World Meteorological Organization
Global Ozone Research and Monitoring Project—Report No. 58

Scientific Assessment of Ozone Depletion: 2018

World Meteorological Organization
United Nations Environment Programme
National Oceanic and Atmospheric Administration
National Aeronautics and Space Administration
European Commission

World Meteorological Organization
7bis avenue de la Paix
Case postale 2300
CH-1211 Geneva 2
Switzerland

United Nations Environment Programme
Ozone Secretariat
P.O. Box 30552
Nairobi, 00100
Kenya

US Department of Commerce
National Oceanic and Atmospheric Administration
14th Street and Constitution Avenue NW
Herbert C. Hoover Building, Room 5128
Washington, D. C. 20230

National Aeronautics and Space Administration
Earth Science Division
NASA Headquarters
300 E. Street SW
Washington, D.C. 20546-0001

European Commission
Directorate-General for Research
B-1049 Bruxelles
Belgium

Published online January 2019
ISBN: 978-1-7329317-1-8
This report is available on the internet at the following locations:
http://ozone.unep.org/science/assessment/sap
https://www.esrl.noaa.gov/csd/assessments/ozone/2018/

This document should be cited as:
WMO (World Meteorological Organization), *Scientific Assessment of Ozone Depletion: 2018*, Global Ozone Research and Monitoring Project–Report No. 58, 588 pp., Geneva, Switzerland, 2018.

Example Chapter Citation:
Engel, A. and M. Rigby (Lead Authors), J.B. Burkholder, R.P. Fernandez, L. Froidevaux, B.D. Hall, R. Hossaini, T. Saito, M.K. Vollmer, and B. Yao, Update on Ozone-Depleting Substances (ODSs) and Other Gases of Interest to the Montreal Protocol, Chapter 1 in *Scientific Assessment of Ozone Depletion: 2018,* Global Ozone Research and Monitoring Project–Report No. 58, World Meteorological Organization, Geneva, Switzerland, 2018.

Inside cover image: Adapted from Adobe Stock photo

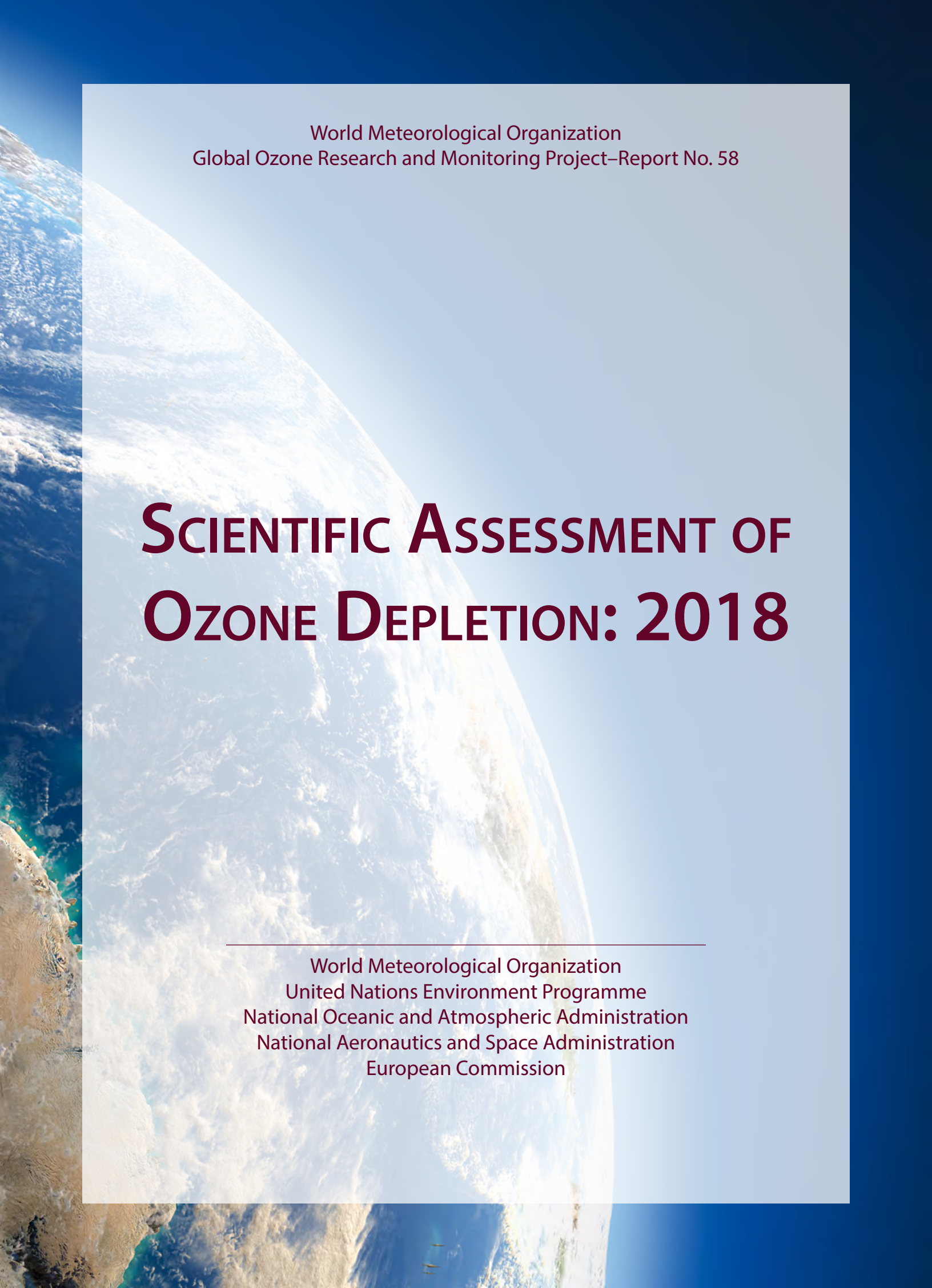

World Meteorological Organization
Global Ozone Research and Monitoring Project–Report No. 58

Scientific Assessment of Ozone Depletion: 2018

World Meteorological Organization
United Nations Environment Programme
National Oceanic and Atmospheric Administration
National Aeronautics and Space Administration
European Commission

This page was intentionally left blank.

Scientific Assessment of Ozone Depletion: 2018

Assessment Co-chairs

David W. Fahey
Paul A. Newman
John A. Pyle
Bonfils Safari

Scientific Steering Committee

David W. Fahey
Paul A. Newman
John A. Pyle
Bonfils Safari
Martyn P. Chipperfield
David J. Karoly
Doug Kinnison
Malcolm K. Ko
Michelle Santee

Assessment Coordinator

Sarah J. Doherty

Chapter Lead Authors

Chapter 1: Update on Ozone-Depleting Substances (ODSs) and Other Gases of Interest to the Montreal Protocol
Andreas Engel and Matthew Rigby

Chapter 2: Hydrofluorocarbons (HFCs)
Stephen A. Montzka and Guus J.M. Velders

Chapter 3: Update on Global Ozone: Past, Present, and Future
Peter Braesicke and Jessica Neu

Chapter 4: Polar Stratospheric Ozone: Past, Present, and Future
Ulrike Langematz and Matthew B. Tully

Chapter 5: Stratospheric Ozone Changes and Climate
Alexey Yu. Karpechko and Amanda C. Maycock

Chapter 6: Scenarios and Information for Policymakers
Lucy J. Carpenter and John S. Daniel

Twenty Questions and Answers About the Ozone Layer: 2018 Update
Ross J. Salawitch

Appendix A: Summary of Abundances, Lifetimes, ODPs, REs, GWPs, and GTPs
James B. Burkholder

Report Design and Production

Debra A. Dailey-Fisher and Ann M. Reiser

Full list of contributors given in Appendix D

This page was intentionally left blank.

Remembrances

It is with sadness that we note the passing of the following scientists who have played leading roles in the international scientific assessments of the ozone layer.

Ralph J. Cicerone (1943–2016) (Retired President of the National Academy of Sciences) passed away on 5 November 2016 in Milburn, New Jersey. Ralph was born in New Castle, Pennsylvania on 2 May 1943. Ralph received his undergraduate degree from the Massachusetts Institute of Technology in 1965, and his doctoral degree from the University of Illinois at Urbana–Champaign in 1970. While at the University of Michigan in 1974, Ralph and his colleague Rich Stolarski showed that chlorine catalysis of ozone destruction could add a crucial piece of the puzzle to the questions about the stratospheric ozone photochemical balance. Subsequently, Ralph moved to the Scripps Institution of Oceanography at UC San Diego, and in 1980 became a senior scientist and director of the Atmospheric Chemistry Division at the National Center for Atmospheric Research in Boulder, Colorado. Ralph migrated west to the University of California, Irvine (UCI), in 1989 where he founded the Department of Earth System Science and eventually became the University Chancellor. In 2005, Ralph became the 21st President of the US National Academy of Science. Amongst Ralph's awards are the 1999 Bower Award and Prize for Achievement in Science; the American Geophysical Union's (AGU) 1979 James B. Macelwane Award; AGU's 2002 Roger Revelle Medal; and the World Cultural Council's 2004 Albert Einstein World Award of Science. Ralph was also recognized in the 1995 Nobel Prize in chemistry awarded to F. Sherwood Rowland, Mario Molina, and Paul Crutzen for his work on chlorine chemistry in the stratosphere. Ralph was a co-author of the very first international assessment "The Stratosphere 1981". Ralph was also a co-author of "Atmospheric Ozone: 1985" that formed the scientific foundation for the Montreal Protocol. He also contributed to the "Report of the International Ozone Trends panel – 1988", and to the "Scientific Assessment of Ozone Depletion: 1994".

Photo credit: Courtesy of the National Academy of Sciences / Photographer: Mark Finkenstaedt

Ivar Sigmund Angell Isaksen (1937–2017) (Professor in the Department of Geosciences at the University of Oslo) passed away on 16 May 2017. Ivar grew up in Djupvik in Lyngen in North Troms. He joined the University of Oslo's Department of Geophysics in 1967 and received his doctoral degree at the University of Oslo in 1973. He then became professor of theoretical meteorology in 1981 at the University of Oslo. Ivar's awards included the National Oceanographic and Administration (NOAA) Award for outstanding scientific achievement in 1975; the 1990 Norwegian Ministry of Environment award for Environmental Research; the University of Thessaloniki Award, 2000, for Scientific Achievement; the European Physical Society and The Balkan Physical Union Award for outstanding contribution in Environmental Physics, 2002; and an Honorary doctorate at the University of Athens, 2009. He was elected to the International Ozone Commission in 1984, and was its President from 2004-2008. Ivar was a major contributor to the Scientific Assessments of Ozone Depletion as an author, co-author, coordinator, and reviewer. He was an author of the very first international assessment "The Stratosphere 1981", and then contributed to every report up to "The Scientific Assessment of Ozone Depletion: 2010". Ivar's final comments were from May 2013, when he recommended that the 2014 Assessment should tackle overlapping topics with the climate community.

Photo credit: CICERO (the Norwegian Center for International Climate Research)

This page was intentionally left blank.

CONTENTS

World Meteorological Organization
Global Ozone Research and Monitoring Project – Report No. 58

Executive Summary

Scientific Assessment of Ozone Depletion: 2018

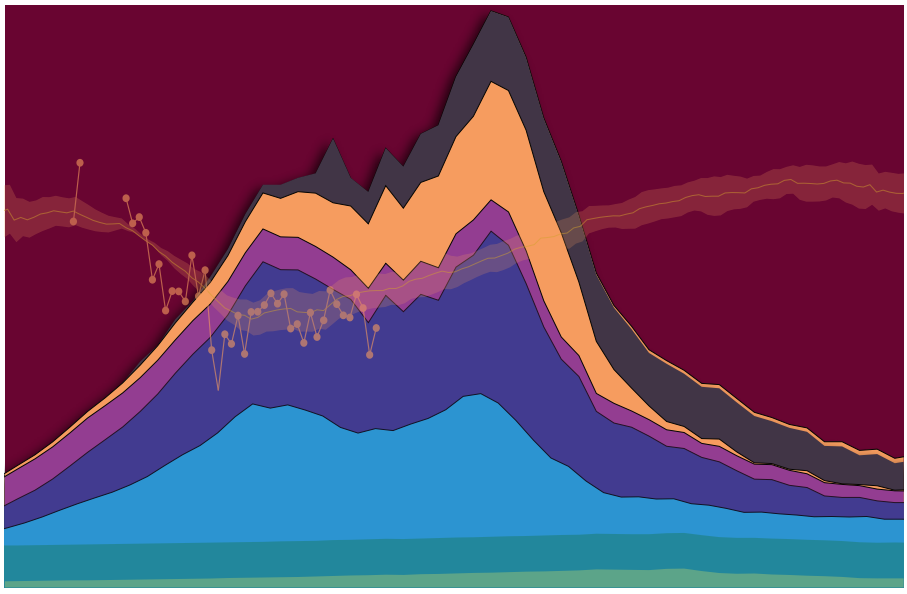

World Meteorological Organization
United Nations Environment Programme
National Oceanic and Atmospheric Administration
National Aeronautics and Space Administration
European Commission

This page was intentionally left blank.

Highlights
Scientific Assessment of Ozone Depletion: 2018

The Assessment documents the advances in scientific understanding of ozone depletion reflecting the thinking of the many international scientific experts who have contributed to its preparation and review. These advances add to the scientific basis for decisions made by the Parties to the Montreal Protocol. It is based on longer observational records, new chemistry-climate model simulations, and new analyses. Highlights since the 2014 Assessment are:

Actions taken under the Montreal Protocol have led to decreases in the atmospheric abundance of controlled ozone-depleting substances (ODSs) and the start of the recovery of stratospheric ozone. The atmospheric abundances of both total tropospheric chlorine and total tropospheric bromine from long-lived ODSs controlled under the Montreal Protocol have continued to decline since the 2014 Assessment. The weight of evidence suggests that the decline in ODSs made a substantial contribution to the following observed ozone trends:

The Antarctic ozone hole is recovering, while continuing to occur every year. As a result of the Montreal Protocol much more severe ozone depletion in the polar regions has been avoided.

Outside the polar regions, upper stratospheric ozone has increased by 1–3% per decade since 2000.

No significant trend has been detected in global (60°S–60°N) total column ozone over the 1997–2016 period with average values in the years since the last Assessment remaining roughly 2% below the 1964–1980 average.

Ozone layer changes in the latter half of this century will be complex, with projected increases and decreases in different regions. Northern Hemisphere mid-latitude total column ozone is expected to return to 1980 abundances in the 2030s, and Southern Hemisphere mid-latitude ozone to return around mid-century. The Antarctic ozone hole is expected to gradually close, with springtime total column ozone returning to 1980 values in the 2060s. [ES Sections 1 and 3]

The Kigali Amendment is projected to reduce future global average warming in 2100 due to hydrofluorocarbons (HFCs) from a baseline of 0.3–0.5 °C to less than 0.1 °C. The magnitude of the avoided temperature increase due to the provisions of the Kigali Amendment (0.2 to 0.4 °C) is substantial in the context of the 2015 Paris Agreement, which aims to keep global temperature rise this century to well below 2 °C above pre-industrial levels. [ES Section 2]

There has been an unexpected increase in global total emissions of CFC-11. Global CFC-11 emissions derived from measurements by two independent networks increased after 2012, thereby slowing the steady decrease in atmospheric concentrations reported in previous Assessments. The global concentration decline over 2014 to 2016 was only two-thirds as fast as it was from 2002 to 2012. While the emissions of CFC-11 from eastern Asia have increased since 2012, the contribution of this region to the global emission rise is not well known. The country or countries in which emissions have increased have not been identified. [ES Section 1]

Sources of significant carbon tetrachloride emissions, some previously unrecognised, have been quantified. These sources include inadvertent by-product emissions from the production of chloromethanes and perchloroethylene, and fugitive emissions from the chlor-alkali process. The global budget of carbon tetrachloride is now much better understood than was the case in previous Assessments, and the previously identified gap between observation-based and industry-based emission estimates has been substantially reduced. [ES Sections 1 and 5]

Continued success of the Montreal Protocol in protecting stratospheric ozone depends on continued compliance with the Protocol. Options available to hasten the recovery of the ozone layer are limited, mostly because actions that could help significantly have already been taken. Remaining options such as complete elimination of controlled and uncontrolled emissions of substances such as carbon tetrachloride and dichloromethane; bank recapture and destruction of CFCs, halons, and HCFCs; and elimination of HCFC and methyl bromide production would individually lead to small-to-modest ozone benefits. Future emissions of carbon dioxide, methane, and nitrous oxide will be extremely important to the future of the ozone layer through their effects on climate and on atmospheric chemistry. Mitigation of nitrous oxide emissions would also have a small-to-modest ozone benefit. [Figure ES-9, ES Section 5]

This page was intentionally left blank.

Contents

Executive Summary

Scientific Assessment of Ozone Depletion: 2018

This page was intentionally left blank.

PREFACE

This document contains information upon which the Parties to the Montreal Protocol on Substances that Deplete the Ozone Layer ("The Parties") will base their future decisions regarding protection of the stratospheric ozone layer and climate from the production and consumption of ozone-depleting substances (ODSs) and their replacements.

The Charge to the Assessment Panels

Specifically, Article 6 of the Montreal Protocol on Substances that Deplete the Ozone Layer states:

> *Beginning in 1990, and at least every four years thereafter, the Parties shall assess the control measures provided for in Article 2 and Articles 2A to 2I on the basis of available scientific, environmental, technical and economic information.*

To provide the mechanisms whereby these assessments are conducted, the Montreal Protocol further states:

> ". . . the Parties shall convene appropriate panels of experts" and "the panels will report their conclusions . . . to the Parties."

To meet this request, the Scientific Assessment Panel (SAP), the Environmental Effects Assessment Panel, and the Technology and Economic Assessment Panel each prepare, about every 3–4 years, major assessments that update the state of understanding in their purviews. These assessments are made available to the Parties in advance of their annual meetings at which they consider amendments and adjustments to the provisions of the Montreal Protocol.

Sequence of Scientific Assessments

The 2018 Assessment is the latest in a series of assessments prepared by the world's leading experts in the atmospheric sciences and under the auspices of the Montreal Protocol in coordination with the World Meteorological Organization (WMO) and/or the United Nations Environment Programme (UN Environment). The 2018 Assessment is the ninth in the series of major assessments that have been prepared by the Scientific Assessment Panel as direct input to the Montreal Protocol process. The chronology of the nine scientific assessments of ozone depletion, along with other relevant reports and international policy decisions, are summarized in Table ES-1.

2018 Assessment Terms of Reference

The terms of reference of the 2018 Assessment were decided at the 27th Meeting of the Parties to the Montreal Protocol in Dubai, United Arab Emirates (1–5 November 2015) in their Decision XXVII/6[1]:

> 5. To request the assessment panels to bring to the notice of the Parties any significant developments which, in their opinion, deserve such notice, in accordance with decision IV/13;
> 7. To request the Scientific Assessment Panel to undertake, in its 2018 report, a review of the scientific knowledge as dictated by the needs of the Parties to the Montreal Protocol, as called for in the terms of reference for the panels, taking into account those factors stipulated in Article 3 of the Vienna Convention, including estimates of the levels of ozone-layer depletion attributed to the remaining potential emissions of ozone-depleting substances and an assessment of the level of global emissions of ozone depleting substances below which the depletion of the ozone layer could be comparable to various other factors such as the natural variability of global ozone, its secular trend over a decadal timescale and the 1980 benchmark level;

[1] Decision XXVII/6: Potential areas of focus for the 2018 quadrennial reports of the Scientific Assessment Panel, the Environmental Effects Assessment Panel and the Technology and Economic Assessment Panel.

and in their Decision XXVII/7[2]:

> 7. To request the Technology and Economic Assessment Panel and the Scientific Assessment Panel to continue their analysis of the discrepancies between observed atmospheric concentrations and reported data on carbon tetrachloride and to report and provide an update on their findings to the Twenty-Eighth Meeting of the Parties.

Significant developments since the 2014 Assessment that are included in the 2018 Assessment are (i) the adoption of the Kigali Amendment in 2016 to phase down global hydrofluorocarbon (HFC) production and consumption; (ii) the recognition of increased global emissions of CFC-11; and (iii) an improved understanding of the budget of carbon tetrachloride (CCl_4).

The Assessment Process

The process of writing the current Assessment started early in 2016. The SAP co-chairs considered suggestions from the Parties regarding experts from their countries who could participate in the process. Further, an ad hoc international scientific advisory group was formed to suggest authors and reviewers from the world scientific community and to help craft the Assessment outline. As in previous Assessments, the participants represented experts from the developed and developing world who bring a special perspective to the process and whose involvement in the Assessment contributes to capacity building. The Appendix provides a listing of the approximately 280 scientists from 31 countries who contributed to the preparation and review of the Assessment.

An initial letter was sent to a large number of scientists and policy makers in November 2016 soliciting comments and inputs on a draft outline along with suggestions for authors for the 2018 Assessment. This was followed by revisions to the outline and recruitment of lead authors and co-authors. The steering committee and lead authors met in London, UK, in May 2017 to review the revised chapter outlines. The chapter writing process produced five drafts between mid-September 2017 and August 2018 aided by two author team meetings (Boulder, Colorado, USA and Les Diablerets, Switzerland). The first and third drafts were formally peer-reviewed by a large number of expert reviewers. The chapters were revised by the author teams based on the extensive review comments (numbering over 5000) and the review editors for each chapter provided oversight of the revision process to ensure that all comments were addressed appropriately.

At a meeting in Les Diablerets, Switzerland, held on 16–20 July 2018, the Executive Summary contained herein was prepared and completed by the 68 attendees of the meeting. These attendees included the steering committee, chapter lead authors, review editors, some chapter co-authors (selected by the chapter leads), reviewers (selected by the review editors), and some leading experts invited by the steering committee. The Executive Summary, initially drafted by the Assessment steering committee, was reviewed, revised, and approved line-by-line. The Highlights section was drafted during the meeting to provide a concise summary of the Executive Summary.

The success of the 2018 Assessment depended on the combined efforts and commitment of a large international team of scientific researchers who volunteered their time as lead authors, contributors, reviewers, and review editors and on the skills and dedication of the assessment coordinator and the editorial and production staff, who are listed at the end of this report.

[2] Decision XXVII/7: Investigation of carbon tetrachloride discrepancies.

Table ES-1. Chronology of scientific reports and policy decisions related to ozone depletion.

Year	Policy Decisions	Scientific Reports
1981		The Stratosphere 1981: Theory and Measurements. WMO No. 11.
1985	Vienna Convention	Atmospheric Ozone 1985. Three volumes. WMO No. 16.
1987	Montreal Protocol	
1988		International Ozone Trends Panel Report 1988. Two volumes. WMO No. 18.
1989		Scientific Assessment of Stratospheric Ozone: 1989. Two volumes. WMO No. 20.
1990	London Adjustment and Amendment	
1991		Scientific Assessment of Ozone Depletion: 1991. WMO No. 25.
1992		Methyl Bromide: Its Atmospheric Science, Technology, and Economics (Montreal Protocol Assessment Supplement). UNEP (1992)
1992	Copenhagen Adjustment and Amendment	
1994		Scientific Assessment of Ozone Depletion: 1994. WMO No. 37.
1995	Vienna Adjustment	
1997	Montreal Adjustment and Amendment	
1998		Scientific Assessment of Ozone Depletion: 1998. WMO No. 44.
1999	Beijing Adjustment and Amendment	
2002		Scientific Assessment of Ozone Depletion: 2002. WMO No. 47.
2006		Scientific Assessment of Ozone Depletion: 2006. WMO No. 50.
2007	Montreal Adjustment	
2010		Scientific Assessment of Ozone Depletion: 2010. WMO No. 52.
2014		Scientific Assessment of Ozone Depletion: 2014. WMO No. 55.
2016	Kigali Amendment	
2018		Scientific Assessment of Ozone Depletion: 2018. WMO No. 58.

This page was intentionally left blank.

INTRODUCTION

The 1985 Vienna Convention for the Protection of the Ozone Layer is an international agreement in which United Nations States recognized the fundamental importance of preventing damage to the stratospheric ozone layer. The 1987 Montreal Protocol on Substances that Deplete the Ozone Layer and its succeeding amendments, adjustments, and decisions were subsequently negotiated to control the consumption and production of anthropogenic ozone-depleting substances (ODSs) and some hydrofluorocarbons (HFCs). The Montreal Protocol Parties base their decisions on scientific, environmental, technical, and economic information that is provided by their technical panels. The Protocol requests quadrennial reports from its Scientific Assessment Panel that update the science of the ozone layer. This Executive Summary (ES) highlights the key findings of the *Scientific Assessment of Ozone Depletion: 2018*, as put together by an international team of scientists. The key findings of each of the six chapters of the Scientific Assessment have been condensed and formulated to make the ES suitable for a broad audience.

Ozone depletion is caused by human-related emissions of ODSs and the subsequent release of reactive halogen gases, especially chlorine and bromine, in the stratosphere. ODSs include chlorofluorocarbons (CFCs), bromine-containing halons and methyl bromide, hydrochlorofluorocarbons (HCFCs), carbon tetrachloride (CCl_4), and methyl chloroform. The substances controlled under the Montreal Protocol are listed in the various annexes to the agreement (CFCs and halons under Annex A and B, HCFCs under Annex C, and methyl bromide under Annex E)[3]. These ODSs are long-lived (e.g., CFC-12 has a lifetime greater than 100 years) and are also powerful greenhouse gases (GHGs). As a consequence of Montreal Protocol controls, the stratospheric concentrations of anthropogenic chlorine and bromine are declining.

In addition to the longer-lived ODSs, there is a broad class of chlorine- and bromine-containing substances known as very short-lived substances (VSLSs) that are not controlled under the Montreal Protocol and have lifetimes shorter than about 6 months. For example, bromoform ($CHBr_3$) has a lifetime of 24 days, while chloroform ($CHCl_3$) has a lifetime of 149 days. These substances are generally destroyed in the lower atmosphere in chemical reactions. In general, only small fractions of VSLS emissions reach the stratosphere where they contribute to chlorine and bromine levels and lead to increased ozone depletion.

The Montreal Protocol's control of ODSs stimulated the development of replacement substances, firstly HCFCs and then HFCs, in a number of industrial sectors. While HFCs have only a minor effect on stratospheric ozone, some HFCs are powerful GHGs. Previous Assessments have shown that HFCs have been increasing rapidly in the atmosphere over the last decade and were projected to increase further as global development continued in the coming decades. The adoption of the 2016 Kigali Amendment to the Montreal Protocol (see Annex F) will phase down the production and consumption of some HFCs and avoid much of the projected global increase and associated climate change.

Observations of atmospheric ozone are made by instruments on the ground and on board balloons, aircraft, and satellites. This network of observations documented the decline of ozone around the globe, with extreme depletions occurring over Antarctica in each spring and occasional large depletions in the Arctic, and they allowed us to report some indications of recovery in stratospheric ozone in the 2014 Assessment. The chemical and dynamical processes controlling stratospheric ozone are well understood, with ozone depletion being fundamentally driven by the atmospheric abundances of chlorine and bromine.

[3] Montreal Protocol Handbook, 2018.

Previous Assessments have shown projections of decreasing ODSs, and models show that global ozone should increase as a result. Models have also demonstrated that increasing concentrations of the GHGs carbon dioxide (CO_2) and methane (CH_4) during this century will cause global ozone levels to increase beyond the natural level of ozone observed in the 1960s, primarily because of the cooling of the upper stratosphere and a change of the stratospheric circulation. On the other hand, the chemical effect of increasing concentrations of nitrous oxide (N_2O), another GHG, will be to deplete stratospheric ozone.

This 2018 Assessment is the ninth in a series that is provided to the Montreal Protocol by its Scientific Assessment Panel. In this Assessment, many of our previous Assessment findings are strengthened and new results are presented. A clear message of the 2018 Assessment is that the Montreal Protocol continues to be effective at reducing the atmospheric abundance of ODSs.

Terminology used in the Executive Summary

Equivalent effective stratospheric chlorine (EESC)

EESC is a metric for representing ODS levels in the stratosphere. It is calculated based upon three factors: surface atmospheric concentrations of individual ODSs and their number of chlorine and bromine atoms, the relative efficiency of chlorine and bromine for ozone depletion, and the time required for the substances to reach different stratospheric regions and break down to release their chlorine and bromine atoms. As EESC continues to decrease in response to Montreal Protocol provisions, stratospheric ozone is expected to increase. In this Assessment, EESC does not include chlorine and bromine from very short-lived substances (VSLSs).

Representative concentration pathways (RCPs)

Representative concentration pathways (RCPs) were developed by the Intergovernmental Panel on Climate Change (IPCC) to help describe how climate change may evolve out to the year 2100. The RCPs define a timeline of atmospheric concentrations of greenhouse gases (GHGs) expressed in units of $GtCO_2$-eq. The four pathways, RCP-2.6, RCP-4.5, RCP-6.0, and RCP-8.5, are labeled by the radiative forcing assumed for 2100 (i.e., RCP-2.6 has a global-mean radiative forcing from GHGs in 2100 of 2.6 W $m^{-2)}$. RCP-2.6 assumes that GHG emissions will peak before 2020; RCP-4.5 assumes a peak around 2040; RCP-6.0 assumes a peak around 2080; and RCP-8.5 assumes no peak before 2100. Each scenario includes certain socio-economic assumptions about fossil-fuel use and other aspects related to GHG emissions.

Ozone-depleting substance (ODS)

An ODS is a substance that leads to stratospheric ozone depletion. Under the Montreal Protocol, most of the widely used ODSs are controlled under Annexes A, B, C, and E. These include, among others, chlorofluorocarbons (CFCs), carbon tetrachloride (CCl_4), methyl chloroform (CH_3CCl_3), halons, methyl bromide (CH_3Br) and hydrochlorofluorocarbons (HCFCs). These ODSs typically have sufficiently long atmospheric lifetimes to reach the stratosphere after being emitted at the surface. Methyl bromide is the shortest-lived of the controlled substances and has natural and anthropogenic sources. Other ODSs are not controlled under the Montreal Protocol.

Ozone depletion potential (ODP)

The Ozone Depletion Potential (ODP) is a metric for determining the relative strength of a chemical to destroy ozone. The ODP of a substance is defined as the ratio of the change in global ozone for a given mass emission of the substance to the change in global ozone for the same mass emission of CFC-11 ($CFCl_3$). ODPs provide a direct method for comparing the impacts of specific substances on the ozone layer.

Halogenated very short-lived substances (VSLSs)

Halogenated very short-lived substances (VSLSs) have atmospheric lifetimes less than 0.5 year and yet make a contribution to stratospheric chlorine or bromine levels. As short-lived ODSs, a large fraction of VSLS emissions are destroyed in the troposphere, limiting the fraction of emissions that reaches the stratosphere and causes ozone depletion. VSLS emissions that occur in regions with rapid transport to the stratosphere will make an enhanced contribution to stratospheric halogen levels. Hence, the ODP of a VSLS is generally dependent on assumptions about the emission source region and time of the year of the emissions. VSLSs are not controlled under the Montreal Protocol.

Global warming potentials (GWPs)

The global warming potential (GWP) is a metric for determining the relative contribution of a substance to climate warming. GWP is defined as the ratio of the radiative forcing for a given mass emission of a substance relative to the same mass emission of CO_2 summed over a given time period (typically 20 or 100 years). In this Assessment, a 100-yr time window is implied unless otherwise stated. For a given mass emissions of a substance, the CO_2-equivalent (CO_2-eq) value is defined as the emissions multiplied by the respective GWP value, noting that the GWP of CO_2 is defined to be unity.

This page was intentionally left blank.

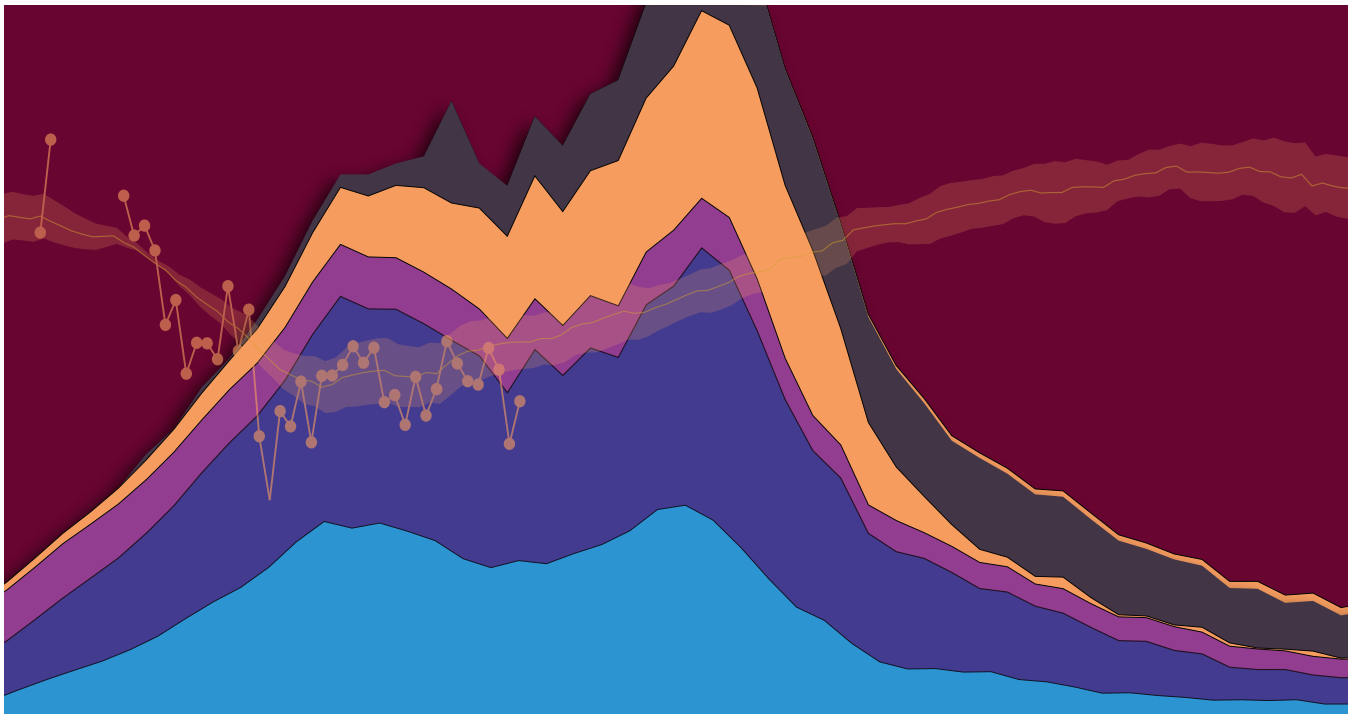

[1] Concentrations and trends in ozone-depleting substances (ODSs)

Total chlorine and total bromine

Our confidence that the Montreal Protocol is continuing to work is based on a sustained network of measurements of the long-lived source gas concentrations over several decades. These measurements allow the determination of global concentrations, their interhemispheric differences, and their trends. Combined with lifetime information, the data allow us to derive historical emissions which can be compared with emissions derived from data reported to UN Environment.

- **The atmospheric abundances of both total tropospheric chlorine and total tropospheric bromine from long-lived ODSs controlled under the Montreal Protocol have continued to decline since the 2014 Assessment (Figure ES-1, panels a, b; Table ES-2).**

- **During the period 2012–2016, the observed rate of decline in tropospheric chlorine due to controlled substances was 12.7 ± 0.9 ppt Cl yr^{-1}, which is very close to the baseline projection from the 2014 Assessment.** The net rate of change was the result of a slower than projected decrease in CFC concentrations and a slower than projected increase in HCFCs relative to the 2014 scenario. That scenario was based on the maximum allowed production of HCFCs from Article 5 countries under the Montreal Protocol.

- **The decrease of chlorine from controlled substances has partly been offset by increases in the mainly natural CH_3Cl and mainly anthropogenic very short-lived gases, which are not controlled under the Montreal Protocol.**

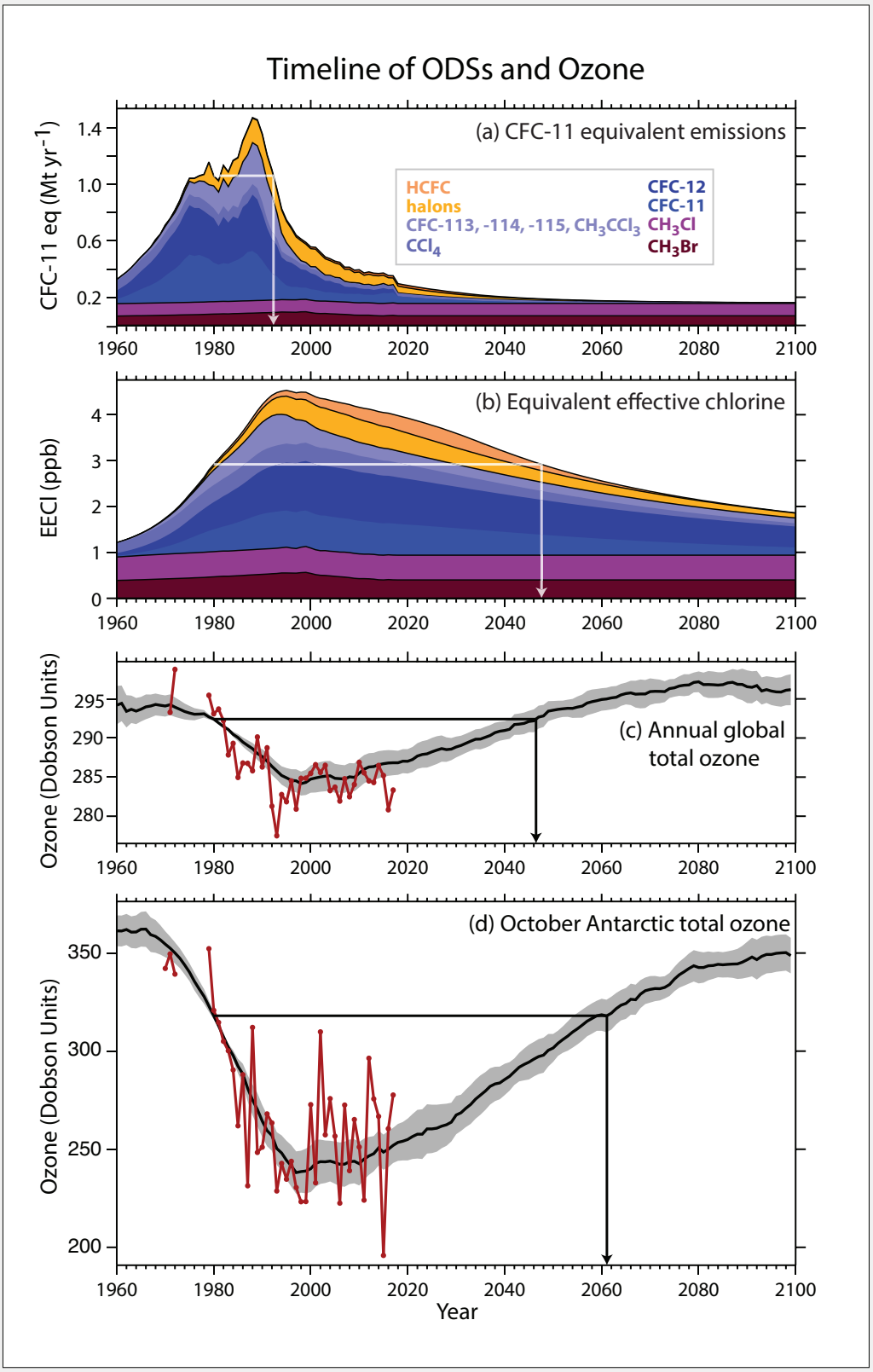
Timeline of ODSs and Ozone
(a) CFC-11 equivalent emissions
CFC-11 eq (Mt yr^{-1})
1.4
1.0
0.6
0.2
HCFC
halons
CFC-113, -114, -115, CH_3CCl_3
CCl_4
CFC-12
CFC-11
CH_3Cl
CH_3Br
(b) Equivalent effective chlorine
EECl (ppb)
4
3
2
1
0
(c) Annual global total ozone
Ozone (Dobson Units)
295
290
285
280
(d) October Antarctic total ozone
Ozone (Dobson Units)
350
300
250
200
1960
1980
2000
2020
2040
2060
2080
2100
Year

Table ES-2. Contributions of various long-lived ozone-depleting substances controlled under the Montreal Protocol to tropospheric organic chlorine and bromine in 2016, and annual average trends between 2012 and 2016.

	Contribution to tropospheric chlorine and bromine in 2016[1] (ppt Cl/Br)	Changes in tropospheric chlorine and bromine (in parts per trillion (ppt) (Cl/Br) yr^{-1}) from early-2012 to late-2016
Controlled chlorine substances by group		
chlorofluorocarbons (CFCs)	1979	−12.0 ± 0.4
methyl chloroform (CH_3CCl_3)	7.8	−2.0 ± 0.5
carbon tetrachloride (CCl_4)	322	−4.5 ± 0.2
hydrochlorofluorocarbons (HCFCs)	309	+5.9 ± 1.3
halon-1211	3.6	−0.1 ± 0.01
Total Chlorine from controlled substances	**2621**	**−12.7 ± 0.9**
Controlled bromine substances by group		
halons	7.8	−0.1 ± 0.01
methyl bromide (CH_3Br)[2]	6.8	−0.04 ± 0.05
Total bromine from controlled substances	**14.6**	**−0.15 ± 0.04**

[1] Values are annual averages.

[2] Not all CH_3Br emissions are controlled. Some anthropogenic uses of CH_3Br are exempted from Montreal Protocol controls, and CH_3Br has natural sources, which results in a natural background concentration.

Figure ES-1. Timeline of: a) CFC-11-equivalent emissions, b) equivalent effective chlorine, c) global total ozone, and d) October Antarctic total ozone. Annual CFC-11-equivalent emissions are computed for the ODSs shown in the legend by multiplying mass emissions of a substance by its ODP *(panel a)*. Historical emissions are derived from the measured atmospheric concentrations of individual ODSs from measurement networks. The future projections of emissions assume full compliance with the Montreal Protocol and use standard methodologies based on reported production, inventory-estimates of the banks and release rates. The annual abundances of equivalent effective chlorine (EECl), shown for the global surface, are based on surface abundances (measured or derived from projected emissions and lifetimes) of the chlorine- and bromine-containing substances *(panel b)*. The bromine abundances are weighted by a factor of 65 to account for the greater efficiency of bromine in ozone destruction reactions in the atmosphere. Global total column ozone represents an average over 60°N to 60°S latitudes *(panel c)* and Antarctic total column ozone represents an average over 60°S to 80°S latitudes *(panel d)*. *Panels (c) and (d)* include a comparison of chemistry-climate model results (black lines with gray shadings indicating uncertainty ranges) and available observations (data points). The model projections into the future assume compliance with the Montreal Protocol and an increase in GHGs following the RCP-6.0 scenario. The lines with arrows mark when CFC-11-equivalent emissions *(a)*, EECl *(b)* and ozone abundances *(c and d)* return to their 1980 values. [Data sources are: *panel (a)* mixing ratios in Figure 6-2 and ODPs and lifetimes in Table A-1; *panel (b)* following Figure 6-2 with an alpha factor of 65; *panel (c)* Figure 3-28; and *panel (d)* Figure 4-18.]

Unexpected increase in global total emissions of CFC-11

Observations of the persistent slowdown in the decline of CFC-11 concentrations have only recently allowed the robust conclusion that emissions of CFC-11 have increased in recent years, as opposed to other possible causes for the slowdown such as changing atmospheric circulation.

- **Global CFC-11 emissions, derived from measurements by two independent networks, increased after 2012 contrary to projections from previous Assessments, which showed decreasing emissions (Figure ES-2).** This conclusion is supported by the observed rise in the CFC-11 hemispheric concentration difference. Global CFC-11 emissions for 2014 to 2016 were approximately 10 Gg yr^{-1} (about 15%) higher than the fairly constant emissions derived for 2002 to 2012; the excess emissions relative to projected emissions for recent years is even larger. The increase in global emissions above the 2002–2012 average resulted in a global concentration decline in CFC-11 over 2014 to 2016 that was only two-thirds as fast as from 2002 to 2012.

- **The CFC-11 emission increase suggests new production not reported to UN Environment because the increase is inconsistent with likely changes in the release of CFC-11 from banks associated with pre-phaseout production**. Depending on how this newly produced CFC-11 is being used, substantial increases in the bank and future emissions are possible.

- **Emissions of CFC-11 from eastern Asia have increased since 2012; the contribution of this region to the global emission rise is not well known.** The country or countries in which emissions have increased have not yet been identified.

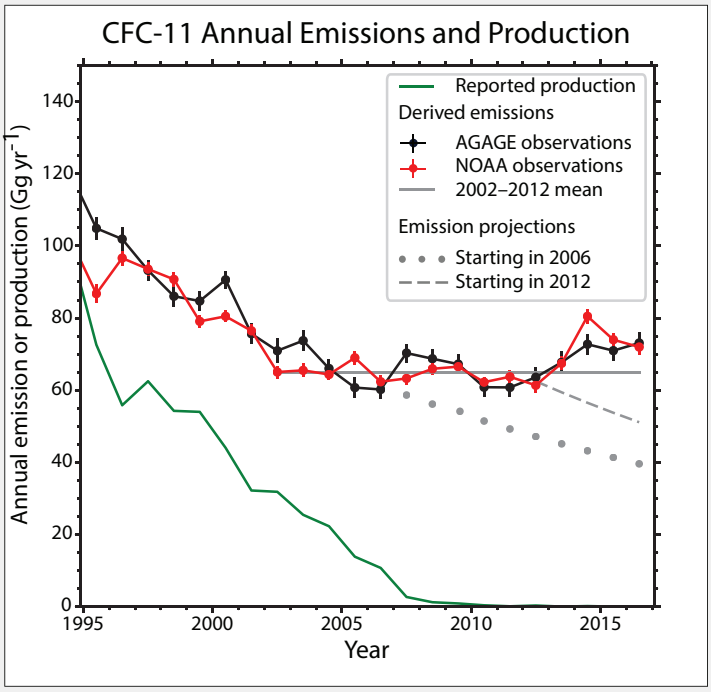

Figure ES-2. CFC-11 global emissions and reported production. Emissions of CFC-11 derived from AGAGE (Advanced Global Atmospheric Gases Experiment; black) and NOAA (National Oceanic and Atmospheric Administration; red) global network measurements of CFC-11 concentrations (see also Figure 1-4 of the Assessment) and a model using a CFC-11 lifetime of 52 years. Also shown are the production history reported to UN Environment for all uses (green), the average of annual emissions over the 2002–2012 period (grey line), and scenario projections based on observations through 2006 or through 2012 (dotted and dashed lines). These emission projections are calculated using standard methodologies based on reported production, inventory estimates of the bank, and an empirically determined release fraction from the bank over the seven years before 2006 or 2012, which is then applied to subsequent years (see Chapter 1 and Chapter 6). Uncertainties in emissions, shown as vertical lines on the data points, include the influence of measurement and model representation uncertainties. The uncertainties are smaller than those presented in Figure 1-4, because uncertainties related to factors constant across the whole time period, such as lifetimes and calibration scale, have been omitted.

Persistent emissions of low abundance CFCs

- **Observation-based analyses show unexpected stable or even increasing emissions of some of the low abundance (less than 20 ppt) CFCs (CFC-13, CFC-113a, CFC-114, CFC-115) between 2012 and 2016.** For CFC-114 and CFC-115, atmospheric observations imply that a substantial fraction of global emissions originated from China.

Ongoing substantial emissions of carbon tetrachloride (CCl_4)

- **Sources of significant CCl_4 emissions, some previously unrecognized, have been quantified.** At least 25 Gg yr^{-1} of emissions have been estimated, mainly originating from the industrial production of chloromethanes, perchloroethylene and chlorine. This value can be compared with total global emissions of approximately 35 Gg yr^{-1}, derived from atmospheric observations. The global CCl_4 budget is now much better understood and the previously identified gap between observation-based and industry-based emission estimates has been substantially reduced compared to the 2014 Assessment.

Hydrochlorofluorocarbons (HCFCs)

- **Total chlorine from HCFCs has continued to increase in the atmosphere since the last Assessment and reached 309 ppt in 2016.** The annual average growth rate of chlorine from HCFCs decreased from 9.2 ± 0.3 ppt yr^{-1} for the 2008 to 2012 period to 5.9 ± 1.3 ppt yr^{-1} for the 2012 to 2016 period.

- **Combined emissions of the major HCFCs have declined since the last Assessment which suggests an effective response to the 2007 Adjustment to the Montreal Protocol that limited HCFC emissions.** Annual emissions of HCFC-22 have remained relatively unchanged since 2012, whilst emissions of HCFC-141b and-142b declined by around 10% and 18%, respectively, between 2012 and 2016. These findings are consistent with a decrease in reported HCFC consumption after 2012, particularly from Article 5 countries.

Tropospheric bromine

- **Total tropospheric bromine from controlled ODSs (halons and methyl bromide) continued to decrease and by 2016 was 14.6 ppt, 2.3 ppt below the peak levels observed in 1998**. In the 4-year period prior to the last Assessment, this decrease was primarily driven by a decline in methyl bromide (CH_3Br) abundance, with a smaller contribution from a decrease in halons. These relative contributions have now reversed, with halons being the main driver of the decrease of 0.15 ± 0.04 ppt yr^{-1} tropospheric bromine between 2012 and 2016.

- **Total bromine from halons has decreased from a peak of 8.5 ppt in 2005 to 7.7 ppt in 2016.** Emissions of halons derived from atmospheric observations declined or remained stable between 2012 and 2016 and are thought to originate primarily from banks.

- **The atmospheric abundance of CH_3Br declined from a peak of 9.2 ppt in 1996–1998 to 6.8 ppt in 2016 as a consequence of controls under the Montreal Protocol.** By 2016, controlled CH_3Br consumption had declined by more than 98% from its peak value. Reported consumption in quarantine and pre-shipment (QPS) uses of CH_3Br, which are not controlled under the Montreal Protocol, has not changed substantially over the last two decades. Total reported anthropogenic emissions (controlled and not-controlled) have declined by about 85% from the peak value, and atmospheric CH_3Br abundance is now near the expected natural background.

Halogenated very short-lived substances (VSLSs)

Halogenated VSLS substances contribute to stratospheric chlorine and bromine loading and are not controlled by the Montreal Protocol. Chlorinated VSLSs are predominantly of anthropogenic origin, while brominated VSLSs have mainly natural sources.

- **Dichloromethane (CH_2Cl_2) is the main component of VSLS chlorine and accounts for the majority of the rise in total chlorine from VSLSs between 2012 and 2016.** A substantial fraction of the global CH_2Cl_2 emissions has been attributed to southern and eastern Asia. The current estimate is that total chlorine from VSLS source gases increased by about 20 ppt between 2012 and 2016 to reach 110 ppt (**Figure ES-3**). The growth rate shows large interannual variability.

- **Several field campaigns conducted since the last Assessment have confirmed that brominated VSLSs contribute 5±2 ppt to stratospheric bromine (Figure ES-3).** There is no indication in measurements of a long-term trend in the contribution of VSLSs to stratospheric bromine.

Total stratospheric chlorine and bromine

Total stratospheric chlorine and bromine both continue to decline. Even though the abundance of bromine is much smaller than that of chlorine, bromine has a significant impact because it is around 60–65 times more efficient than chlorine in destroying ozone.

- **Total chlorine entering the stratosphere from well-mixed ODSs declined by 405 ppt (12%) between the 1993 peak (3582 ppt) and 2016 (3177 ppt). (Figure ES-3)** This decline was driven by decreasing atmospheric abundances of methyl chloroform (CH_3CCl_3), CFC-11 and CCl_4 (in order of importance). The VSLS contribution (primarily anthropogenic) has increased over this period but remains below 4% of the total in 2016. About 80% of the chlorine entering the stratosphere annually is of anthropogenic origin.

- **Total bromine entering the stratosphere from well-mixed ODSs declined by 2.4 ppt (15%) between the 1998 peak (16.9 ppt) and 2016 (14.5 ppt). (Figure ES-3)** This decline was driven by decreasing atmospheric abundances of methyl bromide (CH_3Br), halon-1211, and halon 2402 (in order of importance). The VSLS (primarily biogenic) contribution has no measurable change over this period, contributing about 25% to the total in 2016. The natural components of CH_3Br and VSLSs now contribute more than half of the bromine entering the stratosphere annually.

- **HCl is the major chlorine component in the upper stratosphere. Its concentration in this region decreased by about 6% between 2005 and 2016.** This decrease is consistent with the decline in total chlorine entering the stratosphere.

- **Total stratospheric bromine derived from bromine monoxide (BrO) observations decreased by about 8% from 2004 to 2014.** This decrease is consistent with the decline in total bromine entering the stratosphere.

[2] Hydrofluorocarbons (HFCs)

The Montreal Protocol phaseout of ODSs has led to the development of alternative substances for use in many sector applications. Hydrofluorocarbons (HFCs) are a widely used category of ODS alternatives that do not contain ozone-depleting chlorine or bromine. Long-lived CFCs, HCFCs, and HFCs are all potent greenhouse gases. Ultimately the Kigali Amendment to the Montreal Protocol, which was adopted in 2016 and will come into force in 2019, sets schedules for the phasedown of global production and consumption of specific HFCs. Although the radiative forcing supplied by atmospheric HFC abundances is currently small, the Kigali Amendment is designed to avoid unchecked growth in emissions and associated warming in response to projected increasing demand in coming decades. Discussed here are the anticipated overall effects of Kigali Amendment controls and existing national and regional HFC regulations on future HFC abundances and associated climate warming. HFCs were included as one group within the basket of gases of the 1997 Kyoto Protocol and, as a result, developed (Annex-I) countries supply annual emission estimates of HFCs to the United Nations Framework Convention on Climate Change (UNFCCC). HFC-23 is considered separately in the Kigali Amendment and in this Assessment, primarily because it is emitted to the atmosphere as a by-product of HCFC-22 production. HFC-23 has one of the longest atmospheric lifetimes and highest global warming potentials (GWP) among HFCs. HFC-23 is not included in the projections discussed here.

Observed HFC abundances and associated emissions

- **Atmospheric abundances of most currently measured HFCs are increasing in the global atmosphere.** These increases are similar to those projected in the baseline scenario of the 2014 Assessment. HFC emissions derived from observations increased by 23% from 2012 to 2016 and currently amount to about 1.5% of total emissions from all long-lived greenhouse gases as carbon dioxide-equivalent emissions ($GtCO_2$-eq).

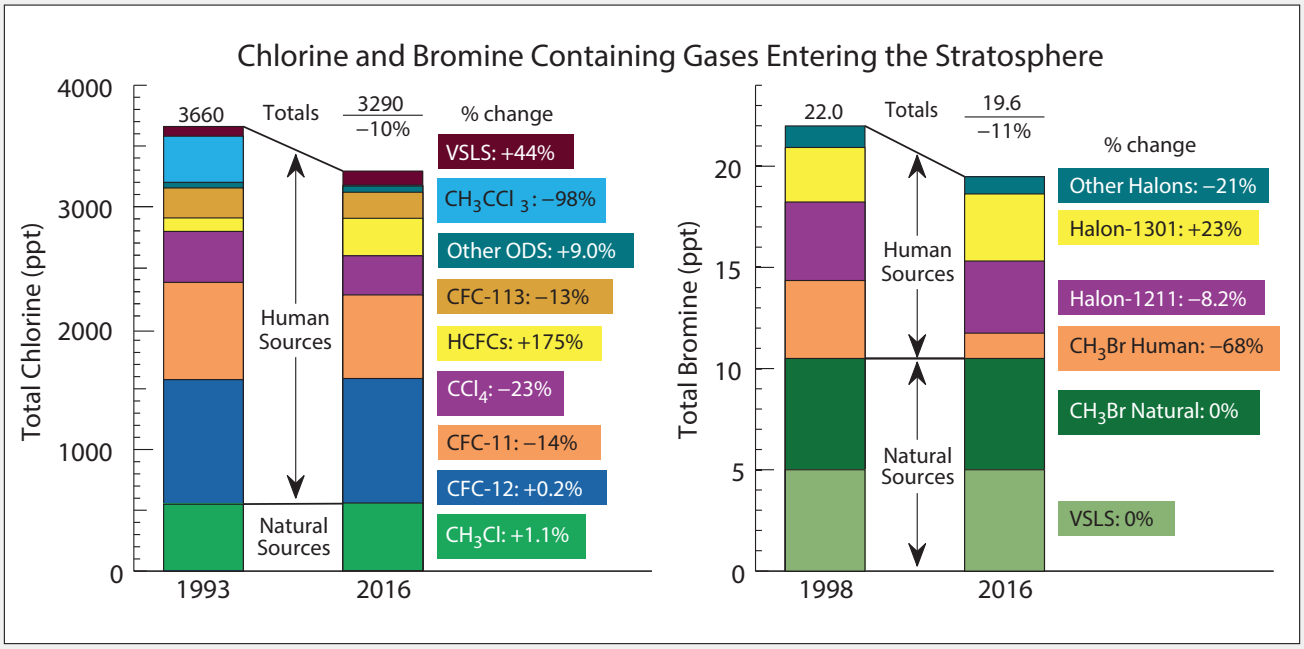

Figure ES-3. Total chlorine and bromine entering the stratosphere from well-mixed ODSs and VSLSs. These partitioned columns show the contributions of various chlorine-containing (left) and bromine-containing (right) substances from natural and human-related sources as derived from surface observations. The displayed amounts are representative of air entering the stratosphere in 2016 and in 1993 or 1998, when chlorine and bromine global abundances were near their respective peak values. Note the large difference between the total abundances of chlorine and bromine. The percentage decline or increase of the abundance of each substance in 2016 relative to the peak year and the total change are shown. Horizontal lines divide natural and human-related contributions. Both total chlorine and bromine have declined substantially from respective peaks in the 1990s (10% and 11%, respectively, when considering the sum of well-mixed ODSs and VSLSs). Human activities are the largest source of chlorine entering the stratosphere and CFCs are the largest fraction of the total; the human contribution to total chlorine is 14% lower in 2016 compared to 1993. Methyl chloride (CH_3Cl) is the largest natural source of chlorine. VSLS chlorine species from human activities are a small fraction of total chlorine (less than a few percent). Methyl bromide (CH_3Br) and halons are the primary sources of stratospheric bromine. Methyl bromide has both natural and human sources whereas halons are entirely due to human activity. The human contribution to total bromine is 22% lower in 2016 compared to 1998. Bromine from VSLSs is entirely of natural origin and is assumed constant at 5 ppt since 1998. In 2016, the sum of bromine from natural methyl bromide and VSLSs supplied more than half of the total entering the stratosphere. Chlorine compounds labeled 'Other ODSs' include minor CFCs and halon-1211. Other chemical terms are carbon tetrachloride (CCl_4) and methyl chloroform (CH_3CCl_3). Bromine compounds labeled 'Other Halons' include halon-1202 and halon-2402. In the vertical axes label, 'ppt' denotes atmospheric abundance in units of parts per trillion. [Derived from Figure 1-17 and Table 6-4]

- **HFC emissions estimated from the combination of inventory reporting and atmospheric observations indicate that the HFC emissions originate from both developed and developing countries.** Only developed (Annex I) countries are required to report HFC emissions to the UNFCCC, and these reported totals account for less than half of global emissions (as CO_2-eq) derived from observations.

- **Radiative forcing from measured HFCs continues to increase; it currently amounts to 1% (0.03 W m^{-2}) of the 3 W m^{-2} supplied by all long-lived greenhouse gases (GHGs) including CO_2, CH_4, N_2O, and halocarbons.** Total HFC radiative forcing in 2016 was about 10% of the 0.33 W m^{-2} supplied by all halocarbons.

- **Global annual emissions of HFC-23, a potent greenhouse gas and a byproduct of HCFC-22 production, have varied substantially in recent years.** This variability in observationally derived global emissions is broadly consistent with the sum of reported HFC-23 emissions associated with HCFC-22 production from developed countries and inventory-based estimates of HFC-23 emissions from developing countries. Future HFC-23 emission trends will largely depend on the magnitude of HCFC-22 production and the effectiveness of HFC-23 destruction associated with that production.

- **Some short-lived, low-GWP replacement substances for long-lived HCFCs and HFCs have been detected in the atmosphere (at concentrations typically below 1 ppt), consistent with the transition to these substances being underway.** Some of these substances are unsaturated HCFCs and unsaturated HFCs, also known as hydrofluoroolefins or HFOs.

Projections of HFC emissions and temperature contributions

- **The HFC phasedown schedule of the 2016 Kigali Amendment to the Montreal Protocol substantially reduces future projected global HFC emissions (Figure ES-4).** Emissions are projected to peak before 2040 and decline to less than 1 $GtCO_2$-eq yr^{-1} by 2100 (**Figure ES-4**). Only marginal increases are projected for CO_2-eq emissions of the low-GWP alternatives (**Figure ES-5**) despite substantial projected increases in their emission mass.

- **The Kigali Amendment, assuming global compliance, is projected to reduce future radiative forcing due to HFCs by about 50% in 2050 compared to a scenario without any HFC controls**. The estimated benefit of the amendment is the avoidance of 2.8 - 4.1 $GtCO_2$-eq yr^{-1} emissions by 2050 and 5.6 - 8.7 $GtCO_2$-eq yr^{-1} by 2100. For comparison, total CH_4 emissions are projected to be 7 - 25 $GtCO_2$-eq yr^{-1} by 2100 in the RCP-6.0 and RCP-8.5 scenarios and total N_2O emissions 5-7 $GtCO_2$-eq yr^{-1} by 2100.

- **The Kigali Amendment is projected to reduce future global average warming in 2100 due to HFCs from a baseline of 0.3-0.5 °C to less than 0.1 °C (Figure ES-4).** If the global production of HFCs were to cease in 2020, the surface temperature contribution of the HFC emissions would stay below 0.02 °C for the whole 21st century. The magnitude of the avoided temperature increase, due to the provisions of the Kigali Amendment (0.2 to 0.4 °C) is substantial in the context of the 2015 UNFCCC Paris Agreement, which aims to limit global temperature rise to well below 2.0 °C above pre-industrial levels and to pursue efforts to limit the temperature increase even further to 1.5 °C.

[3] Stratospheric ozone

The Montreal Protocol and its Amendments and Adjustments have been effective in limiting the abundance of ODSs in the atmosphere. Detecting and attributing ozone trends during this period of slow ODS decline is challenging because of large natural variability in ozone, as well as confounding factors such as climate change and changes in tropospheric ozone. While most natural variability is quasi-periodic, episodic volcanic eruptions can drive large changes in ozone in the presence of elevated halogen abundances. The Antarctic and the upper stratosphere, where the ozone depletion signal has been clearest against the backdrop of natural variability, are now showing evidence of recovery. Although the

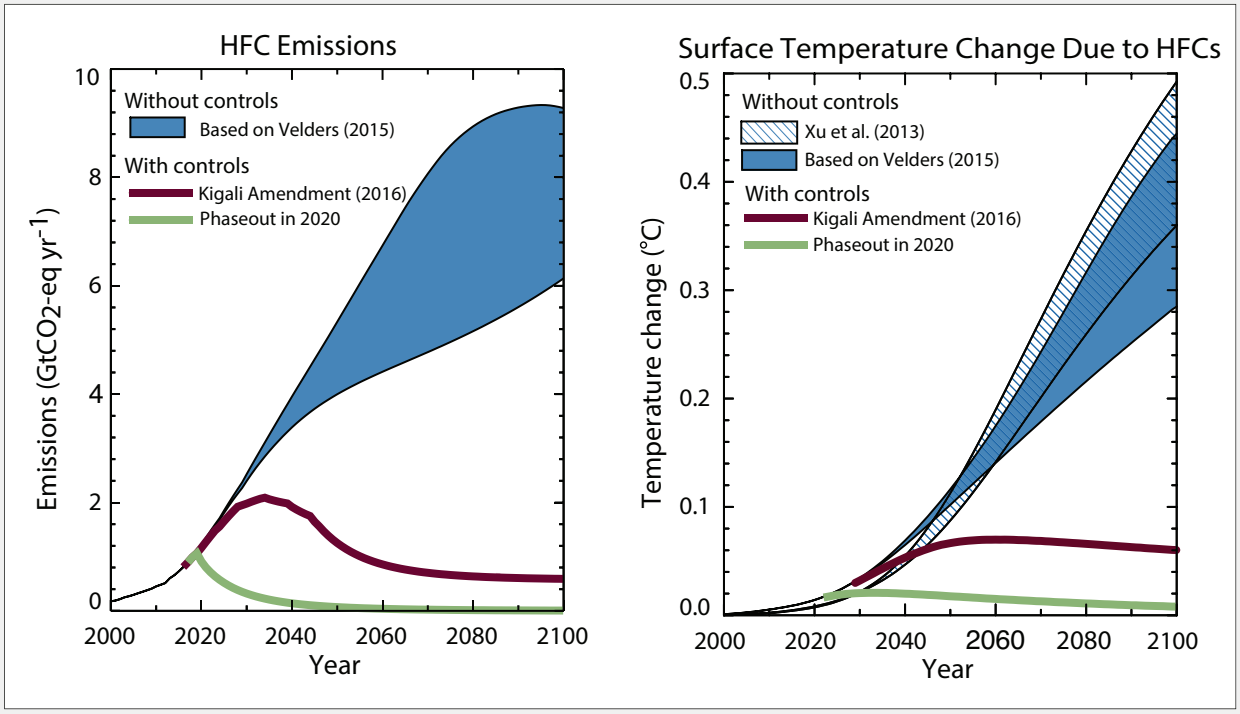

Figure ES-4. Scenarios of HFC emissions and global average surface-temperature response. Shown are global HFC scenarios without global HFC controls and with full compliance with the Kigali Amendment. Also shown is a scenario in which global production of HFCs is phased out in 2020. For comparison, the global surface temperature from all greenhouse gases is projected to increase, relative to the 1986–2005 average, by between 1.4 °C and 4.8 °C by the end of the 21st century in the RCP-6.0 and RCP-8.5 scenarios. The contribution from HFC-23 emissions is not included here. [Figure adapted from Figure 2-20]

Arctic stratosphere is warmer and experiences much more meteorological variability, severe chemical ozone loss can occur when cold conditions persist into March/April (Figure ES-6). Ozone in the tropical lower stratosphere shows little response to changes in ODSs, because halogen-driven ozone depletion is small in this region.

Antarctic and Arctic ozone

- **For the first time, there are emerging indications that the Antarctic ozone hole has diminished in size and depth since the year 2000, with the clearest changes occurring during early spring. Although accounting for natural variability is challenging, the weight of evidence suggests that the decline in ODSs made a substantial contribution to the observed trends.**

- **Even with these early signs of recovery, an Antarctic ozone hole continues to occur every year, with the severity of the chemical loss strongly modulated by meteorological conditions (temperatures and winds) (Figure ES-1).** In 2015, the ozone hole was particularly large and long-lasting, as a result of a cold and undisturbed polar stratospheric vortex. Aerosols from the Calbuco volcanic eruption are also believed to have contributed to the large ozone hole area in 2015. Conversely, in 2017, the Antarctic ozone hole was very small due to a warm and unusually disturbed polar vortex.

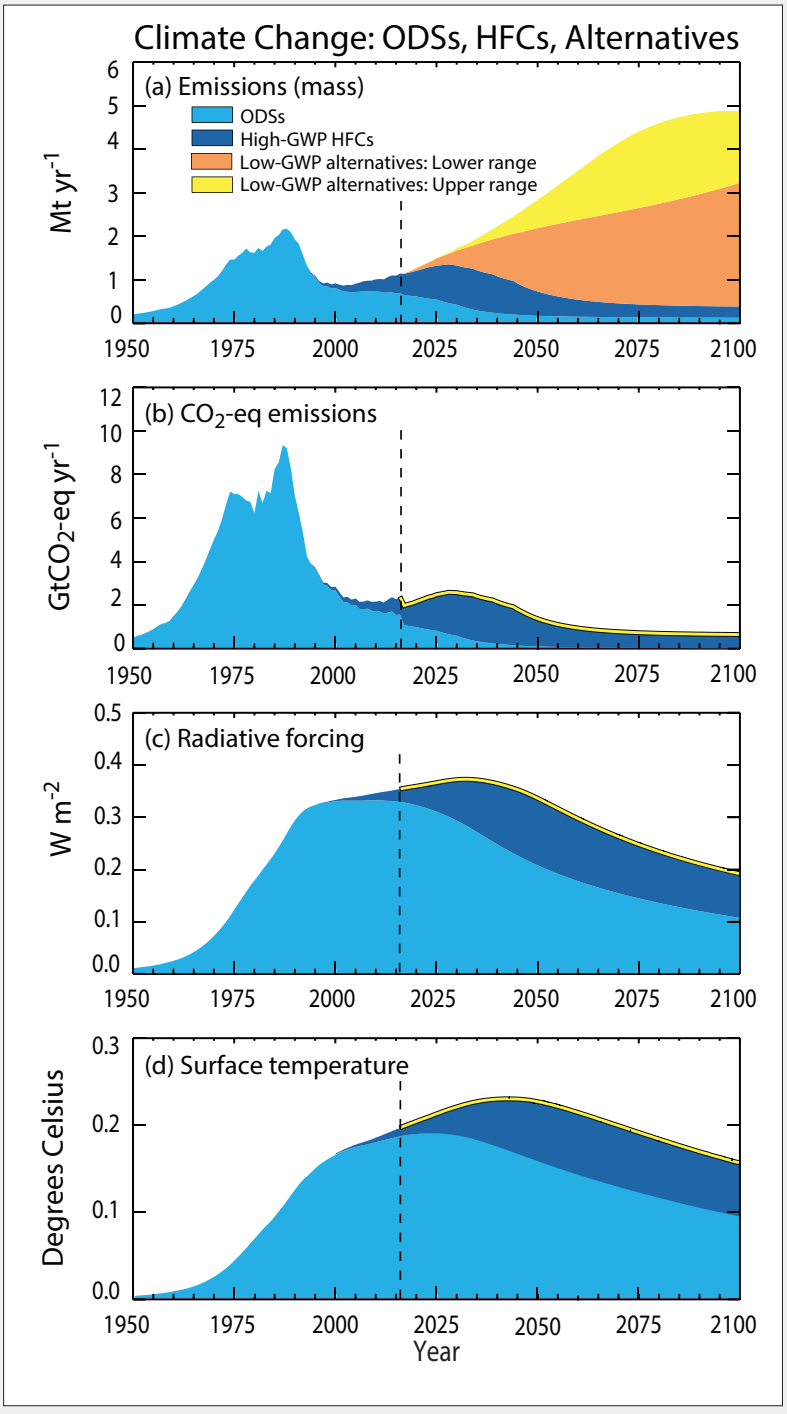

Figure ES-5. Historical and projected emissions, radiative forcing and surface temperature from ODSs, HFCs, and HFC alternatives. Historical and projected contributions to climate change are shown for ODSs and high-GWP HFCs (excluding HFC-23) assuming full compliance with the provisions of the Montreal Protocol, including the Kigali Amendment. Also shown are projections for low-GWP alternatives. Quantities shown are the (a) mass emissions, (b) CO_2-eq emissions, (c) radiative forcing and (d) contributions to surface temperature change, with a dashed vertical line indicating 2016. The surface temperature response is calculated with a parameterized climate model. Note that the values for low-GWP alternatives in the bottom three panels (yellow lines) are sufficiently small that they require enlargement to be visible to the reader. [Figure adapted from Figures 2-20 and 6-8]

- **In the Arctic, year-to-year variability in column ozone is much larger than in the Antarctic, precluding identification of a statistically significant[4] increase in Arctic ozone over the 2000–2016 period.** Exceptionally low ozone abundances, similar to those experienced in Arctic spring 2011, have not been observed in the last four years. Extremely cold conditions in the 2015/2016 winter resulted in rapid chemical ozone loss, but a sudden warming of the polar stratosphere in early March curtailed further losses.

[4] The term 'statistically significant' indicates that there is a very high likelihood (above some confidence limit that is typically 95%) that a quantity has undergone a change over a given time period and has not simply exhibited variability around an unchanged state. For a more detailed discussion of trend uncertainties, see Chapter 3.

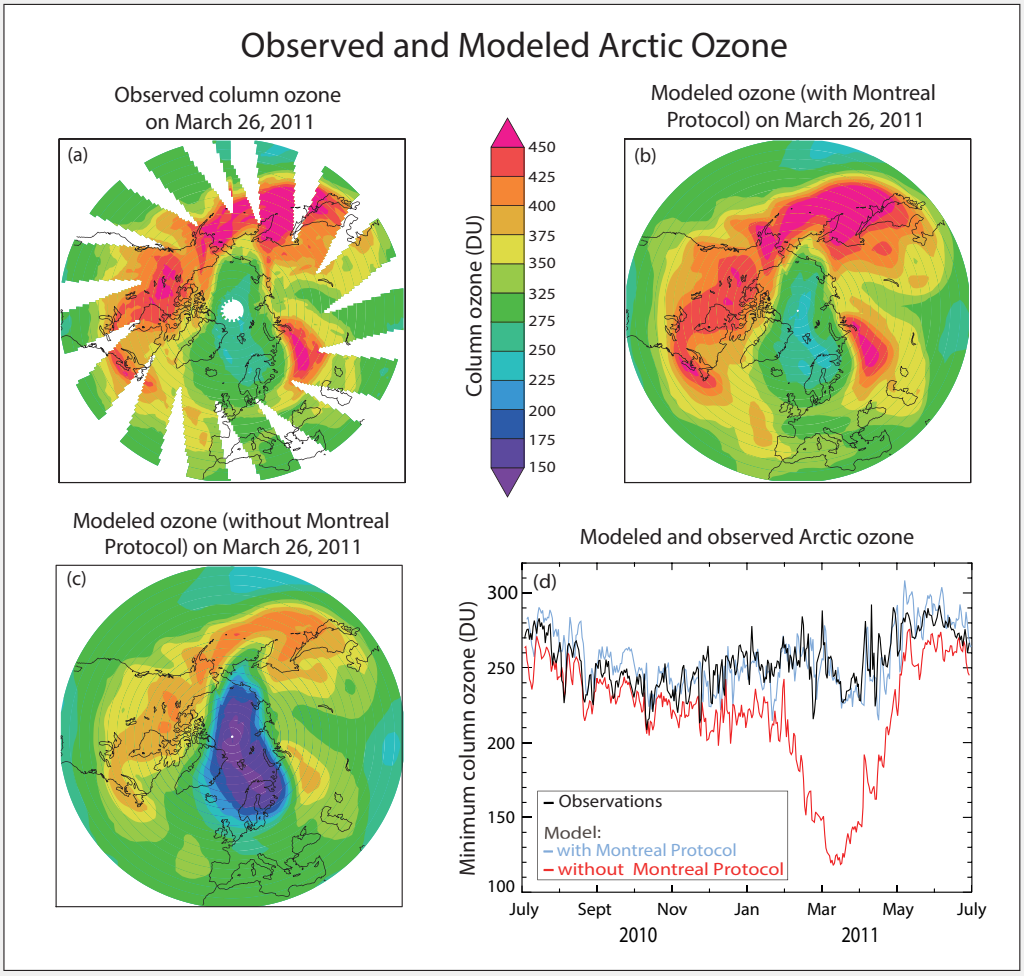

Figure ES-6. Observed and modeled column ozone in the Arctic. Without the success of the Montreal Protocol, a deep ozone hole could have formed in the Arctic in 2011, and smaller Arctic ozone holes would have become a regular occurrence. The 2010/2011 Arctic winter had unusually persistent low temperatures in the stratosphere that led to strong chemical ozone destruction. Satellite observations from the Ozone Monitoring Instrument (OMI) in March 2011 show a region of low column ozone surrounded by regions of higher ozone (*panel (a)*). The March observations are well simulated by a chemistry-transport model run with observed abundances of ODSs, as seen by comparing the maps of *panels (a) and (b)* as well as the black and blue curves in *panel (d)*, which show the measured and modeled timelines for the mid-2010 to mid-2011 period of daily minimum column-ozone values in the Arctic region (latitudes greater than 45°N). If the same model is run with projected ODS abundances in the absence of Montreal Protocol controls, a much more severe and prolonged Arctic ozone hole is seen *(panel (c)* and the red curve in *panel (d)*). [See also Figure 4-17]

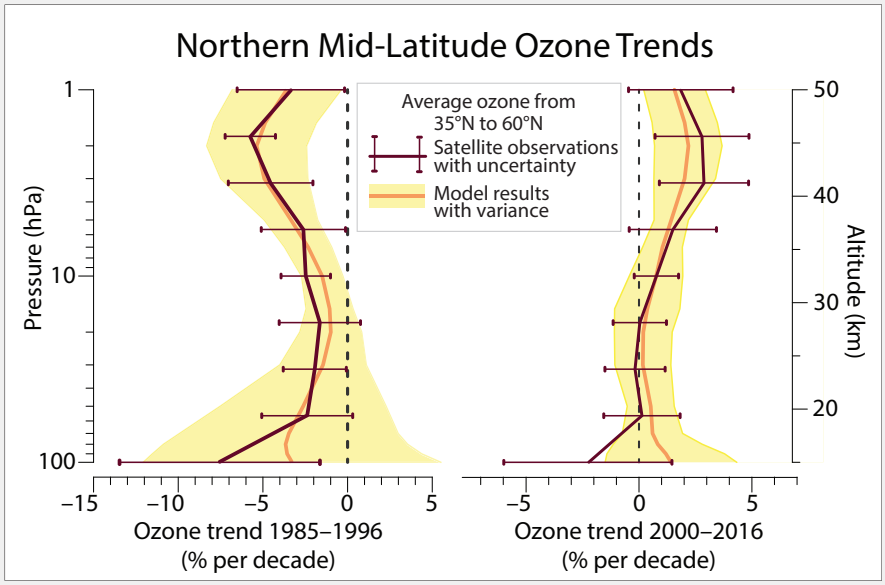

Figure ES-7. Ozone trends in the stratosphere. The largest relative depletion of ozone outside the polar regions occurred prior to 1997 in the northern mid-latitude, upper stratosphere *(left panel)*. The largest recovery has occurred in the same region, with an upward trend of about 3% per decade since 2000 above 40-km altitude *(right panel)*. Ozone trends derived from satellite observations are shown in brown, with uncertainty ranges given by horizontal lines. Ozone trends derived from a set of chemistry-climate models are shown in orange, with the model variance given by the yellow envelope. Ozone trends from chemistry-climate models agree very well with the measured trends. [See also Figure 3-23]

- **Model simulations show that implementation of the Montreal Protocol has prevented much more severe ozone depletion than has been observed in the polar regions of both hemispheres (Figure ES-6).**

Global ozone

- **No statistically significant trend has been detected in global (60°S–60°N) total column ozone over the 1997–2016 period (Figure ES-1).** Average global total column ozone in the years since the last Assessment remain roughly 2.2% below the 1964–1980 average. These findings are expected given our understanding of the processes that control ozone.
    - In the mid-latitudes, the increase in ozone expected to arise from the 15% decline in EESC since 1997 is small (1% per decade) relative to the year-to-year variability (about 5%).
    - In the tropics, where halogen-driven ozone loss is small in the lower stratosphere, total column ozone has not varied significantly with ODS concentrations, except under conditions of high volcanic aerosol loading (e.g., Mt. Pinatubo).
- **Upper stratospheric ozone, which represents only a small fraction of the total column, has increased by 1–3% per decade since 2000 outside of polar regions (Figure ES-7).** Additional and improved data sets and focused studies evaluating trend uncertainties have strengthened our ability to assess ozone profile changes since the last Assessment. The upward trend is largest and statistically significant in northern mid-latitudes and maximizes above 40-km altitude.
    - Model simulations attribute about half of the observed upper stratospheric ozone increase after 2000 to the decline of ODSs since the late 1990s.
    - The other half of the ozone increase is attributed to the slowing of gas-phase ozone destruction, which results from cooling of the upper stratosphere caused by increasing GHGs.
- **There is some evidence for a decrease in global (60°S–60°N) lower stratospheric ozone from 2000 to 2016, but it is not statistically significant in most analyses. Much of the apparent decline in the tropics**

and mid-latitudes was reversed by an abrupt increase in ozone in 2017, showing that longer records are needed to identify robust trends. Model simulations indicate that, on multiannual timescales, variations in ozone in this region are primarily controlled by transport rather than chemistry.

Ozone recovery and ozone-climate interactions

A refined ODS scenario and new GHG emissions scenarios were used in chemistry-climate models for this Assessment, leading to a delay of about 5 to 15 years in the return dates relative to the last Assessment, depending on the latitude region.

- Updated chemistry climate model projections based on full compliance with the Montreal Protocol and assuming the baseline estimate of the future evolution of GHGs (RCP-6.0) show that:
  - **The Antarctic ozone hole is expected to gradually close, with springtime total column ozone returning to 1980 values shortly after mid-century (about 2060) (Figure ES-1)**;
  - **Arctic springtime total ozone is expected to return to 1980 values before mid-century (about 2030s)**. Substantial Arctic ozone loss will remain possible in cold winters as long as ODS concentrations are well above natural levels. In contrast to the Antarctic, the timing of the recovery of Arctic total ozone in spring will be strongly affected by anthropogenic climate change;
  - **Northern-Hemisphere, mid-latitude column ozone is expected to return to 1980 abundances before mid-century (2030s), and Southern Hemisphere, mid-latitude ozone is expected to return around mid-century.**
- **Outside the Antarctic, CO_2, CH_4, and N_2O will be the main drivers of stratospheric ozone changes in the second half of the 21st century, assuming full compliance with the Montreal Protocol.** These gases impact both chemical cycles and the stratospheric overturning circulation, with a larger response in stratospheric ozone associated with stronger climate forcing. By 2100 the stratospheric column is expected to:
  - decrease in the tropics by about 5 DU for RCP-4.5 and about 10 DU for RCP-8.5, with the net total column change projected to be smaller (about 5 DU) because of offsetting increases in tropospheric ozone; and
  - not only to recover but to exceed 1960–1980 average values in mid-latitudes and the Arctic, with springtime Arctic ozone being higher by about 35 DU for RCP-4.5 and about 50 DU for RCP-8.5.

[4] Ozone change and its influence on climate

Ozone is important in the climate system and its changes can influence both the troposphere and the stratosphere. Past Assessments have discussed evidence for how stratospheric ozone depletion has affected Southern Hemisphere climate. The climate impacts of ozone depletion are expected to reverse over coming decades as stratospheric ozone recovers. However, projected increases in atmospheric GHG concentrations will continue to be a key driver of future Southern Hemisphere climate. The relative importance of ozone recovery for future Southern Hemisphere climate will depend on the evolution of atmospheric GHG concentrations.

Influence on stratospheric climate

- **Discrepancies between estimates of stratospheric cooling rates from different satellite temperature retrievals have been substantially reduced since the last Assessment.** This result has led to greater confidence in the attribution of observed stratospheric temperature changes since the late 1970s.

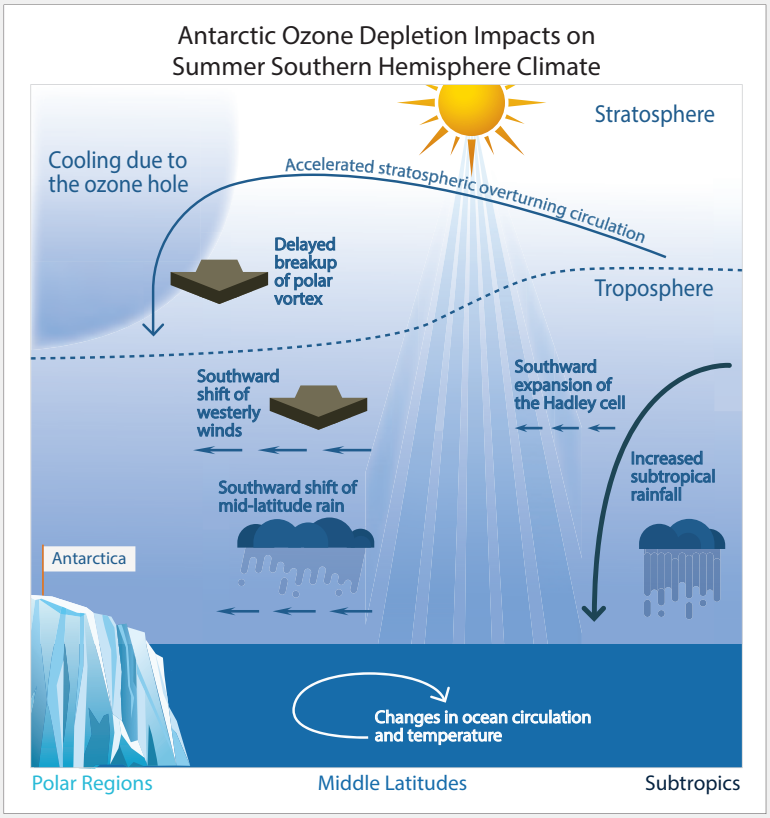

Figure ES-8. Schematic illustration of Southern Hemisphere climate impacts in austral summer associated with Antarctic ozone depletion. Ozone depletion has cooled the Antarctic stratosphere, leading to a delayed breakup of the stratospheric polar vortex and an accelerated stratospheric overturning circulation. Impacts have extended into the troposphere with the region of strong westerly winds and associated rainfall shifted southward, affecting the ocean circulation. The subtropical edge of the tropical circulation has also expanded poleward, leading to reduced precipitation in mid-latitudes and enhanced precipitation in the subtropics. [Also appears as Figure 5-12]

- **Decreases in stratospheric ozone caused by ODS increases have been an important contributor to observed stratospheric cooling.** New studies find that ODSs thereby contributed approximately one third of the observed cooling in the upper stratosphere from 1979 to 2005, with two thirds caused by increases in other GHGs.

- **Satellite temperature records show weaker global-average cooling throughout the depth of the stratosphere between 1998 and 2016 relative to between 1979 and 1997.** The difference in the rate of stratospheric cooling between the two periods is consistent with differences in the observed ozone trends for each period.

Influence on surface climate and oceans

- **New studies strengthen the conclusion from the last Assessment that lower stratospheric cooling due to ozone depletion has very likely been the dominant cause of late 20th century changes in Southern Hemisphere climate in summer.** These changes include the observed poleward shift in Southern Hemisphere tropospheric circulation, with associated impacts on surface temperature and precipitation (**Figure ES-8**). No robust link between stratospheric ozone depletion and long-term surface climate changes in the Northern Hemisphere has been established.

- **Changes in tropospheric circulation driven by ozone depletion have contributed to recent trends in Southern Ocean temperature and circulation; the impact on Antarctic sea ice remains unclear.**

- **New studies since the last Assessment have not found a causal link between ozone depletion and the net strength of the Southern Ocean carbon sink over the last few decades**. This result updates the 2010 Assessment where such a link was suggested.

[5] Policy considerations for stratospheric ozone and climate

Policy-relevant alternative scenarios related to future ozone changes

Changes in total column ozone and GWP-weighted emissions in response to various control measures and alternative scenarios are shown in Figure ES-9. The baseline scenario used here and those used in previous Assessments assume compliance with the Montreal Protocol. The alternative scenarios assessed here include the elimination of banks, production, and emissions of gases that are both controlled and uncontrolled by the Montreal Protocol. Key conclusions are found in the bullet points below.

- **The recently derived increase in global emissions of CFC-11 (Figure ES-2, Section 1) indicates that there is global production that is not reported to UN Environment**. Assuming total emissions of CFC-11 continue at their average level from 2002–2016 (67 Gg yr^{-1}), the return of mid-latitude and polar EESC values to their 1980 values would be delayed by about 7 and 20 years, respectively, compared to the recovery date expected from the continued declining bank emissions expected from the baseline scenario in which no unreported production is considered. Avoiding this scenario (blue bar in top panel of **Figure ES-9**) would have a larger positive impact on future ozone than any of the other mitigation options considered in **Figure ES-9**.

- **Future emissions from ODS banks continue to be a slightly larger contributor than future ODS production to ozone layer depletion over the next four decades in the baseline scenario.** The baseline scenarios assume compliance with the Montreal Protocol. Future emissions from the banks of halons, CFCs, and HCFCs are projected to contribute roughly comparable amounts to EESC over the next few decades.

- **CCl_4 emissions inferred from atmospheric observations continue to be much greater than those assumed from feedstock uses as reported to UN Environment.** A significant part of these additional emissions has been identified as inadvertent by-product emissions from chloromethanes and perchloroethylene plants and fugitive emissions from the chlor-alkali process. Elimination of all CCl_4 emissions in 2020 would accelerate the return of mid-latitude EESC to 1980 levels by almost three years.

- **Elimination of future quarantine and pre-shipment (QPS) production of methyl bromide (CH_3Br) would accelerate the return of mid-latitude EESC to 1980 levels by about a year.** Production for QPS applications is not controlled by the Montreal Protocol. QPS has remained nearly unchanged over the last two decades, and now constitutes almost 90% of the reported production of CH_3Br because of the phaseout of other uses.

A number of gases of anthropogenic origin that are not controlled by the Montreal Protocol can have direct chemical effects on stratospheric ozone, for example dichloromethane (CH_2Cl_2) and N_2O.

- **Emissions of anthropogenic VSLS chlorine contribute to ozone depletion.** Observed growth in the concentrations of CH_2Cl_2, which accounted for the majority of the recent rise in total chlorine from VSLSs, continues to be highly variable and there is insufficient information to confidently predict the future concentrations of CH_2Cl_2 (see Section 1). Response to any action taken to reduce emissions would be rapid and effective in reducing atmospheric concentrations since CH_2Cl_2 is a short-lived substance (**Figure ES-9** upper panel).

- **Reducing N_2O emissions from those in RCP-6.0 to achieve the Concerted Mitigation scenario would have a similar positive impact on stratospheric ozone as eliminating future production of HCFCs from 2020 (Figure ES-9** upper panel**).** The Concerted Mitigation scenario[5] is an average of four scenarios that lead to lower N_2O emissions in 2050 than were experienced in 2005. This N_2O mitigation scenario has a larger benefit to climate (2020 to 2060) than do the ODS alternative scenarios considered (**Figure ES-9** lower panel).

[5] UNEP 2013. Drawing Down N_2O to Protect Climate and the Ozone Layer. A UNEP Synthesis Report. United Nations Environment Programme (UNEP), Nairobi, Kenya.

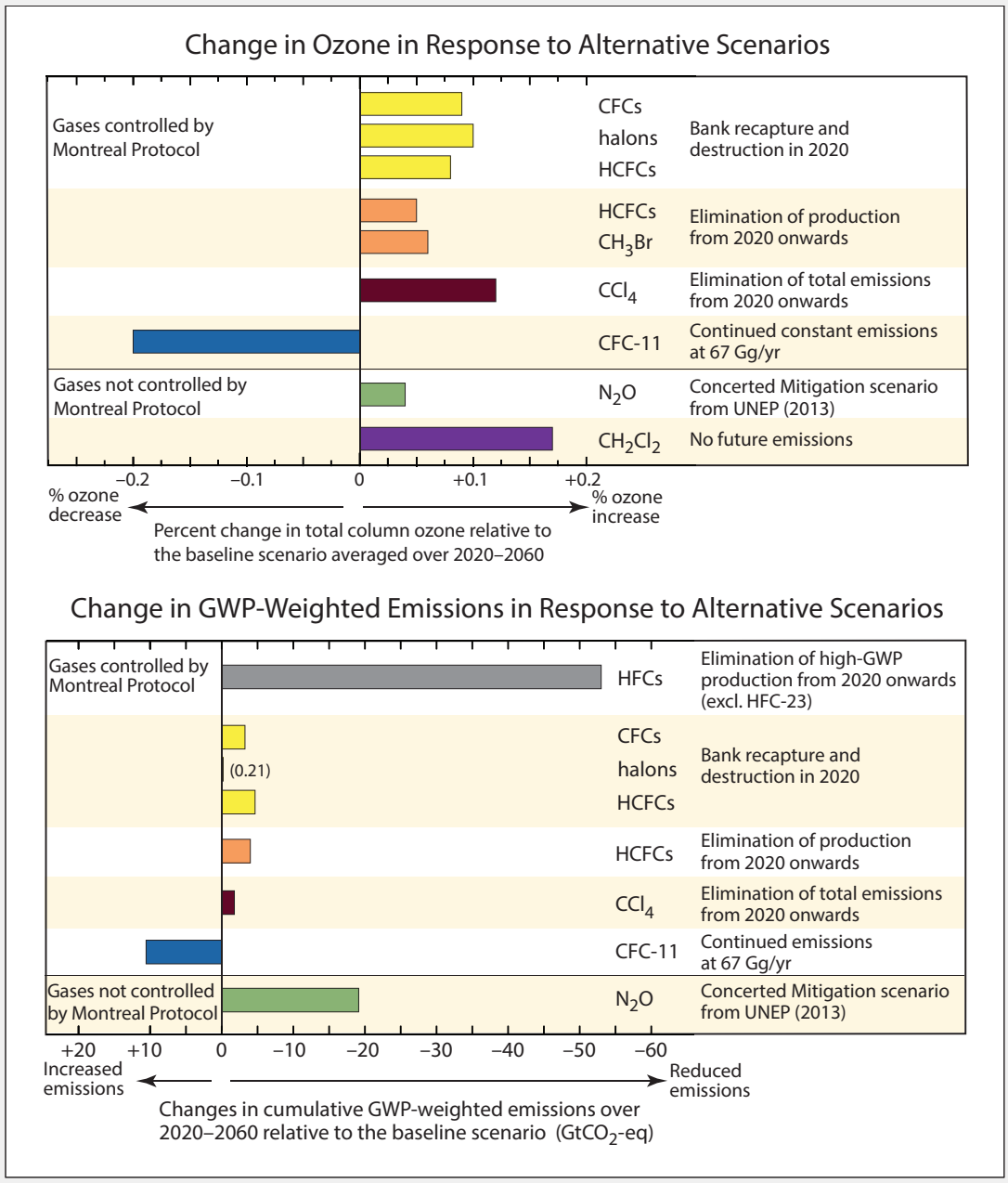

Figure ES-9. Changes in ozone and GWP-weighted emissions for a selection of alternative scenarios. Changes in total column ozone (*upper panel*) and GWP-weighted emissions (*lower panel*) that occur in the alternative scenarios as described in the figure. The values are differences in average ozone (*top panel*) over the period 2020–2060 and cumulative GWP-weighted emission (*lower panel*) over the same period between the alternative scenarios and the baseline scenario. A decrease in total ozone and an increase in GWP-weighted emissions occur when the alternative scenario emissions are higher than in the baseline scenario. Numerical values of these changes are shown in Table 6-5. Note that the change resulting from the elimination of HFC production shown in the *lower panel* is not shown in the *upper panel* because HFCs play such a small role in the chemical destruction of ozone. Chemical terms used in the figure are methyl bromide (CH_3Br), carbon tetrachloride (CCl_4), nitrous oxide (N_2O), and dichloromethane (CH_2Cl_2). [Also Figure 6-1]

Climate impact of gases controlled by the Montreal Protocol

*Historical and projected contributions to climate change from emissions of ODSs, high-GWP HFCs, and low-GWP alternatives have been calculated, assuming full compliance with the Montreal Protocol, including the Kigali Amendment (**Figure ES-5**).*

- **Future CO_2-eq emissions of HFCs from 2020 to 2060 under the Kigali Amendment are about half of those in a scenario without any HFC controls.** Assuming compliance, projected cumulative emissions of HFCs from 2020 to 2060 decrease to approximately 60 $GtCO_2$-eq. CFCs from known banks and HCFCs cumulatively contribute approximately 3 Gt and 9 $GtCO_2$-eq emissions, respectively, over the same time period. For comparison, cumulative CO_2 emissions from fossil fuel usage are projected over this time period to be 760 $GtCO_2$ in the RCP-2.6 scenario and 1700 $GtCO_2$ in the RCP-6.0 scenario. The peak in annual CO_2-eq emissions of all HFCs together is expected to be much smaller than the peak in ODS emissions (**Figure ES-5**).

- **A faster phasedown of HFCs than required by the Kigali Amendment would further limit climate change from HFCs. One way to achieve this phasedown would be more extensive replacement of high-GWP HFCs with commercially available low-GWP alternatives in refrigeration and air-conditioning equipment. Figure ES-9** shows the impact of a complete elimination of production of HFCs starting in 2020, and their substitution with low-GWP HFCs, which would avoid an estimated cumulative 53 $GtCO_2$-eq emission during 2020–2060.

- **Improvements in energy efficiency in refrigeration and air-conditioner equipment during the transition to low-GWP alternative refrigerants can potentially double the climate benefits of the HFC phasedown of the Kigali Amendment.**

- **Total radiative forcing from the controlled ODSs and their replacements continues to be strongly limited by the Montreal Protocol, including the Kigali Amendment.** The radiative forcing from CFCs has been declining since the early 2000s. The sum of CFC and HCFC radiative forcing has been stable for about two decades and is just starting to decline. The total forcing from CFC and HCFCs and their HFC replacements is projected to continue to increase gradually for the next decade or two. After that, the ODS and HFC restrictions of the Montreal Protocol, if adhered to, ensure a continued decline in total RF from ODSs and their replacements through the rest of the century.

- **Global warming potentials, global temperature potentials, and ozone depletion potentials of hundreds of HCFCs have been calculated and are presented, most for the first time in an assessment.** These data include all the HCFCs listed under Annex C, Group I of the Montreal Protocol, many of which did not have estimated GWPs at the time of the adoption of the Kigali Amendment. This information is significant since the Kigali Amendment uses CO_2-eq production and consumption of HFCs and HCFCs as a metric for the baseline determination of the HFC phasedown.

Impacts of climate change and other processes on future stratospheric ozone

Anthropogenic activity associated with climate change could have potentially important impacts on the future of the ozone layer.

- **The wide range of possible future levels of CO_2, CH_4, and N_2O represents an important limitation to making accurate projections of the ozone layer** [see Ozone recovery and ozone-climate interactions section]. Because future ODS atmospheric concentrations are highly constrained by the Montreal Protocol, the range in projected ozone levels across the ODS scenarios is much smaller than that associated with GHG changes.

- **Intentional long-term geoengineering applications that substantially increase stratospheric aerosols to mitigate global warming by reflecting sunlight would alter the stratospheric ozone layer.** The estimated magnitude and even the sign of ozone changes in some regions are uncertain because of the high sensitivity to variables such as the amount, altitude, geographic location, type of injection and the halogen loading. An increase of the stratospheric sulfate aerosol burden in amounts sufficient to substantially reduce global radiative forcing would delay the recovery of the Antarctic ozone hole. Much less is known about the effects on ozone from geoengineering solutions using non-sulfate aerosols.

Chapter 1: Update on Ozone-Depleting Substances (ODSs) and other Gases of Interest to the Montreal Protocol

This chapter concerns atmospheric changes in ozone-depleting substances (ODSs), such as chlorofluorocarbons (CFCs), halons, chlorinated solvents (e.g., CCl_4 and CH_3CCl_3) and hydrochlorofluorocarbons (HCFCs), which are controlled under the Montreal Protocol. Furthermore, the chapter updates information about ODSs not controlled under the Protocol, such as methyl chloride (CH_3Cl) and very short-lived substances (VSLSs). In addition to depleting stratospheric ozone, many ODSs are potent greenhouse gases.

Mole fractions of ODSs and other species are primarily measured close to the surface by global or regional monitoring networks. The surface data can be used to approximate a mole fraction representative of the global or hemispheric tropospheric abundance. Changes in the tropospheric abundance of an ODS result from a difference between the rate of emissions into the atmosphere and the rate of removal from it. For gases that are primarily anthropogenic in origin, the difference between northern and southern hemispheric mole fractions is related to the global emission rate because these sources are concentrated in the northern hemisphere.

- **The abundances of the majority of ODSs that were originally controlled under the Montreal Protocol are now declining, as their emissions are smaller than the rate at which they are destroyed. In contrast, the abundances of most of the replacement compounds, HCFCs and hydrofluorocarbons (HFCs, which are discussed in Chapter 2), are increasing.**

Tropospheric chlorine

Total tropospheric chlorine is a metric used to quantify the combined globally averaged abundance of chlorine in the troposphere due to the major chlorine-containing ODSs. The contribution of each ODS to total tropospheric chlorine is the product of its global tropospheric mean mole fraction and the number of chlorine atoms it contains.

- **Total tropospheric chlorine (Cl) from ODSs continued to decrease between 2012 and 2016.** Total tropospheric chlorine in 2016[1] was 3,287 ppt (where ppt refers to parts per trillion as a dry air mole fraction), 11% lower than its peak value in 1993, and about 0.5% lower than reported for 2012 in the previous Assessment. Of the 2016 total, CFCs accounted for about 60%, CH_3Cl accounted for about 17%, CCl_4 accounted for about 10%, and HCFCs accounted for about 9.5%. The contribution from CH_3CCl_3 has now decreased to 0.2%. Very short-lived source gases (VSL SGs), as measured in the lower troposphere, contributed approximately 3%.
    - During the period 2012–2016, the observed rate of decline in tropospheric Cl due to *controlled substances* was 12.7 ± 0.9[2] ppt Cl yr^{-1}, similar to the 2008–2012 period (12.6 ± 0.3 ppt Cl yr^{-1}). This rate of decrease was close to the projections from the A1 scenario[3] in the previous Assessment. However, the net rate of change was the result of a slower than projected decrease in CFCs and a slower HCFC increase than in the A1 scenario, which assumed that HCFC production from Article 5 countries would follow the maximum amount allowed under the Montreal Protocol.

[1] Here and throughout this chapter, values that are given for a specific year represent annual averages, unless mentioned otherwise.
[2] The ranges given here represent the interannual variability in observed growth rate or rate of decrease.
[3] A1 Scenario is given in Table 5A-2 of Harris and Wuebbles et al. [2014].

- When substances *not controlled* under the Montreal Protocol are also included, the overall decrease in tropospheric chlorine was 4.4 ± 4.1 ppt Cl yr^{-1} during 2012–2016. This is smaller than the rate of decline during the 2008–2012 period (11.8 ± 6.9 ppt Cl yr^{-1}) and smaller than the rate of decline in controlled substances because VSLS, predominantly anthropogenic dichloromethane (CH_2Cl_2), and methyl chloride (CH_3Cl), which is mostly from natural sources, increased during this period.

- **Starting around 2013, the rate at which the CFC-11 mole fraction was declining in the atmosphere slowed unexpectedly, and the interhemispheric difference in its mole fraction increased. These changes are very likely due to an increase in emissions, at least part of which originate from eastern Asia.** Assuming no change in atmospheric circulation, an increase in global emissions of approximately 10 Gg yr^{-1} (~15%) is required for 2014–2016, compared to 2002–2012, to account for the observed trend and interhemispheric difference. The rate of change and magnitude of this increase is unlikely to be explained by increasing emissions from banks. Therefore, these findings may indicate new production not reported to the United Nations Environment Programme (UN Environment). If the new emissions are associated with uses that substantially increase the size of the CFC-11 bank, further emissions resulting from this new production would be expected in future.

- **Compared to 2008–2012, for the period 2012–2016, mole fractions of CFC-114[4] declined more slowly, CFC-13 continued to rise, and CFC-115 exhibited positive growth after previously showing near-zero change. These findings likely indicate an increase or stabilization of the emissions of these relatively low abundance compounds, which is not expected given their phaseout for emissive uses under the Montreal Protocol.** For CFC-114 and -115, regional analyses show that some of these emissions originate from China. There is evidence that a small fraction of the global emissions of CFC-114 and -115 are due to their presence as impurities in some HFCs. However, the primary processes responsible are unknown.

- **The rate at which carbon tetrachloride (CCl_4) has declined in the atmosphere remains slower than expected from its reported use as a feedstock. This indicates ongoing emissions of around 35 Gg yr^{-1}. Since the previous Assessment, the best estimate of the global atmospheric lifetime of CCl_4 has increased from 26 to 32 years, due to an upward revision of its lifetime with respect to loss to the ocean and soils. New sources have been proposed including significant by-product emissions from the production of chloromethanes and perchloroethylene and from chlor-alkali plants.** With these changes in understanding, the gap between top-down and bottom-up emissions estimates has reduced to around 10 Gg yr^{-1}, compared to 50 Gg yr^{-1} previously.

- **Combined emissions of the major HCFCs have declined since the previous Assessment.** Emissions of HCFC-22 have remained relatively stable since 2012, while emissions of HCFC-141b and -142b declined between 2012 and 2016, by around 10% and 18%, respectively. These findings are consistent with a sharp drop in reported HCFC consumption after 2012, particularly from Article 5 countries.

- **Emissions of the compounds HCFC-133a and HCFC-31, for which no current intentional use is known, have been detected from atmospheric measurements.** Research to date suggests that these gases are unintentional by-products of HFC-32, HFC-134a, and HFC-125 production.

Tropospheric bromine

Total tropospheric bromine is defined in analogy to total tropospheric chlorine. Even though the abundance of bromine is much smaller than that of chlorine, it has a significant impact on stratospheric ozone because it is around 60–65 times more efficient than chlorine as an ozone-destroying catalyst.

- **Total tropospheric bromine from controlled ODSs (halons and methyl bromide) continued to decrease and by 2016 was 14.6 ppt, 2.3 ppt below the peak levels observed in 1998.** In the 4-year period prior to the last Assessment, this decrease was primarily driven by a decline in methyl bromide (CH_3Br) abundance, with a

[4] Here, CFC-114 refers to the combination of CFC-114 and CFC-114a isomers.

smaller contribution from a decrease in halons. These relative contributions to the overall trend have now reversed, with halons being the main driver of the decrease of 0.15 ± 0.04 ppt Br yr^{-1} between 2012 and 2016.

- **The mole fractions of halon-1211, halon-2402, and halon-1202 continued to decline between 2012 and 2016. Mole fractions of halon-1301 increased during this period, although its growth rate dropped to a level indistinguishable from zero in 2016.** Emissions of halon-2402, halon-1301, and halon-1211, as derived from atmospheric observations, declined or remained stable between 2012 and 2016.

- **Methyl bromide (CH_3Br) mole fractions continued to decline between 2012 and 2015 but showed a small increase (2–3%) between 2015 and 2016. This overall reduction is qualitatively consistent with the controls under the Montreal Protocol.** The 2016 level was 6.8 ppt, a reduction of 2.4 ppt from peak levels measured between 1996 and 1998. The increase between 2015 and 2016 was the first observation of a positive global change for around a decade or more. The cause of this increase is yet to be explained. However, as it was not accompanied by an increased interhemispheric difference, it is unlikely that this is related to anthropogenic emissions in the Northern Hemisphere. By 2016, controlled CH_3Br consumption dropped to less than 2% of the peak value, and total reported fumigation emissions have declined by more than 85% since their peak in 1997. Reported consumption in quarantine and pre-shipment (QPS) uses of CH_3Br, which are not controlled under the Montreal Protocol, have not changed substantially over the last two decades.

Halogenated very short-lived substances (VSLSs)

VSLSs are defined as trace gases whose local lifetimes are shorter than 0.5 years and have nonuniform tropospheric abundances. These local lifetimes typically vary substantially over time and space. Of the very short-lived source gases (VSL SGs) identified in the atmosphere, brominated and iodinated species are predominantly of oceanic origin, while chlorinated species have significant additional anthropogenic sources. VSLSs will release the halogen they contain almost immediately once they enter the stratosphere and will thus play an important role in the lower stratosphere in particular. Due to their short lifetimes and their atmospheric variability the quantification of their contribution is much more difficult and has much larger uncertainties than for long-lived compounds.

- **Total tropospheric chlorine from VSL SGs in the background lower atmosphere is dominated by anthropogenic sources. It continued to increase between 2012 and 2016, but its contribution to total chlorine remains small.** Global mean chlorine from VSLSs in the troposphere has increased from about 90 ppt in 2012 to about 110 ppt in 2016. The relative VSLS contribution to stratospheric chlorine input derived from observations in the tropical tropopause layer has increased slightly from 3% in 2012 to 3.5% in 2016.

- **Dichloromethane (CH_2Cl_2), a VSL SG that has predominantly anthropogenic sources, accounted for the majority of the change in total chlorine from VSLSs between 2012 and 2016 and is the main source of VSLS chlorine.** The global mean abundance reached approximately 35–40 ppt in 2016, which is about a doubling compared to the early part of the century. The increase slowed substantially between 2014 and 2016. Emissions from southern and eastern Asia have been detected for CH_2Cl_2.

- **There is further evidence that VSLSs contribute ~5 (3–7) ppt to stratospheric bromine, which was about 25% of total stratospheric bromine in 2016. The main sources for brominated VSLSs are natural, and no long-term change is observed.** While the best estimate of 5 ppt has remained unchanged from the last Assessment, the assessed uncertainty range has been reduced. Due to the decline in the abundance of regulated bromine compounds, the relative contribution of VSLSs to total stratospheric bromine continues to increase.

Stratospheric chlorine and bromine

In the stratosphere, chlorine and bromine can be released from organic source gases to form inorganic species, which participate in ozone depletion. In addition to estimates of the stratospheric input derived from the tropospheric observations, measurements of inorganic halogen loading in the stratosphere are used to determine trends of stratospheric chlorine and bromine.

- **Hydrogen chloride (HCl) is the major reservoir of inorganic chlorine (Cl_y) in the mid to upper stratosphere. Satellite-derived measurements of HCl (60°N–60°S) in the middle stratosphere show a long-term decrease of HCl at a rate of around 0.5% yr^{-1}, in good agreement with expectations from the decline in tropospheric chlorine.** In the lower stratosphere, a decrease was observed over the period from 1997 to 2016, while significant differences in the trends are seen over the period 2005 to 2016 between various datasets and altitude/geographical regions. A similar behavior is observed for total column measurements, likely reflecting variability in stratospheric dynamics and chemistry. Total chlorine input to the stratosphere of 3,290 ppt is derived for 2016 from measurements of long-lived ODSs at the surface and VSLSs in the upper troposphere. About 80% of this input is from substances controlled under the Montreal Protocol.

- **Total stratospheric bromine, derived from observations of bromine monoxide (BrO), continued to decrease at a rate of about 0.75% yr^{-1} from 2004 to 2014.** This decline is consistent with the decrease in total tropospheric organic bromine, based on measurements of CH_3Br and the halons. A total bromine input to the stratosphere of 19.6 ppt is derived for 2016, combined from 14.6 ppt of long-lived gases and 5 ppt from VSLSs not controlled under the Montreal Protocol. Anthropogenic emissions of all brominated long-lived gases are controlled, but as CH_3Br also has natural sources, more than 50% of the bromine reaching the stratosphere is now estimated to be from sources not controlled under the Montreal Protocol. There is no indication of a long-term change in natural sources to stratospheric bromine.

Equivalent effective stratospheric chlorine (EESC)

EESC is the chlorine-equivalent sum of chlorine and bromine derived from ODS tropospheric abundances, weighted to reflect their expected depletion of stratospheric ozone. The growth and decline in EESC depends on a given tropospheric abundance propagating to the stratosphere with varying time lags (on the order of years) associated with transport. Therefore, the EESC abundance, its peak timing, and its rate of decline are different in different regions of the stratosphere. Recent suggestions of a refinement in the calculation method for EESC result in somewhat lower estimates on how far the stratospheric reactive halogen loading has recovered.

- **By 2016, EESC had declined from peak values by about 9% for polar winter conditions and by about 13–17% for mid-latitude conditions.** This drop is 31–43% of the decrease required for EESC in mid-latitudes to return to the 1980 benchmark level, and about 18–19% of the decrease required for EESC in polar regions to return to the 1980 benchmark level[5]. The rate at which EESC is decreasing has slowed, in accordance with a slowdown of the decrease in tropospheric chlorine. The ranges given reflect the different methods for calculating EESC. Differences in halogen recovery levels from previous Assessments are also due to differences in assumed fractional release factors.

Tropospheric and stratospheric fluorine

While fluorine has no direct impact on stratospheric ozone, many fluorinated gases are strong greenhouse gases, and their emission is often related to the replacement of chlorinated substances regulated under the Montreal Protocol. For this reason, trends in fluorine are also assessed in this report.

- **The main sources of fluorine in the troposphere and in the stratosphere are CFCs, HCFCs, and HFCs. In contrast to total chlorine, total fluorine in the troposphere continued to increase between 2012 and 2016, at a rate of 1.7% yr^{-1}.** This increase shows the decoupling of the temporal trends in fluorine and chlorine due to the increasing emissions of HFCs (see **Chapter 2**). The total atmospheric-column abundance of inorganic fluorine, which is mainly stratospheric, has continued to increase at a rate of about 1% yr^{-1} over the period 2007–2016.

[5] As in previous Assessments, 1980 levels of EESC are used as a benchmark for recovery, although this value is somewhat arbitrary and some ozone loss has occurred prior to 1980. Also, recovery of EESC to 1980 values does not necessarily imply a recovery of ozone to 1980 levels, as other parameters, e.g. stratospheric circulation, may change.

Effect of ozone-depleting substances (ODSs) on climate

- **The total direct radiative forcing[6] of CFCs continues to be much higher than that of HCFCs.** However, radiative forcing from CFCs has dropped by about 7% since its peak in 2000 to about 250 mW m^{-2} in 2016 (approximately 13% that of CO_2), while radiative forcing from HCFCs increased to 58 mW m^{-2} in 2016 (approximately 3% that of CO_2). The total direct radiative forcing due to CFCs, HCFCs, halons, CCl_4 and CH_3CCl_3 was 327 mW m^{-2} in 2016 (approximately 16% that of CO_2).

- **CO_2-equivalent emissions[7] of CFCs and HCFCs were approximately equal in 2016.** The CO_2-equivalent emission from the sum of all CFCs or the sum of all HCFCs was approximately 0.8 Gt in 2016. The CO_2-equivalent emission from the sum of CFCs, HCFCs, halons, CCl_4 and CH_3CCl_3 was approximately 1.7 Gt in 2016.

Other gases that affect ozone and climate

- **Mole fractions of many other gases that affect both ozone and climate have changed since the previous Assessment.** The atmospheric abundance of methane has continued to increase following a period of stagnation in the early 2000s. The drivers of the changing trend are disputed. Nitrous oxide continues to grow relatively steadily in the atmosphere. The global mole fractions of the fluorinated species sulfur hexafluoride (SF_6), nitrogen trifluoride (NF_3), sulfuryl fluoride (SO_2F_2), and the perfluorocarbons (PFCs such as CF_4 and C_2F_6) have continued to grow. In contrast, the abundance of the sulfur-containing compounds sulfur dioxide (SO_2) and carbonyl sulfide (COS) has not changed substantially.

Chapter 2: Hydrofluorocarbons (HFCs)

The Montreal Protocol is an international agreement designed to heal the ozone layer. It outlines schedules for the phase-out of ozone-depleting substances (ODSs) such as chlorofluorocarbons (CFCs), hydrochlorofluorocarbons (HCFCs), chlorinated solvents, halons, and methyl bromide. As a result of this phase-out, alternative chemicals and procedures were developed by industry for use in many applications including refrigeration, air-conditioning, foam-blowing, electronics, medicine, agriculture, and fire protection. Hydrofluorocarbons (HFCs) were used as ODS alternatives in many of these applications because they were suitable substitutes and they do not contain ozone-depleting chlorine or bromine; in addition, most HFCs have smaller climate impacts per molecule than the most widely used ODSs they replaced. Long-lived HFCs, CFCs, and HCFCs, however, are all potent greenhouse gases, and concerns were raised that uncontrolled future use of HFCs would lead to substantial climate warming.

As a result of these concerns, HFCs were included as one group of greenhouse gases for which emissions controls were adopted by the 1997 Kyoto Protocol under the 1992 United Nations Framework Convention on Climate Change (UNFCCC). Consequently, developed countries (those listed in Annex I to this Convention, or "Annex I" Parties) supply annual emission estimates of HFCs to the UNFCCC.

Since the Kyoto Protocol only specified limits on the sum of all controlled greenhouse gases, emissions of HFCs were not explicitly controlled. However, following the Kyoto Protocol, some countries enacted additional controls specifically limiting HFC use based on their global warming potentials (GWPs). Ultimately the Kigali Amendment to the Montreal Protocol was agreed upon in 2016, and this Amendment supplies schedules for limiting the production and consumption of specific HFCs. Although the radiative forcing supplied by HFCs is currently small, this Amendment was designed to ensure that the radiative forcing from HFCs will not grow uncontrollably in the future. The Kigali Amendment will come into force at the start of 2019. HFC concentrations are currently monitored through atmospheric measurements. All HFCs with large abundances are monitored, as are most with small abundances.

[6] A measure of the change in net irradiance (incoming minus outgoing) at the tropopause.

[7] CO_2 equivalents are determined here by weighting emissions estimates by the global warming potential (GWP) of each gas, integrated over a 100-year time horizon.

Most HFCs that are emitted to the atmosphere are intentionally produced for use in a variety of applications that were once dependent on ODSs. An exception is HFC-23, which is emitted to the atmosphere primarily as a by-product of HCFC-22 production. HFC-23 is also unique in that it has a substantially longer atmospheric lifetime and higher GWP than nearly all other HFCs. As a result, the Kigali Amendment includes different control schedules for HFC-23 production than for other HFCs. To date, HFC-23 emissions have been partially abated in developed countries through regulations or voluntary measures and in developing countries with assistance from the UNFCCC's Clean Development Mechanism (CDM).

- **Atmospheric mole fractions of most currently measured HFCs are increasing in the global atmosphere at accelerating rates, consistent with expectations based on the ongoing transition away from use of ozone-depleting substances.**
    - **HFC-134a remained the most abundant HFC in the atmosphere**, reaching a global mean surface mole fraction of nearly 90 ppt in 2016. Its rate of increase averaged 5.6 ± 0.2 ppt yr^{-1} (7.3 ± 0.2 % yr^{-1}) during 2012–2016, which is about 0.6 ppt yr^{-1} faster than the mean increase for 2008–2012.
    - **The next four most abundant HFCs in 2016 were HFC-23, HFC-125, HFC-143a, and HFC-32.** Their global mean surface mole fractions in 2016 were 28.9 ppt, 20.4 ppt, 19.2 ppt, and 11.9 ppt, respectively. Mole fractions of these HFCs increased during 2012–2016 by an average of 1.0 ppt yr^{-1} for HFC-23, 2.1 ppt yr^{-1} for HFC-125, 1.5 ppt yr^{-1} for HFC-143a, and 1.6 ppt yr^{-1} for HFC-32; for all of these gases, these rates are faster than the average growth rates reported for 2008–2012 in the last Assessment.
    - **Global mole fractions of most HFCs increased through 2016 at rates similar to those projected in the baseline scenario of the last Assessment**, despite the fact that this scenario was created nearly a decade ago. The HFCs for which mole fractions are increasing substantially less rapidly than originally projected include HFC-152a, HFC-365mfc, and HFC-245fa.
- **Radiative forcing from measured HFCs continues to increase; it currently amounts to 1% of the total forcing from all long-lived greenhouse gases.** The radiative forcing arising from measured atmospheric mole fractions of HFCs totaled 0.030 W m^{-2} in 2016, up by 36% from 0.022 W m^{-2} in 2012; HFC-134a accounted for 47% of this forcing in 2016, while the next largest contributors were HFC-23 (17%), HFC-125 (15%) and HFC-143a (10%). Total HFC radiative forcing in 2016 accounted for ~10% of the 0.33 W m^{-2} supplied by ODSs (**see Chapter 1**), and 1.0% of the 3 W m^{-2} supplied by all long-lived GHGs combined, including CO_2, CH_4, N_2O, ODSs and HFCs.
- **Global emissions of nearly all measured HFCs continue to increase; they currently amount to ~1.5% of total emissions from all long-lived greenhouse gases (CO_2, CH_4, N_2O, and long-lived halocarbons) in CO_2-equivalent emissions.** As derived from atmospheric observations, total emissions of HFCs increased by 23% from 2012 to 2016 and summed to 0.88 (± 0.07) $GtCO_2$-eq yr^{-1} in 2016; this increase outpaced decreases in CO_2-eq emissions from CFCs and HCFCs. These CO_2-eq HFC emissions stem primarily from four gases: HFC-134a (34% of total), HFC-125 (24% of total), HFC-23 (18% of total), and HFC-143a (16% of total). HFC CO_2-eq emissions were comparable to those of CFCs (0.8 ± 0.3 $GtCO_2$-eq yr^{-1}) and HCFCs (0.76 ± 0.11 $GtCO_2$-eq yr^{-1}) in 2016.
- **HFC emissions estimated from the combination of inventory reporting and atmospheric observations indicate that the HFC emissions originate from both developed and developing countries**. Large differences are observed between global total emissions derived from atmospheric observations and the totals reported to the UNFCCC. These differences arise primarily because only developed (Annex I) countries are obligated to report HFC emissions to the UNFCCC. When summed, these reported HFC emissions account for less than half of the global total inferred from observations (as CO_2-eq emissions).

- **Annual global emissions of HFC-23 derived from atmospheric measurements have varied substantially in recent years. This variability is mostly consistent with expectations based on reported HCFC-22 production and reported and estimated HFC-23 emissions.** This long-lived HFC is emitted to the atmosphere primarily as a by-product of HCFC-22 production. HFC-23 emissions, after reaching a low of ~10 Gg yr^{-1} (0.13 $GtCO_2$-eq yr^{-1}) 2009–2010, owing in part to destruction in developing countries facilitated under the UNFCCC's Clean Development Mechanism (CDM), increased and subsequently peaked at ~14 Gg yr^{-1} (0.18 $GtCO_2$-eq yr^{-1}) in 2013–2014. The mean global emission rate over 2013–2014 is slightly higher than that derived for 2005–2006, when CDM-facilitated destruction had yet to be fully implemented. Global emissions estimated from observations for 2015 and 2016 dropped below the 2013–2014 peak; emissions in 2016 were 12.3 ± 0.7 Gg yr^{-1} (0.16 $GtCO_2$-eq yr^{-1}), or approximately 2 Gg yr^{-1} below those in 2014. New controls put in place under the Kigali Amendment mandate HFC-23 by-product destruction, to the extent practicable, beginning in 2020. These controls are expected to limit future emissions and thus slow or reverse atmospheric concentration increases of this potent greenhouse gas.

- **Some next-generation substitute chemicals with very low GWPs (unsaturated HCFCs and unsaturated HFCs, also known as hydrofluoroolefins, or HFOs) have now been detected in ambient air, consistent with the transition to these compounds being underway**. Unsaturated HFCs and HCFCs are replacement compounds for some long-lived HCFCs and HFCs. Because unsaturated HFCs have short atmospheric lifetimes (days) and GWPs typically less than 1 they are not included as controlled substances in the Kigali Amendment to the Montreal Protocol. Very low mole fractions (typically below 1 ppt) of two unsaturated HFCs (HFC-1234yf and HFC-1234ze*(E)*) have been measured at a continental background European site.

- **Global adherence to the HFC phasedown schedule of the 2016 Kigali Amendment to the Montreal Protocol would substantially reduce future projected global HFC emissions.** Emissions are projected to peak before 2040 and decline to less than 1 $GtCO_2$-eq yr^{-1} by 2100. Only marginal increases are projected for CO_2-eq emissions of the low-GWP alternatives despite substantial projected increases in their emission mass. The estimated avoided HFC emissions as a result of this Amendment is 2.8–4.1 $GtCO_2$-eq yr^{-1} emissions by 2050 and 5.6–8.7 $GtCO_2$-eq yr^{-1} by 2100. For comparison, total CH_4 emissions in 2100 are projected to be 7.0 and 25 $GtCO_2$-eq yr^{-1} in the RCP-6.0 and RCP-8.5 scenarios, respectively, and total N_2O emissions in 2100 are projected to be 5.0 and 7.0 $GtCO_2$-eq yr^{-1} in these same scenarios.

- **The 2016 Kigali Amendment to the Montreal Protocol, assuming global compliance, is expected to reduce future radiative forcing due to HFCs by about 50% in 2050 compared to the forcing from HFCs in the baseline scenario.** Currently (in 2016), HFCs account for a forcing of 0.025 W m^{-2} not including 0.005 from HFC-23; forcing from these HFCs was projected to increase up to 0.25 W m^{-2} by 2050 (excluding a contribution from HFC-23) with projected increased use and emissions in the absence of controls. With the adoption of the Kigali Amendment, a phasedown schedule has been agreed for HFC production and consumption in developed and developing countries under the Montreal Protocol. With global adherence to this Amendment in combination with national and regional regulations that were already in place in, e.g., Europe, the USA, and Japan, along with additional recent controls in other countries, future radiative forcing from HFCs is projected to reach 0.13 W m^{-2} by 2050 (excluding HFC-23), or about half the forcing projected in the absence of these controls.

- **The Kigali Amendment and national and regional regulations are projected to reduce global average warming in 2100 due to HFCs from 0.3–0.5°C in a baseline scenario to less than 0.1°C.** If the global production of HFCs were to cease in 2020, the surface temperature contribution of HFC emissions would stay below 0.02°C for the whole 21st century. The magnitude of the avoided temperature increase due to the provisions of the Kigali Amendment is substantial in the context of the 2015 UNFCCC Paris Agreement, which aims to limit global temperature rise to well below 2.0°C above pre-industrial levels and to pursue further efforts to limit the temperature increase to 1.5°C.

- **Improvements in energy efficiency in refrigeration and air-conditioning equipment during the transition to low-GWP alternative refrigerants can potentially double the climate benefits of the HFC phasedown of the Kigali Amendment.** The conversion from equipment using HFC refrigerants with high GWPs to refrigerants with lower GWPs, which will most likely result from the Kigali Amendment, provides an opportunity to consider other technological improvements that offer additional climate benefits. The total climate impact related to refrigerant use and associated emissions is not only associated with the radiative properties and lifetime of the refrigerant, but also with CO_2 emissions resulting from the energy used by the equipment over its entire life cycle. The use of a refrigerant with a lower GWP than the currently-used HFCs (i.e., following the Kigali Amendment) offers the opportunity to redesign equipment and improve its energy efficiency. For example, a 30% improvement in the energy efficiency of the global stock of mini-split air conditioners (the most widely used air conditioning systems today) in 2030 would provide a climate benefit comparable to replacing the mix of current HFC refrigerants commonly used in this application (which have GWPs averaging about 2,000) with a mix of alternatives that have GWPs of less than about 5 to about 700. An energy efficiency improvement of 30% is estimated to be technically and economically feasible and cost-effective in many economies.

- **Some HFCs degrade in the environment to produce trifluoroacetic acid (TFA), a persistent toxic chemical. The environmental effects of this source of TFA are currently small and are expected to remain negligible over the next decades.** Atmospheric degradation of HFC-1234yf, a replacement compound for some long-lived HCFCs and HFCs, produces TFA. Potential impacts beyond a few decades of this TFA source could require future evaluation due to the environmental persistence of TFA and uncertainty in future emissions of HFC-1234yf and other HFCs that produce TFA upon degradation.

- **Improvements in the understanding of reaction rates have been incorporated into revised lifetime estimates for saturated and unsaturated HFCs.** Most of these changes are small, although lifetimes of HFC-245cb ($CF_3CF_2CH_3$), octafluorocyclopentene (*cyclo*-$CF{=}C_4F_7$-), *(E)*-HFO-1214yc (*(E)*-$CF_3CH{=}CHCF_3$), and *(E)*-HFO-1438mzz (*(E)*-$CF_3CH{=}CHC_2F_5$) were noticeably changed because the relevant reaction rate information has become available for the first time. Lifetimes for a few HFCs considered here remain estimates based on either analogy with similar compounds or structure–activity relationships.

Chapter 3: Update on Global Ozone: Past, Present, and Future

This chapter deals with the evolution of global ozone outside of the polar regions. The increase of ozone-depleting substance (ODS) concentrations caused the large ozone decline observed from the early satellite era (circa 1980) to the mid-1990s. Since the late 1990s, concentrations of ODSs have been declining due to the successful implementation of the Montreal Protocol. Ozone concentrations show latitudinally dependent increases in the upper stratosphere for the 2000–2016 period; changes in other parts of the stratosphere are not yet statistically significant. A new suite of model simulations confirms previous results for the upper stratosphere that about half of the observed increase is associated with declining ODSs. Ozone column trends are likewise positive but not generally statistically significant. Their overall evolution is, however, compatible with the decline in equivalent effective stratospheric chlorine (EESC).

Over the next decades, we expect increasing global mean stratospheric ozone columns, as ODSs continue to decline. Emissions of greenhouse gases (GHGs), especially carbon dioxide (CO_2), methane (CH_4), and nitrous oxide (N_2O), will also affect the evolution of global stratospheric ozone, particularly in the second half of the 21st century, when ODS concentrations are expected to be low.

Past changes in total column ozone

- **Ground- and space-based observations indicate that there is no statistically significant trend in near-global (60°S–60°N) column ozone over the 1997–2016 period.** These datasets show an increase of between 0.3% and

1.2% decade^{-1} since 1997, with uncertainties of about 1% decade^{-1}. These findings are consistent with our understanding of the processes that control ozone.

  - In middle and high latitudes, the increase in total column ozone expected to arise from the 15% decline in EESC since 1997 is small (~1% decade^{-1}) relative to the large, dynamically forced year-to-year variations of ~5%.

  - In the tropics, where halogen-driven ozone loss is small in the lower stratosphere, total column ozone has not varied significantly with ODS concentrations, except under conditions of high volcanic aerosol loading (e.g., from the eruption of Mt. Pinatubo in 1991).

- Outside the tropics, present-day (2014–2017) total ozone columns from ground-based and space-based observations remain lower than 1964–1980 column ozone by

  - about 2.2% for the near-global average (60°S–60°N)

  - about 3.0% in the Northern Hemisphere mid-latitudes (35°N–60°N)

  - about 5.5% in the Southern Hemisphere mid-latitudes (35°S–60°S)

  These values are essentially the same as in the last Assessment, given uncertainties associated with natural variability and instrumental accuracy. The larger depletion in the Southern Hemisphere is linked to the Antarctic ozone hole.

Past changes in ozone profiles

Additional and improved datasets and focused studies evaluating trend uncertainties have strengthened our ability to assess ozone profile changes. Analysis of data from the upper stratosphere shows increases that are consistent with those suggested in the last Assessment. There is some evidence for a dynamically driven decrease in ozone in the lower stratosphere from 2000 to 2016, but robust trends have not been identified for this region. New chemistry–climate model (CCM) simulations that include realistic time variations of GHG and ODS concentrations are analyzed using the same trend model as for the observations; this allows attribution of changes in ozone to different processes.

- **Measurements show increases of ozone in the upper stratosphere over the period 2000-2016.** Following a large decline of 5 to 7% decade^{-1} through the 1980s and middle 1990s, upper stratospheric ozone has increased by 1 to 3% decade^{-1} since 2000. The largest confidence is in northern mid-latitudes, where the positive trend is statistically significant between 35- and 45-km altitude. Confidence in trends in the tropics and southern mid-latitudes is not as high due to larger discrepancies between trends from individual measurement records.

- **Model simulations attribute about half of the observed upper stratospheric ozone increase after 2000 to the decline of ODSs since the late 1990s.** The other half of the ozone increase is attributed to the slowing of gas-phase ozone destruction cycles, which results from cooling of the upper stratosphere caused by increasing GHGs.

- **There is some evidence for a decrease in lower stratospheric ozone from 2000 to 2016.** This decrease is most consistent across datasets in the tropics, but is not statistically significant in most analyses. Much of the apparent decline was reversed by an abrupt increase in ozone in 2017, indicating that longer records are needed to robustly identify trends in this region. Model simulations attribute the variations in lower stratospheric ozone over this period primarily to dynamical variability.

- **Assessing the consistency between stratospheric profile trends and total column ozone trends requires changes in tropospheric ozone to be well quantified.** A recent assessment of tropospheric column ozone trends,

however, shows large disagreements in the sign and magnitude of the observed trends over the past decade and a half.

Future ozone changes

The baseline climate change scenario used in the new model simulations differs from the previous Assessment, because new emissions scenarios were used. The key drivers of future ozone levels continue to be declining ODS concentrations, upper stratospheric cooling because of increased GHGs, and the possible strengthening of the Brewer-Dobson circulation from climate change. The new emissions scenarios lead to slight differences in the relative contributions of these processes in various latitude and altitude regions and a delay in return dates for ozone compared to the previous Assessment.

- **Estimated dates of return of total column ozone to 1980 values are generally a few years later than given in the previous Assessment and vary considerably between scenarios.** For the baseline scenario (RCP-6.0), they are:
  - around mid-century for near-global mean annually averaged ozone;
  - most likely before the middle of the century (~2035) for annually averaged Northern Hemisphere mid-latitude ozone;
  - around mid-century for annually averaged Southern Hemisphere mid-latitude ozone.
- **CO_2, CH_4, and N_2O will be the main drivers of 60°S–60°N stratospheric ozone changes in the second half of the 21st century.** These gases impact both chemical cycles and the stratospheric overturning circulation, with a larger response in stratospheric ozone associated with stronger climate forcing. By 2100, the stratospheric column is expected to decrease in the tropics by about 5 DU for RCP-4.5 and about 10 DU for RCP-8.5 relative to 1980 values, with the net total column change projected to be smaller (about 5 DU) because of offsetting increases in tropospheric ozone.
- **Given that ODS levels are expected to decline slowly in coming years, a large enhancement of stratospheric sulfate aerosol in the next decades would result in additional chemical ozone losses.** Possible sources of additional stratospheric sulfate aerosol include volcanic eruptions (like Mt. Pinatubo in 1991) and geoengineering. Even when ODS levels have declined substantially, a large injection of volcanic halogens into the stratosphere could drive substantial ozone losses in the presence of aerosol surfaces.
- **Future ozone recovery and the projected strengthening of the Brewer-Dobson circulation (BDC) are likely to lead to increases in the stratosphere-to-troposphere (STT) flux of ozone via increases in mid-latitude lower stratospheric ozone and mass flux.** The net impact of increased STT flux on the tropospheric ozone burden is highly model and scenario dependent. Most studies suggest it will be small relative to other factors, such as concurrent changes in precursor emissions, temperature, and water vapor.

Chapter 4: Update on Polar Ozone: Past, Present, and Future

The chemical and dynamical processes controlling polar ozone are well understood. Polar ozone depletion is fundamentally driven by anthropogenic chlorine and bromine, with the severity of the chemical loss each year in both hemispheres strongly modulated by meteorological conditions (temperatures and winds), and, to a lesser extent, by the stratospheric aerosol loading and the solar cycle. As noted in prior Assessments, the stratospheric halogen concentration resulting from the emission of ozone-depleting substances (ODSs) reached its peak in the polar regions around the turn of the century and has been gradually declining since then in response to actions taken under the Montreal Protocol and its Amendments and adjustments. Early signs of ozone recovery are now beginning to appear in the Antarctic; as the

observational record lengthens, clearer ozone hole recovery trends are expected to emerge against the background of natural variability. Nevertheless, the Antarctic ozone hole will continue to be a recurring phenomenon until the middle of the century. The Arctic is more dynamically variable, precluding identification of a significant increase in Arctic ozone, and cold conditions conducive to substantial ozone loss may still occur in a particular year in the coming decades. New chemistry–climate model (CCM) projections largely confirm previous studies that in both hemispheres, spring polar total column ozone will return to 1980 historical levels in the coming decades, albeit with a delay of a few years due to updated future ODS and greenhouse gas (GHG) emissions scenarios.

Observed changes in polar ozone

- **The characteristics of the October Antarctic ozone hole in the years since 2014 have generally been within the range observed since the early 1990s.** In 2015, however, the ozone hole was particularly large and long-lasting, as a result of a cold and undisturbed polar stratospheric vortex. Aerosols from the Calbuco volcanic eruption in April 2015 are also believed to have contributed to the large ozone hole observed that year. Conversely, in 2017, the Antarctic ozone hole was very small due to a warm and unusually disturbed polar vortex.

- **Several lines of evidence have started to emerge indicating an increase in Antarctic stratospheric ozone during September.** Statistically significant trends since the year 2000 have now been identified showing an increase in observed ozone and a decrease in ozone hole size and depth. Although accounting for the large degree of natural variability is challenging, the weight of evidence from statistical analyses and modeling studies suggests that the decline in ODSs made a substantial contribution to these trends.

- **In the Arctic, the exceptionally low ozone abundances of spring 2011 have not been observed again in the last four years.** Arctic stratospheric springtime ozone is dominated by large year-to-year dynamically induced variability of the polar vortex, with severe ozone loss occurring in very cold years, such as 2011. Extreme meteorological conditions in the early 2015/2016 winter led to rapid ozone loss, but a sudden stratospheric warming (SSW) at the beginning of March 2016 curtailed the chemical processes which lead to ozone destruction about a month earlier than in 2011, keeping ozone above record low levels. Arctic ozone trends are small compared to the dynamical variability, and thus a recovery trend remains undetectable in observations over the 2000–2016 period.

Understanding of factors controlling polar ozone

- **Observations in the Arctic winter have demonstrated that large nitric acid trihydrate (NAT) particles are a regularly occurring phenomenon in the lower stratosphere.** This knowledge improves our understanding of polar stratospheric cloud (PSC) formation and denitrification, which is important for catalytic ozone loss cycles.

- **Bromine-containing very short-lived substances (VSLSs) of natural origin have an important impact on the stratospheric halogen loading and consequently on stratospheric ozone loss in the polar regions.** The inclusion of additional stratospheric bromine from VSLSs is necessary for models to produce a realistic simulation of polar ozone loss.

- **The effects of tropospheric dynamical forcing in winter on Arctic polar ozone are now better quantified.** Ozone depletion in northern winters with SSWs is on average two-thirds less than in winters without SSWs, with depletion ending about one month earlier in the year. Such an SSW was a major influence on ozone levels observed in the Arctic winter of 2015/16.

- **Polar ozone in the middle and upper stratosphere varies by 10–15% from year to year due to energetic particle precipitation (EPP) related to solar variability.** Satellite observations and model results show that NO_y produced in the aurora is transported from the thermosphere down into the stratosphere in each winter, leading to stratospheric ozone decreases modulated by geomagnetic activity. The resulting variation in total column

ozone is small (a few percent) but can persist for 2–3 years. Full EPP-effects were not included in current assessment models.

- **Model simulations show that the Montreal Protocol and its Amendments and adjustments have already brought about substantial ozone benefits.** In the polar regions of both hemispheres, much larger ozone depletion than currently observed has been avoided through implementation of the Protocol.

Future evolution of polar ozone

- **Updated CCM projections based on full compliance with the Montreal Protocol and assuming the baseline estimate of the future evolution of GHGs (RCP-6.0) have confirmed that the Antarctic ozone hole is expected to gradually close, with springtime total column ozone returning to 1980 values shortly after mid-century (about 2060).** The timing of the recovery of the ozone hole will not be significantly affected by increases in GHG concentrations. There are no substantial differences between Antarctic total ozone columns at the end of this century for the various GHG scenarios (Representative Concentration Pathways [RCPs]).

- **The timing of the recovery of Arctic total ozone in spring will be affected by anthropogenic climate change. Based on full compliance with the Montreal Protocol and assuming the baseline estimate of the future evolution of GHGs (RCP-6.0), Arctic springtime total ozone is expected to return to 1980 values before mid-century (2030s).** New model simulations confirm that in the Arctic, enhanced GHG concentrations cause an earlier return of total column ozone to historical values than a reduction of ODSs alone.

- **In the second half of the 21st century CO_2, CH_4, and N_2O will be the dominant drivers of Arctic ozone changes, assuming full compliance with the Montreal Protocol.** These gases impact both chemical cycles and the stratospheric overturning circulation, with a larger response in stratospheric ozone associated with stronger climate forcing. By 2100, the stratospheric ozone column is expected to not only recover but to exceed 1960–1980 average values in the Arctic, with springtime Arctic ozone being higher by about 35 DU for RCP-4.5 and about 50 DU for RCP-8.5.

- **In the coming decades, substantial Arctic ozone loss will remain possible in cold winters as long as ODS concentrations are well above natural levels.** Increasing GHG concentrations may cool the lower stratosphere and lead to enhanced formation of polar stratospheric clouds (PSCs) early in the Arctic winter. However, one recent study indicates that no corresponding cooling is expected in March, which is the month when persistent low temperatures lead to large chemical ozone losses.

Chapter 5: Stratospheric Ozone Changes and Climate

Since the 2014 Ozone Assessment, new research has better quantified the impact of stratospheric ozone changes on climate. Additional model and observational analyses are assessed, which examine the influence of stratospheric ozone changes on stratospheric temperatures and circulation, tropospheric circulation and composition, surface climate, the oceans, and sea ice. The new results support the main conclusions of the previous Assessment; the primary advances are summarized below.

Stratospheric temperatures

- **New estimates of satellite-observed stratospheric temperature changes show net global stratospheric cooling of around 1.5 K (at 25–35 km), 1.5 K (at 35–45 km), and 2.3 K (at 40–50 km) between 1979 and 2005, with differences between datasets of up to 0.6 K.**

    - There are now better estimates of observed stratospheric temperature trends than were available during the last Assessment. Two datasets from satellite measurements have been re-processed and now show greater consistency in long-term temperature trends in the middle and upper stratosphere.

- Satellite temperature records show smaller stratospheric cooling rates over 1998–2015 compared to 1979–1997, consistent with the observed differences in stratospheric ozone trends during these periods.
- Global average temperature in the lower stratosphere (13–22 km) cooled by about 1 K between 1979 and the late 1990s but has not changed significantly since then.

- **In the lower stratosphere (13–22 km), ozone trends were the major cause of the observed cooling between the late 1970s and the mid-1990s. In the middle and upper stratosphere, however, increases in long-lived greenhouse gases played a slightly larger role than ozone changes in cooling trends over this period.** Ozone recovery will continue to play an important role in future stratospheric temperature trends.
  - There is now improved understanding of the causes of stratospheric temperature trends and variability. For the upper stratosphere (40–50 km), new studies suggest that one-third of the observed cooling over 1979–2005 was due to ozone-depleting substances (ODSs) and associated ozone changes, while two-thirds was due to other well-mixed greenhouse gases.
  - Chemistry–climate models show that the magnitude of future stratospheric temperature trends is dependent on future greenhouse gas concentrations, with most greenhouse gas scenarios showing cooling in the middle and upper stratosphere over the 21st century. The projected increase in global stratospheric ozone during this period would offset part of the stratospheric cooling due to increasing greenhouse gases.

Stratospheric overturning circulation

- **There are indications that the overturning circulation in the lower stratosphere has accelerated over the past few decades.**
  - Observations of the latitudinal profile of lower stratospheric temperature trends and changes in constituents show that tropical upwelling in the lower stratosphere has strengthened over the last ~30 years, in qualitative agreement with model simulations and reanalysis datasets.
  - New studies using measurements provide evidence for structural changes in the stratospheric overturning circulation which is comprised of a strengthening in the lower stratosphere and a weakening in the middle and upper stratosphere.
  - According to models, in addition to well-mixed greenhouse gases, changes in ODSs (and associated changes in ozone) are an important driver of past and future changes in the strength of the stratospheric overturning circulation, notably the increase in downwelling over the Antarctic over the late 20th century.
  - Estimates of externally forced long-term changes in the stratospheric overturning circulation from observations remain uncertain, partially due to internal variability.
  - Models project future increases in stratosphere–troposphere exchange of ozone as a consequence of a strengthening of the stratospheric overturning circulation and stratospheric ozone recovery.

Impacts on the troposphere, ocean, and sea ice

- **New research supports the findings of the 2014 Ozone Assessment that Antarctic ozone depletion was the dominant driver of the changes in Southern Hemisphere tropospheric circulation in austral summer during the late 20th century, with associated weather impacts.**

- Over the period 1970 to 2000, tropospheric jets in the Southern Hemisphere shifted poleward and strengthened, the Southern Annular Mode (SAM) index increased, and the southern edge of the Hadley Cell expanded poleward. Since 2000, the SAM has remained in a positive phase.
- For austral summer, most model simulations show a larger contribution to these trends from Antarctic ozone depletion compared to increases in well-mixed greenhouse gases during the last decades of the 20th century. During other seasons, the contribution of ozone depletion to circulation changes is comparable to that from well-mixed greenhouse gases.
- Paleoclimate reconstructions of the SAM index suggest that the current period of prolonged positive summer SAM conditions is unprecedented in at least the past 600 years.
- No robust link between stratospheric ozone depletion and long-term Northern Hemisphere surface climate has been established; there are indications that occurrences of extremely low springtime ozone amounts in the Arctic may have short-term effects on Northern Hemisphere regional surface climate.

- **Changes in tropospheric weather patterns driven by ozone depletion have played a role in recent temperature, salinity, and circulation trends in the Southern Ocean, but the impact on Antarctic sea ice remains unclear.**
  - Progress has been made since the last Assessment in understanding the physical processes involved in the Southern Ocean response to ozone depletion, which is now believed to entail a fast surface cooling followed by a slow long-term warming.
  - Modeling studies indicate that ozone depletion contributes to a decrease in Antarctic sea ice extent and hence cannot explain the observed sea ice increase between 1979 and 2015. This is in agreement with the conclusions of the previous Assessment. However, in general, climate models still cannot reproduce the observed Antarctic sea ice trends since 1979, which limits the confidence in the modeled sea ice response to ozone depletion.

- **New observation-based analyses indicate that a causal link between the strength of the Southern Ocean carbon sink and ozone depletion cannot be established, in contrast to earlier suggestions.**
  - New observation-based analyses confirmed the previously reported slowdown of the carbon sink between the 1980s and early 2000s but also revealed a remarkable reinvigoration of the carbon sink since then. The new results indicate that atmospheric circulation changes (whether driven by ozone depletion or not) have not had a considerable impact on the net strength of the Southern Ocean carbon sink.

Montreal Protocol climate impacts

- **New studies since the 2014 Ozone Assessment have identified that future global sea level rise of at least several centimeters has been avoided as a result of the Montreal Protocol.** This would have arisen from thermal expansion of the oceans associated with additional global warming from unregulated ozone depleted substances emissions.

Chapter 6: Scenarios and Information for Policymakers

In the sections below, we note the significance of various improvements in our understanding concerning actions related to the Montreal Protocol and its Amendments that could alter the recovery of the ozone layer and/or impact Earth's climate. As in previous Assessments, we use equivalent effective stratospheric chlorine (EESC) as a proxy for the amount of stratospheric ozone depletion caused by ozone-depleting substances (ODSs) that contain chlorine and/or bromine and reside in the atmosphere for more than a few months. The return of EESC to 1980 values is used as a metric to compare

the effects of different future scenarios of production and emission of ozone-depleting gases on ozone layer recovery. In this chapter, we also use 2-D model simulations to estimate changes in future ozone depletion for these different scenarios. (Note that 3-D model projections of global and polar ozone and analyses of expected recovery dates are presented in Chapters 3 and 4. These calculations include changes in greenhouse gas levels and in atmospheric transport and are not expected to be equivalent to the EESC recovery dates). Our ability to predict future changes in the ozone layer is limited more by uncertainties in future levels of CO_2, CH_4, and N_2O than by uncertainties in the levels of ODSs, especially as we approach the 1980 values of EESC. Indeed, ozone levels in some regions of the atmosphere could exceed natural levels, due to climate change, with possible consequences to humans and natural ecosystems, assuming natural levels represent a harmonious balance. The influence of CO_2 occurs through its role in the climate system as a driver of change in temperature and atmospheric circulation. The influences of CH_4 and N_2O occur primarily through their roles as chemical reagents in the atmosphere. ODSs themselves are greenhouse gases, and their influence on climate and ozone layer depletion are intricately intertwined, even though we note them separately for clarity of presentation. Lastly, note that the various additional actions discussed below impact future ozone to a much smaller degree than what has already been accomplished by the Montreal Protocol.

Post-Kigali information of interest and concern

- **The Kigali Amendment to the Montreal Protocol, along with regional and national regulatory and voluntary actions taken before Kigali entered into force, is expected to substantially limit future climate forcing by HFCs.** Projections of HFC emissions that include compliance with Kigali Amendment control measures suggest that the radiative forcing (a metric for global warming) from HFCs, currently 0.025 W m^{-2} (not including HFC-23), will reach 0.13 W m^{-2} by 2050, about half as high as that projected without the Kigali Amendment and prior national and regional regulation. The estimated benefit of these actions is 2.8–4.1 Gt CO_2-eq. yr^{-1} of avoided Global Warming Potential (GWP)-weighted emissions by 2050. The projected surface temperature contribution from HFCs (excluding HFC-23) reduces from 0.3–0.5 °C to less than 0.1 °C in 2100 due to entry into force of the Kigali Amendment.

- **Options are available to further decrease the climate impact of HFCs.** Use of commercially available low-GWP alternatives in place of high-GWP HFCs in refrigeration and air-conditioning equipment, thermal insulating foam, metered-dose inhalers, fire protection, and miscellaneous HFC applications during the phasedown would further reduce climate change. Additional benefits would be gained by such actions via development of more energy-efficient equipment and thermal insulating foam that use these low-GWP replacements.

- **Sustained increases in anthropogenic chlorinated very short-lived substances (VSLSs Cl) emissions, as seen for CH_2Cl_2 in the 2000s, would decrease stratospheric ozone levels in the coming decades. However, observed growth rates of CH_2Cl_2 continue to be highly variable, and there is insufficient information to confidently predict future concentrations.** If the growth in emission rates seen during the first decade of this century continues, CH_2Cl_2 is projected to deplete as much column ozone between 2020 and 2060 as that by the controlled ODSs emitted during that period. However, such large growth projections do not account for a more recent reduction in the CH_2Cl_2 growth rate, nor have they been shown to be consistent with expectations for global demand over the coming decades. Any control of CH_2Cl_2 production and consumption under the Montreal Protocol would be rapidly effective, since this VSLS will be cleansed out of the stratosphere within a few years.

Ozone-depleting substances (ODSs) and equivalent effective stratospheric chlorine (EESC)

Below, we discuss potential changes in the projected trajectory of ozone depletion and EESC that result from improvements in our understanding of the emissions or other characteristics of individual gases or groups of gases. We reference these potential changes to the so-called baseline scenario—which should be considered a plausible future pathway for these gases. The baseline scenario for ODSs is developed from atmospheric concentration observations, combined with

estimates of the amounts of ODSs in existing equipment or other products containing ODSs, referred to as banks. The 2018 baseline scenario for HFCs takes into account global control measures introduced by the Kigali Amendment and other regional and national actions. For all baseline scenarios, we assume that the long-lived greenhouse gases N_2O, CH_4, and CO_2 follow the Representative Concentration Pathway (RCP) 6.0 scenario. Note that for some of the metrics the combined consequence of these gases is generally not simply the addition of each of the changes. It is also important to recognize that the return date of EESC to 1980 levels is quite sensitive to any change in EESC concentration because of the relatively small rate at which EESC is projected to decline in the middle of this century.

- **Global emissions of CFC-11 derived from atmospheric observations show an increase in recent years that is not consistent with our understanding of release from its banks and suggests new global production that is not reported to the United Nations Environment Programme (UN Environment). If total emissions of CFC-11 were to continue at levels experienced from 2002–2016 (67 Gg yr^{-1}), the return of mid-latitude and polar EESC to the 1980 value would be delayed by about seven years and 20 years, respectively**. Such an assumption of continuing emissions implicitly assumes that the unidentified emissions will grow to counteract the expected decline in bank emissions.

- **Emissions from current ODS banks continue to be a slightly larger future contribution than ODS production to ozone layer depletion over the next four decades, assuming maximum production levels allowed by the Montreal Protocol.** Future business-as-usual emissions from HCFCs and from banks of CFCs and banks of halons are each projected to contribute roughly comparable amounts to EESC in the next few decades.

- **Elimination of future production of methyl bromide (CH_3Br) for quarantine and pre-shipment (QPS) applications, not controlled by the Montreal Protocol, would accelerate the return of mid-latitude EESC to 1980 levels by about a year**. Production for QPS use has remained relatively stable over the last two decades and now constitutes almost 90% of the reported production of CH_3Br since emissions from other uses have declined dramatically. Non-QPS applications of CH_3Br were completely phased out in 2015, except for approved critical use exemptions, which have declined by a factor of ~30 since 2005.

- **If CCl_4 emissions continue to decline at the rate observed over the last two decades of 2.5% yr^{-1}, future concentrations will be about 14 ppt higher in 2050 than projected in the previous Assessment**. CCl_4 emissions inferred from atmospheric observations continue to be much greater than those assumed from feedstock uses as reported to UN Environment; by-product emissions from chloromethane and perchloroethylene plants and fugitive emissions from the chlor-alkali process have been quantified as significant contributors to these additional emissions. Elimination of all CCl_4 emissions in 2020 would accelerate the return of mid-latitude EESC to 1980 levels by almost three years compared to the baseline scenario of a continued emissions decrease of 2.5% yr^{-1}. Alternatively, if future emissions do not decline but remain at the current level, the return of mid-latitude EESC to 1980 levels would be delayed almost two years.

- **The return of mid-latitude EESC to 1980 levels is estimated to be delayed by almost two years compared to the previous Assessment, due primarily to the higher projected future concentrations of CCl_4.** The mid-latitude EESC change from CCl_4 alone leads to a delay larger than two years, but future CH_3Br baseline projections are now lower than in the previous Assessment and offset some of the effect from CCl_4. The delay in polar EESC returning to 1980 levels is slightly more than two years when compared with the previous Assessment. A new EESC formalism alters the time evolution of EESC and dates when EESC returns to 1980 levels, but it has little effect on the relative impacts of the various alternative future scenarios. When compared with the previous Assessment's EESC formalism, the new EESC formalism leads to a projected EESC return to the 1980 level 11 years later at mid-latitudes and by less than two years later at polar latitudes.

- **Reducing anthropogenic emissions of N_2O from those in RCP-6.0 to the Concerted Mitigation scenario[8] would have a similar positive impact on stratospheric ozone over the next four decades as eliminating production of HCFCs from 2020. This N_2O emissions reduction would have a larger benefit to climate over 2020–2060 than the sum of all the options for controlled ODSs considered (based on GWP-weighted emissions).**

Updates on the climate impact of gases controlled by the Montreal Protocol

- **Future emissions of HFC-23, a potent greenhouse gas and a by-product of HCFC-22 production, are expected to be limited by the Kigali Amendment**, which mandates the destruction of HFC-23 to the extent practicable. Globally, HCFC-22 is currently produced in roughly equal quantities for controlled emissive uses, which are declining, and for the uncontrolled feedstock uses, which grew rapidly over the last few decades but have recently stabilized. Future emission trends will largely depend on the extent to which HFC-23 is destroyed by HCFC-22 production facilities and the amount of HCFC-22 produced.

- **Future emissions of HFCs, HCFCs, and CFCs contribute approximately 60, 9, and 3 cumulative Gt CO_2-equivalent emissions, respectively, from 2020 to 2060 in the baseline scenario.** Of the 60 Gt CO_2-eq emissions from HFCs, 53 arise from future production. For reference, cumulative CO_2 emissions from fossil fuel usage are projected over this time period to be 1,700 Gt CO_2 in the RCP-6.0 scenario and 760 Gt CO_2 in the RCP-2.6 scenario. The total radiative forcing from CFC and HCFCs and their HFC replacements is projected to continue to increase gradually for the next decade or two. After that point, the ODS and HFC restrictions of the Montreal Protocol, if adhered to, ensure a continued decline in total RF from ODSs and their replacements through the rest of the century.

- **Global warming potentials, global temperature change potentials, and ozone depletion potentials of hundreds of HCFCs are presented, most for the first time in an assessment.** This comprehensive assessment includes all the HCFCs listed under Annex C, Group I of the Montreal Protocol, many of which did not have estimated GWPs at the time of the signing of the Kigali Amendment.

Updates on impacts of climate gases and other processes on future stratospheric ozone

In this section, we summarize potentially important impacts on the future of the ozone layer that could result from anthropogenic activity not associated with ODS production or consumption and not controlled by the Montreal Protocol. As noted above, a major issue is that uncertainties in future changes in the ozone layer will be influenced more by uncertainties in CO_2, CH_4, and N_2O levels than by uncertainties in the levels of ODSs, especially as we approach the 1980 values of EESC. Increases in greenhouse gas concentrations are predicted to lead to increases in upper-stratospheric ozone at all latitudes, with a more complex pattern of ozone changes in the lower stratosphere, including a decrease in low latitudes due to changes in dynamics and transport. These processes are discussed in detail in Chapters 3 and 4. Note that natural forces such as large explosive volcanic eruptions could also adversely affect ozone recovery over the next decade, while ODS levels remain high.

- **The wide range of possible future levels of CO_2, CH_4, and N_2O represents an important limitation to making accurate projections of the ozone layer.** Global mean warming as well as stratospheric cooling will drive ozone changes through both atmospheric circulation and chemistry. Future ozone levels depend on the path of greenhouse gas and aerosol emissions as well as the sensitivity of the climate system to these emissions. Future ODS atmospheric concentrations are more certain than atmospheric concentrations of climate forcing emissions, as long as there is adherence to the Montreal Protocol. This chapter considers various climate scenarios, using the Representative Concentration Pathways (RCPs) adopted by the IPCC for its Fifth Assessment Report (AR5). The Paris Agreement, with a stated objective to limit globally averaged warming to less than 2°C, requires emissions closest to RCP-2.6, the lowest emission scenario of all the RCP scenarios.

[8] UNEP 2013. Drawing Down N_2O to Protect Climate and the Ozone Layer. A UNEP Synthesis Report. United Nations Environment Programme (UNEP), Nairobi, Kenya.

- **Intentional long-term geoengineering applications that substantially increase stratospheric aerosols to mitigate global warming by reflecting sunlight would alter stratospheric ozone.** The estimated magnitudes and even the sign of ozone changes in some regions are uncertain because of the high sensitivity to variables such as the amount, altitude, geographic location and type of injection, and the halogen loading. An increase of stratospheric sulfate aerosol burden in amounts sufficient to substantially reduce global radiative forcing would delay the recovery of the Antarctic ozone hole. Much less is known about the effects on ozone from geoengineering solutions using non-sulfate aerosols.

- **Rocket launches presently have a small effect on total stratospheric ozone (much less than 0.1%).** Space industry developments indicate that rocket emissions may increase more significantly than reported in the previous Assessment. Their impacts will depend on rocket design (particularly the altitude of emissions), launch vehicle sizes, launch rates, spaceport locations, and fuel types. Important gaps remain in understanding rocket emissions and their combined chemical, radiative, and dynamical impacts on the global stratosphere and in projections of launch rates. These gaps limit the confidence level of predictions of present and future impacts of rocket emissions on stratospheric ozone and suggest periodic assessments are warranted. The lifetime of the most important rocket emissions is limited, and the stratospheric accumulation of rocket-emitted black carbon and alumina particles varies in correspondence with global launch rates and altitude of emissions.

Update on other environmental impacts of Montreal Protocol gases

Here, we refer to all gases controlled under the Montreal Protocol and its various Amendments, including the Kigali Amendment, as Montreal Protocol Gases.

- **There is increased confidence that trifluoroacetic acid (TFA) produced from degradation of HFCs, HCFCs, and HFOs will not harm the environment over the next few decades.** This assessment is based on the current estimates of future use of hydrocarbons, HCFCs, and HFOs. It is noteworthy that HFCs and HCFCs have atmospheric lifetimes long enough to globally distribute any TFA emissions, while HFOs have atmospheric lifetimes so short that TFA emissions are deposited near the point of emission. Periodic re-evaluation is prudent, given the uncertainties in the sources and sinks of TFA and because of its persistence in the environment.

Summary of the impacts of mitigation options and particular scenarios

Figure 6-1 (**also Figure ES-9**) shows what ozone and climate-relevant changes could be avoided if various actions were taken. These changes are shown as the differences in global total column ozone averaged over 2020–2060 and in cumulative CO_2-equivalent emissions over 2020–2060 relative to the baseline (A1) scenario (which includes the Kigali Amendment for HFCs). The options available to hasten the recovery of the ozone layer are limited, mostly because actions that could help significantly have already been taken.

  - For CFCs, halons, and HCFCs, the most effective mitigation option, not considering technical feasibility, is expanded bank recapture and destruction; elimination of HCFC production starting in 2020 would be somewhat less effective.

  - For CH_3Br, elimination of production for currently uncontrolled quarantine and pre-shipment (QPS) applications is shown.

  - For CCl_4, the impacts of total emissions elimination starting in 2020 are shown.

  - For CH_2Cl_2, an uncontrolled ozone-depleting gas whose exact sources are unknown, we show that immediate emissions elimination would have a greater positive impact on total column ozone than total emissions elimination of CCl_4.

- For N_2O, the impacts of the Concerted Mitigation average scenario from UNEP [2013] are shown, compared to the RCP-6.0 scenario. The Concerted Mitigation scenario was developed by averaging the four published mitigation scenarios (RCP-2.6, SRES B2, and scenarios 4 and 5 from Davidson [2012]) that lead to lower N_2O emissions in 2050 than were experienced in 2005.
- For HFCs, the impact of a hypothetical complete global phaseout of production (excluding HFC-23) starting in 2020 is shown. As discussed in Chapter 2, for this scenario the surface temperature contribution of the HFC emissions would stay below 0.02 °C for the entire 21st century and beyond.

Further detail on these options and scenarios is given in **Section 6.4** and **Table 6-5.**

All the scenarios discussed above hasten the ozone layer recovery (CFCs, halons, HCFCs, CH_3Br, CCl_4, CH_2Cl_2 and N_2O) and reduce warming (HFCs, CFCs, halons, HCFCs, CCl_4, and N_2O). An additional scenario for emissions that may result from a violation of the Montreal Protocol is shown, namely continuing unexplained emissions of CFC-11 at 67 Gg yr^{-1}, which is the average calculated annual emission from atmospheric concentration observations over 2002–2016. This scenario leads to more ozone depletion and climate warming. Avoiding this scenario would have a larger positive impact on future ozone than any of the other mitigation options considered here.

Errata (December 2018)

Executive Summary content:

- In Figure ES-1 (panel (a)), the units label was corrected to (Mt yr^{-1}).
- In the caption of Figure ES-8 the cross-reference was changed to Figure 5-12.
- In Figure ES-1 (panel (b)), the label and caption were changed to EECl (equivalent effective chlorine).

Appendix:

- Addition was made to the Contributors list to include Sydnee Masias, Science and Technology Corporation, NOAA Office of the Chief Administrative Officer, USA.
- Chapter 1 Scientific Summary (pg. ES.34) footnote was changed to "Here, CFC-114 refers to the combination of the CFC-114 and CFC-114a isomers."
- The spelling of Helen Walter-Terrinoni's name was corrected.

Chapter 1

Update on Ozone-Depleting Substances (ODSs) and Other Gases of Interest to the Montreal Protocol

Lead Authors
A. Engel
M. Rigby

Coauthors
J.B. Burkholder
R.P. Fernandez
L. Froidevaux
B.D. Hall
R. Hossaini
T. Saito
M.K. Vollmer
B. Yao

Contributors
E. Altas
P. Bernath
D.R. Blake
G. Dutton
P. Krummel
J.C. Laube
E. Mahieu
S.A. Montzka
J. Mühle
G. Nedoluha
S.J. O'Doherty
D.E. Oram
K. Pfeilsticker
R.G. Prinn
B. Quack
I.J. Simpson
R.F. Weiss

Review Editors
Q. Liang
S. Reimann

Cover photo: View of the high-altitude Jungfraujoch research station, perched at ca. 3,500 m in the Swiss Alps. Both in-situ atmospheric background measurements of halocarbons and related species, as well as remote sensing measurements of halogen species taken at the Jungfraujoch, have contributed to this report. Photo: Courtesy of jungfraujoch.ch.

Chapter 1

Update on Ozone-Depleting Substances (ODSs) and Other Gases of Interest to the Montreal Protocol

CONTENTS

Chapter 1

Update on Ozone-Depleting Substances (ODSs) and Other Gases of Interest to the Montreal Protocol

SCIENTIFIC SUMMARY

This chapter concerns atmospheric changes in ozone-depleting substances (ODSs), such as chlorofluorocarbons (CFCs), halons, chlorinated solvents (e.g., CCl_4 and CH_3CCl_3) and hydrochlorofluorocarbons (HCFCs), which are controlled under the Montreal Protocol. Furthermore, the chapter updates information about ODSs not controlled under the Protocol, such as methyl chloride (CH_3Cl) and very short-lived substances (VSLSs). In addition to depleting stratospheric ozone, many ODSs are potent greenhouse gases.

Mole fractions of ODSs and other species are primarily measured close to the surface by global or regional monitoring networks. The surface data can be used to approximate a mole fraction representative of the global or hemispheric tropospheric abundance. Changes in the tropospheric abundance of an ODS result from a difference between the rate of emissions into the atmosphere and the rate of removal from it. For gases that are primarily anthropogenic in origin, the difference between northern and southern hemispheric mole fractions is related to the global emission rate because these sources are concentrated in the northern hemisphere.

- **The abundances of the majority of ODSs that were originally controlled under the Montreal Protocol are now declining, as their emissions are smaller than the rate at which they are destroyed. In contrast, the abundances of most of the replacement compounds, HCFCs and hydrofluorocarbons (HFCs, which are discussed in Chapter 2), are increasing.**

TROPOSPHERIC CHLORINE

Total tropospheric chlorine is a metric used to quantify the combined globally averaged abundance of chlorine in the troposphere due to the major chlorine-containing ODSs. The contribution of each ODS to total tropospheric chlorine is the product of its global tropospheric mean mole fraction and the number of chlorine atoms it contains.

- **Total tropospheric chlorine (Cl) from ODSs continued to decrease between 2012 and 2016.** Total tropospheric chlorine in 2016[1] was 3,287 ppt (where ppt refers to parts per trillion as a dry air mole fraction), 11% lower than its peak value in 1993, and about 0.5% lower than reported for 2012 in the previous Assessment. Of the 2016 total, CFCs accounted for about 60%, CH_3Cl accounted for about 17%, CCl_4 accounted for about 10%, and HCFCs accounted for about 9.5%. The contribution from CH_3CCl_3 has now decreased to 0.2%. Very short-lived source gases (VSL SGs), as measured in the lower troposphere, contributed approximately 3%.
    - During the period 2012–2016, the observed rate of decline in tropospheric Cl due to *controlled substances* was 12.7 ± 0.9[2] ppt Cl yr^{-1}, similar to the 2008–2012 period (12.6 ± 0.3 ppt Cl yr^{-1}). This rate of decrease was close to the projections from the A1 scenario[3] in the previous Assessment. However, the net rate of change was the result of a slower than projected decrease in CFCs and a slower HCFC increase than in the A1 scenario, which assumed that HCFC production from Article 5 countries would follow the maximum amount allowed under the Montreal Protocol.

[1] Here and throughout this chapter, values that are given for a specific year represent annual averages, unless mentioned otherwise.

[2] The ranges given here represent the interannual variability in observed growth rate or rate of decrease.

[3] A1 Scenario is given in Table 5A-2 of Harris and Wuebbles et al. (2014).

- When substances *not controlled* under the Montreal Protocol are also included, the overall decrease in tropospheric chlorine was 4.4 ± 4.1 ppt Cl yr^{-1} during 2012–2016. This is smaller than the rate of decline during the 2008–2012 period (11.8 ± 6.9 ppt Cl yr^{-1}) and smaller than the rate of decline in controlled substances because VSLSs, predominantly anthropogenic dichloromethane (CH_2Cl_2), and methyl chloride (CH_3Cl), which is mostly from natural sources, increased during this period.

- **Starting around 2013, the rate at which the CFC-11 mole fraction was declining in the atmosphere slowed unexpectedly, and the interhemispheric difference in its mole fraction increased. These changes are very likely due to an increase in emissions, at least part of which originate from eastern Asia.** Assuming no change in atmospheric circulation, an increase in global emissions of approximately 10 Gg yr^{-1} (~15%) is required for 2014–2016, compared to 2002–2012, to account for the observed trend and interhemispheric difference. The rate of change and magnitude of this increase is unlikely to be explained by increasing emissions from banks. Therefore, these findings may indicate new production not reported to the United Nations Environment Programme (UN Environment). If the new emissions are associated with uses that substantially increase the size of the CFC-11 bank, further emissions resulting from this new production would be expected in future.

- **Compared to 2008–2012, for the period 2012–2016, mole fractions of CFC-114[4] declined more slowly, CFC-13 continued to rise, and CFC-115 exhibited positive growth after previously showing near-zero change. These findings likely indicate an increase or stabilization of the emissions of these relatively low abundance compounds, which is not expected given their phaseout for emissive uses under the Montreal Protocol.** For CFC-114 and -115, regional analyses show that some of these emissions originate from China. There is evidence that a small fraction of the global emissions of CFC-114 and -115 are due to their presence as impurities in some HFCs. However, the primary processes responsible are unknown.

- **The rate at which carbon tetrachloride (CCl_4) has declined in the atmosphere remains slower than expected from its reported use as a feedstock. This indicates ongoing emissions of around 35 Gg yr^{-1}. Since the previous Assessment, the best estimate of the global atmospheric lifetime of CCl_4 has increased from 26 to 32 years, due to an upward revision of its lifetime with respect to loss to the ocean and soils. New sources have been proposed including significant by-product emissions from the production of chloromethanes and perchloroethylene and from chlor-alkali plants.** With these changes in understanding, the gap between top-down and bottom-up emissions estimates has reduced to around 10 Gg yr^{-1}, compared to 50 Gg yr^{-1} previously.

- **Combined emissions of the major HCFCs have declined since the previous Assessment.** Emissions of HCFC-22 have remained relatively stable since 2012, while emissions of HCFC-141b and -142b declined between 2012 and 2016, by around 10% and 18%, respectively. These findings are consistent with a sharp drop in reported HCFC consumption after 2012, particularly from Article 5 countries.

- **Emissions of the compounds HCFC-133a and HCFC-31, for which no current intentional use is known, have been detected from atmospheric measurements.** Research to date suggests that these gases are unintentional by-products of HFC-32, HFC-134a, and HFC-125 production.

TROPOSPHERIC BROMINE

Total tropospheric bromine is defined in analogy to total tropospheric chlorine. Even though the abundance of bromine is much smaller than that of chlorine, it has a significant impact on stratospheric ozone because it is around 60–65 times more efficient than chlorine as an ozone-destroying catalyst

[4] Here, CFC-114 refers to the combination of the CFC-114 and CFC-114a isomers.

- **Total tropospheric bromine from controlled ODSs (halons and methyl bromide) continued to decrease and by 2016 was 14.6 ppt, 2.3 ppt below the peak levels observed in 1998.** In the 4-year period prior to the last Assessment, this decrease was primarily driven by a decline in methyl bromide (CH_3Br) abundance, with a smaller contribution from a decrease in halons. These relative contributions to the overall trend have now reversed, with halons being the main driver of the decrease of 0.15 ± 0.04 ppt Br yr^{-1} between 2012 and 2016.

- **The mole fractions of halon-1211, halon-2402, and halon-1202 continued to decline between 2012 and 2016. Mole fractions of halon-1301 increased during this period, although its growth rate dropped to a level indistinguishable from zero in 2016.** Emissions of halon-2402, halon-1301, and halon-1211, as derived from atmospheric observations, declined or remained stable between 2012 and 2016.

- **Methyl bromide (CH_3Br) mole fractions continued to decline between 2012 and 2015 but showed a small increase (2–3%) between 2015 and 2016. This overall reduction is qualitatively consistent with the controls under the Montreal Protocol.** The 2016 level was 6.8 ppt, a reduction of 2.4 ppt from peak levels measured between 1996 and 1998. The increase between 2015 and 2016 was the first observation of a positive global change for around a decade or more. The cause of this increase is yet to be explained. However, as it was not accompanied by an increased interhemispheric difference, it is unlikely that this is related to anthropogenic emissions in the Northern Hemisphere. By 2016, controlled CH_3Br consumption dropped to less than 2% of the peak value, and total reported fumigation emissions have declined by more than 85% since their peak in 1997. Reported consumption in quarantine and pre-shipment (QPS) uses of CH_3Br, which are not controlled under the Montreal Protocol, have not changed substantially over the last two decades.

HALOGENATED VERY SHORT-LIVED SUBSTANCES (VSLSs)

VSLSs are defined as trace gases whose local lifetimes are shorter than 0.5 years and have nonuniform tropospheric abundances. These local lifetimes typically vary substantially over time and space. Of the very short-lived source gases (VSL SGs) identified in the atmosphere, brominated and iodinated species are predominantly of oceanic origin, while chlorinated species have significant additional anthropogenic sources. VSLSs will release the halogen they contain almost immediately once they enter the stratosphere and will thus play an important role in the lower stratosphere in particular. Due to their short lifetimes and their atmospheric variability the quantification of their contribution is much more difficult and has much larger uncertainties than for long-lived compounds.

- **Total tropospheric chlorine from VSL SGs in the background lower atmosphere is dominated by anthropogenic sources. It continued to increase between 2012 and 2016, but its contribution to total chlorine remains small.** Global mean chlorine from VSLSs in the troposphere has increased from about 90 ppt in 2012 to about 110 ppt in 2016. The relative VSLS contribution to stratospheric chlorine input derived from observations in the tropical tropopause layer has increased slightly from 3% in 2012 to 3.5% in 2016.

- **Dichloromethane (CH_2Cl_2), a VSL SG that has predominantly anthropogenic sources, accounted for the majority of the change in total chlorine from VSLSs between 2012 and 2016 and is the main source of VSLS chlorine.** The global mean abundance reached approximately 35–40 ppt in 2016, which is about a doubling compared to the early part of the century. The increase slowed substantially between 2014 and 2016. Emissions from southern and eastern Asia have been detected for CH_2Cl_2.

- **There is further evidence that VSLSs contribute ~5 (3–7) ppt to stratospheric bromine, which was about 25% of total stratospheric bromine in 2016. The main sources for brominated VSLSs are natural, and no long-term change is observed.** While the best estimate of 5 ppt has remained unchanged from the last

Assessment, the assessed uncertainty range has been reduced. Due to the decline in the abundance of regulated bromine compounds, the relative contribution of VSLSs to total stratospheric bromine continues to increase.

STRATOSPHERIC CHLORINE AND BROMINE

In the stratosphere, chlorine and bromine can be released from organic source gases to form inorganic species, which participate in ozone depletion. In addition to estimates of the stratospheric input derived from the tropospheric observations, measurements of inorganic halogen loading in the stratosphere are used to determine trends of stratospheric chlorine and bromine.

- **Hydrogen chloride (HCl) is the major reservoir of inorganic chlorine (Cl_y) in the mid to upper stratosphere. Satellite-derived measurements of HCl (60°N–60°S) in the middle stratosphere show a long-term decrease of HCl at a rate of around 0.5% yr^{-1}, in good agreement with expectations from the decline in tropospheric chlorine.** In the lower stratosphere, a decrease was observed over the period from 1997 to 2016, while significant differences in the trends are seen over the period 2005 to 2016 between various datasets and altitude/geographical regions. A similar behavior is observed for total column measurements, likely reflecting variability in stratospheric dynamics and chemistry. Total chlorine input to the stratosphere of 3,290 ppt is derived for 2016 from measurements of long-lived ODSs at the surface and VSLSs in the upper troposphere. About 80% of this input is from substances controlled under the Montreal Protocol.

- **Total stratospheric bromine, derived from observations of bromine monoxide (BrO), continued to decrease at a rate of about 0.75% yr^{-1} from 2004 to 2014.** This decline is consistent with the decrease in total tropospheric organic bromine, based on measurements of CH_3Br and the halons. A total bromine input to the stratosphere of 19.6 ppt is derived for 2016, combined from 14.6 ppt of long-lived gases and 5 ppt from VSLSs not controlled under the Montreal Protocol. Anthropogenic emissions of all brominated long-lived gases are controlled, but as CH_3Br also has natural sources, more than 50% of the bromine reaching the stratosphere is now estimated to be from sources not controlled under the Montreal Protocol. There is no indication of a long-term change in natural sources to stratospheric bromine.

EQUIVALENT EFFECTIVE STRATOSPHERIC CHLORINE (EESC)

EESC is the chlorine-equivalent sum of chlorine and bromine derived from ODS tropospheric abundances, weighted to reflect their expected depletion of stratospheric ozone. The growth and decline in EESC depends on a given tropospheric abundance propagating to the stratosphere with varying time lags (on the order of years) associated with transport. Therefore, the EESC abundance, its peak timing, and its rate of decline are different in different regions of the stratosphere. Recent suggestions of a refinement in the calculation method for EESC result in somewhat lower estimates on how far the stratospheric reactive halogen loading has recovered.

- **By 2016, EESC had declined from peak values by about 9% for polar winter conditions and by about 13–17% for mid-latitude conditions.** This drop is 31–43% of the decrease required for EESC in mid-latitudes to return to the 1980 benchmark level, and about 18–19% of the decrease required for EESC in polar regions to return to the 1980 benchmark level[5]. The rate at which EESC is decreasing has slowed, in accordance with a slowdown of the decrease in tropospheric chlorine. The ranges given reflect the different methods for calculating EESC. Differences in halogen recovery levels from previous Assessments are also due to differences in assumed fractional release factors.

[5] As in previous Assessments, 1980 levels of EESC are used as a benchmark for recovery, although this value is somewhat arbitrary and some ozone loss had occurred prior to 1980. Also, recovery of EESC to 1980 values does not necessarily imply a recovery of ozone to 1980 levels, as other parameters, e.g. stratospheric circulation, may change.

TROPOSPHERIC AND STRATOSPHERIC FLUORINE

While fluorine has no direct impact on stratospheric ozone, many fluorinated gases are strong greenhouse gases, and their emission is often related to the replacement of chlorinated substances regulated under the Montreal Protocol. For this reason, trends in fluorine are also assessed in this report.

- **The main sources of fluorine in the troposphere and in the stratosphere are CFCs, HCFCs, and HFCs. In contrast to total chlorine, total fluorine in the troposphere continued to increase between 2012 and 2016, at a rate of 1.7% yr^{-1}.** This increase shows the decoupling of the temporal trends in fluorine and chlorine due to the increasing emissions of HFCs (see **Chapter 2**). The total atmospheric-column abundance of inorganic fluorine, which is mainly stratospheric, has continued to increase at a rate of about 1% yr^{-1} over the period 2007–2016.

EFFECT OF OZONE-DEPLETING SUBSTANCES (ODSs) ON CLIMATE

- **The total direct radiative forcing[6] of CFCs continues to be much higher than that of HCFCs.** However, radiative forcing from CFCs has dropped by about 7% since its peak in 2000 to about 250 mW m^{-2} in 2016 (approximately 13% that of CO_2), while radiative forcing from HCFCs increased to 58 mW m^{-2} in 2016 (approximately 3% that of CO_2). The total direct radiative forcing due to CFCs, HCFCs, halons, CCl_4 and CH_3CCl_3 was 327 mW m^{-2} in 2016 (approximately 16% that of CO_2).

- **CO_2-equivalent emissions[7] of CFCs and HCFCs were approximately equal in 2016.** The CO_2-equivalent emission from the sum of all CFCs or the sum of all HCFCs was approximately 0.8 Gt in 2016. The CO_2-equivalent emission from the sum of CFCs, HCFCs, Halons, CCl_4 and CH_3CCl_3 was approximately 1.7 Gt in 2016.

OTHER GASES THAT AFFECT OZONE AND CLIMATE

- **Mole fractions of many other gases that affect both ozone and climate have changed since the previous Assessment.** The atmospheric abundance of methane has continued to increase following a period of stagnation in the early 2000s. The drivers of the changing trend are disputed. Nitrous oxide continues to grow relatively steadily in the atmosphere. The global mole fractions of the fluorinated species sulfur hexafluoride (SF_6), nitrogen trifluoride (NF_3), sulfuryl fluoride (SO_2F_2), and the perfluorocarbons (PFCs such as CF_4 and C_2F_6) have continued to grow. In contrast, the abundance of the sulfur-containing compounds sulfur dioxide (SO_2) and carbonyl sulfide (COS) has not changed substantially.

[6] A measure of the change in net irradiance (incoming minus outgoing) at the tropopause.

[7] CO_2 equivalents are determined here by weighting emissions estimates by the global warming potential (GWP) of each gas, integrated over a 100-year time horizon.

Chapter 1

Update on Ozone-Depleting Substances (ODSs) and Other Gases of Interest to the Montreal Protocol

1.1 SUMMARY OF FINDINGS FROM THE PREVIOUS OZONE ASSESSMENT

Chapter 1 of the 2014 Assessment report (Carpenter and Reimann et al., 2014) provided updates on ozone-depleting substances (ODSs) and other gases of interest to the Montreal Protocol. These included hydrofluorocarbons (HFCs), which have been used to replace ODSs; they are not ozone-depleting substances, but they do add to climate warming.

Chapter 1 from the 2014 Assessment showed that, in the 5-year period 2008–2012, total tropospheric chlorine from substances regulated under the Montreal Protocol had declined at an average rate of 13.4 ± 0.9 ppt yr^{-1} (ppt defined as dry air mole fraction in parts per trillion), while bromine from regulated substances was declining at a rate of 0.14 ± 0.02 ppt yr^{-1}. All major CFCs (chlorofluorocarbons) showed decreasing mole fractions and continued to be the main carriers of chlorine, with a contribution of 61% to total tropospheric chlorine. The only class of compounds that were regulated yet still showed increasing mole fractions were hydrochlorofluorocarbons (HCFCs). A continuing discrepancy in the emissions of CCl_4 inferred from observations versus those derived from reports to the United Nations Environment Programme (UN Environment) was documented.

An increase in lower tropospheric abundances of chlorinated very short-lived substances (VSLSs) was observed. Dichloromethane (CH_2Cl_2) increased particularly strongly; the global mean mole fraction had increased by about 60% between 2001 and 2012. However, the total contribution of VSLSs to stratospheric chlorine remained small at approximately 3% in 2012, including the contribution of inorganic product gases entering the stratosphere.

Total tropospheric bromine showed an overall decline, consistent with the projections from the scenarios in the 2010 Assessment. The decline was driven by the continued decrease of CH_3Br and, for the first-time, an observed decrease in total tropospheric bromine from halons, with all halons except for halon-1301 decreasing in the atmosphere. The relative contribution of brominated VSLSs to total bromine was much larger than the contribution of chlorinated VSLSs to total chlorine, with about 5 ppt of the total 20 ppt of stratospheric bromine attributed to short-lived substances. Input of bromine from VSLSs to the stratosphere in both organic and inorganic forms was included.

Equivalent effective stratospheric chlorine (EECS), which is the chlorine-equivalent sum of chlorine and bromine derived from ODS tropospheric abundances weighted to reflect their expected depletion of stratospheric ozone, was assessed to have declined from its maximum value in polar regions by about 10% and in mid-latitudes by about 15%; this is equivalent to about 20% and 40% of the decline required to return to 1980 benchmark levels, respectively.

The influence of ODS and HFC emissions on climate was assessed in terms of their equivalent in gigatonnes of carbon dioxide (CO_2-equivalent emissions) using 100-year Global Warming Potential (GWP). The CO_2-equivalent emissions of CFCs, HCFCs, and HFCs were roughly equal to each other in 2012 with respect to their climate influence. However, the emissions of HFCs were increasing, while the emissions of CFCs were declining and those of HCFCs remained relatively constant.

1.2 UPDATED ABUNDANCES, TRENDS, LIFETIMES, AND EMISSIONS OF LONGER-LIVED HALOGENATED SOURCE GASES

Observations of ODSs have been carried out over multiple decades by several groups with different sampling strategies, who have, in most cases, developed independent, but regularly compared, calibration scales (**Figure 1-1**, **Table 1-1**). Global and hemispheric mean mole fractions are derived using data from networks with air sampling stations that are distributed

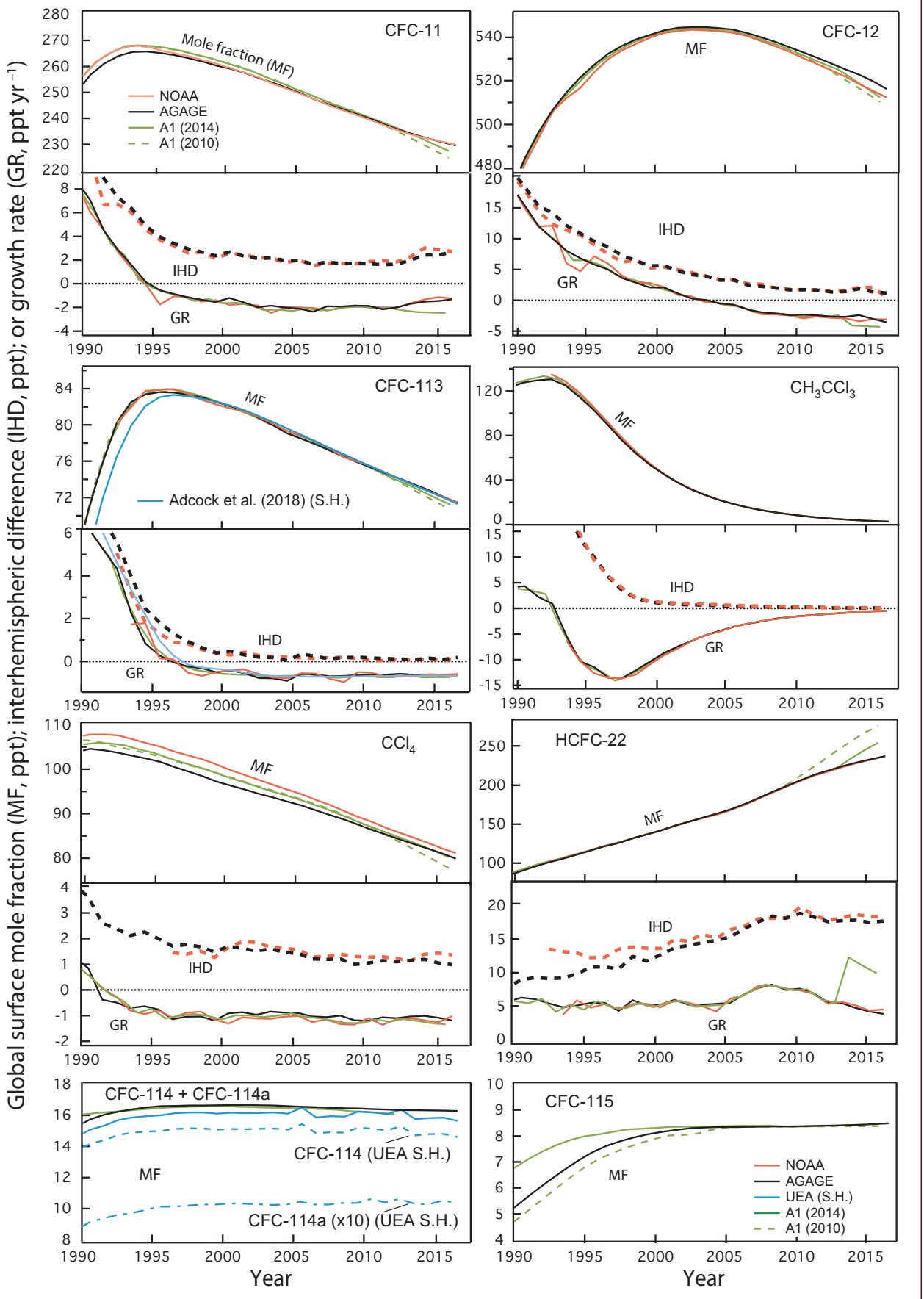
Global surface mole fraction (MF, ppt); interhemispheric difference (IHD, ppt); or growth rate (GR, ppt yr⁻¹)
CFC-11
Mole fraction (MF)
NOAA
AGAGE
A1 (2014)
A1 (2010)
IHD
GR
CFC-12
MF
IHD
GR
CFC-113
MF
Adcock et al. (2018) (S.H.)
IHD
GR
CH3CCl3
MF
IHD
GR
CCl4
MF
IHD
GR
HCFC-22
MF
IHD
GR
CFC-114 + CFC-114a
CFC-114 (UEA S.H.)
MF
CFC-114a (x10) (UEA S.H.)
CFC-115
MF
NOAA
AGAGE
UEA (S.H.)
A1 (2014)
A1 (2010)
Year
Year

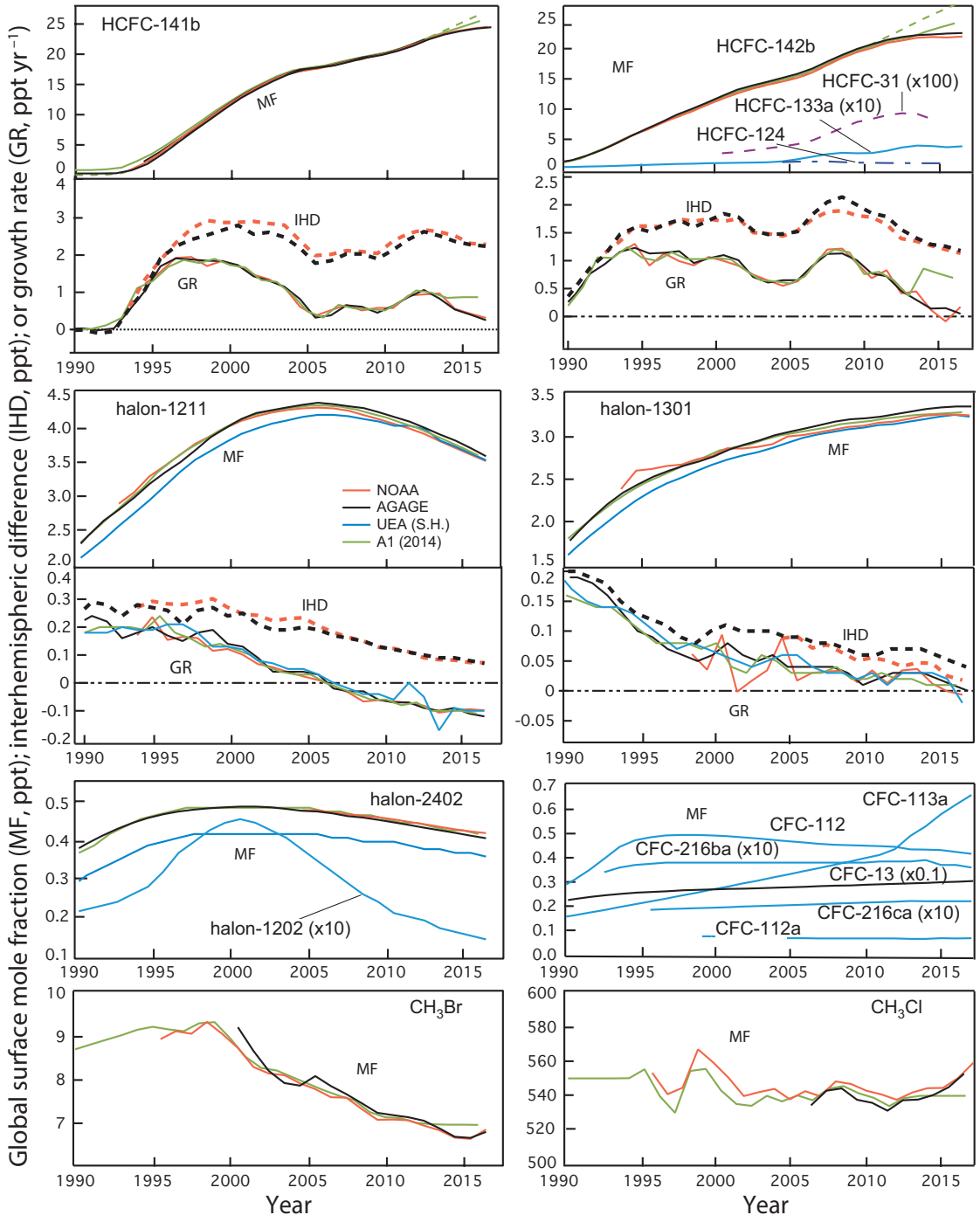

Figure 1-1. Annual mean global surface mole fractions (MF; expressed as dry air mole fractions in parts per trillion or ppt) of ozone-depleting substances from independent sampling networks and from scenario A1 of the previous Ozone Assessments over the past 26 years (1990–2016) (Daniel and Velders, 2011; Harris and Wuebbles et al., 2014). The baseline scenarios from previous Assessments (A1-2010, A1-2014) are projections from 2009 and 2013, respectively. Only A1-2014 data are shown for some species. Shown are measured global surface annual means from the NOAA network (red) and AGAGE network (black). Southern Hemispheric data obtained by the University of East Anglia (UEA) (blue) are shown for some species. NOAA and AGAGE CFC-113 data likely represent some combination of CFC-113 and CFC-113a (although the influence of CFC-113a on NOAA and AGAGE measurements of CFC-113 is likely small), whereas UEA measures CFC-113 and CFC-113a separately (Adcock et al., 2018). UEA CFC-113 data (annual Southern Hemispheric means from Adcock et al., 2018) were adjusted downward by 2% to be consistent with the NOAA scale determined by gas chromatography-mass spectrometry (GC-MS) as opposed to gas chromatography-electron capture detection (GC-ECD). HCFC-124 data were taken from Simmonds et al. (2017). HCFC-31 data were taken from Schoenenberger et al. (2015). For some gases, we also show growth rates (GR) and interhemispheric differences (IHD; NH mean minus SH mean) in a second panel, using the same color scheme as in the corresponding upper panel.

Table 1-1. Measured mole fractions and changes of ozone-depleting gases from ground-based sampling networks (expressed in dry air mole fractions as parts per trillion (ppt), or relative units).

Chemical Formula	Common or Industrial Name	Annual Mean Mole Fraction (ppt) 2012	2015	2016	Change (2015–2016) (ppt yr^{-1})	(% yr^{-1})	Network, Method
CFCs							
CCl_3F	CFC-11	**235.5**	**230.9**	**229.6**	**-1.3**	**-0.6**	AGAGE, in situ[1]
		235.2	**231.1**	**229.8**	**-1.3**	**-0.6**	NOAA[2], flask & in situ
		235.3	**229.2**	**227.4**	**-1.8**	**-0.8**	UCI, flask
CCl_2F_2	CFC-12	**527.8**	**519.7**	**516.1**	**-3.6**	**-0.7**	AGAGE, in situ
		524.7	**515.3**	**512.2**	**-3.1**	**-0.6**	NOAA, flask & in situ
		522.5	**519.5**	**515.6**	**-3.9**	**-0.8**	UCI, flask
$CClF_3$	CFC-13	**2.94**	**3.01**	**3.04**	**0.03**	**1.0**	AGAGE, in situ
CCl_2FCCl_2F	CFC-112	*0.44*	*0.42*	*0.42*	*0.00*	*0.0*	UEA, flask (Cape Grim)
CCl_3CClF_2	CFC-112a	*0.066*	*0.066*	*0.067*	*0.001*	*1.5*	UEA, flask (Cape Grim)
CCl_2FCClF_2	CFC-113	**74.0**	**72.1**	**71.4**	**-0.7**	**-0.9**	AGAGE, in situ[3]
		74.0	**72.1**	**71.5**	**-0.6**	**-0.8**	NOAA, flask[3]
		74.2	**71.8**	**71.1**	**-0.7**	**-1.0**	UCI, flask[3]
CCl_3CF_3	CFC-113a	*0.43*	*0.62*	*0.66*	*0.04*	*6.5*	UEA, flask (Cape Grim)
$CClF_2CClF_2$	CFC-114	**16.3**	**16.3**	**16.3**	**0.0**	**-0.1**	AGAGE, in situ[4]
		15.2	*14.8*	*14.6*	*-0.2*	*-1.4*	UEA, flask (Cape Grim)[5]
CCl_2FCF_3	CFC-114a	*1.05*	*1.05*	*1.04*	*-0.01*	*-1.0*	UEA, flask (Cape Grim)[5]
$CClF_2CF_3$	CFC-115	**8.40**	**8.46**	**8.49**	**0.03**	**0.4**	AGAGE, in situ
		8.48	*8.63*	*8.67*	*0.04*	*0.5*	NIES, in situ (Japan)
HCFCs[6]							
$CHClF_2$	HCFC-22	**219.3**	**233.6**	**237.4**	**3.8**	**1.6**	AGAGE, in situ
		218.0	**233.0**	**237.5**	**4.5**	**1.9**	NOAA, flask
		214.5	**238.0**	**242.3**	**4.3**	**1.8**	UCI, flask
CH_2ClCF_3	HCFC-133a	*0.31*	*0.37*	*0.39*	*0.02*	*5.4*	UEA, flask (Cape Grim)
CH_3CCl_2F	HCFC-141b	**22.45**	**24.22**	**24.47**	**0.25**	**1.0**	AGAGE, in situ
		22.27	**24.22**	**24.53**	**0.31**	**1.3**	NOAA, flask
		21.80	**24.49**	**24.59**	**0.10**	**0.4**	UCI, flask
CH_3CClF_2	HCFC-142b	**21.92**	**22.51**	**22.56**	**0.05**	**0.2**	AGAGE, in situ
		21.36	**21.84**	**22.01**	**0.17**	**0.8**	NOAA, flask
		21.80	**23.26**	**23.16**	**-0.10**	**-0.4**	UCI, flask
Halons							
CBr_2F_2	halon-1202	*0.018*	*0.015*	*0.014*	*-0.001*	*-6.7*	UEA, flask (Cape Grim)[5]
$CBrClF_2$	halon-1211	**4.01**	**3.71**	**3.59**	**-0.12**	**-3.2**	AGAGE, in situ
		3.92	**3.61**	**3.52**	**-0.09**	**-2.5**	NOAA, flask

Chemical Formula	Common or Industrial Name	Annual Mean Mole Fraction (ppt) 2012	2015	2016	Change (2015–2016) (ppt yr^{-1})	(% yr^{-1})	Network, Method
$CBrClF_2$ (continued)	halon-1211 (continued)	**3.96**	**3.66**	**3.54**	**-0.12**	**-3.3**	NOAA, in situ
		3.97	*3.61*	*3.51*	*-0.10*	*-2.8*	UEA, flask (Cape Grim)
		4.14	**3.80**	**3.70**	**-0.10**	**-2.6**	UCI, flask
$CBrF_3$	halon-1301	**3.30**	**3.36**	**3.36**	**0.00**	**0.0**	AGAGE, in situ
		3.19	**3.25**	**3.25**	**0.00**	**-0.1**	NOAA, in situ
		3.10	*3.17*	*3.17*	*0.00*	*0.0*	UEA, flask (Cape Grim)
$CBrF_2CBrF_2$	halon-2402	**0.44**	**0.42**	**0.41**	**-0.01**	**-2.4**	AGAGE, in situ[7]
		0.44	**0.42**	**0.42**	**-0.01**	**-1.2**	NOAA, flask
		0.39	*0.37*	*0.36*	*-0.01*	*-2.7*	UEA, flask (Cape Grim)[5]
Chlorocarbons							
CH_3Cl	methyl chloride	**539.9**	**544.7**	**552.7**	**8.0**	**1.5**	AGAGE, in situ
		541.4	**550.0**	**559.1**	**9.1**	**1.7**	NOAA, flask
CCl_4	carbon tetrachloride	**84.2**	**81.1**	**79.9**	**-1.2**	**-1.5**	AGAGE, in situ
		85.7	**82.2**	**81.2**	**-1.0**	**-1.2**	NOAA, flask & in situ
		86.7	**82.2**	**81.9**	**-0.3**	**-0.3**	UCI, flask
CH_3CCl_3	methyl chloroform	**5.21**	**3.09**	**2.61**	**-0.48**	**-16**	AGAGE, in situ
		5.25	**3.07**	**2.60**	**-0.47**	**-15**	NOAA, flask
		5.7	**3.48**	**3.05**	**-0.43**	**-12**	UCI, flask
Bromocarbons							
CH_3Br	methyl bromide	**7.06**	**6.66**	**6.80**	**0.14**	**2.1**	AGAGE, in situ
		6.95	**6.64**	**6.86**	**0.22**	**3.3**	NOAA, flask

Mole fractions in this table represent independent estimates measured by different groups for the years indicated. Results in bold text are estimates of global surface mean mole fractions. Regional data from relatively unpolluted sites are shown (in italics) where global estimates are not available, where global estimates are available from only one network, or where regional data provide additional long-term records. Absolute changes (ppt yr^{-1}) are calculated as the difference between 2015 and 2016 annual means; relative changes (% yr^{-1}) are the same difference relative to the 2015 value. Small differences between values reported in previous Assessments are due to changes in calibration scale and methods for estimating global mean mole fractions from a limited number of sampling sites.

These observations are published in or are updated from the following sources: (Adcock et al., 2018; Butler et al., 1998; Laube et al., 2016; Laube et al., 2014; Montzka et al., 2003; Montzka et al., 2018; Montzka et al., 2015; Newland et al., 2013; Prinn et al., 2018; Rigby et al., 2014; Simmonds et al., 2017; Simpson et al., 2007; Vollmer et al., 2016, 2018; Yokouchi et al., 2006); AGAGE, Advanced Global Atmospheric Gases Experiment (http://agage.mit.edu/; Prinn et al., 2018); NOAA, National Oceanic and Atmospheric Administration, USA (http://www.esrl.noaa.gov/gmd/dv/site/); UEA, University of East Anglia, United Kingdom (http://www.uea.ac.uk/environmental-sciences/research/marine-and-atmospheric-sciences-group); UCI, University of California, Irvine, USA (http://ps.uci.edu/~rowlandblake/research_atmos.html); NIES, National Institute for Environmental Studies, Japan (http://db.cger.nies.go.jp/gem/moni-e/warm/Ground/st01.html); Cape Grim: Cape Grim Baseline Air Pollution Station, Australia.

Notes:

[1] Global mean estimates from AGAGE are calculated using atmospheric data and a 12-box model (Cunnold et al., 1983; Rigby et al., 2014; Rigby et al., 2013). [2]The NOAA CFC-11 data have been updated following a calibration scale change in 2016 (Montzka et al., 2018). [3]Measurements of CFC-113 likely represent a combination of CFC-113 and CFC-113a due to co-elution, with the effect of CFC-113a on CFC-113 dependent on the analytical method. [4]AGAGE measurements of CFC-114 are a combination of the CFC-114 and CFC-114a isomers, with a relative contribution of ~7% CFC-114a (Laube et al., 2016). At UEA, CFC-114 and CFC-114a are quantified separately. [5]Mole fractions for 2016 represent averages from January to July for UEA data for these compounds. [6]Updates to HCFC-124 mole fractions are not provided as the AGAGE calibration scale has not been finalized. [7]Compared to the previous Assessment, AGAGE halon-2402 data are now on an independent calibration scale.

around the world: the Advanced Global Atmospheric Gases Experiment (AGAGE) network, the National Oceanic and Atmospheric Administration (NOAA) network, and the University of California, Irvine (UCI) network. Further data representative of regional or hemispheric scales are available for some species from the National Institute for Environmental Studies (NIES) and the University of East Anglia (UEA). Because these networks maintain independent calibration scales, and because they have different sampling locations and frequencies, small differences are observed (typically on the order of a few percent or less; see **Table 1-1**) in the burden and trend estimated from each dataset. Therefore, for much of this section, global trends and inferred emissions are given separately for each network. Data from regionally representative (e.g., Southern Hemisphere) sites are used when global network data are not available. In some circumstances, these data can be extrapolated to derive global-scale mole fractions or emissions using an atmospheric transport model (e.g., **Box 1-1**). This is the case where AGAGE mole fraction records have been extended back before Northern Hemispheric air samples were available, through the assimilation of Cape Grim Air Archive (CGAA; Langenfelds et al., 1996) data into an AGAGE 12-box model inversion (e.g. Rigby et al., 2014). Column observations are also available for some species based on ground-based or satellite-based remote sensing methods (**Figure 1-2**, **Table 1-2**).

For the long-lived ODSs that are primarily of anthropogenic origin, we derive radiative forcing from global mean near-surface mole fractions using the methods outlined in Ramaswamy et al. (2001) (**Figure 1-3**). Emissions, along with global and hemispheric mean mole fractions, are estimated using a box model of atmospheric transport and chemistry, constrained using baseline atmospheric data, following Rigby et al. (2014) (**Figure 1-4, Box 1-1**). The model includes estimates of the major loss processes, the magnitudes of which are mostly based on the SPARC Lifetimes assessment (SPARC, 2013) (**Table A-1**, **Figure 1-4**). Emissions estimates were combined with estimates of 100-year time horizon Global Warming Potentials (GWPs) and Ozone Depletion Potentials (ODPs), as summarized in **Table A-1**, to calculate CO_2-equivalent and CFC-11-equivalent emissions of ODSs and related substances (**Figure 1-5**).

1.2.1 Chlorofluorocarbons (CFCs)

Observations of Atmospheric Abundance

Mole fractions of the three most abundant CFCs—CFC-12 (CCl_2F_2), CFC-11 (CCl_3F), and CFC-113 (CCl_2FCClF_2)—continued to decline since 2012, reaching approximately 514 ppt, 230 ppt, and 71 ppt, respectively in 2016 (**Figure 1-1**). The atmospheric abundance of CFC-12 has fallen increasingly rapidly throughout this period, with the rate of decline increasing from 2.9 ppt yr^{-1} in 2011–2012 to around 3.6 ppt yr^{-1} in 2015–2016 (**Figure 1-1**, **Table 1-1**). The

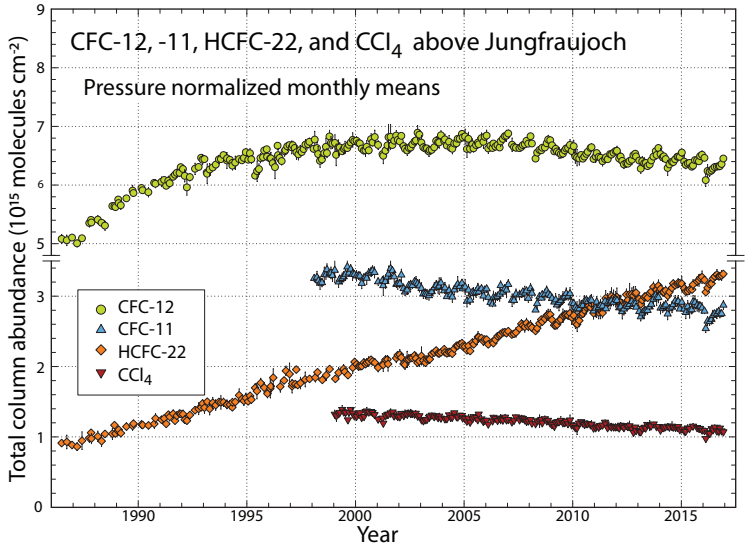

Figure 1-2. Monthly mean total vertical column abundances (in molecules per square centimeter) for CFC-12, CFC-11, CCl_4, and HCFC-22 above Jungfraujoch station, Switzerland, from 1986 to 2016 (updated from Zander et al., 2008 and Rinsland et al., 2012). The bootstrap resampling tool described by Gardiner et al. (2008) and Rinsland et al. (2012) was used for the trend evaluations (see **Table 1-2**). Note the discontinuity in the vertical scale.

rate of decline in CFC-113 has remained relatively constant at around 0.7 ppt yr^{-1}. In contrast, there was a slowdown in the rate at which the global abundance of CFC-11 was falling, starting around 2013 (Montzka et al., 2018): Rates of decline remained relatively close to 2.0 ppt yr^{-1} (0.8% yr^{-1}) between around 2002 and 2012 (±0.2 ppt yr^{-1} interannual variability, 1-sigma), but that rate has since dropped to approximately 1.3 ppt yr^{-1} (0.6% yr^{-1}) between 2014 and 2016. Coincident with this feature, the interhemispheric difference (IHD; the difference between Northern Hemisphere and Southern Hemisphere mean mole fractions) of CFC-11 increased from 1.8 ppt in 2012 to 2.7 ppt in 2016, suggesting that the increase is driven by Northern Hemispheric sources.

Measurements of the 2010–2016 trends in Northern Hemispheric CFC-11 and CFC-12 abundances made using ground-based Fourier transform infrared (FTIR) spectroscopy at Jungfraujoch, Switzerland, agree within uncertainties with those derived using surface-based in situ observations (**Table 1-2**, **Figure 1-2**). However, in contrast to the surface data, column CFC-11 trends were not found to be statistically different between the periods 2008–2012 (–1.24 ± 0.23% yr^{-1}) and 2013–2016 (–1.28 ± 0.42% yr^{-1}). This discrepancy is likely due to the larger interannual variability found in the column data, which complicates the comparison between column and surface trends over short timescales.

A full atmospheric history of CFC-13 ($CClF_3$) has recently been published based on samples from firn, archived air, and AGAGE in situ measurements (Vollmer et al., 2018). This compound increased relatively rapidly in the atmosphere until the mid-1990s, after which growth slowed but remained positive until the most recent measurements in 2016, when the global mole fraction reached 3.04 ppt (mean growth rate since 1996 of 0.02 ppt yr^{-1}). This new

Table 1-2. Comparison of annual trends of ODSs, CF_4, and SF_6 from in situ and remote sensing measurements. Relative trends in ODSs and halogenated greenhouse gases for the 2010–2016 time period derived from surface measurements and remote sensing observations. This time period was selected because interannual variability in remote sensing data makes robust quantification of trends challenging over shorter periods. Surface in situ trends were derived from monthly mean mole fractions, weighted by the surface area in the region 30°N to 90°N. Shown are the averages of trends derived independently from NOAA and AGAGE data (% yr^{-1} relative to 2013 annual mean). Uncertainties were estimated from uncertainties in the linear trends and differences between trends derived from independent networks. For CF_4, only AGAGE in situ data were used, and the uncertainty was derived from the uncertainty in the slope. For remote sensing observations, relative annual rates of change were computed over the 2010–2016 time period from FTIR observations at Jungfraujoch station, Switzerland, with the bootstrap resampling tool described in Gardiner et al. (2008), using the year 2013 as reference. All uncertainties are estimated at 2-sigma.

Annual Trend 2010–2016 (% yr^{-1} relative to 2013)			
Substance	**In situ**	**Remote sensing**	**References**
CFC-11	-0.64 ± 0.05	-0.70 ± 0.17	Updated from Zander et al. (2008) and references in Table 1-1.
CFC-12	-0.55 ± 0.05	-0.47 ± 0.08	Updated from Zander et al. (2008) and references in Table 1-1.
CCl_4	-1.32 ± 0.09	-1.03 ± 0.23	Updated from Rinsland et al. (2012) and references in Table 1-1.
HCFC-22	2.21 ± 0.10	2.54 ± 0.14	Updated from Zander et al. (2008) and references in Table 1-1.
HCFC-142b	0.97 ± 0.17	-0.6 ± 1.1	Updated from Mahieu et al. (2017) and references in Table 1-1.
SF_6	3.90 ± 0.06	4.34 ± 0.19	Updated from Zander et al. (2008) and Hall et al. (2011).
CF_4	0.94 ± 0.01	1.11 ± 0.09	Updated from Mahieu et al. (2014b) and references in Table 1-1.

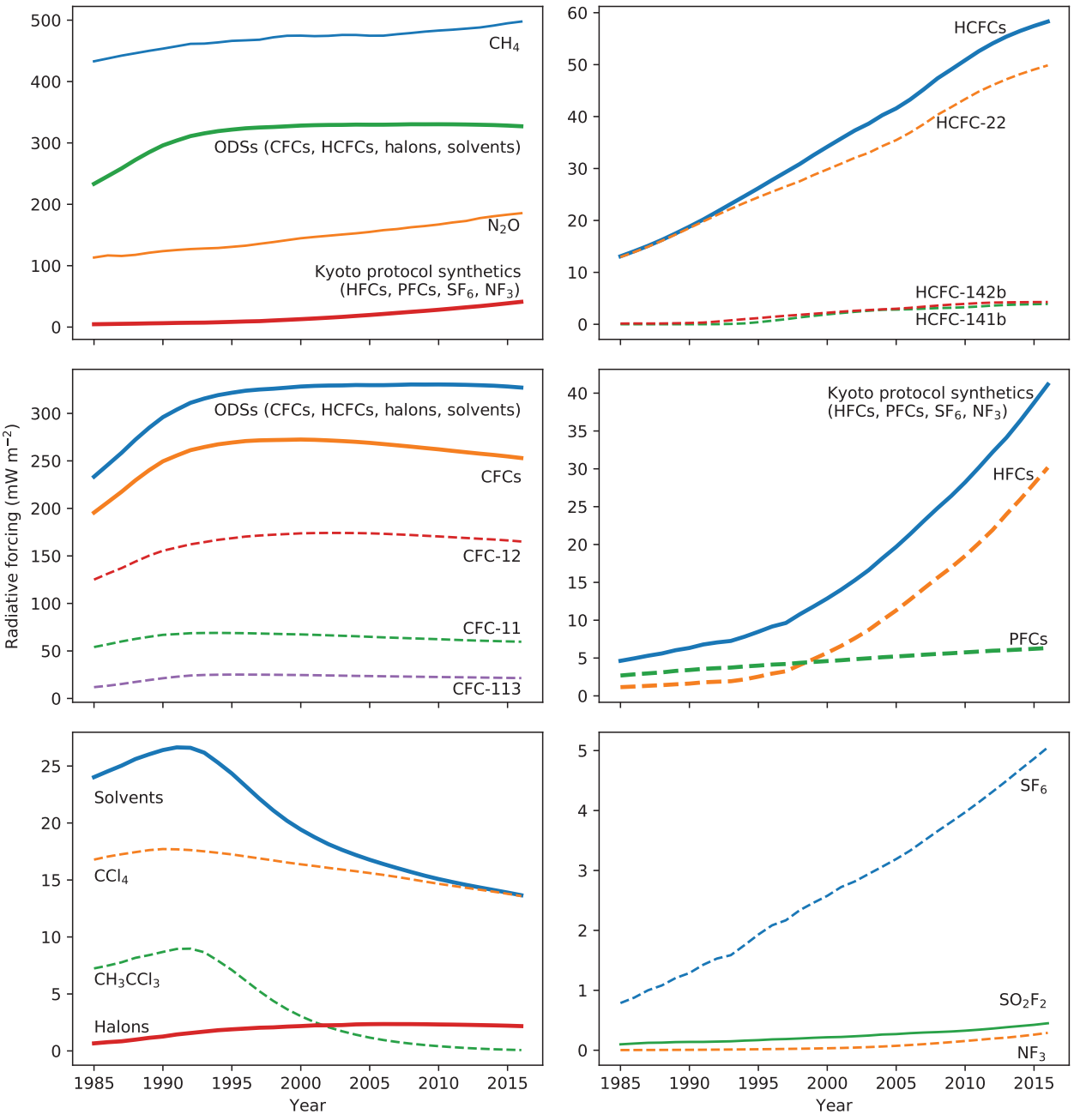

Figure 1-3. Direct radiative forcing due to ODSs, HFCs, CH_4, N_2O, and other greenhouse gases. Selected groupings of gases are shown in bold and selected compounds or collections of compounds that fall within these groupings are shown as dashed lines. The ODS group here refers to combined CFCs, HCFCs, halons, and solvents (CCl_4 and CH_3CCl_3). Kyoto protocol synthetics are defined as HFCs (see **Chapter 2**), perfluorocarbons (PFCs, which include CF_4 and C_2F_6), SF_6, and NF_3 (**Section 1.5**). Lower tropospheric annual mean mole fractions were taken from AGAGE data (**Table 1-1**, **Figure 1-1**). Radiative forcing was calculated using the expressions in Ramaswamy et al. (2001), with radiative efficiencies as summarized in **Table A-1** and preindustrial global surface mean mole fractions of 722 ppb, 270 ppb, and 36 ppt for CH_4, N_2O, and CF_4, respectively. For comparison, the radiative forcing due to CO_2 was approximately 2 W m^{-2} in 2016.

measurement time series is around 25% lower than previous records, due primarily to differences in calibration scales (Culbertson et al., 2004; Oram, 1999).

The previous Assessment reported a slowly declining combined mole fraction of the CFC-114 ($CClF_2CClF_2$) and CFC-114a (CCl_2FCF_3) isomers. This downward trend has continued but at a slower rate than was reported between 2011 and 2012 (**Figure 1-1**, **Table 1-1**; Vollmer et al., 2018). In 2016, the global mean mole fraction of combined CFC-114 and CFC-114a was approximately 16 ppt, and the mole fraction of CFC-114a measured in the CGAA was around 1 ppt. The 2014 Assessment estimated a 10% contribution of CFC-114a to total CFC-114 in the atmosphere. A new study using CGAA samples shows the CFC-114a contribution to total CFC-114 increasing from 4.1% in the late 1970s to 6.5% in the mid-2010s (Laube et al., 2016). The sum of the abundances of the two CFC-114 isomers in the CGAA agree between this and another recently published record of combined-isomer measurements (Laube et al., 2016; Vollmer et al., 2018).

The 2010 and 2014 Assessments found that mole fractions of CFC-115 ($CClF_2CF_3$) had stabilized at approximately 8.4 ppt since around 2000. However, mole fractions have grown since 2012, reaching 8.5 ppt in 2016 (Vollmer et al., 2018). While the magnitude of this change is comparable with the uncertainties on the observations (around 0.1 ppt in 2016), the fact that it is observed at all remote AGAGE stations strongly suggests a renewed global increase (Vollmer et al., 2018).

Since the last Assessment, CFC-112 (CCl_2FCCl_2F), which had a Southern Hemispheric mole fraction of 0.42 ppt in 2016, has continued to decline in the atmosphere, and CFC-112a ($CClF_2CCl_3$) has remained relatively stable at close to 0.07 ppt in the Southern Hemisphere (update to Laube et al., 2014; see **Table 1-1**). In contrast, CFC-113a has continued to increase in the Southern Hemisphere at an accelerated rate since 2012, reaching 0.68 ppt in 2016 (Adcock et al., 2018).

CFC-216ba ($CClF_2CClFCF_3$) and CFC-216ca ($CClF_2CF_2CClF_2$) were measured for the first time in the CGAA (Kloss et al., 2014). The Southern Hemispheric mole fraction of CFC-216ba was found to be relatively constant over the last 20 years at 0.04 ppt. CFC-216ca exhibited a small positive trend, with a mole fraction in the CGAA of 0.02 ppt in 2012.

With respect to their influence on climate, in 2016, CFCs contributed 77% of the total direct radiative forcing due to ODSs regulated under the Montreal Protocol, with a combined radiative forcing of 250 mW m^{-2} (**Figure 1-3**). The radiative forcing due to CFCs has declined by 7% since its peak in 2000, driven primarily by the reduction in abundance of CFC-11 and CFC-12; by 2016 the radiative forcing due to each gas had declined by 9 mW m^{-2} from their respective peaks in 1994 and 2002.

Emissions and Lifetimes

Since the previous Assessment, there has been little new work on CFC lifetimes. Therefore, our lifetimes estimates for these compounds are still based on SPARC (2013), as summarized in **Table A-1**.

Given the global phaseout of the production of CFCs for dispersive uses under the Montreal Protocol, emissions to the atmosphere are now expected to be due only to leakage from banks. These emissions are generally expected to decline with time as the size of the banks decrease, as is reflected in the monotonically decreasing emissions in previous baseline (A1) scenarios of CFC emissions (Harris and Wuebbles et al., 2014). One potential exception was identified in the IPCC/TEAP Special Report: Safeguarding the Ozone Layer and the Global Climate System (Ashford et al., 2005), where a global increase in emissions could coincide with the decommissioning of buildings with foams containing CFCs (primarily CFC-11).

Broadly in line with the expectation of declining emissions from banks, inferred emissions of CFC-12 have continued to fall since the previous Assessment, with 2016 emissions being approximately 35 Gg yr^{-1}, around 20% lower than in 2012, and 93% lower than their peak value in 1988 (**Figure 1-4**). Emissions of CFC-113 have remained at very low levels (<10 Gg yr^{-1}, compared to a maximum of around 243 Gg yr^{-1} in 1988).

The findings, since the previous Assessment, of a slowdown in the rate of decline of CFC-11 and an increase in the IHD suggest an increase in emissions, although changes in atmospheric transport could also play a role (Montzka et al., 2018; Prinn et al., 2018). **Figure 1-4** shows CFC-11 emissions inferred from AGAGE and NOAA data, assuming interannually repeating transport and a global lifetime of 52 years (also shown

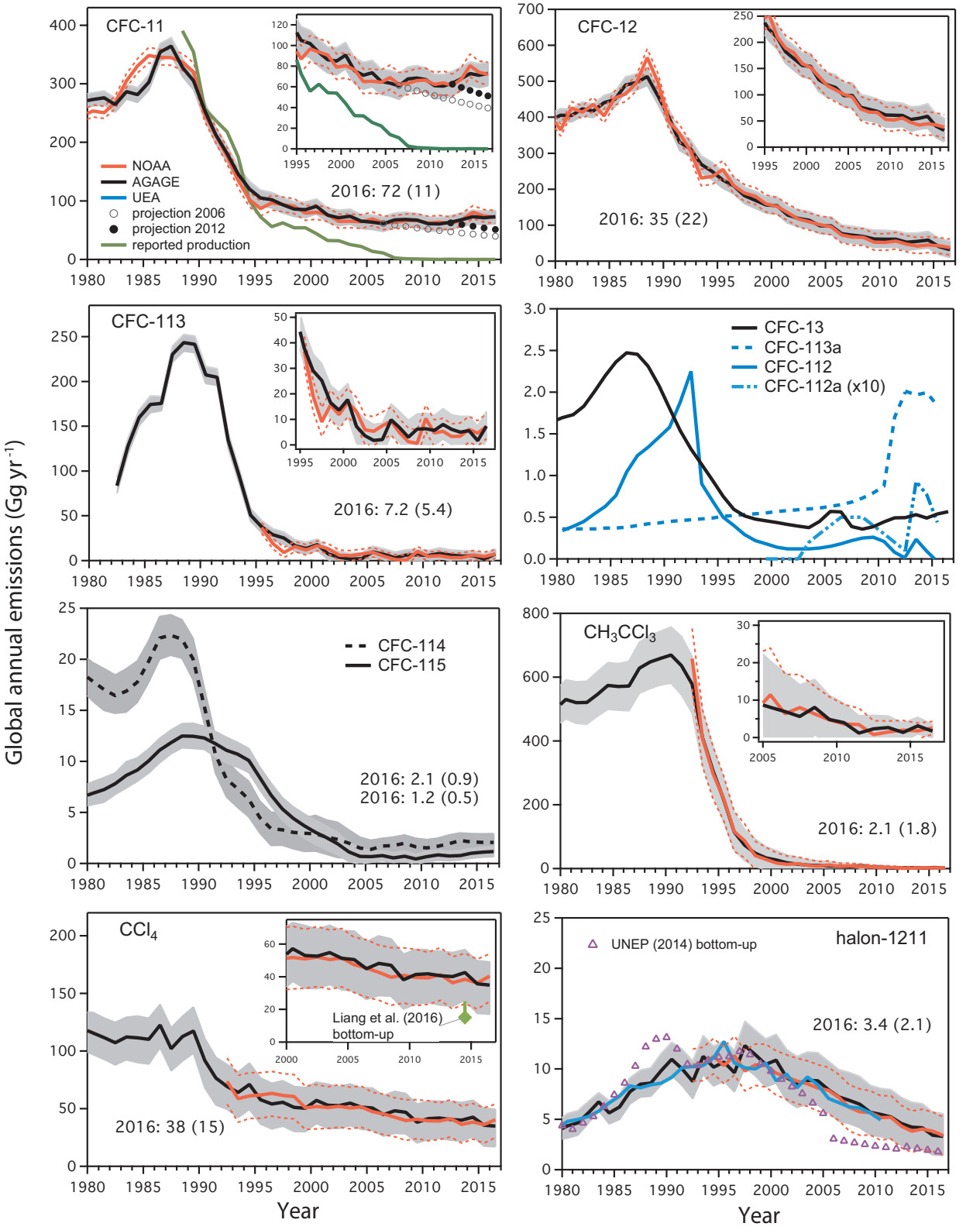
CFC-11
NOAA
AGAGE
UEA
projection 2006
projection 2012
reported production
2016: 72 (11)
CFC-12
2016: 35 (22)
CFC-113
2016: 7.2 (5.4)
CFC-13
CFC-113a
CFC-112
CFC-112a (x10)
CFC-114
CFC-115
2016: 2.1 (0.9)
2016: 1.2 (0.5)
CH3CCl3
2016: 2.1 (1.8)
CCl4
Liang et al. (2016) bottom-up
2016: 38 (15)
UNEP (2014) bottom-up
halon-1211
2016: 3.4 (2.1)
Global annual emissions (Gg yr-1)
Year

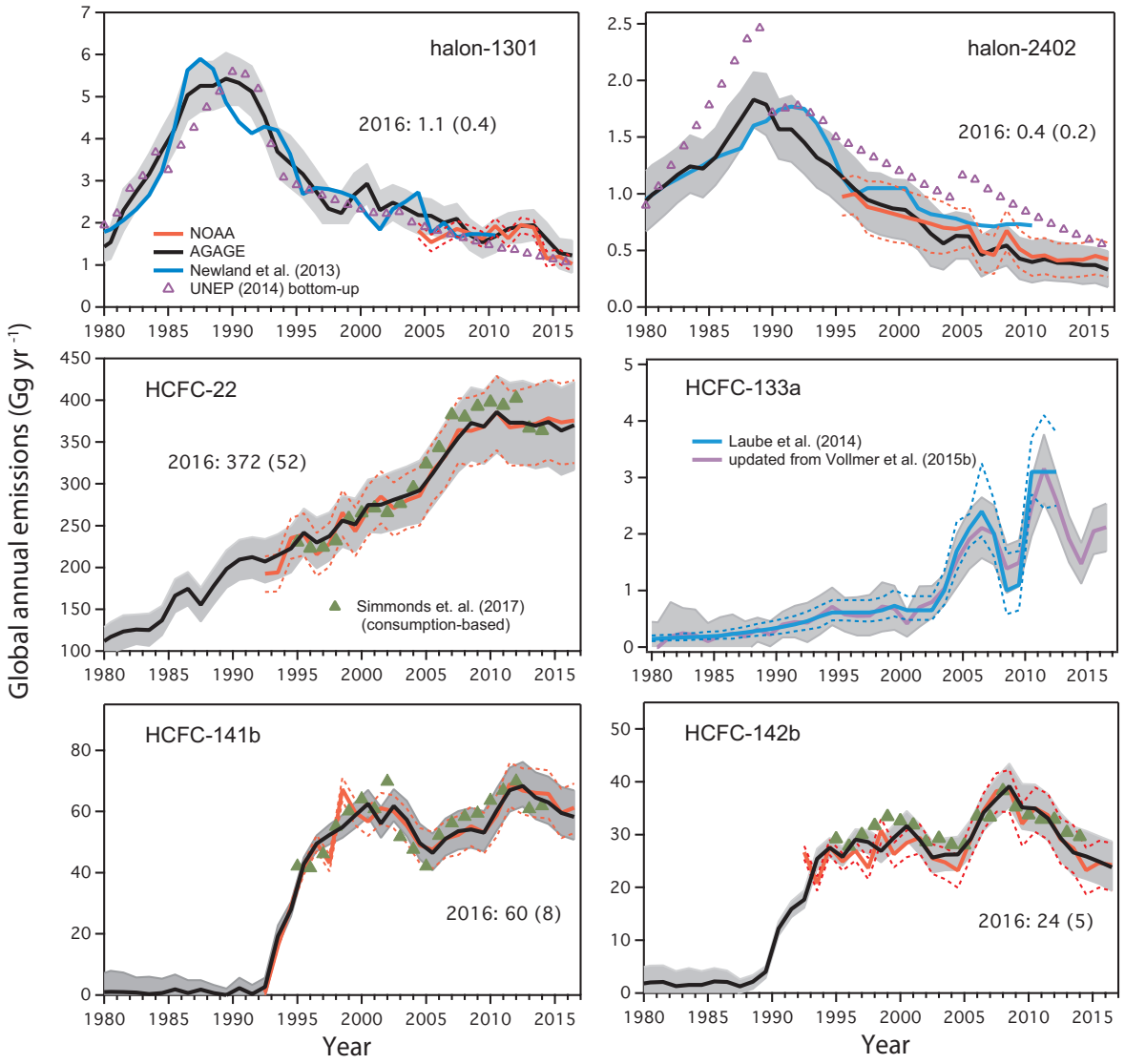

Figure 1-4. Top-down and bottom-up global emission rate estimates (Gg yr^{-1}) for ozone-depleting substances. Top-down emissions rates from AGAGE (black) and NOAA (red) atmospheric data were calculated using a global 12-box model (**Box 1-1;** Cunnold et al., 1983; Rigby et al., 2013). For the CFCs, stratospheric lifetimes were assumed to be equal to the total lifetimes from **Table A-1** (no other losses were assumed). For the halons, lifetimes are summarized in Vollmer et al. (2016). A lifetime of 32 years was used, derived from stratospheric, ocean, and soil lifetimes of CCl_4 (Butler et al., 2016; Rhew and Happell, 2016; SPARC, 2013). For the other species, stratospheric lifetimes from **Table A-1** were imposed, with OH rate constants from Burkholder et al. (2015). Global steady-state lifetimes for each species were: CFC-11 (52 years), CFC-12 (101 years), CFC-13 (640 years), CFC-113 (93 years), combined CFC-114/CFC-114a (189 years), CFC-115 (540 years), halon-1211 (16 years), halon-1301 (72 years), halon-2402 (28 years), HCFC-22 (11.6 years), HCFC-141b (9.2 years), HCFC-142b (17.6 years), and HCFC-133a (4.6 years). For some of these species, small differences can be seen between these global steady-state lifetimes calculated using the 12-box model and those in Appendix **Table A-1**, due to differences in assumed OH and model transport. Emissions were estimated using a Bayesian inverse method, in which the emissions growth rates from bottom-up inventories were used as *a priori* constraints (Rigby et al., 2011; Rigby et al., 2014) with minor update in Vollmer et al. (2018). Descriptions of bottom-up datasets are given in Rigby et al. (2014); Rigby et al. (2013); Simmonds et al. (2017); Vollmer et al. (2016); and

Vollmer et al. (2018). As described in Vollmer et al. (2018), the uncertainty in the *a priori* emissions growth rate was assumed to be 20% of maximum prior emissions. Posterior uncertainties (gray shading for AGAGE and red dashed lines for NOAA) include contributions from the observations, the model, the prior constraint, and the lifetime uncertainties from SPARC (2013), using the method in Rigby et al. (2014). For CFC-11, uncertainties are larger here than presented in the Executive Summary, as the systematic components of the uncertainty (i.e. due to lifetime and calibration scale) are omitted from Figure ES.2. For CFC-112, CFC-112a, CFC-113a, and the halons, emissions were calculated using UEA data from the Southern Hemisphere (blue; Laube et al. 2014). Emissions were calculated from 2013 to 2015 for CFC-112, CFC-112a, and CFC-113a using a 1-box model and scaled to match those reported in Laube et al. (2014) for previous years. HCFC-133a emissions were taken from Vollmer et al. (2015b) and Laube et al. (2014). Uncertainties for CFC-112, CFC-112a, and CFC-113a are not shown for clarity (see Laube et al., 2014). Numerical values of emissions estimates for 2016, shown in some panels, were calculated as the mean of estimates based on AGAGE and NOAA network data, with 1-sigma uncertainties (in parentheses) taken from the AGAGE estimates. For CCl_4, the bottom-up industrial estimate from Liang et al. (2016) is shown as a green diamond in the CCl_4 inset, with the potential magnitude of legacy emissions shown as a green bar extending upwards. Bottom-up estimates for halons (violet triangles) were updated from (UNEP, 2014a). For the major HCFCs, consumption-based estimates from Simmonds et al. (2017) are shown (solid green triangles). These estimates are calculated from reported consumption and estimates of immediate and ongoing release rates that were chosen to be consistent with the top-down emissions estimates.

in Executive Summary Figure ES.2). Following an initial decline after the late 1980s, emissions did not drop substantially after about 2002–2005, with the 2002–2012 average being 66 Gg yr^{-1} or 64 Gg yr^{-1} (using AGAGE or NOAA observations, respectively), which is about 82% lower than the peak in 1987. The inversions then show an increase in emissions beginning around 2013 and reaching an average of 72 or 75 Gg yr^{-1} between 2014 and 2016 (for AGAGE or NOAA data, respectively). This represents a 7 Gg yr^{-1} (or 10%) to 11 Gg yr^{-1} (or 17%) increase in emissions over the 2002 to 2012 average. These emissions are higher overall than the NOAA-data-based estimate of Montzka et al. (2018), who assumed a longer lifetime than the SPARC (2013) estimate used here. However, due to the use of a different inverse modeling approach, they found a slightly larger magnitude of the post-2013 increase, of 13 ± 5 Gg yr^{-1} (25 ± 13%) for 2014–2016 compared to 2002–2012. Considered together, these estimates using AGAGE and NOAA data show an increase in emissions of around 10 Gg yr^{-1} between these two periods. Following the methodology used in previous Assessments and Montzka et al. (2018), two projections were created to examine the expected decline in emissions after 2006 (near the beginning of the period during which emissions did not decline) and 2012 (after which emissions increased) (**Figure 1-4** and Executive Summary Figure ES-2). These projections are based on reported CFC-11 production history, an estimate of the magnitude of the bank for the year 2002 (IPCC/TEAP, 2005), and the assumption of a constant release fraction from the bank following 2006 or 2012. The release fractions used in the projections were estimated as the mean release fractions during the 7-year periods prior to 2006 or 2012 and were based on the yearly inferred bank size and top-down emissions over these periods. The projections indicate that emissions may have been higher than expected since the mid-2000s, although this has only recently become clear given the relatively large uncertainties considered in the past on top-down emissions and on projections. The projections also highlight that the recent emissions increase may be significantly larger than 10 Gg yr^{-1}, when considered relative to the expected emissions decline during this period. Montzka et al. (2018) argue that the recent increase is too large and too rapid to be explained by the release of CFC-11 from its bank, including from the decommissioning of old buildings, given our understanding of the bank size and past release rates. Therefore, they propose that new production is taking place that has not been reported to the UN Environment Ozone Secretariat. This would be inconsistent with the CFC-11 phaseout agreed under

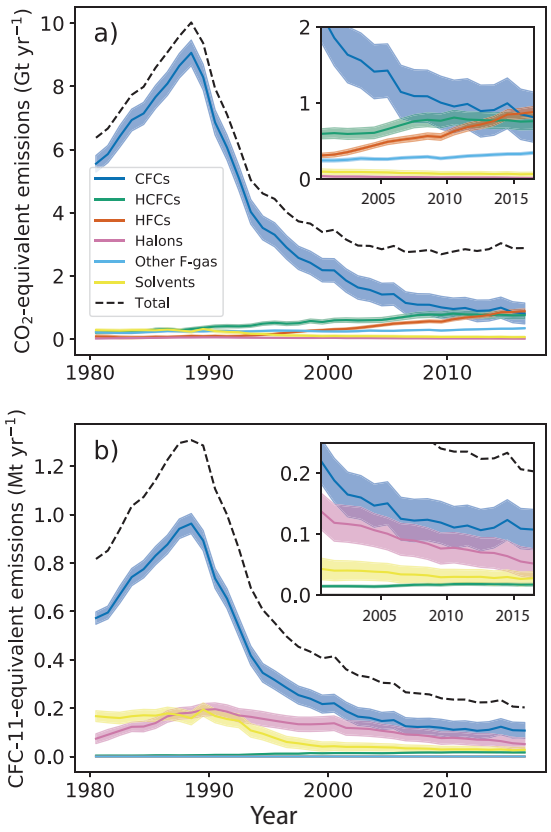

Figure 1-5. (a) 100-year GWP-weighted emissions and (b) ODP-weighted emissions. Emissions are the average of those derived from AGAGE and NOAA data, converted to CO_2-equivalents and CFC-11-equivalents using 100-year time horizon GWPs and ODPs from **Table A-1.** Species are grouped into CFCs, HCFCs, HFCs (see **Chapter 2**), halons, solvents (CCl_4 and CH_3CCl_3), and other F-gases (SF_6, CF_4, C_2F_6, C_3F_8, NF_3, SO_2F_2, see **Section 1.5**). Totals are shown as dashed black lines and shading indicates the 1-sigma uncertainty.

the Montreal Protocol. If the new emissions are associated with uses that substantially increase the size of the CFC-11 bank, further emissions resulting from this new production would be expected in future. The recent increase in emissions and any associated future emissions will delay the expected rate of recovery of stratospheric ozone relative to previous projections.

Inferred emissions of the lower-abundance compound CFC-13 show a strong decline in the first decade following a maximum in emissions in the late 1980s of 2.5 Gg yr^{-1} (Vollmer et al., 2018). However, for the last decade, emissions have plateaued at around 0.5 Gg yr^{-1} (approximately 85% lower than their peak value). CFC-13 was used primarily in refrigeration; the size of the CFC-13 bank and rate of release from it were expected to continue to decline with time.

Emissions of the combined CFC-114/CFC-114a isomers have plateaued for at least the last decade, at 1.9 Gg yr^{-1}, which is about 10% of the maximum value, reached in the late 1980s (Vollmer et al., 2018). Based on a study that can separate the two isomers (Laube et al., 2016), stagnant emissions were found for CFC-114 (1.8 Gg yr^{-1}; data through 2014), while those of the minor CFC-114a isomer have slightly declined. This indicates that the sources of the two isomers are, at least in part, decoupled. Laube et al. (2016) speculated that emissions of CFC-114a could be linked to the production of HFC-125 and HFC-143a.

Global emissions of CFC-113a increased strongly between 2009 and 2012 and since then have remained at approximately 1.7 Gg yr^{-1} (Adcock et al., 2018). This is opposite to the trend exhibited by the major isomer CFC-113 and, similar to the relative changes in CFC-114 and CFC-114a, indicates that the two isomers may have some different sources.

Emissions of CFC-115 appear to have increased since the previous Assessment, with Vollmer et al. (2018) reporting mean emissions for 2015–2016 of 1.14 ± 0.5 Gg yr^{-1}, which is approximately double that of the period 2007–2010, when emissions were at a minimum (**Figure 1-4**). Recent emissions are around 5–10% of the maximum, found in the late 1980s. While some CFC-115 was found as an impurity in samples of the refrigerant HFC-125 (CHF_2CF_3), this was not thought to be significant enough of a source to explain global emissions. Therefore, the cause of this emissions increase is unknown.

Several regional studies have examined CFC emissions using atmospheric observations. Between 2008 and 2014, emissions within the USA of the three major CFCs (CFC-11, CFC-12, and CFC-113) were estimated to have declined (L. Hu et al., 2017). These results suggest that the USA is unlikely to be the

Box 1-1. Inferring Emissions Using Atmospheric Data

In this Assessment, as in previous reports, emissions of ODSs (and of HFCs in Chapter 2) are inferred using atmospheric observations and a model of atmospheric transport and chemistry. Here, we describe the principle considerations behind these "top-down," or "inverse," calculations. An overview of the various methods for estimating ODS emissions can be found in Montzka and Reimann et al. (2010).

If we assume that the atmosphere consists of a single box into which trace gases are emitted, and within which some loss takes place, mass balance considerations allow the rate of change in the burden (B, the total mass of the gas in the atmosphere) to be written as:

$$\frac{dB}{dt} = Q - \frac{B}{\tau}$$

Here, Q is the globally integrated emission rate (in mass per unit time) and τ is the overall lifetime of the gas in the atmosphere. The latter is determined by a variety of sinks such as photolysis (e.g., in the stratosphere), reaction with oxidants (e.g., the hydroxyl radical), and loss at the surface (e.g., to soils or the ocean). The previous Assessment discussed how the lifetimes from these different processes can be combined to calculate overall lifetimes.

For long-lived gases ($\tau \geq 0.5$yr) that are relatively well mixed throughout the atmosphere, surface mole fraction data from global networks such AGAGE and NOAA provide estimates of the trace gas global burden and its rate of change.

For the majority of gases in this chapter, the magnitudes of the global lifetimes are relatively well known, compared to uncertainties in bottom-up emissions estimates. These lifetimes estimates, primarily taken from the SPARC Lifetimes assessment (SPARC, 2013), are based on a combination of satellite observations, in situ measurements of tracer-tracer correlations, photochemical model simulations, and estimates of oceanic and terrestrial fluxes, which are independent of the observations used to infer emissions in this chapter. However, it should be noted that SPARC (2013) also included lifetimes estimates inferred using AGAGE and NOAA observations for some species, which leads to some circularity if used to infer emissions.

We can rearrange Equation 1 to infer global emissions rates (Q) from the information on the global burden (B) and its trend (dB/dt) and estimates of the global lifetime (τ). Such emissions estimates are sensitive to uncertainties in the observed burden (e.g., random and representation errors in the observations and systematic calibration scale errors) and uncertainties in the lifetime, both of which should be propagated through to the uncertainties in the inferred emissions (e.g. Rigby et al., 2014).

While this discussion illustrates the broad principles behind the inference of emissions at the global scale, some additional factors are introduced in the calculations presented in this chapter. Firstly, a model of atmospheric transport and chemistry is used to simulate the nonuniform distribution of gases in the atmosphere, improving our estimates of the global burden compared to the single-box approach above. The model primarily used in this chapter is the AGAGE 12-box model, which separates the atmosphere into boxes with latitudinal boundaries at 90°N, 30°N, 0°N, 30°S, and 90°S, and vertical boundaries at 1000 hPa, 500 hPa, 200 hPa and 0 hPa (Cunnold et al., 1994; Cunnold et al., 1983; Rigby et al., 2013). Transport of each gas occurs via parameterized mixing and advection between boxes. Removal from the atmosphere takes place via reaction with the hydroxyl radical, via first-order processes parameterizing non-OH photochemical losses and via loss to the ocean or land. This model was designed to simulate baseline mole fractions (i.e.,

Box 1-1, continued.

observations that have not been strongly influenced by nearby sources and can be considered representative of zonal averages) for long-lived gases that have small spatial gradients in the atmosphere. However, for shorter-lived substances, which exhibit strong spatial and temporal variability, atmospheric distributions may be more poorly represented. Secondly, a Bayesian statistical approach is employed that allows prior beliefs about emissions to be incorporated into the inversion and provides a framework for propagating prior and observational uncertainty through to the derived emissions estimates (e.g., see the supplementary materials in Rigby et al., 2014).

Regional emissions estimates are possible where spatially and/or temporally dense measurements are made within or downwind of certain areas (e.g., Graziosi et al., 2015; L. Hu et al., 2017). The regional approach requires a model that can simulate the three-dimensional atmospheric transport of a gas from the source to the measurement points. Such simulations can then be compared to the data and fluxes at regional and national scales inferred through examination of the difference between the two. In contrast to global estimates, for long-lived compounds, regional flux inversions are insensitive to uncertainties in the atmospheric lifetime. However, significant uncertainties can arise through the need to accurately simulate trace gas transport at high resolution.

source of the increase in global CFC-11 emissions that started in 2013. In aggregate, the emissions of these gases agreed well with bottom-up estimates by the US Environmental Protection Agency (EPA). However, species-specific differences were found, particularly for CFC-113. Where the emissions inventory had predicted negligible emissions since 1996, emissions inferred from atmospheric concentrations were statistically higher than zero (by around 0.5–3 Gg yr^{-1}) until 2013. While regional inverse modeling of CFC-11 emissions from eastern Asia has not yet been carried out, Montzka et al. (2018) note increased variability in CFC-11 measured at Mauna Loa, Hawai'i, beginning after 2012, along with emerging correlations with other anthropogenic species during the autumn months, when this site is strongly influenced by flows from eastern Asia. These signals are consistent with an increase in CFC-11 emissions from eastern Asia. Regional inverse modeling using data from the Gosan Station, South Korea, showed evidence of emissions of combined CFC-114/CFC-114a and CFC-115 from China (Vollmer et al., 2018). The inferred emissions for each of these gases were of a magnitude that was a significant fraction of the respective global total. Persistent sources of CFC-113a and CFC-114a from eastern Asia were also identified (Adcock et al., 2018; Laube et al., 2016).

In summary, while emissions of almost all CFCs have declined substantially since their peaks in the 1980s or 1990s, and emissions of CFC-12 and -113 continue to decline, there are strong indications that emissions of several CFCs are no longer following the downward trajectory expected under a scenario of globally depleting banks. Most important, CFC-11 emissions have increased by around 10 Gg yr^{-1} for 2014–2016, relative to 2002–2012. A study into these CFC-11 trends proposes that new production not reported to the UN Environment Ozone Secretariat may be taking place and that at least some of the new emissions originate from eastern Asia (Montzka et al., 2018). Regional studies find evidence for continuing or increasing emissions of some of the more minor CFCs from eastern Asia (Vollmer et al., 2018).

In terms of both CO_2- and CFC-11-equivalents, inferred combined emissions of all CFCs have declined markedly since the late 1980s (**Figure 1-5**). In 2016, CO_2-equivalent emissions of the CFCs were 0.8 ± 0.3 Gt yr^{-1}, approximately 90% lower than the highest inferred value of 9.1 ± 0.4 Gt yr^{-1} in 1988. If the recent change in the CFC-11 growth rate is due to emissions alone, the increase since 2013 has added around 0.05 Gt yr^{-1} CO_2-equivalent to this total. Total ODP-weighted emissions for all CFCs dropped by around 90% since the peak (in 1987) and reached 110 ± 30 Gg yr^{-1} CFC-11-equivalent in 2016.

1.2.2 Halons

Observations of Atmospheric Abundance

Halon-1211 ($CBrClF_2$), halon-2402 ($CBrF_2CBrF_2$), and halon-1202 (CBr_2F_2) abundances continued to decline from their peak values, observed in the early and mid-2000s. Global surface mean mole fractions of approximately 3.5 ppt and 0.42 ppt were observed for halon-1211 and -2402, respectively, in 2016, and Southern Hemispheric mole fractions of approximately 0.014 ppt were recorded for halon-1202 (**Table 1-1**, **Figure 1-1**) (Newland et al., 2013; Vollmer et al., 2016). Halon-1301 (CF_3Br) growth rates, which were reported as being positive in the previous Assessment, declined to <0.01 ppt yr^{-1} in 2016, when a global mean mole fraction of 3.36 ppt or 3.25 ppt was reached for AGAGE and NOAA, respectively.

New measurements of halon-2311 ($CF_3CHClBr$, halothane, an anesthetic that is no longer widely used) show low abundances in the atmosphere with a mole fraction that declined from 0.025 ppt in 2000 to <0.01 ppt in 2016 in the Northern Hemisphere (update of Vollmer et al., 2015c).

The direct contribution of halons to global radiative forcing was small, 2.2 mW m^{-2} in 2016, equivalent to 0.9% of the radiative forcing of CFCs (**Figure 1-3**). When their influence on ozone depletion is also considered, radiative forcing due to halons is negative (Daniel et al., 1995).

Emissions and Lifetimes

Lifetimes of the three most abundant halons are taken from SPARC (2013), and are summarized in **Table A-1.** For these three halons, emissions derived from observations generally agree within their uncertainties for the estimates made from NOAA, AGAGE, and UEA measurements (**Figure 1-4;** Vollmer et al., 2016; Newland et al., 2013). For each gas, these emissions have continued to decline since the previous Assessment. Bottom-up emissions were revised in 2014 by the Halon Technical Options Committee (HTOC), and updates are provided here (UNEP, 2014a).

Top-down estimates of emissions of halon-1211 show a decline to 3.4 ± 2.1 Gg yr^{-1} in 2016 (average of emissions inferred from AGAGE and NOAA data), 70% lower than the peak value in 1998. Compared to previous bottom-up estimates (UNEP, 2011), the most recent HTOC emissions for this species have been revised downward for the last decade, creating a larger gap (~50%) with the observation-based values. In contrast, for halon-1301, bottom-up and observation-based emissions now show closer agreement than in the previous Assessment, with top-down values for 2016 of 1.1 ± 0.4 Gg yr^{-1} and HTOC estimates of 1.1 Gg yr^{-1}. The 2016 top-down values are 80% lower than their peak of 5.4 ± 0.6 in 1989. Halon-2402 bottom-up emissions are now available for a longer time period than in the previous Assessment and are significantly larger than previously estimated (UNEP, 2014a). They show a similar trend to emissions inferred from observations, which grew until 1988 and then declined. However, the HTOC estimates were larger throughout, at 0.56 Gg yr^{-1} in 2016, compared to top-down estimates of 0.37 ± 0.2 Gg yr^{-1}; these are 80% lower than their peak value.

Global emissions of the lower-abundance halon-2311 inferred from atmospheric observations declined from 0.49 Gg yr^{-1} in 2000 to 0.25 Gg yr^{-1} in 2014, likely reflecting a continuing reduction of its use as an anesthetic (Vollmer et al., 2015c).

Total CO_2-equivalent halon emissions were small in 2016, 2% that of CFCs, as shown in **Figure 1-5**. However, due to their high ODPs (**Table A-1**), their contribution to ozone depletion remains significant, with ODP-weighted emissions of 50 ± 20 Gg yr^{-1} CFC-11-equivalent in 2016, just under half that of global CFC emissions.

1.2.3 Carbon Tetrachloride (CCl_4)

Observations of Atmospheric Abundance

Carbon tetrachloride (CCl_4) has continued to decline at a rate similar to that reported in the previous Assessment. AGAGE observations showed a decline of 1.5% between 2015 and 2016, with a mole fraction of 79.9 ppt in 2016, and NOAA reported a decline of 1.2% during the same period and a 2016 mole fraction of 81.2 ppt (**Table 1-1**, **Figure 1-1**). These differences are broadly consistent with known calibration scale differences, although the level of agreement has changed over time, suggesting some drift in one or both scales or time-dependent analytical issues. Data from UCI show a smaller decline, of 0.3%, between

these years and a 2016 mole fraction of 81.9 ppt. The IHD, estimated from AGAGE and NOAA networks, has exhibited a gradual decline since 2000, with a rate of 0.04 and 0.03 ppt yr^{-1}, respectively, for each network.

Ground-based remote sensing observations of CCl_4 from Jungfraujoch show a slightly lower rate of decline between 2010 and 2016 than the AGAGE and NOAA networks, although the uncertainties overlap at the 2-sigma level (**Table 1-2**). New observations with global coverage in the upper troposphere and lower stratosphere have become available from the MIPAS instrument, onboard the Envisat satellite (Eckert et al., 2017; Valeri et al., 2017). The upper-tropospheric trends derived from these observations between 2002 and 2012 confirm that atmospheric mole fractions declined during this period with a magnitude that was broadly consistent with the ground-based measurements (Valeri et al., 2017). However, stratospheric trends derived from these observations were found to be nonuniform, with some (generally non-statistically significant) positive trends even being found in the middle stratosphere in the Southern Hemisphere (Eckert et al., 2017). This high variability, compared to surface data, reflects the additional impact of variability in transport on the temporal evolution of trace gases in the stratosphere.

Radiative forcing due to CCl_4 declined to 14 mW m^{-2} in 2016, equivalent to 6% of the radiative forcing due to CFCs (**Figure 1-3**).

Emissions and Lifetime

Previous Assessments highlighted a significant discrepancy between CCl_4 trends observed in atmospheric data and those calculated from known sources and our understanding of atmospheric sinks (Carpenter and Reimann et al., 2014; Montzka and Reimann et al., 2010). In the previous Assessment, the best estimate of the CCl_4 lifetime was 26 years, which led to a top-down global emissions estimate of 57 (40–74) Gg yr^{-1}. In contrast, bottom-up estimates of emissions due to feedstock use, based on the difference between reported production and destruction (Montzka and Reimann et al., 2010), were less than 4 Gg yr^{-1} in 2012 (Carpenter and Reimann et al., 2014). In light of these discrepancies, the CCl_4 budget was re-examined in the 2016 SPARC Report on the Mystery of Carbon Tetrachloride (Liang et al., 2016). Here we summarize the primary findings of this report, along with additional studies that have been carried out in the interim period.

The global lifetime of CCl_4 has been revised upward from 26 years, initially to 33 (28–41) years in Liang et al. (2016), primarily due to an increase in the estimated lifetime due to ocean loss and uptake from soils. This has subsequently been reduced slightly to 32 (26–43) years, following a revision to the lifetime with respect to ocean loss, the best estimate for which is now 183 (147–241) years (Butler et al., 2016). The current best estimate for the lifetime due to soil uptake is 375 (228–536) years, which has increased from the previously estimated 195 years (Rhew and Happell, 2016). Estimates of the lifetime due to stratospheric loss remained unchanged at 44 (36–58) years (SPARC, 2013). Of these sinks, the remaining uncertainties in the ocean uptake were found to have the potential to most significantly alter model estimates of the atmospheric trend (Chipperfield et al., 2016).

Global emissions, derived from atmospheric trends and a model parameterized with a 33-year lifetime, were reduced to 40 ± 15 Gg yr^{-1} (2007–2014 average) in Liang et al. (2016), compared to 57 ± 17 Gg yr^{-1} in the previous Assessment (2011–2012 average). Estimates based on the observed atmospheric IHD were found to be similar to the trend-based estimate, at 30 ± 5 Gg yr^{-1} (2010–2014 average; update of Liang et al., 2014b). Updated estimates (**Figure 1-4**), using the new lifetime of 32 years and AGAGE and NOAA observations, show a relatively rapid drop in emissions in the late-1980s and early-1990s, then a relatively slow decline since the late-1990s. Since 2000, emissions have been declining at a rate of ~1.2 Gg yr^{-1} per year (**Figure 1-4**). Emissions inferred here for 2016 from the AGAGE and NOAA data, respectively, were 35 ± 16 Gg yr^{-1} and 40 ± 15 Gg yr^{-1} (around 30% of the peak value, which occurred in the mid-to-late 1980s).

Since the previous Assessment, global bottom-up estimates have been made of emissions from a range of industrial sources. Liang et al. (2016) and Sherry et al. (2017) proposed that 13 Gg yr^{-1} may be due to unreported, non-feedstock emissions from chloromethane and perchloroethylene production plants. In addition, unreported, inadvertent emissions during chlorine production (e.g., from chlor-alkali plants) and usage (e.g., in industrial and domestic bleaching) and legacy

emissions from landfills and contaminated soil were estimated to contribute up to 10 Gg yr^{-1} (which is towards the lower end of estimates previously made by Fraser et al. (2014)). Similar to previous Assessments, 2 Gg yr^{-1} fugitive emissions from feedstock usage were estimated (e.g., in the production of HFCs and other compounds). Together, these sources could total around 25 Gg yr^{-1}.

Regional studies of CCl_4 emissions have been carried out for the USA, Europe, and East Asia. NOAA observations across the USA were used to infer fluxes of 4.0 (2.0–6.5) Gg yr^{-1} from 2008 to 2012 (L. Hu et al., 2016a), a value two orders of magnitude larger than reported by the US Environmental Protection Agency (EPA) and around 10% of the global top-down value estimated here during the same period. The spatial distribution of emissions derived for the USA was found to be more consistent with the location of industrial sources in the EPA reports (e.g., chlor-alkali plants) than other potential sources that would be more widely distributed (e.g., uncapped landfill). This suggests that emissions may be underreported for these industries. Similarly, using European AGAGE data, Graziosi et al. (2016) found that the spatial distribution of emissions in Europe was similar to that of industrial sources in the European Pollutant Release and Transfer Register and the location of chlor-alkali plants. Also in common with the USA, these top-down emissions estimates are significantly larger than the bottom-up reports. The top-down mean European emission rate was estimated to be 2.2 ± 0.8 Gg yr^{-1} from 2006 to 2014 (around 5% of the global mean estimated here during the same period), declining at an average rate of 6.9% yr^{-1}. Bottom-up estimates for China showed an increase in emissions during the 1990s, which reached a peak in 2002 of 14.0 (9.1–19.5) Gg yr^{-1} (Bie et al., 2017). This was followed by a decline to 5.2 (2.4–8.8) Gg yr^{-1} in 2014, with the sharpest drop occurring between 2009 and 2011. It was proposed that this decrease was primarily due to a reduction in CCl_4 use as a process agent. Top-down estimates for China from late 2006 to early 2008 by Vollmer et al. (2009) are consistent with these bottom-up values, within uncertainties (15 (10–22) Gg yr^{-1}). However, the subsequent decline estimated by Bie et al. (2017) has not yet been confirmed by atmospheric observations at the national scale. The sum of the available regional top-down studies suggests emissions of around 20 Gg yr^{-1}, although it should be emphasized that these studies cover different time periods and that this cannot be considered a global total, as several potentially important regions are not observed by the current monitoring network (e.g., India, Russia, Africa, and South America).

In summary, the upward revision of the atmospheric lifetime and the proposal of significant emissions from sources such as chloromethane, perchloroethylene, and chlor-alkali plants have substantially reduced the gap in the CCl_4 budget since the previous Assessment. Regional inverse modeling studies in the USA and Europe support the idea that reported emissions are significantly underestimated and that industrial sources could be much larger than previously thought. However, there remains a difference of around 10 Gg yr^{-1} between the global top-down estimate, based on our updated knowledge of the sinks, and recent global bottom-up estimates.

CO_2-equivalent CCl_4 emissions were relatively small in 2016, 8% that of the CFCs (**Figure 1-5**). However, ODP-weighted emissions were significant, at 27 ± 10 Gg yr^{-1} in 2016, 23% as large as the CFCs.

1.2.4 Methyl Chloroform (CH_3CCl_3)

Observations of Atmospheric Abundance

The global mean mole fraction of methyl chloroform (1,1,1-trichloroethane, CH_3CCl_3) continued to decline between 2012 and 2016, decreasing to 2.6 ± 0.7 ppt in 2016, 2% of its maximum value of 133 ± 4 ppt, which was reached in 1992 (**Figure 1-1**, **Table 1-1**). The IHD reached a maximum in 1990 (28 ppt) and has since declined to 0.078 ppt in 2016. The radiative forcing due to methyl chloroform is now negligible (**Figure 1-3**).

Emissions and Lifetime

Assuming a constant CH_3CCl_3 global lifetime of 5.0 years (SPARC, 2013), we infer emissions that have continued to decline since 2012 (**Figure 1-1**, **Table 1-1**), with mean values of 1.7 and 2.5 Gg yr^{-1} in 2016 (AGAGE and NOAA, respectively); the emissions are not statistically different from zero at the 1-sigma level. Using global box models, non-zero emissions have been inferred for up to at least 2014 (Rigby et

al., 2017; Turner et al., 2017), with estimated global emissions in the range of 0.5 to 2 Gg yr^{-1} in 2014. Observations of above-baseline mole fractions at one AGAGE station (Scripps Institution of Oceanography, La Jolla, California, USA) confirm the continued release of CH_3CCl_3 near this location until at least 2014 (Rigby et al., 2017). Above-baseline events were also found up until 2012 at Monte Cimone, Italy, and Jungfraujoch, Switzerland, with inferred emissions in Europe declining from around 1.1 Gg yr^{-1} in 2002 to 0.2 Gg yr^{-1} in 2012 (Maione et al., 2014).

Rigby et al. (2017) and Turner et al. (2017) used methyl chloroform observations from AGAGE and NOAA to infer changes in tropospheric hydroxyl radical (OH) concentrations, the primary sink for CH_3CCl_3, between the 1980s and the mid-2000s. They both found maximum likelihood tropospheric concentrations of OH that increased during the late 1990s and early 2000s and fell afterwards. However, both studies noted that the uncertainty in these inferred changes was large, such that a solution with no OH variability (and therefore no change in CH_3CCl_3 lifetime) was also possible. Rigby et al. (2017) inferred a global mean OH concentration that was 5–10% higher than was estimated in Rigby et al. (2013) and SPARC (2013), suggesting that the CH_3CCl_3 lifetime (and that of many other compounds whose primary sink is OH) may be shorter than the SPARC estimate, although their uncertainties suggest that this difference is not statistically significant.

The influence of CH_3CCl_3 emissions on climate and ozone depletion is now very small (**Figure 1-5**). In 2016, 100-year-GWP-weighted emissions were 0.3 ± 0.3 Mt yr^{-1} (0.04% as large as the CFCs), and ODP-weighted emissions were 0.3 ± 0.3 Gg yr^{-1} (0.3% as large as the CFCs).

1.2.5 Hydrochlorofluorocarbons (HCFCs)

Observations of Atmospheric Abundance

The global surface mean mole fraction of the most abundant HCFC, HCFC-22 ($CHClF_2$), has continued to increase since the previous Assessment and was around 237 ppt in 2016 (**Figure 1-1**, **Table 1-1**). However, its growth rate has declined relative to previous years (**Figure 1-1**) and is now comparable to the growth rate observed in the early 2000s. Growth rates of the less abundant HCFCs—HCFC-141b (CH_3CCl_2F) and HCFC-142b (CH_3CClF_2)—have declined substantially since 2012 (**Figure 1-1**). Global mean mole fractions of these two gases were about 24.5 ppt and 22 ppt in 2016, respectively. Abundances of all three HCFCs have grown more slowly than projected in the previous Assessment, with 2016 mole fractions being about 7.5%, 4.5%, and 8% lower than the A1-2014 scenario for HCFC-22, HCFC-141b, and HCFC-142b, respectively. This scenario assumed that after 2012, all Article 5 countries would continue producing HCFCs at the maximum level allowed under the Montreal Protocol.

Recent trends of HCFC-22 and HCFC-142b are compared between surface in situ (including grab samples) and ground-based total column remote sensing methods (**Table 1-2**). Trends calculated during the period 2010–2016 are similar for the two methods for HCFC-22 but do not agree for HCFC-142b. For HCFC-142b, the remote sensing observations show a trend that is not statistically different from zero, while in situ observations show a small positive (1% yr^{-1}) trend.

Upper tropospheric trends based on global satellite observations of HCFC-22 from MIPAS agree with surface trends measured by AGAGE and NOAA networks for the period from 2005 to 2012 (Chirkov et al., 2016). Stratospheric trends determined from satellite data largely reflect tropospheric trends but with additional variability, possibly caused by variability in stratospheric circulation.

HCFC-133a (CH_2ClCF_3), which is an intermediate in HFC-125, HFC-134a, and HFC-143a production, has increased only slightly since 2012, and its abundance remains less than 1 ppt. HCFC-31 (CH_2ClF), a relatively short-lived compound with an atmospheric lifetime of 1.2 years, is an intermediate in the synthesis of HFC-32 (CH_2F_2) and was first reported by Schoenenberger et al. (2015). It was found to be present in the Northern Hemisphere at 0.17 ppt in 2011, and updates to these measurements have shown a decline to 0.11 ppt in 2016. The compound HCFC-225ca ($CF_3CF_2CHCl_2$), which was used as a drop-in replacement for CFC-113, has been measured in the CGAA since the previous Assessment (Kloss et al., 2014). It appeared in the observational record in the early 1990s, and its abundance peaked at 0.05 ppt in

2001, after which it declined to 0.02 ppt in 2012.

The radiative forcing due to HCFCs reached 58 mW m^{-2} in 2016 (**Figure 1-3**), which is comparable to that of CFC-11 (60 mW m^{-2}) and 23% as large as total CFC radiative forcing. The major contributor to total HCFC radiative forcing was HCFC-22, which was responsible for 50 mW m^{-2} in 2016.

Emissions and Lifetimes

Lifetimes of the major of HCFCs have not been significantly updated since (SPARC, 2013), the values from which are used here (**Table A-1**).

Emissions of HCFC-22 inferred from atmospheric observations have remained relatively constant at ~370 Gg yr^{-1} since 2012 (**Figure 1-4**), while emissions of HCFC-141b and HCFC-142b have declined by approximately 10 Gg yr^{-1} (~10%) and 6 Gg yr^{-1} (~18%), respectively, between 2012 and 2016, reaching values of around 60 Gg yr^{-1} and 24 Gg yr^{-1} in 2016. For all three of these gases, the top-down emissions trends generally agree with consumption-based estimates (Simmonds et al., 2017) (**Figure 1-4**).

Emissions of HCFCs as a whole, expressed as CO_2-equivalent, have declined since the previous Assessment (**Figure 1-5**). This is contrary to the projected increase in emissions in the A1 scenarios, which were based on the assumption that Article 5 countries would produce the maximum amount of HCFCs allowed under the Montreal Protocol (Harris and Wuebbles et al., 2014; Simmonds et al., 2017). This emissions decrease is consistent with a sharp drop in reported HCFC consumption after 2012, particularly in Article 5 countries. By 2016, reported HCFC consumption in Article 5 countries declined by 30% compared to the 2008–2012 average (UNEP, 2017). These recent changes suggest that the 2007 adjustment to the Montreal Protocol has been highly effective in limiting emissions of these gases (Montzka et al., 2015; Simmonds et al., 2017).

Emissions trends have been inferred for some of the more minor HCFCs. Emissions of HCFC-124 ($CHClFCF_3$) have declined from ~7 Gg yr^{-1} in 2003 to ~3.5 Gg yr^{-1} in 2015 (Simmonds et al., 2017). Emissions of HCFC-133a (**Figure 1-4**), which had been reported as increasing prior to the previous Assessment (Laube et al., 2014), were found to suddenly decline after reaching a peak of 3 Gg yr^{-1} in 2011 and were at 1.5 Gg in 2014 (Vollmer et al., 2015b). As this compound is thought to be an intermediate during the manufacture of HFC-134a, HFC-143a, and HFC-125, this reduction may be related to better containment during production of these HFCs (Vollmer et al., 2015b). However, the trend appears to have reversed again after 2014. (**Figure 1-4**). Emissions of the compound HCFC-31 were recently inferred for the first time from atmospheric observations (Schoenenberger et al., 2015). Emissions were found to increase from 2000 to 2011, reaching 0.9 (0.7–1.0) Mg yr^{-1}, before declining until the last available measurements in 2014. The reasons for the decline are unknown but may be related to changes in HFC-32 production methods. Emissions of HCFC-225ca were inferred to increase between 1992 and 1999, reaching 1.5 Gg yr^{-1} before declining to 0.5 Gg yr^{-1} in 2011 (Kloss et al., 2014). This trend was thought to be consistent with an increase due to its use as a CFC replacement, then subsequent phasedown due to controls on HCFCs.

Regional emissions estimates using atmospheric observations indicate substantial declines in HCFC-22 and HCFC-142b emissions in the USA and HCFC-22 emissions in Europe, as would be expected from the phasedown schedule for non–Article 5 countries (**Figure 1-6**) (Graziosi et al., 2015; Hu et al., 2017). However, in both regions, significant differences with the bottom-up estimates were found, perhaps indicating incomplete or inaccurate reporting and assumptions relating to release rates and/or atmospheric modeling uncertainties. Because the phaseout of HCFCs in Article 5 countries is delayed compared to non–Article 5 countries (e.g., the USA and European countries), recent emissions estimates using bottom-up methods suggest a continued increase of HCFC-22, HCFC-141b, and HCFC-142b emissions from China since the 1990s (**Figure 1-6**) (Han et al., 2014; Li et al., 2016; Wang et al., 2015b). A number of observation-based estimates are generally consistent with these bottom-up estimates (Fang et al., 2012; Li et al., 2011; Liu et al., 2015; Stohl et al., 2010; Stohl et al., 2009; Vollmer et al., 2009; Wang et al., 2014; Yokouchi et al., 2006).

In terms of CO_2-equivalent emissions, HCFCs were comparable to the CFCs (and HFCs; **Chapter 2**) in 2016, at 0.8 ± 0.1 Gt CO_2 yr^{-1} (**Figure 1-5**). The major

contributor to this total was HCFC-22, with emissions of 0.7 ± 0.1 Gt yr^{-1} CO_2-equivalent in 2016. CO_2-equivalent emissions due to all HCFCs peaked in 2010 and then declined 6% by 2016. When weighted by their ODPs, emissions of HCFCs were relatively small in 2016, at 17 ± 2 Gg yr^{-1}, 16% as large as the CFCs. ODP-weighted emissions reached a maximum in 2011 and have declined by 6% since.

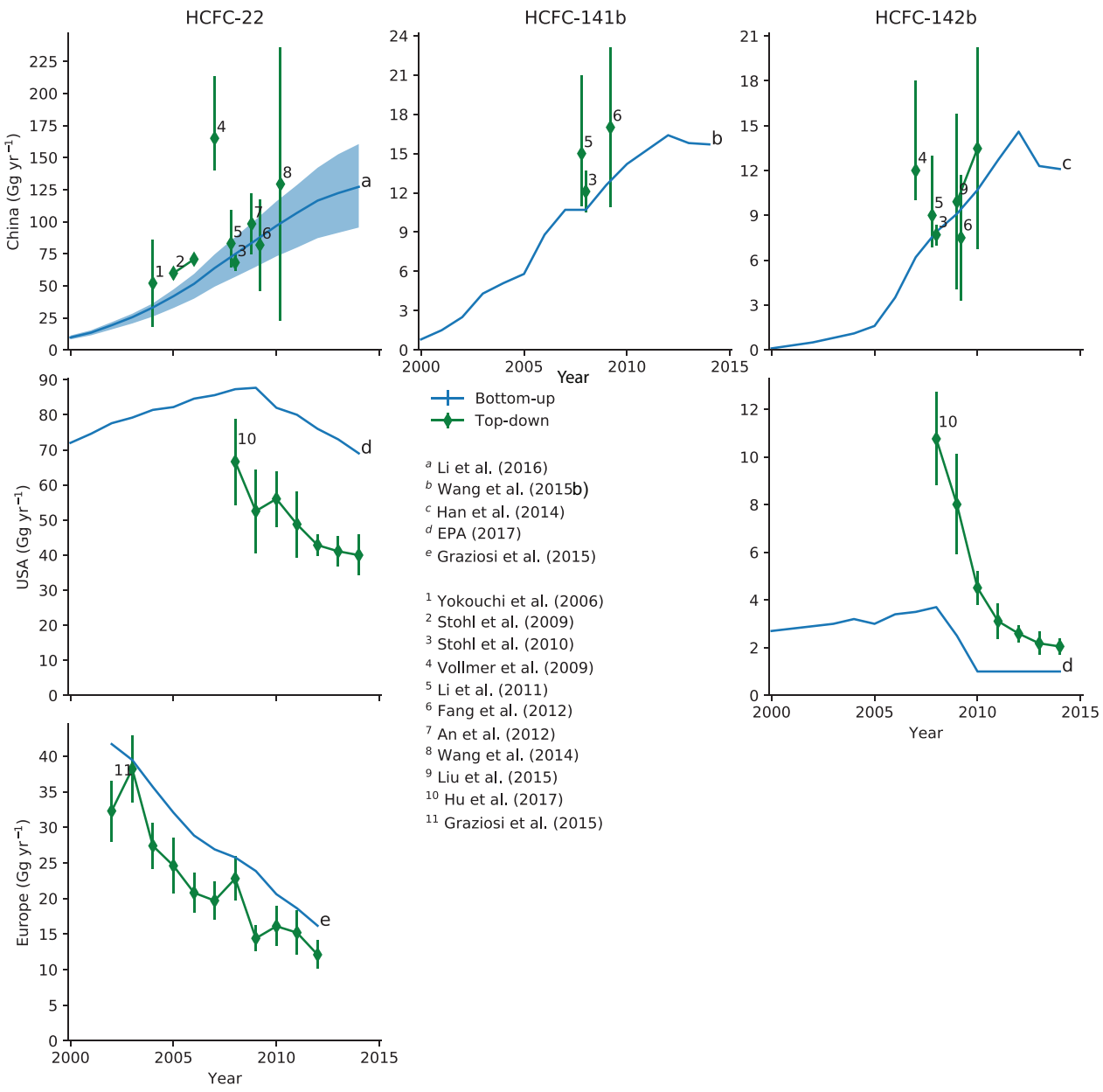

Figure 1-6. Regional emissions estimates of (*left to right*) HCFC-22, HCFC-141b, and HCFC-142b from (*top to bottom*) China, USA, and Europe. Bottom-up estimates are shown as solid blue lines with shading indicating uncertainty (where available). Top-down estimates from a variety of studies and 1-sigma uncertainties are shown in green.

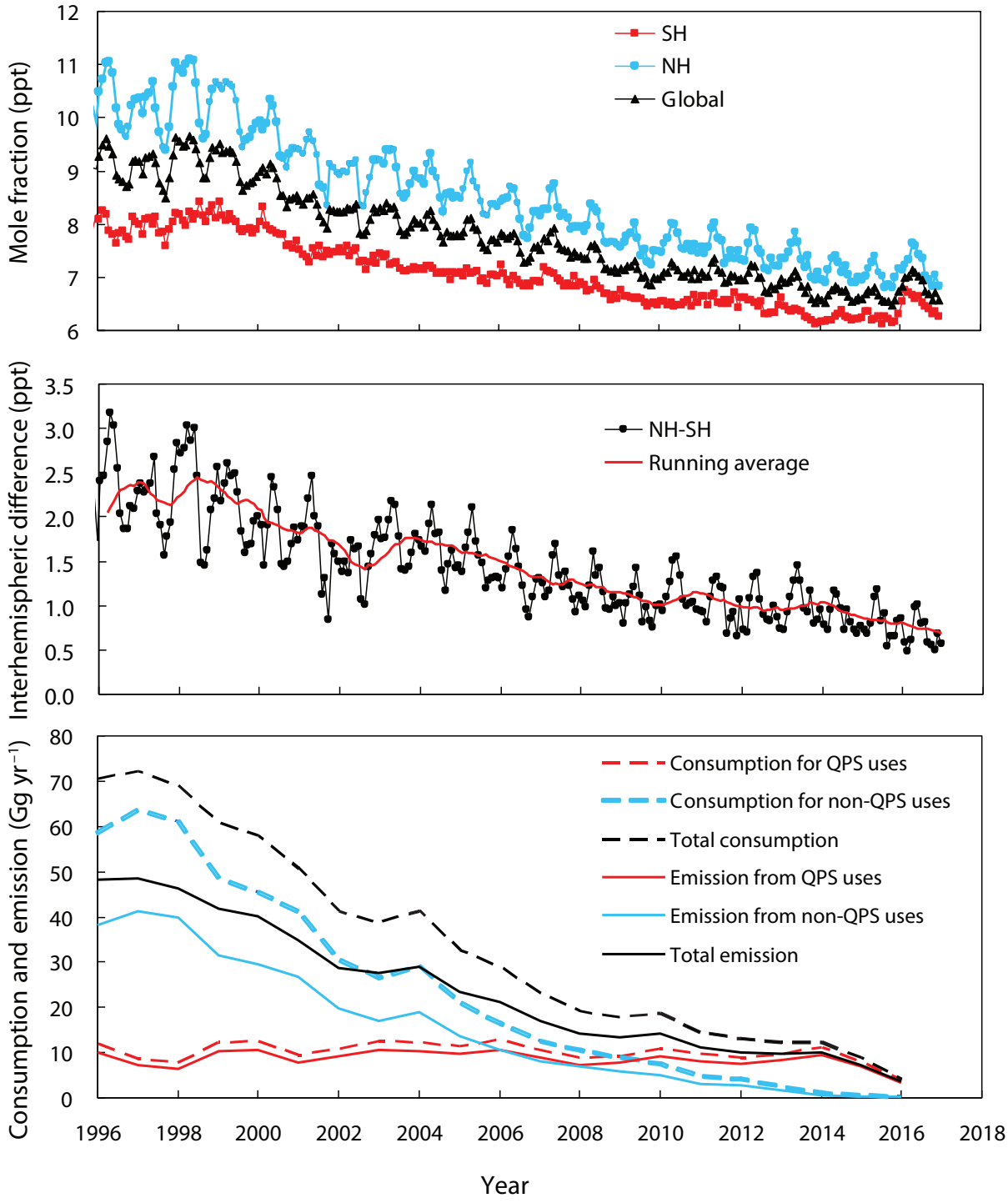

Figure 1-7. *Upper panel:* Trends in methyl bromide monthly mean mole fractions for the NH (blue), SH (red), and globe (black) from NOAA data (Montzka et al., 2003, updated). *Middle panel*: Interhemispheric difference (NH–SH) as monthly means (black) and as a 12-month running average (red). *Lower panel*: Consumption (dashed lines) as reported in the UNEP database (UNEP, 2017), for non-QPS uses (blue) and QPS uses (red), and emissions (solid lines) from non-QPS uses (blue) and QPS uses (red). Total consumption and emissions are shown as black dashed and solid lines, respectively. Soil fumigation emission rates are estimated as 65% of reported consumption (UNEP, 2006) and QPS emission rates are estimated as 84% of reported consumption (UNEP, 2006).

1.2.6 Methyl Chloride (CH_3Cl)

Observations of Atmospheric Abundance

Methyl chloride (CH_3Cl) is largely natural in origin and is not controlled under the Montreal Protocol. The 2016 global mean mole fraction determined from the AGAGE and NOAA global networks was 553 and 559 ppt, respectively (**Table 1-1**). These values are around 2–3% higher than the 2012 values reported in the previous Assessment, although such changes are consistent with historical variability (**Figure 1-1**).

Emissions and Lifetime

The estimate of the total global lifetime of CH_3Cl (0.9 years) remains unchanged from the previous Assessment. Major sinks include oxidation by the hydroxyl radical, uptake by soils, degradation in oceans, and photolysis in the stratosphere. Among the sinks, only the partial lifetime due to loss in the stratosphere has been addressed since the last Assessment. The estimate of a 35 ± 7-year stratospheric lifetime (Umezawa et al., 2015) is consistent with the 30.4-year estimate in the last Assessment.

The major sources of methyl chloride are tropical and subtropical plants, biomass burning, the ocean, salt marshes, and fungi. The major anthropogenic source is thought to be coal combustion (McCulloch et al., 1999). The previous Assessment summarized known CH_3Cl sources, highlighting that the global source strength is about 20% lower than the magnitude of known sinks. A recent study based on atmospheric observations from Gosan, South Korea, found that CH_3Cl emissions from industrialized regions of China may have been underestimated (Li et al., 2017) and suggested that the chemical industry may be a source that has not been accounted for in previous budgets. If confirmed, these findings could substantially reduce the gap in the CH_3Cl budget. Emissions from bread-baking have also been proposed, although the magnitude was thought to be small compared to other sources (Thornton et al., 2016).

Some process-level studies have investigated emissions of CH_3Cl from a range of natural and anthropogenic sources, including coastal salt marshes and an invasive plant (perennial pepperweed) in North America (Khan et al., 2013; Rhew et al., 2014), a fern species (Yokouchi et al., 2015), and coastal heathland fires in Australia (Lawson et al., 2015). However, the implications of these studies for the global budget have not yet been established.

1.2.7 Methyl Bromide (CH_3Br)

Observations of Atmospheric Abundance

The 2016 global mean surface mole fractions of methyl bromide from the AGAGE and NOAA networks, respectively, were 6.80 ppt and 6.86 ppt (**Figure 1-1**, **Figure 1-7,** and **Table 1-1**), ~25% lower than the peak of about 9.2 ppt observed between 1996-1998 and around 1.3 ppt (~25%) higher than the preindustrial Southern Hemisphere mole fraction of 5.5 ± 0.2 ppt from ice core measurements (Carpenter and Reimann et al., 2014). The global mean mole fraction declined until 2015, when it reached 6.6 ppt. However, between 2015 and 2016, NOAA and AGAGE observations showed positive growth rates of 0.22 ppt yr^{-1} (3.3%) and 0.14 ppt yr^{-1} (2.1%), respectively. This is the highest growth rate observed in the last decade or more. The annual mean IHD has continued to decline since the previous Assessment, with the NOAA value reaching 0.68 ppt in 2016, 70% lower than the peak in 1996–1998. The increase in growth between 2015 and 2016 does not appear to coincide with an increase in IHD.

Emissions and Lifetime

The global total lifetime of CH_3Br is estimated to be 0.8 years, unchanged from the previous Assessment.

Atmospheric CH_3Br has both natural and anthropogenic sources. Its use is controlled under the Montreal Protocol for the fumigation of soils, post-harvest storage of commodities, and the fumigation of structures, although some "critical use" exemptions from these controls have been awarded (e.g.UNEP, 2014b). Quarantine and pre-shipment (QPS) use of CH_3Br, mainly for pest control for the transport of agricultural products, is exempt from the phaseout. Natural or partly anthropogenic sources include biomass burning and emissions from oceanic and terrestrial ecosystems (for further details, see Table 1-4 in the previous Assessment; Carpenter and Reimann et al., 2014). Reported non-QPS consumption dropped to 0.94 Gg in 2016, around 1% of its peak value (UNEP, 2017; **Figure 1-7**). The reported consumption for QPS

was 8.4 Gg yr^{-1} in 2016. Compared to the non-QPS consumption, this value has been relatively stable for the previous two decades (UNEP, 2017). Combined reported consumption from these uses has decreased by approximately 87% since its peak, which occurred in the late-1990s. This decrease is qualitatively consistent with the observed decline in atmospheric mole fraction and IHD. The cause of the anomalous growth observed between 2015 and 2016 is not yet known. However, the fact that the growth increase did not coincide with an increase in IHD suggests that the associated changes in sources and/or sink must be distributed across hemispheres.

The previous Assessments noted a discrepancy between total known sources of CH_3Br and its total loss rate, with the sinks being around 39 Gg yr^{-1} larger than emissions. Some recent studies have investigated potentially new or poorly studied sources that could reduce this gap. Thornton et al. (2016) found a relatively minor contribution to the global budget from emissions occurring during bread-baking (<1%). Similarly, seagrass meadows are not thought to contribute significantly to the global budget (Weinberg et al., 2015). Several regional or process-level studies have been carried out focusing on subtropical salt marshes, peatland pastures, heathland fires, or the photochemical halogenation of terrestrial dissolved organic matter in estuarine outflow (Khan et al., 2013; Lawson et al., 2015; Mendez-Diaz et al., 2014; Rhew et al., 2014). However, the implications of these studies for the global budget have not yet been established. Therefore, the cause of the discrepancy identified in the previous Assessment remains unknown.

1.3 VERY SHORT-LIVED HALOGENATED SUBSTANCES (VSLSs)

As in the last Assessment, VSLSs are considered to include source gases (SGs; i.e., very short-lived halogenated substances present in the atmosphere in the form they were emitted from natural and anthropogenic sources), halogenated product gases (PGs) arising from SG degradation, and other sources of tropospheric inorganic halogens. VSLSs have tropospheric lifetimes of around 0.5 years or less. While longer-lived ODSs account for the majority of the present-day stratospheric halogen loading, there is strong evidence that VSLSs make a significant contribution to stratospheric bromine and that they contribute to stratospheric chlorine (Carpenter and Reimann et al., 2014; Montzka and Reimann et al., 2010), and possibly iodine. These gases thus contribute to stratospheric ozone destruction, but their radiative forcing is small due to their short lifetimes. Also, due to their short lifetimes, VSLSs show much higher variability in the troposphere than long-lived ODSs and are partly chemically broken down during the transport to the stratosphere. In order to assess the amount of halogen delivered to the stratosphere, the sources, transport pathways, and the chemical transformation of VSLSs during transit need to be understood. In this section, we use data from global networks to assess the mean tropospheric mixing ratios, whereas observations close to the tropical tropopause are used to infer the input of VSL SGs to the stratosphere.

1.3.1 Tropospheric Abundance, Trends, and Emissions of Very Short-Lived Source Gases (VSL SGs)

For the principal VSL SGs, a detailed compilation of local lifetimes was given in Table 1-5 of Carpenter and Reimann et al. (2014), and is updated in **Table A-1** of this Assessment. Box 1-1 in the 2014 Assessment provides a discussion of different VSL SGs' lifetimes.

1.3.1.1 Chlorine-Containing Very Short-Lived Source Gases

This section focuses on the chlorinated VSLSs most widely reported in the background atmosphere: dichloromethane (CH_2Cl_2), chloroform (trichloromethane, $CHCl_3$), tetrachloroethene (perchloroethylene, CCl_2CCl_2, shortened to C_2Cl_4), trichloroethene (C_2HCl_3) and 1,2-dichloroethane (CH_2ClCH_2Cl). Long-term measurements are available from both the NOAA and AGAGE surface networks for CH_2Cl_2 and C_2Cl_4, while $CHCl_3$ is available from AGAGE only. Hemispheric mean mole fractions and annual emissions derived from these data using a global 12-box model (see **Box 1-1**) are shown in **Figure 1-8** and **Table 1-3**. It should be noted that because these relatively short-lived compounds exhibit spatial gradients that will not be well represented at the coarse resolution of a box model, these estimates are likely to be subject to significant, but poorly quantified, representation uncertainties. Industrial emissions dominate over natural sources for these gases except for

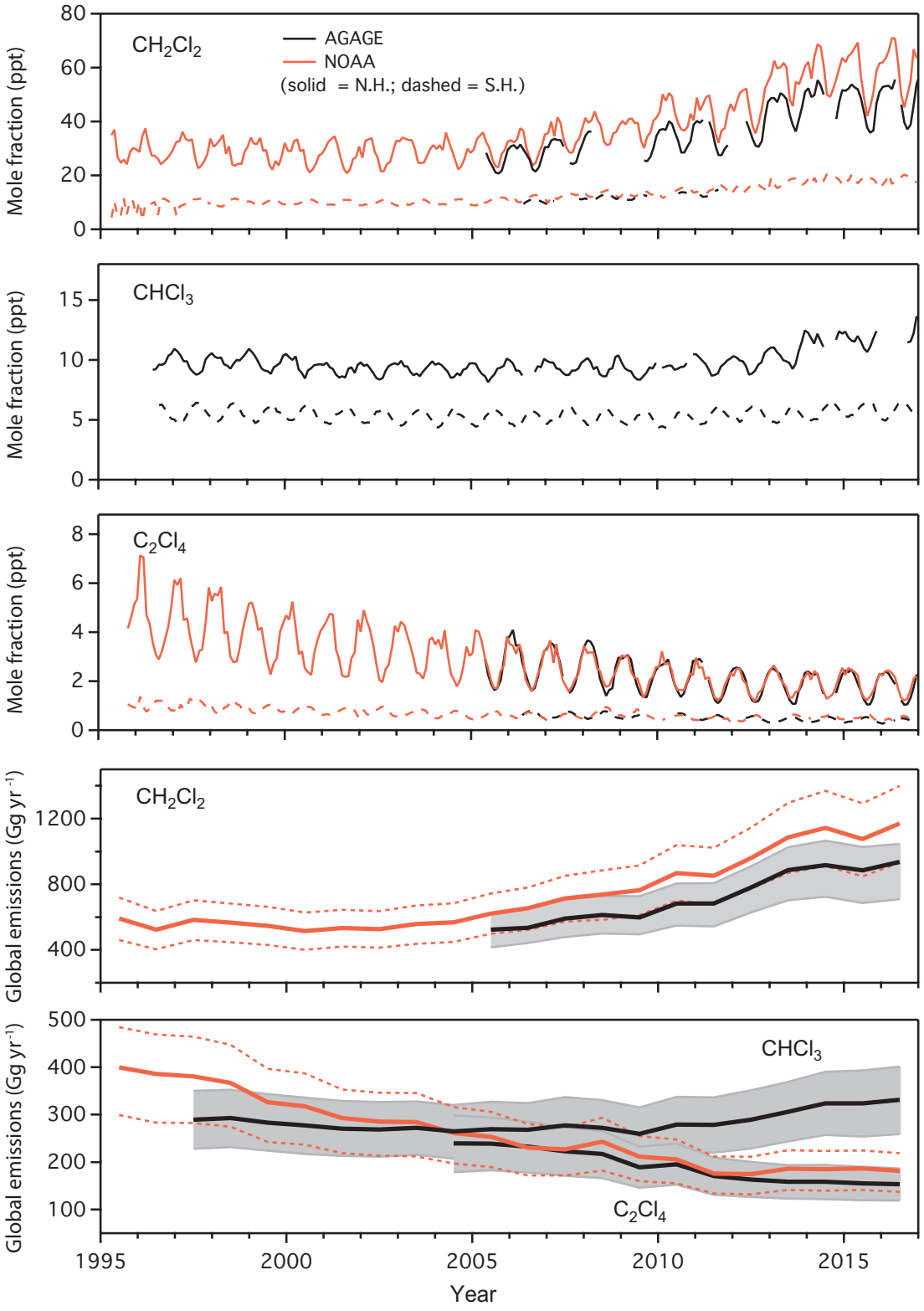

Figure 1-8. *Upper three panels:* Monthly hemispheric mean mole fractions of CH_2Cl_2, $CHCl_3$, and C_2Cl_4 derived from AGAGE (black) and NOAA (red) observations in the NH (solid lines) and SH (dashed lines). *Lower two panels:* Global emissions estimates (Gg yr^{-1}) calculated using a global 12-box model (using methods described in **Box 1-1** and **Figure 1-4**), with 1-sigma uncertainties indicated by shading (AGAGE) or dotted lines (NOAA).

Table 1-3. Annual global mean mole fractions of chlorinated VSL source gases and estimated emissions from the global networks. Emissions based on AGAGE and NOAA surface data were calculated using a global 12-box model (Cunnold et al., 1983; Rigby et al., 2013), identical to the global emissions shown in **Figure 1-4** for longer-lived ODSs. The calculations assume parameterized global total steady-state lifetimes of 0.54, 0.58, and 0.38 years for CH_2Cl_2, $CHCl_3$, and C_2Cl_4, respectively.

Formula	Annual Mean Mole Fraction (ppt)			Growth (2015–2016)		Annual Global Emissions (Gg yr^{-1})			Network
	2012	2015	2016	ppt yr^{-1}	% yr^{-1}	2012	2015	2016	
CH_2Cl_2	26.0	32.0	32.7	0.7	2.2	780 (±135)	885 (±164)	937 (±172)	AGAGE
	30.4	37.8	39.2	1.4	3.7	881 (±169)	957 (±204)	1037 (±213)	NOAA
$CHCl_3$	7.6	8.7	8.9	0.2	2.3	290 (±60)	324 (±69)	331 (±70)	AGAGE
C_2Cl_4	1.17	1.10	1.07	-0.03	-2.7	87 (±18)	84 (±17)	83 (±17)	AGAGE
	1.16	1.22	1.20	-0.02	-1.6	97 (±20)	103 (±22)	103 (±21)	NOAA

$CHCl_3$ (Montzka and Reimann et al., 2010). Detailed information on industrial uses is available on the U.S. Environmental Protection Agency's (https://www.epa.gov) and the EU European Chemicals Agency's (https://echa.europa.eu/) websites.

Dichloromethane (CH_2Cl_2) exhibits a strong IHD, with NH (Northern Hemisphere) mole fractions a factor of ~3 larger than those in the SH (Southern Hemisphere), reflecting NH industrial sources (e.g., **Figure 1-8**; Hossaini et al., 2017). Measurements from the NOAA network suggest CH_2Cl_2 emissions increased by a factor of ~2 between 2000 (~508 ± 109 Gg yr^{-1}) and 2016 (1037 ± 213 Gg yr^{-1}). The annual mean mole fraction in 2016 was 39.2 ppt based on the NOAA network, which is about a doubling compared to the beginning of the century. Global mean mole fractions increased by 12.3 ppt between 2007 and 2016 (a relative increase of 60%), reaching 32.7 ppt in 2016 based on the AGAGE record. Particularly large CH_2Cl_2 growth occurred between 2012 and 2013 (~6 ppt yr^{-1} from NOAA and ~4 ppt yr^{-1} from AGAGE), though more recent growth rates (2015 to 2016) are comparatively small (1.4 ppt yr^{-1} for NOAA and 0.7 ppt yr^{-1} for AGAGE) (**Table 1-3**). At present, it cannot be assessed if this recent decrease in growth rate reflects a stabilization of emissions or is a transient effect reflecting the large atmospheric variability. The discrepancy between the two CH_2Cl_2 datasets of about 13 ppt of tropospheric chlorine in 2016 reflects differences in calibration scales, which are on the order of 10%, and also differences in sampling locations between the networks. The latter is particularly evident in the 0–30° northern latitude band, where NOAA observations (from the Pacific: Mauna Loa and Cape Kumukahi, Hawai'i) are around 30% higher than the AGAGE measurements (from the Atlantic: Ragged Point, Barbados). It is beyond the capability of the 12-box model used here to resolve such differences, which may be due to longitudinal gradients in the atmosphere.

The upward CH_2Cl_2 trend during the last decade is corroborated by upper tropospheric aircraft data from the CARIBIC (Civil Aircraft for the Regular Investigation of the atmosphere Based on an Instrument Container) mission (Leedham Elvidge et al., 2015a; Oram et al., 2017). The contribution of regional CH_2Cl_2 sources to global emission trends are not well quantified, though emissions from the Indian subcontinent may have increased by a factor of 2–4 between 1998–2000 and 2008 (Leedham Elvidge et al., 2015a) and substantial emissions from eastern Asia have been proposed (Oram et al., 2017).

Table 1-4. Summary of observed mole fractions (in ppt) of VSL source gases from the marine boundary layer (MBL) to the tropical tropopause layer (TTL) and above. Note, many of the upper tropospheric measurements were made at least one decade ago in the case of brominated and iodinated SGs. As chlorinated SGs have significant anthropogenic sources and some show trends, data are based on measurements from 2013/2014 only.

	Marine Boundary Layer (MBL)		Lower TTL		LZRH (z_0)[1]		Upper TTL		Tropical Tropopause	
Height Range			**12–14 km**		**14.5–15.5 km**		**15.5–16.5 km**		**16.5–17.5 km**	
Potential Temperature Range			**340–355 K**		**355–365 K**		**365–375 K**		**375–385 k**	
	Median[2]	**Range[3]**	**Mean[2]**	**Range[3]**	**Mean[2]**	**Range[3]**	**Mean[2]**	**Range[3]**	**Mean[2]**	**Range[3]**
CH_2Cl_2	57.5	46.6–68.1	42.0	36.4–47.6	36.4	29.6–44.3	33.9	28.4–41.6	32.5	26.3–38.5
$CHCl_3$	10.3	8.5–12.3	7.9	7.1–8.7	7.1	6.4–8.0	6.8	6.2–7.8	6.5	5.7–7.2
CH_2ClCH_2Cl	12.8	10.4–18.3	9.0	6.8–11.3	7.4	5.2–9.5	6.9	5.4–8.3	6.6	5.7–7.5
C_2HCl_3	0.2	0.1–0.9	0.14	0.02–0.25	0.08	0.00–0.16	0.06	0.0–0.13	0.04	0.00–0.08
C_2Cl_4	1.3	1.0–2.2	0.87	0.68–1.05	0.73	0.49–0.95	0.66	0.49–0.83	0.52	0.38–0.71
CH_2Br_2	0.9	0.6–1.7	0.96	0.72–1.15	0.81	0.59–0.98	0.73	0.43–0.94	0.64	0.32–0.89
$CHBr_3$	1.2	0.4–4.0	0.57	0.30–1.11	0.36	0.05–0.72	0.28	0.02–0.64	0.19	0.01–0.54
CH_2BrCl	0.10	0.07–0.12	0.12	0.07–0.16	0.13	0.08–0.20	0.14	0.10–0.20	0.12	0.07–0.20
$CHBr_2Cl$	0.3	0.1–0.8	0.12	0.06–0.23	0.09	0.04–0.19	0.08	0.02–0.16	0.05	0.02–0.14
$CHBrCl_2$	0.3	0.1–0.9	0.26	0.18–0.55	0.18	0.08–0.49	0.15	0.07–0.31	0.12	0.05–0.32
CH_3I	0.8	0.3–2.1	0.16	0.00–0.49	0.08	0.0–0.32	0.04	0.0–0.25	0.03	0.00–0.14
Total Cl	177	144–221	130	111–149	112	91–136	105	88–127	100 (92)[4]	83–117 (75–110)[4]
Anthrop. Cl[5]	150	122–189	109	93–126	98	75–127	93	73–118	88	69–108
Total Br	6.5	2.8–18.0	4.3	2.7–6.8	3.2	1.6–5.2	2.8	1.1–4.6	2.2	0.8–4.2
Total I	0.8	0.3–2.1	0.16	0.00–0.49	0.08	0.0–0.32	0.04	0.0–0.25	0.03	0.00–0.14

Notes:

[1] LZRH (z_0) corresponds to the level of zero clear-sky radiative heating (see Box 1-3 of Carpenter and Reimann et al. (2014)). As in the previous Assessment, this level is at about 15 km or 360 K, where there is a transition from clear-sky radiative cooling to clear-sky radiative heating. In general, air masses above this level are expected to enter the stratosphere.

[2] Abundances in the MBL are median values. MBL CH_2Cl_2, $CHCl_3$, CH_2ClCH_2Cl, C_2HCl_3, and C_2Cl_4 data are from the CAST and CONTRAST missions (Andrews et al., 2016; Pan et al., 2017). MBL $CHBr_3$, CH_2Br_2, and CH_3I data are from the compilation of Ziska et al. (2013). MBL CH_2BrCl, $CHBr_2Cl$, and $CHBrCl_2$ data are from the previous (Carpenter and Reimann et al., 2014) Assessment. In and above the TTL, abundances are mean values. For brominated VSLSs and CH_3I, data have been compiled from observations obtained during the Pre-AVE, CR-AVE, TC4, HIPPO, SHIVA, CONTRAST, and ATTREX aircraft campaigns (Navarro et al., 2015; Pan et al., 2017; Sala et al., 2014; Wofsy et al., 2011), and from balloon observations (Brinckmann et al., 2012). ATTREX values used here differ from those used in Wales et al. (2018), as they have been filtered by altitude instead of applying any tracer-tracer correlation. For chlorinated VSLSs, data are from the CONTRAST (2014) and ATTREX (2013/2014) missions in 2013/2014 only (Navarro et al., 2015), with the exception of CH_2ClCH_2Cl, which does not include data from ATTREX 2013. See below for definitions of field mission acronyms. Note that calibration scales for VSLSs may differ among different research groups (e.g. Hall et al., 2014; Jones et al., 2011).

[3] In the MBL the stated observed range is 10^{th} to 90^{th} percentile. Above the MBL, the stated observed range represents the smallest mean minus 1 standard deviation and the largest mean plus 1 standard deviation.

[4] Values for 2016 based on the model by (Hossaini et al., 2017), which are used to derive total stratospheric VSL SGI for chlorine, as explained in section 1.3.2.1, in order to reduce variability from individual campaigns in assessing total Cl input to the stratosphere.

[5] The anthropogenic fraction of VSLS (Anthrop. Cl) is approximate and has been calculated from the sum of 90% of CH_2Cl_2, 50% of $CHCl_3$, and 100% of other compounds.

Pre-AVE = Pre-Aura Validation Experiment (2004); CR-AVE = Costa Rica-Aura Validation Experiment (2006); TC4 = Tropical Composition, Cloud and Climate Coupling missions (2007); HIPPO = HIAPER (High-Performance Instrumented Airborne Platform for Environmental Research) Pole-to-Pole Observations (2009–2011); SHIVA = Stratospheric Ozone: Halogen Impacts in a Varying Atmosphere; ATTREX = Airborne Tropical Tropopause Experiment (2011, 2013, and 2014); CAST = Co-ordinated Airborne Studies in the Tropics (2014); CONTRAST = Convective Transport of Active Species in the Tropics (2014).

In contrast to CH_2Cl_2, global perchloroethylene (C_2Cl_4) emissions and mole fractions in background air have largely been in decline at least since the mid-1990s (**Figure 1-8**). C_2Cl_4 observations from AGAGE are only available from 2004, though relative (−44%) and absolute (−0.8 ppt) changes since then are comparable to NOAA trends over the same period (−32%, −0.6 ppt). The global mean C_2Cl_4 mole fraction was ~1 ppt in 2016 (**Table 1-3**).

For chloroform ($CHCl_3$), AGAGE measurements show stable global mean mole fractions in the range of 7.3–7.7 ppt over the 1997–2010 period, followed by a subsequent increase to 8.9 ppt in 2016. Emissions between 2011 and 2016 are estimated to have increased by ~20% (**Figure 1-8**). During this period, the IHD of surface $CHCl_3$ mole fractions increased from 4.3 ppt to 6.3 ppt, suggesting an increase in NH anthropogenic emissions.

No 1,2-dichloroethane (CH_2ClCH_2Cl) measurements are available from either AGAGE or NOAA, thus its budget and emissions are poorly constrained. Based on recent aircraft observations, boundary layer CH_2ClCH_2Cl mole fractions are of the order ~10–20 ppt in the NH (**Table 1-4**), with SH mole fractions a factor of ~6 lower (Hossaini et al., 2016a), indicative of dominant anthropogenic sources. Given these abundances, CH_2ClCH_2Cl is potentially an important source of chlorine to the troposphere (smaller than CH_2Cl_2 but comparable to $CHCl_3$). However, owing to its relatively short lifetime compared to other VSLSs **(Table A-1)**, its importance as a source of stratospheric chlorine is estimated to be lower.

Trichloroethene (C_2HCl_3) is a relatively minor tropospheric chlorine source. A limited set of AGAGE measurements show NH surface mole fractions of

~1.1 ppt in the early 2000s (Simmonds et al., 2006), with recent aircraft data confirming its low abundance (**Table 1-4**).

Short-lived halogenated unsaturated hydrocarbons (halogenated olefins) have recently been used to replace high-GWP HCFCs and HFCs. In this Assessment, hydrofluoroolefins (HFOs) are discussed in **Chapter 2**. Hydrochlorofluoroolefins (HCFOs) are also in use, and the only atmospheric record currently available is that for HCFO-1233zd(E) (trans-$CF_3CH{=}CHCl$) from central Europe (Vollmer et al., 2015a). While this compound was detectable in only 30% of the samples measured at Jungfraujoch in 2013, this increased to 100% by 2016, with a mean mole fraction of 0.03 ppt in that year (update from Vollmer et al., 2015a).

While measurements of VSLSs from NOAA and AGAGE largely reflect background concentrations (e.g. see Simmonds et al., 2006), regional emissions may lead to higher and more variable abundances. Elevated levels in urban air and at sites likely influenced by regional industrial/commercial processes are reported over the USA (Logue et al., 2010) and China, with the latter including up to several tens of ppt of C_2Cl_4 and several hundred ppt or more of CH_2Cl_2, $CHCl_3$ and CH_2ClCH_2Cl (Mao et al., 2009; M. Yang et al., 2016; Zhang et al., 2014). The regional sum of chlorine from CH_2Cl_2, $CHCl_3$, C_2Cl_4, and CH_2ClCH_2Cl can therefore exceed the background global mean (**Table 1-3**) by up to an order of magnitude, as observed, e.g., over Malaysia and the island of Taiwan and (see e.g. Oram et al., 2017)). Oram et al. (2017) estimated anthropogenic CH_2Cl_2 emissions from China to be 455 ± 46 Gg yr^{-1} in 2015 (i.e., ~40–50% of the top-down derived global emissions in **Table 1-3**. Similarly, CH_2ClCH_2Cl emissions from China of 203 (±20) Gg yr^{-1} were derived for 2015.

Natural $CHCl_3$ sources from marine (phytoplankton) and terrestrial (e.g., soils, peatlands, and plants) environments have been identified (e.g. Albers et al., 2017; Forczek et al., 2015; Khalil et al., 1999; Khan et al., 2011) and account for 50–90% of global emissions (McCulloch, 2003; Worton et al., 2006). For CH_2Cl_2, biomass burning may be a small (Lobert et al., 1999) or negligible global source (Leedham Elvidge et al., 2015a; Lawson et al., 2015; Simpson et al., 2011), though oceanic emissions may be more significant. Based on limited observational data, estimates of ocean CH_2Cl_2 emissions range from 124 ± 38 Gg yr^{-1} (Xiao, 2008) to 192 Gg yr^{-1} (Khalil et al., 1999). Natural CH_2Cl_2 sources are therefore uncertain but are likely small relative to industrial emissions, which are estimated to account for 90% of total CH_2Cl_2 emissions (Carpenter and Reimann et al., 2014; Montzka and Reimann et al., 2010). An increase in industrial emissions is the most probable cause of recent CH_2Cl_2 growth.

Global combined tropospheric chlorine from the three VSLSs measured by the NOAA and AGAGE

networks (CH_2Cl_2, $CHCl_3$ and C_2Cl_4) was 92–110 ppt Cl in 2016 (**Table 1-3**), with a 4.0 ± 1.5 ppt Cl yr^{-1} increase over the 5-year period 2012 to 2016. The given uncertainty range includes the differences in the NOAA and AGAGE calibration scales. In the NH tropical boundary layer, total tropospheric chlorine from VSLSs in 2014, including additional contributions from CH_2ClCH_2Cl and C_2HCl_3, is estimated from aircraft observations at 177 (144–221) ppt Cl (**Table 1-4**).

1.3.1.2 Bromine-Containing Very Short-Lived Source Gases

Bromoform ($CHBr_3$) and dibromomethane (methylene dibromide, CH_2Br_2) are the principal brominated VSL SGs. Along with bromochloromethane (CH_2BrCl), dibromochloromethane ($CHBr_2Cl$), and bromodichloromethane ($CHBrCl_2$), these VSL SGs are predominantly of natural marine origin, with ocean phytoplankton and macroalgae being the dominant sources (e.g. Carpenter et al., 2007; Leedham Elvidge et al., 2015b; Hamed et al., 2017; Quack et al., 2007)). Typical tropospheric mole fractions of the above brominated compounds are summarized in **Table 1-4**. Though poorly characterized, minor terrestrial sources include peatland and organic-rich soils (Albers et al., 2017; Carpenter et al., 2005) and production due to water chlorination processes (Worton et al., 2006). In coastal zones, industrial discharge of chlorinated effluents to seawater is also identified as a source of several brominated VSL SGs, in particular $CHBr_3$ (Boudjellaba et al., 2016; Hamed et al., 2017; Yang, 2001). The importance of this source on a global scale is not clear (Liu et al., 2011).

Since the last Assessment, brominated VSL SG emissions in several oceanic regions have been reported from ship cruises, including the Yellow, Sulu, and South China Seas (Nadzir et al., 2014; Yang et al., 2014), the tropical Atlantic (Hepach et al., 2015) Pacific Peruvian coastal waters (Fuhlbrugge et al., 2016a), and the west Indian Ocean (Fiehn et al., 2017). CH_2Br_2 emissions derived in these studies were in some cases significantly larger than those estimated from previous studies (Butler et al., 2007; 2015; Hepach et al., 2014; Tegtmeier et al., 2012) and confirm large spatiotemporal variability in sea–air VSL SG fluxes (e.g. Montzka and Reimann et al., 2010), varying by an order of magnitude or more during a given cruise. Many factors contribute to such variability, including subsurface biogeochemical processes, proximity to coastal sources, wind speed, and sea surface temperature, among others (Stemmler et al., 2015). The correlation between $CHBr_3$ and CH_2Br_2 concentrations in background air suggests the two compounds are largely derived from a common process at the global scale (Carpenter and Liss, 2000; Yokouchi et al., 2017).

While there is evidence for seasonal variations in oceanic VSL SG emissions from observations (Hughes et al., 2009; Yang et al., 2014; Yokouchi et al., 2017) and ocean biogeochemical models (Stemmler et al., 2015), much of the observed seasonality of background surface $CHBr_3$ and CH_2Br_2 is well explained by seasonal changes in OH and other chemical sinks (Hossaini et al., 2016b).

Recent bottom-up estimates of global $CHBr_3$ emissions are a factor of two lower than top-down estimates, most likely due to poor temporal and spatial data coverage, resulting in missing sources and emission hot spots (Stemmler et al., 2015; Ziska et al., 2013). There is no clear evidence for long-term changes in the atmospheric abundance of brominated VSLSs, although small increases in global emissions (~6–8% between 1979 and 2013 for CHBr3 and CH_2Br_2) are suggested to have occurred due predominantly to increases in surface wind speed (Ziska et al., 2017). For $CHBr_3$, the global source estimate of 120–820 Gg Br yr^{-1} given in the last Assessment is unchanged (Carpenter and Reimann et al., 2014). For CH_2Br_2, the range from the last Assessment (57–280 Gg Br yr^{-1}) is reduced to 57–100 Gg Br yr^{-1}, reflecting the most up-to-date emission climatologies (e.g. Lennartz et al., 2015; Ziska et al., 2013) and supported by the fact that global models reproduce tropospheric CH_2Br_2 observations well using emissions at the lower end (Hossaini et al., 2016b). Global CH_2BrCl, $CHBr_2Cl$, and $CHBrCl_2$ emissions are estimated at 4–6 Gg Br yr^{-1}, 15–43 Gg Br $yr^{-1,}$ and 8–11 Gg Br yr^{-1}, respectively (Brinckmann et al., 2012; Ordonez et al., 2012; Warwick et al., 2006; Yokouchi et al., 2005).

1.3.1.3 Iodine-Containing Very Short-Lived Source Gases

Methyl iodide (CH_3I), with mainly oceanic sources, is the main iodine-containing VSL SG. Since the last Assessment, further evidence for oceanic CH_3I

Box 1-2. Regional Variability and Modeling of VSLS Transport to the Stratosphere

Eleven global models participated in the first concerted VSLS multi-model intercomparison (Hossaini et al., 2016b), testing a range of prescribed emissions and using a common chemistry scheme. Despite differences in transport schemes, most of the models were capable of reproducing observed $CHBr_3$ and CH_2Br_2 mole fractions in the TTL, providing confidence in a proper representation of the average transport processes affecting VSLS stratospheric injection.

While the average transport is thus rather well represented, global and trajectory models have intrinsic limitations in properly representing very deep convection of air parcels from the boundary layer to the stratosphere (Feng et al., 2011; Hosking et al., 2010; Hoyle et al., 2011; Orbe et al., 2017), although increasing the model resolution has been found to improve the representation of the strength and location of convective events (Russo et al., 2015).

Modeled SG concentrations in the TTL do not depend only on total emissions, but in particular also on the geographical distribution of the sources. These are mainly natural oceanic sources for bromine; for the input of VSLS chlorine to the stratosphere on a regional scale, the transport of anthropogenic pollution plumes to the upper atmosphere plays a crucial role (Anderson et al., 2016; Ashfold et al., 2015; Chen et al., 2016; Oram et al., 2017). For brominated and iodinated species, which have mostly natural sources, the collocation of natural, mainly oceanic, sources and effective vertical transport is important. The Maritime Continent (Indonesia, Philippines, New Guinea, and other Southeast Asia islands) (Tegtmeier et al., 2012, 2015), the tropical Indian Ocean (Liang et al., 2014a), and the Tropical Western Pacific (Fernandez et al., 2014) have been suggested as particularly important source regions in this respect. The collocation of elevated emissions with the Asian monsoon circulation during boreal summer and with the tropical pacific warm pool during boreal winter also likely provides oceanic VSL SGs an efficient transport route to the stratosphere (Fiehn et al., 2017; Hossaini et al., 2016b; Liang et al., 2014a).

production via biotic (e.g., phytoplankton and cyanobacteria) and abiotic (e.g., photochemical breakdown of dissolved organic matter) processes has been provided by laboratory and field studies (e.g. Allard and Gallard, 2013; Hepach et al., 2015; Mendez-Diaz et al., 2014; Ooki et al., 2015; Shi et al., 2014; Yuan et al., 2016). Terrestrial CH_3I sources are poorly quantified, though include soils/vegetation, rice paddies, wetlands, salt marshes, and biomass burning (e.g. Akagi et al., 2011; Lawson et al., 2015; Lee-Taylor and Redeker, 2005; Manley et al., 2006; Sive et al., 2007), accounting for up to 30% of total CH_3I emissions in some inventories (Bell et al., 2002).

In the marine boundary layer (MBL), recently observed mean CH_3I mole fractions of 0.59 ± 0.30 ppt over the Tropical Western Pacific (Fuhlbrugge et al., 2016b) and 0.84 ± 0.12 ppt over the Indian Ocean (Fiehn et al., 2017) are generally consistent with previous observations (**Table 1-4**). Generally, larger mole fractions are observed at low latitudes than toward the poles (Hu et al., 2016b). No new information on long-term atmospheric CH_3I trends has been reported since the last Assessment (Carpenter and Reimann et al., 2014), when trends were shown to have varied over the past decades (Yokouchi et al., 2012). The best estimate of coastal plus open-oceans emissions is unchanged and is in the range of 157–550 Gg I yr^{-1} (Carpenter and Reimann et al., 2014).

Several other iodinated VSLSs have been detected in the MBL, including CH_2ICl, CH_2IBr, CH_2I_2 and C_2H_5I (Allan et al., 2015; Jones et al., 2010; Shimizu et al., 2017). Owing to their short lifetimes (minutes to hours at the surface) these VSL SGs are not expected to reach the upper troposphere. However, their photolysis is a significant source of tropospheric inorganic iodine (Carpenter et al., 2013; Saiz-Lopez et al., 2014; Sherwen et al., 2016) and may contribute to particulate iodine (Sherwen et al., 2016) observed in the upper troposphere and stratosphere (Murphy et al., 2014; Murphy and Thomson, 2000).

1.3.2 Input of VSLS Halogen to the Stratosphere

VSL SGs can be chemically broken down during transport to the stratosphere. We differentiate between stratospheric halogen input arising from halogen atoms crossing the tropopause in the form of the emitted source gases (source gas injection, SGI) and in the form of product gases released from source gas photodecomposition (product gas injection, PGI). Since the last Assessment, new observations of brominated, chlorinated, and iodinated SGs have been obtained in the tropical troposphere, including the near-tropopause region, allowing constraints on SGI especially from chlorinated and brominated SGs. New measurements of brominated PGs have also been reported from several aircraft campaigns, and global models with a more explicit treatment of PG chemistry have reported PGI estimates. In situ measurements of chlorinated and iodinated PGs remain sparse. Transport processes relevant to the input of VSLSs to the stratosphere show a large regional and seasonal variability, which is discussed in **Box 1-2.** In this subsection, we assess the magnitude of both SGI and PGI for the different halogens.

Dynamical processes relevant to the transport of VSLSs from the marine boundary layer (MBL) to the tropical tropopause layer (TTL) and from the TTL to the stratosphere have been discussed in detail in previous Assessments (see Section 1.3.2 in Montzka and Reimann et al., 2010; see also Carpenter and Reimann et al., 2014). Briefly, the TTL is the region between the lapse rate minimum (~12 km / θ = 345 K) and the cold point tropopause (CPT; ~17 km, θ = 380 K) (see Fueglistaler et al., 2009). The level of zero radiative heating (LZRH; ≈ 15 km / θ = 360 K) marks the transition from clear-sky radiative cooling (below) to clear-sky radiative heating (above). Once a tropospheric air parcel crosses the LZRH, it is expected to reach the lower tropical stratosphere.

1.3.2.1 Source Gas Injection (SGI)

SGI describes the stratospheric input of halogenated SGs in the same form as they were emitted at the surface. The efficiency of SGI is different for each compound and depends on its tropospheric loss rate (mainly through reaction with OH or photolysis) and the timescales for troposphere-to-stratosphere transport (Aschmann and Sinnhuber, 2013; Schofield et al., 2011). SGI—the global average halogen mixing ratio

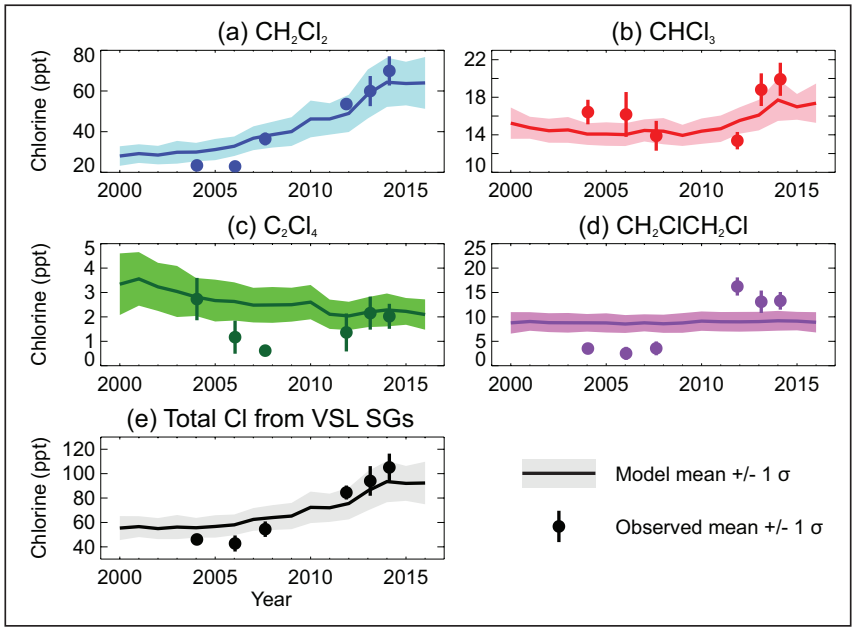

Figure 1-9. Modeled and observed stratospheric chlorine SGI (ppt Cl) evaluated at the tropical tropopause from (a) CH_2Cl_2, (b) $CHCl_3$, (c) C_2Cl_4, (d) CH_2ClCH_2Cl, and (e) total. Update of Hossaini et al. (2015).

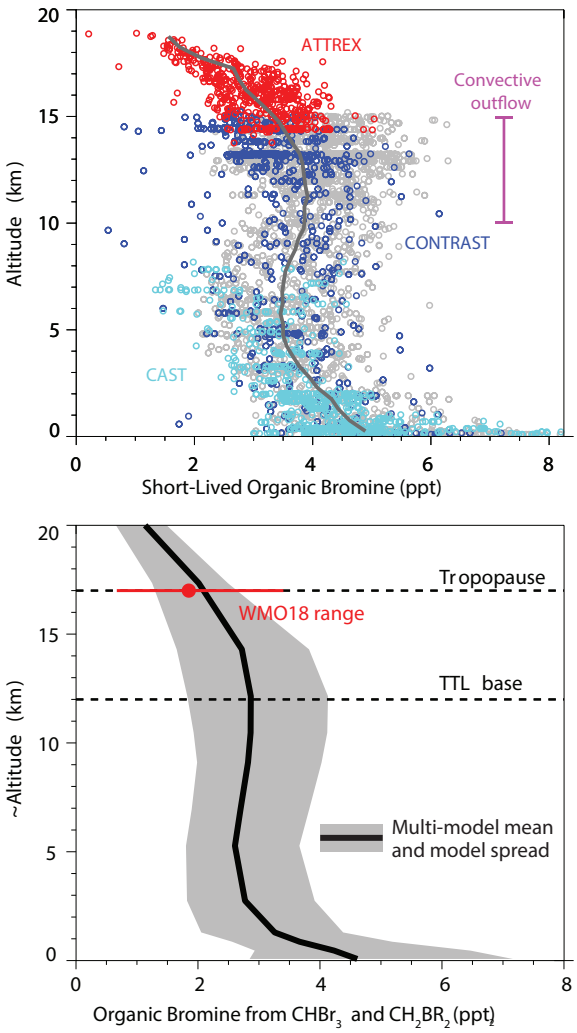

Figure 1-10. *Top panel:* Vertical profile of total organic bromine (ppt Br) from brominated VSL SGs ($CHBr_3$, CH_2Br_2, $CHBr_2Cl$, CH_2BrCl, and $CHBrCl_2$) observed during 2014 CAST, CONTRAST, and ATTREX missions over the Tropical Western Pacific (modified from Pan et al., 2017). *Bottom panel:* Organic bromine from the two main source gases $CHBr_3$ and CH_2Br_2 (ppt Br) from the TransCom-VSLS model intercomparison. The multi-model mean (black line) and model spread (gray shading) are shown, along with the best estimate (red circle) and range (red line) from this Assessment (**Table 1-4**). Modified from Hossaini et al. (2016b).

transported into the stratosphere—can be quantified from SG measurements around the tropical tropopause (~17 km) or from global models.

Since the last Assessment, new aircraft measurements of chlorinated, brominated, and iodinated SGs in the tropical upper troposphere have been reported. These are from the 2013 and 2014 NASA Airborne Tropical TRopopause EXperiment (ATTREX) in the Eastern and Western Pacific (Jensen et al., 2017; Jensen et al., 2013), the 2014 CONTRAST (Convective Transport of Active Species in the Tropics) mission, located in the Western Pacific (Pan et al., 2017), and the 2014 CAST (Coordinated Airborne Studies in the Tropics) mission, also in the Western Pacific (Harris et al., 2017). These campaigns provide new information on the abundance of VSL SGs from the MBL to the TTL and around the tropical tropopause (**Table 1-4**).

SGI from Chlorinated VSLs

Observation-based chlorine SGI from VSLSs is 100 (83–117) ppt Cl based on recent ATTREX measurements only (**Table 1-4**), due to the recent increases of mainly anthropogenic chlorinated VSLSs (see **Section 1.3.1.1**). CH_2Cl_2, $CHCl_3$, and CH_2ClCH_2Cl account for ~65%, ~20%, and ~13% of this total, respectively; the remaining ~2% is from C_2Cl_4 and C_2HCl_3. This chlorine SGI estimate is ~40% larger than the 72 (50–95) ppt Cl derived in the last Assessment and predominantly reflects larger observed mole fractions of CH_2Cl_2 and CH_2ClCH_2Cl around the tropical tropopause during ATTREX compared to the previous measurement compilation. Local upper tropospheric (10–12 km) enhancements of CH_2Cl_2, $CHCl_3$, C_2Cl_4, and CH_2ClCH_2Cl over Southeast Asia have been observed (Oram et al., 2017), with a sum of chlorine in these VSLSs of up to 330 ppt Cl (compared to the average 111–149 ppt Cl from **Table 1-4** in the lower TTL).

An estimate of chlorine SGI (2000 to 2016) from the TOMCAT chemical transport model is shown in **Figure 1-9** (update of Hossaini et al., 2015). The model is constrained by time-dependent, latitudinal-varying boundary conditions, based on NOAA and AGAGE surface measurements (except CH_2ClCH_2Cl, whose emissions were assumed to remain constant). The model reproduces observed CH_2Cl_2 mole fractions around the tropical tropopause reasonably well and shows that chlorine SGI from CH_2Cl_2 increased from 28 (23–33) ppt Cl to 64 (52–76) ppt Cl between 2000 and 2014. Total modeled chlorine SGI is 94 (77–110) ppt Cl in 2014 and is thus in reasonable agreement with the measurement-derived 100 (83–117) ppt Cl

assessed here (**Table 1-4**). Due to the high variability of VSLS observations in the TTL and near the tropical tropopause (see **Figure 1-9e**), the use of SG observations from individual campaigns will lead to large year-to-year variability, which may not be representative of the global mean input to the stratosphere and may not be a good basis for trend estimates. For this Assessment, we therefore use the model data constrained by surface boundary conditions, as the model is able to reproduce the observations from various campaigns reasonably well (see **Figure 1-9**) but at the same time eliminates the variability from the individual campaigns. Based on this model, the total VSL SG injection to the stratosphere is thus assessed to be 92 (75–110) ppt for the year 2016.

SGI from Brominated VSLSs

Total organic bromine from $CHBr_3$, CH_2Br_2, $CHBr_2Cl$, CH_2BrCl, and $CHBrCl_2$ observed during the CAST, CONTRAST, and ATTREX campaigns is shown in **Figure 1-10**. These campaigns were conducted around the Tropical Western Pacific warm pool, a region characterized by strong convective activity where the troposphere-to-stratosphere transport of brominated VSLSs is particularly rapid (e.g. Fernandez et al., 2014; Hosking et al., 2010; Tegtmeier et al., 2015). Intercalibration of standards during CAST, CONTRAST, and ATTREX revealed generally good agreement between VSLS measurements performed by different instruments (relative standard deviation of <10%) (Andrews et al., 2016). CONTRAST measurements show a total of ~4.3 (2.1–7.7) ppt Br in the lower TTL for the five VSL SGs noted above, similar to previous estimates obtained over Southeast Asia (Sala et al., 2014; Wisher et al., 2014). At the LZRH, the CONTRAST mean is ~3.6 (2.0–5.9) ppt Br, ~30% larger than that reported by Carpenter and Reimann et al., (2014). Similarly, both 2013 and 2014 ATTREX data (Navarro et al., 2015) showed roughly equal SGI for bromine over the Western (~3.3 ± 0.5 ppt Br) and Eastern Pacific (~3.0 ± 0.4 ppt Br), which lie around the upper limit of the previously assessed range. These higher values most likely reflect spatiotemporal variability of VSLS sources and transport and should not be taken as an indicator of long-term growth in abundance.

Incorporating the new ATTREX measurements (Navarro et al., 2015) with previously compiled data (Carpenter and Reimann et al., 2014), our best estimate of SGI from brominated VSLSs has increased from 1.4 (0.7–3.4) ppt Br to 2.2 (0.8–4.2) ppt Br. $CHBr_3$ and CH_2Br_2 dominate this supply, accounting for ~84% of the total (**Table 1-4**). The factor of ~5 uncertainty (of similar magnitude to the last Assessment) likely reflects spatiotemporal variability in VSL SG surface emissions (Fiehn et al., 2017; Tegtmeier et al., 2012), tropospheric VSL SG sinks (Aschmann and Sinnhuber, 2013; Rex et al., 2014), and transport processes (Ashfold et al., 2012; Kruger et al., 2008), all of which influence the amount of VSLSs reaching the tropical tropopause.

The revised bromine SGI estimate of 2.2 (0.8–4.2) ppt Br is in broad agreement with a ~2.0 ppt Br estimate from recent global modeling (Fernandez et al., 2014) and the 2.9 ± 0.6 ppt Br derived from recent tracer-tracer correlation of stratospheric VSLS and CFC-11 observations (Wales et al., 2018). For $CHBr_3$ and CH_2Br_2, it is also in good agreement with the climatological multi-model mean of 2.0 (1.2–2.5) ppt Br from the TransCom-VSLS model intercomparison (**Figure 1-10b**; Hossaini et al., 2016b).

SGI from Iodinated VSLSs

With the exception of CH_3I, there is no evidence that significant levels of iodinated VSLSs are present in the TTL (Carpenter and Reimann et al., 2014). From **Table 1-4**, mean CH_3I mole fractions are below 0.1 ppt at 15 km, decreasing to below 0.05 ppt around the tropical tropopause. Iodine SGI is assessed to be in the range of 0 to 0.1 ppt, in agreement with modeling (Saiz-Lopez et al., 2015; Tegtmeier et al., 2013).

1.3.2.2 Product Gas Injection (PGI)

A variable fraction of the halogenated PGs, which arise from the degradation of source gases (SGs), experience efficient dry and wet scavenging during transit to the stratosphere. In principle, PGs can be produced from any halocarbon, but VSL SGs are the main source of PGs. Recent aircraft campaigns have provided new information regarding the vertical distribution of halogenated PGs; these are complemented by box- and global-modeling studies to provide new constraints on stratospheric PGI.

PGI from Chlorinated VSLSs

Product gases arising from chlorinated SGs include phosgene ($COCl_2$) and hydrogen chloride (HCl) and

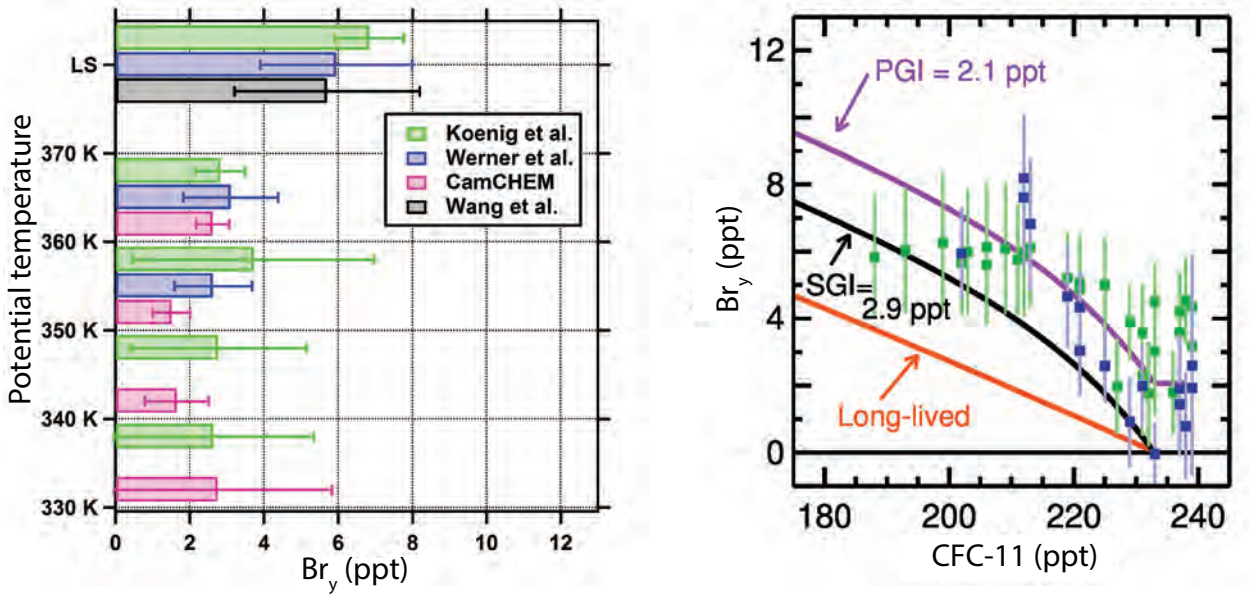

Figure 1-11. *Left panel:* Vertical variation of inferred inorganic bromine (Br_y) from VSLSs within the TTL during the CONTRAST and ATTREX missions (adapted from Koenig et al., 2017). *Right panel:* SGI and PGI inferred from the correlation between stratospheric VSLSs and CFC-11 measured in the Tropical Western Pacific. Inferred Br_y from DOAS (green) and CIMS (blue) instruments are shown, together with the tracer-tracer correlation for VSL SGs (black line) and the SGI + PGI best estimation (purple line). Modified from Wales et al. (2018).

may contribute to PGI. In the last two Assessments, PGI was estimated from $COCl_2$ (up to 32 ppt Cl) and HCl (up to 20 ppt Cl) observations around the LZRH (Brown et al., 2011; Marcy et al., 2007; Mébarki et al., 2010). Since both $COCl_2$ and HCl are also produced from degradation of long-lived ODSs, an unknown amount of these products could be recirculated from the stratosphere into the troposphere. VSLS-derived products were estimated to contribute 0–100%, or ~25 (0–50) ppt, to the observed chlorine PGI (Carpenter and Reimann et al., 2014).

Using a chemical transport model, Hossaini et al. (2015) derived a total VSLS PGI of ~18 (±8) ppt Cl in 2013, with equivalent contributions from $COCl_2$ and HCl and a small contribution from other chlorinated organic PGs that have yet to be observed (~2 ± 0.8 ppt Cl). Simulated chlorinated PGI increased by ~50% between 2005 and 2013, owing to surface trends in SGs, notably CH_2Cl_2, during this period (see **Section 1.3.1.1**, **Figure 1-8**).

All recent studies estimate a non-zero PGI contribution from chlorinated VSLSs. We have therefore increased the lower limit of total chlorine PGI from VSLSs but maintained the upper limit with respect to previous Assessments, giving a best estimate of 25 (8–50) ppt Cl PGI from VSLSs. The lower limit reflects the lower limit from the above modeling work (Hossaini et al., 2015), considering $COCl_2$ and HCl only. This estimate does not include a possible additional chlorine input from ClO or $ClONO_2$, both of which can be strongly influenced by heterogeneous chlorine activation in the upper troposphere and lower stratosphere (Solomon et al., 2016; von Hobe et al., 2011).

PGI from Brominated VSLSs

Several aircraft campaigns targeting brominated PGs in the tropical free troposphere and TTL have been performed since the last Assessment (Chen et al., 2016; Koenig et al., 2017; Le Breton et al., 2017; Volkamer et al., 2015; Wang et al., 2015a; Werner et al., 2017). Bromine monoxide (BrO) and total inorganic bromine (Br_y) mole fractions rapidly increased with altitude, doubling from ~2.5 ppt at the bottom of the TTL to ~5 ppt above the CPT. PGI inferred from BrO (**Figure 1-11**) ranged from 3.4 ± 1.2 ppt within the Tropical Eastern Pacific during ATTREX (Werner et

al. (2017) to 2.7 (2.4–3.0) ppt in the Tropical Western Pacific during CONTRAST (Koenig et al., 2017). Based on the relationship between inferred stratospheric Br_y and CFC-11, measurements obtained during CONTRAST and ATTREX (Wales et al., 2018) estimated a global PGI from brominated VSLSs of 2.1 ± 2.1 ppt (**Figure 1-11**). This is well reproduced by a wide range of Chemistry Climate Models (CCMs), mostly from those considering an explicit treatment of tropospheric chemistry and sources of VSLSs (**Figure 1-11**).

The previous Assessment (Carpenter and Reimann et al., 2014) estimated a global PGI contribution between 1.1 and 4.3 ppt Br, based mainly on global modeling studies that considered only the two major VSL SGs ($CHBr_3$ and CH_2Br_2) and a simplified treatment of gas-phase Br_y speciation and washout (Aschmann and Sinnhuber, 2013; Hossaini et al., 2012; Liang et al., 2014a). New model developments, including a comprehensive heterogeneous recycling scheme on upper-tropospheric ice crystals (**Box 1-3**), suggest a Br_y injection of 3.0 (±1.9) ppt Br in the Eastern Pacific and 2.0 (±0.2) ppt Br in the Western Pacific (Navarro et al., 2015). The contribution from minor VSLSs ($CHBr_2Cl$, $CHBrCl_2$, CH_2BrCl, and CH_2BrI) to PGI was modeled to be ~0.3 ppt Br (Fernandez et al., 2014), which matches the upper limit of previous estimates (Carpenter and Reimann et. al., 2014; Montzka and Reimann et al. (2010).

In summary, there is now consistent observational evidence confirming the prevalence of gas-phase inorganic bromine throughout the free troposphere and TTL. This finding is consistent with previous PGI model estimates and with the amount of bromine required to reconcile Br_y inferred from stratospheric BrO retrievals with the input from long-lived brominated source gases to the stratosphere (see **Section 1.4**). Based on both modeling and measurement studies, our current best estimate of total PGI is thus ~2.7 (1.7–4.2) ppt Br.

PGI from Iodinated VSLSs

The possible injection of significant amounts of inorganic iodine to the stratosphere is under debate. New daytime iodine monoxide (IO) aircraft observations at low solar zenith angles (SZA <45°) within the tropical upper troposphere and lower TTL suggest that significant levels of total reactive iodine (between 0.25 and 0.7 ppt I_y) could be injected to the stratosphere (Saiz-Lopez et al., 2015). This value is 2 to 5 times larger than the recommended PGI upper limit given in the previous Assessment (PGI <0.1 ppt I_y), which was based on balloon-borne solar occultation (SZA ≈ 90°) measurements performed in the tropical lower stratosphere (Bösch et al., 2003; Butz et al., 2009). The discrepancy between the new and previous studies lies in the different chemical scheme used to derive I_y (particularly the treatment of higher-order iodine

Table 1-5. Summary of estimated VSL source gas injection (SGI) and product gas injection (PGI) contributions to stratospheric halogens (based on observations and model results).

VSLS Best Estimate (ppt)	SGI[1]	PGI[2]	Total (SGI + PGI)[3]
Chlorine	92 (75–110)	25 (8–50)	**115 (75–160)**
Bromine	2.2 (0.8–4.2)	2.7 (1.7–4.2)	**5 (3–7)**
Iodine	0–0.1	0–0.7	**0–0.8**

Notes:

[1] Due mainly to the increasing trend in chlorinated compounds, the SGI estimate for chlorinated VSL SGs is representative of year 2016 based on model data (see **Table 1.4**). SGI for bromine and iodine represent the global mean from 2004 onwards as there are no reports of long-term trends.

[2] PGI for chlorine has been estimated based on HCl and $COCl_2$ only (additional input from ClO and $ClONO_2$ has not been considered). PGI for bromine and iodine has been estimated by box- and global-modeling studies based on BrO and IO measurements, respectively.

[3] The SGI and PGI lower/upper limits are not strictly additive because whenever SGI increases (for example due to rapid lifting), the correspondent PGI arising from SG photodecomposition decreases (and vice-versa).

Box 1-3. Heterogeneous Chemistry of Very Short-Lived Product Gases

Atmospheric particles (such as cloud droplets, ice crystals, and aerosols) can affect the tropospheric burden of inorganic product gases (PGs) arising from the degradation of halogenated very short-lived source gases (SGs). The competition, fate, and efficiency of heterogeneous reactions occurring on these particles are still some of the largest uncertainties affecting the stratospheric halogen burden from PGI (Aschmann and Sinnhuber, 2013; Fernandez et al., 2014; Koenig et al., 2017; Liang et al., 2014a; Saiz-Lopez et al., 2015; Schmidt et al., 2016; Wang et al., 2015a).

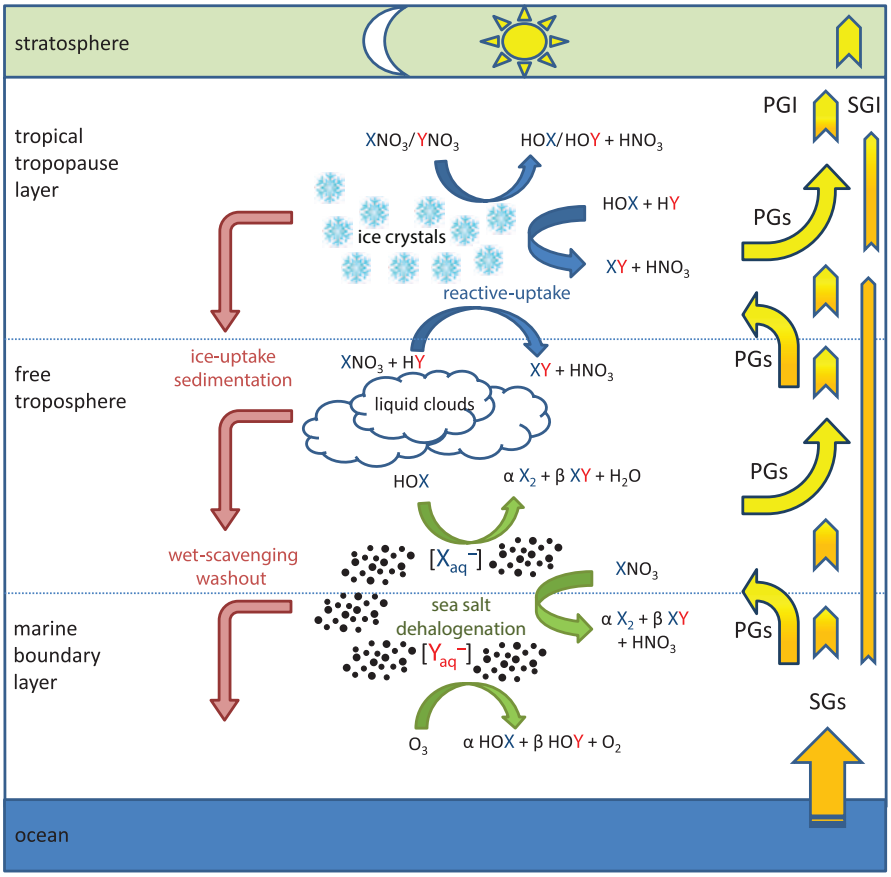

Box 1-3 Figure 1. Schematic representation of tropospheric heterogeneous recycling processes affecting PGI. The upward arrows on the right represent the vertical ascent of halogenated inorganic PGs (yellow) arising from VSL SGs (orange) decomposition. The different transport regimes within each region (e.g., convective lifting and large-scale ascent) are shown by different arrow lengths, while the color gradient indicates the relative SG/PG partitioning. Green arrows indicate the occurrence of sea salt dehalogenation, which constitute an additional source of inorganic PGs (α and β denote the variability in the aerosol enrichment for each halogen family, specified by X and Y). Red downward arrows represent the net sinks of soluble PGs occurring through uptake on liquid/ice clouds followed by precipitation/sedimentation. Blue arrows represent the ice/aerosol mediated repartitioning of inorganic reservoirs, which do not necessarily represent either a net sink or a source of PGs. Note that the distinction of the height at which each heterogeneous process occurs is qualitative, and all processes can occur during the day and night.

Box 1-3, continued.

Oceanic halides comprising the bulk of sea-salt aerosols can be released to the atmosphere as an additional inorganic halogen source through heterogeneous oxidation (**Box 1-3, Figure 1**) (Vogt et al., 1996). The efficiency of this process, usually referred to as sea-salt aerosol dehalogenation, depends on the total halogen fraction prevailing in the aerosol (the so-called enrichment factor), the net rate of gas-phase halogen adsorption and reactive uptake, and the concurrence/collocation of significant sea-salt production and convective transport throughout the troposphere (Yang et al., 2005). Sea-salt recycling has been estimated to provide an additional tropospheric chlorine source of ~5–6 Tg Cl yr^{-1} (Hossaini et al., 2016a; Schmidt et al., 2016) and between 1.4 to 3.5 Tg Br yr^{-1} for the case of bromine (Chen et al., 2017; Fernandez et al., 2014; Parrella et al., 2012; Schmidt et al., 2016; Yang et al., 2005). In the case of bromine, this source has been estimated to be between two and four times larger than the global tropospheric emissions from brominated VSL SGs (Schmidt et al., 2016; Yang et al., 2005). Inclusion of this source in models has helped to reduce differences between models and observations of tropospheric BrO columns densities (Koenig et al., 2017; Schmidt et al., 2016; Wang et al., 2015a).

The processes involved in heterogeneous processing of halogen species are complex. The adsorption followed by effective washout of hydrophilic reservoir species depends on the aqueous/gas-phase partial pressure equilibrium of each individual halogen species (Sander, 2015). However, if the adsorption of reservoirs occurs on top of ice crystals or sulfate/nitrate aerosols, many heterogeneous reactions can proceed (**Box 1-3 Figure 1**), reducing the washout efficiency by transforming the soluble reservoir species into more volatile and photolabile compounds. Inclusion of heterogeneous recycling on ice crystals and upper-tropospheric aerosols has been reported as a necessary process to be considered in box and chemistry-climate models in order to reconcile satellite tropospheric columns with model tropospheric abundances (Parrella et al., 2012; Schmidt et al., 2016), as well as to reproduce the inorganic bromine (Fernandez et al., 2014; Koenig et al., 2017) and iodine (Dix et al., 2013; Saiz-Lopez et al., 2015) vertical profiles throughout the tropical upper troposphere and TTL. Concurrent estimation of gas-phase inorganic PGs and aerosol halide content at high altitudes is required to close the halogen budget in the TTL and lower stratosphere and thus to improve the assessment of PGI. However, as many of the heterogeneous processes are poorly constrained and the uncertainty involved in their parameterization is very large, the evaluation of the overall effect of heterogeneous chemistry on VSLS halogen input to the stratosphere is currently difficult to be quantified.

oxides) as well as on the different temporal field of view (i.e., SZA range) of the measurement technique deployed on each field campaign.

In light of the new results, we cannot provide a central value for iodinated PGI but only a wide interval ranging from zero to an upper limit (0–0.7 ppt I_y). If the maximum PGI value is considered, the impact of iodine on the lower tropical stratosphere could be as large as that of brominated VSLSs.

1.3.2.3 Total Halogen Input into the Stratosphere from VSLSs

Table 1-5 presents the current best estimate of the total injection to the stratosphere from halogenated VSLSs, discriminating SGI and PGI contributions. The relative importance of PGI to SGI depends on the chemical transformation processes during transport from the sources to the stratosphere. The fraction of PGI to total VSLS halogen derived here is higher for bromine than it is for chlorine. While the uncertainty associated with iodine PGI has increased since the previous Assessment, the uncertainty range for the stratospheric flux of organic and inorganic bromine and chlorine has in general been reduced with respect to the previous Assessment.

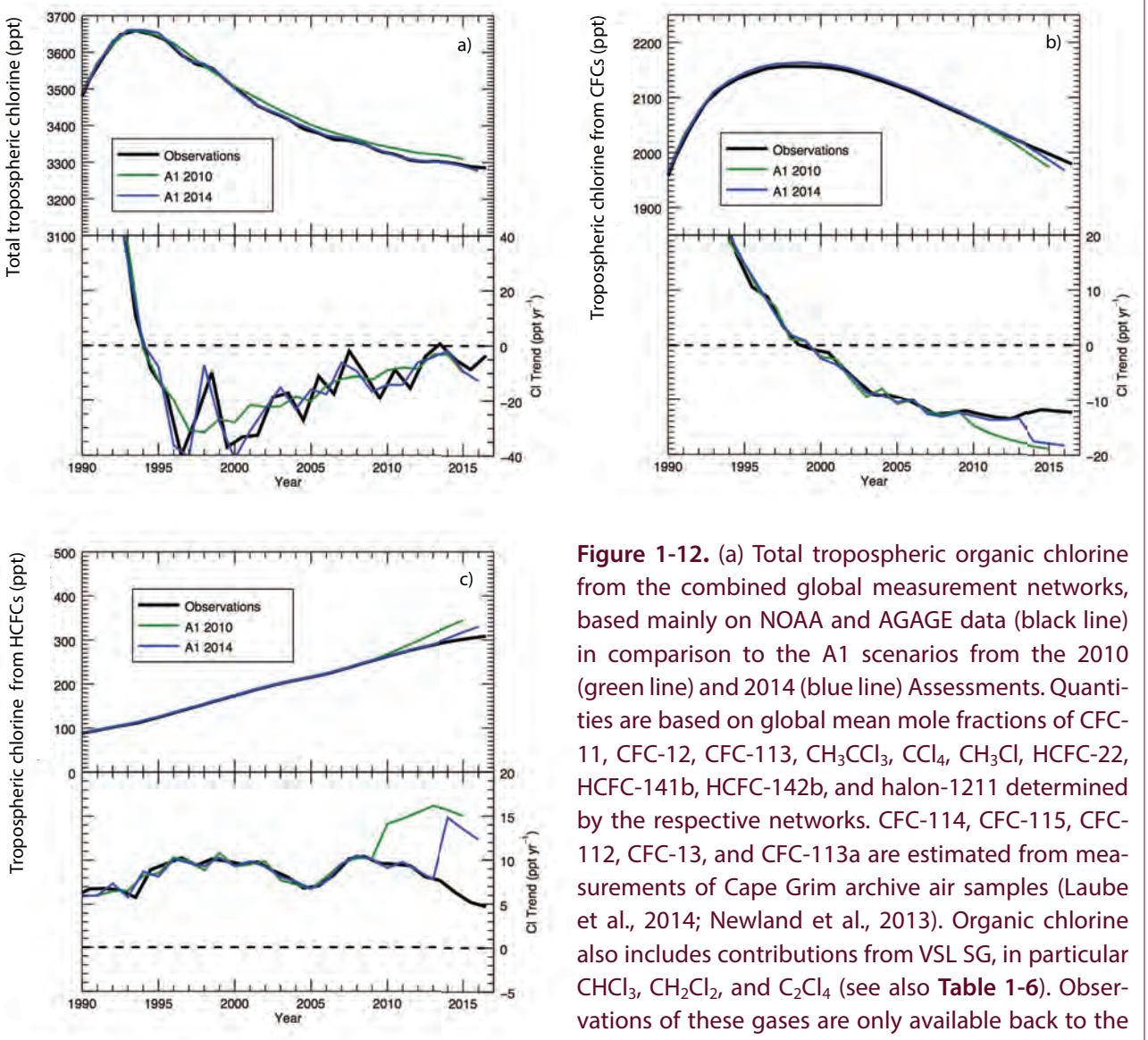

Figure 1-12. (a) Total tropospheric organic chlorine from the combined global measurement networks, based mainly on NOAA and AGAGE data (black line) in comparison to the A1 scenarios from the 2010 (green line) and 2014 (blue line) Assessments. Quantities are based on global mean mole fractions of CFC-11, CFC-12, CFC-113, CH_3CCl_3, CCl_4, CH_3Cl, HCFC-22, HCFC-141b, HCFC-142b, and halon-1211 determined by the respective networks. CFC-114, CFC-115, CFC-112, CFC-13, and CFC-113a are estimated from measurements of Cape Grim archive air samples (Laube et al., 2014; Newland et al., 2013). Organic chlorine also includes contributions from VSL SG, in particular $CHCl_3$, CH_2Cl_2, and C_2Cl_4 (see also **Table 1-6**). Observations of these gases are only available back to the mid-1990s. Before that, constant mixing ratios are assumed. For species which are not included in the scenarios (some minor CFCs and VSLSs), the observed values were included here in order to provide a comparison based on the same set of compounds. (b) and (c) Show the same as panel a for the sum of the tropospheric chlorine contents of the CFCs and the tropospheric chlorine content of all HCFCs, respectively.

Total Input from Chlorinated VSLSs

A "best estimate" of total chlorine (SGI + PGI) from VSLSs reaching the stratosphere is obtained by summing the contribution from individual SGs around the tropopause (**Table 1-4** and **Section 1.3.2.1**) and adding the estimated PG contribution from $COCl_2$ and HCl (see **Section 1.3.2.2).** As explained in **Section 1.3.2.1**, we use model data of SGI, constrained by surface observations (update of Hossaini et al., 2015) here rather than individual campaign observations, since campaign-based estimates are subject to seasonal and regional variability. This yields total Cl from VSLSs entering the stratosphere of 115 (75–160) ppt Cl for 2016 **(Table 1-5)**. This value is very similar to the global average of chlorine VSLSs of 110 ppt derived in **Section 1.4.1.** Around the tropopause, the anthropogenic contribution to the total stratospheric chlorine injection is estimated to be ~85% (**Table 1-4**). The overall

contribution of chlorine from VSLSs has increased to about 3.5% (see discussion in **Section 1.4**).

Total Input from Brominated VSLSs

Various lines of evidence show that brominated VSLSs may provide ~2.2 (0.4–4.2) ppt Br to the stratosphere via SGI and ~2.7 (1.7–4.2) ppt Br via PGI. The best estimate of global stratospheric bromine from VSLSs is ~5 (3–7) ppt Br (see **Table 1.5**), with approximately half due to SGI and half due to PGI. While the central value is unchanged with respect to previous reports, the uncertainty range is reduced based on recent observations and modeling studies. The overall SGI and PGI partitioning is well reproduced by a wide range of Chemistry Climate Models (CCMs), mostly from those considering an explicit treatment of VSL tropospheric chemistry and sources (Wales et al., 2018). Although many of the new aircraft campaigns yielded a total VSLS bromine injection lying in the upper half of the assessed range (Navarro et al., 2015; Werner et al., 2017), this should not be taken as an indication of a positive trend in the contribution from VSLSs to stratospheric Br_y in recent years: Most measurements were performed within regions where the source strength is larger and the vertical transportation of VSLSs is faster. The 5 (3–7) ppt Br global mean also matches the indirect estimate derived from total stratospheric bromine abundances as described in **Section 1.4.** Due to the decline in the abundance of regulated long-lived bromine compounds, the relative contribution of VSLSs to total stratospheric bromine has continued to increase, reaching ~26% by year 2016 (see **Figure 1-17**).

Total Input from Iodinated VSLSs

While the SGI of iodine in the form of CH_3I is expected to be very low (<0.1 ppt), there is a new debate regarding the possible injection of iodine from VSLSs to the stratosphere through PGI. New measurements of IO confirm rather low IO levels, but model calculations suggest an additional impact of higher iodine oxides to the total I_y fraction (Saiz-Lopez et al., 2015). The revised upper limit of total iodine input from VSLSs is therefore extended to 0.8 ppt (0.1 ppt SGI + 0.7 ppt PGI, see **Table 1.5**), which is considerably larger than the upper limit given in previous Assessments (total iodine injection < 0.15 ppt, PGI < 0.1 ppt) (Carpenter and Reimann et al., 2014; Montzka and Reimann et al., 2010).

1.4 CHANGES IN ATMOSPHERIC HALOGENS

In this section we discuss the total halogen loading in the atmosphere and its changes. These are discussed separately for chlorine, bromine, and iodine in **Sections 1.4.1–1.4.3** for the troposphere based on organic sources (ODSs and VSL SGs) and for the stratosphere based on inorganic halogen observations. The total chlorine and bromine input to the stratosphere, including contributions from VSLSs, is then discussed in **Section 1.4.4.** This input should be reflected in inorganic halogen levels, especially in the upper stratosphere, where virtually all halogen has been transferred to the inorganic form. **Section 1.4.4** also discusses equivalent effective stratospheric chlorine (EESC), which is used as a proxy to describe the halogen impact on stratospheric ozone (see **Box 1-4**). EESC does not include contributions from VSLSs. Finally, fluorine, while not contributing to ozone depletion, is discussed in **Section 1.4.5**.

Estimates of tropospheric halogen loading primarily originate from the global surface networks, which are averaged together when mole fractions from multiple networks are available. In general, a simple average is used; however, where data from one network are available for some years but not others, existing network data are scaled to remain consistent with the two-network average (consistent with previous Assessments).

1.4.1 Tropospheric and Stratospheric Chlorine Changes

1.4.1.1 Tropospheric Chlorine Changes

As stated in previous Assessments (e.g., Carpenter and Reimann et. al., 2014; Montzka and Reimann et al., 2010), the total tropospheric chlorine has been decreasing continuously since its peak abundance observed during the years 1993–1994 (**Figure 1-12a**). The maximum annual average total chlorine observed was about 3,660 ppt in 1993. The maximum rate of decrease in total tropospheric organic chlorine was close to 40 ppt yr^{-1} in the years 1995 and 1996, mainly driven by the decrease of the rather short-lived CH_3CCl_3 (lifetime of about 5 years). As expected, the rate of decrease has since slowed and has continued to slow down since the last Assessment. Total chlorine from controlled ODSs declined at an average rate of 12.7 ppt yr^{-1} between early 2012 and late 2016 (**Table 1-6**).

Table 1-6. Contributions of long-lived ODSs and VSL SGs to total chlorine in the troposphere.

	Total Cl (ppt)[1]			Contribution to Total (%)			Average Rate of Change of Total Cl_2 (ppt yr^{-1})		
	2008	2012	2016	2008	2012	2016	2004–2008	2008–2012	2012–2016
All CFCs	2079	2027	1979	62.1	61.4	60.2	–11.6 (1.5)	–12.9 (0.7)	–12.0 (0.4)
CCl_4	359	340	322	10.7	10.3	9.8	–4.4 (0.4)	–4.7 (0.3)	–4.5 (0.2)
HCFCs	248	285	309	7.4	8.6	9.4	9.1 (1.6)	9.2 (0.7)	5.9 (1.3)
CH_3CCl_3	32	16	7.8	1.0	0.5	0.2	–8.3 (2.0)	–4.1 (0.8)	–2.0 (0.5)
halon-1211	4.25	3.96	3.55	0.13	0.12	0.11	–0.02 (0.03)	–0.07 (0.01)	–0.1 (0.01)
Total Controlled Chlorine	2722	2672	2621	81.3	80.9	79.7	–15.2 (1.9)	–12.6 (0.3)	–12.7 (0.9)
CH_3Cl	545	539	556	16.3	16.3	16.9	2.7 (5.2)	–1.8 (4.7)	4.0 (3.6)
VSLSs	82	91	110	2.4	2.8	3.3	2.5 (1.1)	2.6 (3.1)	4.3 (4.9)
Total Chlorine	3349	3302	3287				–10.0 (6.7) (–0.29% yr^{-1})	–11.8 (6.9) (–0.35% yr^{-1})	–4.4 (4.1) (–0.13% yr^{-1})

[1] Chlorine mid-year mole fractions were derived using AGAGE, NOAA, and archive data.

[2] Total and relative Cl changes over 5-year periods, as indicated. The values in parentheses represent the standard deviation of the annual growth rates during the respective period, which reflects the observed variability. Relative changes in total chlorine (in percent per year) were calculated relative to values at the beginning of each period (3,390 ppt total chlorine in 2004). We refer to these periods as 5-year periods, as they are based on annual average values, e.g., from the beginning of 2012 to the end of 2016.

Values for past years differ slightly from previous Assessments because of updated calibration information, different methods for determining global mean mole fractions, rounding errors, and the inclusion of CFC-112 (Kloss et al., 2014) and CFC-113a (Adcock et al., 2018). Total Cl also includes 82, 91, and 110 ppt as VSLSs in 2008, 2012, and 2016, respectively.

This recent decrease of chlorine from controlled substances has been partly offset by an increase in substances not controlled under the Montreal Protocol (e.g., CH_3Cl and VSLSs). In addition to the mainly natural CH_3Cl (which increased at 4.0 ppt yr^{-1}), chlorine from chlorine-containing VSLSs also increased at an average rate of 4.3 ppt yr^{-1} between 2012 and 2016. While chlorine from controlled substances has decreased by 12.7 ppt yr^{-1}, these increases in chlorine from compounds not controlled under the Montreal Protocol have partly offset this decrease, leading to a decrease of total chlorine of only 4.4 ppt yr^{-1} (0.13% yr^{-1}) during this 5-year period. Overall, the fractional contribution of substances not controlled under the Montreal Protocol to total tropospheric chlorine has increased and is now above 20%, mainly due to CH_3Cl (16.9%).

Figure 1-12a compares the observed decrease in total chlorine with the projected trend based on the A1 scenarios from the 2010 and 2014 Assessments. Total chlorine from controlled substances is decreasing at close to the expected overall rate. However, this is partially due to the offsetting effects of a slower than projected increase in HCFCs (**Figure 1-12c**; note that the A1 scenarios for the HCFCs in previous Assessments assumed that Article 5 countries would produce the maximum amount allowed under the Montreal Protocol) and a slower than projected decrease in CFCs (**Figure 1-12b**). This slower than expected decrease in chlorine from CFCs is dominated by CFC-11 but CFC-12 and CFC-113 have also recently contributed to this difference.

1.4.1.2 Stratospheric Chlorine Changes

As mentioned above, total organic chlorine in the troposphere peaked in the early 1990s and has since been declining, although the rate of decline is not constant in time. One would expect a similar global long-term response in stratospheric inorganic chlorine, shifted

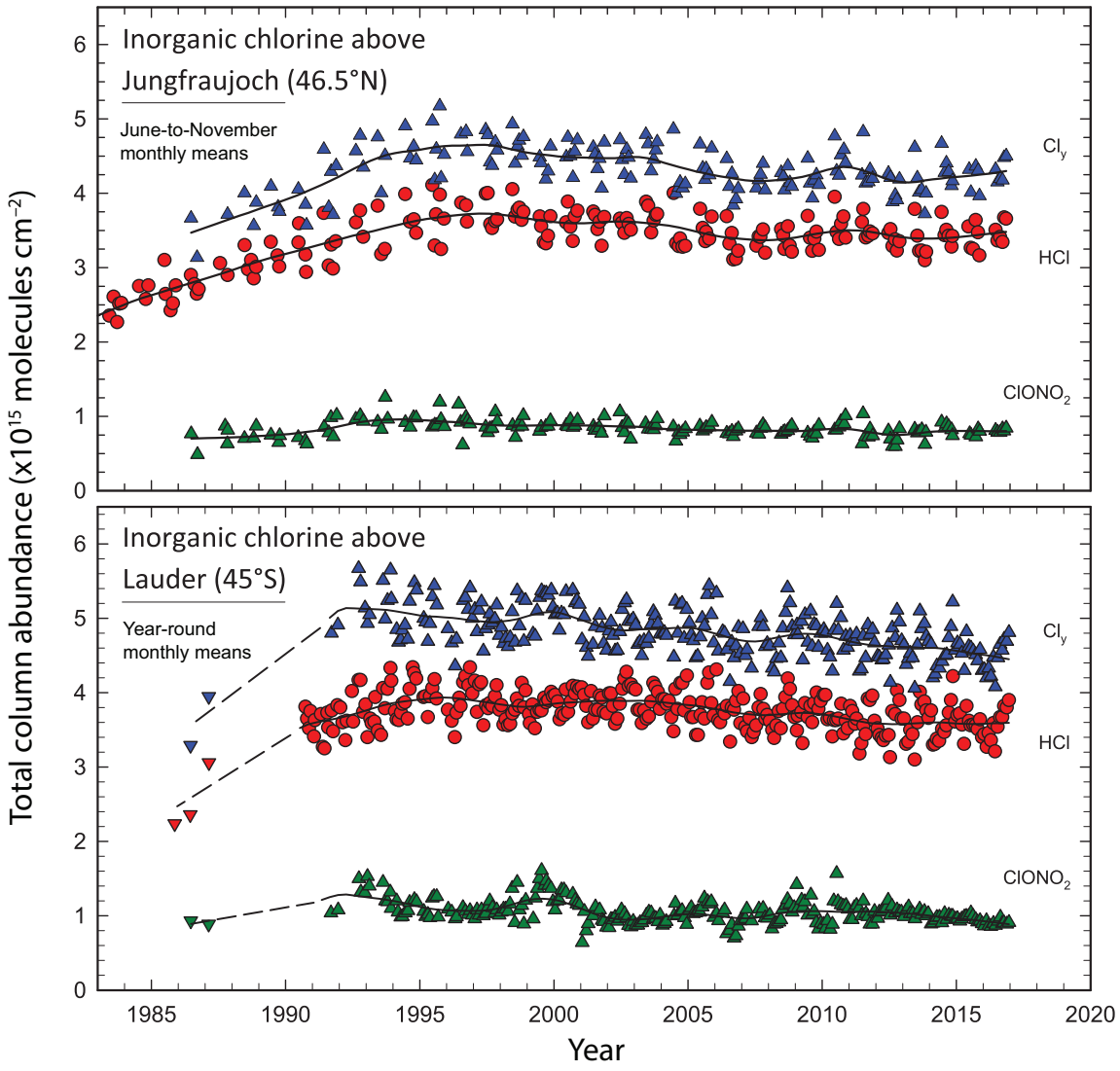

Figure 1-13. Multi-decadal monthly mean total column time series of the two main chlorine reservoirs, HCl and $ClONO_2$, and their summation, as monitored at the Jungfraujoch station (Swiss Alps, 46.5°N, 3,580 m altitude) and the Lauder station (New Zealand, 45.0°S, 370 m altitude), in the framework of the NDACC network. For the Jungfraujoch, in contrast to the data shown in Figure 1-2, the datasets are restricted to the June to November months in an effort to limit the variability caused by atmospheric transport and subsidence during winter and spring. The continuous lines come from non-parametric least-squares fits involving an integration time of about 3 years and help to visualize the non-monotonic and non-linear changes in stratospheric chlorine after the peak from 1996 to 1997.

by a timescale relating to transport into that region (age of air) and photochemical conversion. Significant short-term temporal and latitudinal variability in inorganic chlorine was noted in the lower stratosphere, based on HCl measured from ground-based column data (mostly sensitive to the lower stratosphere) and satellites (Mahieu et al., 2014a). Based on the latter work, increases were observed in total column and lower-stratospheric northern mid-latitude HCl from about 2005 to 2011. These increases were attributed

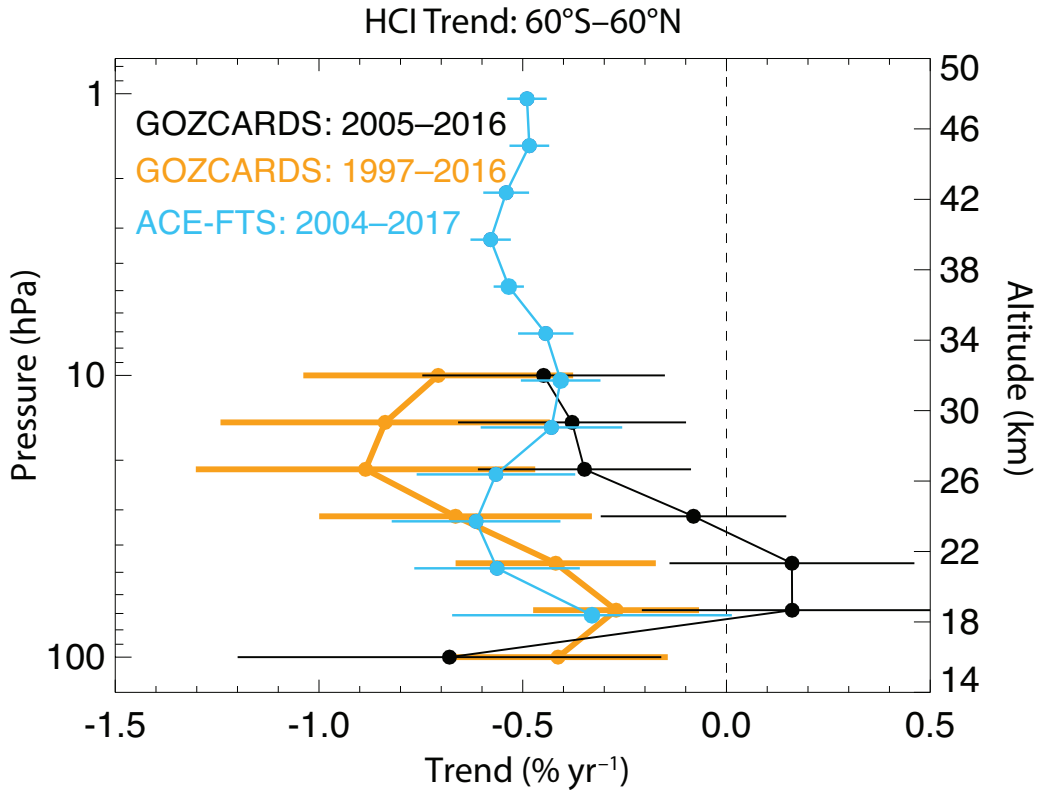

Figure 1-14. Trends (% yr^{-1}) in near-global (60°S to 60°N) HCl abundances, based on different satellite-based datasets and time periods. The longer-term (1997–2016) average linear trend profile (orange dots) is obtained from GOZCARDS merged HCl lower-stratospheric data (updated from Froidevaux et al. (2015), using additional Aura MLS data through 2016). The same dataset is also analyzed for 2005–2016 (black dots). The GOZCARDS trends are derived using a multi-linear regression model that includes seasonal and shorter period cycles, as well as QBO-type variations. The blue dots arise from a linear trend calculation (Bernath and Fernando, 2018) for a seasonally-averaged (and de-seasonalized) ACE-FTS time series (60°S to 60°N, 2005 through 2017) based on version 3.5/3.6 data; these trends do not change appreciably if the 2005–2016 period is used instead. The ACE-FTS trend errors are 2-sigma estimates, taking into account the auto-correlation of the residuals. The GOZCARDS error bars provided here are 2-sigma estimates, based on a bootstrap resampling method (using 20,000 resampling cases from blocks of data).

to variability in the circulation affecting the Northern Hemisphere. **Figure 1-13** shows an update to the long-term total column data for HCl and $ClONO_2$ and their sum, which represents most of the inorganic chlorine in the stratosphere, at Jungfraujoch (46.5°N) and at Lauder (45°S), through the end of 2016. At the Jungfraujoch station, statistically significant decreases are observed for both species for the period from 1997 through 2016: –0.42±0.23% yr^{-1} for HCl and –0.60±0.39% yr^{-1} for $ClONO_2$ (based on June to November data; updated from Mahieu et al., 2014a). The trend over the past decade is, however, not significant. Similar trends have been reported for the mid-latitudes of the Northern Hemisphere from other NDACC (Network for the Detection of Atmospheric Composition Change) stations (Kohlhepp et al. (2012). For the same period (1997–2016), slightly larger negative trends are derived from the Lauder data (including all months) for the Southern Hemisphere, with a decrease of –0.51 ± 0.12% yr^{-1} for HCl and –0.74 ± 0.59% yr^{-1} for $ClONO_2$. HCl from the Global Ozone Chemistry And Related trace gas Data records for the Stratosphere (GOZCARDS), based on the HALOE, ACE-FTS, and Aura MLS satellite instruments (Froidevaux et al., 2015), shows similar trends (1997–2016) for Northern Hemisphere mid-latitudes.

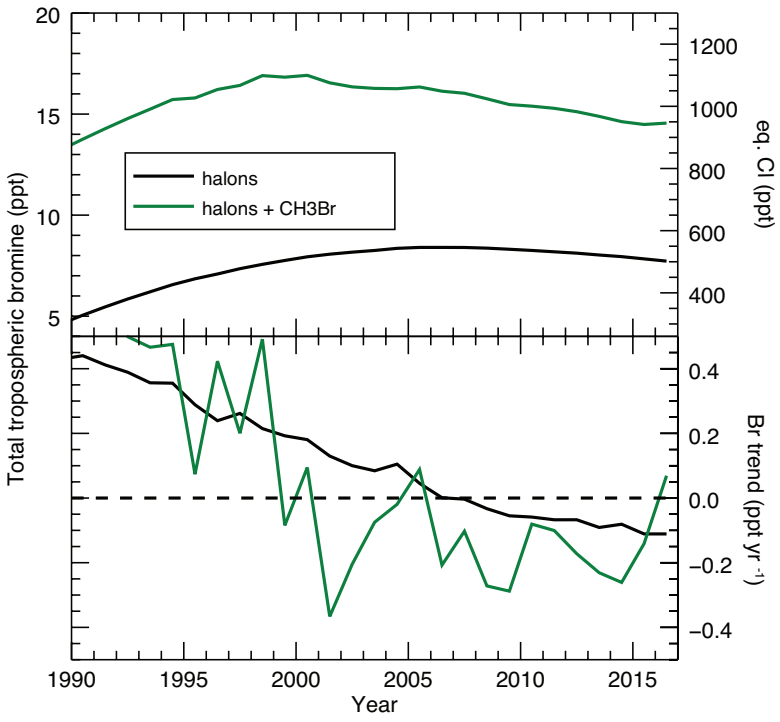

Figure 1-15. Tropospheric bromine time series and annual changes from long-lived gases, separated by contributions due to halons and CH_3Br. No contribution from VSLS species is included here. The values are also shown expressed in equivalent chlorine (right-hand axis of upper panel), adapting a value of α=65 to account for the higher efficiency of bromine in catalyzing ozone destruction. All values are derived from a merged dataset based on NOAA, AGAGE, and UEA data.

GOZCARDS also shows latitude-dependent, short-term lower-stratospheric HCl changes (for different 6- to 8-year periods), with steadier/larger decreases at southern latitudes contrasting with increases at northern mid-latitudes.

Near-global (60°S–60°N) trends of HCl from GOZCARDS and ACE-FTS are compared for the 12-year period 2005–2016 in **Figure 1-14**. While GOZCARDS is dominated by MLS results, as a merged satellite product it also contains some information from ACE-FTS, so the two estimates are not completely independent. ACE-FTS shows a decrease in the uppermost stratosphere at a rate of about –0.48 ± 0.02% yr^{-1} (Bernath and Fernando, 2018) and good agreement with the GOZCARDS result near 10 hPa. Taking into account the time shift between the troposphere and the upper stratosphere of about 5 years, this rate of decrease is in good agreement with the average rate of decrease in tropospheric chlorine over the time period from 2000–2010. There is increasing divergence between these two satellite-based datasets at the lower altitudes, although not significant at the 2-sigma level. In the ACE-FTS trend calculation, dynamical variability has been removed based on a regression model using N_2O time series (Stolarski et al., 2018). Such a procedure was not applied to the GOZCARDS results in **Figure 1-14**, but it would likely reduce the differences in lower-stratospheric trends versus the ACE-FTS result. Sampling differences between MLS and ACE-FTS, and instrument or retrieval issues, could also play a role in explaining these differences. Long-term changes in HCl could also be influenced by changes in stratospheric dynamics and chlorine partitioning, especially in the ratio between $ClONO_2$ and HCl. There is also evidence for significant latitudinal differences in the trends obtained from various FTIR column $ClONO_2$ time series (Kohlhepp et al., 2012), although the ratio between HCl and $ClONO_2$ at Jungfraujoch does not show any significant trend within the 95% confidence interval. Variability in atmospheric circulation has been suggested as a reason for the lack of a significant trend at Northern Hemisphere mid-latitude HCl over the past decade (Mahieu et al., 2014a). This is corroborated by observed changes in the mean age of air in Northern Hemisphere mid-latitudes over the same time period (Haenel et al., 2015; Stiller et al., 2012) and smaller

than expected trends in source gases (Chirkov et al., 2016; Nedoluha et al., 2015).

We conclude that, despite some complications in the lower-stratospheric HCl measurement comparisons, there is continuing evidence for locally non-monotonic latitude-dependent HCl changes in this region, with a slowdown in the decrease of lower-stratospheric HCl since the initial period (about 1997–2005) after its peak concentrations. Upper-stratospheric HCl (close to the abundance of inorganic chlorine, Cl_y) is continuing to decrease steadily, based on ACE-FTS HCl data.

Other evidence for continuing decreases in stratospheric inorganic chlorine comes from ground-based and satellite ClO measurements over Antarctica (Nedoluha et al., 2016). ClO trend detection in this region is complicated by large, meteorologically driven, interannual variability. Temperature-adjusted ClO (as a rough proxy for Cl_y) over that region shows a trend from the Scott Base data of –0.6 ± 0.8 (2 sigma) % yr^{-1} for 1996–2015 and –0.5 ± 0.4% yr^{-1} for 2004–2015 as measured zonally by Aura MLS at the Scott Base latitudes. Based on millimeter-wave emission measurements at Mauna Kea, Hawai'i, ClO near 33–37 km continued to show decreases (Connor et al., 2013). Updated ClO trends (from day-minus-night data) are as follows: –1.08 ± 0.40% yr^{-1} for the early period from 1995 to 2004 (unchanged from the above reference), –0.49 ± 0.12% yr^{-1} for 1995–2015, and –0.32 ± 0.26% yr^{-1} for the 2005–2015 period, 2-sigma uncertainties. To first order at least (since upper-stratospheric ClO is not an exact proxy for Cl_y), these results suggest broad agreement, with other evidence pointing to a continuing decrease with a gradual slowdown in the rate of decrease in stratospheric (and tropospheric) chlorine.

1.4.2 Tropospheric and Stratospheric Bromine Changes

1.4.2.1 Tropospheric Bromine Changes

As stated in previous Assessments, total tropospheric bromine from CH_3Br and halons, the brominated substances controlled under the Montreal Protocol, reached a maximum in 1998 with an annual average value of 16.9 ppt. Since 1998, its abundance has been decreasing at an average rate of 0.15 ± 0.1 ppt yr^{-1} (1% yr^{-1}) over the period from 2000 to 2016 (**Figure 1-15**), reaching a value of 14.6 ppt by mid-2016. This value does not include bromine from VSLSs, such as CH_2Br_2 and $CHBr_3$, which are not regulated under the Montreal Protocol. While bromine from CH_3Br has been decreasing since the late 1990s, bromine from halons did not start to decrease until 2006. For the period from 2008 to 2012, total bromine decreased at a rate of 0.16 ppt yr^{-1}. Halons contributed ~38% to this decline, while CH_3Br contributed ~62%. In the more recent period from 2012 to 2016, total bromine declined at a rate of 0.15 ± 0.04 ppt yr^{-1} (1% yr^{-1}). However, the contributions of halons and CH_3Br were nearly reversed compared to the previous period: halons contributed ~70% (–0.10 ppt yr^{-1}), while CH_3Br contributed ~30% (–0.04 ppt yr^{-1}). For the first time, the decrease in total bromine over the past 5-year period was thus not dominated by a decrease in CH_3Br but rather by a decrease in halons. The reduced contribution of CH_3Br to the decline in total bromine was caused by an as-yet-unexplained increase in CH_3Br in 2016 (see **Section 1.2.7**). The observed decrease in halons is in overall good agreement with the decrease projected by the A1 scenarios from the 2014 Assessment (Harris and Wuebbles et al., 2014).

1.4.2.2 Stratospheric Bromine Changes

Bromine is transported to the stratosphere in the form of long-lived ODSs, mainly the halons and CH_3Br as well as from VSLSs, both in organic and inorganic forms. In general, the amount of bromine in the stratosphere can either be determined by summing up the long-lived ODSs and VSLSs (Brinckmann et al., 2012; Navarro et al., 2015; Pfeilsticker et al., 2000; Sala et al., 2014; Wamsley et al., 1998) or by combining measurements of BrO with a modeled ratio of BrO/Br_y (Dorf et al., 2006; Dorf et al., 2008; Höpfner et al., 2009; Kreycy et al., 2013; Millán et al., 2012; Stachnik et al., 2013; Werner et al., 2017). Br_y is the sum of all inorganic bromine species. The BrO-based method will also yield an estimate of total bromine if the measurements are performed in the upper stratosphere, where all organic long-lived ODSs and VSL SGs are broken down and all bromine is thus in the inorganic form. If this method is applied in the lower stratosphere, additional measurements of the remaining long-lived ODSs and VSL SGs are needed to determine total bromine (Wales et al., 2018; Werner et al., 2017).

In the case of the source gas-based technique, the determination of the contribution from the long-lived

ODSs is straightforward, as they are sufficiently long-lived to be transported into the stratosphere and their stratospheric entry mole fraction can thus be estimated using the global mean from the observational networks (see **Sections 1.2** and **1.4.2.1**). For the contribution from the VSLS gases, both organic (SGI) and inorganic (PGI) forms need to be considered. The sum of these two was assessed to be 5 (3–7) ppt in **Section 1.3** (see **Table 1-5**). As there is no indication of a long-term change in this value, total organic bromine input to the stratosphere is thus derived by adding 5 ppt to the respective sum of the long-lived source gases.

Figure 1-16 compares studies that have used the BrO-based technique, based on total column and vertically resolved measurements, with source gas observations of CH_3Br and halons. **Figure 1-16** is an update

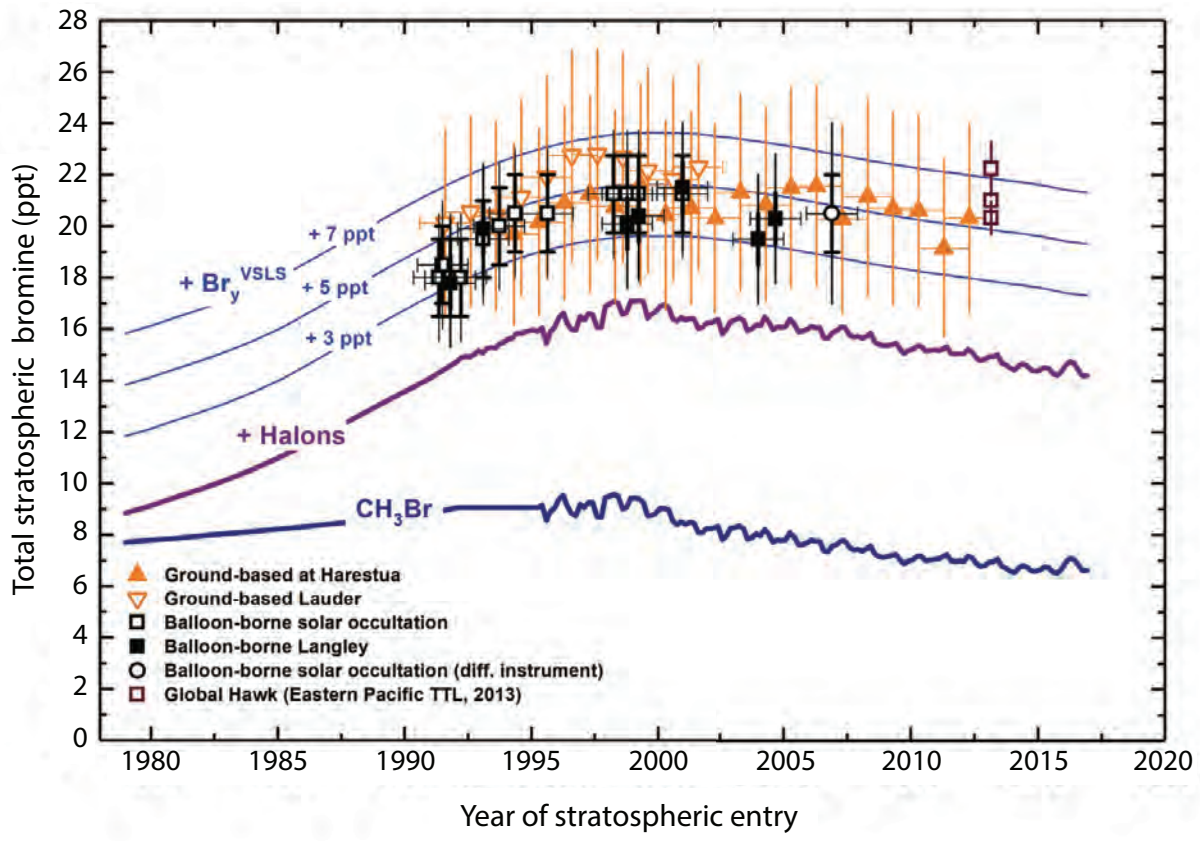

Figure 1-16. Changes in total stratospheric Br_y (ppt) derived from balloon-borne (black squares) (update of Dorf et al., 2006) and airborne (purple open squares) (Werner et al., 2017) BrO observations and annual mean mole fractions calculated from ground-based UV-visible measurements of stratospheric BrO made at Harestua (60°N) and Lauder (45°S) stations (filled and open orange triangles, respectively (adapted from Hendrick et al., 2007 and Hendrick et al., 2008). All UV-visible measurements of stratospheric BrO were evaluated using a common BrO absorption cross section (based on Wahner et al., 1988), frequency-shifted to match the wavelength scale (Wilmouth et al., 1999). For the balloon-borne observations, bold/faint error bars correspond to the precision/accuracy of the estimates, respectively. For the ground-based measurements (triangles), the error bars correspond to the total uncertainties in the Br_y estimates. For stratospheric data, the date corresponds to the time when the air was last in the troposphere, i.e., sampling date minus estimated mean age of the stratospheric air parcel. Time series of CH_3Br and halons have been updated (see Carpenter and Reimann et al. (2014) for details). The blue lines show the expected stratospheric Br_y, assuming an additional input of 3, 5, and 7 ppt of brominated VSLSs, respectively. For tropospheric data, the date corresponds to the sampling time. This figure updates Figure 1-20 from the previous Assessment (Carpenter and Reimann et al., 2014).

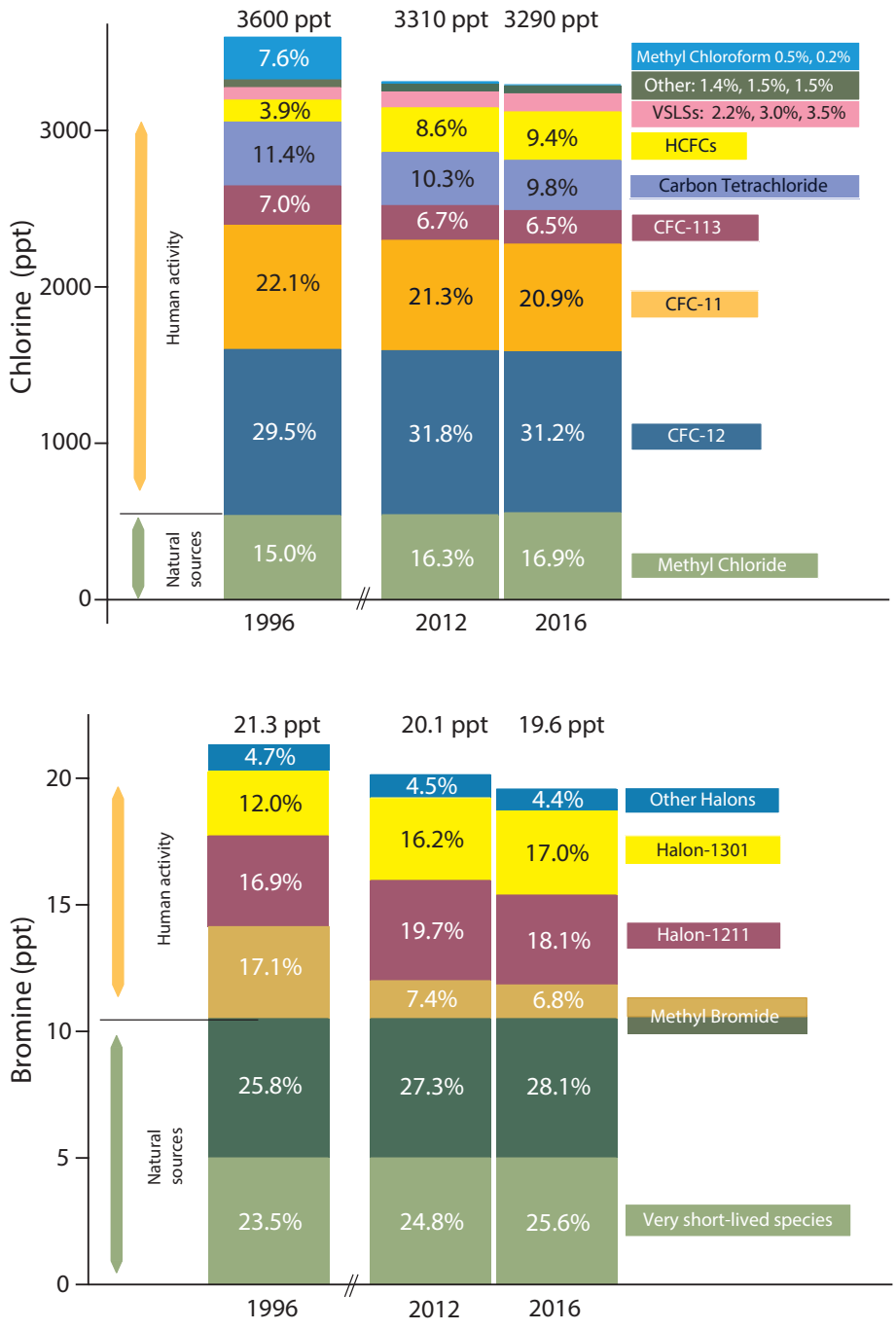

Figure 1-17. Chlorine and bromine input to the stratosphere for 1996, 2012, and 2016 for different species and classes of compounds. The year 1996 represents a reference which is close to the maximum of both chlorine and bromine loading of the troposphere. Mole fractions of long-lived gases are derived from surface observations (global networks). VSLS contributions for bromine are included as a constant 5 ppt, as discussed in **Section 1.3** and summarized in **Table 1-5.** The VSLS chlorine contribution is based on the VSL SG input from a model constrained by observed surface boundary conditions (update of Hossaini et al., 2015), see discussion in **Section 1.3.2.1**). Total VSLS Cl input derived in this way is 80 ppt, 100 ppt, and 115 ppt for years 1996, 2012, and 2016, respectively. For chlorine, "other" includes minor CFCs and halon-1211. For bromine, "other halons" is the sum of bromine contained in halon-1202 and halon-2402. Methyl chloride is counted as having purely natural sources, despite some indications of anthropogenic contributions (see **Section 1.2.6**).

of data presented in the last Assessment (Carpenter and Reimann et. al, 2014; Dorf et al., 2006; Hendrick et al., 2008; Hendrick et al., 2007) and includes new data from the ATTREX campaign (Werner et al., 2017). The stratospheric data are plotted against the "year of stratospheric entry" (respective air mass age) in order to take into account the time to transport air upward in the stratosphere, as characterized by the mean age of air. From these data, a long-term decrease of stratospheric bromine of –0.16 ± 0.07 ppt yr^{-1} is derived for the period from 2004 to 2014, in excellent agreement with the trend in tropospheric bromine derived for the same time period. A value of 19–20 ppt for total bromine in the stratosphere is deduced for the year 2016, in good agreement with the bottom-up method if an input of about 5 ppt from VSLSs (sum of PGI and SGI) is added to the long-lived ODSs. This good agreement enhances the confidence in our overall understanding of bromine input to the stratosphere due to VSLSs. It should also be noted that due to the decline in the compounds regulated under the Montreal Protocol, less than 50% of bromine entering the stratosphere is now due to anthropogenic emissions.

1.4.3 Tropospheric and Stratospheric Iodine Changes

The main organic source gas for iodine is CH_3I. There are no updated data on tropospheric trends since those published by Yokouchi et al. (2012), and there is consensus that the direct input of CH_3I to the stratosphere is small, i.e., below 0.1 ppt (Carpenter and Reimann et al., 2014; Tegtmeier et al., 2013). Observations also agree on the amount of IO in the TTL, which is on the order of 0.15 ppt or less (Bösch et al., 2003; Butz et al., 2009; Dix et al., 2013; Saiz-Lopez et al., 2015). The recent debate about the possibility of a higher PGI to the stratosphere of up to 0.7 ppt (Saiz-Lopez et al., 2015) (see Section 1.3) does not concern a long-term change but rather a different partitioning of total iodine to IO. If the mechanism suggested by Saiz-Lopez et al. (2015), involving higher oxides of iodine, is effective, this would imply a higher iodine content of the stratosphere but not necessarily a long-term change.

1.4.4 Changes in Ozone-Depleting Halogen Abundance in the Stratosphere

Chlorine and Bromine Input to the Stratosphere

Due to the regulations of the Montreal Protocol, many long-lived ODSs that contribute chlorine and bromine to the stratosphere are now decreasing in the atmosphere. Aside from some minor CFCs (**Table 1-1**), the exception to this are HCFCs, which are still increasing, though the rates of increase are slowing down (see **Section 1.2**). On the other hand, chlorinated VSL SGs have shown significant increases during the past decade. This has resulted in changes in the total burden and the relative contributions of different species to total chlorine and bromine in the troposphere and thus to the input of halogens to the stratosphere. **Figure 1-17** shows the changes in total bromine and total chlorine input to the stratosphere. This input is derived by assuming that the global average values derived for long-lived compounds are representative of the amount transported to the stratosphere. For chlorine and bromine from short-lived substances, VSLS input is included from measurements and modeling at the tropical tropopause, as discussed in **Section 1.3** and shown in **Table 1-5**, considering both source gas injection (SGI) and product gas injection (PGI). For bromine, the absolute contribution from VSL SGs is constant, but the relative contribution is increasing, reaching about 25% in 2016. For chlorine, both the absolute and relative contribution of VSL SGs is increasing, although the relative contribution remains small compared to bromine, at 3.9% in 2016. For both bromine and chlorine, there have been no signs of significant long-term changes in the natural sources, so the absolute contributions of natural sources to stratospheric chlorine and bromine remain constant, but their relative contribution is increasing. In the case of bromine, it is now estimated that more than half of the stratospheric bromine input is due to natural sources.

Equivalent Effective Stratospheric Chlorine (EESC)

While the total amount of chlorine and bromine transported to the stratosphere is important, the most relevant metric for the impact on stratospheric ozone is the inorganic halogen loading. The inorganic halogen loading depends not only on the amount of

Box 1-4. Equivalent Effective Stratospheric Chlorine (EESC) and Fractional Release Factors

EESC is a metric used to describe the combined impact of chlorine and bromine on stratospheric ozone and the temporal development of this effect due to tropospheric trends. The basic concept of EESC, as well as that of fractional release factors, which are needed for the calculation of EESC, has been presented and discussed in previous Assessments (Daniel and Velders et al., 2011; Harris and Wuebbles et al., 2014). EESC is expressed as an equivalent chlorine and is commonly defined as "the sum of the time-dependent chlorine and bromine derived from ODSs tropospheric abundances, weighted to reflect their potential influence on ozone" (Harris and Wuebbles et al., 2014). EESC is derived from observed or projected tropospheric mole fractions of ODSs. The calculation of EESC does not take into account changes in stratospheric transport or photochemistry. Therefore, it is important to emphasize that any discussion of EESC changes and

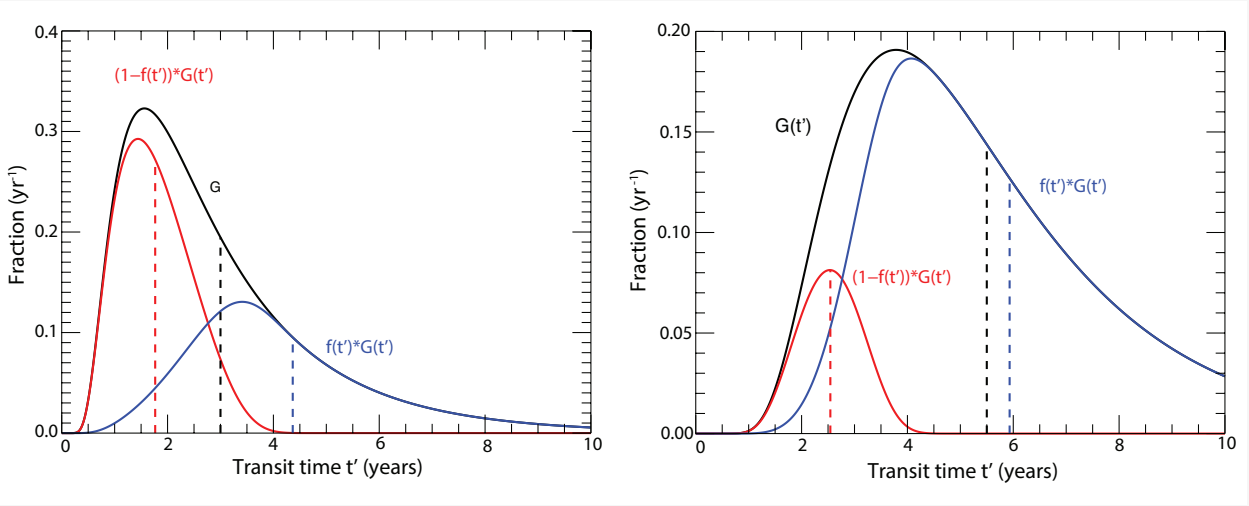

Box 1-4 Figure 1. Age spectra G (black line) for an inert tracer compared to the transit time distributions weighted with chemical loss (red and blue line) for a mean age of 3 years (a), and 5.5 years (b). The red line represents the transit time distribution for the remaining organic fraction of a source gas; the blue line represents the fraction which has been released and is thus in the inorganic form. The loss function has been approximated as a function of transit time in order to represent a tracer similar to CFC-11 (Engel et al., 2018). The first moments of the three functions differ substantially: the first moment of the red curve (representing the remaining organic fraction) is younger, and that of the blue curve (describing the inorganic halogen released from the source gas) is older than the mean age value. Note that this figure is purely for illustrative purposes, as the loss function has been approximated.

percentage reductions of EESC does not imply a similar response of ozone. Such a relationship between EESC and ozone would only be expected in the absence of any other factors influencing ozone. The formulation used in the previous Assessments to calculate EESC was based on Newman et al. (2007), which takes into account the time delay and mixing during transport in the stratosphere by adapting an age spectrum. For polar winter conditions, a mean age value of 5.5 years is used, and a value of 3 years is adapted for mid-latitudes, in line with previous Assessments. The efficiency with which each chlorine or bromine compound releases their halogen content is taken into account using age-of-air-dependent fractional release factors in the calculation of EESC. These fractional release factors describe the fraction of a halogen-carrying source gas that is photochemically lost as a function of mean age. Fractional release factors are higher for 5.5 years of mean age, leading to overall higher values of EESC under polar winter conditions in comparison to mid-latitude conditions.

Box 1-4, continued.

Fractional release factors are mostly derived from observations, again taking into account the age spectrum to compensate for the time-lag between the troposphere and the stratosphere and the tropospheric trends. Fractional release factors should be constant in time as long as stratospheric transport and chemistry do not change, thus representing a molecular property for a given atmospheric state. In particular, they should be independent of the tropospheric trend of a trace gas; i.e., fractional release factors derived during different periods should be very similar, as atmospheric transport is expected to change much less rapidly than tropospheric trends of the source gases. It has recently been shown by Ostermöller et al. (2017) that this is not the case for the current formulation used to calculate fractional release factors (Newman et al., 2007), because the age spectrum used to calculate fractional release is that of an inert tracer and does not take into account chemical loss. Based on the work of Plumb et al. (1999), Ostermöller et al. (2017) suggested that a different transit time distribution should be used to better take into account the interaction of tropospheric trends, chemical breakdown, and stratospheric transport. They presented a new method to calculate fractional release based on a different age spectrum, which is weighted by the chemical loss. As discussed by Engel et al. (2018), the actual loss function will depend on both transit time and the transport pathway of the individual fluid elements of an air parcel, with transport pathways that reached higher altitudes generally showing larger fractional loss. Nevertheless, it has been shown (Engel et al., 2018) that when describing the loss only as a function of transit time, a much better agreement between EESC calculated from model-derived fractional release factors and inorganic halogen loading from model calculations can be achieved. **Box 1-4 Figure 1** shows age spectra for mean ages of 3 and 5.5 years for a compound with a loss function $f(t')$ approximated as function of transit time t' which is approximately representative of CFC-11. As chemical loss is more pronounced in the fraction having long transit times, the transit time distribution describing the remaining organic fraction is weighted more strongly at shorter transit times and thus has a lower mean value. The mean value of this distribution has been termed the "mean arrival time" (Plumb et al., 1999); and the distribution itself, the "arrival time distribution." Using this formulation, fractional release factors can be derived that are largely independent of the tropospheric trend (Ostermöller et al., 2017).

Based on the same concept that the age spectrum is weighted with chemical loss, Engel et al. (2018) showed that the calculation method for EESC could also be improved. While the arrival time distribution used to describe the remaining organic fraction is weighted with the remaining fraction $(1–f(t'))$ (red curve in **Box 1-4 Figure 1**), the fraction describing the released inorganic halogen fraction is weighted with the loss function $f(t')$ (blue curve in **Box 1-4 Figure 1**). The transit time distribution describing the released inorganic halogen has been termed the "release time distribution," in analogy to the arrival time distribution, and its first moment has been termed the "mean release time." The mean release time will always be longer than the mean age.

In this Assessment we present results for EESC from the method presented by Newman et al. (2007) and the method suggested by Engel et al. (2018).

source gases transported into the stratosphere but also on the efficacy with which halogens are released from the source gases. Furthermore, both transport from the troposphere to the stratosphere and transport and mixing in the stratosphere need to be considered, with timescales for the latter being on the order of several years. The different efficiencies with which ODSs and VSLSs release their halogen content are described by *fractional release factors*. Stratospheric transport and mixing are described by an *age-of-air spectrum*. While mean age is the average time it takes for an air parcel to be transported from the troposphere to a certain location in the stratosphere, this age spectrum describes the probability distribution for different transit times. Furthermore, it has to be taken into account that bromine is a much more effective

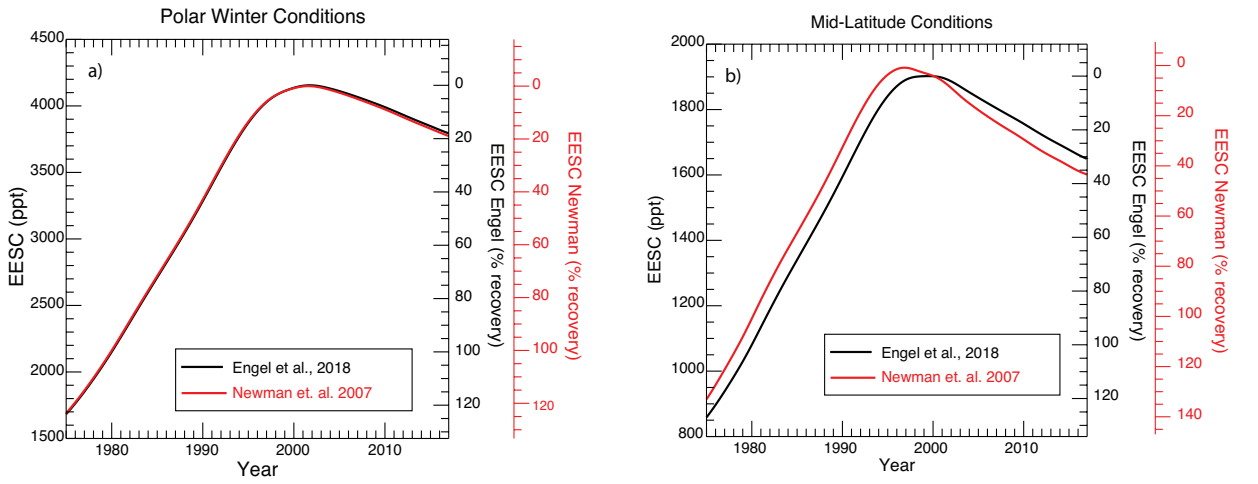

Figure 1-18. Level of EESC recovery towards 1980 benchmark values comparing the EESC calculation as used in the 2014 Assessment (Carpenter and Reimann et al., 2014; Newman et al., 2007) to the new method suggested by Engel et al. (2018). Plot (a) is for 3 years of mean age, representative of mid-latitude conditions, while plot (b) is for 5.5 years of mean age, representative of polar winter conditions. In all cases, the different age spectra (see **Box 1-2**) were parameterized as suggested by Newman et al. (2007) using half of the mean age as width of the age spectrum and an inverse Gaussian function as the shape of the age spectrum. The age spectrum has been integrated over a time period of 20 years. Fractional release factors were used as in the last Assessment report and in Velders and Daniel (2014) for the formulation according to Newman et al. (2007). In the calculation using the formulation suggested by Engel et al. (2018), the same fractional release factors were used, but these were modified to be consistent with the formulation of fractional release suggested by Ostermöller et al. (2017), as explained in Engel et al. (2018). The same tropospheric data were used as in **Section 1.4.1.1** and **Section 1.4.2.1**. VSLS contributions to EESC are not included in this calculation. In the calculation of EESC, the higher efficiency of bromine to destroy stratospheric ozone is taken into account. As in previous Assessments, we adopt a factor of 60 for mid-latitude conditions and a factor of 65 for polar winter conditions.

Table 1-7. EESC values for early 1980 and early 2017 as well as the value when EESC was at its maximum. Values are given for 3 and 5.5 years of mean age and for the two calculation methods discussed (see text in **Section 1.4** for details). Also shown are decreases achieved by early 2017 with respect to the maximum and the percent recovery with respect to the 1980 values. The calculated decreases and recovery rates for 3 years of mean age are significantly smaller using the new method of Engel et al. (2018) than when using the Newman et al. (2007) method.

3 Years of Mean Age; Mid-Latitude Conditions					
	EESC 1980	EESC maximum	EESC early 2017	% decrease from maximum	% Recovery to 1980
Newman et al. (2007)	1161	1928	1601	–17%	43%
Engel et al. (2018)	1080	1902	1649	–13%	31%
5.5 Years of Mean Age; Polar Winter Conditions					
	EESC 1980	EESC maximum	EESC early 2017	% decrease from maximum	% Recovery to 1980
Newman et al. (2007)	2161	4148	3774	–9%	19%
Engel et al. (2018)	2151	4154	3794	–9%	18%

ozone destruction catalyst than chlorine. As in previous Assessments, we adopt a factor of 60 for mid-latitudes and 65 for high-latitude polar winter conditions for the relative efficiency of bromine versus chlorine with respect to ozone destruction. These factors are combined in the metric of equivalent effective stratospheric chlorine (EESC). New formulations to derive fractional release factors (Ostermöller et al., 2017) and EESC (Engel et al., 2018) have recently been proposed (see **Box 1-4**), with a refined treatment of the interaction between chemistry and transport. In the past, different fractional release factors have also been used, mainly based on work by Newman et al. (2007) and Laube et al. (2013). The work by Laube et al. (2013) has recently been re-evaluated using a new method (Ostermöller et al., 2017) and taking into account possible offsets in mean age of air in this work due to the use of SF_6-derived mean age (Leedham Elvidge et al., 2018). With this there is much better agreement with the fractional release values used in (Engel et al., 2018; Newman et al., 2007; Velders and Daniel, 2014) and recent WMO reports.

A refinement in the method to calculate EESC has recently been suggested by Engel et al. (2018). The concept of EESC, the methods of calculation, and the changes in the concept suggested by Engel et al. (2018) are explained in **Box 1-4**. Here, we will present results from both methods. Significant differences in these methods are derived for mid-latitude conditions only, while for polar winter conditions both methods yield very similar results. We have retained the same parameterization of the age spectrum as in previous Assessments; i.e., the width of the distribution is taken as half the value of the mean age. Here, we integrate the age spectrum over 20 years instead of 10 years, as was done in the previous Assessment. As can be seen in **Box 1-4 Figure 1**, a significant fraction of air has transit times greater than 10 years for a mean age of 5.5 years. We use a 20-year integration period to better account for all contributing air parcels.

The different methods in how EESC is calculated, and the integration periods considered, result in slightly different maximum EESC values as well as different benchmark values calculated for the year 1980. EESC in 1980 has been used as a benchmark in many previous Assessments, although this is certainly somewhat arbitrary, as ozone loss occurred prior to 1980. We also note that a return to 1980 EESC levels does not imply a recovery of the ozone layer to the 1980 state, as ozone is influenced by additional parameters like changes in stratospheric dynamics and chemistry. Independent of the formulation used to calculate EESC and the time

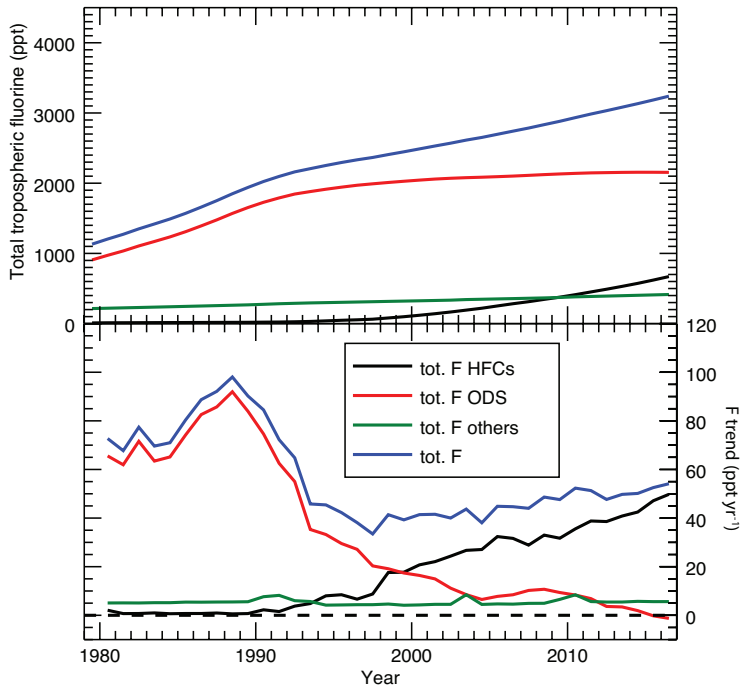

Figure 1-19. Tropospheric total fluorine time series and annual changes from long-lived gases, separated by contributions due to ODS, HFCs (see **Chapter 2**), and other fluorinated gases (such as SF_6, NF_3, and CF_4). ODS mole fractions were derived from a merged dataset based on NOAA, AGAGE, and UEA data. HFC mole fractions were derived from AGAGE and NOAA data. HFC records prior to regular global measurements were supplemented with estimates from Miller et al. (2010); Mühle et al. (2010); O'Doherty et al. (2009); Oram et al. (1996); Simmonds et al. (1998); Vollmer et al. (2011); and Weiss et al. (2008).

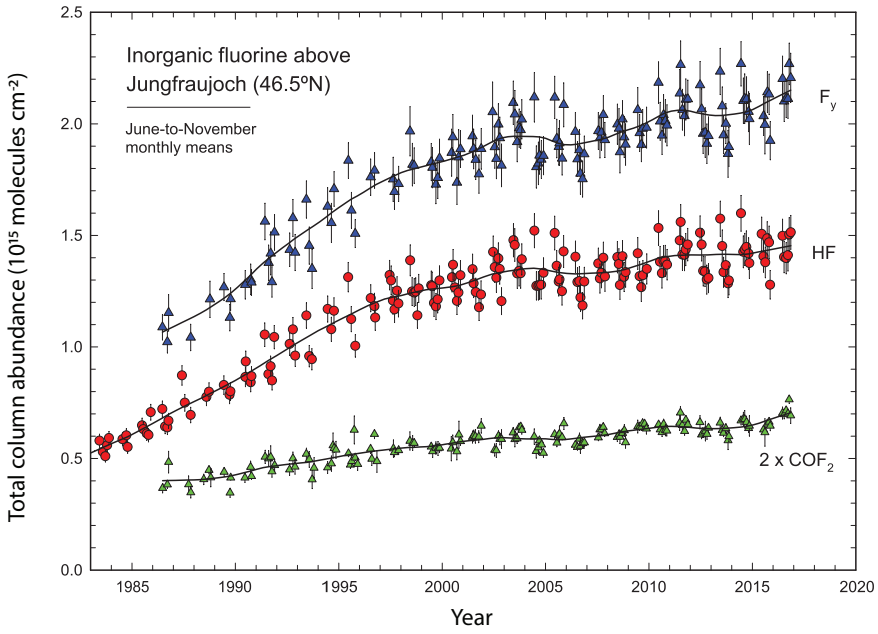

Figure 1-20. Multi-decadal monthly mean total column time series of the two main fluorine reservoirs, HF and COF_2, and their summation (F_y), as monitored at the Jungfraujoch station (Swiss Alps, 46.5°N, 3,580 m altitude), in the framework of the NDACC network. The datasets are restricted to the June to November months, so as to reduce the variability caused by atmospheric transport and subsidence during winter and spring. The continuous lines come from non-parametric least-squares fits involving an integration time of about 3 years and help to visualize the non-monotonic and non-linear changes in stratospheric chlorine after the peak in 1996–1997.

over which the spectrum is integrated, a continuous decline of EESC is derived. For a mean age of 5.5 years, as used for typical polar winter conditions, fractional release is nearly complete, and both formulations of EESC converge. However, in the case of a 3-year mean age, which is typically used for mid-latitude conditions, there are significant differences. Applying the new formulation, inorganic chlorine is expected to lag the tropospheric source gases more than expected based on a mean age representation of an inert tracer (see discussion in **Box 1-4**). One consequence of this is that a lower EESC is derived for the 1980 benchmark. Using the formulation for EESC from Newman et al. (2007) as in the last Assessment, but with a 20-year integration time, an early-1980 benchmark value of 1,160 ppt is calculated for a 3-year mean age, while 1,080 ppt is calculated using the new formulation of EESC suggested by Engel et al. (2018) (**Figure 1-18**, **Table 1-7**). This lower EESC value implies that it will take longer for EESC to decline to 1980 benchmark values. Accordingly, the percentage rate of recovery already achieved is also lower. For a mean age of 5.5 years, very similar values are derived with both methods (see **Table 1-7**). Using the new method, by 2017 we derive recovery of 31% towards 1980 values of EESC for mid-latitudes and of 18% for polar winter conditions; using the formulation by Newman et al. (2007) as in the previous Assessment, but with a 20-year integration time, by early 2017 we derive recovery of 43% for mid-latitude conditions and 19% for polar winter conditions.

Changes in EESC over the past 5 years (early 2012 to early 2017) are very similar for both methods, with maximum differences of 0.1%. The average change derived from both methods is given here. EESC, excluding contributions from short-lived substances, declined 4.3% from early 2012 to late 2016 in mid-latitudes and by 3.6% in high latitudes. The main driver of the decrease in EESC between early 2012 and early 2017 were the CFCs, which contributed 1.3% and 1.4% to this decline for mid-latitude and polar conditions,

respectively. CH_3Br was the second-most important contributor to changes in EESC, reducing EESC by 1.2% and 1% for mid-latitude and polar conditions, respectively. The impact of decreases in CH_3CCl_3 has now decreased to 0.8% (it was an important contributor during the period 2008–2012, with a decrease of about 1.5% for both polar winter conditions and mid-latitudes). EESC from halons decreased by 0.9% and 0.3% for mid-latitude and polar conditions, respectively. This is the first time that a decrease in EESC from halons is now also calculated for polar winter conditions. The decrease in tropospheric CCl_4 has resulted in a decrease of 0.8% in EESC at mid-latitudes and 0.6% in polar latitudes. The continuing increase in HCFCs has offset the total decrease by 0.4% at mid-latitudes and 0.6% for polar winter conditions.

1.4.5 Tropospheric and Stratospheric Fluorine Changes

Fluorine is not an efficient catalyst for stratospheric ozone depletion, due to the stability of the inorganic reservoir gases HF and COF_2, which are breakdown products of fluorine-containing source gases. However, many fluorinated source gases have a high radiative efficiency and are thus strong greenhouse gases, and most important fluorine gases are regulated under the Montreal Protocol. This regulation under the Montreal Protocol for chlorine- and fluorine-containing CFCs and HCFCs was motivated by the chlorine content. The regulation of HFCs, which are also included in the Kyoto Protocol, has only recently been added to the Montreal Protocol (see details in **Chapter 2**) in the framework of the Kigali Amendment, as these gases are replacement compounds for substances already regulated under the Montreal Protocol.

Figure 1-19 shows the time series of tropospheric fluorine in organic and some inorganic (SF_6 and NF_3, see **Section 1.5**) gases, separated by compound classes. In contrast to chlorine, a continuing increase in tropospheric fluorine is observed. A trend in total fluorine of 51.6 ± 2.3 ppt yr^{-1}, or 1.7 ± 0.07% yr^{-1}, is derived for the time period 2012–2016, which is comparable to the trend of 50.1 (±1.9) ppt yr^{-1}, or 1.7 (±0.07) % yr^{-1}, for the period 2008–2012. However, the drivers of this trend have changed. From 2008 to 2012, this increase was due to increases in ODSs (CFCs and HCFCs; 7.8 ppt yr^{-1}), HFCs (36.4 ppt yr^{-1}), and other fluorinated gases (6.6 ppt yr^{-1}). For the most recent 5-year period (2012–2016), it is more strongly dominated by HFCs (45 ppt yr^{-1}). Total fluorine input from ODSs has decreased to an average of 0.9 ± 1.9 ppt yr^{-1}, and the contribution from other fluorinated gases has been relatively stable at 5 ppt yr^{-1}. Total tropospheric fluorine and total tropospheric chlorine do not follow the same trajectory, largely because the largest contribution to a decrease in total Cl since ~1988 results from changes in CH_3CCl_3, which does not contain fluorine. However, the contribution to total tropospheric fluorine from all ODSs has been declining since the late 1980s, and the trend went from positive to negative in the last year (**Figure 1-19**, lower panel).

As can be seen from **Figure 1-19**, the contributions of different compounds and classes of compounds to the total tropospheric fluorine have changed significantly over time. As different gases release their fluorine with different efficiency, this implies that a direct reflection of tropospheric trends of fluorinated compounds in the inorganic fluorine content of the stratosphere is not necessarily expected.

A good proxy for the total inorganic fluorine (F_y) in the stratosphere is obtained by the weighted combination of the two most abundant fluorinated reservoirs, i.e., hydrogen fluoride (HF) and two times carbonyl fluoride (COF_2); this can thus be used as an independent check of the fluorine budget. **Figure 1-20** shows the multi-decadal monthly mean total column time series of inorganic fluorine above the Jungfraujoch station (Swiss Alps, 46.5°N, 3,580 m altitude), restricted to the June-to-November months, when atmospheric variability is at a minimum. A non-parametric least-squares fit to the time series helps to identify fluctuations in the rise of the fluorine loading in the Northern Hemisphere, fluctuations which are related to short-term variability in the atmospheric circulation and dynamics. The total column of HF increased at an average rate of 0.89 ± 0.17% yr^{-1} and that of COF_2 at 1.07 ± 0.14% yr^{-1} (update from Duchatelet et al., 2010; Duchatelet et al., 2009), as calculated using a bootstrap method (Gardiner et al., 2008). Total inorganic fluorine (F_y) has increased at a rate of 0.98 ± 0.15% yr^{-1} between 2007 and 2016.

Based on datasets from HALOE and ACE-FTS and a merged dataset from GOZCARDS, (Harrison et al., 2016) found a substantial slowdown in the rate of

Table 1-8. Measured mole fractions of selected fluorinated compounds (PFCs, SF_6, NF_3, SO_2F_2, SF_5CF_3) and other gases of interest.

Chemical Formula	Common or Industrial Name	Annual Mean Mole Fraction (ppt) 2012	2015	2016	Change (2015–2016) ppt yr^{-1}	% yr^{-1}	Network, Method
Perfluorocarbons (PFCs)							
CF_4	PFC-14	**79.7**	**81.9**	**82.7**	**0.8**	**1.0**	AGAGE in situ (Global)
C_2F_6	PFC-116	**4.2** *3.7*	**4.5** *3.9*	**4.6** *4.0*	**0.1** **0.1**	**2.1** **1.9**	AGAGE in situ (Global) *UEA, Cape Grim*[1]
C_3F_8	PFC-218	**0.57** **0.54**	**0.62** **0.60**	**0.63** **0.60**	**0.02** **0.00**	**2.6** **0.7**	AGAGE in situ (Global) UEA, Cape Grim
c-C_4F_8	PFC-c318	*1.26*	*1.39*	*1.44*	*0.05*	*3.6*	*UEA, Cape Grim*
n-C_5F_{12}	PFC-41-12	*0.142*	*0.149*	*0.148*	*–0.001*	*–0.7*	*UEA, Cape Grim*[1]
Other fluorinated compounds							
SF_6	sulfur hexafluoride	**7.6** **7.6**	**8.6** **8.6**	**8.9** **8.9**	**0.3** **0.3**	**3.8** **3.9**	AGAGE, flask and in situ (Global) NOAA, flask and in situ (Global)
NF_3	nitrogen trifluoride	**0.9**	**1.3**	**1.5**	**0.1**	**11.5**	AGAGE in situ (Global)
SO_2F_2	sulfuryl fluoride	**1.8**	**2.1**	**2.3**	**0.1**	**6.2**	AGAGE in situ (Global)
SF_5CF_3		*0.153*	*0.154*	*0.153*	*-0.001*	*-0.65*	*UEA, Cape Grim*
Other compounds							
CH_4 (ppb)	methane	**1809** **1808** **1808** **1806** **1819**	**1834** **1834** **1830** **1833** **1844**	**1842** **1843** **1840** **1841** **1853**	**8** **9** **10** **8** **9**	**0.4** **0.5** **0.5** **0.4** **0.5**	AGAGE in situ (Global) NOAA, flask and in situ (Global) UCI, flask (Global) CSIRO, flask (Global) WMO/GAW (Global)
N_2O (ppb)	nitrous oxide	**325.6** **325.0** **324.9** **325.1**	**328.5** **328.1** **327.8** **328.1**	**329.3** **328.9** **328.6** **328.9**	**0.8** **0.8** **0.8** **0.8**	**0.2** **0.2** **0.2** **0.2**	AGAGE in situ (Global) NOAA, flask and in situ (Global) CSIRO, flask (Global) WMO/GAW (Global)
COS (ppt)	carbonyl sulfide	**501**	**499**	**505**	**6**	**1.2**	NOAA, flask and in situ (Global)

Mole fractions in this table are from various monitoring networks that measure long-term trends in these gases. Results in bold text are estimates of global surface mean mole fractions. Values in italics represent observations from only one site and therefore do not represent a global mean. AGAGE (Advanced Global Atmospheric Gases Experiment, https://agage.mit.edu/) data are described in Arnold et al. (2013), Cunnold et al. (2002), Mühle et al. (2010), Mühle et al. (2009), Prinn et al. (2018) and Rigby et al. (2010), and global averages are calculated using data from five baseline AGAGE stations, assimilated into an atmospheric box model (extension of Rigby et al., 2014). NOAA (National Oceanic and Atmospheric Administration, USA, http://www.esrl.noaa.gov/gmd/dv/site/) data are described in Dlugokencky et al. (2011), Hall et al. (2011), and Montzka et al. (2007), global means are calculated as area-weighted means from observations at 12 sites for SF_6, and 45 sites for CH_4 (including shipboard sampling). UCI (University of California, Irvine, USA, http://ps.uci.edu/~rowlandblake/research_atmos.html) data are described in Simpson et al. (2012). UEA (University of East Anglia, United Kingdom, http://www.uea.ac.uk/environmental-sciences/research/marine-and-atmospheric-sciences-group) data are described in Laube et al. (2012); Leedham Elvidge et al. (2017), Oram et al. (2012), and Sturges et al. (2012). CSIRO data (Commonwealth Scientific and Industrial Research Organisation) are described in Francey et al. (2003). Cape Grim refers to the Cape Grim Baseline Air Pollution Station, Australia; WMO/GAW, World Meteorological Organization, Global Atmosphere Watch, World Data Centre for Greenhouse Gases, (http://ds.data.jma.go.jp/gmd/wdcgg and https://public.wmo.int/en/resources/library/wmo-greenhouse-gas-bulletin). Differences between each network are due to calibration scales, differences in spatial and temporal sampling strategies, and the different methods for estimating global means.

Note:

[1] Mole fractions for 2016 represent averages from January to July for UEA data for these compounds.

increase of global stratospheric HF. Trends of 0.52 ± 0.03% yr^{-1} were obtained from 2004–2012, in comparison to 1.12 ± 0.08% yr^{-1} for 1998–2005 and 4.97 ± 0.12% yr^{-1} for 1991–1997. The observed trends and the slowdown are in good overall agreement with results from modeled HF time series, although the model calculated a slightly lower increase for the 1991–1997 period. Significant short-term and latitudinal variability was observed in the trends of HF, which is attributed to dynamical variability in the stratosphere.

Overall, these data show a continuing increase in total fluorine. The magnitudes of the total tropospheric fluorine and stratospheric inorganic fluorine trends are somewhat different. As explained above, this may be due to the changing relative importance of different fluorinated gases, with different efficiencies of fluorine release in the stratosphere. The tropospheric increase is now mainly driven by increases in HFCs (**Chapter 2**).

1.5 CHANGES IN OTHER TRACE GASES THAT INFLUENCE OZONE AND CLIMATE

This section describes recent trends in gases that are not covered by the Montreal Protocol but that indirectly affect ozone. The gases nitrous oxide (N_2O) and methane (CH_4) play a role in stratospheric ozone chemistry and contribute to climate change and are discussed in **Sections 1.5.1** and **1.5.2**. **Section 1.5.3** addresses the sulfur-containing gases carbonyl sulfide (COS) and sulfur dioxide (SO_2), which are transported to the stratosphere where they contribute to stratospheric sulfuric acid aerosol. Finally, changes in some fluorine-containing greenhouse gases (GHGs), which indirectly influence ozone through their contribution to global warming (**Chapter 5**), are discussed in **Section 1.5.4**. Carbon dioxide (CO_2) is not discussed here, as it is described in detail elsewhere (e.g., Ciais and Sabine et al., 2013; Le Quéré et al., 2018). In contrast to previous Assessments, HFCs are no longer covered in this section, as they are now the subject of **Chapter 2**.

1.5.1 Nitrous Oxide (N_2O)

N_2O is the dominant source of reactive nitrogen to the stratosphere, which can lead to depletion of stratospheric ozone. Currently, natural and anthropogenic emissions of N_2O make a larger contribution to stratospheric ozone depletion than emissions of any of the individual ODSs discussed in **Section 1.2** (Ravishankara et al., 2009). While it is likely to remain a major contributor to ozone depletion throughout the 21st century, due to changes in stratospheric chemistry and dynamics brought about by increasing GHG concentrations, there remains some uncertainty about its long-term impact on ozone (Revell et al., 2015). Owing to its relatively high GWP, N_2O is the third-most important long-lived GHG after CO_2 and CH_4 (Myhre and Shindell et al., 2013; Ravishankara et al., 2009). The previous Assessment noted that N_2O had been growing relatively steadily, at a rate of around 0.8 ppb yr^{-1}. This trend has continued through 2016, for which an annual surface global mean mole fraction of around 329 ppb was reached (**Table 1-8**). As a result of this growth, the contribution of N_2O to radiative forcing has continued to rise, reaching 0.19 W m^{-2} in 2016 (**Figure 1-3**), approximately 10% that of CO_2.

Recent studies have attempted to better constrain N_2O sources and sinks. The previous Assessment summarized the findings of the SPARC Lifetimes Assessment, which estimated the N_2O lifetime to be 123 (104–152) years (2-sigma "most likely" range, SPARC (2013)). Based on observations from the Microwave Limb Sounder (MLS) and a radiative transfer model, Prather et al. (2015) recommend a lifetime of 116 ± 9 years, which is lower than the maximum likelihood SPARC estimate but within their uncertainties. Emissions of N_2O originate primarily from natural and agricultural soils and the ocean, with approximately one-third of emissions from anthropogenic sources (Ciais and Sabine et al., 2013). Thompson et al. (2014) produced top-down estimates of N_2O emissions using four different chemical transport models. Their estimate of global annual emissions of between 16.1 and 18.7 TgN yr^{-1} was broadly in agreement with IPCC AR5 (Ciais and Sabine et al., 2013) and therefore does not substantially alter our previous understanding of the global budget. More recently, Wagner-Riddle et al. (2017) proposed a 1.07 ± 0.59 TgN yr^{-1} source of N_2O induced by freeze-thaw cycles over croplands, which has not been included in previous budgets.

1.5.2 Methane (CH_4)

Methane, the second-most important anthropogenic GHG, is a source of water vapor and HO_x (OH and HO_2) radicals to the stratosphere and thereby also influences stratospheric ozone. Methane has continued to grow between 2012 and 2016, with the global mean mole fraction increasing between 32 and 35 ppb during this period (**Table 1-8**). The radiative forcing due to CH_4 was 0.5 W m^{-2} in 2016 (**Figure 1-3**), 25% the value of CO_2.

A recent study re-evaluated the global CH_4 budget from 2000–2012 and concluded that around 60% of global emissions are anthropogenic, although there remains a mismatch between emissions estimated using bottom-up and top-down methods (Saunois et al., 2016). Major sources of uncertainty in the CH_4 budget were found to be due to wetland CH_4 emissions and the magnitude and variability of the global hydroxyl radical (OH) concentration. Several recent studies have focused on the causes of the pause in CH_4 growth that occurred between 2000 and 2007, and the subsequent renewed rise. Nisbet et al. (2016) and Schaefer et al. (2016) used data from CH_4 isotopologues to conclude that the renewed growth was likely being driven by an increase in tropical

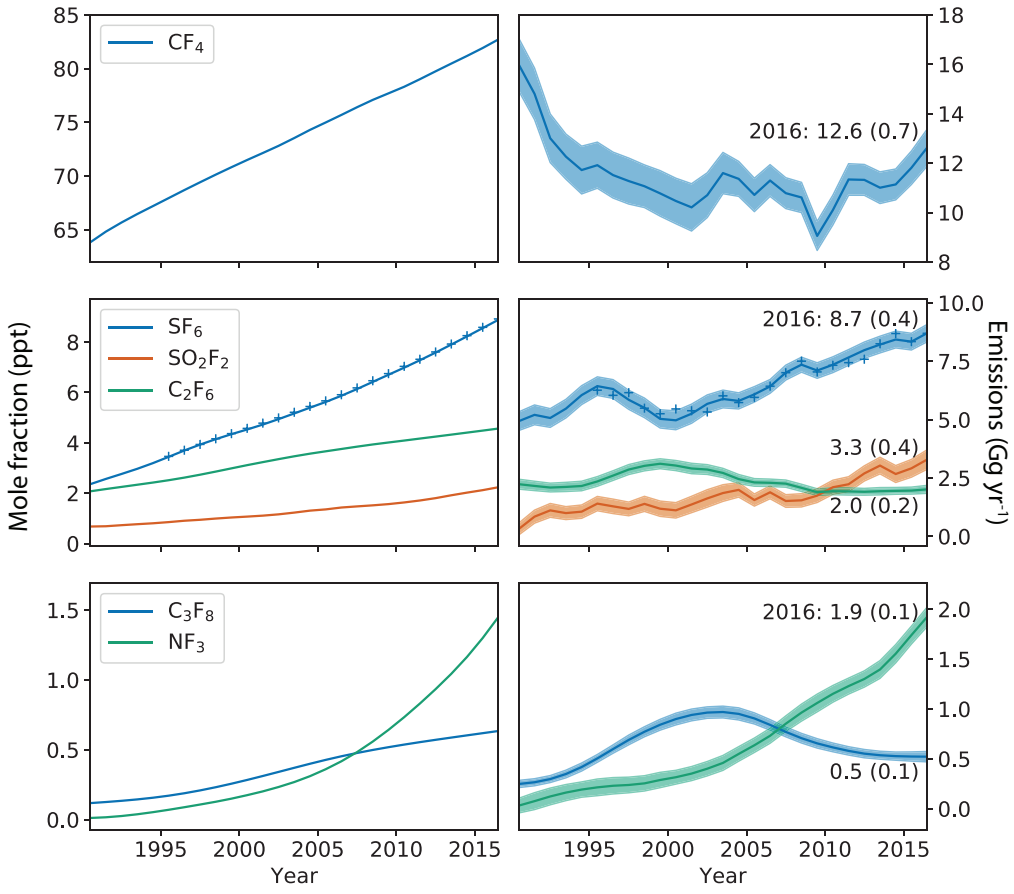

Figure 1-21. Global mean mole fractions (*left panels*) and emissions (*right panels*) for fluorinated greenhouse gases (excluding CFCs, HCFCs, and HFCs). Mole fractions are output from the AGAGE 12-box model (Cunnold et al., 1983; Rigby et al., 2013) and constrained using AGAGE data described in Arnold et al. (2013); Mühle et al. (2010); Mühle et al. (2009); Prinn et al. (2018); and Rigby et al. (2010). For SF_6, pluses represent data from NOAA (Hall et al., 2011, extended). Emissions were estimated using the Bayesian method described above **(Figure 1-4),** with atmospheric lifetimes as summarized in **Table A-1.**

wetland or agricultural (primarily ruminant animal) emissions, respectively. By analyzing global livestock populations and revising emissions factors, Wolf et al. (2017) also proposed that growing emissions from animals could be a significant contributor to the rise. Hausmann et al. (2016) pointed to the coincident growth in atmospheric ethane (C_2H_6) to infer an increase in CH_4 emissions related to oil and gas extraction since 2008, while Dalsoren et al. (2016) proposed an increase in anthropogenic emissions from East Asia. Schwietzke et al. (2016) used new estimates of isotopic source signatures to revise upwards the contribution of fossil fuel to the global CH_4 budget, compared to bottom-up inventories. They inferred a gradual decline in fossil fuel emission since the early 2000s, coincident with a gradual rise in emissions from microbial sources. In contrast, Worden et al. (2017) proposed that recent trends are consistent with a decline in biomass burning emissions and increase in fossil fuel emissions. McNorton et al. (2016), Rigby et al. (2017), and Turner et al. (2017) inferred global OH concentrations using AGAGE and NOAA methyl chloroform (CH_3CCl_3) data. They found an increase in OH in the 1990s and early 2000s, followed by a decline in OH that could explain much of the pause and renewed growth, although the uncertainties were found to be large compared to the magnitude of the inferred change. Overall, the uncertainty in the global CH_4 budget remains considerable, and there is no consensus on the drivers of recent trends.

1.5.3 Aerosol Precursors: Carbonyl Sulfide (COS) and Sulfur Dioxide (SO_2)

The sulfur-containing gases COS and SO_2, which are transported to the stratosphere, can be oxidized to yield sulfuric acid, which can condense on preexisting particles or nucleate to form new particles. Injection of sulfur gases occurs sporadically during volcanic eruptions, as well as more continuously through the atmospheric transport of tropospheric sulfur-containing gases to the stratosphere. As particles can interact with solar and terrestrial radiation, this has an influence on both tropospheric and stratospheric temperatures. In addition, heterogeneous reactions on aerosol surfaces in liquid aerosol particles can influence stratospheric chemistry. A review of stratospheric aerosols and their precursor gases has recently been published by Kremser et al. (2016).

Carbonyl sulfide (COS) is the most important substance responsible for transporting sulfur into the stratosphere. Recent modeling estimates of the sulfur fluxes from COS suggest that this accounts for 56% (Sheng et al., 2015) to 70% (Brühl et al., 2012) of the stratospheric aerosol burden. The magnitude of the sulfur fluxes calculated in the models is in agreement with sulfur fluxes from COS derived from observations (Barkley et al., 2008; Krysztofiak et al., 2015). There are large uncertainties in the global sources and sinks of carbonyl sulfide, with current sink estimates surpassing the source assessments, due to a recent factor-of-two upward revision in the global surface sink estimate (Kremser et al., 2016). While Berry et al. (2013) and Launois et al. (2015) suggested that missing sources may be due to oceanic emissions, this was not confirmed by Lennartz et al. (2017). Therefore, there are currently remaining uncertainties concerning the sinks and sources of COS. The main anthropogenic source of COS is thought to be CS_2 emissions from rayon production, which are rapidly oxidized to form COS in the atmosphere (Campbell et al., 2015). The main source region for these emissions is thought to have shifted to China during the past decades (Campbell et al., 2015).

Recent atmospheric observations of COS confirm that there is currently no or only a very small long-term trend in tropospheric COS (Lejeune et al., 2017). Between 2015 and 2016, tropospheric background values of COS increased by about 6 ppt (**Table 1-8**), but this is more likely a short-term variability than a sign of a long-term increase. Preindustrial levels of COS are confirmed to have been significantly lower than this based on ice core and firn air measurements (Aydin et al., 2014; Campbell et al., 2017). Comprehensive observations of COS in the stratosphere have recently become available from the MIPAS instrument onboard Envisat for June 2002 to April 2012. These observations also do not show a significant trend in the stratosphere (Glatthor et al., 2017). Balloon measurements reveal less than 5% change in stratospheric COS over the past 25 years (Toon et al., 2017).

Following volcanic eruptions, it has been shown that stratospheric sulfur loading from the upper troposphere to the upper stratosphere is enhanced (Höpfner et al., 2015; Höpfner et al., 2013). A large fraction of the SO_2 observed in the stratosphere in the absence of recent volcanic emission is from oxidation of COS in

the stratosphere. The relevance of the direct transport of SO_2 to the stratosphere remains unclear, with large variations between different models (Kremser et al., 2016; Sheng et al., 2015); however, an analysis of model results combining in situ measurements with MIPAS data indicates that it is near negligible (Rollins et al., 2017). Consequently, the impact of changes in tropospheric emissions—for example, the recent reduction in Chinese emissions of SO_2 (van der A et al., 2017)—remains unclear.

1.5.4 Other Fluorine-Containing Gases (SF_6, PFCs, NF_3, SO_2F_2, SF_5CF_3, HFEs)

Sulfur Hexafluoride (SF_6)

Sulfur hexafluoride, which was regulated under the Kyoto Protocol, is used primarily for electrical insulation (e.g. Ko et al., 1993). Its atmospheric global surface mean mole fraction increased from 7.6 to 8.9 ppt between 2012 and 2016, contributing 5.1 mW m^{-2} to global radiative forcing in 2016 (**Table 1-8, Figure 1-3, Figure 1-21**). During the period from 2010 to 2016, FTIR measurements above Jungfraujoch showed an increase in the atmospheric column mean mole fraction of 4.34 ± 0.19% yr^{-1}, which is slightly higher than the corresponding increase in the lower troposphere of 3.90 ± 0.06% yr^{-1} based on ground-based measurements (see **Table 1-2**). Emissions inferred from AGAGE and NOAA observations show that SF_6 global emissions have increased during this period, reaching 8.7 ± 0.4 Gg yr^{-1}, equivalent to 205 ± 9 Mt CO_2 yr^{-1}, in 2016 (**Figure 1-21**). These emissions are now 72% higher than a minimum inferred around the year 2000 (Levin et al., 2010; Rigby et al., 2010).

Using atmospheric SF_6 observations, Fang et al. (2014) estimated increasing emissions from East Asia, from 2.4 Gg in 2006 to 4.1 Gg in 2012, which is on average ~50% of the global emissions for this period. Recent studies have suggested a significant downward revision of the SF_6 lifetime, for which a value of 3,200 years has been widely used (Ravishankara et al., 1993). Using a 3-D model with updated atmospheric electron density, Kovacs et al. (2017) estimated an average lifetime of 1,278 years, with a range 1,120 to 1,475 years. From observations of SF_6 in the Arctic polar vortex, Ray et al. (2017) estimated a lifetime of 850 (580–1,400) years. Since the lifetime remains very long, these estimates will not significantly influence SF_6 emissions derived using observed atmospheric trends, or GWPs over a 100-year time horizon or shorter. However, climate impacts over longer timescales will be influenced.

Perfluorocarbons (PFCs)

Perfluorocarbons are compounds that consist of only carbon and fluorine and typically have very long lifetimes and high radiative efficiencies. The major PFCs are primarily emitted during aluminum and semiconductor production, and they were regulated under the Kyoto Protocol (e.g. Mühle et al., 2010). Since the previous Assessment, atmospheric abundances of all major PFCs have continued to increase (**Table 1-8, Figure 1-21**). CF_4 (PFC-14; lifetime greater than 50,000 years) increased by 0.8 ppt yr^{-1} between 2015 and 2016, reaching 82.7 ppt in 2016; C_2F_6 (PFC-116; lifetime greater than 10,000 years), at 0.1 ppt yr^{-1} to 4.6 ppt; and C_3F_8 (PFC-218; lifetime 2,600 years), at ~0.02 ppt yr^{-1} to 0.63 ppt. *c*-C_4F_8 (PFC-c318; lifetime 3,200 years) has reached 1.44 ppt at Cape Grim (update to Oram et al., 2012). Collectively, the PFCs contributed 6.3 mW m^{-2} to global radiative forcing in 2016 **(Figure 1-3)**. FTIR-based remote sensing observations at Jungfraujoch showed an increase of 1.11 ± 0.09% yr^{-1} for CF_4, which is slightly higher than the rate of 0.94 ± 0.01% yr^{-1} over the period from 2010 to 2016 derived from ground-based measurements (see **Table 1-2**). Emissions of the major PFCs have remained relatively stable since 2012 **(Figure 1-21)**. In 2016, emissions of CF_4, C_2F_6, and C_3F_8 were 12.6 ± 0.7, 2.0 ± 0.2, and 0.52 ± 0.05 Gg yr^{-1}, respectively, equivalent to CO_2 emissions of 84 ± 5, 22 ± 2, 4.6 ± 0.5 Mt yr^{-1}.

Trudinger et al. (2016) used measurements of CF_4, C_2F_6, and C_3F_8 from ice cores, firn, archived air samples, and field stations to reconstruct atmospheric abundances since 1800. They inferred an increase in emissions during the 20th century for these compounds until the early 1980s (CF_4) or early 2000s (C_2F_6 and C_3F_8), after which emissions declined. The growth in emissions of CF_4 and C_2F_6 was found not to have kept pace with global aluminum production (the major source of these gases), suggesting a decrease in the emissions factor from this industry. Apart from an apparent drop in emissions in 2009, attributed to

the global financial crisis, aggregate emissions of these compounds were found to be relatively stable from the late 2000s onwards (also shown in **Figure 1-21**).

Nitrogen Trifluoride (NF_3)

Since the previous Assessment, NF_3 (lifetime 569 years, GWP_{100} 15,750), which is primarily used in semiconductor manufacture and was included in the Kyoto Protocol (Arnold et al., 2013), has grown by more than 10% yr^{-1}, to 1.5 ppt in 2016 (**Table 1-8, Figure 1-21**). Its contribution to radiative forcing remained relatively small in 2016 at 0.3 mW m^{-2} (**Figure 1-3**). Emissions of NF_3 inferred for 2016 reached 1.9 ± 0.1 Gg yr^{-1}, equivalent to 30 ± 2 Mt CO_2 yr^{-1} (**Figure 1-21**). The compound is primarily used in the electronics industry as a source of reactive fluorine, in place of C_2F_6. Arnold et al. (2013) estimated a considerable climate benefit of this transition, due to the higher efficiency at which reactive fluorine can be extracted from NF_3, compared to C_2F_6. However, they also estimated global emissions that were significantly larger than expected under industrial "best practices." Both the atmospheric abundance and inferred emissions reported here for 2016 are more than 60% higher than the values for 2011 in Arnold et al. (2013).

Sulfuryl Fluoride (SO_2F_2)

SO_2F_2 is used as a fumigant for structural and post-harvest agricultural fumigation. It is increasingly being used in place of the ozone-depleting methyl bromide. The first atmospheric observations of SO_2F_2 were reported by Mühle et al. (2009), who estimated a lifetime of 36 ± 11 years, primarily due to loss to the oceans. The rate of growth of SO_2F_2 has increased since the previous Assessment. The 2016 atmospheric abundance was 2.25 ppt, 25% higher than in 2012 (**Table 1-8**, **Figure 1-21**). In 2016, sulfur fluoride contributed 0.45 mW m^{-2} to radiative forcing of climate (**Figure 1-3**). Inferred emissions increased by 35% between 2012 and 2016, from 2.7 ± 0.3 Gg yr^{-1} to 3.6 ± 0.4 Gg yr^{-1}, which is equivalent to 14 ± 2 Mt CO_2 yr^{-1} (**Figure 1-21**).

(Trifluoromethyl) Sulfur Pentafluoride (SF_5CF_3)

This compound has a long lifetime (650–950 years), a very high radiative efficiency (0.59 W m^{-2} ppb^{-1}), and may have been emitted to the atmosphere during the production of perfluorooctanyl sulfonate (Sturges et al., 2012). Data from the Southern Hemisphere show that SF_5CF_3 has remained at 0.153 ppt for the last four years (**Table 1-8)**, contributing around 0.09 mW m^{-2} to radiative forcing. This observed abundance is similar to that given by Sturges et al. (2012), who showed that growth, and therefore emissions, ceased around the late 1990s.

Halogenated Ethers (HFEs)

Information on atmospheric halogenated ethers (HFEs) is sparse. The first atmospheric observations of three inhalation anesthetics—desflurane (HFE-236ea2, $CHF_2OCHFCF_3$), isoflurane (HCFE-235da2, $CHF_2OCHClCF_3$), and sevoflurane (HFE-347 isomer, $(CF_3)_2CHOCH_2F$)—were published by Vollmer et al. (2015c). Using flask samples from the Northern Hemisphere and Antarctica, combined with in situ measurements from Jungfraujoch, 15-year records showed an increase in global mean abundances to levels in 2014 of 0.097 ppt, 0.30 ppt, and 0.13 ppt for isoflurane, desflurane, and sevoflurane. Using radiative efficiencies in **Table A-1**, these mole fractions equate to radiative forcings of 0.04, 0.14, and 0.04 mW m^{-2}, respectively. Using a box model and updated lifetimes from Sulbaek Andersen et al. (2010) and Sulbaek Andersen et al. (2012), global emissions for 2014 were estimated at 0.88 Gg yr^{-1}, 0.96 Gg yr^{-1}, and 1.2 Gg yr^{-1} for the three anesthetics, respectively, equivalent to approximately 3 Mt CO_2 yr^{-1} in total.

REFERENCES

Adcock, K.E., C.E. Reeves, L.J. Gooch, E.C. Leedham Elvidge, M.J. Ashfold, C.A.M. Brenninkmeijer, C. Chou, P.J. Fraser, R.L. Langenfelds, N. Mohd Hanif, S. O'Doherty, D.E. Oram, C.F. Ou-Yang, S.M. Phang, A.A. Samah, T. Röckmann, W.T. Sturges, and J.C. Laube, Continued increase of CFC-113a (CCl_3CF_3) mixing ratios in the global atmosphere: emissions, occurrence and potential sources, *Atmos. Chem. Phys.*, *18*(7), 4737–4751, doi:10.5194/acp-18-4737-2018, 2018.

Akagi, S.K., R.J. Yokelson, C. Wiedinmyer, M.J. Alvarado, J.S. Reid, T. Karl, J.D. Crounse, and P.O. Wennberg, Emission factors for open and domestic biomass burning for use in atmospheric models, *Atmos. Chem. Phys.*, *11*(9), 4039–4072, doi:10.5194/acp-11-4039-2011, 2011.

Albers, C.N., O.S. Jacobsen, E.M.M. Flores, and A.R. Johnsen, Arctic and subarctic natural soils emit chloroform and brominated analogues by alkaline hydrolysis of trihaloacetyl compounds, *Environ. Sci. Technol.*, *51*(11), 6131–6138, doi:10.1021/acs.est7b00144, 2017.

Allan, J.D., P.I. Williams, J. Najera, J.D. Whitehead, M.J. Flynn, J.W. Taylor, D. Liu, E. Darbyshire, L.J. Carpenter, R. Chance, S.J. Andrews, S.C. Hackenberg, and G. McFiggans, Iodine observed in new particle formation events in the Arctic atmosphere during ACCACIA, *Atmos. Chem. Phys.*, *15*(10), 5599–5609, doi:10.5194/acp-15-5599-2015, 2015.

Allard, S., and H. Gallard, Abiotic formation of methyl iodide on synthetic birnessite: A mechanistic study, *Sci. Total Environ.*, 463, 169–175, doi:10.1016/j.scitotenv.2013.05.079, 2013.

Anderson, D.C., J.M. Nicely, R.J. Salawitch, T.P. Canty, R.R. Dickerson, T.F. Hanisco, G.M. Wolfe, E.C. Apel, E. Atlas, T. Bannan, S. Bauguitte, N.J. Blake, J.F. Bresch, T.L. Campos, L.J. Carpenter, M.D. Cohen, M. Evans, R.P. Fernandez, B.H. Kahn, D.E. Kinnison, S.R. Hall, N.R.P. Harris, R.S. Hornbrook, J.-F. Lamarque, M. Le Breton, J.D. Lee, C. Percival, L. Pfister, R.B. Pierce, D.D. Riemer, A. Saiz-Lopez, B.J.B. Stunder, A.M. Thompson, K. Ullmann, A. Vaughan, and A.J. Weinheimer, A pervasive role for biomass burning in tropical high ozone/low water structures, *Nat. Commun.*, 10267, doi:10.1038/ncomms10267, 2016.

Andrews, S.J., L.J. Carpenter, E.C. Apel, E. Atlas, V. Donets, J.R. Hopkins, R.S. Hornbrook, A.C. Lewis, R.T. Lidster, R. Lueb, J. Minaeian, M. Navarro, S. Punjabi, D. Riemer, and S. Schauffler, A comparison of very short lived halocarbon (VSLS) and DMS aircraft measurements in the tropical west Pacific from CAST, ATTREX and CONTRAST, *Atmos. Meas. Tech.*, *9*(10), 5213–5225, doi:10.5194/amt-9-5213-2016, 2016.

Arnold, T., C.M. Harth, J. Mühle, A.J. Manning, P.K. Salameh, J. Kim, D.J. Ivy, L.P. Steele, V.V. Petrenko, J.P. Severinghaus, D. Baggenstos, and R.F. Weiss, Nitrogen trifluoride global emissions estimated from updated atmospheric measurements, *Proc. Natl. Acad. Sci.*, *110*(6), 2029–2034, doi:10.1073/pnas.1212346110, 2013.

Aschmann, J., and B.M. Sinnhuber, Contribution of very short-lived substances to stratospheric bromine loading: uncertainties and constraints, *Atmos. Chem. Phys.*, *13*(3), 1203–1219, doi:10.5194/acp-13-1203-2013, 2013.

Ashfold, M.J., N.R.P. Harris, E.L. Atlas, A.J. Manning, and J.A. Pyle, Transport of short-lived species into the Tropical Tropopause Layer, *Atmos. Chem. Phys.*, *12*(14), 6309–6322, doi:10.5194/acp-12-6309-2012, 2012.

Ashfold, M.J., J.A. Pyle, A.D. Robinson, E. Meneguz, M.S.M. Nadzir, S.M. Phang, A.A. Samah, S. Ong, H.E. Ung, L.K. Peng, S.E. Yong, and N.R.P. Harris, Rapid transport of East Asian pollution to the deep tropics, *Atmos. Chem. Phys.*, *15*(6), 3565–3573, doi:10.5194/acp-15-3565-2015, 2015.

Ashford, P., A. Ambrose, M. Jeffs, B. Johnson, S. Kocchi, S. Lee, D. Nott, P. Vodianitskaia, and J. Wu, Foams, Chapter 7 in *IPCC/TEAP Special Report on Safeguarding the Ozone Layer and the Global Climate System: Issues Related to Hydrofluorocarbons and Perfluorocarbons*, Cambridge University Press, Cambridge, United Kingdom, 2005.

Aydin, M., T.J. Fudge, K.R. Verhulst, M.R. Nicewonger, E.D. Waddington, and E.S. Saltzman, Carbonyl sulfide hydrolysis in Antarctic ice cores and an atmospheric history for the last 8000 years, *J. Geophys. Res. Atmos.*, *119*(13), 8500–8514, doi:10.1002/2014JD021618, 2014.

Barkley, M.P., P.I. Palmer, C.D. Boone, P.F. Bernath, and P. Suntharalingam, Global distributions of carbonyl sulfide in the upper troposphere and stratosphere, *Geophys. Res. Lett.*, *35*(14),

doi:10.1029/2008GL034270, 2008.

Bell, N., L. Hsu, D.J. Jacob, M.G. Schultz, D.R. Blake, J.H. Butler, D.B. King, J.M. Lobert, and E. Maier-Reimer, Methyl iodide: Atmospheric budget and use as a tracer of marine convection in global models, *J. Geophys. Res. Atmos.*, *107*(D17), doi:10.1029/2001JD001151, 2002.

Bernath, P., and A.M. Fernando, Trends in stratospheric HCl from the ACE satellite mission, *J. Quant. Spectrosc.* Radiat. Trans., 217, 126–129, doi:10.1016/j.jqsrt.2018.05.027, 2018.

Berry, J., A. Wolf, J.E. Campbell, I. Baker, N. Blake, D. Blake, A.S. Denning, S.R. Kawa, S.A. Montzka, U. Seibt, K. Stimler, D. Yakir, and Z. Zhu, A coupled model of the global cycles of carbonyl sulfide and CO_2: A possible new window on the carbon cycle, *J. Geophys. Res. Biogeosci.*, *118*(2), 842–852, doi:10.1002/jgrg.20068, 2013.

Bie, P.J., X.K. Fang, Z.F. Li, Z.Y. Wang, and J.X. Hu, Emissions estimates of carbon tetrachloride for 1992-2014 in *China, Environ. Pollut.*, *224*, 670–678, doi:10.1016/j.envpol.2017.02.051, 2017.

Bösch, H., C. Camy-Peyret, M.P. Chipperfield, R. Fitzenberger, H. Harder, U. Platt, and K. Pfeilsticker, Upper limits of stratospheric IO and OIO inferred from center-to-limb-darkening-corrected balloon-borne solar occultation visible spectra: Implications for total gaseous iodine and stratospheric ozone, *J. Geophys. Res.*, *108*(D15), doi:10.1029/2002JD003078, 2003.

Boudjellaba, D., J. Dron, G. Revenko, C. Demelas, and J.L. Boudenne, Chlorination by-product concentration levels in seawater and fish of an industrialised bay (Gulf of Fos, France) exposed to multiple chlorinated effluents, *Sci. Total Environ., 541*, 391–399, doi:10.1016/j.scitotenv.2015.09.046, 2016.

Brinckmann, S., A. Engel, H. Bonisch, B. Quack, and E. Atlas, Short-lived brominated hydrocarbons - observations in the source regions and the tropical tropopause layer, *Atmos. Chem. Phys.*, *12*(3), 1213-1228, doi:10.5194/acp-12-1213-2012, 2012.

Brown, A.T., M.P. Chipperfield, C. Boone, C. Wilson, K.A. Walker, and P.F. Bernath, Trends in atmospheric halogen containing gases since 2004, *J. Quant. Spectrosc. Radiat. Trans.*, *112*(16), 2552–2566, doi:10.1016/j.jqsrt.2011.07.005, 2011.

Brühl, C., J. Lelieveld, P.J. Crutzen, and H. Tost, The role of carbonyl sulphide as a source of stratospheric sulphate aerosol and its impact on climate, *Atmos. Chem. Phys.*, *12*(3), 1239–1253, doi:10.5194/acp-12-1239-2012, 2012.

Burkholder, J.B., S.P. Sander, J. Abbat, J.R. Barker, R.E. Huie, C.E. Kolb, M.J. Kurylo, V.L. Orkin, D. Wilmouth, and P.H. Wine, Chemical Kinetics and Photochemical Data for Use in Atmospheric Studies – Evaluation Number 18, edited by J.B. Burkholder, 1392 pp, JPL Publication, Pasadena, California, 2015.

Butler, J.H., S.A. Montzka, A.D. Clarke, J.M. Lobert, and J.W. Elkins, Growth and distribution of halons in the atmosphere, *J. Geophys. Res. Atmos.*, *103*(D1), 1503–1511, doi:10.1029/97JD02853, 1998.

Butler, J.H., D.B. King, J.M. Lobert, S.A. Montzka, S.A. Yvon-Lewis, B.D. Hall, N.J. Warwick, D.J. Mondeel, M. Aydin, and J.W. Elkins, Oceanic distributions and emissions of short-lived halocarbons, *Global Biogeochem. Cycles*, *21*(1), doi:10.1029/2006gb002732, 2007.

Butler, J.H., S.A. Yvon-Lewis, J.M. Lobert, D.B. King, S.A. Montzka, J.L. Bullister, V. Koropalov, J.W. Elkins, B.D. Hall, L. Hu, and Y.N. Liu, A comprehensive estimate for loss of atmospheric carbon tetrachloride (CCl_4) to the ocean, *Atmos. Chem. Phys.*, *16*(17), 10899-10910, doi:10.5194/acp-16-10899–2016, 2016.

Butz, A., H. Bösch, C. Camy-Peyret, M.P. Chipperfield, M. Dorf, S. Kreycy, L. Kritten, C. Prados-Román, J. Schwärzle, and K. Pfeilsticker, Constraints on inorganic gaseous iodine in the tropical upper troposphere and stratosphere inferred from balloon-borne solar occultation observations, *Atmos. Chem. Phys.*, *9*(18), 7229–7242, doi:10.5194/acp-9-7229-2009, 2009.

Campbell, J.E., M.E. Whelan, U. Seibt, S.J. Smith, J.A. Berry, and T.W. Hilton, Atmospheric carbonyl sulfide sources from anthropogenic activity: Implications for carbon cycle constraints, *Geophys. Res. Lett.*, *42*(8), 3004–3010, doi:10.1002/2015GL063445, 2015.

Campbell, J.E., J.A. Berry, U. Seibt, S.J. Smith, S.A. Montzka, T. Launois, S. Belviso, L. Bopp, and M. Laine, Large historical growth in global terrestrial gross primary production, *Nature*, *544*, 84, doi:10.1038/nature22030, 2017.

Carpenter, L.J., and P.S. Liss, On temperate sources of bromoform and other reactive organic bromine gases, *J. Geophys. Res. Atmos.*, *105*(D16), 20539–20547, doi:10.1029/2000JD900242, 2000.

Carpenter, L.J., D.J. Wevill, S. O'Doherty, G. Spain, and P.G. Simmonds, Atmospheric bromoform at Mace Head, Ireland: seasonality and evidence for a peatland source, *Atmos. Chem. Phys.*, *5*, 2927–2934, 2005.

Carpenter, L.J., D.J. Wevill, J.R. Hopkins, R.M. Dunk, C.E. Jones, K.E. Hornsby, and J.B. McQuaid, Bromoform in tropical Atlantic air from 25 degrees N to 25 degrees S, *Geophys. Res. Lett.*, *34*(11), doi:10.1029/2007GL029893, 2007.

Carpenter, L.J., S.M. MacDonald, M.D. Shaw, R. Kumar, R.W. Saunders, R. Parthipan, J. Wilson, and J.M.C. Plane, Atmospheric iodine levels influenced by sea surface emissions of inorganic iodine, *Nat. Geosci.*, *6*(2), 108–111, doi:10.1038/ngeo1687, 2013.

Carpenter, L.J., and S. Reimann (Lead Authors), J.B. Burkholder, C. Clerbaux, B.D. Hall, R. Hossaini, J.C. Laube, and S.A. Yvon-Lewis, Update on Ozone-Depleting Substances (ODSs) and Other Gases of Interest to the Montreal Protocol, Chapter 1 in *Scientific Assessment of Ozone Depletion: 2014*, Global Ozone Research and Monitoring Project–Report No. 55, World Meteorological Organization, Geneva, Switzerland, 2014.

Chen, D., L.G. Huey, D.J. Tanner, R.J. Salawitch, D.C. Anderson, P.A. Wales, L.L. Pan, E.L. Atlas, R.S. Hornbrook, E.C. Apel, N.J. Blake, T.L. Campos, V. Donets, F.M. Flocke, S.R. Hall, T.F. Hanisco, A.J. Hills, S.B. Honomichl, J.B. Jensen, L. Kaser, D.D. Montzka, J.M. Nicely, J.M. Reeves, D.D. Riemer, S.M. Schauffler, K. Ullmann, A.J. Weinheimer, and G.M. Wolfe, Airborne measurements of BrO and the sum of HOBr and Br_2 over the Tropical West Pacific from 1 to 15km during the CONvective TRansport of Active Species in the Tropics (CONTRAST) experiment, *J. Geophys. Res.*, *121*(12560–12578), doi:10.1002/2016JD025561.

Chen, Q., J.A. Schmidt, V. Shah, L. Jaeglé, T. Sherwen, and B. Alexander, Sulfate production by reactive bromine: Implications for the global sulfur and reactive bromine budgets, *Geophys. Res. Lett.*, *44*, 7069–7078, doi:10.1002/2017GL073812, 2017.

Chipperfield, M.P., Q. Liang, M. Rigby, R. Hossaini, S.A. Montzka, S. Dhomse, W.H. Feng, R.G. Prinn, R.F. Weiss, C.M. Harth, P.K. Salameh, J. Mühle, S. O'Doherty, D. Young, P.G. Simmonds, P.B. Krummel, P.J. Fraser, L.P. Steele, J.D. Happell, R.C. Rhew, J. Butler, S.A. Yvon-Lewis, B. Hall, D. Nance, F. Moore, B.R. Miller, J. Elkins, J.J. Harrison, C.D. Boone, E.L. Atlas, and E. Mahieu, Model sensitivity studies of the decrease in atmospheric carbon tetrachloride, *Atmos. Chem. Phys.*, *16*(24), 15741–15754, doi:10.5194/acp-16-15741-2016, 2016.

Chirkov, M., G.P. Stiller, A. Laeng, S. Kellmann, T. von Clarmann, C.D. Boone, J.W. Elkins, A. Engel, N. Glatthor, U. Grabowski, C.M. Harth, M. Kiefer, F. Kolonjari, P.B. Krummel, A. Linden, C.R. Lunder, B.R. Miller, S.A. Montzka, J. Mühle, S. O'Doherty, J. Orphal, R.G. Prinn, G. Toon, M.K. Vollmer, K.A. Walker, R.F. Weiss, A. Wiegele, and D. Young, Global HCFC-22 measurements with MIPAS: retrieval, validation, global distribution and its evolution over 2005–2012, *Atmos. Chem. Phys.*, *16*(5), 3345–3368, doi:10.5194/acp-16-3345-2016, 2016.

Ciais, P., C. Sabine (Coordinating Lead Authors), G. Bala, L. Bopp, V. Brovkin, J. Canadell, A. Chhabra, R. DeFries, J. Galloway, M. Heimann, C. Jones, C.L. Quéré, R.B. Myneni, S. Piao, and P. Thornton, Carbon and Other Biogeochemical Cycles, Chapter 6 in *Climate Change 2013: The Physical Science Basis. Contribution of Working Group I to the Fifth Assessment Report of the Intergovernmental Panel on Climate Change*, edited by T.F. Stocker, D. Qin, G.K. Plattner, M. Tignor, S.K. Allen, J. Boschung, A. Nauels, Y. Xia, V. Bex, and P.M. Midgley, 465–570, Cambridge University Press, Cambridge, United Kingdom, 2013.

Connor, B.J., T. Mooney, G.E. Nedoluha, J.W. Barrett, A. Parrish, J. Koda, M.L. Santee, and R.M. Gomez, Re-analysis of ground-based microwave ClO measurements from Mauna Kea, 1992 to early 2012, *Atmos. Chem. Phys.*, *13*(17), 8643–8650, doi:10.5194/acp-13-8643-2013, 2013.

Culbertson, J.A., J.M. Prins, E.P. Grimsrud, R.A. Rasmussen, M.A.K. Khalil, and M.J. Shearer, Observed trends for CF_3-containing compounds in background air at Cape Meares, Oregon, Point Barrow, Alaska, and Palmer Station, Antarctica, *Chemosphere*, *55*(8), 1109–1119, doi:10.1016/j.chemosphere.2003.11.002, 2004.

Cunnold, D.M., R.G. Prinn, R.A. Rasmussen, P.G. Simmonds, F.N. Alyea, C.A. Cardelino, A.J. Crawford, P.J. Fraser, and R.D. Rosen, The atmospheric lifetime experiment: 3. lifetime methodology and application to 3 years of $CFCl_3$ data, *J. Geo-*

phys. Res. Oceans, *88*, 8379–8400, doi:10.1029/JC088iC13p08379, 1983.

Cunnold, D.M., P.J. Fraser, R.F. Weiss, R.G. Prinn, P.G. Simmonds, B.R. Miller, F.N. Alyea, and A.J. Crawford, Global trends and annual releases of CCl_3F and CCl_2F_2 estimated from ALE/GAGE and other measurements from July 1978 to June 1991, *J. Geophys. Res. Atmos.*, *99*(D1), 1107–1126, doi:10.1029/93JD02715, 1994.

Cunnold, D.M., L.P. Steele, P.J. Fraser, P.G. Simmonds, R.G. Prinn, R.F. Weiss, L.W. Porter, S. O'Doherty, R.L. Langenfelds, P.B. Krummel, H.J. Wang, L. Emmons, X.X. Tie, and E.J. Dlugokencky, In situ measurements of atmospheric methane at GAGE/AGAGE sites during 1985-2000 and resulting source inferences, *J. Geophys. Res. Atmos.*, *107*(D14), doi:10.1029/2001JD001226, 2002.

Dalsoren, S.B., C.L. Myhre, G. Myhre, A.J. Gomez-Pelaez, O.A. Sovde, I.S.A. Isaksen, R.F. Weiss, and C.M. Harth, Atmospheric methane evolution the last 40 years, *Atmos. Chem. Phys.*, *16*(5), 3099–3126, doi:10.5194/acp-16-3099-2016, 2016.

Daniel, J.S., S. Solomon, and D.L. Albritton, On the evaluation of halocarbon radiative forcing and global warming potentials, *J. Geophys. Res. Atmos.*, *100*(D1), 1271–1285, doi:10.1029/94JD02516, 1995.

Daniel, J.S., G.J.M. Velders (Lead Authors), O. Morgenstern, D.W. Toohey, T.J. Wallington, and D.J. Wuebbles, A Focus on Information and Options for Policymakers, Chapter 5 in *Scientific Assessment of Ozone Depletion: 2010*, Global Ozone Research and Monitoring Project–Report No. 52, World Meteorological Organization, Geneva, Switzerland, 2011.

Dix, B., S. Baidar, J.F. Bresch, S.R. Hall, K.S. Schmidt, S. Wang, and R. Volkamer, Detection of iodine monoxide in the tropical free troposphere, *Proc. Natl. Acad. Sci.*, *110*(6), 2035–2040, doi:10.1073/pnas.1212386110, 2013.

Dlugokencky, E.J., E.G. Nisbet, R. Fisher, and D. Lowry, Global atmospheric methane: Budget, changes and dangers, *Philos. Trans. Roy. Soc. A*, *369*(1943), 2058–2072, doi:10.1098/rsta.2010.0341, 2011.

Dorf, M., J.H. Butler, A. Butz, C. Camy-Peyret, M.P. Chipperfield, L. Kritten, S.A. Montzka, B. Simmes, F. Weidner, and K. Pfeilsticker, Long-term observations of stratospheric bromine reveal slow down in growth, *Geophys. Res. Lett.*, *33*(24), L24803, doi:10.1029/2006GL027714, 2006.

Dorf, M., A. Butz, C. Camy-Peyret, M.P. Chipperfield, L. Kritten, and K. Pfeilsticker, Bromine in the tropical troposphere and stratosphere as derived from balloon-borne BrO observations, *Atmos. Chem. Phys.*, *8*(23), 7265–7271, doi:10.5194/acp-8-7265-2008, 2008.

Duchatelet, P., E. Mahieu, R. Ruhnke, W. Feng, M. Chipperfield, P. Demoulin, P. Bernath, C.D. Boone, K.A. Walker, C. Servais, and O. Flock, An approach to retrieve information on the carbonyl fluoride (COF_2) vertical distributions above Jungfraujoch by FTIR multi-spectrum multi-window fitting, *Atmos. Chem. Phys.*, *9*(22), 9027–9042, doi:10.5194/acp-9-9027-2009, 2009.

Duchatelet, P., P. Demoulin, F. Hase, R. Ruhnke, W. Feng, M.P. Chipperfield, P.F. Bernath, C.D. Boone, K.A. Walker, and E. Mahieu, Hydrogen fluoride total and partial column time series above the Jungfraujoch from long-term FTIR measurements: Impact of the line-shape model, characterization of the error budget and seasonal cycle, and comparison with satellite and model data, *J. Geophys. Res. Atmos.*, *115*, doi:10.1029/2010JD014677, 2010.

Eckert, E., T. von Clarmann, A. Laeng, G.P. Stiller, B. Funke, N. Glatthor, U. Grabowski, S. Kellmann, M. Kiefer, A. Linden, A. Babenhauserheide, G. Wetzel, C. Boone, A. Engel, J.J. Harrison, P.E. Sheese, K.A. Walker, and P.F. Bernath, MIPAS IMK/IAA carbon tetrachloride (CCl_4) retrieval and first comparison with other instruments, *Atmos. Meas. Tech.*, *10*(7), 2727–2743, doi:10.5194/amt-10-2727-2017, 2017.

Engel, A., H. Bönisch, J. Ostermöller, M.P. Chipperfield, S. Dhomse, and P. Jöckel, A refined method for calculating equivalent effective stratospheric chlorine, *Atmos. Chem. Phys.*, *2018*, 601–609, doi:10.5194/acp-18-601-2018, 2018.

Fang, X., R.L. Thompson, T. Saito, Y. Yokouchi, J. Kim, S. Li, K.R. Kim, S. Park, F. Graziosi, and A. Stohl, Sulfur hexafluoride (SF_6) emissions in East Asia determined by inverse modeling, *Atmos. Chem. Phys.*, *14*(9), 4779–4791, doi:10.5194/acp-14-4779-2014, 2014.

Fang, X.K., J. Wu, S.S. Su, J.R. Han, Y.S. Wu, Y.H. Shi, D. Wan, X.Z. Sun, J.B. Zhang, and J.X. Hu, Estimates of major anthropogenic halocarbon emissions from China based on interspecies correla-

tions, *Atmos. Environ., 62*, 26–33, doi:10.1016/j.atmosenv.2012.08.010, 2012.

Feng, W., M.P. Chipperfield, S. Dhomse, B.M. Monge-Sanz, X. Yang, K. Zhang, and M. Ramonet, Evaluation of cloud convection and tracer transport in a three-dimensional chemical transport model, *Atmos. Chem. Phys.*, *11*(12), 5783–5803, doi:10.5194/acp-11-5783-2011, 2011.

Fernandez, R.P., R.J. Salawitch, D.E. Kinnison, J.F. Lamarque, and A. Saiz-Lopez, Bromine partitioning in the tropical tropopause layer: Implications for stratospheric injection, *Atmos. Chem. Phys.*, *14*(24), 13391–13410, doi:10.5194/acp-14-13391-2014, 2014.

Fiehn, A., B. Quack, H. Hepach, S. Fuhlbrügge, S. Tegtmeier, M. Toohey, E. Atlas, and K. Krüger, Delivery of halogenated very short-lived substances from the west Indian Ocean to the stratosphere during the Asian summer monsoon, *Atmos. Chem. Phys.*, *17*(11), 6723–6741, doi:10.5194/acp-17-6723-2017, 2017.

Forczek, S.T., F. Laturnus, J. Dolezalova, J. Holik, and Z. Wimmer, Emission of climate relevant volatile organochlorines by plants occurring in temperate forests, *Plant Soil Environ.*, *61*(3), 103–108, doi:10.17221/900/2014-pse, 2015.

Francey, R.J., L.P. Steele, D.A. Spencer, R.L. Langenfelds, R.M. Law, P.B. Krummel, P.J. Fraser, D.M. Etheridge, N. Derek, S.A. Coram, L.N. Cooper, C.E. Allison, L. Porter, and S. Baly, The CSIRO (Australia) measurement of greenhouse gases in the global atmosphere, in *Baseline Atmospheric Program Australia 1999-2000*, edited by N.W. Tindale, N. Derek, and P.J. Fraser, 42–53, Bureau of Meteorology and CSIRO Atmospheric Research, Melbourne, Australia, 2003.

Fraser, P., B. Dunse, A.J. Manning, R. Wang, P. Krummel, P. Steele, L. Porter, C. Allison, S. O'Doherty, P.G. Simmonds, J. Mühle, and R. Prinn, Australian carbon tetrachloride (CCl_4) emissions in a global context, *Environ. Chem.*, *11*, doi:10.1071/EN13171, 2014.

Froidevaux, L., J. Anderson, H.J. Wang, R.A. Fuller, M.J. Schwartz, M.L. Santee, N.J. Livesey, H.C. Pumphrey, P.F. Bernath, J.M. Russell, and M.P. McCormick, Global OZone Chemistry And Related trace gas Data records for the Stratosphere (GOZCARDS): Methodology and sample results with a focus on HCl, H_2O, and O_3, *Atmos. Chem. Phys.*, *15*(18), 10471–10507, doi:10.5194/acp-15-10471-2015, 2015.

Fueglistaler, S., A.E. Dessler, T.J. Dunkerton, I. Folkins, Q. Fu, and P.W. Mote, Tropical tropopause layer, *Rev. Geophys.*, *47*(1), doi:10.1029/2008rg000267, 2009.

Fuhlbrugge, S., B. Quack, E. Atlas, A. Fiehn, H. Hepach, and K. Kruger, Meteorological constraints on oceanic halocarbons above the Peruvian upwelling, *Atmos. Chem. Phys.*, *16*(18), 12205–12217, doi:10.5194/acp-16-12205-2016, 2016a.

Fuhlbrugge, S., B. Quack, S. Tegtmeier, E. Atlas, H. Hepach, Q. Shi, S. Raimund, and K. Kruger, The contribution of oceanic halocarbons to marine and free tropospheric air over the tropical West Pacific, *Atmos. Chem. Phys.*, *16*(12), 7569–7585, doi:10.5194/acp-16-7569-2016, 2016b.

Gardiner, T., A. Forbes, M. de Mazière, C. Vigouroux, E. Mahieu, P. Demoulin, V. Velazco, J. Notholt, T. Blumenstock, F. Hase, I. Kramer, R. Sussmann, W. Stremme, J. Mellqvist, A. Strandberg, K. Ellingsen, and M. Gauss, Trend analysis of greenhouse gases over Europe measured by a network of ground-based remote FTIR instruments, *Atmos. Chem. Phys.*, *8*(22), 6719–6727, doi:10.5194/acp-8-6719-2008, 2008.

Glatthor, N., M. Höpfner, A. Leyser, G.P. Stiller, T. von Clarmann, U. Grabowski, S. Kellmann, A. Linden, B.M. Sinnhuber, G. Krysztofiak, and K.A. Walker, Global carbonyl sulfide (OCS) measured by MIPAS/Envisat during 2002–2012, *Atmos. Chem. Phys.*, *17*(4), 2631–2652, doi:10.5194/acp-17-2631-2017, 2017.

Graziosi, F., J. Arduini, F. Furlani, U. Giostra, L.J.M. Kuijpers, S.A. Montzka, B.R. Miller, S.J. O'Doherty, A. Stohl, P. Bonasoni, and M. Maione, European emissions of HCFC-22 based on eleven years of high frequency atmospheric measurements and a Bayesian inversion method, *Atmos. Environ., 112*, 196–207, doi:10.1016/j.atmosenv.2015.04.042, 2015.

Graziosi, F., J. Arduini, P. Bonasoni, F. Furlani, U. Giostra, A.J. Manning, A. McCulloch, S. O'Doherty, P.G. Simmonds, S. Reimann, M.K. Vollmer, and M. Maione, Emissions of carbon tetrachloride from Europe, *Atmos. Chem. Phys.*, *16*(20), 12849–12859, doi:10.5194/acp-16-12849-2016, 2016.

Haenel, F.J., G.P. Stiller, T. von Clarmann, B. Funke, E. Eckert, N. Glatthor, U. Grabowski, S. Kellmann, M. Kiefer, A. Linden, and T. Reddmann,

Reassessment of MIPAS age of air trends and variability, *Atmos. Chem. Phys.*, *15*, 13161–13176, doi:10.5194/acp-15-13161-2015, 2015.

Hall, B.D., G.S. Dutton, D.J. Mondeel, J.D. Nance, M. Rigby, J.H. Butler, F.L. Moore, D.F. Hurst, and J.W. Elkins, Improving measurements of SF_6 for the study of atmospheric transport and emissions, *Atmos. Meas. Tech.*, *4*(11), 2441–2451, doi:10.5194/amt-4-2441-2011, 2011.

Hall, B.D., A. Engel, J. Mühle, J.W. Elkins, F. Artuso, E. Atlas, M. Aydin, D. Blake, E.G. Brunke, S. Chiavarini, P.J. Fraser, J. Happell, P.B. Krummel, I. Levin, M. Loewenstein, M. Maione, S.A. Montzka, S. O'Doherty, S. Reimann, G. Rhoderick, E.S. Saltzman, H.E. Scheel, L.P. Steele, M.K. Vollmer, R.F. Weiss, D. Worthy, and Y. Yokouchi, Results from the International Halocarbons in Air Comparison Experiment (IHALACE), *Atmos. Meas. Tech.*, *7*(2), 469-490, doi:10.5194/amt-7-469-2014, 2014.

Hamed, M.A., M.E. Moustafa, Y.A. Soliman, M.A. El-Sawy, and A.I. Khedr, Trihalomethanes formation in marine environment in front of Nuweibaa desalination plant as a result of effluents loaded by chlorine residual, *Egyptian J. Aquatic Res.*, *43*(1), 45–54, doi:10.1016/j.ejar.2017.01.001, 2017.

Han, J.R., L. Li, S.S. Su, J. Wu, X.K. Fang, S.L. Jia, J.B. Zhang, and J.X. Hu, Estimated HCFC-142b emissions in China: 2000-2050, *Chinese Sci. Bull.*, *59*(24), 3046–3053, doi:10.1007/s11434-014-0337-z, 2014.

Harris, N.R.P., and D. Wuebbles (Lead Authors), J.S. Daniel, J. Hu, LJ.M. Kuijpers, K.S. Law, M.J. Prather, and R. Schofield, Scenarios and information for policymakers, Chapter 5 in *Scientific Assessment of Ozone Depletion: 2014*, Global Ozone Research and Monitoring Project – Report No. 55, World Meteorological Organization, Geneva, Switzerland, 2014.

Harris, N.R.P., L.J. Carpenter, J.D. Lee, G. Vaughan, M.T. Filus, R.L. Jones, B. OuYang, J.A. Pyle, A.D. Robinson, S.J. Andrews, A.C. Lewis, J. Minaeian, A. Vaughan, J.R. Dorsey, M.W. Gallagher, M. Le Breton, R. Newton, C.J. Percival, H.M.A. Ricketts, S.J.B. Bauguitte, G.J. Nott, A. Wellpott, M.J. Ashfold, J. Flemming, R. Butler, P.I. Palmer, P.H. Kaye, C. Stopford, C. Chemel, H. Boesch, N. Humpage, A. Vick, A.R. MacKenzie, R. Hyde, P. Angelov, E. Meneguz, and A.J. Manning, Coordinated Airborne Studies in the Tropics (CAST), *Bull. Am. Meterol. Soc.*, *98*(1), 145–162, doi:10.1175/bams-d-14-00290.1, 2017.

Harrison, J.J., M.P. Chipperfield, C.D. Boone, S.S. Dhomse, P.F. Bernath, L. Froidevaux, J. Anderson, and J. Russell, Satellite observations of stratospheric hydrogen fluoride and comparisons with SLIMCAT calculations, *Atmos. Chem. Phys.*, *16*(16), 10501–10519, doi:10.5194/acp-16-10501-2016, 2016.

Hausmann, P., R. Sussmann, and D. Smale, Contribution of oil and natural gas production to renewed increase in atmospheric methane (2007–2014): Top-down estimate from ethane and methane column observations, *Atmos. Chem. Phys.*, *16*(5), 3227–3244, doi:10.5194/acp-16-3227-2016, 2016.

Hendrick, F., M. Van Roozendael, M.P. Chipperfield, M. Dorf, F. Goutail, X. Yang, C. Fayt, C. Hermans, K. Pfeilsticker, J.P. Pommereau, J.A. Pyle, N. Theys, and M. De Mazière, Retrieval of stratospheric and tropospheric BrO profiles and columns using ground-based zenith-sky DOAS observations at Harestua, 60° N, *Atmos. Chem. Phys.*, *7*(18), 4869–4885, doi:10.5194/acp-7-4869-2007, 2007.

Hendrick, F., P.V. Johnston, M. De Mazière, C. Fayt, C. Hermans, K. Kreher, N. Theys, A. Thomas, and M. Van Roozendael, One-decade trend analysis of stratospheric BrO over Harestua (60°N) and Lauder (45°S) reveals a decline, *Geophys. Res. Lett.*, *35*(14), L14801, doi:10.1029/2008GL034154, 2008.

Hepach, H., B. Quack, F. Ziska, S. Fuhlbrugge, E.L. Atlas, K. Kruger, I. Peeken, and D.W.R. Wallace, Drivers of diel and regional variations of halocarbon emissions from the tropical North East Atlantic, *Atmos. Chem. Phys.*, *14*(3), 1255–1275, doi:10.5194/acp-14-1255-2014, 2014.

Hepach, H., B. Quack, S. Raimund, T. Fischer, E.L. Atlas, and A. Bracher, Halocarbon emissions and sources in the equatorial Atlantic Cold Tongue, *Biogeosci.*, *12*(21), 6369-6387, doi:10.5194/bg-12-6369–2015, 2015.

Höpfner, M., J. Orphal, T. von Clarmann, G. Stiller, and H. Fischer, Stratospheric $BrONO_2$ observed by MIPAS, *Atmos. Chem. Phys.*, *9*(5), 1735–1746, doi:10.5194/acp-9-1735-2009, 2009.

Höpfner, M., N. Glatthor, U. Grabowski, S. Kellmann, M. Kiefer, A. Linden, J. Orphal, G. Stiller, T. von Clarmann, B. Funke, and C.D. Boone, Sulfur dioxide SO_2 as observed by MIPAS/Envisat: Tem-

poral development and spatial distribution at 15–45 km altitude, *Atmos. Chem. Phys.*, *13*(20), 10405–10423, doi:10.5194/acp-13-10405-2013, 2013.

Höpfner, M., C.D. Boone, B. Funke, N. Glatthor, U. Grabowski, A. Günther, S. Kellmann, M. Kiefer, A. Linden, S. Lossow, H.C. Pumphrey, W.G. Read, A. Roiger, G. Stiller, H. Schlager, T. von Clarmann, and K. Wissmüller, Sulfur dioxide SO_2 from MIPAS in the upper troposphere and lower stratosphere 2002–2012, *Atmos. Chem. Phys.*, *15*(12), 7017–7037, doi:10.5194/acp-15-7017-2015, 2015.

Hosking, J.S., M.R. Russo, P. Braesicke, and J.A. Pyle, Modelling deep convection and its impacts on the tropical tropopause layer, *Atmos. Chem. Phys.*, *10*(22), 11175–11188, doi:10.5194/acp-10-11175-2010, 2010.

Hossaini, R., M.P. Chipperfield, W. Feng, T.J. Breider, E. Atlas, S.A. Montzka, B.R. Miller, F. Moore, and J. Elkins, The contribution of natural and anthropogenic very short-lived species to stratospheric bromine, *Atmos. Chem. Phys.*, *12*(1), 371–380, doi:10.5194/acp-12-371-2012, 2012.

Hossaini, R., M.P. Chipperfield, A. Saiz-Lopez, J.J. Harrison, R. von Glasow, R. Sommariva, E. Atlas, M. Navarro, S.A. Montzka, W. Feng, S. Dhomse, C. Harth, J. Mühle, C. Lunder, S. O'Doherty, D. Young, S. Reimann, M.K. Vollmer, P.B. Krummel, and P.F. Bernath, Growth in stratospheric chlorine from short-lived chemicals not controlled by the Montreal Protocol, *Geophys. Res. Lett.*, *42*(11), 4573–4580, doi:10.1002/2015gl063783, 2015.

Hossaini, R., M.P. Chipperfield, A. Saiz-Lopez, R. Fernandez, S. Monks, W. Feng, P. Brauer, and R. von Glasow, A global model of tropospheric chlorine chemistry: Organic versus inorganic sources and impact on methane oxidation, *J. Geophys. Res. Atmos.*, *121*(23), 14,271–214,297, doi:10.1002/2016JD025756, 2016a.

Hossaini, R., P.K. Patra, A.A. Leeson, G. Krysztofiak, N.L. Abraham, S.J. Andrews, A.T. Archibald, J. Aschmann, E.L. Atlas, D.A. Belikov, H. Bönisch, L.J. Carpenter, S. Dhomse, M. Dorf, A. Engel, W. Feng, S. Fuhlbrügge, P.T. Griffiths, N.R.P. Harris, R. Hommel, T. Keber, K. Krüger, S.T. Lennartz, S. Maksyutov, H. Mantle, G.P. Mills, B. Miller, S.A. Montzka, F. Moore, M.A. Navarro, D.E. Oram, K. Pfeilsticker, J.A. Pyle, B. Quack, A.D. Robinson, E. Saikawa, A. Saiz-Lopez, S. Sala, B.M. Sinnhuber, S. Taguchi, S. Tegtmeier, R.T. Lidster, C. Wilson, and F. Ziska, A multi-model intercomparison of halogenated very short-lived substances (TransCom-VSLS): Linking oceanic emissions and tropospheric transport for a reconciled estimate of the stratospheric source gas injection of bromine, *Atmos. Chem. Phys.*, *16*(14), 9163–9187, doi:10.5194/acp-16-9163-2016, 2016b.

Hossaini, R., M.P. Chipperfield, S.A. Montzka, A.A. Leeson, S.S. Dhomse, and J.A. Pyle, The increasing threat to stratospheric ozone from dichloromethane, *Nat. Commun.*, *8*, doi:10.1038/ncomms15962, 2017.

Hoyle, C.R., V. Marécal, M.R. Russo, G. Allen, J. Arteta, C. Chemel, M.P. Chipperfield, F. D'Amato, O. Dessens, W. Feng, J.F. Hamilton, N.R.P. Harris, J.S. Hosking, A.C. Lewis, O. Morgenstern, T. Peter, J.A. Pyle, T. Reddmann, N.A.D. Richards, P.J. Telford, W. Tian, S. Viciani, A. Volz-Thomas, O. Wild, X. Yang, and G. Zeng, Representation of tropical deep convection in atmospheric models – Part 2: Tracer transport, *Atmos. Chem. Phys.*, *11*(15), 8103–8131, doi:10.5194/acp-11-8103-2011, 2011.

Hu, L., S.A. Montzka, B.R. Miller, A.E. Andrews, J.B. Miller, S.J. Lehman, C. Sweeney, S.M. Miller, K. Thoning, C. Siso, E.L. Atlas, D.R. Blake, J. de Gouw, J.B. Gilman, G. Dutton, J.W. Elkins, B. Hall, H.L. Chen, M.L. Fischer, M.E. Mountain, T. Nehrkorn, S.C. Biraud, F.L. Moore, and P. Tans, Continued emissions of carbon tetrachloride from the United States nearly two decades after its phaseout for dispersive uses, *Proc. Natl. Acad. Sci.*, *113*(11), 2880–2885, doi:10.1073/pnas.1522284113, 2016a.

Hu, L., S.A. Montzka, S.J. Lehman, D.S. Godwin, B.R. Miller, A.E. Andrews, K. Thoning, J.B. Miller, C. Sweeney, C. Siso, J.W. Elkins, B.D. Hall, D.J. Mondeel, D. Nance, T. Nehrkorn, M.E. Mountain, M.L. Fischer, S.C. Biraud, H.L. Chen, and P.P. Tans, Considerable contribution of the Montreal Protocol to declining greenhouse gas emissions from the United States: U.S. CFCs, HCFCs, and HFCs Emissions, *Geophys. Res. Lett.*, *44* (15), doi:10.1002/2017GL074388, 2017.

Hu, Q., Z. Xie, X. Wang, J. Yu, and Y. Zhang, Methyl iodine over oceans from the Arctic Ocean to the maritime Antarctic, *Sci. Rep.*, *6*, 26007, doi:10.1038/srep26007, 2016b.

Hughes, C., A.L. Chuck, H. Rossetti, P.J. Mann, S.M.

Turner, A. Clarke, R. Chance, and P.S. Liss, Seasonal cycle of seawater bromoform and dibromomethane concentrations in a coastal bay on the western Antarctic Peninsula, *Global Biogeochem. Cycles*, *23*, doi:10.1029/2008gb003268, 2009.

IPCC/TEAP, *Special Report on Safeguarding the Ozone Layer and the Global Climate System: Issues Related to Hydrofluorocarbons and Perfluorocarbons*, (Intergovernmental Panel on Climate Change, and the Technical and Economic Assessment Panel) Cambridge University Press, Cambridge, United Kingdom, 2005.

Jensen, E.J., L. Pfister, D.E. Jordan, D.W. Fahey, P. Newman, T.D. Thornberry, A.W. Rollins, G.S. Diskin, T.V. Bui, M.J. McGill, D.L. Hlavka, R.P. Lawson, R.S. Gao, P. Pilewskie, J. Elkins, E.J. Hintsa, F. Moore, M.J. Mahoney, E. Atlas, J. Stutz, K. Pfeilsticker, S.C. Wofsy, S. Evan, and K. Rosenlof, The NASA Airborne Tropical TRopopause EXperiment (ATTREX), in *SPARC Newsletter No. 41*, pp. 10, SPARC, 2013.

Jensen, E.J., L. Pfister, D.E. Jordan, T.V. Bui, R. Ueyama, H.B. Singh, T.D. Thornberry, A.W. Rollins, R.S. Gao, D.W. Fahey, K.H. Rosenlof, J.W. Elkins, G.S. Diskin, J.P. DiGangi, R.P. Lawson, S. Woods, E.L. Atlas, M.A.N. Rodriguez, S.C. Wofsy, J. Pittman, C.G. Bardeen, O.B. Toon, B.C. Kindel, P.A. Newman, M.J. McGill, D.L. Hlavka, L.R. Lait, M.R. Schoeberl, J.W. Bergman, H.B. Selkirk, M.J. Alexander, J.E. Kim, B.H. Lim, J. Stutz, and K. Pfeilsticker, The NASA Airborne Tropical Tropopause Experiment: High-Altitude Aircraft Measurements in the Tropical Western Pacific, *Bull. Am. Meterol. Soc.*, *98*(1), doi:10.1175/Bams-D-14-00263.1, 2017.

Jones, C.E., K.E. Hornsby, R. Sommariva, R.M. Dunk, R. Von Glasow, G. McFiggans, and L.J. Carpenter, Quantifying the contribution of marine organic gases to atmospheric iodine, *Geophys. Res. Lett.*, *37*, doi:10.1029/2010GL043990, 2010.

Jones, C.E., S.J. Andrews, L.J. Carpenter, C. Hogan, F.E. Hopkins, J.C. Laube, A.D. Robinson, T.G. Spain, S.D. Archer, N.R.P. Harris, P.D. Nightingale, S.J. O'Doherty, D.E. Oram, J.A. Pyle, J.H. Butler, and B.D. Hall, Results from the first national UK inter-laboratory calibration for very short-lived halocarbons, *Atmos. Meas. Tech.*, *4*(5), 865–874, doi:10.5194/amt-4-865-2011, 2011.

Khalil, M.A.K., R.M. Moore, D.B. Harper, J.M. Lobert, D.J. Erickson, V. Koropalov, W.T. Sturges, and W.C. Keene, Natural emissions of chlorine-containing gases: Reactive Chlorine Emissions Inventory, *J. Geophys. Res. Atmos.*, *104*(D7), 8333–8346, doi:10.1029/1998JD100079, 1999.

Khan, M.A.H., R.C. Rhew, M.E. Whelan, K. Zhou, and S.J. Deverel, Methyl halide and chloroform emissions from a subsiding Sacramento–San Joaquin Delta island converted to rice fields, *Atmos. Environ.*, *45*(4), 977–985, doi:10.1016/j.atmosenv.2010.10.053, 2011.

Khan, M.A.H., R.C. Rhew, K. Zhou, and M.E. Whelan, Halogen biogeochemistry of invasive perennial pepperweed (Lepidium latifolium) in a peatland pasture, *J. Geophys. Res. Biogeosci.*, *118*(1), 239-247, doi:10.1002/jgrg.20020, 2013.

Kloss, C., M.J. Newland, D.E. Oram, P.J. Fraser, C.A.M. Brenninkmeijer, T. Rockmann, and J.C. Laube, Atmospheric abundances, trends and emissions of CFC-216ba, CFC-216ca and HCFC-225ca, *Atmos.*, *5*(2), 420–434, doi:10.3390/atmos5020420, 2014.

Ko, M.K.W., N.D. Sze, W.C. Wang, G. Shia, A. Goldman, F.J. Murcray, D.G. Murcray, and C.P. Rinsland, Atmospheric sulfur hexafluoride: Sources, sinks and greenhouse warming, *J. Geophys. Res. Atmos.*, *98*(D6), 10499–10507, doi:10.1029/93JD00228, 1993.

Koenig, T.K., R. Volkamer, S. Baidar, B. Dix, S. Wang, D.C. Anderson, R.J. Salawitch, P.A. Wales, C.A. Cuevas, R.P. Fernandez, A. Saiz-Lopez, M.J. Evans, T. Sherwen, D.J. Jacob, J. Schmidt, D. Kinnison, J.-F. Lamarque, E.C. Apel, J.C. Bresch, T. Campos, F.M. Flocke, S.R. Hall, S.B. Honomichl, R. Hornbrook, J.B. Jensen, R. Lueb, D.D. Montzka, L.L. Pan, J.M. Reeves, S.M. Schauffler, K. Ullmann, A.J. Weinheimer, E.L. Atlas, V. Donets, M.A. Navarro, D. Riemer, N.J. Blake, D. Chen, L.G. Huey, D.J. Tanner, T.F. Hanisco, and G.M. Wolfe, BrO and By profiles over the Western Pacific: Relevance of Inorganic Bromine Sources and a Bry Minimum in the Aged Tropical Tropopause Layer, *Atmos. Chem. Phys.*, *17* (24) 1–46, doi:10.5194/acp-2017-572, 2017.

Kohlhepp, R., R. Ruhnke, M.P. Chipperfield, M. De Maziere, J. Notholt, S. Barthlott, R.L. Batchelor, R.D. Blatherwick, T. Blumenstock, M.T. Coffey, P. Demoulin, H. Fast, W. Feng, A. Goldman, D.W.T. Griffith, K. Hamann, J.W. Hannigan, F. Hase, N.B.

Jones, A. Kagawa, I. Kaiser, Y. Kasai, O. Kirner, W. Kouker, R. Lindenmaier, E. Mahieu, R.L. Mittermeier, B. Monge-Sanz, I. Morino, I. Murata, H. Nakajima, M. Palm, C. Paton-Walsh, U. Raffalski, T. Reddmann, M. Rettinger, C.P. Rinsland, E. Rozanov, M. Schneider, C. Senten, C. Servais, B.M. Sinnhuber, D. Smale, K. Strong, R. Sussmann, J.R. Taylor, G. Vanhaelewyn, T. Warneke, C. Whaley, M. Wiehle, and S.W. Wood, Observed and simulated time evolution of HCl, $ClONO_2$, and HF total column abundances, *Atmos. Chem. Phys.*, *12*(7), 3527–3556, doi:10.5194/acp-12-3527-2012, 2012.

Kovacs, T., W.H. Feng, A. Totterdill, J.M.C. Plane, S. Dhomse, J.C. Gomez-Martin, G.P. Stiller, F.J. Haenel, C. Smith, P.M. Forster, R.R. Garcia, D.R. Marsh, and M.P. Chipperfield, Determination of the atmospheric lifetime and global warming potential of sulfur hexafluoride using a three-dimensional model, *Atmos. Chem. Phys.*, *17*(2), 883–898, doi:10.5194/acp-17-883-2017, 2017.

Kremser, S., L.W. Thomason, M. von Hobe, M. Hermann, T. Deshler, C. Timmreck, M. Toohey, A. Stenke, J.P. Schwarz, R. Weigel, S. Fueglistaler, F.J. Prata, J.-P. Vernier, H. Schlager, J.E. Barnes, J.-C. Antuña-Marrero, D. Fairlie, M. Palm, E. Mahieu, J. Notholt, M. Rex, C. Bingen, F. Vanhellemont, A. Bourassa, J.M.C. Plane, D. Klocke, S.A. Carn, L. Clarisse, T. Trickl, R. Neely, A.D. James, L. Rieger, J.C. Wilson, and B. Meland, Stratospheric aerosol—Observations, processes, and impact on climate, *Rev. Geophys.*, *54*(2), 278-335, doi:10.1002/2015RG000511, 2016.

Kreycy, S., C. Camy-Peyret, M.P. Chipperfield, M. Dorf, W. Feng, R. Hossaini, L. Kritten, B. Werner, and K. Pfeilsticker, Atmospheric test of the $J(BrONO_2)/k(BrO+NO_2)$ ratio: Implications for total stratospheric Br_y and bromine-mediated ozone loss, *Atmos. Chem. Phys.*, *13*(13), 6263–6274, doi:10.5194/acp-13-6263-2013, 2013.

Kruger, K., S. Tegtmeier, and M. Rex, Long-term climatology of air mass transport through the Tropical Tropopause Layer (TTL) during NH winter, *Atmos. Chem. Phys.*, *8*(4), 813–823, 2008.

Krysztofiak, G., Y.V. Té, V. Catoire, G. Berthet, G.C. Toon, F. Jégou, P. Jeseck, and C. Robert, Carbonyl Sulphide (OCS) Variability with Latitude in the Atmosphere, *Atmos. Ocean*, *53*(1), 89–101, doi:10.1080/07055900.2013.876609, 2015.

Langenfelds, R.L., P.J. Fraser, R.J. Francey, L.P. Steele, L.W. Porter, and C.E. Allison, The Cape Grim Air Archive: The first seventeen years, 1978-1995, edited by R.J. Francey, A.L. Dick, N. Derek, p. 53-70, Baseline Atmospheric Program Australia. [Melbourne]: Bureau of Meteorology and CSIRO Division of Atmospheric Research, 1996.

Laube, J.C., C. Hogan, M.J. Newland, F.S. Mani, P.J. Fraser, C.A.M. Brenninkmeijer, P. Martinerie, D.E. Oram, T. Rockmann, J. Schwander, E. Witrant, G.P. Mills, C.E. Reeves, and W.T. Sturges, Distributions, long term trends and emissions of four perfluorocarbons in remote parts of the atmosphere and firn air, *Atmos. Chem. Phys.*, *12*(9), 4081–4090, doi:10.5194/acp-12-4081-2012, 2012.

Laube, J.C., A. Keil, H. Bönisch, A. Engel, T. Röckmann, C.M. Volk, and W.T. Sturges, Observation-based assessment of stratospheric fractional release, lifetimes, and ozone depletion potentials of ten important source gases, *Atmos. Chem. Phys.*, *13*(5), 2779–2791, doi:10.5194/acp-13-2779-2013, 2013.

Laube, J.C., M.J. Newland, C. Hogan, C.A.M. Brenninkmeijer, P.J. Fraser, P. Martinerie, D.E. Oram, C.E. Reeves, T. Rockmann, J. Schwander, E. Witrant, and W.T. Sturges, Newly detetecd ozone-depleting substances in the atmosphere, *Nat. Geosci.*, *7*(4), 266–269, doi:10.1038/ngeo2109, 2014.

Laube, J.C., N.M. Hanif, P. Martinerie, E. Gallacher, P.J. Fraser, R. Langenfelds, C.A.M. Brenninkmeijer, J. Schwander, E. Witrant, J.L. Wang, C.F. Ou-Yang, L.J. Gooch, C.E. Reeves, W.T. Sturges, and D.E. Oram, Tropospheric observations of CFC-114 and CFC-114a with a focus on long-term trends and emissions, *Atmos. Chem. Phys.*, *6*(23), 15347–15358, doi:10.5194/acp-16-15347-2016, 2016.

Launois, T., P. Peylin, S. Belviso, and B. Poulter, A new model of the global biogeochemical cycle of carbonyl sulfide – Part 2: Use of carbonyl sulfide to constrain gross primary productivity in current vegetation models, *Atmos. Chem. Phys.*, *15*(16), 9285-9312, doi:10.5194/acp-15-9285-2015, 2015.

Lawson, S.J., M.D. Keywood, I.E. Galbally, J.L. Gras, J.M. Cainey, M.E. Cope, P.B. Krummel, P.J. Fraser, L.P. Steele, S.T. Bentley, C.P. Meyer, Z. Ristovski, and A.H. Goldstein, Biomass burning emissions of trace gases and particles in marine air at Cape Grim, Tasmania, *Atmos. Chem. Phys.*, *15*(23), 13393–13411, doi:10.5194/acp-15-13393-2015, 2015.

Le Breton, M., T.J. Bannan, D.E. Shallcross, M.A. Khan, M.J. Evans, J. Lee, R. Lidster, S. Andrews, L.J. Carpenter, J. Schmidt, D. Jacob, N.R.P. Harris, S. Bauguitte, M. Gallagher, A. Bacak, K.E. Leather, and C.J. Percival, Enhanced ozone loss by active inorganic bromine chemistry in the tropical troposphere, *Atmos. Environ., 155*, 21–28, doi:10.1016/j.atmosenv.2017.02.003, 2017.

Leedam Elvidge, E.C., D.E. Oram, J.C. Laube, A.K. Baker, S.A. Montzka, S. Humphrey, D.A. O'Sullivan, and C.A.M. Brenninkmeijer, Increasing concentrations of dichloromethane, CH_2Cl_2, inferred from CARIBIC air samples collected 1998-2012, *Atmos. Chem. Phys.*, *15*(4), 1939–1958, doi:10.5194/acp-15-1939-2015, 2015a.

Leedam Elvidge, E.C., S.M. Phang, W.T. Sturges, and G. Malin, The effect of desiccation on the emission of volatile bromocarbons from two common temperate macroalgae, *Biogeosci.*, *12*(2), 387–398, doi:10.5194/bg-12-387-2015, 2015b.

Leedham Elvidge, E.C., H. Bönisch, C.A.M. Brenninkmeijer, A. Engel, P.J. Fraser, E. Gallacher, R. Langenfelds, J. Mühle, D.E. Oram, E.A. Ray, A.R. Ridley, T. Röckmann, W.T. Sturges, R.F. Weiss, and J.C. Laube, Evaluation of stratospheric age of air from CF_4, C_2F_6, $C3F_8$, CHF_3, HFC-125, HFC-227ea and SF_6: Implications for the calculations of halocarbon lifetimes, fractional release factors and ozone depletion potentials, *Atmos. Chem. Phys.*, *18*(5), 3369–3385, doi:10.5194/acp-18-3369-2018, 2018.

Le Quéré, C., R.M. Andrew, P. Friedlingstein, S. Sitch, J. Pongratz, A.C. Manning, J.I. Korsbakken, G.P. Peters, J.G. Canadell, R.B. Jackson, T.A. Boden, P.P. Tans, O.D. Andrews, V.K. Arora, D.C.E. Bakker, L. Barbero, M. Becker, R.A. Betts, L. Bopp, F. Chevallier, L.P. Chini, P. Ciais, C.E. Cosca, J. Cross, K. Currie, T. Gasser, I. Harris, J. Hauck, V. Haverd, R.A. Houghton, C.W. Hunt, G. Hurtt, T. Ilyina, A.K. Jain, E. Kato, M. Kautz, R.F. Keeling, K. Klein Goldewijk, A. Körtzinger, P. Landschützer, N. Lefèvre, A. Lenton, S. Lienert, I. Lima, D. Lombardozzi, N. Metzl, F. Millero, P.M.S. Monteiro, D.R. Munro, J.E.M.S. Nabel, S.I. Nakaoka, Y. Nojiri, X.A. Padin, A. Peregon, B. Pfeil, D. Pierrot, B. Poulter, G. Rehder, J. Reimer, C. Rödenbeck, J. Schwinger, R. Séférian, I. Skjelvan, B.D. Stocker, H. Tian, B. Tilbrook, F.N. Tubiello, I.T. van der Laan-Luijkx, G.R. van der Werf, S. van Heuven, N. Viovy, N. Vuichard, A.P. Walker, A.J. Watson, A.J. Wiltshire, S. Zaehle, and D. Zhu, Global Carbon Budget 2017, *Earth Syst. Sci. Data*, *10*(1), 405–448, doi:10.5194/essd-10-405-2018, 2018.

Lee-Taylor, J., and K.R. Redeker, Reevaluation of global emissions from rice paddies of methyl iodide and other species, *Geophys. Res. Lett.*, *32*(15), doi:10.1029/2005GL022918, 2005.

Lejeune, B., E. Mahieu, M.K. Vollmer, S. Reimann, P.F. Bernath, C.D. Boone, K.A. Walker, and C. Servais, Optimized approach to retrieve information on atmospheric carbonyl sulfide (OCS) above the Jungfraujoch station and change in its abundance since 1995, *J. Quant. Spectrosc. Radiat. Trans.*, *186*, 81–95, available at: https://www.sciencedirect.com/science/article/pii/S0022407316300899, 2017.

Lennartz, S.T., G. Krysztofiak, C.A. Marandino, B.M. Sinnhuber, S. Tegtmeier, F. Ziska, R. Hossaini, K. Krüger, S.A. Montzka, E. Atlas, D.E. Oram, T. Keber, H. Bönisch, and B. Quack, Modelling marine emissions and atmospheric distributions of halocarbons and dimethyl sulfide: the influence of prescribed water concentration vs. prescribed emissions, *Atmos. Chem. Phys.*, *15*(20), 11753–11772, doi:10.5194/acp-15-11753-2015, 2015.

Lennartz, S.T., C.A. Marandino, M. von Hobe, P. Cortes, B. Quack, R. Simo, D. Booge, A. Pozzer, T. Steinhoff, D.L. Arevalo-Martinez, C. Kloss, A. Bracher, R. Röttgers, E. Atlas, and K. Krüger, Direct oceanic emissions unlikely to account for the missing source of atmospheric carbonyl sulfide, *Atmos. Chem. Phys.*, *17*(1), 385-402, doi:10.5194/acp-17-385-2017, 2017.

Levin, I., T. Naegler, R. Heinz, D. Osusko, E. Cuevas, A. Engel, J. Ilmberger, R.L. Langenfelds, B. Neininger, C. Von Rohden, L.P. Steele, R. Weller, D.E. Worthy, and S.A. Zimov, The global SF_6 source inferred from long-term high precision atmospheric measurements and its comparison with emission inventories, *Atmos. Chem. Phys.*, *10*(6), 2655–2662, 2010.

Li, S., J. Kim, K.R. Kim, J. Mühle, S.K. Kim, M.K. Park, A. Stohl, D.J. Kang, T. Arnold, C.M. Harth, P.K. Salameh, and R.F. Weiss, Emissions of halogenated compounds in East Asia determined from measurements at Jeju Island, Korea, *Environ. Sci. Technol., 45*(13), 5668–5675, doi:10.1021/es104124k, 2011.

Li, S., M. Park, C.O. Jo, and S. Park, Emission estimates of methyl chloride from industrial sources in China based on high frequency atmospheric observations, *J. Atmos. Chem.*, *74*(2), 227–243, doi:10.1007/s10874-016-9354-4, 2017.

Li, Z., P. Bie, Z. Wang, Z. Zhang, H. Jiang, W. Xu, J. Zhang, and J. Hu, Estimated HCFC-22 emissions for 1990–2050 in China and the increasing contribution to global emissions, *Atmos. Environ., 132*, 77–84, doi:10.1016/j.atmosenv.2016.02.038, 2016.

Liang, Q., E. Atlas, D. Blake, M. Dorf, K. Pfeilsticker, and S. Schauffler, Convective transport of very short lived bromocarbons to the stratosphere, *Atmos. Chem. Phys.*, *14*(11), 5781–5792, doi:10.5194/acp-14-5781-2014, 2014a.

Liang, Q., P.A. Newman, J.S. Daniel, S. Reimann, B.D. Hall, G. Dutton, and L.J.M. Kuijpers, Constraining the carbon tetrachloride (CCl_4) budget using its global trend and inter-hemispheric gradient, *Geophys. Res. Lett.*, *41*(14), 5307–5315, doi:10.1002/2014GL060754, 2014b.

Liang, Q., S. Reimann, and P.A. Newman, SPARC Report on the Mystery of Carbon Tetrachloride, SPARC, Volume 7, doi:10.3929/ethz-a-01069-0647, 2016.

Liu, Y., S.A. Yvon-Lewis, L. Hu, J.E. Salisbury, and J.E. O'Hern, $CHBr_3$, $CH2Br_2$, and $CHClBr_2$ in U.S. coastal waters during the Gulf of Mexico and East Coast Carbon cruise, *J. Geophys. Res. Oceans*, *116*(C10), doi:10.1029/2010JC006729, 2011.

Liu, Z., B. Yao, X. An, L. Zhou, T. Luan, H. Wang, G. Zhang, and S. Cheng, Study of Chinese HCFC-142b emission by inverse model, in Chinese with English abstract, *China Envirnomental Science*, *35*(4), 1040–1046, 2015.

Lobert, J.M., W.C. Keene, J.A. Logan, and R. Yevich, Global chlorine emissions from biomass burning: Reactive Chlorine Emissions Inventory, *J. Geophys. Res. Atmos.*, *104*(D7), 8373–8389, doi:10.1029/1998JD100077, 1999.

Logue, J.M., M.J. Small, D. Stern, J. Maranche, and A.L. Robinson, Spatial Variation in Ambient Air Toxics Concentrations and Health Risks between Industrial-Influenced, Urban, and Rural Sites, *J. Air Waste Manag. Assoc.*, *60*(3), 271–286, doi:10.3155/1047-3289.60.3.271, 2010.

Mahieu, E., M.P. Chipperfield, J. Notholt, T. Reddmann, J. Anderson, P.F. Bernath, T. Blumenstock, M.T. Coffey, S.S. Dhomse, W. Feng, B. Franco, L. Froidevaux, D.W.T. Griffith, J.W. Hannigan, F. Hase, R. Hossaini, N.B. Jones, I. Morino, I. Murata, H. Nakajima, M. Palm, C. Paton-Walsh, J.M.R. III, M. Schneider, C. Servais, D. Smale, and K.A. Walker, Recent Northern Hemisphere stratospheric HCl increase due to atmospheric circulation changes, *Nature*, *515*(7525), 104–107, doi:10.1038/nature13857, 2014a.

Mahieu, E., R. Zander, G.C. Toon, M.K. Vollmer, S. Reimann, J. Mühle, W. Bader, B. Bovy, B. Lejeune, C. Servais, P. Demoulin, G. Roland, P.F. Bernath, C.D. Boone, K.A. Walker, and P. Duchatelet, Spectrometric monitoring of atmospheric carbon tetrafluoride (CF_4) above the Jungfraujoch station since 1989: Evidence of continued increase but at a slowing rate, *Atmos. Meas. Tech.*, *7*(1), 333–344, doi:10.5194/amt-7-333-2014, 2014b.

Mahieu, E., B. Lejeune, B. Bovy, C. Servais, G.C. Toon, P.F. Bernath, C.D. Boone, K.A. Walker, S. Reimann, M.K. Vollmer, and S. O'Doherty, Retrieval of HCFC-142b (CH_3CClF_2) from ground-based high-resolution infrared solar spectra: Atmospheric increase since 1989 and comparison with surface and satellite measurements, *J. Quant. Spectrosc. Radiat. Trans.*, *186*, 96–105, doi:10.1016/j.jqsrt.2016.03.017, 2017.

Maione, M., F. Graziosi, J. Arduini, F. Furlani, U. Giostra, D.R. Blake, P. Bonasoni, X. Fang, S.A. Montzka, S.J. O'Doherty, S. Reimann, A. Stohl, and M.K. Vollmer, Estimates of European emissions of methyl chloroform using a Bayesian inversion method, *Atmos. Chem. Phys.*, *14*(18), 9755–9770, doi:10.5194/acp-14-9755-2014, 2014.

Manley, S.L., N.Y. Wang, M.L. Walser, and R.J. Cicerone, Coastal salt marshes as global methyl halide sources from determinations of intrinsic production by marsh plants, *Global Biogeochem. Cycles*, *20*(3), doi:10.1029/2005gb002578, 2006.

Mao, T., Y.S. Wang, H.H. Xu, J. Jiang, F.K. Wu, and X.B. Xu, A study of the atmospheric VOCs of Mount Tai in June 2006, *Atmos. Environ., 43*(15), 2503–2508, doi:10.1016/j.atmosenv.2009.02.013, 2009.

Marcy, T.P., P.J. Popp, R.S. Gao, D.W. Fahey, E.A. Ray, E.C. Richard, T.L. Thompson, E.L. Atlas, M. Loewenstein, S.C. Wofsy, S. Park, E.M. Weinstock, W.H. Swartz, and M.J. Mahoney, Measurements of trace gases in the tropical tropopause layer, *Atmos. Environ., 41*(34), 7253–7261, doi:10.1016/j.

atmosenv.2007.05.032, 2007.

McCulloch, A., M.L. Aucott, C.M. Benkovitz, T.E. Graedel, G. Kleiman, P.M. Midgley, and Y.-F. Li, Global emissions of hydrogen chloride and chloromethane from coal combustion, incineration and industrial activities: Reactive Chlorine Emissions Inventory, *J. Geophys. Res. Atmos.*, *104*(D7), 8391–8403, doi:10.1029/1999JD900025, 1999.

McCulloch, A., Chloroform in the environment: occurrence, sources, sinks and effects, *Chemosphere*, *50*(10), 1291–1308, doi:10.1016/s0045-6535(02)00697-5, 2003.

McNorton, J., E. Gloor, C. Wilson, G.D. Hayman, N. Gedney, E. Comyn-Platt, T. Marthews, R.J. Parker, H. Boesch, and M.P. Chipperfield, Role of regional wetland emissions in atmospheric methane variability, *Geophys. Res. Lett.*, *43*(21), 11433–11444, doi:10.1002/2016GL070649, 2016.

Mébarki, Y., V. Catoire, N. Huret, G. Berthet, C. Robert, and G. Poulet, More evidence for very short-lived substance contribution to stratospheric chlorine inferred from HCl balloon-borne in situ measurements in the tropics, *Atmos. Chem. Phys.*, *10*, 397–409, doi:10.5194/acpd-9-16163-2009, 2010.

Mendez-Diaz, J.D., K.K. Shimabuku, J. Ma, Z.O. Enumah, J.J. Pignatello, W.A. Mitch, and M.C. Dodd, Sunlight-driven photochemical halogenation of dissolved organic matter in seawater: A natural abiotic source of organobromine and organoiodine, *Environ. Sci. Technol.*, *48*(13), 7418–7427, doi:10.1021/es5016668, 2014.

Millán, L., N. Livesey, W. Read, L. Froidevaux, D. Kinnison, R. Harwood, I.A. MacKenzie, and M.P. Chipperfield, New Aura Microwave Limb Sounder observations of BrO and implications for Br_y, *Atmos. Meas. Tech.*, *5*(7), 1741-1751, doi:10.5194/amt-5-1741–2012, 2012.

Miller, B.R., M. Rigby, L.J.M. Kuijpers, P.B. Krummel, L.P. Steele, M. Leist, P.J. Fraser, A. McCulloch, C. Harth, P. Salameh, J. Mühle, R.F. Weiss, R.G. Prinn, R.H.J. Wang, S. O'Doherty, B.R. Greally, and P.G. Simmonds, HFC-23 (CHF_3) emission trend response to HCFC-22 ($CHClF_2$) production and recent HFC-23 emission abatement measures, *Atmos. Chem. Phys.*, *10*(16), 7875–7890, doi:10.5194/acp-10-7875-2010, 2010.

Montzka, S.A., J.H. Butler, B.D. Hall, D.J. Mondeel, and J.W. Elkins, A decline in tropospheric organic bromine, *Geophys. Res. Lett.*, *30*(15), doi:10.1029/2003GL017745, 2003.

Montzka, S.A., P. Calvert, B.D. Hall, J.W. Elkins, T.J. Conway, P.P. Tans, and C. Sweeney, On the global distribution, seasonality, and budget of atmospheric carbonyl sulfide (COS) and some similarities to CO_2, *J. Geophys. Res. Atmos.*, *112*(D9), doi:10.1029/2006JD007665, 2007.

Montzka, S.A., S. Reimann, (Coordinating Lead Authors) A. Engel, K. Krüger, S. O`Doherty, and W.T. Sturges, Ozone-Depleting Substances (ODSs) and Related Chemicals, Chapter 1 in *Scientific Assessment of Ozone Depletion: 2010*, Global Ozone Research and Monitoring Project–Report No. 52, World Meteorological Organization, Geneva, Switzerland, 2010.

Montzka, S.A., M. McFarland, S.O. Andersen, B.R. Miller, D.W. Fahey, B.D. Hall, L. Hu, C. Siso, and J.W. Elkins, Recent trends in global emissions of hydrochlorofluorocarbons and hydrofluorocarbons: Reflecting on the 2007 adjustments to the Montreal Protocol, *J. Phys. Chem. A*, *119*(19), 4439–4449, doi:10.1021/jp5097376, 2015.

Montzka, S.A., G.S. Dutton, P. Yu, E. Ray, R.W. Portmann, J.S. Daniel, L. Kuijpers, B.D. Hall, D. Mondeel, C. Siso, J.D. Nance, M. Rigby, A.J. Manning, L. Hu, F. Moore, B.R. Miller, and J.W. Elkins, An unexpected and persistent increase in global emissions of ozone-depleting CFC-11, *Nature*, *557*(7705), 413–417, doi:10.1038/s41586-018-0106-2, 2018.

Mühle, J., J. Huang, R.F. Weiss, R.G. Prinn, B.R. Miller, P.K. Salameh, C.M. Harth, P.J. Fraser, L.W. Porter, B.R. Greally, S. O'Doherty, and P.G. Simmonds, Sulfuryl fluoride in the global atmosphere, *J. Geophys. Res. Atmos.*, *114* D05306, doi:10.1029/2008JD011162, 2009.

Mühle, J., A.L. Ganesan, B.R. Miller, P.K. Salameh, C.M. Harth, B.R. Greally, M. Rigby, L.W. Porter, L.P. Steele, C.M. Trudinger, P.B. Krummel, S. O'Doherty, P.J. Fraser, P.G. Simmonds, R.G. Prinn, and R.F. Weiss, Perfluorocarbons in the global atmosphere: tetrafluoromethane, hexafluoroethane, and octafluoropropane, *Atmos. Chem. Phys.*, *10*(11), 5145–5164, doi:10.5194/acp-10-5145–2010, 2010.

Murphy, D.M., and D.S. Thomson, Halogen ions and NO+ in the mass spectra of aerosols in the upper troposphere and lower stratosphere, *Geophys. Res. Lett.*, *27*(19), 3217–3220,

doi:10.1029/1999GL011267, 2000.

Murphy, D.M., K.D. Froyd, J.P. Schwarz, and J.C. Wilson, Observations of the chemical composition of stratospheric aerosol particles, *Q. J. R. Meteorol. Soc.*, *140*(681), 1269–1278, doi:10.1002/qj.2213, 2014.

Myhre, G., and D.T. Shindell (Coordinating Lead Authors), F.-M. Bréon, W. Collins, J. Fuglestvedt, J. Huang, D. Koch, J.-F. Lamargue, D. Lee, B. Mendoza, T. Nakajima, A. Robock, G. Stephens, T. Takemura, and H. Zhang, Anthropogenic and Natural Radiative Forcing, Chapter 8 in *Climate Change 2013: The Physical Science Basis. Contribution of Working Group I to the Fifth Assessment Report of the Intergovernmental Panel on Climate Change*, edited by D.J. Jacob, A.R. Ravishankara, and K. Shine, p. 659–740, Cambridge University Press, Cambridge, United Kingdom, 2013.

Nadzir, M.S.M., S.M. Phang, M.R. Abas, N.A. Rahman, A. Abu Samah, W.T. Sturges, D.E. Oram, G.P. Mills, E.C. Leedham, J.A. Pyle, N.R.P. Harris, A.D. Robinson, M.J. Ashfold, M.I. Mead, M.T. Latif, M.F. Khan, A.M. Amiruddin, N. Banan, and M.M. Hanafiah, Bromocarbons in the tropical coastal and open ocean atmosphere during the 2009 Prime Expedition Scientific Cruise (PESC-09), *Atmos. Chem. Phys.*, *14*(15), 8137–8148, doi:10.5194/acp-14-8137-2014, 2014.

Navarro, M.A., E.L. Atlas, A. Saiz-Lopez, X. Rodriguez-Lloveras, D.E. Kinnison, J.F. Lamarque, S. Tilmes, M. Filus, N.R.P. Harris, E. Meneguz, M.J. Ashfold, A.J. Manning, C.A. Cuevas, S.M. Schauffler, and V. Donets, Airborne measurements of organic bromine compounds in the Pacific tropical tropopause layer, *Proc. Natl. Acad. Sci.*, *112*(45), 13789–13793, doi:10.1073/pnas.1511463112, 2015.

Nedoluha, G.E., I.S. Boyd, A. Parrish, R.M. Gomez, D.R. Allen, L. Froidevaux, B.J. Connor, and R.R. Querel, Unusual stratospheric ozone anomalies observed in 22 years of measurements from Lauder, New Zealand, *Atmos. Chem. Phys.*, *15*(12), 6817–6826, doi:10.5194/acp-15-6817-2015, 2015.

Nedoluha, G.E., B.J. Connor, T. Mooney, J.W. Barrett, A. Parrish, R.M. Gomez, I. Boyd, D.R. Allen, M. Kotkamp, S. Kremser, T. Deshler, P. Newman, and M.L. Santee, 20 years of ClO measurements in the Antarctic lower stratosphere, *Atmos. Chem. Phys.*, *16*(16), 10725–10734, doi:10.5194/acp-16-10725-2016, 2016.

Newland, M.J., C.E. Reeves, D.E. Oram, J.C. Laube, W.T. Sturges, C. Hogan, P. Begley, and P.J. Fraser, Southern hemispheric halon trends and global halon emissions, 1978–2011, *Atmos. Chem. Phys.*, *13*(11), 5551-5565, doi:10.5194/acp-13-5551-2013, 2013.

Newman, P.A., J.S. Daniel, D.W. Waugh, and E.R. Nash, A new formulation of equivalent effective stratospheric chlorine (EESC), *Atmos. Chem. Phys.*, *7*(17), 4537–4552, doi:10.5194/acp-7-4537-2007, 2007.

Nisbet, E.G., E.J. Dlugokencky, M.R. Manning, D. Lowry, R.E. Fisher, J.L. France, S.E. Michel, J.B. Miller, J.W.C. White, B. Vaughn, P. Bousquet, J.A. Pyle, N.J. Warwick, M. Cain, R. Brownlow, G. Zazzeri, M. Lanoiselle, A.C. Manning, E. Gloor, D.E.J. Worthy, E.G. Brunke, C. Labuschagne, E.W. Wolff, and A.L. Ganesan, Rising atmospheric methane: 2007-2014 growth and isotopic shift, *Global Biogeochem. Cycles*, *30*(9), 1356–1370, doi:10.1002/2016gb005406, 2016.

O'Doherty, S., D.M. Cunnold, B.R. Miller, J. Mühle, A. McCulloch, P.G. Simmonds, A.J. Manning, S. Reimann, M.K. Vollmer, B.R. Greally, R.G. Prinn, P.J. Fraser, L.P. Steele, P.B. Krummel, B.L. Dunse, L.W. Porter, C.R. Lunder, N. Schmidbauer, O. Hermansen, P.K. Salameh, C.M. Harth, R.H.J. Wang, and R.F. Weiss, Global and regional emissions of HFC-125 (CHF_2CF_3) from in situ and air archive atmospheric observations at AGAGE and SOGE observatories, *J. Geophys. Res.*, *114*, D23304, doi:10.1029/2009JD012184, 2009.

Ooki, A., D. Nomura, S. Nishino, T. Kikuchi, and Y. Yokouchi, A global-scale map of isoprene and volatile organic iodine in surface seawater of the Arctic, Northwest Pacific, Indian, and Southern Oceans, *J. Geophys. Res. Oceans*, *120*(6), 4108–4128, doi:10.1002/2014jc010519, 2015.

Oram, D.E., C.E. Reeves, W.T. Sturges, S.A. Penkett, P.J. Fraser, and R.L. Langenfelds, Recent tropospheric growth rate and distribution of HFC-134a (CF_3CH_2F), *Geophys. Res. Lett.*, *23*(15), 1949–1952, doi:10.1029/96GL01862, 1996.

Oram, D.E., Trends of Long-Lived Anthropogenic Halocarbons in the Southern Hemisphere and Model Calculation of Global Emissions, Ph.D. thesis, University of East Anglia, Norwich, United Kingdom, 249 pp., 1999.

Oram, D.E., F.S. Mani, J.C. Laube, M.J. Newland, C.E. Reeves, W.T. Sturges, S.A. Penkett, C.A.M. Brenninkmeijer, T. Rockmann, and P.J. Fraser, Long-term tropospheric trend of octafluorocyclobutane (c-C4F8 or PFC-318), *Atmos. Chem. Phys.*, *12*(1), 261–269, doi:10.5194/acp-12-261-2012, 2012.

Oram, D.E., M.J. Ashfold, J.C. Laube, L.J. Gooch, S. Humphrey, W.T. Sturges, E. Leedham-Elvidge, G.L. Forster, N.R.P. Harris, M.I. Mead, A. Abu Samah, S.M. Phang, O.Y. Chang-Feng, N.H. Lin, J.L. Wang, A.K. Baker, C.A.M. Brenninkmeijer, and D. Sherry, A growing threat to the ozone layer from short-lived anthropogenic chlorocarbons, *Atmos. Chem. Phys.*, *2017*, 1–20, doi:10.5194/acp-2017–497, 2017.

Orbe, C., D.W. Waugh, H. Yang, J.-F. Lamarque, S. Tilmes, and D.E. Kinnison, Tropospheric transport differences between models using the same large-scale meteorological fields, *Geophys. Res. Lett.*, *44*(2), 1068–1078, doi:10.1002/2016GL071339, 2017.

Ordonez, C., J.F. Lamarque, S. Tilmes, D.E. Kinnison, E.L. Atlas, D.R. Blake, G.S. Santos, G. Brasseur, and A. Saiz-Lopez, Bromine and iodine chemistry in a global chemistry-climate model: Description and evaluation of very short-lived oceanic sources, *Atmos. Chem. Phys.*, *12*(3), 1423–1447, doi:10.5194/acp-12-1423-2012, 2012.

Ostermöller, J., H. Bönisch, P. Jöckel, and A. Engel, A new time-independent formulation of fractional release, *Atmos. Chem. Phys.*, *17*(6), 3785–3797, doi:10.5194/acp-17-3785-2017, 2017.

Pan, L.L., E.L. Atlas, R.J. Salawitch, S.B. Honomichl, J.F. Bresch, W.J. Randel, E.C. Apel, R.S. Hornbrook, A.J. Weinheimer, D.C. Anderson, S.J. Andrews, S. Baidar, S.P. Beaton, T.L. Campos, L.J. Carpenter, D. Chen, B. Dix, V. Donets, S.R. Hall, T.F. Hanisco, C.R. Homeyer, L.G. Huey, J.B. Jensen, L. Kaser, D.E. Kinnison, T.K. Koenig, J.F. Lamarque, C. Liu, J. Luo, Z.J. Luo, D.D. Montzka, J.M. Nicely, R.B. Pierce, D.D. Riemer, T. Robinson, P. Romashkin, A. Saiz-Lopez, S. Schauffler, O. Shieh, M.H. Stell, K. Ullmann, G. Vaughan, R. Volkamer, and G. Wolfe, The Convective Transport of Active Species in the Tropics (CONTRAST) Experiment, *Bull. Am. Meteorol. Soc.*, *98*(1), 106–128, doi:10.1175/bams-d-14-00272.1, 2017.

Parrella, J.P., D.J. Jacob, Q. Liang, Y. Zhang, L.J. Mickley, B. Miller, M.J. Evans, X. Yang, J.A. Pyle, N. Theys, and M. Van Roozendael, Tropospheric bromine chemistry: Implications for present and pre-industrial ozone and mercury, *Atmos. Chem. Phys.*, *12*(15), 6723–6740, doi:10.5194/acp-12-6723-2012, 2012.

Pfeilsticker, K., W.T. Sturges, H. Bosch, C. Camy-Peyret, M.P. Chipperfield, A. Engel, R. Fitzenberger, M. Muller, S. Payan, and B.M. Sinnhuber, Lower stratospheric organic and inorganic bromine budget for the Arctic winter 1998/99, Geophys. Res. Lett., 27(20), 3305–3308, doi:10.1029/2000GL011650, 2000.

Plumb, I.C., P.F. Vohralik, and K.R. Ryan, Normalization of correlations for atmospheric species with chemical loss, *J. Geophys. Res. Atmos. 104*(D9), 11723–11732, doi:10.1029/1999JD900014, 1999.

Prather, M.J., J. Hsu, N.M. DeLuca, C.H. Jackman, L.D. Oman, A.R. Douglass, E.L. Fleming, S.E. Strahan, S.D. Steenrod, O.A. Sovde, I.S.A. Isaksen, L. Froidevaux, and B. Funke, Measuring and modeling the lifetime of nitrous oxide including its variability, *J. Geophys. Res. Atmos.*, *120*(11), 5693–5705, doi:10.1002/2015JD023267, 2015.

Prinn, R.G., R.F. Weiss, J. Arduini, T. Arnold, H.L. DeWitt, P.J. Fraser, A.L. Ganesan, J. Gasore, C.M. Harth, O. Hermansen, J. Kim, P.B. Krummel, S. Li, Z.M. Loh, C.R. Lunder, M. Maione, A.J. Manning, B.R. Miller, B. Mitrevski, J. Mühle, S. O'Doherty, S. Park, S. Reimann, M. Rigby, T. Saito, P.K. Salameh, R. Schmidt, P.G. Simmonds, L.P. Steele, M.K. Vollmer, R.H. Wang, B. Yao, Y. Yokouchi, D. Young, and L. Zhou, History of chemically and radiatively important atmospheric gases from the Advanced Global Atmospheric Gases Experiment (AGAGE), *Earth Syst. Sci. Data*, *10*(2), 985–1018, doi:10.5194/essd-10-985-2018, 2018.

Quack, B., E. Atlas, G. Petrick, and D.W.R. Wallace, Bromoform and dibromomethane above the Mauritanian upwelling: Atmospheric distributions and oceanic emissions, *J. Geophys. Res. Atmos.*, *112*(D9), doi:10.1029/2006JD007614, 2007.

Ramaswamy, V. (Coordinating Lead Author), O. Boucher, J.D. Haigh, D.A. Hauglustaine, J.M. Haywood, G. Myrhe, T. Nakajima, G.Y. Shi, and S. Solomon, Radiative Forcing of Climate Change, Chapter 6 in *Climate Change 2001: The Scientific Basis. Contribution of Working Group I to the Third Assessment Report of the Intergovernmental Panel on Climate Change,* edited by F. Joos and J. Srinivasan, Cambridge University Press, Cambridge,

United Kingdom and New York, New York, 2001.

Ravishankara, A.R., S. Solomon, A.A. Turnipseed, and R.F. Warren, Atmospheric Lifetimes of Long-Lived Halogenated Species, *Science*, *259*(5092), 194–199, doi: 10.1126/science.259.5092.194, 1993.

Ravishankara, A.R., J.S. Daniel, and R.W. Portmann, Nitrous Oxide (N_2O): The dominant ozone-depleting substance emitted in the 21st century, *Science*, *326*(5949), 123–125, doi:10.1126/science.1176985, 2009.

Ray, E.A., F.L. Moore, J.W. Elkins, K.H. Rosenlof, J.C. Laube, T. Rockmann, D.R. Marsh, and A.E. Andrews, Quantification of the SF_6 lifetime based on mesospheric loss measured in the stratospheric polar vortex, *J. Geophys. Res. Atmos.*, *122*(8), 4626–4638, doi:10.1002/2016JD026198, 2017.

Revell, L.E., F. Tummon, R.J. Salawitch, A. Stenke, and T. Peter, The changing ozone depletion potential of N_2O in a future climate, *Geophys. Res. Lett.*, *42*(22), 10,047-010,055, doi:10.1002/2015GL065702, 2015.

Rex, M., I. Wohltmann, T. Ridder, R. Lehmann, K. Rosenlof, P. Wennberg, D. Weisenstein, J. Notholt, K. Kruger, V. Mohr, and S. Tegtmeier, A tropical West Pacific OH minimum and implications for stratospheric composition, *Atmos. Chem. Phys.*, *14*(9), 4827–4841, doi:10.5194/acp-14-4827-2014, 2014.

Rhew, R.C., M.E. Whelan, and D.H. Min, Large methyl halide emissions from south Texas salt marshes, *Biogeosci.*, *11*(22), 6427–6434, doi:10.5194/bg-11-6427-2014, 2014.

Rhew, R.C., and J.D. Happell, The atmospheric partial lifetime of carbon tetrachloride with respect to the global soil sink, *Geophys. Res. Lett.*, *43*(6), 2889–2895, doi:10.1002/2016GL067839, 2016.

Rigby, M., J. Mühle, B.R. Miller, R.G. Prinn, P.B. Krummel, L.P. Steele, P.J. Fraser, P.K. Salameh, C.M. Harth, R.F. Weiss, B.R. Greally, S. O'Doherty, P.G. Simmonds, M.K. Vollmer, S. Reimann, J. Kim, K.R. Kim, H.J. Wang, J.G.J. Olivier, E.J. Dlugokencky, G.S. Dutton, B.D. Hall, and J.W. Elkins, History of atmospheric SF_6 from 1973 to 2008, *Atmos. Chem. Phys.*, *10*(21), 10305–10320, doi:10.5194/acp-10-10305-2010, 2010.

Rigby, M., A.L. Ganesan, and R.G. Prinn, Deriving emissions time series from sparse atmospheric mole fractions, *J. Geophys. Res. Atmos.*, *116*, doi:10.1029/2010JD015401, 2011.

Rigby, M., R.G. Prinn, S. O'Doherty, S.A. Montzka, A. McCulloch, C.M. Harth, J. Mühle, P.K. Salameh, R.F. Weiss, D. Young, P.G. Simmonds, B.D. Hall, G.S. Dutton, D. Nance, D.J. Mondeel, J.W. Elkins, P.B. Krummel, L.P. Steele, and P.J. Fraser, Re-evaluation of the lifetimes of the major CFCs and CH_3CCl_3 using atmospheric trends, *Atmos. Chem. Phys.*, *13*(5), 2691–2702, doi:10.5194/acp-13-2691-2013, 2013.

Rigby, M., R.G. Prinn, S. O'Doherty, B.R. Miller, D. Ivy, J. Mühle, C.M. Harth, P.K. Salameh, T. Arnold, R.F. Weiss, P.B. Krummel, L.P. Steele, P.J. Fraser, D. Young, and P.G. Simmonds, Recent and future trends in synthetic greenhouse gas radiative forcing, *Geophys. Res. Lett.*, *41*(7), 2623–2630, doi:10.1002/2013GL059099, 2014.

Rigby, M., S.A. Montzka, R.G. Prinn, J.W.C. White, D. Young, S. O'Doherty, M.F. Lunt, A.L. Ganesan, A.J. Manning, P.G. Simmonds, P.K. Salameh, C.M. Harth, J. Mühle, R.F. Weiss, P.J. Fraser, L.P. Steele, P.B. Krummel, A. McCulloch, and S. Park, Role of atmospheric oxidation in recent methane growth, *Proc. Natl. Acad. Sci.*, *114*(21), 5373–5377, doi:10.1073/pnas.1616426114, 2017.

Rinsland, C.P., E. Mahieu, P. Demoulin, R. Zander, C. Servais, and J.-M. Hartmann, Decrease of the carbon tetrachloride (CCl_4) loading above Jungfraujoch, based on high resolution infrared solar spectra recorded between 1999 and 2011, *J. Quant. Spectrosc. Radiat. Trans.*, *113*(11), 1322–1329, doi:10.1016/j.jqsrt.2012.02.016, 2012.

Rollins, A.W., T.D. Thornberry, L.A. Watts, P. Yu, K.H. Rosenlof, M. Mills, E. Baumann, F.R. Giorgetta, T.V. Bui, M. Höpfner, K.A. Walker, C. Boone, P.F. Bernath, P.R. Colarco, P.A. Newman, D.W. Fahey, and R.S. Gao, The role of sulfur dioxide in stratospheric aerosol formation evaluated by using in situ measurements in the tropical lower stratosphere, *Geophys. Res. Lett.*, *44*(9), 4280–4286, doi:10.1002/2017GL072754, 2017.

Russo, M.R., M.J. Ashfold, N.R.P. Harris, and J.A. Pyle, On the emissions and transport of bromoform: sensitivity to model resolution and emission location, *Atmos. Chem. Phys.*, *15*(24), 14031–14040, doi:10.5194/acp-15-14031-2015, 2015.

Saiz-Lopez, A., R.P. Fernandez, C. Ordóñez, D.E. Kinnison, J.C. Gómez Martín, J.F. Lamarque, and S. Tilmes, Iodine chemistry in the troposphere and its effect on ozone, *Atmos. Chem. Phys.*, *14*(23), 13119-

13143, doi:10.5194/acp-14-13119-2014, 2014.

Saiz-Lopez, A., S. Baidar, C.A. Cuevas, T.K. Koenig, R.P. Fernandez, B. Dix, D.E. Kinnison, J.F. Lamarque, X. Rodriguez-Lloveras, T.L. Campos, and R. Volkamer, Injection of iodine to the stratosphere, *Geophys. Res. Lett.*, *42*(16), 6852–6859, doi:10.1002/2015GL064796, 2015.

Sala, S., H. Bönisch, T. Keber, D.E. Oram, G. Mills, and A. Engel, Deriving an atmospheric budget of total organic bromine using airborne in situ measurements from the western Pacific area during SHIVA, *Atmos. Chem. Phys.*, *14*(13), 6903–6923, doi:10.5194/acp-14-6903-2014, 2014.

Sander, R., Compilation of Henry's law constants (version 4.0) for water as solvent, *Atmos. Chem. Phys.*, *15*, 4399–4981, doi:10.5194/acp-15-4399-2015, 2015.

Saunois, M., P. Bousquet, B. Poulter, A. Peregon, P. Ciais, J.G. Canadell, E.J. Dlugokencky, G. Etiope, D. Bastviken, S. Houweling, G. Janssens-Maenhout, F.N. Tubiello, S. Castaldi, R.B. Jackson, M. Alexe, V.K. Arora, D.J. Beerling, P. Bergamaschi, D.R. Blake, G. Brailsford, V. Brovkin, L. Bruhwiler, C. Crevoisier, P. Crill, K. Covey, C. Curry, C. Frankenberg, N. Gedney, L. Hoglund-Isaksson, M. Ishizawa, A. Ito, F. Joos, H.S. Kim, T. Kleinen, P. Krummel, J.F. Lamarque, R. Langenfelds, R. Locatelli, T. Machida, S. Maksyutov, K.C. McDonald, J. Marshall, J.R. Melton, I. Morino, V. Naik, S. O'Doherty, F.J.W. Parmentier, P.K. Patra, C.H. Peng, S.S. Peng, G.P. Peters, I. Pison, C. Prigent, R. Prinn, M. Ramonet, W.J. Riley, M. Saito, M. Santini, R. Schroeder, I.J. Simpson, R. Spahni, P. Steele, A. Takizawa, B.F. Thornton, H.Q. Tian, Y. Tohjima, N. Viovy, A. Voulgarakis, M. van Weele, G.R. van der Werf, R. Weiss, C. Wiedinmyer, D.J. Wilton, A. Wiltshire, D. Worthy, D. Wunch, X.Y. Xu, Y. Yoshida, B. Zhang, Z. Zhang, and Q. Zhu, The global methane budget 2000-2012, *Earth Syst. Sci. Data*, *8*(2), 697-751, doi:10.5194/essd-8-697–2016, 2016.

Schaefer, H., S.E.M. Fletcher, C. Veidt, K.R. Lassey, G.W. Brailsford, T.M. Bromley, E.J. Dlugokencky, S.E. Michel, J.B. Miller, I. Levin, D.C. Lowe, R.J. Martin, B.H. Vaughn, and J.W.C. White, A 21st-century shift from fossil-fuel to biogenic methane emissions indicated by $^{13}CH_4$, *Science*, *352*(6281), 80–84, doi:10.1126/science.aad2705, 2016.

Schmidt, J.A., D.J. Jacob, H.M. Horowitz, L. Hu, T. Sherwen, M.J. Evans, Q. Liang, R.M. Suleiman, D.E. Oram, M. Le Breton, C.J. Percival, S. Wang, B. Dix, and R. Volkamer, Modeling the observed tropospheric BrO background: Importance of multiphase chemistry and implications for ozone, OH, and mercury, *J. Geophys. Res. Atmos.*, *121*(19), 11,819–11,835, doi:10.1002/2015JD024229, 2016.

Schoenenberger, F., M.K. Vollmer, M. Rigby, M. Hill, P.J. Fraser, P.B. Krummel, R.L. Langenfelds, T.S. Rhee, T. Peter, and S. Reimann, First observations, trends, and emissions of HCFC-31 (CH_2ClF) in the global atmosphere, *Geophys. Res. Lett.*, *42*(18), 7817–7824, doi:10.1002/2015GL064709, 2015.

Schofield, R., S. Fueglistaler, I. Wohltmann, and M. Rex, Sensitivity of stratospheric Br-y to uncertainties in very short lived substance emissions and atmospheric transport, *Atmos. Chem. Phys.*, *11*(4), 1379–1392, doi:10.5194/acp-11-1379-2011, 2011.

Schwietzke, S., O.A. Sherwood, L.M.P.B. Ruhwiler, J.B. Miller, G. Etiope, E.J. Dlugokencky, S.E. Michel, V.A. Arling, B.H. Vaughn, J.W.C. White, and P.P. Tans, Upward revision of global fossil fuel methane emissions based on isotope database, *Nature*, *538*(7623), 88-91, 10.1038/nature19797, 2016.

Sheng, J.-X., D.K. Weisenstein, B.-P. Luo, E. Rozanov, A. Stenke, J. Anet, H. Bingemer, and T. Peter, Global atmospheric sulfur budget under volcanically quiescent conditions: Aerosol-chemistry-climate model predictions and validation, *J. Geophys. Res. Atmos.*, *120*(1), 256–276, 10.1002/2014JD021985, 2015.

Sherry, D., A. McCulloch, Q. Liang, S. Reimann, and P.A. Newman, Current Sources of Carbon Tetrachloride (CCl_4) in our Atmosphere, *Environ. Res. Lett.,* 13, doi:10.1088/1748-9326/oa9c87.

Sherwen, T., M.J. Evans, L.J. Carpenter, S.J. Andrews, R.T. Lidster, B. Dix, T.K. Koenig, R. Sinreich, I. Ortega, R. Volkamer, A. Saiz-Lopez, C. Prados-Roman, A.S. Mahajan, and C. Ordóñez, Iodine's impact on tropospheric oxidants: a global model study in GEOS-Chem, *Atmos. Chem. Phys., 16*(2), 1161–1186, doi:10.5194/acp-16-1161-2016, 2016.

Shi, Q., G. Petrick, B. Quack, C. Marandino, and D. Wallace, Seasonal variability of methyl iodide in the Kiel Fjord, *J. Geophys. Res. Oceans, 119*(3), doi:10.1002/2013jc009328,2014,2014.

Shimizu, Y., A. Ooki, H. Onishi, T. Takatsu, S. Tanaka, Y. Inagaki, K. Suzuki, N. Kobayashi, Y. Kamei, and K. Kuma, Seasonal variation of volatile organic

iodine compounds in the water column of Funka Bay, Hokkaido, Japan, *J. Atmos. Chem.*, *74*(2), 205–225, doi:10.1007/s10874-016-9352-6, 2017.

Simmonds, P.G., S. O'Doherty, J. Huang, R. Prinn, R.G. Derwent, D. Ryall, G. Nickless, and D. Cunnold, Calculated trends and the atmospheric abundance of 1,1,1,2-tetrafluoroethane, 1,1-dichloro-1-fluoroethane, and 1-chloro-1, 1-difluoroethane using automated in-situ gas chromatography-mass spectrometry measurements recorded at Mace Head, Ireland, from October 1994 to March 1997, *J. Geophys. Res. Atmos.*, *103*(D13), 16029–16037, doi:10.1029/98JD00774, 1998.

Simmonds, P.G., A.J. Manning, D.M. Cunnold, A. McCulloch, S. O'Doherty, R.G. Derwent, P.B. Krummel, P.J. Fraser, B. Dunse, L.W. Porter, R.H.J. Wang, B.R. Greally, B.R. Miller, P. Salameh, R.F. Weiss, and R.G. Prinn, Global trends, seasonal cycles, and European emissions of dichloromethane, trichloroethene, and tetrachloroethene from the AGAGE observations at Mace Head, Ireland, and Cape Grim, Tasmania, *J. Geophys. Res. Atmos.*, *111*(D18), doi:10.1029/2006JD007082, 2006.

Simmonds, P.G., M. Rigby, A. McCulloch, S. O'Doherty, D. Young, J. Mühle, P.B. Krummel, P. Steele, P.J. Fraser, A.J. Manning, R.F. Weiss, P.K. Salameh, C.M. Harth, R.H.J. Wang, and R.G. Prinn, Changing trends and emissions of hydrochlorofluorocarbons (HCFCs) and their hydrofluorocarbon (HFCs) replacements, *Atmos. Chem. Phys.*, *17*(7), 4641–4655, doi:10.5194/acp-17-4641-2017, 2017.

Simpson, I.J., N.J. Blake, D.R. Blake, S. Meinardi, M.P.S. Andersen, and F.S. Rowland, Strong evidence for negligible methyl chloroform (CH_3C-Cl_3) emissions from biomass burning, *Geophys. Res. Lett.*, *34*(10), doi:10.1029/2007GL029383, 2007.

Simpson, I.J., S.K. Akagi, B. Barletta, N.J. Blake, Y. Choi, G.S. Diskin, A. Fried, H.E. Fuelberg, S. Meinardi, F.S. Rowland, S.A. Vay, A.J. Weinheimer, P.O. Wennberg, P. Wiebring, A. Wisthaler, M. Yang, R.J. Yokelson, and D.R. Blake, Boreal forest fire emissions in fresh Canadian smoke plumes: C-1-C-10 volatile organic compounds (VOCs), CO_2, CO, NO_2, NO, HCN and CH_3CN, *Atmos. Chem. Phys.*, *11*(13), 6445–6463, doi:10.5194/acp-11-6445-2011, 2011.

Simpson, I.J., M.P.S. Andersen, S. Meinardi, L. Bruhwiler, N.J. Blake, D. Helmig, F.S. Rowland, and D.R. Blake, Long-term decline of global atmospheric ethane concentrations and implications for methane, *Nature*, *488*(7412), 490–494, doi:10.1038/nature11342, 2012.

Sive, B.C., R.K. Varner, H. Mao, D.R. Blake, O.W. Wingenter, and R. Talbot, A large terrestrial source of methyl iodide, *Geophys. Res. Lett.*, *34*(17), doi:10.1029/2007GL030528, 2007.

Solomon, S., D. Kinnison, R.R. Garcia, J. Bandoro, M. Mills, C. Wilka, R.R. Neely, A. Schmidt, J.E. Barnes, J.-P. Vernier, and M. Höpfner, Monsoon circulations and tropical heterogeneous chlorine chemistry in the stratosphere, *Geophys. Res. Lett.*, *43*(24), 12,624–612,633, doi:10.1002/2016GL071778, 2016.

SPARC, (Stratospheric Processes And their Role in Climate), *Lifetimes of Stratospheric Ozone-Depleting Substances, Their Replacements, and Related Species*, edited by M.K.W. Ko, P.A. Newman, S. Reimann, and S.E. Strahan, *SPARC Report No. 6*, WCRP-15/2013, 2013.

Stachnik, R.A., L. Millán, R. Jarnot, R. Monroe, C. McLinden, S. Kühl, J. Puķīte, M. Shiotani, M. Suzuki, Y. Kasai, F. Goutail, J.P. Pommereau, M. Dorf, and K. Pfeilsticker, Stratospheric BrO abundance measured by a balloon-borne submillimeterwave radiometer, *Atmos. Chem. Phys.*, *13*(6), 3307–3319, doi:10.5194/acp-13-3307-2013, 2013.

Stemmler, I., I. Hense, and B. Quack, Marine sources of bromoform in the global open ocean-global patterns and emissions, *Biogeosci.*, *12*(6), 1967–1981, doi:10.5194/bg-12-1967-2015, 2015.

Stiller, G.P., T. von Clarmann, F. Haenel, B. Funke, N. Glatthor, U. Grabowski, S. Kellmann, M. Kiefer, A. Linden, S. Lossow, and M. Lopez-Puertas, Observed temporal evolution of global mean age of stratospheric air for the 2002 to 2010 period, *Atmos. Chem. Phys.*, *12*(7), 3311–3331, doi:10.5194/acp-12-3311-2012, 2012.

Stohl, A., P. Seibert, J. Arduini, S. Eckhardt, P. Fraser, B.R. Greally, C. Lunder, M. Maione, J. Mühle, S. O'Doherty, R.G. Prinn, S. Reimann, T. Saito, N. Schmidbauer, P.G. Simmonds, M.K. Vollmer, R.F. Weiss, and Y. Yokouchi, An analytical inversion method for determining regional and global emissions of greenhouse gases: Sensitivity studies

and application to halocarbons, *Atmos. Chem. Phys.*, *9*(5), 1597–1620, doi:10.5194/acp-9-1597-2009, 2009.

Stohl, A., J. Kim, S. Li, S. O'Doherty, J. Mühle, P.K. Salameh, T. Saito, M.K. Vollmer, D. Wan, R.F. Weiss, B. Yao, Y. Yokouchi, and L.X. Zhou, Hydrochlorofluorocarbon and hydrofluorocarbon emissions in East Asia determined by inverse modeling, *Atmos. Chem. Phys.*, *10*(8), 3545–3560, doi:10.5194/acp-10-3545-2010, 2010.

Stolarski, R.S., A.R. Douglass, and S.E. Strahan, Using satellite measurements of N_2O to remove dynamical variability from HCl measurements, *Atmos. Chem. Phys.*, *18*(8), 5691–5697, doi:10.5194/acp-18-5691-2018, 2018.

Sturges, W.T., D.E. Oram, J.C. Laube, C.E. Reeves, M.J. Newland, C. Hogan, P. Martinerie, E. Witrant, C.A.M. Brenninkmeijer, T.J. Schuck, and P.J. Fraser, Emissions halted of the potent greenhouse gas SF_5CF_3, *Atmos. Chem. Phys.*, *12*(8), 3653–3658, doi:10.5194/acp-12-3653-2012, 2012.

Sulbaek Andersen, M.P., S.P. Sander, O.J. Nielsen, D.S. Wagner, T.J. Sanford, and T.J. Wallington, Inhalation anaesthetics and climate change, *Brit. J. Anaesth.*, *105*(6), 760–766, doi:10.1093/bja/aeq259, 2010.

Sulbaek Andersen, M.P., O.J. Nielsen, B. Karpichev, T.J. Wallington, and S.P. Sander, Atmospheric chemistry of isoflurane, desflurane, and sevoflurane: Kinetics and mechanisms of reactions with chlorine atoms and OH radicals and global warming potentials, *J. Phys. Chem. A*, *116*(24), 5806-5820, doi:10.1021/jp2077598, 2012.

Tegtmeier, S., K. Krüger, B. Quack, E.L. Atlas, I. Pisso, A. Stohl, and X. Yang, Emission and transport of bromocarbons: From the West Pacific ocean into the stratosphere, *Atmos. Chem. Phys.*, *12*(22), 10633–10648, doi:10.5194/acp-12-10633-2012, 2012.

Tegtmeier, S., K. Krüger, B. Quack, E. Atlas, D.R. Blake, H. Boenisch, A. Engel, H. Hepach, R. Hossaini, M.A. Navarro, S. Raimund, S. Sala, Q. Shi, and F. Ziska, The contribution of oceanic methyl iodide to stratospheric iodine, *Atmos. Chem. Phys.*, *13*(23), 11869-11886, doi:10.5194/acp-13-11869-2013, 2013.

Tegtmeier, S., F. Ziska, I. Pisso, B. Quack, G.J.M. Velders, X. Yang, and K. Krüger, Oceanic bromoform emissions weighted by their ozone depletion potential, *Atmos. Chem. Phys.*, *15*(23), 13647–13663, doi:10.5194/acp-15-13647-2015, 2015.

Thompson, R.L., K. Ishijima, E. Saikawa, M. Corazza, U. Karstens, P.K. Patra, P. Bergamaschi, F. Chevallier, E. Dlugokencky, R.G. Prinn, R.F. Weiss, S. O'Doherty, P.J. Fraser, L.P. Steele, P.B. Krummel, A. Vermeulen, Y. Tohjima, A. Jordan, L. Haszpra, M. Steinbacher, S. Van der Laan, T. Aalto, F. Meinhardt, M.E. Popa, J. Moncrieff, and P. Bousquet, TransCom N_2O model inter-comparison - Part 2: Atmospheric inversion estimates of N_2O emissions, *Atmos. Chem. Phys.*, *14*(12), 6177–6194, doi:10.5194/acp-14-6177-2014, 2014.

Thornton, B.F., A. Horst, D. Carrizo, and H. Holmstrand, Methyl chloride and methyl bromide emissions from baking: An unrecognized anthropogenic source, *Sci. Total Environ., 551*, 327–333, doi:10.1016/j.scitotenv.2016.01.213, 2016.

Toon, G.C., J.F.L. Blavier, and K. Sung, Atmospheric Carbonyl Sulphide (OCS) measured remotely by FTIR solar absorption spectrometry, *Atmos. Chem. Phys.*, *2017*, 1–37, doi:10.5194/acp-2017-404, 2017.

Trudinger, C.M., P.J. Fraser, D.M. Etheridge, W.T. Sturges, M.K. Vollmer, M. Rigby, P. Martinerie, J. Mühle, D.R. Worton, P.B. Krummel, L.P. Steele, B.R. Miller, J. Laube, F.S. Mani, P.J. Rayner, C.M. Harth, E. Witrant, T. Blunier, J. Schwander, S. O'Doherty, and M. Battle, Atmospheric abundance and global emissions of perfluorocarbons CF_4, C_2F_6 and C_3F_8 since 1800 inferred from ice core, firn, air archive and in situ measurements, *Atmos. Chem. Phys.*, *16*(18), 11,733–11,754, doi:10.5194/acp-16-11733-2016, 2016.

Turner, A.J., C. Frankenbergb, P.O. Wennberg, and D.J. Jacob, Ambiguity in the causes for decadal trends in atmospheric methane and hydroxyl, *Proc. Natl. Acad. Sci.*, *114*(21), 5367–5372, doi:10.1073/pnas.1616020114, 2017.

Umezawa, T., A.K. Baker, C.A.M. Brenninkmeijer, A. Zahn, D.E. Oram, and P.F.J. van Velthoven, Methyl chloride as a tracer of tropical tropospheric air in the lowermost stratosphere inferred from IAGOS-CARIBIC passenger aircraft measurements, *J. Geophys. Res. Atmos.*, *120*(23), doi:10.1002/2015JD023729, 2015.

UNEP (United Nations Environment Programme), *Report of the Methyl Bromide Technical Options Committee*, United Nations Environment Programme,

Ozone Secretariat, Nairobi, Kenya, 2006.

UNEP (United Nations Environment Programme), *2010 Report Of The Halons Technical Options Committee*, 187 pp., United Nations Environment Programme, Ozone Secretariat, Nairobi, Kenya, 2011.

UNEP (United Nations Environment Programme), *2014 Report of the Methyl Bromide Technical Options Committee,* edited by M. Pizano, I. Porter, and M. Besri, Nairobi, Kenya, 2014a.

UNEP (United Nations Environment Programme), *2014 Report Of The Halons Technical Options Committee*, United Nations Environment Programme, Ozone Secretariat, Nairobi, Kenya, 2014b.

UNEP(United Nations Environment Programme), Ozone Secretariat Country Data Centre (https://ozone.unep.org/countries/data), Nairobi, Kenya, 2017.

Valeri, M., F. Barbara, C. Boone, S. Ceccherini, M. Gai, G. Maucher, P. Raspollini, M. Ridolfi, L. Sgheri, G. Wetzel, and N. Zoppetti, CCl_4 distribution derived from MIPAS ESA v7 data: Intercomparisons, trend, and lifetime estimation, *Atmos. Chem. Phys.*, *17*(16), 10143–10162, doi:10.5194/acp-17-10143-2017, 2017.

van der A, R.J., B. Mijling, J. Ding, M.E. Koukouli, F. Liu, Q. Li, H. Mao, and N. Theys, Cleaning up the air: Effectiveness of air quality policy for SO_2 and NOx emissions in China, *Atmos. Chem. Phys.*, *17*(3), 1775–1789, doi:10.5194/acp-17-1775-2017, 2017.

Velders, G.J.M., and J.S. Daniel, Uncertainty analysis of projections of ozone-depleting substances: Mixing ratios, EESC, ODPs, and GWPs, *Atmos. Chem. Phys.*, *14*(6), 2757–2776, doi:10.5194/acp-14-2757-2014, 2014.

Vogt, R., P.J. Crutzen, and R. Sander, A mechanism for halogen release from sea-salt aerosol in the remote marine boundary layer, *Nature*, *383*, 327–330, doi:10.1038/383327a0, 1996.

Volkamer, R., S. Baidar, T.L. Campos, S. Coburn, J.P. DiGangi, B. Dix, E.W. Eloranta, T.K. Koenig, B. Morley, I. Ortega, B.R. Pierce, M. Reeves, R. Sinreich, S. Wang, M.A. Zondlo, and P.A. Romashkin, Aircraft measurements of BrO, IO, glyoxal, NO_2, H_2O, O_2-O_2 and aerosol extinction profiles in the tropics: comparison with aircraft-/ship-based in situ and lidar measurements, *Atmos. Meas. Tech.*, *8*(5), 2121–2148, doi:10.5194/amt-8-2121-2015, 2015.

Vollmer, M.K., L.X. Zhou, B.R. Greally, S. Henne, B. Yao, S. Reimann, F. Stordal, D.M. Cunnold, X.C. Zhang, M. Maione, F. Zhang, J. Huang, and P.G. Simmonds, Emissions of ozone-depleting halocarbons from China, *Geophys. Res. Lett.*, *36*, doi:10.1029/2009GL038659, 2009.

Vollmer, M.K., S. Reimann, M. Hill, and D. Brunner, First observations of the fourth generation synthetic halocarbons HFC-1234yf, HFC-1234ze(E), and HCFC-1233zd(E) in the atmosphere, *Environ. Sci. Technol.*, *49*(5), 2703–2708, doi:10.1021/es505123x, 2015a.

Vollmer, M.K., M. Rigby, J.C. Laube, S. Henne, T.S. Rhee, L.J. Gooch, A. Wenger, D. Young, L.P. Steele, R.L. Langenfelds, C.A.M. Brenninkmeijer, J.L. Wang, C.F. Ou-Yang, S.A. Wyss, M. Hill, D.E. Oram, P.B. Krummel, F. Schoenenberger, C. Zellweger, P.J. Fraser, W.T. Sturges, S. O'Doherty, and S. Reimann, Abrupt reversal in emissions and atmospheric abundance of HCFC-133a (C_3FCH_2Cl), *Geophys. Res. Lett.*, *42*(20), 8702–8710, doi:10.1002/2015GL065846, 2015b.

Vollmer, M.K., T.S. Rhee, M. Rigby, D. Hofstetter, M. Hill, F. Schoenenberger, and S. Reimann, Modern inhalation anesthetics: Potent greenhouse gases in the global atmosphere, *Geophys. Res. Lett.*, *42*(5), 1606–1611, doi:10.1002/2014GL062785, 2015c.

Vollmer, M.K., J. Mühle, C.M. Trudinger, M. Rigby, S.A. Montzka, C.M. Harth, B.R. Miller, S. Henne, P.B. Krummel, B.D. Hall, D. Young, J. Kim, J. Arduini, A. Wenger, B Yao., S. Reimann., S. O'Doherty, M. Maione, D.M. Etheridge, S. Li, D.P. Verdonik, S. Park, G.S. Dutton, L.P. Steele, C.P. Lunder, T.S. Rhee, O. Hermansen, N. Schmidbauer , R.H.J. Wang, M. Hill, P.K. Salameh, R.L. Langenfelds, Z. L.X. Zhou, T. Blunier, J. Schwander, J.W. Elkins, J.H. Butler, P.G. Simmonds, R.F. Weiss, R.G. Prinn, and P.J. Fraser, Atmospheric histories and global emissions of halons H-1211 ($CBrClF_2$), H-1301 ($CBrF_3$), and H-2402 ($CBrF_2CBrF_2$), *J. Geophys. Res. Atmos.*, *121*, 3663–3686, doi:10.1002/2015JD0024488, 2016.

Vollmer, M.K., D. Young, C.M. Trudinger, J. Mühle, S. Henne, M. Rigby, S. Park, S. Li, M. Guillevic, B. Mitrevski, C.M. Harth, B.R. Miller, S.Reimann, B. Yao, L.P. Steele, S.A. Wyss, C.R. Lunder, J. Arduini, A. McCulloch, S. Wu, T.S. Rhee, R.H.J. Wang, P.K. Salameh, O. Hermansen, M. Hill, R.L. Lan-

genfelds, D. Ivy, S. O'Doherty, P.B. Krummel, M. Maione, D.M. Etheridge, L. Zhou, P.J. Fraser, R.G. Prinn, R.F. Weiss, and P.G. Simmonds, Atmospheric histories and emissions of the chlorofluorocarbons CFC-13 ($CClF_3$), ΣCFC-114 ($C_2Cl_2F_4$), and CFC-115 (C_2ClF_5), *Atmos. Chem. Phys.*, *18*, 979–1002, doi:10.5194/acp-18-979-2018, 2018.

von Hobe, M., J.U. Grooß, G. Günther, P. Konopka, I. Gensch, M. Krämer, N. Spelten, A. Afchine, C. Schiller, A. Ulanovsky, N. Sitnikov, G. Shur, V. Yushkov, F. Ravegnani, F. Cairo, A. Roiger, C. Voigt, H. Schlager, R. Weigel, W. Frey, S. Borrmann, R. Müller, and F. Stroh, Evidence for heterogeneous chlorine activation in the tropical UTLS, *Atmos. Chem. Phys.*, *11*(1), 241–256, doi:10.5194/acp-11-241-2011, 2011.

Wagner-Riddle, C., K.A. Congreves, D. Abalos, A.A. Berg, S.E. Brown, J.T. Ambadan, X.P. Gao, and M. Tenuta, Globally important nitrous oxide emissions from croplands induced by freeze-thaw cycles, *Nat. Geosci.*, *10*(4), 279–283, doi:10.1038/Ngeo2907, 2017.

Wahner, A., A.R. Ravishankara, S.P. Sander, and R.R. Friedl, Absorption cross-section of BrO between 312 and 385 nm at 298 and 223 K, *Chem. Phys. Lett.*, *152*, 507–510, 1988.

Wales, P.A., R.J. Salawitch, J.M. Nicely, D.C. Anderson, T.P. Canty, S. Baidar, B. Dix, T.K. Koenig, R. Volkamer, D. Chen, L.G. Huey, D.J. Tanner, C.A. Quevas, R.P. Fernandez, D.E. Kainnison, J.-F. Lamarque, A. Saiz-Lopez, E.L. Atlas, S.R. Hall, M.A. Navarro, L.L. Pan, S.M. Schauffler, M. Stell, S. Tilmes, K. Ullmann, A.J. Weinheimer, H. Akiyoshi, M.P. Chipperfield, M. Deushi, S.S. Dhomse, W. Feng, P. Graf, R. Hossaini, P. Jöckel, E. Mancini, M. Michou, O. Morgenstern, L.D. Oman, G. Pitari, D.A. Plummer, L.E. Revell, E. Rozanov, D. Saint-Martin, R.Schofield, A. Stenke, K.A. Stone, D. Visioni, Y. Yamashita, G. Zeng, Stratospheric injection of brominated very short-lived substances: Aircraft observations in the Western Pacific and representation in global models, *J. Geophys. Res.*, doi:10.1029/2017JD027978, 2018.

Wamsley, P.R., J.W. Elkins, D.W. Fahey, G.S. Dutton, C.M. Volk, R.C. Myers, S.A. Montzka, J.H. Butler, A.D. Clarke, P.J. Fraser, L.P. Steele, M.P. Lucarelli, E.L. Atlas, S.M. Schauffler, D.R. Blake, F.S. Rowland, W.T. Sturges, J.M. Lee, S.A. Penkett, A. Engel, R.M. Stimpfle, K.R. Chan, D.K. Weisenstein, M.K.W. Ko, and R.J. Salawitch, Distribution of halon-1211 in the upper troposphere and lower stratosphere and the 1994 total bromine budget, *J. Geophys. Res. Atmos.*, *103*(D1), 1513–1526, doi:10.1029/97JD02466, 1998.

Wang, C., M. Shao, D.K. Huang, S.H. Lu, L.M. Zeng, M. Hu, and Q. Zhang, Estimating halocarbon emissions using measured ratio relative to tracers in China, *Atmos. Environ., 89*, 816–826, doi:10.1016/j.atmosenv.2014.03.025, 2014.

Wang, S., J.A. Schmidt, S. Baidar, S. Coburn, B. Dix, T.K. Koenig, E. Apel, D. Bowdalo, T.L. Campos, E. Eloranta, M.J. Evans, J.P. DiGangi, M.A. Zondlo, R.-S. Gao, J.A. Haggerty, S.R. Hall, R.S. Hornbrook, D. Jacob, B. Morley, B. Pierce, M. Reeves, P. Romashkin, A. ter Schure, and R. Volkamer, Active and widespread halogen chemistry in the tropical and subtropical free troposphere, *Proc. Natl. Acad. Sci.*, *112*(30), 9281–9286, doi:10.1073/pnas.1505142112, 2015a.

Wang, Z.Y., H.H. Yan, X.K. Fang, L.Y. Gao, Z.H. Zhai, J.X. Hu, B.Y. Zhang, and J.B. Zhang, Past, present, and future emissions of HCFC-141b in China, *Atmos. Environ., 109*, 228–233, doi:10.1016/j.atmosenv.2015.03.019, 2015b.

Warwick, N.J., J.A. Pyle, G.D. Carver, X. Yang, N.H. Savage, F.M. O'Connor, and R.A. Cox, Global modeling of biogenic bromocarbons, *J. Geophys. Res. Atmos.*, *111*(D24), doi:10.1029/2006jd007264, 2006.

Weinberg, I., E. Bahlmann, T. Eckhardt, W. Michaelis, and R. Seifert, A halocarbon survey from a seagrass dominated subtropical lagoon, Ria Formosa (Portugal): flux pattern and isotopic composition, *Biogeosci.*, *12*(6), 1697–1711, doi:10.5194/bg-12-1697-2015, 2015.

Weiss, R.F., J. Mühle, P.K. Salameh, and C.M. Harth, Nitrogen trifluoride in the global atmosphere, *Geophys. Res. Lett.*, *35*(20), doi:10.1029/2008GL035913, 2008.

Werner, B., J. Stutz, M. Spolaor, L. Scalone, R. Raecke, J. Festa, S.F. Colosimo, R. Cheung, C. Tsai, R. Hossaini, M.P. Chipperfield, G.S. Taverna, W. Feng, J.W. Elkins, D.W. Fahey, R.-S. Gao, E.J. Hintsa, T.D. Thornberry, F.L. Moore, M.A. Navarro, E. Atlas, B.C. Daube, J. Pittman, S. Wofsy, and K. Pfeilsticker, Probing the subtropical lowermost stratosphere and the tropical upper troposphere

and tropopause layer for inorganic bromine, *Atmos. Chem. Phys.*, *17*(2), 1161–1186, doi:10.5194/acp-17-1161-2017, 2017.

Wilmouth, D.M., T.F. Hanisco, N.M. Donahue, and J.G. Anderson, Fourier Transform Ultraviolet Spectroscopy of the A 2Π3/2 ← X 2Π3/2 Transition of BrO, *J. Phys. Chem. A*, *103*(45), 8935–8945, doi:10.1021/jp991651o, 1999.

Wisher, A., D.E. Oram, J.C. Laube, G.P. Mills, P. van Velthoven, A. Zahn, and C.A.M. Brenninkmeijer, Very short-lived bromomethanes measured by the CARIBIC observatory over the North Atlantic, Africa and Southeast Asia during 2009–2013, *Atmos. Chem. Phys.*, *14*(7), 3557–3570, doi:10.5194/acp-14-3557-2014, 2014.

Wofsy, S.C., and HIPPO Science Team and Cooperating Modellers, and Satellite Teams, HIAPER Pole-to-Pole Observations (HIPPO): Fine-grained, global-scale measurements of climatically important atmospheric gases and aerosols, *Philos. Trans. Roy. Soc. A*, *369*(1943), 2073–2086, doi:10.1098/rsta.2010.0313, 2011.

Wolf, J., G.R. Asrar, and T.O. West, Revised methane emissions factors and spatially distributed annual carbon fluxes for global livestock, *Carbon Balance Manag.*, *12*(1), 16, doi:10.1186/s13021-017-0084-y, 2017.

Worden, J.R., A.A. Bloom, S. Pandey, Z. Jiang, H.M. Worden, T.W. Walker, S. Houweling, and T. Röckmann, Reduced biomass burning emissions reconcile conflicting estimates of the post-2006 atmospheric methane budget, *Nat. Commun.*, *8*(1), 2227, doi:10.1038/s41467-017-02246-0, 2017.

Worton, D.R., W.T. Sturges, J. Schwander, R. Mulvaney, J.M. Barnola, and J. Chappellaz, 20th century trends and budget implications of chloroform and related tri-and dihalomethanes inferred from firn air, *Atmos. Chem. Phys.*, *6*, 2847–2863, doi:10.5194/acp-6-2847-2006, 2006.

Xiao, X., Optimal estimation of the surface fluxes of chloromethanes using a 3-D global atmospheric chemical transport model, Ph.D. thesis, Massachusetts Institute of Technology, Cambridge, Massachusetts, 2008.

Yang, G.P., B. Yang, X.L. Lu, H.B. Ding, and Z. He, Spatio-temporal variations of sea surface halocarbon concentrations and fluxes from southern Yellow Sea, *Biogeochem.*, *121*(2), 369–388, doi:10.1007/s10533-014-0007-x, 2014.

Yang, J.S., Bromoform in the effluents of a nuclear power plant: A potential tracer of coastal water masses, *J. Hydrobiologia*, *464*(1-3), 99-105, 2001.

Yang, M.M., Y. Wang, J.M. Chen, H.L. Li, and Y.H. Li, Aromatic Hydrocarbons and Halocarbons at a Mountaintop in Southern China, *Aerosol Air Qual. Res.*, *16*(3), 478–491, doi:10.4209/aaqr.2015.03.0197, 2016.

Yang, X., R.A. Cox, N.J. Warwick, J.A. Pyle, G.D. Carver, F.M. O'Connor, and N.H. Savage, Tropospheric bromine chemistry and its impacts on ozone: A model study, *J. Geophys. Res., 110*(D23), doi:10.1029/2005JD006244, 2005.

Yokouchi, Y., F. Hasebe, M. Fujiwara, H. Takashima, M. Shiotani, N. Nishi, Y. Kanaya, S. Hashimoto, P. Fraser, D. Toom-Sauntry, H. Mukai, and Y. Nojiri, Correlations and emission ratios among bromoform, dibromochloromethane, and dibromomethane in the atmosphere, *J. Geophys. Res. Atmos.*, *110*(D23), doi:10.1029/2005JD006303, 2005.

Yokouchi, Y., S. Taguchi, T. Saito, Y. Tohjima, H. Tanimoto, and H. Mukai, High frequency measurements of HFCs at a remote site in east Asia and their implications for Chinese emissions, *Geophys. Res. Lett.*, *33*(21), doi:10.1029/2006GL026403, 2006.

Yokouchi, Y., Y. Nojiri, D. Toom-Sauntry, P. Fraser, Y. Inuzuka, H. Tanimoto, H. Nara, R. Murakami, and H. Mukai, Long-term variation of atmospheric methyl iodide and its link to global environmental change, *Geophys. Res. Lett.*, *39*(23), L23805, doi:10.1029/2012GL053695, 2012.

Yokouchi, Y., A. Takenaka, Y. Miyazaki, K. Kawamura, and T. Hiura, Emission of methyl chloride from a fern growing in subtropical, temperate, and cool-temperate climate zones, *J. Geophys. Res. Biogeosci.*, *120*(6), 1142–1149, doi:10.1002/2015JG002994, 2015.

Yokouchi, Y., T. Saito, J.Y. Zeng, H. Mukai, and S. Montzka, Seasonal variation of bromocarbons at Hateruma Island, Japan: Implications for global sources, *J. Atmos. Chem.*, *74*(2), 171–185, doi:10.1007/s10874-016-9333-9, 2017.

Yuan, D., G.P. Yang, and Z. He, Spatio-temporal distributions of chlorofluorocarbons and methyl iodide in the Changjiang (Yangtze River) estuary and its adjacent marine area, *Marine Poll.*

Bull., *103*(1-2), 247–259, doi:10.1016/j.marpolbul.2015.12.012, 2016.

Zander, R., E. Mahieu, P. Demoulin, P. Duchatelet, G. Roland, C. Servais, M. De Maziere, S. Reimann, and C.P. Rinsland, Our changing atmosphere: Evidence based on long-term infrared solar observations at the Jungfraujoch since 1950, *Sci. Total Environ.*, *391*(2-3), 184–195, doi:10.1016/j.scitotenv.2007.10.018, 2008.

Zhang, J.K., Y. Sun, F.K. Wu, J. Sun, and Y.S. Wang, The characteristics, seasonal variation and source apportionment of VOCs at Gongga Mountain, China, *Atmos. Environ., 88*, 297–305, doi:10.1016/j.atmosenv.2013.03.036, 2014.

Ziska, F., B. Quack, K. Abrahamsson, S.D. Archer, E. Atlas, T. Bell, J.H. Butler, L.J. Carpenter, C.E. Jones, N.R.P. Harris, H. Hepach, K.G. Heumann, C. Hughes, J. Kuss, K. Kruger, P. Liss, R.M. Moore, A. Orlikowska, S. Raimund, C.E. Reeves, W. Reifenhauser, A.D. Robinson, C. Schall, T. Tanhua, S. Tegtmeier, S. Turner, L. Wang, D. Wallace, J. Williams, H. Yamamoto, S. Yvon-Lewis, and Y. Yokouchi, Global sea-to-air flux climatology for bromoform, dibromomethane and methyl iodide, *Atmos. Chem. Phys.*, *13*(17), 8915–8934, doi:10.5194/acp-13-8915-2013, 2013.

Ziska, F., B. Quack, S. Tegtmeier, I. Stemmler, and K. Krüger, Future emissions of marine halogenated very-short lived substances under climate change, *J. Atmos. Chem.*, *74*(2), 245–260, doi:10.1007/s10874-016-9355-3, 2017.

Chapter 2

Hydrofluorocarbons (HFCs)

Lead Authors
S.A. Montzka
G.J.M. Velders

Coauthors
P.B. Krummel
J. Mühle
V.L. Orkin
S. Park
N. Shah
H. Walter-Terrinoni

Contributors
P. Bernath
C. Boone
L. Hu
M.J. Kurylo
E. Leedham Elvidge
M. Maione
B.R. Miller
S. O'Doherty
M. Rigby
I.J. Simpson
M.K. Vollmer
R.F. Weiss

Review Editors
L.J.M. Kuijpers
W.T. Sturges

Cover photo: Plenary discussion during the 28th Meeting of the Parties to the Montreal Protocol in Kigali, Rwanda. The historic Kigali Amendment was adopted on 15 October 2016 limiting future production and consumption of hydrofluorocarbons. Photo: Courtesy of IISD/ENB | Kiara Worth at http://enb.iisd.org/ozone/resumed-oewg38-mop28/11oct.html

CHAPTER 2

HYDROFLUOROCARBONS (HFCS)

CONTENTS

Chapter 2

Hydrofluorocarbons (HFCs)

SCIENTIFIC SUMMARY

The Montreal Protocol is an international agreement designed to heal the ozone layer. It outlines schedules for the phase-out of ozone-depleting substances (ODSs) such as chlorofluorocarbons (CFCs), hydrochlorofluorocarbons (HCFCs), chlorinated solvents, halons, and methyl bromide. As a result of this phase-out, alternative chemicals and procedures were developed by industry for use in many applications including refrigeration, air-conditioning, foam-blowing, electronics, medicine, agriculture, and fire protection. Hydrofluorocarbons (HFCs) were used as ODS alternatives in many of these applications because they were suitable substitutes and they do not contain ozone-depleting chlorine or bromine; in addition, most HFCs have smaller climate impacts per molecule than the most widely used ODSs they replaced. Long-lived HFCs, CFCs, and HCFCs, however, are all potent greenhouse gases, and concerns were raised that uncontrolled future use of HFCs would lead to substantial climate warming.

As a result of these concerns, HFCs were included as one group of greenhouse gases for which emissions controls were adopted by the 1997 Kyoto Protocol under the 1992 United Nations Framework Convention on Climate Change (UNFCCC). Consequently, developed countries (those listed in Annex I to this Convention, or "Annex I" Parties) supply annual emission estimates of HFCs to the UNFCCC.

Since the Kyoto Protocol only specified limits on the sum of all controlled greenhouse gases, emissions of HFCs were not explicitly controlled. However, following the Kyoto Protocol, some countries enacted additional controls specifically limiting HFC use based on their global warming potentials (GWPs). Ultimately the Kigali Amendment to the Montreal Protocol was agreed upon in 2016, and this Amendment supplies schedules for limiting the production and consumption of specific HFCs. Although the radiative forcing supplied by HFCs is currently small, this Amendment was designed to ensure that the radiative forcing from HFCs will not grow uncontrollably in the future. The Kigali Amendment will come into force at the start of 2019. HFC concentrations are currently monitored through atmospheric measurements. All HFCs with large abundances are monitored, as are most with small abundances.

Most HFCs that are emitted to the atmosphere are intentionally produced for use in a variety of applications that were once dependent on ODSs. An exception is HFC-23, which is emitted to the atmosphere primarily as a by-product of HCFC-22 production. HFC-23 is also unique in that it has a substantially longer atmospheric lifetime and higher GWP than nearly all other HFCs. As a result, the Kigali Amendment includes different control schedules for HFC-23 production than for other HFCs. To date, HFC-23 emissions have been partially abated in developed countries through regulations or voluntary measures and in developing countries with assistance from the UNFCCC's Clean Development Mechanism (CDM).

- **Atmospheric mole fractions of most currently measured HFCs are increasing in the global atmosphere at accelerating rates, consistent with expectations based on the ongoing transition away from use of ozone-depleting substances.**
    - **HFC-134a remained the most abundant HFC in the atmosphere**, reaching a global mean surface mole fraction of nearly 90 ppt in 2016. Its rate of increase averaged 5.6 ± 0.2 ppt yr^{-1} (7.3 ± 0.2 % yr^{-1}) during 2012–2016, which is about 0.6 ppt yr^{-1} faster than the mean increase for 2008–2012.
    - **The next four most abundant HFCs in 2016 were HFC-23, HFC-125, HFC-143a, and HFC-32.** Their global mean surface mole fractions in 2016 were 28.9 ppt, 20.4 ppt, 19.2 ppt, and 11.9 ppt, respectively. Mole fractions of these HFCs increased during 2012–2016 by an average of 1.0 ppt yr^{-1} for

HFC-23, 2.1 ppt yr^{-1} for HFC-125, 1.5 ppt yr^{-1} for HFC-143a, and 1.6 ppt yr^{-1} for HFC-32; for all of these gases, these rates are faster than the average growth rates reported for 2008–2012 in the last Assessment.

- **Global mole fractions of most HFCs increased through 2016 at rates similar to those projected in the baseline scenario of the last Assessment**, despite the fact that this scenario was created nearly a decade ago. The HFCs for which mole fractions are increasing substantially less rapidly than originally projected include HFC-152a, HFC-365mfc, and HFC-245fa.

- **Radiative forcing from measured HFCs continues to increase; it currently amounts to 1% of the total forcing from all long-lived greenhouse gases.** The radiative forcing arising from measured atmospheric mole fractions of HFCs totaled 0.030 W m^{-2} in 2016, up by 36% from 0.022 W m^{-2} in 2012; HFC-134a accounted for 47% of this forcing in 2016, while the next largest contributors were HFC-23 (17%), HFC-125 (15%) and HFC-143a (10%). Total HFC radiative forcing in 2016 accounted for ~10% of the 0.33 W m^{-2} supplied by ODSs (**see Chapter 1**), and 1.0% of the 3 W m^{-2} supplied by all long-lived GHGs combined, including CO_2, CH_4, N_2O, ODSs and HFCs.

- **Global emissions of nearly all measured HFCs continue to increase; they currently amount to ~1.5% of total emissions from all long-lived greenhouse gases (CO_2, CH_4, N_2O, and long-lived halocarbons) in CO_2-equivalent emissions.** As derived from atmospheric observations, total emissions of HFCs increased by 23% from 2012 to 2016 and summed to 0.88 (± 0.07) $GtCO_2$-eq yr^{-1} in 2016; this increase outpaced decreases in CO_2-eq emissions from CFCs and HCFCs. These CO_2-eq HFC emissions stem primarily from four gases: HFC-134a (34% of total), HFC-125 (24% of total), HFC-23 (18% of total), and HFC-143a (16% of total). HFC CO_2-eq emissions were comparable to those of CFCs (0.8 ± 0.3 $GtCO_2$-eq yr^{-1}) and HCFCs (0.76 ± 0.11 $GtCO_2$-eq yr^{-1}) in 2016.

- **HFC emissions estimated from the combination of inventory reporting and atmospheric observations indicate that the HFC emissions originate from both developed and developing countries**. Large differences are observed between global total emissions derived from atmospheric observations and the totals reported to the UNFCCC. These differences arise primarily because only developed (Annex I) countries are obligated to report HFC emissions to the UNFCCC. When summed, these reported HFC emissions account for less than half of the global total inferred from observations (as CO_2-eq emissions).

- **Annual global emissions of HFC-23 derived from atmospheric measurements have varied substantially in recent years. This variability is mostly consistent with expectations based on reported HCFC-22 production and reported and estimated HFC-23 emissions.** This long-lived HFC is emitted to the atmosphere primarily as a by-product of HCFC-22 production. HFC-23 emissions, after reaching a low of ~10 Gg yr^{-1} (0.13 $GtCO_2$-eq yr^{-1}) 2009–2010, owing in part to destruction in developing countries facilitated under the UNFCCC's Clean Development Mechanism (CDM), increased and subsequently peaked at ~14 Gg yr^{-1} (0.18 $GtCO_2$-eq yr^{-1}) in 2013–2014. The mean global emission rate over 2013–2014 is slightly higher than that derived for 2005–2006, when CDM-facilitated destruction had yet to be fully implemented. Global emissions estimated from observations for 2015 and 2016 dropped below the 2013–2014 peak; emissions in 2016 were 12.3 ± 0.7 Gg yr^{-1} (0.16 $GtCO_2$-eq yr^{-1}), or approximately 2 Gg yr^{-1} below those in 2014. New controls put in place under the Kigali Amendment mandate HFC-23 by-product destruction, to the extent practicable, beginning in 2020. These controls are expected to limit future emissions and thus slow or reverse atmospheric concentration increases of this potent greenhouse gas.

- **Some next-generation substitute chemicals with very low GWPs (unsaturated HCFCs and unsaturated HFCs, also known as hydrofluoroolefins, or HFOs) have now been detected in ambient air, consistent with the transition to these compounds being underway**. Unsaturated HFCs and HCFCs are replacement compounds for some long-lived HCFCs and HFCs. Because unsaturated HFCs have short atmospheric

lifetimes (days) and GWPs typically less than 1 they are not included as controlled substances in the Kigali Amendment to the Montreal Protocol. Very low mole fractions (typically below 1 ppt) of two unsaturated HFCs (HFC-1234yf and HFC-1234ze(E)) have been measured at a continental background European site.

- **Global adherence to the HFC phasedown schedule of the 2016 Kigali Amendment to the Montreal Protocol would substantially reduce future projected global HFC emissions.** Emissions are projected to peak before 2040 and decline to less than 1 $GtCO_2$-eq yr^{-1} by 2100. Only marginal increases are projected for CO_2-eq emissions of the low-GWP alternatives despite substantial projected increases in their emission mass. The estimated avoided HFC emissions as a result of this Amendment is 2.8–4.1 $GtCO_2$-eq yr^{-1} emissions by 2050 and 5.6–8.7 $GtCO_2$-eq yr^{-1} by 2100. For comparison, total CH_4 emissions in 2100 are projected to be 7.0 and 25 $GtCO_2$-eq yr^{-1} in the RCP-6.0 and RCP-8.5 scenarios, respectively, and total N_2O emissions in 2100 are projected to be 5.0 and 7.0 $GtCO_2$-eq yr^{-1} in these same scenarios.

- **The 2016 Kigali Amendment to the Montreal Protocol, assuming global compliance, is expected to reduce future radiative forcing due to HFCs by about 50% in 2050 compared to the forcing from HFCs in the baseline scenario.** Currently (in 2016), HFCs account for a forcing of 0.025 W m^{-2} not including 0.005 from HFC-23; forcing from these HFCs was projected to increase up to 0.25 W m^{-2} by 2050 (excluding a contribution from HFC-23) with projected increased use and emissions in the absence of controls. With the adoption of the Kigali Amendment, a phasedown schedule has been agreed for HFC production and consumption in developed and developing countries under the Montreal Protocol. With global adherence to this Amendment in combination with national and regional regulations that were already in place in, e.g., Europe, the USA, and Japan, along with additional recent controls in other countries, future radiative forcing from HFCs is projected to reach 0.13 W m^{-2} by 2050 (excluding HFC-23), or about half the forcing projected in the absence of these controls.

- **The Kigali Amendment and national and regional regulations are projected to reduce global average warming in 2100 due to HFCs from 0.3–0.5°C in a baseline scenario to less than 0.1°C.** If the global production of HFCs were to cease in 2020, the surface temperature contribution of HFC emissions would stay below 0.02°C for the whole 21st century. The magnitude of the avoided temperature increase due to the provisions of the Kigali Amendment is substantial in the context of the 2015 UNFCCC Paris Agreement, which aims to limit global temperature rise to well below 2.0°C above pre-industrial levels and to pursue further efforts to limit the temperature increase to 1.5°C.

- **Improvements in energy efficiency in refrigeration and air-conditioning equipment during the transition to low-GWP alternative refrigerants can potentially double the climate benefits of the HFC phasedown of the Kigali Amendment.** The conversion from equipment using HFC refrigerants with high GWPs to refrigerants with lower GWPs, which will most likely result from the Kigali Amendment, provides an opportunity to consider other technological improvements that offer additional climate benefits. The total climate impact related to refrigerant use and associated emissions is not only associated with the radiative properties and lifetime of the refrigerant, but also with CO_2 emissions resulting from the energy used by the equipment over its entire life cycle. The use of a refrigerant with a lower GWP than the currently-used HFCs (i.e., following the Kigali Amendment) offers the opportunity to redesign equipment and improve its energy efficiency. For example, a 30% improvement in the energy efficiency of the global stock of mini-split air conditioners (the most widely used air conditioning systems today) in 2030 would provide a climate benefit comparable to replacing the mix of current HFC refrigerants commonly used in this application (which have GWPs averaging about 2,000) with a mix of alternatives that have GWPs of less than about 5 to about 700. An energy efficiency improvement of 30% is estimated to be technically and economically feasible and cost-effective in many economies.

- **Some HFCs degrade in the environment to produce trifluoroacetic acid (TFA), a persistent toxic chemical. The environmental effects of this source of TFA are currently small and are expected to remain negligible over the next decades.** Atmospheric degradation of HFC-1234yf, a replacement compound for some long-lived HCFCs and HFCs, produces TFA. Potential impacts beyond a few decades of this TFA source could require future evaluation due to the environmental persistence of TFA and uncertainty in future emissions of HFC-1234yf and other HFCs that produce TFA upon degradation.

- **Improvements in the understanding of reaction rates have been incorporated into revised lifetime estimates for saturated and unsaturated HFCs.** Most of these changes are small, although lifetimes of HFC-245cb ($CF_3CF_2CH_3$), octafluorocyclopentene (*cyclo*-$CF{=}C_4F_7$-), *(E)*-HFC-1214yc (*(E)*-$CF_3CH{=}CHCF_3$), and *(E)*-HFC-1438mzz (*(E)*-$CF_3CH{=}CHC_2F_5$) were noticeably changed because the relevant reaction rate information has become available for the first time. Lifetimes for a few HFCs considered here remain estimates based on either analogy with similar compounds or structure–activity relationships.

CHAPTER 2

HYDROFLUOROCARBONS (HFCS)

2.1 SUMMARY OF FINDINGS FROM PREVIOUS ASSESSMENTS

Information pertaining to HFCs was included in Chapter 1 and Chapter 5 of the 2014 Assessment report. That Assessment reported that tropospheric mole fractions of HFCs continued to increase, adding to the warming of Earth's climate. The radiative forcing supplied by HFCs in 2012, the last year assessed in that report, was small compared to that from CFCs and HCFCs, but projections suggested the potential for significant increases in HFC-associated warming in the future. Furthermore, the documented climate benefits achieved by the Montreal Protocol through reductions in the production and emission of CFCs and HCFCs might be substantially offset if emissions of the substitute HFCs were allowed to continue unabated. The sum of HFC emissions in 2012 had reached 0.72 ± 0.05 $GtCO_2$-equivalent yr^{-1} (for CO_2-eq considering a 100-yr time horizon) after having increased by nearly 7% yr^{-1} from 2008 to 2012. This total was similar to the magnitude of emissions from CFCs (0.9 ± 0.3 $GtCO_2$ yr^{-1}) and HCFCs (0.78 ± 0.10 $GtCO_2$-eq yr^{-1}) for 2012. This total included a global emission of approximately 0.16 ± 0.01 $GtCO_2$-eq yr^{-1} from the potent greenhouse gas HFC-23 (CHF_3), which is emitted primarily as a by-product during the production of HCFC-22 and not as a result of use in industrial applications and products. Although global emissions of this HFC had decreased from 2005 to 2009, they increased after 2009 and by 2012 were ~40% above the minimum recorded for 2009.

2.2 INTRODUCTION

Hydrofluorocarbons have been used in refrigeration, air conditioning, thermal insulating foam, and miscellaneous applications since the 1990s, replacing the CFCs and HCFCs that were traditionally used in these applications. The first widespread HFC use was of HFC-134a beginning in the early 1990s, as a substitute for CFC-12 in mobile air conditioning (Montzka et al., 1996; Oram et al., 1996; Andersen et al., 2013). Within a decade most mobile air conditioners used this HFC (Papasavva et al., 2009), and this remains true today. With the global CFC phase-out in 2010 and the ongoing HCFC phase-out, the use of HFCs has increased substantially, not only for various refrigeration and air conditioning applications, but also as foam blowing agents, as medical aerosols, and to a lesser extent as cleaning, etching, and fire-fighting agents. As was true for ODSs, emissions of HFCs follow production and consumption with a delay of months to decades, depending on the type of application in which the HFCs are used.

HFCs do not contain ozone-depleting chlorine or bromine, but are potent greenhouse gases (Harris and Wuebbles et al., 2014). To ensure that radiative forcing from the substitute HFCs does not offset climate gains provided by the Montreal Protocol phase-out of CFCs and HCFCs, Parties to the Montreal Protocol agreed to an Amendment in Kigali, Rwanda in October 2016, to include some HFCs as controlled substances and to phase down their production and consumption (GWP-weighted) in coming decades (UNEP, 2016a; for a list of controlled HFCs, see footnote to **Table 2-1** [or HFCs with asterisks in **Table 2-2**]). The Kigali Amendment will enter into force on January 1, 2019, since more than 20 Parties have ratified, accepted, or approved this Amendment. Limiting climate change is not the primary goal of the 1985 Vienna Convention for the Protection of the Ozone layer, but climate change considerations are addressed in this Convention. Limiting climate change was also a contributing factor to the 2007 Adjustment of the Montreal Protocol for an accelerated HCFC phase-out (UNEP, 2007).

Since 1997, HFCs have been included in the Kyoto Protocol to the United Nations Framework Convention on Climate Change as one group among many greenhouse gases for which emissions overall should be reduced by up to 8% in the period 2008–2012 by some developed countries relative to baseline levels (mostly the year 1990). HFC emissions were not directly controlled by the Kyoto Protocol, however, since controls applied to the sum of all greenhouse gases.

Table 2-1. Base level and phasedown schedule for production and consumption of controlled HFCs[1], expressed as CO_2-eq, under the Kigali Amendment to the Montreal Protocol (UNEP, 2016a).

	Developing Countries*		Developed Countries*
	A5 Group 1 Countries[2]	A5 Group 2 Countries[3]	Non-A5 Countries[4]
Base level:	Average HFCs 2020–2022 plus 65% of HCFC base level	Average HFCs 2024–2026 plus 65% of HCFC base level	Average HFCs 2011–2013 plus 15% of HCFC base level[5]
Freeze:	2024	2028	-
1st step:	2029: 10% reduction	2032: 10% reduction	2019: 10% reduction
2nd step:	2035: 30% reduction	2037: 20% reduction	2024: 40% reduction
3rd step:	2040: 50% reduction	2042: 30% reduction	2029: 70% reduction
4th step:			2034: 80% reduction
Plateau:	2045: 80% reduction	2047: 85% reduction	2036: 85% reduction

* In the UNFCCC, developing countries are referred to as "non-Annex I" countries, and developed countries are referred to as "Annex I countries."

[1] HFCs controlled by the Kigali Amendment include: HFC-23, HFC-134, HFC-134a, HFC-143, HFC-245fa, HFC-365mfc, HFC-227ea, HFC-236cb, HFC-236ea, HFC-236fa, HFC-245ca, HFC-43-10mee, HFC-32, HFC-125, HFC-143a, HFC-41, HFC-152, HFC-152a. This Amendment also specifies that emissions of HFC-23 generated during production of HCFCs or HFCs be destroyed to the extent practicable beginning January 2020.

[2] Group 1: Article 5 (developing) countries not part of Group 2. Article 5 of the Montreal Protocol.

[3] Group 2: Article 5 (developing) countries: Bahrain, India, the Islamic Republic of Iran, Iraq, Kuwait, Oman, Pakistan, Qatar, Saudi Arabia and the United Arab Emirates.

[4] Non-A5 countries, also referred to as A2 countries (developed). Article 2J of the Montreal Protocol.

[5] For Belarus, Russian Federation, Kazakhstan, Tajikistan, Uzbekistan 25% HCFC component of base level and different initial two steps (1) 5% reduction in 2020 and (2) 35% reduction in 2025. Article 2J of the Montreal Protocol.

Note: Non-Article 5 (developed) and UNFCCC Annex I (developed) countries include all EU-28 countries, Australia, Belarus, Canada, Iceland, Japan, Liechtenstein, Monaco, New Zealand, Norway, the Russian Federation, Switzerland, Ukraine, and the USA. Further, non-Article 5 countries are Andorra, Azerbaijan, the Holy See, Israel, Kazakhstan, San Marino, Tajikistan, and Uzbekistan. Turkey is solely an Annex I country.

In previous Assessments, observed concentrations, derived emissions, and atmospheric effects of HFCs were discussed together with those of ozone-depleting substances. In this Assessment, issues related to HFCs are covered in this separate chapter, with the main foci being updating observations of HFC atmospheric mole fractions and understanding what they imply for emissions on global to regional scales; determining if the observed mole fraction changes are consistent with expectations and emission magnitudes reported to UNFCCC and elsewhere; quantifying the associated climate- and environmental-related effects arising from HFC emissions and associated atmospheric changes; and considering how these influences might change in the future, especially in light of controls on HFC production and consumption specified in the Kigali Amendment to the Montreal Protocol.

With respect to climate influences, increases in radiative forcing resulting from recent increases in HFC atmospheric mole fractions are documented in this chapter. For HFCs with lifetimes longer than 1 year (e.g., those that are well mixed in the lower atmosphere), radiative forcing is linearly proportional to global mean surface mole fractions and the efficiency of the particular HFC in trapping outgoing terrestrial radiation (i.e., its radiative efficiency; see **Table A-1**). Total emission rates are also derived from these global-scale observations with consideration of lifetime-determined loss rates (**Table 2-2**) in an inverse budget analysis performed with box models (**see Box 1-1**). Emission magnitudes are considered here on a mass basis and with mass emissions weighted by 100-yr GWPs to enable an assessment of integrated radiative forcing supplied by an HFC emission relative to an equivalent CO_2 emission over a 100-year time horizon

(CO_2-eq emissions, **Figure 2-1; Table 2-2**). GWPs associated with a 20-year time horizon are also tabulated, but they are not considered further in this chapter.

Determining if atmospheric concentrations of ODSs or HFCs are changing as expected has always been an important remit for authors of this Assessment. For HFCs, this task is facilitated by the reporting by developed countries (Annex I Parties) to the UNFCCC of national emission magnitudes derived from country-specific analyses of production, imports, sales, exports, and use. For HFC-23, emission estimates for developing countries derived from information collected by the Montreal Protocol's Multilateral Fund[1] are also considered. In this chapter, these inventory-based HFC emission totals are compared to national and global totals derived from atmospheric data on both a compound-specific and aggregate basis. Factors contributing to differences between UNFCCC-reported and observation-derived emissions for individual HFCs are discussed; they include inaccuracies in methods for deriving emissions from atmospheric mole fraction measurements, inaccuracies in emissions reporting by Annex I (developed) countries, reporting emissions as aggregated mixes of HFCs or HFCs and perfluorocarbons (PFCs), and the potential for significant emissions from non-Annex I (developing) countries not obligated to report their HFC emissions to the UNFCCC[2]. Recent inverse analyses of atmospheric measurements made in the USA and Europe provide a means to assess UNFCCC inventory reporting from these regions. Similar observations from other regions are also considered and add to our understanding of emission magnitudes from countries not required to report emissions to the UNFCCC.

In **Chapter 6** of this Assessment, as in related chapters in previous Assessments, scenarios are constructed for ODS concentrations in the future as part of the Assessment itself, since such scenarios are usually not available in the literature. Also consistent with previous Assessments, new HFC scenarios have not been constructed here or in **Chapter 6**. Instead, projections of HFC use and emission magnitudes are taken from the literature and are discussed in this chapter. These scenarios were created based on data available at the time they were created, and they have not been updated to consider the most recent observational data. As a result, discrepancies between projected and observed HFC concentrations and emissions are apparent in years after the scenarios were created.

Discussions in this chapter extend those presented in specific chapters of the most recent Intergovernmental Panel on Climate Change (IPCC) assessment report (Hartmann, Tank, and Rusticucci et al., 2013; Myhre and Shindell et al., 2013) by updating observed mixing ratios and associated radiative forcings through 2016. Laboratory kinetic data published since that time are considered in providing updated lifetime estimates. Furthermore, the scenarios discussed here are based on more recent analyses, whereas those in the IPCC report are from the Representative Concentration Pathways (RCPs) scenarios (Meinshausen et al., 2011).

2.3 ATMOSPHERIC OBSERVATIONS AND DERIVED EMISSION ESTIMATES

2.3.1 Global HFC Concentration Changes and Estimated Emissions on Regional to Global Scales

Atmospheric abundances of HFCs are regularly measured throughout the global atmosphere by a few surface-based measurement networks at remote sites, by aircraft, and by satellite-borne instruments (**Figure 2-2** and **Table 2-3**). These results imply substantial emissions of HFCs on a global scale, when independently-determined atmospheric removal rates (or lifetimes) are considered (**Figure 2-1; Table 2-2**). Emission rates are also derived on regional spatial scales using trace-gas measurements in non-remote regions (see **Box 1-1**). These results can provide estimates of region-specific HFC emissions that are independent of inventory-based approaches used in reporting to UNFCCC. Regional emission rates are typically derived from data analysis methods such as inter-species correlation and inverse modeling. Regional emission estimates typically have larger relative uncertainties

[1] The Multilateral Fund (MLF) for the implementation of the Montreal Protocol was established in 1991 to assist developing countries (Article 5 countries) to meet their Montreal Protocol commitments. Financial contributions to the MLF come from developed countries (non-Article 5 countries).

[2] UNFCCC Parties listed in Annex I (as amended in 1998) include all the developed countries in the Organization for Economic Cooperation and Development, it also includes Economies in Transition, which are characterized as national economies in the process of changing from a planned economic system to a market economy. By default, other countries are referred to as non-Annex I countries.

Table 2-2. Trace gas lifetimes for selected halocarbons: partially fluorinated alkanes, partially fluorinated olefins, and perfluorinated olefins.

Industrial Designation of Chemical Name	Chemical Formula	Total Lifetime,[a] WMO-2014 (years, unless otherwise indicated)	Total Lifetime,[b,c] this Assessment (years, unless otherwise indicated)	Radiative Efficiency[d] (W m^{-2} ppb^{-1})	GWP at Given Time Horizon, this Assessment		Notes
					20-yr	100-yr	
Hydrofluorocarbons							
HFC-23 **	CHF_3	228	228	0.18	11,085	12,690	1
HFC-32 **	CH_2F_2	5.4	5.4	0.11	2,530	705	1
HFC-41 **	CH_3F	2.8	2.8	0.02	430	116	1
HFC-125 **	CHF_2CF_3	31	30	0.23	6,280	3,450	1
HFC-134 **	CHF_2CHF_2	9.7	10	0.19	3,625	1,135	1
HFC-134a **	CH_2FCF_3	14	14	0.16	3,810	1,360	1
HFC-143 **	CH_2FCHF_2	3.5	3.6	0.13	1,250	340	1
HFC-143a **	CH_3CF_3	51	51	0.16	7,050	5,080	1
HFC-152 **	CH_2FCH_2F	146 days (114–335 days)	172 days	0.04	64	17	1, b
HFC-152a **	CH_3CHF_2	1.6	1.6	0.10	545	148	1
HFC-161	CH_3CH_2F	66 days (51–154 days)	80 days	0.02	20	6	1, b
HFC-227ca	$CF_3CF_2CHF_2$	28.2	30	0.27	5,260	2,865	2
HFC-227ea **	CF_3CHFCF_3	36	36	0.26	5,250	3,140	1
HFC-236cb **	$CH_2FCF_2CF_3$	~13	13.4	0.23	3,540	1,235	1
HFC-236ea **	CHF_2CHFCF_3	11.0	11.4	0.30	4,190	1,370	1
HFC-236fa **	$CF_3CH_2CF_3$	222	213	0.24	6,785	7,680	1
HFC-245ca **	$CH_2FCF_2CHF_2$	6.5	6.6	0.24	2,530	720	1
HFC-245cb	$CF_3CF_2CH_3$	47.1	39.9	0.24	6,340	4,000	1
HFC-245ea	$CHF_2CHFCHF_2$	3.2	3.3	0.16	880	240	1
HFC-245eb	$CH_2FCHFCF_3$	3.2	3.2	0.20	1,070	290	1
HFC-245fa **	$CHF_2CH_2CF_3$	7.9	7.9	0.24	2,980	880	1
HFC-263fb	$CH_3CH_2CF_3$	1.1	1.1	0.10	250	68	1
HFC-272ca	$CH_3CF_2CH_3$	2.6	~9	0.07	1,580	480	3
HFC-281ea	CH_3CHFCH_3	23 days (19-46 days)	27 days	–	–	–	1, b
HFC-329p	$CHF_2CF_2CF_2CF_3$	~30	32	0.31	4,720	2,630	4
HFC-338pcc	$CHF_2CF_2CF_2CHF_2$	12.9	13.5	–	–	–	1
HFC-356mcf	$CH_2FCH_2CF_2CF_3$	1.2	1.2	–	–	–	1

HFC-356mff	$CF_3CH_2CH_2CF_3$	8.3	8.5	–	–	–	1
HFC-365mfc **	$CH_3CF_2CH_2CF_3$	8.7	8.9	0.22	2,660	810	1
HFC-43-10mee **	$CF_3CHFCHF$-CF_2CF_3	16.1	17.0	0.359	3,770	1,470	1, 19
HFC-458mfcf	$CF_3CH_2CF_2CH_2CF_3$	22.9	23.8	–	–	–	1
HFC-55-10mcff	$CF_3CF_2CH_2CH_2$-CF_2CF_3	7.5	7.7	–	–	–	1
HFC-52-13p	$CHF_2CF_2CF_2$-$CF_2CF_2CF_3$	32.7	35.2	–	–	–	5
HFC-72-17p	$CHF_2(CF_2)_6CF_3$		23.8	–	–	–	6
Fluorinated Olefinic HFCs – indicated here as HFOs							
HFO-1123	$CHF=CF_2$	–	1.5 days	0.0019	<1	<1	1, 7, b
HFO-1132a	$CH_2=CF_2$	4.0 days (3.0–5.7 days)	4.6 days	0.004	<1	<1	1, b
HFO-1141	$CH_2=CHF$	2.1 days (1.4–3.1 days)	2.5 days	0.002	<1	<1	1, b
HFO-1234ye*(E)*	*(E)*-$CHF=CFCHF_2$	<5 days	<5 days	–	–	–	8, b
HFO-1234ye*(Z)*	*(Z)*-$CHF=CFCHF_2$	<5 days	<5 days	–	–	–	8, b
HFO-1225ye*(E)*	*(E)*-$CF_3CF=CHF$	4.9 days (3.7–6.9 days)	5.7 days	0.01	<1	<1	1, b
HFO-1225ye*(Z)*	*(Z)*-$CF_3CF=CHF$	8.5 days (6.2–12 days)	10 days	0.02	<1	<1	1, b
HFO-1234ze*(E)*	*(E)*-$CF_3CH=CHF$	16.4 days (12.8-24 days)	19 days	0.04	4	<1	1, b
HFO-1234ze*(Z)*	*(Z)*-$CF_3CH=CHF$	10.0 days	10 days	0.02	1	<1	9, b
HFO-1234yf	$CF_3CF=CH_2$	10.5 days (8.4–16 days)	12 days	0.02	1	<1	1
HFO-1261zf	$CH_2FCH=CH_2$	0.7 days (0.5–1.0 days)	0.8 days	–	–	–	1, b
HFO-1234yc	$CF_2=CFCH_2F$	~2 days	~2 days	–	–	–	8, b
HFO-1225zc	$CF_2=CHCF_3$	~2 days	~2 days	–	–	–	8, b
HFO-1234zc	$CF_2=CHCHF_2$	<5 days	<5 days	–	–	–	8, b
HFO-1336mzz*(E)*	*(E)*-$CF_3CH=CHCF_3$	(16–30 days)	122 days	0.13	60	16	10, b
HFO-1336mzz*(Z)*	*(Z)*-$CF_3CH=CHCF_3$	(16–32 days)	27 days	0.07	6	2	1, b
HFO-1243zf	$CHCF_3=CH_2$	7.6 days (5.5–11 days)	9 days	0.01	<1	<1	1, b
HFO-1345fz	$CHC_2F_5=CH_2$	7.9 days (5.8–11.4 days)	9 days	0.01	<1	<1	1, b
HFO-1438mzz*(E)*	*(E)*-$CF_3CH=CHCF_2CF_3$	(16–30 days)	~122 days	–	–	–	11, b
HFO-1447fz	$CH_2=CHCF_2CF_2CF_3$	(6–10 days)	9 days	–	–	–	12, b

HFO-1549fz 1H,1H,2H-Perfluorohexene	$CHC_4F_9=CH_2$	7.6 days	9 days	0.03	<1	<1	13, b
HFO-174-13fz 1H,1H,2H-Perfluoro-1-octene	$CHC_6F_{13}=CH_2$	7.6 days	9 days	0.03	<1	<1	13, b
HFO-194-17fz 1H,1H,2H-Heptadecafluoro-1-decene	$CHC_8F_{17}=CH_2$	7.6 days	9 days	0.03	<1	<1	13, b
HFO-1438ezy*(E)*	*(E)*-$(CF_3)_2CFCH=CHF$		43 days	0.34	42	11	14, b
Perfluorinated Olefins							
PFC-1114	$CF_2=CF_2$	1.1 days (0.7–1.6 days)	1.2 days	0.002	<1	<1	1, b
PFC-1216	$CF_3CF=CF_2$	4.9 days (3.3–7.1 days)	5.5 days	0.01	<1	<1	1, b
Perfluoro buta-1,3-diene	$CF_2=CFCF=CF_2$	1.1 days (0.8–1.6 days)	1.1 days	0.003	<1	<1	1, b
Perfluoro but-1-ene	$CF_3CF_2CF=CF_2$	6 days	6 days	0.02	<1	<1	15, b
Perfluorobut-2-ene (isomer blend: 71% *(E)* and 29% *(Z)*)	$CF_3CF=CFCF_3$				4.8	1.3	16
(E)-Perfluro -2-butene	*(E)*-$CF_3CF=CFCF_3$	–	22 days	0.05	3.6	1.0	1, b
(Z)-Perfluro -2-butene	*(Z)*-$CF_3CF=CFCF_3$	–	35 days	0.07	7.8	2.1	1, b
Perfluoro (2-methyl-2-pentene)	$(CF_3)_2C=CFCF_2CF_3$	–	192 days	–	–	–	1, b
Fluorinated Cycloolefins							
3,3,4,4-Tetrafluro-cyclobut-1-ene 1H,2H-Tetrafluro cyclobutene	*cyclo*-$CH=CHCF_2CF_2$-		84 days	0.09	37	10	17, b
2,3,3,4,4-Pentafluoro cyclobut-1-ene 1H-Pentafluoro-cyclobutene	*cyclo*-$CH=CFCF_2CF_2$-		270 days	0.19	214	58	17
Hexafluorocy-clobutene	*cyclo*-$CF=CFCF_2CF_2$-		1.2	0.25	420	110	17

Octafluorocyclo-pentene	*cyclo*-CF=$CFCF_2CF_2CF_2$-	31 days	1.05	0.27	300	82	18

Table Heading Footnotes:

Although the designation HFC is applicable to both saturated and unsaturated chemicals, it is used to refer only to partially fluorinated alkanes in this table. Partially fluorinated unsaturated compounds, hydrofluoroolefins, are designated as HFO in this table for easier identification.

** Those HFCs listed as controlled substances in Annex F of the Kigali Amendment to the Montreal Protocol. Additional reporting requirements were adopted at the 29th Meeting of the Parties of the Montreal Protocol (Decision XXIX/12) on consideration of HFCs not listed as controlled substances. This decision requested that production and consumption of HFCs with GWPs higher than the smallest GWP listed in Annex F also be reported to the Ozone Secretariat for informational purposes.

[a] Total lifetime, τ_{HFC}, reported in the 2014 Assessment (indicated as "WMO-2014"; Carpenter and Reimann et al., 2014).

[b] Lifetimes for VSLSs (values given in days) are calculated relative to the methyl chloroform (MCF) partial lifetime due to reaction with OH with the same procedure that is used for long-lived gases. Local lifetimes for VSLSs will depend on the season and location of the emission. Nevertheless, the characteristic values are within the range of likely lifetimes for an emission between the equator and midlatitudes. More detailed modeling is required to derive VSLS lifetimes associated with emission from a specific region and season. A representative range of local lifetimes taken from the 2014 Assessment (Carpenter and Reimann et al., 2014) (**Tables 1-5** and **1-11**) is given in parentheses where available.

[c] Italicized values indicate estimated lifetimes when no experimental data on OH reactivity is available.

[d] Radiative efficiency values are taken from recommendations given in Hodnebrog et al. (2013) based on a literature review of experimental data and a reanalysis of this information, unless another source is specified in notes to the table.

Lifetime Footnotes:

[1] OH reaction rate constant was taken from JPL Publication 15-10 (Burkholder et al., 2015b).

[2] OH reactivity assumed the same as CHF_2CF_3 (HFC-125).

[3] OH reactivity calculated using the structure activity relationships of DeMore (DeMore, 1996) assuming an *E*/R of 1700 K.

[4] OH reactivity calculated using the room-temperature rate constant reported by Young et al. (2009a) assuming an *E*/R of 1700 K, which is similar to that of CHF_2CF_3.

[5] OH reactivity taken from the IUPAC (Ammann et al., 2017) recommendation.

[6] OH reaction rate constant was taken from Chen et al. (2011).

[7] Radiative metrics calculated using the infrared spectrum from Baasandorj and Burkholder (2016).

[8] No experimental data were available for OH reaction rate constants, so lifetimes were estimated based on reactivity trends of fluorinated ethenes and propenes.

[9] OH reaction rate constant was taken from Zhang et al. (2015).

[10] The atmospheric lifetime and radiative efficiency were calculated using the kinetic and infrared data reported by Baasandorj et al. (2018).

[11] OH reactivity assumed the same as (*E*)-CF_3CH=$CHCF_3$.

[12] OH reactivity assumed the same as CH_2=$CHCF_3$.

[13] OH reactivity was recommended by JPL Publication 15-10 based on the room temperature rate constant reported by Sulbaek and Andersen et al. (2005) assuming *E*/R of -170, which is similar to that of CH_2=$CHCF_3$.

[14] OH reaction rate constant and radiative efficiency values were taken from Papadimitriou and Burkholder (2016).

[15] OH reactivity calculated using the room temperature OH rate constant reported by Young et al. (2009b) assuming *E*/R of -415 K, which is similar to that of CF_3CF=CF_2.

[16] Industrial Perfluorobut-2-ene is a mixture of two stereo-isomers, *(E)*-Perfluoro-2-butene and *(Z)*-Perfluoro-2-butene, with the ratio of ~71% and ~29%, respectively. Atmospheric lifetimes of individual isomers are given in **Table 2-2**.

GWP of the mixture was calculated based on estimated GWPs of individual isomers for each time horizon. The radiative efficiency recommended by Hodnebrog et al. (2013) for CF_3CF=$CFCF_3$ was used to estimate this parameter for each stereo-isomer, after corresponding corrections to account for its dependence upon lifetimes of the individual stereo-isomers.

[17] OH reaction rate constant was taken from Jia et al. (2013). Radiative efficiency was taken from Jia et al. (2013), and lifetime given here includes the correction suggested by Hodnebrog et al. (2013).

[18] OH reaction rate constant was taken from Zhang et al. (2017). Radiative efficiency was taken from Zhang et al. (2017) and lifetime given here includes the correction suggested by Hodnebrog et al. (2013).

[19] Radiative efficiency was taken from Le Bris et al. (2017).

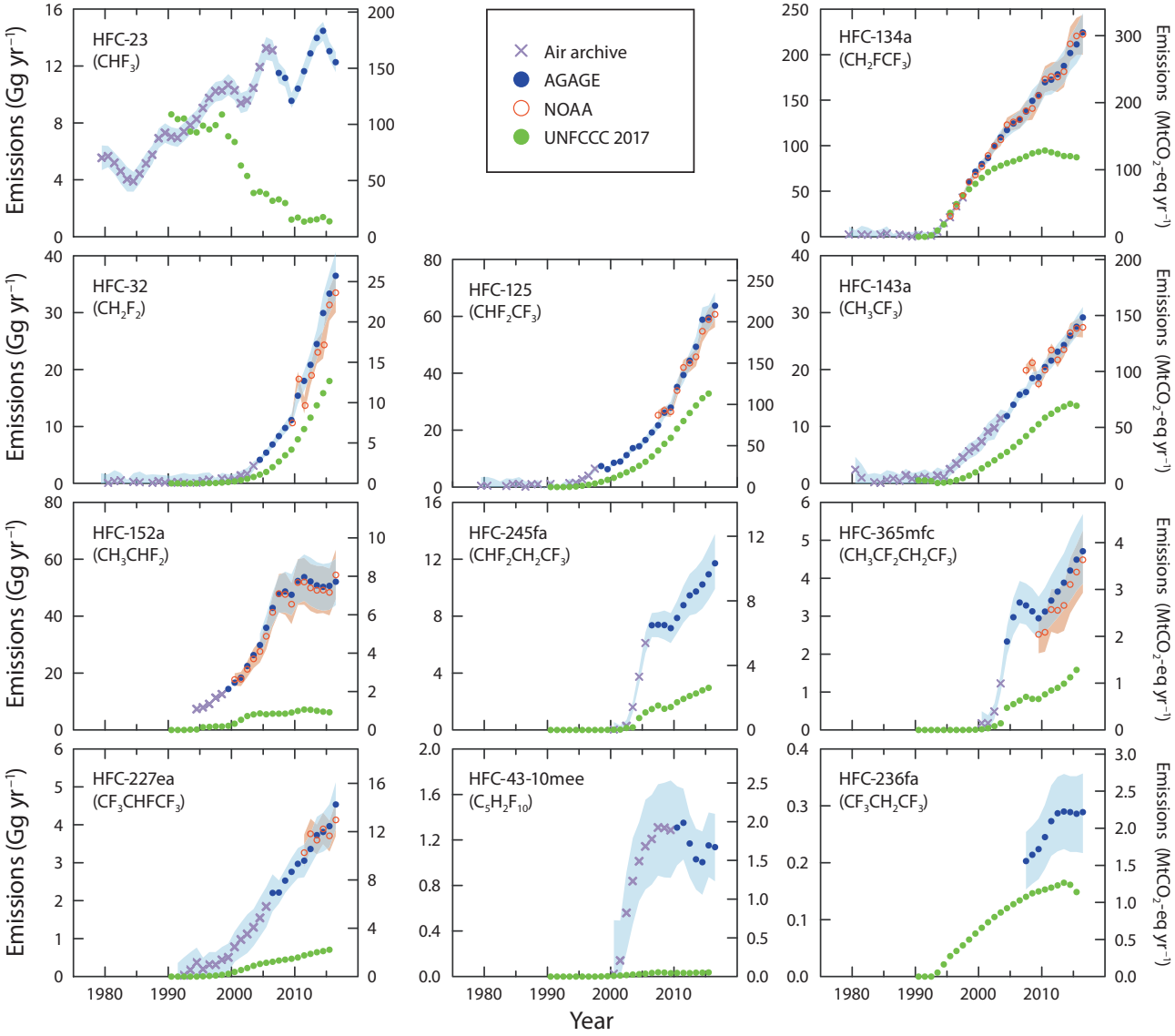

Figure 2-1. Total global emissions estimated from a budget analysis of atmosphere measurements at remote sites (those in **Figure 2-2**) compared to total emissions reported to UNFCCC (2017). Atmospheric measurement-based emissions are derived with a 12-box model and the lifetimes in **Table 2-2**; the methods and model used here are discussed by Rigby et al. (2014). Emissions are presented in units of Gg compound yr^{-1} on the left-hand axis, and the right-hand axis has been scaled by chemical-specific 100-yr GWPs (**Table 2-2**) to indicate emission magnitudes in MtCO$_2$-eq yr^{-1} (1 Mt = 10^{12} g). Shaded regions represent 1 standard deviation in global emissions derived from measured mole fractions and a 12-box model (Rigby et al., 2014). Uncertainties in mole fractions and their model representation are propagated through to the posterior emissions estimates using a Bayesian framework. These uncertainties are augmented by lifetime and calibration scale uncertainties following Rigby et al. (2014). The model uses interannually repeating meteorology and, therefore, errors may be underestimated for periods with large circulation changes, although this will likely affect short-term (e.g., annual) variations more than long-term trends.

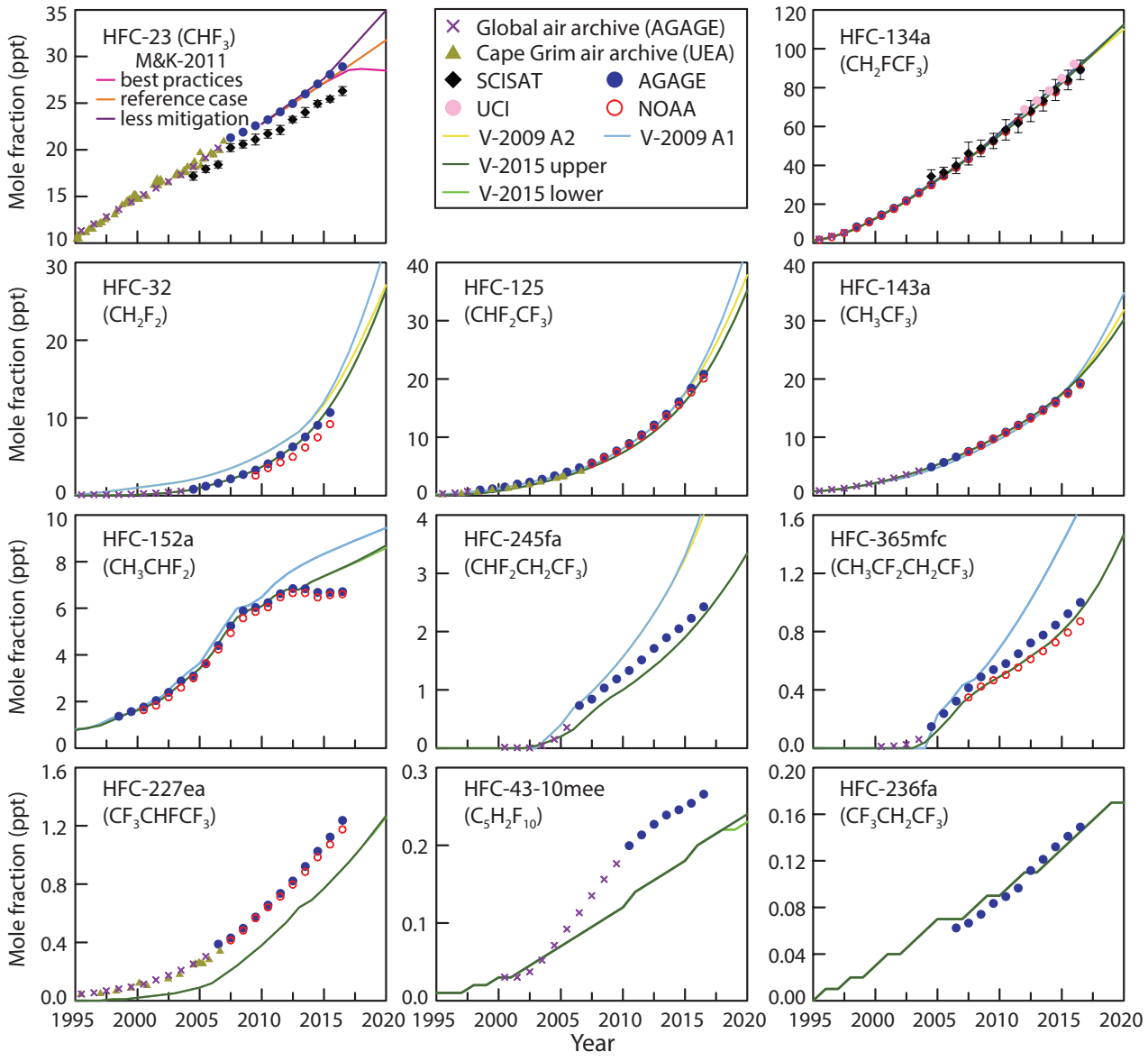

Figure 2-2. Annual mean mole fractions of HFCs and recent projections. Shown are global means estimated from in-situ instrumentation at five remote sites (AGAGE, dark blue filled circles) and independent estimates derived from weekly flasks filled at 8 remote sites (NOAA, open red circles). Global means for HFC-134a from quarterly sampling in the Pacific Basin are also shown (pink filled circles; UCI = the University of California at Irvine; Simpson et al., 2014). Global means derived from air archives in both hemispheres (AGAGE, purple crosses) (Arnold et al., 2014; O'Doherty et al., 2014; Rigby et al., 2014; Simmonds et al., 2016; Simmonds et al., 2018; Vollmer et al., 2011) are calculated using a 12-box model (Cunnold et al., 1983; Rigby et al., 2013). Results reported for the southern hemisphere from analyses of the Cape Grim Air Archive only are also shown (UEA data, khaki triangles; Oram et al., 1998; Leedham Elvidge et al., 2018). Results from satellite absorption retrievals (SCISAT) represent upper troposphere-lower stratosphere means averaged from 60°N to 60°S (black diamonds; Nassar et al., 2006; Harrison et al., 2012). Uncertainties on these satellite retrievals represent statistical variability in the data used in the averaging and do not include any systematic errors. Also shown are projections for global means that were considered in the previous Ozone Assessment (V-2009 = Velders et al., 2009; Carpenter and Reimann et al., 2014) and updated projections based on observations through 2012 (V-2015 = Velders et al., 2015; M&K-2011 = Miller and Kuijpers, 2011). Data are updates to published measurement records (see **Table 2-1** for sources not mentioned here).

Table 2-3. Global surface mean mole fractions of hydrofluorocarbons estimated from ground-based air sampling networks.

Chemical Formula	Common or Industrial Name	Annual Mean Mole Fraction (ppt) 2012	2015	2016	Change (2015–2016) ppt yr^{-1}	% yr^{-1}	Network, Method
CHF_3	HFC-23	24.9	28.1	28.9	0.8	2.9%	AGAGE, in situ (Global)
CH_2F_2	HFC-32	6.28	10.7	12.6	1.9	18%	AGAGE, in situ (Global)
		4.97	9.18	11.2	2.0	22%	NOAA, flasks (Global)
CHF_2CF_3	HFC-125	12.1	18.4	20.8	2.4	13.0%	AGAGE, in situ (Global)
		11.7	17.7	20.1	2.4	13.4%	NOAA, flasks (Global)
CH_2FCF_3	HFC-134a	67.7	83.3	89.3	6.0	7.2%	AGAGE, in situ (Global)
		67.5	83.4	89.6	6.1	7.4%	NOAA, flasks (Global)
		68.9	84.9	92.1	7.2	8.5%	UCI, flasks, (global)
CH_3CF_3	HFC-143a	13.4	17.7	19.3	1.6	9.2%	AGAGE, in situ (Global)
		13.2	17.4	19.0	1.6	9.0%	NOAA, flasks (Global)
CH_3CHF_2	HFC-152a	6.84	6.68	6.72	0.03	0.5%	AGAGE, in situ (Global)
		6.65	6.57	6.61	0.04	0.6%	NOAA, flasks (Global)
$CHF_2CH_2CF_3$	HFC-245fa	1.71	2.23	2.43	0.20	8.9%	AGAGE, in situ (Global)
$CH_3CF_2CH_2CF_3$	HFC-365mfc	0.72	0.92	1.00	0.08	8.4%	AGAGE, in situ (Global)
		0.61	0.79	0.87	0.08	9.9%	NOAA, flasks (Global)
CF_3CHFCF_3	HFC-227ea	0.82	1.12	1.24	0.11	10.2%	AGAGE, in situ (Global)
		0.80	1.07	1.17	0.10	9.6%	NOAA, flasks (Global)
$CF_3(CHF)_2CF_2CF_3$	HFC-43-10mee	0.23	0.25	0.27	0.01	4.6%	AGAGE, in situ (Global)
$CF_3CH_2CF_3$	HFC-236fa	0.11	0.14	0.15	0.01	5.7%	AGAGE, in situ (Global)

Notes:
Stated mole fractions represent independent estimates of global surface means determined by different observational networks at different sampling locations; annual values represent calendar year means. Absolute changes (ppt yr^{-1}) are calculated as the difference in annual means; relative changes (% yr^{-1}) are that same difference relative to the 2015 value. Small differences between values from previous Assessments are due to changes in calibration scale and methods for estimating global mean mole fractions from a limited number of sampling sites. These observations are updated from the following sources: Montzka et al., 1996; Miller et al., 2008; Miller et al., 2010; Vollmer et al., 2011; Arnold et al., 2014; Rigby et al., 2014; Simpson et al., 2014; Montzka et al., 2015; Simmonds et al., 2016, 2017, 2018. They are available at http://agage.mit.edu/ (for AGAGE data); at http://www.esrl.noaa.gov/gmd/dv/site/ (for NOAA data); and at http://ps.uci.edu/~rowlandblake/research_atmos.html (for UCI data). Global mean estimates from AGAGE are calculated using atmospheric data and a 12-box model (Cunnold et al., 1983; Rigby et al., 2013). AGAGE calibrations are as specified in CDIAC (2016) and related primary publications. NOAA-determined values are directly estimated from measurements made at 8 to 12 remote surface sites with cosine-of-latitude weighting.

than global-scale emission estimates. Uncertainties associated with regional-scale inverse analyses, for example, include the inversion setup, the assumed priors, the uncertainty assumed for those priors and for the observations, the geographic extent of the sampling network, and sampling frequency, among other parameters. Furthermore, some emission estimates are derived from observations that have limited spatial coverage and limited sensitivity to emissions across an entire region of interest (countrywide, for example) or incomplete coverage across all seasons. While uncertainties in regional-scale emission estimates would ideally encompass all of these factors, this is often not feasible as this entails estimating uncertainties in parameters with insufficient objective information.

2.3.1.1 HFC-134a (CH_2FCF_3)

HFC-134a remains the most abundant HFC in the global atmosphere and has the largest annual growth rate and emission. The global annual mean mole fraction reached 89.5 ppt in 2016, up from 67.7 ppt in 2012 (AGAGE and NOAA data; UCI results over this period are ~3% higher; **Table 2-3**). The rate of increase averaged 5.6 ± 0.2 ppt yr^{-1} (7.3 ± 0.2% yr^{-1}) during 2012–2016, which is about 0.6 ppt yr^{-1} larger than the

mean increase for 2008–2012, as reported in the last Assessment. This observed increase in global mole fraction is similar to that projected nearly a decade ago (Velders et al., 2009) and more recently (Velders et al., 2015); it is also consistent with the largest increases projected in the Representative Concentration Pathways (RCPs), namely RCP8.5 (**Figure 2-2**; Carpenter and Reimann et al., 2014; Velders et al., 2009; Meinshausen et al., 2011).

Mixing ratios of HFC-134a have been estimated from the ACE-FTS instrument on board SCISAT for recent years (updates to Nassar et al., 2006) using updated absorption cross sections (Harrison, 2015). The upper tropospheric annual means derived for HFC-134a from SCISAT are very consistent with mean mole fractions measured by the surface networks; differences between results from SCISAT and the surface networks are much smaller than the uncertainties associated with the satellite retrievals. Rates of change in HFC-134a mixing ratios determined for 2012–2016 from these independent measurements systems are also consistent, with 7.0 ± 0.8 % yr^{-1} derived from annual changes in SCISAT results, 7.3 ± 0.1 % yr^{-1} derived from NOAA data, and 7.2 ± 0.2 % yr^{-1} derived from AGAGE data (**Figure 2-2**).

Globally, HFC-134a contributed a radiative forcing (RF) of 14.3 mW m^{-2} in 2016. This is the largest radiative forcing contributed by any other HFC or other fluorinated gas (i.e., PFCs, SF_6, SO_2F_2, and NF_3; see **Chapter 1**). The mean rate of increase has been slightly larger over the past 4 years (5.4–5.8 ppt yr^{-1}) than during 2008–2012 (4.9–5.1 ppt yr^{-1}). HFC-134a has been used as a substitute for CFC-12 since the mid-1990s in mobile air conditioning (MAC), in stationary refrigeration and air conditioning, in metered-dose inhalers, and in foam-blowing applications; it has also been used as a fire suppressant and for dry etching. Due to its high GWP (**Table 2-2**), controls on HFC-134a use have been adopted in some sectors in the E.U., USA, Japan, and other countries (see **Section 2.5.1**). Refrigerants with substantially lower GWPs such as HFC-1234yf and HFC-1234ze(E), among others, are starting to replace HFC-134a in various applications (see below) (UNEP, 2017a).

Total global emissions of HFC-134a estimated from a budget analysis of measured mole fractions at remote sites increased nearly linearly from 177 ± 17 Gg yr^{-1} in 2012 to 223 ± 22 Gg yr^{-1} in 2016 (**Figure 2-1**; update from Rigby et al., 2014; Montzka et al., 2015; Simmonds et al., 2017; AGAGE and NOAA data). Global emissions have increased by an average of 10 Gg yr^{-1} since 2008, faster than emissions of any other HFC. Global emissions derived with different modeling frameworks (but these same network data) are consistent with the emissions derived here (Fortems-Cheiney et al., 2015; Lunt et al., 2015; Xiang et al., 2014).

The total global emissions derived for HFC-134a from atmospheric observations are over two times larger than total emissions reported to UNFCCC from Annex I countries (see **Figure 2-3**). Furthermore, this emission gap has become larger over time; the

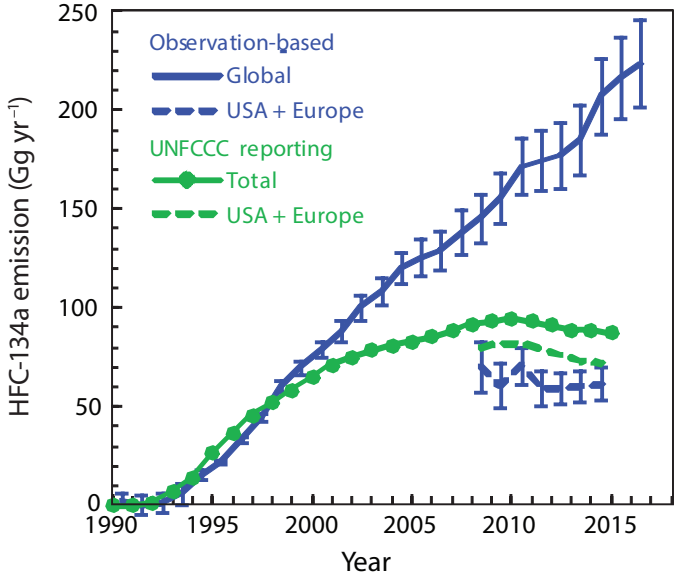

Figure 2-3. A comparison of HFC-134a emission totals reported to UNFCCC (UNFCCC, 2017; green lines) and derived from atmospheric observations (blue lines; from **Figure 2-1**). Totals are indicated as solid lines (total reported for UNFCCC and global total for observation-based). The sum of emissions from the U.S. and Europe are indicated with a dashed green line for UNFCCC reporting and a dashed blue line for the atmospheric measurement-based estimate (from **Figure 2-4** and **Figure 2-5**).

HFC-134a totals reported to UNFCCC have decreased slightly since 2010, in contrast to the increases derived for global total emissions from the atmospheric data (**Figure 2-1** and **Figure 2-3**).

The difference between UNFCCC reporting and atmosphere-based global total emission is not likely from underreporting of emissions from the USA and Europe, the two regions that account for most (~80%) emissions reported to the UNFCCC (**Figure 2-3**). Regional emissions derived from inverse modeling analysis of measurements within the USA and Europe suggest that the inventory-based reporting from these regions is accurate or slightly high (Graziosi et al., 2017; Hu et al., 2017; Say et al., 2016) (**Figure 2-4, Figure 2-5**). A similar conclusion was derived for HFC-134a from all Annex I countries from an inverse modeling analysis of measurements at globally-distributed sites (Lunt et al., 2015). For 2014, emissions of HFC-134a from the USA and Europe summed together were 71 Gg yr^{-1} in UNFCCC reporting, and they were 61 ± 8 Gg yr^{-1} from inversion-based modeling analyses of atmospheric observations. The observation-based emissions derived for the USA totaled 43 ± 6 Gg yr^{-1} (Hu et al., 2017) and for Europe totaled 18 ± 6 yr^{-1} (Graziosi et al., 2017) in 2014. Other inversion-based analyses of atmospheric data in Europe suggest European HFC-134a emissions that are consistent with those derived in Graziosi et al. for 2009 (Keller et al., 2012); they are between 9 and 16 Gg yr^{-1} higher in other years (Brunner et al., 2017 for 2011; and Fortems-Cheiney et al., 2015 for multiple years). Slightly higher European emissions

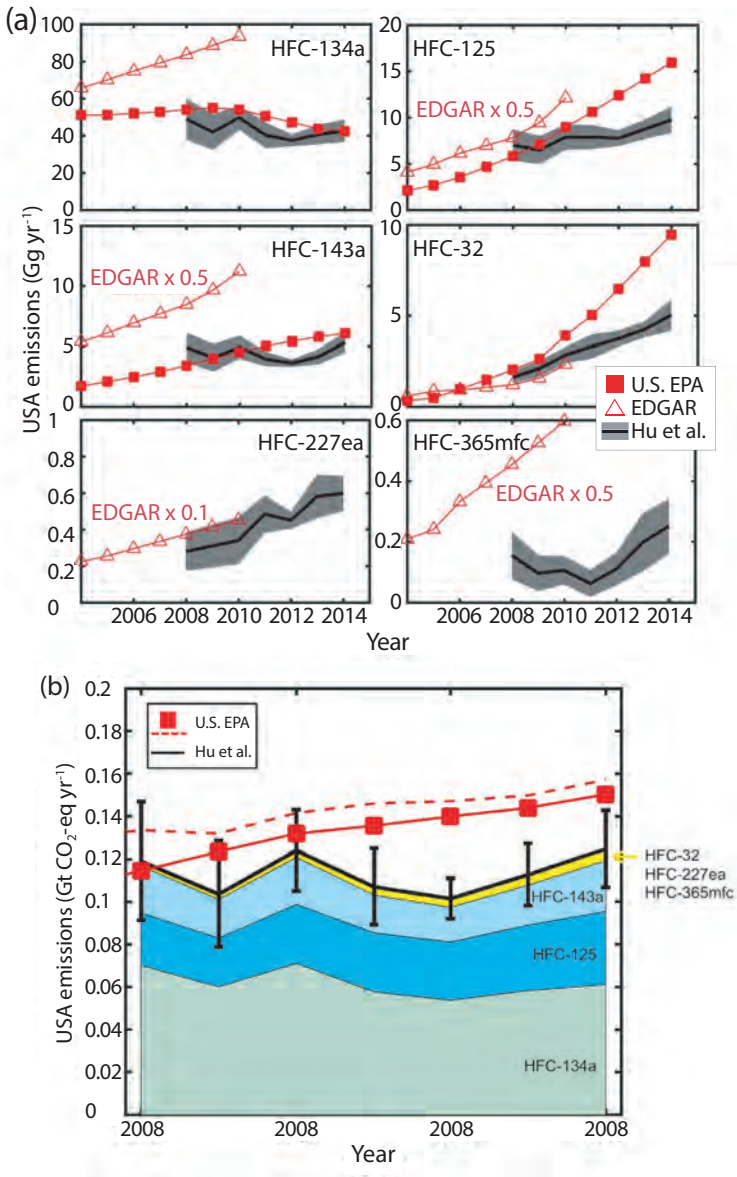

Figure 2-4. USA national HFC emissions estimated from an atmospheric sampling network and from two inventory-based analyses: EDGAR (Emissions Database for Global Atmospheric Research) and U.S. EPA, which is subsequently reposted by UNFCCC (adapted from Hu et al., 2017). a) These six panels show results by compound. b) Aggregated results as Gt CO_2-eq emissions yr^{-1}, with contributions from these six different gases indicated by the different colors. The EPA inventory result for these six gases (solid red line and red-filled symbols in both panels) is shown for comparison, as is the contribution to the inventory totals of additional HFCs not included in the Hu et al., 2017 study (dashed red line). Uncertainties in both panels represent ranges in derived emissions based on multiple inversions, given uncertainties associated with the sampling network, assumed prior emissions, upwind mole fractions (background conditions), transport models, and meteorology.

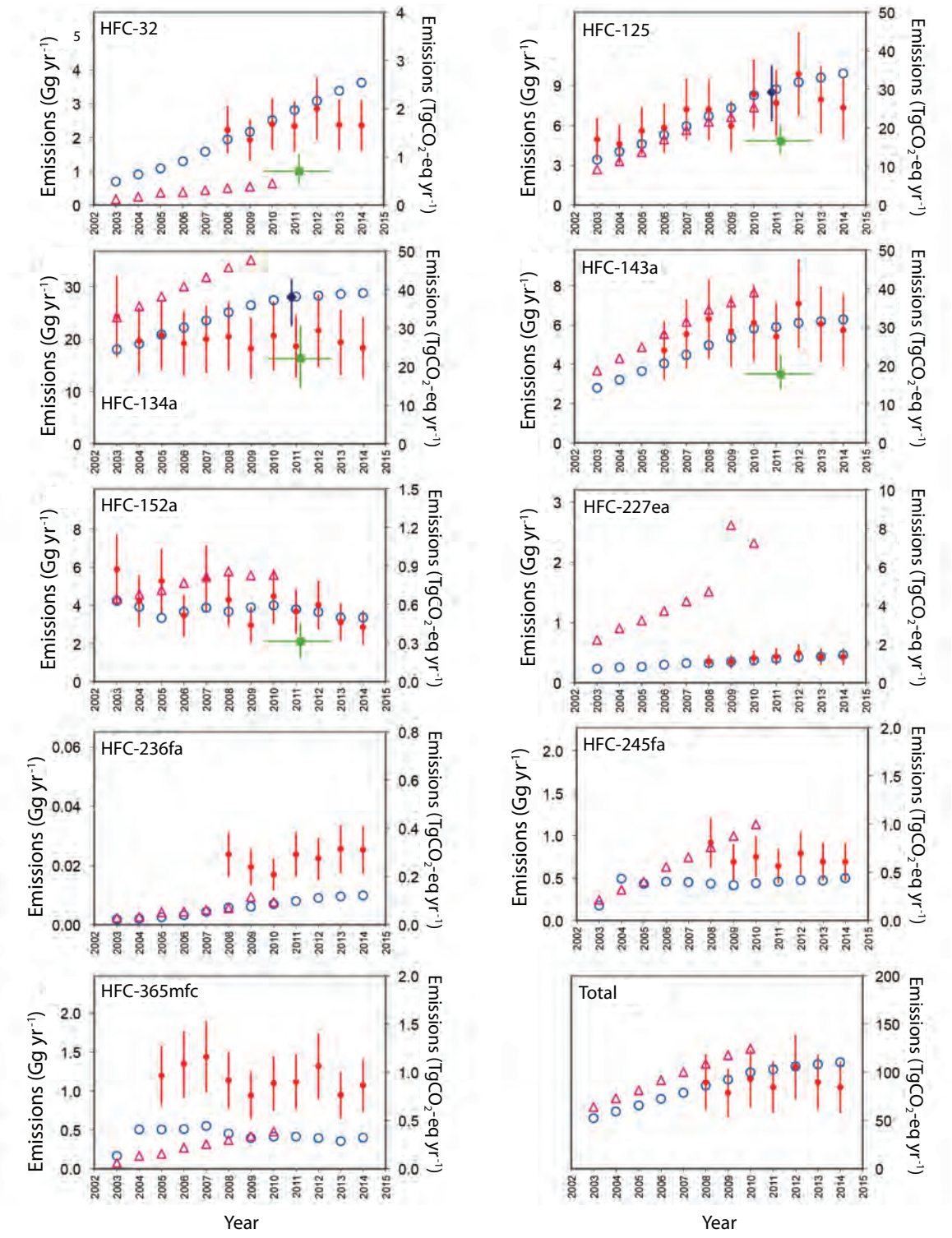

Figure 2-5. Emissions of nine HFCs from the European geographic domain, and related uncertainties, from January 2003 to December 2014. Emissions are given in Gg yr^{-1} (left axis) and in TgCO$_2$-eq yr^{-1} (right axis). The lower right panel (labeled "total") shows aggregated CO$_2$-eq emissions yr^{-1} from the nine HFCs. Emissions derived from atmospheric measurements are given as red filled circles: Graziosi et al. (2017); green filled squares: Lunt et al. (2015); and dark blue filled diamonds: Brunner et al. (2017). Emissions derived from inventories are shown as light blue unfilled circles (UNFCCC) and purple unfilled triangles (EDGAR v4.2 FT2010). Note that Lunt et al. (2015) and Brunner et al. (2017) data are shifted slightly in time for clarity; the Lunt et al. data are a 3-yr average and the Brunner et al. (2017) data refer to a smaller domain. Note that 100 Tg = 0.1 Gt.

of HFC-134a would make the sum of European and USA emissions more consistent with reporting to the UNFCCC (**Figure 2-3**). The only other recent analysis of USA emissions based on USA observations (Fortems-Cheiney et al., 2015) suggests between 10 and 20 Gg yr^{-1} larger emissions than derived in Hu et al. for the overlapping years of 2008–2010, but these higher values may be less representative of the USA total as they are derived from observations at a smaller number of USA sites.

Most of the remaining HFC-134a emissions reported to the UNFCCC (20% of reported total) come from Canada, Japan, Australia, and Russia and have ranged from 1.5 to 4 Gg yr^{-1} per country in recent years. Of these countries, atmosphere measurement-based estimates are available for Japan and Australia. Japanese emissions during 2008 have been estimated at 3.1 ± 0.2 Gg yr^{-1} in one study (Stohl et al., 2010) and 4.7 (4.5–5) Gg yr^{-1} in another (Li et al., 2011); emissions during 2010-2012 were estimated at 3.7 (0.6–7.4) Gg yr^{-1} in one study (Lunt et al., 2015) and between 2.1 and 4.3 Gg yr^{-1} in another (Saito et al., 2015). These estimates are not significantly different from the 2.5 to 2.9 Gg yr^{-1} reported to UNFCCC by Japan in these years, although higher amounts were inferred for 2010 in one study (12 ± 2 Gg yr^{-1}; Fortems-Cheiney et al., 2015). Atmosphere-based estimates for Australia for 2006 (4.5 Gg yr^{-1}; Stohl et al., 2009) indicate comparable emissions to Japan's, but they are higher than the 1.9 Gg reported by Australia to UNFCCC for that year.

The absence of substantial underestimates in national emissions reported to UNFCCC, as is implied from the above discussion, indicates that the factor of approximately two difference (> 100 Gg^{-1}) between totals reported to UNFCCC and atmosphere-based global totals likely stems from significant emissions of HFC-134a from non-reporting countries (i.e., non-Annex I, developing countries). Regional atmospheric studies in Asia support this conclusion. Emissions for 2008 from East Asia were estimated to be 15–20 Gg yr^{-1} (based on values from Li et al., 2011 of 15.2 [12.5–18.6] Gg yr^{-1} and from Stohl et al., 2010 of 19.2 ± 2.5 Gg yr^{-1}). Atmosphere-based estimates suggest that emissions from China accounted for 8–13 Gg of these East Asian HFC-134a emissions during 2008 (based on estimates of 8.3 [6.2–11] Gg yr^{-1} from Li et al., 2011, 8.7 [6.5–12] Gg yr^{-1} from Kim et al., 2010, and 12.9 ± 1.7 Gg yr^{-1} from Stohl et al., 2010). Emissions at the higher end of this range were derived for 2010-2012 (12 [5–21] Gg yr^{-1} in Lunt et al., 2015). Based on emissions derived from atmospheric observations, South Korea has accounted for approximately 1–3 Gg yr^{-1} of HFC-134a in recent years (1.5–2.2 Gg yr^{-1} for 2008 [Stohl et al., 2010 and Li et al., 2011] and (1.83 [0.58-3.13] Gg yr^{-1} for 2010-2012 [Lunt et al., 2015]).

An analysis of HFC production and consumption in China also indicates significant Chinese emissions of HFC-134a and suggests increasing emissions over time with 9.2–11 Gg in 2008 and 33 Gg in 2013 (Su et al., 2015 and Fang et al., 2016). These results and the atmosphere measurement-based estimates, however, suggest that emissions from China account for less than half of the difference between global emissions and totals reported to UNFCCC from Annex I countries (**Figure 2-6**). As such, they imply that significant emissions of HFC-134a, perhaps as much of 30% of the global total, are currently arising from non-Annex I countries other than China that are not required to report HFC emissions to the UNFCCC.

2.3.1.2 HFC-23 (CHF_3)

HFC-23 is emitted into the atmosphere primarily as a by-product from over-fluorination during HCFC-22 production; much smaller emissions are associated with HFC-23 use as feedstock for halon-1301 production, in semiconductor fabrication (plasma etching and chamber cleaning), in very low-temperature refrigeration, and in specialty fire suppression systems (Miller et al., 2010; Montzka et al., 2010; Oram et al., 1998; Simmonds et al., 2018; US EPA, 2017).

Atmospheric mole fractions of HFC-23 continue to increase in the global atmosphere and reached 28.9 ppt in 2016 (up from 25 ppt in 2012; AGAGE data only; **Table 2-3**). This global abundance accounted for 5.2 mW m^{-2} in 2016, the second largest radiative forcing of all individual HFCs and other F-gases (PFCs, SF_6, NF_3, SO_2F_2, SF_5CF_3; see **Chapter 1**). The HFC-23 global mole fraction increased by 0.83 ppt yr^{-1} (2.9% yr^{-1}) in 2015–2016, similar to the 0.9 ppt yr^{-1} increase measured for 2011–2012 (Carpenter and Reimann et al., 2014), but less than the peak rate of 1.1 ppt yr^{-1} observed during 2014. The average rate of increase for 2012–2016 was 1.0 ppt yr^{-1}, which is slightly faster than the 0.8 ppt yr^{-1} reported in the previous Assessment for 2008–2012. In recent years, observed global mole

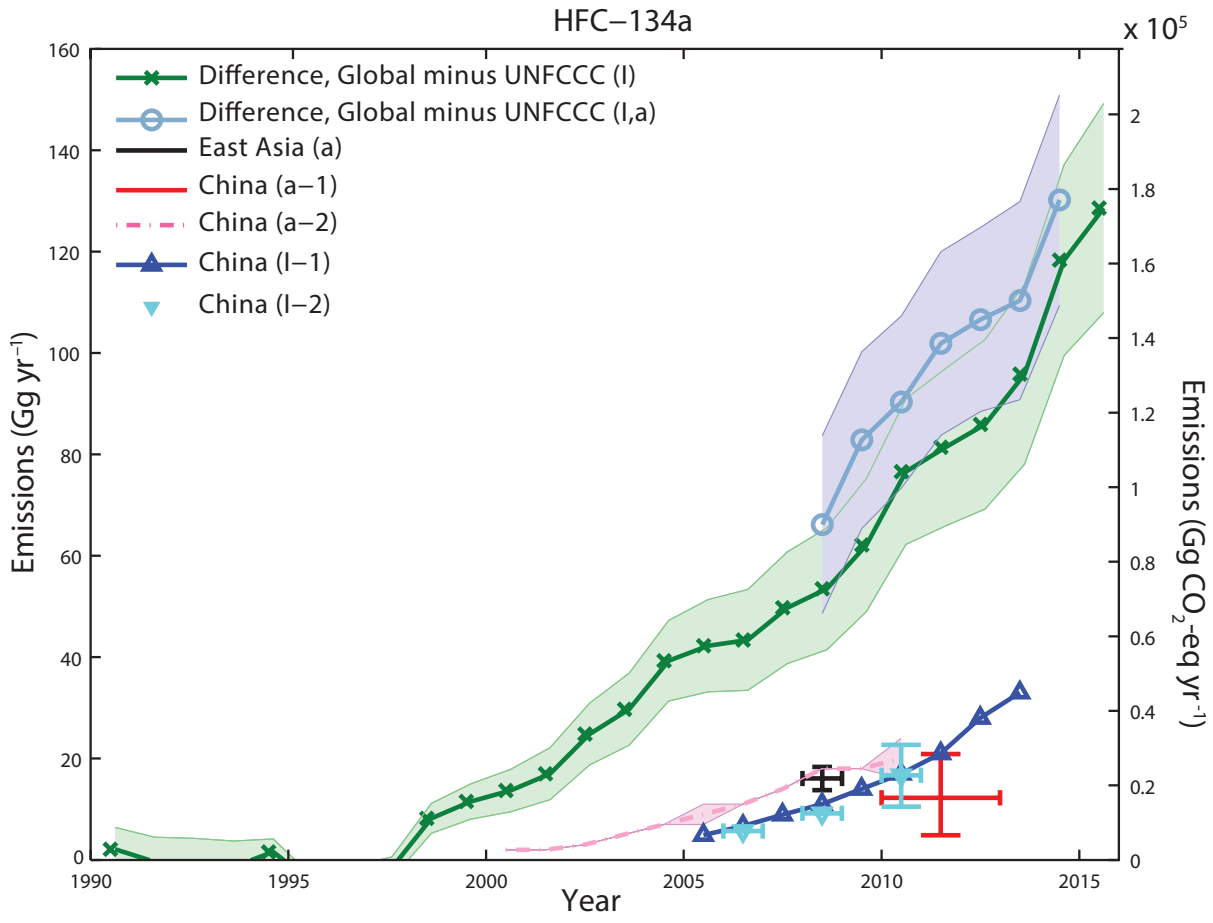

Figure 2-6. Differences between the global emissions derived from atmospheric measurements and the total emissions reported to UNFCCC (UNFCCC, 2017) for HFC-134a. Annual differences between atmosphere-based global total HFC-134a emissions (from **Figure 2-1**) and inventory-reported totals (UNFCCC, 2017) are plotted as the green line and shading (Global minus UNFCCC(I); shading reflects global emission uncertainties); the dark blue line with shading (Global minus UNFCCC(I,a)) represents a similar quantity, but with UNFCCC reporting for the USA and Europe replaced by the regional emission estimates supplied by atmospheric observations in these regions (Hu et al., 2017; Graziosi et al., 2017). Also shown are emissions derived from atmospheric measurements (or other inventory-based estimates) for China and East Asia, which are not obligated to report emissions to the UNFCCC. (These estimates do not represent emissions from all regions not obligated to report to the UNFCCC). East Asian (Stohl et al., 2010, a, black) and Chinese emissions are from inventory-based and atmosphere-based approaches (Lunt et al., 2015, a-1, red; Fortems-Cheiney et al., 2015, a-2, pink and shading; Su et al., 2015, I-2, light blue upside down triangles; Fang et al., 2016, I-1, dark blue triangles).

fractions of HFC-23 are also consistent with the largest emissions projected in the RCPs, which are in RCP8.5 (Meinshausen et al., 2011).

Mixing ratios of HFC-23 have been estimated over time from the ACE-FTS instrument on board the SCISAT satellite (Harrison et al., 2012) using updated absorption cross sections (Harrison, 2013). The upper tropospheric means are approximately 2 ppt below those estimated from surface-based data (AGAGE), although the relative rate of change averaged over 2012–2016 from the two independent measurements is not significantly different (3.1 ± 0.8% yr^{-1} from SCISAT versus 3.8 ± 0.6% yr^{-1} from AGAGE) (**Figure 2-2**).

Total global HFC-23 emissions derived from a budget analysis of measured mole fractions at remote sites show gradual increases before 1999 and then substantial variations, with minima in 2001–2002 and in 2009–2010 and maxima in 2005–2006 and 2013–2014. Derived peak emissions were 14.5 ± 0.7 Gg yr^{-1} in 2014, and have since decreased, with 12.3 ± 0.7 Gg yr^{-1} estimated for 2016 (**Figure 2-1**, Simmonds et al., 2018).

A comparison between atmospheric measurement-based global emission estimates and Annex I country totals reported to UNFCCC shows fairly good consistency during 1990–1995 (**Figure 2-1**). After 2000, however, UNFCCC totals decrease and atmospheric measurement-derived global emissions increase. UNFCCC totals were between 1 and 1.5 Gg yr^{-1} for 2009–2015 while measurement-based global emission totals ranged between 9.5 and 15 Gg yr^{-1}. This difference increased concurrently with the substantial increases in HCFC-22 production and associated HFC-23 emission from developing countries not required to report HFC emissions to the UNFCCC (i.e., non-Annex I countries) (Miller et al., 2010; Montzka et al., 2010; Simmonds et al., 2018).

Inventory-based emissions of HFC-23 from countries not obligated to report emissions to the UNFCCC are derivable from information provided to the Montreal Protocol's Multilateral Fund (MLF) by these countries (UNEP, 2017b; Simmonds et al., 2018). These inventory emissions of HFC-23 are estimated in some countries and, in others, are derived from a combination of country-based reporting of HCFC-22 production for all uses, HFC-23 production rates, and quantities of HFC-23 destroyed or otherwise transformed as feedstock.

The sum of inventory-based emissions derived from reporting to the UNFCCC and estimated using the information collected by the Montreal Protocol's MLF fairly closely tracks the wide swings in global emissions derived from atmospheric mole fraction measurements (**Figure 2-7**), although emissions in a few years (e.g., 2008, 2013, and 2015) are significantly underestimated by these inventories (Simmonds et al., 2018). This overall consistency suggests that the inventory-derived HFC-23 emissions associated with HCFC-22 production are fairly accurately estimated (within ± 2 Gg in total) in both developed and developing countries.

This consistency also provides an understanding of HFC-23 emission changes over the past decade. The minimum in emissions centered around 2009–2010 stems from a significant decrease in the ratio of HFC-23 emission relative to HCFC-22 production (E_{23}/P_{22}) (**Figure 2-7**), which was primarily the result of HFC-23 destruction facilitated by the UNFCCC's CDM projects (Miller et al., 2010; Montzka et al., 2010). The subsequent increase in HFC-23 emissions after 2010 appears to be the result of increases in total HCFC-22 production and slight increases in the E_{23}/P_{22} ratio as the CDM projects were terminated. The ~2 Gg decrease in annual emissions after 2014 is associated with slightly reduced total HCFC-22 production as dispersive-use production was capped in 2013, although a much larger emission decline was expected in 2015 from inventory reporting than is apparent in the measurement-derived emission estimate for that year. The decline in reported emissions in 2015 is due primarily to a drop in the reported E_{23}/P_{22} ratio (**Figure 2-7**).

The inventory-based reporting totals also suggest a significant shift in regions emitting HFC-23 in the past. Emissions were primarily from the USA, Russia, the UK, and Japan during the early 1990s. Since 2009, however, between 84% and 89% of global HFC-23 emissions have come from China, which is consistent with China being the largest producer of HCFC-22 in recent years in reporting to the UN Environment Ozone Secretariat (UNEP, 2017b; Simmonds et al., 2018).

Independent evidence for substantial HFC-23 emissions from non-Annex I countries in recent years comes from a number of observational studies, although measurements have not been conducted near all developing countries reporting HFC-23 emission (i.e., Argentina, China, India, Mexico, North Korea, and Venezuela). Emissions from China, for example, were estimated for 2008 from observations in eastern Asian countries and different data analysis methods and range between 6 and 12 Gg yr^{-1} (based on estimates from Stohl et al. [2010] of 6.2 ± 0.7 Gg yr^{-1}, Fang et al., [2015] of 6.2 ± 0.6 Gg yr^{-1}, Li et al. [2011] of 10 (7.2–13) Gg yr^{-1}, and Kim et al. [2010] of 12 (8.6–15) Gg yr^{-1}). The lower end of this range is in good agreement with the inventory-based estimates provided to the MLF from China of 5.7 Gg yr^{-1} for 2008 (UNEP, 2017b; Simmonds et al., 2018). For comparison, total global emissions derived from

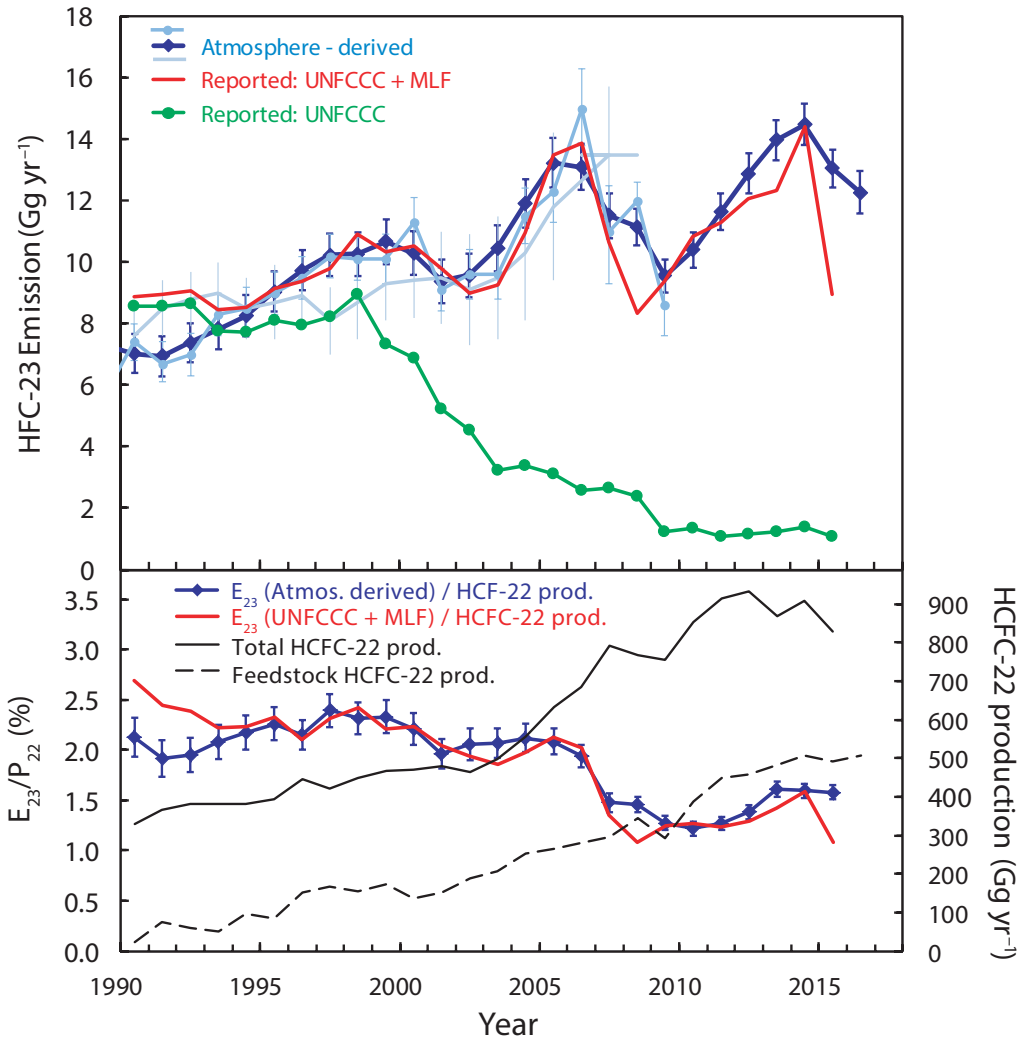

Figure 2-7. *Top panel:* Emissions of HFC-23 derived from atmospheric measurements (blue lines) and inventories (red and green lines). Measurement-based emissions are derived from analyses of southern-hemispheric firn air (light-blue line; Montzka et al., 2010), a southern-hemispheric air archive before 2007 coupled with ongoing results from multiple sites during 2007–2009 (light blue circles; Miller et al., 2010), and from a combination of air-archive, firn air, and ongoing measurements (dark blue diamonds; Simmonds et al., 2018). Uncertainties are one standard deviation of estimates. Inventory results are from Annex I reporting to UNFCCC (green line with filled circles; UNFCCC, 2017) and from the sum of reporting to UNFCCC and to the Montreal Protocol's Multilateral Fund (MLF; red line, Simmonds et al., 2018). *Bottom panel:* the ratio of HFC-23 emissions relative to HCFC-22 production for all uses (E_{23}/P_{22} by mass, left-hand axis; with emissions being the total from inventories (red) or global magnitudes estimated from atmospheric measurements and their uncertainty (blue line) from the upper panel, and total global HCFC-22 production reported for all uses (black line; right-hand axis) and for feedstock only (black dashed line; right-hand axis).

measured atmospheric changes at remote sites was 11.2 ± 0.6 Gg yr^{-1} in 2008.

By 2012, atmospheric measurement-based analyses indicated that HFC-23 emissions from China accounted for at least two-thirds of global HFC-23 emissions. Atmospheric observations in that year suggest Chinese emissions of 8.8 ± 0.8 Gg yr^{-1} (Fang et al., 2015) compared to the 10.8 Gg yr^{-1} estimate provided to the MLF (UNEP, 2017b; Simmonds et al., 2018), while the atmosphere measurement-based global estimate in 2012 was 12.9 ± 0.7 Gg yr^{-1} and UNFCCC

Annex I reporting totaled 1.2 Gg yr^{-1}. A small fraction of the global emission arises from other non-Annex I countries such as South Korea and Taiwan (Stohl et al., 2010; Li et al., 2011; Fang et al., 2015), ~0.1–0.2 Gg yr^{-1} in 2008 (compared to the estimates derived from information provided to the MLF of less than 0.1 Gg yr^{-1} for South Korea). Analyses of atmospheric observations also indicate that emissions from Japan were ~0.2–0.3 Gg yr^{-1} in 2008 (Stohl et al., 2010; Li et al., 2011; Fang et al., 2015), somewhat larger than the 0.04 Gg yr^{-1} reported to UNFCCC, while European emissions (Keller et al., 2011; Simmonds et al., 2018) are similar or slightly larger than the UNFCCC submission values.

2.3.1.3 HFC-32 (CH_2F_2), HFC-125 (CHF_2CF_3), HFC-143a (CH_3CF_3)

Global mean mole fractions of HFC-32, HFC-125, and HFC-143a continue to rise in the atmosphere primarily because these chemicals are used as HCFC substitutes in major refrigeration blends (HFC-125 also has a minor application for fire protection) (O'Doherty et al., 2014; Montzka et al., 2015; Simmonds et al., 2015, 2017; US EPA, 2017). In 2016, average global mean mole fractions were 11.9 (11.2–12.6) ppt for HFC-32, 20.4 (20.1–20.8 ppt) for HFC-125, and 19.2 (19.0–19.3) ppt for HFC-143a (NOAA and AGAGE data; **Table 2-3**). These mole fractions are approximately twice the 2012 values for HFC-32 and HFC-125, and are 50% higher for HFC-143a. Mole fractions of these HFCs increased during 2012–2016 by an average of 1.6 ppt yr^{-1} for HFC-32, 1.5 ppt yr^{-1} for HFC-143a, and 2.1 ppt yr^{-1} for HFC-125. These rates are considerably larger than measured during 2008–2012 as reported in the previous Assessment, by a factor of 1.7 for HFC-32 and HFC-125, and by a factor of 1.2 for HFC-143a.

The mole fraction increases observed for these gases since 2007 are similar to the scenario projections discussed in the previous Assessment (**Figure 2-2**; Carpenter and Reimann et al., 2014; Velders et al., 2009) and to those in newer scenarios (Velders et al., 2015), although projected HFC-32 mole fractions were slightly higher than observed.

The radiative forcings associated with these 2016 global mole fractions were 1.31 (1.23–1.39) mW m^{-2} from HFC-32, 4.70 (4.62–4.79) mW m^{-2} from HFC-125, and 3.06 (3.04–3.09) mW m^{-2} from HFC-143a.

Total global emissions of these three HFCs derived from a budget analysis of measured mole fractions at remote sites continue to increase, with estimates for 2016 of 35 ± 4 Gg yr^{-1} for HFC-32, 62 ± 5 Gg yr^{-1} for HFC-125 and 28 ± 2 Gg yr^{-1} for HFC-143a. These were higher than their 2012 emissions of 20 Gg yr^{-1}, 44 Gg yr^{-1}, and 22 Gg yr^{-1}, respectively (**Figure 2-1**; update from O'Doherty et al., 2009, 2014; Rigby et al., 2014; Lunt et al., 2015; Montzka et al., 2015; and Simmonds et al., 2017). In 2014, the global emission estimates for each of these three gases were about two times higher than the corresponding UNFCCC totals from reporting countries.

As was true for HFC-134a, the difference between UNFCCC reporting and atmosphere-based global total emission for these three gases is not likely from underreporting of emissions from the USA and Europe, the two regions that account for most emissions reported to UNFCCC (~83–90%). Regional emission magnitudes derived from measurements within the USA and Europe suggest that the inventory-based reporting from these regions is accurate or even overestimated. In Europe, atmosphere-based emissions estimated for these gases have been consistent with values reported to UNFCCC in most recent years; an exception is that UNFCCC reporting for HFC-32 has increased above the atmosphere-based estimates in the most recent years (**Figure 2-5**) (Graziosi et al, 2017; Brunner et al., 2017). A similar divergence is observed in the USA for HFC-32 and HFC-125, with the UNFCCC inventory increasing faster than atmosphere-based estimates (**Figure 2-4**); this divergence is less pronounced for HFC-143a. For Japan, both atmosphere-based estimates (Saito et al., 2015; Lunt et al., 2015) and UNFCCC reporting suggest Japanese emissions are < 2 Gg yr^{-1} for each of these gases.

The absence of substantial underestimates in national emissions reported to UNFCCC for these three HFCs indicates that the factor of approximately two difference in reporting totals versus atmosphere-based global totals likely stems from significant emissions from developing countries not required to report their emissions to UNFCCC (non-Annex I). This conclusion has also been reached in an analysis of production estimates and market demand in developing countries, based on the Montreal Protocol phase-out schedules for ODSs (Fang et al., 2016; Zhang and Wang, 2014; Velders et al., 2015).

Emissions estimates based on atmospheric measurements in East Asia confirm substantial HFC-32 emissions from non-Annex I countries. Averaged over 2010–2012, Chinese emissions of HFC-32 were estimated to be 7.0 (4.9–9.2) Gg yr^{-1} and those from South Korea were estimated at 0.43 (0.1–0.52) Gg yr^{-1} (Lunt et al., 2015). These Chinese emissions are larger than the mean emissions estimated for the USA of 3.3 ± 0.5 Gg yr^{-1} (Hu et al., 2017) or for Europe of 2.5 ± 0.9 Gg yr^{-1} (Graziosi et al., 2017) during these same years. They also are significantly larger than those from Japan (0.5–0.7 Gg yr^{-1}) (Lunt et al., 2015; Saito et al., 2015).

Consideration of HFC-32 production and consumption magnitudes along with use patterns has allowed inventory-based emission estimates in China. This analysis suggests emissions of 12 Gg yr^{-1} of HFC-32 in 2013 and 7.7 Gg yr^{-1} for 2010–2012 (Fang et al., 2016), consistent with the atmosphere-based regional estimate from Lunt et al. quoted above (7.0 [4.9–9.2] Gg yr^{-1} for 2010–2012). These results suggest that substantial emissions of HFC-32 have arisen from China as a result of the phase-out of ODSs and that these Chinese emissions explain most if not all of the difference between global estimates and totals being reported to UNFCCC for this chemical (**Figure 2-8**).

Atmosphere-based studies also suggest substantial emissions of HFC-125 from non-Annex I countries (**Figure 2-9**). Emissions from China averaged over 2010–2012 were 5.7 (4.0–7.7) Gg yr^{-1}, and those from South Korea were substantially smaller (0.5 [0.3–0.7] Gg yr^{-1}; Lunt et al., 2015). By comparison, average emission during this period was estimated to be 7.9 ± 1.2 Gg yr^{-1} from the USA (Hu et al., 2017) and 8.6 ± 2.7 Gg yr^{-1} from Europe (Graziosi et al., 2017). Smaller emissions of 0.8 (0.3–1.5) Gg yr^{-1} were estimated from Japan for 2010–2012 (Lunt et al., 2015).

Consideration of HFC-125 production and consumption magnitudes along with use patterns has allowed inventory-based emission estimates in China. This analysis suggests emissions of 6.3 Gg yr^{-1} averaged over 2010–2012 and 12 Gg yr^{-1} of HFC-125 in 2013 (Fang et al., 2016), consistent with the atmosphere-based regional estimate from Lunt et al. (2015). While these

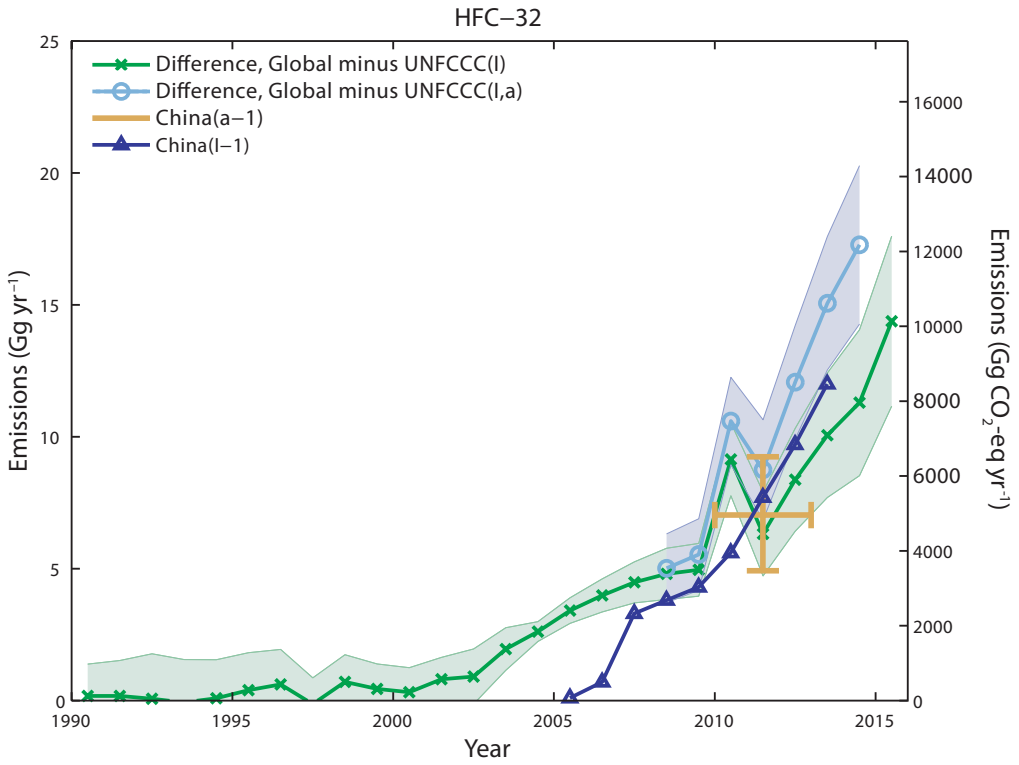

Figure 2-8. As in **Figure 2-6**, but for HFC-32. Here Chinese emissions are from inventory-based (Fang et al., 2016; I-1, blue triangles) and atmosphere-based (Lunt et al., 2015, a-1, yellow) estimates.

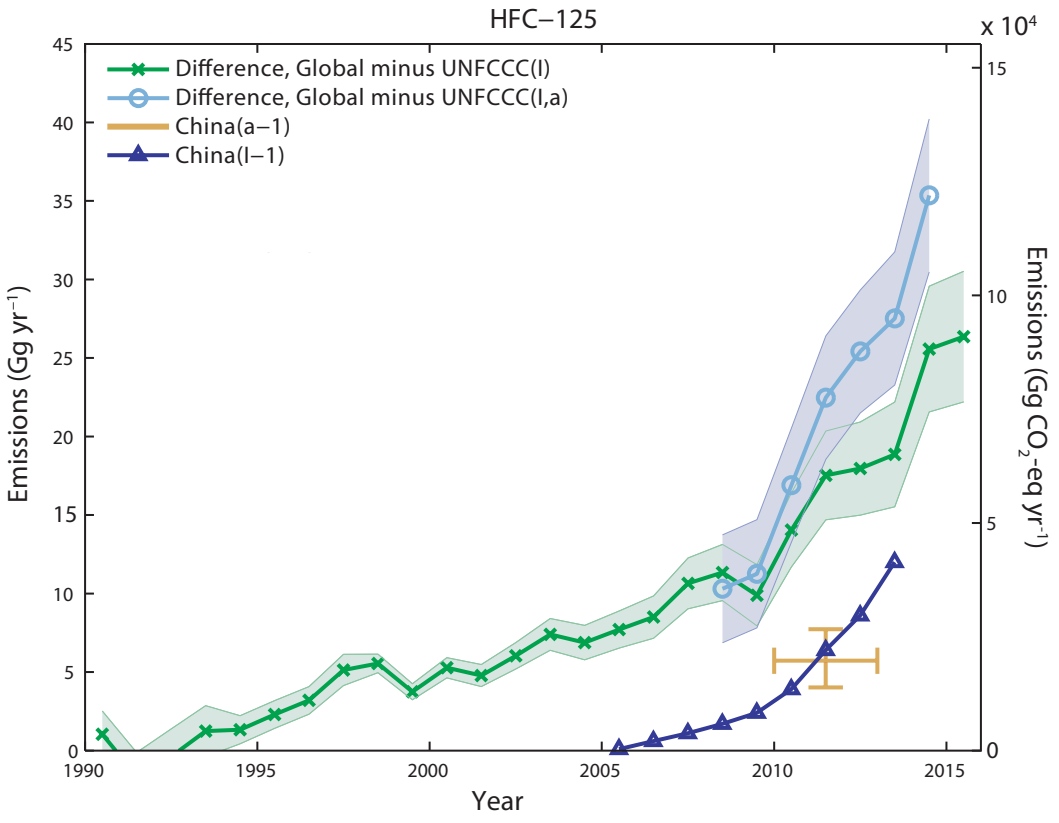

Figure 2-9. As in **Figure 2-8**, but for HFC-125.

results indicate increasing emissions of HFC-125 from China during the phase-out of ODSs, they also demonstrate that Chinese emissions explain only approximately half of the difference between global emissions of HFC-125 and totals reported to UNFCCC (**Figure 2-9**). This difference suggests substantial emissions of HFC-125 from other non-Annex I countries not required to report emissions to the UNFCCC.

Atmosphere-based studies also suggest substantial emissions of HFC-143a from non-Annex I countries (**Figure 2-10**). Emissions from China averaged over 2010–2012 were 2.1 (1.3–3.1) Gg yr^{-1}, and those from South Korea were 0.13 (0.06–0.21) Gg yr^{-1} (Lunt et al., 2015). By comparison, during this period emissions of 4.2 ± 0.7 Gg yr^{-1} were estimated from the USA (Hu et al., 2017) and 6.2 ± 2.1 Gg yr^{-1} from Europe (Graziosi et al., 2017). Smaller emissions were estimated from Japan (0.3 [0.1–0.6] Gg yr^{-1}) and S.E. Australia (0.2 [0.1–0.5] Gg yr^{-1}) for 2010–2012 (Lunt et al., 2015).

Consideration of HFC-143a production and consumption magnitudes along with use patterns has allowed inventory-based emission estimates in China. This analysis suggests Chinese emissions of 3 Gg yr^{-1} of HFC-143a in 2012 (Fang et al., 2016), consistent with the atmosphere-based regional estimate from Lunt et al. (2015), likely as a result of the phase-out of ODSs. As was true for HFC-125, Chinese emissions account for less than half of the difference between global estimates and totals being reported to UNFCCC for HFC-143a (**Figure 2-10**).

2.3.1.4 HFC-152a (CH_3CHF_2)

The global annual average HFC-152a mole fraction has varied relatively little over the past 4 years, between 6.5 and 6.8 ppt (AGAGE and NOAA data; 6.8 ppt was measured in 2012; Carpenter and Reimann et al., 2014). This is notably different from projections, which have suggested HFC-152a mole fractions would increase over time (**Figure 2-2**; Carpenter and Reimann et al., 2014; Velders et al., 2009, 2015). The global abundance in 2014 contributed a radiative forcing of 0.67 mW m^{-2}, relatively little compared to the HFCs discussed above. HFC-152a is used as a foam-blowing agent,

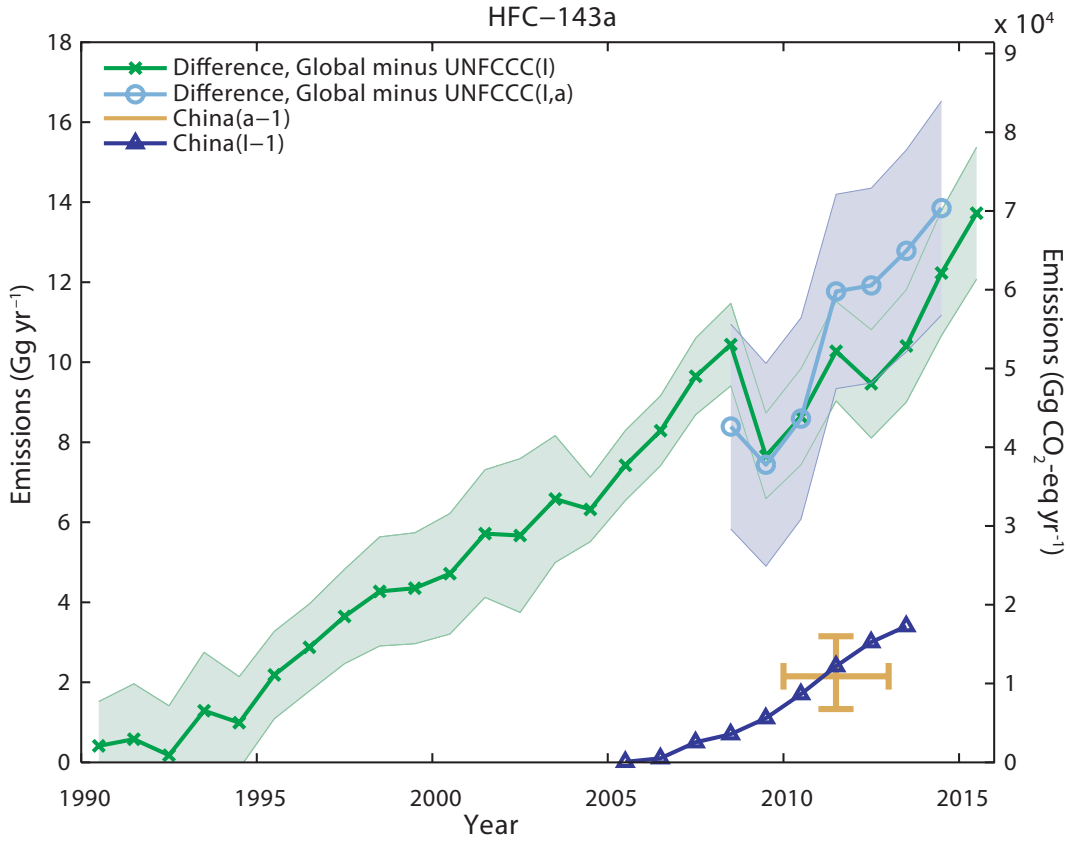

Figure 2-10. As in **Figure 2-8**, but for HFC-143a.

aerosol propellant, and in some refrigeration blends to replace CFCs, HCFCs, and recently HFC-134a in automobile air conditioners (Simmonds et al., 2016; UNEP, 2017a; US EPA, 2017).

Total global HFC-152a emission derived from a budget analysis of measured mole fractions at remote sites was 53 Gg yr^{-1} in 2016, not appreciably different from the 51 ± 8 Gg yr^{-1} estimated for all years since 2010 (**Figure 2-1**, update from Rigby et al., 2014, Lunt et al., 2015, Montzka et al., 2015 and Simmonds et al., 2016). While HFC-152a emissions are larger than most other HFCs, its impact on atmospheric concentrations and climate is relatively small because its lifetime (1.6 yr) and associated GWP (100-yr GWP = 148) are small compared to most other HFCs whose production and consumption is also controlled by the Kigali Amendment to the Montreal Protocol.

HFC-152a emissions reported to UNFCCC account for only 10 to 15% (6 to 7 Gg yr^{-1} for 2009–2015) of the global totals derived from measured atmospheric changes in the remote atmosphere. A likely reason for this large difference is that emissions of HFC-152a from the USA are not included in UNFCCC totals considered here and displayed in **Figure 2-1**. This is because emissions totals of HFC-152a are only reported by the U.S. Environmental Protection Agency (EPA) to the UNFCCC together with other chemicals (HFC-227ea, HFC-245fa, HFC-43-10mee, some hydrofluoroolefins (HFOs), and some minor PFCs) owing to confidentiality issues. If half of the 10.7 $MtCO_2$-eq total reported by the USA for this mix in 2015 was due to emissions of HFC-152a, it would account for approximately 36 Gg yr^{-1} of HFC-152a emission, or most of the ~45 Gg difference shown in **Figure 2-1** between reported and atmosphere measurement-derived estimates in recent years.

Atmospheric observations from limited regions using different modeling/inversion techniques provide evidence for substantial USA HFC-152a emissions in recent years: 10–15 Gg yr^{-1} in 2005–2006 (Stohl et al., 2009), 25 (11–50) Gg yr^{-1} in 2004–2009 (Miller et al., 2012), 32 ± 4 Gg yr^{-1} in 2008 (Barletta et al., 2011), 28

(23–33) Gg yr^{-1} in 2007–2009 and 32 (25–39) Gg yr^{-1} in 2010–2012 (Lunt et al., 2015; Simmonds et al., 2016).

HFC-152a emissions from Europe have been estimated at 2.9 Gg yr^{-1} in 2009 (Keller et al., 2012), 4.1–7.5 Gg yr^{-1} in 2007–2012 (Lunt et al., 2015; Simmonds et al., 2016), and an average of 4.1 ± 1.0 Gg yr^{-1} over 2003–2014, with a slight decreasing trend over this period (Graziosi et al., 2017; uncertainty represents 1 standard deviation of annual estimates). These magnitudes and the decreasing trend are consistent with values reported to UNFCCC over this period (Graziosi et al., 2017).

Evidence exists for substantial HFC-152a emissions from countries not required to report emissions to the UNFCCC. Atmospheric measurements in eastern Asia suggest emissions of ~5 Gg yr^{-1} (Stohl et al., 2010) and 6.8 Gg yr^{-1} (Li et al., 2011) in 2008, 6.2 (5–9) Gg yr^{-1} in 2007–2009 and 7.0 (5–10) Gg yr^{-1} in 2010–2012 (Lunt et al., 2015; Simmonds et al., 2016). A sizable fraction of these eastern Asian emissions arises from China, with estimates of 2.0–2.9 Gg yr^{-1} in 2010–2011 (Yao et al., 2012) and 3.4–5.7 Gg yr^{-1} in 2004–2005 (Yokouchi et al., 2006) and 2008 (Kim et al., 2010; Stohl et al., 2010).

2.3.1.5 HFC-245fa ($CHF_2CH_2CF_3$), HFC-365mfc ($CH_3CF_2CH_2CF_3$), HFC-227ea (CF_3CHFCF_3), HFC-236fa ($CF_3CH_2CF_3$)

HFC-245fa and HFC-365mfc (normally blended with HFC-227ea to reduce flammability) replace HCFC-141b in polyurethane structural foam blowing, and they have potential uses in solvent applications and medical aerosols; HFC-245fa is also used in small quantities in centrifugal chillers (Vollmer et al., 2006; Stemmler et al., 2007; Laube et al., 2010; UNEP, 2010; Vollmer et al., 2011; UNEP, 2016b). The global mean mole fraction of both gases continues to steadily increase. The global mean estimated for HFC-245fa (AGAGE data) for 2016 was 2.4 ppt, up from 1.7 ppt in 2012, with an annual increase of +0.2 ppt yr^{-1} (8.9% yr^{-1}) from 2015 to 2016 (**Table 2-3**). For HFC-365mfc, networks report a global average of 0.94 (0.87–1.00) ppt, up from 0.67 ppt in 2012, with a growth rate of +0.08 ppt yr^{-1} (9.2% yr^{-1}) (NOAA and AGAGE data; **Table 2-3**).

HFC-227ea and HFC-236fa are used as fire retardants to replace halon-1211 and halon-1301; HFC-227ea is also used in mixtures with other HFCs as a propellant in metered-dose inhalers and in blends with HFC-365mfc in polyurethane foam blowing; HFC-236fa is also used as a coolant in specialized applications (UNEP, 2010; Vollmer et al., 2011; UNEP, 2014b, 2016b; US EPA, 2017). Global mean mole fractions of both compounds are relatively small but continue to increase steadily in the atmosphere. For 2016, a global average of 1.21 (1.17–1.24) ppt is estimated for HFC-227ea, up from 0.81 ppt in 2012 (NOAA and AGAGE data). The global mean estimated for HFC-236fa in 2016 was 0.15 ppt (AGAGE data), up from 0.11 ppt in 2012. Growth rates were 0.11 ppt yr^{-1} (9.9% yr^{-1}) for HFC-227ea and 0.01 ppt yr^{-1} (8.9% yr^{-1}) for HFC-236fa in 2015–2016 (**Table 2-3**). In 2016, the radiative forcings from these four HFCs were still very small with 0.58 mW m^{-2} from HFC-245fa, 0.21 mW m^{-2} from HFC-365mfc, 0.31 mW m^{-2} from HFC-227ea, and 0.04 mW m^{-2} from HFC-236fa.

Increases projected for global mole fractions of HFC-227ea and HFC-236fa have been fairly accurate over time, whereas those for HFC-245fa and HFC-365mfc were initially overestimated (**Figure 2-2**; Carpenter and Reimann et al., 2014; Velders et al., 2009, 2015) because of the lack of observations and production statistics for these HFCs being available when the initial projections were developed.

Total global emissions derived from a budget analysis of measured mole fractions at remote sites have increased nearly linearly in recent years for HFC-245fa (from 9.5 ± 1.5 Gg yr^{-1} in 2012 to 11.7 ± 1.9 Gg yr^{-1} in 2016), HFC-365mfc (from 3.4 ± 0.7 Gg yr^{-1} in 2012 to 4.6 ± 0.9 Gg yr^{-1} in 2016), and HFC-227ea (from 3.6 ± 0.4 Gg yr^{-1} in 2012 to 4.3 ± 0.5 Gg yr^{-1} in 2016). By contrast, HFC-236fa emissions have remained at 0.29 ± 0.07 Gg yr^{-1} since 2012 (**Figure 2-1**, update from Vollmer et al., 2011, Rigby et al., 2014 and Montzka et al., 2015).

Emissions reported to UNFCCC for these HFCs account for only a small fraction of global totals inferred from measurements at remote sites (**Figure 2-1**). Some of these discrepancies may arise because several countries report significant CO_2-eq emissions of "unspecified mix of HFCs" and "unspecified mix of HFCs and PFCs", likely due to confidentiality concerns. For example, the U.S. National Inventory Reports specifies that the latter category includes HFC-227ea and HFC-245fa emissions.

Few regional emission estimates exist for these four HFCs, and they only explain a small fraction of global emissions.

HFC-245fa emissions in 2014 from Europe were estimated to be 0.7 ± 0.5 Gg yr^{-1} from observations at European sites (Graziosi et al., 2017) compared to ~10 Gg yr^{-1} globally in that year. An inventory-based analysis suggests Chinese emissions of 0.07 Gg yr^{-1} in 2009 (Fang et al., 2016) compared to ~7 Gg yr^{-1} globally in that year.

HFC-365mfc emissions in 2014 were estimated to be 1.1 ± 0.4 Gg yr^{-1} from Europe (Graziosi et al., 2017) and 0.25 ± 0.1 Gg yr^{-1} from the USA (Hu et al., 2017), based on observations in these regions, compared to ~4 Gg yr^{-1} globally in that year. For 2008, Li et al. (2011) estimated East Asian emissions of 0.2–0.3 Gg yr^{-1} based on atmospheric measurements in that region, mostly from Japan, compared to global estimates of ~3 Gg yr^{-1} in that year.

HFC-227ea emissions in 2014 were estimated at 0.6 ± 0.1 Gg yr^{-1} from the USA (Hu et al., 2017) and 0.4 ± 0.2 Gg yr^{-1} from Europe (Graziosi et al., 2017) based on atmospheric measurements in those regions, compared to ~3.9 Gg yr^{-1} globally for that year. For 2009, Fang et al. (2016) estimated 0.5 Gg yr^{-1} from China based on an analysis of inventories and markets, compared to the global estimate of ~2.8 Gg yr^{-1} for that year.

HFC-236fa emissions in 2014 were 0.025 ± 0.019 Gg yr^{-1} from Europe compared to ~0.29 Gg yr^{-1} globally for that year (Graziosi et al., 2017).

2.3.1.6 HFC-43-10mee ($CF_3CHFCHFCF_2CF_3$)

HFC-43-10mee is used for cleaning applications in the electronics industry where it replaces CFC-113, methyl chloroform, and HCFC-141b; it is also used in aerosol sprays and is an alternative to PFCs in certain applications (Arnold et al., 2014; UNEP, 2016b; Le Bris et al., 2017). It continues to slowly accumulate in the atmosphere. In 2016, a global mean mole fraction of 0.27 ppt was measured, slightly up from 0.23 ppt in 2012, with a very small growth rate of 0.01 ppt yr^{-1} (4.6% yr^{-1}) in 2015–2016 (AGAGE data only; **Table 2-3**). In 2016, the resulting radiative forcing was still small at 0.10 mW m^{-2} relative to the other HFCs discussed here. Total global emissions derived from a budget analysis of measured mole fractions at remote sites were 1.1 ± 0.3 Gg yr^{-1} in 2016 and have not increased appreciably since 2007 (**Figure 2-1**, update from Arnold et al., 2014).

2.3.2 Summed Radiative Forcing and CO_2-eq Emissions Attributable to HFCs

The contribution to climate change from the atmospheric concentration of a long-lived trace gas at a particular point in time is expressed as a radiative forcing (Myhre and Shindell et al., 2013). Radiative forcing from all HFCs in the atmosphere approximately doubled over the past decade, reaching 30 mW m^{-2} in 2016 (**Figure 2-11**); this climate warming influence is 36% larger than the 22 mW m^{-2} reported for 2012 in the last Assessment (Carpenter and Reimann et al., 2014). Nearly half (47%) of the radiative forcing from HFCs in 2016 is attributable to HFC-134a; the next three largest contributors are HFC-23, HFC-125, and HFC-143a, which together account for 42% of the total. Total radiative forcing from HFCs in 2016 accounted for ~10% of the 0.33 W m^{-2} from ODSs (**see Chapter 1**), and it was approximately 1.0% of the 3 W m^{-2} supplied in recent years by all long-lived GHGs combined, including CO_2, CH_4, N_2O, ozone-depleting substances, and HFCs (Myhre and Shindell et al., 2013; more recent values are posted at: https://www.esrl.noaa.gov/gmd/aggi/aggi.html).

The time-integrated radiative forcing supplied from the emission of a given HFC includes consideration of the persistence or lifetime of HFCs. The GWP is the metric commonly used to express the time-integrated forcing from the emission of a trace gas relative to the forcing arising from the equivalent emission of CO_2 over a given time interval. One-hundred years is often the time interval considered, although GWPs considered over shorter time intervals (e.g., 20-yr GWPs) are substantially larger for all HFCs except one, HFC-23 (see **Table 2-2**). CO_2-eq emissions of HFCs have increased over time (**Figure 2-12**) and totaled 0.88 ± 0.07 $GtCO_2$-eq yr^{-1} emissions in 2016, up 23% from the 0.72 ± 0.05 $GtCO_2$-eq yr^{-1} estimated for 2012 (Carpenter and Reimann et al., 2014). HFC-134a accounted for 0.30 ± 0.03 $GtCO_2$-eq yr^{-1} in 2016, or 34% of the CO_2-eq emissions from all HFCs considered here. The next three largest contributors were HFC-125 (0.21 ± 0.02 $GtCO_2$-eq yr^{-1}), HFC-143a (0.14 ± 0.01 $GtCO_2$-eq yr^{-1}), and HFC-23 (0.16 ± 0.01 $GtCO_2$-eq yr^{-1}); these

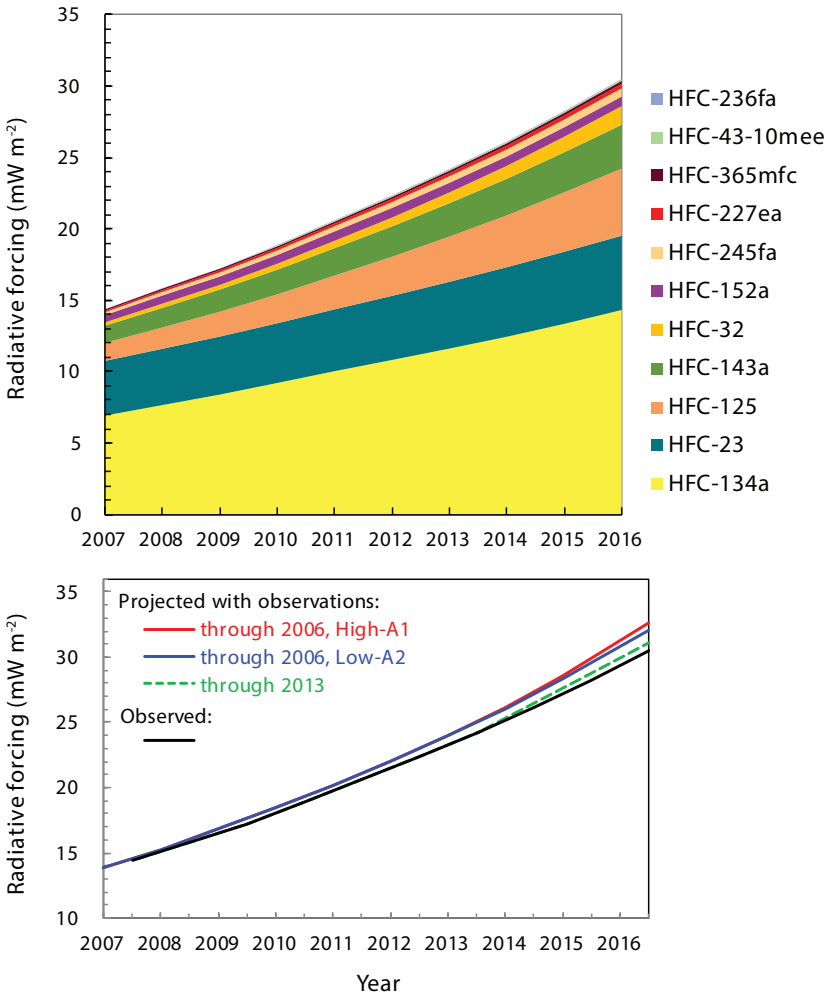

Figure 2-11. *Upper panel:* Radiative forcing supplied by individual HFCs and their sum during the past decade based on observed global mole fractions and their change over time (as given in **Figure 2-2**). These forcings are derived by multiplying measured mole fractions by radiative efficiencies (**Tables 2-1** and **2-2**). *Lower panel:* the overall observed increase in summed radiative forcing from HFCs in the upper panel (black line) was slightly less rapid than was projected nearly a decade ago based on observations through the end of 2006 and a market analysis done at that time (high and low projections from baseline scenarios in Velders et al., 2009; see **Section 2.5**). This projection analysis was updated in 2015 based on observations through 2013 (Velders et al., 2015; high and low projections overlay one another on this time scale). Radiative forcings for HFCs are derived assuming pre-industrial concentrations of zero ppt, which is consistent with the atmospheric measurement records and no known natural sources of HFCs.

top four contributors accounted for 93% of total CO_2-eq yr^{-1} emissions from HFCs in 2016.

In 2016, HFC CO_2-eq emissions were comparable to those of CFCs (0.8 ± 0.3 $GtCO_2$-eq yr^{-1}) and HCFCs (0.76 ± 0.11 $GtCO_2$-eq yr^{-1}; see **Chapter 1**), and the emissions of these HFCs represent ~1.5% of the sum all emissions from long-lived greenhouse gases in recent years (CO_2, CH_4, N_2O, and halocarbons; Montzka et al., 2011, updated).

2.3.3 Comparison of Recent Observed Changes Versus Projections Made in the Past

Large increases in emissions, mole fractions, and radiative forcing from HFCs were projected for the future before an amendment to the Montreal Protocol was agreed in Kigali in 2016 (Velders et al., 2009; Gschrey et al., 2011; Velders et al., 2015; UNEP, 2014c; see **Section 2.3**). Atmospheric measurements through

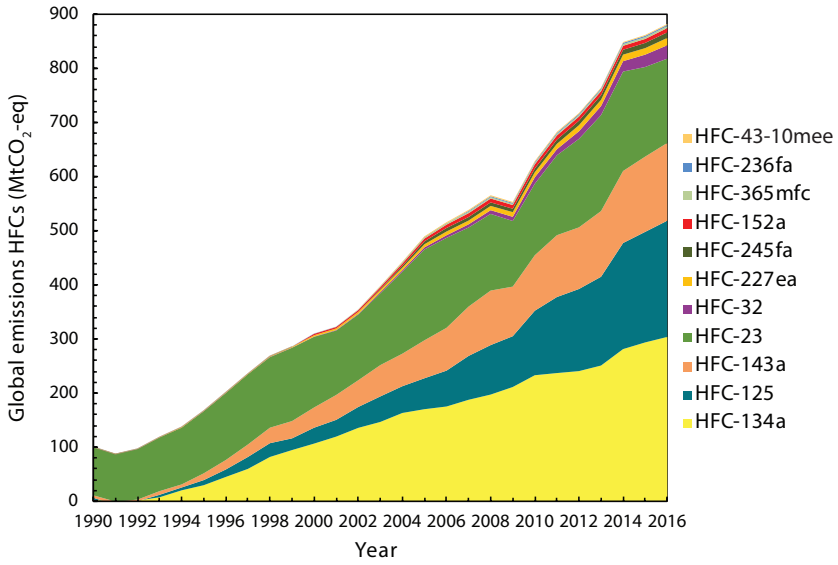

Figure 2-12. Global emissions of HFCs ($MtCO_2$-eq) derived from a budget analysis of global observations (see **Figure 2-1**; mean of AGAGE & NOAA network results when both are available) using the AGAGE 12-box model (Rigby et al., 2016). Emissions are weighted by 100-yr GWP to consider the heating supplied by these chemicals integrated over a 100-yr period relative to an equivalent emission of CO_2.

2016 show that mole fractions of most HFCs increased over the previous decade at rates similar to those projected in a baseline scenario created nearly a decade earlier based on an analysis of atmospheric data and market trends through 2006 (Velders et al., 2009). This baseline scenario has been updated to include data through 2012 (Velders et al., 2015). This consistency is noted for those HFCs currently contributing the most to radiative forcing and CO_2-eq emissions (**Figures 2-1 and 2-2**). Some less abundant HFCs (e.g., HFC-152a, HFC-245fa, and HFC-365mfc) have increased substantially more slowly than was projected. As a result, radiative forcing from the sum of HFCs used as ODS substitutes (i.e., not including HFC-23) increased slightly more slowly than in the baseline projections created nearly a decade ago (**Figure 2-11**).

These results indicate that mole fractions and emissions for most HFCs have continued to change in a fairly predictable manner during the global phase-out of CFC and HCFC production and consumption. These projections included a slowdown in the HFC emission increases from non-Article 5 countries (also referred to as Article 2 countries or Parties to the Montreal Protocol) and, beginning in the mid-2000s, significant contributions from Article 5 countries that were projected to increase substantially after the 2013 cap on global HCFC production. These projections did not include country- and region-specific controls that were introduced or were being considered during that decade (see **Section 2.5.1.2**), except the 2006 EU MAC directive (EU, 2006), and this likely explains in part the slightly slower increases in summed radiative forcing from HFCs in observations compared to projections in **Figure 2-11**. While production and consumption of some HFCs are capped in the future by controls outlined in the Kigali Amendment (see **Section 2.5.1.3** and **Table 2-1**), they may temporarily increase in some countries in the future, particularly those countries for which caps on production and consumption limit these quantities beginning in 2024 or 2028 based on baseline magnitudes determined for future years (e.g., 2020–2022 or 2024–2026, depending on developing country Group; **Table 2-1**).

2.3.4 Aggregate Sums of HFC Emissions Reported to the UNFCCC and Contributions from Non-Reporting Countries

Throughout **Section 2.3**, substantial differences were noted for all HFCs between total emissions reported to the UNFCCC and global total emissions estimated from atmospheric data. Those differences have

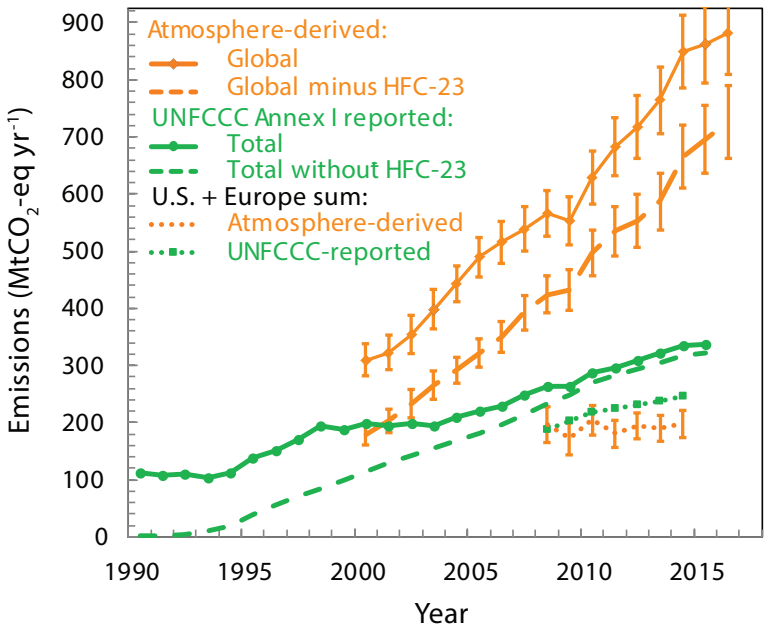

Figure 2-13. Summed HFC emissions, expressed as CO_2-eq, reported to UNFCCC (UNFCCC 2017) and based on atmospheric measurements, for the global and for the sum of the U.S. and European regions. (Global emission values from **Figure 2-1**; measurement-based regional estimates for the U.S. and Europe are taken from **Figure 2-4** and **Figure 2-5**). Sums including emissions of HFC-23 (solid lines) and without HFC-23 (dashed lines) are shown. Uncertainties on global estimates represent one standard deviation of estimates (see **Figure 2-1**); Uncertainties on regional estimates are approximate, based on the range and standard deviation quoted in the original sources (Graziosi et al., 2017 and Hu et al., 2017).

continued to grow over time for most gases (**Figure 2-1**) and in the aggregate of total HFC emission (**Figure 2-13**). On a CO_2-eq basis, aggregate HFC emissions reported to the UNFCCC in 2015, the latest year for which UNFCCC reporting is available, accounted for only 39% of the total global HFC emissions derived from global atmospheric mole fraction changes measured in the remote atmosphere; this value increases to 46% if emissions of only those HFCs used as ODS substitutes are considered (i.e., not HFC-23) (**Figure 2-13**).

Inverse analyses of atmospheric measurements made in the USA and in Europe suggest aggregate HFC emissions from these regions may actually be somewhat lower (by 10 to 20% in recent years, excluding HFC-23 emissions) than the totals reported to UNFCCC. Given that HFC emissions from the USA and Europe accounted for over 80% of total HFC emission reported to the UNFCCC for 2015 (excluding HFC-23; **Figure 2-13**), it is unlikely that inaccurate emission reporting from Annex I countries explains the increasing gap between global emissions derived from atmospheric data and totals reported to UNFCCC.

The dramatic increase in this emission gap over time is consistent with substantial increases in HFC use in developing countries not obligated to report emissions to the UNFCCC, as had been projected (Velders et al., 2009, 2015; Gschrey et al., 2011). Inverse analyses of atmospheric measurements of HFCs in East Asia support this conclusion (see **Section 2.3.1**). Furthermore, for some HFCs, such as HFC-23 and HFC-32, emissions from China or East Asia explain most, if not all, of the unreported emissions (see **Figures 2-7 and 2-8**). For other HFCs (HFC-134a, HFC-125, and HFC-143a), emissions from China or East Asia account for only a fraction of unreported emissions (see **Figures 2-9 and 2-10**).

2.3.5 Next Generation Substitutes

2.3.5.1 HFC-1234yf ($CF_3CF=CH_2$) and HFC-1234ze*(E)* (*(E)*-$CF_3CH=CHF$)

Unsaturated HFCs, also known as hydrofluoroolefins (HFOs), are being used as substitutes for higher GWP-HFCs in a number of applications. Given their short lifetimes and small GWPs, they are not included as controlled substances in the Kigali Amendment to the Montreal Protocol. HFC-1234yf and HFC-1234ze(E) are hydrofluoroolefins with estimated tropospheric OH-lifetimes of 12 days and 19 days, respectively, (**Table 2-2**) and 100-yr GWPs of less than 1 (Hodnebrog et al., 2013). HFC-1234yf has been identified as the main replacement for HFC-134a in MAC

Table 2-4. Composition of HFC blends referenced in this chapter

HFC Blend	Composition	100-yr GWP *
R-404A	44% HFC-125, 52% HFC-143a, 4% HFC-134a	4,210
R-407A	20% HFC-32, 40% HFC-125, 40% HFC-134a	2,070
R-407C	23% HFC-32, 25% HFC-125, 52% HFC-134a	1,730
R-407F	30% HFC-32, 30% HFC-125, 40% HFC-134a	1,790
R-410A	50% HFC-32, 50% HFC-125	2,080
R-446A of L-41 or L-41-1	68% HFC-32, 29% HFC=1234ze(E), 3% isobutane	480
R-447A or L-41-2	68% HFC-32, 3.5% HFC-125, 28.5 HFC-1234ze(e)	600
R-448A	26% HFC-32, 26% HFC-125, 20% HFC-1234yf, 21% HFC-134a, 7% HFC-1234ze(E)	1,370
R-449A	24.3% HFC-32, 24.7% HFC-125, 25.3% HFC-1234yf, 25.7% HFC-134a	1,370
R-449B	25.2% HFC-32, 24.3% HFC-125, 23.2% HFC-1234yf, 27.3% HFC-134a	1,390
R-450A	58% HFC-1234ze(E), 42% HFC-134a	570
R-452B or DR55	67% HFC-32, 7% HFC-125, 26% HFC-1234yf	715
R-459A or ARM71a	68% HFC-32, 26% HFC-1234yf, 6% HFC-1234ze(E)	480
R-513A	56% HFC-1234yf, 44% HFC-134a	600
DR5	72.5% HFC-32, 27.5% HFC-1234yf	510
L-41a	73% HFC-32, 15% HFC-1234yf, 12% HFC-1234ze(E)	515
L-41b	73% HFC-32, 27% HFC-1234ze(E)	515
ARM70a	50% HFC-32, 10% HFC-134a, 40% HFC-1234yf	490
D2Y60	40% HFC-32, 60% HFC-1234yf	282
HPR2A	76% HFC-32, 6% HFC-134a, 18% 1234ze(E)	615
HPR1D	60% HFC-32, 6% CO_2, 34% HFC-1234ze(E)	425

* 100-yr GWPs (Global Warming Potentials from this assessment) are calculated as the global warming influence of this gas relative to that by an equivalent mass emission of CO_2. See additional text in the Introduction.

systems in Europe, the USA (US EPA, 2017), and other countries, although use in developing countries may be limited because of current high production costs (UNEP, 2017a). HFC-1234ze(E) could replace HFC-134a for extruded polystyrene foam blowing (possibly in blends) and perhaps in metered-dose inhalers if toxicology, flammability, and cost concerns can be addressed (US EPA, 2017; UNEP, 2017a). Both compounds are also being investigated for use in refrigeration blends with saturated HFCs to replace fluids with high GWPs (UNEP, 2017a); various blends have been found to be non-flammable and acceptable for use (R-448A, R-449A, R-449B, R-450A, R-513A) even in domestic applications (US EPA, 2015b; 2016). See **Table 2-4** for the composition of HFC blends.

The first ambient-air measurements of these new olefinic HFCs were reported by Vollmer et al. (2015) from two sites in Switzerland (**see Figure 2-14**). In 2011, HFC-1234yf was undetectable at the high-altitude Jungfraujoch observatory, but by mid-2016 observed mole fractions were often in the 0.02–0.20 ppt range; higher values were observed at the urban Dübendorf site where they were often in the 1–4 ppt

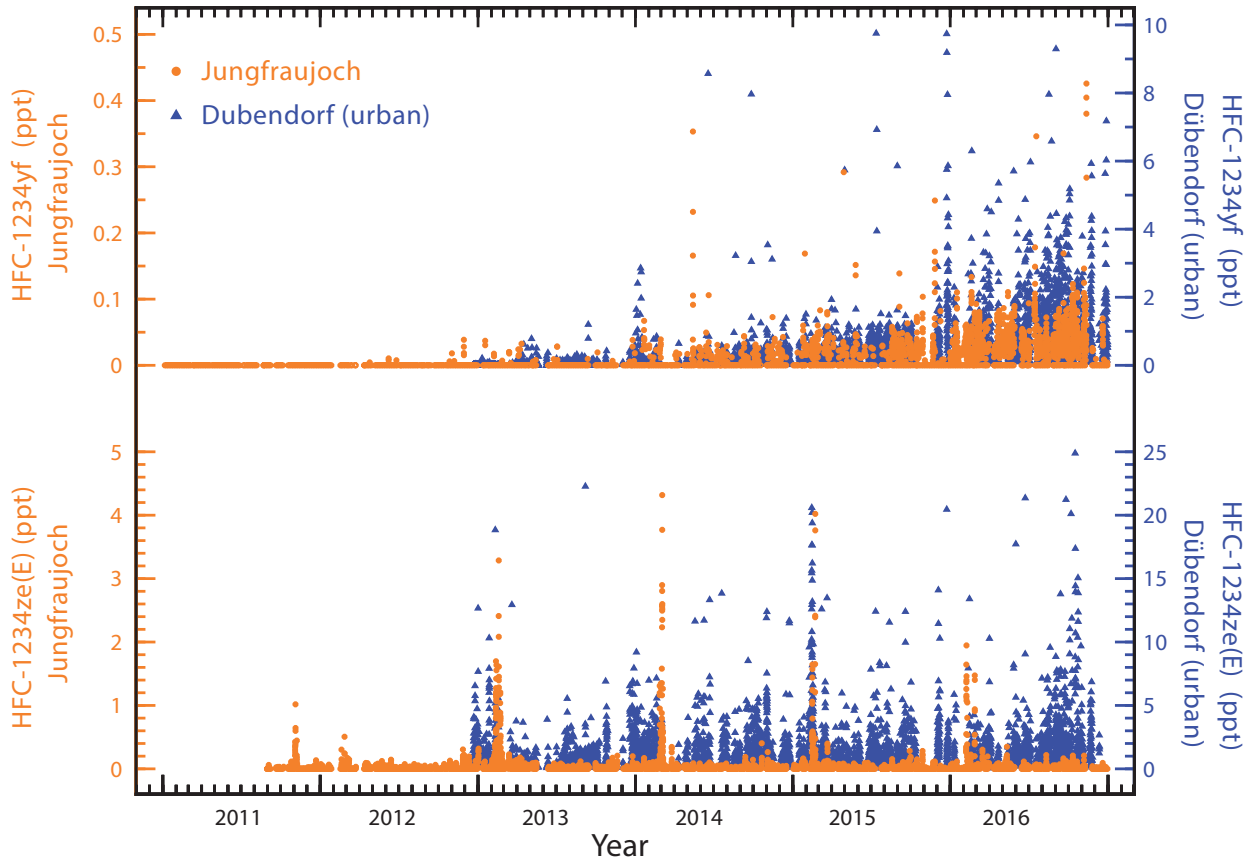

Figure 2-14. The emergence of HFC-1234yf and HFC-1234ze(e) in the atmosphere at two European sites, the mountaintop site Jungfraujoch (3,580 meters above sea level) and the urban Dübendorf site (updated from Vollmer et al., 2015). Different colors indicate results from different sites. Results at or below the detection limit (~0.003 ppt) are plotted at 0.003 ppt. By mid-2016, 1 to 4 ppt of HFC-1234yf and ~1 ppt of HFC-1234ze(E) were regularly observed at Dübendorf, with pollution events containing up to 20 ppt of HFC-1234ze(E), suggesting that it is more prevalently used in this region.

range. HFC-1234ze(E) has been observed in most samples since the beginning of dedicated ongoing observations. By mid-2016, ~0.025 ppt was commonly observed at Jungfraujoch and ~1 ppt at Dübendorf, where pollution events containing up to 20 ppt of this HFC have been seen, suggesting more prevalent use of HFC-1234ze(E) in this region (Vollmer et al., 2015).

2.4 ATMOSPHERIC CHEMISTRY OF HFCs

2.4.1 New Developments on Loss Rates and Lifetimes

HFCs are removed from the atmosphere mainly by their reactions with hydroxyl radicals (OH) in the troposphere. The residence times of HFCs in the atmosphere determined by reaction with tropospheric OH, τ_{HFC}^{OH}, are derived from the corresponding lifetime of methyl chloroform, CH_3CCl_3, (Spivakovsky et al., 2000) as described in previous Assessments (e.g., Box 1-1 in Carpenter and Reimann et al., 2014).

Although HFCs do not absorb stratospheric UV radiation, stratospheric loss processes, such as reactions with OH and $O(^1D)$, can contribute to the loss rate of long-lived HFCs and, therefore, slightly affect their lifetimes. Photolysis at the Lyman-a wavelength (121.6 nm) can only affect lifetimes of very long-lived species (such as perfluorinated compounds) that are inert enough to reach the mesosphere (≥ 70 km) in appreciable quantities; it has a negligible effect on the lifetimes of HFCs. Recent intensive modeling efforts (SPARC, 2013) provide detailed information on model-derived total lifetimes for a number of compounds, partial lifetimes due to specific photochemical

removal processes (reactions with OH, reactions with $O(^1D)$, and photolysis), and partial lifetimes associated with the atmospheric removal regions (troposphere and stratosphere). These results have been used to derive empirical correlations for estimating partial lifetimes due to stratospheric reactions of other HFCs, τ^{str}_{HFC}. The total atmospheric lifetimes, τ_{HFC}, reported in **Table 2-2** have been calculated as $(\tau_{HFC})^{-1} = (\tau^{OH}_{HFC})^{-1} + (\tau^{str}_{HFC})^{-1}$ to account for the stratospheric loss of HFCs.

Table 2-2 presents updated estimates of the lifetimes for partially fluorinated alkanes (HFCs), partially fluorinated olefins (HFCs that are also called HFOs) and perfluorinated olefins. The abundances of HFOs and perfluorinated olefins are also primarily controlled by their reactions with the hydroxyl radical. Compounds with atmospheric lifetimes shorter than ~0.5 years have been designated as very short-lived substances (VSLSs) as in previous Assessments. These compounds generally have non-uniform tropospheric distributions because their lifetimes are comparable to or shorter than the characteristic time of mixing processes in the troposphere.

The lifetime of VSLSs released into the atmosphere depends on local atmospheric conditions at the emission location and, therefore, the concept of a single global lifetime is inappropriate (e.g., Hodnebrog et al., 2013 and previous Ozone Assessment reports). Hence, the VSLS lifetimes presented in **Table 2-2** (with units of days) should not be considered as the global average atmospheric lifetime of a VSLS once emitted. Nevertheless, these estimates provide a useful scaling among such compounds and distinguish them from longer-lived HFCs that are well mixed in the troposphere. It should be noted that the local lifetimes of VSLSs tabulated in this report are ~10–20% longer than in previous Assessments primarily because they have now been calculated with the same approach that is used for longer-lived HFCs (i.e., relative to the global mean lifetime of methyl chloroform against OH oxidation), thereby avoiding arbitrary differences arising from the use of two different approaches.

For a few compounds in **Table 2-2**, experimental data on OH reactivity are not available. Lifetimes for these gases have been estimated based on either structure activity relationships or reactivity trends among similar compounds and appear in italics in **Table 2-2**.

OH reactivity for several compounds has been revised since the last Assessment based on new experimental data and/or analyses. However, these revisions do not substantially change the recommended atmospheric lifetimes. Other changes since the previous Assessment are listed below. (References related to these updates can be found in the notes to **Table 2-2**):

- HFC-72-17p, $CHF_2(CF_2)_6CF_3$, has been added.
- The lifetime of HFC-245cb is 15% shorter than estimated previously based on an analogy to HFC-143a. This revision reflects a new recommendation (Burkholder et al., 2015b), which is now based on laboratory-measured OH reactivity data.
- The estimated lifetime of HFC-272ca ($CH_3CF_2CH_3$) is based on OH reactivity calculated using the structure activity relationships. There are no experimental data.
- Lifetimes of shorter-lived HFC-152 (CH_2FCH_2F), HFC-161 (CH_3CH_2F), and HFC-281ea (CH_3CHFCH_3) are estimated to be ~18% longer than previous estimates. This revision is the result of the estimates now being made in a manner consistent with other HFCs.
- The list of fluorinated olefins has been expanded to include 7 new chemicals including stereo-isomers with different lifetimes and cyclic unsaturated fluorocarbons.
- The lifetimes of *(E)*-$CF_3CH{=}CHCF_3$ and *(E)*-$CF_3CH{=}CHCF_2CF_3$ are a factor of ~6 longer because experimental data on the OH reactivity of *(E)*-$CF_3CH{=}CHCF_3$ became available for the first time since the last Assessment.
- The lifetime of perfluorocyclopentene is more than an order of magnitude longer because experimental data on its reactivity toward OH became available for the first time since the last Assessment.

2.4.2 Updates on TFA Formation and Tropospheric Ozone Formation

Trifluoroacetic acid (TFA; CF_3COOH) is produced as the result of the breakdown in the atmosphere of several HCFCs and HFCs, such as HCFC-123 and HCFC-124, HFC-134a, HFC-143a, HFC-1234yf, and possibly HFC-1234ze (Burkholder et al., 2015a; Wallington et

al., 2015; Javadi et al., 2008). TFA is also produced as a breakdown product of a large number of other chemicals and is produced synthetically by the chemical industry, resulting, in many cases, in direct release to the atmosphere (Solomon et al., 2016). TFA also arises from natural processes. TFA is a stable compound that can accumulate in lakes and the ocean. As an acid or as a salt, TFA is of low to moderate toxicity to a range of organisms. The salts of TFA are inert and not of toxicological or environmental concern in the small concentrations (~200 ng L^{-1}) that are present in the ocean (UNEP, 2014a). The contribution of most sources to the total TFA budget is uncertain, although the source strength from atmospheric oxidation of HCFCs and HFCs is now better quantified.

Solomon et al. (2016) estimated TFA added to the oceans as a result of unregulated use of HCFCs and HFCs (including HFOs) up to 2050. Under an upper range scenario of global HFC use (Velders et al., 2015), it was estimated that by 2050 the total additional contribution of TFA to the oceans would be less than 7.5% of the approximately 200 ng acid equivalents L^{-1} estimated to be present at the start of the millennium (Solomon et al., 2016). With the 2016 Kigali Amendment to the Montreal Protocol, the projected use of HFCs is expected to be much lower (see **Section 3.1**) with consequently lower estimated TFA production from HFCs. Increased use of HFOs could augment TFA production and partially offset reductions in TFA production from saturated HFCs. The environmental effects of TFA, from the breakdown of HCFCs and HFCs, are therefore considered too small to be a risk to the environment over the next few decades (Solomon et al., 2016). However, potential longer-term impacts could require future evaluation due to the environmental persistence of TFA, uncertainty in future uses of HFOs, and because of uncertainties in the global budget of TFA. See **Section 6.2.6** for more information on TFA.

The atmospheric degradation of HFC-1234yf (an HFO) can also contribute tropospheric ozone and thereby contribute to reduced air quality. Luecken et al. (2010) showed that the additional tropospheric ozone from the conversion of HFC-134a to HFC-1234yf in mobile air conditioners in the USA is small compared with ambient ozone levels in cities in the USA.

2.5 POTENTIAL FUTURE CHANGES

Projections have suggested that the use and emissions of HFCs could increase substantially with the phase-out of HCFCs in developed countries by 2030 and in developing countries by 2040 (Velders et al., 2009; Gschrey et al. 2011; Rigby et al., 2014; Velders et al., 2015; UNEP, 2014c; Fang et al., 2016; Purohit and Höglund-Isaksson, 2017). Because many HFCs in use currently have high GWPs and these HFCs leak from appliances and other applications, they contribute to the radiative forcing (RF) of climate. The 2016 Kigali Amendment requires large reductions (up to 85% by 2035 or 2045 relative to a base level) for GWP-weighted HFC production and consumption for all developed and developing countries.

2.5.1 Scenarios

In this section, HFC scenarios developed elsewhere—with and without the implementation of the Kigali Amendment—are discussed, including their implications for radiative forcing of climate. Also discussed are alternatives to HFCs and factors that might be relevant for future HFC use.

2.5.1.1 HFC Scenarios Without Consideration of Controls: "Baseline" Scenarios

The Kigali Amendment of October 2016, assuming global implementation, will significantly affect the future demand for HFCs in developed and developing countries and consequently their emissions, mixing ratios, and radiative forcing of climate. The effects of the Amendment can be viewed relative to HFC baseline scenarios that were constructed in the past without including specific global control measures on HFC production or consumption. Here the results of several of these HFC baseline scenarios are compared before discussing the effects of the Kigali Amendment on future HFC emissions (**Section 2.5.1.3**). HFC-23 is not considered in these scenarios since it is not used as a replacement compound in applications that traditionally used ODSs, and it is also in a separate group in the Kigali Amendment (see **Section 2.5.1.5**).

In **Figure 2-15** the GWP-weighted emissions and corresponding radiative forcings are shown for HFCs in several of these baseline scenarios. The projected emissions in Velders et al. (2015) are an update of

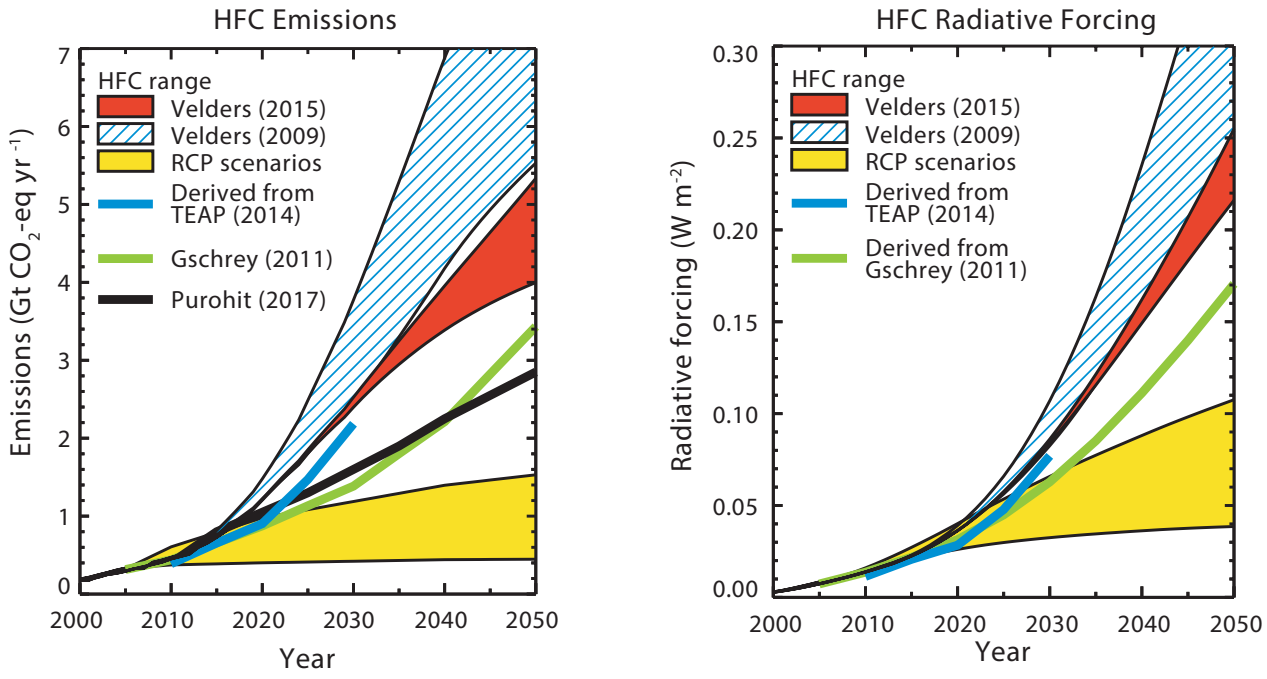

Figure 2-15. HFC emissions and radiative forcing scenarios from baseline scenarios (excluding HFC-23) from Velders et al. (2009), Gschrey et al. (2011), RCPs (Meinshausen et al., 2011), UNEP (2014c), Velders et al. (2015), and Purohit and Höglund-Isaksson (2017). The Velders et al. (2009) scenarios are shown, because they were the reference scenarios in the previous (2014) Assessment. The emissions and radiative forcing shown here are based on the GWPs and radiative efficiencies in the corresponding publications, which may differ from those in **Table 2-2**; the difference in CO_2-eq emissions is less than 1%.

those of Velders et al. (2009) based on more detailed and more current information on HFC use by sector and region. The scenarios of Velders et al. (2009) are shown here because they were the reference scenarios in the previous Assessment (Harris and Wuebbles et al., 2014). The HFC emissions in Velders et al. (2015) are similar to those in UNEP (2014c); they are slightly higher than projected in other sector-specific scenarios (Gschrey et al., 2011; Purohit and Höglund-Isaksson, 2017; Höglund-Isaksson et al., 2017); and they are significantly higher than in the Representative Concentration Pathways (RCPs) scenarios (Meinshausen et al., 2011). The latter two scenarios included different assumptions for the HCFC replacement pattern and/or different growth rate projections for HFC use in applications. In these scenarios, the lifetimes of the HFCs are kept constant. Model calculations show that HFC lifetimes might change towards 2100 due to changes in temperatures and OH abundances. Most models show a decrease in lifetime by 5–10% in 2100 relative to 2000 (SPARC, 2013). These changes depend on the future greenhouse gas abundances and are highly uncertain.

The recent sector- and region-specific HFC baseline scenarios of Velders et al. (2015) (**Figure 2-16**) assume that current uses (substances and technologies) of HFCs for specific sectors would continue without control measures and that developing countries would follow the same transitions from HCFCs to HFCs and not-in-kind alternatives as has occurred in developed countries, but at a later time. So these scenarios do not take into account the 2016 Kigali Amendment or the recent regulations of HFC use in the EU (revised F-gas regulation of the European Union; EU, 2014), USA (US EPA, 2015a) and Japan (METI, 2015). The scenarios are based on (1) robust historical HFC consumption data by sector for developed countries derived from their UNFCCC National Inventory Submissions (UNFCCC, 2014), (2) historical HFC consumption

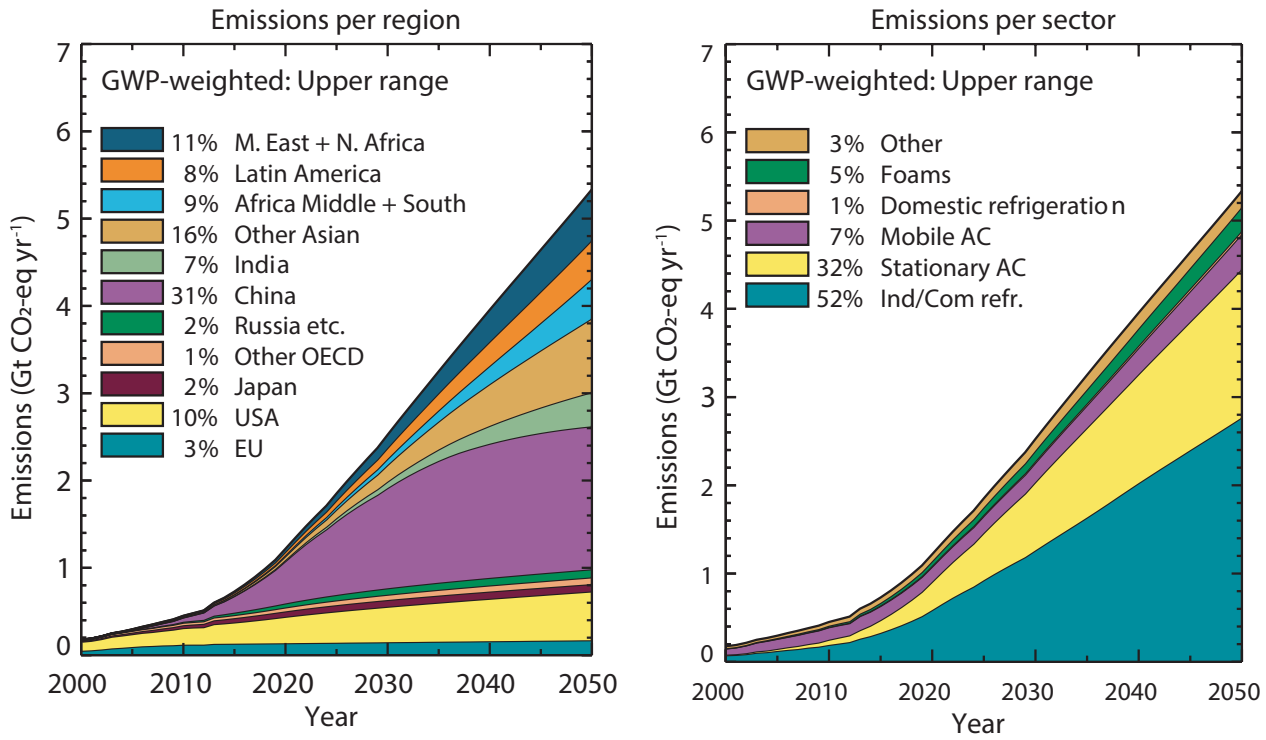

Figure 2-16. Regional and sectoral contributions to HFC GWP-weighted emissions for the upper-range baseline scenario of Velders et al. (2015), excluding HFC-23. The percentages refer to the global average relative contributions of each sector to the total GWP-weighted emissions in 2050. In the scenario, 10 HFCs are considered. The 11 regions are Europe, USA, Japan, other OECD countries, States of the former Soviet Republics and Yugoslavia (Russia), China, India, other Asian countries, Middle and Southern Africa, Latin America, and the Middle East plus Northern Africa. The six use sectors are (1) industrial, commercial (open compressor), commercial (hermetically sealed compressor), and transport refrigeration, (2) stationary AC, (3) mobile AC, (4) domestic refrigeration, (5) foams—extruded polystyrene, polyurethane, and open cell foams, and (6) other—aerosol products, fire extinguishing systems, and solvents. The emissions shown here are based on the GWPs used in Velders et al. (2015), which differ somewhat from those in **Table 2-2**; the difference in CO_2-eq emissions is less than 1%.

data for China (Zhang and Wang, 2014) and some other developing countries, (3) historical HCFC consumption data from UNEP (2015), (4) replacements pattern of HCFCs by HFCs and not-in-kind technologies (Velders et al., 2009; 2015), (5) scenarios of gross domestic product (GDP) and population from Shared Socioeconomic Pathway (SSP) projections (O'Neill et al., 2012) as drivers for the demand for HFCs, (6) observed atmospheric abundances of HFCs from 1990 to the beginning of 2013 as constraints on the historical consumption data, and (7) leakage rates (i.e., emission factors) derived from the UNFCCC National Inventory Submissions; these are kept constant over time in the scenarios.

The largest historical HFC use and emissions are in the developed countries, primarily the USA, EU, and Japan (**Figure 2-16**). In the baseline scenario, China is projected to become the largest emitter of HFCs by 2020, and Chinese emissions are projected to reach 31% of total CO_2-eq emissions (100-yr time horizon) of all HFCs by 2050 in the upper range HFC scenario (Velders et al., 2015). In all countries or regions, the largest contributions in CO_2-eq emissions come from industrial and commercial refrigeration (range of 40–58% for the different regions by 2050), because of the large use of HFCs and relatively large leakage rates from these applications, while the second largest HFC source comes from stationary air conditioning (AC) (21–40% by 2050) (**Figure 2-16**). Historically, mobile

AC has been responsible for the largest fraction of CO_2-eq HFC emissions, but this sector is projected to account for only 10–18% of developed country emissions by 2050. In developing countries in these scenarios, mobile AC contributes only 3–12% of total CO_2-eq HFC emissions in 2050. It should be noted that this baseline scenario does not include the effects in the EU and potentially around the globe of the EU MAC directive which has recently banned the use of HFC-134a in new cars (see **Section 2.5.1.2**).

In 2050, in the scenarios of Velders et al. (2015), CO_2-eq HFC emissions (excluding HFC-23) sum to 0.8–1.0 $GtCO_2$-eq yr^{-1} for the developed countries and 3.2–4.4 $GtCO_2$-eq yr^{-1} for the developing countries, resulting in a global total of 4.0–5.3 $GtCO_2$-eq yr^{-1}. In comparison, these values are equivalent to 5–11% of the global CO_2 emissions in 2050 in the RCP6.0 and RCP8.5 scenarios. The HFC radiative forcing (RF) (excluding HFC-23) in 2050 in these scenarios is 0.22–0.25 W m^{-2}. In comparisons of projected growth, the 2015–2050 increase in HFC CO_2-eq emissions is 9–29% of that for CO_2 over the same time period in the RCP scenarios. These CO_2-eq emissions represent only the direct emissions of the HFCs. Indirect CO_2 emissions associated with the production of fossil fuel-derived energy used by the appliances or in other applications need to also be considered for the overall impact of HFCs on radiative forcing (see **Section 2.5.2.3**).

In the refrigeration and air conditioning sectors, pure HFCs or blends of HFCs are used as refrigerants. The most-used HFC refrigerants in the scenarios are HFC-134a and the blends R-404A (mix of HFC-125, HFC-134a, HFC-143a) and R-410A (mix of HFC-32 and HFC-125). Consequently, these HFCs are projected to have the largest future emissions by mass or CO_2-eq (**Figure 2-17**). See **Table 2-4** for more detail about the composition of HFC blends.

The assumptions about market saturation are important aspects for the projections of HFCs. In the scenarios of Velders et al. (2015) the demand for HFCs per capita in developing countries is limited to the demand per capita in the developed countries. These scenarios do not take into account the potentially higher future demand for stationary AC as a result of increased ambient temperatures due to climate change. They also do

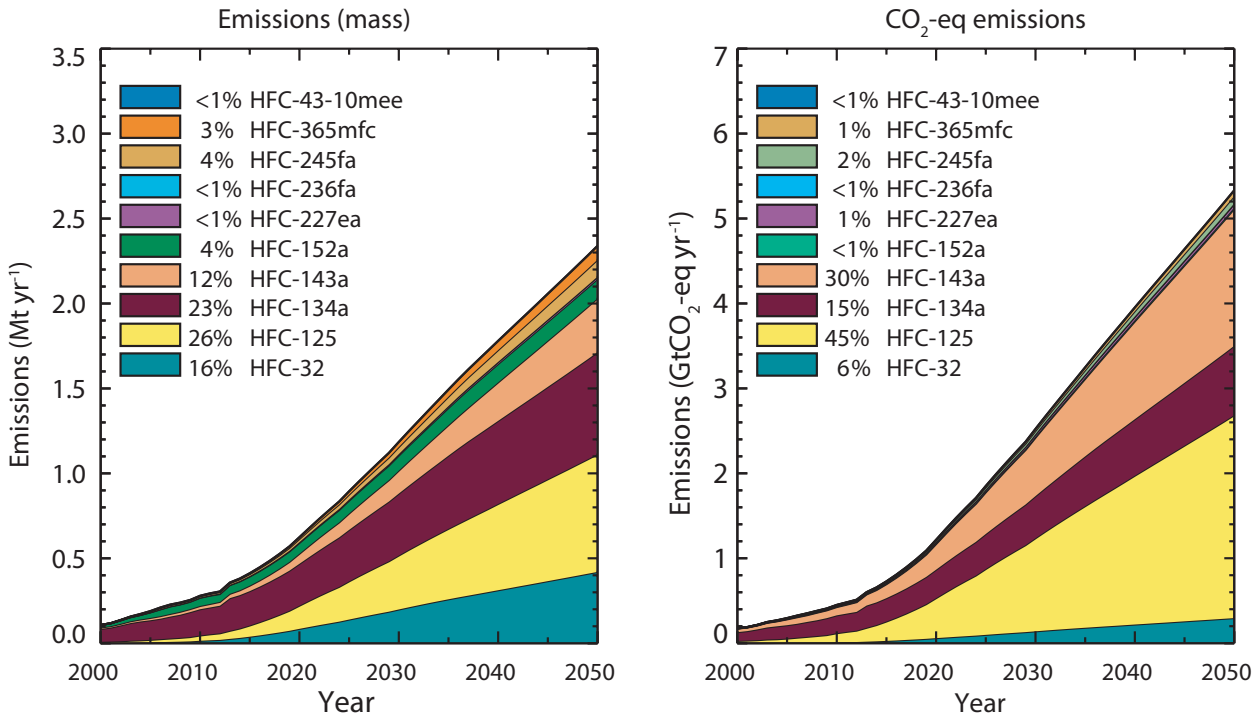

Figure 2-17. Contributions of the different HFCs to global emissions (in Mt yr^{-1} and $GtCO_2$-eq yr^{-1}) in the upper range baseline scenario of Velders et al. (2015). The percentages refer to the relative contributions in 2050.

not consider the fact that many developing countries have higher ambient temperatures than the developed countries and could, therefore, have a higher demand for stationary AC and higher emissions per capita.

2.5.1.2 Effect of National and Regional HFC Control Measures on Future Projections

In the EU, the 2006 MAC Directive, which addresses the use of mobile air conditioning (EU, 2006), and the 2014 revised F-gas Regulation (EU, 2014) ban the use of high-GWP HFCs in certain sectors. Although there is no common definition of high- or low-GWP, in the European Union Fluorinated Greenhouse Gas Regulations, a value of 150 or higher is often referred to as high. In addition to these bans on specific HFC use, there is an HFC phasedown schedule reducing the allowable amount (GWP-weighted) of HFCs placed on the EU market starting from a cap at the 2009–2012 average in 2015 and reaching a 79% reduction by 2030 relative to that average. The USA has already implemented incentive credits for use of low-GWP refrigerants (US EPA, 2012) in support of greenhouse gas emission standards for light duty vehicles; it also removed certain high-GWP HFCs from the Significant New Alternatives Policy (SNAP) list of allowable technologies for specific sectors as of 2015 (US EPA, 2015a)[3]. Japan also adopted a regulation in 2015 to limit the use of high-GWP HFCs for specific sectors (METI, 2015).

The regulations in the EU, USA, Japan, and elsewhere likely will drive changes in sector technologies (i.e., technologies and HFC-blends that currently use high-GWP HFCs) such as refrigeration, stationary and mobile AC, and foams. Consequently, these new technologies will likely also be available for other countries, thereby increasing the climate benefits of these national regulations. With global adoption of these technologies in a revised scenario, the 2050 emissions (excluding HFC-23) in the baseline scenario of 4.0–5.3 $GtCO_2$-eq yr^{-1} are reduced to 1.5–1.9 $GtCO_2$-eq yr^{-1} following the regulations in the EU, to 1.9–2.5 $GtCO_2$-eq yr^{-1} following the regulations in the USA, and to 2.0–2.6 $GtCO_2$-eq yr^{-1} following the regulations in Japan (**Figure 2-18**). These regulations will also lead to slower increases in radiative forcing from HFCs. The GWP-weighted emissions following the regulations are anticipated to more or less level off after 2030, at slightly more than half (reduction of 51–65%) the emissions of the baseline scenario; however, the radiative forcing continues to increase and is only reduced by 28–41% in 2050 compared to the baseline scenario because of the long atmospheric lifetimes (5–50 years) of the major high-GWP HFCs (**Figure 2-18**).

[3] In the USA, a process in the U.S. Court of Appeals is underway for SNAP rule 20, related to enabling a transition away from HFCs under Section 612 of the Clean Air Act. Implementation of the Court's direction is unclear under the EPA SNAP structure, so EPA has provided guidance stating that they will not enforce the HFC aspects of the rule while it is rewritten in compliance with the decision. (US EPA, 2018).

2.5.1.3 Projected Impact of the Kigali Amendment

Under the Kigali Amendment there are different base level years and phasedown schedules for developed countries (non-A5 Parties) and two groups of developing countries (A5 Parties) (**Table 2-1**). Following the Amendment, the allowable GWP-weighted HFC production and consumption will have to be reduced to 15–20% of the base level by 2045–2047 for developing countries and to 15% of the base level by 2036 for developed countries.

The Kigali Amendment requires global implementation to significantly limit future radiative forcing from HFCs. The national (e.g., USA and Japan) and regional (EU) regulations (see **Section 2.5.1.3**) that are already in place will aid and accelerate developed and developing countries' efforts to meet the provisions of the Amendment. The largest effect from the Kigali Amendment, though, is expected from the reductions in HFC production and consumption in developing countries. Some reductions in HFC use might have occurred in developing countries as a result of regulations in developed countries through technology transfer, but quantifying such reductions is difficult. Instead, the Kigali Amendment ensures legally binding reductions in HFC production for the first time in both developed and developing countries. Therefore, we discuss here the reductions in emissions and radiative forcing that result from applying the phasedown of the Kigali Amendment to the global baseline scenario, acknowledging that national and regional regulations also play an important role in limiting future climate forcing from HFCs.

With compliance to the Kigali Amendment controls (**Table 2-1**) and national and regional regulations, the

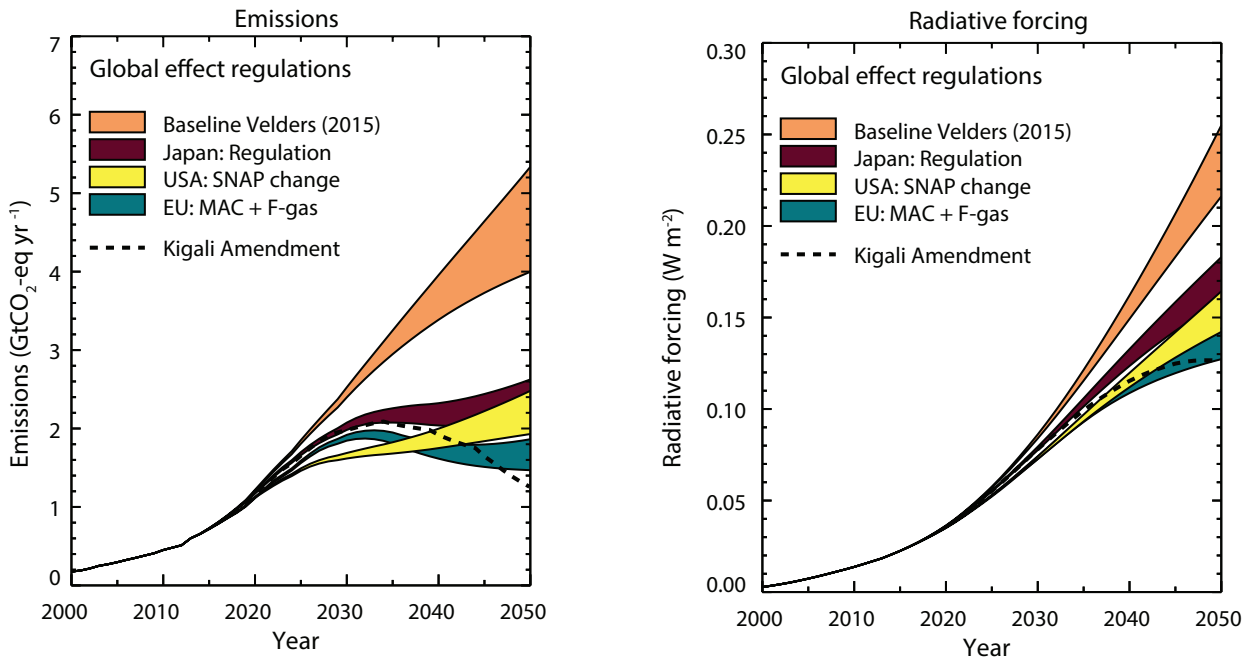

Figure 2-18. Response of global HFC emissions ($GtCO_2$-eq yr^{-1}) and global radiative forcing (W m^{-2}) in the baseline scenario of Velders et al. (2015) to global implementation of three national regulations and of the Kigali Amendment (HFC-23 not included). In each case, the national regulation is applied to all countries, with a 5-year delay of the regulations for developing countries. The emissions and radiative forcing shown here are based on the GWPs and radiative efficiencies used in Velders *et al.* (2015), which differ somewhat from those in **Table 2-2**. (Note: see **Section 2.5.1.2** for the status of the HFC regulations under SNAP).

peak in global production and consumption of HFCs is expected to occur around 2025. HFC emissions are projected to peak about a decade later (**Figures 2-18 and 2-19**; note these figures do not include HFC-23) because HFCs used as refrigerants in refrigeration and air conditioning systems are emitted gradually over a period of about a decade from the equipment during and after use (so-called banks). The total HFC bank, therefore, represents a potentially substantial source of emissions and radiative forcing even after production ceases (Velders et al., 2014). Despite this bank, adherence to controls in the Kigali Amendment results in HFC emissions from developed countries that are reduced from the baseline scenario level of 0.8–1.0 $GtCO_2$-eq yr^{-1} to 0.16 $GtCO_2$-eq yr^{-1} by 2050, and in developing countries, emissions are reduced from 3.2–4.4 $GtCO_2$-eq yr^{-1} to 1.1 $GtCO_2$-eq yr^{-1}, for a total reduction from 4.0–5.3 $GtCO_2$-eq yr^{-1} to 1.3 $GtCO_2$-eq yr^{-1}. The total reduction by 2100 is from 6.1–9.3 $GtCO_2$-eq yr^{-1} to 0.6 $GtCO_2$-eq yr^{-1}. So, the estimated benefit of the Amendment is the avoidance of 2.8–4.1 $GtCO_2$-eq yr^{-1} emissions by 2050 and 5.6–8.7 $GtCO_2$-eq yr^{-1} by 2100. For comparison, total CH_4 emissions are projected to be 7.0–25 $GtCO_2$-eq yr^{-1} by 2100 in the RCP6.0 and RCP8.5 scenarios and total N_2O emissions 5.0–7.0 $GtCO_2$-eq yr^{-1} by 2100 (RCP emissions from Meinshausen et al., 2011; GWPs of N_2O and CH_4 from Myhre and Shindell et al., 2013).

Radiative forcing from HFCs is projected to peak around the middle of the century, or a decade after the peak in emissions, due to continued emissions from the banks and the slow breakdown of the HFCs in the atmosphere (i.e., lifetimes up to about 50 years for HFCs used as ODS substitutes). The response of the global HFC radiative forcing to the Kigali Amendment and national controls is a reduction from 0.22–0.25 W m^{-2} in the baseline scenario to 0.13 W m^{-2} by 2050, and from 0.48–0.77 W m^{-2} to 0.08 W m^{-2} by 2100. The effects of the Kigali Amendment on global emissions and RF through 2050 are similar to the effects of the different national regulations (discussed above) when implemented globally (**Figure 2-18**).

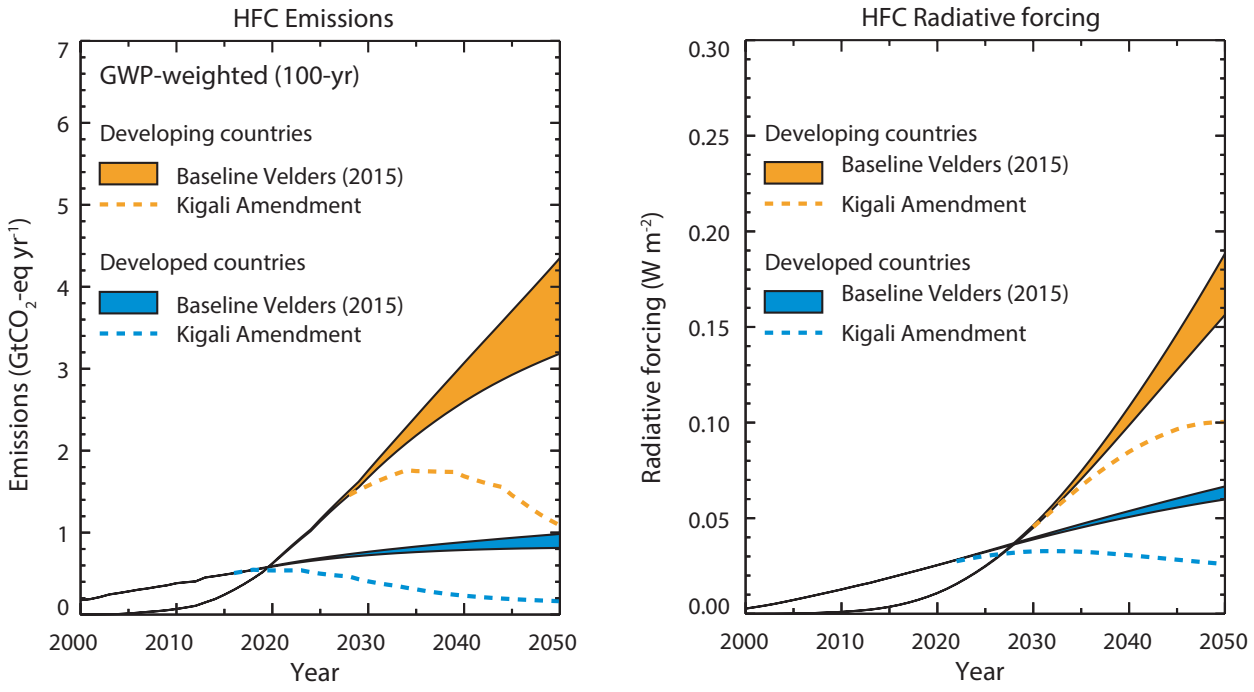

Figure 2-19. Response of HFC emissions ($GtCO_2$-eq yr^{-1}) and radiative forcing in the baseline scenario (Velders et al., 2015) for developed and developing countries to implementation of the Kigali Amendment to the Montreal Protocol (excluding HFC-23). Extending the scenarios beyond 2050 under the same assumptions gives a radiative forcing for the baseline scenario of 0.07–0.12 W m^{-2} and 0.40–0.65 W m^{-2} in 2100 for the developed and developing countries, respectively. The 2100 radiative forcing under the Kigali Amendment is 0.01 W m^{-2} and 0.06–0.07 W m^{-2} for the developed and developing countries, respectively. The emissions and radiative forcing shown here are based on the GWPs and radiative efficiencies used in Velders et al. (2015), which differ somewhat from those in **Table 2-2**.

2.5.1.4 Climate Impacts of HFCs

The radiative forcing from HFCs contributes to changes in atmospheric circulation, temperature, and sea level (see **Chapter 5**). Atmospheric changes in temperature and circulation arising from HFC emissions lead to a weak, indirect depletion of stratospheric ozone (Hurwitz et al. 2015). Ozone Depletion Potentials (ODPs) of the most relevant HFCs range from 0.00039 for HFC-32 to 0.03 for HFC-23 (see **Chapter 1**).

Xu et al. (2013) calculate, using a parameterized integrated carbon and radiant energy balance model, a global average surface warming by HFCs of about 0.1°C by 2050 and 0.35–0.50°C by 2100, based on the scenarios of Velders et al. (2009) (**Figure 2-20**). With a different parameterized climate model, they calculated a surface temperature change of 0.10–0.12°C for 2050 and 0.28–0.44°C for 2100 based on the scenarios of Velders et al. (2015). These scenarios differ in their assumption for the projections of the demand for HFCs past 2050 and the way potential market saturation is taken into account. To calculate the temperature response of HFCs in 2100, the emissions over the whole period from 2000 to 2100 are important. In **Figure 2-20** HFC emissions and temperature changes are shown based on the Velders et al. (2015) scenario in which the same assumptions and model are used for the period past 2050 as for 2000–2050.

With the Kigali Amendment and national and regional regulations, the future production and consumption of HFCs is strongly limited (**Table 2-1**). Under the provisions of the Amendment, the contribution of HFCs to the global average surface temperature is projected to reach a maximum around 2060, after which it slowly decreases to about 0.06°C by 2100 (**Figure**

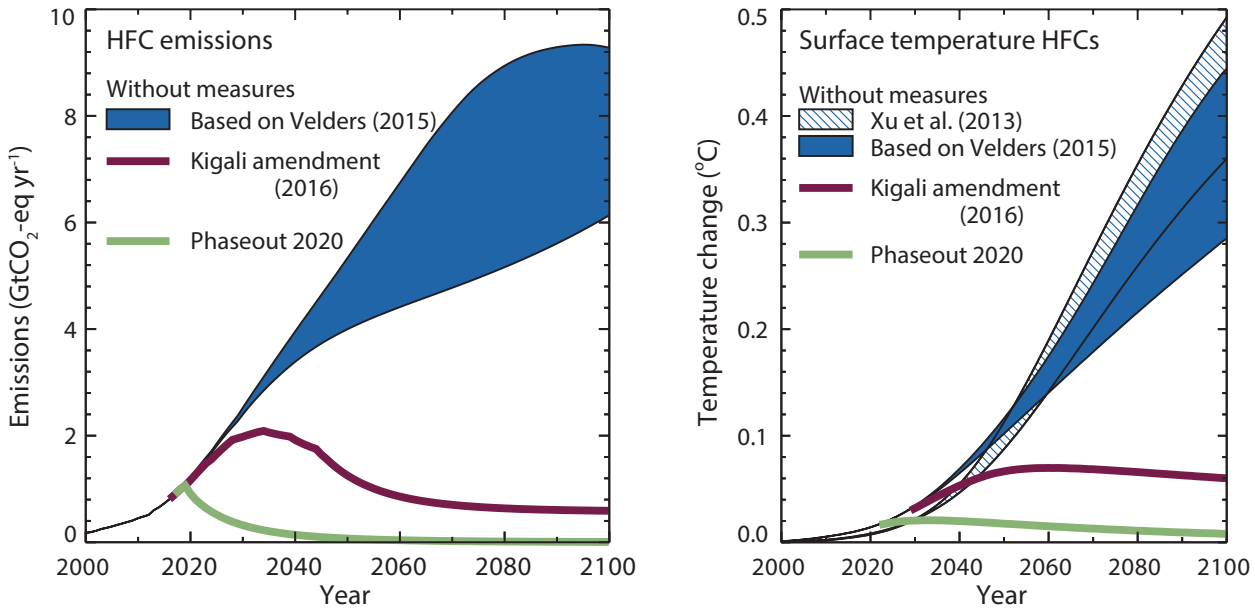

Figure 2-20. HFC emissions and the contribution of HFCs to the global average surface warming of Earth with and without the Kigali Amendment. The scenarios without the measures are based on Xu et al. (2013) and Velders et al. (2015) which differ in their assumptions for the projections of the demand for HFCs past 2050. Also shown is a hypothetical scenario assuming that the global production of HFCs would cease in 2020. The surface temperature change based on Velders et al. (2015) is calculated using the MAGICC6 model. For comparison, the total warming from all greenhouse gases is projected to be 1.4–4.8°C by the end of the 21st century following the RCP6.0 and RCP8.5 scenarios (Collins and Knutti et al., 2013). The contribution from HFC-23 is not included here. The emissions shown here are based on the GWPs used in Velders et al. (2015), which differ somewhat from those in **Table 2-2**; the difference in CO_2-eq emissions is less than 1%.

2-20). In contrast, the surface temperature contribution from HFCs in the baseline scenario is 0.3–0.5°C in 2100 (based on Xu et al., 2013 and Velders et al., 2015). The difference in projected temperatures is relevant in the context of the 2015 UNFCCC Paris Agreement, which aims to limit the global temperature increase to well below 2°C relative to pre-industrial levels.

In **Figure 2-20**, the effects are also shown of a hypothetical scenario in which the global production of HFCs ceases in 2020. In this case, the emissions start decreasing immediately and the surface temperature contribution of the accumulated HFC emissions is projected to stay below 0.02°C for the whole 21st century. These calculated surface warmings do not include emissions from HFC-23.

Due to the thermal inertia of the ocean, the response of surface temperature and even more so sea level rise through thermal expansion is even slower than changes in radiative forcing from the controls on HFC production. After HFCs, or any other greenhouse gas, stop being emitted, the climate system is not initially in equilibrium with radiative forcing, and the ocean will continue to take up heat until equilibrium is reached (see, e.g., Zickfeld et al., 2017 and Hu et al., 2013).

Historical and projected concentrations, emissions, and contributions to climate change have been calculated for ODSs, high-GWP HFCs, and low-GWP alternatives (**Figure 2-21**), assuming full compliance with the Montreal Protocol, including the Kigali Amendment. The phase-down schedule for HFC production and consumption substantially reduces future projected global HFC emissions. Summed HFC emissions are expected to peak before 2040 and decline to less than 1 $GtCO_2$-eq yr^{-1} by 2100. This peak emission is well below summed ODS emissions at their peak

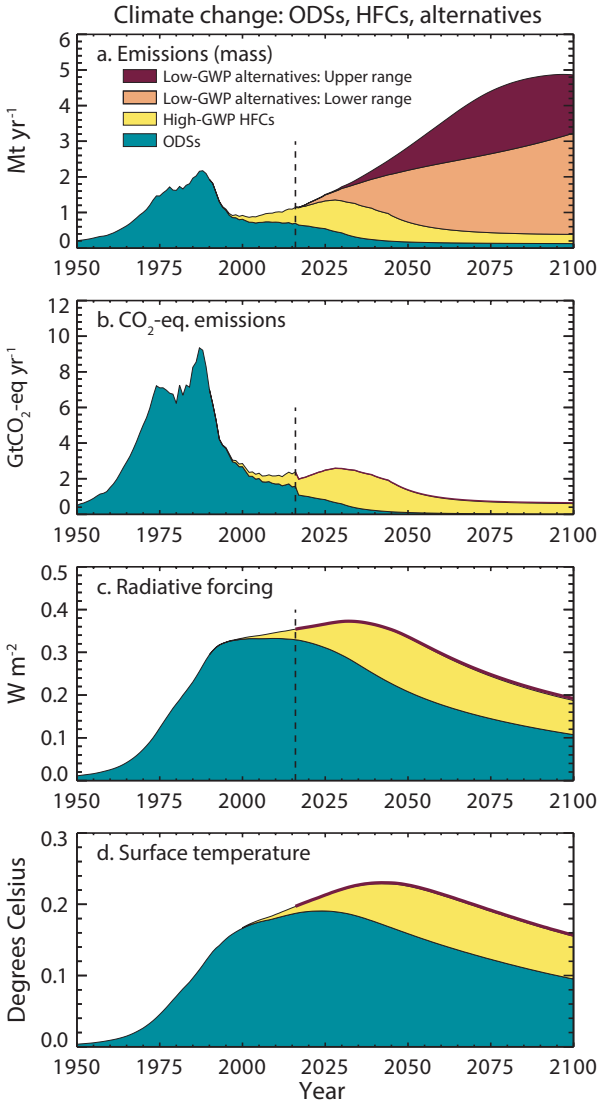

Figure 2-21. Projected contributions to climate change from ODSs, high-GWP HFCs, and low-GWP alternatives assuming full compliance to the provisions of the Montreal Protocol, including the Kigali Amendment. Shown are (a) emissions by mass, (b) CO_2-eq emissions, (c) radiative forcing, and (d) average surface temperature contributions. Only the direct GWP-weighted emissions, radiative forcing, and temperature effects of the ODSs and HFCs are shown. The ODS data are from the baseline (A1) scenario of **Chapter 6** of this Assessment. The ODS emissions from around 1980 through 2016 are derived from atmospheric observations and after 2016 are from the scenario (distinction indicated by dashed vertical lines). The projected HFC quantities follow the controls of the Kigali Amendment assuming full compliance (**Figure 2-20**). The projections of the low-GWP alternatives result from imposing the controls of the Kigali Amendment to the HFC baseline scenario (curve in **Figure 2-20** labeled 'without measures'; Velders et al., 2015). The difference between the HFC baseline scenario and the Kigali Amendment scenario are assigned here to the low-GWP alternatives. These could be chemicals with a GWP of less than 20 or alternative technologies. The low-GWP alternatives scenario assumes that the alternatives use the same amount (by mass) per application as the HFCs they replace. The curve with the low-GWP alternatives is based on the upper and lower range scenarios from Velders et al. (2015) and **Figure 2-20**. The contributions of the low-GWP alternatives in panels b, c, and d are smaller than the thickness of the green curves. Not included here are contributions from HFC-23, indirect radiative effects from ozone depletion, and indirect effects associated with the energy used by equipment and the associated CO_2 emissions.

in the 1980s. Only marginal increases are projected for CO_2-eq emissions of the low-GWP alternatives despite substantial projected increases in the mass of their emissions.

A more complete understanding of the climate impact of refrigerant-using equipment can be accomplished through more detailed analysis of, for example, the Life Cycle Climate Performance (LCCP), which includes direct and indirect emissions (i.e., those associated with energy use) as well as associated emissions from production and disposal (see e.g., Papasavva et al., 2010; **Section 2.5.2.3**).

2.5.1.5 HFC-23 Projection

Emissions of HFC-23 originate predominantly as a by-product of HCFC-22 production, and they have continued despite mitigation efforts. HFC-23 is a strong infrared absorber and has the longest lifetime (228 years) and highest GWP (12,690 for a 100-year time horizon; **Table 2-2**; see **Section 2.3**) of the HFCs considered in this Assessment. The amount of HFC-23 emitted depends on the amount of HCFC-22 produced, the yield of HFC-23 from the production process, and the degree to which produced HFC-23 is incinerated. Although HFC-23 is included under the phasedown schedule with other HFCs (**Table 2-1**), a separate provision is additionally included for HFC-23 in the Amendment that states: "Each country manufacturing HCFC-22 or HFCs shall ensure that starting in 2020 the emissions of HFC-23 generated in production facilities are destroyed to the extent practicable using technology approved by the Montreal Protocol" (UNEP, 2016a). Without abatement, HFC-23 emissions were projected to increase to ~20 Gg yr^{-1} by 2016 and ~24 Gg yr^{-1} by 2035 (Miller and Kuijpers, 2011). Emissions for 2016, derived from atmospheric observations, are 12.3 Gg yr^{-1}, well below the worst-case scenario, but above the best-practice scenario of ~11 Gg yr^{-1}. With implementation of the provisions of the Kigali Amendment, future HFC-23 emissions are expected to be limited significantly.

Recently, developments in chemical synthesis may have opened up the use of HFC-23 as feedstock for the production of a wide range of -CF_3 containing fluorochemicals (Grushin, 2014), which may affect future HFC-23 emissions.

2.5.2 HFC Alternatives

2.5.2.1 Alternatives: HFOs, Hydrocarbons, CO_2, NH_3, Not-in-Kind Alternatives

Commercially-available alternatives with low- to medium-GWPs are available for high-GWP HFCs for many refrigeration and AC sector applications; however, more supporting work (e.g., standards development and code adoption) is needed for use of some of the lowest GWP options and fastest growing sectors, such as certain air conditioning sectors. Efforts to optimize cooling capacity and energy efficiency performance of refrigeration and air conditioning equipment containing low-GWP and zero-ODP refrigerants continue to make progress, as do standards development in all sectors.

In recent years, there has been a focus on natural refrigerants (CO_2, hydrocarbons, and ammonia), low-GWP HFCs, and HFOs alone or in blends with saturated HFCs to replace fluids with high-GWP. The use of hydrocarbons (e.g., iso-butane [R-600a] and propane [R-290]), ammonia (R-717), and carbon dioxide (R-744) continues.

European domestic refrigerator and freezer manufacturers have been required to use refrigerants with a GWP less than 150 since 2015 (EU, 2014). In the USA, domestic appliance manufacturers have created a voluntary commitment to convert away from HFC-134a use as a refrigerant (AHAM, 2016). A charge size of up to 57 g of iso-butane (R-600a) has been allowed in refrigeration and has been in commercial use for some time in self-contained refrigerated food cases and smaller domestic refrigerators (US EPA, 2011). Other options to replace HFC-134a include HFC-1234yf, HFC-152a, and non-flammable blends of HFOs and HFCs. European commercial refrigeration GWP limits are phased in gradually; limits are initially placed on HFCs with GWPs greater than 2,500, and in 2020, on HFCs with GWPs larger than 150 in applications where alternatives are available and affordable. In addition, there is a service ban on HFCs having GWPs greater than 2,500 starting in 2020 (EU, 2014). In the USA, the HFC-blend R-404A is not allowed in new equipment as of 1 January 2017 for supermarkets, as of 1 January 2018 for condensing units, and as of 1 January 2019 for self-contained systems (2020 for larger systems). High-GWP blends such as R-404A

are not allowed in new refrigerated food processing and dispensing equipment from 1 January 2021 and in new warehouse applications from 1 January 2023 (US EPA, 2015a). Canada has published draft recommendations that limit the use of fluids having GWPs above 650 starting in 2020 for stand-alone, medium temperature commercial refrigeration systems and they limit the use of fluids having GWPs above 1,500 in stand-alone low temperature commercial refrigeration (Environment and Climate Change Canada, 2017).

Low-GWP refrigerant blends of HFC/HFO/hydrochlorofluoroolefins (such as R-448A, R-449A, R-449B, R-450A, and R-513A; **Table 2-4**) have GWPs that are 50–70% lower than refrigerants they typically replace, and they are in commercial use in refrigeration equipment. The use of R-407A and R-407F (at approximately half the GWP of R-404A) continues to grow in many parts of the world. Non-halocarbon refrigerants such as CO_2 (R-744) and propane (R-290) are increasingly being used in supermarkets.

2.5.2.2 Safety Issues

Some alternatives to high-GWP HFCs (e.g., water and inert gases) pose no safety risk to handle but others do entail some risk. According to safety ratings, hydrocarbons have higher flammability than most HFCs, while ammonia and some HFOs have lower flammability, and CO_2 is non-flammable. Safety ratings also indicate higher toxicity for ammonia than for most HFCs and lower toxicity for hydrocarbons, HFC-1234yf, and CO_2 (ASHRAE, 2016). Safety issues can be resolved by changes in design of equipment, limiting the refrigerant charge sizes, and limiting potential emissions (UNEP, 2011).

2.5.2.3 Energy Efficiency vis-à-vis GWP

The overall life-cycle climate impact of refrigeration and air conditioning applications that use halocarbons as refrigerants depends on many factors including, but not limited to

- the GWP of the refrigerant used,
- the loss (or recovery) of the refrigerant at the end of life of the equipment,
- the leakage rate of the refrigerant and recharge rates during service,
- the energy required to operate the coolant device,
- the number of hours that the equipment is used, and
- the carbon intensity of the electricity used to power the equipment.

Of these, for most applications, emissions due to the energy use of the equipment tend to dominate the life-cycle emissions (unless the grid is exceptionally free of carbon-emitting energy sources or the hours of use are very low). For example, Goetzler et al. (2016) estimated 73–76% of global CO_2–eq emissions from AC systems in 2010 to be indirect emissions from the energy use. Hence the energy efficiency resulting from the use of specific refrigerants is a very important consideration.

In the context of the Montreal Protocol, energy efficiency[4] has had a range of commonly accepted meanings, which include, but are not limited to the following:

1. The performance of a refrigerant relative to an HFC, HCFC, or CFC refrigerant being replaced such that it **consumes less energy to perform the same service** in the same (or similar) refrigeration or air-conditioning equipment, henceforth referred to as "refrigerant energy efficiency".
2. The performance of refrigeration or air-conditioning equipment by replacing one or more components other than the refrigerant such that it **consumes less energy to perform the same service**, henceforth referred to as "equipment energy efficiency".

There are other methods to reduce energy consumption in refrigeration, air conditioning, or other applications in which halocarbons are used, which fall under a broader consideration of "energy efficiency", such as using building insulation or maintenance to ensure optimal operation. Such methods (sometimes called "not-in-kind") are less germane to a discussion of energy efficiency in the context of the Montreal

[4] Sometimes "energy efficiency" is also used to denote a metric or quantitative measure designed to measure the amount of energy used to perform a particular service, e.g., reduce the temperature of one ton of chilled water by 1 degree C. The less energy used to perform the same service, the more energy efficient the technology being used.

Protocol, since the influence of these approaches is generally independent of the chemical chosen as coolant.

Many studies have been conducted to evaluate both types of energy efficiency improvement mentioned above (e.g., Schultz, 2016; Abdelaziz et al., 2015). For example, in a study of refrigerant energy efficiency in air conditioners, Schultz (2016) found that some alternate low-GWP refrigerants, e.g., HFC-32 and R-452B (blend of 67% HFC-32, 7% HFC-125, and 26% HFC-1234yf, also referred to as DR-55), perform as well as or better than the HFC refrigerant R-410A (blend of 50% HFC-32 and 50% HFC-125). Meanwhile, Abdelaziz et al. (2015) found that the low-GWP refrigerant R-290 (propane) achieved a slightly higher efficiency than HCFC-22, but with a slightly lower cooling capacity under test conditions.

Equipment energy efficiency has been evaluated mainly under the aegis of market transformation programs for energy efficiency such as those run by the EU Ecodesign program (EuP, 2008) and the U.S. Department of Energy (DOE, 2017). Shah et al. (2013) found that a ~30% efficiency improvement, relative to current technologies, for air conditioners was cost-effective in many economies.

The conversion from using HFC refrigerants with high GWPs to refrigerants with lower GWPs, which will most likely result from the Kigali Amendment, provides an opportunity to consider other technological improvements that offer additional climate benefits through improvements in equipment energy efficiency.

Shah et al. (2015) found that if, in 2030, the world mini-split AC stock (i.e., the total number of installed and operational mini-split ACs[5]) transitioned from high-GWP, low-efficiency equipment to low-GWP refrigerants such as HFC-32 or propane (R-290), coupled with improved equipment that was 30% more efficient, the climate benefit over the ~10 year lifetime of the ACs would be over 25 $GtCO_2$-eq emissions. This would roughly double the CO_2-eq emission reductions in comparison with either policy (refrigerant transition or equipment energy efficiency improvement) implemented in isolation. The combined direct and indirect emissions abatement from both policies implemented together for mini-split ACs would be roughly 98 $GtCO_2$-eq emissions by 2050, as a result of the large projected growth in ACs in developing countries (**Figure 2-22**). Regions with higher hours of use or more carbon-intensive electricity grids would benefit more from energy efficiency improvement.

Based on the various alternate refrigerant testing programs listed above and the various energy efficiency market transformation studies, similar results (in % terms) may also be found for other air-conditioning and refrigeration equipment. Results are dependent on hours of use, emissions during operation or at end of life, grid carbon intensity, growth rates, and other relevant factors.

In conclusion, improvements in energy efficiency in refrigeration and air conditioning equipment during the transition to low-GWP alternative refrigerants can potentially double the climate benefits of the HFC phasedown of the Kigali Amendment. The potential magnitude of these combined benefits would contribute to achieving the targets of the UNFCCC 2015 Paris Agreement, which aims to keep global temperature rise this century well below 2°C above pre-industrial levels.

[5] Mini-split ACs are the most widely used type of AC system, representing roughly ~70% of sales by unit worldwide.

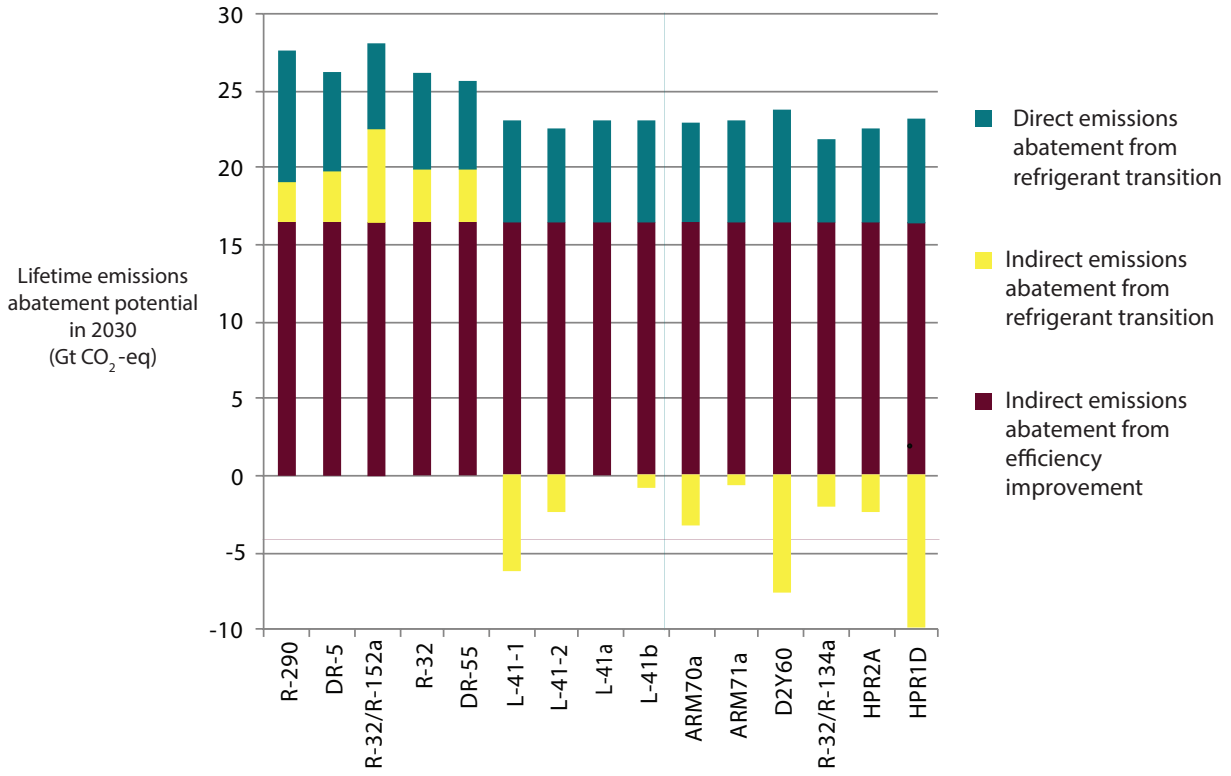

Figure 2-22. Estimated emissions abatement potential of air conditioning (AC) Stock in 2030 over 10-year AC lifetime. Positive numbers indicate CO_2 emission reductions while negative numbers indicate increases in CO_2 emissions[1]. Source: Shah et al. (2015). The purple bar indicates the "indirect" emissions abatement from the ~30% equipment efficiency improvement (compared with current technologies) while the yellow bar indicates the "indirect" emissions abatement refrigerant energy efficiency improvement (or reduction), and the blue bar indicates the direct emissions abatement due to the lower GWP of the refrigerant compared to the commonly used AC refrigerant R-410A[2]. See **Table 2-4** for the acronyms of the different refrigerants. R32/R152a is a blend of 95% HFC-32 and 5% HFC-152a. R32/R134a is a blend of 95% HFC-32 and 5% HFC-134a.

[1] Shah et al. (2015) estimated the world AC stock (# of installed units) will grow from ~900 million units in 2015 to roughly 1.6 billion units in 2030.

[2] Indirect emissions are emissions from the electricity grid due to the energy consumption of the equipment, while direct emissions are emissions of the refrigerant from the equipment due to leakage or at the end of life.

REFERENCES

Abdelaziz, O., S.S. Shrestha, J.D. Munk, R.L. Linkous, W. Goetzler, M. Guernsey, and T. Kassuga, *Alternative Refrigerant Evaluation for High-Ambient-Temperature Environments: R-22 and R-410A Alternatives for Mini-Split Air Conditioners,* No. ORNL/TM-2015/536, Oak Ridge National Laboratory, Oak Ridge, Tennessee, USA, https://energy.gov/sites/prod/files/2015/10/f27/bto_pub59157_101515.pdf, 2015.

AHAM (Association of Home Appliance Manufacturers), *Home Appliance Industry Sets Goal to Eliminate Use of HFC Refrigerants*, http://www.aham.org/AHAM/News/Latest_News/Home_Appliance_Industry_Sets_Goals_to_Eliminate_Use_of_HFC_Refrigerants.aspx, 2016.

Ammann, M., R.A. Cox, J.N. Crowley, H. Herrmann, M.E. Jenkin, V.F. McNeil, A. Mellouki, M.J. Rossi, J. Troe, and T.J. Wallington, IUPAC Task Group on Atmospheric Chemical Kinetic Data Evaluation, http://iupac.pole-ether.fr, 2017.

Andersen, S.O., M.L. Halberstadt, and N. Borgford-Parnell, Stratospheric ozone, global warming, and the principle of unintended consequences—An ongoing science and policy success story, *J. Air Waste Manag. Assoc.*, *63* (6), 607-647, doi:10.1080/10962247.2013.791349, 2013.

Arnold, T., D.J. Ivy, C.M. Harth, M.K. Vollmer, J. Mühle, P.K. Salameh, L.P. Steele, P.B. Krummel, R.H.J. Wang, D. Young, C.R. Lunder, O. Hermansen, T.S. Rhee, J. Kim, S. Reimann, S. O'Doherty, P.J. Fraser, P.G. Simmonds, R.G. Prinn, and R.F. Weiss, HFC-43-10mee atmospheric abundances and global emission estimates, *Geophys. Res. Lett.*, *41* (6), 2228-2235, doi:10.1002/2013GL059143, 2014.

ASHRAE (American Society of Heating, and Refrigerating and Air-Conditioning Engineers), *Refrigerant Designations, ANSI/ASHRAE 34-2016m*, http://www.ashrae.org/technical-resources/standards-and-guidelines/ashrae-refrigerant-designations, 2016.

Baasandorj, M., and J.B. Burkholder, Rate coefficient for the gas-phase OH + $CHF=CF_2$ reaction between 212 and 375 K, *Int. J. Chem. Kinet.*, *48* (11), 714-723, doi:10.1002/kin.21027, 2016.

Baasandorj, M., P. Marshall, R.L. Waterland, A.R. Ravishankara, and J.B. Burkholder, Rate coefficient measurements and theoretical analysis of the OH + *(E)*-$CF_3CH=CHCF_3$ reaction, *J. Phys. Chem. A*, *122*(19), 4635-4646, doi:10.1021/acs.jpca.8b02771, 2018.

Barletta, B., P. Nissenson, S. Meinardi, D. Dabdub, F. Sherwood Rowland, R.A. VanCuren, J. Pederson, G.S. Diskin, and D.R. Blake, HFC-152a and HFC-134a emission estimates and characterization of CFCs, CFC replacements, and other halogenated solvents measured during the 2008 ARCTAS campaign (CARB phase) over the South Coast Air Basin of California, *Atmos. Chem. Phys.*, *11* (6), 2655-2669, doi:10.5194/acp-11-2655-2011, 2011.

Brunner, D., T. Arnold, S. Henne, A. Manning, R.L. Thompson, M. Maione, S. O'Doherty, and S. Reimann, Comparison of four inverse modelling systems applied to the estimation of HFC-125, HFC-134a, and SF_6 emissions over Europe, *Atmos. Chem. Phys.*, *17* (17), 10651-10674, doi:10.5194/acp-17-10651-2017, 2017.

Burkholder, J.B., R.A. Cox, and A.R. Ravishankara, Atmospheric degradation of ozone depleting substances, their substitutes, and related species, *Chem. Rev.*, *115* (10), 3704-3759, doi:10.1021/cr5006759, 2015a.

Burkholder, J.B., S.P. Sander, J. Abbatt, J.R. Barker, R.E. Huie, C.E. Kolb, M.J. Kurylo, V.L. Orkin, D.M. Wilmouth, and P.H. Wine, *Chemical Kinetics and Photochemical Data for Use in Atmospheric Studies, Evaluation No. 18*, JPL Publication 15-10, Jet Propulsion Laboratory, Pasadena, Calif., http://jpldataeval.jpl.nasa.gov/, 2015b.

Carpenter, L.J., S. Reimann (Lead Authors), J.B. Burkholder, C. Clerbaux, B.D. Hall, R. Hossaini, J.C. Laube, S.A. Yvon-Lewis, Update on Ozone-Depleting Substances (ODSs) and Other Gases of Interest to the Montreal Protocol, Chapter 1 in *Scientific Assessment of Ozone Depletion: 2014*, Global Ozone Research and Monitoring Project–Report No. 55, World Meteorological Organization, Geneva, Switzerland, 2014.

CDIAC (Carbon Dioxide Information Analysis Center), *The ALE / GAGE / AGAGE Network (DB1001)*, Investigators: R.G. Prinn, R.F. Weiss, P.B. Krummel, S. O'Doherty, P.J. Fraser, J. Mühle, S. Reimann, M.K. Vollmer, P.G. Simmonds, M. Maione, J. Arduini, C.R. Lunder, N. Schmidbauer, D. Young, H.J. Wang, J. Huang, M. Rigby, C.M. Harth, P.K. Salameh, T.G. Spain, L.P. Steele, T. Ar-

nold, J. Kim, O. Hermansen, N. Derek, B. Mitrevski, and R. Langenfelds, Oak Ridge National Laboratory, doi:10.3334/CDIAC/atg.db1001, 2016.

Chen, L., T. Uchimaru, S. Kutsuna, K. Tokuhashi, A. Sekiya, and H. Okamoto, Kinetics and mechanism of gas-phase reaction of $CF_3CF_2CF_2CF_2$-$CF_2CF_2CF_2CF_2H$ with OH radicals in an environmental reaction chamber at 253–328K, *Chem. Phys. Lett.*, *501* (4), 263-266, doi:10.1016/j.cplett.2010.12.009, 2011.

Collins, M., R. Knutti, (Lead Authors), J. Arblaster, J.-L. Dufresne, T. Fichefet, P. Friedlingstein, X. Gao, W.J. Gutowski, T. Johns, G. Krinner, M. Shongwe, C. Tebaldi, A.J. Weaver, M. Wehner, Long-term Climate Change: Projections, Commitments and Irreversibility, Chapter 12 in *Climate Change 2013: The Physical Science Basis: Contribution of Working Group I to the Fifth Assessment Report of the Intergovernmental Panel on Climate Change*, edited by T.F. Stocker, D. Qin, G.-K. Plattner, M. Tignor, S.K. Allen, J. Boschung, A. Nauels, Y. Xia, V. Bex, and P.M. Midgley, Cambridge University Press, Cambridge, United Kingdom, 2013.

Cunnold, D.M., R.G. Prinn, R.A. Rasmussen, P.G. Simmonds, F.N. Alyea, C.A. Cardelino, A.J. Crawford, P.J. Fraser, and R.D. Rosen, The Atmospheric Lifetime Experiment: 3. Lifetime methodology and application to three years of $CFCl_3$ data, *J. Geophys. Res.*, *88* (C13), 8379-8400, doi:10.1029/JC088iC13p08379, 1983.

DeMore, W.B., Experimental and estimated rate constants for the reactions of hydroxyl radicals with several halocarbons, *J. Phys. Chem.*, *100* (14), 5813-5820, doi:10.1021/jp953216+, 1996.

DOE (U.S. Department of Energy), *Technical Support Document: Energy Efficiency Program for Consumer Products: Residential Central Air Conditioners and Heat Pumps*, Washington, D.C., http://www.regulations.gov/contentStreamer?documentId=EERE-2014-BT-STD-0048-0098&attachmentNumber=1&contentType=pdf, 2017.

EDGAR, European Commission, Joint Research Centre / Netherlands Environmental Assessment Agency, *Emission Database for Global Atmospheric Research (EDGAR), release version 4.2 FT2010*, http://edgar.jrc.ec.europa.eu/overview.php?v=42FT2010, 2013.

Environment and Climate Change Canada, *Canada Environmental Protection Act, 1999, Regulations Amending the Ozone-Depleting Substances and Halocarbon Alternatives Regulations,* Part II Vol. 151, http://www.puntofocal.gov.ar/notific_otros_miembros/can507a1_t.pdf, 2017.

EU (European Union), Directive 2006/40/EC of the European Parliament and of the Council of 17 May 2006 relating to emissions from air-conditioning systems in motor vehicles, *OJEU*, *L161*, 14.6.2006, 12-18, 2006.

EU (European Union), Regulation (EU) No 517/2014 of the European Parliament and of the Council of 16 April 2014 on fluorinated greenhouse gases and repealing Regulation (EC) No 842/2006, *OJEU*, *L150, 195-230*, http://eur-lex.europa.eu/legal-content/EN/TXT/PDF/?uri=CELEX-:32014R0517&from=EN, 2014.

EuP, Preparatory study on the environmental performance of residential room conditioning appliances (airco and ventilation), *Final Report of Task 6*, http://www.eup-network.de/fileadmin/user_upload/Produktgruppen/Aircon_Final_report_of_Task_6.pdf, European Commission Ecodesign Directive, 2008.

Fang, X., A. Stohl, Y. Yokouchi, J. Kim, S. Li, T. Saito, S. Park, and J. Hu, Multiannual top-down estimate of HFC-23 emissions in East Asia, *Environ. Sci. Technol.*, *49* (7), 4345-4353, doi:10.1021/es505669j, 2015.

Fang, X., G.J.M. Velders, A.R. Ravishankara, M.J. Molina, J. Hu, and R.G. Prinn, Hydrofluorocarbons (HFCs) emissions in China: An inventory for 2005–2013 and projections to 2050, *Environ. Sci. Technol.*, *50* (4), 2027-2034, doi:10.1021/acs.est.5b04376, 2016.

Fortems-Cheiney, A., M. Saunois, I. Pison, F. Chevallier, P. Bousquet, C. Cressot, S.A. Montzka, P.J. Fraser, M.K. Vollmer, P.G. Simmonds, D. Young, S. O'Doherty, R.F. Weiss, F. Artuso, B. Barletta, D.R. Blake, S. Li, C. Lunder, B.R. Miller, S. Park, R. Prinn, T. Saito, L.P. Steele, and Y.C.J. Yokouchi, Increase in HFC-134a emissions in response to the success of the Montreal Protocol, *J. Geophys. Res.*, *120* (22), 11,728-11,742, doi:10.1002/2015JD023741, 2015.

Goetzler, W., M. Guernsey, J. Young, J. Fuhrman, and O. Abdelaziz., *The Future of Air Conditioning for Buildings-Executive Summary (DOE/EE-1394)*, Oak Ridge National Laboratory, Oak Ridge, Tennessee, USA, https://energy.gov/sites/prod/

files/2016/07/f33/The%20Future%20of%20AC%20Report%20-%20Executive%20Summary_0.pdf, 2016.

Graziosi, F., J. Arduini, F. Furlani, U. Giostra, P. Cristofanelli, X. Fang, O. Hermanssen, C. Lunder, G. Maenhout, S. O'Doherty, S. Reimann, N. Schmidbauer, M.K. Vollmer, D. Young, and M. Maione, European emissions of the powerful greenhouse gases hydrofluorocarbons inferred from atmospheric measurements and their comparison with annual national reports to UNFCCC, *Atmos. Environ.*, *158*, 85-97, doi:10.1016/j.atmosenv.2017.03.029, 2017.

Grushin, V.V., Fluoroform as a feedstock for high-value fluorochemicals: Novel trends and recent developments, *Chimi. Oggi-Chem. Today*, *32* (3), 81-88, 2014.

Gschrey, B., W. Schwarz, C. Elsner, and R. Engelhardt, High increase of global F-gas emissions until 2050, *Greenhouse Gas Meas. and Mgmt.*, *1* (2), 85-92, doi:10.1080/20430779.2011.579352, 2011.

Harris, N.R.P., D.J. Wuebbles (Lead Authors), J.S. Daniel, J. Hu, L.J.M. Kuijpers, K.S. Law, M.J. Prather, and R. Schofield, Scenarios and information for policymakers, Chapter 5 in *Scientific Assessment of Ozone Depletion: 2014*, Global Ozone Research and Monitoring Project–Report No. 55, World Meteorological Organization, Geneva, Switzerland, 2014.

Harrison, J.J., C.D. Boone, A.T. Brown, N.D.C. Allen, G.C. Toon, and P.F. Bernath, First remote sensing observations of trifluoromethane (HFC-23) in the upper troposphere and lower stratosphere, *J. Geophys. Res.*, *117* (D5), D05308, doi:10.1029/2011JD016423, 2012.

Harrison, J.J., Infrared absorption cross sections for trifluoromethane, *J. Quant. Spect. Rad. Trans.*, *130*, 359-364, doi: 10.1016/j.jqsrt.2013.05.026, 2013.

Harrison, J.J., Infrared absorption cross sections for 1,1,1,2-tetrafluoroethane, *J. Quant. Spect. Rad. Trans.*, *151*, 210-216, doi:10.1016/j.jqsrt.2014.09.023, 2015.

Hartmann, D.L., A.M.G.K. Tank, M. Rusticucci (Coordinating Lead Authors), L.V. Alexander, S. Brönnimann, Y.A.-R. Charabi, F.J. Dentener, E.J. Dlugokencky, D.R. Esaterling, A. Kaplan, B.J. Soden, P.W. Thorne, M. Wild, P, Zhai, Observations: Atmosphere and Surface, Chapter 2 in *Climate Change 2013: The Physical Science Basis: Contribution of Working Group I to the Fifth Assessment Report of the Intergovernmental Panel on Climate Change*, edited by T.F. Stocker, D. Qin, G.-K. Plattner, M. Tignor, S.K. Allen, J. Boschung, A. Nauels, Y. Xia, V. Bex, and P.M. Midgley, Cambridge University Press, Cambridge, United Kingdom, 2013.

Hodnebrog, Ø., M. Etminan, J.S. Fuglestvedt, G. Marston, G. Myhre, C.J. Nielsen, K.P. Shine, and T.J. Wallington, Global warming potentials and radiative efficiencies of halocarbons and related compounds: A comprehensive review, *Rev. Geophys.*, *51* (2), 300-378, doi:10.1002/rog.20013, 2013.

Höglund-Isaksson, L., P. Purohit, M. Amann, I. Bertok, P. Rafaj, W. Schöpp, and J. Borken-Kleefeld, Cost estimates of the Kigali Amendment to phase-down hydrofluorocarbons, *Environ. Sci. Policy*, *75*, 138-147, doi:10.1016/j.envsci.2017.05.006, 2017.

Hu, A., Y. Xu, C. Tebaldi, W.M. Washington, and V. Ramanathan, Mitigation of short-lived climate pollutants slows sea-level rise, *Nature Clim. Change*, *3*, 730-734, doi:10.1038/nclimate1869, 2013.

Hu, L., S.A. Montzka, S.J. Lehman, D.S. Godwin, B.R. Miller, A.E. Andrews, K. Thoning, J.B. Miller, C. Sweeney, C. Siso, J.W. Elkins, B.D. Hall, D.J. Mondeel, D. Nance, T. Nehrkorn, M. Mountain, M.L. Fischer, S.C. Biraud, H. Chen, and P.P. Tans, Considerable contribution of the Montreal Protocol to declining greenhouse gas emissions from the United States, *Geophys. Res. Lett.*, *44* (15), 8075-8083, doi:10.1002/2017GL074388, 2017.

Hurwitz, M.M., E.L. Flemming, P.A. Newman, F. Li, E. Mlawer, K. Cady-Pereira, and R. Bailey, Ozone depletion by hydrofluorocarbons, *Geophys. Res. Lett.*, *42*, 8686-8692, doi:10.1002/2015GL065856, 2015.

Javadi, M.S., R. Søndergaard, O.J. Nielsen, M.D. Hurley, and T.J. Wallington, Atmospheric chemistry of trans-CF_3CH=CHF: Products and mechanisms of hydroxyl radical and chlorine atom initiated oxidation, *Atmos. Chem. Phys.*, *8* (12), 3141-3147, doi:10.5194/acp-8-3141-2008, 2008.

Jia, X., L. Chen, J. Mizukado, S. Kutsuna, and K. Tokuhashi, Rate constants for the gas-phase reactions of *cyclo*-CX=CXCF_2CF_2– (X=H, F) with OH radicals at a temperature range of 253–328K, *Chem. Phys. Lett.*, *572*, 21-25, doi:10.1016/j.cplett.2013.04.020, 2013.

Keller, C.A., D. Brunner, S. Henne, M.K. Vollmer, S. O'Doherty, and S. Reimann, Evidence for under-

reported western European emissions of the potent greenhouse gas HFC-23, *Geophys. Res. Lett.*, *38* (15), L15808, doi:10.1029/2011GL047976, 2011.

Keller, C.A., M. Hill, M.K. Vollmer, S. Henne, D. Brunner, S. Reimann, S. O'Doherty, J. Arduini, M. Maione, Z. Ferenczi, L. Haszpra, A.J. Manning, and T. Peter, European emissions of halogenated greenhouse gases inferred from atmospheric measurements, *Environ. Sci. Technol.*, *46* (1), 217-225, doi:10.1021/es202453j, 2012.

Kim, J., S. Li, K.-R. Kim, A. Stohl, J. Mühle, S.-K. Kim, M.-K. Park, D.-J. Kang, G. Lee, C.M. Harth, P.K. Salameh, and R.F. Weiss, Regional atmospheric emissions determined from measurements at Jeju Island, Korea: Halogenated compounds from China, *Geophys. Res. Lett.*, *37* (12), L12801, doi:10.1029/2010GL043263, 2010.

Laube, J.C., P. Martinerie, E. Witrant, T. Blunier, J. Schwander, C.A.M. Brenninkmeijer, T.J. Schuck, M. Bolder, T. Röckmann, C. van der Veen, H. Bönisch, A. Engel, G.P. Mills, M.J. Newland, D.E. Oram, C.E. Reeves, and W.T. Sturges, Accelerating growth of HFC-227ea (1,1,1,2,3,3,3-heptafluoropropane) in the atmosphere, *Atmos. Chem. Phys.*, *10* (13), 5903-5910, doi:10.5194/acp-10-5903-2010, 2010.

Le Bris, K., J. DeZeeuw, P.J. Godin, and K. Strong, Infrared absorption cross-sections, radiative efficiency and global warming potential of HFC-43-10mee, *J. Mol. Spectrosc.*, *348*, 64-67, doi:10.1016/j.jms.2017.06.004, 2017.

Leedham Elvidge, E., H. Bönisch, C.A.M. Brenninkmeijer, A. Engel, P.J. Fraser, E. Gallacher, R. Langenfelds, J. Mühle, D.E. Oram, E.A. Ray, A.R. Ridley, T. Röckmann, W.T. Sturges, R.F. Weiss, and J.C. Laube, Evaluation of stratospheric age of air from CF_4, C_2F_6, C_3F_8, CHF_3, HFC-125, HFC-227ea and SF_6; implications for the calculations of halocarbon lifetimes, fractional release factors and ozone depletion potentials, *Atmos. Chem. Phys.*, *18* (5), 3369-3385, doi:10.5194/acp-18-3369-2018, 2018.

Li, S., J. Kim, K.-R. Kim, J. Mühle, S.-K. Kim, M.-K. Park, A. Stohl, D.-J. Kang, T. Arnold, C.M. Harth, P.K. Salameh, and R.F. Weiss, Emissions of halogenated compounds in east Asia determined from measurements at Jeju Island, Korea, *Environ. Sci. Technol.* (13), 5668-5675, doi:10.1021/es104124k, 2011.

Luecken, D.J., R.L. Waterland, S. Papasavva, K.N. Taddonio, W.T. Hutzell, J.P. Rugh, and S.O. Andersen, Ozone and TFA impacts in North America from degradation of 2,3,3,3-tetrafluoropropene (HFO-1234yf), a potential greenhouse gas replacement, *Environ. Sci. Technol.*, *44* (1), 343-348, doi:10.1021/es902481f, 2010.

Lunt, M.F., M. Rigby, A.L. Ganesan, A.J. Manning, R.G. Prinn, S. O'Doherty, J. Mühle, C.M. Harth, P.K. Salameh, T. Arnold, R.F. Weiss, T. Saito, Y. Yokouchi, P.B. Krummel, L.P. Steele, P.J. Fraser, S. Li, S. Park, S. Reimann, M.K. Vollmer, C. Lunder, O. Hermansen, N. Schmidbauer, M. Maione, J. Arduini, D. Young, and P.G. Simmonds, WΣWΣReconciling reported and unreported HFC emissions with atmospheric observations, *Proc. Natl. Acad. Sci.*, *112* (19), 5927-5931, doi:10.1073/pnas.1420247112, 2015.

Meinshausen, M., S. Smith, K. Calvin, J. Daniel, M. Kainuma, J.F. Lamarque, K. Matsumoto, S. Montzka, S. Raper, K. Riahi, A. Thomson, G. Velders, and D.P. van Vuuren, The RCP greenhouse gas concentrations and their extensions from 1765 to 2300, *Clim. Change.*, *109* (1), 213-241, doi:10.1007/s10584-011-0156-z, 2011.

METI, *Act on the rational use and proper management of fluorocarbons* (Act No. 64 of 2001), Ministry of Economy, Trade and Industry, Japan, http://conf.montreal-protocol.org/meeting/workshops/hfc_management/presentations/Statements by Heads of Delegations/M. Ohki Session 4, 2014.

Miller, B.R., R.F. Weiss, P.K. Salameh, T. Tanhua, B.R. Greally, J. Muhle, and P.G. Simmonds, Medusa: A sample preconcentration and GC/MS detector system for in situ measurements of atmospheric trace halocarbons, hydrocarbons, and sulfur compounds, *Anal. Chem.*, *80* (5), 1536-1545, doi:10.1021/ac702084k, 2008.

Miller, B.R., M. Rigby, L.J.M. Kuijpers, P.B. Krummel, L.P. Steele, M. Leist, P.J. Fraser, A. McCulloch, C. Harth, P. Salameh, J. Mühle, R.F. Weiss, R.G. Prinn, R.H.J. Wang, S. O'Doherty, B.R. Greally, and P.G. Simmonds, HFC-23 (CHF_3) emission trend response to HCFC-22 ($CHClF_2$) production and recent HFC-23 emission abatement measures, *Atmos. Chem. Phys.*, *10* (16), 7875-7890, doi:10.5194/acp-10-7875-2010, 2010.

Miller, B.R., and L.J.M. Kuijpers, Projecting future

HFC-23 emissions, *Atmos. Chem. Phys.*, *11* (24), 13259-13267, doi:10.5194/acp-11-13259-2011, 2011.

Miller, J.B., S.J. Lehman, S.A. Montzka, C. Sweeney, B.R. Miller, A. Karion, C. Wolak, E.J. Dlugokencky, J. Southon, J.C. Turnbull, and P.P. Tans, Linking emissions of fossil fuel CO_2 and other anthropogenic trace gases using atmospheric $^{14}CO_2$, *J. Geophys. Res.*, *117* (D8), D08302, doi: 10.1029/2011JD017048, 2012.

Montzka, S.A., R.C. Myers, J.H. Butler, J.W. Elkins, L.T. Lock, A.D. Clarke, and A.H. Goldstein, Observations of HFC-134a in the remote troposphere, *Geophys. Res. Lett.*, *23* (2), 169-172, doi: 10.1029/95gl03590, 1996.

Montzka, S.A., L. Kuijpers, M.O. Battle, M. Aydin, K.R. Verhulst, E.S. Saltzman, D.W. Fahey, Recent increases in global HFC-23 emissions, *Geophys. Res. Lett.*, *37*, L02808, doi:10.1029/2009GL041195, 2010.

Montzka, S.A., E.J. Dlugokencky, J.H. Butler, Non-CO_2 greenhouse gases and climate change, *Nature*, 476, 43-50, doi:10.1038/nature10322, 2011.

Montzka, S.A., M. McFarland, S.O. Andersen, B.R. Miller, D.W. Fahey, B.D. Hall, L. Hu, C. Siso, and J.W. Elkins, Recent trends in global emissions of hydrochlorofluorocarbons and hydrofluorocarbons: Reflecting on the 2007 adjustments to the Montreal Protocol, *J. Phys. Chem. A*, *119* (19), 4439-4449, doi:10.1021/jp5097376, 2015.

Myhre, G., D. Shindell (Coordinating Lead Authors), F.-M. Bréon, W. Collins, J. Fuglestvedt, J. Huang, D. Koch, J.-F. Lamarque, D. Lee, B. Mendoza, T. Nakajima, A. Robock, G. Stephens, T. Takemura, and H. Zhang, Anthropogenic and Natural Radiative Forcing, Chapter 8 in *Climate Change 2013: The Physical Science Basis: Contribution of Working Group I to the Fifth Assessment Report of the Intergovernmental Panel on Climate Change*, edited by T.F. Stocker, D. Qin, G.-K. Plattner, M. Tignor, S.K. Allen, J. Boschung, A. Nauels, Y. Xia, V. Bex, and P.M. Midgley, Cambridge University Press, Cambridge, United Kingdom, 2013.

Nassar, R., P.F. Bernath, C.D. Boone, S.D. McLeod, R. Skelton, K.A. Walker, C.P. Rinsland, and P. Duchatelet, A global inventory of stratospheric fluorine in 2004 based on Atmospheric Chemistry Experiment Fourier transform spectrometer (ACE-FTS) measurements, *J. Geophys. Res.*, *111* (D22), D22313, doi:10.1029/2006JD007395, 2006.

O'Doherty, S., D.M. Cunnold, B.R. Miller, J. Mühle, A. McCulloch, P.G. Simmonds, A.J. Manning, S. Reimann, M.K. Vollmer, B.R. Greally, R.G. Prinn, P.J. Fraser, L.P. Steele, P.B. Krummel, B.L. Dunse, L.W. Porter, C.R. Lunder, N. Schmidbauer, O. Hermansen, P.K. Salameh, C.M. Harth, R.H.J. Wang, and R.F. Weiss, Global and regional emissions of HFC-125 (CHF_2CF_3) from in situ and air archive atmospheric observations at AGAGE and SOGE observatories, *J. Geophys. Res.*, *114*, D23304, doi: 10.1029/2009JD012184, 2009.

O'Doherty, S., M. Rigby, J. Mühle, D.J. Ivy, B.R. Miller, D. Young, P.G. Simmonds, S. Reimann, M.K. Vollmer, P.B. Krummel, P.J. Fraser, L.P. Steele, B. Dunse, P.K. Salameh, C.M. Harth, T. Arnold, R.F. Weiss, J. Kim, S. Park, S. Li, C. Lunder, O. Hermansen, N. Schmidbauer, L.X. Zhou, B. Yao, R.H.J. Wang, A.J. Manning, and R.G. Prinn, Global emissions of HFC-143a (CH_3CF_3) and HFC-32 (CH_2F_2) from in situ and air archive atmospheric observations, *Atmos. Chem. Phys.*, *14* (17), 9249-9258, doi:10.5194/acp-14-9249-2014, 2014.

O'Neill, B.C., T.R. Carter, K.L. Ebi, J. Edmonds, S. Hallegatte, E. Kemp-Benedict, E. Kriegler, L. Mearns, R. Moss, K. Riahi, B. van Ruijven, and D. van Vuuren, *Meeting Report of the Workshop on The Nature and Use of New Socioeconomic Pathways for Climate Change Research*, 110 pp., Boulder, Colorado, November 2-4, 2011, available at http://www.isp.ucar.edu/socioeconomic-pathways, 2012.

Oram, D.E., C.E. Reeves, W.T. Sturges, S.A. Penkett, P.J. Fraser, and R.L. Langenfelds, Recent tropospheric growth rate and distribution of HFC-134a (CF_3CH_2F), *Geophys. Res. Lett.*, *23* (15), 1949-1952, doi:10.1029/96GL01862, 1996.

Oram, D.E., W.T. Sturges, S.A. Penkett, A. McCulloch, and P.J. Fraser, Growth of fluoroform (CHF_3, HFC-23) in the background atmosphere, *Geophys. Res. Lett.*, *25* (1), 35-38, doi: 10.1029/97GL03483, 1998.

Papadimitriou, V.C., and J.B. Burkholder, OH radical reaction rate coefficients, infrared spectrum, and global warming potential of $(CF_3)_2CFCH{=}CHF$ (HFO-1438ezy(*E*)), *J. Phys. Chem. A*, *120* (33), 6618-6628, doi:10.1021/acs.jpca.6b06096, 2016.

Papasavva, S., D.J. Luecken, R.L. Waterland, K.N.

Taddonio, and S.O. Andersen, Estimated 2017 refrigerant emissions of 2,3,3,3-tetrafluoropropene (HFC-1234yf) in the United States resulting from automobile air conditioning, *Environ. Sci. Technol.*, *43* (24), 9252-9259, doi:10.1021/es902124u, 2009.

Papasavva, S., W.R. Hill, and S.O. Andersen, GREEN-MAC-LCCP: A tool for Assessing the life cycle climate performance of MAC Systems, *Environ. Sci. Technol.*, *44* (19), 7666-7672, doi:10.1021/es100849g, 2010.

Purohit, P., and L. Höglund-Isaksson, Global emissions of fluorinated greenhouse gases 2005–2050 with abatement potentials and costs, *Atmos. Chem. Phys.*, *17* (4), 2795-2816, doi:10.5194/acp-17-2795-2017, 2017.

Rigby, M., R.G. Prinn, S. O'Doherty, S.A. Montzka, A. McCulloch, C.M. Harth, J. Mühle, P.K. Salameh, R.F. Weiss, D. Young, P.G. Simmonds, B.D. Hall, G.S. Dutton, D. Nance, D.J. Mondeel, J.W. Elkins, P.B. Krummel, L.P. Steele, and P.J. Fraser, Re-evaluation of the lifetimes of the major CFCs and CH_3CCl_3 using atmospheric trends, *Atmos. Chem. Phys.*, *13* (5), 2691-2702, doi:10.5194/acp-13-2691-2013, 2013.

Rigby, M., R.G. Prinn, S. O'Doherty, B.R. Miller, D. Ivy, J. Mühle, C.M. Harth, P.K. Salameh, T. Arnold, R.F. Weiss, P.B. Krummel, L.P. Steele, P.J. Fraser, D. Young, and P.G. Simmonds, Recent and future trends in synthetic greenhouse gas radiative forcing, *Geophys. Res. Lett.*, *41* (7), 2623-2630, doi:10.1002/2013GL059099, 2014.

Saito, T., X. Fang, A. Stohl, Y. Yokouchi, J. Zeng, Y. Fukuyama, and H. Mukai, Extraordinary halocarbon emissions initiated by the 2011 Tohoku earthquake, *Geophys. Res. Lett.*, *42* (7), 2500-2507, doi:10.1002/2014GL062814, 2015.

Say, D., A.J. Manning, S. O'Doherty, M. Rigby, D. Young, and A. Grant, Re-evaluation of the UK's HFC-134a emissions inventory based on atmospheric observations, *Environ. Sci. Technol.*, *50* (20), 11129-11136, doi:10.1021/acs.est.6b03630, 2016.

Schultz, K., Summary of High Ambient Temperature (HAT) Tests Conducted under AREP II, AHRI Low-GWP Alternate Refrigerant Evaluation Program Conference, Orlando, Florida, available at http://www.ahrinet.org/App_Content/ahri/files/RESEARCH/AREP_II/REF-3_HAT_Summary_Ingersol_Rand.pdf, 2016.

Shah, N., P. Waide, and A. Phadke, *Cooling the Planet: Opportunities for Deployment of Superefficient Room Air Conditioners*, Report No. LBNL–6164E, Lawrence Berkeley National Laboratory, https://eta.lbl.gov/sites/default/files/publications/lbnl-6164e.pdf, 2013.

Shah, N., M. Wei, V.E. Letschert, and A.A. Phadke, *Benefits of Leapfrogging to Superefficiency and Low Global Warming Potential Refrigerants in Room Air Conditioning*, Report No. LBNL-1003671, Energy Technology Areas, Lawrence Berkeley National Laboratory, https://eta.lbl.gov/sites/default/files/publications/lbnl-1003671.pdf, 2015.

Simmonds, P.G., R.G. Derwent, A.J. Manning, A. McCulloch, and S. O'Doherty, USA emissions estimates of CH_3CHF_2, CH_2FCF_3, CH_3CF_3 and CH_2F_2 based on in situ observations at Mace Head, *Atmos. Environ.*, *104*, 27-38, doi:10.1016/j.atmosenv.2015.01.010, 2015.

Simmonds, P.G., M. Rigby, A.J. Manning, M.F. Lunt, S. O'Doherty, A. McCulloch, P.J. Fraser, S. Henne, M.K. Vollmer, J. Mühle, R.F. Weiss, P.K. Salameh, D. Young, S. Reimann, A. Wenger, T. Arnold, C.M. Harth, P.B. Krummel, L.P. Steele, B.L. Dunse, B.R. Miller, C.R. Lunder, O. Hermansen, N. Schmidbauer, T. Saito, Y. Yokouchi, S. Park, S. Li, B. Yao, L.X. Zhou, J. Arduini, M. Maione, R.H.J. Wang, D. Ivy, and R.G. Prinn, Global and regional emissions estimates of 1,1-difluoroethane (HFC-152a, CH_3CHF_2) from in situ and air archive observations, *Atmos. Chem. Phys.*, *16* (1), 365-382, doi:10.5194/acp-16-365-2016, 2016.

Simmonds, P.G., M. Rigby, A. McCulloch, S. O'Doherty, D. Young, J. Mühle, P.B. Krummel, P. Steele, P.J. Fraser, A.J. Manning, R.F. Weiss, P.K. Salameh, C.M. Harth, R.H.J. Wang, and R.G. Prinn, Changing trends and emissions of hydrochlorofluorocarbons (HCFCs) and their hydrofluorocarbon (HFCs) replacements, *Atmos. Chem. Phys.*, *17* (7), 4641-4655, doi:10.5194/acp-17-4641-2017, 2017.

Simmonds, P.G., M. Rigby, A. McCulloch, M.K. Vollmer, S. Henne, J. Mühle, B.R. Miller, S. O'Doherty, A.J. Manning, P.B. Krummel, P.J. Fraser, D. Young, R.F. Weiss, P.K. Salameh, C.M. Harth, S. Reimann, C.M. Trudinger, L.P. Steele, R.H.J. Wang, D. Ivy, R.G. Prinn, B. Mitrevski and D.M. Etheridge, Recent increases in the growth rate and emissions of HFC-23 (CHF_3) and the link to HCFC-22 ($CHClF_2$) production, *Atmos. Chem. Phys.*, *18*, 4153–

4169, doi:10.5194/acp-18-4153-2018, 2018.

Simpson, I.J., O.S. Aburizaiza, A. Siddique, B. Barletta, N.J. Blake, A. Gartner, H. Khwaja, S. Meinardi, J. Zeb, and D.R. Blake, Air quality in Mecca and surrounding holy places in Saudi Arabia during Hajj: Initial survey, *Environ. Sci. Technol.*, *48* (15), 8529-8537, doi:10.1021/es5017476, 2014.

Solomon, K.R., G.J.M. Velders, S.R. Wilson, S. Madronich, J. Longstreth, P.J. Aucamp, and J.F. Bornman, Sources, fates, toxicity, and risks of trifluoroacetic acid and its salts: Relevance to substances regulated under the Montreal and Kyoto Protocols, *J. Toxicol. Environ. Health Part A*, *19* (7), 1-16, doi:10.1080/10937404.2016.1175981, 2016.

SPARC (Stratosphere-troposphere Processes And their Role in Climate), *SPARC Report on the Lifetimes of Stratospheric Ozone-Depleting Substances, Their Replacements, and Related Species*, edited by M. Ko, P. Newman, S. Reimann, and S. Strahan, SPARC Report No. 6, WCRP-15/2013, 2013.

Spivakovsky, C.M., J.A. Logan, S.A. Montzka, Y.J. Balkanski, M. Foreman-Fowler, D.B.A. Jones, L.W. Horowitz, A.C. Fusco, C.A.M. Brenninkmeijer, M.J. Prather, S.C. Wofsy, and M.B. McElroy, Three-dimensional climatological distribution of tropospheric OH: Update and evaluation, *J. Geophys. Res.*, *105* (D7), 8931-8980, doi:10.1029/1999JD901006, 2000.

Stemmler, K., D. Folini, S. Ubl, M.K. Vollmer, S. Reimann, S. O'Doherty, B.R. Greally, P.G. Simmonds, and A.J. Manning, European emissions of HFC-365mfc, a chlorine-free substitute for the foam blowing agents HCFC-141b and CFC-11, *Environ. Sci. Technol.*, *41* (4), 1145-1151, doi:10.1021/es061298h, 2007.

Stohl, A., P. Seibert, J. Arduini, S. Eckhardt, P. Fraser, B.R. Greally, C. Lunder, M. Maione, J. Mühle, S. O'Doherty, R.G. Prinn, S. Reimann, T. Saito, N. Schmidbauer, P.G. Simmonds, M.K. Vollmer, R.F. Weiss, and Y. Yokouchi, An analytical inversion method for determining regional and global emissions of greenhouse gases: Sensitivity studies and application to halocarbons, *Atmos. Chem. Phys.*, *9* (5), 1597-1620, doi:10.5194/acp-9-1597-2009, 2009.

Stohl, A., J. Kim, S. Li, S. O'Doherty, J. Mühle, P.K. Salameh, T. Saito, M.K. Vollmer, D. Wan, R.F. Weiss, B. Yao, Y. Yokouchi, and L.X. Zhou, Hydrochlorofluorocarbon and hydrofluorocarbon emissions in East Asia determined by inverse modeling, *Atmos. Chem. Phys.*, *10* (8), 3545-3560, doi:10.5194/acp-10-3545-2010, 2010.

Su, S., X. Fang, L. Li, J. Wu, J. Zhang, W. Xu, and J. Hu, HFC-134a emissions from mobile air conditioning in China from 1995 to 2030, *Atmos. Environ.*, *102*, 122-129, doi:10.1016/j.atmosenv.2014.11.057, 2015.

Sulbaek Andersen, M.P., O.J. Nielsen, A. Toft, T. Nakayama, Y. Matsumi, R.L. Waterland, R.C. Buck, M.D. Hurley, and T.J. Wallington, Atmospheric chemistry of $C_xF_{2x+1}CHCH_2$ (x=1, 2, 4, 6, and 8): Kinetics of gas-phase reactions with Cl atoms, OH radicals, and O_3, *J. Photochem. Photobio.*, *176* (1), 124-128, doi:10.1016/j.jphotochem.2005.06.015, 2005.

UNEP (United Nations Environment Programme), *Report of the Nineteenth Meeting of the Parties to the Montreal Protocol on Substances that Deplete the Ozone Layer*, UNEP/OzL.Pro.19/7, Montreal, Canada, http://ozone.unep.org/Meeting_Documents/mop/19mop/MOP-19-7E.pdf, 2007.

UNEP (United Nations Environment Programme), Technology and Economic Assessment Panel: Assessment of HCFCs and Environmentally Sound Alternatives, Scoping Study on Alternatives to HCFC Refrigerants Under High Ambient Temperature Conditions, in *TEAP 2010 Progress Report*, Volume 1, 178 pp., coordinated by S.O. Andersen, L. Kuijpers, and J. Pons-Pons, Nairobi, Kenya, 2010.

UNEP (United Nations Environment Programme), *HFCs: A Critical Link in Protecting Climate and the Ozone Layer*, 40 pp., Nairobi, Kenya, http://wedocs.unep.org/bitstream/handle/20.500.11822/8014/-HFCs_%20A%20Critical%20Link%20in%20Protecting%20%20Climate%20and%20the%20Ozone%20Layer-20111072.pdf, 2011.

UNEP (United Nations Environment Programme), *Environmental Effects Assessment Panel, Environmental Effects of Ozone Depletion and its Interactions with Climate Change: 2014 Assessment*, Nairobi, Kenya, http://ozone.unep.org/Assessment_Panels/EEAP/eeap_report_2014.pdf, 2014a.

UNEP (United Nations Environment Programme), *Halons Technical Options Committee: 2014 Assessment Report*, Volume 1, 46 pp., Nairobi, Kenya, http://ozone.unep.org/en/Assessment_Panels/

TEAP/Reports/HTOC/HTOC%202014%20Assessment%20Report.pdf, 2014b.

UNEP (United Nations Environment Programme), *Technology and Economic Assessment Panel: October 2014 Decision XXV/5 task force report additional information to alternatives on ODSs*, Nairobi, Kenya, http://ozone.unep.org/Assessment_Panels/TEAP/Reports/TEAP_Reports/TEAP_Task%20Force%20XXV5-October2014.pdf, 2014c.

UNEP (United Nations Environment Programme), *Production and consumption of ozone depleting substances under the Montreal Protocol*, Nairobi, Kenya, http://ozone.unep.org/en/data-reporting/data-centre, 2015.

UNEP (United Nations Environment Programme), *Report of the Twenty-Eighth Meeting of the Parties to the Montreal Protocol on Substances that Deplete the Ozone Layer*, UNEP/OzL.Pro.28/12, Kigali, Rwanda, http://conf.montreal-protocol.org/meeting/mop/mop-28/final-report/SitePages/Home.aspx, 2016a.

UNEP (United Nations Environment Programme), *Technology and Economic Assessment Panel: September 2016 Decision XXVII/4 Task Force Update Report Further Information On Alternatives To Ozone-Depleting Substances, Volume 1*, 179 pp., Nairobi, Kenya, http://conf.montreal-protocol.org/meeting/mop/mop-28/presession/Background%20Documents%20are%20available%20in%20English%20only/TEAP_TFXXVII-4_Report_September2016.pdf, 2016b.

UNEP (United Nations Environment Programme), *2017 Progress Report of the Technology and Economic Assessment Panel*, 105 pp., coordinated by B. Maranion, M. Pizano, and A. Woodcock, Volume 1, Nairobi, Kenya, http://conf.montreal-protocol.org/meeting/oewg/oewg-39/presession/Background-Documents/TEAP-Progress-Report-May2017.pdf, 2017a.

UNEP (United Nations Environment Programme), *Report to the Executive Committee of the Multilateral Fund for the Implementation of the Montreal Protocol, Key Aspects Related to HFC-23 By-Product Control Technologies (Decision 78/5)*, UNEP/OzL.Pro/ExCom/79/48, Bangkok, Thailand, 2017b.

UNFCCC (United Nations Framework Convention on Climate Change), *National Inventory Submissions 2014*, last access: November 2014, Climate Change Secretariat, Bonn, Germany, http://unfccc.int/national_reports/annex_i_ghg_inventories/national_inventories_submissions/items/8108.php, 2014.

UNFCCC (United Nations Framework Convention on Climate Change), *National Inventory Submissions 2017*, last access: June 2017, http://unfccc.int/national_reports/annex_i_ghg_inventories/national_inventories_submissions/items/10116.php, 2017.

US EPA (U.S. Environmental Protection Agency), *Protection of the Stratospheric Ozone: Change of Listing Status for Certain Substitutes Under the Significant New Alternatives Policy Program; Final Rule, Federal Register*, *76* (244), Part II 2040 Part CFR 2082, https://www.gpo.gov/fdsys/pkg/FR-2011-12-20/pdf/2011-32175.pdf, 2011.

US EPA (U.S. Environmental Protection Agency), *2017 and Later Model Year Light-Duty Vehicle Greenhouse Gas Emissions and Corporate Average Fuel Economy Standards, Federal Register, 77* (199), https://www.gpo.gov/fdsys/pkg/FR-2012-10-15/pdf/2012-21972.pdf, 2012.

US EPA (U.S. Environmental Protection Agency), *Protection of Stratospheric Ozone: Change of listing status for certain substitutes under the significant new alternatives policy program*, EPA–HQ–OAR–2014–0198, https://www.federalregister.gov/documents/2014/09/19/2014-22382/protection-of-stratospheric-ozone-change-of-listing-status-for-certain-substitutes-under-the, 2015a.

US EPA (U.S. Environmental Protection Agency), *Protection of Stratospheric Ozone: Determination 30 for Significant New Alternatives Policy Program*, *Federal Register*, *80*, (136), https://www.gpo.gov/fdsys/pkg/FR-2015-07-16/pdf/2015-17469.pdf, 2015b.

US EPA (U.S. Environmental Protection Agency), *Protection of Stratospheric Ozone: Determination 32 for Significant New Alternatives Policy Program, Federal Register*, *81*, (196), 40 CFR Part 82, https://www.gpo.gov/fdsys/pkg/FR-2016-10-11/pdf/2016-24381.pdf, 2016.

US EPA (U.S. Environmental Protection Agency), *Inventory of U.S. Greenhouse Gas Emissions and Sinks: 1990 – 2015,* EPA 430-P-17-001, https://www.epa.gov/sites/production/files/2017-02/documents/2017_complete_report.pdf, 2017.

US EPA (U.S. Environmental Protection Agency), *Advance version of Notice of Guidance and a Stakeholder Meeting Concerning the Significant New Alternatives Policy Program,* EPA-HQ-OAR-2003-0118, https://www.epa.gov/snap/advance-version-notice-guidance-and-stakeholder-meeting-concerning-significant-new-alternatives, 2018.

Velders, G.J.M., D.W. Fahey, J.S. Daniel, M. McFarland, and S.O. Andersen, The large contribution of projected HFC emissions to future climate forcing, *Proc. Natl. Acad. Sci.*, *106* (27), 10949-10954, doi:10.1073/pnas.0902817106, 2009.

Velders, G.J.M., S. Solomon, and J.S. Daniel, Growth of climate change commitments from HFC banks and emissions, *Atmos. Chem. Phys.*, *14* (9), 4563-4572, doi:10.5194/acp-14-4563-2014, 2014.

Velders, G.J.M., D.W. Fahey, J.S. Daniel, S.O. Andersen, and M. McFarland, Future atmospheric abundances and climate forcings from scenarios of global and regional hydrofluorocarbon (HFC) emissions, *Atmos. Environ.*, *123*, 200-209, doi:10.1016/j.atmosenv.2015.10.071, 2015.

Vollmer, M.K., S. Reimann, D. Folini, L.W. Porter, and L.P. Steele, First appearance and rapid growth of anthropogenic HFC-245fa ($CHF_2CH_2CF_3$) in the atmosphere, *Geophys. Res. Lett.*, *33* (20), L20806, doi:10.1029/2006GL026763, 2006.

Vollmer, M.K., B.R. Miller, M. Rigby, S. Reimann, J. Mühle, P.B. Krummel, S. O'Doherty, J. Kim, T.S. Rhee, R.F. Weiss, P.J. Fraser, P.G. Simmonds, P.K. Salameh, C.M. Harth, R.H.J. Wang, L.P. Steele, D. Young, C.R. Lunder, O. Hermansen, D. Ivy, T. Arnold, N. Schmidbauer, K.-R. Kim, B.R. Greally, M. Hill, M. Leist, A. Wenger, and R.G. Prinn, Atmospheric histories and global emissions of the anthropogenic hydrofluorocarbons HFC-365mfc, HFC-245fa, HFC-227ea, and HFC-236fa, *J. Geophys. Res.*, *116* (D8), D08304, doi:10.1029/2010JD015309, 2011.

Vollmer, M.K., S. Reimann, M. Hill, and D. Brunner, First observations of the fourth generation synthetic halocarbons HFC-1234yf, HFC-1234ze(E), and HCFC-1233zd(E) in the atmosphere, *Environ. Sci. Technol.*, *49* (5), 2703-2708, doi:10.1021/es505123x, 2015.

Wallington, T.J., M.P.S. Andersen, and O.J. Nielsen, Atmospheric chemistry of short-chain haloolefins: Photochemical ozone creation potentials (POCPs), global warming potentials (GWPs), and ozone depletion potentials (ODPs), *Chemosphere*, *129*, 135-141, doi:10.1016/j.chemosphere.2014.06.092, 2015.

Xiang, B., P.K. Patra, S.A. Montzka, S.M. Miller, J.W. Elkins, F.L. Moore, E.L. Atlas, B.R. Miller, R.F. Weiss, R.G. Prinn, and S.C. Wofsy, Global emissions of refrigerants HCFC-22 and HFC-134a: Unforeseen seasonal contributions, *Proc. Natl. Acad. Sci.*, *111* (49), 17379-17384, doi:10.1073/pnas.1417372111, 2014.

Xu, Y., D. Zaelke, G.J.M. Velders, and V. Ramanathan, The role of HFCs in mitigating 21st century climate change, *Atmos. Chem. Phys.*, *13* (12), 6083-6089, doi:10.5194/acp-13-6083-2013, 2013.

Yao, B., M.K. Vollmer, L.X. Zhou, S. Henne, S. Reimann, P.C. Li, A. Wenger, and M. Hill, In-situ measurements of atmospheric hydrofluorocarbons (HFCs) and perfluorocarbons (PFCs) at the Shangdianzi regional background station, China, *Atmos. Chem. Phys.*, *12* (21), 10181-10193, doi:10.5194/acp-12-10181-2012, 2012.

Yokouchi, Y., S. Taguchi, T. Saito, Y. Tohjima, H. Tanimoto, and H. Mukai, High frequency measurements of HFCs at a remote site in east Asia and their implications for Chinese emissions, *3. Res. Lett.*, *33* (21), L21814, doi:10.1029/2006GL026403, 2006.

Young, C.J., M.D. Hurley, T.J. Wallington, and S.A. Mabury, Atmospheric chemistry of CF_3CF_2H and $CF_3CF_2CF_2CF_2H$: Kinetics and products of gas-phase reactions with Cl atoms and OH radicals, infrared spectra, and formation of perfluorocarboxylic acids, *Chem. Phys. Lett.*, *473* (4), 251-256, doi:10.1016/j.cplett.2009.04.001, 2009a.

Young, C.J., M.D. Hurley, T.J. Wallington, and S.A. Mabury, Atmospheric chemistry of perfluorobutenes ($CF_3CF=CFCF_3$ and $CF_3CF_2CF=CF_2$): Kinetics and mechanisms of reactions with OH radicals and chlorine atoms, IR spectra, global warming potentials, and oxidation to perfluorocarboxylic acids, *Atmos. Environ.*, *43* (24), 3717-3724, doi:10.1016/j.atmosenv.2009.04.025, 2009b.

Zhang, J., and C. Wang, China's hydrofluorocarbon challenge, *Nature Clim. Change*, *4* (11), 943-945, doi:10.1038/nclimate2377, 2014.

Zhang, N., L. Chen, J. Mizukado, H. Quan, and H. Suda, Rate constants for the gas-phase reactions of *(Z)*-CF_3CHCHF and *(E)*-CF_3CHCHF with OH radicals at 253–328K, *Chem. Phys. Lett.*, *621*, 78-

84, doi:10.1016/j.cplett.2014.12.044, 2015.

Zhang, N., T. Uchimaru, Q. Guo, F. Qing, L. Chen, and J. Mizukado, Atmospheric chemistry of perfluorocyclopentene (cyc-$CF_2CF_2CF_2CF$=CF–): Kinetics, products and mechanism of gas-phase reactions with OH radicals, and atmospheric implications, *Atmos. Environ.*, *160*, 46-54, doi: 10.1016/j.atmosenv.2017.04.012, 2017.

Zickfeld, K., S. Solomon, and D.M. Gilford, Centuries of thermal sea-level rise due to anthropogenic emissions of short-lived greenhouse gases, *Proc. Natl. Acad. Sci.*, *114* (4), 657-662, doi:10.1073/pnas.1612066114, 2017.

Chapter 3

Update on Global Ozone: Past, Present, and Future

Lead Authors
P. Braesicke
J. Neu

Coauthors
V. Fioletov
S. Godin-Beekmann
D. Hubert
I. Petropavlovskikh
M. Shiotani
B.-M. Sinnhuber

Contributors
W. Ball
K.-L. Chang
R. Damadeo
S. Dhomse
S. Frith
A. Gaudel
B. Hassler
R. Hossaini
S. Kremser
S. Misios
O. Morgenstern
R. Salawitch
V. Sofieva
K. Tourpali
O. Tweedy
D. Zawada

Review Editors
W. Steinbrecht
M. Weber

Cover photo: Image of Earth from space. The ozone layer is a small part of the atmosphere which is a very thin layer surrounding the planet. Photo: Adapted from an Adobe Stock photo.

Chapter 3

Update on Global Ozone: Past, Present, and Future

CONTENTS

Chapter 3

Update on Global Ozone: Past, Present, and Future

SCIENTIFIC SUMMARY

This chapter deals with the evolution of global ozone outside of the polar regions. The increase of ozone-depleting substance (ODS) concentrations caused the large ozone decline observed from the early satellite era (circa 1980) to the mid-1990s. Since the late 1990s, concentrations of ODSs have been declining due to the successful implementation of the Montreal Protocol. Ozone concentrations show latitudinally dependent increases in the upper stratosphere for the 2000–2016 period; changes in other parts of the stratosphere are not yet statistically significant. A new suite of model simulations confirms previous results for the upper stratosphere that about half of the observed increase is associated with declining ODSs. Ozone column trends are likewise positive but not generally statistically significant. Their overall evolution is, however, compatible with the decline in equivalent effective stratospheric chlorine (EESC).

Over the next decades, we expect increasing global mean stratospheric ozone columns, as ODSs continue to decline. Emissions of greenhouse gases (GHGs), especially carbon dioxide (CO_2), methane (CH_4), and nitrous oxide (N_2O), will also affect the evolution of global stratospheric ozone, particularly in the second half of the 21st century, when ODS concentrations are expected to be low.

PAST CHANGES IN TOTAL COLUMN OZONE

- **Ground- and space-based observations indicate that there is no statistically significant trend in near-global (60°S–60°N) column ozone over the 1997–2016 period.** These datasets show an increase of between 0.3% and 1.2% decade^{-1} since 1997, with uncertainties of about 1% decade^{-1}. These findings are consistent with our understanding of the processes that control ozone:
    - In middle and high latitudes, the increase in total column ozone expected to arise from the 15% decline in EESC since 1997 is small (~1% decade^{-1}) relative to the large, dynamically forced year-to-year variations of ~5%;
    - In the tropics, where halogen-driven ozone loss is small in the lower stratosphere, total column ozone has not varied significantly with ODS concentrations, except under conditions of high volcanic aerosol loading (e.g., from the eruption of Mt. Pinatubo in 1991).
- Outside the tropics, present-day (2014–2017) total ozone columns from ground-based and space-based observations remain lower than 1964–1980 column ozone by:
    - about 2.2% for the near-global average (60°S–60°N);
    - about 3.0% in the Northern Hemisphere mid-latitudes (35°N–60°N);
    - about 5.5% in the Southern Hemisphere mid-latitudes (35°S–60°S).

  These values are essentially the same as in the last Assessment, given uncertainties associated with natural variability and instrumental accuracy. The larger depletion in the Southern Hemisphere is linked to the Antarctic ozone hole.

PAST CHANGES IN OZONE PROFILES

Additional and improved datasets and focused studies evaluating trend uncertainties have strengthened our ability to assess ozone profile changes. Analysis of data from the upper stratosphere shows increases that are consistent with

those suggested in the last Assessment. There is some evidence for a dynamically driven decrease in ozone in the lower stratosphere from 2000 to 2016, but robust trends have not been identified for this region. New chemistry–climate model (CCM) simulations that include realistic time variations of GHG and ODS concentrations are analyzed using the same trend model as for the observations; this allows attribution of changes in ozone to different processes.

- **Measurements show increases of ozone in the upper stratosphere over the period 2000-2016.** Following a large decline of 5 to 7% decade^{-1} through the 1980s and middle 1990s, upper stratospheric ozone has increased by 1 to 3% decade^{-1} since 2000. The largest confidence is in northern mid-latitudes, where the positive trend is statistically significant between 35- and 45-km altitude. Confidence in trends in the tropics and southern mid-latitudes is not as high due to larger discrepancies between trends from individual measurement records.

- **Model simulations attribute about half of the observed upper stratospheric ozone increase after 2000 to the decline of ODSs since the late 1990s.** The other half of the ozone increase is attributed to the slowing of gas-phase ozone destruction cycles, which results from cooling of the upper stratosphere caused by increasing GHGs.

- **There is some evidence for a decrease in lower stratospheric ozone from 2000 to 2016.** This decrease is most consistent across datasets in the tropics, but is not statistically significant in most analyses. Much of the apparent decline was reversed by an abrupt increase in ozone in 2017, indicating that longer records are needed to robustly identify trends in this region. Model simulations attribute the variations in lower stratospheric ozone over this period primarily to dynamical variability.

- **Assessing the consistency between stratospheric profile trends and total column ozone trends requires changes in tropospheric ozone to be well quantified.** A recent assessment of tropospheric column ozone trends, however, shows large disagreements in the sign and magnitude of the observed trends over the past decade and a half.

FUTURE OZONE CHANGES

The baseline climate change scenario used in the new model simulations differs from the previous Assessment, because new emissions scenarios were used. The key drivers of future ozone levels continue to be declining ODS concentrations, upper stratospheric cooling because of increased GHGs, and the possible strengthening of the Brewer-Dobson circulation from climate change. The new emissions scenarios lead to slight differences in the relative contributions of these processes in various latitude and altitude regions and a delay in return dates for ozone compared to the previous Assessment.

- **Estimated dates of return of total column ozone to 1980 values are generally a few years later than given in the previous Assessment and vary considerably between scenarios.** For the baseline scenario (RCP-6.0), they are:
    - around mid-century for near-global mean annually averaged ozone;
    - most likely before the middle of the century (~2035) for annually averaged Northern Hemisphere mid-latitude ozone;
    - around mid-century for annually averaged Southern Hemisphere mid-latitude ozone.

- **CO_2, CH_4, and N_2O will be the main drivers of 60°S–60°N stratospheric ozone changes in the second half of the 21st century.** These gases impact both chemical cycles and the stratospheric overturning circulation, with a larger response in stratospheric ozone associated with stronger climate forcing. By 2100, the stratospheric column is expected to decrease in the tropics by about 5 DU for RCP-4.5 and about 10 DU for

RCP-8.5 relative to 1980 values, with the net total column change projected to be smaller (about 5 DU) because of offsetting increases in tropospheric ozone.

- **Given that ODS levels are expected to decline slowly in coming years, a large enhancement of stratospheric sulfate aerosol in the next decades would result in additional chemical ozone losses.** Possible sources of additional stratospheric sulfate aerosol include volcanic eruptions (like Mt. Pinatubo in 1991) and geo-engineering. Even when ODS levels have declined substantially, a large injection of volcanic halogens into the stratosphere could drive substantial ozone losses in the presence of aerosol surfaces.

- **Future ozone recovery and the projected strengthening of the Brewer-Dobson circulation (BDC) are likely to lead to increases in the stratosphere-to-troposphere (STT) flux of ozone via increases in mid-latitude lower stratospheric ozone and mass flux.** The net impact of increased STT flux on the tropospheric ozone burden is highly model and scenario dependent. Most studies suggest it will be small relative to other factors, such as concurrent changes in precursor emissions, temperature, and water vapor.

Chapter 3

Update on Global Ozone: Past, Present, and Future

3.1. INTRODUCTION

This chapter updates the corresponding chapter from the previous Assessment (Chapter 2, WMO, 2014); it describes our current understanding of past changes in global (60°S–60°N) ozone and its expected future development. The chapter focuses on detection and attribution of ozone changes and the robustness of ozone trends and their associated uncertainties. The chapter also describes how ozone is expected to change in the future. This includes the modeled response to the continuing decline in stratospheric chlorine- and bromine-containing compounds and the response of ozone to climate change. A key benchmark, as always, is the date of return of ozone to its 1980 value.

3.1.1 Summary of Findings from the Previous Ozone Assessment

The 2014 Assessment (WMO, 2014) for the first time provided evidence that stratospheric ozone concentrations have increased in response to reductions in the emissions of ozone-depleting substances (ODSs) imposed by the Montreal Protocol. In particular, measurements of ozone in the upper stratosphere showed a statistically significant positive trend, which chemistry–climate models (CCMs) suggested is attributable equally to decreased ODS concentrations and to colder temperatures resulting from increased greenhouse gases (GHGs). Total column ozone had not increased significantly (1%±1.7%). Large dynamic variability and differences between datasets were shown to make trend detection difficult given the ~1% expected increase in column ozone associated with ODS decline.

CCM results indicated that a large enhancement of sulfate aerosol from either a volcanic eruption or geoengineering would result in significant ozone loss while ODS levels remain high. CCM simulations were also used to examine how assumptions about future GHG emissions affect ozone in the late 21st century, when chemical ozone destruction by halogens will be negligible. The effects of increasing nitrous oxide (N_2O), which chemically depletes global ozone, compete against the effects of increasing carbon dioxide (CO_2) and methane (CH_4), which increase ozone in the extratropics via both changes in chemistry and strengthening of the circulation. CCMs showed differences of 7% in global average total column ozone for the year 2100 between maximum and minimum radiative forcing Representative Concentration Pathways (RCPs). Significant decreases in tropical column ozone were projected under all scenarios despite increases in the upper stratosphere associated with GHG-induced cooling. The column reductions occurred primarily because strengthening of the circulation decreases tropical ozone in the lower stratosphere.

3.1.2 Major New Developments Since 2014

With four additional years of data and the advent of both new and consolidated merged datasets, this chapter revisits evidence for the detectability of positive ozone trends that might be attributable to decreases in stratospheric chlorine- and bromine-containing compounds.

The Long-term Ozone Trends and Uncertainties in the Stratosphere (LOTUS) initiative has undertaken a systematic assessment of the significance of observed ozone profile trends. LOTUS (2018) robustly quantified the degree to which ozone variability can be attributed to the various proxies used to represent natural process that drive ozone changes. It also examined available trend models and formulated a best practice, applying a common methodology to updated satellite and ground-based datasets (including merged and homogenized data). The resulting trend profiles include a traceable error characterization for the assessment of significant (recovery) trends. The new analysis confirms the general trends derived for the 2014 Ozone Assessment, but with larger estimated uncertainties, in particular in the upper stratosphere. In addition, the LOTUS trend model used for the profile observations is applied to model integrations of ozone under various scenarios, allowing a consistent

comparison of observed and modeled trends up to the present day.

The Chemistry-Climate Model Initiative Phase 1 (CCMI-1; Morgenstern et al., 2017) provides new model integrations that simulate past, present, and future ozone. For the past, free-running and "specified dynamics" model integrations are available and capture many important features of the observed ozone variability and trends. The baseline future projections use the RCP-6.0 scenario to represent climate change. In this respect, this chapter deviates from the 2014 and 2011 Ozone Assessments (WMO, 2014; WMO, 2011), where CCMVal-2 integrations were used, which are based on the SRES A1B scenario. However, the response of ozone to different climate change scenarios is evaluated using additional RCP scenarios and idealized sensitivity studies (e.g., fixed ODSs or fixed GHGs). Return dates are derived in a comprehensive way by calculating filtered multi-model mean time series and analyzing if and when 1980 ozone values are reached (Dhomse et al., 2018).

3.1.3 Data Sources

This Assessment relies on essentially the same ground-based, in situ and satellite ozone datasets as were used for the 2014 Assessment. Since then, all records have been extended to the present, and some have been revised and reprocessed, in part or in full. In addition, a few new data records have emerged. **Appendix 3A** summarizes the data records used in this chapter. Because single-instrument records do not provide sufficient temporal and/or spatial coverage to assess global long-term trends, merging is required; quantification of uncertatinties associated with merging is discussed in **Section 3.1.4**. Each approach has its merits and weaknesses, and the availability of a number of complementary, independent global ozone datasets is essential to comprehensively quantifying uncertainties in trend assessments.

3.1.4 Data Quality

Data quality is one of the key drivers of trend uncertainty, with other important contributions coming from natural variability, methodological choices in the regression analyses, and assumptions on how trend results are combined (see **Section 3.2**). Merged datasets provide comprehensive multi-instrument records, with improved temporal and spatial coverage and reduced uncertainties compared to a single-instrument data record (Tummon et al., 2015). The challenges of merged records highlighted in the last Assessment, however, are still relevant: Inter-instrument biases and drift, differences or changes in spatiotemporal sampling patterns, different (vertical) coordinate systems, and different spatiotemporal resolutions can all impact the accuracy of trends derived from merged records.

Instrument biases lead to time-dependent artifacts ("jumps") when continuous or partially overlapping records are merged without prior adjustment to a common absolute reference (Ball et al., 2017; Weatherhead et al., 2017). The accuracy of such bias corrections increases with the amount of data available and depends on the length of the overlap periods for different records. Many single-instrument records were revised in recent years (**Appendix 3A**), and a series of intercomparisons revisited and refined the estimated biases between satellite data records (Kramarova et al., 2013; Frith et al., 2014, 2017; Tegtmeier et al., 2013; Coldewey-Egbers et al., 2015; Rahpoe et al., 2015; Froidevaux et al., 2015; Davis et al., 2016; Sofieva et al., 2017), ground-based datasets (Van Malderen et al., 2016; Deshler et al., 2017), and ground-based and satellite data records (Koukouli et al., 2015; Hubert et al., 2016; Thompson et al., 2017; Garane et al., 2018; Sterling et al., 2018). Single-sensor ozone profile datasets agree to within about 5% in the height range of 20–45 km. Once adjustments are made by the merging algorithms, the residual inter-instrument biases are reduced considerably. However, it is likely that uncertainties associated with bias corrections are, in some cases, not negligible; e.g., for the merged SBUV satellite data records (due to short overlap periods; Ball et al., 2017; Frith et al., 2017) and for the SAGE-MIPAS-OMPS satellites (due to a sparse sampler that acts as transfer standard between MIPAS and OMPS; LOTUS, 2018).

Removing inter-instrument drift is a challenge that requires considerable temporal overlap of data records and a reliable statistical analysis (Stolarski and Frith, 2006). Drift correction schemes have been developed for combined data from dense nadir-viewing samplers (Coldewey-Egbers et al., 2015), but thus far such corrections have only rarely been tested for limb merging algorithms (Eckert et al., 2014; Damadeo

et al., 2018). Intercomparisons between single records generally show inter-instrument drifts below 1% decade^{-1} for total column data (Frith et al., 2014; Koukouli et al., 2015; Garane et al., 2018) and less than 3–5% decade^{-1} for profilers (Kramarova et al., 2013; Rahpoe et al., 2015; Hubert et al., 2016; Frith et al., 2017). Large drifts (i.e., 5% decade^{-1} or more) found in previous versions of the OSIRIS and SCIAMACHY satellite data records (Hubert et al., 2016) have been corrected, improving agreement with other datasets (Sofieva et al., 2017; Bourassa et al., 2018; LOTUS, 2018). Instabilities in the NCEP temperature data in the 1980s (McLinden et al., 2009; Maycock et al., 2016) have been shown to have introduced a ~6% decade^{-1} systematic error on the trend in SAGE II v6.2 volume mixing ratio data in the tropical upper stratosphere (Froidevaux et al., 2015; Ball et al., 2017). The current SAGE II v7.00 release, used by all merged limb records considered here, utilizes MERRA temperature profiles that substantially reduce this systematic error.

Time-dependent biases can appear in datasets that are based on a collection of observations with non-homogeneous sampling (e.g., SAGE, HALOE, and ACE-FTS). This can also be true for an instrument such as SBUV that drifts in local overpass time. Ignoring SBUV data close to the terminator avoids most, but not all, of this issue. A study comparing trends regressed from monthly zonal mean (MZM) solar occultation data to those from data close to the native resolution of the measurements (**Figure 3-1**) inferred that diurnal sampling biases that change over time affect the MZM-derived trends by about 1% decade^{-1} in the mid-latitude upper stratosphere, which

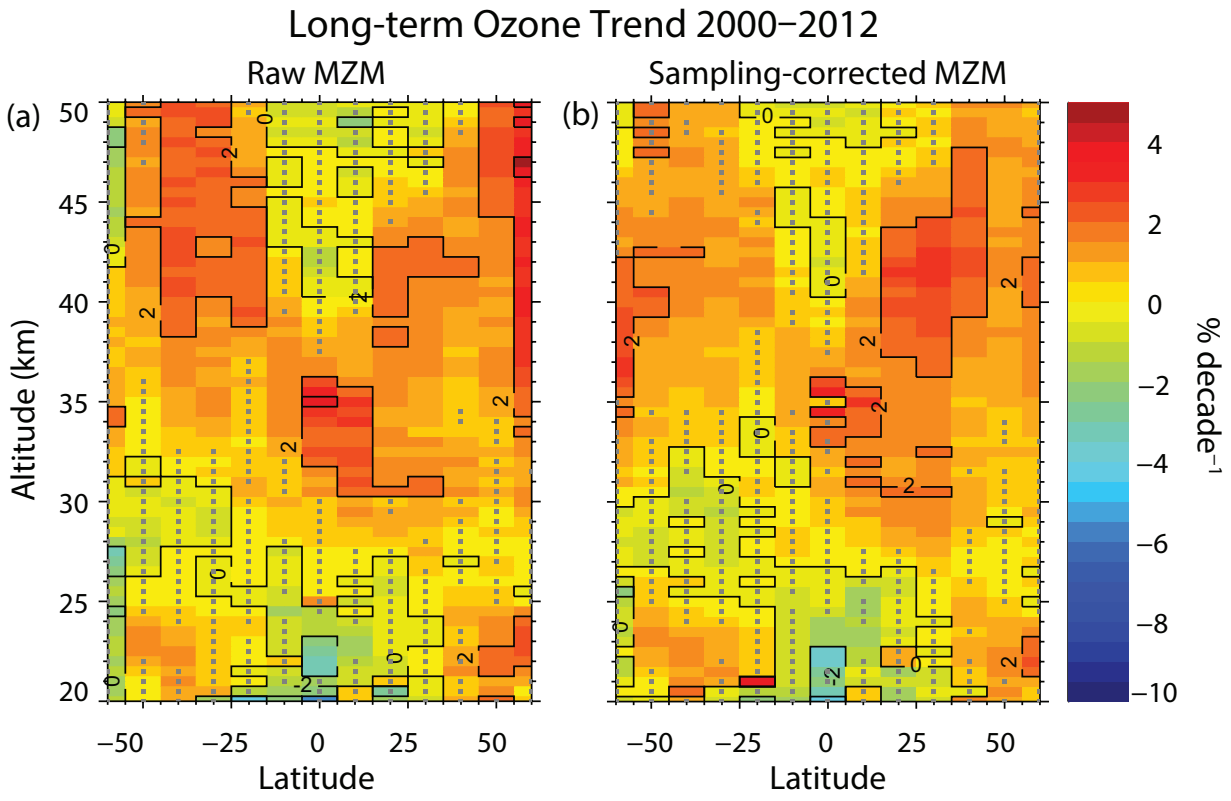

Figure 3-1. Long-term ozone trends in % decade^{-1} for the period 2000–2012 derived from both (a) a regression of monthly zonal mean data (MZM) and (b) monthly zonal mean data corrected for sampling biases due to the diurnal and seasonal cycle. The diurnal correction has the greatest influence on the upper stratosphere, while the seasonal correction has the greatest influence at higher latitudes. Stippling denotes areas where the trend results are not significant at the 2σ level. Contour lines are plotted at 2% decade^{-1} intervals. Adapted from Damadeo et al. (2018).

constitutes about half of the trend in past two decades (Damadeo et al., 2018). Seasonal sampling biases were shown to be more prevalent at higher latitudes and in the tropical middle stratosphere. The analysis led to a sampling bias correction scheme for the SAGE II dataset, which was used for the SAGE-OSIRIS-OMPS record, but not for other limb records. Sampling biases in total column or limb profile data records are generally considered random in nature but are not fully quantified (Coldewey-Egbers et al., 2015; Millán et al., 2016).

The coherent propagation of uncertainties through merging algorithms is a complex challenge. Addressing this challenge by applying a Monte Carlo technique to simulate the SBUV error time series for two different merging algorithms results in a trend uncertainty of 1–2.4% decade^{-1} (1σ), which explains the differences in profile trends for the merged SBUV MOD and SBUV COH records (Frith et al., 2014, 2017; see also **Appendix 3A** and **Figure 3-2**). So far, a comprehensive error propagation analysis has not been done for the merged limb profile records. The most advanced attempt, based on singular value decomposition of the differences between four merged limb and nadir profile data records, estimated uncertainties of up to 5% for earlier versions of MZM data from the GOZCARDS and SWOOSH data records (Ball et al., 2017). However, the impact of measurement uncertainties on trends was not investigated.

Differences in merged data records are dominated by the selection of instruments rather than the choice of the merging technique (Tummon et al., 2015). Differences are smallest in the mid-latitude lower and middle stratosphere (5%) and increase in the upper stratosphere (8%) and tropical lower stratosphere (10%), consistent with the biases between single-instrument data records. Recent modifications to profile records have addressed, at least partially, some of the identified issues, and current versions of merged ozone profile records are in better agreement than the versions used in the previous Assessment (LOTUS, 2018). Differences between merged space- and ground-based total column records (compared as monthly zoone mean total column datasets) are on average less than 1–2% and they drift apart less than 0.5–1% decade^{-1} (Chiou et al., 2014; Bai et al., 2017).

Recent reanalysis datasets (Dee et al., 2011; Dragani 2011; and Wargan et al., 2017) have been shown to produce a "realistic representation of total ozone" (Davis et al., 2017), but they are not included in this Assessment.

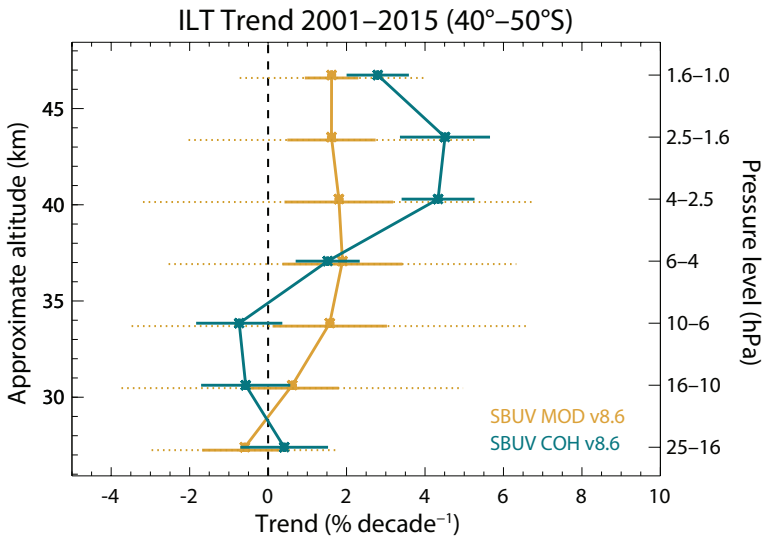

Figure 3-2. Independent linear trends (ILTs) fit from 2001 to 2015 using SBUV MOD (dark yellow) and SBUV COH (green) merged ozone records. Trends are in % decade^{-1} and plotted as a function of pressure layers for 40–50°S. Horizontal lines indicate trend uncertainty (2σ): Solid lines represent the statistical uncertainty from the unexplained variability in the multiple linear regression (MLR) analysis (**Section 3.2.1**), and dotted lines show the total uncertainty obtained by adding the statistical and merging uncertainty in quadrature. The latter is estimated from Monte Carlo simulations that model how uncertainties in individual SBUV data records propagate through the merging chain. Adapted from Frith et al. (2017).

3.2 NATURAL OZONE VARIATIONS AND TREND DETECTION

3.2.1 Natural Variability

The natural variation and long-term trends of stratospheric ozone are generally quantified using multiple linear regression (MLR) models. Such models have been discussed in previous ozone assessments (e.g., WMO, 2014). They use explanatory variables (i.e., predictors) to describe natural and anthropogenic variability in long-term ozone time series. The typical multi-linear regression can be written in the following form (e.g., Chehade et al., 2014, Steinbrecht et al., 2017, Weber et al., 2018):

$$Z(t) = Z_o + Trend \cdot (t - t_o) + \sum_{i=0}^{n} a_i P_i(t) + \varepsilon(t) \quad (1)$$

where $Z(t)$ represents a monthly or yearly averaged ozone time series and Z_0 is the value at t_0. The time series usually describes deviations from a climatology rather than the absolute amount of ozone. The *Trend* term is discussed in **Section 3.2.2**. The predictors, or proxies, $P_i(t)$ are the variables used to explain ozone interannual and long-term variability. The predictors most commonly used in ozone trend studies are listed in **Table 3-1** and are discussed in detail below. The last term, $\varepsilon(t)$, is the residual variability not explained by the MLR, which most analyses assume to be first order autoregressive noise. The terms in the model must be linearly independent and are assumed to be sufficiently orthogonal to provide independent pieces of information such that the regression can attribute, with confidence, ozone variability in the observed or modeled time record (see **Section 3.2.2**). When terms exhibit significant covariations, as is the case, for example, for the quasi-biennial oscillation (QBO) and the El Niño–Southern Oscillation (ENSO) over particular time periods, the ability of MLR to determine attribution is detrimentally impacted and confidence intervals, which take into account the covariance matrix of the regression coefficients, are correspondingly larger.

While MLR models are often applied to zonally averaged satellite data, there can be large longitudinal asymmetries in the influence of some of the processes represented by the various proxies on ozone. In particular, ENSO and the North Atlantic Oscillation (NAO) have large regional impacts that can be seen in non-zonally averaged data, as discussed in more detail in the sections below.

3.2.1.1 Solar Variability

The solar cycle influences ozone through photochemical and dynamical processes in the stratosphere (Haigh, 1994; Hood and Soukharev, 2003). Ozone in the upper-middle atmosphere is produced at wavelengths shorter than 242 nm, and it is primarily destroyed at longer wavelengths through photochemical processes. Understanding changes in UV irradiance is therefore important for the ozone and radiation budget. The solar ozone response (SOR) to changes in solar irradiance further plays a potentially important role in climate variability through modulation of stratospheric temperatures and wind. These changes in the stratosphere can influence tropospheric climate through both direct radiative effects and dynamical coupling, with impacts on extratropical modes of variability (e.g., Gray et al., 2010). Thus, understanding of the coupling between solar cycle variability, ozone changes, and circulation is of great importance for assessing the climate response to solar cycle change.

The 2014 Assessment reported a 2–4% variation of SOR in the upper stratosphere (3% in total ozone) in phase with the 11-year solar cycle. However, it was stated that the "exact shape of the solar response profile depends on the type of data and/or analysis, the length of data records, and the time periods under investigation." In the 2014 Assessment, the uncertainties regarding solar-induced variability in observed ozone fields were related to the brevity of ozone records (spanning only a few solar cycles) as well as incomplete understanding of the accuracy of modern solar spectral irradiance (SSI) observed records (i.e., data from the SORCE satellite; McClintock et al., 2005). The lack of sufficient spectral resolution in the radiation schemes of global climate models was also noted as the reason for the models not being able to reproduce the solar–ozone relationship detected in observations.

Since the last Assessment, several papers have re-evaluated SOR estimates using both updated satellite observations and models. Uncertainties in the magnitude and structure of SOR estimates remain and continue to complicate the validation of atmospheric chemistry models (Dhomse et al., 2016). The primary

Table 3-1. Table of proxies used in Equation (1), including representative data sources. The proxies and data sources used in analyses presented in **Section 3.3** are shaded in dark orange.

Proxy	Parameter	Data Sources
Solar cycle	10.7 cm solar radio flux	NOAA National Centers for Environmental Information: https://www.ngdc.noaa.gov/stp/solar/flux.html National Research Council Canada Dominion Radio Astrophysical Observatory: ftp://ftp.geolab.nrcan.gc.ca/data/solar_flux/
	30 cm solar radio flux	CNES Collecte Localisation Satellites Space Weather Services: https://spaceweather.cls.fr/services/radioflux/
	Core-to-wing ratio of Mg II doublet (280 nm)	University of Bremen: http://www.iup.uni-bremen.de/UVSAT/Datasets/mgii
QBO1 and QBO2 (orthogonal components of the quasi- biennial oscillation, QBO)	EOF1 and EOF2	Free University of Berlin: www.geo.fu-berlin.de/en/met/ag/strat/produkte/qbo/
	Tropical zonal winds at 2 pressure levels (e.g., 30 hPa and 50 hPa or 10 hPa and 30 hPa)	NOAA National Weather Service Climate Prediction Center: http://www.cpc.ncep.noaa.gov/data/indices/
ENSO	Multivariate ENSO index	NOAA Earth System Research Laboratory: https://www.esrl.noaa.gov/psd/enso/mei/
	Niño 3.4 index	NOAA National Weather Service Climate Prediction Center: http://www.cpc.noaa.gov/data/indices/ http://www.cpc.ncep.noaa.gov/products/precip/CWlink/MJO/enso.shtml
	Southern Oscillation index	
Aerosols	Mean aerosol optical depth at 550 nm	NASA Goddard Institute for Space Studies: https://data.giss.nasa.gov/modelforce/strataer/tau.line_2012.12.txt
		Khaykin et al. (2017) https://www.atmos-chem-phys.net/17/1829/2017/acp-17-1829-2017.pdf
Other Dynamical Proxies	Brewer–Dobson circulation (BDC): eddy heat flux (EHF) at 100 hPa	NOAA National Weather Service Climate Prediction Center: http://www.cpc.ncep.noaa.gov/products/stratosphere/polar/polar_body.html
	North Atlantic Oscillation (NAO) index (daily or monthly)	NOAA National Weather Service Climate Prediction Center: http://www.cpc.ncep.noaa.gov/products/precip/CWlink/pna/nao.shtml
	Arctic Oscillation (AO) index (daily or monthly)	NOAA National Weather Service Climate Prediction Center: http://www.cpc.ncep.noaa.gov/products/precip/CWlink/daily_ao_index/ao.shtml
	Antarctic Oscillation (AAO) index (daily or monthly)	NOAA National Weather Service Climate Prediction Center: http://www.cpc.ncep.noaa.gov/products/precip/CWlink/daily_ao_index/aao/aao.shtml
	Tropopause pressure (TP)	NOAA Earth System Research Laboratory https://www.esrl.noaa.gov/psd/data/gridded/data.ncep.reanalysis.tropopause.html NASA Global Modeling and Assimilation Office: https://gmao.gsfc.nasa.gov/reanalysis/MERRA/data_access/ https://gmao.gsfc.nasa.gov/reanalysis/MERRA-2/data_access/

new result, shown by two studies, is that updated SAGE II and SBUV mixing ratio datasets suggest a decrease in the magnitude of the SOR in the tropical upper stratosphere relative to earlier assessments (from ~4% in the 2014 Assessment to ~1% here) (Maycock et al., 2016; Dhomse et al., 2016). The SAGE II v7.0 number density dataset is consistent with v6.2, but the mixing ratio dataset exhibits a smaller signal, largely due to the use of a different temperature reanalysis product to convert ozone number densities to mixing ratios. SBUV MOD VN8.6 also shows a smaller and less significant SOR in the tropical upper stratosphere than the SBUV Merged Cohesive VN8.5 and closely resembles the SAGE II v7.0 mixing ratio data. However, given known issues with reanalysis temperatures, the authors concluded that the use of number density is more robust for SOR analyses than converting to mixing ratio for data records for which number density is the native coordinate, in agreement with previous findings (Remsberg et al., 2014). One of the studies also showed that the SAGE–GOMOS merged number density datasets are consistent with the SOR in SAGE II alone while SAGE-OSIRIS is not (Maycock et al., 2016). It further notes that limb sampling is too sparse to extract sub-annual variations in the SOR but that the SBUV MOD VN8.6 dataset suggests substantial month-to-month variations, particularly in the winter extratropics.

The investigations of SSI data and their reproducibility by solar models is important for the simulation of solar cycle effects on both stratospheric ozone and surface climate (e.g. Ermolli et al., 2013, and Matthes et al., 2017). Two new studies find that at pressures <5 hPa, the ozone response to solar variability simulated using output from solar models, such as SATIRE-S and NRLSSI, as forcings in climate models is consistent with observations, while simulations using SORCE data are not (**Figure 3-3;** Dhomse et al., 2016; Ball et al., 2016). These studies support earlier evidence that SORCE measurements strongly overestimate solar cycle variability in the UV range. Large differences in the amplitude and spectral features of the most recent solar cycle (C24, which began in December 2008) from earlier periods, including a reduction in total solar irradiance amplitude of 35% from the previous cycle, are an area of active investigation.

Previous studies have reported a secondary maximum in the ozone response to the solar cycle in the tropical lower stratosphere (e.g., Soukharev and Hood, 2006; Gray et al., 2010). This lower stratospheric signal is generally attributed to a dynamical response to increased heating in the upper stratosphere during solar maxima, but it could be a result of aliasing in MLR analyses due to the presence of volcanic eruptions at solar maxima (Chiodo et al., 2014). However, further evidence for the dynamical response comes from the fact that the secondary peak has also been seen in IASI satellite data (2008–2013) using daily solar flux measurements in the regression analysis (Wespes et al., 2016).

3.2.1.2 Quasi-Biennial Oscillation (QBO)

The quasi-biennial oscillation (QBO) influences stratospheric ozone through its impact on dynamical and chemical processes. The QBO signal in tropical ozone consists of a primary maximum in amplitude at a pressure of ~7 hPa, a secondary maximum near 20–30 hPa, and a minimum near 15 hPa (e.g., Naoe et al., 2017). However, other modes of variability such as ENSO can also influence tropical stratospheric ozone (e.g., Oman et al., 2013; **Section 3.2.1.3**), and anomalies do not always show a direct correlation with the QBO phase (Nedoluha et al., 2015a). The QBO proxy in MLR analyses (**Table 3-1**) is often represented by the wind speeds measured at two different pressure levels by radiosonde soundings in Singapore (Baldwin, 2001) or, alternatively, by two orthogonal QBO time series derived from principal component analyses (Wallace et al., 1993; Randel and Wu, 1996).

The period since the last Assessment was marked by an unprecedented disruption of the QBO during the NH winter of 2015–2016 (Newman et al., 2016; Osprey et al., 2016; Dunkerton et al., 2016). Usually, alternating westerly and easterly zonal wind regimes propagate downward with time with a ~28-month period. In 2016, an anomalous upward displacement of the westerly phase occurred from ~30 hPa to 15 hPa, and easterly winds appeared at 40 hPa (see **Figure 3-4**). Such a disruption of the QBO has never before been observed in tropical wind measurements, which began in 1953. The first two empirical orthogonal functions (EOFs) of the QBO, which describe the primary modes of variability in tropical zonal winds, typically account for ~95% of the variance in these winds; in 2016, they explain only 71% of the variance (Tweedy et al., 2017).

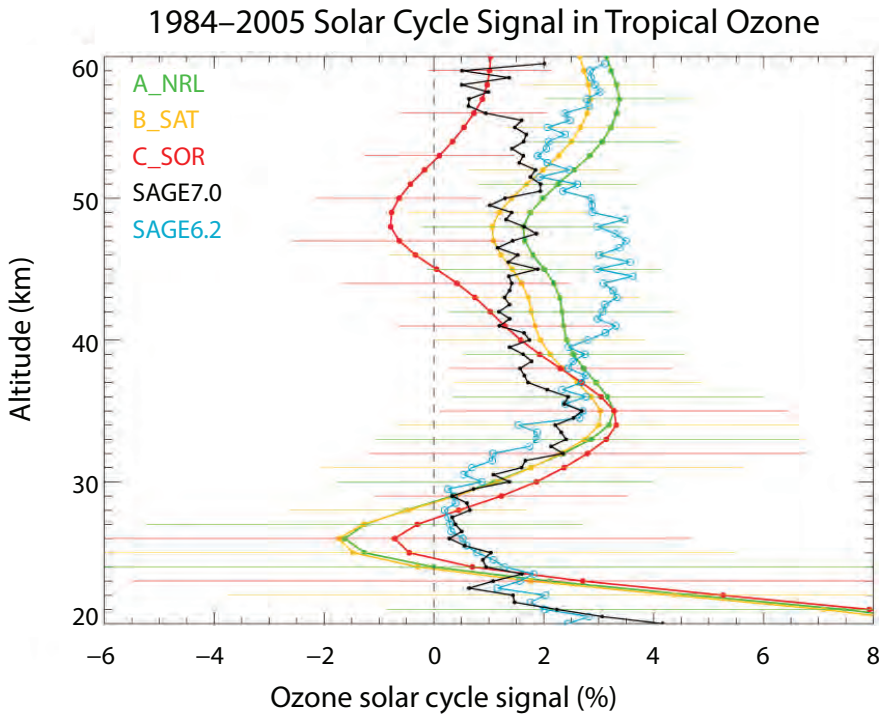

Figure 3-3. Estimated solar cycle signal in tropical ozone volume mixing ratio (VMR) from SAGE II (1984–2005) v7.0 (black) and v6.2 (light blue). The signal was dervied using a recently developed regression model (Damadeo et al., 2014). All error bars are 2-σ; none are shown for SAGE data. The modeled ozone solar cycle signals for climate model simulations using output from the NRLSSI (green) and SATIRE-S (orange) solar models and from SORCE data (red) for the 1984–2005 period are also shown. Adapted from Dhomse et al. (2016).

The anomalous zonal wind pattern drove a decrease in tropical upwelling from 50 to 30 hPa, which was associated with a positive ozone anomaly, and increased upwelling at pressures >50 hPa, which was associated with a negative ozone anomaly (**Figure 3-5**) (Tweedy et al., 2017). In the extratropics, reduced downwelling balanced the decrease in tropical ascent from 50 to 30 hPa, resulting in a negative ozone anomaly. In fact, SBUV observations show near-record low levels of total ozone in the subtropics in August 2016 of both hemispheres (Tweedy et al., 2017). At nearly the same time as the QBO disruption, there was a very strong El Niño event and a very strong stratospheric polar vortex in early to mid-winter (Nedoluha et al, 2015; Cheung et al., 2016; Hu et al., 2016; Scaife et al., 2017), which may have also contributed to ozone variability. In fact, while ENSO and QBO are assumed to be orthogonal terms in MLR analyses, they are sometimes in phase for long periods of time, complicating attribution of ozone changes (e.g., Neu et al., 2014).

The occurrence of the 2016 QBO cycle, as well as other less pronounced anomalies in the magnitude and phase of the QBO in the past decade (Nedoluha et al., 2015), are possible indications of changes in the normal behavior of the processes that impact the global stratospheric ozone distribution and inter-annual variability. The causes of this anomalous behavior and its potential implications for the future evolution of ozone are still under investigation.

3.2.1.3 El Niño–Southern Oscillation (ENSO)

El Niño–Southern Oscillation (ENSO) affects tropical upwelling, which in turn leads to fluctuations in temperature and ozone in the tropical lower stratosphere (Bodeker et al., 1998; Randel et al., 2009; and references therein). ENSO is generally represented in MLR analyses either by the Niño 3.4 index or by the multivariate ENSO index (MEI) (Wolter, 2013), which is based on the first principle component of six atmospheric parameters (**Table 3-1**). In the tropical upper troposphere and lower stratosphere (UTLS), the ENSO coefficient is negative, with low ozone during El Niño years and high ozone during La Niña years; the opposite signal is seen in mid-latitudes (e.g., Neu et al., 2014; Oman et al., 2013; Olsen et al., 2016; Wespes et al., 2016). Regression of MLS satellite measurements suggests up to a ~20 ppb K^{-1} response of ozone in the tropical lower stratosphere to changes

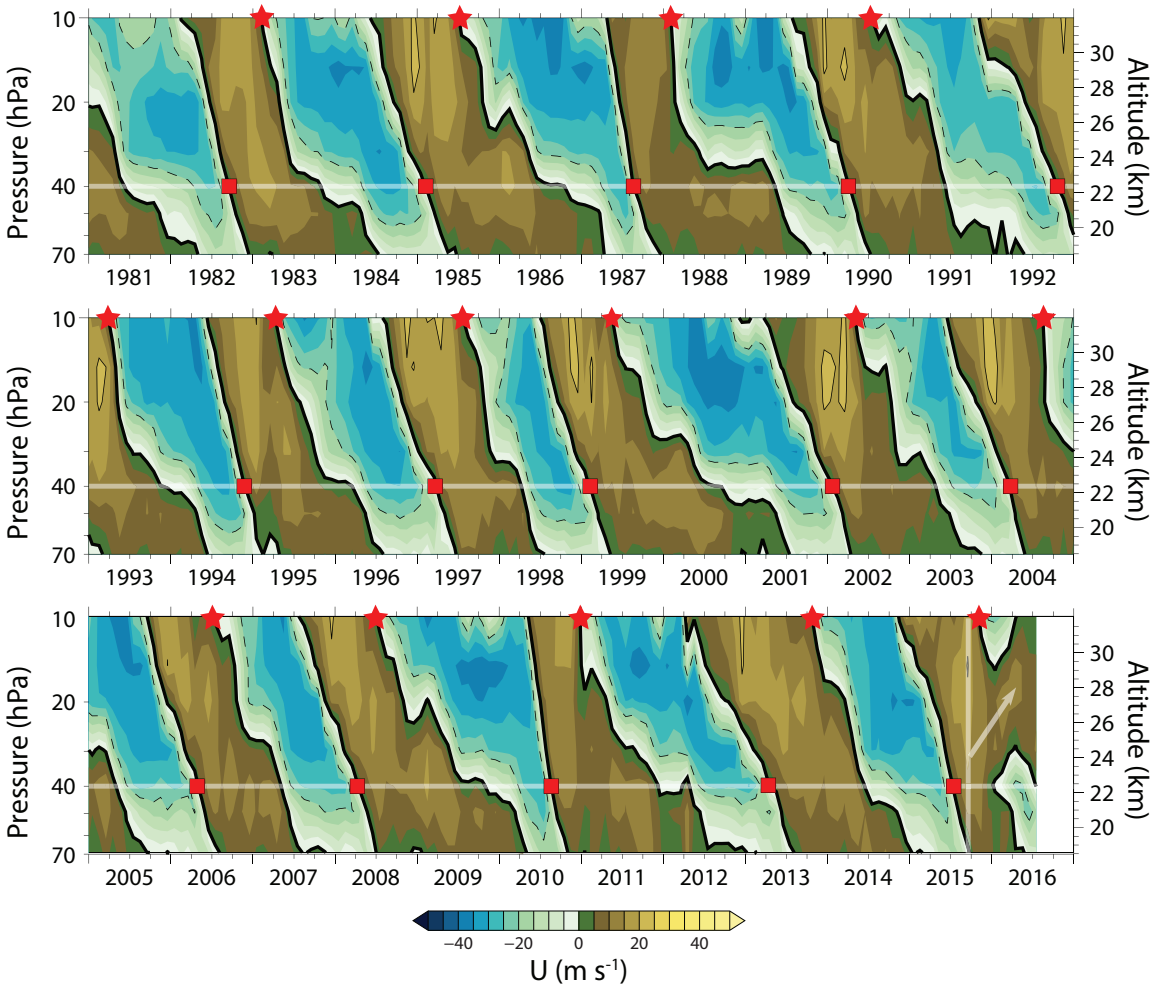

Figure 3-4. Monthly mean zonal wind U(m s^{-1}) derived from Singapore radiosondes (1°N, 104°E) between 70 and 10 hPa for 1981 through July 2016. Easterlies are shown in cyan/blue, while westerlies are shown in green/brown. Contours are every 20 m s^{-1}, with easterlies dashed and westerlies solid, and a thick black line for zero wind. The red squares show the dates of the 40 hPa easterly-to-westerly transition, while the red stars show the dates of the 10 hPa westerly-to-easterly transition. From Newman et al. (2016).

in sea surface temperatures in the Niño 3.4 region (Oman et al., 2013). This likely represents a maximum value, as ENSO and the QBO were in phase throughout much of the analyzed period, making it impossible to separate their contributions to ozone variability through linear regression (Neu et al., 2014). The period since the last Assessment has seen not only the disruption of the QBO described in **Section 3.2.1.2** but also the 2015 El Niño, which was the strongest on record since 1997 and the third strongest since 1950. The impact of this event on stratospheric ozone has not yet been assessed.

The lag between the ENSO signal in atmospheric composition and the ENSO index increases with height, and optimizing the lag has been shown to reduce trend uncertainty in the lower stratosphere (Sioris et al, 2014; Sofieva et al., 2017). One study, however, did not find that inclusion of the lag in an MLR model improved the fit to the 8-year long IASI ozone time series, perhaps due either to the brevity of the record or the broad vertical smoothing of IASI (Wespes et al. 2016). This second possibility is consistent with another analysis that found the ENSO contribution to ozone variability to be statistically insignificant in many geographical regions in low-vertical-resolution NDACC FTIR ground-based data (Vigouroux et al. 2015).

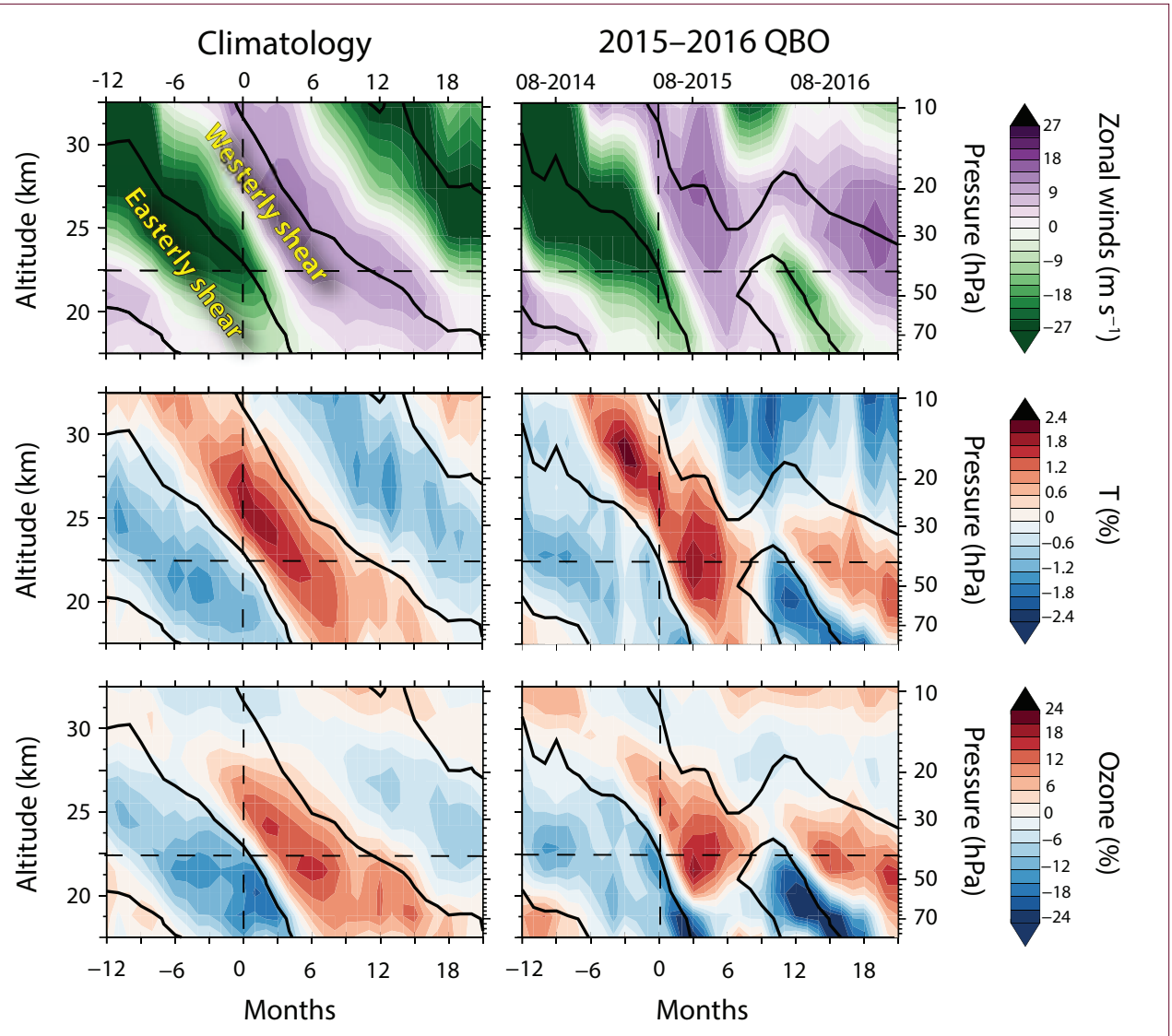

Figure 3-5. Impact of the 2015–2016 QBO disruption on stratospheric variables. The rows show (*top*) the MERRA-2 zonal-mean zonal wind component (in m s^{-1}), (*middle*) deseasonalized MLS temperature anomalies (in %), and (*bottom*) ozone anomalies (in %) as a function of time and pressure (relative to the long-term monthly averages), averaged over 5°S–5°N. The *left column* shows the composite of the easterly-to-westerly shear transitions based on 4 shear transitions at 40 hPa. The *right column* shows the 2015–2016 QBO cycle, which includes the data from April 2014 to September 2016, with month 0 (vertical dashed lines) being May 2016. The thick black contours denote the zero wind shear. The horizontal dashed lines indicate the 40 hPa level. Adapted from Tweedy et al. (2017).

Even in vertically resolved datasets, however, the ENSO impact on stratospheric ozone is regional. It changes sign between the eastern and western regions of the Pacific Ocean (Oman et al., 2013), and even in the extratropics there are large regions of both positive and negative coefficient estimates in total column ozone (Rieder et al., 2013; Frossard et al., 2013). Thus, the ENSO signal, while important for regional ozone variability, is typically small in zonal averaged ozone time series that are analyzed in this chapter (e.g, Sioris et al., 2014). LOTUS (2018) shows that inclusion of an unlagged ENSO proxy in MLR trend analyses of vertically resolved datasets changes trends by 1–2% $decade^{-1}$ and reduces trend uncertainties by 1% $decade^{-1}$.

3.2.1.4 Effects of Stratospheric Aerosol Loading

Volcanic eruptions are a major source of sulfate aerosol in the stratosphere. In the absence of volcanic eruptions, the background stratospheric aerosol layer is attributed to sulfuric gas precursors such as carbonyl sulfide (OCS) and sulfur dioxide (SO_2) that are emitted at the surface and lofted into the stratosphere by deep convection. See **Box 3-1** for a general description of the origin of stratospheric aerosols and their impacts on ozone through radiative processes and heterogeneous chemistry (e.g., Kremser et al., 2016 and references therein). Aerosol surface area has tended to undergo significant variations on decadal timescales, with major eruptions in the 1970s (Fuego), 1980s (El Chichón), and 1990s (Mount Pinatubo). There is thus potential for significant aliasing between the solar cycle and aerosol terms in MLR analysis (Solomon, 1996).

Long-term observational records of stratospheric aerosol are very important for the interpretation of global temperature changes and ozone layer variability. Ground-based lidar observations provide stable, high-quality measurements of stratospheric aerosol. Satellite data are also a very important source of information because they provide the global distribution of aerosols, although the derived aerosol surface area from satellite extinction measurements is rather uncertain (Kremser et al., 2016). In situ stratospheric aerosol measurements from optical particle counters (OPCs) have been extensively used to validate satellite measurements from SAGE II and HALOE (e.g., SPARC, 2006). The discrepancies between aerosol properties inferred from in situ and SAGE II measurements during volcanically quiescent periods have been reduced recently due to improvements in both data records (Thomason et al., 2008; Kovilakam and Deshler, 2015).

One study presented a new combined data record from continuous stratospheric aerosol lidar observations spanning 1994–2015 at the French Haute-Provence Observatory (OHP; 44°N, 6°E) compared with satellite data from SAGE II, GOMOS, OSIRIS, CALIOP, and OMPS (Khaykin et al., 2017). **Figure 3-6**, modified from this study, shows the time series of monthly averaged stratospheric aerosol optical depth between 17- and 30-km altitude derived from OHP lidars and satellite datasets. Remarkable agreement is found between all datasets despite the large variety of measurement techniques. Merged datasets such as the Global Space-based Stratospheric Aerosol Climatology (described by Thomason et al., 2018), provide input to the construction of stratospheric aerosol forcing datasets for chemistry–climate model simulations. Gap-filling of the record after the 1991 Mount Pinatubo eruption, when the stratosphere was too optically opaque for SAGE II measurements, has typically been done with ground-based lidar data. A new study finds that using CLAES measurements from the UARS satellite instead of these ground-based lidar measurements leads to less aerosol loading in the tropical lower stratosphere and less ozone loss following the eruption, in better agreement with observations (Revell et al., 2017).

As discussed in **Box 3-1**, enhanced aerosol levels following major volcanic eruptions cause ozone changes via heterogeneous chemical processes on the particle surfaces and dynamical effects related to the radiative heating of the lower stratosphere (e.g., SPARC, 2006). Ensemble sensitivity simulations using a coupled atmosphere–ocean chemistry–climate model have been used to assess how these dynamical and chemical processes affect stratospheric ozone and NH polar vortex dynamics (Muthers et al., 2015). The study found that ozone is affected globally by a volcanic eruption for several years. At current ODS levels, the dominant ozone response is depletion linked to heterogeneous chemistry involving halogen compounds, with radiative and dynamical perturbations playing a less important role. However, a major volcanic eruption could directly inject volcanic HCl into the stratosphere, triggering substantial ozone loss even when ODS levels are significantly lower than today (Klobas et al., 2017).

As seen in **Figure 3-6**, there has been no volcanic eruption with Volcanic Explosivity Index (VEI) >5 since Mount Pinatubo (VEI 6), but some small eruptions occurred in the last decade. Studies have shown that smaller volcanic eruptions can inject aerosol into the stratosphere (e.g.,Vernier et al., 2011). Therefore, it is thought that these eruptions may have impacted the ozone column at mid-latitudes over the past decade, as atmospheric chlorine levels have slowly decreased. The Calbuco volcano, which erupted in southern Chile on 22 April 2015, increased the stratospheric aerosol optical depth by a factor of 2, with an e-folding time of 90 days (Bègue et al., 2017).

Box 3-1. Origin of Stratospheric Aerosols at Mid-latitudes

C. Junge (Junge et al., 1961) discovered the presence of a layer of aqueous sulfuric acid aerosols in the stratosphere in the early 1960s. The composition of these aerosols is dominated by droplets of sulfuric acid/water (H_2SO_4–H_2O) solution, with smaller amounts of meteoritic and non-sulfate materials. The main precursors of sulfate aerosols are sulfur dioxide (SO_2) and carbonyl sulfide (OCS), which are transported to the stratosphere through dynamical transport mechanisms occurring mainly in the tropics. Volcanic eruptions can also directly inject SO_2 into the stratosphere. SO_2 and OCS are then oxidized to form H_2SO_4, which rapidly nucleates to form condensation nuclei. These nuclei grow into larger aerosol particles through condensation and coagulation mechanisms.

The key processes relating to the origin of stratospheric aerosols (adapted from Kremser et al., 2016) are given in **Box 3-1 Figure 1**:

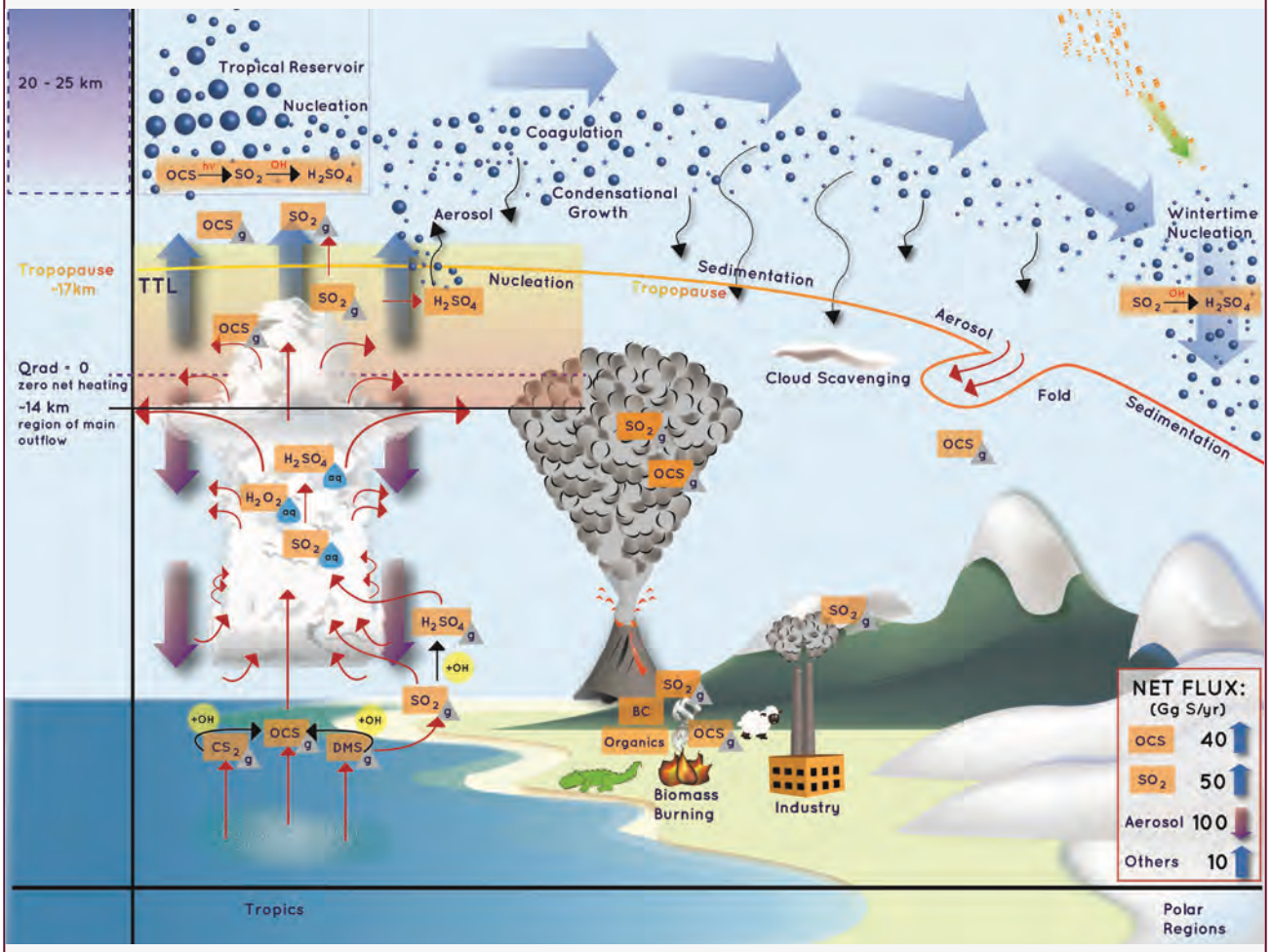

Impact of Stratospheric Aerosols on Ozone

Stratospheric aerosols play a role on the stratospheric ozone budget through chemical, radiative, and dynamical processes:

- **Chemical processes**
  - Nitrogen oxides (e.g., N_2O_5) are converted to HNO_3 through heterogeneous chemical reaction at the surface of the particles. This slows down NO_X catalytic cycles and enhances ozone in the middle stratosphere.

Box 3-1, continued.

- In the lower stratosphere, the removal of nitrogen oxides leads to increased production and decreased loss of reactive chlorine via HO_X and Cl_X cycles. This results in ozone loss in the presence of ODSs.

- **Radiative and dynamical processes**
  - Enhancement of the stratospheric aerosol layer by volcanic eruptions increases atmospheric optical depth in the solar shortwave radiation domain, inducing a cooling at Earth's surface. At the same time, volcanic aerosols increase the absorption of solar longwave radiation, inducing a heating of the lower stratosphere.
  - For volcanic eruptions occurring in the tropics, the warming of the tropical stratosphere enhances the meridional temperature gradient, which perturbs the stratospheric circulation. The enhanced upwelling linked to heating of the lower tropical stratosphere results in lower ozone levels in the tropics and higher ozone at mid-latitudes. At polar latitudes, the strengthening of the vortex due to the larger meridional gradient enhances polar ozone destruction under present-day ODS levels.

The Asian monsoon circulation has been highlighted recently as an important pathway for transport of aerosols into the stratosphere (e.g., Vernier et al., 2015, 2011). Both the Asian and North American summer monsoon circulations are accompanied by low temperatures in the lowermost stratosphere subtropics. Using a nudged chemistry–climate model, one study showed that significant heterogeneous chlorine activation on volcanic and non-volcanic particles could occur along the southeastern flank of the monsoon anticyclones (Solomon et al., 2016a). This conversion of HCl into reactive chlorine led to small modeled ozone decreases of 1.5–2.5% in the 16- to 18-km altitude range when averaged over 2009–2012 and 0°–30°N.

3.2.1.5 Other Dynamical Variations

The Brewer–Dobson circulation (BDC) is a residual meridional circulation driven largely by the deposition of momentum by planetary-scale waves. Changes in the BDC drive variations in ozone both through transport and chemistry. For example, variations in tropical upwelling have been shown to have a statistically significant impact on ozone in the mid-latitude lower stratosphere (Neu et al., 2014); Nedoluha et al. (2015) hypothesized that a significant decrease in tropical ozone from 2004 to 2013 seen near 10 hPa in measurements from MLS and other satellites (Kyrola et al., 2013; Gebhardt et al., 2014; Eckert et al., 2014), for which an increase in tropical upwelling was deemed an insufficient explanation (Eckert et al., 2014), could have instead resulted from chemical changes associated with a decrease in upwelling over the period (Aschmann et al., 2014). Using a 2-dimensional model, this study showed that such a decrease in upwelling would increase the residence time of N_2O and therefore its conversion into NO_y, which would in turn deplete ozone near the ozone maximum, where it is very sensitive to NO_y.

Because year-to-year variations in the BDC can have such an important influence on ozone variability (e.g., Fusco and Salby, 1999; Newman et al., 2001; Dhomse et al., 2006), they are often taken into account in MLR analyses. However, variability in middle-stratospheric tropical upwelling associated with the QBO and ENSO can be as large as 40% (Flury et al., 2013; Neu et al., 2014; Minschwaner et al., 2016), making it unclear to what degree BDC proxies provide information independent of these terms in MLR analyses, particularly in the tropics. As discussed in **Section 3.2.1**, the LOTUS study found that inclusion of an eddy heat flux (EHF) proxy, which is a measure of the vertical group velocity of planetary-scale waves and is proportional to the vertical component of the BDC, has a negligible impact on ozone profile trends computed from zonal average ozone fields (LOTUS, 2018). However,

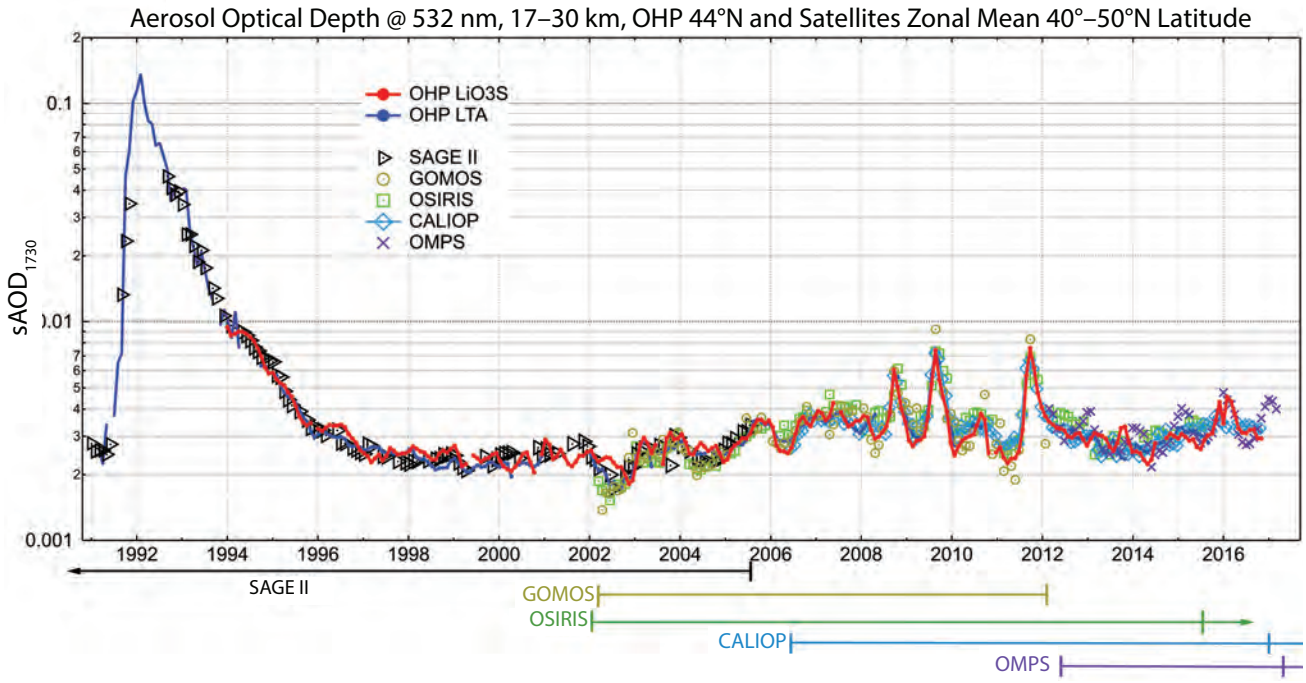

Figure 3-6. Time series of monthly mean stratospheric aerosol optical depth between 17- and 30-km altitude ($sAOD_{1730}$) from OHP lidars and monthly and zonal mean $sAOD_{1730}$ within 40–50°N from satellite sounders. From Khaykin et al. (2017).

another study found that while the QBO dominates total column ozone (TCO) variability in the tropics, using a winter-mean EHF at 100 hPa as a proxy for the BDC accounts for most of the variability in TCO from 50 to 60° in both hemispheres, with an explained variance of up to 7 DU in the SBUV MOD v8.6 and GSG datasets and a 15–35% larger signal in SBUV MOD 8.0 (Chehade et al. 2014; see **Appendix 3A** for a description of these datasets). While studies that utilize a BDC proxy tend to focus on interannual changes in ozone and on the lower-stratospheric circulation, Ball et al. (2016) developed a new upper-branch Brewer–Dobson circulation (UBDC) index based on mid-latitude temperature variations near 5 hPa that reflect rapid changes in the upper branch of the BDC that occur on timescales of a month or less. They found that this index explains more of the variability in ozone at 2 hPa (up to 60%) than the QBO index and reduces uncertainties on the estimated trend in upper-stratospheric equatorial ozone by up to 20%.

Other dynamical terms in MLR analyses include tropopause pressure, which has been shown to be a strong predictor of short-term variability in Fourier transform infrared (FTIR) ground-based ozone records (Vigouroux et al., 2015), and the Arctic Oscillation (AO), North Atlantic Oscillation (NAO), and Antarctic Oscillation (AAO) indices. The AO and NAO are essentially different ways of describing NH high-latitude pressure gradients, which influence the zonality of the jet stream. The AAO is the SH counterpart of the AO (e.g., Weiss et al., 2001; Frossard et al., 2013; Rieder et al., 2013; and references therein). The NAO/AO and AAO contributions to zonally averaged ozone variations are generally small (Chehade et al., 2014; Wespes et al., 2016; LOTUS, 2018), but these oscillations explain much of the variability in ozone at individual ground stations (Petropavlovskikh et al., 2015; Vigouroux et al., 2015). This is likely due to the fact that there are large regions of both positive and negative coefficients for the NAO north of 40°N and for the AAO south of 50°S that are associated with the shift in the jet stream between positive and negative phases (Rieder et al., 2013; Frossard et al., 2013).

3.2.1.6 Attributing Variability in Regression Analysis

In addition to there being covariances between the various proxies describing natural variability, these proxies are not fully orthogonal to the trend term and thereby influence trend estimates and their sensitivity. This long-recognized issue has been the subject of continued efforts in recent years to quantify trend sensitivity to the combination and description of natural proxies (de Laat et al., 2015; LOTUS, 2018). **Figure 3-7** shows an example of an ozone time series, the proxies for natural variability used in the LOTUS analysis (scaled by their regression coefficients), and the ozone fit residuals resulting from subtraction of those proxy terms.

As discussed in **Section 3.2.1.5**, inclusion of the AO, AAO, NAO, or EHF proxies has a negligible impact on trends for most zonally averaged satellite profile datasets (LOTUS, 2018). Trend uncertainties are slightly affected by these terms but not to the extent that insignificant trends become significant, or vice versa. The use of solar, QBO, and ENSO proxies is well established. Their omission results in 1–2% decade^{-1} changes in piecewise linear profile trends and a decrease in overall significance levels (LOTUS, 2018). The impact of the solar cycle term on upper-stratospheric trends diminishes to 0.5% decade^{-1} for regression analyses of data extending past 2014. Furthermore, the choice of solar proxy is found to be not particularly important for time series of this length (LOTUS, 2018). Using a lag for the ENSO term (see **Section 3.2.1.3**) mainly affects trend uncertainties, not the trends, but no consistent picture emerges regarding the magnitude of the impact or the parts of the atmosphere for which a lag is important. Adding a third QBO EOF into the regression has negligible impacts on the trend and uncertainty results (LOTUS, 2018).

Including an aerosol proxy primarily affects trend results in the lower stratosphere. Some aerosol dependence is seen across datasets in the middle to upper stratosphere, and coherence of this dependence across datasets adds confidence that it is likely real (LOTUS, 2018). The proxy terms for El Chichón and Mount Pinatubo scale differently, and it is often necessary to separate them and use different time lags for each term. It is quite important to accurately represent the Pinatubo event, because it tends to have a large impact on the trend term, especially when using piecewise linear trends. In recent years, there have been numerous small volcanic eruptions (Solomon et al., 2016b; **Section 3.2.1.4**), and the aerosol proxy time series have not yet been extended to cover these events. A pragmatic approach used in LOTUS is to repeat the last month of the aerosol proxy time series (September 2012) to extend the record (LOTUS, 2018). This choice has a negligible effect on trend results since the aerosol regression term is primarily constrained by the period immediately following the Pinatubo eruption rather than by aerosol loading during the last five years (**Figure 3-7**).

3.2.2 Trend Models

The proxies discussed in **Section 3.2.1** describe periodic or transient variations in ozone in Equation (1), with the longer-term evolution characterized by the *Trend* term in Equation (1). Trends are often modeled as two linear terms that are either connected (piecewise linear trend, PLT) or disconnected (independent linear trend, ILT). Alernatively, an additional proxy function (e.g., equivalent effective stratospheric chlorine, EESC) can be used to attribute long-term changes in ozone to a particular process, such as changes in ODSs.

Both PLT and ILT trend estimates are sensitive to the start- and endpoints of the time series, but this sensitivity decreases as the length of the time series increases. For stratospheric ozone trends, the advantages of ILT over PLT are that outliers in the mid 1990s affect only one trend, not both, and that no linear model is forced during the turnaround period, when the time series behaves nonlinearly. The inflection time in the PLT model is generally fixed to ~1997 (Harris et al., 2008; Kyrölä et al., 2013; Chehade et al., 2014; Damadeo et al., 2014), coinciding with the turnaround in ODS concentrations (see **Chapter 1**). Changing this inflection point impacts PLT trends in the upper stratosphere; for datasets that end in 2016, PLT trends systematically increase by up to 0.3% decade^{-1} (at mid-latitudes) for every forward shift in inflection time of one year. Changing the start year for recovery in the ILT analyses from 1997 to 2000 leads to a change in the trends of up to 1–1.5% decade^{-1} (**Figure 3-8**; LOTUS, 2018). Hence, trends calculated over different time periods are not directly comparable, and the level of disagreement depends on the trend model and the dataset (LOTUS, 2018).

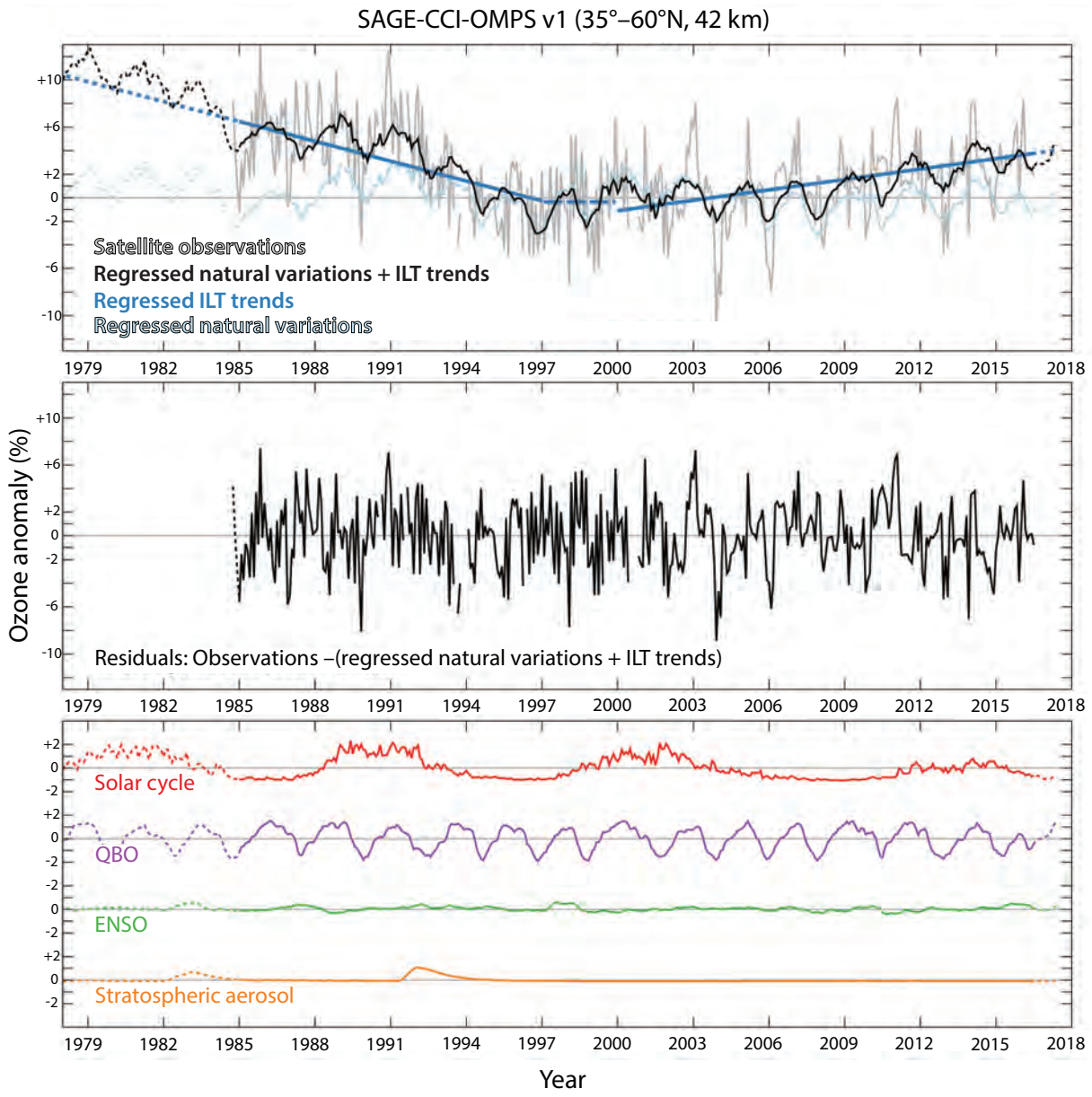

Figure 3-7. Terms in the regression of monthly deseasonalized ozone anomalies from SAGE-CCI-OMPS at 42 km in the 35°–60°N zonal band. The *top panel* shows observed monthly mean anomalies (in %; gray line) relative to the annual cycle of ozone. The black line is the result of the regression model including the independent linear trends (ILTs; thick blue lines). The light blue line shows the sum of the terms of the regression model without the ILTs included. The *middle panel* shows the residual in the observed ozone when the long-term trend and regressed natural variations are subtracted. The *bottom panel* shows the relative contributions of (from *top to bottom*) the solar flux, QBO, ENSO, and aerosols to the reconstructed time series (light blue line) in the top panel. The same vertical scale is used for all time series. Dashed lines fall outside the period used by the MLR. Observations and regression model are those used by LOTUS (2018).

This issue should not be overlooked when comparing trends and their significance from different analyses.

Long-term changes in ozone can also be represented as a nonlinear process; e.g., proportional to a measure of total stratospheric halogen loading such as an EESC proxy. EESC is calculated from emission rates of chlorofluorocarbons and related halogenated compounds, given their individual Ozone Depletion Potentials (ODPs) and certain assumptions regarding transport

times into the stratosphere. EESC-derived trends are primarily used for attribution studies. They are not well suited to detection of recent trends because the model uses a single fit coefficient, which is primarily constrained by the early period of large EESC increases and ozone depletion rates. The small ozone changes observed in recent years are poorly described by the modest post-turnaround decline in EESC (Damadeo et al., and 2014; Frith et al., 2017). In fact, the strong anti-correlation between EESC and ozone in the early period can force an erroneous, statistically significant positive trend in the latter period, even through synthetic time series in which EESC does not decrease (Kuttippurath et al., 2015). Models with two orthogonal EESC terms avoid such trend bias by effectively leaving the turnaround time and ozone depletion/recovery rate as free parameters (Damadeo et al., 2014, 2018), but this renders attribution of trends to changes in ODSs less straightforward. Adaptive techniques, such as dynamic linear regression models (DLMs; Laine et al., 2014, and Ball et al., 2017) and ensemble empirical mode decomposition (EEMD) methods

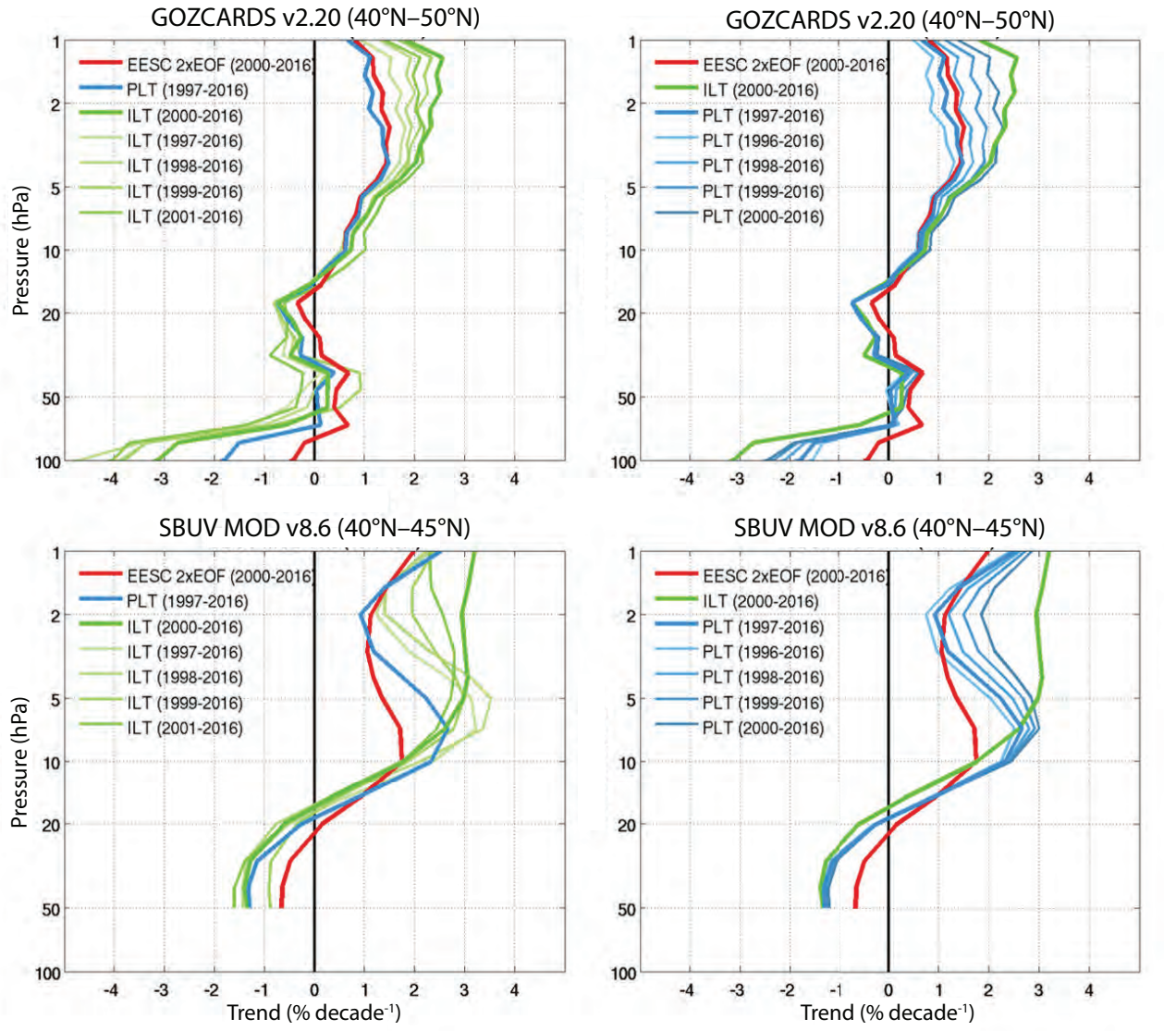

Figure 3-8. Sensitivity of ozone profile trend estimates to the modeling of the trend in the regression (independent, piecewise, or EESC) and its starting point. Results are shown for GOZCARDS v2.20 (*top row*) and SBUV MOD v8.6 (*bottom row*) at mid-northern latitudes for the past two decades. Trends in the upper stratosphere vary by 1–2 % decade^{-1} depending on the trend model and regression period. Adapted from LOTUS (2018).

(Bai et al., 2017), do not rely on a priori information for the long-term behavior of ozone. Trends are allowed to evolve over time, more accurately reflecting observed changes, especially when compared to single EESC models (Bai et al., 2017). The diagnosed difference of several percent per decade between PLT and DLM trends is not significant. However, uncertainties of DLM trends are generally larger, such that they are more likely to be insignificant than PLT trends. Tests on synthetic data hint that the DLM method provides more accurate errors (Ball et al., 2017).

Artifacts in the time series—such as sudden changes in the mean value or noise level, or more gradual changes due to drifting satellite orbits or instrument performance (e.g., Weatherhead et al., 2017)—are usually not modeled in a regression. Some artifacts are large and contribute considerably to the random component of the trend uncertainty budget, while others contribute to the systematic error. Accurate estimates of the latter remain challenging for a number of reasons, despite considerable progress in recent years, particularly in analysis of data from the middle and upper stratosphere (**Section 3.1.4**).

Random errors derived from regression residuals are typically in the range of 0.5–1% decade^{-1} (1σ). Discrepancies in trends for individual merged data records are estimated to range from 1.1 to 3.2% decade^{-1} (1σ). Uncertainties in the regression analysis contribute 0.5–1% decade^{-1}, and uncertainty in the long-term stability of satellite profile data records is currently thought to be about 1–3% decade^{-1} (LOTUS, 2018). Averaging different trend results reduces some of the biases, assuming they are uncorrelated between the data analyses, but the assumptions going into the combination of trends derived from individual data records can play a considerable role in quantifying uncertainties in long-term changes (Harris et al., 2015; Steinbrecht et al., 2017; and LOTUS, 2018). This is further discussed in **Section 3.3.2**.

3.3 PAST OZONE IN OBSERVATIONS

3.3.1 Changes in Total Column Ozone

The time series for (near) global mean, mid-latitude, and tropical total column ozone are shown in **Figure 3-9** (Weber et al., 2018).

3.3.1.1 Interannual Variations

As discussed in **Section 3.2.1**, a large fraction of the total ozone variability is related to natural processes. The impact of these processes on the ozone layer depends on season and latitude. To illustrate this, **Figure 3-10** shows a time–latitude cross section of total ozone deviations from the 1964–1980 annual cycle, clearly showing a large degree of interannual variability. However, the ozone deviations in the extratropics are mostly negative (relative to pre-1980 levels) after the mid-1980s, indicating an overall decrease in ozone.

Polar ozone depletion contributes to these negative anomalies as ozone-depleted polar air moves into lower latitudes. Strong negative anomalies at SH high latitudes in late 2015 to early 2016 reflect a large Antarctic ozone hole, whose extent was close to the all-time record. Record low temperatures likewise occurred in the Arctic stratosphere in late 2015 to early 2016 (see **Chapter 4**). In the Arctic, however, one study estimates that polar ozone depletion is responsible for only about one-third of the variability in NH mid-latitude ozone in spring, with dynamically driven differences in ozone transport between warm and cold winters responsible for the other two-thirds (Strahan et al., 2016).

The 2015–2016 boreal winter was also characterized by an unprecedented disruption in the downward propagation of the QBO westerly phase (Newman et al., 2016; see **Section 3.2.1.2**). The associated decrease in tropical upwelling led to a positive perturbation in tropical total ozone, while weaker extratropical downwelling decreased extratropical total ozone from April to September 2016 (Tweedy et al., 2017; and Weber et al., 2017).

3.3.1.2 Total Ozone Trends

The total ozone trend estimates presented below are based on the ILT approach (Weber et al., 2018). The regression model (see **Section 3.2.1**) also includes seasonal, QBO, solar, and ENSO terms using the proxy data sources described in **Table 3-1**.

The five bias-corrected merged time series (**Appendix 3A**) for the tropical (20°S–20°N) and mid-latitude (35–60°S and N) zonal bands, along with ILT trend fits to the time series, are shown in **Figure 3-11**. Prior to 1997, total ozone trends over the mid-latitudes of both

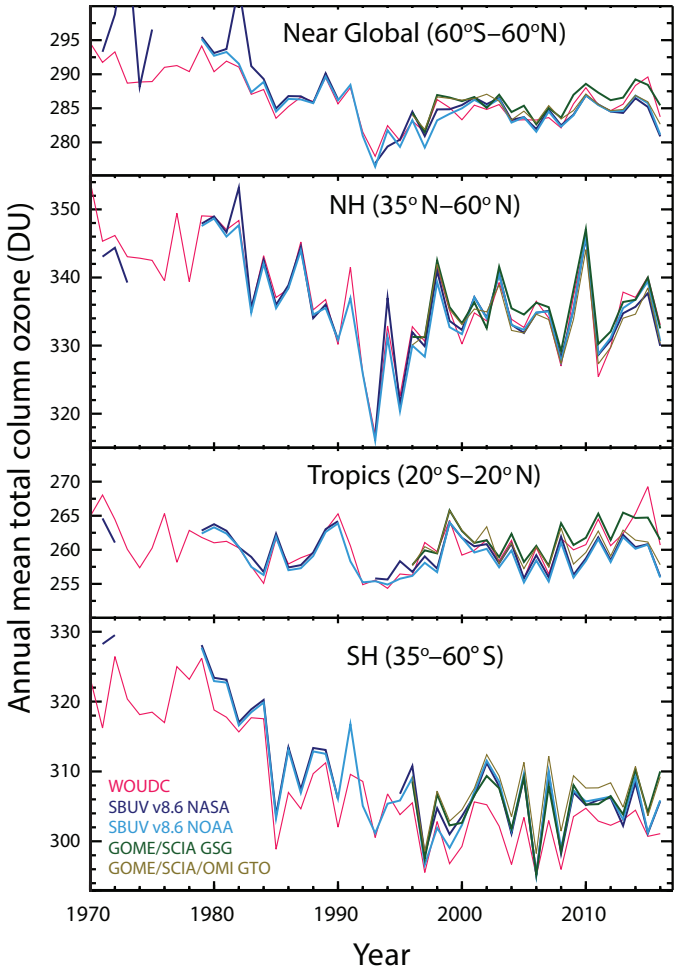

Figure 3-9. Time series of annual mean total ozone in four zonal bands. Data are from WOUDC ground-based measurements combining Brewer, Dobson, SAOZ, and filter spectrometer data (red lines; Fioletov et al. 2002); the BUV-SBUV-SBUV/2 v8.6 merged products from NASA (MOD v8.6; dark blue lines; Chiou et al., 2014, Frith et al., 2014), and NOAA (light blue lines; Wild et al., 2016); the GOME-SCIAMACHY-GOME-2 (GSG) product from the University of Bremen (dark green lines; Weber et al., 2011) and GTO product from ESA/DLR (light green lines; Coldewey-Egbers et al., 2015). WOUDC values for 2016 are preliminary because not all ground station data were available. From Weber et al. (2018).

hemispheres were about −3% ± 1.5% (2σ) decade^{-1}. The 35°–60°S and 35°–60°N trends for 1997–2016 are about +0.6% decade^{-1} and +0.2% decade^{-1}, respectively, based on the average of trend estimates for five datasets. The total column ozone trends are not statistically significant except for the GSG and GTO datasets (**Appendix 3A**) in the SH, which show a +0.7% ± 0.7% decade^{-1} increase that just reaches the 2σ uncertainty level. Given the large (~5%) year-to-year variability in mid-latitude total column ozone, the observed trends for 1997–2016 are consistent with the expected trends from EESC changes, which are about +1% decade^{-1}. Note that the two independent linear fits are almost joined together in the SH but not in the NH. The tropical belt trends are nearly zero.

Total ozone trends for the same five datasets are shown as a function of latitude for 5-degree latitude bins in **Figure 3-12.** The latitudinal dependence of the pre-1997 decrease was discussed in previous Assessments. The trend is nearly zero at the equator and becomes negative and statistically significant toward the poles. The trends over middle and high latitudes are about −3 to −6% decade^{-1}, or about −5.5 to −11% over the entire 1979–1996 period. The trends over the 1997–2016 period, on the other hand, do not show any clear latitudinal dependence. They are close to zero over the equator and NH middle and high latitudes (35°–60°N). Positive values of up to 0.8% decade^{-1} are seen over the 30°–60°S latitude band, though they are not statistically significant. The trend at 20°N is positive and statistically significant in some datasets. An increase at that latitude can also been seen in **Figure 3-10,** where ozone values in the mid-1990s are noticeably lower than in recent years.

As discussed in **Section 3.2.2**, a common approach to estimating total ozone trends is to fit the ozone time

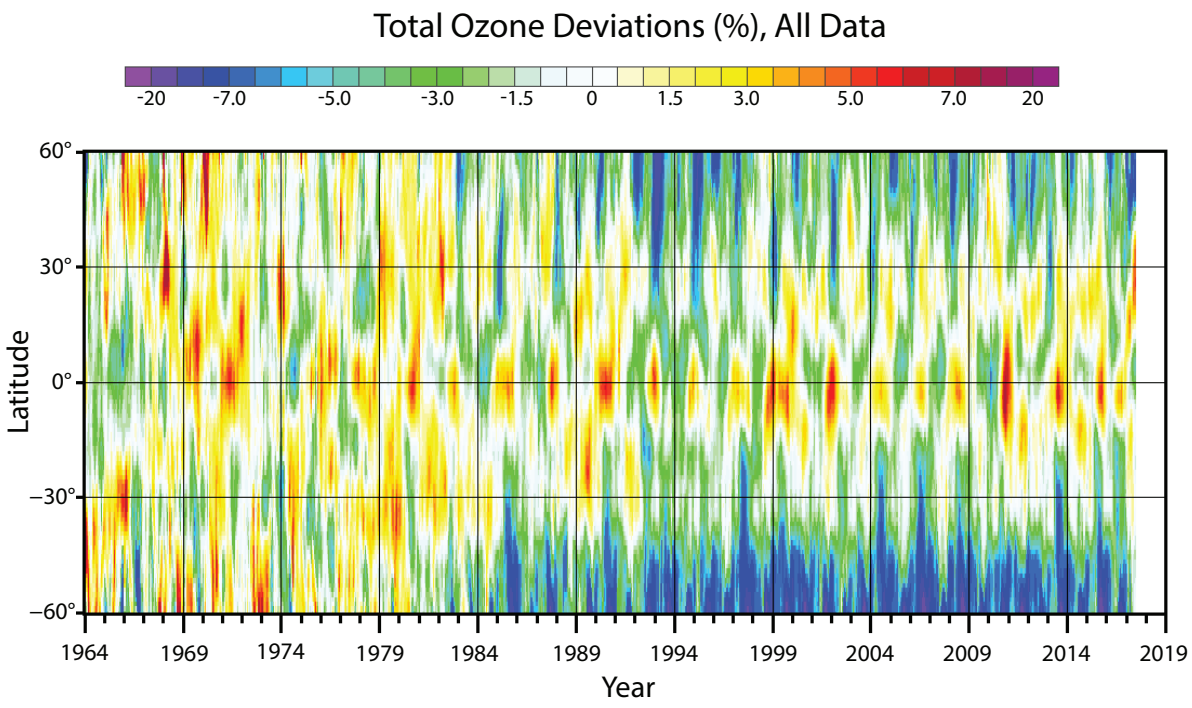

Figure 3-10. Latitude–time cross section of deviations (%) of total ozone from the long-term (1964–1980) mean, estimated from the five datasets shown in Figure 3-9. Measurements from 1964–1970 are from the WOUDC ground-based dataset. Zonal averages were calculated for each dataset for each month of the year using data averaged over the years 1997-2016, when data from all five data sets are available. These monthly zonal averages for each dataset were subtracted from the original data, yielding monthly deviations (in percent) for the entirety of each data record. The deviations then were averaged over all of the datasets for each zonal band to form a single set of monthly zonal deviations. Finally, baseline monthly mean, zonal mean deviations were calculated from the 1964-1980 average, and differences from these baseline deviations were plotted.

series using EESC. This approach works particularly well for ozone data integrated over the globe (with or without the polar regions), because dynamical fluctuations are largely reduced by the global integration. **Figure 3-13** shows global ozone with seasonal, QBO, solar, and volcanic effects removed and the best fit for the EESC curve overlaid, providing a picture of the extent of "unexplained" ozone variability (updated from WMO, 2011). While this method does not estimate the rates of ozone change prior to and after the turning point separately, it is useful as an illustration because it indicates the overall agreement of ozone and ODS changes.

One study used a different technique, called a four-step adaptive ozone trend estimation scheme, to isolate the long-term zonal ozone variability related to anthropogenic forcing (Bai et al, 2017). The technique does not require any a priori assumptions about the shape of the ozone trend. With this technique, the turning point of the ozone change was determined to occur in the year 2000; i.e., later than the maximum of stratospheric ODSs and also later than the turning point typically used in ILT analyses. Otherwise, the study's conclusions were similar to those from conventional methods. It finds that the rate of ozone change is positive after 2000 but that the record is still too short to identify a significant trend.

The datasets discussed above are based on measurements in the UV or visible parts of the spectrum. Fourier transform infrared (FTIR) measurements of the solar spectrum can also provide total ozone columns. The records of ground-based FTIR measurements are now long enough to examine the trends. Data from eight FTIR sites with records starting from

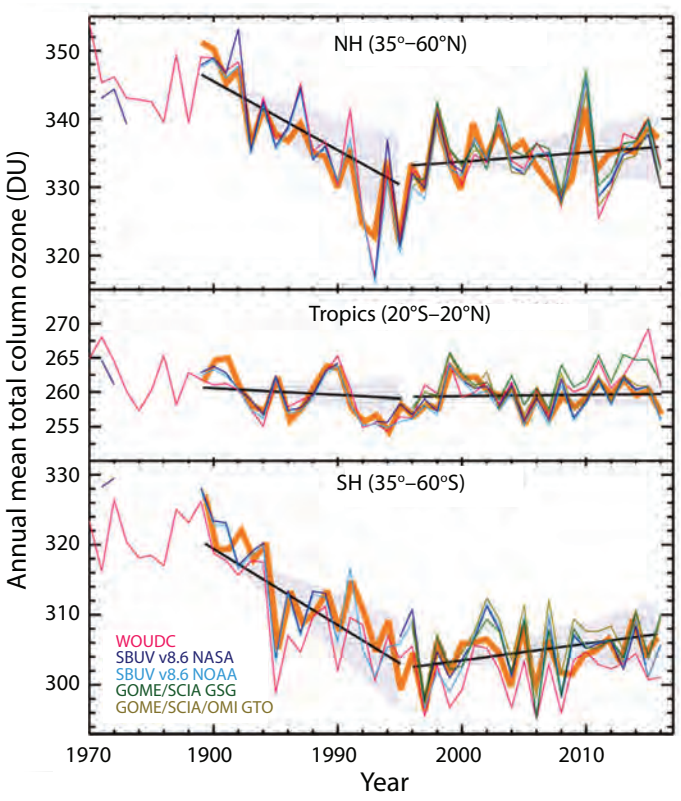

Figure 3-11. Annual mean total ozone time series of five bias-corrected, merged datasets in the 35°–60°S, 35°–60°N and 20°S–20°N latitude bands. The thick orange lines are the result from applying a multiple linear regression (MLR) model. The solid black lines indicate the linear trends before and after the ODS peak in 1997, respectively. The shaded areas show the 2σ uncertainty of the MLR trend estimates. Adapted from Weber et al. (2018).

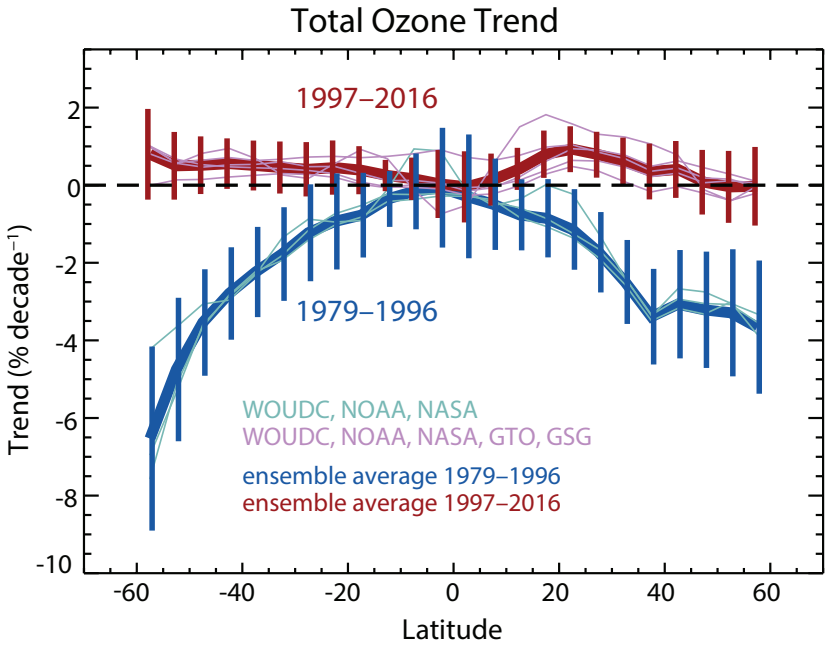

Figure 3-12. Total ozone linear trend in % decade^{-1} as a function of latitude for 1979–1996 (bluish colors) and 1997–2016 (reddish colors) estimated for NASA MOD, NOAA SBUV, GTO, GSC, and WOUDC datasets. The thick blue line with blue 2σ error bars and the thick red line with red 2σ error bars represent a weighted mean trend from the five (or three before 1996) datasets for 1979–1996 and 1997–2016, respectively. The weights are the inverses of the trend uncertainties from the individual datasets. Trends estimated using the individual datasets are shown by the thin lines as indicated. The 1979–1996 trends are not shown, as the GSG and GTO are available only after 1995. The uncertainty of the mean trend is the weighted standard deviation resulting from the averaging. However, the uncertainties are sometimes very small, as all datasets agree at some latitudes very well. Therefore, the larger value of the weighted standard deviation and the mean of the individual uncertainties is plotted (in most cases, it is the latter). Adapted from Weber et al. (2018).

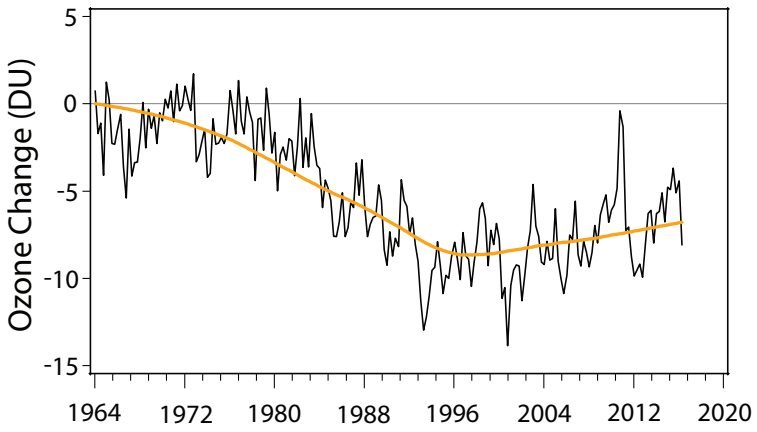

Figure 3-13. Deseasonalized, area-weighted total ozone deviations for 60°S–60°N from the WOUDC dataset, adjusted for seasonal, solar, volcanic, and QBO effects (black line). The orange line represents the component of ozone variability due to changes in the equivalent effective stratospheric chlorine (EESC) based on a fit to data from 1964–2016. The EESC curve for the mid-latitude lower stratosphere is used for this plot.

around 1995 have been found to be consistent with UV/VIS measurements (Vigouroux et al., 2015). The total ozone trends over middle and low latitudes are small and not significant for all stations except for Wollongong, located at 34°S, where the 1996–2012 trend was 1.9% ± 1.1% decade^{-1}.

Total ozone changes during the solstice seasons for 35°–60°S and 35°–60°N for the period 1970–2016 are shown in **Figure 3-14**. The ozone variability over mid-latitudes is highest during winter and is much lower during summer, though the winter and summer deviations are highly correlated. The long-term ozone decline in the Northern Hemisphere shows a seasonal dependence, with the average winter and spring 1997–2016 deviations from pre-1980 levels of 3–4% and summer and autumn deviations of ~2–2.5%. In contrast, there is no seasonal difference in the ozone decline in the Southern Hemisphere. The average 1997–2016 values are about 6% lower than the pre-1980 level for all seasons. In the Northern Hemisphere, large winter–spring ozone deviations such as those seen in 1993 and 1995 (**points a** and **b** in **Figure 3-14**) which were related to the Mount Pinatubo eruption, have not occurred recently. Summer deviations in 2011 and 2016 (**points c** and **d** in **Figure 3-14**) however, are among the largest in the record and comparable to those that occurred in 1993 and 1995. The large Arctic ozone depletion events in 2011 and 2016, as well as the QBO disruption in 2016 (**Section 3.2.1.2**) and the large 2015 ENSO event (**Section 3.2.1.3**) may have contributed to these large deviations. However, it is difficult to quantify these effects. Unlike in the Northern Hemisphere, summertime ozone values in the Southern Hemisphere are affected by the ozone hole and dilution of polar ozone to mid-latitudes (e.g., Fioletov and Shepherd, 2003).

Long-term total ozone variations and trends are generally determined from zonal or global averages, but zonal asymmetries do exist. One study investigated the ENSO impact on the detectability of regional trends in total ozone (Coldewey-Egbers et al., 2014). Both it and another study (Knibbe et al., 2014) that used a different dataset (van der A et al., 2010, 2015) found that the effect of ENSO on total ozone is primarily seen over the Pacific. The contributions from most other factors showed little longitudinal dependence.

In summary, the main results of this Assessment related to total column ozone are similar to those from the 2014 Assessment (WMO, 2014): column ozone remains below pre-1980 levels by 2–3% over NH mid-latitudes (35°–60°N) and by 5–6% over SH mid-latitudes (35°–60°S), with no major changes over the tropical region (20°S–20°N). Despite the fact that it has been nearly 20 years since the ODS turning point in 1997, we still do not see a statistically significant positive total ozone trend over the NH mid-latitudes. The trend is only +0.2% decade^{-1}, which is consistent with expectations given the slow rate of ODS decline and large interannual variability. The trend over the

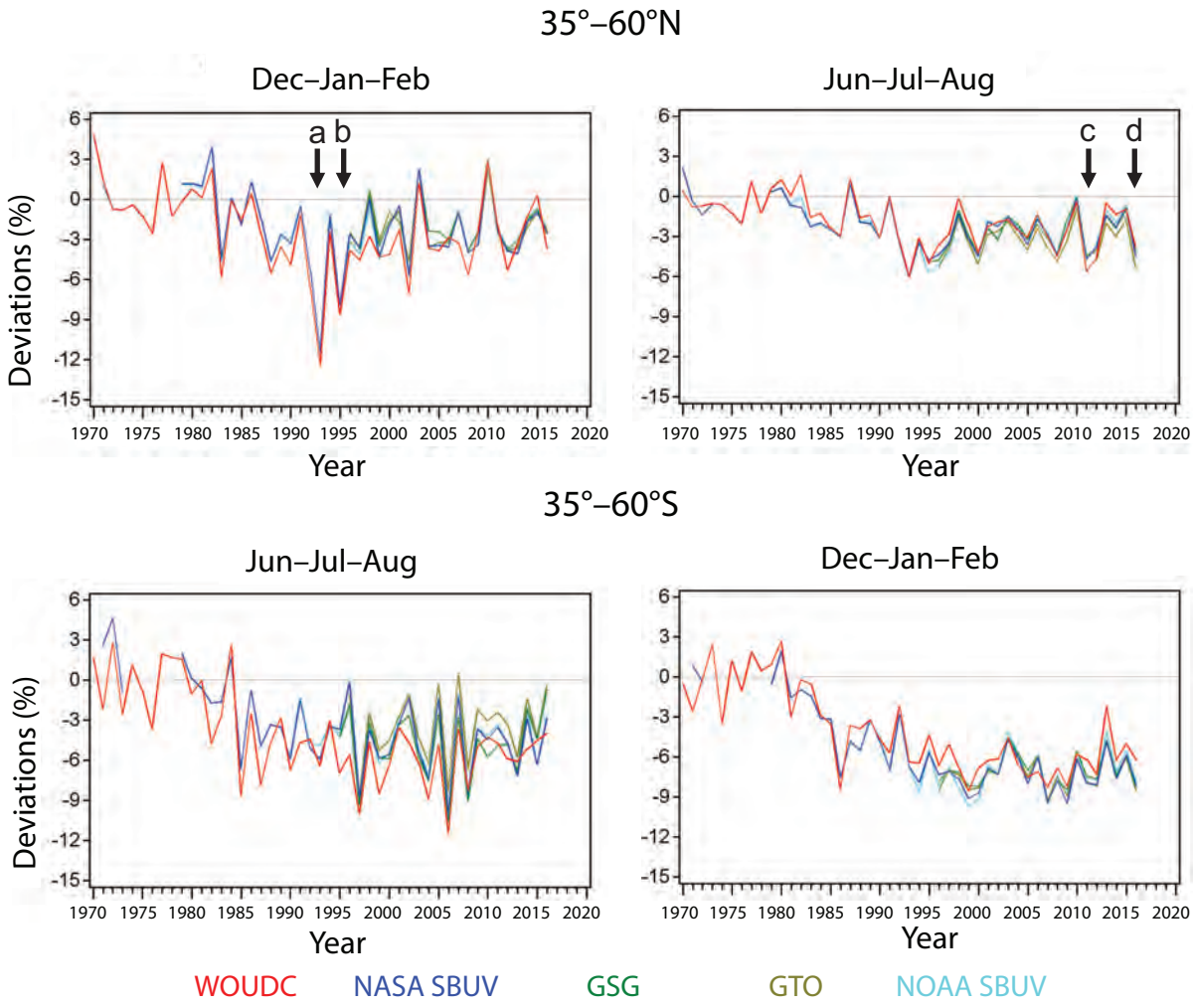

Figure 3-14. Seasonal, area-weighted total ozone deviations from the 1964–1980 means, calculated for four seasonal averages for the latitude bands 35°–60°N (*top row*) and 35°–60°S (*bottom row*). The years on the horizontal scale correspond to the first month of the season. The arrows indicate large NH ozone deviations that occurred in the winter–spring of 1993 (a) and 1995 (b), as well as in the summer of 2011 (c) and 2016 (d) that are discussed in the text. Updated from WMO (2007).

SH mid-latitudes is about +0.7% decade^{-1}, which is just above the 2σ uncertainty level.

3.3.2 Trends in Ozone Profiles

3.3.2.1 Time Series

Figures 3-15 and 3-16 show time series of annual mean ozone concentration anomalies at four pressure levels from 70 to 2 hPa from various ground-based and satellite-based measurements records (**Appendix 3A**), averaged over four latitude bands (LOTUS, 2018). Chemistry–climate model simulations from CCMI-1 are also shown. Ozone anomalies are relative to the 1998 to 2008 climatology of each individual dataset. **Figures 3-15** and **3-16** show overall consistency among observations and between observations and models at the various pressure levels and latitude bands. The relatively narrow model ranges, as compared to the interannual variability of the observations, can be explained to some extent by the lack of volcanic perturbations in some of the CCMI-1 simulations, as well as by a 3-year smoothing applied to the model output. The larger variability of ground-based

observations relative to the satellite measurements is expected, given the small number of measurement stations providing long-term ozone measurements. As in the last Assessment, all datasets show an ozone decline up to the late 1990s, with a leveling off since then. At 2 hPa, most records indicate a slight increase of ozone over the 2000–2016 period that is most pronounced in the Northern Hemisphere. In the CCMI-1 simulations, the ozone decline before 2000 is linked to increasing ODS levels. After 2000, the ozone increase due to ODS decline is enhanced by upper-stratospheric cooling associated with increases in GHGs (e.g., Randel et al., 2016) (**Section 3.3.3**). At pressures greater than 10 hPa, no increase in ozone is seen in the observational records, in broad agreement with the range of model simulations at these pressure levels.

Figure 3-15. Evolution of annual mean deseasonalized ozone anomalies at the 2-hPa/42-km (*left column*) and 10-hPa/31-km (*right column*) levels. Satellite data and measurements from ground-based stations are averaged over four different latitude bands. Gray shadings correspond to the 10th–90th percentiles of the CCMI-1 model results. The model mean and median are also plotted, together with the ±2σ range of the models (gray lines). All anomalies are calculated relative to the base period 1998–2008; CCMI-1 model data are shown as 3-year weighted running means with a double weight for the central year (i.e., 1-2-1 weighting). Adapted from LOTUS (2018).

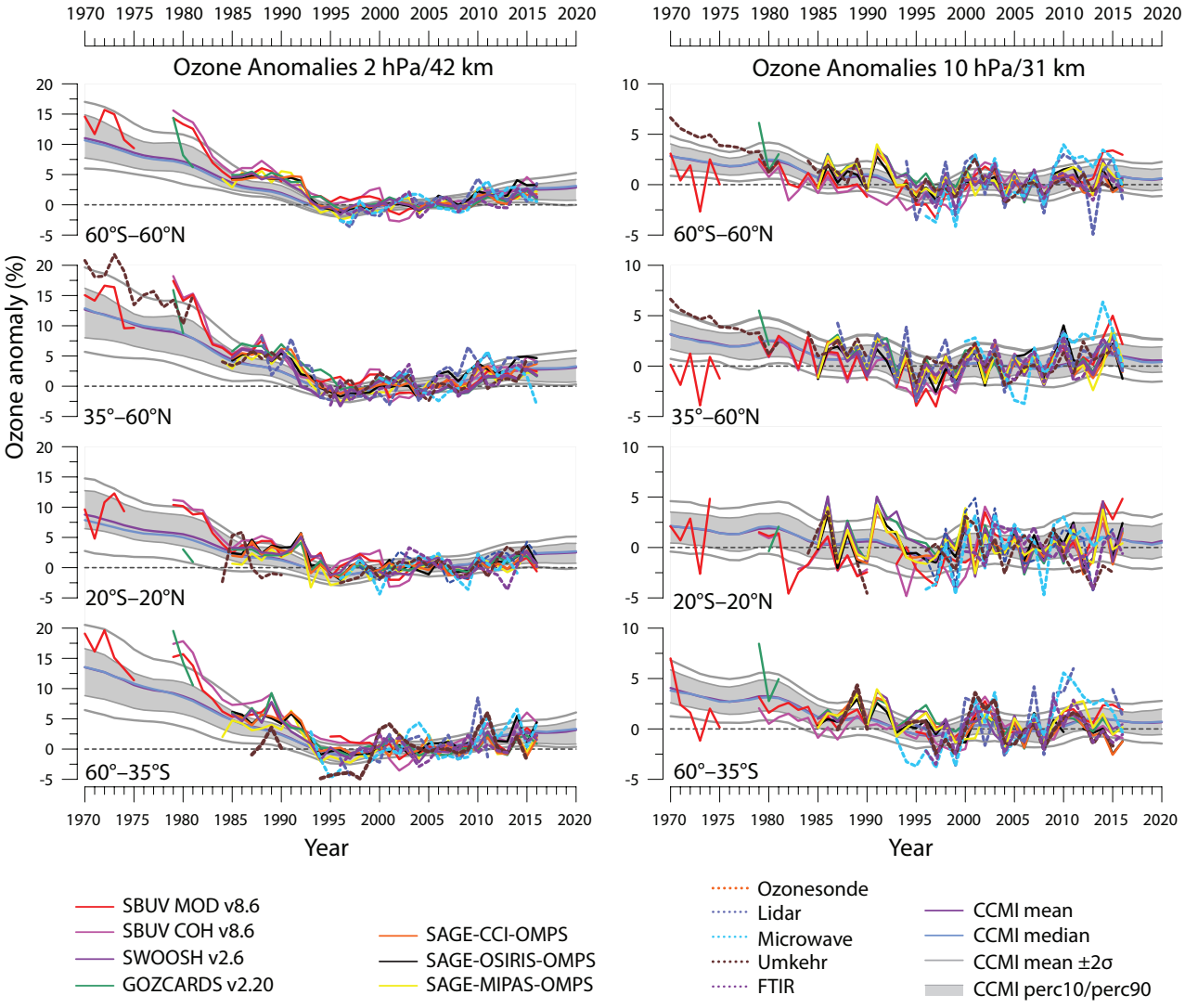

3.3.2.2 Ozone Trends 2000–2016

The last Assessment examined ozone profile trends for both the period of ODS increases, up to about 1997, and after the turnaround in ODS concentrations. For the first part of the record, it confirmed the large negative trends of about −6 to −8% decade^{-1} in the upper stratosphere (around 2 hPa or 35–45 km altitude) that had been found in previous Assessments. For the period after the ODS peak, it reported a significant increase in ozone of 2.5–5% at around the same altitudes in the mid-latitudes and in the tropics. These findings were in agreement with CCMVal-2 model simulations, which attributed about half of this upper-stratospheric ozone increase to declining ODSs. The other half was attributed to increasing GHGs, which cool the upper stratosphere and reduce catalytic ozone loss rates.

Shortly after the release of the 2014 Assessment, several papers that reassessed ozone trends were published as part of the SPARC/IO3C/IGACO-O3/NDACC (SI2N) initiative. The most prominent study re-evaluated long-term ozone profile trends from ground-based, single-satellite and merged satellite ozone records over the period 1979–2012 (Harris et al., 2015). Trends obtained before the ODS peak

Figure 3-16. Same as **Figure 3-15** but for levels 20 hPa/26 km (*left*) and 70 hPa/19 km (right). Adapted from LOTUS (2018).

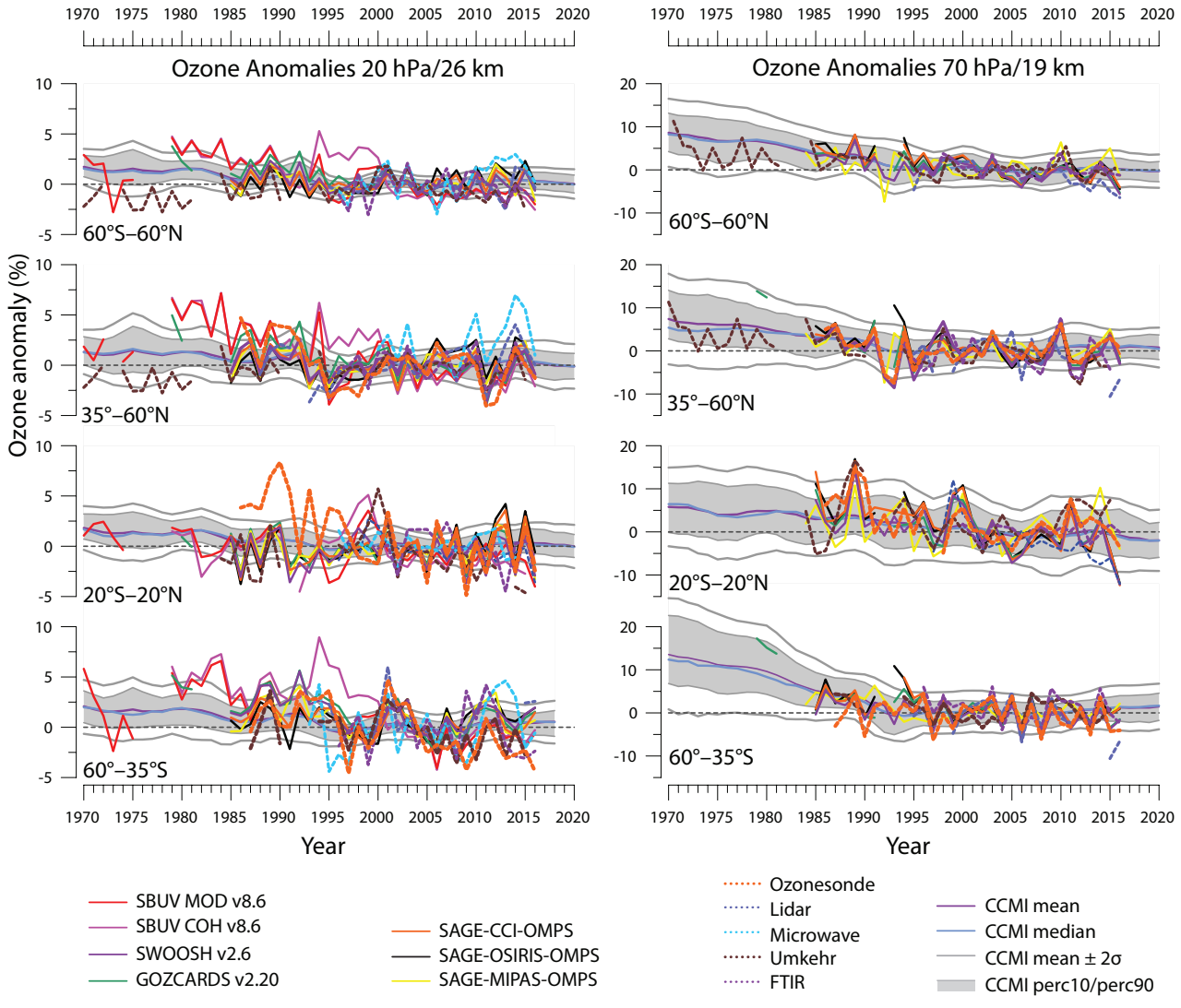

were found to be similar to those reported previously, including in the 2014 Assessment. For the period after the peak in ODS concentrations, positive trends of ~2% decade^{-1} in mid-latitudes and ~3% decade^{-1} in the tropics were found in the upper stratosphere. However, several methods were used to investigate the significance of the increasing trends and in all cases they were found to be insignificant throughout the stratosphere. One method, similar to that used in the previous Assessment, estimated the uncertainty of average trends from the weighted mean of the individual variances but added an extra term for measurement drift, which was found to be ±3–5% decade^{-1} in the 20–40 km altitude range and larger elsewhere (Hubert et al., 2016). A second method used the joint distribution of the individual variances around the arithmetic mean of the estimators e.g., (SPARC 2013). The main conclusion of the Harris et al. (2015) study was that the analyses included in the 2014 Assessment had underestimated the uncertainties in the combined ozone records and that, given these uncertainties, it was too early to detect a significant trend given the length of the "recovery" period (1997–2012).

The differences in the conclusions regarding the significance of increasing ozone trends between the 2014 Assessment and Harris et al. (2015) were revisited under the LOTUS initiative (LOTUS, 2018). In parallel, one study using both newly released merged satellite records and ground-based datasets (Steinbrecht et al., 2017) and another using just satellite records (Sofieva et al., 2017) re-evaluated ozone profile trends using multi-linear regression analyses. Both studies found significant ozone increases in the upper stratosphere of about 2–2.5% decade^{-1} in the mid-latitudes of both hemispheres. Other recent analyses using ground-based datasets have also reported significant positive trends of ozone in the upper stratosphere (e.g., Moreira et al., 2015; Nair et al., 2015; Vigouroux et al., 2015).

However, at least in the case of SBUV long-term observations, inclusion of uncertainties in the calibration and drift of individual instruments in ozone profile merged datasets can result in relatively large errors in ozone trend results. When Monte Carlo simulations are used to estimate uncertainties in ozone trends based on the SBUV MOD merged dataset over the period 2000–2015, the significant ozone trends derived over the 1.6–1.0 hPa range from standard multi-linear regression analyses become insignificant at the 2σ level (Frith et al., 2017).

Altitude–latitude cross sections of ozone trends derived from the merged satellite ozone datsets considered in the LOTUS initiative are shown in **Figures 3-17** and **3-18** for the periods 1985–1997 and 2000–2016, respectively. Trends were determined using the ILT regression model (**Section 3.2.2**). In **Figure 3-17**, the negative trends obtained in the upper stratosphere (e.g., above 35 km) are consistent in magnitude with previous studies. These trends range from −4 to −9% decade^{-1}, depending on the satellite record, with larger negative trends in the Southern Hemisphere in some cases. For the 2000–2016 period (**Figure 3-18**), most records show significant positive ozone trends in the upper stratosphere, consistent with the recent studies discussed above. These positive trends are largest in the mid-latitudes of both hemispheres and range from 2 to 4% decade^{-1}. Both SBUV merged records also show significant positive trends in the tropical upper stratosphere, although the significance is likely overestimated due to omission of the merging uncertainies of the SBUV datasets (**Section 3.1.4**; Frith et al., 2017). Some significant negative trends are found in the tropical middle to lower stratosphere; these are seen primarily in the SBUV and SWOOSH records (LOTUS, 2018). While merging uncertainties were not available for all datasets and thus not explicitly considered within LOTUS, they are to some extent taken into account in that the final trend uncertainty (**Section 3.3.2.3**) was derived from the trend ensemble using the noise in the regression residuals and the spread in the derived trends.

3.3.2.3 Trend Profiles

Figure 3-19 shows individual trend profiles derived from the various data records used in LOTUS (2018) in four broad latitude bands. The pre-1997 trends are very similar across the datasets, within the uncertainties of the measurements; the exceptions are both SBUV merged records, which show large differences from the other datasets in some regions due to larger merging uncertainty in the mid 1990s (LOTUS, 2018). In the post-2000 period, all individual merged records show significant trends, ranging from 2 to 5% decade^{-1}, in the 5–2 hPa pressure range for 35°–60°N. Smaller positive trends are found in the other latitude bands, and some trend values are not significant,

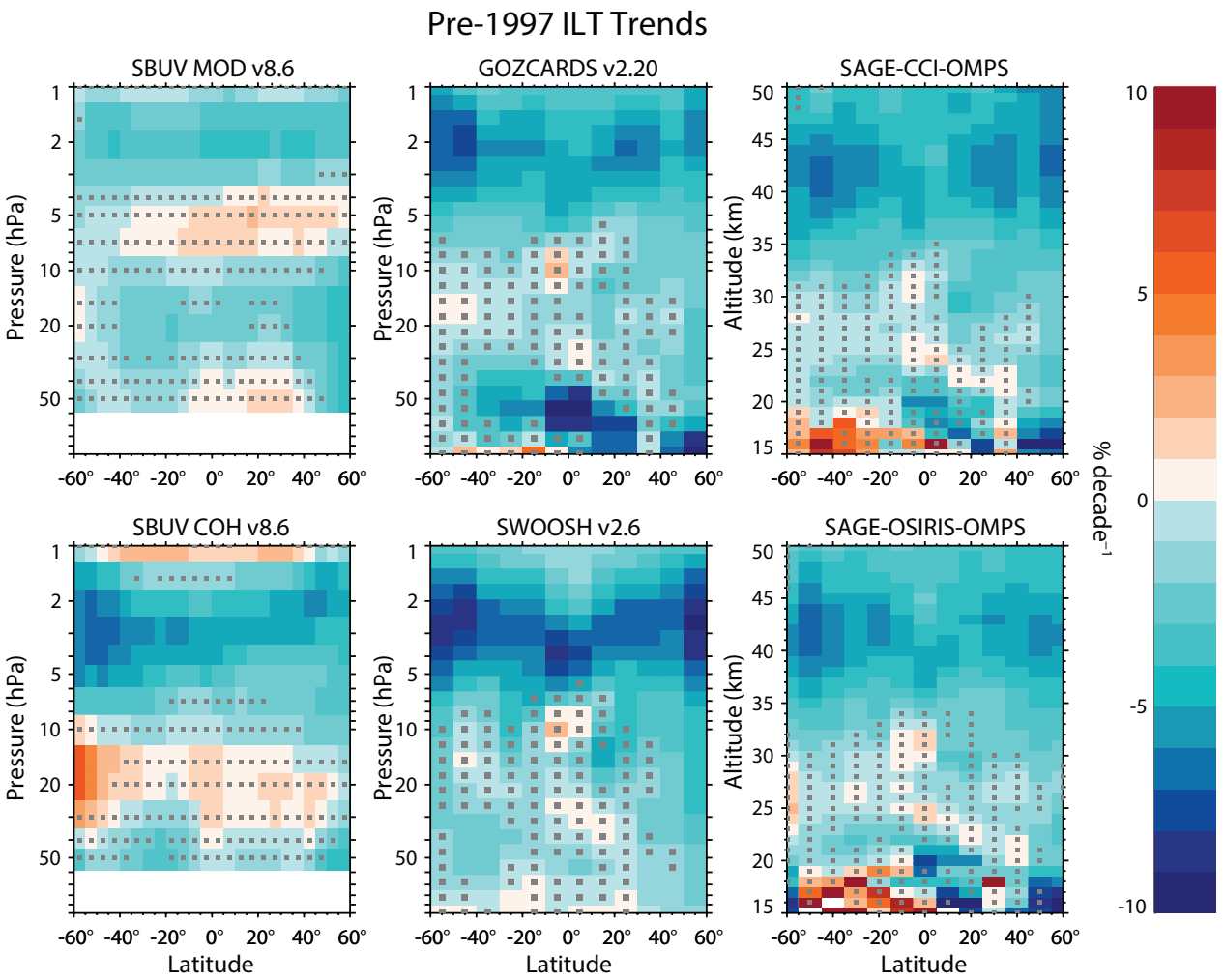

Figure 3-17. Ozone trends for the period 1985–1997 estimated from six satellite data records using the independent linear trend (ILT) model. Gray stippling denotes results that are not significant at the 2σ level. Data are presented on the latitudinal grid and vertical coordinates associated with each dataset. Adapted from LOTUS (2018).

especially in the tropics. In the middle and lower stratosphere, trends are generally not significantly different from zero. This includes the NH mid-latitudes, where most records show negative but not significant trends below 70 hPa.

To facilitate comparison with model simulations, it is useful to calculate an average ozone trend profile from the individual trends derived from each observational record. However, the use of different averaging techniques and different approaches to the calculation of average trend uncertainties can result in contradicting statements regarding the significance of ozone recovery in the stratosphere (**Figure 3-20**). Various techniques have been used to merge the uncertainties in the past (e.g., Harris et al., 2015; Steinbrecht et al., 2017); LOTUS (2018) introduced a new, more statistically robust method. This method includes both simple error propagation, which captures uncertainties introduced by the data and the analyses, and the standard error of the mean, which captures systematic uncertainties such as those introduced by drifts between datasets. Another important parameter that impacts the uncertainty of combined trends is the estimated number of independent datasets. In LOTUS (2018), this number is determined from the correlation of the fit residuals from the trend simulations; it

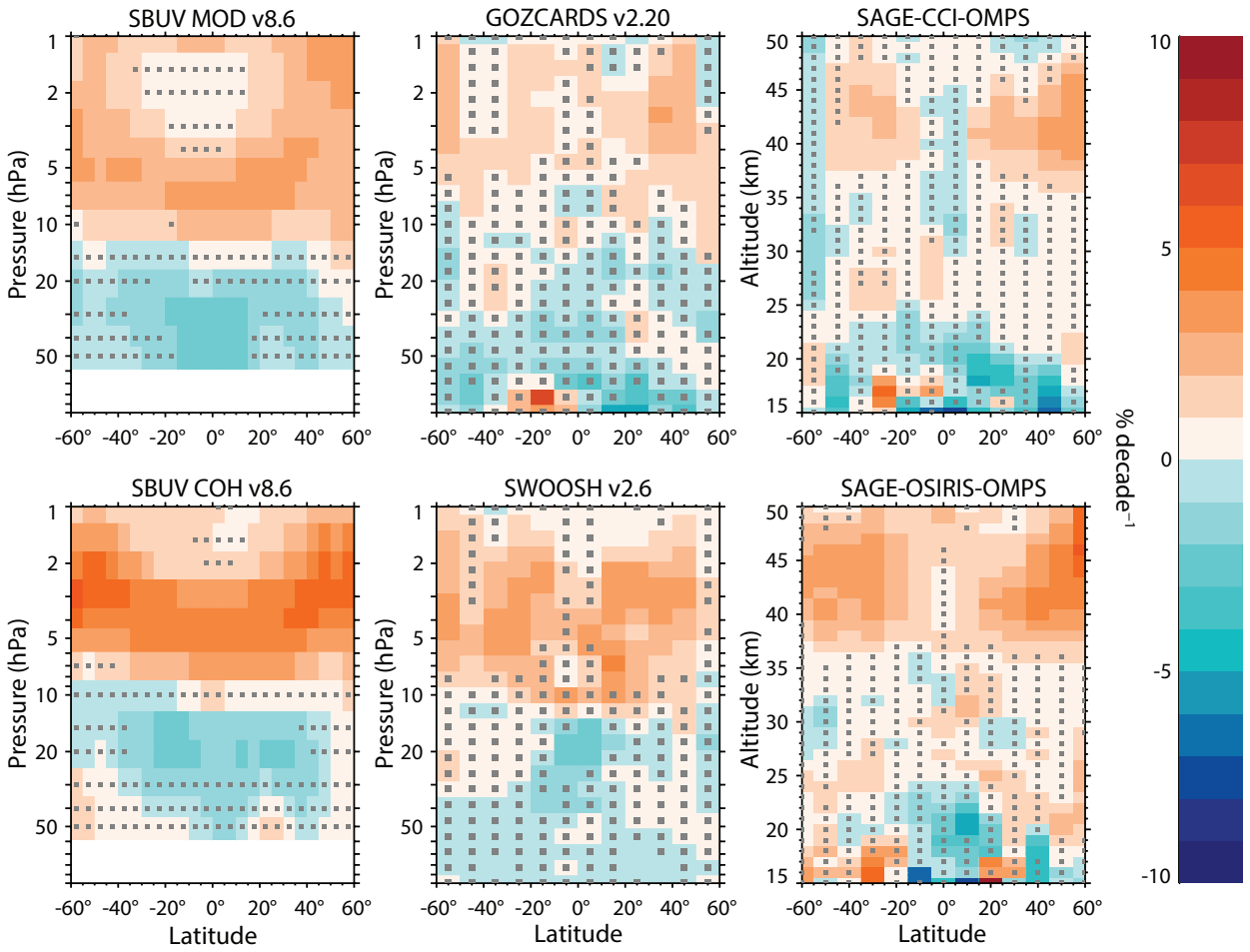

Figure 3-18. Ozone trends for the period 2000–2016 estimated from six satellite data records using the independent linear trend (ILT) model. Gray stippling denotes results that are not significant at the 2σ level. Data are presented on the latitudinal grid and vertical coordinates associated with each dataset. Adapted from LOTUS (2018).

has been more subjectively determined in previous studies (Steinbrecht et al., 2017). The combined trends from the merged satellite datasets used in the LOTUS (2018) study are shown in **Figure 3-21** and compared to the results from the last Ozone Assessment, as well as from the two major studies on ozone profile trends published since then (Harris et al., 2015; Steinbrecht et al., 2017). A significant ozone increase is found in the NH mid-latitude upper stratosphere regardless of the method used. In the tropics and SH mid-latitude upper stratosphere, however, trends are smaller, and their degree of significance depends on the method used to evaluate combined uncertainties.

3.3.2.4 Consistency of Total Column Trends and Integrated Profile Trends

As shown in **Figure 3-12**, total ozone trends for the 1997–2016 period are close to zero over all latitudes, with small positive but not statistically significant values at middle and high latitudes. Despite the small magnitude of these trends, the time series of global mean total ozone is, in fact, consistent with changes in EESC resulting from ODS changes (**Figure 3-13**).

However, ozone profile trends (**Section 3.3.2**) show a significant increase in ozone mixing ratios in the upper stratosphere; this is also thought to be due

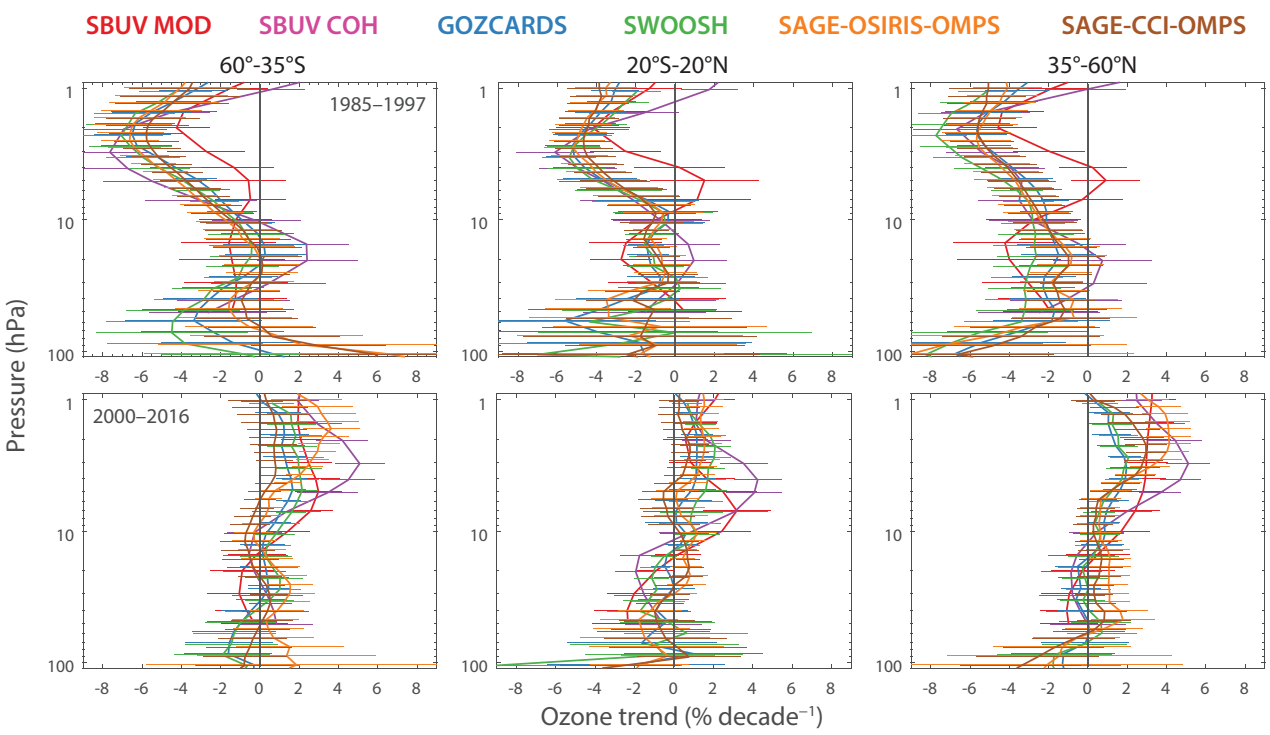

Figure 3-19. Ozone profile trends with 2σ uncertainties for the 1985–1997 (*top row*) and 2000–2016 time periods (*bottom row*) from the ILT regression for latitude bands 35°–60°S (*left column*), 20°S–20°N (*center column*), and 35°–60°N (*right column*). Colored lines are the trend estimates from six individual merged datasets on their original vertical grid. Adapted from LOTUS (2018).

to the decline in ODSs, with enhancement of upper-stratospheric cooling associated with increases in GHGs (**Section 3.3.3**). Though the contribution of the upper stratosphere to column ozone changes is small, it is necessary to understand the consistency or lack thereof among ozone trends in the upper, middle, and lower stratosphere and their relationship to total column changes.

There is recent evidence for a continuous decline in lower-stratospheric ozone, based on merged SWOOSH-GOZCARDS-SAGE II-CCI-OMPS and SAGE II-OSIRIS-OMPS data (Ball et al., 2018). Partial column ozone anomalies (60°S–60°N) were calculated for three layers: the upper stratosphere (10–1 hPa), the middle stratosphere (32–10 hPa), and the lower stratosphere (100–32 hPa). The study found that for the 1998–2016 period, there was a highly probable recovery in the upper stratosphere, a relatively flat trend in the middle stratosphere, and a continuous decrease in ozone in the lower stratosphere.

Similar observational results showing a decline in lower-stratospheric ozone have also been noted by others (e.g., Bourassa et al., 2014, 2018; Steinbrecht et al., 2017; Sofieva et al., 2017) and can be seen in **Figures 3-18** and **3-19** of this report. These figures show that the decline is largest and most consistent across datasets in the tropics. Several studies have addressed attribution of ozone trends in the tropical lower stratosphere (see **Section 3.3.3.2**).

Ball et al. (2017) also found that stratospheric column ozone, which is dominated by lower-stratospheric ozone, decreased from 1998 to 2016. Using the OMI/MLS tropospheric ozone residual column (Ziemke et al., 2006), the study suggests that the total column change is near zero because of increases in tropospheric ozone that compensate for the decline in the stratosphere.

Though there does appear to be evidence from merged satellite datasets for a decrease in lower-stratospheric

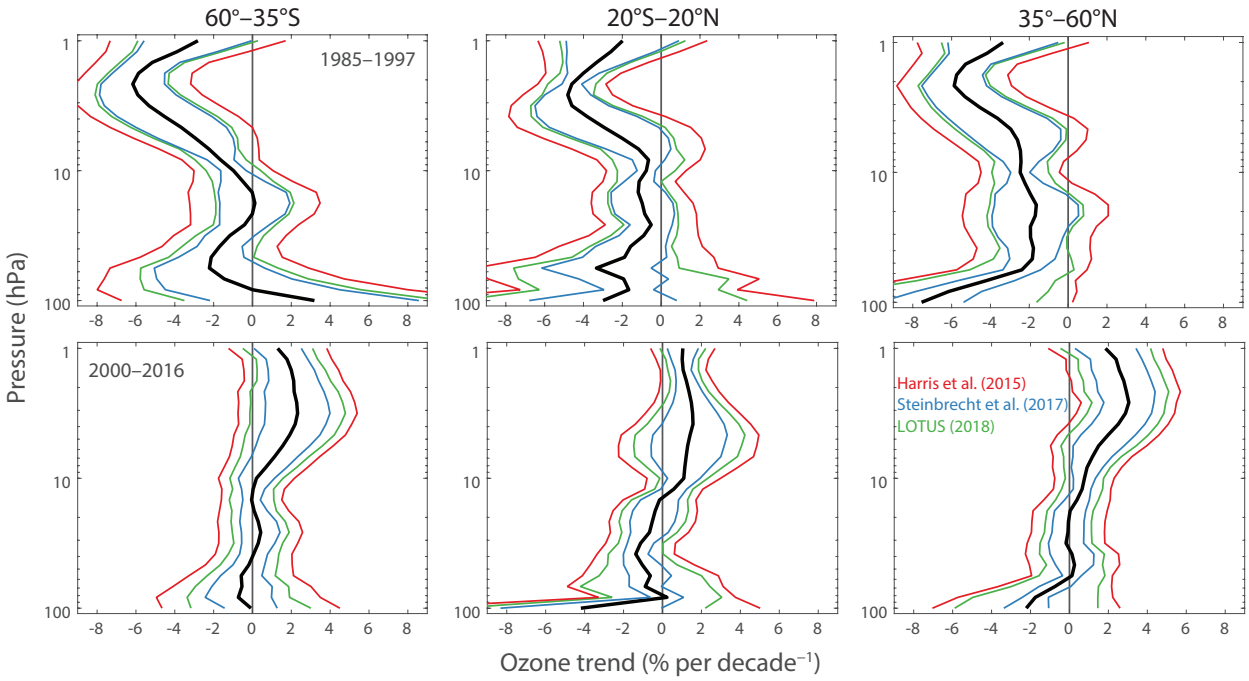

Figure 3-20. Combined trends of six satellite data records with 2σ uncertainties for the pre-1997 period (*top row*) and the post-2000 period (*bottom row*) from the LOTUS analysis for three latitude bands 35°–60°S (*left column*), 20°S–20°N (*center column*) and 35°–60°N (*right column*). Central trend estimates are identical for all methods (black lines). Green lines represent uncertainties calculated using the LOTUS method (Equation 5.1 in LOTUS, 2018); Blue lines represent the method of Steinbrecht et al. (2017) with the number of independent datasets estimated as 2 for pre-1997 and 3 for post-2000 trends; and red lines represent the J-distribution method used by Harris et al. (2015). Results shown here for the latter two methods were obtained using formulae that were modified to use an unbiased estimator of sample variance. Adapted from LOTUS (2018).

ozone over the 1998–2016 period, it is not easy to assert the statistical significance of the trends because the uncertainties are very large there, as seen in **Figure 3-19**. In particular, the lower stratosphere is one of the most difficult regions for obtaining accurate satellite observations because of steep vertical gradients in various atmospheric parameters around the tropopause. Natural variability is also large in the lower stratosphere. In fact, in a 9-member ensemble of a free-running CCM, 1998–2016 trends in the lower stratosphere varied from −6% decade^{-1} to +6% decade^{-1} among the ensemble members (Stone et al., 2018). Furthermore, a recent study showed that lower-stratospheric ozone and the total ozone column both increased sharply from 2016 to 2017, reversing much of the apparent decline in recent years (Chipperfield et al., 2018). Using a chemistry-transport model, that study concluded that the observed changes in lower-stratospheric ozone have been dominated by dynamically driven variability and that there is no need to invoke the VSLS-driven ozone loss suggested by Ball et al. (2018) to explain them. Enhanced isentropic transport between the tropical and extratropical lower stratosphere from 1998 to 2016, particularly in the NH mid-latitudes, has been proposed as a mechanism for this dynamically driven decrease in ozone in the lower stratosphere (Wargan et al., 2018).

The tropospheric ozone trend and its role in total column changes require further investigation. OMI/MLS

is the only record of tropospheric ozone to show continuous, near-global, monotonic increases in tropospheric ozone since 2004 (Gaudel et al., 2018). Other OMI records based on profile retrievals show much smaller increases, and IASI measurements actually show a decline in tropospheric ozone since 2008. There is currently no consistent picture of changes in ozone throughout the troposphere over the past decade (**Figure 3-22**).

3.3.3 Impacts of Changes in Ozone-Depleting Substances and Greenhouse Gases on Ozone Trends

A comprehensive interpretation of observational records must be supported by chemistry–climate or chemistry-transport modeling. CCMI-1 modeled ozone profile trends are in excellent agreement with the observed trends (**Section 3.3.2.3**), except in the

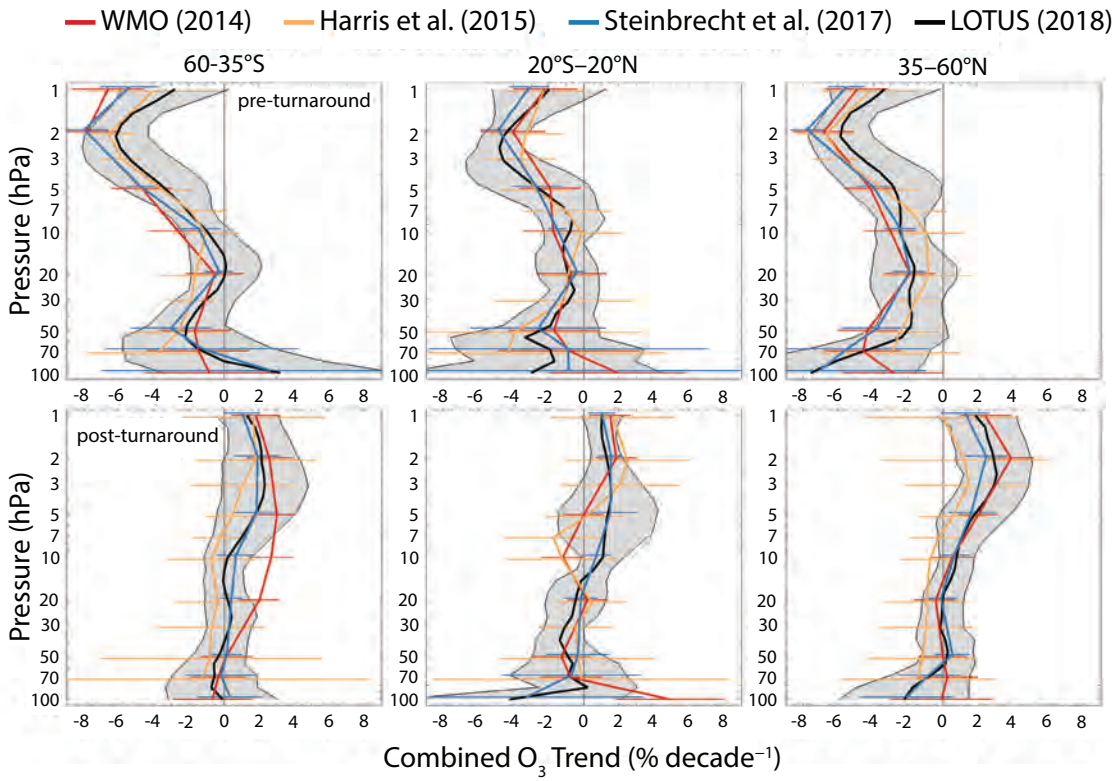

Figure 3-21. Ozone profile trends from WMO (2014), Harris et al. (2015), Steinbrecht et al. (2017), and LOTUS (2018) are shown in red, orange, blue, and black, respectively[1]. The top row shows trends before the turnaround of ODSs; the bottom row shows trends since the turnaround. Shaded areas and error bars represent the 95% confidence interval for the combined trend. Colored profiles are slightly offset on the vertical axis for display purposes. Steinbrecht et al. (2017) did not report or discuss pre-1997 trends but did calculate them and made them available for comparison here. Adapted from LOTUS (2018).

[1]Data included in the trends from each study are from the following periods:

	Pre-turnaround	**Post-turnaround**
WMO (2014)	May 1970 / Feb 1979 / Oct 1984–1997	Jan 2000–Dec 2013
Harris et al. (2015) (Sections 2.1 & 2.2)	Feb 1979 / Oct 1984–Dec 1997	Jan 1998–Dec 2012
Steinbrecht et al. (2017) (Table 3)	May 1970 / Feb 1979 / Oct 1984–Dec 1996	Jan 2000–Dec 2016
LOTUS (2018) (Table ES.1)	Jan 1985–Dec 1996	Jan 2000–Dec 2016

SH lowermost stratosphere during the period of ozone depletion (**Figure 3-23**). Idealized scenarios run by a subset of these models allow the attribution of ODS and GHG effects on ozone changes.

The evolution of stratospheric ozone in a changing climate depends on (in addition to ODS change): cooling of the stratosphere due to increases in GHGs; changes in transport (Brewer–Dobson circulation); and changes in ozone chemistry (N_2O/NO_x and CH_4/HO_x).

While past changes in stratospheric ozone were primarily due to anthropogenic emissions of ozone-depleting substances (ODSs), the evolution of stratospheric ozone in the 21st century will be controlled not only by the decline in ODSs but also, to a large extent, by the increase in greenhouse gases (GHGs) such as CO_2, CH_4, and N_2O. This section updates the attribution of past changes in ozone to changes in ODSs and GHGs, separated for the periods 1979–1996 and 2000–2016. This attribution is based on a multi-model analysis of simulations from CCMI-1 (**Figure 3-24**).

Figure 3-24 provides an update of the attribution of ozone trends due to ODS and GHG changes, based on output from the seven CCMI-1 models that performed all of the required simulations. In addition to the standard (REF-C2) model simulations including all forcings (ODSs and GHGs), a set of sensitivity simulations was run with either changes in ODSs only (i.e., with fixed GHGs) or with changes in GHGs only (i.e., with fixed ODSs). In the REF-C2 simulations, ODS and GHG concentrations follow the RCP-6.0 scenario, consistent with observed concentrations before 2005. Sea surface temperatures were either prescribed from an offline model simulation, which was performed using either the same model or a different model, or they were internally calculated via a coupled ocean model (Morgenstern et al., 2017). Trends were calculated as independent linear trends (ILTs) consistent with observed trends, using proxies derived from the variability in each model for QBO, ENSO, solar cycle, and aerosol optical depth.

In line with previous results, this analysis shows that negative ozone trends over the period 1979–1996 are primarily due to the increase in ODS concentrations. Model simulations with fixed ODSs exhibit small, statistically insignificant trends, except in the tropical lower stratosphere. In this region, the simulations indicate that the 1979–1996 ozone decrease may mostly

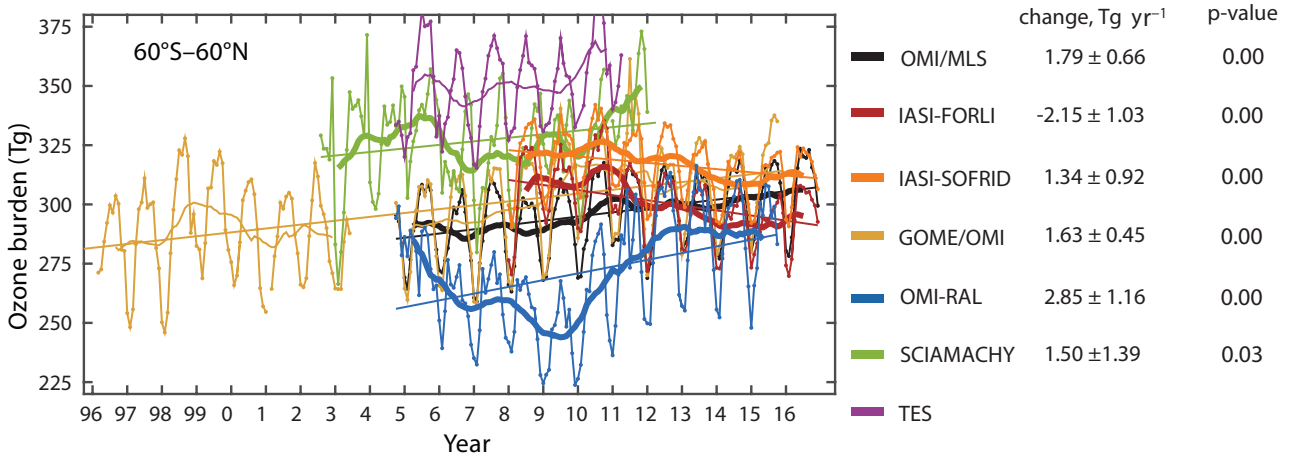

Figure 3-22. Time series of the tropospheric ozone burden, calculated from measured tropospheric ozone columns for seven satellite records. All instruments are nadir-viewing and have differing vertical sensitivities. The black line is the OMI/MLS tropospheric ozone residual product; the dark red and orange lines are IASI retrievals using the Fast Optimal Retrievals on Layers (FORLI) and SOftware for a Fast Retrieval (SOFRID) algorithms; respectively; the blue line is the OMI optimal estimation retrieval from Rutherford Appleton Laboratories (RAL); and the gold line is a combined GOME and OMI time series from Smithsonian Astrophysical Observatory. The green and purple lines are standard products from SCIAMACHY and TES, respectively. See Gaudel et al. (2018) and references therein. Adapted from Gaudel et al. (2018).

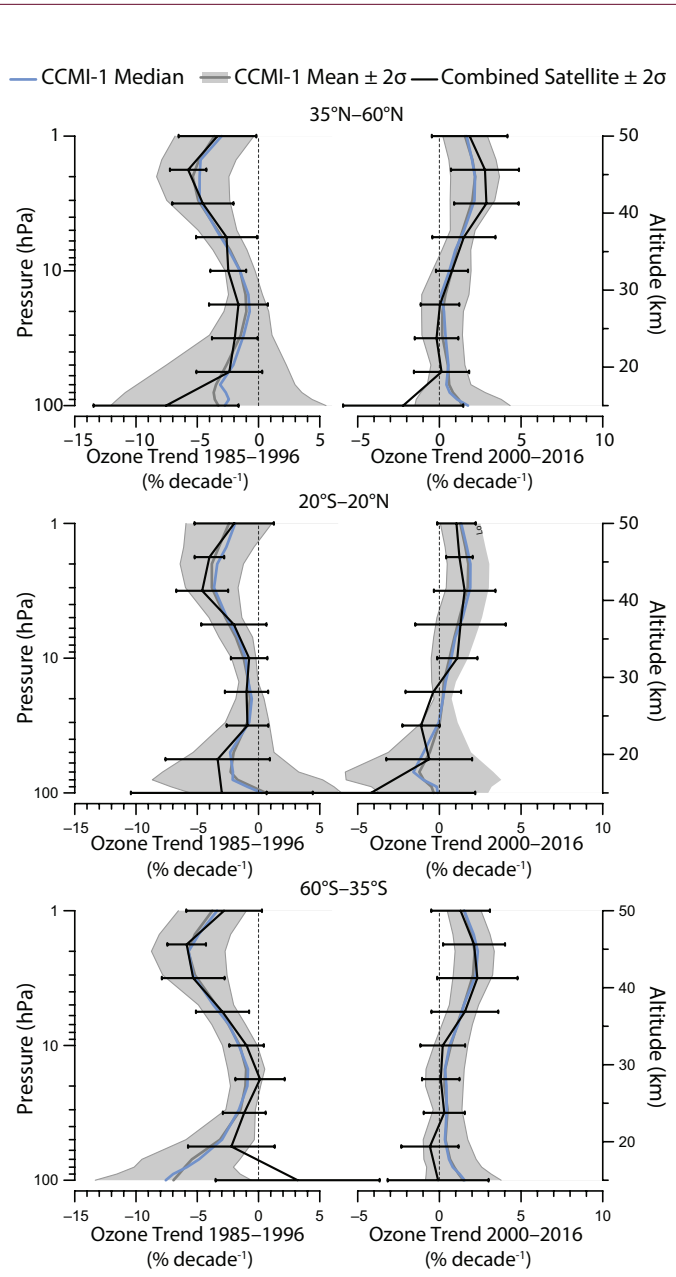

Figure 3-23. Measured and modeled ozone trends for the NH mid-latitudes (*top row*), tropics (*middle row*), and SH mid-latitudes (*bottom row*) for the pre-1997 (*left column*) and post-2000 (*right column*) periods. The black line is the combined satellite-based ozone trend from LOTUS, with 2σ uncertainties, the blue line is the median model, and the gray line is the multi-model mean. The gray envelope shows the 2σ variance of the models. CCMI-1 REF-C2 simulations are shown.

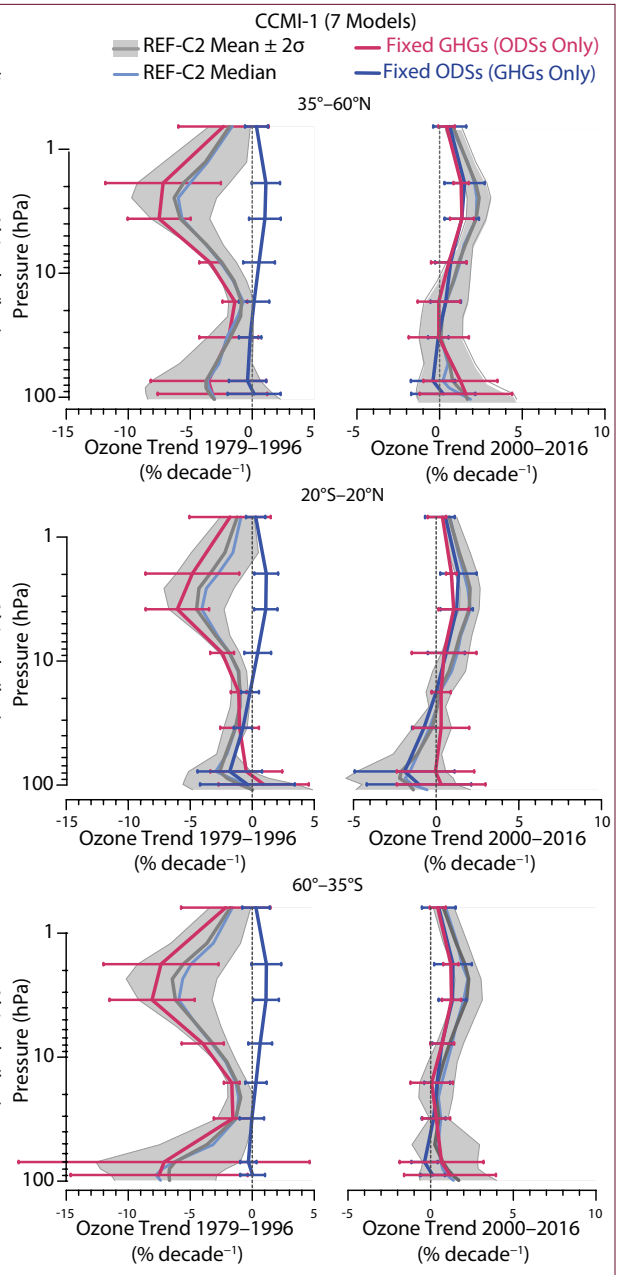

Figure 3-24. Attribution of stratospheric ozone profile trends for 1979–1996 (*left column*) and 2000–2016 (*right column*) due to ODSs and GHGs based on CCMI-1 model simulations. The top row shows the trends for NH mid-latitudes (35°–60°N); the middle row, for the tropics (20°N–20°S); and the bottom row, for SH mid-latitudes (60°–35°S). The gray lines show the multi-model mean of seven REF-C2 simulations including all forcings, with the shading indicating the 2σ range. The light blue lines show the median for all forcings. The red and blue lines represent the median trends due to ODSs only (i.e., with fixed GHGs) and due to GHGs only (i.e., with fixed ODSs), respectively. The same subset of seven models are used in all cases. Adapted from LOTUS (2018).

be due to an increase in GHGs. However, uncertainties in the lower stratosphere are large, as expressed by the relatively large spread in model results. Positive ozone trends in the lower stratosphere over the 2000–2016 period in the mid-latitudes of both hemispheres are consistent with the decline in ODSs, as the all-forcing REF-C2 simulations show positive ozone trends in this region similar to the ODS-only simulations.

In the upper stratosphere, ODS and GHG changes both contribute more or less equally to the positive ozone trends over the 2000–2016 period, again largely in agreement with previous results. The GHG-induced ozone increase in the upper stratosphere is primarily a result of cooling associated with GHGs, which reduces catalytic ozone loss rates. Furthermore, these simulations confirm previous findings that in the upper stratosphere, the effects of declining ODSs and increasing GHGs add approximately linearly.

3.3.3.1 Effects of Very Short-Lived Substances

Halogens from very short-lived substances (VSLSs; i.e., from halogenated ozone-depleting substances with lifetimes shorter than a few months) may contribute to ozone trends, in particular in the lowermost stratosphere, even when the concentrations of VSLSs themselves exhibit no trend (e.g., Dvortsov et al., 1999; Salawitch et al., 2005; Sinnhuber et al., 2009). They do so by providing additional chemical reaction partners for bromine and chlorine from anthropogenic long-lived source gases. One study described simulations with the chemistry–climate model EMAC over the timeframe 1960–2005 with and without the inclusion of brominated VSLSs (Sinnhuber and Meul, 2015). It found that a constant contribution of brominated VSLSs, producing about 6 ppt of additional bromine, led to column ozone changes in better agreement with observations and a stronger negative ozone trend in the mid-latitude lowermost stratosphere for the 1979–1995 period. The study also found a stronger positive trend for the 1996–2005 period, but the considered time period was too short for a robust estimate of the effect on ozone trends. The largest effect of brominated VSLSs on ozone was found for polar winter–spring ozone loss in the lower stratosphere and, in particular, the Antarctic ozone hole (**Chapter 4, Sections 4.3.3** and **4.5.3.4**).

Model calculations show that column ozone is reduced by about 1% at low latitudes and about 5% at high latitudes relative to a model simulation without VSLSs when best estimates for the present-day stratospheric loading of brominated and chlorinated VSLSs are used (**Figure 3-25;** Hossaini et al., 2015). The largest ozone reductions due to VSLSs occur in the lowermost stratosphere below 20-km altitude, where present-day ozone reductions due to VSLSs could be almost half as large as the ozone depletion due to long-lived ODSs, depending on the assumed VSLS scenario (**Figure 3-25**). Although the effectiveness of VSLSs to deplete ozone depends on the anthropogenic halogen loading, VSLSs have contributed to the lower-stratospheric ozone decrease since preindustrial times. Lower-stratospheric ozone changes due to the presence of brominated VSLSs have resulted in an estimated radiative forcing of about 0.02 W m^{-2} since the preindustrial period (Hossaini et al., 2015).

Brominated VSLSs are emitted primarily from biogenic oceanic sources (such as phytoplankton and seaweed) and contribute significantly to the current stratospheric bromine loading (see **Chapter 1**); in contrast, chlorinated VSLSs are emitted primarily from anthropogenic sources (although there are also significant natural sources of methyl chloride) and currently contribute little to stratospheric chlorine loading. However, some of the chlorinated VSLSs, and in particular CH_2Cl_2, have shown relatively large increases in recent years (Hossaini et al., 2015; Hossaini et al., 2017; Oram et al., 2017). The impact of anthropogenic chlorinated VSLSs on past ozone trends is still small (Hossaini et al., 2015), but may become important in the future if the observed increase in emissions of CH_2Cl_2 continues (Hossaini et al., 2017).

All CCMI-1 models now include additional bromine from VSLSs (Morgenstern et al., 2017). Two studies have investigated the impact of VSLSs on ozone recovery in chemistry–climate model simulations, with a focus on polar ozone, where the effects are largest (Oman et al., 2016; Fernandez et al., 2017; see **Chapter 4, Section 4.5.3.4**).

3.3.3.2 Tropical Ozone Changes

Past Assessments (WMO, 2011; WMO, 2014) have reported observed negative ozone trends in the tropical lower stratosphere, in overall agreement with available chemistry–climate model simulations. Modeled changes in tropical stratospheric ozone columns using the CMAM chemistry–climate model over the

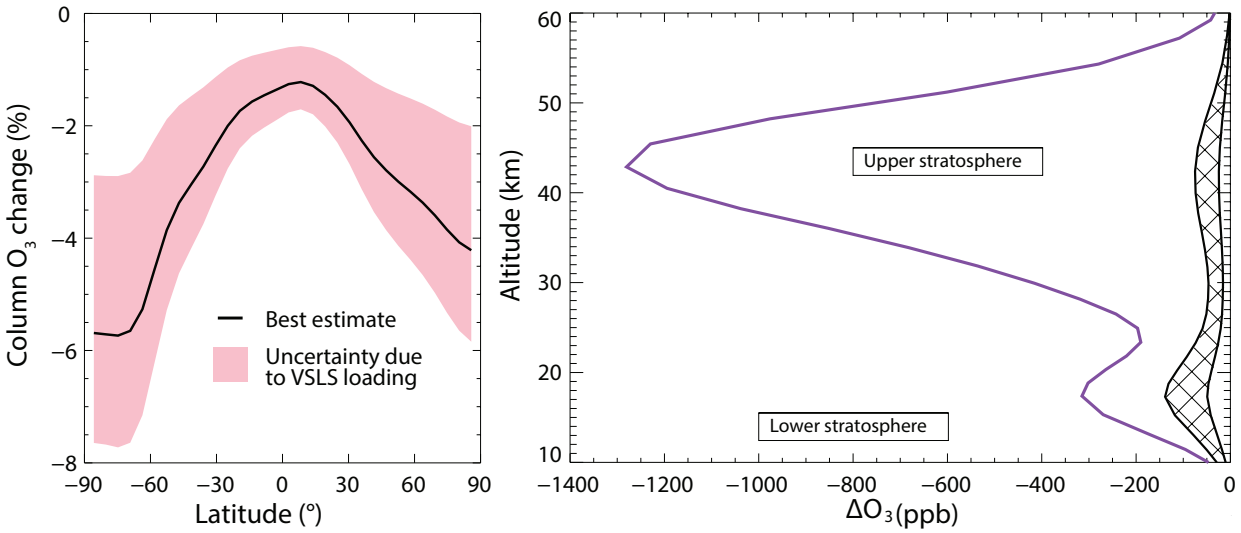

Figure 3-25. Effect of VSLSs on present-day (2011) ozone columns (calculated as the difference between simulations with and without VSLSs) as a function of latitude (*left*), and the impact of ODSs (purple) and VSLSs (black) on global mean ozone profiles (*right*). Shading indicates the range of current estimates of the contribution of VSLSs to stratospheric bromine. Adapted from Hossaini et al. (2015).

1960–2010 period are broadly consistent with satellite observations based on LIMS, SAGE I and II, and MIPAS, although the modeled decrease in tropical ozone is smaller than that deduced from SAGE II (Shepherd et al., 2014). The model shows a decrease of tropical (25°S–25°N) stratospheric ozone of 5.2 ± 1.7 DU between the 1964–1978 and 1996–2002 periods, with the largest decrease in tropical stratospheric ozone before 1990 and little change since the mid-1990s. This is consistent with results presented in this Assessment and with the analysis in the last Assessment (WMO, 2014); while both model simulations and observations show negative trends in the tropical lower stratosphere since 2000 (**Figure 3-23**), these trends are not significant except at 30–50 hPa in the SBUV MOD dataset. In CMAM, the 1990s decrease in stratospheric ozone is partly compensated by a modeled increase in tropical tropospheric ozone of 2.9 ± 0.7 DU over the same period (Shepard et al., 2014). The modeled decrease in stratospheric ozone can be largely attributed to the increase in ODSs; a model simulation with constant ODSs shows only a small and insignificant decrease in the tropical stratospheric ozone column of 0.3 ± 1.8 DU between the 1964–1978 average and the 1996–2002 average.

Another study similarly demonstrated that observed variations in tropical lower-stratospheric ozone are captured by a chemistry-transport model driven with meteorological reanalysis fields (Aschmann et al., 2014). The lack of ozone decline after the mid-1990s was explained by changes in not only the strength but also the location of the tropical upwelling region. This argument, that structural changes in upwelling are responsible for changes in tropical ozone trends, is supported by another analysis using satellite observations (Stiller et al., 2017). MIPAS measurements indicate a southward shift of up to 5 degrees in the lower- to middle-stratospheric upwelling region during the period 2002–2012. This shift also appears to explain observed hemispheric asymmetries in trends in other long-lived trace gases (Stiller et al., 2017).

Separating chemical- and transport-related effects (in particular ozone reductions due to an increase in tropical upwelling; **Chapter 5, Section 5.3.2**) is not trivial, as recent papers (Oberländer-Hayn et al., 2015; Polvani et al., 2017) have emphasized that ODS changes may have had a significant or even dominant impact on changes in tropical upwelling, thus leading to the observed decreases in tropical lower-stratospheric ozone. One study used a set of simulations from the

GEOSCCM with small ensembles of single forcings and concluded that dynamical responses to ODSs are the main driver for past changes in tropical upwelling (Polvani et al., 2017). It suggests that the mechanism of such a response may relate to changes in the thermal structure of the lower stratosphere caused by polar ozone depletion, which could alter the propagation and dissipation of planetary-scale waves. Another study, based on simulations with the EMAC chemistry–climate model, finds that ODSs contributed about equally with other GHGs to past changes in tropical lower-stratospheric upwelling (Oberländer-Hayn et al., 2015).

3.4 PROJECTED OZONE CHANGES

Models have always been tools to test process understanding and to project possible future developments. **Box 3-2** summarizes the evolution of models used in Ozone Assessments since 2002 and introduces the model runs used in this Assessment.

Box 3-2. Modelling past and future changes in ozone: Model heritage and application

Modelling in support of the Ozone Assessments has a long tradition. For example, the 2002 Assessment used a selection of early 3-dimensional (3-D) Chemistry-Climate Models (CCMs) to assess polar ozone changes. However, a large amount of information, in particular in the global ozone chapter, was derived from 2-dimensional (2-D) models. In the 2006 Assessment, 3-D Chemistry Transport Models (CTMs) were extensively used to discuss past ozone changes and were complemented with 3-D CCMs. The projected changes for the 21st century were extensively discussed in a separate chapter that used 2-D models and (very extensively) 3-D CCM results, largely emerging from the CCMVal (CCM Validation) activity. The model results were used to characterize future changes in ozone, including the return dates. The 3-D CCM modelling results for the 2010 Assessment were produced in the context of a comprehensive model evaluation in the framework CCMVal-2 (SPARC, 2010). A summary of the participating models can be found in Morgenstern et al. (2010). In the 2014 Assessment, results from this exercise were also used and complemented with results from newer publication. Prior to the 2014 report the CCMVal activity was superseded by the Chemistry-Climate Modelling Initiative (CCMI), which has a wider remit than CCMVal.

Earlier versions of most models contributing to CCMI in the context of stratospheric ozone variability and trends were evaluated in CCMVal-2. As can be expected, some models have been changed more than others; however their fidelity is always assessed by modelling the recent past. A summary of relevant models and their configurations can be found in Morgenstern et al. (2017). Generally, there is a trend to higher spatial resolution, more processes and the option to run more models with interactive ocean and sea-ice coupling. In previous CCM projections there was a clearer disjoint between model configurations used for CCMVal and model configurations used for CMIP (Coupled Model Intercomparison Project). Often, when projecting ozone changes, CCMs prescribed the future sea-surface temperatures and sea-ice coverage from their nearest CMIP relative. The CMIP model would be run without chemistry (prescribing ozone – perhaps from CCM integrations – in the radiation), but with an interactive ocean and sea-ice. This circularity can now be overcome by running atmosphere-ocean CCMs consistently. However, it is important to remember that the ozone projection will rely in both cases on the chosen climate change scenario (see table below and Meinshausen et al., 2011 for the definition of the RCPs).

Other model changes relate to the complexity of the chemistry (more emitted species, more reactions in the troposphere) and to a better understanding of the halogen budget, including the role of VSLSs. The impact of concentration and flux boundary conditions on lifetimes of halogen-containing species was evaluated in the SPARC Report No. 6 using a subset of CCMs from CCMVal-2/CCMI.

Box 3-2, continued.

Name of Simulation	Type of Simulation	Purpose	Features
REF-C1	Hindcast simulation of the period 1960–2010	To produce realistic simulations of the past atmospheric state	GHG*, ODS*, background and volcanic aerosol, solar variability, ozone and aerosol precursors, SST*, SIC*, VSLSs* are prescribed from observations
REF-C1SD	Hindcast simulation of the period 1980–2010	Same as REF-C1, but with the CCM dynamics nudged to observed meteorology	Same as in REF-C1; SSTs and SIC are consistent with meteorological reanalyses
REF-C2	Consistent simulation from the past into the future for the period 1960–2100	To produce best estimates of the future ozone and climate changes under specific assumptions of GHG and ODS evolution	Observations until 2005; then prescribed future scenarios for GHG and ozone/aerosol precursors (medium RCP6.0), ODS (WMO, 2011), background aerosol, projected solar variability, VSLSs; SST and SIC modeled
SEN-C2-RCP2.6	Same as in REF-C2 but for the period 2000–2100	To assess the future evolution of ozone and climate change under GHG scenarios other than RCP6.0	Same as in REF-C2, but GHG and ozone/aerosol precursors according to RCP2.6 scenario; SST and SIC consistent with RCP2.6 scenario
SEN-C2-RCP4.5	Same as in REF-C2 but for the period 2000–2100	To assess the future evolution of ozone and climate change under GHG scenarios other than RCP6.0	Same as in REF-C2, but GHG and ozone/aerosol precursors according to RCP4.5 scenario; SST and SIC consistent with RCP4.5 scenario
SEN-C2-RCP8.5	Same as in REF-C2 but for the period 2000–2100	To assess the future evolution of ozone and climate change under GHG scenarios other than RCP6.0	Same as in REF-C2, but GHG and ozone/aerosol precursors according to RCP8.5 scenario; SST and SIC consistent with RCP8.5 scenario
SEN-C2-fODS	Same as in REF-C2 for the period 1960-2100	To assess the effect of halogens on stratospheric ozone and climate change in the presence of climate change	Same as in REF-C2, but with halogens (ODS) fixed at 1960 levels
SEN-C2-fGHG	Same as in REF-C2 for the period 1960–2100	To assess the impact of halogens on the atmosphere in the absence of climate change	Same as in REF-C2, but with GHG fixed at 1960 levels and 1955–1964 average values from REF-C2 for SST and SIC repeating each year

*GHG: Greenhouse gases; ODS: Ozone depleting substances; SST: Sea surface temperature; SIC: Sea-ice concentration; VSLSs: Very short- lived halogenated substances

3.4.1 Expected Return to 1980 Levels and Ozone Recovery

One of the most critical roles that models play in the assessment process is to provide projections of the future evolution of ozone, with the return to 1980 values being a convenient definition of an ozone recovery milestone. Previous Assessments have discussed tropical and global annual mean total column ozone time series from individual models or multi-model means (see **Box 3-2** for a timeline of modeling and current experimental setups). In the last two Assessments, the results of the CCMVal-2 initiative have been utilized. Here, we provide an update using recent integrations from CCMI-1. The increased availability of simulations from models and ensemble integrations within CCMI-1 provides a new resource for assessing past and future ozone changes. However, the ability to discern the robustness of ozone return dates is limited by the newness of the results and the resulting lack of comprehensive validation across models.

Figure 3-26 presents the modeled total column ozone time series from 1960 to 2100 from bias-adjusted CCMI-1 multi-model means for the tropical belt and for global annual means. To provide a measure of the spread that is realistic but not overly influenced by outliers, the envelope is calculated from models that fall within 1σ of the multi-model mean (denoted MMM1S; see Dhomse et al., 2018 for details). The MMM1S return dates are generally found to be consistent with those derived from the median model (Dhomse et al., 2018).

The most appropriate (based on the chosen boundary conditions) free-running model representation of past total ozone is REF-C1 (blue lines in **Figure 3-26**). REF-C1SD (green lines) should be an even more accurate representation, as the individual models' circulation and thermal structure are relaxed toward analyzed values, thus providing extra information about "realistic" temporal changes to the models. Theoretically, REF-C1SD should provide the best representation of observed ozone anomalies (in particular the timing of low/high ozone events). However, there are large differences among models in how the specified dynamics were implemented. REF-C1 is still able to capture the long-term variability as imposed by the boundary conditions, but it does not accurately capture extremes or particular events. By construction, REF-C2 (red lines in **Figure 3-26**) should be similar to REF-C1 for the past. However, the boundary conditions are extended into the future following the RCP-6.0 scenario in REF-C2, allowing the identification of possible return thresholds in total ozone. A common point of reference is the occurrence of ozone values at 1980 levels (indicated by the horizontal dashed lines in **Figure 3-26**). For a more detailed discussion of the use of return dates, see **Box 3-3** on "Ozone return dates".

Figure 3-27 provides a comparison of the 1980 total column ozone return dates from the last Assessment (WMO, 2014) with the corresponding MMM1S results from CCMI-1 (Dhomse et al., 2018) (see also details in **Box 3-3**). Many of the 20 CCMs analyzed provided ensemble integrations of the REF-C2 scenario; if only a single model integration was available, then a 3-year boxcar smoothing algorithm was applied before ensemble mean model output and individual integrations were brought together (Dhomse et al., 2018). Due to the large number of model realizations that are combined to derive the multi-model mean, internal variability contributes only a small amount to the uncertainty in return dates (indicated by range bars in **Fig. 3-27**). However, when determining whether the 1980s total ozone threshold has been met with either measurements or output from an individual model, the year-to-year variability of ozone due to internal atmospheric variability must be considered (e.g., Keeble et al., 2018). The multi-model median return dates are in good agreement with the MMM1S results, demonstrating the robustness of the analysis, but they have larger uncertainties (Dhomse et al., 2018). The MMM1S return year is used in this Assessment because it is a more comparable metric to the analysis in the last Assessment than the median return year.

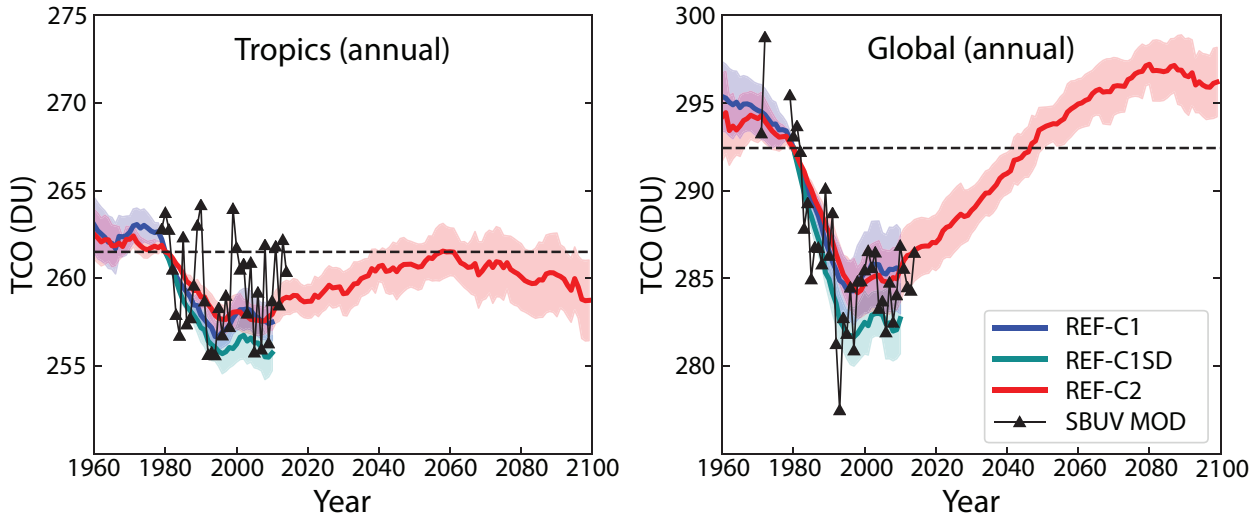

Figure 3-26. Adjusted and smoothed multi-model mean time series of annual mean tropical (*left*) and global (*right*) total column ozone (TCO) from CCMI models (colored lines) and from observations (solid black lines and symbols). Note that the multi-model mean uses a 1σ threshold (MMM1S) for filtering (for method see Dhomse et al., 2018, Figure 2, bottom). The dashed black lines represent 1980 values of TCO.

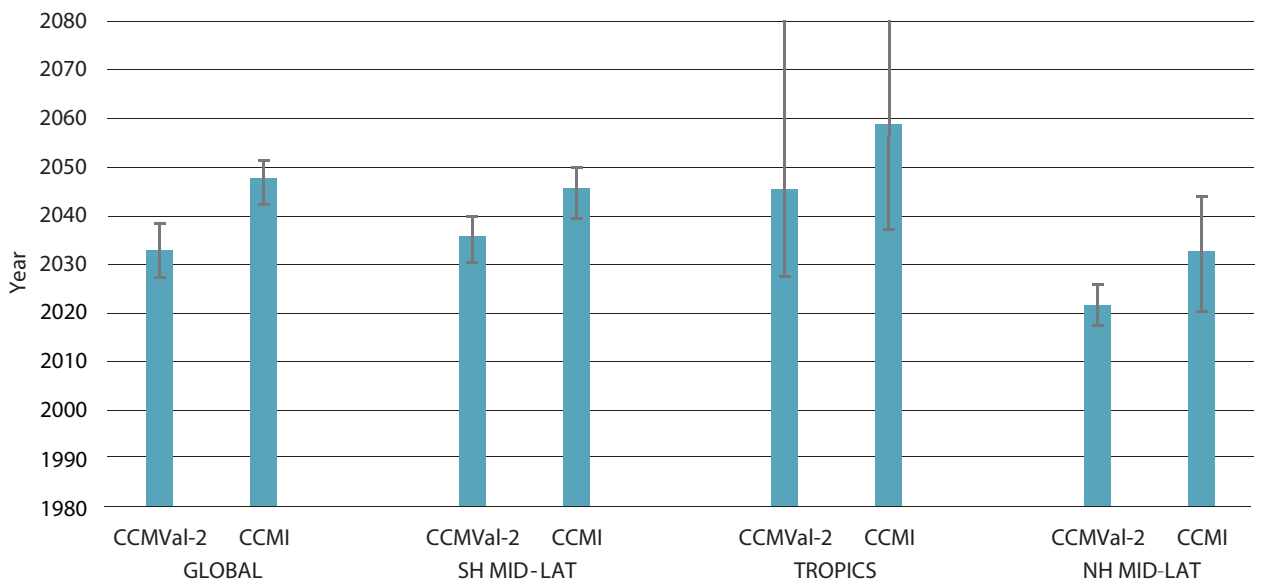

Figure 3-27. Bar chart comparing WMO (2014) projected 1980 return dates (labeled CCMVal-2) to this Assessment's CCMI-1 1980 return dates as analyzed from the multi-model mean (MMM1S) time series. The global mean refers to 90°S–90°N for WMO (2014) and to a near-global mean (60°S–60°N), consistent with the observations presented in this chapter) in the case of MMM1S. The true and near-global mean should be very similar (Dhomse et al., 2018). A comprehensive table with more details is provided by Dhomse et al. (2018).

The delay in return dates seen in this Assessment relative to the 2014 Assessment results primarily from different assumptions made in the scenarios (see **Box 3-3)**. The current best estimates for the range of years in which total ozone will return to 1980 values are 2042–2051 for the near-global mean, 2039–2050 for the SH mid-latitudes, and 2020–2044 for the NH mid-latitudes. The systematic delay of return years relative to the last Assessment (WMO, 2014) does not imply deficits in understanding, but rather reflects updates to prescribed scenarios describing the future evolution of GHGs (chosen to be in line with CMIP5) and ODSs. The extended range of return dates for the tropical belt reflects the fact that some models will not return to their 1980 ozone values in the projected time window given the competing effects of climate change (declining lower-stratospheric ozone) and declining ODSs (increasing ozone) in the tropics.

3.4.2 Effects of Future Stratospheric Temperature and Circulation Changes

As mentioned throughout this chapter, the evolution of stratospheric ozone in the 21st century will be controlled not only by the decline of ODSs but also, to a large extent, by changes in GHG concentrations, most importantly CO_2, CH_4, and N_2O. These GHGs affect stratospheric ozone through temperature and subsequent changes in dynamics and transport; CH_4 and N_2O also affect ozone chemistry (e.g., Butler et al., 2016), as discussed in more detail in **Section 3.4.3.2**. The impact of possible future GHG scenarios described by different Representative Concentration Pathways (RCPs) is discussed in **Section 3.4.3.1**.

The effects of GHG-induced temperature and circulation changes on ozone are compared to the effects of declining ODSs in **Figure 3-28,** which shows results from time-slice simulations with different forcings from the UM-UKCA chemistry–climate model

(Banerjee et al., 2016). The decrease in ODSs between the years 2000 and 2100 will lead to an ozone increase essentially everywhere in the atmosphere, with the largest percentage changes in the upper stratosphere at around 40 km and in the lower stratosphere at high latitudes, particularly in the Southern Hemisphere, where recovery of the Antarctic ozone hole is most notable. In contrast, changes in GHG concentrations will lead to a more complex pattern of ozone changes, with increases in the upper stratosphere at

Box 3-3. Ozone Return Dates

A critical role of Ozone Assessments is to provide years at which (column) ozone is expected to return to a particular, historic level – so-called return dates. This Assessment tabulates ozone return to 1980 values only. Here, we explain how return dates are computed and clarify why our current estimate for when global, total ozone will return to the 1980 level is systematically delayed relative to the 1980 return given in the prior two Assessments.

Comprehensive Chemistry-Climate Models (CCMs) project climate, and interactively calculate ozone, for prescribed future abundances of greenhouse gases (GHGs) and ozone depleting substances (ODSs). Three types of uncertainties must be considered for return date estimates: internal variability, structural uncertainty, and scenario uncertainty.

Internal Variability. CCMs exhibit internally-generated variability that impacts ozone (e.g., polar stratospheric warmings). If multiple runs from one model exist for the same climate scenario, these so-called ensembles are averaged together. If only one run is available, the model output is smoothed with respect to time, prior to being combined with results from other models. Due to the large number of runs and models that are combined to derive the multi-model mean, internal variability contributes only a small amount to the uncertainty of return dates.

Structural Uncertainty. CCMs represent processes, and their interactions, differently. This may lead to different return dates, for the same prescribed future levels of GHGs and ODSs. Several of the latest CCMs have interactive oceans and/or sea-ice modules, enlarging the degrees of freedom. In this and prior Assessments, structural uncertainty is quantified by examining output from many different models. While structural uncertainty is certainly important for quantifying the range of expected return years, the introduction of three additional CCMs for this Assessment is not responsible for the delay of the return dates relative to prior Assessments. Structural uncertainty is, however, the driving factor of lower and upper limits for the range of years given in **Table 3-4**.

Scenario Uncertainty. CCM projections use prescribed scenarios for future ODSs and GHGs. The return dates reported in WMO (2011) and WMO (2014) were based on ODSs from the baseline scenario of WMO (2007) with an adjustment for HCFCs and GHGs from the Special Report on Emissions Scenarios (SRES) A1b scenario developed in IPCC (2000). Here, we use ODSs from the baseline scenario of WMO (2011) and GHGs from the Representation Concentration Pathway (RCP) 6.0 scenario developed by Masui et al. (2011) for IPCC (2013). As illustrated below, differences in future specifications of CO_2, CH_4, and ODSs are the likely cause of the obvious delay in return of ozone to the 1980 value relative to the projections of the previous Assessments.

Most CCMs prescribe future abundances of GHGs and ODSs at the surface and compute the concentrations in the atmosphere as a function of time. Panels a) and b) on the next page show significant differences in the assumed evolution of CO_2 and CH_4 as used in model runs for the previous assessments (SRES A1b) and this assessment (RCP 6.0). Note that these differences in CO_2 and CH_4 have both direct and indirect

Box 3-3, continued.

consequences for the climate change impact on ozone. Panel c) shows effective equivalent stratospheric chlorine (EESC) that can be used as a proxy of how the halogen loading evolves within the CCMs. The approximately 5-year delay in EESC drawdown in the WMO (2011) baseline scenario used in this assessment relative to the previously-used scenario reflects new knowledge of lifetimes and emissions of various ODSs. This is another factor contributing to the overall delay in return dates.

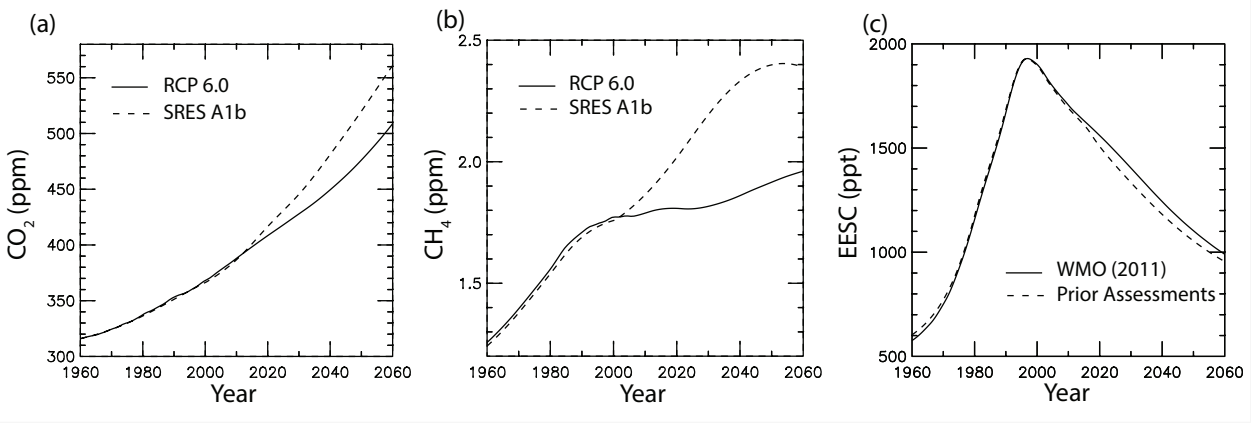

Time series of a) CO_2, b) CH_4, and c) equivalent effective stratospheric chlorine (EESC) used as boundary conditions for the CCM simulations analyzed for ozone return dates of this assessment (black solid) and of the prior two assessments (black dashed). For the baseline return dates of this assessment, future abundances of CO_2, CH_4, and all other GHGs are from the RCP 6.0 scenario developed for IPCC (2013) and ODS mixing ratios that drive EESC originate from WMO (2011). The prior two Assessments utilized time series of GHGs from the SRES A1b scenario and ODSs from WMO (2007) with an adjustment for HCFCs. The EESC curves in this figure were calculated for mid-latitude air with a lifetime of 3 years, using the Newman et al. (2007) release factors.

all latitudes, primarily due to GHG-induced cooling that slows down gas-phase ozone loss reactions. In the low-latitude lower stratosphere, however, ozone is projected to decrease due to changes in dynamics and transport, and, in particular, a strengthening of the BDC. This increase in the strength of the BDC is a robust finding in the CCMI-1 models, although there are still uncertainties in the magnitude (Morgenstern et al., 2018) and attribution of the strengthening (**Chapter 5, Section 5.3.2**). Lower-stratospheric ozone in middle to high latitudes may either increase or decrease, depending on the hemisphere and on the GHG scenario. In the more extreme RCP-8.5 scenario, the upper-stratospheric increase in ozone due to GHGs is larger than that due to ODS decline. In the tropical lower stratosphere, ozone changes due to BDC alteration that are potentially driven by GHG increases will dominate (see also **Section 3.4.3**).

A study diagnosing ozone sensitivity to varying GHGs and ODSs in CCMI-1 simulations finds varying degrees of consistency in the models' responses in ozone to individual forcings, including some considerable disagreement. It is suggested that some of these differences could be linked to circulation differences between the models (Morgenstern et al., 2018). The results in **Figure 3-28** (Banerjee et al., 2016) are therefore an illustration of principle and not a universally valid result.

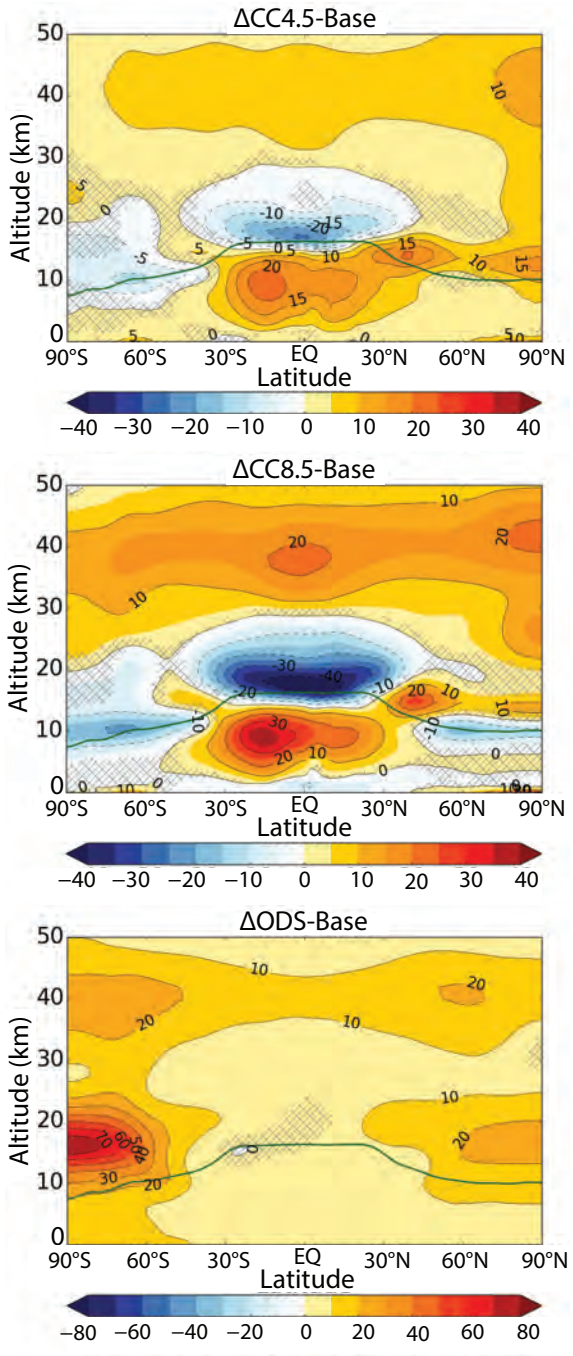

Figure 3-28. Modeled percent changes in annual mean ozone between 2000 and 2100 due to GHG changes according to RCP-4.5 (*top*) and RCP-8.5 (*middle*) and due to ODS changes (*bottom*). Shown are differences between a year-2000 baseline simulation with single forcing changes for year-2100 conditions: RCP-4.5 and RCP-8.5 assume year-2100 SST, sea-ice, and GHG concentrations with year-2000 ODS and ozone precursor emissions. From Banerjee et al. (2016).

3.4.3 Sensitivity to the Specification of Different Future Scenarios

3.4.3.1 Effects of Different Representative Concentration Pathways

A number of CCMI-1 models provide estimates of the sensitivity of ozone to changes in other traces gases using simulations with different scenarios. The different RCPs are GHG concentration trajectories first chosen for the Coupled Model Intercomparison Project Phase 5 (CMIP5) to span a range of corresponding radiative forcings by the year 2100 (see **Box 3-2**). While the standard reference simulations of CCMI-1 use the RCP-6.0 scenario, sensitivity simulations for RCP-2.6, RCP-4.0, and RCP-8.5 have also been carried out. **Figure 3-29** summarizes the evolution of total ozone columns for the different RCPs (Dhomse et al., 2018). For global mean total ozone columns, the return to 1980 values is faster and the possibility of super-recovery (i.e., the increase of ozone above historical levels) is higher for the RCPs with larger GHG increases. This effect is largest in mid-latitudes, where RCP-8.5 results in ozone increases of more than 20 DU above average 1980 levels at the end of the 21st century. RCP-4.5, in contrast, results in a return to 1980 global mean ozone columns in NH mid-latitudes by the middle of the 21st century and shows little change afterwards. Tropical ozone columns for the multi-model mean do not fully return to pre-1980 levels in any of the scenarios.

One study shows changes in tropical total column ozone for three altitude ranges (upper stratosphere, lower stratosphere, and troposphere) for three RCPs (4.5, 6.0, 8.5) from calculations with the chemistry–climate model EMAC (Meul et al., 2016; **Figure 3-30**). Upper-stratospheric ozone columns ($p<10$ hPa) recover to 1980 levels as early as ~2025 in all scenarios and show a super-recovery afterwards, with the largest super-recovery for RCP-8.5. In contrast, ozone columns in the lower stratosphere ($10\ \text{hPa} < p < 100\ \text{hPa}$) do not return to pre-1980 levels at all but continue to decrease, with the largest decrease for RCP-8.5. (These simulations show a small increase in tropical lower-stratospheric ozone columns between the late 1990s and around 2025, but it is not clear if this is significant.) Tropical total ozone columns also depend critically on the evolution of tropospheric partial column ozone, which is either decreasing or increasing in the future, depending on the RCP scenario (Igelsias-Suarez et al.,

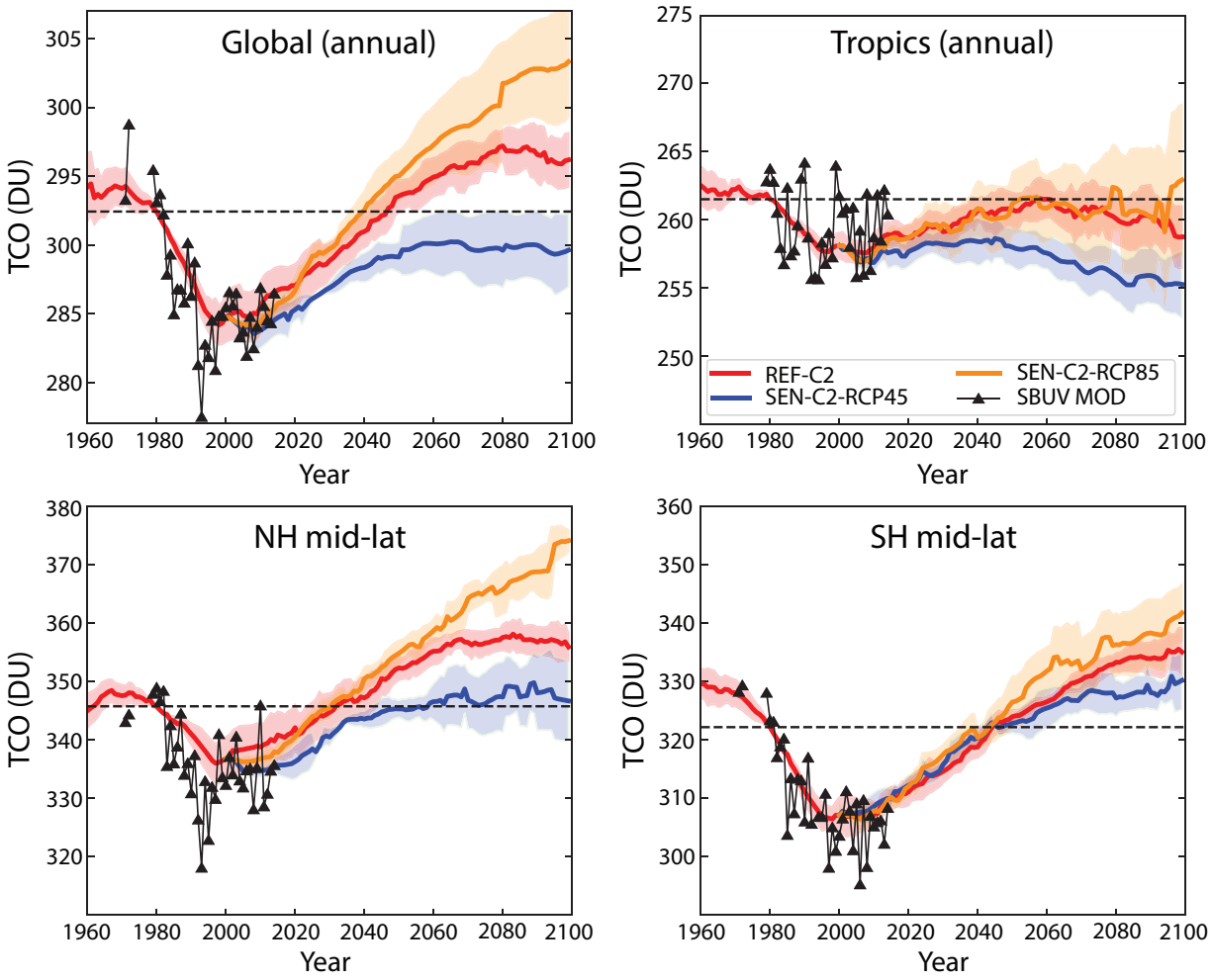

Figure 3-29. Adjusted and smoothed multi-model mean time series of annual mean TCO from observations (solid black lines and symbols) and for RCP scenarios from CCMI models: REF-C2=RCP-6.0 (red lines), SEN-C2-RCP45=RCP-4.5 (blue lines), and SEN-C2-RCP85=RCP-8.5 (orange lines). The black dashed lines represent 1980 values of TCO. From Dhomse et al. (2018).

2016; Meul et al., 2016). In most scenarios, tropical tropospheric ozone columns decrease during the second half of the 21st century, though there are large differences among models (**Section 3.4.4**). The exception is RCP-8.5, which shows a strong increase in tropical tropospheric ozone in most models due to a strong increase in methane. There is some cancelation between the projected upper-stratospheric increase in tropical ozone (e.g., due to GHG-induced cooling) and the projected decrease in lower-stratospheric ozone, but the overall effect on stratospheric ozone columns depends on the RCP scenario (Banerjee et al., 2016).

3.4.3.2 Influence of Nitrous Oxide and Methane

Methane (CH_4) and nitrous oxide (N_2O) affect stratospheric ozone not only through the temperature changes associated with their radiative forcing, but also through chemistry: N_2O is the main source of odd nitrogen (NO_y) in the stratosphere, while CH_4 is an important source for hydroxyl radicals (HO_x) but is also involved in chlorine deactivation into HCl. Currently, N_2O is the most important ODS emitted in terms of its Ozone Depletion Potential (ODP). However, the ODP metric was traditionally developed for long-lived halogen-containing ODSs. It uses CFC-11 as a reference gas, and it is not an optimal metric

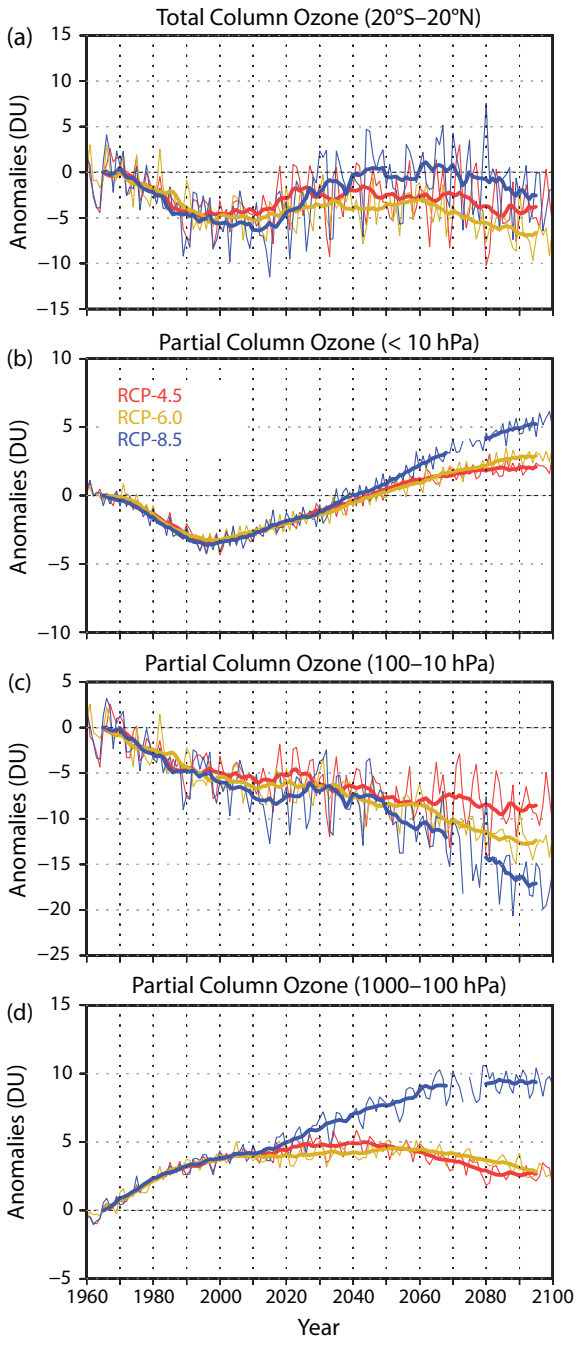

Figure 3-30. Past and projected tropical ozone for different RCPs: (a) total-column ozone, (b) upper-stratospheric partial column ozone, (c) lower-stratospheric partial column ozone, and (d) tropospheric partial column ozone. From Meul et al. (2016).

for assessing the impact of future N_2O emissions. Specifically, the ODP value for N_2O depends critically on the level of other GHGs and the degree of halogen loading. This sensitivity is due to the chemical interactions of NO_x with HO_x and ClO_x, as well as the temperature dependence of those interactions (Revell et al., 2015). The ODP of N_2O was calculated using the chemistry–climate model SOCOL (Revell et al., 2015) for year-2100 conditions under a range of different CH_4 and CO_2 concentrations (**Figure 3-31**). **Figure 3-31a** shows the calculated global mean total ozone column as a function of CO_2 and CH_4 global mean surface mixing ratios, with all other parameters held constant according to RCP-6.0. Global mean total ozone increases for increasing CO_2 and increasing CH_4 concentrations. Reductions in global mean total ozone relative to the modeled value for the year 2000 of 314 DU (white contour) are primarily due to reductions in tropospheric ozone columns resulting from reductions in ozone precursor emissions in the model scenarios (Revell et al., 2015). **Figure 3-31b** shows the calculated ODP of N_2O in the year 2100 as a function of CO_2 and CH_4. The ODP of N_2O for 2100 will, under essentially all conditions, be larger than the calculated value of 0.015 for the year 2000 because of interactions of NO_x chemistry with chlorine chemistry. Under high chlorine loading, increasing NO_x reduces ozone depletion by deactivating reactive chlorine. Higher CO_2 levels induce cooling of the stratosphere, which increases the chemical destruction of NO_x and reduces the efficiency of ozone destruction by N_2O (Stolarski et al., 2015). Higher levels of CH_4 also slow NO_x-driven ozone loss, but they lead to an increased ODP of N_2O. This is because increased CH_4 reduces the efficiency of CFC-11 at destroying ozone, and CFC-11 is used as a reference gas in the ODP concept (Revell et al., 2017).

One study analyzing the effect of N_2O and CH_4 changes on ozone from a range of CCMI-1 models shows that the global-average impact of N_2O increases on total column ozone is highly model-dependent (Morgenstern et al., 2017). Another analysis of simulations from the WACCM model with different N_2O and CH_4 scenarios concludes that extratropical total ozone could either remain weakly depleted or even

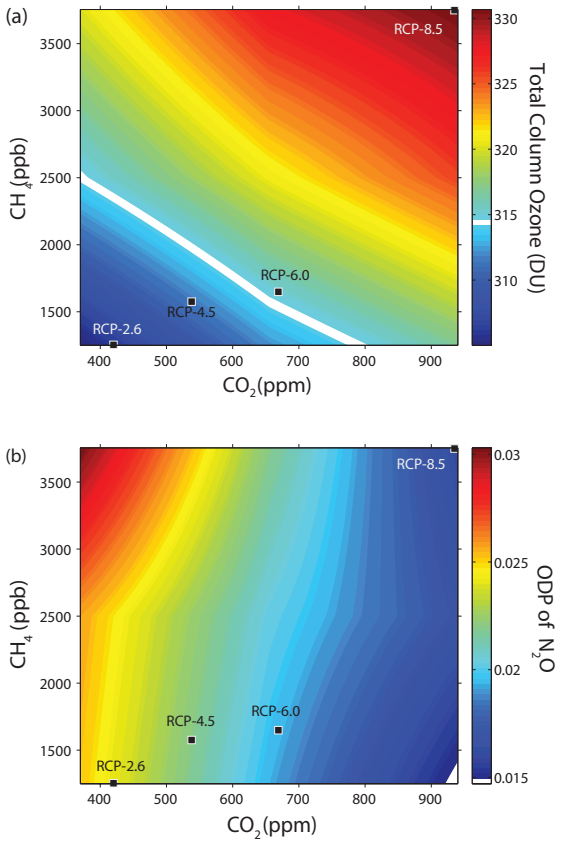

Figure 3-31. Effect of different abundances of CO_2 and CH_4 on (a) global mean total column ozone and on the (b) ODP of N_2O in 2100. Black squares indicate the CO_2 and CH_4 surface concentrations in 2100 for the various RCP scenarios. White contour lines show values of ozone (314 DU) and the ODP of N_2O (0.015) for year-2000 conditions. From Revell et al. (2015)

increase well above historical levels, depending on the CH_4 and N_2O scenario (Butler et al., 2016).

3.4.3.3 Sensitivity to Geoengineering/Solar Radiation Management

Deliberate increases in stratospheric aerosol loading to counter the effects of GHG-induced global warming have been discussed in recent years. This is often termed geoengineering or, more specifically, solar radiation management (SRM; see also **Chapter 6**). These schemes would impact stratospheric ozone in a number of ways: 1) through chemical effects of the increased aerosol loading, 2) through resulting changes in stratospheric temperature as well as changes in solar radiation and corresponding photolysis rates, both of which impact ozone chemistry, and 3) through resulting changes in stratospheric dynamics and transport. The most discussed and studied SRM schemes involve enhancement of stratospheric sulfate aerosols. **Chapter 6, Section 6.2.5** provides a detailed overview of the impact of deliberate climate interventions. A number of recent chemistry–climate modeling studies, including coordinated multi-model studies (GeoMIP, Kravitz et al., 2013), have been performed to study the impact of deliberate stratospheric sulfate aerosol enhancements on the ozone layer (e.g., Pitari et al., 2014). The effect on stratospheric ozone depends critically on the assumed stratospheric halogen loading; i.e., it will be different under a scenario where halogen loading is enhanced (e.g., for the middle of the 21st century) than under a scenario with little halogen loading (e.g., corresponding to the end of the 21st century). While much can be learned from the effects of enhanced sulfate aerosol loading following volcanic eruptions (see also **Chapter 5, Section 5.2.3**), the long-term effects of deliberate sulfate aerosol increases will be different from volcanic effects due to the different timescales involved (Pitari et al., 2014). In addition to their use in studying stratospheric chemistry perturbations taking place through the enhanced surface area density of the sulfuric acid aerosols, chemistry–climate models have been used to examine the impact on long-lived species transport due to the aerosol-driven surface cooling coupled to the stratospheric warming (Visioni et al., 2017). Perturbed concentrations of CH_4, N_2O, and other long-lived tracers would feed back on short-lived species that regulate stratospheric ozone depletion. Any significant reduction in stratospheric ozone associated with sulfate aerosol enhancement would further lead to decreases in tropospheric ozone through decreased stratosphere-to-troposphere transport (STT) of ozone and increased UV radiation (Xia et al., 2017).

More recent studies have explored strategic injections of sulfate aerosols into the stratosphere at locations other than the equator. One examination of a scenario in which injection at 15°N, 15°S and 30°N was steadily increased over the 21st century found that mean surface temperature and the equator-to-pole temperature gradients were kept near 2020 levels despite the strong climate forcing of the RCP-8.5 scenario (Richter et al., 2018). Polar column ozone

recovered to pre-ozone hole conditions by the end of the century but, in contrast to RCP-8.5, did not exceed pre-1980 levels. In the middle and high latitudes, ozone recovered and even exceeded RCP-8.5 values in some latitude bands and some months. Another study looked at differences between high- and low-altitude injections, assuming injection latitudes of 15°N and 15°S (Tilmes et al., 2018). Ozone destruction was less severe when sulfate aerosols were injected at 70 hPa rather than 30 hPa, and for middle and high latitudes, the low-altitude injections resulted in more column ozone than without geoengineering in winter.

A number of studies have also investigated the effect of solid particles for SRM schemes (e.g., Tang et al., 2014; Tang et al., 2016; Keith et al., 2016; Weisenstein et al., 2015). These highly refractive particles will lead to much less warming of the tropical lower stratosphere compared to sulfate aerosols (Keith et al., 2016). In particular salts of alkaline metals such as calcite ($CaCO_3$) have been proposed for SRM; these would have the side effect of chemically removing acids such as HCl or HNO_3 that are involved in ozone depletion. Model simulations have been used to investigate and compare the impact of proposed geoengineering schemes using sulfate, titania, and black carbon particles on the stratosphere (Jones et al., 2016). However, so far not enough information is available to assess how these proposed SRM schemes with solid aerosol particles will affect the evolution of stratospheric ozone under different GHG and ODS scenarios.

A recent chemistry–climate modeling study investigated the effect of solar radiation management schemes on stratospheric and surface ozone. It focused on the generic impact of SRM schemes; i.e., ozone changes due to the reduction in solar radiation, stratospheric temperature changes, and resulting changes in dynamics and transport (Nowack et al., 2016). In this study, the radiative forcing due to increased GHGs was balanced by a reduction in solar radiation at the top of the atmosphere without explicit treatment of stratospheric aerosol enhancements (an implementation colloquially termed space mirrors). This generic scheme thus shows some general aspects of SRM schemes without the particular chemical and radiative aspects that are specific to sulfate or other aerosol enhancements. The study shows that this generic SRM scheme would lead to strong enhancements in stratospheric ozone, with a calculated global total column increase of about 8% (Nowack et al., 2016). Because SRM schemes will not substantially reduce the upper-stratospheric cooling due to GHG increases, stratospheric ozone will strongly increase. In addition, reduced solar radiation under SRM would lead to further chemical ozone enhancement, according to this study. Increases in tropical upwelling (BDC) would be reduced with SRM, mediating the climate change-induced reduction in tropical lower-stratospheric ozone.

3.4.4 Impacts on Tropospheric Ozone

Both ozone recovery and the projected strengthening of the stratospheric circulation associated with GHG increases act to increase the downward transport of ozone from the stratosphere to the troposphere in the extratropics (e.g., Zeng and Pyle, 2003; Hegglin and Shepherd, 2009; Banerjee et al., 2016; see also **Chapter 5, Section 5.3.3**). The impact on tropospheric ozone is greatest in the upper troposphere (UT), where ozone's radiative effect is largest. Climate change has the largest impact in the subtropics, and ozone recovery primarily affects UT ozone in the extratropics (Banerjee et al., 2016). The net impacts of these processes, however, given concurrent changes in precursor emissions, temperature, and water vapor, are highly model- and scenario-dependent, as described below. **Figure 3-32** shows the sensitivity of ozone to ODSs and long-lived GHGs for seven CCMI-1 models (Morgenstern et al., 2018). There are sizable discrepancies among the models throughout the atmosphere, but these discrepancies are particularly large in the troposphere. A separate set of simulations showed a somewhat surprising sensitivity of tropospheric ozone to changes in N_2O; this sensitivity was dominated by chemical depletion of stratospheric ozone by N_2O (Morgenstern et al., 2018).

Using the UM-UKCA model under both RCP-4.5 and RCP-8.5 emissions scenarios in which the methane boundary condition was held constant, a recent study found that the projected increase in STT associated with climate change and ozone recovery offsets decreases in net chemical production associated with reductions in ozone precursor emissions (Banerjee et al., 2016), in agreement with earlier work (Sekiya and Sudo, 2014). Enhanced STT increases the global tropospheric lifetime of ozone (τ_{O3}) because it

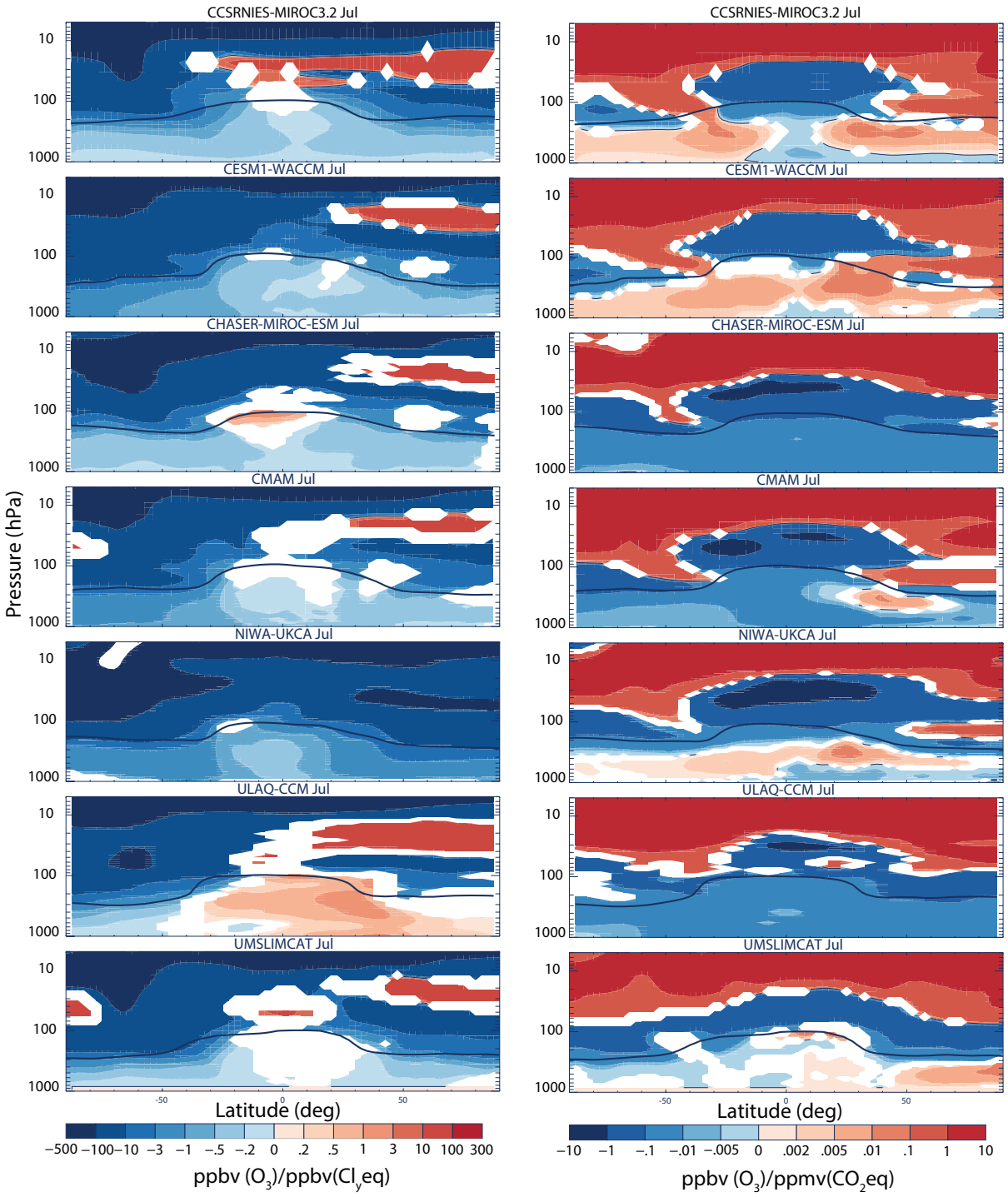

Figure 3-32. Ratio of zonal mean ozone volume mixing ratio (VMR) changes to VMR in (*left column*) equivalent Cl (Newman et al., 2007) and (*right column*) equivalent CO_2 (sum of CO_2, HFCs, PFCs, and SF_6) for seven CCMI-1 models for July. The solid black lines indicate 150 ppbv of ozone. Adapted from Morgenstern et al. (2018).

increases the ozone burden in the UT, where ozone is long lived. For climate change, this enhancement is offset by greater water vapor-induced loss of tropospheric ozone (reduction in lifetime of 0.4–6.7%, depending on scenario); for ozone recovery, the increase in τ_{O3} is enhanced by decreases in OH associated with decreased photolysis rates (increase of ~0.5%) (Bannerjee et al., 2016; Zhang et al., 2014). This decrease in OH may enhance the intercontinental transport of ozone and other pollutants, increasing ozone attributable to Asian emissions by up to 15%, or 0.3 ppbv, in the Northern Hemisphere (Zhang et al., 2014). It should be noted, however, that global models differ by nearly a factor of 2 in their predictions of OH changes associated with stratospheric ozone recovery (Madronich et al., 2015).

While ozone recovery and projected increases in the ozone flux associated with STT have a clear influence on τ_{O3}, the net change in lifetime depends strongly on changes in precursor emissions, temperature, and humidity and is highly scenario-dependent. Uncertainties in the future evolution of CH_4 dominate differences in tropospheric ozone among RCP scenarios (e.g., Revell et al., 2012, 2015; Young et al., 2013; Naik et al., 2013). Within any given scenario, changes in tropospheric ozone depend primarily on changes in ozone precursors. The SOCOL CCM, using RCP-6.0, simulates a 23% decrease in global mean tropospheric ozone between 1990 and 2060. This decrease is dominated by reductions in NO_x emissions. The increased STT associated with climate change contributes <1 ppb of additional ozone at 500 hPa between 1960 and 2090. This additional ozone, as well as that attributable to increased production of NO_x by lightning, was largely offset by increases in ozone chemical loss driven by higher temperatures in the model. Under a "solar mirror" geoengineering scenario in the HadGEM3 CCM, higher stratospheric ozone levels combined with lower atmospheric-specific humidity resulted in an overall increase in surface ozone of ~5% (Nowack et al., 2016), assuming no change in precursor emissions.

Observations cannot yet be used to evaluate projections of the tropospheric ozone response to strengthening of the stratospheric circulation and ozone recovery. However, satellite observations have been used to quantify the link between year-to-year variations in circulation strength and lower-stratospheric ozone abundances, with a 40% increase in circulation associated with a ~25% increase in NH mid-latitude lower-stratospheric ozone (Neu et al., 2014). These changes are similar to the long-term increases in circulation and ozone predicted by CCMs from 1960 to 2100 (Hegglin and Shepherd, 2009) and are associated with a ~2% increase in tropospheric ozone (Neu et al., 2014). Taken together with the modeling studies described above, this study suggests that future changes in tropospheric ozone are likely to be dominated by changes in precursor emissions, with the stratosphere playing a relatively minor role in increasing tropospheric ozone abundances and lifetime.

REFERENCES

Arosio, C., A. Rozanov, E. Malinina, K.-U. Eichmann, T. von Clarmann, and J.P. Burrows, Retrieval of ozone profiles from OMPS limb scattering observations, *Atmos. Meas. Tech.*, *11*, 2135–2149, doi:10.5194/amt-11-2135-2018, 2018.

Aschmann, J., J.P. Burrows, C. Gebhardt, A. Rozanov, R. Hommel, M. Weber, and A.M. Thompson, On the hiatus in the acceleration of tropical upwelling since the beginning of the 21st century, *Atmos. Chem. Phys.*, *14*, 12,803–12,814, doi:10.5194/acp-14-12803-2014, 2014.

Bai, K., N.-B. Chang, R. Shi, H. Yu, and W. Gao, An intercomparison of multidecadal observational and reanalysis datasets for global total ozone trends and variability analysis, *J. Geophys. Res. Atmos.*, *122*, 7119–7139, doi:10.1002/2016JD025835, 2017.

Baldwin, M.P., L.J. Gray, T.J. Dunkerton, K. Hamilton, P.H. Haynes, W.J. Randel, J.R. Holton, M.J. Alexander, I. Hirota, T. Hoinouchi, D.B.A. Jones, J.S. Kinnersely, C. Marquardt, K. Sato, and M. Takahasi, The Quasi-Biennial Oscillation, *Rev. Geophys.*, 39 (2), 179–229, doi:10.1029/1999RG000073, 2001.

Ball, W.T., J.D. Haigh, E.V. Rozanov, A. Kuchar, T. Sukhodolov, F. Tummon, A.V. Shapiro, and W. Schmutz, High solar cycle spectral variations inconsistent with stratospheric ozone observations, *Nat. Geosci., 9*, 206–209, doi:10.1038/ngeo2640, 2016.

Ball, W.T., J. Alsing, D.J. Mortlock, E.V. Rozanov, F. Tummon, and J.D. Haigh, Reconciling differences in stratospheric ozone composites, *Atmos. Chem. Phys.*, *17*, 12,269–12,302, doi:10.5194/acp-17-12269-2017, 2017.

Ball, W.T., J. Alsing, D.J Mortlock, J. Staehelin, J.D.Haigh, T. Peter, F. Tummon, R. Stübi, A. Stenke, J. Anderson, A. Bourassa, S.M. Davis, D. Degenstein, S. Frith, L. Froidevaux, C. Roth, V. Sofieva, R. Wang, J. Wild, P. Yu, J.R. Ziemke, and E.V. Rozanov, Evidence for a continuous decline in lower stratospheric ozone offsetting ozone layer recovery, *Atmos. Chem. Phys.*, *18*, 1379–1394, doi:10.5194/acp-18-1379-2018, 2018.

Banerjee, A., A.C. Maycock, A.T. Archibald, N.L. Abraham, P. Telford, P. Braesicke, and J.A. Pyle, Drivers of changes in stratospheric and tropospheric ozone between year 2000 and 2100, *Atmos. Chem. Phys.*, *16*, 2727–2746, 2016, doi:10.5194/acp-16-2727-2016

Bègue, N., D. Vignelles, G. Berthet, T. Portafaix, G. Payen, F. Jégou, H. Benchérif, J. Jumelet, J.P. Vernier, T. Lurton, J.-B. Renard, L. Clarisse, V. Duverger, F. Posny, J.-M. Metzger, and S. Godin-Beekmann, Long-range transport of stratospheric aerosols in the Southern Hemisphere following the 2015 Calbuco eruption, *Atmos. Chem. Phys.*, *17*, 15019–15036, doi:10.5194/acp-17-15019-2017, 2017.

Bhartia, P.K., R.D. McPeters, L.E. Flynn, S. Taylor, N.A. Kramarova, S. Frith, B. Fisher, and M. DeLand, Solar Backscatter UV (SBUV) total ozone and profile algorithm, *Atmos. Meas. Tech.*, *6*, 2533–2548, doi:10.5194/amt-6-2533-2013, 2013.

Bodeker, G.E., I.S. Boyd, and W.A. Matthews, Trends and variability in vertical ozone and temperature profiles measured by ozonesondes at Lauder, New Zealand: 1986 to 1996, *J. Geophys. Res.*, *103*, 28,661–28,681, doi:10.1029/98JD02581, 1998.

Bodeker, G.E., J.C. Scott, K. Kreher, and R.L. McKenzie, Global ozone trends in potential vorticity coordinates using TOMS and GOME intercompared against the Dobson network: 1978–1998, *J. Geophys. Res.*, *106*, 23,029–23,042, doi:10.1029/2001JD900220, 2001.

Bojkov, R.D., V.E. Fioletov, and A.M. Shalamjansky, Total ozone changes over Eurasia since 1973 based on re-evaluated filter ozonometer data, *J. Geophys. Res.*, *99* (D11), 22,985–22,999, doi:10.1029/94JD02006, 1994.

Boone, C.D., K. Walker, P.F. Bernath, Version 3 Retrievals for the Atmospheric Chemistry Experiment Fourier Transform Spectrometer (ACE-FTS), in The Atmospheric Chemistry Experiment ACE at 10: A Solar Occultation Anthology, edited by P.F. Bernath, 103–127, A. Deepak Publishing, Hampton, Virginia, 2013.

Bourassa, A.E., D.A. Degenstein, W.J. Randel, J.M. Zawodny, E. Kyrölä, C.A. McLinden, C.E. Sioris, and C.Z. Roth, Trends in stratospheric ozone derived from merged SAGE II and Odin-OSIRIS satellite observations, *Atmos. Chem. Phys.*, *14*, 6983–6994, doi:10.5194/acp-14-6983-2014, 2014.

Bourassa, A.E., C.Z. Roth, D.J. Zawada, L.A. Rieger, C.A. McLinden, and D.A. Degenstein, Drift-corrected Odin-OSIRIS ozone product: Algorithm

and updated stratospheric ozone trends, *Atmos. Meas. Tech.*, *11*, 489–498, doi:10.5194/amt-11-489-2018, 2018.

Boynard, A., D. Hurtmans, M.E. Koukouli, F. Goutail, J. Bureau, S. Safieddine, C. Lerot, J. Hadji-Lazaro, C. Wespes, J.-P. Pommereau, A. Pazmino, I. Zyrichidou, D. Balis, A. Barbe, S.N. Mikhailenko, D. Loyola, P. Valks, M. van Roozendael, P.-F. Coheur, and C. Clerbaux, Seven years of IASI ozone retrievals from FORLI: validation with independent total column and vertical profile measurements, *Atmos. Meas. Tech.*, *9*, 4327–4353, doi:10.5194/amt-9-4327-2016, 2016.

Butler, A.H., J.S. Daniel, R.W. Portmann, A.R. Ravishankara, P.J. Young, D.W. Fahey, and K.H. Rosenlof, Diverse policy implications for future ozone and surface UV in a changing climate, *Environ. Res. Lett.*, *11*, doi:10.1088/1748-9326/11/6/064017, 2016.

Calisesi, Y., D. Ruffieux, N. Kämpfer, and P. Viatte, The Stratospheric Ozone Monitoring Radiometer SOMORA: First validation results, in Proceedings of the Sixth European Symposium on Stratospheric Ozone, Göteborg, Sweden, 2002, *Air Pollution Research Report 79*, edited by N.R.P. Harris, G.T. Amanatidis and J.G. Levine, 92–95 pp., European Commission, 2003.

Chehade, W., M. Weber, and J.P. Burrows, Total ozone trends and variability during 1979–2012 from merged datasets of various satellites, *Atmos. Chem. Phys.*, *14*, 7059–7074, doi:10.5194/acp-14-7059-2014, 2014.

Cheung, H.H.N., W. Zhou, M.Y.T. Leung, C.M. Shun, S.M. Lee, and H.W. Tong, A strong phase reversal of the Arctic Oscillation in midwinter 2015/2016: Role of the stratospheric polar vortex and tropospheric blocking, *J. Geophys. Res. Atmos.*, *121*, 13,443–13,457, doi:10.1002/2016JD025288, 2016.

Chiodo, G., D.R. Marsh, R. Garcia-Herrera, N. Calvo, and J.A. García, On the detection of the solar signal in the tropical stratosphere, *Atmos. Chem. Phys.*, *14*, 5251–5269, doi:10.5194/acp-14-5251-2014, 2014.

Chipperfield, M.P., S. Dhomse, R. Hossaini, W. Feng, M.L. Santee, M. Weber, J.P. Burrows, J.D. Wild, D. Loyola, M. Coldewey-Egbers, On the cause of recent variations in lower stratospheric ozone, *Geophys. Res. Lett.*, *45*, doi:10.1029/2018GL078071, 2018.

Chiou, E.W., P.K. Bhartia, R.D. McPeters, D.G Loyola, M. Coldewey-Egbers, V.E. Fioletov, M. Van Roozendael, R. Spurr, C. Lerot, S.M. and Frith, Comparison of profile total ozone from SBUV (v8.6) with GOME-type and ground-based total ozone for a 16-year period (1996 to 2011), *Atmos. Meas. Tech.*, *7*, 1681–1692, doi:10.5194/amt-7-1681-2014, 2014.

Claude, H., U. Köhler, and W. Steinbrecht, New trend analyses of the homogenized ozone records at Hohenpeissenberg, in Proceedings of the XVIII Quadrennial Ozone Symposium 1996 in L'Aquila, Italy, edited by R.D. Bojkov and G. Visconti, 21–24 pp., International Ozone Commission, 1988.

Clerbaux, C., A. Boynard, L. Clarisse, M. George, J. Hadji-Lazaro, H. Herbin, D. Hurtmans, M. Pommier, A. Razavi, S. Turquety, C. Wespes, and P.-F. Coheur, Monitoring of atmospheric composition using the thermal infrared IASI/MetOp sounder, *Atmos. Chem. Phys.*, *9*, 6041 –6054, doi:10.5194/acp-9-6041-2009, 2009.

Coldewey-Egbers, M., M. Weber, L.N. Lamsal, R. de Beek, M. Buchwitz, and J.P. Burrows, Total ozone retrieval from GOME UV spectral data using the weighting function DOAS approach, *Atmos. Chem. Phys.*, *5*, 1015–1025, doi:10.5194/acp-5-1015-2005, 2005.

Coldewey-Egbers, M., Diego G., Loyola R., P. Braesicke, M. Dameris, M. van Roozendael, C. Lerot, and W. Zimmer, A new health check of the ozone layer at global and regional scales, *Geophys. Res. Lett.*, *41*, 4363–4372, doi:10.1002/2014GL060212, 2014.

Coldewey-Egbers, M., D. Loyola, M. Koukouli, D. Balis, J.-C. Lambert, T. Verhoelst, J. Granville, M. van Roozendael, C. Lerot, R. Spurr, S.M. Frith, and C. Zehner, The GOME-type Total Ozone Essential Climate Variable (GTO-ECV) data record from the ESA Climate Change Initiative, *Atmos. Meas. Tech.*, *8*, 3923–3940, doi:10.5194/amt-8-3923-2015, 2015.

Damadeo, R.P., J.M. Zawodny, L.W. Thomason, and N. Iyer, SAGE version 7.0 algorithm: Application to SAGE II, *Atmos. Meas. Tech.*, *6*, 3539–3561, doi:10.5194/amt-6-3539-2013, 2013.

Damadeo, R.P., J.M. Zawodny, and L.W. Thomason, Re-evaluation of stratospheric ozone trends from SAGE II data using a simultaneous temporal and spatial analysis, *Atmos. Chem. Phys.*, *14*, 13,455–13,470, doi:10.5194/acp-14-13455-2014, 2014.

Damadeo, R.P., J.M. Zawodny, E.E. Remsberg, and K.A. Walker, The impact of nonuniform sampling on stratospheric ozone trends derived from occultation instruments, *Atmos. Chem. Phys.*, *18*, 535–554, doi:10.5194/acp-18-535-2018, 2018.

Davis, S.M., K.H. Rosenlof, B. Hassler, D.F. Hurst, W.G. Read, H. Vömel, H. Selkirk, M. Fujiwara, and R. Damadeo, The Stratospheric Water and Ozone Satellite Homogenized (SWOOSH) database: A long-term database for climate studies, *Earth Syst. Sci. Data*, *8*, 461–490, doi:10.5194/essd-8-461-2016, 2016.

Davis, S.M., M.I. Hegglin, M. Fujiwara, R. Dragani, Y. Harada, C. Kobayashi, C. Long, G.L. Manney, E.R. Nash, G.L. Potter, S. Tegtmeier, T. Wang, K. Wargan, and J.S. Wright, Assessment of upper tropospheric and stratospheric water vapor and ozone in reanalyses as part of S-RIP, *Atmos. Chem. Phys.*, *17*, 12,743–12,778, doi:10.5194/acp-17-12743-2017, 2017.

Dee, D.P., S.M. Uppala, A.J. Simmons, P. Berrisford, P. Poli, S. Kobayashi, U. Andrae, M.A. Balmaseda, G. Balsamo, P. Bauer, P. Bechtold, A.C. Beljaars, L. van de Berg, J. Bidlot, N. Bormann, C. Delsol, R. Dragani, M. Fuentes, A.J. Geer, L. Haimberger, S.B. Healy, H. Hersbach, E.V. Hólm, L. Isaksen, P. Kållberg, M. Köhler, M. Matricardi, A.P. McNally, B.M. Monge-Sanz, J. Morcrette, B. Park, C. Peubey, P. de Rosnay, C. Tavolato, J. Thépaut, and F. Vitart, The ERA-Interim reanalysis: Configuration and performance of the data assimilation system. *Q. J .R. Meteorol. Soc.*, *137*, 553–597, doi:10.1002/qj.828, 2011.

de Laat, A.T.J., R.J. van der A, and M. van Weele, Tracing the second stage of ozone recovery in the Antarctic ozone-hole with a "big data" approach to multivariate regressions, *Atmos. Chem. Phys.*, *15*, 79–97, doi:10.5194/acp-15-79-2015, 2015.

Deshler, T., J. Mercer, H.G.J. Smit, R. Stuebi, G. Levrat, B.J. Johnson, S.J. Oltmans, R. Kivi, J. Davies, A.M. Thompson, J. Witte, F.J. Schmidlin, G. Brothers, and T. Sasaki, Atmospheric comparison of electrochemical cell ozonesondes from different manufacturers, and with different cathode solution strengths: The Balloon Experiment on Standards for Ozonesondes, *J. Geophys. Res.*, *113* (D4), D04307, doi:10.1029/2007JD008975, 2008.

Deshler, T., Observations for Chemistry (In Situ), in *Particles, Encyclopedia of Atmospheric Science, 2nd Edition*, *Vol. 1*, edited by G.R. North, J. Pyle, and F. Zhang, 379–386, Academic Press, Cambridge, Masseachusetts, 2015.

Deshler, T., R. Stübi, F.J. Schmidlin, J.L. Mercer, H.G.J. Smit, B.J. Johnson, R. Kivi, and B. Nardi, Methods to homogenize electrochemical concentration cell (ECC) ozonesonde measurements across changes in sensing solution concentration or ozonesonde manufacturer, *Atmos. Meas. Tech.*, *10*, 2021–2043, doi:10.5194/amt-10-2021-2017, 2017.

Dhomse, S., M. Weber, I. Wohltmann, M. Rex, and J.P. Burrows, On the possible causes of recent increases in northern hemispheric total ozone from a statistical analysis of satellite data from 1979 to 2003, *Atmos. Chem. Phys.*, *6*, 1165–1180, doi:10.5194/acp-6-1165-2006, 2006.

Dhomse, S.S., M.P. Chipperfield, R.P. Damadeo, J.M. Zawodny, W.T. Ball, W. Feng, R. Hossaini, G.W. Mann, and J.D. Haigh, On the ambiguous nature of the 11-year solar cycle signal in upper stratospheric ozone, *Geophys. Res. Lett.*, *43*, 7241–7249, doi:10.1002/2016GL069958, 2016.

Dhomse, S.S., D. Kinnison, M.P. Chipperfield, R.J. Salawitch, I. Cionni, M.L. Hegglin, N.L. Abraham, H. Akiyoshi, A.T. Archibald, E.M. Bednarz, S. Bekki, P. Braesicke, N. Butchart, M. Dameris, M. Deushi, S. Frith, S.C. Hardiman, B. Hassler, L.W. Horowitz, R.-M. Hu, P. Jöckel, B. Josse, O. Kirner, S. Kremser, U. Langematz, J. Lewis, M. Marchand, M. Lin, E. Mancini, V. Marécal, M. Michou, O. Morgenstern, F.M. O'Connor, L. Oman, G. Pitari, D.A. Plummer, J.A. Pyle, L.E. Revell, E. Rozanov, R. Schofield, A. Stenke, K. Stone, K. Sudo, S. Tilmes, D. Visioni, Y. Yamashita, and G. Zeng, Estimates of ozone return dates from Chemistry-Climate Model Initiative simulations, *Atmos. Chem. Phys.*, *18*, 8409–8438, doi:10.5194/acp-18-8409-2018, 2018.

Dragani, R., On the quality of the ERA-Interim ozone reanalyses: Comparisons with satellite data. *Q. J .R. Meteorol. Soc.*, *137*, 1312–1326, doi:10.1002/qj.821, 2011.

Dufour, G., M. Eremenko, A. Griesfeller, B. Barret, E. LeFlochmoën, C. Clerbaux, J. Hadji-Lazaro, P.-F. Coheur, and D. Hurtmans, Validation of three different scientific ozone products retrieved from IASI spectra using ozonesondes, *Atmos. Meas. Tech.*, *5*, 611–630, doi:10.5194/amt-5-611-2012, 2012.

Dunkerton, T.J., The quasi-biennial oscillation of 2015–2016: Hiccup or death spiral?, *Geophys. Res. Lett.*, *43*, 10,547–10,552, doi:10.1002/2016GL070921, 2016.

Dvortsov, V.L., M.A. Geller, S. Solomon, S.M. Schauffler, E.L. Atlas, and D.R. Blake, Rethinking reactive halogen budgets in the mid-latitude lower stratosphere, *Geophys. Res. Lett.*, *26*, 1699–1702, doi:10.1029/1999GL900309, 1999.

Eckert, E., T. von Clarmann, M. Kiefer, G.P. Stiller, S. Lossow, N. Glatthor, D.A. Degenstein, L. Froidevaux, S. Godin-Beekmann, T. Leblanc, S. McDermid, M. Pastel, W. Steinbrecht, D.P.J. Swart, K.A. Walker, and P.F. Bernath, Drift-corrected trends and periodic variations in MIPAS IMK/IAA ozone measurements, *Atmos. Chem. Phys.*, *14*, 2571–2589, doi:10.5194/acp-14-2571-2014, 2014.

Ermolli, I., K. Matthes, T. Dudok de Wit, N.A. Krivova, K. Tourpali, M. Weber, Y.C. Unruh, L. Gray, U. Langematz, P. Pilewskie, E. Rozanov, W. Schmutz, A. Shapiro, S.K. Solanki, and T.N. Woods, Recent variability of the solar spectral irradiance and its impact on climate modelling, *Atmos. Chem. Phys.*, *13*, 3945–3977, doi:10.5194/acp-13-3945-2013, 2013.

Fernandez, R., D.E. Kinnison, J.-F. Lamarque, S. Tilmes, and A. Saiz-Lopez, Impact of biogenic very short-lived bromine on the Antarctic ozone hole during the 21st century, *Atmos. Chem Phys.*, *17*, 1673–1688, doi:10.5194/acp-17-1673-2017, 2017.

Fioletov, V.E., G.E. Bodeker, A.J. Miller, R.D. McPeters, and R. Stolarski, Global and zonal total ozone variations estimated from ground-based and satellite measurements: 1964–2000, *J. Geophys. Res.*, *107*, doi:10.1029/2001JD001350, 2002.

Fioletov, V.E., and T.G. Shepherd, Seasonal persistence of midlatitude total ozone anomalies, *Geophys. Res. Lett.*, *30* (7), doi:10.1029/2002GL016739, 2003.

Fioletov, V.E., G. Labow, R. Evans, E.W. Hare, U. Köhler, C.T. McElroy, K. Miyagawa, A. Redondas, V. Savastiouk, A.M. Shalamyansky, J. Staehelin, K.Vanicek, M. Weber, Performance of the ground-based total ozone network assessed using satellite data, *J. Geophys. Res.*, *113*, D14313, doi:10.1029/2008JD009809, 2008.

Flury, T., D.L. Wu, and W.G. Read, Variability in the speed of the Brewer–Dobson circulation as observed by Aura/MLS, *Atmos. Chem. Phys.*, *13*, 4563–4575, doi:10.5194/acp-13-4563-2013, 2013.

Frith, S.M., N.A. Kramarova, R.S. Stolarski, R.D. McPeters, P.K. Bhartia, and G.J. Labow, Recent changes in column ozone-based on the SBUV version 8.6 merged ozone dataset, *J. Geophys. Res. Atmos.*, *119*, 9735–9751, doi:10.1002/2014JD021889, 2014.

Frith, S.M., R.S. Stolarski, N.A. Kramarova, and R.D. McPeters, Estimating uncertainties in the SBUV Version 8.6 merged profile ozone dataset, *Atmos. Chem. Phys.*, *17*, 14,695–14,707, doi:10.5194/acp-17-14695-2017, 2017.

Froidevaux, L., J. Anderson, H.-J. Wang, R.A. Fuller, M.J. Schwartz, M.L. Santee, N.J. Livesey, H.C. Pumphrey, P.F. Bernath, J.M. Russell III, and M.P. McCormick, Global OZone Chemistr And Related trace gas Data records for the Stratosphere (GOZCARDS): Methodology and sample results with a focus on HCl, H_2O, and O_3, *Atmos. Chem. Phys.*, *15*, 10,471–10,507, doi:10.5194/acp-15-10471-2015, 2015.

Frossard, L., H.E. Rieder, M. Ribatet, J. Staehelin, J.A. Maeder, S. Di Rocco, A.C. Davison, and T. Peter, On the relationship between total ozone and atmospheric dynamics and chemistry at mid-latitudes – Part 1: Statistical models and spatial fingerprints of atmospheric dynamics and chemistry, *Atmos. Chem. Phys.*, *13*, 147–164, doi:10.5194/acp-13-147-2013, 2013.

Fusco, A.C., and M.L. Salby, 1999: Interannual variations of total ozone and their relationship to variations of planetary wave activity, *J. Clim.*, *12*, 1619–1629. doi:10.1175/1520-0442(1999)012<1619:IVOTOA>2.0.CO;2, 1999.

Garane, K., C. Lerot, M. Coldewey-Egbers, T. Verhoelst, M.E. Koukouli, I. Zyrichidou, D.S. Balis, T. Danckaert, F. Goutail, J. Granville, D. Hubert, A. Keppens, J.-C. Lambert, D. Loyola, J.-P. Pommereau, M. Van Roozendael, and C. Zehner, Quality assessment of the Ozone_cci Climate Research Data Package (release 2017) – Part 1: Ground-based validation of total ozone column data products, *Atmos. Meas. Tech.*, *11*, 1385–1402, doi:10.5194/amt-11-1385-2018, 2018.

Gaudel A., O.R. Cooper, G. Ancellet, B. Barret, A. Boynard, J.P. Burrows, C. Clerbaux, P.-F. Coheur,

J. Cuesta, E. Cuevas, S. Doniki, G. Dufour, F. Ebojie, G. Foret, O. Garcia, M.J. Granados Muños, J.W. Hannigan, F. Hase, G. Huang, B. Hassler, D. Hurtmans, D. Jaffe, N. Jones, P. Kalabokas, B. Kerridge, S.S. Kulawik, B. Latter, T. Leblanc, E. Le Flochmoën, W. Lin, J. Liu, X. Liu, E. Mahieu, A. McClure-Begley, J.L. Neu, M. Osman, M. Palm, H. Petetin, I. Petropavlovskikh, R. Querel, N. Rahpoe, A. Rozanov, M.G. Schultz, J. Schwab, R. Siddans, D. Smale, M. Steinbacher, H. Tanimoto, D.W. Tarasick, V. Thouret, A.M. Thompson, T. Trickl, E. Weatherhead, C. Wespes, H.M. Worden, C. Vigouroux, X. Xu, G. Zeng, and J. Ziemke, Tropospheric Ozone Assessment Report: Present-day distribution and trends of tropospheric ozone relevant to climate and global atmospheric chemistry model evaluation, *Elem-Sci. Anthrop.*, *6* (1), doi:10.1525/elementa.291, 2018.

Gebhardt, C., A. Rozanov, R. Hommel, M. Weber, H. Bovensmann, J.P. Burrows, D. Degenstein, L. Froidevaux, and A.M. Thompson, Stratospheric ozone trends and variability as seen by SCIAMACHY from 2002 to 2012, *Atmos. Chem. Phys.*, *14*, 831–846, doi:10.5194/acp-14-831-2014, 2014.

Godin, S., G. Mégie, and J. Pelon, Systematic lidar measurements of the stratospheric ozone vertical distribution, *Geophys. Res. Lett.*, *16* (6), 547–550, doi:10.1029/GL016i006p00547, 1989.

Gray, L.J., J. Beer, M. Geller, J.D. Haigh, M. Lockwood, K. Matthes, U. Cubasch, D. Fleitmann, G. Harrison, L. Hood, J. Luterbacher, G.A. Meehl, D. Shindell, B. van Geel, W. White, Solar influences on climate, *Rev. Geophys.*, *48* (4), RG4001, doi:10.1029/2009RG000282, 2010.

Haigh, J.D., The role of stratospheric ozone in modulating the solar radiative forcing of climate, *Nature*, *370*, 544–546, doi:10.1038/370544a0, 1994.

Harris, N.R.P., E. Kyrö, J. Staehelin, D. Brunner, S.-B. Andersen, S. Godin-Beekmann, S. Dhomse, P. Hadjinicolaou, G. Hansen, I. Isaksen, A. Jrrar, A. Karpetchko, R. Kivi, B. Knudsen, P. Krizan, J. Lastovicka, J. Maeder, Y. Orsolini, J.A. Pyle, M. Rex, K. Vanicek, M. Weber, I. Wohltmann, P. Zanis, and C. Zerefos, Ozone trends at northern mid- and high latitudes – a European perspective, *Ann. Geophys.*, *26*, 1207–1220, doi:10.5194/angeo-26-1207-2008, 2008.

Harris, N.R.P., B. Hassler, F. Tummon, G.E. Bodeker, D. Hubert, I. Petropavlovskikh, W. Steinbrecht, J. Anderson, P.K. Bhartia, C.D. Boone, A. Bourassa, S.M. Davis, D. Degenstein, A. Delcloo, S.M. Frith, L. Froidevaux, S. Godin-Beekmann, N. Jones, M.J. Kurylo, E. Kyrölä, M. Laine, S.T. Leblanc, J.-C. Lambert, B. Liley, E. Mahieu, A. Maycock, M. de Mazière, A. Parrish, R. Querel, K.H. Rosenlof, C. Roth, C. Sioris, J. Staehelin, R.S. Stolarski, R. Stübi, J. Tamminen, C. Vigouroux, K.A. Walker, H.J. Wang, J. Wild, and J.M. Zawodny, Past changes in the vertical distribution of ozone – Part 3: Analysis and interpretation of trends, *Atmos. Chem. Phys.*, *15*, 9965–9982, doi:10.5194/acp-15-9965-2015, 2015.

Hase, F., T. Blumenstock, and C. Paton-Walsh, Analysis of the instrumental line shape of high-resolution Fourier transform IR spectrometers with gas cell measurements and new retrieval software, *Appl. Opt.*, *38*, 3417–3422, doi:10.1364/AO.38.003417, 1999.

Hassler, B., I. Petropavlovskikh, J. Staehelin, T. August, P.K. Bhartia, C. Clerbaux, D. Degenstein, M.D. Mazière, B.M. Dinelli, A. Dudhia, G. Dufour, S.M. Frith, L. Froidevaux, S. Godin-Beekmann, J. Granville, N.R.P. Harris, K. Hoppel, D. Hubert, Y. Kasai, M.J. Kurylo, E. Kyrölä, J.-C. Lambert, P.F. Levelt, C.T. McElroy, R.D. McPeters, R. Munro, H. Nakajima, A. Parrish, P. Raspollini, E.E. Remsberg, K.H. Rosenlof, A. Rozanov, T. Sano, Y. Sasano, M. Shiotani, H.G.J. Smit, G. Stiller, J. Tamminen, D.W. Tarasick, J. Urban, R.J. van der A, J.P. Veefkind, C. Vigouroux, T. von Clarmann, C. von Savigny, K.A.Walker, M.Weber, J. Wild, J.M., and Zawodny, Past changes in the vertical distribution of ozone – Part 1: Measurement techniques, uncertainties and availability, *Atmos. Meas. Tech.*, 7, 1395–1427, doi:10.5194/amt-7-1395-2014, 2014.

Hegglin, M. I., and T.G. Shepherd, Large climate-induced changes in ultraviolet index and stratosphere-to-troposphere ozone flux. *Nat. Geosci.*, *2* (10), 687–691, doi:10.1038/NGEO604, 2009.

Hendrick, F., J.-P. Pommereau, F. Goutail, R.D. Evans, D. Ionov, A. Pazmino, E. Kyrö, G. Held, P. Eriksen, V. Dorokhov, M. Gil, and M. Van Roozendael, NDACC/SAOZ UV-visible total ozone measurements: Improved retrieval and comparison with correlative ground-based and satellite observations, *Atmos. Chem. Phys.*, *11*, 5975–5995, doi:10.5194/acp-11-5975-2011, 2011.

Hood, L.L., and B.E. Soukharev, Quasi-decadal variability of the tropical lower stratosphere: The role of extratropical wave forcing, *J. Atmos. Sci.*, *60*, 2389–2403, doi:10.1175/1520-0469(2003)060<2389:QVOTTL>2.0.CO;2, 2003.

Hossaini, R., M.P. Chipperfield, S.A. Montzka, A. Rap, S. Dhomse, and W. Feng, Efficiency of short-lived halogens at influencing ozone through depletion of stratospheric ozone, *Nat. Geosci.*, *8*, 186–190, doi:10.1038/NGEO2363, 2015.

Hossaini, R., M.P. Chipperfield, S.M. Montzka, A.A. Leeson, S.S. Dhomse, J.A. Pyle, The increasing threat to stratospheric ozone from dichloromethane, *Nat. Commun.*, *8*, doi:10.1038/ncomms15962, 2017.

Hu, D., W. Tian, Z. Guan, Y. Guo, and S. Dhomse, Longitudinal asymmetric trends of tropical cold-point tropopause temperature and their link to strengthened walker circulation, *J. Clim., 29*, 7755–7771, doi:10.1175/JCLI-D-15-0851.1, 2016.

Hubert, D., J.-C. Lambert, T. Verhoelst, J. Granville, A. Keppens, J.-L. Baray, A.E. Bourassa, U. Cortesi, D.A. Degenstein, L. Froidevaux, S. Godin-Beekmann, K.W. Hoppel, B.J. Johnson, E. Kyrölä, T. Leblanc, G. Lichtenberg, M. Marchand, C.T. McElroy, D. Murtagh, H. Nakane, T. Portafaix, R. Querel, J.M. Russell III, J. Salvador, H.G.J. Smit, K. Stebel, W. Steinbrecht, K.B. Strawbridge, R. Stübi, D.P.J. Swart, G. Taha, D.W. Tarasick, A.M. Thompson, J. Urban, J.A.E. van Gijsel, R. Van Malderen, P. von der Gathen, K.A. Walker, E. Wolfram, J.M. and Zawodny, Ground-based assessment of the bias and long-term stability of 14 limb and occultation ozone profile data records, *Atmos. Meas. Tech.*, *9*, 2497–2534, doi:10.5194/amt-9-2497-2016, 2016.

IPCC (Intergovernmental Panel on Climate Change), *Emissions Scenerios. A Special Report of Working Group III of the International Panel on Climate Change,* edited by N. Nakicenovic, and R. Swart, 570 pp., Cambridge University Press, Cambridge, United Kingdom, 2000.

IPCC (Intergovenmental Panel on Climate Change), *Climate Change 2013: The Physical Science Basis. Contribution of Working Group I to the Fifth Assessment Report of the Intergovernmental Panel on Climate Change*, edited by T.F. Stocker, D. Qin, G.-K. Plattner, M. Tignor, S.K. Allen, J. Boschung, A. Nauels, Y. Xia, V. Bex, and P.M. Midgley, 1535 pp., Cambridge University Press, Cambridge, United Kingdom, 2013.

Jaross, G., P.K. Bhartia, G. Chen, M. Kowitt, M. Haken, Z. Chen, P. Xu, J. Warner, and T. Kelly, OMPS Limb profiler instrument performance assessment, *J. Geophys. Res. Atmos.*, *119*, 4399–4412, doi:10.1002/2013JD020482, 2014.

Jia, J., A. Rozanov, A. Ladstätter-Weißenmayer, and J.P. Burrows, Global validation of SCIAMACHY limb ozone data (versions 2.9 and 3.0, IUP Bremen) using ozonesonde measurements, *Atmos. Meas. Tech.*, *8*, 3369–3383, doi:10.5194/amt-8-3369-2015, 2015.

Jones, A.C., J.M. Haywood, and A. Jones, Climatic impacts of stratospheric geoengineering with sulfate, black carbon and titania injection, *Atmos. Chem. Phys.*, *16*, 2843–2862, doi:10.5194/acp-16-2843-2016, 2016.

Keeble, J., Brown, H., Abraham, N. L., Harris, N. R. P., and Pyle, J. A.: On ozone trend detection: using coupled chemistry–climate simulations to investigate early signs of total column ozone recovery, Atmos. Chem. Phys., 18, 7625-7637, doi: 10.5194/acp-18-7625-2018, 2018

Keith, D.W., D.K. Weisenstein, J.A. Dykema, and F.N. Keutsch, Stratospheric solar geoengineering without ozone loss, *Proc. Natl. Acad. Sci.*, *113*, 14,910–14,914, doi:10.1073/pnas.1615572113, 2016.

Khaykin S., S. Godin-Beekmann, P. Keckhut, A. Hauchecorne, J. Jumelet, J.-P. Vernier, A. Bourassa, D.A. Degenstein, L.A. Rieger, C. Bingen, F. Vanhellemont, C. Robert, M. DeLand, and P.K. Bhartia, Variability and evolution of the midlatitude stratospheric aerosol budget from 22 years of ground-based lidar and satellite observations, *Atmos. Chem. Phys.*, *17*, 1829–1845, doi:10.5194/acp-17-1829-2017, 2017.

Kiesewetter, G., B.-M. Sinnhuber, M. Weber, J.P. and Burrows, Attribution of stratospheric ozone trends to chemistry and transport: A modelling study, *Atmos. Chem. Phys.*, 10, 12,073–12,089, doi:10.5194/acp-10-12073-2010, 2010.

Klobas, J.E., D.M. Wilmouth, D.K. Weisenstein, J.G. Anderson, and R.J. Salawitch, Ozone depletion following future volcanic eruptions, *Geophys. Res. Lett.*, *44*, 7490–7499, doi:10.1002/2017GL073972, 2017.

Knibbe, J.S., R.J. van der A, and A.T.J. de Laat, Spatial regression analysis on 32 years total column

ozone data, *Atmos. Chem. Phys., 14*, 5323–5373, doi:10.5194/acpd- 14-5323-2014, 2014.

Komhyr, W.D., Electrochemical concentration cells for gas analysis, *Am Geoph. 25*, 203-210, 1969.

Koukouli, M.E., C. Lerot, J. Granville, F. Goutail, J.-C. Lambert, J.-P. Pommereau, D. Balis, I. Zyrichidou, M. Van Roozendael, M. Coldewey-Egbers, D. Loyola, G. Labow, S. Frith, R. Spurr, and C. Zehner, Evaluating a new homogeneous total ozone climate data record from GOME/ERS-2, SCIAMACHY/Envisat, and GOME-2/MetOp-A, *J. Geophys. Res. Atmos.*, *120*, 12,296–12,312, doi:10.1002/2015JD023699, 2015.

Kovilakam, M., and T. Deshler, On the accuracy of stratospheric aerosol extinction derived from in situ size distribution measurements and surface area density derived from remote SAGE II and HALOE extinction measurements, *J. Geophys. Res. Atmos.*, *120*, 8426–8447, doi:10.1002/2015JD023303, 2015.

Kramarova, N.A., S.M. Frith, P.K. Bhartia, R.D. McPeters, S.L. Taylor, B.L. Fisher, G.J. Labow, and M.T. DeLand, Validation of ozone monthly zonal mean profiles obtained from the version 8.6 Solar Backscatter Ultraviolet algorithm, *Atmos. Chem. Phys.*, *13*, 6887–6905, doi:10.5194/acp-13-6887-2013, 2013.

Kramarova, N.A., E.R. Nash, P.A. Newman, P.K. Bhartia, R.D. McPeters, D.F. Rault, C.J. Seftor, P.Q. Xu, and G.J. Labow, Measuring the Antarctic ozone hole with the new Ozone Mapping and Profiler Suite (OMPS), *Atmos. Chem. Phys.*, *14*, 2353–2361, doi:10.5194/acp-14-2353-2014, 2014.

Kramarova, N.A., P.K. Bhartia, G. Jaross, L. Moy, P. Xu, Z. Chen, M. DeLand, L. Froidevaux, N. Livesey, D. Degenstein, A. Bourassa, K.A. Walker, and P. Sheese, Validation of ozone profile retrievals derived from the OMPS LP version 2.5 algorithm against correlative satellite measurements, *Atmos. Meas. Tech.*, *11*, 2837–2861, doi:10.5194/amt-11-2837-2018, 2018.

Kravitz, B., A. Robock, P.M. Forster, J.M. Haywood, M.G. Lawrence, and H. Schmidt, An overview of the Geoengineering Model Intercomparison Project (GeoMIP), *J. Geophys. Res.*, *118*, 13,103–13,107, doi:10.1020/2013JD020569, 2013.

Kremser, S., L.W. Thomason, M. von Hobe, M. Hermann, T. Deshler, C. Timmreck, M. Toohey, A. Stenke, J.P. Schwarz, R. Weigel, S. Fueglistaler, F.J. Prata, J.-P. Vernier, H. Schlager, J.E. Barnes, J.-C. Antuña-Marrero, D. Fairlie, M. Palm, E. Mahieu, J. Notholt, M. Rex, C. Bingen, F. Vanhellemont, A. Bourassa, J.M.C. Plane, D. Klocke, S.A. Carn, L. Clarisse, T. Trickl, R. Neely, A.D. James, L. Rieger, J.C. Wilson, B. Meland, Stratospheric aerosol-observations, processes, and impact on climate, *Rev. Geophys.*, *54*, 278–335, doi:10.1002/2015RG000511, 2016.

Kuttippurath, J., G.E. Bodeker, H.K. Roscoe, and P.J. Nair, A cautionary note on the use of EESC-based regression analysis for ozone trend studies, *Geophys. Res. Lett.*, *42*, 162–168, doi:10.1002/2014GL062142, 2015.

Kyrölä, E., M. Laine, V. Sofieva, J. Tamminen, S.-M. Päivärinta, S. Tukiainen, J. Zawodny, and L. Thomason, Combined SAGE II–GOMOS ozone profile dataset for 1984–2011 and trend analysis of the vertical distribution of ozone, *Atmos. Chem. Phys.*, *13*, 10,645–10,658, doi:10.5194/acp-13-10645-2013, 2013.

Laine, M., N. Latva-Pukkila, and E. Kyrölä, Analysing time-varying trends in stratospheric ozone time series using the state space approach, *Atmos. Chem. Phys.*, *14*, 9707–9725, doi:10.5194/acp-14-9707-2014, 2014.

Lerot, C., M. Van Roozendael, R. Spurr, D. Loyola, M. Coldewey-Egbers. S. Kochenova, J. van Gent, M. Koukouli, D. Balis, J.-C. Lambert, J. Granville, C. Zehner, Homogenized total ozone data records from the European sensors GOME/ERS-2, SCIAMACHY/Envisat, and GOME-2/MetOp-A, *J. Geophys. Res. Atmos.*, *119* (3), 1639–1662, doi:10.1002/2013JD020831, 2014.

Livesey, N.J., W.G. Read, P.A. Wagner, L. Froidevaux, A. Lambert, G.L. Manney, L.F. Millán Valle, H.C. Pumphrey, M.L. Santee, M.J. Schwartz, S.Wang, R.A. Fuller, R.F. Jarnot, B.W. Knosp, E. Martinez, R.R. Lay, Earth Observing System (EOS) Aura Microwave Limb Sounder (MLS) Version 4.2x level 2 data quality and description document, JPL D-33509 Rev. D, available at https://mls.jpl.nasa.gov/data/v4-2_data_quality_document.pdf, 2018.

LOTUS (2018): *SPARC/IO3C/GAW report on Long-term Ozone Trends and Uncertainties in the Stratosphere,* edited by I. Petropavlovskikh, S. Godin-Beekmann, D. Hubert, R. Damadeo, B. Hassler, V. Sofieva, *SPARC Report No. 9, WCRP-*

17/2018, GAW Report No. 241, doi:10.17874/f899e57a20b, (accepted in May 2019), available at: http://www.sparc-climate.org/publications/sparc-reports.

Madronich, S., M. Shao, S.R. Wilson, K.R. Solomon, J.D. Longstreth, and X.Y. Tang, Changes in air quality and tropospheric composition due to depletion of stratospheric ozone and interactions with changing climate: implications for human and environmental health, *Photochem. Photobiol. Sci.*, *14*, 149–169, doi:10.1039/C4PP90037E, 2015.

Masui T., K. Matsumoto, Y. Hijioka, T. Kinoshita, T. Nozawa, S. Ishiwatari, E. Kato, P.R. Shukla, Y. Yamagata, M. Kainuma, An emission pathway for stabilization at 6 Wm−2 radiative forcing, *Clim. Change*, *109* (12), 59–76, doi:10.1007/s10584-011-0150-5, 2011.

Maycock, A.C., K. Matthes, S. Tegtmeier, R. Thiéblemont, and L. Hood, The representation of solar cycle signals in stratospheric ozone – Part 1: A comparison of recently updated satellite observations, *Atmos. Chem. Phys.*, *16*, 10,021–10,043, doi:10.5194/acp-16-10021-2016, 2016.

Matthes, K., B. Funke, M.E. Andersson, L. Barnard, J. Beer, P. Charbonneau, M.A. Clilverd, T. Dudok de Wit, M. Haberreiter, A. Hendry, C.H. Jackman, M. Kretzschmar, T. Kruschke, M. Kunze, U. Langematz, D.R. Marsh, A.C. Maycock, S. Misios, C.J. Rodger, A.A. Scaife, A. Seppälä, M. Shangguan, M. Sinnhuber, K. Tourpali, I. Usoskin, M. van de Kamp, P.T. Verronen, and S. Versick, Solar forcing for CMIP6 (v3.2), *Geosci. Model Dev.*, *10*, 2247–2302, doi:10.5194/gmd-10-2247-2017, 2017.

McClintock, W.E., G.J. Rottman, and T.N. Woods, Solar-Stellar Irradiance Comparison Experiment II (SOLSTICE II): Instrument concept and design, *Sol. Phys.*, *230*, 225–258, doi:10.1007/0-387-37625-9_12, 2005.

McDermid, I.S., S.M. Godin, and T.D. Walsh, Lidar measurements of stratospheric ozone and intercomparisons and validation, *Appl. Opt.*, *29* (33), 4914–4923, doi:10.1364/AO.29.004914, 1990.

McDermid, I.S., J.B. Bergwerff, G. Bodeker, I.S. Boyd, E.J. Brinksma, B.J. Connor, R. Farmer, M.R. Gross, P. Kimvilakani, W.A. Matthews, T.J. McGee, F.T. Ornel, A. Parrish, U. Singh, D.P.J. Swart, J.J. Tsou, P.H. Wang, and J. Zawodny, OPAL: Network for the detection of stratospheric change ozone profiler assessment at Lauder, New Zealand. Intercomparison of revised results, *J. Geophys. Res.*, *103*, 28,693–28,699, doi:10.1029/98JD02707, 1998.

McLinden, C.A., S. Tegtmeier, and V. Fioletov, Technical Note: A SAGE-corrected SBUV zonal-mean ozone dataset, *Atmos. Chem. Phys.*, *9*, 7963–7972, doi:10.5194/acp-9-7963-2009, 2009.

McPeters, R.D., D.J. Hofmann, M. Clark, L. Froidevaux, M. Gross, B. Johnson, G. Koenig, S. McDermid, F. Murcray, S. Oltmans, A. Parrish, U. Singh, J.J. Tsou, and J. Zawodny, Results from the 1995 stratospheric ozone profile intercomparison at Mauna Loa, *J. Geophys. Res.*, *104*, 30,505–30,514, doi:10.1029/1999JD900760, 1999.

Meinshausen, M., S.J. Smith, K. Calvin, J.S. Daniel, M.L.T. Kainuma, J.-F. Lamarque, K. Matsumoto, S.A. Montzka, S.C.B. Raper, K. Riahi, A. Thomson, G.J.M. Velders, D.P.P. van Vuuren, *Clim. Change*, *109*, doi:10.1007/s10584-011-0156-z, 2011.

Meul, S., M. Dameris, U. Langematz, J. Abalichin, A. Kerschbaumer, A. Kubin, and S. Oberländer-Hayn, Impact of rising greenhouse gas concentrations on future tropical ozone and UV exposure, *Geophys. Res. Lett.*, *43*, 2919–2927, doi:10.1002/2016GL067997, 2016.

Millán, L.F., N.J. Livesey, M.L. Santee, J.L. Neu, G.L. Manney, and R.A. Fuller, Case studies of the impact of orbital sampling on stratospheric trend detection and derivation of tropical vertical velocities: Solar occultation vs. limb emission sounding, *Atmos. Chem. Phys.*, *16*, 11,521–11,534, doi:10.5194/acp-16-11521-2016, 2016.

Minschwaner, K., H. Su, and J.H. Jiang, The upward branch of the Brewer-Dobson circulation quantified by tropical stratospheric water vapor and carbon monoxide measurements from the Aura Microwave Limb Sounder, *J. Geophys. Res. Atmos.*, *121*, 2790–2804, doi:10.1002/2015JD023961, 2016.

Moreira, L., K. Hocke, E. Eckert, T. von Clarmann, and N. Kämpfer, Trend analysis of the 20-year time series of stratospheric ozone profiles observed by the GROMOS microwave radiometer at Bern, *Atmos. Chem. Phys.*, *15*, 10,999-11,009, doi:10.5194/acp-15-10999-2015, 2015.

Morgenstern, O., H. Akiyoshi, S. Bekki, P. Braesicke, N. Butchart, M.P. Chipperfield, D. Cugnet, M. Deushi, S.S. Dhomse, R.R. Garcia, A. Gettel-

man, N.P. Gillett, S.C. Hardiman, J. Jumelet, D.E. Kinnison, J.-F. Lamarque, F. Lott, M. Marchand, M. Michou, T. Nakamura, D. Olivié, T. Peter, D. Plummer, J.A. Pyle, E. Rozanov, D. Saint-Martin, J.F. Scinocca, K. Shibata, M. Sigmond, D. Smale, H. Teyssèdre, W. Tian, A. Voldoire, Y. Yamashita, Anthropogenic forcing of the Northern Annular Mode in CCMVal-2 models, *J. Geophys. Res.*, *115* (D3), doi:10.1029/2009JD013347, 2010.

Morgenstern, O., M.I. Hegglin, E. Rozanov, F.M. O'Connor, N.L. Abraham, H. Akiyoshi, A.T. Archibald, S. Bekki, N. Butchart, M.P. Chipperfield, M. Deushi, S.S. Dhomse, R.R. Garcia, S.C. Hardiman, L.W. Horowitz, P. Jöckel, B. Josse, D. Kinnison, M. Lin, E. Mancini, M.E. Manyin, M. Marchand, V. Marécal, M. Michou, L.D. Oman, G. Pitari, D.A. Plummer, L.E. Revell, D. Saint-Martin, R. Schofield, A. Stenke, K. Stone, K. Sudo, T.Y. Tanaka, S. Tilmes, Y. Yamashita, K. Yoshida, and G. Zeng, Review of the global models used within phase 1 of the Chemistry–Climate Model Initiative (CCMI-1), *Geosci. Model Dev.*, *10*, 639–671, doi:10.5194/gmd-10-639-2017, 2017.

Morgenstern, O., K.A. Stone, R. Schofield, H. Akiyoshi, Y. Yamashita, D.E. Kinnison, R.R. Garcia, K. Sudo, D.A. Plummer, J. Scinocca, L.D. Oman, M.E. Manyin, G. Zeng, E. Rozanov, A. Stenke, L.E. Revell, G. Pitari, E. Mancini, G. Di Genova, D. Visioni, S.S. Dhomse, and M.P. Chipperfield, Ozone sensitivity to varying greenhouse gases and ozone-depleting substances in CCMI-1 simulations, *Atmos. Chem. Phys.*, *18*, 1091–1114, doi:10.5194/acp-18-1091-2018, 2018.

Muthers S., F. Arfeuille, C.C. Raible, and E. Rozanov, The impacts of volcanic aerosol on stratospheric ozone and the Northern Hemisphere polar vortex: Separating radiative-dynamical changes from direct effects due to enhanced aerosol heterogeneous chemistry, *Atmos. Chem. Phys.*, *15*, 11,461–11,476, doi:10.5194/acp-15-11461-2015, 2015.

Naik, V., A.Voulgarakis, A.M. Fiore, L.W. Horowitz, J.-F. Lamarque, M. Lin, M.J. Prather, P.J. Young, D. Bergmann, P.J. Cameron-Smith, I. Cionni, W.J. Collins, S.B. Dalsøren, R. Doherty, V. Eyring, G. Faluvegi, G.A. Folberth, B. Josse, Y.H. Lee, I.A. MacKenzie, T. Nagashima, T.P.C. van Noije, D.A. Plummer, M. Righi, S.T. Rumbold, R. Skeie, D.T. Shindell, D.S. Stevenson, S. Strode, K. Sudo, S. Szopa, and G. Zeng, Preindustrial to present-day changes in tropospheric hydroxyl radical and methane lifetime from the Atmospheric Chemistry and Climate Model Intercomparison Project (ACCMIP), *Atmos. Chem. Phys.*, *13*, 5277–5298, doi:10.5194/acp-13-5277-2013, 2013.

Nair, P. J., L. Froidevaux, J. Kuttippurath, J. M. Zawodny, J. M. Russell III, W. Steinbrecht, H. Claude, T. Leblanc, J.A.E. van Gijsel, B. Johnson, D.P.J. Swart, A. Thomas, R. Querel, R. Wang, and J. Anderson, Subtropical and midlatitude ozone trends in the stratosphere: Implications for recovery. *J. Geophys. Res. Atmos.*, *120*, 7247–7257, doi:10.1002/2014JD022371, 2015.

Naoe, H., M. Deushi, K. Yoshida, and K. Shibata, Future changes in the ozone quasi-biennial oscillation with increasing GHGs and ozone recovery in CCMI simulations, *J. Clim.*, *30*, 6977–6997, doi:10.1175/JCLI-D-16-0464.1, 2017.

Nédélec, P., R. Blot, D. Boulanger, G. Athier, J.-M. Cousin, B. Gautron, A. Petzold, A.Volz-Thomas, and V. Thouret, Instrumentation on commercial aircraft for monitoring the atmospheric composition on a global scale: The IAGOS system, technical overview of ozone and carbon monoxide measurements, *Tellus B: Chem. Phys. Meteorol.*, *67* (1), doi:10.3402/tellusb.v67.27791, 2015.

Nedoluha, G.E., I.S. Boyd, A. Parrish, R.M. Gomez, D.R. Allen, L. Froidevaux, B.J. Connor, and R.R Querel, Unusual stratospheric ozone anomalies observed in 22 years of measurements from Lauder, New Zealand, *Atmos. Chem. Phys.*, *15*, 6817–6826, doi:10.5194/acp-15-6817-2015, 2015, 2015a.

Nedoluha, G.E., D.E. Siskind, A. Lambert, and C. Boone, The decrease in mid-stratospheric tropical ozone since 1991, *Atmos. Chem. Phys.*, *15* (8), 4215–4224, doi:10.5194/acp-15-4215-2015, 2015b.

Neu, J.L., T. Flury, G.L. Manney, M.L. Santee, N.J. Livesey, and J. Worden, Tropospheric ozone variations governed by changes in stratospheric circulation, *Nat. Geosci.*, *7*, 340–344, doi:10.1038/ngeo2138, 2014.

Newman, P.A., E.R. Nash, and J.E. Rosenfield, What controls the temperature of the Arctic stratosphere during the spring?, *J. Geophys. Res.*, 106 (D17), 19,999–20,010, doi:10.1029/2000JD000061, 2001.

Newman, P.A., J.S. Daniel, D.W. Waugh, and E.R. Nash, A new formulation of equivalent effective

stratospheric chlorine (EESC), *Atmos. Chem. Phys.*, *7*, 4537–4552, doi:10.5194/acp-7-4537-2007, 2007.

Newman, P., L. Coy, S. Pawson, and L. Lait, The anomalous change in the QBO in 2015–2016, *Geophys. Res. Lett.*, *43*, 8791–8797, doi:10.1002/2016GL070373, 2016.

Nowack, P.J., N.L. Abraham, P. Braesicke, and J.A. Pyle., Stratospheric ozone changes under solar geoengineering: Implications for UV exposure and air quality, *Atmos. Chem. Phys.*, *16*, 4191–4203, doi:10.5194/acp-16-4191-2016, 2016.

Oberländer-Hayn, S., S. Meul, U. Langematz, J. Abalichin, and F. Haenel, A chemistry-climate model study of past changes in the Brewer-Dobson circulation, *J. Geophys. Res. Atmos.*, *120*, 6742–6757, doi:10.1002/2014JD022843, 2015.

Olsen, M.A., K. Wargan, and S. Pawson, Tropospheric column ozone response to ENSO in GEOS-5 assimilation of OMI and MLS ozone data, *Atmos. Chem. Phys.*, *16*, 7091–7103, doi:10.5194/acp-16-7091-2016, 2016.

Oman, L.D., A.R. Douglass, J.R. Ziemke, J.M. Rodriguez, D.W. Waugh, and J.E. Nielsen, The ozone response to ENSO in Aura satellite measurements and a chemistry-climate simulation, *J. Geophys. Res.*, *118*, 965–976, doi:10.1029/2012JD018546, 2013.

Oman, L.D., A.R. Douglass, R.J., Salawitch, T.P. Canty, J.R. Ziemke, and M. Manyin, The effect of representing bromine from VSLS on the simulation and evolution of Antarctic ozone, *Geophys. Res. Lett.*, *43*, 9869–9876, doi:10.1002/2016GL070471, 2016.

Oram, D.E., M.J Ashfold, J.C. Laube, L.J. Gooch, S. Humphrey, W.T. Sturges, E. Leedham-Elvidge, G.L. Forster, N.R.P. Harris, M.I. Mead, A.A. Samah, S.M. Phang, C.-F. Ou-Yang, N.-H. Lin, J.-L. Wang, A.K. Baker, C.A.M. Brenninkmeijer, and D. Sherry, A growing threat to the ozone layer from short-lived anthropogenic chlorocarbons, *Atmos. Chem. Phys.*, *17*, 11,929–11,941, doi:10.5194/acp-17-11929-2017, 2017.

Osprey, S.M., N. Butchart, J.R. Knight, A.A. Scaife, K. Hamilton, J.A. Anstey, V. Schenzinger, and C. Zhang, An unexpected disruption of the atmospheric quasi-biennial oscillation, *Science*, *353*, 1424–1427, doi:10.1126/science.aah4156, 2016.

Parrish, A., B.J. Connor, J.J. Tsou, I.S. Mcdermid, and W.P. Chu, Ground-based microwave monitoring of stratospheric ozone, *J. Geophys. Res.*, *97*, 2541–2546, doi:10.1029/91JD02914, 1992.

Petropavlovskikh, I., P.K. Bhartia, and J. DeLuisi, New Umkehr ozone profileretrieval algorithm optimized for climatological studies, *Geophys. Res. Lett.*, *32* (16), L16808, doi:10.1029/2005GL023323, 2005.

Petropavlovskikh, I., R. Evans, G. Mcconville, K. Miyagawa, S. Oltmans, Effect of the out-of-band stray light on the retrieval of the Umkehr Dobson ozone profiles, *Int. J. Remote Sens.*, *30* (24), 6461–6482, doi:10.1080/01431160902865806, 2009.

Petropavlovskikh, I., R. Evans, G. McConville, S. Oltmans, D. Quincy, K. Lantz, P. Disterhoft, M. Stanek, and L. Flynn, Sensitivity of Dobson and Brewer Umkehr ozone profile retrievals to ozone cross-sections and stray light effects, *Atmos. Meas. Tech.*, *4*, 1841–1853, doi:10.5194/amt-4-1841-2011, 2011.

Petropavlovskikh, I., R. Evans, G. McConville, G.L. Manney, and H.E. Rieder, The influence of the North Atlantic Oscillation and El Niño–Southern Oscillation on mean and extreme values of column ozone over the United States, *Atmos. Chem. Phys.*, *15*, 1585–1598, doi:10.5194/acp-15-1585-2015, 2015.

Pitari, G., V. Aquila, B. Kravitz, A. Robock, S. Watanabe, N.D. Luca, G.D. Genova, E. Mancini, S. Tilmes, and I. Cionni, Stratospheric ozone response to sulfate geoengineering: Results from the Geoengineering Model Intercomparison Project (GeoMIP), *J. Geophys. Res.*, *119*, 2629–2653, doi:10.1002/2013JD020566, 2014.

Polvani, L.M., L. Wang, V. Aquila, D.W. Waugh, The impact of ozone-depleting substances on tropical upwelling, as revealed by the absence of lower-stratospheric cooling since the late 1990s, *J. Clim.*, *30*, 2523–2534, doi:10.1175/JCLI-D-16-0532.1, 2017.

Rahpoe, N., M. Weber, A.V. Rozanov, K. Weigel, H. Bovensmann, J.P. Burrows, A. Laeng, G. Stiller, T. von Clarmann, E. Kyrölä, V.F. Sofieva, J. Tamminen, K. Walker, D. Degenstein, A.E. Bourassa, R. Hargreaves, P. Bernath, J. Urban, and D.P. Murtagh, Relative drifts and biases between six ozone limb satellite measurements from the last decade, *Atmos. Meas. Tech.*, *8*, 4369–4381,

doi:10.5194/amt-8-4369-2015, 2015.

Randel, W.J., and F. Wu, Isolation of the Ozone QBO in SAGE II Data by Singular-Value Decomposition, *J. Atmos. Sci.*, *53*, 2546–2559, doi:10.1175/1520-0469, 1996.

Randel, W.J., K.P. Shine, J. Austin, J. Barnett, C. Claud, N.P. Gillett, P. Keckhut, U. Langematz, R. Lin, C. Long, C. Mears, A. Miller, J. Nash, D.J. Seidel, D.W.J. Thompson, F. Wu, and S. Yoden, An update of observed stratospheric temperature trends, *J. Geophys. Res.*, *114* (D2), D010421, doi:10.1029/2008JD010421, 2009.

Randel, W.J., A.K. Smith, F. Wu, C. Zou, and H. Qian, Stratospheric Temperature Trends over 1979–2015 Derived from Combined SSU, MLS, and SABER Satellite Observations, *J. Climate*, *29*, 4843–4859, doi:10.1175/JCLI-D-15-0629.1, 2016.

Remsberg, E.E., Decadal-scale responses in middle and upper stratospheric ozone from SAGE II version 7 data, *Atmos. Chem. Phys.*, *14*, 1039–1053, doi:10.5194/acp-14-1039-2014, 2014.

Revell, L.E., G.E. Bodeker, P.E. Huck, B.E. Williamson, and E. Rozanov, The sensitivity of stratospheric ozone changes through the 21st century to N_2O and CH_4, *Atmos. Chem. Phys.*, *12*, 11,309–11,317, doi:10.5194/acp-12-11309-2012, 2012.

Revell, L.E., F. Tummon, R.J. Salawitch, A. Stenke, and T. Peter, The changing ozone depletion potential of N_2O in a future climate, *Geophys. Res. Lett.*, *42*, 10,047–10,055, doi:10.1002/2015GL065702, 2015.

Revell, L.E., A. Stenke, B. Luo, S. Kremser, E. Rozanov, T. Sukhodolov, and T. Peter, Impacts of Mt Pinatubo volcanic aerosol on the tropical stratosphere in chemistry–climate model simulations using CCMI and CMIP6 stratospheric aerosol data, *Atmos. Chem. Phys.*, *17*, 13,139–13,150, doi:10.5194/acp-17-13139-2017, 2017.

Richter, J.H., S. Tilmes, A. Glanville, B. Kravitz, D.G. MacMartin, M.J. Mills, I.R. Simpson, F. Vitt, J.J. Tribbia, J.-F. Lamarque, Stratospheric response in the first geoengineering simulation meeting multiple surface climate objectives, *J. Geophys. Res. Atmos.*, *123*, 5762–5782, doi:10.1029/2018JD028285, 2018.

Rieder, H.E., L. Frossard, M. Ribatet, J. Staehelin, J.A. Maeder, S. Di Rocco, A.C. Davison, T. Peter, P. Weihs, and F. Holawe, On the relationship between total ozone and atmospheric dynamics and chemistry at mid-latitudes – Part 2: The effects of the El Niño/Southern Oscillation, volcanic eruptions and contributions of atmospheric dynamics and chemistry to long-term total ozone changes, *Atmos. Chem. Phys.*, *13*, 165–179, doi:10.5194/acp-13-165-2013, 2013.

Salawitch, R.J., D.K. Weisenstein, L.J. Kovalenko, C.E. Sioris, P.O. Wennberg, K. Chance, M.K.W. Ko, and C.A. McLinden, Sensitivity of ozone to bromine in the lower stratosphere, *Geophys. Res. Lett.*, *32*, L05811, doi:10.1029/2004GL021504, 2005.

Scaife, A.A., R. Comer, N. Dunstone, D. Fereday, C. Folland, E. Good, M. Gordon, L. Hermanson, S. Ineson, A. Karpechko, J. Knight, C. MacLachlan, A. Maidens, K.A. Peterson, D. Smith, J. Slingo, and B. Walker, Predictability of European winter 2015/2016, *Atmos. Sci. Lett.*, *18*, 38–44, doi:10.1002/asl.721, 2017.

Sekiya, T., and K. Sudo, Roles of transport and chemistry processes in global ozone change on interannual and multidecadal time scales, *J. Geophys. Res. Atmos.*, *119*, 4903–4921, doi:10.1002/2013JD020838, 2014.

Sheese, P.E., C.D. Boone, and K.A. Walker, Detecting physically unrealistic outliers in ACE-FTS atmospheric measurements, *Atmos. Meas. Tech.*, *8*, 741–750, doi:10.5194/amt-8-741-2015, 2015.

Shepherd, T.G., D.A. Plummer, J.F. Scinocca, M.I. Hegglin, V.E. Fioletov, M.C. Reader, E. Remsberg, T. von Clarmann, and H. J. Wang, Reconciliation of halogen-induced ozone loss with the total-column ozone record, *Nat. Geosci.*, *7*, 443–449, doi:10.1038/ngeo2155, 2014.

Sinnhuber, B.-M., N. Sheode, M. Sinnhuber, M.P. Chipperfield, and W. Feng, The contribution of anthropogenic bromine emissions to past stratospheric ozone trends: A modelling study, *Atmos. Chem. Phys.*, *9*, 2863–2871, doi:10.5194/acp-9-2863-2009, 2009.

Sinnhuber, B.-M., and S. Meul, Simulating the impact of emissions of brominated very short-lived substances on past stratospheric ozone trends, *Geophys. Res. Lett.*, 42 (7), 2449–2456, doi:10.1002/2014GL062975, 2015.

Sioris, C.E., C.A. McLinden, V.E. Fioletov, C. Adams, J.M. Zawodny, A.E. Bourassa, C.Z. Roth, and D.A. Degenstein, Trend and variability in ozone in the tropical lower stratosphere over 2.5 solar cycles observed by SAGE II and OSIRIS, *Atmos. Chem.*

Phys., *14*, 3479–3496, doi:10.5194/acp-14-3479-2014, 2014.

Smit, H.G.J., W. Straeter, B. Johnson, S. Oltmans, J. Davies, D.W. Tarasick, B. Hoegger, R. Stubi, F. Schmidlin, T. Northam, A. Thompson, J. Witte, I. Boyd, F. Posny, Assessment of the performance of ECC-ozonesondes under quasi-flight conditions in the environmental simulation chamber: Insights from the Jülich Ozone Sonde Intercomparison Experiment (JOSIE), *J. Geophys. Res.*, *112*, D19306, doi:10.1029/2006JD007308, 2007.

Sofieva, V.F., E. Kyrölä, M. Laine, J. Tamminen, D. Degenstein, A. Bourassa, C. Roth, D. Zawada, M. Weber, A. Rozanov, N. Rahpoe, G. Stiller, A. Laeng, T. von Clarmann, K.A. Walker, P. Sheese, D. Hubert, M. van Roozendael, C. Zehner, R. Damadeo, J. Zawodny, N. Kramarova, and P.K. Bhartia, Merged SAGE II, Ozone_cci and OMPS ozone profile dataset and evaluation of ozone trends in the stratosphere, *Atmos. Chem. Phys.*, *17*, 12,533–12,552, doi:10.5194/acp-17-12533-2017, 2017.

Solomon, S., R.W. Portmann, R.R. Garcia, L.W. Thomason, L.R. Poole, and M.P. McCormick, The role of aerosol variations in anthropogenic ozone depletion at northern midlatitudes, *J. Geophys. Res.*, *101* (D3), 6713–6727, doi:10.1029/95JD03353, 1996.

Solomon, S., D. Kinnison, R. Garcia, J. Bandoro, M. Mills, C. Wilka, R. Neely III, A. Schmidt, J.E. Barnes, J.-P. Vernier, and M. Höpfner, Monsoon circulations and tropical heterogeneous chlorine chemistry in the stratosphere, *Geophys. Res. Lett.*, *43*, 12,624–12,633, doi:10.1002/2016GL071778, 2016a.

Solomon, S., D.J. Ivy, D. Kinnison, M.J. Mills, R.R. Neely III, and A.Schmidt, Emergence of healing in the Antarctic ozone layer, *Science*, *353*, 269–274, doi:10.1126/science.aae0061, 2016b.

Soukharev, B.E., and L.L. Hood, Solar cycle variation of stratospheric ozone: Multiple regression analysis of long-term satellite datasets and comparisons with models, *J. Geophys. Res.*, *111* (D20), D20314, doi:10.1029/2006JD007107, 2006.

SPARC (Stratospheric Processes And their Role in Climate), *SPARC Assessment of Stratospheric Aerosol Properties (ASAP)*, edited by L. Thomason and T. Peter, *SPARC Report No. 4*, WCRP-124, WMO/TD No. 1295, available at: www.sparc-climate.org/publications/sparc-reports/, 2006.

SPARC (Stratospheric Processes And their Role in Climate), *SPARC CCMVal Report on Evaluation Chemistry -Climate Models*, edited by V. Eyring, T. Shepherd, and D. Waugh, *SPARC Report No. 5*, WCRP-30/2010, WMO/TD-No. 40, available at: https://www.sparc-climate.org/publications/sparc-reports/, 2010.

SPARC (Stratopshere-troposphere Processes And their Role in Climate), *SPARC Report on the Lifetimes of Stratospheric Ozone-Depleting Substances, Their Replacements, and Related Species*, edited by M.K.W. Ko, P.A. Newman, S. Reimann, and S.E. Strahan, *SPARC Report No. 6*, WCRP-15/2013, available at: https://www.sparc-climate.org/publications/sparc-reports/sparc-report-no-6/, 2013.

Steinbrecht, W., L. Froidevaux, R. Fuller, R. Wang, J. Anderson, C. Roth, A. Bourassa, D. Degenstein, R. Damadeo, J. Zawodny, S. Frith, R. McPeters, P. Bhartia, J. Wild, C. Long, S. Davis, K. Rosenlof, V. Sofieva, K. Walker, N. Rahpoe, A. Rozanov, M. Weber, A. Laeng, T. von Clarmann, G. Stiller, N. Kramarova, S. Godin-Beekmann, T. Leblanc, R. Querel, D. Swart, I. Boyd, K. Hocke, N. Kämpfer, E. Maillard Barras, L. Moreira, G. Nedoluha, C. Vigouroux, T. Blumenstock, M. Schneider, O. García, N. Jones, E. Mahieu, D. Smale, M. Kotkamp, J. Robinson, I. Petropavlovskikh, N. Harris, B. Hassler, D. Hubert, and F. Tummon, An update on ozone profile trends for the period 2000 to 2016, *Atmos. Chem. Phys.*, *17*, 10,675–10,690, doi:10.5194/acp-17-10675-2017, 2017.

Sterling, C.W., B.J. Johnson, S.J. Oltmans, H.G.J. Smit, A.F. Jordan, P.D. Cullis, E.G. Hall, A.M. Thompson, and J.C. Witte, Homogenizing and estimating the uncertainty in NOAA's long- term vertical ozone profile records measured with the electrochemical concentration cell ozonesonde, *Atmos. Meas. Tech.*, *11*, 3661–3687, doi:10.5194/amt-11-3661-2018, 2018.

Stiller, G.P., F. Fierli, F. Ploeger, C. Cagnazzo, B. Funke, F.J. Haenel, T. Reddmann, M. Riese, and T. von Clarmann, Shift of subtropical transport barriers explains observed hemispheric asymmetry of decadal trends of age of air, *Atmos. Chem. Phys.*, *17*, 11,177–11,192, doi:10.5194/acp-17-11177-2017, 2017.

Stolarski, R.S., and S.M. Frith, Search for evidence of trend slow-down in the long-term TOMS/SBUV

total ozone data record: The importance of instrument drift uncertainty, *Atmos. Chem. Phys.*, *6*, 4057–4065, doi:10.5194/acp-6-4057-2006, 2006.

Stolarski R.S., A.R. Douglass, L.D. Oman, and D.W. Waugh, Impact of future nitrous oxide and carbon dioxide emissions on the stratospheric ozone layer, *Environ. Res. Lett.*, *10*, doi:10.1088/1748-9326/10/3/034011, 2015.

Stone, K.A., S. Solomon, and D.E. Kinnison, On the Identification of Ozone Recovery, *Geophys. Res. Lett.*, 45 (10), 5158–5165, doi:10.1029/2018GL077955, 2018.

Strahan, S.E., A.R. Douglass, and S.D. Steenrod, Chemical and dynamical impacts of stratospheric sudden warmings on Arctic ozone variability, *J. Geophys. Res. Atmos.*, *121*, 11,836–11,851, doi:10.1002/2016JD025128, 2016.

Studer, S., K. Hocke, M. Pastel, S. Godin-Beekmann, and N. Kämpfer, Intercomparison of stratospheric ozone profiles for the assessment of the upgraded GROMOS radiometer at Bern, *Atmos. Meas. Tech.*, *6*, 6097–6146, doi:10.5194/amtd-6-6097-2013, 2013.

Tang, M.J., P.J. Telford, F.D. Pope, L. Rkiouak, N.L. Abraham, A.T. Archibald, P. Braesicke, J.A. Pyle, J. McGregor, I.M. Watson, R.A. Cox, and M. Kalberer, Heterogeneous reaction of N_2O_5 with airborne TiO_2 particles and its implication for stratospheric particle injection, *Atmos. Chem. Phys.*, *14*, 6035–6048, doi:10.5194/acp-14-6035-2014, 2014.

Tang, M., J. Keeble, P.J. Telford, F.D. Pope, P. Braesicke, P.T. Griffiths, N.L. Abraham, J. McGregor, I.M. Watson, R.A. Cox, J.A. Pyle, and M. Kalberer, Heterogeneous reaction of $ClONO_2$ with TiO_2 and SiO_2 aerosol particles: Implications for stratospheric particle injection for climate engineering, *Atmos. Chem. Phys.*, *16*, 15,397–15,412, doi:10.5194/acp-16-15397-2016, 2016.

Tarasick, D.W., J. Davies, H.G.J. Smit, S.J. Oltmans, A re-evaluated Canadian ozonesonde record: Measurements of the vertical distribution of ozone over Canada from 1966 to 2013, *Atmos. Meas. Tech.*, *9*, 195–214, doi:10.5194/amt-9-195-2016, 2016.

Tegtmeier, S., M.I. Hegglin, J. Anderson, A. Bourassa, S. Brohede, D. Degenstein, L. Froidevaux, R. Fuller, B. Funke, J. Gille, A. Jones, Y. Kasai, K. Krüger, E. Kyrölä, G. Lingenfelser, J. Lumpe, B. Nardi, J. Neu, D. Pendlebury, E. Remsberg, A. Rozanov, L. Smith, M. Toohey, J. Urban, T. von Clarmann, K.A. Walker, R.H.J. Wang, SPARC Data Initiative: A comparison of ozone climatologies from international satellite limb sounders, *J. Geophys. Res. Atmos.*, *118*, 12,229–12,247, doi:10.1002/2013JD019877, 2013.

Thomason, L.W., S.P. Burton, B.-P. Luo, and T. Peter, SAGE II measurements of stratospheric aerosol properties at non-volcanic levels, *Atmos. Chem. Phys.*, *8*, 983–995, doi:10.5194/acp-8-983-2008, 2008.

Thomason, L.W., N. Ernest, L. Millán, L. Rieger, A. Bourassa, J.-P. Vernier, G. Manney, B. Luo, F. Arfeuille, and T. Peter, A global space-based stratospheric aerosol climatology: 1979–2016, *Earth Syst. Sci. Data*, *10*, 469–492, doi:10.5194/essd-10-469-2018, 2018.

Thompson, A.M., J.C. Witte, C. Sterling, A. Jordan, B.J. Johnson, S.J. Oltmans, M. Fujiwara, H. Vömel, M. Allaart, A. Piters, G.J.R. Coetzee, F. Posny, E. Corrales, J.A. Diaz, C.F.N. Komala, N. Lai, H.T.A. Nguyen, M. Maata, F. Mani, Z. Zainal, S-Y. Ogino, F. Paredes, T.L.B. Penha, F. Raimundo da Silva, S. Sallons-Mitro, H.B. Selkirk, F.J. Schmidlin, R. Stübi, K. Thiongo, First reprocessing of Southern Hemisphere Additional Ozonesondes (SHADOZ) ozone profiles (1998–2016): 2. Comparisons with satellites and ground-based instruments, *J. Geophys. Res. Atmos.*, *122*, 13,000–13,025, doi:10.1002/2017JD027406, 2017.

Thouret, V., A. Marenco, J.A. Logan, P. Nédélec, and C. Grouhel, Comparisons of ozone measurements from the MOZAIC airborne program and the ozone sounding network at eight locations, *J. Geophys. Res.*, *103* (D19), 25,695–25,720, doi:10.1029/98JD02243, 1998.

Tilmes, S., J.H. Richter, M.J. Mills, B. Kravitz, D.G. Macmartin, R.R. Garcia, D.E. Kinnison, J.-F. Lamarque, J. Tribbia, F. Vitt, Effects of different stratospheric SO_2 injection altitudes on stratospheric chemistry and dynamics, *J. of Geophys. Res. Atmos.*, *123*, 4654–4673, doi:10.1002/2017JD028146, 2018.

Tummon, F., B. Hassler, N.R.P. Harris, J. Staehelin, W. Steinbrecht, J. Anderson, G.E. Bodeker, A. Bourassa, S.M. Davis, D. Degenstein, S.M. Frith, L. Froidevaux, E. Kyrölä, M. Laine, C. Long, A.A. Penckwitt, C.E. Sioris, K.H. Rosenlof, C. Roth,

H.-J. Wang, and J. Wild, Intercomparison of vertically resolved merged satellite ozone datasets: Interannual variability and long-term trends, *Atmos. Chem. Phys.*, *15*, 3021–3043, doi:10.5194/acp-15-3021-2015, 2015.

Tweedy, O.V., N.A. Kramarova, S.E. Strahan, P.A. Newman, L. Coy, W.J. Randel, M. Park, D.W. Waugh, and S.M. Frith, Response of trace gases to the disrupted 2015–2016 quasi-biennial oscillation, *Atmos. Chem. Phys.*, *17*, 6813–6823, doi:10.5194/acp-17-6813-2017, 2017.

van der A, R.J., M.A.F. Allaart, and H.J. Eskes, Multi sensor reanalysis of total ozone, *Atmos. Chem. Phys.*, *10* (22), 11,277–11,294, doi:10.5194/acp-10-11277-2010, 2010.

van der A, R.J., M.A.F. Allaart, and H.J. Eskes, Extended and refined multi sensor reanalysis of total ozone for the period 1970–2012, *Atmos. Meas. Tech.*, *8*, 3021–3035, doi:10.5194/amt-8-3021-2015, 2015.

Van Malderen, R., M.A.F. Allaart, H. De Backer, H.G.J. Smit, D. De Muer, On instrumental errors and related correction strategies of ozonesondes: Possible effect on calculated ozone trends for the nearby sites Uccle and De Bilt, *Atmos. Meas. Tech.*, *9*, 3793–3816, doi:10.5194/amt-9-3793-2016, 2016.

Vernier, J.-P., L.W. Thomason, J.-P. Pommereau, A. Bourassa, J. Pelon, A. Garnier, A. Hauchecorne, L. Blanot, C. Trepte, D. Degenstein, F. Vargas, Major influence of tropical volcanic eruptions on the stratospheric aerosol layer during the last decade, *Geophys. Res. Lett.*, *38* (12), L12807, doi:10.1029/2011GL047563, 2011.

Vernier, J.-P., T.D. Fairlie, M. Natarajan, F.G. Wienhold, J. Bian, B.G. Martinsson, S. Crumeyrolle, L.W. Thomason, and K.M. Bedka, Increase in upper tropospheric and lower stratospheric aerosol levels and its potential connection with Asian pollution, *J. of Geophys. Res. Atmos.*, *120* (4), 1608–1619, doi.org/10.1002/2014JD022372, 2015.

Vigouroux, C., T. Blumenstock, M. Coffey, Q. Errera, O. García, N.B. Jones, J.W. Hannigan, F. Hase, B. Liley, E. Mahieu, J. Mellqvist, J. Notholt, M. Palm, G. Persson, M. Schneider, C. Servais, D. Smale, L. Thölix, and M. De Mazière, Trends of ozone total columns and vertical distribution from FTIR observations at eight NDACC stations around the globe, *Atmos. Chem. Phys.*, *15*, 2915–2933, doi:10.5194/acp-15-2915-2015, 2015.

Visioni, D., G. Pitari, and V. Aquila, Sulfate geoengineering: A review of the factors controlling the needed injection of sulfur dioxide, *Atmos. Chem. Phys.*, *17*, 3879–3889, doi:10.5194/acp-17-3879-2017, 2017.

Wallace, J.M., R.L. Panetta, and J. Estberg, Representation of the equatorial stratospheric quasi-biennial oscillation in EOF phase space, *J. Atmos. Sci.*, *50*, 1751–1762, doi: 10.1175/1520-0469(1993)050<1751:ROTESQ>2.0.CO;2, 1993.

Wargan, K., G. Labow, S. Frith, S. Pawson, N. Livesey, and G. Partyka, Evaluation of the Ozone Fields in NASA's MERRA-2 Reanalysis, *J. Clim.*, *30*, 2961–2988, doi:10.1175/JCLI-D-16-0699.1, 2017.

Wargan, K., C. Orbe, S. Pawson, J.R. Ziemke, L.D. Oman, M.A. Olsen, L. Coy, K.E. Knowland, Recent decline in extratropical lower stratospheric ozone attributed to circulation changes. *Geophys. Res. Lett.*, *45*, 5166–5176, doi:10.1029/2018GL077406, 2018.

Weatherhead, E.C., J. Harder, E.A. Araujo-Pradere, G. Bodeker, J.M. English, L.E. Flynn, S.M. Frith, J.K. Lazo, P. Pilewskie, M. Weber, and T.N. Woods, How long do satellites need to overlap? Evaluation of climate data stability from overlapping satellite records, *Atmos. Chem. Phys.*, *17*, 15,069–15,093, doi:10.5194/acp-17-15069-2017, 2017.

Weber, M., L.N. Lamsal, M. Coldewey-Egbers, K. Bramstedt, and J.P. Burrows, Pole-to-pole validation of GOME WFDOAS total ozone with ground-based data, *Atmos. Chem. Phys.*, *5*, 1341–1355, doi:10.5194/acp-5-1341-2005, 2005.

Weber, M., S. Dikty, J.P. Burrows, H. Garny, M. Dameris, A. Kubin, J. Abalichin, and U. Langematz, The Brewer-Dobson circulation and total ozone from seasonal to decadal time scales, *Atmos. Chem. Phys.*, *11*, 11,221–11,235, doi:10.5194/acp-11-11221-2011, 2011.

Weber, M., W. Steinbrecht, C. Roth, M. Coldewey-Egbers, D. Degenstein, Y.E. Fioletov, S.M. Frith, L. Froidevaux, J. de Laat, C.S. Long, D. Loyola, and J.D. Wild, [Global Climate] Stratospheric ozone [in "State of the Climate in 2015"], *Bull. Am. Meteorol. Soc.*, *97* (8), S49–S51, doi:10.1175/2016BAMSStateoftheClimate.1, 2016.

Weber, M., W. Steinbrecht, S.M. Frith, O. Tweedy, M.

Coldewey-Egbers, S. Davis, D. Degenstein, V.E. Fioletov, L. Froidevaux, J. de Laat, C.S. Long, D. Loyola, C. Roth, and J.D. Wild, [Global Climate] Stratospheric ozone [in "State of the Climate in 2016"], *Bull. Amer. Meteorol. Soc.*, 98, S49–S51, doi:10.1175/2017BAMSStateoftheClimate.1, 2017.

Weber, M., M. Coldewey-Egbers, V.E. Fioletov, S.M. Frith, J.D. Wild, J.P. Burrows, C.S. Long, and D. Loyola, Total ozone trends from 1979 to 2016 derived from five merged observational datasets – the emergence into ozone recovery, *Atmos. Chem. Phys.*, *18*, 2097–2117, doi:10.5194/acp-18-2097-2018, 2018.

Weisenstein, D.K., D.W. Keith, and J.A. Dykema, Solar geoengineering using solid aerosol in the stratosphere, *Atmos. Chem. Phys.*, *15*, 11,835–11,859, doi:10.5194/acp-15-11835-2015, 2015.

Weiss, A.K., J. Staehelin, C. Appenzeller, and N.R.P. Harris, Chemical and dynamical contributions to ozone profile trends of the Payerne (Switzerland) balloon soundings, *J. Geophys. Res.*, *106* (D19), 22,685–22,694, doi:10.1029/2000JD000106, 2001.

Wespes, C., D. Hurtmans, L.K. Emmons, S. Safieddine, C. Clerbaux, D.P. Edwards, and P.-F. Coheur, Ozone variability in the troposphere and the stratosphere from the first 6 years of IASI observations (2008–2013), *Atmos. Chem. Phys.*, *16*, 5721–5743, doi:10.5194/acp-16-5721–2016, 2016.

Wespes, C., D. Hurtmans, C. Clerbaux, A. Boynard, and P.-F. Coheur, Decrease in tropospheric O_3 levels in the Northern Hemisphere observed by IASI, *Atmos. Chem. Phys.*, *18*, 6867–6885, doi:10.5194/acp-18-6867-2018, 2018.

Wild, J.D., S.-K. Yang, and C.S. Long, Ozone Profile Trends: An SBUV/2 Perspective, in Proceedings of the Quadrennial Ozone Symposium, International Ozone Commission, Edinburgh, Scottland, QOS2016-133, 2016.

Witte, J.C., A.M. Thompson, H.G.J. Smit, M. Fujiwara, F. Posny, G.J.R. Coetzee, E.T. Northam, B.J. Johnson, C.W. Sterling, M. Mohamad, S.-Y. Ogino, A. Jordan, F.R. da Silva, First reprocessing of Southern Hemisphere ADditional OZonesondes (SHADOZ) profile records (1998–2015): 1. Methodology and evaluation, *J. Geophys. Res. Atmos.*, *122*, 6611–6636, doi:10.1002/2016JD026403, 2017.

WMO (World Meteorological Organization), *Scientific Assessment of Ozone Depletion: 2006*, Global Ozone Research and Monitoring Project - Report No. 50, 572 pp., Geneva, Switzerland, 2007.

WMO (World Meteorological Organization), *Scientific Assessment of Ozone Depletion: 2010*, Global Ozone Research and Monitoring Project-Report No. 52, 516 pp., Geneva, Switzerland, 2011.

WMO (World Meteorological Organization), *Scientific Assessment of Ozone Depletion: 2014*, World Meteorological Organization, Global Ozone Research and Monitoring Project-Report No. 55, 416 pp., Geneva, Switzerland, 2014.

Wolter, K., MultiMultivariate ENSO Index (MEI), available at: www.esrl.noaa.gov/psd/enso/mei/table.html (last access: 10 May 2013), 2013.

Xia, L., P.J. Nowack, S. Tilmes, and A. Robock, Impacts of stratospheric sulfate geoengineering on tropospheric ozone, *Atmos. Chem. Phys.*, *17*, 11,913–11,928, doi:10.5194/acp-17-11913-2017, 2017.

Young, P.J., A.T. Archibald, K.W. Bowman, J.-F. Lamarque, V. Naik, D.S. Stevenson, S. Tilmes, A. Voulgarakis, O. Wild, D. Bergmann, P. Cameron-Smith, I. Cionni, W.J. Collins, S.B. Dalsøren, R.M. Doherty, V. Eyring, G. Faluvegi, L.W. Horowitz, B. Josse, Y.H. Lee, I.A. MacKenzie, T. Nagashima, D.A. Plummer, M. Righi, S.T. Rumbold, R.B. Skeie, D.T. Shindell, S.A. Strode, K. Sudo, S. Szopa, and G. Zeng, Pre-industrial to end 21st century projections of tropospheric ozone from the Atmospheric Chemistry and Climate Model Intercomparison Project (ACCMIP), *Atmos. Chem. Phys.*, *13*, 2063–2090, doi:10.5194/acp-13-2063-2013, 2013.

Zawada, D.J., L.A. Rieger, A.E. Bourassa, and D.A. Degenstein, Tomographic retrievals of ozone with the OMPS Limb Profiler: Algorithm description and preliminary results, *Atmos. Meas. Tech.*, *11*, 2375–2393, doi:10.5194/amt-11-2375-2018, 2018.

Zeng, G., and J.A. Pyle, Changes in tropospheric ozone between 2000 and 2100 modeled in a chemistry-climate model, *Geophys. Res. Lett.*, *30* (7), doi:10.1029/2002GL016708, 2003.

Zhang, L., D.J. Jacob, X. Yue, N.V. Downey, D.A. Wood, and D. Blewitt, Sources contributing to background surface ozone in the US Intermountain West, *Atmos. Chem. Phys.*, *14*, 5295–5309,

doi:10.5194/acp-14-5295-2014, 2014.

Ziemke, J.R., S. Chandra, B.N. Duncan, L. Froidevaux, P.K. Bhartia, P.F. Levelt, and J.W. Waters, Tropospheric ozone determined from Aura OMI and MLS: Evaluation of measurements and comparison with the Global Modeling Initiative's Chemical Transport Model, *J. Geophys. Res.*, *111* (D19), D19303, doi:10.1029/2006JD007089, 2006.

Appendix 3A

Data Sources

3A.1 Ground-based Measurements

Ground-based instruments at numerous stations around the globe monitor changes in total column and profile ozone amounts at local to regional scales (WMO, 2014; Hassler et al., 2014). These instruments include:

- **remote-sensing instruments** such as Dobson and Brewer spectrophotometers (Fioletov et al., 2002, 2008; Petropavlovskikh et al., 2005, 2009, 2011), SAOZ spectrometers (Hendrick et al., 2011), filter ozonometers (Bojkov et al., 1994), FTIR spectrometers (Hase et al., 1999; Vigouroux et al., 2015), lidars (Claude et al., 1988; Godin et al., 1989; McDermid et al., 1990), and microwave radiometers (MWR; Parrish et al., 1992; McDermid et al., 1998a,b; McPeters et al., 1999; Calisesi et al, 2003; Studer et al., 2013; Nedoluha et al., 2015); and
- **in situ instruments** such as balloon-borne ozonesondes (Komhyr, 1969; Smit et al., 2007; Deshler et al., 2008, 2017) and aircraft-mounted sensors (Thouret et al., 1998; Nédélec et al., 2015).

Since the last Assessment, most ground-based data records were merely extended in time. However, several station records were revised to address inhomogeneities in time (changes in measurement process at the site) or in space (differences in measurement process between sites in the network). Such revisions were done for 2 MWR stations and for about 30 ozonesonde sites. The Bern microwave instrument was upgraded and the entire time series was referenced to the current spectrometer (Moreira et al., 2015). The Payerne microwave data changed as a result of improvements in the retrieval method and in the integration of the measurements (private communications with PI Maillard-Barras). Both revised MWR records were used for this Assessment. Over the past few years, the ozonesonde community has put considerable effort into reducing uncertainties in the measurements to 5–10%. Biases between different types of ozonesonde instrumentation have been characterized, correction schemes developed, and the ozone profile records of 30 stations in the NDACC, GAW, and SHADOZ networks reprocessed accordingly (Tarasick et al., 2016; Van Malderen et al., 2016; Deshler et al., 2017; Witte et al., 2017; Sterling et al., 2018). Further efforts to assess the outcome of this homogenization activity are ongoing. At the time of this Assessment, not all reprocessed sonde data were available.

The profile trends assessed here are based on observations at the sites listed in **Table 3A-1**, most of which have operated continuously for at least 20 years. Zonally averaged, ground-based data records, one for each measurement technique, were computed from deseasonalized anomaly time series at each site in a given latitude band (Fioletov et al., 2002, 2008; WMO, 2014; Steinbrecht et al., 2017; LOTUS, 2018). Such an approach reduces the impact of station-dependent instrument biases, temporal coverage, and sampling.

The **WOUDC** ground-based total column dataset is based on available Dobson, Brewer, SAOZ, and filter ozonometer data that have been averaged monthly and zonally (using a TOMS v7 climatology to translate deviations in ozone at a single point into zonal mean deviations) and then binned in 5-degree intervals (Fioletov et al., 2002). Time series based on these relatively sparse ground-based measurements may not always reproduce monthly zonal fluctuations well, particularly in the tropics and Southern Hemisphere. However, seasonal (and longer) averages can be estimated with a precision comparable with satellite-based datasets (~1%) (Chiou et al., 2014).

3A.2 Space-Based Ozone Profiles

Space-based observations of stratospheric ozone are performed in nadir-, limb-, or occultation-viewing geometry in different wavelength ranges using different measurement techniques (Chiou et al., 2014; Hassler et al., 2014;

Table 3A-1. Overview of the sources of ozone profile observations by ground-based techniques used for the monthly zonal mean data considered in this Assessment. Stations are sorted by instrument type and chronologically by the starting year of the record. Those with an asterisk are located outside the attributed latitude zones.

Instruments and Data Archives	Stations (Start of Data Record)		
	35°–60°S	20°S–20°N	35°–60°N
Ozonesonde (0– 30 km) http://www.ndsc.ncep.noaa.gov/data, http://www.woudc.org/data/explore.php?lang=en, https://tropo.gsfc.nasa.gov/shadoz/Archive.html	Lauder (1986), Macquarie Island (1994), Broadmeadows (1999)	Hilo (1982), Ascension Island (1998), Kuala Lumpur (1998), Nairobi (1998), Natal (1998), Pago Pago (1998), Suva (1998), Hong Kong Observatory* (2000)	Goose Bay (1963), Uccle (1965), Hohenpeißenberg (1966), Payerne (1968), Edmonton (1970), Wallops Island (1970), Lindenberg (1975), Legionowo (1979), Praha (1979), Boulder (1991), De Bilt (1992), Valentia (1994), Huntsville* (1999)
Lidar (15–50 km) http://www.ndsc.ncep.noaa.gov/data	Lauder (1994)	Mauna Loa (1993)	OHP (1986), Hohenpeißenberg (1987), Table Mountain (1988)
Microwave (MWR) (20–70 km) http://www.ndsc.ncep.noaa.gov/data	Lauder (1992)	Mauna Loa (1995)	Bern (1994), Payerne (2000)
FTIR (0–50 km) http://www.ndsc.ncep.noaa.gov/data	Wollongong (1996), Lauder (2001)	Izaña* (1999)	Jungfraujoch (1995)
Dobson/Brewer Umkehr (0–50 km) ftp://aftp.cmdl.noaa.gov/data/ozwv/DobsonUmkehr/Stray%20light%20corrected/monthlymean	Perth (1984), Lauder (1987)	Mauna Loa (1984)	Arosa (1956), Boulder (1984), OHP (1984), Fairbanks (1994)

Table 3A-2. Merged satellite vertical ozone profile datasets used in this Assessment (monthly zonal mean data).

Merged Data Set	Instruments and Data Version	Ozone Representation	Latitude Coverage and Sampling	Altitude Coverage and Sampling	Temporal Coverage
SBUV-NASA MOD v8.6 (release 6)	Nimbus 4 BUV v8.6 Nimbus 7 SBUV v8.6 NOAA 11 SBUV/2 v 8.6 NOAA 14 SBUV/2 v8.6 NOAA 16 SBUV/2 v8.6 NOAA 17 SBUV/2 v8.6 NOAA 18 SBUV/2 v8.6 NOAA 19 SBUV/2 v8.6	Partial columns over pressure layers	80°N–80°S 5 deg	50–0.5 hPa, 9 layers (~6–15 km thick)	1970–2016
SBUV-NOAA COH v8.6	Nimbus 4 BUV v8.6 Nimbus 7 SBUV v8.6 NOAA 11 SBUV/2 v 8.6 NOAA 14 SBUV/2 v8.6 NOAA 16 SBUV/2 v8.6 NOAA 17 SBUV/2 v8.6 NOAA 18 SBUV/2 v8.6 NOAA 19 SBUV/2 v8.6	Partial columns over pressure layers	80°N–80°S 5 deg	50–0.5 hPa, 13 layers (~6–15 km thick)	1978–2016
GOZCARDS v2.20	SAGE I v5.9_rev, SAGE II v7.0, HALOE v19, Aura MLS v4.2	Mixing ratio at pressure levels	90°S–90°N, 10 deg	215–0.2 hPa	1979–2016
SWOOSH v2.60	SAGE II v7.0, HALOE v19, UARS MLS v5, SAGE III v4, Aura MLS v4.2	Mixing ratio at pressure levels	90°S–90°N, 10 deg (also 5 and 2.5 deg)	316–1 hPa, ~3 km	1984–2016
SAGE II-OSIRIS- OMPS	SAGE II v7.0, OSIRIS v5.10, OMPS USask-2D v1.0.2	Number density (anomaly) at altitude levels	60°S–60°N, 10 deg	0–50 km, 1 km	1984–2016
SAGE II-CCI-OMPS	SAGE II v7.0, OSIRIS v5.10, GOMOS ALGOM2s v1, MIPAS IMK/IAA v7, SCIAMACHY UBr v3.5, ACE-FTS v3.5/3.6, OMPS USask-2D v1.0.2	Number density (anomaly) at altitude levels	90°S–90°N, 10 deg	10–50 km, 1 km	1984–2016
SAGE II-MIPAS- OMPS	SAGE II v7.0, MIPAS IMK/IAA v7, OMPS NASA v2.0	Deseasonalized ozone anomalies at altitude levels	60°S–60°N, 10 deg	10–50 km, 1 km	1984–2017

Table 3A-3. Merged total ozone column datasets used in this Assessment (annual zonal mean data).

Merged dataset	Instruments	Record length	Reference	URL
WOUDC	Dobson, Brewer, SAOZ, Filter ozonometer	1964–2016	Fioletov et al. (2002, 2008)	http://woudc.org/archive/Projects-Campaigns/ZonalMeans
SBUV NASA MOD v8.6 (release 6)	Nimbus 4 BUV Nimbus 7 SBUV NOAA 11 SBUV/2 NOAA 14 SBUV/2 NOAA 16 SBUV/2 NOAA 17 SBUV/2 NOAA 18 SBUV/2 NOAA 19 SBUV/2	1970–2016	Frith et al. (2014)	http://acdb-ext.gsfc.nasa.gov/Data_services/merged
SBUV NOAA COH v8.6	Nimbus 4 BUV Nimbus 7 SBUV NOAA 11 SBUV/2 NOAA 14 SBUV/2 NOAA 16 SBUV/2 NOAA 17 SBUV/2 NOAA 18 SBUV/2 NOAA 19 SBUV/2	1978–2016	Wild et al. (2016)	ftp://ftp.cpc.ncep.noaa.gov/SBUV_CDR
GTO	GOME, SCIAMACHY, GOME-2A, OMI	1995–2016	Coldewey-Egbers et al. (2015)	http://www.esa-ozone-cci.org/?q=node/163
GSG	GOME, SCIAMACHY, GOME-2A	1995–2016	Weber et al. (2011, 2016)	http://www.iup.uni-bremen.de/gome/wfdoas

Weber et al., 2017; Garane et al., 2018). Revised datasets have been released for most instruments in recent years: (nadir) GOME, SCIAMACHY, GOME-2, OMI (Wever et al., 2017; Garane et al., 2018); (limb) OSIRIS v5.10 (Bourassa et al., 2018), SCIAMACHY IUP v3.5 (Jia et al., 2015), Aura MLS v4.2 (Livesey et al., 2018); (occultation) SAGE II v7.0 (Damadeo et al., 2013, 2014), GOMOS ALGOM2s v1 (Sofieva et al., 2017), and ACE-FTS v3.6 (Boone et al., 2013; Sheese et al.; 2015). Revisions include modification of calibration and altitude-registration data as well as updates to radiative transfer models, retrieval and screening algorithms, and meteorological datasets used to convert retrieved ozone values to different units. The largest improvements in stability of the data record were achieved for OSIRIS (altitude registration), MIPAS (calibration data), SCIAMACHY (retrieval algorithm), and SAGE II (meteorological data).

The records of two additional instruments have now reached sufficient length and maturity to be used in trend assessments: The Ozone Mapping and Profiler Suite (OMPS), onboard the Suomi-NPP platform launched in 2011, provides total column data (nadir) in addition to profile data in nadir and limb geometry (Jaross et al., 2014; Kramarova et al., 2014, 2018; Arosio et al., 2018; Zawada et al., 2018). The Infrared Atmospheric Sounding Interferometer (IASI), on the MetOp-A platform launched in 2006, provides nadir ozone profiles (Clerbaux et al., 2009; Dufour et al., 2012; Boynard et al., 2016; Wespes et al., 2016, 2018).

Merged, space- and time-gridded profile records can be categorized in a number of ways, depending on the type of instruments used (nadir versus limb), the profile representation (altitude/pressure, partial columns/volume mixing ratio/number density), the adjustment procedure (single versus multiple references) and the averaging

method (absolute versus anomaly-based, weighted versus unweighted). The following families of merged profile records are used in **Chapter 3** (see **Table 3A-2**):

SBUV MOD and SBUV COH. These records are based on the series of SBUV/2 v8.6 data. Since the last Assessment, NOAA-19 data were added, but only minor changes were made to the merging algorithms of the Merged Ozone Data (MOD) release 6 (Frith et al., 2017) and Cohesive data record (COH; Wild et al., 2016). The approach used for the MOD dataset is to average data from different records during overlap periods; the approach used for COH is to adjust and chain contiguous records sequentially. SBUV COH also incorporates some corrections to individual satellite profiles and excludes measurements from some SBUV instruments (e.g., the NOAA-9 ascending node data).

GOZCARDS and SWOOSH. A second family of merged datasets is built around SAGE II and Aura MLS: GOZCARDS v2.20 and SWOOSH v2.6 (Froidevaux et al., 2015; Davis et al., 2016). Both records use SAGE II as an absolute reference, but differences are expected from their use of different instruments, adjustment procedures, and averaging methods. For GOZCARDS, each record is weighted equally in the average after adjusting derived monthly zonal mean data during the overlap period. For SWOOSH, space–time collocated profile pairs are used for the adjustments, and weighting is done according to the number of observations. Current versions of GOZCARDS and SWOOSH differ considerably from those used in the previous Assessment; these differences are largely a result of revisions in the input data records and/or a different selection of instruments.

SOO, SCO, and SMO. The last family comprises records constructed from SAGE II and two (or more) other instruments: SAGE-OSIRIS-OMPS (SOO), SAGE-CCI-OMPS (SCO), SAGE-MIPAS-OMPS (SMO) (Bourassa et al., 2014, 2018; Sofieva et al., 2017). All of these were constructed by 1) adjusting deseasonalized anomalies of individual records to those of SAGE II and then 2) either computing an unweighted (SOO) or weighted (SMO) average or the median (SCO). The latter exploits the larger ensemble of up to five instruments in the 2002–2012 period. The MIPAS-based record requires using ACE-FTS as a transfer standard between MIPAS and OMPS, which leads to larger uncertainties in the adjustments. This 3-member family can be considered new to the WMO Assessment. Besides the addition of OMPS data, the previously used SAGE-GOMOS and SAGE-OSIRIS records were based on older and less stable versions of GOMOS and OSIRIS data.

3A.3 Space-Based Total Ozone Columns

Zonal and global total ozone time series are regularly updated and reported; e.g., in the annual State of the Climate reports published in the Bulletin of the American Meteorological Society (BAMS) (Weber et al., 2016, 2017). They are based on ground-based measurements, as well as merged data from multiple satellite instruments. The following total ozone datasets are used in this report (**Table 3A-3**; see Weber et al., 2018 for details).

SBUV MOD and **SBUV COH**. Both datasets are based on integrated vertical ozone profiles from the SBUV MOD and SBUV COH datasets described in **Section 3A.2** (Bhartia et al., 2013).

GTO. The GOME-type Total Ozone Essential Climate Variable (GTO-ECV) data record (Coldewey-Egbers et al., 2015) is based on GOME, SCIAMACHY, OMI, and GOME-2A measurements. The total ozone columns were retrieved using the GOME-type Direct FITting (GODFIT) version 3 algorithm (Lerot et al., 2014). Adjustments to OMI measurements were used to merge data from different instruments into one record in order to correct for small remaining inter-sensor biases and temporal drifts. The record was validated using ground-based measurements (Coldewey-Egbers et al., 2015; Koukouli et al., 2015; Garane et al., 2018).

GSG. The merged GOME-SCIAMACHY-GOME-2A (GSG) total ozone time series (Kiesewetter et al., 2010; Weber et al., 2011, 2016) consists of total ozone data that were retrieved using the University of Bremen Weighting Function DOAS algorithm (Coldewey-Egbers et al., 2005; Weber et al., 2005). The SCIAMACHY and GOME-2A observations were successively adjusted for apparent offsets to be continuous with the original

GOME data. These offsets were determined as a function of latitude in steps of 1 degree using monthly zonal means and then smoothed over 10-degree latitude bands (Weber et al., 2018).

Thus, similar to the SBUV MOD and COH datasets, GTO and GSG are not independent and are in fact based on almost the same measurements by GOME, SCIAMACHY, and GOME-2A, although GTO also uses OMI data. The main difference is in the processing algorithms and/or how the data from different satellites were merged together.

Chapter 4

Polar Stratospheric Ozone: Past, Present, and Future

Lead Authors
U. Langematz
M. Tully

Coauthors
N. Calvo
M. Dameris
A.T.J. de Laat
A. Klekociuk
R. Müller
P. Young

Contributors
S. Alexander
S. Dhomse
B. Funke
J.-U. Grooß
S. Kremser
G.L. Manney
S. Molleker
E. Nash
M.C. Pitts
A. Saiz-Lopez
F. Schmidt
M. Sinnhuber
R. Spang
I. Tritscher
P. von der Gathen
M. Weber

Review Editors
W. Randel
S. Solomon

Cover photo: An ozonesonde launch on a small balloon from Davis Station in Antarctica. Ozonesondes provide high-resolution measurements of the vertical profile of ozone concentrations in the atmosphere. Long-term monitoring, conducted at a small number of stations in the Arctic and Antarctic as part of the WMO Global Atmosphere Watch Programme, provides essential data for understanding the processes that affect polar ozone and ozone changes over time. Photo: Courtesy of V. Heinrich, Bureau of Meteorology, Australia

Chapter 4

Polar Stratospheric Ozone: Past, Present, and Future

CONTENTS

Chapter 4

Update on Polar Ozone: Past, Present, and Future

SCIENTIFIC SUMMARY

The chemical and dynamical processes controlling polar ozone are well understood. Polar ozone depletion is fundamentally driven by anthropogenic chlorine and bromine, with the severity of the chemical loss each year in both hemispheres strongly modulated by meteorological conditions (temperatures and winds), and, to a lesser extent, by the stratospheric aerosol loading and the solar cycle. As noted in prior Assessments, the stratospheric halogen concentration resulting from the emission of ozone-depleting substances (ODSs) reached its peak in the polar regions around the turn of the century and has been gradually declining since then in response to actions taken under the Montreal Protocol and its Amendments and adjustments. Early signs of ozone recovery are now beginning to appear in the Antarctic; as the observational record lengthens, clearer ozone hole recovery trends are expected to emerge against the background of natural variability. Nevertheless, the Antarctic ozone hole will continue to be a recurring phenomenon until the middle of the century. The Arctic is more dynamically variable, precluding identification of a significant increase in Arctic ozone, and cold conditions conducive to substantial ozone loss may still occur in a particular year in the coming decades. New chemistry–climate model (CCM) projections largely confirm previous studies that in both hemispheres, spring polar total column ozone will return to 1980 historical levels in the coming decades, albeit with a delay of a few years due to updated future ODS and greenhouse gas (GHG) emissions scenarios.

OBSERVED CHANGES IN POLAR OZONE

- **The characteristics of the October Antarctic ozone hole in the years since 2014 have generally been within the range observed since the early 1990s.** In 2015, however, the ozone hole was particularly large and long-lasting, as a result of a cold and undisturbed polar stratospheric vortex. Aerosols from the Calbuco volcanic eruption in April 2015 are also believed to have contributed to the large ozone hole observed that year. Conversely, in 2017, the Antarctic ozone hole was very small due to a warm and unusually disturbed polar vortex.

- **Several lines of evidence have started to emerge indicating an increase in Antarctic stratospheric ozone during September.** Statistically significant trends since the year 2000 have now been identified showing an increase in observed ozone and a decrease in ozone hole size and depth. Although accounting for the large degree of natural variability is challenging, the weight of evidence from statistical analyses and modeling studies suggests that the decline in ODSs made a substantial contribution to these trends.

- **In the Arctic, the exceptionally low ozone abundances of spring 2011 have not been observed again in the last four years.** Arctic stratospheric springtime ozone is dominated by large year-to-year dynamically induced variability of the polar vortex, with severe ozone loss occurring in very cold years, such as 2011. Extreme meteorological conditions in the early 2015/2016 winter led to rapid ozone loss, but a sudden stratospheric warming (SSW) at the beginning of March 2016 curtailed the chemical processes which lead to ozone destruction about a month earlier than in 2011, keeping ozone above record low levels. Arctic ozone trends are small compared to the dynamical variability, and thus a recovery trend remains undetectable in observations over the 2000–2016 period.

UNDERSTANDING OF FACTORS CONTROLLING POLAR OZONE

- **Observations in the Arctic winter have demonstrated that large nitric acid trihydrate (NAT) particles are a regularly occurring phenomenon in the lower stratosphere.** This knowledge improves our understanding of polar stratospheric cloud (PSC) formation and denitrification, which is important for catalytic ozone loss cycles.

- **Bromine-containing very short-lived substances (VSLSs) of natural origin have an important impact on the stratospheric halogen loading and consequently on stratospheric ozone loss in the polar regions.** The inclusion of additional stratospheric bromine from VSLSs is necessary for models to produce a realistic simulation of polar ozone loss.

- **The effects of tropospheric dynamical forcing in winter on Arctic polar ozone are now better quantified.** Ozone depletion in northern winters with SSWs is on average two-thirds less than in winters without SSWs, with depletion ending about one month earlier in the year. Such an SSW was a major influence on ozone levels observed in the Arctic winter of 2015/16.

- **Polar ozone in the middle and upper stratosphere varies by 10–15% from year to year due to energetic particle precipitation (EPP) related to solar variability.** Satellite observations and model results show that NO_y produced in the aurora is transported from the thermosphere down into the stratosphere in each winter, leading to stratospheric ozone decreases modulated by geomagnetic activity. The resulting variation in total column ozone is small (a few percent) but can persist for 2–3 years. Full EPP-effects were not included in current assessment models.

- **Model simulations show that the Montreal Protocol and its Amendments and adjustments have already brought about substantial ozone benefits.** In the polar regions of both hemispheres, much larger ozone depletion than currently observed has been avoided through implementation of the Protocol.

FUTURE EVOLUTION OF POLAR OZONE

- **Updated CCM projections based on full compliance with the Montreal Protocol and assuming the baseline estimate of the future evolution of GHGs (RCP-6.0) have confirmed that the Antarctic ozone hole is expected to gradually close, with springtime total column ozone returning to 1980 values shortly after mid-century (about 2060).** The timing of the recovery of the ozone hole will not be significantly affected by increases in GHG concentrations. There are no substantial differences between Antarctic total ozone columns at the end of this century for the various GHG scenarios (Representative Concentration Pathways [RCPs]).

- **The timing of the recovery of Arctic total ozone in spring will be affected by anthropogenic climate change. Based on full compliance with the Montreal Protocol and assuming the baseline estimate of the future evolution of GHGs (RCP-6.0), Arctic springtime total ozone is expected to return to 1980 values before mid-century (2030s).** New model simulations confirm that in the Arctic, enhanced GHG concentrations cause an earlier return of total column ozone to historical values than a reduction of ODSs alone.

- **In the second half of the 21st century CO_2, CH_4, and N_2O will be the dominant drivers of Arctic ozone changes, assuming full compliance with the Montreal Protocol.** These gases impact both chemical cycles and the stratospheric overturning circulation, with a larger response in stratospheric ozone associated with stronger climate forcing. By 2100, the stratospheric ozone column is expected to not only recover but to exceed 1960–1980 average values in the Arctic, with springtime Arctic ozone being higher by about 35 DU for RCP-4.5 and about 50 DU for RCP-8.5.

- **In the coming decades, substantial Arctic ozone loss will remain possible in cold winters as long as ODS concentrations are well above natural levels.** Increasing GHG concentrations may cool the lower stratosphere and lead to enhanced formation of polar stratospheric clouds (PSCs) early in the Arctic winter. However, one recent study indicates that no corresponding cooling is expected in March, which is the month when persistent low temperatures lead to large chemical ozone losses.

Chapter 4

Polar Stratospheric Ozone: Past, Present, and Future

4.1 INTRODUCTION

This chapter builds on the long sequence of chapters in most of the previous Assessments that have specifically considered stratospheric ozone in the polar regions of the earth. This history reflects the large scientific effort that has been dedicated to observing and understanding polar ozone changes, as well as the great long-standing interest in polar ozone among policymakers and the general public.

4.1.1 Summary of Findings from the Previous Ozone Assessment

WMO (2014) reported that the Antarctic ozone hole had continued to appear each spring, with year-to-year changes in the depth and area of the hole predominantly controlled by temperature variations, given the slow rate of decrease of equivalent effective stratospheric chlorine (EESC; see **Chapter 1**) expected in Antarctica since its peak value around the year 2000. Somewhat reduced ozone depletion was observed in the years 2010, 2012, and 2013, but not in 2011. These observations of less severe ozone depletion were broadly consistent with the anticipated effects of the declining levels of ozone-depleting substances (ODSs) due to the Montreal Protocol and its Amendments and adjustments. However, a definitive conclusion that the observed changes were due to EESC decline could not yet be reached. Nonetheless, WMO (2014) stated that an estimate of the increase of springtime Antarctic total ozone of 10 to 25 Dobson Units (DU) could be made over the years 2000 to 2010 by attempting to remove the effects of natural variability.

In the Arctic, exceptionally low ozone concentrations were observed in the winter and spring of 2010/2011 between 15 and 23 km, but importantly, WMO (2014) reported that chemistry transport models (CTMs) were able to successfully reproduce the measured depletion, given the observed meteorological conditions. This was seen as providing confidence that the understanding of Arctic ozone depletion processes was largely correct.

Continued observations from satellites and aircraft campaigns had further refined knowledge of PSC formation and polar chemical processes. Although several important scientific questions had not been resolved, these uncertainties did not hinder the successful simulation of polar ozone destruction, which is ultimately driven by temperatures falling below threshold values for the activation of chlorine. Previous issues surrounding conflicting values of the ClOOCl absorption cross-section were considered by WMO (2014) to be resolved, with more recent observational studies and laboratory investigations confirming the role of the catalytic ozone destruction cycle initiated by the ClO+ClO reaction, with a significant contribution also from the cycle initiated by BrO+ClO.

Additionally, WMO (2014) stated the apparent trend towards Arctic cold winters becoming colder, as expressed through the V_{PSC} diagnostic, had become less certain, as subsequent research found statistically weaker results.

While WMO (2011) made extensive use of model results from the SPARC Chemistry-Climate Model Validation-2 (CCMVal-2) initiative, no such large suite of results was available for WMO (2014). However, it was reported that no work subsequent to CCMVal-2 had significantly challenged the previous findings pointing to an earlier recovery of ozone to 1980 levels in the Arctic than the Antarctic (2030 and 2050, respectively), with future levels of Arctic ozone also showing a greater sensitivity to the greenhouse gas (GHG) scenario used in model projections.

4.1.2 Scope of Chapter

This chapter updates the state of our knowledge about stratospheric ozone in the polar regions of both hemispheres, taking advantage of systematic observational programs and special measurement campaigns, laboratory studies, and a wide array of computer

modeling. The long-term record of meteorological conditions and ozone depletion in the polar vortex of both hemispheres is presented, updated for the years following the last Assessment. The particular winter–spring seasons of 2015 and 2017 in the Antarctic and 2015/2016 in the Arctic are considered in more detail. Progress in the understanding of the many chemical and physical processes underlying and influencing polar ozone depletion is then reported. Recent studies seeking to identify a statistically significant trend due to declining anthropogenic halogen levels (known as the second stage of Antarctic ozone recovery as set out in WMO (2007)) are discussed, before the chapter concludes with the presentation of results from the SPARC/IGAC Chemistry-Climate Model Initiative (CCMI) and the latest projections of polar ozone over the coming decades.

4.2 RECENT POLAR OZONE CHANGES

4.2.1 Measurements of Ozone and Related Constituents

Scientific study of polar ozone is made possible by the continuation of long-term measurements of ozone made by ground-based, balloon, aircraft, and satellite instruments, supplemented by measurements of related chemical constituents and meteorological parameters. In general, these measurement programs have largely been maintained since WMO (2014).

Long-standing ground-based and balloon measurements of both total column and vertically resolved ozone have continued under the WMO Global Atmosphere Watch and its contributing network NDACC (Network for the Detection of Atmospheric Composition Change). Observational data from these networks are freely available from the World Ozone and Ultraviolet Radiation Data Centre (www.woudc.org). A summary of available satellite measurements relevant to polar ozone was provided in Table 3A-1 of WMO (2014). Many satellite missions launched in the early 2000s have continued to collect data well beyond their expected lifetimes. A number of specific measurement campaigns have also been conducted in addition to long-term monitoring programs. The understanding that these missions and campaigns have contributed to will be discussed in **Section 4.3**.

It is also important to note the contribution of recent work that has combined observational ozone data from different instruments into single homogeneous long-term data sets (**Sections 4.2.3, 4.2.4,** and **4.4**) and the extra insight and usefulness obtained by assimilating meteorological observations and producing reanalysis products (discussed more fully in **Section 4.2.2**).

4.2.2 Evolution of Polar Temperatures and Vortex Characteristics

4.2.2.1 Temperatures and PSC Volume

Polar ozone depletion is highly dependent on stratospheric temperature, as this acts as a strong control on the potential for polar stratospheric cloud (PSC) formation and thus the rate of heterogeneous reactions. **Figure 4-1** shows the annual climatological cycle (1979–2017) of 50 hPa polar minimum temperature for both the Arctic and Antarctic, with four recent years highlighted.

As is well established, winter and spring temperatures show a far higher degree of interannual variability over the Arctic than over Antarctica, indicative of the large year-to-year variability in dynamics and the more frequent disturbances to the Arctic vortex in the form of sudden stratospheric warmings (SSWs) (Labitzke and van Loon, 1999). Since the last Assessment (WMO, 2014), Arctic minimum temperatures have been in the 10–90% envelope about the climatological mean, except for winter/spring of 2015/2016. This period was characterized by December and January minimum temperatures that were close to, or at, the lowest minimum values for the whole period, with a strong and undisturbed vortex (Manney and Lawrence, 2016; Matthias et al., 2016). However, a major final SSW occurred on 5–6 March 2016 and the vortex broke up in early April (Manney and Lawrence, 2016). After the SSW, the polar minimum temperatures were then near, or at, their highest for the 1979–2017 period. The effects of these conditions on Arctic ozone levels will be further discussed in **Section 4.2.4.1**.

The less dynamically disturbed Antarctic vortex shows much lower interannual temperature variability. Recent winter/spring temperatures over Antarctica have typically been within 30–70% of the long-term climatological mean, with the exception of the 2015 spring where they were close to, or at, the lowest

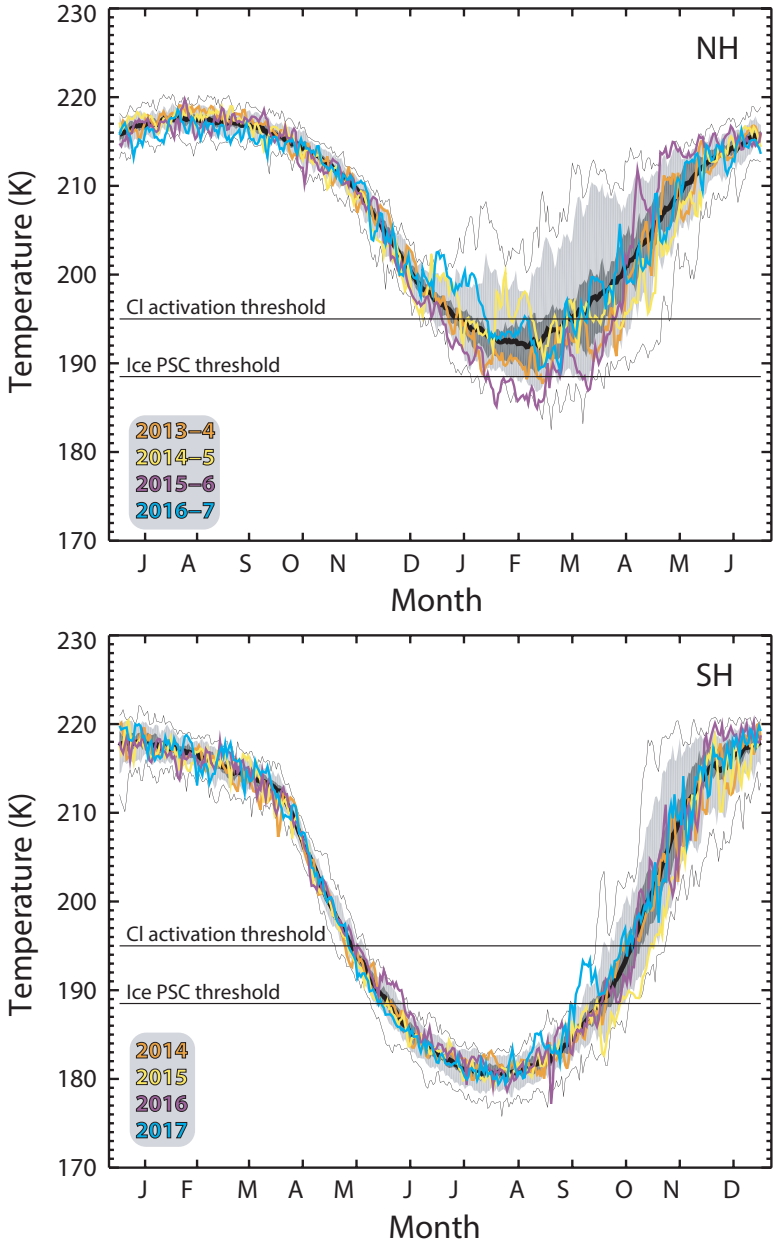

Figure 4-1. Annual cycle and variability at 50 hPa (~20 km) of minimum temperature for the Northern Hemisphere (50°N–90°N, *top*) and the Southern Hemisphere (50°S–90°S, *bottom*) from ERA-Interim reanalysis data (Dee et al., 2011). The thick black line shows the climatological mean annual cycle, with the dark and light gray shaded areas to indicate the 30–70% and 10–90% probabilities, respectively; the thin gray lines indicate the record maximum and minimum values for the period; and the colored lines show the annual cycle of temperatures for recent years. The data cover the periods 1978/1979 to 2016/2017 for the Northern Hemisphere and 1979–2017 for the Southern Hemisphere. Also indicated are the threshold temperatures for chlorine activation and ice PSC formation. Updated from Figure 3-1 in WMO (2014).

minimum temperatures during October and early November, and 2017, when they were above the previous maximum during September. The effects on ozone of the 2015 low temperature in combination with the volcanic eruption of Calbuco in southern Chile are discussed in **Section 4.2.3.1**.

A vortex-wide and season-long picture of the potential for ozone depletion in a winter/spring period is given by a measure of the time-integrated volume of air within the vortex, between the 400 K and 700 K isentropic surfaces, where heterogeneous ozone loss can occur. This metric, hereafter integrated V_{PSC}, is defined using height-resolved temperature data from radiosondes or reanalyses, together with a standard, non-denitrified profile of nitric acid, in order to estimate the temperature threshold for existence of nitric acid trihydrate (NAT) PSCs (Rex et al., 2002). (Due to the use of a non-denitrified nitric acid profile, this does not strictly define threshold temperatures for NAT existence, but rather is a proxy for low temperatures.)

Figure 4-2 shows the long-term evolution of Arctic integrated V_{PSC}, updating the similar figure from WMO (2014), which used V_{PSC}, rather than integrated V_{PSC}. The addition of the time integration emphasizes the importance of duration of the low temperatures (see

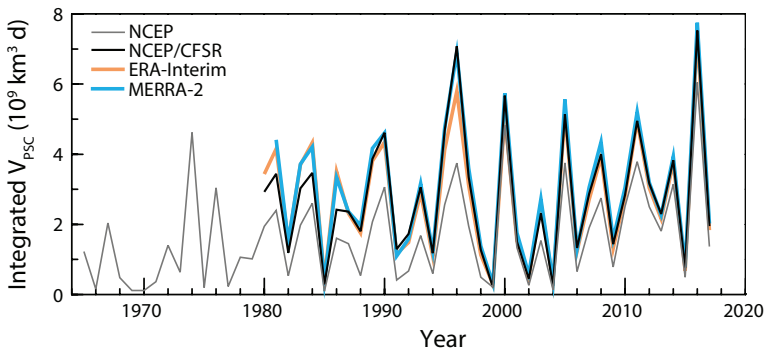

Figure 4-2. Time-integrated Arctic V_{PSC}, integrated by day (d) from 1 November to 30 April for each winter/spring, on isentropic surfaces from 400 to 700 K. Results are shown for different meteorological reanalyses: NCEP (Kalnay et al., 1996), NCEP/CFSR (Saha et al., 2010), MERRA-2 (Gelaro et al., 2017), and ERA-Interim (Dee et al., 2011). The figure is an update from WMO (2014) with the refinement of time integrating V_{PSC} and the addition of new reanalysis products. The V_{PSC} metric is calculated based on the method described by Rex et al. (2006) and estimates the volume within the vortex in which the temperature is low enough for NAT PSCs to exist, based on a standardized non-denitrified nitric acid profile.

also Strahan et al., 2016). The figure shows integrated V_{PSC} calculated from several reanalysis products to provide an idea about structural uncertainty arising from the different reanalysis systems. The three more recent reanalyses (NCEP/CFSR, ERA-Interim, and MERRA-2) are in closer agreement with each other than they are with the earlier NCEP reanalysis (see the figure caption for references). NCEP is shown for comparison with earlier reports but is no longer recommended for stratospheric analyses due to the availability of more recent reanalyses that have been shown to be more suitable (Lawrence et al., 2015; Long et al., 2017).

Apparent from **Figure 4-2** is the large integrated V_{PSC} value for the 2015/2016 winter/spring, driven by the particularly cold December and January in 2015/2016 (Manney and Lawrence, 2016). It exceeds the corresponding value associated with the stronger Arctic ozone depletion of 2011, even though March total ozone values were not anomalously low (**Figure 4-4**). This suggests an instance where the integrated V_{PSC} metric alone is insufficient as an ozone depletion proxy. Arctic ozone depletion in the winter and spring of 2015/2016 is discussed in **Section 4.2.4.1**. In the last Assessment, the evidence for a significant climate change-driven trend towards larger V_{PSC} values occurring in the coldest winters (Rex et al., 2004; 2006) was challenged by studies using extreme value statistics (Rieder and Polvani, 2013) or sunlit vortex volumes (Pommereau et al., 2013). Since then, there have been no in-depth analyses of the V_{PSC} metric and despite the large (integrated) V_{PSC} value for 2015/2016, due to the large year-to-year variability no significant trend can be detected. More recent studies have explored the drivers of polar stratospheric trends using observations and model simulations; these are discussed in **Section 4.5.3**.

4.2.2.2 Polar Vortex Breakup Dates

Figure 4-3 shows the date at which the Arctic and Antarctic polar vortices breakup each spring, due to strong planetary wave breaking and the returning sun resulting in a warming of the polar stratosphere. As in **Figure 4-2**, the dates are calculated from a range of different reanalysis products, using wind data along the vortex edge (Nash et al., 1996). Similar to polar temperature variability, there is a higher degree of interannual variability of the vortex breakup date for the Arctic, compared to the Antarctic. As noted in the previous Assessment, this Arctic variability is greater since 2000 (average standard deviation across the reanalyses: 30.7 days) compared to the 1990s (average standard deviation: 18.8 days), although the amount depends on the reanalysis product. Breakup dates over Antarctica also show a degree of interannual variability, which is more marked after the first decade of the record shown, although again this varies between the reanalysis products. Overall, there is evidence of decadal variability in both hemispheres.

In general, there is better agreement between the different reanalyses for the Antarctic vortex breakup dates (average max–min range between the reanalyses of 5.6 days) than the Arctic (average max–min range of 16.7 days), with the Arctic having some years where the range between different reanalyses exceeds one month. Differences in the simulation of stratospheric

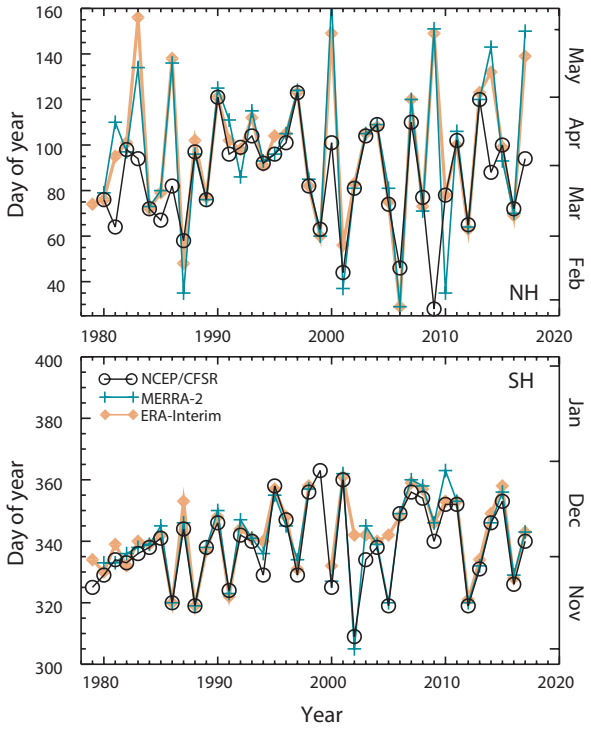

Figure 4-3. Breakup dates for the Arctic (*top*) and Antarctic (*bottom*) polar vortices, defined as when the wind speed on the 500 K isentropic surface falls below 15.2 m s^{-1}, as per Nash et al. (1996). Dates are determined using reanalysis data from NCEP/CFSR (Saha et al., 2010), MERRA-2 (Gelaro et al., 2017), and ERA-Interim (Dee et al., 2011). Note that the Nash et al. (1996) definition does not yield a breakup date in all reanalyses for certain years. Updated from Figure 3-2 of WMO (2014).

winds between the reanalysis products (e.g., Butler et al., 2017; Long et al., 2017) explain the differences between the lines in **Figure 4-3**. There are a range of definitions for breakup date, but no systematic comparison exists in the literature. Other definitions, such as a temperature-based metric (e.g., Haigh and Roscoe, 2009) or computer image analysis techniques (Lawrence and Manney, 2017) may yield better agreement between reanalyses.

4.2.3 Ozone Depletion in Antarctic Springs (2014–2017)

Figures 4-4 and **4-5**, updates to figures that have been used in previous Assessments, represent the evolution of polar ozone loss in both hemispheres. **Figure 4-4** shows mean polar cap (63°–90° latitude) total column ozone averaged for the months of March (for the Arctic) and October (for the Antarctic) compiled from various satellite datasets since 1970. For the Antarctic, generally reliable and well-sampled satellite measurements of total ozone have been available for October since 1979 from the TOMS/OMI/OMPS series of instruments, with some gaps in 1993 and 1995 where alternate instruments were used.

In **Figure 4-5**, rather than mean ozone, the minimum of the daily mean ozone is shown, and further, an attempt is made to confine the averaging region to within the polar vortex through use of a threshold for equivalent latitude on the 475 K isentrope (Müller et al., 2008).

In the Antarctic, both metrics share the general

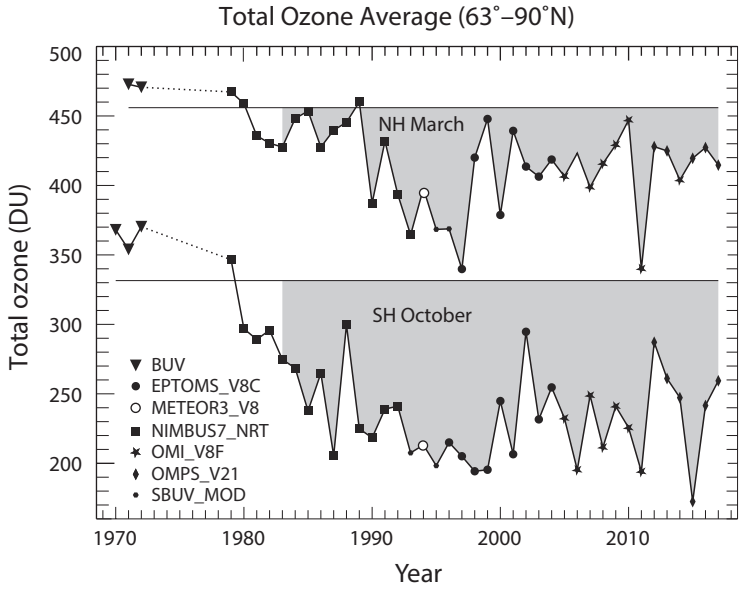

Figure 4-4. Total ozone average (Dobson units) over 63°–90° latitude in March (Northern Hemisphere, NH) and October (Southern Hemisphere, SH). Symbols indicate the satellite data that have been used in different years. The horizontal gray lines represent the average total ozone for the years prior to 1983 in March for the NH and in October for the SH. Updated from Figure 3-4, WMO (2014).

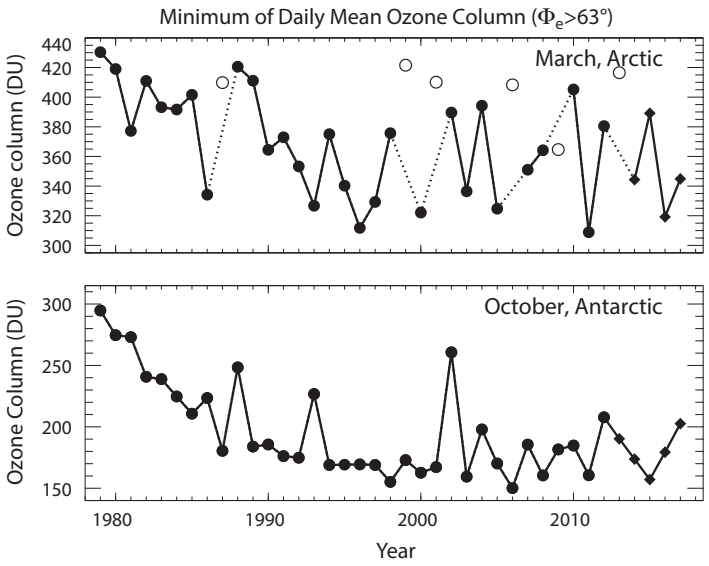

Figure 4-5. Time series of the minimum of the daily average column ozone (Dobson units) within the 63° contour of equivalent latitude (Φ_e) in (*top*) March in the Arctic and (*bottom*) October in the Antarctic. Arctic winters in which the polar vortex broke up before March (1987, 1999, 2001, 2006, 2009, and 2013) are shown by open symbols; dotted lines connect surrounding years. Adapted from WMO (2014), updated using the Bodeker Scientific combined total column ozone data base (version 3.0; circles; Müller et al., 2008) through March 2013 and Aura OMI measurements thereafter (diamonds).

features of a clear decline over the 1980s and 1990s, followed by a period without a clear trend but showing increased year-to-year variability, with the variability reduced in **Figure 4-5** relative to **Figure 4-4** due to the use of equivalent latitude. For 1988, 2002, and 2012, relatively high temperatures in the winter stratosphere limited the severity of ozone loss in the following spring (Klekociuk et al., 2015); in the case of 2002, an unprecedented major sudden stratospheric warming in September disrupted the polar vortex and allowed unusually strong transport of ozone-rich air into the polar cap (Newman and Nash, 2005; WMO, 2007).

Mean October ozone values for three of the last four years since the last Assessment—2014, 2016, and 2017—were all at the higher end of the range of values observed since the year 2000, as were the two preceding years 2012 and 2013. In contrast, the October mean value for 2015 was the lowest on record. The relative positions are similar for minimum daily vortex-averaged ozone **(Figure 4-5)**, although 2014 and 2016 are closer to the middle of the range, and the 2015 minimum is not as low as 2006, which is the record low value for this metric.

The evolution of Antarctic ozone has also been represented in previous Assessments by the time series of three standard metrics: area of the ozone hole, minimum ozone within the ozone hole and ozone hole mass deficit (**Figure 4-6**—refer to the caption for the specific definitions and time periods of the metrics shown). For ozone hole area, the last four years have varied within the general range observed since the early 1990s, with 2015 being among the largest recorded and 2017 the second smallest since the late 1980s. Ozone hole minimum is similar in **Figure 4-6** to the minimum vortex average shown in **Figure 4-5** but shows a greater general increase since 2000. Several years from the period 2000–2013 had lower ozone hole minimum values than all four years 2014–2017. Ozone hole mass deficit (OMD) shows the most evident change since 2000, with the 2017 value being the smallest since 1988. To illustrate the development of the Antarctic ozone hole over winter and spring in the four years, **Figure 4-7** shows the estimated daily ozone mass deficit for July to December in years 2014 to 2017 and also the extreme years of 2002 and 2006 for comparison. This metric is the difference in column ozone from 220 DU expressed as a mass integrated over the area of the ozone hole. A similar figure was last presented in WMO (2007). The onset of significant ozone depletion in the Antarctic normally occurs between the beginning and middle of August, when total column abundances usually begin to drop below the 220 DU threshold that was introduced by Stolarski et al. (1990) as a definition of the Antarctic ozone hole (see Uchino et al. (1999), Bodeker et al. (2005), and Huck et al. (2007) for additional definitions, and Pazmiño et al. (2018) for different thresholds). Ozone loss typically maximizes at the beginning of October after which ozone concentrations tend to increase through the remainder of

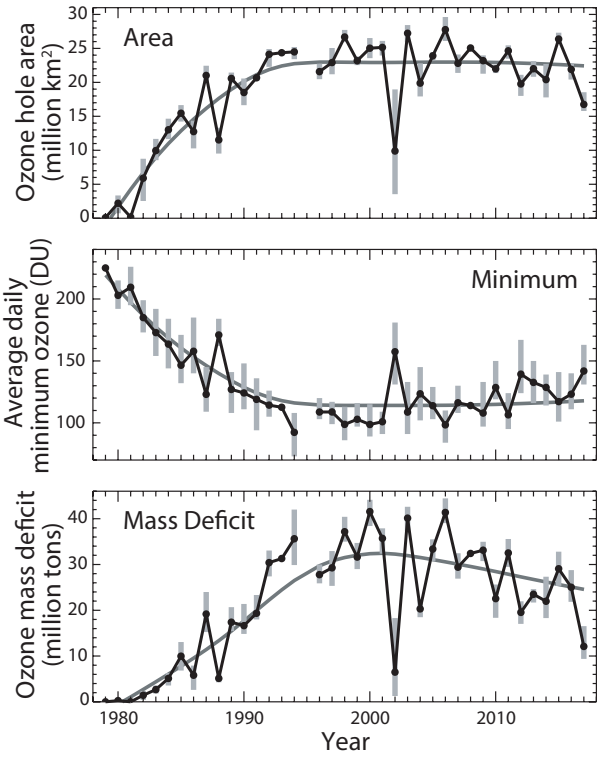

Figure 4-6. (*top*) Area of the Antarctic ozone hole for 1979–2017, averaged from daily total ozone area values contained by the 220 DU contour for 21–30 September. (*middle*) An average of daily minimum ozone values over Antarctica during the period from 21 September to 16 October. (*bottom*) Ozone mass deficit (OMD) averaged over the 21–30 September period. For all three panels, the vertical gray bars indicate the range of values over the same time period. The dark gray curves show the fits to each quantity as was shown in Newman et al. (2004) using EESC, as derived in Newman et al. (2006), updated with the current baseline A1 scenario. The EESC has a mean age of 5.5 years, an age spectrum width of 2.75 years, and a bromine-scaling factor of 65. The fit is quadratic in EESC. This figure was generated from TOMS (1979–2004), Aura OMI (2005–2015), and Suomi NPP OMPS (2016–2017) data. Updated from Figure 4-8 from WMO (2007).

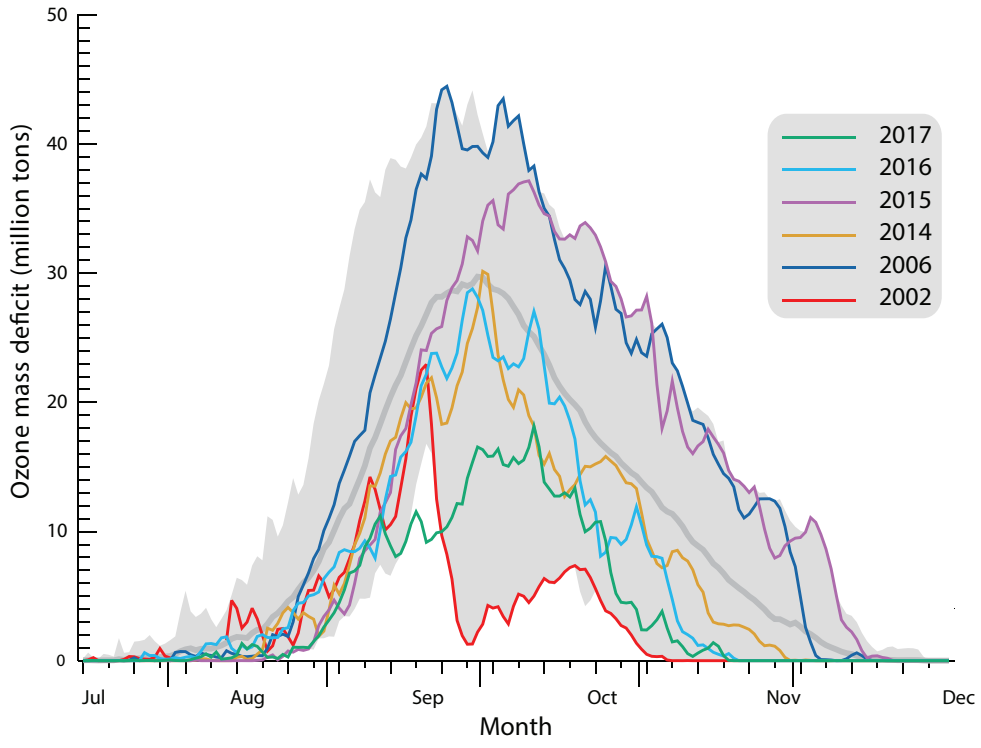

Figure 4-7. Daily ozone mass deficit over Antarctica for various years compared with the range of values over the period 1990–2016 (gray shaded area). The thick dark gray line shows daily values averaged over the 1990–2016 period. Values have been computed using data from TOMS, Aura OMI, and Suomi NPP OMPS. Updated from Figure 4-9 from WMO (2007).

the year, but do often show significant variability on timescales of days to weeks due to disturbance of the polar vortex by Rossby wave activity.

The growth and decline of daily ozone mass deficit in 2014 and 2016 were generally similar to each other, and took place over a somewhat contracted period relative to the long-term mean, with a 1-2 weeks slower development in early September and an earlier zero-crossing in November (**Figure 4-7**). In terms of the broad features of the daily time series of deficit and area, these specific ozone holes exhibited behavior similar to some years in the early 1990s, although their total ozone mass deficits were generally greater than pre-1990 levels (**Figure 4-6**; Newman et al., 2015; Weber et al., 2015; Newman et. al., 2017; Weber et al., 2017). In 2016, the latest date for which total column ozone values were below 220 DU was November 20 (**Figure 4-7**), which was the earliest such date for the period 2014-2017. This early elevation of levels above the 220 DU threshold was brought about by an episode of strong warming in the polar cap during late November of that year (**Figure 4-1**). Some evidence of a shift in the timing of the formation and growth of the ozone hole towards a later date since 2000 has also been presented (Solomon et al., 2016). The evolution of the ozone mass deficit in years 2015 and 2017, which were distinctly different to 2014 and 2016, are discussed in **Sections 4.2.3.1** and **4.2.3.2**, respectively.

4.2.3.1 Antarctic Spring 2015: Volcanic and Dynamical Influence on Ozone

In terms of total annual ozone mass deficit, the 2015 Antarctic ozone hole was the largest of the period 2014–2017 (**Figure 4-7**). The 2015 ozone hole was notable in achieving a large maximum area, being comparable to the largest values observed for 2003 and 2006 (**Figure 4-6**). Through much of the period from early October to mid-December, the Antarctic ozone hole of 2015 set records in daily area and mass deficit and had unusually low minimum column abundances (Nash et al., 2016; Weber et al., 2016). Additionally, its onset was approximately two weeks later than typical (Nash et al., 2016).

The large area of the 2015 Antarctic ozone hole was influenced in part by the chemical effects in the lowermost stratosphere (particularly around the 100–150 hPa pressure level) of aerosols that were entrained in the polar vortex from the eruption of the Calbuco volcano in southern Chile in April 2015 (Solomon et al., 2016; Ivy et al., 2017; Stone et al., 2017). Studies comparing ozone hole metrics with and without the inclusion of prescribed aerosol loading derived from observed volcanic SO_2 emissions found simulations with prescribed aerosols provide an ozone hole area that closely matches observations, and concluded that chemical ozone depletion enhanced by heterogeneous processes associated with the volcanic aerosols was the primary factor behind the ozone hole achieving record size. Dynamical and temperature feedbacks from the ozone loss were less important (Solomon et al., 2016; Ivy et al., 2017). Measurements by ozonesondes and the Aura MLS satellite instrument are consistent with the model results and indicate that the aerosol-influenced ozone loss was most significant in the lowermost stratosphere (Stone et al., 2017).

It should be noted that the contribution of volcanic aerosol particles took place in the setting of a notably cold and stable Antarctic vortex in 2015 (**Figures 4-1** and **4-12**). The level of disturbance to the Antarctic vortex was relatively low in the winter and spring. The eddy heat flux at 100 hPa was generally below the long-term average from July to October, and particularly in October, which favored the ozone hole having greater persistence than on average (Nash et al., 2016). Much of 2015 was marked by a positive value for the Southern Annular Mode index, which did not favor Rossby wave propagation to high (> 60°S) southern latitudes (Fogt, 2016).

4.2.3.2 Antarctic Spring 2017: Dynamical Influences on Ozone

Antarctic ozone loss in the spring of 2017 was unusually low and comparable in some metrics, particularly mass deficit, with that for 2002 (when the stratospheric vortex exhibited an unprecedented major warming as noted earlier) and most years prior to 1989. The small size of the ozone hole in terms of its maximum area and total mass deficit compared with other years can be seen in **Figure 4-6**. The rate of increase of ozone mass deficit in 2017 was notably below average throughout September (**Figure 4-7**), during the majority of which time stratospheric temperatures were the warmest in the 1979–2017 record (**Figure 4-1**). Unusually for the Southern Hemisphere, the ratio of September to March ozone from 50° to 90°S

was greater than one, consistent with the high value of poleward eddy heat flux integrated over winter (**Figure 4-12**).

4.2.4 Ozone Depletion in Arctic Springs (2014–2017)

The annual time series of polar cap mean and minimum ozone in March for the Arctic are shown in the upper panels of **Figures 4-4** and **4-5.** Some issues around the interpretation of these figures in the Arctic are discussed in Section 3.2.3 of WMO (2014). These averages have been used to assess the long-term behavior of Arctic stratospheric ozone as chemical depletion normally peaks in March, unless the polar vortex dissipates earlier. In the Arctic polar cap, ozone concentrations in the lower stratosphere are more strongly influenced by horizontal transport than in the Antarctic, owing to the relatively weak and disturbed nature of the northern polar vortex. The Arctic vortex is smaller and more spatially variable than the Antarctic vortex, and variability in the amount of ozone transported to the polar cap can complicate the interpretation of total column measurements. In spite of these limitations, which can be minimized by considering partial columns (e.g., Strahan et al., 2016), these metrics have been used to highlight years where ozone concentrations in the Arctic are notably low. However, as discussed in detail in WMO (2014), years of particularly low Arctic ozone in March, such as 1997 and 2011, can show distinctly different behavior in chemical ozone loss (which was strong in 2011 but only moderate in 1997) and dynamical influences (which reduced ozone levels in the latter part of the 1997 winter). More recently, chemical depletion of ozone has been shown to account for one-third of the difference from the pre-1983 mean (the gray shaded area in **Figure 4-4**) in most years, with the remainder being due to variations in dynamical resupply of ozone (Strahan et al., 2016; see also WMO, 2010 Figure 2-15).

As for the Antarctic, **Figures 4-4** and **4-5** display an evident negative trend in ozone in the 1980s which did not continue past the late 1990s. In terms of March mean ozone across the geographic polar cap **(Figure 4-4)**, the four years since the last Assessment have all been well within the range of typical values observed since 2000, with only small differences between each of the years and significantly above the value for 2011 which experienced very large ozone depletion. The differences between the four years are much larger in **Figure 4-5** however, with minimum ozone in March 2015 now at the higher end of the range of values since 1990 and March 2016 being one of the lowest values.

To consider the development of Arctic ozone in winter and spring over these four recent years, **Figure 4-8** shows time series of the daily average concentration of specific species relevant to ozone chemistry at a height of approximately 18 km—representative for the lower stratosphere within the Arctic polar vortex. The 2013/2014 Arctic vortex was large, cold (see also **Figure 4-1**), and relatively strong throughout the winter; temperatures near 18-km altitude were below chlorine activation thresholds until approximately mid-March. The observed decrease in ozone was slightly more than the average up until April 2014 (Bernhard et al., 2015). Over the period December 2014 to April 2015, ozone concentrations in the Arctic lower stratosphere near 18 km altitude were the highest in the Aura MLS record (which started in August 2004; **Figure 4-8**) (Manney et al., 2015b; Bernhard et al., 2016). A minor sudden stratospheric warming (SSW) event in early January 2015 (**Figure 4-1**) raised temperatures and limited further development of ozone-depleting chemistry within the polar vortex. Additionally, Aura MLS data showed evidence for above average transport of ozone-rich air into the polar cap through the upper branch of the Brewer-Dobson circulation (Manney et al., 2015b), which also elevated HNO_3 concentrations to levels in the lower stratosphere not previously observed in the Aura MLS record. The enhanced temperatures and transport were both the result of increased high-latitude wave activity (Manney et al., 2015b).

The early part of the 2016/2017 Arctic winter was unusually warm in the lower stratosphere with a weak vortex, although with a cold and strong vortex in the middle and upper stratosphere. Several minor SSWs occurred, with two of them near the threshold to be defined as "major" (according to definitions by Butler et al., 2015). Temperatures below chlorine activation thresholds in the lower stratosphere did not appear until late December. However, cold conditions were consistently present thereafter until early March, and significant chlorine activation and ozone loss were observed. As indicated by relatively high levels of HNO_3 in the lower stratosphere (top panel of **Figure**

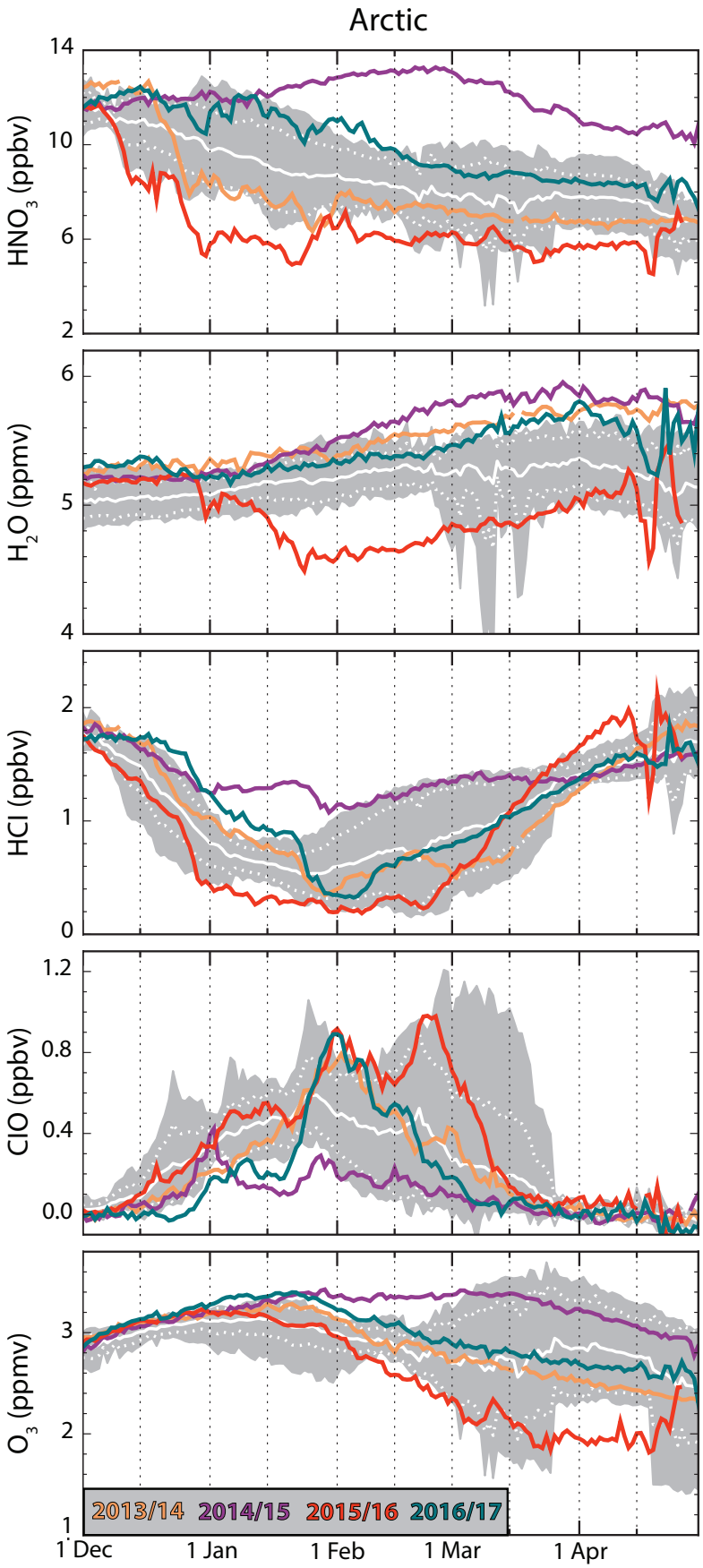

Figure 4-8. Time series of vortex-averaged HNO_3, H_2O, HCl, ClO, and O_3 from Aura Microwave Limb Sounder (MLS) on the 480 K potential temperature surface (~18 km, ~50 hPa) for winters and spring in the Arctic. Gray shading shows the envelope of behavior observed by Aura MLS over the 2005–2013 period. A data gap from 27 March to 18 April 2011 has produced a noticeable artefact in the envelope of some panels. The last four winters are highlighted by colored lines as indicated in the legend, for which the given year refers to January to April. Updated from Figure 3-6 from WMO (2014).

4-8), denitrification was not particularly pronounced within the vortex during 2016/2017.

4.2.4.1 Arctic Spring 2016: Record Ozone Depletion Halted by Major Warming

The 2015/2016 Arctic winter had significant potential for large ozone loss (Manney and Lawrence, 2016). Exceptionally low temperatures occurred throughout the period from December 2015 to February 2016, which were the lowest in the 68-year observational record (Matthias et al., 2016). Strong denitrification and dehydration occurred (Manney and Lawrence, 2016; **Figure 4-8**), which were associated with extensive PSC formation (Khosrawi et al., 2017; Bernhard et al., 2017). The low stratospheric temperatures, particularly in November and December of 2015, were linked with weak planetary wave-1 activity associated with the prevailing enhanced tropospheric meridional temperature gradient that appears to have increased the vertical wind shear at northern mid-latitudes and reduced the ability of the planetary waves to propagate upward (Matthias et al., 2016).

The cold conditions led to very strong chlorine activation within the polar vortex in 2015/2016 until the end of February. Levels of HCl at the 480 K surface in the vortex in January were the lowest in the Aura MLS record, below those of 2010/2011 when ozone loss was exceptional and levels of ClO were correspondingly high (**Figure 4-8**). The amount of ozone depletion was enhanced by the strong level of denitrification (Manney and Lawrence, 2016). However, the overall ozone loss in this season was halted by a major final SSW in early March, which terminated stratospheric chlorine activation approximately a month earlier than was the case for the 2010/2011 season (Bernhard et al., 2017). From this point on, ClO levels dropped rapidly (**Figure 4-8**). As a result of the warming, record Arctic ozone depletion that might have occurred with such high levels of chlorine activation earlier in the season, did not take place.

4.3 UNDERSTANDING OF POLAR OZONE PROCESSES

4.3.1 Polar Stratospheric Clouds

Polar stratospheric clouds (PSCs) and cold sulfate aerosols impact polar ozone and chlorine chemistry by converting chlorine from inactive reservoir species (mainly hydrochloric acid (HCl) and chlorine nitrate ($ClONO_2$)) to active ozone-destroying species. Furthermore, PSCs can both temporarily sequester HNO_3 from the gas phase (substantially reducing gas-phase concentrations of HNO_3 as long as the PSCs exist) and irreversibly redistribute HNO_3 by gravitational sedimentation of large nitric acid trihydrate (NAT) particles (referred to as "denitrification"; WMO (2014), Box 3-1). These impacts on polar ozone and chlorine chemistry are now considered to be well understood. However, many aspects of the microphysics of PSCs and their formation still remain unclear, such as the nucleation mechanism for NAT particles (in particular, large NAT particles), the impact of rapid cooling rates (gravity waves), and the origin and nature of refractory (that is, non-volatile) particles in the polar vortex. As well, the substantial uncertainties in the reactivity on NAT surfaces (particularly the heterogeneous reaction HCl + $ClONO_2$) identified many years ago (WMO, 1998; Carslaw and Peter, 1997) remain unresolved. Most results, such as comparisons of chemical transport models to observations, are generally robust to the details of the assumptions employed regarding PSCs and heterogeneous chemistry (e.g., Kirner et al., 2015a; Wohltmann et al., 2013). Nonetheless, there are conditions where the exact rates of heterogeneous chlorine activation reactions and thus also PSC composition will be significant; for example, when chlorine activation occurs in the Arctic within a limited spatial or temporal region (Wegner et al., 2016) or in the Antarctic under conditions of a direct competition of the rate of gas-phase deactivation and heterogeneous activation of chlorine (Solomon et al., 2015). Further, an accurate representation of PSC processes in models is required to ensure the reliability of projections of the future development of polar ozone under conditions of changed atmospheric concentrations of key species. The contribution of the latest observational, laboratory, and modeling studies to addressing these questions is described in the following sections.

4.3.1.1 Observations of PSC Extent and Composition

Long-term data sets of the occurrence of different types of PSC particles over the polar regions are now available from both satellite and ground-based observations. The MIPAS instrument, which was carried by the ENVISAT satellite, was an infrared limb

sounder providing a pole-covering day and night time climatology of PSC distributions and their composition from July 2002 until April 2012. The CALIOP instrument onboard CALIPSO is a two-wavelength polarization-sensitive lidar that provides night-time high-resolution vertical profiles of PSCs with data collection beginning in mid-June 2006 and lasting until the present day. In addition, ground-based lidar systems provide important long-term information on PSC properties; measurements are available since 1997 at Esrange, Sweden (Achtert and Tesche, 2014) and for 1995–2001 and 2006–2010 at McMurdo, Antarctica (Di Liberto et al., 2014). Data from these ground-based systems are compared with satellite-based measurements and are used to test and develop PSC classification schemes.

The most recent data products from MIPAS and CALIOP (Spang et al., 2016; Lambert et al., 2016) show a very good agreement regarding PSC classification and occurrence as seen in the daily altitude-resolved time series of three PSC classes in 2009 for the two instruments **(Figure 4-9)** (Spang et al., 2018). Given the very different measurement principles used by CALIOP and MIPAS, the agreement between the two data sets is encouraging and will allow analyses on the temporal and spatial development of PSCs over multiple winters to be performed with the potential for the validation and improvement of PSC schemes in CTMs and CCMs (e.g., Zhu et al., 2017a).

WMO (2014) reported on the detection of unusually large particles (up to 35 μm), so-called "NAT-rocks", in synoptic-scale PSC fields during aircraft campaigns in the Arctic in 2010 and 2011 (von Hobe et al., 2013). It has been argued for a long time that the sequestering of major amounts of nitric acid in relatively large particles leads to efficient denitrification (Salawitch et al., 1989). Further analysis of these observations (Molleker et al., 2014) showed that the optically measured size distribution (**Figure 4-10**) could only be explained by either strong asphericity of the particles or an alternate composition (e.g., water ice coated with NAT). While there has been previous evidence (Fahey et al., 2001; Brooks et al., 2003) for NAT-rocks, their observational basis has been expanded by these measurements and the occurrence of large NAT particles now appears to be a regular feature of synoptic-scale PSCs in the Arctic.

Further, analysis of the spectral signature of the PSC field over northern Scandinavia obtained by airborne passive infrared limb emission measurements in December 2011 revealed a distinctive "shoulder-like" signature in the spectral region around 820 cm^{-1} (Woiwode et al., 2016). This observed signature is best explained by the combination of the absorption, emission, and scattering characteristics of large (log-normal distribution with a mode radius of 4.8 μm) highly aspherical (aspect ratios of 0.1 or 10) NAT particles. The measurement of excess gas-phase HNO_3 observed in a nitrification layer directly below the observed PSCs further supports the role of such large aspherical particles in denitrification.

Comparison of CALIOP observations for the Antarctic in winter 2010 with model simulations suggests that two major NAT particle formation mechanisms must exist. Homogeneous nucleation from supercooled ternary solution (STS; see WMO (2014), Box 3-1) droplets produces large NAT particles which are needed to reproduce the observed rates of denitrification, while heterogeneous nucleation of NAT on ice produces small particles which account for the large backscattering ratio from NAT observed by CALIOP (Zhu et al., 2017a; 2017b).

It has also previously been proposed that refractory particles of meteoric origin could serve as condensation nuclei of NAT-rocks (Curtius et al., 2005). Laboratory experiments using analogues of meteoric materials show that such surfaces have the capacity to nucleate nitric acid hydrates (James et al., 2018). As reported in WMO (2014), aircraft measurements made in the Arctic in late winter 2010 detected a large number of refractory particles with diameters above 500 nm (von Hobe et al., 2013). The abundance of refractory aerosols in the lower stratosphere during late winter in the Arctic vortex appears to be a regular feature rather than an exception (Weigel et al., 2014). At the time of these measurements, the air mass subsidence inside the Arctic winter vortex from the upper stratosphere and mesosphere was well-advanced, leading to the conclusion that the refractory particles had been transported from higher altitudes into the lower stratosphere. In contrast, in the flight samples collected in an early winter situation (December 2011, and therefore a young vortex in which the air masses had seen much less descent), no large refractory particles were observed (Ebert et al., 2016). The observed general

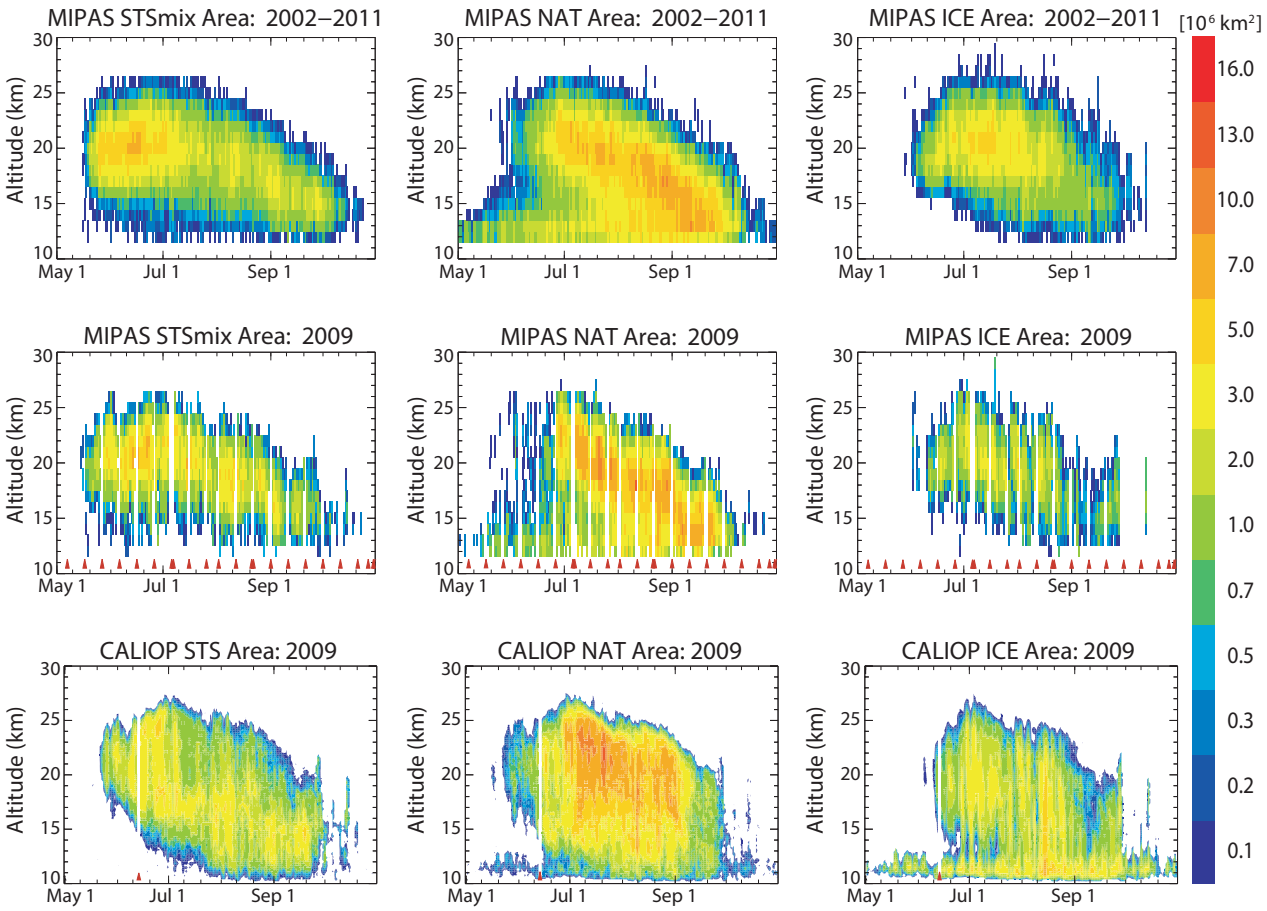

Figure 4-9. Time series of the daily Antarctic PSC areas (*top row*) from MIPAS climatology (10-year mean [2002, 2003, and 2005–2011]; MIPAS data weighted by the area of the applied latitude bins south of 55°S in the altitude range 12–30 km), (*middle row*) from MIPAS for the year 2009, and (*bottom row*) CALIOP V2 for the year 2009, based on the identical computation of PSC area for each data set. Presented are all relevant PSC classes for the MIPAS and CALIOP satellite retrievals (ice, NAT, and STSmix). For better comparability with CALIOP, MIPAS observations in the middle row are restricted to latitudes north of 82°S, the latitude coverage of CALIOP. Red triangles at 10.5 km altitude in the MIPAS and CALIOP time series (*middle and bottom rows*) mark data gaps caused by the measurement mode. Adapted from Spang et al. (2018).

tendency of a lower abundance of refractory particles during PSC events compared to non-PSC situations supports the hypothesis that such particles can provide a surface for heterogeneous nucleation during PSC formation. Further, recent analysis of particles originally collected in the Arctic stratosphere from January until March 2000 found a high abundance of carbonaceous refractory particles. Based on their chemistry and nanostructure, many non-meteoric sources for these carbonaceous particles can be excluded (Schütze et al., 2017). However, the exact source of the large refractory particles in the stratosphere and their impact on PSC formation remain to be accurately determined.

4.3.1.2 Gravity Waves and Orographic Forcing

Atmospheric gravity waves yield substantial small-scale temperature fluctuations that can trigger the formation of PSCs (e.g., Murphy and Gary, 1995). Orr et al. (2015), based on case studies over the Antarctic Peninsula, investigated the representation of stratospheric mountain-wave-induced temperature fluctuations by the UK Met Office Unified Model (UM) at climate scale and mesoscale, compared to observations. They found that, at high horizontal resolution (4 km), the regional mesoscale configuration of the UM is able to correctly simulate the magnitude, timing,

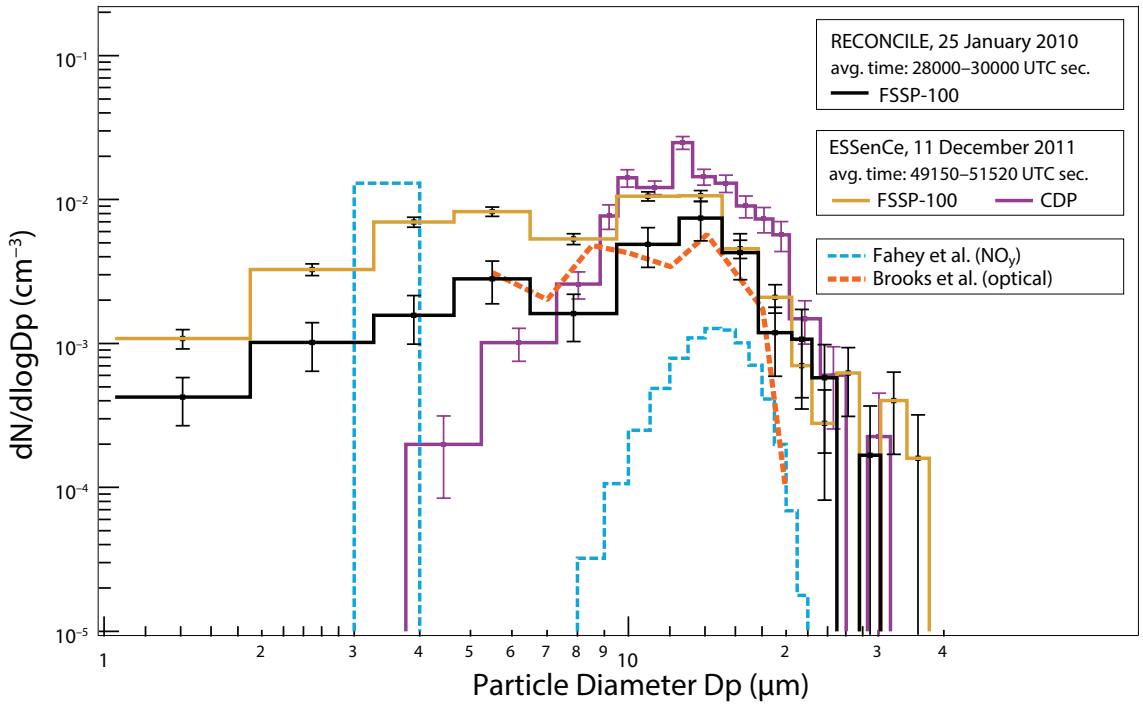

Figure 4-10. Size distributions of large HNO_3-containing PSC particles with high number densities from in situ airborne measurements in 2010 and 2011. These measurements are compared to previous measurements by Fahey et al. (2001) (retrieved from total NO_y) and Brooks et al. (2003) (optical measurements). Adapted from Molleker et al. (2014).

and location of the measured temperature fluctuations. While a climate configuration of the model with lower horizontal resolution was not able to resolve the fluctuations, in this case, the use of a mountain wave parameterization scheme gave reasonable agreement with observations. A 10-year satellite record of gravity wave activity in the polar lower stratosphere based on AIRS indicates that orography as well as jet and storm sources are the main causes of the observed gravity waves. There is a strong seasonal cycle in wave activity with wintertime maxima at high latitudes, the cycle lasting 2–6 months in the Northern Hemisphere and 5–9 months in the Southern Hemisphere (Hoffmann et al., 2017). A comparison of the satellite observations with temperature fluctuations in the ECMWF operational analysis (16-km horizontal resolution) showed that gravity wave patterns occur in the right locations, but that wave amplitudes were typically underestimated by a factor of 2–3 (Hoffmann et al., 2017). Further, Lambert and Santee (2018) find that the potential to form ice PSCs in model studies driven by various reanalyses varies significantly because of the underlying differences in the representation of mountain wave activity. Moreover, CALIOP data indicate that simulations are missing clouds containing small NAT particles with large number densities; such particles are most likely to form from ice clouds or STS in gravity waves (Zhu et al., 2017b).

These recent findings emphasize the importance of high spatial resolution, state-of-the-art meteorological reanalyses, and high-quality schemes for the representation of gravity waves in model studies aimed at PSC formation and existence.

4.3.2 Polar Chemistry

4.3.2.1 Observations of Polar Chemistry

Measurements taken with balloon-borne MIPAS-B and TELIS instruments in northern Sweden on 31 March 2011 inside the polar vortex provided vertical profiles of inorganic and organic chlorine species over the whole altitude range in which chlorine had been undergoing activation and deactivation (Wetzel et al., 2015). A total chlorine (Cl_y) concentration of 3.41 ± 0.30 ppbv is inferred above 24 km from the

measurements. This value is consistent with the slightly reduced chlorine loading of the stratosphere in 2011 compared to its peak value a decade earlier (see **Chapter 1**).

Strahan et al. (2014) reported Aura MLS-inferred Cl_y showed large variations from year to year due to the variability of transport to the Antarctic vortex. The mean expected annual Cl_y decline due to the Montreal Protocol is estimated to be –20 ppt yr^{-1}; however, fluctuations of the concentration in a given year have varied up to 200 ppt below and 150 ppt above the mean. (The concentration of Cl_y in 2013 at 450 K in the vortex was estimated by this method to have been 2650 ppt.) Because of this large interannual variability of Cl_y, it requires at least 10 years of chlorine decline after the chlorine maximum for an Antarctic ozone recovery (in the sense of an ozone increase caused by halocarbon reductions) to be attributable to a decline of stratospheric chlorine in a statistically significant manner (Strahan et al., 2014).

In the Arctic vortex of the 2009/2010 winter, satellite observations showed the initial activation of chlorine occurred in association with the formation of PSCs over the eastern coast of Greenland at the beginning of January 2010 (Wegner et al., 2016). Although this area of PSCs covered only a small fraction of the vortex, it was responsible for almost the entire initial chlorine activation throughout the vortex. Observations show that HCl mixing ratios decreased rapidly in and downstream of this region. Simulations of heterogeneous reaction rates along trajectories intersecting with the PSCs indicate that the initial phase of chlorine activation occurred in just a few hours. These calculations further suggest that the very rapid chlorine activation in Arctic winter 2009/2010 can only be explained by an increase in surface area density due to PSC formation (Wegner et al., 2016), as reactions on the background binary aerosol would have been too slow.

4.3.2.2 Laboratory Studies, Theoretical Basis, and Models

Laboratory, PSCs

New experiments on the heterogeneous kinetics of H_2O, HNO_3, and HCl on HNO_3 hydrates have been performed using a multidiagnostic stirred-flow reactor in which the gas phase as well as the condensed phase have been simultaneously investigated for stratospheric temperatures in the range 175–200 K (Iannarelli and Rossi, 2016). In these experiments, NAT was investigated in two phases; α-NAT, which exists at temperatures below 185 K and is metastable and β-NAT, which exists above this temperature and is the form predominantly found in PSCs (see also the following section). In the laboratory experiments, initial spontaneous formation of α-NAT was found, followed by the gradual transformation of α- to β-NAT at $T > 185$ K; further nitric acid dihydrate (NAD) was spontaneously formed at somewhat larger partial pressures of HNO_3 deposited on pure H_2O ice (Iannarelli and Rossi, 2016). The improved experimental instrumentation suggests, in contrast to previous studies, the formation of α-NAT proceeds without prior formation of an amorphous HNO_3/H_2O layer and always results in the formation of β-NAT.

Chlorine Chemistry and Heterogeneous Reactions

Chlorine activation and subsequent ozone depletion only occur because of heterogeneous reactions (Solomon et al., 1986); chlorine activation rates are mainly controlled by temperature, with only a limited dependence on PSC type (e.g., Salawitch et al., 1988; Kawa et al., 1997; WMO, 2014). Beyond heterogeneous chemistry, NAT particles have an impact on gas-phase chemistry through removal of HNO_3 (denitrification). Initial chlorine activation is not directly related to chemical ozone loss and chlorine activation is often saturated because of the lack of available $ClONO_2$, so that gas-phase chemistry becomes important (Solomon et al., 2015; Müller et al. 2018). However, strong polar ozone loss requires both a nearly complete activation of chlorine and the maintenance of high levels of active chlorine for an extended period (e.g., Solomon et al., 2015; Müller et al., 2018). Recent work has focused on the sensitivity of simulated ozone loss on PSC types, temperature thresholds and the maintenance of high levels of activated chlorine, and the chemical processes responsible for chlorine activation (Solomon et al., 2015; Kirner et al., 2015a; Wegner et al., 2016; Wohltmann et al., 2017; Müller et al., 2018).

Multi-year simulations of a CCM (nudged to ERA-Interim reanalysis meteorological fields) show the impact that the various types of PSCs (Box 3.1 in WMO (2014)) have on Antarctic chlorine activation and

ozone loss (Kirner et al., 2015a). In these simulations, in high southern latitudes, heterogeneous chemistry on liquid particles accounts for more than 90% of ozone depletion, with reactions on ice particles adding less than 5% of further ozone depletion and NAT particles less than 1%, although NAT particles play an essential role in denitrification. Simulations of HNO_3, ClO, and ozone agree closely with observations from MLS (Kirner et al., 2015a).

Polar ozone depletion simulations based on the WACCM model for the year 2011 indicate that total ozone depletion in both hemispheres is dependent on low temperatures (below 192 K) and associated heterogeneous chemistry on polar stratospheric cloud particles (Solomon et al., 2015). Reactions limited to temperatures above 192 K, or on binary (sulfate/water) liquid aerosols, yield little simulated polar ozone depletion in this model in either hemisphere. The simulated ozone loss is sensitive to sulfate, which provides additional surface area for heterogeneous reactions (Tabazadeh et al., 2002); enhancing stratospheric sulfate by a factor of three increases ozone loss by up to 20 Dobson Units (DU) in the Antarctic and 15 DU in the Arctic. These assumed enhanced sulfate levels are similar to those observed following recent relatively small volcanic eruptions since 2005. Ozone losses in the model are strongly sensitive to temperature, with a test case cooler by 2 K producing as much as 30 DU additional ozone loss in the Antarctic and 40 DU in the Arctic. The modeled result compares with an earlier analysis of observations that calculated the mean dependence on stratospheric temperature of Arctic ozone loss as 15.6 DU K^{-1} (Rex et al., 2006).

Moreover, Solomon et al. (2015) corroborate earlier findings (Jaeglé et al., 1997) that in the edge region of the Antarctic vortex, transport of $ClONO_2$ from lower latitudes to higher latitudes as well as latitudinal excursions of air parcels in and out of sunlight during winter enhances $ClONO_2$ and HOCl available for reaction with HCl and hence net chlorine activation. The onset of chlorine activation by heterogeneous processes is mostly limited by the amount of available $ClONO_2$, as confirmed by a recent combination of CALIOP PSC and MLS HCl and ClO observations with model simulations (Nakajima et al., 2016).

Recent studies focus on a quantitative analysis of the chemical reactions involved in polar ozone depletion in the stratosphere (for specific winters) and of the relevant reaction pathways and cycles (Wohltmann et al., 2017; Müller et al., 2018). Wohltmann et al. (2017), based on NASA's Jet Propulsion Laboratory (JPL) 2011 recommendation (Sander et al., 2011), find that the ClO dimer cycle contributes about 50% to the vortex-averaged ozone loss at 54 hPa in both hemispheres, while the BrO–ClO cycle contributes about 40%. Further, in the Southern Hemisphere, there is a clear shift from chlorine activation by the $ClONO_2$ + HCl reaction in early winter to activation by the HOCl + HCl reaction later in winter (Wohltmann et al., 2017; Müller et al., 2018). The HOCl + HCl reaction accounts for about 70% of the activation of Cl in the Southern Hemisphere, while it accounts for 30% of the activation in the Northern Hemisphere (Wohltmann et al., 2017). In the core of the Antarctic vortex, in the lowermost stratosphere, high levels of active chlorine are maintained by effective chemical cycles (HCl null-cycles) where the formation of HCl is balanced by immediate reactivation, which allows active chlorine levels to be maintained and thus rapid ozone destruction to occur. For the observed almost complete activation of stratospheric chlorine in the lower stratosphere, the production of HOCl via HO_2 + ClO, with the HO_2 resulting from photolysis of CH_2O, is essential (Müller et al., 2018).

In the dark core of the polar vortex MLS observations show a much faster depletion of HCl than simulated by current state-of-the-art models (ATLAS, CLaMS, WACCM, and TOMCAT/SLIMCAT) (Wohltmann et al., 2017; Grooß et al., 2018). This points to some unknown process that is currently not fully represented. There is only a minor impact of about 2% on the overall ozone column loss over the course of Antarctic winter and spring, however, because the HCl discrepancy and the associated underestimation of chlorine activation occur in early winter, when ozone loss rates are slow.

Reaction Kinetics

Canty et al. (2016) showed that the most recent recommendations for the kinetics that govern the partitioning of ClO and ClOOCl (put forth by the JPL panel) (Burkholder et al., 2015) are in extremely good agreement with the atmospheric observations of ClO and ClOOCl. The most important difference with respect to calculations that rely on older recommendations is

the temperature at which loss of ozone by the ClOOCl catalytic cycle terminates. The current recommendation (Burkholder et al., 2015) suggests that ClOOCl is less stable than previously assumed, resulting in an approximate 2 K downward shift in the termination temperature of polar ozone loss due to the ClOOCl catalytic cycle (Canty et al., 2016).

4.3.3 Very Short-Lived Halogenated Substances

Recent observations show that the atmospheric concentration of dichloromethane (CH_2Cl_2)—an ozone-depleting gas not controlled by the Montreal Protocol—is increasing (Leedham Elvidge et al., 2015; Hossaini et al., 2017; **Chapter 1** of this Assessment). The future evolution of atmospheric dichloromethane is uncertain, but for the present day (2015) the simulated contribution of dichloromethane to total inorganic chlorine in the polar lower stratosphere (100 hPa) is about 3% (Hossaini et al., 2017). Using atmospheric model simulations, Hossaini et al. (2017) show that the largest ozone decreases attributable to dichloromethane are simulated in the Southern Hemisphere. The impact of dichloromethane in these simulations is modest at the present time, with springtime zonal mean column ozone in the Southern Hemisphere up to 3%, or 6 DU, lower in simulations in which dichloromethane is considered (Hossaini et al., 2017).

Beyond dichloromethane, a number of very short-lived substances (VSLSs; for example, 1,2-Dichloroethane, $C_2H_4Cl_2$) have also been detected in Earth's atmosphere, although atmospheric measurements of these compounds are sparse (Hossaini et al., 2015a). While the major contribution to stratospheric chlorine from chlorine-containing VSLSs comes from dichloromethane, these other VSLSs also contribute. The additional chlorine loading from all chlorine-containing VSLSs in 2013 amounted to about 100 ppt (Hossaini et al., 2015a).

It is also important to account for the contribution of bromine-containing VSLSs to the stratospheric halogen loading (e.g., Frieler et al., 2006). Recent CCM simulations of the evolution of the Antarctic ozone hole show a significant additional reduction of the total ozone column over the polar cap and better agreement with observations, when brominated VSLSs are considered (**Figure 4-11**, Braesicke et al., 2013; Yang et al., 2014; Sinnhuber and Meul, 2015; Oman et al., 2016; Fernandez et al., 2017). For instance, Sinnhuber and Meul (2015) found that due to the inclusion of VSLSs, up to 25% more ozone was destroyed locally in the southern polar lower stratosphere (60°–90°S) in October in the period 1979 to 1995, leading to a regional reduction of total column ozone by about 10% (October) due to bromine-containing VSLSs. Compared to OMI satellite measurements, Oman et al. (2016) obtained better agreement in the very low ozone concentrations in the deep Antarctic lower stratospheric polar vortex during late September to early October from the late 1990s to the early 2000s when bromine from natural VSLSs was considered in their model. At the time of maximum chlorine loading around the year 2000, the 5 ppt of very short-lived Br_y increased the ozone hole area by about 40% (5 million km^2) and enhanced the ozone mass deficit by about 75% (8 million tons) (Fernandez et al., 2017, **Figure 4-11**). Although the strongest impact of bromine-containing VSLSs is in the Antarctic, there is also an impact on Arctic ozone levels in spring (e.g., Yang et al., 2014). However, it should be noted that the impact of bromine on stratospheric ozone occurs through the ClO/BrO–ClO chemical cycle and thus is only strong for enhanced stratospheric chlorine levels.

4.3.4 Polar Dynamical Processes

4.3.4.1 Dynamical Control of Polar Ozone

Year-to-year variability of stratospheric polar ozone is controlled by dynamical and chemical processes. Both are coupled to temperature changes which, in turn, are strongly influenced by wave activity (WMO, 2014). Recent studies of the dynamical contribution to temperature trends and ozone variability in Arctic spring essentially confirmed the important role of dynamics (Bohlinger et al., 2014; Bednarz et al., 2016; Ivy et al., 2016; Strahan et al., 2016). Ozonesonde measurements over Belgrano (Antarctica) show, for example, that the largest ozone depletion occurs in the coldest years (55–60% decrease of total ozone column in spring in the years 2000, 2003, and 2006), while the ozone loss in warm winters is smaller (20% in 2002 due to the Southern Hemisphere (SH) major sudden stratospheric warming) (Parrondo et al., 2014).

Planetary wave driving of the polar stratosphere is generally stronger and more variable in Northern

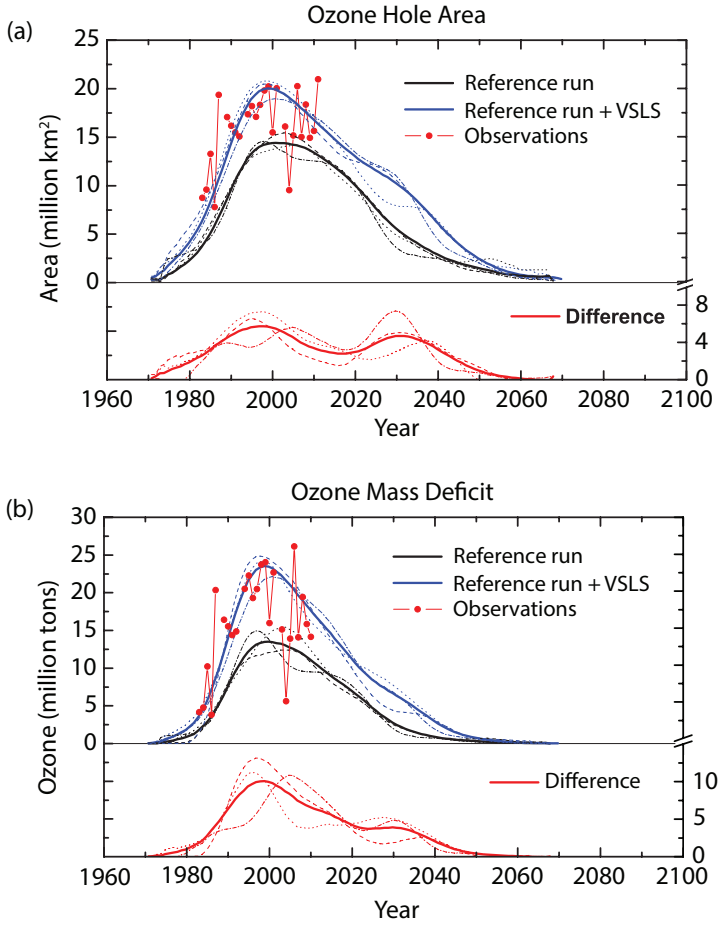

Figure 4-11. Temporal evolution of (a) the Antarctic ozone hole area and (b) ozone mass deficit for model experiments with the Community Atmosphere Model with Chemistry (CAM) without brominated VSLSs (black, reference) and with brominated VSLSs (blue, reference + VSLS) on the left axis, as well as the difference between runs (red) on the right axis. Solid thick lines show the ensemble mean for each experiment, while the dashed, dotted, and dashed-dotted thin lines correspond to each of the three independent simulations for each run. Red dots in the upper panels show observations. From Fernandez et al. (2017).

Hemisphere (NH) than in SH winter, leading to a warmer Arctic polar vortex and less chemical ozone depletion (see **Figures 4-1, 4-4, and 4-5**). In contrast, in austral winter and spring, Antarctic lower stratospheric temperatures are low enough for continuing heterogeneous ozone depletion, as the Antarctic vortex is much less disturbed by wave forcing (WMO, 2014; Solomon et al., 2014). The inter-hemispheric differences in the relationship between wave activity and the spring-to-fall ozone ratio are illustrated in **Figure 4-12** (update of Weber et al., 2011 and Figure 3-13 in WMO, 2014). **Figure 4-12** shows the compact linear relationship between the mean winter eddy heat flux at 100 hPa and the spring-to-fall high-latitude ozone ratio, combining data from both hemispheres. The winter eddy heat flux is consistently lower in the SH than in the NH. As a result, chemical ozone loss dominates in the SH lower stratosphere, and ozone values are lower in spring than in fall (except for 2002 and 2017). In contrast, the larger NH eddy heat flux leads to enhanced transport of ozone throughout the winter. As shown in **Figure 4-12**, this relationship held for all Antarctic and Arctic winters since the last Assessment, including the year 2015 (with the eruption of the Chilean volcano Calbuco enhancing Antarctic ozone depletion (see **Section 4.2.3.1**) and the northern winter 2015/2016 (see **Section 4.2.4.1**).

4.3.4.2 Refined Understanding of Dynamical Variability

The mechanisms involved in the generation, propagation, and dissipation of planetary waves are well known from theoretical, observational, and modeling approaches. Nevertheless, our understanding of the processes that determine the degree and interannual variability of wave driving of the polar stratosphere is still incomplete (WMO, 2014). Investigating the sources of interannual variability of wave activity in the stratosphere is still an intense area of research. The following sections report on advances since the last Assessment.

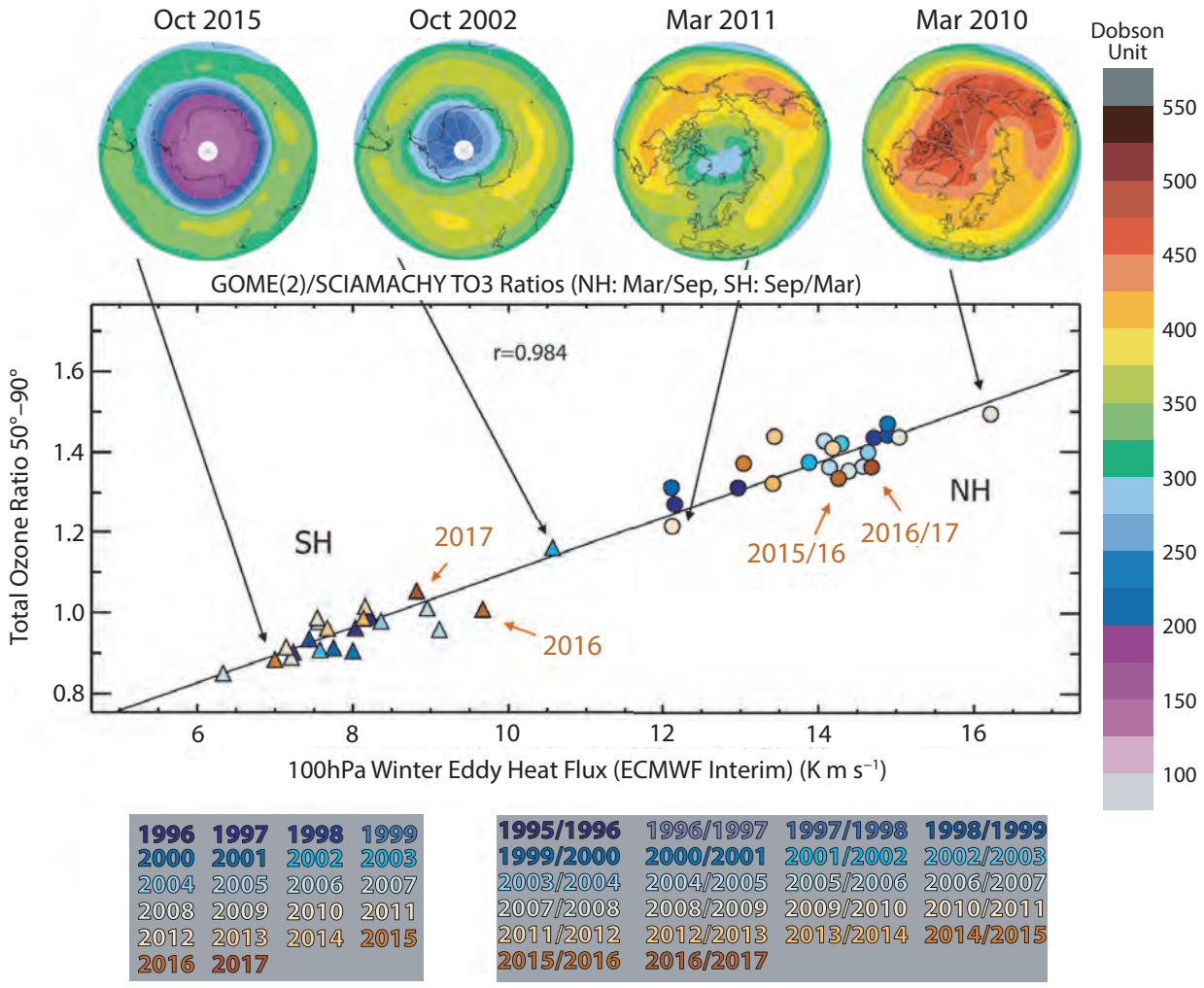

Figure 4-12. Spring-to-autumn ratio of observed high latitude total ozone (>50º latitude) as a function of the absolute extratropical winter mean eddy heat flux (September to March in the Northern Hemisphere and March to September in the Southern Hemisphere) derived from ECMWF ERA-Interim data. Data from the Southern Hemisphere are shown as triangles (September over March ozone ratios) and from the Northern Hemisphere as solid circles (March over September ratios). Polar total ozone distributions for select years are shown at the top. Updated from Weber et al. (2011).

Sources of Dynamical Variability: SSTs and ENSO

Since van Loon and Labitzke (1987), it is well known that variations in sea surface temperatures (SSTs) lead to anomalous stratospheric polar vortices, affecting stratospheric polar ozone. Recent studies have refined previous work by addressing in more detail the underlying mechanisms linking SST anomalies to stratospheric polar vortex variability, the role of the location of SST anomalies and differences in the impact of SSTs on the Arctic and Antarctic polar vortices and on stratospheric ozone.

SST anomalies generate anomalous upward wave flux into the stratosphere. Hence, increasing global SSTs and their latitudinal gradients modulate the polar vortices through an enhancement of the Brewer-Dobson circulation in both hemispheres. While globally uniform SST changes have a stronger impact on the Southern Hemisphere, changes in the SST gradients affect the Arctic vortex more significantly. This asymmetry is due to differences in the properties and transmission of the waves in both hemispheres (Hu et al., 2014).

Moreover, depending on the longitudinal position of the SST anomalies, they can either enhance or weaken upward wave propagation into the stratosphere through positive or negative interference with the climatological wave patterns. Hemispheric differences in the extratropical impact of regional tropical SST anomalies have been linked to differences in transient eddy forcing and stationary wave activity between the hemispheres (Li et al., 2010). Thus, higher SSTs in either the tropical Eastern Pacific Ocean (e.g., Calvo et al., 2017) or the North Atlantic (Omrani et al., 2014), or lower SSTs in either the North Pacific (e.g. Hurwitz et al., 2012) or the Indian Ocean (Fletcher and Kushner, 2011) lead to a weaker Arctic polar vortex. Using satellite observations and reanalysis data, Tian et al. (2017) reported a high correlation between SSTs in the East Asian marginal seas and lower stratospheric ozone over Antarctica in austral spring, with high SSTs reducing planetary wave activity in the SH, strengthening the stratospheric polar vortex, and thereby enhancing chemical ozone loss (with the opposite effects for low SSTs). According to their model simulations, ~17% of the decline of Antarctic lower stratospheric ozone between 1955 and 2005 may be associated with increasing SSTs over the marginal seas of East Asia.

Recent studies of the El Niño–Southern Oscillation (ENSO) highlighted the role of the location of the strongest SST anomalies (i.e., in the Eastern Pacific [EP] or the central Pacific [CP]) for the effects of ENSO on polar ozone. 'Canonical' EP El Niño events tend to weaken the polar vortex (e.g., Calvo et al., 2017 and references therein) and enhance stratospheric column ozone at high latitudes (e.g., Cagnazzo et al., 2009), while during La Niña events (characterized by negative SST anomalies in the central-eastern Pacific area), a stronger and colder polar Arctic vortex is observed (Iza et al., 2016), implying a reduced polar total ozone column. Compared to canonical El Niño events, CP El Niño events are more effective in the Antarctic where they lead to higher stratospheric temperatures and ozone in the lower stratosphere during austral summer and autumn (Zubiaurre and Calvo, 2012; Evtushevsky et al., 2015). However, the effects of CP El Niño on the Arctic stratosphere are still under debate (Hurwitz et al., 2014).

Dynamical Variability in NH Stratospheric Winters

Sudden stratospheric warmings (SSWs) in northern winter are induced by anomalously strong upward wave propagation from the troposphere and dissipation in the middle and high latitudes of the stratosphere. They weaken the polar vortex, warm the polar stratosphere, and enhance the Brewer-Dobson circulation (BDC) (e.g., Andrews et al., 1987; Charlton and Polvani, 2007). Since the previous Assessment, a growing number of studies investigated the impact of SSWs on polar processes and polar ozone. The enhanced temperature and BDC around the SSW date lead to a reduction of ozone loss and more ozone transported towards the pole (e.g., Strahan et al., 2016; Manney et al., 2015b; Damiani et al., 2014; Tao et al., 2015). In addition, meridional mixing increases during and after SSWs although its impact on ozone is not clear due to large case-to-case variability (Tao et al., 2015; Damiani et al., 2014; Manney et al., 2015a; Manney and Lawrence, 2016).

By comparing simulations with a CTM driven with observed meteorological conditions with and without heterogeneous chemistry, Strahan et al. (2016) quantified the chemical ozone depletion over the Arctic cap for the recent past (2005–2015). They showed that the linear relationship between the chemical ozone loss rate and the number of days cold enough for PSC particle formation within the polar vortex, found in earlier studies (Rex et al., 2004, 2006; Tilmes et al., 2003), still holds. While enhanced chemical ozone loss takes place in an undisturbed, cold, and stable polar vortex, the occurrence of a major SSW in mid-winter limits the number of cold days. As a result, ozone depletion in winters with a stable and cold polar vortex is roughly three times greater than in winters with a major SSW before mid-February. With five cold Arctic winters (2005, 2007, 2008, 2011, and 2014) and six winters with SSWs occurring in the period 2005–2015, a large part of the interannual variability of Arctic ozone over this period is explained (correlation of 0.97 between the maximum seasonal Arctic cap column ozone depletion and the number of cold days) (Strahan et al., 2016). Ozone loss in cold Arctic winters can additionally be amplified by high water vapor mixing ratios in the lower stratosphere, further increasing the probability of PSC formation and effective heterogeneous chlorine activation, as derived by Khosrawi et al. (2016) from satellite observations.

Particularly strong SSWs may perturb the mesosphere for many weeks. These events are characterized by an elevated stratopause which forms at pressure levels as high as 0.5 Pa (~70 km) about 10–14 days after the peak of the SSW. During the recovery phase of such elevated stratopause events, observations show a strong descent of polar mesospheric NO_x-rich air into the stratosphere (e.g., Pérot et al., 2014; Orsolini et al., 2017), inducing polar Arctic upper stratospheric ozone loss.

Recently, Siskind et al. (2016) proposed a new mechanism by which dynamical variability in northern spring may affect polar ozone in the following summer. In winters with strong mesospheric descent that are followed by dynamically quiet spring seasons (as in boreal winter 2009), relatively low values of CH_4 and high values of ClO may persist in the upper stratosphere throughout the summer. In 2009, these variations caused up to a 5% reduction in upper stratospheric ozone throughout the summer and early fall.

Downward Planetary Wave Reflection

As discussed in the previous section, the upward propagation and dissipation of planetary waves is *the* important driver of the BDC in the boreal winter stratosphere and largely determines the dynamical resupply of Arctic ozone in winter and spring. However, the overall effect of the planetary wave forcing on Arctic ozone levels in midwinter and spring not only depends on the tropospheric planetary wave sources but also on the stratospheric conditions for wave propagation, as highlighted in a recent CCM study by Lubis et al. (2017). Downward planetary wave reflection may occur in the stratosphere when upward pulses of wave activity decelerate the flow in the upper stratosphere, forming a downward-reflecting surface that redirects waves back to the troposphere (e.g., Harnik and Lindzen, 2001). These types of events lead to a weaker BDC and a colder polar vortex. Thus, there is a direct effect by planetary wave reflection on ozone due to transport, such that less ozone is advected towards the polar region, and an indirect effect due to the induced lower temperatures in the polar vortex, which enhance heterogeneous chemical ozone loss (Lubis et al., 2017).

4.3.5 Other Factors Affecting Polar Ozone

4.3.5.1 Solar Variability by Energetic Particle Precipitation

In addition to the impact on global ozone by decadal variations in solar ultraviolet irradiance (see **Chapter 3.2.1.1**), polar ozone can be destroyed by energetic particle precipitation (EPP) resulting in total ozone loss up to 10–20 DU after strong solar proton events (SPEs) (Vogel et al., 2008). EPP is strongly linked to solar activity either directly by coronal mass ejections (CMEs) producing sporadically large fluxes of solar energetic particles or indirectly by the quasi-continuous impact of the solar wind on Earth's magnetosphere resulting in precipitation of energetic electrons (see e.g., the review by Mironova et al., 2015). The presence of EPP affects the ionization levels in the middle and upper polar atmosphere, leading to significant changes of the chemical composition including ozone (see e.g., the review by Sinnhuber et al., 2012).

Solar proton events caused by CMEs are particularly frequent around the maximum of the solar cycle. A recent intercomparison study demonstrated the overall ability of specialized atmospheric models to reproduce the direct EPP effect by solar protons after the 2003 "Halloween" SPE in late October and early November 2003 (Funke et al., 2011). This event was characterized by short-term (days) mesospheric ozone depletions up to 70%, followed by longer-lasting (weeks to months) depletions of up to 35% in the upper stratosphere. After the "Halloween" event, which has been discussed in detail in WMO (2006), SPE-related composition changes of smaller magnitude have also been observed and modeled in other occasions, namely in November 2004 (Hocke, 2017), January 2005 (Jackman et al., 2011; Verkhoglyadova et al., 2015), as well as in January and March 2012 (von Clarmann et al., 2013; Jackman et al., 2014; Päivärinta et al., 2016). A statistical investigation of average changes in ozone from sonde measurements following 191 SPEs from 1989 to 2016 was carried out by Denton et al. (2018). Their results indicate that SPEs are linked to a ~5–10% decrease in ozone at ~20 km altitude during the polar winter. The greatest decrease occurs ~10–20 days following SPEs with ozone depleted for ~30 days on average.

Energetic electron precipitation is associated with geomagnetic storms and occurs mainly in the polar

auroral and sub-auroral regions with an intensity being largest about two years after the maximum of the solar cycle. Precipitation from mid-energy and from auroral electrons affects the mesosphere (50–100 km) and the lower thermosphere (95–120 km), respectively. The NO_x produced by EPP at these altitudes is long-lived during polar winter and transported down into the stratosphere to altitudes well below 30 km. Satellite observations have provided clear evidence of this EPP indirect effect (IE) occurring in every polar winter with a magnitude modulated by the solar cycle (e.g., Randall et al., 2007; Hendrickx et al., 2015; Funke et al., 2016). The EPP-generated NO_y contributes to the polar winter NO_y column at 20–70 km by 10–40% in the Southern Hemisphere (SH) (see **Figure 4-13**, top panel) (Funke et al., 2014). Stronger wave activity in Arctic winters is responsible for the generally smaller and more variable contributions in the Northern Hemisphere (up to 30%). Recently, observational evidence of polar ozone losses due to the EPP IE has

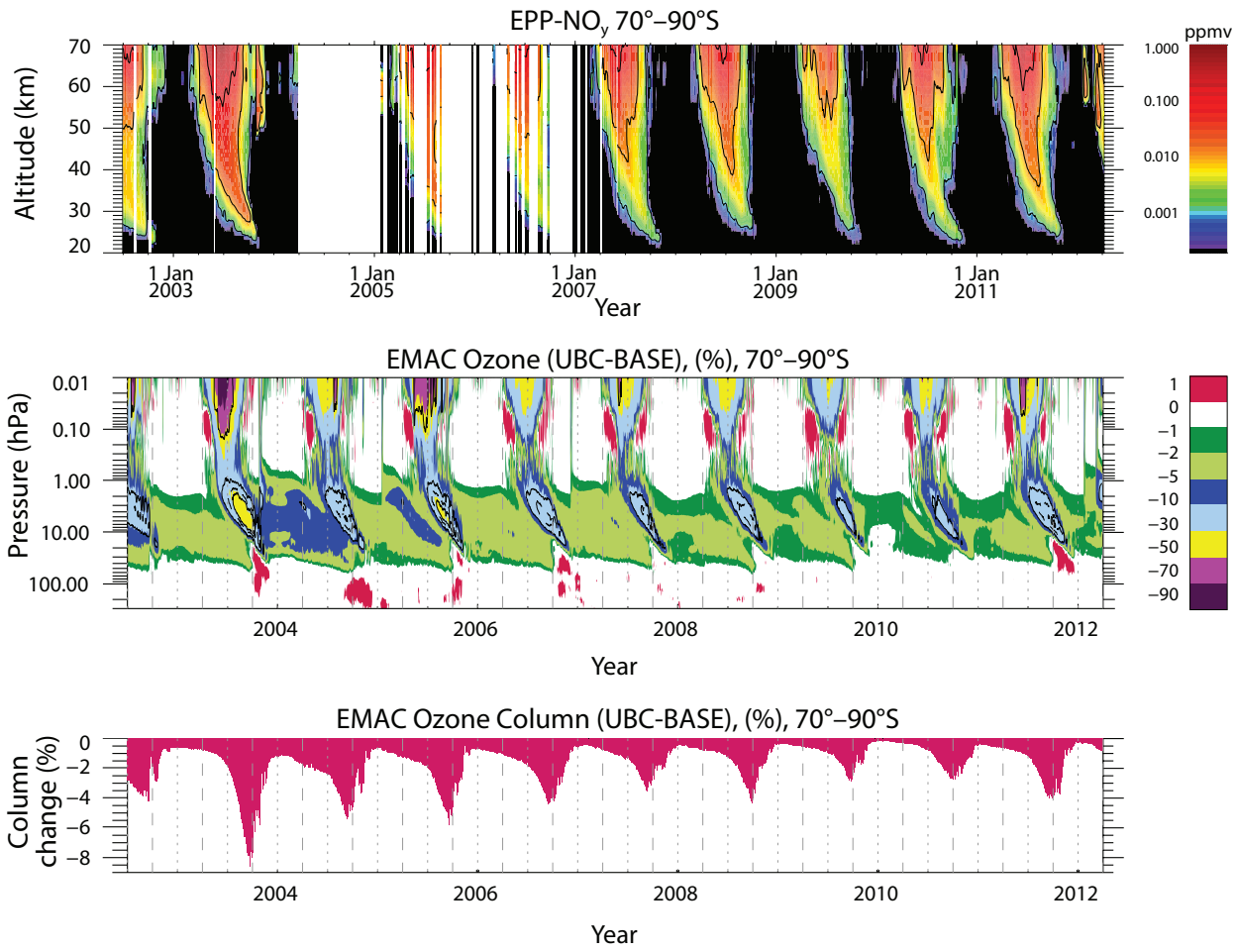

Figure 4-13. (*top*) Temporal evolution of the NO_y contribution produced by energetic particle precipitation (EPP-NO_y) (in ppmv) at 70°–90°S taken by the Michelson Interferometer for Passive Atmospheric Sounding (MIPAS) on board the Envisat satellite during 2002–2012. The contribution of EPP-NO_y has been discriminated from that produced by N_2O oxidation using a tracer correlation method based on MIPAS CH_4 and CO observations. (Adapted from Funke et al., 2014). (*middle and bottom*) Ozone loss due to EPP as a function of pressure level (*middle*) and for the total ozone column (*bottom*) at southern high latitudes (70°–90°S). Shown is the percentage difference between EMAC model simulations with and without EPP impact. The EPP effect is prescribed as an upper boundary condition of NO_y based on MIPAS observations; solar proton events (e.g., in October/November 2003 or January 2005) are prescribed by modeled ionization rates. Adapted from Sinnhuber et al. (2018).

been provided: SH polar stratospheric ozone loss due to the EPP IE peaks around 30–40 km in late winter with an average magnitude of about 10–15% (Fytterer et al., 2015; Damiani et al., 2016). Chemistry–climate models accounting for the EPP IE are able to reproduce the observed effects reasonably well. Forced by EPP-induced NO_y anomalies from satellite data between 2002 and 2012, Sinnhuber et al. (2018) show a recurring average decrease in Antarctic total column ozone around 4% in each winter/spring (ranging between 2% and 3% in 2009 and 2010, and 8% in 2003; see **Figure 4-13,** middle and bottom panel, adapted from Sinnhuber et al., 2018). Although the decrease in total column ozone by EPP-generated NO_y is less than one-tenth of the halogen-induced ozone depletion in the Antarctic polar vortex (see Figure 2-29 in WMO, 2010), the EPP effect needs to be considered in models to simulate realistic total ozone columns in polar winter. However, most CCMI models do not yet incorporate the effects of EPP-generated NO_y on polar ozone loss.

4.3.5.2 Volcanic Eruptions

Sulfate aerosols increase in the stratosphere after volcanic eruptions, providing surfaces on which heterogeneous chemical reactions occur favoring ozone loss (Hofmann and Solomon, 1989). In addition, volcanic aerosols also reduce polar ozone by an indirect dynamical mechanism through radiative heating of the lower stratosphere which increases the equator-to-pole temperature gradient. This leads to a strengthening of the polar vortex—either by thermal wind balance (Kodera, 1995) or reduced planetary wave forcing (Bittner et al., 2016)—and thus to more ozone loss.

While some climate models are able to reproduce the robust response of the polar vortex to volcanic eruptions (Pitari et al., 2016; Muthers et al., 2015; Raible et al., 2016), others are not (Driscoll et al., 2012; Charlton-Perez et al., 2013; Toohey et al., 2014), or their response depends on the size of the eruption (Bittner et al., 2016). The reasons for these discrepancies are still not well understood. Some models tend to overestimate the warming of the tropical stratosphere and thus magnify the polar dynamical response (Muthers et al., 2015). Moreover, the polar vortex response seems to be very sensitive to the spatio-temporal distribution of the volcanic forcing (Toohey et al., 2014) and also to the choice of the ozone climatology in climate models without interactive chemistry (Muthers et al., 2014).

While no major volcanic eruptions comparable in size to Mt. Pinatubo have occurred since 1991, satellite measurements revealed further injections of volcanic SO_2 into the stratosphere by a number of moderate eruptions at different latitudes during the past decade (WMO, 2011; Carn et al., 2016). Solomon et al. (2016) showed that including the SO_2 emissions from these moderate eruptions in specified-dynamics CCM simulations enlarged the size of the modeled Antarctic ozone hole in September and led to better agreement with the observed ozone hole. Moreover, they found about a 10% reduction of the modeled post-2000 healing of the Antarctic ozone hole in September as a result of the chemical effects of increased volcanic activity in the latter part of 2000–2014. Likewise, observations from ozonesondes and the Aura MLS suggest that stratospheric volcanic particles from the 2015 eruption of the Chilean volcano Calbuco enhanced Antarctic ozone depletion and contributed to the record-large Antarctic ozone hole in October 2015 (Stone et al., 2017) (see also **Section 4.2.3.1**). This ozone loss after volcanic eruptions is driven by heterogeneous chemical processes associated with SO_2 emissions, while radiative and dynamical feedbacks only play a minor role (Ivy et al., 2017).

A further potential impact of explosive volcanic eruptions on stratospheric ozone is the direct injection of halogens into the stratosphere. Recent developments in measurement technology allowed for improved estimates of halogen ejections from large historical eruptions (Kutterolf et al., 2015). As these substances are diluted on their transport from the troposphere to the stratosphere through scavenging by hydrometeors (Tabazadeh and Turco, 1993), estimates of the injection efficiency into the stratosphere vary widely for individual eruptions. Nevertheless, direct injections of significant quantities of volcanic halogens have recently been confirmed by remote sensing: MLS recorded stratospheric $HCl:SO_2$ ratios of 0.01–0.03 for 14 eruptions spanning the years 2005 to 2014 (Carn et al., 2016). Based on petrological constraints, Cadoux et al. (2015) found that the Late Bronze Age 'Minoan' eruption of the Santorini volcano released far more halogens than sulfur. Even if only 2% of these halogens had reached the stratosphere, they would have

resulted in reductions in ozone columns of 20% to >90% at northern high latitudes.

Recent Assessments have not considered the impact of the volcanic halogen loading on stratospheric ozone partly because of the large uncertainties in its magnitude and also because this process was determined to be small compared to anthropogenic halogen loading after the eruptions of El Chichón (in 1982) and Mt. Pinatubo (in 1991). However, volcanic halogens are expected to become more relevant in the future as anthropogenic halogens decline. The response of the total ozone column to the injection of SO_2 results from two chemical regimes causing opposite ozone changes: (1) in the lower stratosphere (pressures >30 hPa), heterogeneous chemistry on sulfate aerosol surfaces leads to chlorine activation and ozone depletion and (2) in the upper stratosphere (pressures <30 hPa), catalytic ozone depletion in the NO_x cycle is suppressed (Tie and Brasseur, 1995). Hence, in an atmosphere with low chlorine levels, such as in the era before industrial halogen production, upper stratospheric chemistry dominates and the total polar ozone column is expected to increase after volcanic eruptions (WMO, 2014; Muthers et al, 2015). Similarly, in the future, when anthropogenic halogen is expected to decrease, major volcanic eruptions that inject SO_2 into the stratosphere may cause an ozone increase (e.g., Naik et al., 2017). However, Klobas et al. (2017) found that in a future medium Representative Concentration Pathway RCP-6.0 GHG scenario there is still significant net loss of total column ozone after volcanic SO_2 emissions after mid-century. With increasing GHG concentrations, the post-volcanic chemical ozone depletion weakens due to stratospheric cooling and increased methane concentrations (Klobas et al., 2017; Naik et al., 2017). Klobas et al. (2017) further show that in a future low-halogen environment, the presence in the stratosphere of bromine from natural, very short-lived biogenic compounds is critically important for determining whether future eruptions will lead to ozone depletion. The additional injection of volcanic halogens would induce substantial ozone reductions, particularly in polar regions. Projecting how future volcanic eruptions might affect stratospheric polar ozone remains highly uncertain due to the complex interactions between volcanic aerosols, rising GHG concentrations and VSLSs.

4.4 RECOVERY OF POLAR OZONE

4.4.1 Polar Ozone Recovery in Previous Assessments

WMO (2007) defined three stages of current and future stratospheric ozone recovery: (1) a slowing in the rate of ozone decline, (2) the onset of ozone increases above the previous minimum values (so-called "turnaround") due to declining EESC, and (3) full recovery from ODSs. WMO (2007) concluded that, while stabilization of Antarctic ozone levels had been observed at a similar time as the expected peak of EESC, due to the influence of both saturation of depletion and anomalously high temperatures, the attribution was inconclusive and it was therefore not possible to state that either the first or second stages of recovery had yet occurred. WMO (2007) also included predictions of a slow recovery of Antarctic total column ozone, with an increase in springtime ozone of 5–10% between 2000 and 2020, or 0.25–0.5% yr^{-1} (approximately 0.5–1 DU yr^{-1}) over that period.

WMO (2011) concluded that the leveling off of Antarctic stratospheric ozone since the late 1990s could be attributed to the slight decline in Antarctic stratospheric ODSs, based on the analysis of Yang et al. (2008).

WMO (2014) discussed recovery of Antarctic springtime stratospheric ozone in more detail. Further studies of both vertically resolved and total column ozone had been published since WMO (2011), generally making use of multiple linear regression methods to account for non-chemical effects. It was concluded that Antarctic total column ozone appeared to have started to increase since reaching a minimum at the beginning of the 21st century and that the rate of increase appeared consistent with declining ODSs. The definitive conclusion that Antarctic stratospheric ozone was increasing due to declining ODSs could not yet be reached, however, due to uncertainties in measurements and statistical methods.

Compared to the Antarctic, the Arctic shows larger interannual variability in springtime ozone and smaller ozone depletion, and detection of changes in ozone due to decreases in EESC are therefore expected to take longer than in the Antarctic. WMO (2007) reported that no slowing of the decline in Arctic stratospheric ozone had yet been found. WMO

(2011) and WMO (2014) both reported little progress in assessing Arctic stratospheric ozone recovery since WMO (2007).

4.4.2 Long-Term Antarctic Ozone Trend

4.4.2.1 Onset of Antarctic Ozone Depletion

As noted in previous Assessments, the general choice of 1980 as the reference year for ozone levels should not be taken to mean that there was no anthropogenic ozone depletion in Antarctica prior to that year. Comparing simulations from 17 CCMVal-2 models with total column ozone measurements from four long-term Dobson sites in the Antarctic (Faraday, Halley, South Pole, and Syowa) combined with measurements from multiple space-based instruments (Bodeker et al., 2005), it was estimated that about half of the ozone loss attributable to halogens between 1960 and 2000 actually took place before 1980 (Langematz et al., 2016). Updated results of this study for more years of observations and new CCMI model simulations are shown in **Figure 4-14**. The observed halogen-induced, pre-1980 Antarctic spring total ozone depletion reaches about 54% of that in the 1960–2000 period, comparable in size to the previous estimate. Similar to the CCMVal-2 models, the CCMI models slightly underestimate the observed estimate, with a comparable spread in both model groups.

4.4.2.2 Onset of Antarctic Ozone Recovery

Since WMO (2014), several studies have taken advantage of the increasing length of record to identify parameters that quantify various aspects of ozone loss, which show a positive trend in ozone (i.e. a decrease in ozone depletion) since the year 2000. Different sources of data have been used to derive these parameters, such as ozonesondes or ground-based data from the global Dobson and Brewer networks. Merged multi-year ozone time series were generated from different satellite instruments, which allowed the quantification of long-term trends in total column ozone and vertical ozone profiles before and after the turnaround of Antarctic EESC. More details of the applied ozone data sets are given in the respective studies

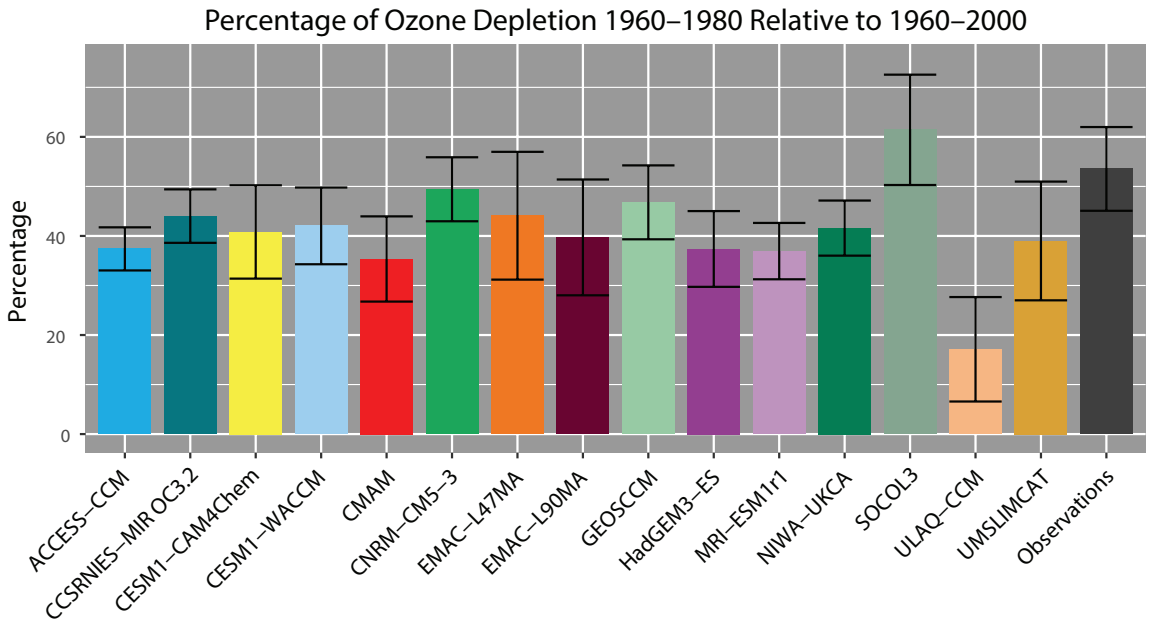

Figure 4-14. Halogen-induced Antarctic ozone depletion in September to November for the period 1960–1980 in % of the depletion for the period 1960–2000 in CCMI simulations and observations. Uncertainties of 1σ were derived by applying error propagation rules. For the analysis, the extended observational data base until 2016 (Bodeker et al., 2005) has been used. Adapted from Langematz et al. (2016).

listed in **Table 4-1**. From these ozone observations, long-term changes in Antarctic ozone were derived by applying various mathematical methods that provide estimates of trends in a number of ozone parameters (e.g., total column ozone, ozone within the particular height range at which depletion has previously been greatest, or metrics used to describe the severity of the Antarctic ozone hole) for specific Antarctic locations (e.g., Antarctic ground-based or ozonesonde stations or polar cap (60°–90°S) average) and season (e.g., September, October, or September to November average) and trend periods (i.e., different starting and finishing years). **Box 4-1** describes in more detail the methods applied to calculate Antarctic ozone trends.

Although the recent studies have differed in their approaches, they have found broadly consistent results. **Table 4-1** gives an overview of some of the identified trends discussed in the following subsections, including the ranges of uncertainty. It should be noted that the table only gives a subset of results, with most of the studies reported on having also considered additional or differently defined parameters and variations of method such as filtering criteria. There is consensus among all studies that, particularly in the month of September, several metrics of Antarctic ozone have shown reductions of depletion in the years following the peak in EESC. In contrast, in October, no significant trends in metrics of Antarctic ozone have been found to this time.

Individual studies find positive trends in Antarctic total column ozone in September that are significant at the 90% or 95% confidence levels (e.g., Solomon et al. 2016; Kuttipurath and Nair, 2017), while other metrics do not yield trends significant at the 2σ level. Apart from the impact of dynamical variability, uncertainties in derived trends arise from the formulation of the regression model, the use of different proxies, and the time period of the trend (Knibbe et al., 2014; de Laat et al., 2015; Chipperfield et al., 2017; Weber at al., 2018). Other factors not incorporated in the purely statistical uncertainty range include possible drifts in the observational data sets (Hubert et al., 2016), the procedures used to merge and homogenize data records from different instruments (e.g., Hassler et al., 2014; Frith et al., 2017), or the representativeness of sparse ground-based data particularly in light of changes to the structure of the vortex over time (Hassler et al., 2011a).

Total Column Ozone

Total column ozone over Antarctica in springtime has increased since 2000 at a mean rate estimated to be between 5 and 10% decade^{-1}, approximately equivalent to 1–2 DU yr^{-1} (Knibbe et al., 2014; Solomon et al., 2016; Kuttipurath and Nair, 2017; Chipperfield et al., 2017; Weber et al., 2018; Pazmiño et al., 2018).

Solomon et al. (2016) found a positive trend in total column ozone in the month of September over the period 2000–2014 as measured by ozonesondes at South Pole of 2.5 ± 1.5 DU yr^{-1}, and SBUV measurements over the polar cap (as available) of 2.5 ± 1.6 DU yr^{-1}, with both ranges at the 90% confidence level. These results are in good agreement with Pazmiño et al. (2018) who derived total column ozone trends inside the Antarctic polar vortex ranging between 1.85 and 2.67 DU yr^{-1} depending on the methods and data sets over the 2001–2016 period. Their trends are statistically significant at the 2σ level. Kuttippurath and Nair (2017) found a positive trend in September to November total column ozone of 1.72 to 1.80 ± 0.80% yr^{-1} (95% confidence level), depending on how the vortex is defined, over the period 2001–2013. The value of the calculated trend was not greatly sensitive to the choice of proxies.

Knibbe et al. (2014) derived a range of positive total column ozone trends depending on the inflection year in their piecewise linear trend (PWLT) analysis. Using 2001 (i.e., the year with maximum EESC over the SH polar cap), they found an increase of 3.1 ± 5.8 DU yr^{-1} for the period 2001–2010. The trend was, therefore, not statistically significant at the 95% confidence level.

More recently, Chipperfield et al. (2017) and Weber et al. (2018) both derived independent linear trends (ILTs) for September in Antarctica. Chipperfield et al. (2017) calculated the September Antarctic (60°–90°S) trend from 2000 to 2015 to be 4.7 ± 9.1% decade^{-1} using NASA SBUV data, while Weber et al. (2018), using five merged data sets from satellite and ground-based observations, found the 2000–2016 trend in September across the five data sets ranged between 8 to 10% decade^{-1} with a 2σ uncertainty of 7%. By contrast, the trend in October was only 3% decade^{-1} and not statistically significant (**Figure 4-15**). The fact that these two studies used almost the same data sets and similar methods but determined different results

Table 4-1. Trends in a selection of metrics of Antarctic ozone in spring since 2000 (the year with maximum halogen loading), derived from various data sets and using a variety of analysis methods. **Box 4-1** gives descriptions of the methods used. Note that only a subset of the results for the polar regions of each study are shown, each of which also considered additional parameters not shown here.

Parameter	Data Source	Trend	Confidence Level	Time Period	Method	Reference
TOTAL COLUMN OZONE						
Total column ozone September–November Antarctic	MSR + SCIAMACHY	3.1 ± 5.8 DU year^{-1}	±2σ	2001–2010	MLR (PWLT)	Knibbe et al. (2014)
Total column ozone September South Pole	Ozonesondes	2.5 ± 1.5 DU year^{-1}	90%	2000–2014	Linear trend excluding 2002	Solomon et al. (2016)
Total column ozone September, south of 63°S	SBUV	2.5 ± 1.6 DU year^{-1}				
Total column ozone locations of Antarctic stations September–November	TOMS/OMI	1.72-1.80 ± 0.8 % year^{-1}	95%	2001–2013	MLR (PWLT) with vortex filtering	Kuttipurath and Nair (2017)
Total column ozone September, 60°–90°S	NASA SBUV	4.7 ± 9.1 % decade^{-1}	±2σ	2000–2015	MLR (ILT)	Chipperfield et al. (2017)
Total column ozone September, 60°–90°S	Merged satellite data and WOUDC	8.1–10.1 ± 7 % decade^{-1}	±2σ	2000–2016	MLR (ILT)	Weber et al. (2018)
Total column ozone 15 September–15 October Antarctic vortex	MSR-2	1.42 ± 0.92 DU year^{-1}	±2σ	2001–2017	MLR (PWT) with vortex filtering	Pazmiño et al. (2018)
VERTICALLY RESOLVED OZONE						
Ozone mixing ratio September–November Antarctic vortex	Ozonesondes	Up to 8 % year^{-1}, significant between 325 and 550 K levels	95%	2001–2013	MLR (PWLT) with vortex filtering	Kuttipurath and Nair (2017)
Ozone partial column September South Pole, Syowa	Ozonesondes	"Clear increase" from 100 to 50 hPa	90%	2000–2015	Linear trend excluding 2002	Solomon et al. (2016)
OZONE HOLE METRICS						
Ozone hole area late September in cold years	AURA-MLS	Smaller in 2008, 2011 due to decreased Cl_y	—	2004–2012	Linear relationship	Strahan et al. (2014)
Ozone hole area September	TOMS/OMI	–4.5 ± 4.1 million km^2	90%	2000–2015	Linear trend excluding 2002	Solomon et al. (2016)
Ozone hole mass deficit between days 220 and 280	MSR-2 +GOME-2	–0.77 ± 0.17 Mt year^{-1}	±2σ	2000–2015	Linear trend 6 warmest years filtered	de Laat et al. (2017)
Ozone hole mass deficit 15 September–15 October	MSR-2	–0.68 ± 0.37 Mt year^{-1}	±2σ	2001–2017	MLR (PWT) with vortex filtering	Pazmiño et al. (2018)

Box 4-1. Methods Applied to Calculate Polar Ozone Trends

- ***Linear Trend***

  Linear trends since the year 2000 were used by Solomon et al. (2016), with the extreme year of 2002 filtered out. Similarly, de Laat et al. (2017) calculated a linear trend since 2000, after removing the six warmest years of the 1979–2015 record (1986, 1988, 2002, 2004, 2010, and 2012).

- ***MLR (Multiple Linear Regression)***

  Multiple linear regression is the most commonly used method to calculate the Antarctic ozone trend remaining after removing the influence of known sources of variability, such as eddy heat flux, solar variability, the Quasi-Biennial Oscillation (QBO), El Niño–Southern Oscillation (ENSO), and stratospheric aerosol loading. The significance of the resulting trend is sensitive to the choice of proxies used to represent physical processes, and the choices of spatial and temporal averaging and time period (de Laat et al., 2015). In previous Assessments, EESC was often used as a regressor variable.

- ***MLR with PWLT (Piecewise Linear Trends)***

  Following Kuttippurath et al. (2015), who warned that the fit of EESC to ozone time series was determined mostly by the years prior to turnaround, and therefore could result in an inaccurate recovery trend, fits to EESC are not used in this Assessment. Regression using PWLT instead fits two linear trends to the ozone time series before and after an appropriate "turnaround" year, usually either 2000 or 2001. The trends are constrained to give a common value at the turnaround year. PWLT was used by Knibbe et al. (2014).

- ***MLR with ILT (Independent Linear Trends)***

  Independent linear trends differ from PWLT in that the two linear trends are not constrained to meet at a common value at the turnaround year. This introduces an additional degree of freedom to the regression. Both Chipperfield et al. (2017) and Weber at al. (2018) used ILT.

- ***MLR with PWT (Piecewise Trends)***

  The "modified PWLT" model used by Pazmiño et al. (2018) is similar to ILT, but instead joins the two linear trends with a parabolic curve. This allows an overall improved regression result, as EESC and ozone show a non-linear growth rate around the period of the EESC peak.

reflects the uncertainty of the multiple linear regression method—in this case, the results show some sensitivity to the length of the time period and the treatment of the proxies.

Vertically Resolved Ozone

WMO (2014) reported the results of Hassler et al. (2011b) showing that ozone loss rates in springtime (measured by ozonesondes at South Pole between 100 and 40 hPa) had reached a maximum in the period 1991–1995 and had subsequently stabilized but had not shown any significant reduction between 2001 and 2010. The additional years of observational data from ozonesondes (Solomon et al., 2016; Kuttipurath and Nair, 2017) and Aura MLS (Strahan and Douglass, 2018) do now show evidence that Antarctic ozone within this height range has significantly increased since the year 2000.

Solomon et al. (2016) studied ozonesonde measurements from Syowa and South Pole stations in the month of September. They found a statistically significant increase in ozone over the period 2000–2015

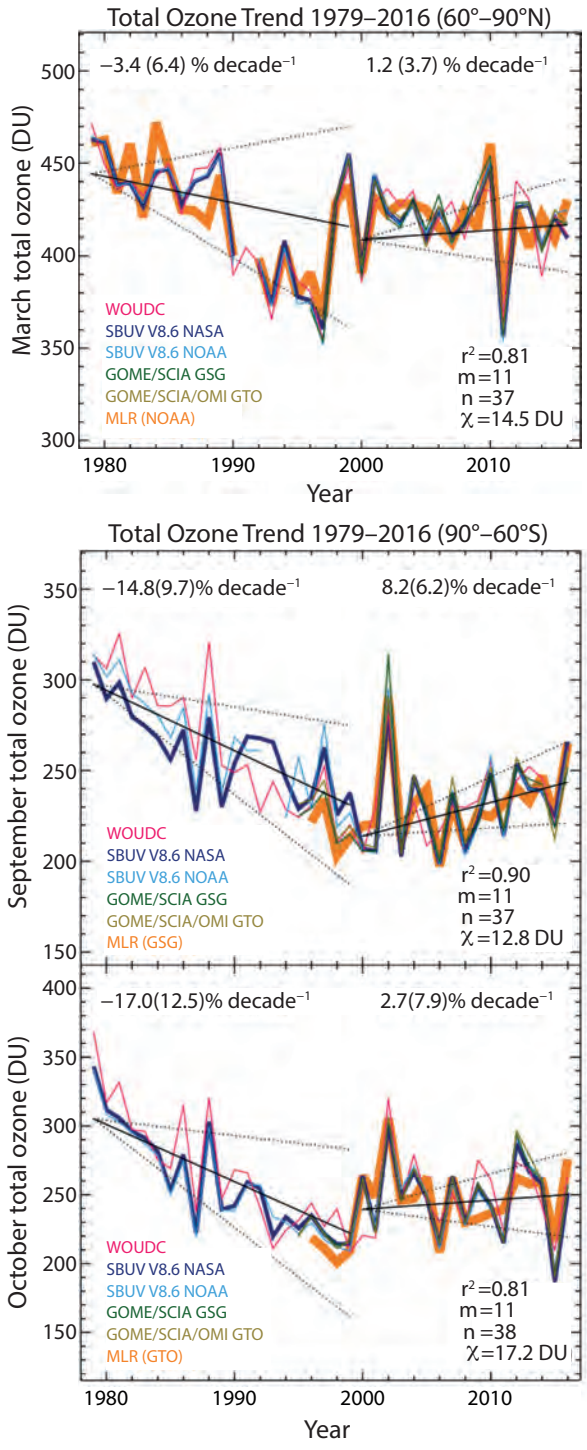

Figure 4-15. Total ozone time series for (*top panel*) the Arctic (60°–90°N) in the month of March and (*bottom two panels*) for Antarctica (60°–90°S) in the months of September and October, derived from five long-term observational data sets: WOUDC (based on the GAW network of ground-based Dobson and Brewer instruments), SBUV 8.6 processed by NASA, SBUV 8.6 processed by NOAA, GOME-SCIAMACHY-GOME-2(GSG) and GOME-type Total Ozone (GTO). In each panel, one data set has been chosen as labelled to show the results of applying a multiple linear regression with independent linear trends analysis (orange). Regressor terms include the solar cycle, QBO, ENSO, volcanic aerosol, and the strength of the Brewer-Dobson circulation. From Weber et al. (2018).

between 100 and 50 hPa, approximately half the size of the decrease measured in Syowa at this height between 1980 and 2000 **(Figure 4-16)**. Kuttipurath and Nair (2017) also found positive trends since 2001 reversing the pre-2000 vertically resolved trend using ozone profiles from ozonesonde stations distributed across Antarctica during the period 1979–2013 filtered according to their location as inside or outside of the Antarctic vortex at each altitude. For 2001–2013, they found the largest trends of up to 8% yr^{-1} around 15 km, with trends being significant at the 95% confidence level between approximately 12 and 22 km. Using simple linear trends without any dynamical or aerosol proxies gave similar results but increased the uncertainty of the trend, such that the trend was no longer significant over some of the height range.

Ozone Hole Metrics

Three metrics that have been widely used for many years to report on the state of the ozone hole from year to year are shown in **Figure 4-6**—the daily ozone hole area averaged from 21 to 30 September, the average of daily minimum ozone values from 21 September to 16 October, and the daily ozone mass deficit (OMD) averaged from 21 to 30 September. A fit of Antarctic EESC to each metric is also shown. It is apparent that all three metrics show a clear stabilization after the year 2000 when Antarctic EESC is calculated to have peaked, with the OMD showing both the greatest apparent turnaround since that date but also the largest variability. Note that in this figure, the fit has not taken into account dynamical variability, most evident for all three metrics in the year 2002 when the Antarctic vortex experienced an unprecedented major sudden stratospheric warming. Negative trends (that is, towards a smaller ozone hole) can now be seen in ozone hole area (Strahan et

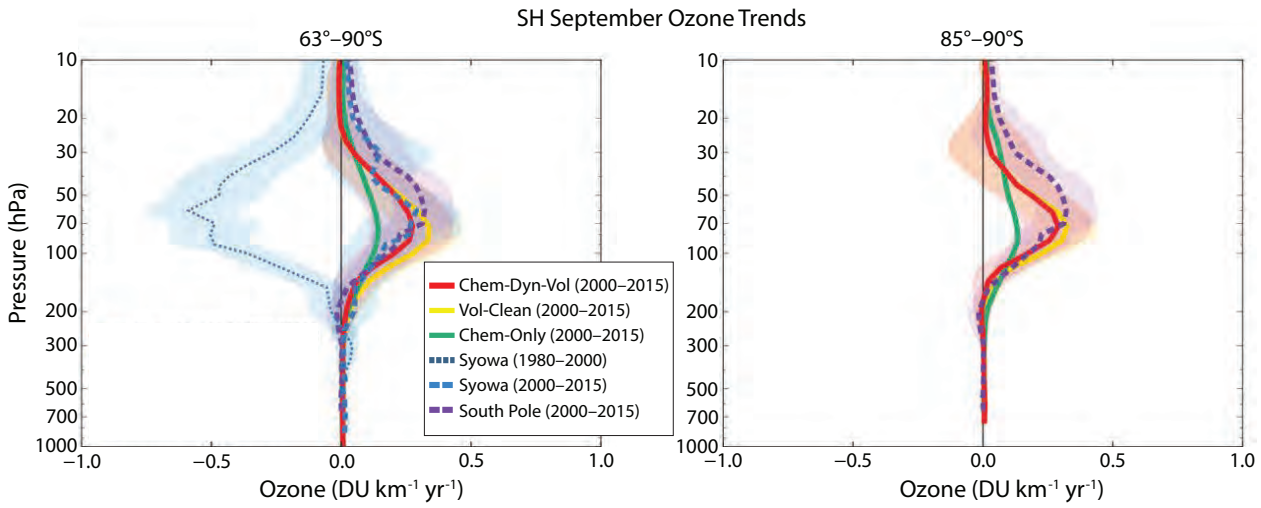

Figure 4-16. Trends in ozonesonde data from Syowa (69°S, 39.58°E) and South Pole stations with years as marked, with shading indicating the 90% confidence interval. Overlaid are model results from the WACCM model for regions 60°–90°S (*left*) and 85°–90°S (*right*) forced with different combinations of halogen changes ("chem"), specified dynamics ("dyn"), and injection of aerosols from volcanic eruptions ("vol"). (From Solomon, S., D.J. Ivy, D. Kinnison, M.J. Mills, R.R. Neely III, and A. Schmidt (2016), Emergence of healing in the Antarctice ozone layer, *Science*, *353* (6296), 269-274. Reprinted with permission from AAAS.)

al., 2014; Solomon et al., 2016) and ozone hole mass deficit (de Laat et al., 2017) once temperature fluctuations have been taken into account. The closeness with which particular ozone hole metrics follow the evolution of EESC varies with different choices of threshold and period of the year, due to saturation effects and, as already noted, the increased influence of dynamics in October compared to September (Solomon et al., 2016; Pazmiño et al., 2018).

Strahan et al. (2014) found that, comparing the ozone hole area in the very cold years of 2006, 2008, and 2011, the progressive reduction in size was proportional to declining EESC inferred from Aura MLS observations. Solomon et al. (2016) considered the size of the Antarctic ozone hole in September of each year, derived from TOMS/OMI data. From 2000 to 2015, the area decreased by 4.5 ± 4.1 million km^2.

The OMD between days 220 and 280 (from early August to early October) of each year was considered by de Laat et al. (2017) as derived from total column ozone measurements from multiple satellite instruments. Including all years in the trend, the decrease from 2000 to 2015 was 0.52 ± 0.50 Mt yr^{-1}. When excluding the six warmest years (1986, 1988, 2002, 2004, 2010, and 2012) from the record in order to remove the largest fluctuations caused by meteorological variability, the OMD decreased by 0.77 ± 0.17 Mt yr^{-1} (2σ). From 2000 to 2015, OMD defined in this way was estimated to have decreased about 30% from its peak value. Similar values were calculated using MLR with PWT (**Box 4-1**) by Pazmiño et al. (2018), who found a negative trend of OMD in September of 0.86 ± 0.36 Mt yr^{-1} since 2001, or 0.65 ± 0.33 Mt yr^{-1} if averaged over the period of maximum depletion, 15 September to 15 October.

Attribution to Decline in EESC

Attributing the trends in Antarctic ozone discussed in the previous sections to a decline in stratospheric halogen abundances is challenging, as the trend in EESC is small compared to the large variability in Cl_y due to transport, as derived from Aura MLS measurements between 2004 and 2012 (Strahan et al., 2014). Nevertheless, Strahan and Douglass (2018) using a longer Aura MLS data set until 2016, showed that vortex-averaged ozone loss (defined as the observed changes in partial column ozone between 261 and 12 hPa from July to mid-September) decreased over the 12-year data record because of the decline in lower stratospheric Cl_y levels. By analyzing ozone changes

over this seasonal average, dynamical contributions to ozone change are minimized.

Further evidence of a response of Antarctic ozone to declining ODSs was given by Solomon et al. (2016) by comparing measurements with CCM sensitivity simulations with different specified forcings. They showed (using model runs that held the dynamical conditions, temperatures, and volcanic aerosols constant at 1999 levels) about half of the lower stratospheric ozone increase in September observed between 2000 and 2014 was due to halogen decrease, with the remainder attributed to changes in dynamics and temperature (**Figure 4-16**). Likewise, the model results suggest that about half of the total column increase in September observed over that period is due to declining ODS levels (~ +1.3 DU yr^{-1}). The ozone hole was estimated to have decreased by 3.5 ± 0.3 million km^2 as the result of decreasing chlorine and bromine.

Further, Solomon et al. (2017) analyzed the seasonality of modeled and observed trends in Antarctic stratospheric ozone and stratospheric temperatures. The changes observed prior to 2000 were followed by oppositely signed changes after 2000 very similarly patterned in terms of season and altitude. These "mirrored" changes were largely able to be replicated by CCM runs only when forced with measured ODS levels, with a relatively small role being played by unforced dynamical changes. This finding is supported by de Laat et al. (2017) who found in their analysis of OMD in multi-sensor reanalysis (MSR) data that the ratio of pre- and post-2000 trends in OMD matched those in Antarctic EESC, seconded by regression results suggesting long-term changes in PSC volume and pre-winter ozone levels had played only minimal roles.

Modeling results (Solomon et al., 2017; Randel et al., 2017) suggest that observed changes in Antarctic ozone have significantly contributed to the observed cooling in Antarctic stratospheric springtime temperature from 1979 to the late 1990s and the subsequent warming trend to the present time. A component of the temperature variability discussed in the context of detecting ozone recovery should therefore be considered a feedback from EESC changes rather than being purely unforced.

4.4.2.3 Summary

While in the prior Assessment only two to three studies claimed to have found early signs of Antarctic ozone recovery, a number of studies has been presented since then. These used various new merged data sets and observations, including four more years since WMO (2014), as well as chemistry–climate model simulations to attribute the observed changes.

It is noteworthy that independent of the data set, time period, and analysis method, all studies derive trends in different metrics of Antarctic ozone of the same overall sign; i.e., they all show increasing total column ozone and ozone in the lower stratosphere, decreasing ozone hole area, and decreasing ozone mass deficit since about 2000 in Antarctic springtime. Some trends are statistically significant at the 2σ level, while others are either barely significant or not significant for various reasons, with differences arising for example from the applied regression model or the time period. However, it was found that the significance of the derived trends rises for the month of September when dynamical activity of the Antarctic polar vortex is small and chemical ozone depletion not saturated as in October. Particularly in the month of September, several metrics of Antarctic ozone have shown significant reductions of depletion in the years following the peak in EESC. By employing model simulations or other means, it has been shown that a portion of the positive trend in ozone can now be attributed to declining ODS levels. Therefore, it can now be concluded that the early signs of the second stage of Antarctic ozone recovery are becoming apparent.

4.4.3 Long-Term Arctic Ozone Trend

As stated in previous Assessments, detection of ozone recovery in the Arctic is much more difficult than the Antarctic, chiefly because of the much larger dynamical variability. Knibbe et al. (2014) analyzed spatial variations in monthly total column ozone for the period 1979–2012 in the Arctic but did not find any trend. Solomon et al. (2016) did not find statistically significant trends in springtime Arctic SBUV data (63°–90°N) for the period 2000–2014, with their model results suggesting the small positive trend expected from EESC decline is currently overwhelmed by dynamical effects. The study of Weber et al. (2018) described above found trends in the Arctic in March

were less than 1% decade^{-1} and not significant (**Figure 4-15**).

4.4.4 Benefits Achieved by the Montreal Protocol

By comparing model simulations using an uncontrolled growth of ODSs (unaffected by the Montreal Protocol) with simulations using ODS mixing ratios controlled by the Montreal Protocol, it is possible to identify how polar ozone would have developed in a "world avoided" with continuously growing ODS abundances. Moreover, the extent to which the polar ozone layer has already (in the recent past) benefited from the Montreal Protocol can be derived. CCM simulations assuming either a total chlorine loading of 9 ppbv for ~2025 or a growth rate of 3% yr^{-1} (leading to 9 ppbv in 2019) showed that uncontrolled growth in the emissions of ODSs would lead to ozone depletion in the coming decades much larger than projected for a controlled chlorine loading (Morgenstern et al., 2008; Newman et al., 2009; WMO, 2011; Garcia et al., 2012).

Chipperfield et al. (2015) used a state-of-the-art 3D chemistry transport model to investigate a "world avoided" scenario, comparing a simulation based on observed atmospheric ODS loading to one in which continued growth in ODS production of 3% yr^{-1} after 1987 is assumed (**Figure 4-17**). In Arctic winter 2010/2011, when the OMI satellite instrument shows a local ozone column of around 230 DU, the integration without Montreal Protocol regulation indicates a greatly reduced ozone column below 120 DU (**Figure 4-17e**). On 26 March 2011, a region of relatively low column ozone (250–275 DU) emerges in the observations (**Figure 4-17a**) and the model run with observed ODSs (**Figure 4-17b**). With the "world avoided" scenario, however, a further dramatic decrease in column ozone by up to 130 DU over a wide region of the Arctic occurs. Without the Montreal Protocol, a deep Arctic ozone hole would have developed in 2011 (**Figure 4-17c**). The Antarctic ozone hole would have been 40% larger by 2013 (with enhanced loss at subpolar latitudes) and longer-lived each year. Smaller Arctic ozone holes would have become a regular occurrence as chemical ozone depletion would have a stronger effect on Arctic ozone in spring than dynamic variability.

4.5 FUTURE CHANGES IN POLAR OZONE

This section discusses the future evolution of polar ozone as projected by new chemistry–climate model (CCM) simulations coordinated within the IGAC/SPARC Chemistry-Climate Model Initiative CCMI (Eyring et al., 2013a). The CCMI model data set provides an update of previous ozone projections obtained from the second phase of the SPARC Chemistry-Climate Model Validation (CCMVal, referred to as CCMVal-2; SPARC CCMVal, 2010) activity that formed the basis of projections of future ozone for the prior two Assessments (WMO, 2011; 2014).

4.5.1 New Ozone Projections from Chemistry–Climate Models

As a result of continuing global CCM activities, new model simulations have been produced. The majority of CCMs that participated in CCMI had already been part of CCMVal-2; many of these models have been further refined since the earlier activity. Improvements of some of the CCMI models compared to their CCMVal-2 versions include

- more detailed chemistry schemes, with enhanced tropospheric chemistry, a more consistent representation of sulfate surface area densities, and the consideration of the effects of naturally produced very short-lived (bromine) substances (VSLSs) on ozone depletion, and
- interactive coupling of the atmosphere-only CCMs to deep-ocean models, hence improving the representation of climate feedbacks in particular (as in 'classical' Coupled Model Intercomparison Project Phase 5 (CMIP5)-type climate models).

A detailed overview of the applied CCMs including model expansions and improvements since CCMVal-2 is given in Morgenstern et al. (2017).

The performance of the previous CCM generation that provided the ozone projections for the prior two Assessments has been evaluated in detail within the SPARC CCMVal activity. SPARC CCMVal (2010) compared the quality of the dynamics and transport, as well as of the radiation and chemistry schemes, and offered a useful baseline for evaluating the results of later model studies. So far, a similar coordinated

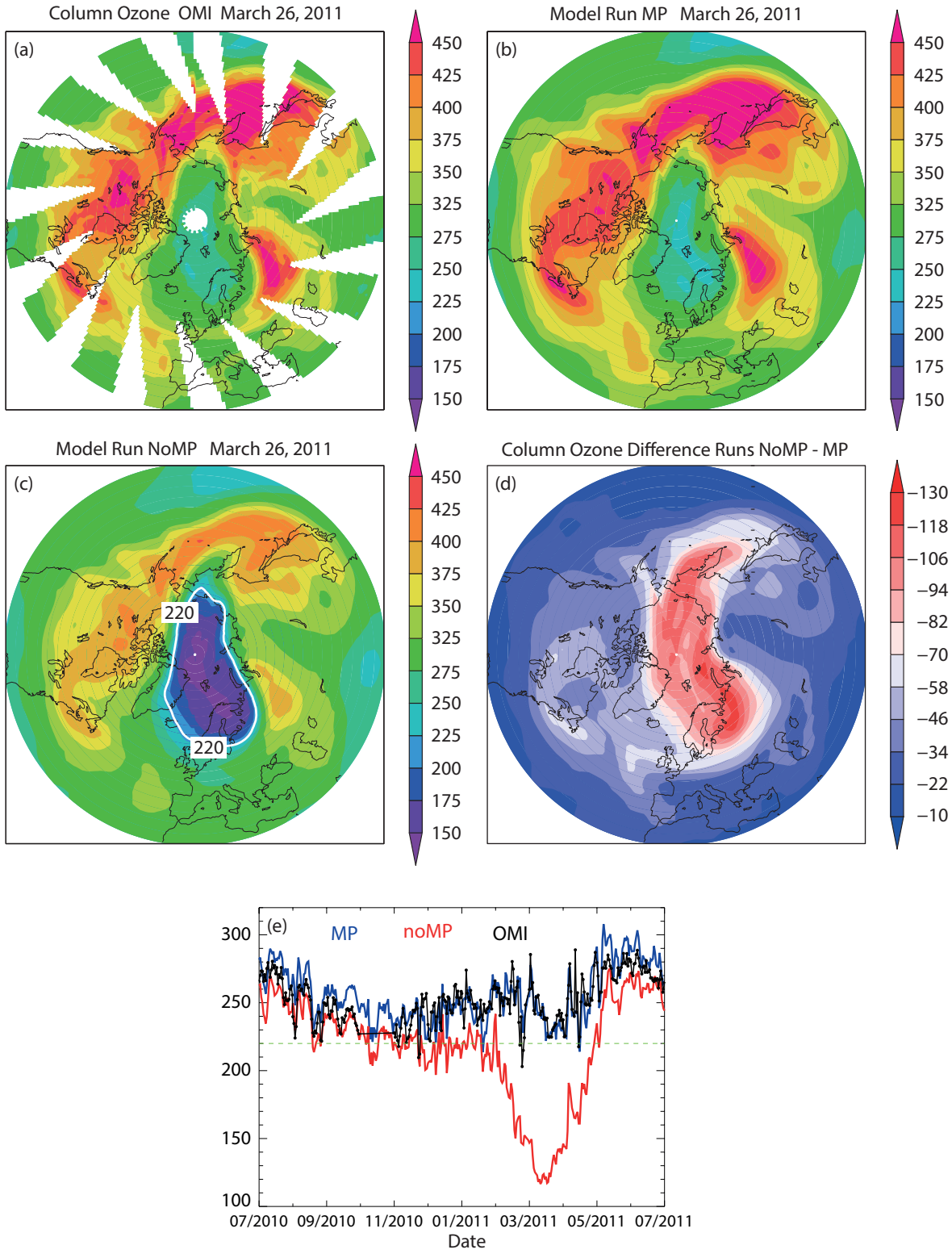

Figure 4-17. Evolution of column ozone in the Arctic from satellite observations and model simulations for winter 2010/2011. Column ozone (DU) on 26 March 2011 (a) observed by OMI, (b) from model run with ODSs controlled by the Montreal Protocol (MP), and (c) from model run with uncontrolled ODSs (NoMP) (with the 220 DU contour indicated in white). (d) Difference in column ozone between runs NoMP and MP. (e) The daily minimum ozone column in the Arctic region (latitude >45°N) from mid-2010 to mid-2011 as observed by the Ozone Monitoring Instrument (OMI) (black points), along with equivalent model results from run MP (blue) and run NoMP (red). From Chipperfield et al. (2015).

evaluation has not been completed for the current CCM versions, though a large number of analyses of the CCMI models focusing on different topics is underway (e.g., Wales et al., 2018; Dietmüller et al., 2018) A comprehensive comparison of ozone return dates in the CCMI, CMIP5, and CCMVal-2 simulations is presented in Dhomse et al. (2018).

A suite of CCMI simulations has been performed by the modeling groups using a standard set of specific forcings according to the recommendations in Eyring et al. (2013a); the relevant simulations and forcings for this Assessment are summarized in **Box 3-2**, "Modeling past and future changes in ozone: Model heritage and application". The most probable projections of the future evolution of polar ozone rely on the reference simulations (REF-C2) that are driven by an assumed decline of ODSs (WMO, 2011), the effects of brominated VSLSs, and a concurrent increase in GHG concentrations according to the RCP-6.0 scenario (Meinshausen et al., 2011). Sensitivity (SEN) simulations address the uncertainty of polar ozone recovery induced by different GHG scenarios and the attribution of ozone recovery to future changes in ODSs and GHGs.

As a novel aspect of CCMI, CCM simulations with specified dynamics (SD) have been performed for the historical period (1960–2010). The setup of these REF-C1SD simulations is specified in **Box 3-2.** The

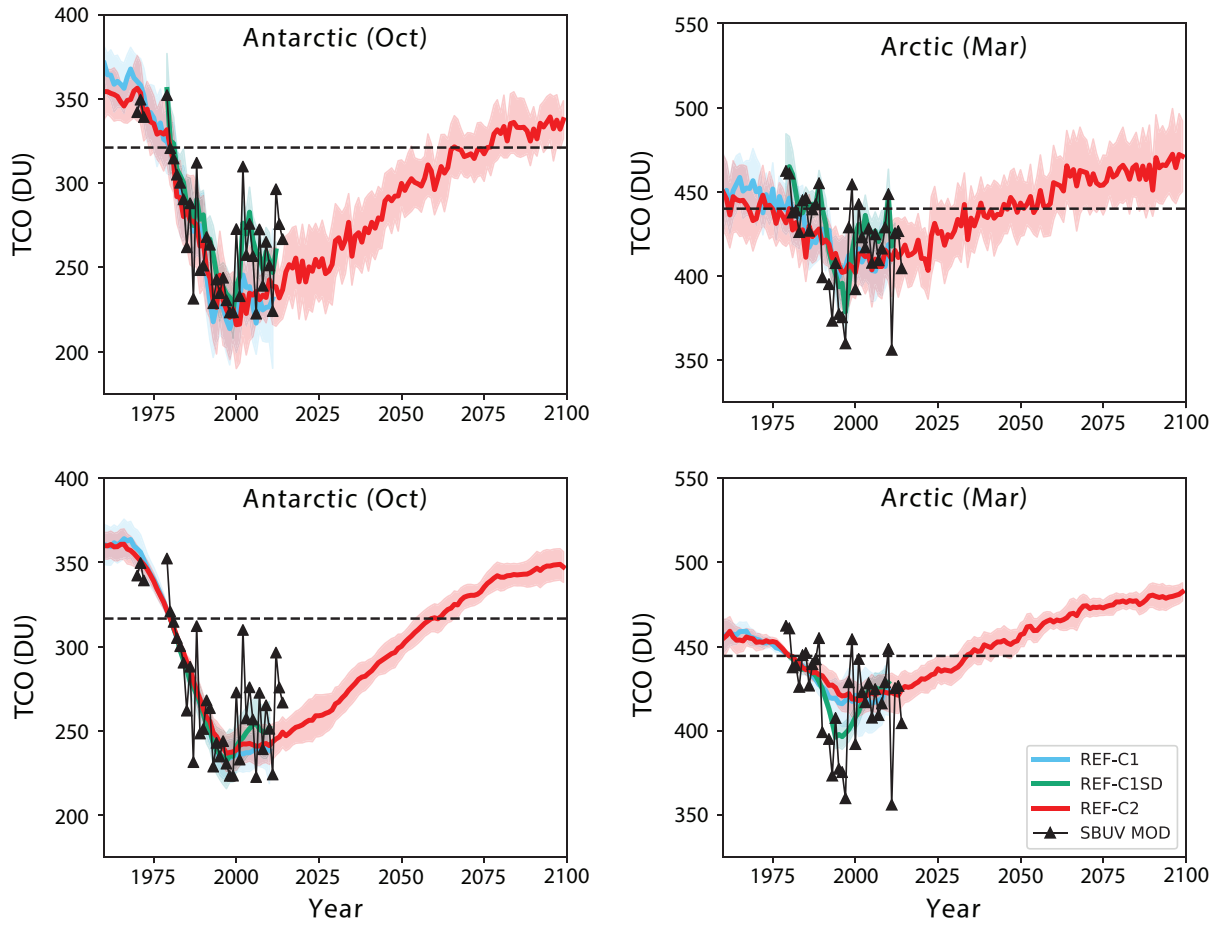

Figure 4-18. Multi-model mean (MMM1S) total column ozone time series (in Dobson Units, DU) from CCMI REF-C1 (light blue), REF-C1SD (green) and REF-C2 (red) simulations for the (*left*) SH polar (October) and (*right*) NH polar (March) regions. The dashed black lines show the 1980 reference value for each latitude band. The *top row* shows the unadjusted modeled values and the *bottom row* shows the time series adjusted with respect to mean 1980–1984 observations. Also shown are the merged SBUV observations. From Dhomse et al. (2018).

dynamics in the REF-C1SD simulations are adjusted ("nudged") towards observations or reanalysis data that represent the observed dynamical behavior of the atmosphere. Through the nudging, the model dynamics in the REF-C1SD simulations are forced to closely follow observed dynamical variability from year to year. These simulations thus provide realistic variability in the transport of chemical compounds and temperatures, in contrast to free-running CCMs that develop their own internal dynamical variability. The REF-C1SD runs therefore allow for a more detailed evaluation of the chemical processes (e.g., Solomon et al., 2015). A comparison of the REF-C1SD results with those from free-running REF-C1 simulations also helps to identify inaccuracies in the representation of dynamical processes in CCMs.

Figure 4-18 presents the multi-model mean (MMM1S) total column ozone time series from the REF-C1 (light blue) and REF-C1SD (green) simulations. MMM1S results represent the mean of the models that lie within one standard deviation (1σ) of the multi-model mean (MMM). Time series are shown for the unadjusted multi-model means (MMM1S) of the REF-C1, REF-C1SD, and REF-C2 simulations (top row) and the same MMM1S adjusted with respect to the mean 1980–1984 observations (bottom row) in Antarctic October (left) and Arctic March (right) (for more details see Dhomse et al., 2018). The top panels demonstrate that, as expected, the REF-C1SD simulations (i.e., in which the models are nudged towards analyzed meteorology) better reproduce the observed evolution of total column ozone than the REF-C1 simulations (i.e., the free-running CCMs). Both sets of simulations show the decline of the total ozone column until about the year 2000 in spring of the Northern and Southern Hemispheres. The REF-C1SD runs, however, better capture the observed year-to-year variability. Due to the averaging of individual model results, enhanced total ozone variability is suppressed in the MMM1S of the REF-C1SD simulations, as for example in the Arctic around the turn of the century and in the Antarctic during the following decade. Nevertheless, with constrained dynamics, the CCMs perform well in simulating the ozone evolution in the Antarctic and Arctic, giving confidence that the basic chemical processes and the ozone response to long-term ODS changes are understood.

4.5.2 Long-Term Projections of Polar Ozone

This section focuses on the future evolution of Antarctic and Arctic polar ozone projected by state-of-the-art CCMs following the best estimates of future decline in ODSs and increase in GHG concentrations. For this purpose, the CCMI REF-C2 simulations are analyzed for which the medium RCP-6.0 GHG scenario has been prescribed. Apart from refinements of the models, the experimental setup differs from the projections shown in WMO (2011) and WMO (2014) due to updates in the ODS and GHG scenarios (see also **Box-3-3**, "Ozone Return Dates") and the consideration of brominated VSLSs. The potential implications of these changes on the ozone return to historical values will be discussed in **Section 4.5.4**.

4.5.2.1 Future Antarctic Spring Total Column Ozone

Figure 4-18 (left) shows the future evolution of total column ozone (TCO) in the Antarctic (60°–90°S) in October for the multi-model mean of the REF-C2 simulations (red lines in **Figure 4-18**) from 20 CCMs (Dhomse et al., 2018). In the past (1960–2010), the multi-model mean (MMM1S) TCO shows good agreement with observations including the strong decrease of Antarctic ozone in the 1980s and early 1990s. A broad TCO minimum occurs around the year 2000. It is about 80 DU lower than the 1980 value, confirming the results presented in WMO (2011). In the future, the ozone hole will recover and a return of TCO to values of the year 1980 is expected to occur shortly after mid-century (between 2055 and 2066). Compared to the last Assessments (WMO, 2011, 2014), the current estimate is postponed by about 10 years. The previous earliest and latest projected return dates of Antarctic TCO (referring to the 1980 level) in October are also delayed by about 5 years (see also **Figure 4-22**). Possible reasons for these discrepancies are discussed in **Section 4.5.4**.

4.5.2.2 Future Arctic Spring Total Column Ozone

The temporal evolution of Arctic spring TCO derived from the CCMI simulations is presented for March in **Figure 4-18** (right). It shows the TCO MMM1S (60°–90°N) until 2100 derived from the REF-C2

simulations (red lines in **Figure 4-18**) of 20 CCMs (Dhomse et al., 2018). Again, model results representing the past are indicating qualitative agreement with observations concerning the long-term behavior, although the strong decrease of TCO in the 1990s, particularly in the years after the eruption of Pinatubo, is underestimated by the MMM1S. In the future, a return to TCO values of 1980 is expected before mid-century (between 2025 and 2043). Hence, the new projections suggest a return date for Arctic spring TCO that is delayed by 4 years compared to the CCMVal-2 estimate (WMO, 2011; 2014) (see also **Figure 4-22**). The range of potential TCO return dates is broader in the CCMI models, extending from 2025 (as for the CCMVal-2 models) to 2043, i.e., 8 years later than the CCMVal-2 models.

4.5.3 Factors Controlling Future Polar Ozone

4.5.3.1 Changing Roles of ODSs and GHGs

Whereas ODSs are expected to continue to decrease due to the controls of the Montreal Protocol, GHG concentrations are expected to continue to rise. Hence, the relative effects of ODSs and GHGs on polar ozone will change with time. For the most likely scenario of future ODS and GHG changes (i.e., REF-C2) the models project a return of TCO to historical values in the coming decades (see **Figure 4-18**). In this section, CCMI sensitivity simulations with separated forcings are discussed in order to disentangle the individual impacts of the ODS and GHG changes on the evolution of ozone.

In simulations with constant ODSs between 1960 and 2100 and growing GHG abundances (i.e., SEN-C2-fODS simulations), Antarctic total column ozone (TCO) in October shows only a small, non-significant positive long-term trend with weak year-to-year variations (**Figure 4-19**, top panel). A slight ozone increase after the middle of the 21st century results from stratospheric cooling forced by rising GHG

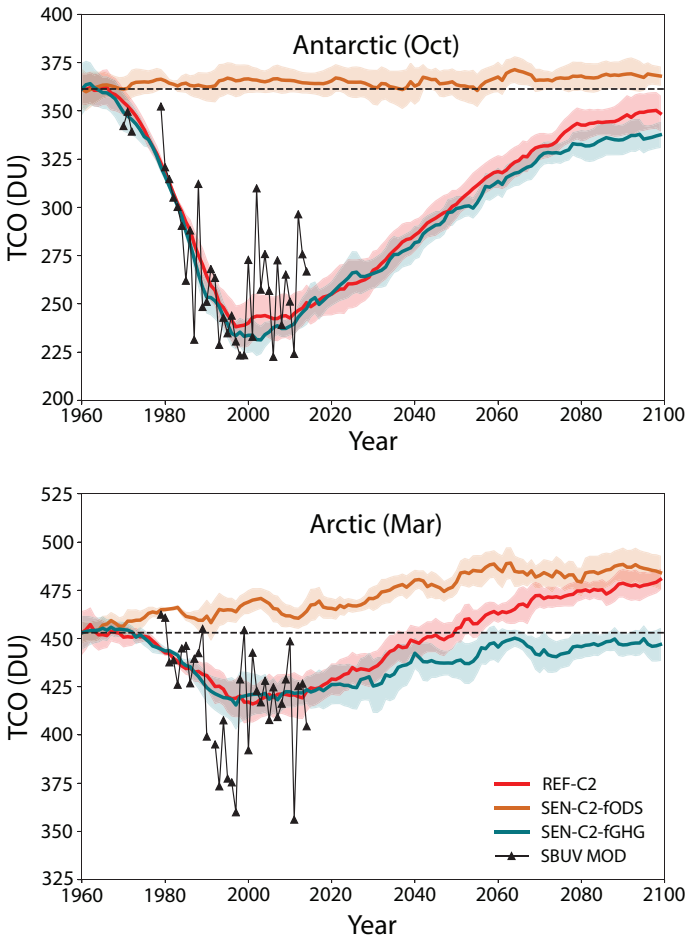

Figure 4-19. Temporal evolution of multi-model means (MMM1S) of total column ozone (in Dobson Units, DU) derived from REF-C2 (red), SEN-C2-fODS (brown), and SEN-C2-fGHG (green) CCMI scenario calculations for Antarctic spring (October, *top panel*) and Arctic spring (March, *bottom panel*). SEN-C2-fODS simulations use fixed ODS levels of the year 1960, while SEN-C2-fGHG simulations use fixed GHG levels of the year 1960. Black triangles indicate observations derived from SBUV MOD data. The black dashed lines denote the 1960 reference values for each region. Adapted from Dhomse et al. (2018).

concentrations. When GHGs are held constant at their 1960 values but ODSs vary according to the prescribed reference scenario (i.e., SEN-C2-fGHG simulations), the evolution of TCO closely follows that of the REF-C2 reference simulation. After the middle of the century, the GHG effect in the REF-C2 simulations accelerates Antarctic ozone recovery and leads to about 10 DU higher TCO around 2100 than with constant 1960 GHG concentrations. Hence, the evolution of the ODSs exerts the dominant influence on Antarctic TCO change modulated by a minor effect of GHGs in the second half of the century. Although the GHG effect strengthens Antarctic ozone recovery from ODSs, the 1960 baseline value will not be reached by the year 2100.

In Arctic spring, TCO gradually increases with time in the SEN-C2-fODS simulation with constant 1960 ODS levels (**Figure 4-19**, bottom panel). This ozone increase is caused by rising GHG concentrations which (a) cool the stratosphere, thereby reducing chemical gas-phase ozone depletion and (b) strengthen the Brewer-Dobson circulation (BDC) leading to a growing poleward and downward transport of ozone in Arctic spring (e.g., Oman et al., 2010; Oberländer et al., 2013). When prescribing GHG values for the 1960s (i.e., in SEN-C2-fGHG) throughout the whole projection, TCO closely follows the values of the REF-C2 reference simulation until about 2020. Afterwards, TCO in the simulation with constant 1960 GHG concentrations gradually approaches its 1960 values until the end of the 21st century, in contrast to the reference simulation where the rising GHG abundances induce an additional ozone increase, as described above. Hence, as in the Antarctic, the ODSs have been the primary driver of observed Arctic TCO trends in the past. However, in contrast to Antarctica, changes in GHGs will exert the dominant control over Arctic ozone distributions by the late 21st century. As demonstrated in CCM sensitivity studies with specified single or combined forcings (Rieder et al., 2014; Douglass et al., 2014; Kirner et al., 2015b; see also **Section 4.5.3.2**), past ODS changes mainly affected Arctic lower stratospheric ozone, while changes of GHG concentrations mainly affect the upper stratosphere. In addition, the growing GHG abundances in the REF-C2 scenario drive a stronger transport of ozone into the Arctic stratosphere. In total, whereas the decline in ODSs allows TCO to recover towards its 1960 baseline in the Arctic, the concurrent increase in GHGs induces not only an earlier return of Arctic TCO to its 1960 baseline value (in the 2040s for the REF-C2 MMM1S) but also a further TCO increase by about 20 DU by the end of the century.

These results reinforce the major findings of Eyring et al. (2010a) which were based on similar sensitivity simulations from a limited number of CCMVal-2 models. The additional CCMI simulations thus enhance the confidence in the models' responses to changing ODS and GHG concentrations.

4.5.3.2 Dynamic Variability in Arctic Spring

Particularly in the Arctic, CCM results show that the role of dynamical processes for determining springtime ozone will increase in the future. Individual CCM simulations indicate that even after 2040, when Arctic ozone is expected to have increased due to the effects of declining ODSs and rising GHGs, early springtime Arctic total column ozone can episodically drop by about 50 to 100 DU below the long-term mean for that period, reaching stratospheric ozone values characteristic of the near-present-day average ozone level (e.g., Langematz et al., 2014; Bednarz et al., 2016). This is due to the large year-to-year variability of the Arctic polar vortex. In the presence of a very cold, strong, and persistent polar vortex in late winter and early spring (as observed during March of 1997, 2011, and 2015), enhanced formation of polar stratospheric clouds (PSCs), and elevated halogen-induced ozone losses well above the long-term mean continue to occur. Together with reduced poleward transport of ozone, these factors contribute to the low total column ozone values as for instance measured in spring 1997.

For the future, CCM studies project a significant cooling trend in the Arctic winter mid- and upper stratosphere due to enhanced GHG concentrations (e.g., Oberländer et al., 2013; Rieder et al., 2014). There is, however, less confidence in the projected temperature trends in the Arctic lower stratosphere (e.g., Langematz et al., 2014; Rieder et al., 2014; Bednarz et al., 2016). Langematz et al. (2014) found in their CCM study that rising GHG concentrations lead to a cooling of the Arctic lower stratosphere in early winter.

However, their model did not show any significant temperature changes in late winter or spring. Neither was a statistically significant increase in the volume of PSCs (V_{PSC}), a temperature-dependent metric that is linearly correlated with wintertime chemical ozone loss (Rex et al., 2004), found throughout the 21st century. Nevertheless, CCM projections suggest the possibility that in the presence of a cold and strong polar vortex higher V_{PSC} and halogen-induced ozone losses may occur in individual Arctic winter/spring seasons until the middle of the 21st century (Langematz et al., 2014) or even into the second part of the century (Bednarz et al., 2016).

4.5.3.3 The Role of GHG Scenarios

As discussed in the previous sections, rising GHG concentrations influence the future recovery of stratospheric polar ozone. Ozone is not only affected by carbon dioxide (CO_2) through cooling of the upper stratosphere and modifying ozone transport but also by the GHGs methane (CH_4) and nitrous oxide (N_2O) through both radiative and chemical effects (Chapter 2 in WMO, 2014). Therefore, a projection of the return of ozone to a historical baseline will depend on the specific GHG scenario. Three different climate change scenarios (representative concentration pathways, RCPs, Meinshausen et al., 2011), i.e. RCP-4.5, RCP-6.0 (= REF-C2), and RCP-8.5 have been discussed in Dhomse et al. (2018). Note that the modest RCP-2.6 scenario was not included in the analysis because the number of model realizations for this scenario was too low. In **Figure 4-20** the total column ozone (TCO) (top row) as well as the partial column ozone (PCO) for the upper (second row) and lower stratosphere (third row) and the troposphere (bottom row) are presented for the subset of CCMI models that carried out simulations with different RCPs.

In Antarctic spring (October) (left column in **Figure 4-20**) slight differences between the RCPs begin to emerge in the upper stratosphere (US) and the troposphere in the middle of the century. In the US, ozone directly responds to the RCP scenario with the smallest ozone increase in the RCP-4.5 scenario and the largest ozone increase in RCP-8.5. In the RCP-8.5 scenario, the GHG-induced cooling is most pronounced, and subsequently, the temperature-dependent reduction in chemical ozone depletion strongest. All RCP scenarios project higher US partial ozone columns by the end of the century than existed in the US before the start of ODS-induced ozone depletion. In the troposphere, the assumed strong increase in CH_4 of the RCP-8.5 scenario will enhance ozone production more than in the other scenarios. No significant differences between the RCPs appear, however, in the lower stratosphere (LS). The projected warming of the Antarctic LS in spring, particularly in the first half of the 21st century when the ozone hole starts to diminish (see **Figure 5-8** in Chapter 5 of this Assessment), more than offsets a potential GHG-induced cooling (leading to heterogeneous ozone depletion). When integrated over the layers, TCO in Antarctic spring does not reveal significant differences between the GHG scenarios throughout the century. In the US, where ozone differences by the RCPs are most pronounced, PCO returns earlier to its 1980 values than TCO. However, differences in the US PCO return dates between the RCPs are not significant. As discussed in the previous section, ODSs are the dominant driver of ozone recovery in the South Polar lower stratosphere, even with more extreme future GHG abundance.

In Arctic spring, the effects of the extreme RCP-8.5 scenario become progressively more important for TCO and the stratospheric and tropospheric PCOs in the second half of the century (**Figure 4-20**, right column). While the stratospheric cooling in the RCP-8.5 scenario drives the stronger increase of US PCOs, the LS ozone growth is related to the projected strengthening of the Brewer-Dobson circulation with enhanced ozone transport into the LS. Tropospheric ozone increase is strongest in the RCP-8.5 scenario due to steadily rising levels of atmospheric CH_4 that reach 3.7 ppm by the end of the century. Adding the ozone changes in the different atmospheric layers yields higher TCO for the RCP-8.5 scenario compared to the more moderate scenarios. In the second half of the 21st century, the impact of GHGs is the dominant driver of stratospheric ozone changes. For all GHG scenarios, a "super-recovery" of Arctic spring TCO (i.e., an ozone increase above its concentrations in the 1960s and 1970s, when anthropogenic ozone depletion started) is projected. By 2100, the Arctic springtime stratospheric ozone column is expected to exceed 1960–1980 average values by about 35 DU for RCP-4.5 and about 50 DU for RCP-8.5 (Dhomse et al., 2018).

The different hemispheric sensitivity of future polar TCO to the climate change scenario was also found

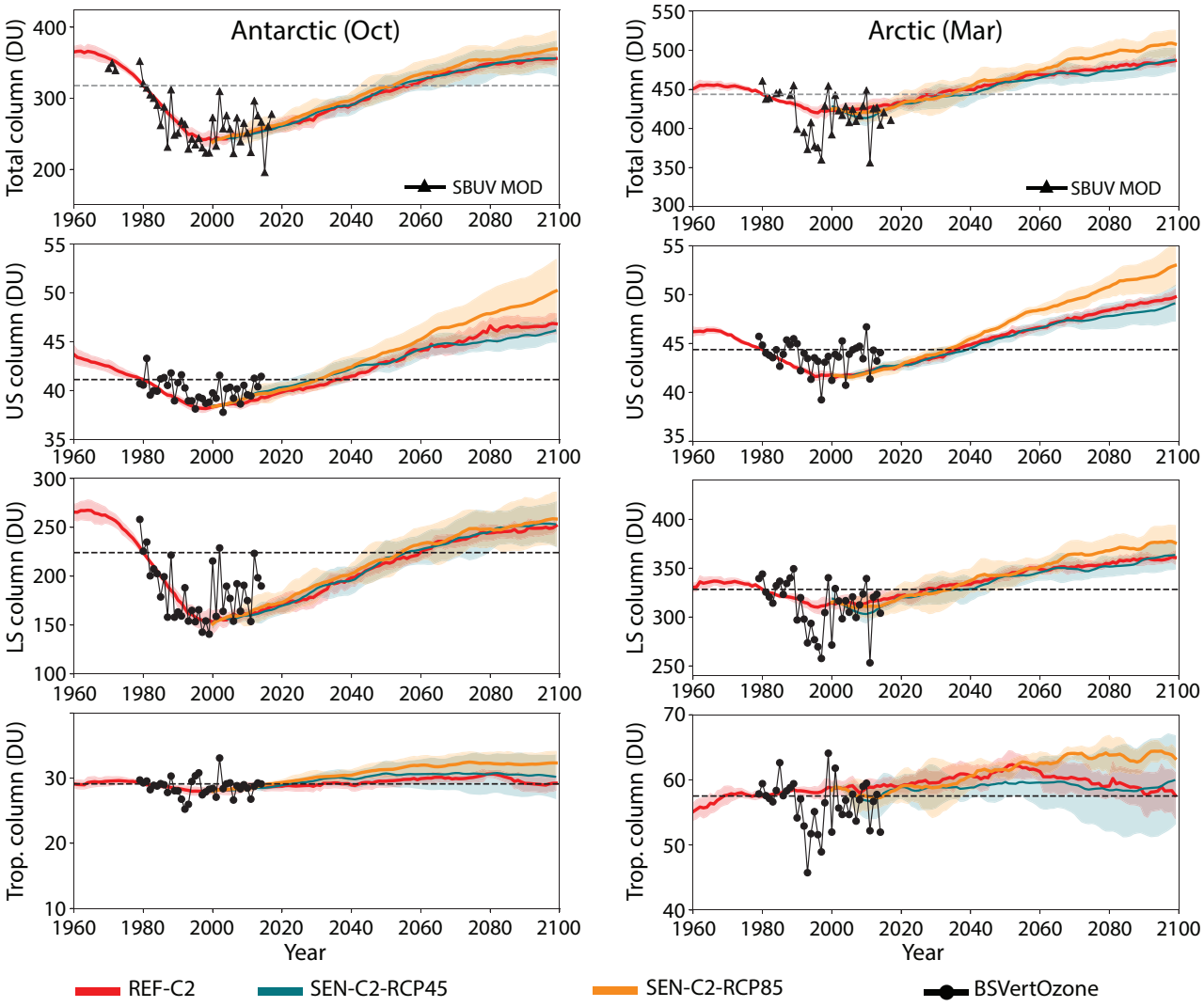

Figure 4-20. (*top*) Evolution of total column ozone (in Dobson Units, DU) MMM1S for the CCMI REF-C2 simulation (red lines) and the CCMI RCP scenario simulations SEN-C2-RCP45 (blue-green lines) and SEN-C2-RCP85 (orange lines). The REF-C2 simulation uses the RCP-6.0 scenario. Also shown are the partial ozone columns for the upper stratosphere (*second row*), the lower stratosphere (*third row*) and the troposphere (*bottom*). For comparison the respective total and partial ozone columns are shown. The black dashed lines denote the 1980 reference values for each region and layer. Adapted from Dhomse et al. (2018).

in analyses of the CMIP5 model subset with interactive chemistry (e.g., Eyring et al., 2013b), as well as in the ACCMIP model ensemble (Iglesias-Suarez et al., 2016). In the CCMI projections, however, the influence of the RCPs on TCO starts later in the century, and the TCO spread between RCPs is smaller than for the CMIP5 models in both hemispheres.

The RCP scenarios consist of projected concentration changes for a number of GHGs (most importantly CO_2, CH_4, and N_2O), which all have similar radiative effects, but differ in their chemical effects on ozone. As discussed previously, during the latter half of the 21st century, as ODS concentrations are expected to decline, GHGs become more relevant for ozone. Model studies indicate that in particular the future CO_2, N_2O, and CH_4 will have significant impacts on global total ozone (e.g., Fleming et al., 2011). The quantification of the net impact of these gases on future polar ozone is complicated by competing effects: Increasing N_2O concentrations will produce more NO_y and enhance ozone depletion, thereby reducing

the ozone increase due to CO_2-induced cooling and increases in CH_4 (Oman et al., 2010; Revell et al., 2012). However, ozone depletion by NO_y is less effective with decreasing temperature in the middle and upper stratosphere (Rosenfield and Douglass, 1998). In addition, chemical feedback processes reduce the efficiency of increasing N_2O to deplete ozone, as with increasing CO_2, less NO_y is produced (e.g., Portmann et al., 2012; Stolarski et al., 2015). Nevertheless, Revell et al. (2015) show that the ozone depletion potential (ODP) of N_2O for the year 2100 varies under different scenarios and is mostly larger than for the year 2000. Butler et al. (2016) describe how mitigation strategies may be adapted to the evolution of the individual gases: if reductions of CO_2 and CH_4 concentrations to RCP-2.6 levels (a low emissions scenario) could be achieved by the end of the 21st century, no super-recovery of stratospheric ozone is expected and N_2O mitigation would become important to avoid further ozone depletion. On the other hand, if CO_2 and N_2O were reduced to RCP-2.6 levels but CH_4 concentrations increased, stratospheric ozone would increase toward historical levels and large increases in global tropospheric ozone would be expected.

4.5.3.4 The Role of VSLSs

Since the last Assessment, considerable progress has been made in implementing the effects of bromine-containing very short-lived substances (VSLSs) on ozone (see also **Section 4.3.3**) into CCMs. Model simulations show clear signatures of brominated VSLSs in stratospheric ozone (e.g., Hossaini et al., 2015a; Sinnhuber and Meul, 2015; Oman et al., 2016; Fernandez et al., 2017; Falk et al., 2017). Brominated VSLSs are projected to affect the Antarctic ozone hole area and depth until about the middle of the century (Fernandez et al., 2017). As the abundance of long-lived halogens declines, the relative importance of brominated VSLSs regarding ozone reduction is predicted to increase in the coming decades and surpass ozone destruction by chlorine by about 2070 (Fernandez et al., 2017). However, as the depletion of stratospheric ozone due to brominated VSLSs depends also on the availability of chlorine, the impact of bromine on stratospheric ozone will continuously fade. Therefore, Fernandez et al. (2017) do not find a significant change in the return date of Antarctic ozone to 1980 values. This result is in contrast to model projections by Yang et al. (2014) and Oman et al. (2016) which show that active bromine from VSLSs is expected to delay the return of TCO to historical values by about 6–8 years (Yang et al., 2014) to a decade (Oman et al., 2016). The differences between these projections may be due to the applied models, the number of model realizations, or the specifications of future VSLSs. Hence more model studies are needed for a robust projection of the effect of brominated VSLSs on the Antarctic ozone return date.

As discussed in WMO (2014), increasing emissions of synthetic, chlorine-containing VSLSs, in particular dichloromethane (CH_2Cl_2), represent another, more recently detected component of VSLSs that affects polar ozone. Recent observations indicate that the atmospheric concentration of dichloromethane (which is not controlled by the Montreal Protocol) is growing (see **Chapter 1** for further details). Using CTM and CCM simulations, Hossaini et al. (2017) showed that the impact of dichloromethane on stratospheric ozone has clearly increased in recent years from a relative ozone decrease by dichloromethane of 3 DU in 2010 to 6 DU in 2016. Assuming a continuous increase of dichloromethane in coming decades at the mean rate observed over the 2004–2014 period, they found a delay of the return of Antarctic ozone to the 1980 baseline by nearly 20 years compared to a simulation without CH_2Cl_2 abundance (**Figure 4-21**). A sustained future increase in atmospheric concentrations of dichloromethane would therefore further slow the recovery of the Antarctic ozone hole. The future evolution of dichloromethane is however uncertain, given its recent decline in growth rate between 2014 and 2016 (see **Chapter 1**).

While the above cited studies have clearly shown that brominated and chlorinated VSLSs have a significant impact on stratospheric polar ozone, their consequences for the return dates of polar ozone to historical baseline values will depend on the future abundances of VSLSs in the atmosphere and are therefore uncertain, as addressed in more detail in **Section 4.5.4.2**.

4.5.4 Uncertainty in Polar Ozone Projections

Future ozone projections are affected by uncertainty due to internal variability of the atmosphere, structural

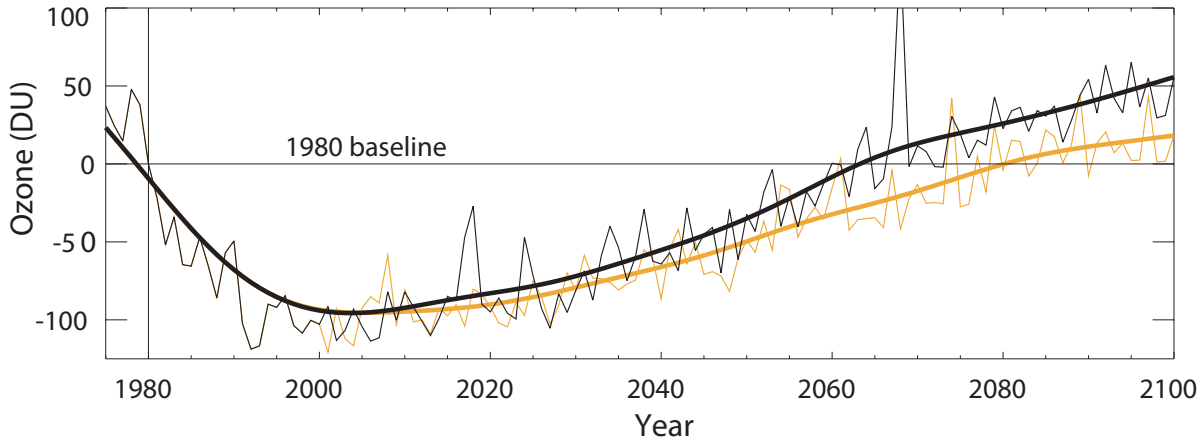

Figure 4-21. Future impact of growth in dichloromethane (CH_2Cl_2) on Antarctic column ozone and ozone trend derived from a CCM study. Results are shown for two UMSLIMCAT simulations: one run without CH_2Cl_2 and another where surface CH_2Cl_2 concentrations continue to increase at the mean rate observed over the 2004–2014 period. The figure shows the temporal evolution of October mean Antarctic stratospheric ozone column (in Dobson Units, DU) relative to 1980. While interannual variability is large, the two ozone time series are statistically different at the 95% significance level according to a Student's t-test (P_{value} = 0.02). Ozone returns to the 1980 baseline in the year 2064 (without CH_2Cl_2; black line) and in 2081 (with CH_2Cl_2; gold line). Adapted from Hossaini et al. (2017).

uncertainty due to differences between models and uncertainty in the future scenarios for ODSs and GHGs (see also **Box 3-3**). The role of internal dynamical variability in particular for Arctic polar ozone has been addressed in **Section 4.3.4**. In the following, the aspect of model uncertainty will be revisited for the new CCMI model simulations (**Section 4.5.4.1**) and the new ozone return dates will be discussed in the context of the ODS and GHG scenarios used (**Section 4.5.4.2**).

4.5.4.1 Model Uncertainty

As discussed in **Section 4.5.1**, CCMs differ in their treatment of the relevant physical, dynamical, and chemical processes. The broad range of total column ozone projections in the new CCMI simulations could be a result of the enhanced complexity of the applied CCMs. Most of the models participating in CCMI have been improved since CCMVal-2, being now more physically based, with enhanced resolution and more frequently coupled to ocean models, which leads to enhanced diversity in model results (Morgenstern et al., 2017).

In particular, the responses in total column ozone of the CCMI models to anthropogenic forcings, such as changes in ODSs and GHGs, were found to be less consistent across the different CCMs than those of the ozone profiles (Morgenstern et al., 2018). The likely cause of this is lower-stratospheric transport and dynamical responses, such as in the Brewer-Dobson circulation, exhibiting substantial inter-model differences. Good agreement of CCM results was found in the middle and upper stratosphere. Obvious differences were identified particularly in the troposphere, possibly caused by differences in the formulation and complexity of the tropospheric chemistry modules used in the CCMs.

These conclusions are confirmed by Dhomse et al. (2018) who investigate ozone recovery of partial columns in the lower stratosphere (LS, from the tropopause up to 10 hPa) and in the upper stratosphere (US, at 10 hPa and lower pressures) from 14 individual CCMI models. In the LS, where ozone has a long photochemical lifetime, the adjusted results from the CCMs show clear differences among the models in the polar regions. This suggests issues with the descriptions of dynamical (transport) and chemical

(heterogeneous chemistry) processes due to temperature biases in the CCMs. For the upper stratosphere, ozone in the polar regions behaves more similarly in the different models, as dynamical processes are less important for ozone, while the feedback of temperature changes on ozone becomes more important (Haigh and Pyle, 1982).

A further source of uncertainty in the CCMI ozone projections lies in existing uncertainties of rate constants for the N_2O and CH_4 reactions, which have been reassessed recently (SPARC, 2013). The CCMI models generally used the kinetic rate constants recommended at the time of the simulations (Sander et al., 2011). However, using updated estimates of kinetic and photochemical parameters, Fleming et al. (2015) report that uncertainties in the commonly used recommendations for the rates of chemical loss processes of N_2O and CH_4 lead to a substantial range in model ozone, both for present day and long-term projections of future ozone recovery. For October SH polar ozone, the largest uncertainty is due to the Cl + CH_4 reaction, which impacts the amount of chlorine in reservoir versus radical forms, resulting in a total ozone range of ±6% for present day chlorine loading. However, this range will diminish to less than ±1% by 2100 as atmospheric chlorine decreases.

4.5.4.2 Uncertainty in Ozone Return Dates

The return date of total or stratospheric ozone to a historical baseline is an important indicator to assess the success of the Montreal Protocol and its Amendments and adjustments. Ozone return dates have been presented previously based on CCMVal-2 projections (Eyring et al., 2010a, b; WMO, 2011) and CMIP5 simulations using different GHG scenarios (Eyring et al., 2013b; WMO, 2014). Estimates of ozone return dates from the new CCMI simulations have been derived in Dhomse et al. (2018). This section compares the different estimates of ozone return dates and discusses reasons generating uncertainty in the derived dates. It is important to note that all model projections use prescribed scenarios for future abundances of ODSs assuming a future decline of ODSs according to the regulations of the Montreal Protocol. This section does not assess the uncertainty in ozone return dates arising from potential non-compliance with the Montreal Protocol. (For more information on this topic see **Chapter 6**). The return dates for polar total column ozone from the CCMVal-2 projections in WMO (2011) and from the CCMI REF-C2 simulations as well as their estimated ranges are shown in **Figure 4-22**.

To account for model uncertainty, it is a common approach to give ozone return dates in terms of their mean value plus uncertainty range. Three different measures of ozone return dates were provided by Dhomse et al. (2018) for the CCMI simulations: (1) the multi-model mean (MMM) with the 1σ standard deviation defining the model range of recovery dates, (2) the median with the 10th and 90th percentiles defining the range of recovery dates, and (3) the multi-model mean including only models within one standard deviation of the MMM (MMM1S) with the 1σ standard deviation of the MMM1S defining the model range of recovery dates. For both polar regions, the median and MMM1S approaches provide (near) identical return dates giving confidence in the derived results.

Sensitivity to ODS and GHG Scenarios

As shown in **Sections 4.5.2.1** and **4.5.2.2**, the return dates of polar total column ozone (TCO) to 1980 baseline values are delayed in the CCMI models (MMM1S) by 4 years in the Arctic and 10 years in the Antarctic compared to the CCMVal-2 models (SPARC CCMVal, 2010; WMO, 2011). This delay in polar ozone recovery can partially be ascribed to updates in the ODS and GHG scenarios prescribed to the CCMI reference simulations (for more details see **Box 3-3** and Dhomse et al., 2018). The change in the ODS scenario from the adjusted A1 scenario of WMO (2007) used in CCMVal-2 to the A1 scenario of WMO (2011) in CCMI caused a delayed decline in stratospheric halogen levels. In addition, the transition from the SRES-A1b GHG scenario used in CCMVal-2 to the RCP-6.0 scenario in CCMI reduces the chemically driven increase of ozone due to a slower rise of CO_2 and CH_4 in the RCP-6.0 scenario, explaining a further delay in TCO recovery in the CCMI models.

The expected effect of rising N_2O concentrations in the REF-C2 simulations (about 40% between 1960 and 2100) is to delay the ozone return date due to an enhanced production of NO_x and catalytic ozone depletion. However, while the return date of global and northern mid-latitude stratospheric column ozone is

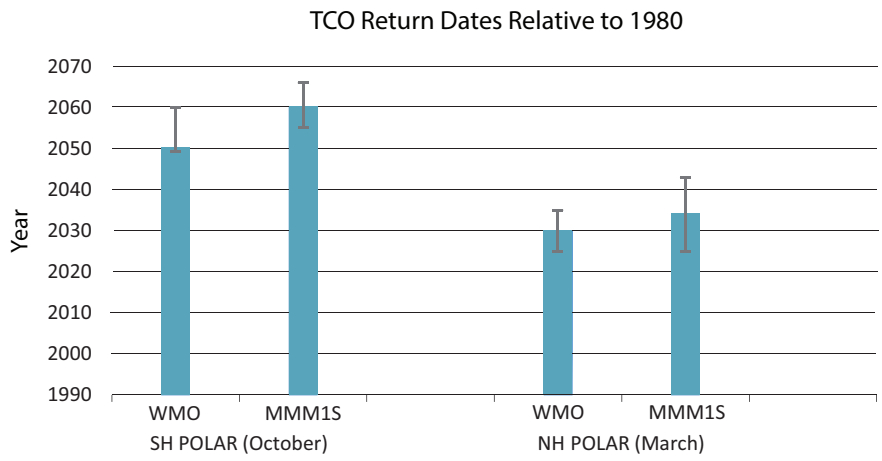

Figure 4-22. Estimated return years of total column ozone (TCO) to 1980 historical levels for the SH polar cap in October and the NH polar cap in March based on CCMVal-2 simulations (WMO) and on CCMI REF-C2 simulations (MMM1S). The estimated 1-σ uncertainties are shown with black vertical lines. Adapted from Dhomse et al. (2018).

significantly earlier in a scenario with fixed 1960 N_2O surface mixing ratios than in the REF-C2 simulations, it remains nearly unchanged in both polar areas (see Table 4 in Dhomse et al., 2018). Morgenstern et al. (2018) suggest that the negative effect of N_2O increases on ozone in the upper stratosphere might be compensated by a self-healing effect in the lower stratosphere initiated by the upper stratosphere ozone decline. However, the detailed processes leading to a zero response of the polar ozone return date to N_2O increases still need to be understood.

CH_4 concentrations increase in the RCP-6.0 scenario of the REF-C2 simulations by 57% between 1960 and their maximum in 2070, and by 128% between 1960 and 2100 in the RCP-8.5 scenario. Consistent with previous work (e.g., Revell et al., 2012), stratospheric ozone returns earlier in the CCMI simulations with rising CH_4 concentrations than in the constant-1960 scenario. This effect is stronger for the more extreme CH_4 increase in the RCP-8.5 scenario and stronger in Arctic spring (about 10 years) than in Antarctic spring (6 years). Note, however, that for the N_2O- and CH_4-sensitivity simulations only one realization by a limited number of models was available, reducing the robustness of the stated return dates.

Sensitivity to VSLSs

Section 4.5.3.4 revealed that both bromine- and chlorine-containing VSLSs have the potential to delay the return of the Antarctic ozone hole to historical values by somewhere between several years and up to three decades. Hence, the future evolution of the VSLS emissions represents a further source of uncertainty for the projection of the ozone return date. While the CCMVal-2 models generally did not include the effects of brominated VSLSs on ozone, most CCMI models took their effects into account. The additional ozone depletion by the VSLSs could therefore be a further contribution to the delay in CCMI TCO return dates (e.g., Oman et al., 2016).

The concentrations of the oceanic brominated VSLSs seem to have remained relatively stable over the past decades (see **Figure 1-16 in Chapter 1**). Based on this fact, most model studies assume a constant mixing ratio of brominated VSLSs of 5 ppt in simulations of past and future ozone. Based on present day, observed global oceanic and atmospheric concentrations (ERA-Interim) and historical and future data from three CMIP5 models, Ziska et al. (2017) derived, however, an increase of brominated VSLSs for the period 1979–2005. For the RCP-8.5 scenario, oceanic brominated VSLS emissions could increase by 30% from 2010 to 2100 (Tegtmeier et al., 2015; Ziska et al., 2017). In a transient CCM study using the RCP-6.0 GHG scenario and interactive VSLS emissions, an increase of the ocean–atmosphere flux of brominated VSLSs of about 8–10% by the end of the 21st century compared to present day was found (Falk et al., 2017). However, under the low chlorine loading at the end of the century, brominated VSLSs are projected to have less impact on total Antarctic stratospheric ozone depletion than in the present day (in agreement with studies using constant VSLS

mixing ratios) and may not act as a major source of future stratospheric ozone depletion (Falk et al., 2017). More CCM studies including the effects of climate change on VSLS emissions from the ocean need to be carried out to provide a robust estimate of the impact of future changes in brominated VSLSs on the return of polar ozone to historical values.

Chlorine-containing VSLSs are predominantly produced by industry. Among those, dichloromethane (CH_2Cl_2), has increased rapidly in recent years. Between 2000 and 2012, surface concentrations of CH_2Cl_2 increased at a global mean rate of almost 8% yr^{-1}, with the largest growth in South and Southeast Asia (Hossaini et al., 2015b; Oram et al., 2017). As discussed in **Section 4.5.3.4**, Hossaini et al. (2017) obtained a substantial delay of Antarctic ozone return, if the recently observed global mean CH_2Cl_2 growth rate of 2 ppt yr^{-1} continues. Whether such a growth rate would be likely to continue until the end of the century is arguable given the current global production capacity for CH_2Cl_2.

REFERENCES

Achtert, P., and M. Tesche, Assessing lidar-based classification schemes for polar stratospheric clouds based on 16 years of measurements at Esrange, Sweden, *J. Geophys. Res. Atmos.*, *119*, 1386–1405, doi:10.1002/2013JD020355, 2014.

Andrews, D.G., J.R. Holton, and C.B. Leovy, *Middle Atmosphere Dynamics*, vol. 40, 1st Edition, 489 pp., ISBN: 9780080211672, Academic Press, London, 1987.

Bednarz, E.M., A.C. Maycock, N.L. Abraham, P. Braesicke, O. Dessens, and J.A. Pyle, Future Arctic ozone recovery: The importance of chemistry and dynamics, *Atmos. Chem. Phys.*, *16*, 12159–12176, doi:10.5194/acp-16-12159-2016, 2016.

Bernhard, G., G. Manney, J.-U. Grooß, R. Müller, K. Lakkala, V. Fioletov, T. Koskela, A. Heikkilä, and B. Johnsen, Ozone and UV Radiation [in "State of the Climate in 2014"], *Bull. Am. Meteorol. Soc.*, *96* (7), S131–S133, doi:10.1175/2015BAMSStateof theClimate.1, 2015.

Bernhard, G., I. Ialongo, J.-U. Grooß, J. Hakkarainen, B. Johnsen, G.L. Manney, V. Fioletov, A. Heikkilä, and K. Lakkala, Ozone and UV Radiation [in "State of the Climate in 2015"], *Bull. Am. Meteorol. Soc.*, *97* (8), S152–S153, doi:10.1175/2016BAMS-Stateof theClimate.1, 2016.

Bernhard, G., V.E. Fioletov, J.-U. Grooß, I. Ialongo, B. Johnsen, K. Lakkala, G. Manney, and R. Müller, Ozone and UV radiation [in "State of the Climate in 2016"], *Bull. Am. Meteorol. Soc.*, *98*, S151–S154, doi:10.1175/2017BAMSStateoftheClimate.1, 2017.

Bittner, M., C. Timmreck, H. Schmidt, M. Toohey, and K. Krüger, The impact of wave-mean flow interaction on the Northern Hemisphere polar vortex after tropical volcanic eruptions, *J. Geophys. Res. Atmos.*, *121*, doi:10.1002/2015JD0244603, 2016.

Bodeker, G.E., H. Shiona, and H. Eskes, Indicators of Antarctic ozone depletion, *Atmos. Chem. Phys.*, *5*, 2603–2615, doi:10.5194/acp-5-2603-2005, 2005.

Bohlinger, P., B.-M. Sinnhuber, R. Ruhnke, and O. Kirner, Radiative and dynamical contributions to past and future Arctic stratospheric temperature trends, *Atmos. Chem. Phys.*, *14*, 1679–1688, doi:10.5194/acp-14-1679-2014, 2014.

Braesicke, P., J. Keeble, X. Yang, G. Stiller, S. Kellmann, N.L. Abraham, A. Archibald P. Telford, and J.A. Pyle, Circulation anomalies in the Southern Hemisphere and ozone changes, *Atmos. Chem. Phys.*, *13*, 10,677–10,688, doi:10.5194/acp-13-10677-2013, 2013.

Brooks, S.D., D. Baumgardner, B. Gandrud, J.E. Dye, M.J. Northway, D.W. Fahey, T.P. Bui, O.B. Toon, and M.A. Tolbert, Measurements of large stratospheric particles in the Arctic polar vortex, *J. Geophys. Res., 108* (D20), doi:10.1029/2002JD003278, 2003.

Burkholder, J.B., S.P. Sander, J. Abbatt, J.R. Barker, R.E. Huie, C.E. Kolb, M.J. Kurylo, V.L. Orkin, D.M. Wilmouth, and P.H. Wine, *Chemical kinetics and photochemical data for use in atmospheric studies, Evaluation No. 18*, JPL Publication 15-10, Jet Propulsion Laboratory, Pasadena, California, 2015. [Available at http://jpldataeval.jpl.nasa.gov.]

Butler, A.H., D.J. Seidel, S.C. Hardiman, N. Butchart, T. Birner, and A. Match, Defining sudden stratospheric warmings, *Bull. Amer. Meteorol. Soc., 96*, 1913–1928, doi:10.1175/BAMS-D-13-00173.1, 2015.

Butler, A.H., J.S. Daniel, R.W. Portmann, A.R. Ravishankara, P.J. Young, D.W. Fahey, and K.H. Rosenlof, Diverse policy implications for future ozone and surface UV in a changing climate, *Environ. Res. Lett.*, *11* (6), doi:10.1088/1748-9326/11/6/064017/meta, 2016.

Butler, A.H., J.P. Sjoberg, D.J. Seidel, and K.H. Rosenlof, A sudden stratospheric warming compendium, *Earth Syst. Sci. Data*, *9*, 63–76, doi:10.5194/essd-9-63-2017, 2017.

Cadoux, A., B. Scaillet, S. Bekki, C. Oppenheimer, and T.H. Druitt, Stratospheric Ozone destruction by the Bronze-Age Minoan eruption (Santorini Volcano, Greece), *Sci. Rep.*, *5*, 12243, doi:10.1038/srep12243, 2015.

Cagnazzo, C., E. Manzini, N. Calvo, A. Douglass, H. Akiyoshi, S. Bekki, M. Chipperfield, M. Dameris, M. Deushi, A.M. Fischer, H. Garny, A. Gettelman, M.A. Giorgetta, D. Plummer, E. Rozanov, T.G. Shepherd, K. Shibata, A. Stenke, H. Struthers, and W. Tian, Northern winter stratospheric temperature and ozone responses to ENSO inferred from an ensemble of Chemistry Climate Models, *Atmos. Chem. Phys.*, *9*, 8935–8948, doi:10.5194/acp-9-8935-2009, 2009.

Calvo, N., M. Iza, M.M. Hurwitz, E. Manzini, C. Peña-Ortiz, A.H. Butler, C. Cagnazzo, S. Ineson, and C.I. Garfinkel, Northern Hemisphere strato-

spheric pathway of different El Niño flavors in stratosphere resolving CMIP5 models, *J. Clim.*, –, 4351–4371, doi:10.1175/JCLI-D.16-0132.1, 2017.

Canty, T.P., R.J. Salawitch, and D.M. Wilmouth, The kinetics of the ClOOCl catalytic cycle, *J. Geophys. Res.*, *121*, 13 768–13 783, doi:10.1002/2016JD025710, 2016.

Carslaw, K.S., and T. Peter, Uncertainties in reactive uptake coefficients for solid stratospheric particles, 1. Surface chemistry, *Geophys. Res. Lett., 24* (14), 1743–1746, doi:10.1029/97GL01683, 1997.

Carn, S.A., L. Clarisse, and A.J. Prata, Multi-decadal satellite measurements of global volcanic degassing, *J. Volcanol. Geotherm. Res.*, *311*, 99–134, doi:10.1016/j.jvolgeores.2016.01.002, 2016.

Charlton, A.J., and L.M. Polvani, A new look at stratospheric sudden warmings, Part I: Climatology and modeling benchmarks, *J. Clim.*, *20*, 449–469, doi:10.1175/JCLI3996.1, 2007.

Charlton-Perez, A.J., M.P. Baldwin, T. Birner, R.X. Black, A.H. Butler, N. Calvo, N.A. Davis, E.P. Gerber, N. Gillett, S. Hardiman, J. Kim, K. Krüger, Y.-Y. Lee, E. Manzini, B.A. McDaniel, L. Polvani, T. Reichler, T.A. Shaw, M. Sigmond, S.-W. Son, M. Toohey, L. Wilcox, S. Yoden, B. Christiansen, F. Lott, D. Shindell, S. Yukimoto, S. Watanabe, On the lack of stratospheric dynamical variability in low-top versions of the CMIP5 models, *J. Geophys. Res. Atmos.*, *118*, 2494–2505, doi:10.1002/jgrd.50125, 2013.

Chipperfield, M.P., S.S. Dhomse, W. Feng, R.L. McKenzie, G.J.M. Velders, and J.A. Pyle, Quantifying the ozone and ultraviolet benefits already achieved by the Montreal Protocol. *Nat. Commun.*, *6*, 7233, doi:10.1038/ncomms8233, 2015.

Chipperfield, M., S. Bekki, S. Dhomse, N. Harris, B. Hassler, R. Hossaini, W. Steinbrecht, R. Thiéblemont, and M. Weber, Detecting recovery of the stratospheric ozone layer, *Nature*, *549*, 211–218, doi:10.1038/nature23681, 2017.

Curtius, J., R. Weigel, H.-J. Vössing, H. Wernli, A. Werner, C.-M. Volk, P. Konopka, M. Krebsbach, C. Schiller, A. Roiger, H. Schlager, V. Dreiling, and S. Borrmann, Observations of meteoric material and implications for aerosol nucleation in the winter Arctic lower stratosphere derived from in situ particle measurements, *Atmos. Chem. Phys.*, *5*, 3053–3069, doi:10.5194/acp-5-3053-2005, 2005.

Damiani, A., B. Funke, M. Lopez-Puertas, A. Gardini, T. von Clarmann, M.K. Santee, L. Froidevaux, and R.R. Cordero, Changes in the composition of the northern polar upper stratosphere in February 2009 after a sudden stratospheric warming, *J. Geophys. Res.*, *119*, 11,429–11,444, doi:10.1002/2014JD021698, 2014.

Damiani, A., B. Funke, M.L. Santee, R.R. Cordero, and S. Watanabe, Energetic particle precipitation: A major driver of the ozone budget in the Antarctic upper stratosphere, *Geophys. Res. Lett.*, *43* (7), 3554–3562, doi:10.1002/2016GL068279, 2016.

Dee, D.P., S.M. Uppala, A.J. Simmons, P. Berrisford, P. Poli, S. Kobayashi, U. Andrae, M.A. Balmaseda, G. Balsamo, P. Bauer, P. Bechtold, A.C.M. Beljaars, L. van de Berg, J. Bidlot, N. Bormann, C. Delsol, R. Dragani, M. Fuentes, A.J. Geer, L. Haimberger, S.B. Healy, H. Hersbach, E.V. Hólm, L. Isaksen, P. Kållberg, M. Köhler, M. Matricardi, A.P. McNally, B.M. Monge-Sanz, J.-J. Morcrette, B.-K. Park, C. Peubey, P. de Rosnay, C. Tavolato, J.-N. Thépaut, and F. Vitart, The ERA-Interim reanalysis: Configuration and performance of the data assimilation system, *Q. J. R. Meteorol. Soc.*, *137*, 553–597, doi:10.1002/qj.828, 2011.

de Laat, A.T.J., R.J. van der A, and M. van Weele, Tracing the second stage of ozone recovery in the Antarctic ozone-hole with a "big data" approach to multivariate regressions, *Atmos. Chem. Phys.*, *15* (1), 79–97, doi:10.5194/acp-15-79-2015, 2015.

de Laat, A.T.J., M. van Weele, and R.J. van der A, Onset of stratospheric ozone recovery in the Antarctic ozone hole in assimilated daily total ozone columns. *J. Geophys. Res. Atmos.*, *122,* 11,880–11,899, doi:10.1002/2016JD025723, 2017.

Denton, M.H., R. Kivi, T. Ulich, M.A. Clilverd, C.J. Rodger, and P. von der Gathen, Northern Hemisphere stratospheric ozone depletion caused by solar proton events: The role of the polar vortex, *Geophys. Res. Lett.*, *45*, 2115–2124, doi:10.1002/2017GL075966, 2018.

Dhomse, S., D. Kinnison, M.P. Chipperfield, I. Cionni, M. Hegglin, N.L. Abraham, H. Akiyoshi, A.T. Archibald, E.M. Bednarz, S. Bekki, P. Braesicke, N. Butchart, M. Dameris, M. Deushi, S. Frith, S.C. Hardiman, B. Hassler, L.W. Horowitz, R.-M. Hu, P. Jöckel, B. Josse, O. Kirner, S. Kremser, U. Langematz, J. Lewis, M. Marchand, M. Lin, E. Mancini, V. Marécal, M. Michou, O. Morgenstern, F.M.

O'Connor, L. Oman, G. Pitari, D.A. Plummer, J.A. Pyle, L.E. Revell, E. Rozanov, R. Schofield, A. Stenke, K. Stone, K. Sudo, S. Tilmes, D. Visioni, Y. Yamashita, and G. Zeng, Estimates of ozone return dates from Chemistry-Climate Model Initiative simulations, *Atmos. Chem. Phys.*, *18*, 8409–8438, doi:10.5194/acp-18-5408-218, 2018.

Dietmüller, S., R. Eichinger, H. Garny, T. Birner, H. Boenisch, G. Pitari, E. Mancini, D. Visioni, A. Stenke, L. Revell, E. Rozanov, D.A. Plummer, J. Scinocca, P. Jöckel, L. Oman, M. Deushi, S. Kiyotaka, D.E. Kinnison, R. Garcia, O. Morgenstern, G. Zeng, K.A. Stone, and R. Schofield, Quantifying the effect of mixing on the mean age of air in CCMVal-2 and CCMI-1 models, *Atmos. Chem. Phys.*, *18*, 6699–6720, doi:10.5194/acp-18-6699-2018, 2018.

Di Liberto, L., F. Cairo, F. Fierli, G. DiDonfrancesco, M. Viterbini, T. Deshler, and M. Snels, Observations of polar stratosperic clouds over McMurdo (77.85°S, 166.67°E) (2006-2010), *J. Geophys. Res. Atmos., 119 (9)*, 5528-5541, doi:10.1002/2013JD019892, 2014

Douglass, A.R., S.E. Strahan, L.D. Oman, and R.S. Stolarski, Understanding differences in chemistry climate model projections of stratospheric ozone, *J. Geophys. Res. Atmos.*, *119*, 4922–4939, doi:10.1002/2013JD021159, 2014.

Driscoll, S., A. Bozzo, L.J. Gray, A. Robock, and G. Stenchikov, Coupled Model Intercomparison Project 5 (CMIP5) simulations of climate following volcanic eruptions, *J. Geophys. Res.*, *117*, D17105, doi:10.1029/2012JD017607, 2012.

Ebert, M., R. Weigel, K. Kandler, G. Günther, S. Molleker, J.-U. Grooß, B. Vogel, S. Weinbruch, and S. Borrmann, Chemical analysis of refractory stratospheric aerosol particles collected within the arctic vortex and inside polar stratospheric clouds, *Atmos. Chem. Phys.*, *16* (13), 8405–8421, doi:10.5194/acp-16-8405-2016, 2016.

Evtushevsky, O.M., V.O. Kravchenko, L.L. Hood, and G.P. Milinevsky, Teleconnection between the central tropical Pacific and the Antarctic stratosphere: Spatial patterns and time lags, *Clim. Dyn.*, *44*, 1841–1855, doi:10.1007/s00382-014-2375-2, 2015.

Eyring, V., I. Cionni, G.E. Bodeker, A.J. Charlton-Perez, D.E. Kinnison, J.F. Scinocca, D.W. Waugh, H. Akiyoshi, S. Bekki, M.P. Chipperfield, M. Dameris, S. Dhomse, S.M. Frith, H. Garny, A. Gettelman, A. Kubin, U. Langematz, E. Mancini, M. Marchand, T. Nakamura, L.D. Oman, S. Pawson, G. Pitari, D.A. Plummer, E. Rozanov, T.G. Shepherd, K. Shibata, W. Tian, P. Braesicke, S.C. Hardiman, J.F. Lamarque, O. Morgenstern, J.A. Pyle, D. Smale, and Y. Yamashita, Multi-model assessment of stratospheric ozone return dates and ozone recovery in CCMVal-2 models, *Atmos. Chem. Phys.*, *10*, 9451–9472, doi:10.5194/acp-10-9451-2010, 2010a.

Eyring, V., I. Cionni, J.F. Lamarque, H. Akiyoshi, G.E. Bodeker, A.J. Charlton-Perez, S.M. Frith, A. Gettelman, D.E. Kinnison, T. Nakamura, L.D. Oman, S. Pawson, and Y. Yamashita, Sensitivity of 21st century stratospheric ozone to greenhouse gas scenarios, *Geophys. Res. Lett.*, *37*, L16807, doi:10.1029/2010GL044443, 2010b.

Eyring, V., J.-F. Lamarque, P. Hess, F. Arfeuille, K. Bowman, M.P. Chipperfield, B. Duncan, A. Fiore, A. Gettelman, M.A. Giorgetta, C. Granier, M. Hegglin, D. Kinnison, M. Kunze, U. Langematz, B. Luo, R. Martin, K. Matthes, P.A. Newman, T. Peter, A. Robock, T. Ryerson, A. Saiz-Lopez, R. Salawitch, M. Schultz, T.G. Shepherd, D. Shindell, J. Staehelin, S. Tegtmeier, L. Thomason, S. Tilmes, J.-P. Vernier, D.W. Waugh, and P.J. Young, Overview of IGAC/SPARC Chemistry-Climate Model Initiative (CCMI) community simulations in support of upcoming ozone and climate assessments, SPARC Newsletter, *40*, 48–66, 2013a.

Eyring, V., J.M. Arblaster, I. Cionni, J. Sedlácek, J. Perlwitz, P.J. Young, S. Bekki, D. Bergmann, P. Cameron-Smith, W.J. Collins, G. Faluvegi, K.-D. Gottschaldt, L.W. Horowitz, D.E. Kinnison, J.-F. Lamarque, D.R. Marsh, D. Saint-Martin, D.T. Shindell, K. Sudo, S. Szopa, and S. Watanabe, Long-term ozone changes and associated climate impacts in CMIP5 simulations, *J. Geophys. Res. Atmos.*, *118* (10), 5029–5060, doi:10.1002/jgrd.50316, 2013b.

Fahey, D.W., R.S. Gao, K.S. Carslaw, J. Kettleborough, P.J. Popp, M.J. Northway, J.C. Holecek, S.C. Ciciora, R.J. McLaughlin, T.L. Thompson, R.H. Winkler, D.G. Baumgardner, B. Gandrud, P.O. Wennberg, S. Dhaniyala, K. McKinley, T. Peter, R.J. Salawitch, T.P. Bui, J.W. Elkins, C.R. Webster, E.L. Atlas, H. Jost, J.C. Wilson, R.L. Herman, A. Kleinböhl, and M. von König, The detection of

large HNO_3-containing particles in the winter Arctic stratosphere, *Science*, *291*, 1026–1031, doi:10.1126/science.1057265, 2001.

Falk, S., B.-M. Sinnhuber, G. Krysztofiak, P. Jöckel, P. Graf, and S.T. Lennartz, Brominated VSLs and their influence on ozone under a changing climate, *Atmos. Chem. Phys.*, *17*, 11,313–11,329, doi:10.5194/acp-17-11313-2017, 2017.

Fernandez, R.P., D.E. Kinnison, J.-F. Lamarque, S. Tilmes, and A. Saiz-Lopez, Impact of biogenic very short-lived bromine on the Antarctic ozone hole during the 21st century, *Atmos. Chem. Phys.*, *17* (3), 1673–1688, doi:10.5194/acp-17-1673-2017, 2017.

Fleming E.L., C.H. Jackman, R.S. Stolarski, and A.R. Douglass, A model study of the impact of source gas changes on the stratosphere for 1850–2100, *Atmos. Chem. Phys., 11,* 8515–8541, doi:10.5194/acp-11-8515-2011, 2011.

Fleming, E.L., C. George, D.E. Heard, C.H. Jackman, M.J. Kurylo, W. Mellouki, V.L. Orkin, W.H. Swartz, T.J. Wallington, P.H. Wine, and J.B. Burkholder, The impact of current CH_4 and N_2O atmospheric loss process uncertainties on calculated ozone abundances and trends, *J. Geophys. Res.*, *120*, 5267–5293, doi:10.1002/2014JD022067, 2015.

Fletcher, C., and P. Kushner, The role of linear interference in the annular mode response to tropical SST forcing, *J. Clim*, *24*, 778–794, doi: 10.1175/2010JCLI3735.1, 2011.

Fogt, R.L., El Niño and Antarctica [in "State of the Climate in 2015"], *Bull. Am. Meteorol. Soc.*, *97* (8), S162, doi:10.1175/2016BAMSStateoftheClimate.1, 2016.

Frieler, K., M. Rex, R.J. Salawitch, T. Canty, M. Streibel, R.M. Stimpfle, K. Pfeilsticker, M. Dorf, D.K. Weisenstein, and S. Godin-Beekmann, Toward a better quantitative understanding of polar stratospheric ozone loss, *Geophys. Res. Lett.*, *33*, L10812, doi:10.1029/2005GL025466, 2006.

Frith, S.M., R.S. Stolarski, N.A. Kramarova, and R.D. McPeters, Estimating uncertainties in the SBUV Version 8.6 merged profile ozone data set, *Atmos. Chem. Phys.*, *17*, 14,695–14,707, doi:10.5194/acp-17-14695-2017, 2017.

Funke, B., A. Baumgaertner, M. Calisto, T. Egorova, C.H. Jackman, C.J. Kieser, A. Krivolutsky, M. López-Puertas, D.R. Marsh, T. Reddmann, E. Rozanov, S.-M. Salmi, M. Sinnhuber, G.P. Stiller, P.T. Verronen, S. Versick, T. von Clarmann, T.Y. Vyushkova, N. Wieters, and J.M. Wissing, Composition changes after the "Halloween" solar proton event: The High-Energy Particle Precipitation in the Atmosphere (HEPPA) model versus MIPAS data intercomparison study, *Atmos. Chem. Phys.*, *11*, 9089–9139, doi:10.5194/acp-11-9089-2011, 2011.

Funke, B., M. López-Puertas, G.P. Stiller, and T. von Clarmann, Mesospheric and stratospheric NO_y produced by energetic particle precipitation during 2002–2012, *J. Geophys. Res.*, *119*, doi:10.1002/2013JD021404, 2014.

Funke, B., M. López-Puertas, G.P. Stiller, S. Versick, and T. von Clarmann, A semi-empirical model for mesospheric and stratospheric NO_y produced by energetic particle precipitation, *Atmos. Chem. Phys.*, *16* (13), 8667–8693, doi:10.5194/acp-16-8667-2016, 2016.

Fytterer, T., M.G. Mlynczak, H. Nieder, K. Pérot, M. Sinnhuber, G. Stiller, and J. Urban, Energetic particle induced intra-seasonal variability of ozone inside the Antarctic polar vortex observed in satellite data, *Atmos. Chem. Phys.*, *15* (6), 3327–3338, doi:10.5194/acp-15-3327-2015, 2015.

Garcia, R.R., D.E. Kinnison, and D.R. Marsh, "World avoided" simulations with the Whole Atmosphere Community Climate Model, *J. Geophys. Res.*, *117*, D23303, doi:10.1029/2012JD018430, 2012.

Gelaro, R., W. McCarty, M.J. Suárez, R. Todling, A. Molod, L. Takacs, C.A. Randles, A. Darmenov, M.G. Bosilovich, R. Reichle, K. Wargan, L. Coy, R. Cullather, C. Draper, S. Akella, V. Buchard, A. Conaty, A.M. da Silva, W. Gu, G. Kim, R. Koster, R. Lucchesi, D. Merkova, J.E. Nielsen, G. Partyka, S. Pawson, W. Putman, M. Rienecker, S.D. Schubert, M. Sienkiewicz, and B. Zhao, The Modern-Era Retrospective Analysis for Research and Applications, Version 2 (MERRA-2), *J. Clim.*, 30, 5419–5454, doi: 10.1175/JCLI-D-16-0758.1, 2017.

Grooß, J.-U., R. Müller, R. Spang, I. Tritscher, T. Wegner, M.P. Chipperfield, W. Feng, D.E. Kinnison, and S. Madronich, On the discrepancy of HCl processing in the core of the wintertime polar vortices, *Atmos. Chem. Phys.*, *18*, 8647–8666, doi:10.5194/acp-18-8647-2018, 2018.

Haigh, J.D., and J. Pyle, Ozone perturbation experiments in a two-dimensional circulation model, *Q. J. R. Meteorol. Soc.*, *108* (457), 551–574,

doi:10.1002/qj.49710845705, 1982.

Haigh, J.D., and H.K. Roscoe, The final warming date of the Antarctic polar vortex and influences on its interannual variability, *J. Clim.*, *22*, 5809–5819, doi:10.1175/2009JCLI2865.1, 2009.

Harnik, N., and R.S. Lindzen, The effect of reflecting surfaces on the vertical structure and variability of stratospheric planetary waves, *J. Atmos. Sci.*, *58*, 2872–2894, doi:10.1175/1520-0469(2001)058<2872:TEORSO>2.0.CO;2, 2001.

Hassler, B., G.E. Bodeker, S. Solomon, and P.J. Young, Changes in the polar vortex: Effects on Antarctic total ozone observations at various stations, *Geophys. Res. Lett.*, *38* (1), L01805, doi:10.1029/2010GL045542, 2011a.

Hassler, B., J.S. Daniel, B.J. Johnson, S. Solomon, and S.J. Oltmans, An assessment of changing ozone loss rates at South Pole: Twenty-five years of ozonesonde measurements, *J. Geophys. Res.*, *116* (D22), D22301, doi:10.1029/2011JD016353, 2011b.

Hassler, B., I. Petropavlovskikh, J. Staehelin, T. August, P.K. Bhartia, C. Clerbaux, D. Degenstein, M.D. Mazière, B.M. Dinelli, A. Dudhia, G. Dufour, S.M. Frith, L. Froidevaux, S. Godin-Beekmann, J. Granville, N.R.P. Harris, K. Hoppel, D. Hubert, Y. Kasai, M.J. Kurylo, E. Kyrölä, J.-C. Lambert, P.F. Levelt, C.T. McElroy, R.D. McPeters, R. Munro, H. Nakajima, A. Parrish, P. Raspollini, E.E. Remsberg, K.H. Rosenlof, A. Rozanov, T. Sano, Y. Sasano, M. Shiotani, H.G.J. Smit, G. Stiller, J. Tamminen, D.W. Tarasick, J. Urban, R.J. van der A, J.P. Veefkind, C. Vigouroux, T. von Clarmann, C. von Savigny, K.A. Walker, M. Weber, J. Wild, and J.M. Zawodny, Past changes in the vertical distribution of ozone, Part 1: Measurement techniques, uncertainties and availability, *Atmos. Meas. Tech.*, *7*, 1395–1427, doi:10.5194/amt-7-1395-2014, 2014.

Hendrickx, K., L. Megner, J. Gumbel, D.E. Siskind, Y.J. Orsolini, H.N. Tyssøy, and M. Hervig, Observation of 27-day solar cycles in the production and mesospheric descent of EPP-produced NO, *J. Geophys. Res. Space Phys.*, *120* (10), 8978–8988, doi:10.1002/2015JA021441, 2015.

Hocke, K., Response of the middle atmosphere to the geomagnetic storm of November 2004, *J. Atmos. Terr. Phys.*, *154*, 86–91, doi: 10.1016/j.jastp.2016.12.013 2017.

Hofmann, D.J., and S. Solomon, Ozone destruction through heterogeneous chemistry following the eruption of El Chichón, *J. Geophys. Res.*, *94* (D4), 5029–5041, doi:10.1029/JD094iD04p05029, 1989.

Hoffmann, L., R. Spang, A. Orr, M.J. Alexander, L.A. Holt, and O. Stein, A decadal satellite record of gravity wave activity in the lower stratosphere to study polar stratospheric cloud formation, *Atmos. Chem. Phys.*, *17* (4), 2901–2920, doi:10.5194/acp-17-2901-2017, 2017.

Hossaini, R., M.P. Chipperfield, S.A. Montzka, A. Rap, S. Dhomse, and W. Feng, Efficiency of short-lived halogens at influencing climate through depletion of stratospheric ozone, *Nat. Geosci.*, *8*, 186–190, doi:10.1038/ngeo2363, 2015a.

Hossaini, R., M.P. Chipperfield, A. Saiz-Lopez, J.J. Harrison, R. von Glasow, R. Sommariva, E. Atlas, M. Navarro, S.A. Montzka, W. Feng, S. Dhomse, C. Harth, J. Mühle, C. Lunder, S. O'Doherty, D. Young, S. Reimann, M.K. Vollmer, P.B. Krummel, and P.F. Bernath, Growth in stratospheric chlorine from short-lived chemicals not controlled by the Montreal protocol, *Geophys. Res. Lett.*, *42* (11), 4573–4580, doi:10.1002/2015GL063783, 2015b.

Hossaini, R., M.P. Chipperfield, S.A. Montzka, A.A. Leeson, S.S. Dhomse, and J.A. Pyle, The increasing threat to stratospheric ozone from dichloromethane, *Nat. Comm.*, *8*, 186–190, doi:10.1038/ncomms15962, 2017.

Hu, D., W. Tian, F. Xie, J. Shu, and S. Dhomse, Effects of meridional sea surface temperature change on stratospheric temperature and circulation, *Adv. Atmos. Sci.*, *31*, 888–900, doi:10.007/s00376-013-3152-6, 2014.

Hubert, D., J.-C. Lambert, T. Verhoelst, J. Granville, A. Keppens, J.-L. Baray, A.E. Bourassa, U. Cortesi, D.A. Degenstein, L. Froidevaux, S. Godin-Beekmann, K.W. Hoppel, B.J. Johnson, E. Kyrölä, T. Leblanc, G. Lichtenberg, M. Marchand, C.T. McElroy, D. Murtagh, H. Nakane, T. Portafaix, R. Querel, J.M. Russell III, J. Salvador, H.G. Smit, K. Stebel, W. Steinbrecht, K.B. Strawbridge, R. Stübi, D.P.J. Swart, G. Taha, D.W. Tarasick, A.M. Thompson, J. Urban, J.A.E. van Gijsel, R. Van Malderen, P. von der Gathen, K.A. Walker, E. Wolfram, and J.M. Zawodny, Ground-based assessment of the bias and long-term stability of 14 limb and occultation ozone profile data records, *Atmos. Meas. Tech.*, *9*, 2497–2534, doi:10.5194/amt-9-2497-2016, 2016.

Huck, P.E., S. Tilmes, G.E. Bodeker, W.J. Randel, A.J.

McDonald, and H. Nakajima, An improved measure of ozone depletion in the Antarctic stratosphere, *J. Geophys. Res.*, *112*, D11104, doi:10.1029/2006JD007860, 2007.

Hurwitz, M., P. Newman, and C. Garfinkel, On the influence of the North Pacific sea surface temperatures on the Arctic winter climate, *J. Geophys. Res.*, *117*, D19110, doi:10.1029/2012JD017819, 2012.

Hurwitz, M.M., N. Calvo, C.I. Garfinkel, A.H. Butler, S. Ineson, C. Cagnazzo, E. Manzini, and C. Peña-Ortiz, Extra-tropical atmospheric response to ENSO in the CMIP5 models, *Clim. Dyn.*, *43*, doi:10.1007/s00382-014-2110-z, 2014.

Iannarelli, R., and M.J. Rossi, Heterogeneous kinetics of H_2O, HNO_3 and HCl on HNO_3 hydrates (α-NAT, β-NAT, NAD) in the range 175–200 K, *Atmos. Chem. Phys.*, *16* (18), 11,937–11,960, doi:10.5194/acp-16-11937-2016, 2016.

Iglesias-Suarez, F, P.J. Young, and O. Wild, Stratospheric ozone change and related climate impacts over 1850–2100 as modelled by the ACCMIP ensemble, *Atmos. Chem. Phys.*, *16*, 343–363, doi:10.5194/acp-16-343-2016, 2016.

Ivy, D.J., S. Solomon, and H.E. Rieder, Radiative and dynamical influences on polar stratospheric temperature trends, *J. Clim.*, *29* (13), 4927–4938, doi:10.1175/jcli-d-15-0503.1, 2016.

Ivy, D.J., S. Solomon, D. Kinnison, M.J. Mills, A. Schmidt, and R.R. Neely III, The influence of the Calbuco eruption on the 2015 Antarctic ozone hole in a fully coupled chemistry-climate model, *Geophys. Res. Lett.*, *44*, 2556–2561, doi:10.1002/2016GL071925, 2017.

Iza, M., N. Calvo, and E. Manzini, The stratospheric pathway of La Niña, *J. Clim.*, *29*, doi:10.1175/JCLI-D.16-0230.1, 2016.

Jackman, C.H., D.R. Marsh, F.M. Vitt, R.G. Roble, C.E. Randall, P.F. Bernath, B. Funke, M. López-Puertas, S. Versick, G.P. Stiller, A.J. Tylka, and E. L. Fleming, Northern Hemisphere atmospheric influence of the solar proton events and ground level enhancement in January 2005, *Atmos. Chem. Phys.*, *11*, 6153–6166, doi:10.5194/acp-11-6153-2011, 2011.

Jackman, C.H., C.E. Randall, V.L. Harvey, S. Wang, E.L. Fleming, M. López-Puertas, B. Funke, and P.F. Bernath, Middle atmospheric changes caused by the January and March 2012 solar proton events, *Atmos. Chem. Phys.*, *14* (2), 1025–1038, doi:10.5194/acp-14-1025-2014, 2014.

Jaeglé, L., C.R. Webster, R.D. May, D.C. Scott, R.M. Stimpfle, D.W. Kohn, P.O. Wennberg, T.F. Hanisco, R.C. Cohen, M.H. Proffitt, K.K. Kelly, J. Elkins, D. Baumgardner, J.E. Dye, J.C. Wilson, R.F. Pueschel, K.R. Chan, R.J. Salawitch, A.F. Tuck, S.J. Hovde, and Y.L. Yung, Evolution and stoichiometry of heterogeneous processing in the Antarctic stratosphere, *J. Geophys. Res.*, *10* (102), 13,235–13,253, doi:10.1029/97JD00935, 1997.

James, A.D., J.S.A. Brooke, T.P. Mangan, T.F. Whale, J.M.C. Plane, and B.J. Murray, Nucleation of nitric acid hydrates in polar stratospheric clouds by meteoric material, *Atmos. Chem. Phys.*, *18*, 4519–4531, doi:10.5194/acp-18-4519-2018, 2018.

Kalnay, E., M. Kanamitsu, R. Kistler, W. Collins, D. Deaven, L. Gandin, M. Iredell, S. Saha, G. White, J. Woollen, Y. Zhu, A. Leetmaa, R. Reynolds, M. Chelliah, W. Ebisuzaki, W. Higgins, J. Janowiak, K.C. Mo, C. Ropelewski, J. Wang, R. Jenne, and D. Joseph, The NCEP/NCAR 40-Year Reanalysis Project, *Bull. Am. Meteorol. Soc.*, *77*, 437–471, doi:10.1175/1520-0477(1996)077<0437:TNYRP>2.0.CO;2, 1996.

Kawa, S.R., P.A. Newman, L.R. Lait, M.R. Schoeberl, R.M. Stimpe, D.W. Kohn, C.R. Webster, R.D. May, D. Baumgardner, J.E. Dye, J.C. Wilson, K.R. Chan, and M. Loewenstein, Activation of chlorine in sulfate aerosol as inferred from aircraft observations, *J. Geophys. Res.*, *102* (D3), 3921–3933, doi:10.1029/96JD01992, 1997.

Khosrawi, F., J. Urban, S. Lossow, G. Stiller, K. Weigel, P. Braesicke, M.C. Pitts, A. Rozanov, J.P. Burrows, and D. Murtagh, Sensitivity of polar stratospheric cloud formation to changes in water vapour and temperature, *Atmos. Chem. Phys.*, *16*, 101–121, doi:10.5194/acp-16-101-2016, 2016.

Khosrawi, F., O. Kirner, B.-N. Sinnhuber, S. Johansson, M. Höpfner, M.L. Santee, L. Froidevaux, J. Ungermann, R. Ruhnke, W. Woiwode, H, Oelhaf, and P. Braesicke, Denitrification, dehydration and ozone loss during the 2015/2016 Artic winter, *Atmos. Chem. Phys.*, *17*, 12,893-12,910, doi:10.5194/acp-17-12893-2017, 2017.

Kirner, O., R. Müller, R. Ruhnke, and H. Fischer, Contribution of liquid, NAT and ice particles to chlorine activation and ozone depletion in Antarctic winter and spring, *Atmos. Chem. Phys.*, *15* (4), 2019–2030, doi:10.5194/acp-15-2019-2015,

2015a.

Kirner, O., R. Ruhnke, and B.-M. Sinnhuber, Chemistry-climate interactions of stratospheric and mesospheric ozone in EMAC long-term simulations with different boundary conditions for CO_2, CH_4, N_2O, and ODS, *Atmos. Ocean*, *53* (1), 140–152, doi:10.1080/07055900.2014.9807, 2015b.

Klekociuk, A.R., M.B. Tully, P.B. Krummel, H.P. Gies, S.P. Alexander, P.J. Fraser, S.I. Henderson, J. Javorniczky, J.D. Shanklin, R. Schofield, and K.A. Stone, The Antarctic ozone hole during 2013, *Aust. Meteorol. Ocean*, *65*, 247–266, 2015.

Klobas, J.E., D.M. Wilmouth, D.K. Weisenstein, J.G. Anderson, and R.J. Salawitch, Ozone depletion following future volcanic eruptions, *Geophys. Res. Lett*., *44*, doi:10.1002/2017GL073972, 2017.

Knibbe, J.S., R.J. van der A, and A.T. J. de Laat, Spatial regression analysis on 32 years of total column ozone data, *Atmos. Chem. Phys*., *14*, 8461–8482, doi:10.5194/acp-14-8461-2014, 2014.

Kodera, K., On the origin and nature of the interannual variability of the winter stratospheric circulation in the Northern Hemisphere, *J. Geophys. Res*., *100*, 14,077–14,087, 1995.

Kutterolf, S., T. Hansteen, A. Freundt, H. Wehrmann, K. Appel, K. Krüger, and W. Perez, Bromine and chlorine emissions from Plinian eruptions along the Central American volcanic arc: From source to atmosphere, *Earth Planet. Sci. Lett.*, *429,* 234–246, doi:10.1016/j.epsl.2015.07.064, 2015.

Kuttippurath, J., and P.J. Nair, The signs of Antarctic ozone recovery, *Sci. Rep.*, *7*, 585, doi:10.1038/s41598-017-00722-7, 2017.

Kuttippurath, J., G.E. Bodeker, H.K. Roscoe, and P.J. Nair, A cautionary note on the use of EESC-based regression analysis for ozone trend studies, *Geophys. Res. Lett*., *42*, 162–168, doi:10.1002/2014GL062142, 2015.

Labitzke, K.G., and H. van Loon, *The Stratosphere: Phenomena, History, and Relevance*, Springer-Verlag Berlin Heidelberg GmbH, New York, New York, doi:10.1007/978-3-642-58541-8, 1999.

Lambert, A., and M.L. Santee, Accuracy and precision of polar lower stratospheric temperatures from reanalyses evaluated from A-Train CALIOP and MLS, COSMIC GPS RO, and the equilibrium thermodynamics of supercooled ternary solutions and ice clouds, *Atmos. Chem. Phys*., *18*, 1945–1975, doi:10.5194/acp-18-1945-2018, 2018.

Lambert, A., M.L. Santee, and N.J. Livesey, Interannual variations of early winter Antarctic polar stratospheric cloud formation and nitric acid observed by CALIOP and MLS, *Atmos. Chem. Phys*., *16* (23), 15,219–15,246, doi:10.5194/acp-16-15219-2016, 2016.

Langematz, U., S. Meul, K. Grunow, E. Romanowsky, S. Oberländer, J. Abalichin, and A. Kubin, Future Arctic temperature and ozone: The role of stratospheric composition changes, *J. Geophys. Res. Atmos*., *119*, 2092–2112, doi:10.1002/2013JD021100, 2014.

Langematz, U., F. Schmidt, M. Kunze, G.E. Bodeker, and P. Braesicke, Antarctic ozone depletion between 1960 and 1980 in observations and chemistry-climate model simulations, *Atmos. Chem. Phys.*, *16* (24), 15,619–15,627, doi:10.5194/acp-16-15619-2016, 2016.

Lawrence, Z.D., and G.L. Manney, Characterizing stratospheric polar vortex variability with computer vision techniques, *J. Geophys. Res.*, *122*, doi:10.1002/2017JD027556, 2017.

Lawrence, Z.D., G.L. Manney, K. Minschwarner, M.L. Santee, and A. Lambert, Comparisons of polar processing diagnostics from 34 years of the ERA-Interim and MERRA reanalyses, *Atmos. Chem. Phys.*, *17*, 3873–3892, doi:10.5194/acp-15-3873-2015, 2015.

Leedham Elvidge, E.C., D.E. Oram, J.C. Laube, A.K. Baker, S.A. Montzka, S. Humphrey, D.A. O'Sullivan, and C.A.M. Brenninkmeijer, Increasing concentrations of dichloromethane, CH_2Cl_2, inferred from CARIBIC air samples collected 1998–2012, *Atmos. Chem. Phys*., *15* (4), 1939–1958, doi:10.5194/acp-15-1939-2015, 2015.

Li, S., J. Perlwitz, M.P. Hoerling, and X. Chen, Opposite annular responses on the Northern and Southern Hemispheres to Indian Ocean warming, *J. Clim*., *23*, 3720–3738, doi:10.1175/2010JCLI3410.1, 2010.

Long, C.S., M. Fujiwara, S. Davis, D.M. Mitchell, and C.J. Wright, Climatology and interannual variability of dynamic variables in multiple reanalyses evaluated by the SPARC Reanalysis Intercomparison Project (S-RIP), *Atmos. Chem. Phys.*, *17*, 14,593–14,629, doi:10.5194/acp-17-14593-2017, 2017.

Lubis, S.W., V. Silverman, K. Matthes, N. Harnik, N.-

E. Omrani, and S. Wahl, How does downward planetary wave coupling affect polar stratospheric ozone in the Arctic winter stratosphere?, *Atmos. Chem. Phys.*, *17*, 2437–2458, doi:10.5194/acp-17-2437-2017, 2017.

Manney, G.K., and Z.D. Lawrence, The major stratospheric final warming in 2016: Dispersal of vortex air and termination of Arctic chemical ozone loss, *Atmos. Chem. Phys.*, *16*, 15,371–15,396, doi:10.5194/acp-16-15371-2016, 2016.

Manney, G.K., Z.D. Lawrence, M.L. Santee, N.J. Livesey, A. Lambert, and M.C. Pitts, Polar processing in a split vortex: Arctic ozone loss in early winter 2012/2013, *Atmos. Chem. Phys.*, *15*, 5381–5403, doi:10.5194/acp-15-5381-2015, 2015a.

Manney, G.L., Z.D. Lawrence, M.L. Santee, W.G. Read, N.J. Livesey, A. Lambert, L. Froidevaux, H.C. Pumphrey, and M.J. Schwartz, A minor sudden stratospheric warming with a major impact: Transport and polar processing in the 2014/2015 Arctic winter, *Geophys. Res. Lett.*, *42*, 7808–7816, doi:10.1002/2015GL065864, 2015b.

Matthias, V., A. Dörnbrack, and G. Stober, The extraordinarily strong and cold polar vortex in the early northern winter 2015/2016, *Geophys. Res. Lett.*, *43*, 12,287–12,294, doi:10.1002/2016GL071676, 2016.

Meinshausen, M., S.J. Smith, K. Calvin, J.S. Daniel, M.L.T. Kainuma, J.-F. Lamarque, K. Matsumoto, S.A. Montzka, S.C.B. Raper, K. Riahi, A. Thomson, G.J.M. Velders, and D.P.P. van Vuuren, The RCP greenhouse gas concentrations and their extensions from 1765 to 2300, *Clim. Change*, *109* (1/2), 213-241, doi:10.1007/s10584-011-0156-z, 2011.

Mironova, I.A., K.L. Aplin, F. Arnold, G.A. Bazilevskaya, R.G. Harrison, A.A. Krivolutsky, K.A. Nicoll, E.V. Rozanov, E. Turunen, and I.G. Usoskin, Energetic particle influence on the Earth's atmosphere, *Space Sci. Rev.*, *194*, 1–96, doi:10.1007/s11214-015-0185-4, 2015.

Molleker, S., S. Borrmann, H. Schlager, B. Luo, W. Frey, M. Klingebiel, R. Weigel, M. Ebert, V. Mitev, R. Matthey, W. Woiwode, H. Oelhaf, A. Dörnbrack, G. Stratmann, J.-U. Grooß, G. Günther, B. Vogel, R. Müller, M. Krämer, J. Meyer, and F. Cairo, Microphysical properties of synoptic-scale polar stratospheric clouds: In situ measurements of unexpectedly large HNO_3-containing particles in the Arctic vortex, *Atmos. Chem. Phys.*, *14* (19), 10,785–10,801, doi:10.5194/acp-14-10785-2014, 2014.

Morgenstern, O., P. Braesicke, M.M. Hurwitz, F.M. O'Connor, A.C. Bushell, C.E. Johnson, and J.A. Pyle, The world avoided by the Montreal Protocol, *Geophys. Res. Lett.*, *35*, L16811, doi:10.1029/2008GL034590, 2008.

Morgenstern, O., M.I. Hegglin, E. Rozanov, F.M. O'Connor, N.L. Abraham, H. Akiyoshi, A.T. Archibald, S. Bekki, N. Butchart, M.P. Chipperfield, M. Deushi, S.S. Dhomse, R.R. Garcia, S.C. Hardiman, L.W. Horowitz, P. Jöckel, B. Josse, D. Kinnison, M. Lin, E. Mancini, M.E. Manyin, M. Marchand, V. Marécal, M. Michou, L.D. Oman, G. Pitari, D.A. Plummer, L.E. Revell, D. Saint-Martin, R. Schofield, A. Stenke, K. Stone, K. Sudo, T.Y. Tanaka, S. Tilmes, Y. Yamashita, K. Yoshida, and G. Zeng, Review of the global models used within phase 1 of the Chemistry–Climate Model Initiative (CCMI), *Geosci. Model Dev.*, *10*, 639–671, doi:10.5194/gmd-10-639-2017, 2017.

Morgenstern, O., K.A. Stone, R. Schofield, H. Akiyoshi, Y. Yamashita, D.E. Kinnison, R.R. Garcia, K. Sudo, D.A. Plummer, J. Scinocca, L.D. Oman, M.E. Manyin, G. Zeng, E. Rozanov, A. Stenke, L.E. Revell, G. Pitari, E. Mancini, G. Di Genova, D. Visioni, S.S. Dhomse, and M.P. Chipperfield, Ozone sensitivity to varying greenhouse gases and ozone-depleting substances in CCMI-1 simulations, *Atmos. Chem. Phys.*, *18*, 1091–1114, doi:10.5194/acp-18-1091-2018, 2018.

Müller, R., J.-U. Grooß, C. Lemmen, D. Heinze, M. Dameris, and G. Bodeker, Simple measures of ozone depletion in the polar stratosphere, *Atmos. Chem. Phys.*, *8*, 251–264, doi:10.5194/acp-8-251-2008, 2008.

Müller, R., J.-U. Grooß, A.M. Zafar, S. Robrecht, and R. Lehmann, The maintenance of elevated active chlorine levels in the Antarctic lower stratosphere through HCl null cycles, *Atmos. Chem. Phys.*, *18*, 2985–2997, doi:10.5194/acp-18-2985-2018, 2018.

Murphy, D.M., and B.L. Gary, Mesoscale temperature fluctuations and polar stratospheric clouds, *J. Atmos. Sci.*, *52* (10), 1753–1760, doi:10.1175/1520-0469(1995)<1753:mtfapd>2.0.co;2, 1995.

Muthers, S., J.G. Anet, C.C. Raible, S. Brönnimann, E. Rozanov, F. Arfeuille, T. Peter, A.I. Shapiro, J. Beer, F. Steinhilber, Y. Brugnara, and W. Schmutz,

Northern hemispheric winter warming pattern after tropical volcanic eruptions: Sensitivity to the ozone climatology, *J. Geophys. Res. Atmos.*, *119*, 1340–1355, doi:10.1002/2013JD020138, 2014.

Muthers, S., F. Arfeuille, C.C. Raibel, and E. Rozanov, The impacts of volcanic aerosol on stratospheric ozone and the Northern Hemisphere polar vortex: Separating radiative-dynamical changes from direct effects due to enhanced aerosol heterogeneous chemistry, *Atmos. Chem. Phys.*, *15*, 11,461–11,476, doi:10.5194/acp-15-11461-2015, 2015.

Naik V., L.W. Horowitz, M.D. Schwarzkopf, and M. Lin, Impact of volcanic aerosols on stratospheric ozone recovery, *J. Geophys. Res. Atmos.*, *122*, doi:10.1002/2016JD025808, 2017.

Nakajima, H., I. Wohltmann, T. Wegner, M. Takeda, M.C. Pitts, L.R. Poole, R. Lehmann, M.L. Santee, and M. Rex, Polar stratospheric cloud evolution and chlorine activation measured by CALIPSO and MLS, and modeled by ATLAS, *Atmos. Chem. Phys., 16*, 3311–3325, doi:10.5194/acp-16-3311-2016, 2016.

Nash, E.R., P.A. Newman, J.E. Rosenfield, and M.R. Schoeberl, An objective determination of the polar vortex using Ertel's potential vorticity, *J. Geophys. Res.*, *101*, 9471–9478, doi:10.1029/96JD00066, 1996.

Nash, E.R., S.E. Strahan, N. Kramarova, C.S. Long, M.C. Pitts, P.A. Newman, B. Johnson, M.L. Santee, I. Petropavlovskikh, and G.O. Braathen, Antarctic Ozone Hole [in "State of the Climate in 2015"], *Bull. Am. Meteorol. Soc.*, *97* (8), S188–S172, 2016.

Newman, P.A., and E.R. Nash, The unusual Southern Hemisphere stratosphere winter of 2002, *J. Atmos. Sci.*, *62*, 614-628, doi:10.1175/JAS-3323.1, 2005.

Newman, P.A., S.R. Kawa, and E.R. Nash, On the size of the Antarctic ozone hole, *Geophys. Res. Lett., 31*, L21104, doi:10.1029/2004GL020596, 2004.

Newman, P.A., E.R. Nash, S.R. Kawa, S.A. Montzka, and S.M. Schauffler, When will the Antarctic ozone hole recover?, *Geophys. Res. Lett.*, *33*, L12814, doi:10.1029/2005GL025232, 2006.

Newman, P.A., L.D. Oman, A.R. Douglass, E.L. Fleming, S.M. Frith, M.M. Hurwitz, S.R. Kawa, C.H. Jackman, N.A. Krotkov, E.R. Nash, J.E. Nielsen, S. Pawson, and G.J.M. Velders, What would have happened to the ozone layer if chlorofluorocarbons had not been regulated?, *Atmos. Chem. Phys.*, *9*, 2113–2128, doi:10.5194/acp-9-2113-2009, 2009.

Newman, P.A., E.R. Nash, S.E. Strahan, N. Kramarova, C.S. Long, M.C. Pitts, B. Johnson, M.L. Santee, I. Petropavlovskikh, and G.O. Braathen, Stratospheric Ozone [in "State of the Climate in 2014"], *Bull. Am. Meteorol. Soc.*, *96* (7), S165–S167, 2015.

Newman, P.A., E.R. Nash, S.E. Strahan, N. Kramarova, C.S. Long, M.C. Pitts, B. Johnson, M.L. Santee, I. Petropavlovskikh, and G.O. Braathen, 2016 Antarctic ozone [in "State of the Climate in 2016"], *Bull. Am. Meteorol. Soc.*, *98* (8), S169–S172, doi:10.1175/2017BAMSStateoftheClimate.1, 2017.

Oberländer, S., U. Langematz, and S. Meul, Unraveling impact factors for future changes in the Brewer-Dobson circulation, *J. Geophys. Res. Atmos.*, *118*, 10,296–10,312, doi:10.1002/jgrd.50775, 2013.

Oman, L.D., D.A. Plummer, D.W. Waugh, J. Austin, J.F. Scinocca, A.R. Douglass, R.J. Salawitch, T. Canty, H. Akiyoshi, S. Bekki, P. Braesicke, N. Butchart, M.P. Chipperfield, D. Cugnet, S. Dhomse, V. Eyring, S. Frith, S.C. Hardiman, D.E. Kinnison, J.-F. Lamarque, E. Mancini, M. Marchand, M. Michou, O. Morgenstern, T. Nakamura, J.E. Nielsen, D. Olivié, G. Pitari, J. Pyle, E. Rozanov, T.G. Shepherd, K. Shibata, R.S. Stolarski, H. Teyssèdre, W. Tian, Y. Yamashita, and J.R. Ziemke, Multimodel assessment of the factors driving stratospheric ozone evolution over the 21st century, *J. Geophys. Res. Atmos.*, *115*, D24306, doi:10.1029/2010JD014362, 2010.

Oman, L.D., A.R. Douglass, R.J. Salawitch, T.P. Canty, J.R. Ziemke, and M. Manyin, The effect of representing bromine from VSLs on the simulation and evolution of Antarctic ozone, *Geophys. Res. Lett.*, *43*, 9869–9876, doi:10.1002/2016GL070471, 2016.

Omrani, N.-E., N.S. Keenlyside, J. Bader, and E. Manzini, Stratosphere key for wintertime atmospheric response to warm Atlantic decadal conditions, *Clim. Dyn.*, *42*, 649–663, doi:10.1007/s00382-013-1860-3, 2014.

Oram, D.E., M.J. Ashford, J.C. Laube, L.J. Gooch, S. Humphrey, W.T. Surges, E. Leedham-Elvidge, G.L. Forster, N.R.P. Harris, M.I., Mead, A.A. Samah, S.M. Phang, C.-F. Ou-Yang, N.-H. Lin, J.-L. Wang, A.K. Baker, C.A.M. Brenninkmeijer, and D. Sherry, A growing threat to the ozone layer from

short-lived anthropogenic chlorocarbons, *Atmos. Chem. Phys.*, *17*, 11,929-11,941, doi:10.5194/acp-17-11929-2017, 2017.

Orr, A., J.S. Hosking, L. Homann, J. Keeble, S.M. Dean, H.K. Roscoe, N.L. Abraham, S. Vosper, and P. Braesicke, Inclusion of mountain wave-induced cooling for the formation of PSCs over the Antarctic Peninsula in a chemistry-climate model, *Atmos. Chem. Phys.*, *15* (2), 1071–1086, doi:10.5194/acp-15-1071-2015, 2015.

Orsolini, Y.J., V. Limpasuvan, K. Pérot, P. Espy, R. Hibbins, S. Lossow, K. Raaholt Larsson, and D. Murtagh, Modelling the descent of nitric oxide during the elevated stratopause event of January 2013, *J. Atmos. Terr. Sci.*, *155*, 50–61, doi:10.1016/j.jastp.2017.01.006, 2017.

Päivärinta, S.M., P.T. Verronen, B. Funke, A. Gardini, A. Seppälä, and M.E. Andersson, Transport versus energetic particle precipitation: Northern polar stratospheric NO_x and ozone in January–March 2012, *J. Geophys. Res. Atmos.*, *121* (10), 6085–6100, doi:10.1002/2015JD024217, 2016.

Parrondo, M.C., M. Gil, M. Yela, B.J. Johnson, and H.A. Ochoa, Antarctic ozone variability inside the polar vortex estimated from balloon measurements, *Atmos. Chem. Phys.*, *14* (1), 217–229, doi:10.5194/acp-14-217-2014, 2014.

Pazmiño, A., S. Godin-Beekmann, A. Hauchecorne, C. Claud, S. Khaykin, F. Goutail, E. Wolfram, J. Salvador, and E. Quel, Multiple symptoms of total ozone recovery inside the Antarctic vortex during austral spring, *Atmos. Chem. Phys., 18*, 7557–7572, doi:10.5194/acp-18-7557-2018, 2018.

Pérot, K., J. Urban, and D.P. Murtagh, Unusually strong nitric oxide descent in the Arctic middle atmosphere in early 2013 as observed by Odin/SMR, *Atmos. Chem. Phys.*, *14* (15), 8009–8015, doi:10.5194/acp-14-8009-2014, 2014.

Pitari, G., G. Di Genova, E. Mancini, D. Visioni, I. Gandolfi, and I. Cionni, Stratospheric aerosols from major volcanic eruptions: A Composition-Climate Model Study of the aerosol cloud dispersal and e-folding time, *Atmos.*, *7* (75), doi:10.3390/atmos7060075, 2016.

Pommereau, J.-P., F. Goutail, F. Lefèvre, A. Pazmiño, C. Adams, V. Dorokhov, P. Eriksen, R. Kivi, K. Stebel, X. Zhao, and M. van Roozendael, Why unprecedented ozone loss in the Arctic in 2011? Is it related to climate change?, *Atmos. Chem. Phys.*, *13*, 5299–5308, doi:10.5194/acp-13-5299-2013, 2013.

Portmann, R.W., J.S. Daniel, and A.R. Ravishankara, Stratospheric ozone depletion due to nitrous oxide: Influences of other gases, *Philos. Trans. Roy. Soc. B*, *367* (1593), 1256–1264, doi:10.1098/rstb.2011.0377, 2012.

Raible, C.C., S. Brönnimann, R. Auchmann, P. Brohan, T.L. Froelicher, H.-F. Graf, P. Jones, J. Luterbacher, S. Muthers, R. Neukom, A. Robock, S. Self, A. Sudrajat, C. Timmreck, and M. Wegmann, Tambora 1815 as a test case for high impact volcanic eruptions: Earth system effects, *WIREs Clim. Change*, *7*, 569–589, doi:10.1002/wcc.407, 2016.

Randall, C.E., V.L. Harvey, C.S. Singleton, S.M. Bailey, P.F. Bernath, M. Codrescu, H. Nakajima, and J.M. Russell, Energetic particle precipitation effects on the Southern Hemisphere stratosphere in 1992–2005, *J. Geophys. Res.*, *112*, D08308, doi:10.1029/2006JD007696, 2007.

Randel, W.J., L. Polvani, F. Wu, D.E. Kinnison, C.-Z. Zou, and C. Mears, Troposphere-stratosphere temperature trends derived from satellite data compared with ensemble simulations from WACCM, *J. Geophys. Res. Atmos.*, *122* (18), 9651-9667, doi: 10.1002/2017JD027158, 2017.

Revell, L.E., G.E. Bodeker, P.E. Huck, B.E. Williamson, and E. Rozanov, The sensitivity of stratospheric ozone changes through the 21st century to N_2O and CH_4, *Atmos. Chem. Phys.*, *12,* 11,309–11,317, doi:10.5194/acp-12-11309-2012, 2012.

Revell, L.E., F. Tummon, R.J. Salawitch, A. Stenke, and T. Peter, The changing ozone depletion potential of N_2O in a future climate, *Geophys. Res. Lett., 42*, 10,047–10,055, doi:10.1002/2015GL065702, 2015.

Rex, M., R.J. Salawitch, N.R.P. Harris, P. von der Gathen, G.O. Braathen, A. Schulz, H. Deckelmann, M. Chipperfield, B.-M. Sinnhuber, E. Reimer, R. Alfier, R. Bevilacqua, K. Hoppel, M. Fromm, J. Lumpe, H. Küllmann, A. Kleinböhl, H. Bremer, M. von König, K. Künzi, D. Toohey, H. Vömel, E. Richard, K. Aikin, H. Jost, J.B. Greenblatt, M. Loewenstein, J.R. Podolske, C.R. Webster, G.J. Flesch, D.C. Scott, R.L. Herman, J.W. Elkins, E.A. Ray, F.L. Moore, D.F. Hurst, P. Romashkin, G.C. Toon, B. Sen, J.J. Margitan, P. Wennberg, R. Neuber, M. Allart, B.R. Bojkov, H. Claude, J. Davies, W. Davies, H. De Backer, H. Dier, V. Dorokhov, H. Fast,

Y. Kondo, E. Kyrö, Z. Litynska, I.S. Mikkelsen, M.J. Molyneux, E. Moran, T. Nagai, H. Nakane, C. Parrondo, F. Ravegnani, P. Skrivankova, P. Viatte, and V. Yushkov, Chemical depletion of Arctic ozone in winter 1999/2000, *J. Geophys. Res.*, *107* (D20), doi:10.1029/2001JD000533, 2002.

Rex, M., R.J. Salawitch, P. von der Gathen, N.R.P. Harris, M.P. Chipperfield, and B. Naujokat, Arctic ozone loss and climate change, *Geophys. Res. Lett.*, *31*, L04116, doi:10.1029/2003GL018844, 2004.

Rex, M., R.J. Salawitch, H. Deckelmann, P. von der Gathen, N.R.P. Harris, M.P. Chipperfield, B. Naujokat, E. Reimer, M. Allaart, S.B. Andersen, R. Bevilacqua, G.O. Braathen, H. Claude, J. Davies, H. De Backer, H. Dier, V. Dorokhov, H. Fast, M. Gerding, S. Godin-Beekmann, K. Hoppel, B. Johnson, E. Kyrö, Z. Litynska, D. Moore, H. Nakane, M.C. Parrondo, A.D. Risley Jr., P. Skrivankova, R. Stübi, P. Viatte, V. Yushkov, and C. Zerefos, Arctic winter 2005: Implications for stratospheric ozone loss and climate change, *Geophys. Res. Lett.*, *33*, L23808, doi:10.1029/2006GL026731, 2006.

Rieder, H.E., and L.M. Polvani, Are recent Arctic ozone losses caused by increasing greenhouse gases?, *Geophys. Res. Lett.*, *40*, 4437–4441, doi:10.1002/grl.50835, 2013.

Rieder, H.E., L.M. Polvani, and S. Solomon, Distinguishing the impacts of ozone-depleting substances and well-mixed greenhouse gases on Arctic stratospheric ozone and temperature trends, *Geophys. Res. Lett.*, *41*, 2652–2660, doi:10.1002/2014GL059367, 2014.

Rosenfield, J.E., and A.R. Douglass, Doubled CO_2 effects on NO_y in a coupled 2-D model, *Geophys. Res. Lett., 25*, 4381–4384, doi:10.1029/1998GL900147, 1998.

Saha, S., S. Moorthi, H. Pan, X. Wu, J. Wang, S. Nadiga, P. Tripp, R. Kistler, J. Woollen, D. Behringer, H. Liu, D. Stokes, R. Grumbine, G. Gayno, J. Wang, Y. Hou, H. Chuang, H.H. Juang, J. Sela, M. Iredell, R. Treadon, D. Kleist, P. van Delst, D. Keyser, J. Derber, M. Ek, J. Meng, H. Wei, R. Yang, S. Lord, H. van den Dool, A. Kumar, W. Wang, C. Long, M. Chelliah, Y. Xue, B. Huang, J. Schemm, W. Ebisuzaki, R. Lin, P. Xie, M. Chen, S. Zhou, W. Higgins, C. Zou, Q. Liu, Y. Chen, Y. Han, L. Cucurull, R.W. Reynolds, G. Rutledge, and M. Goldberg, The NCEP Climate Forecast System Reanalysis, *Bull. Am. Meteorol. Soc.*, *91*, 1015–1058, doi:10.1175/2010BAMS3001.1, 2010.

Salawitch, R.J., S.C. Wofsy, and M.B. McElroy, Influence of polar stratospheric clouds on the depletion of Antarctic ozone, *Geophys. Res. Lett.*, *15*, 871–874, doi:10.1029/GL015i008p00871, 1988.

Salawitch, R.J., G.P. Gobbi, S.C. Wofsy, and M.B. McElroy, Denitrification in the Antarctic stratosphere, *Nature, 339*, 525–527, doi:10.1038/339525a0, 1989.

Sander, S.P., J. Abbatt, J.R. Barker, J.B. Burkholder, R.R. Friedl, D.M. Golden, R.E. Huie, C.E. Kolb, M.J. Kurylo, G.K. Moortgat, V.L. Orkin, and P.H. Wine, Chemical Kinetics and Photochemical Data for Use in Atmospheric Studies, Evaluation No. 17, *JPL Publication 10-6*, Jet Propulsion Laboratory, Pasadena, California. [available at: http://jpldataeval.jpl.nasa.gov], 2011.

Schütze, K., J.C. Wilson, S. Weinbruch, N. Benker, M. Ebert, G. Günther, R. Weigel, and S. Borrmann, Sub-micrometer refractory carbonaceous particles in the polar stratosphere, *Atmos. Chem. Phys.*, *17*, 12,475–12,493, doi:10.5194/acp-17-12475-2017, 2017.

Sinnhuber, B.-M., and S. Meul, Simulating the impact of emissions of brominated very short lived substances on past stratospheric ozone trends, *Geophys. Res. Lett.*, *42*, 2449–2456, doi:10.1002/2014GL062975, 2015.

Sinnhuber, M., H. Nieder, and N. Wieters, Energetic particle precipitation and the chemistry of the mesosphere / lower thermosphere, *Surv. Geophys.*, *33*, doi:10.1007/s10712-012-9201-3, 2012.

Sinnhuber, M., U. Berger, B. Funke, H. Nieder, T. Reddmann, G. Stiller, S. Versick, T. von Clarmann, and J.M. Wissing, NO_y production, ozone loss and changes in net radiative heating due to energetic particle precipitation in 2002–2010, *Atmos. Chem. Phys.*, *18*, 1115–1147, doi:10.5194/acp-18-1115-2018, 2018.

Siskind, D.E., GE. Nedoluha, F. Sassi, P. Rong, S.M. Bailey, M.E. Hervig, and C.E. Randall, Persistence of upper stratospheric wintertime tracer variability into the Arctic spring and summer, *Atmos. Chem. Phys.*, *16*, 7957–7967, doi:10.5194/acp-16-7957-2016, 2016.

Solomon, S., R.R. Garcia, F.S. Rowland, and D.J. Wuebbles, On the depletion of Antarctic ozone, *Nature*, *321*, 755–758, doi:10.1038/321755a0,

1986.

Solomon, S., J. Haskins, D.J. Ivy, and F. Min, Fundamental differences between Arctic and Antarctic ozone depletion, *Proc. Natl. Acad. Sci.*, *111* (17), 6220–6225, doi:10.1073/pnas.1319307111, 2014.

Solomon, S., D. Kinnison, J. Bandoro, and R. Garcia, Simulation of polar ozone depletion: An update, *J. Geophys. Res.*, *120*, 7958–7974, doi:10.1002/2015JD023365, 2015.

Solomon, S., D.J. Ivy, D. Kinnison, M.J. Mills, R.R. Neely III, and A. Schmidt, Emergence of healing in the Antarctic ozone layer, *Science*, *353* (6296), 269–274, doi:10.1126/science.aae0061, 2016.

Solomon, S., D. Ivy, M. Gupta, J. Bandoro, B. Santer, Q. Fu, P. Lin, R.R. Garcia, D. Kinnison, and M. Mills, Mirrored changes in Antarctic ozone and stratospheric temperature in the late 20th versus early 21st centuries, *J. Geophys. Res. Atmos.*, *122*, doi:10.1002/2017JD026719, 2017.

Spang, R., L. Hoffmann, M. Höpfner, S. Griessbach, R. Müller, M.C. Pitts, A.M.W. Orr, and M. Riese, A multi-wavelength classification method for polar stratospheric cloud types using infrared limb spectra, *Atmos. Meas. Tech.*, *9* (8), 3619–3639, doi:10.5194/amt-9-3619-2016, 2016.

Spang, R., L. Hoffmann, R. Müller, J.-U. Grooß, I. Tritscher, M. Höpfner, M. Pitts, A. Orr, and M. Riese, A climatology of polar stratospheric cloud composition between 2002 and 2012 based on MIPAS/Envisat observations, *Atmos. Chem. Phys.*, *18*, 5089–5113, doi:10.5194/acp-18-5089-2018, 2018.

SPARC CCMVal (Stratosphere-troposphere Processes And their Role in Climate), *SPARC Report on the Evaluation of Chemistry-Climate Models*, edited by V. Eyring, T.G. Shepherd, and D.W. Waugh, SPARC Report No. 5, WCRP-132, WMO/TD-No. 1526, 478 pp., [available at: http://www.atmosp.physics.utoronto.ca/SPARC/ccmval_final/index.php], 2010.

SPARC (Stratosphere-troposphere Processes And their Role in Climate), *SPARC Report on the Lifetimes of Stratospheric Ozone-Depleting Substances, Their Replacements, and Related Species*, edited by M.K.W. Ko, P.A. Newman, S. Reimann, S.E. Strahan, SPARC Report No. 6, WCRP-15/2013, 2013.

Stolarski, R., M. Schoeberl, P. Newman, R. McPeters, and A. Krueger, The 1989 Antarctic ozone hole as observed by TOMS, *Geophys. Res. Lett.*, *17* (9), 1267–1270, doi:10.1029/GL017i009p01267, 1990.

Stolarski, R.S., A.R. Douglass, L.D. Oman, and D. Waugh, Impact of future nitrous oxide and carbon dioxide emissions on the stratospheric ozone layer, *Environ. Res. Lett., 10* (3), doi:10.1088/1748-9326/10/3/03011, 2015.

Stone, K.A., S. Solomon, D.E. Kinnison, M.C. Pitts, L.R. Poole, M.J. Mills, A. Schmidt, R.R. Neely III, D. Ivy, M.J. Schwartz, B.J. Johnson, M.B. Tully, A.R. Klekociuk, G. König-Langlo, and S. Hagiya, Observing the impact of Calbuco volcanic aerosols on South Polar ozone depletion in 2015, *J. Geophys. Res.*, *122*, 11,862–11,879, doi:10.1002/2017JD026987, 2017.

Strahan, S.E., and A.R. Douglass, Decline in Antarctic ozone depletion and lower stratospheric chlorine determined from Aura Microwave Limb Sounder observations, *Geophys. Res. Lett.*, *45*, 382–390, doi:10.1002/2017GL074830, 2018.

Strahan, S.E., A.R. Douglass, P.A. Newman, and S.D. Steenrod, Inorganic chlorine variability in the Antarctic vortex and implications for ozone recovery, *J. Geophys. Res. Atmos.*, *119* (24), doi:10.1002/2014JD022295, 2014.

Strahan, S.E., A.R. Douglass, and S.D. Steenrod, Chemical and dynamical impacts of stratospheric sudden warmings on Arctic ozone variability, *J. Geophys. Res. Atmos.*, *121*, 11,836–11,851, doi:10.1002/2016JD025128, 2016.

Tabazadeh, A., and R.P. Turco, A model for heterogeneous chemical processes on the surfaces of ice and nitric acid trihydrate particles, *J. Geophys. Res.*, *98* (D7), 12727–12740, doi:10.1029/93JD00947, 1993.

Tabazadeh. A., K. Drdla, M.R. Schoeberl, P. Hamill, and O.B. Toon, Arctic "ozone hole" in a cold volcanic stratosphere, *Proc. Natl. Acad. Sci.*, *99* (5), 2609–2612; doi:10.1073/pnas.052518199, 2002.

Tao, M., P. Konopka, F. Ploeger, J.-U. Grooß, R. Müller, C.M. Volk, K.A. Walker, and M. Riese, Impact of the 2009 major sudden stratospheric warming on the composition of the stratosphere, *Atmos. Chem. Phys.*, *15*, 8695–8715, doi: 10.5194/acp-15-8695-2015, 2015.

Tegtmeier, S., F. Ziska, I. Pisso, B. Quack, G.J.M. Velders, X. Yang, and K. Krüger, Oceanic bromoform emissions weighted by their ozone depletion potential, *Atmos. Chem. Phys.*, *15*, 13,647–13,663,

doi:10.5194/acp-15-13647-2015, 2015.

Tian, W., Y. Li, F. Xie, J. Zhang, M.P. Chipperfield, W. Feng, Y. Hu, S. Zhao, X. Zhou, Y. Yang, and X. Ma, The relationship between lower-stratospheric ozone at southern high latitudes and sea surface temperature in the East Asian marginal seas in austral spring, *Atmos. Chem. Phys.*, *17*, 6705–6722, doi:10.5194/acp-17-6705-2017, 2017.

Tie, X.-X., and G. Brasseur, The response of stratospheric ozone to volcanic eruptions: Sensitivity to atmospheric chlorine loading, *Geophys. Res. Lett.*, *22 (22)*, 3035–3038, doi:10.1029/95GL03057, 1995.

Tilmes, S., R. Müller, J.-U. Grooß, M. Höpfner, G.C. Toon, and J.M. Russell III, Very early chlorine activation and ozone loss in the Arctic winter 2002–2003, *Geophys. Res. Lett.*, *30* (23), 2201–2205, doi:10.1029/2003GL018079, 2003.

Toohey, M., K. Krüger, M. Bittner, C. Timmreck, and H. Schmidt, The impact of volcanic aerosols on the Northern Hemisphere stratospheric polar vortex: Mechanisms and sensitivity forcing structure, *Atmos. Chem. Phys.*, *14*, 13,063–13,079, doi:10.5194/acp-14-13063-2014, 2014.

Uchino, O., R.D. Bojkov, D.S. Balis, K. Akagi, M. Hayashi, and R. Kajihara, Essential characteristics of the Antarctic-spring ozone decline: Update to 1998, *Geophys. Res. Lett.*, *26* (10), 1377–1380, doi:10.1029/1999GL900277, 1999.

van Loon, H., and K. Labitzke, The Southern Oscillation, Part V: The anomalies in the lower stratosphere of the Northern Hemisphere in winter and a comparison with the Quasi-Biennial Oscillation, *Mon. Wea. Rev., 115*, 357–369, doi:10.1175/1520-0493(1987)115<0357:TSOPVT>2.0.CO;2, 1987.

Verkhoglyadova, O.P., S. Wang, M.G. Mlynczak, L.A. Hunt, and G.P. Zank, Effects of two large solar energetic particle events on middle atmosphere nighttime odd hydrogen and ozone content: Aura/MLS and TIMED/SABER measurements, *J. Geophys. Res. Space Phys.*, *120* (1), 12–29, doi:10.1002/2014JA020609, 2015.

Vogel, B., P. Konopka, J.-U. Grooß, R. Müller, B. Funke, M. López-Puertas, T. Reddmann, G. Stiller, T. von Clarmann, and M. Riese, Model simulations of stratospheric ozone loss caused by enhanced mesospheric NOx during Arctic Winter 2003/2004, *Atmos. Chem. Phys.*, *8*, 5279–5293, doi:10.5194/acp-8-5279-2008, 2008.

von Clarmann, T., B. Funke, M. López-Puertas, S. Kellmann, A. Linden, G.P. Stiller, C.H. Jackman, and V.L. Harvey, The Solar proton events in 2012 as observed by MIPAS, *Geophys. Res. Lett.*, *40*, 1–5, doi:10.1002/grl.50119, 2013.

von Hobe, M., S. Bekki, S. Borrmann, F. Cairo, F. D'Amato, G. Di Donfrancesco, A. Dörnbrack, A. Ebersoldt, M. Ebert, C. Emde, I. Engel, M. Ern, W. Frey, S. Genco, S. Griessbach, J.-U. Grooß, T. Gulde, G. Günther, E. Hösen, L. Hoffmann, V. Homonnai, C.R. Hoyle, I.S.A. Isaksen, D.R. Jackson, I.M. Janosi, R.L. Jones, K. Kandler, C. Kalicinsky, A. Keil, S.M. Khaykin, F. Khosrawi, R. Kivi, J. Kuttippurath, J.C. Laube, F. Lefevre, R. Lehmann, S. Ludmann, B.P. Luo, M. Marchand, J. Meyer, V. Mitev, S. Molleker, R. Müller, H. Oelhaf, F. Olschewski, Y. Orsolini, T. Peter, K. Pfeilsticker, C. Piesch, M.C. Pitts, L.R. Poole, F.D. Pope, F. Ravegnani, M. Rex, M. Riese, T. Röckmann, B. Rognerud, A. Roiger, C. Rolf, M.L. Santee, M. Scheibe, C. Schiller, H. Schlager, M. Siciliani de Cumis, N. Sitnikov, O.A. Svde, R. Spang, N. Spelten, F. Stordal, O. Suminska-Ebersoldt, A. Ulanovski, J. Ungermann, S. Viciani, C.M. Volk, M. vom Scheidt, P. von der Gathen, K. Walker, T. Wegner, R. Weigel, S. Weinbruch, G. Wetzel, F.G. Wienhold, I. Wohltmann, W. Woiwode, I.A.K. Young, V. Yushkov, B. Zobrist, and F. Stroh, Reconciliation of essential process parameters for an enhanced predictability of Arctic stratospheric ozone loss and its climate interactions (RECONCILE): Activities and results, *Atmos. Chem. Phys.*, *13* (18), 9233–9268, doi:10.5194/acp-13-9233-2013, 2013.

Wales, P.A., R.J. Salawitch, J.M. Nicely, D.C. Anderson, T.P. Canty, S. Baidar, B. Dix, T.K. Koenig, R. Volkamer, D. Chen, L.G. Huey, D.J. Tanner, C.A. Cuevas, R.P. Fernandez, D.E. Kinnison, J.-F. Lamarque, A. Saiz-Lopez, E.L. Atlas, S.R. Hall, M.A. Navarro, L.L. Pan, S.M. Schauffler, M. Stell, S. Tilmes, K. Ullmann, A.J. Weinheimer, H. Akiyoshi, M.P. Chipperfield, M. Deushi, S.S. Dhomse, W. Feng, P. Graf, R. Hossaini, P. Jöckel, E. Mancini, M. Michou, O. Morgenstern, L.D. Oman, G. Pitari, D.A. Plummer, L.E. Revell, E. Rozanov, D. Saint-Martin, R. Schofield, A. Stenke, K.A. Stone, D. Visioni, Y. Yamashita, and G. Zeng, Stratospheric injection of brominated very short-lived

substances: Aircraft observations in the Western Pacific and representation in global models, *J. Geophys. Res.*, *123*, doi:10.1029/2017JD027978, 2018.

Weber, M., S. Dikty, J.P. Burrows, H. Garny, M. Dameris, A. Kubin, J. Abalichin, and U. Langematz, The Brewer-Dobson circulation and total ozone from seasonal to decadal time scales, *Atmos. Chem. Phys.*, *11*, 11,221–11,235, doi:10.5194/acp-11-11221-2011, 2011.

Weber, M., W. Steinbrecht, C. Roth, M. Coldewey-Egbers, R.J. van der A, D. Degenstein, V.E. Fioletov, S.M. Frith, L. Froidevaux, C.S. Long, D. Loyola, and J.D. Wild, Stratospheric Ozone, [in "State of the Climate in 2014"], *Bull. Amer. Meteorol. Soc.*, *96* (7), S44–S46, doi:10.1175/2015BAMSStateoftheClimate.1, 2015.

Weber, M., W. Steinbrecht, C. Roth, M. Coldewey-Egbers, D. Degenstein, Y.E. Fioletov, S.M. Frith, L. Froidevaux, J. de Laat, C.S. Long, D. Loyola, and J.D. Wild, Stratospheric Ozone, [in "State of the Climate in 2015"], *Bull. Amer. Meteorol. Soc.*, *97* (8), S49–S51, doi:10.1175/2016BAMSStateoftheClimate.1, 2016.

Weber M., W. Steinbrecht, S.M. Frith, O. Tweedy, M. Coldewey-Egbers, S. Davis, D. Degenstein, Y.E. Fioletov, L. Froidevaux, J. de Laat, C.S. Long, D. Loyola, C. Roth, and J.D. Wild, Stratospheric Ozone, [in "State of the Climate in 2016"], *Bull. Amer. Meteorol. Soc.*, *98* (8), S49–S51, doi:10.1175/2017BAMSStateoftheClimate.1, 2017.

Weber, M., M. Coldewey-Egbers, V.E. Fioletov, S. Frith, J.D. Wild, J.P. Burrows, C.S. Long, and D. Loyola, Total ozone trends from 1979 to 2016 derived from five merged observational datasets – the emergence into ozone recovery, *Atmos. Chem. Phys.*, *18*, 2097–2117, doi:10.5194/acp-18-2097-2018, 2018.

Wegner, T., M.C. Pitts, L.R. Poole, I. Tritscher, J.-U. Grooß, and H. Nakajima, Vortex-wide chlorine activation by a mesoscale PSC event in the Arctic winter of 2009/10, *Atmos. Chem. Phys.*, *16* (7), 4569–4577, doi:10.5194/acp-16-4569-2016, 2016.

Weigel, R., C.M. Volk, K. Kandler, E. Hösen, G. Günther, B. Vogel, J.-U. Grooß, S. Khaykin, G.V. Belyaev, and S. Borrmann, Enhancements of the refractory submicron aerosol fraction in the Arctic polar vortex: Feature or exception?, *Atmos. Chem. Phys.*, *14*, 12,319–12,342, doi:10.5194/acp-14-12319-2014, 2014.

Wetzel, G., H. Oelhaf, M. Birk, A. de Lange, A. Engel, F. Friedl-Vallon, O. Kirner, A. Kleinert, G. Maucher, H. Nordmeyer, J. Orphal, R. Ruhnke, B.-M. Sinnhuber, and P. Vogt, Partitioning and budget of inorganic and organic chlorine species observed by MIPAS-B and TELIS in the Arctic in March 2011, *Atmos. Chem. Phys.*, *15* (14), 8065–8076, doi:10.5194/acp-15-8065-2015, 2015.

WMO (World Meteorological Organization), *Scientific Assessment of Ozone Depletion: 2006*, Global Ozone Research and Monitoring Project–Report No. 50, 572 pp., Geneva, Switzerland, 2007.

WMO (World Meteorological Organization), *Scientific Assessment of Ozone Depletion: 2010*, Global Ozone Research and Monitoring Project–Report No. 52, 516 pp., Geneva, Switzerland, 2011.

WMO (World Meteorological Organization), *Scientific Assessment of Ozone Depletion: 2014,* Global Ozone Research and Monitoring Project Report–No. 55, 416 pp., Geneva, Switzerland, 2014

Wohltmann, I., T. Wegner, R. Müller, R. Lehmann, M. Rex, G.L. Manney, M.L. Santee, P. Bernath, O. Sumińska-Ebersoldt, F. Stroh, M. von Hobe, C.M. Volk, E. Hösen, F. Ravegnani, A. Ulanovsky, and V. Yushkov, Uncertainties in modelling heterogeneous chemistry and Arctic ozone depletion in the winter 2009/2010, *Atmos. Chem. Phys., 13*, 3909–3929, doi:10.5194/acp-13-3909-2013, 2013.

Wohltmann, I., R. Lehmann, and M. Rex, A quantitative analysis of the reactions involved in stratospheric ozone depletion in the polar vortex core, *Atmos. Chem. Phys.*, *17*, 10,535–10,563, doi:10.5194/acp-17-10535-2017, 2017.

Woiwode, W., M. Höpfner, L. Bi, M.C. Pitts, L.R. Poole, H. Oelhaf, S. Molleker, S. Borrmann, M. Klingebiel, G. Belyaev, A. Ebersoldt, S. Griessbach, J.-U. Grooß, T. Gulde, M. Krämer, G. Maucher, C. Piesch, C. Rolf, C. Sartorius, R. Spang, and J. Orphal, Spectroscopic evidence of large aspherical β-NAT particles involved in denitrification in the December 2011 Arctic stratosphere, *Atmos. Chem. Phys.*, *16* (14), 9505–9532, doi:10.5194/acp-16-9505-2016, 2016.

Yang, E.-S., D.M. Cunnold, M.J. Newchurch, R.J. Salawitch, M.P. McCormick, J.M. Russell III, J.M. Zawodny, and S.J. Oltmans, First stage of Antarctic ozone recovery, *J. Geophys. Res.*, *113*, D20308, doi:10.1029/2007JD009675, 2008.

Yang, X., N.L. Abraham, A.T. Archibald, P. Braesicke, J. Keeble, P.J. Telford, N.J. Warwick, and J.A. Pyle, How sensitive is the recovery of stratospheric ozone to changes in concentrations of very shortlived bromocarbons?, *Atmos. Chem. Phys.*, *14* (19), 10,431–10,438, doi:10.5194/acp-14-10431-2014, 2014.

Ziska, F., B. Quack, I. Stemmler, S. Tegtmeier, and K. Krüger, Future emissions of marine halogenated very short-lived substances under climate change, *J. Atmos. Chem.*, *74*, 245, doi:10.1007/s10874-016-9355-3, 2017.

Zhu, Y., O.B. Toon, A. Lambert, D.E. Kinnison, C. Bardeen, and M.C. Pitts, Development of a polar stratospheric cloud model within the Community Earth System Model: Assessment of 2010 Antarctic winter, *J. Geophys. Res.*, *122*, 10,418–10,438. doi:10.1002/2017JD027003, 2017a.

Zhu, Y., O.B. Toon, M.C. Pitts, A. Lambert, C. Bardeen, and D.E. Kinnison, Comparing simulated PSC optical properties with CALIPSO observations during the 2010 Antarctic winter, *J. Geophys. Res. Atmos.*, *122*, 1175–1202, doi:10.1002/2016JD025191, 2017b.

Zubiaurre, I., and N. Calvo, The ENSO Modoki signal in the stratosphere, *J. Geophys. Res. Atmos.*, *117,* D06109, doi:10.1029/2011JD016690, 2012

Chapter 5

Stratospheric Ozone Changes and Climate

Lead Authors
A.Yu. Karpechko
A.C. Maycock

Coauthors
M. Abalos
H. Akiyoshi
J.M. Arblaster
C.I. Garfinkel
K.H. Rosenlof
M. Sigmond

Contributors
V. Aquila
A. Banerjee
A. Chrysanthou
D. Ferreira
H. Garny
N. Gillett
P. Landschützer
E.-P. Lim
M.J. Mills
W.J. Randel
E. Ray
W. Seviour
S.-W. Son
N. Swart

Review Editors
C. Cagnazzo
L. Polvani

Cover photo: An image of a cyclone off the coast of Antarctica from the MODIS satellite instrument. Stratospheric ozone depletion has led to a poleward shift in summertime cyclone frequency over the Southern Ocean. Photo: NASA

Chapter 5

Stratospheric Ozone Changes and Climate

CONTENTS

Chapter 5

Stratospheric Ozone Changes and Climate

SCIENTIFIC SUMMARY

Since the 2014 Ozone Assessment, new research has better quantified the impact of stratospheric ozone changes on climate. Additional model and observational analyses are assessed, which examine the influence of stratospheric ozone changes on stratospheric temperatures and circulation, tropospheric circulation and composition, surface climate, the oceans, and sea ice. The new results support the main conclusions of the previous Assessment; the primary advances are summarized below.

STRATOSPHERIC TEMPERATURES

- **New estimates of satellite-observed stratospheric temperature changes show net global stratospheric cooling of around 1.5 K (at 25–35 km), 1.5 K (at 35–45 km), and 2.3 K (at 40–50 km) between 1979 and 2005, with differences between datasets of up to 0.6 K.**
    - There are now better estimates of observed stratospheric temperature trends than were available during the last Assessment. Two datasets from satellite measurements have been re-processed and now show greater consistency in long-term temperature trends in the middle and upper stratosphere.
    - Satellite temperature records show smaller stratospheric cooling rates over 1998–2015 compared to 1979–1997, consistent with the observed differences in stratospheric ozone trends during these periods.
    - Global average temperature in the lower stratosphere (13–22 km) cooled by about 1 K between 1979 and the late 1990s but has not changed significantly since then.
- **In the lower stratosphere (13–22 km), ozone trends were the major cause of the observed cooling between the late 1970s and the mid-1990s. In the middle and upper stratosphere, however, increases in long-lived greenhouse gases played a slightly larger role than ozone changes in cooling trends over this period.** Ozone recovery will continue to play an important role in future stratospheric temperature trends.
    - There is now improved understanding of the causes of stratospheric temperature trends and variability. For the upper stratosphere (40–50 km), new studies suggest that one-third of the observed cooling over 1979–2005 was due to ozone-depleting substances (ODSs) and associated ozone changes, while two-thirds was due to other well-mixed greenhouse gases.
    - Chemistry–climate models show that the magnitude of future stratospheric temperature trends is dependent on future greenhouse gas concentrations, with most greenhouse gas scenarios showing cooling in the middle and upper stratosphere over the 21st century. The projected increase in global stratospheric ozone during this period would offset part of the stratospheric cooling due to increasing greenhouse gases.

STRATOSPHERIC OVERTURNING CIRCULATION

- **There are indications that the overturning circulation in the lower stratosphere has accelerated over the past few decades.**

- Observations of the latitudinal profile of lower stratospheric temperature trends and changes in constituents show that tropical upwelling in the lower stratosphere has strengthened over the last ~30 years, in qualitative agreement with model simulations and reanalysis datasets.
- New studies using measurements provide evidence for structural changes in the stratospheric overturning circulation which is comprised of a strengthening in the lower stratosphere and a weakening in the middle and upper stratosphere.
- According to models, in addition to well-mixed greenhouse gases, changes in ODSs (and associated changes in ozone) are an important driver of past and future changes in the strength of the stratospheric overturning circulation, notably the increase in downwelling over the Antarctic over the late 20th century.
- Estimates of externally forced long-term changes in the stratospheric overturning circulation from observations remain uncertain, partially due to internal variability.
- Models project future increases in stratosphere–troposphere exchange of ozone as a consequence of a strengthening of the stratospheric overturning circulation and stratospheric ozone recovery.

IMPACTS ON THE TROPOSPHERE, OCEAN, AND SEA ICE

- **New research supports the findings of the 2014 Ozone Assessment that Antarctic ozone depletion was the dominant driver of the changes in Southern Hemisphere tropospheric circulation in austral summer during the late 20th century, with associated weather impacts.**
  - Over the period 1970 to 2000, tropospheric jets in the Southern Hemisphere shifted poleward and strengthened, the Southern Annular Mode (SAM) index increased, and the southern edge of the Hadley Cell expanded poleward. Since 2000, the SAM has remained in a positive phase.
  - For austral summer, most model simulations show a larger contribution to these trends from Antarctic ozone depletion compared to increases in well-mixed greenhouse gases during the last decades of the 20th century. During other seasons, the contribution of ozone depletion to circulation changes is comparable to that from well-mixed greenhouse gases.
  - Paleoclimate reconstructions of the SAM index suggest that the current period of prolonged positive summer SAM conditions is unprecedented in at least the past 600 years.
  - No robust link between stratospheric ozone depletion and long-term Northern Hemisphere surface climate has been established; there are indications that occurrences of extremely low springtime ozone amounts in the Arctic may have short-term effects on Northern Hemisphere regional surface climate.
- **Changes in tropospheric weather patterns driven by ozone depletion have played a role in recent temperature, salinity, and circulation trends in the Southern Ocean, but the impact on Antarctic sea ice remains unclear.**
  - Progress has been made since the last Assessment in understanding the physical processes involved in the Southern Ocean response to ozone depletion, which is now believed to entail a fast surface cooling followed by a slow long-term warming.
  - Modeling studies indicate that ozone depletion contributes to a decrease in Antarctic sea ice extent and hence cannot explain the observed sea ice increase between 1979 and 2015. This is in agreement with the conclusions of the previous Assessment. However, in general, climate models still cannot

reproduce the observed Antarctic sea ice trends since 1979, which limits the confidence in the modeled sea ice response to ozone depletion.

- **New observation-based analyses indicate that a causal link between the strength of the Southern Ocean carbon sink and ozone depletion cannot be established, in contrast to earlier suggestions.**
    - New observation-based analyses confirmed the previously reported slowdown of the carbon sink between the 1980s and early 2000s but also revealed a remarkable reinvigoration of the carbon sink since then. The new results indicate that atmospheric circulation changes (whether driven by ozone depletion or not) have not had a considerable impact on the net strength of the Southern Ocean carbon sink.

MONTREAL PROTOCOL CLIMATE IMPACTS

- **New studies since the 2014 Ozone Assessment have identified that future global sea level rise of at least several centimeters has been avoided as a result of the Montreal Protocol.** This would have arisen from thermal expansion of the oceans associated with additional global warming from unregulated ozone depleted substances emissions.

Chapter 5

Stratospheric Ozone Changes and Climate

5.1 INTRODUCTION AND SCOPE

The 2006 Ozone Assessment was the first to include a dedicated chapter on ozone–climate interactions (Baldwin and Dameris et al., 2007). The focus of that chapter was mostly on how anthropogenic climate change affects stratospheric ozone. Ozone–climate interactions were considered in a broader perspective in both the 2010 and 2014 Ozone Assessments. Chapter 4 of the 2014 Assessment (Arblaster and Gillett et al., 2014) addressed changes in stratospheric climate, their coupling with stratospheric ozone changes, and the impacts of stratospheric changes on tropospheric climate. This chapter is similar in scope and provides an assessment of the advances in scientific understanding of ozone–climate coupling since the last Assessment. To provide a basis for discussing these advances in the subsequent sections, the main conclusions from Chapter 4 of the 2014 Assessment are summarized here.

5.1.1 Summary of Findings from the Previous Ozone Assessment

The last Assessment concluded that the lower stratosphere (near 20 km) cooled in the global mean by approximately 1 K over the period 1979–1995, after which temperatures remained approximately constant. It also concluded that the middle (25–35 km) and upper (35–50 km) stratosphere have cooled in the global mean over this period; however, the available satellite datasets showed substantial differences in the estimated magnitude of cooling. In agreement with previous Ozone Assessments, it was concluded that stratospheric ozone changes were the primary cause of the observed lower-stratospheric cooling, while both ozone decreases and greenhouse gas (GHG) increases (primarily carbon dioxide, CO_2) made more comparable contributions to cooling in the middle and upper stratosphere.

The 2014 Ozone Assessment concluded from observations of composition and temperature that over the past several decades there has been an increase in tropical lower-stratospheric upwelling, consistent with a strengthening of the shallow branch of the stratospheric overturning circulation. At the same time, long-term changes in the deep branch of the overturning circulation were concluded to be uncertain. No long-term changes were found in stratospheric water vapor concentrations since 2000.

In agreement with the findings of earlier Assessments, the 2014 Assessment concluded that the ozone-induced springtime cooling of the Antarctic lower stratosphere has strongly affected the Southern Hemisphere (SH) tropospheric climate in austral summer. It was assessed that stratospheric temperature changes due to ozone depletion were likely the dominant driver of the observed summertime poleward shift of the mid-latitude tropospheric jet and have contributed to the poleward expansion of the SH Hadley Cell. It was noted that, in response to ozone depletion, some climate models simulate a poleward shift of subtropical precipitation patterns and that consistent changes are seen in observations. Changes in the Southern Ocean were discussed, and it was concluded that changes in surface wind stress, associated with the tropospheric circulation response to ozone depletion, likely caused the intensification of the subtropical ocean gyres, the meridional overturning circulation, and subsurface warming. Contrary to the findings of the 2010 Assessment, the 2014 Assessment concluded, though with low confidence, that stratospheric ozone depletion induces a decrease in Antarctic sea ice extent and therefore cannot explain the small observed increase in Antarctic sea ice extent over the past several decades. Possible impacts of ozone depletion-induced surface wind stress changes on carbon uptake in the Southern Ocean were also assessed to be uncertain. The 2014 Assessment did not find a robust link between ozone changes and tropospheric climate in the Northern Hemisphere.

The 2014 Assessment concluded that stratospheric ozone depletion contributed to a decrease in the flux of ozone into the troposphere but that coincident increases in emissions of ozone precursor species led to an

overall increase in the tropospheric ozone burden. The overall global radiative forcing (RF) between 1850 and 2011 due to the effect of long-lived ozone-depleting substances (ODSs) on both stratospheric and tropospheric ozone was estimated to be about –0.15 W m^{-2}.

For the future, the 2014 Assessment concluded that the impacts of ozone depletion on tropospheric climate will reverse as a result of ozone recovery and that this will offset part of the GHG-induced changes in SH tropospheric circulation in summer during the first half of this century. The projected strengthening of the stratospheric overturning circulation was assessed to have important implications for future stratospheric and tropospheric ozone abundances. The RF due to future stratospheric ozone changes was assessed to be uncertain even regarding its sign, due to uncertainty in model projections of tropical lower-stratospheric ozone trends.

5.1.2 Scope of the Chapter

Following Chapter 4 of the 2014 Ozone Assessment, this chapter begins with an assessment of changes in stratospheric constituents and external forcings (**Section 5.2**). Only a brief discussion of changes in ODSs and stratospheric ozone is given here, since these are assessed in detail in **Chapter 1** (ODS changes) and **Chapters 3 and 4** (ozone changes). **Section 5.3** assesses changes in stratospheric temperatures and circulation. That section includes an attribution of observed temperature and circulation changes to different drivers and also an analysis of projected changes. Stratosphere–troposphere exchange of ozone is also discussed, but since changes in tropospheric ozone have been recently assessed in detail in the Tropospheric Ozone Assessment Report (TOAR), led by the International Global Atmospheric Chemistry (IGAC) project (Young et al., 2018), the discussion of tropospheric chemistry is limited to assessing the effects of stratospheric ozone on the tropospheric ozone budget. **Section 5.4** discusses the effects of stratospheric ozone on tropospheric circulation, surface climate, the ocean, and sea ice, as well as the current scientific understanding of physical mechanisms for the downward dynamical coupling between the stratosphere and troposphere. Lastly, **Section 5.5** assesses the climate impacts that have been avoided as a result of the successful regulation of ODS emissions under the Montreal Protocol, as well as the future climate impacts that will be avoided if nations adhere to the phasedown of hydrofluorocarbons under the 2016 Kigali Amendment (see also **Chapter 2**).

5.2 OBSERVED CHANGES IN ATMOSPHERIC CONSTITUENTS AND EXTERNAL FORCINGS THAT RELATE TO CLIMATE

The species detailed in this section play a role in climate through their effects on radiative and chemical processes. Changes in these species can alter stratospheric ozone concentrations either through direct effects on ozone chemistry and/or via their effect on stratospheric temperatures and transport.

5.2.1 Long-Lived Greenhouse Gases and Ozone-Depleting Substances

Carbon dioxide (CO_2), methane (CH_4), and nitrous oxide (N_2O) are the three most important anthropogenically emitted GHGs in the atmosphere in terms of historical RF (Myhre and Shindell et al., 2013); however, it should be noted that ODSs and their replacement compounds are also significant GHGs. Such gases are more transparent to incoming (shortwave) radiation from the sun compared to outgoing infrared (longwave) radiation. Increases in the atmospheric concentrations of these gases lead to warming at the surface, producing a direct global climate response. These gases may also cause changes in stratospheric temperatures through effects on the local radiative balance; for example, increasing CO_2 cools the stratosphere (see **Box 5-1**). Ozone photochemistry responds to stratospheric temperature changes, as well as to changes in abundances of ODSs. Similarly, changes in ozone affect the stratospheric radiative balance; decreases in ozone will result in stratospheric cooling due to less absorption of solar ultraviolet radiation. Changes in the stratospheric overturning (Brewer–Dobson) circulation may be forced by changes in well-mixed GHGs and ozone concentrations (see **Section 5.3.2**); this may also impact the distributions of stratospheric and tropospheric ozone through transport changes (see **Section 5.3.3**).

Recent concentrations and growth rates for ODSs, including N_2O, are described in **Chapter 1** and for ODS replacement compounds in **Chapter 2**. Globally averaged annual average mole fraction values for 2017

were 405 ppm (parts per million) for CO_2 and 1,850 ppb (parts per billion) for CH_4. Global concentrations and growth rates for CO_2 and CH_4 are shown in **Figure 5-1**. These show that 2015 and 2016 had high CO_2 growth rates relative to the 1980–2016 average. This is likely related, at least in part, to the El Niño conditions that persisted from late 2014 through early 2016 (Le Quéré et al., 2018); the CO_2 growth rate is known to increase during El Niño conditions and decrease during La Niña conditions (Kim et al., 2016; Betts et al., 2016; Le Quéré et al., 2018). The CH_4 growth rate peaked in 2014 but remained positive and greater than 5 ppb yr^{-1} in 2015 and 2016. Multiple drivers have been suggested for the higher CH_4 growth rates since the 2000s and are discussed in **Section 1.5.2** (see also Saunois et al., 2016). These include changes in the atmospheric concentrations of the hydroxyl (OH) radical, increased emissions from oil and gas extraction, increased emissions from wetlands, and increased emissions from anthropogenic sources in East Asia.

5.2.2 Stratospheric Water Vapor

Stratospheric water vapor (SWV) modulates Earth's climate directly, mainly through longwave radiative processes, and indirectly through its influence on stratospheric ozone abundances. It impacts stratospheric ozone chemistry through its role as the major source of reactive hydrogen oxide molecules (HO_x) in the stratosphere and through the formation of polar stratospheric clouds (see **Chapter 4**). Changes to

Box 5-1. Why Does Increasing CO_2 Cool the Stratosphere?

Although carbon dioxide (CO_2) in the stratosphere plays only a small direct role in chemical processes, it is very important for the atmosphere's radiative balance. CO_2 emits and absorbs radiation mainly in the infrared part of the electromagnetic spectrum, with the strongest emission and absorption at wavelengths close to 15 μm. At these wavelengths, the absorption of infrared radiation by CO_2 is so efficient that most radiation emitted by Earth's surface is absorbed in the troposphere and does not reach the stratosphere. Radiation entering the stratosphere from below therefore comes from the relatively cold upper troposphere. At the same time, CO_2 in the stratosphere emits radiation to space, cooling the stratosphere. The largest cooling rates are in the upper stratosphere, where temperatures are highest due to absorption of incoming ultraviolet radiation by ozone. Since this local emission is not balanced by the absorption of upwelling radiation from below, CO_2 contributes a net cooling in the stratosphere. When the atmospheric CO_2 concentration increases, there is only a small increase in the absorption of radiation from the troposphere, which does not compensate for a relatively larger increase in local emission, leading to a greater loss of radiation to space. An increase in CO_2 therefore radiatively cools the stratosphere at all altitudes, with the largest cooling in the upper stratosphere.

Increases in other greenhouse gases (GHGs) that absorb and emit infrared radiation, such as methane, nitrous oxide, and chlorofluorocarbons (CFCs), also contribute to cooling in the upper stratosphere, because at stratospheric altitudes they emit more radiation to space than they absorb from below. However, when in the lower stratosphere, these gases, whose absorption bands lie at wavelengths between 7 and 12 μm, can absorb radiation from the warm lower troposphere and from Earth's surface. Therefore, an increase in these gases can contribute to warming of the lower stratosphere, although their contribution is usually small. Some non-CO_2 GHGs are also chemically reactive (such as methane, nitrous oxide, and CFCs) and thus have an indirect effect on stratospheric temperatures through changing ozone abundances (see **Chapters 3 and 4**). In some cases, this indirect effect on stratospheric temperatures via changes to ozone may be larger than the direct radiative effect of the gas itself.

In summary, increases in stratospheric CO_2 and other GHGs lead to stratospheric cooling, with the largest changes occurring in the upper stratosphere.

SWV also impact ozone indirectly by changing stratospheric temperatures, which in turn alter the rates of photochemical reactions.

Air enters the stratosphere with a water vapor concentration largely controlled by tropical tropopause temperatures. The primary source of SWV internal to the stratosphere is in situ oxidation of CH_4, yielding two water molecules for each CH_4 molecule oxidized. Convective overshooting of ice particles and transport across the extratropical tropopause are minor sources of SWV. The primary loss process internal to the stratosphere is dehydration through ice particle formation and sedimentation in polar regions (mostly in the Antarctic) during winter.

SWV has been measured by multiple in situ and remote sensing techniques, starting with World War II measurements aimed at understanding contrails using a manually operated aircraft-borne frost point hygrometer (FPH) (Brewer, 1946). The Boulder FPH record extends from 1980 to present day. A detailed analysis of time variations in the Boulder record using breakpoints revealed periods of both increases and decreases in SWV and variations in trends with altitude (Hurst et al., 2011). While the net source of SWV from CH_4 oxidation was found to vary with time, it is estimated to have caused about 25% of the increase in SWV in the altitude range 16–26 km between 1980 and 2010 (Hurst et al., 2011). Although the lack of continuous long-term measurements complicates SWV trend determination, several studies have shown an overall long-term increasing trend (Oltmans et al., 2000; Rosenlof et al., 2001; Hurst et al., 2014). In terms of the consistency between in situ and satellite measurements of SWV, a comparison of balloon FPH measurements with retrievals from the Aura Microwave Limb Sounder (MLS) satellite instrument for the period 2004–2012 revealed there was no statistically significant drift (Hurst et al., 2014). Subsequent analysis including more recent data (Hurst et al., 2016) shows a trend in the difference between the balloon FPH measurements and the Aura MLS measurements, the reasons for which are still under investigation.

Although it is known that tropical cold point temperatures and in situ production from CH_4 oxidation largely control SWV concentrations, there are still issues reproducing the absolute value of measured SWV using global temperature analyses. To produce accurate simulations (to within 0.5–1 ppmv [parts per million by volume]) of tropical stratospheric water vapor entry concentrations using trajectory models driven by global temperature analyses, proper representation of waves, convective influences, and microphysical processes are needed (Ueyama et al., 2014). There is also evidence (Avery et al., 2017) that injections of ice can at times impact SWV during extreme events.

Tropical Pacific sea surface temperature (SST) variability affects SWV entry through impacts on tropical tropopause temperatures; it has been suggested that SST changes contributed to the observed decrease in SWV in the lower stratosphere around the year 2000 (Rosenlof and Reid, 2008; Brinkop et al., 2016; Ding and Fu, 2017; Garfinkel et al., 2018). Variations of SWV are detailed in the State of the Climate reports published annually in the *Bulletin of the American Meteorological Society*; the most recent update (Blunden and Arndt, 2017) shows recent extreme variability of SWV in the tropical lower stratosphere, where water vapor enters the stratosphere, ranging from very high values to very low values between December 2015 and December 2016 (**Figure 5-2**); part of this change may be related to the transition from extreme El Niño conditions to weak La Niña conditions at the end of the period (Konopka et al., 2016; Garfinkel et al., 2018).

Trends in tropical tropopause temperature and atmospheric CH_4 concentrations are expected to be the major drivers of future SWV trends, but there are also suggestions from model simulations that trends in overshooting ice particles could contribute to trends in SWV (Dessler et al., 2016). Climate models predict that tropical lower-stratospheric humidity will increase in the future due to increased transport through the tropical tropopause layer (Smalley et al., 2017), though it should be noted that many climate models do not properly capture the processes that affect tropical tropopause temperatures (Kim et al., 2013). The magnitude of modeled increases in SWV over the 21st century, particularly in the middle and upper stratosphere, is strongly affected by future atmospheric CH_4 concentrations (Revell et al., 2016).

It has been suggested that convective injection of water vapor into the lower stratosphere could lead to enhanced heterogeneous destruction of ozone and

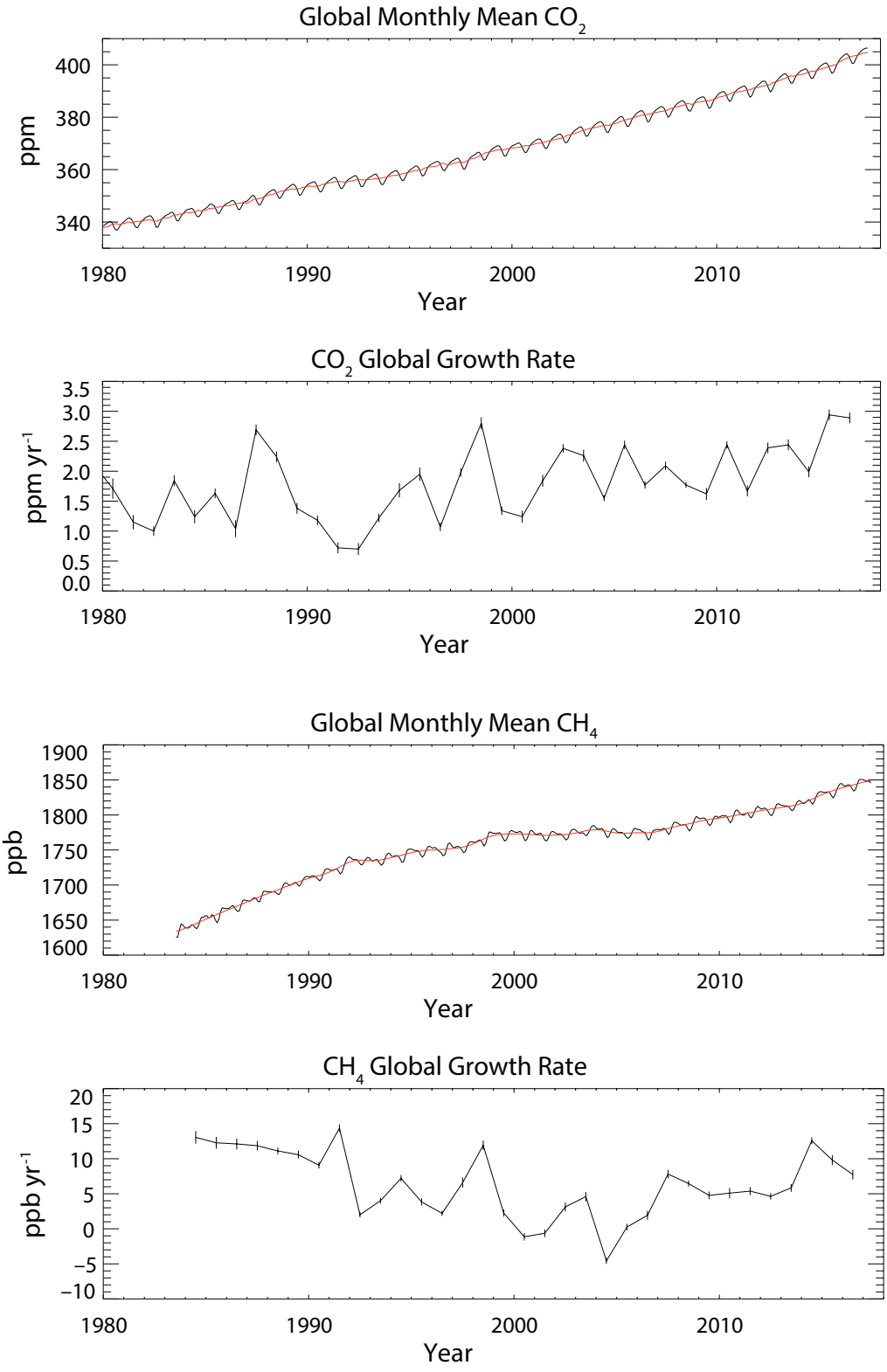

Figure 5-1. Time series of concentrations and growth rates for globally averaged CO_2 (*top two panels*) and CH_4 (*bottom two panels*). These time series were constructed with data provided by Ed Dlugokencky and Pieter Tans, NOAA/ESRL, and are available at www.esrl.noaa.gov/gmd/ccgg/trends/. See Masarie and Tans (1995) and Dlugokencky et al. (1994) for details of measurements.

reduced Northern Hemisphere (NH) mid-latitude column ozone amounts (Anderson et al., 2012, 2017; Anderson and Clapp, 2018). However, observational evidence that synoptic convective systems lead to enhanced catalytic ozone destruction in mid-latitudes is currently inconsistent (Schwartz et al., 2013; Solomon et al., 1997; Anderson et al., 2012, 2017). Though it has been posited that this mechanism may be enhanced in a warmer climate (Anderson and Clapp, 2018), the lack of evidence for any role for this mechanism in the current climate and the fact that in the future there will be lower atmospheric chlorine levels and hence reduced catalytic ozone destruction mean that there is low confidence in this proposed feedback.

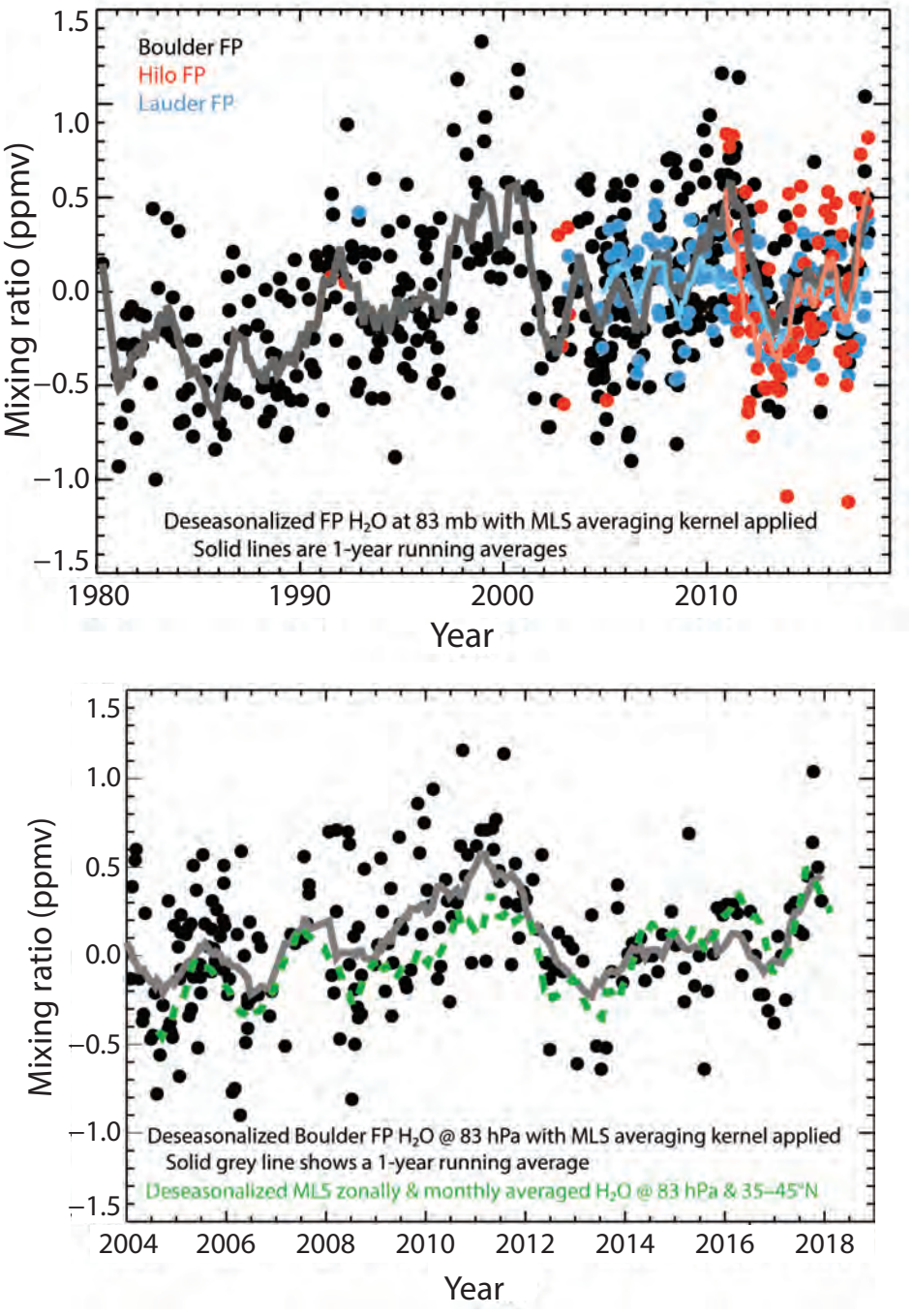

Figure 5-2. *Top panel:* Lower-stratospheric water vapor anomalies (black, red, and blue circles, plotted as difference from the monthly mean over the period 2004–2018) from balloon measurements taken between 1980 and 2018 at Boulder, Colorado (USA); Hilo, Hawaii (USA); and Lauder (New Zealand). *Bottom panel:* This graph is the same as the one above but shows only Boulder measurements (black circles) between 2004 and 2018, as well as zonally averaged water vapor anomalies (35–45°N) from the Aura Microwave Limb Sounder (MLS; green dashes). The frost point (FP) data extend the information plotted in Figure 2.55 of Blunden and Arndt (2017).

5.2.3 Stratospheric Aerosols

Stratospheric aerosols influence climate by scattering sunlight back to space, by modifying cloud microphysical processes, and by altering ozone chemistry. Trends and variability in stratospheric aerosols and their impact on ozone are discussed in detail in **Chapters 3** and **4** (see **Sections 3.2.1.4**, **4.2.3.1**, and **4.3.5.2**). Because they reflect sunlight, artificial enhancement of stratospheric aerosols has been proposed as a possible method for solar radiation management to cool the planet (see **Chapter 6**, **Section 6.2.5.2**). Stratospheric aerosols also warm the stratosphere by absorbing infrared radiation, and as such, they are important drivers of the observed stratospheric temperature variability (see **Section 5.3.1.2**). Major increases in stratospheric aerosols result from volcanic eruptions. The last major volcanic eruption that significantly perturbed stratospheric aerosols was Mount Pinatubo (in the Philippines) in 1991. What are believed to be background levels of stratospheric aerosols were reached in the late 1990s (Kremser et al., 2016), and since then, there have been moderate eruptions that have increased stratospheric aerosol loading (Neely et al., 2013). **Figure 5-3** (from Mills et al., 2016) shows the progression of the global aerosol burden from 1980 to 2015. Peak aerosol loading follows the Pinatubo eruption in 1991, with several shorter-lived increases following moderate eruptions during the early 21st century, the largest of which occurred in 2008. Sulfur-rich particles dominate stratospheric aerosols, but recent work has also highlighted the importance of organic aerosols (Murphy et al., 2014; Vernier et al., 2015; Yu et al., 2016) and has shown that they have likely increased significantly since the preindustrial period (Yu et al., 2016).

Increases in stratospheric aerosols in the presence of elevated stratospheric chlorine produce ozone loss. For example, the large October 2015 Antarctic ozone hole has been attributed to the presence of volcanic aerosols from the Calbuco eruption (in southern Chile) (Solomon et al., 2016). The potential for aerosols to enhance ozone loss is expected to decrease as chlorine loadings continue to decrease in the future (Klobas et al., 2017), but uncertainty in future levels of volcanic aerosol introduces uncertainty to determining when ozone recovery to 1980 levels is expected to occur (Naik et al., 2017).

Since the 2014 Ozone Assessment, there have been significant improvements in understanding of the existence of the Asian Tropopause Aerosol Layer (ATAL) (Vernier et al., 2011), which became evident only after aerosol concentrations returned to pre-Pinatubo concentrations. The ATAL is hypothesized to have a significant anthropogenic origin (Vernier et al., 2015) and, according to one study, likely contributes as much to the background aerosol in the Northern Hemisphere as small to moderate volcanic eruptions (Yu et al., 2017).

5.2.4 Ozone

Stratospheric ozone changes can impact climate by changing the large-scale atmospheric state, including impacts on the tropospheric circulation and ultimately surface weather (see **Section 5.4**), or by changing the amount of UV radiation that reaches the surface, both impacting surface temperatures and biogenic processes.

Since the late 1990s, concentrations of ODSs have declined in response to the implementation of the Montreal Protocol (see **Chapter 1**). **Chapter 3** reports that global (60°S–60°N) column ozone has been increasing by between 0.3% and 1.2% per decade since the late 1990s, but this increase is not statistically significant, owing to the comparatively large uncertainty of 1% per decade arising from dynamically forced interannual variability. Global column ozone is expected to increase with further reductions in the abundance of ODSs in the stratosphere. Current tropical column ozone is found to be unchanged compared to the period 1964–1980, consistent with the findings of the 2014 Assessment. Upper-stratospheric (35–45 km altitude) ozone in the tropics and mid-latitudes has increased by 1–3% per decade over the 2000–2016 period; these increases are statistically significant and are thought to be caused by a combination of reductions in ODSs and GHG-induced cooling. Climate models predict a decrease in tropical lower-stratospheric ozone due to a modeled increase in strength of the stratospheric overturning circulation. However, due to large internal variability, which is also seen in models, this decrease has not been detected in a statistically significant manner since 2000. As noted in **Chapter 4**, the characteristics of the Antarctic ozone hole in October during recent years are similar to those in the early 1990s; its size and duration are still

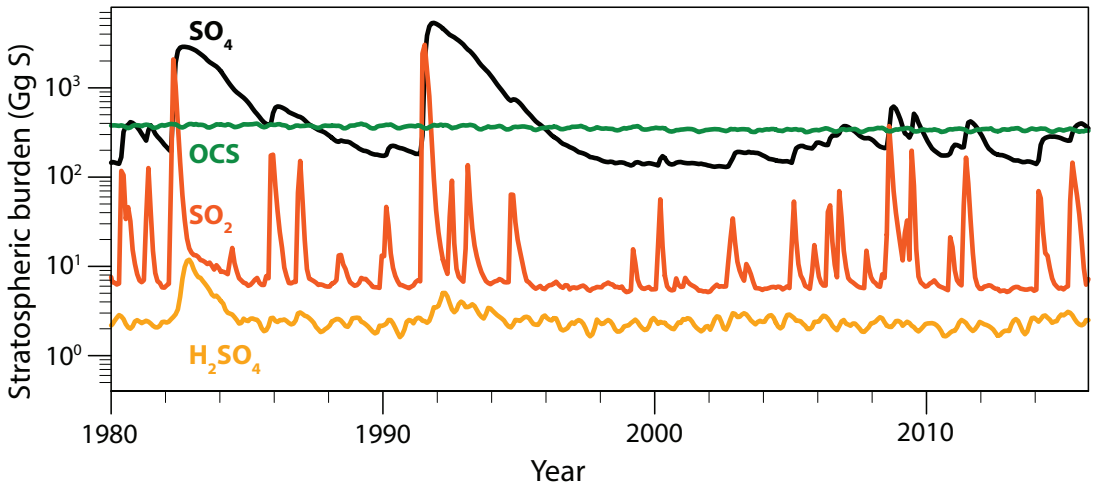

Figure 5-3. Calculated global mass burdens of major sulfur-bearing species from a specified dynamics (SD-) WACCM VOLC simulation above the tropopause, shown as a function of time from 1 January 1980 to 31 December 2015 (updated from Mills et al., 2016). The black line shows SO_4 (sulfate); the green line, OCS (carbonyl sulfide); the yellow line, H_2SO_4 (sulfuric acid); and the red line, SO_2 (sulfur dioxide). Mass burdens are shown in units of Gg (=10^9 g) of S. Note that the burden of dimethylsulfide in the stratosphere (10^{-3}–10^{-2} Gg S) is too small to be shown. The spikes in the SO_2 trace (red line) indicate where volcanic eruptions reached the stratosphere. The actual eruptions used are detailed in Mills et al. (2016). Note: there was an error in the originally published version due to an incorrect adjustment for molecular weights, so the burdens of the gases have shifted.

impacted in cases of high volcanic aerosol loading, such as from the Calbuco eruption in 2015 (Solomon et al., 2016). However, statistically significant positive trends in ozone have been observed in the Antarctic in September since 2000 (Solomon et al., 2016). Overall, there have been minimal long-term ozone changes found in the Arctic, where dynamically forced interannual variability in ozone in winter and spring is large compared to the long-term changes.

5.2.5 Solar Activity

Total solar irradiance (TSI), which measures the amount of solar radiation at the top of Earth's atmosphere, has been directly monitored by satellites since 1978. TSI varies on a wide range of timescales, the most relevant of which for understanding recent stratospheric climate and ozone changes is the approximately 11-year cycle during which TSI varies by about 1 W m^{-2} (<0.1%) between solar cycle maximum and minimum (Haigh, 2007). When solar activity is high, incoming solar UV radiation is enhanced, impacting ozone production in the stratosphere and mesosphere (Haigh, 2007). Changes in the absorption of UV radiation by ozone then impacts stratospheric temperature distributions and, consequently, circulation and climate (Gray et al., 2010). The impact of solar cycle variations on ozone depends on solar spectral irradiance (SSI) and, in particular, the fraction of variance in the UV spectral region. The peak of the current 24th 11-year solar cycle, which started in December 2008, was weaker than previous cycles (Hathaway, 2015). At present, the sun is approaching a minimum phase of the solar cycle.

5.3 OBSERVED AND SIMULATED CHANGES IN STRATOSPHERIC CLIMATE

Section 5.2 reviewed observed changes in some of the major constituents and external drivers of stratospheric climate. This section describes the current understanding from observations and model simulations of recent and future changes in stratospheric climate and their drivers.

5.3.1 Stratospheric Temperatures

Stratospheric temperature trends are a key marker for anthropogenic effects on the climate system (IPCC, 2013; USGCRP, 2017). Moreover, stratospheric temperature trends affect stratospheric ozone abundances through effects on the rates of photochemical reactions (see **Chapters 3** and **4**). The 2014 Assessment concluded that over the past several decades, increases in atmospheric GHGs and decreases in stratospheric ozone abundances have been the major radiative drivers of global mean cooling in the middle and upper stratosphere. In the lower stratosphere, observed global mean cooling was largely attributed to stratospheric ozone changes over the past few decades. The latitudinal structure of stratospheric temperature trends is strongly influenced by changes in the stratospheric overturning circulation (see **Section 5.3.2**), which may be externally forced and/or associated with internal variability. This section focuses on what has been learned about stratospheric temperature trends since the 2014 Ozone Assessment, notably, improved constraints on satellite-observed temperature trends and new efforts to attribute observed and model-simulated temperature variability and trends to natural and anthropogenic drivers.

5.3.1.1 Observed Temperature Changes

Observations of stratospheric temperatures come from operational radiosondes, operational polar orbiting satellites, GPS Radio Occultation satellite networks, and from research satellites and rocket sondes. Radiosonde observations span the longest time period (starting in the late 1950s), but there are discontinuities due to changes in instrumentation and location of stations, and they cover only the lower part of the stratosphere. Consequently, homogenized datasets based on radiosondes have been constructed to improve the accuracy of radiosonde temperature time series, e.g., IUK (Sherwood and Nishant, 2015); RATPAC (Lanzante et al., 2003); RAOBCORE and RICH (Haimberger et al., 2012); and HADAT2 (Thorne et al., 2005). Global temperature data for the stratosphere are available from the Microwave Sounding Unit (MSU) and Stratospheric Sounding Unit (SSU) satellite instruments that flew on operational polar orbiters and provided coverage from late 1978 to 2005. MSU and SSU measure stratospheric temperatures over four broad layers covering the lower stratosphere (MSU Channel 4 [MSU4], 13–22 km; and SSU Channel 1 [SSU1], 25–35 km), the middle stratosphere (SSU Channel 2 [SSU2], 35–45 km), and the upper stratosphere (SSU Channel 3 [SSU3], 40–50 km). These instruments were replaced by the Advanced Microwave Sounding Unit (AMSU), which started flying in 1998. Continuing the record has required merging the MSU/SSU data with AMSU data or with measurements from other recent satellite records (see below).

The 2014 Ozone Assessment highlighted a significant discrepancy in global long-term temperature trends in the middle stratosphere between the two independent analyses of the SSU record from the UK Met Office and the National Oceanographic and Atmospheric Administration (NOAA). The NOAA Center for Satellite Applications and Research (STAR) SSU v1.0 dataset (Wang et al., 2012) showed temperature trends over 1979–2006 of -1.24 ± 0.13, -0.93 ± 0.14, and -1.01 ± 0.19 K decade^{-1} in SSU1, SSU2, and SSU3, respectively (Wang et al., 2012). These could be compared with trends in the UK Met Office SSU dataset available at that time of -0.52 ± 0.23, -0.40 ± 0.23, and -1.27 ± 0.33 K decade^{-1} (Wang et al., 2012). The NOAA STAR dataset therefore showed substantially larger cooling trends in SSU1 and SSU2 and a weaker cooling trend in SSU3 compared to the UK Met Office dataset.

Since the 2014 Ozone Assessment, both groups have published revised versions of their SSU datasets (Nash and Saunders, 2015; Zou et al., 2014). The reprocessed SSU records show much greater consistency in the estimated global and annual mean temperature trends throughout the stratosphere than was reported in the 2014 Assessment (Seidel et al., 2016) (**Figure 5-4**). This reflects substantial progress in understanding the sources of differences in temperature trends between the two SSU datasets, but differences remain that are larger than the uncertainty estimates provided by each research team (Seidel et al., 2016). The satellite observations in **Figure 5-4** show global stratospheric cooling of about 1.5 K (25–35 km), 1.5 K (35–45 km), and 2.3 K (40–50 km) between 1979 and 2005. The largest outstanding discrepancies are in SSU2 and SSU3, where the NOAA dataset shows stronger cooling in SSU2 by about 0.6 K and weaker cooling in SSU3 by about 0.3 K than in the UK Met Office dataset. However, the reprocessed NOAA SSU dataset shows a vertical coherency in stratospheric temperatures that is more consistent with model simulations

than the UK Met Office dataset (Seidel et al., 2016), suggesting that the NOAA SSU dataset provides a more physically consistent representation of stratospheric temperatures.

Since the 2014 Assessment, there have been efforts to extend the SSU record, which ended in 2006, to near-present day using more recent satellite measurements, including AMSU-A (Zou et al., 2016; McLandress et al., 2015), SABER, and MLS (Randel et al., 2016). The signal weightings as a function of altitude of the more recent satellite instruments are different from those of the SSU instruments. Recent studies have focused on developing methods to map the current satellite retrievals onto the SSU weighting functions in order to produce a consistent merged record. Analysis of stratospheric temperature trends in satellite records covering the recent past has revealed weaker trends after around 1997 (Zou et al., 2016; McLandress et al., 2015; Randel et al., 2016; Khaykin et al., 2017) (**Figure 5-5**), which is consistent with current understanding of the timing of peak atmospheric chlorine loading (see **Chapter 1**), the coincident changes in stratospheric ozone trends (see **Chapters 3** and **4**), and associated effects on stratospheric temperatures (Ferraro et al., 2015; Randel et al., 2017).

In the lower stratosphere (13–22 km), the three MSU4 records, NOAA/STAR v4.0 (Zou et al., 2006), the Remote Sensing Systems (RSS) v3.3 (Mears et al., 2011), and the University of Alabama in Huntsville (UAH) v6.0 data sets (Christy et al., 2003), show a net cooling in the global mean between 1979 and 2016 of about 1 K. The majority of the observed global lower stratospheric cooling in the MSU4 record occurred before the mid-1990s (**Figure 5-4**). Since then there has been little overall global temperature change in the MSU4 record (Seidel et al., 2016; Polvani et al., 2017). The long-term cooling is interspersed by short-term global stratospheric warming for a few years following the two major tropical volcanic eruptions in the epoch (El Chichón in 1982 and Mt. Pinatubo in 1991). The stratospheric heating from volcanic aerosols peaks in the lower stratosphere (**Figure 5-4d**) but is also evident in the middle and upper stratosphere (**Figure 5.4a–5.4c**).

The University of Alabama in Huntsville (UAH) MSU4 dataset shows slightly stronger cooling over the record, by about 0.2 K, compared to the NOAA STAR and Remote Sensing Systems (RSS) MSU4 datasets (**Figure 5-4d**) (Seidel et al., 2016). The majority of the differences in temperature trends between the three MSU4 datasets are associated with temperature changes at high latitudes (Seidel et al., 2016). The three MSU4 records agree reasonably well, in the global mean, with the radiosonde datasets RAOBCORE and RICH (**Figure 5-4d**), but the comparison with the radiosonde data is problematic because the disagreement between the two radiosonde datasets is as large as the difference between either of them and the MSU4 datasets.

As reported in the last Assessment, long-term MSU4 temperature trends show considerable structure in latitude and by season. **Figure 5-6a** shows MSU4 temperature trends over 1979–1997. The trends show significant cooling throughout most of the year in the tropics and also in mid-latitudes, with enhanced cooling in the Antarctic in austral spring and summer. An enhanced cooling in the Arctic in mid-winter as well as a warming in SH high latitudes in August are also observed, but these are not reproduced by the chemistry–climate models (**Figure 5-6b**), suggesting this is likely a manifestation of the large internal variability in the polar stratosphere during winter affecting the calculated trends over a relatively short 19-year period (see **Section 5.3.1.3**). Over the period 1998–2016 (**Figure 5-6c**), the tropics is the only region where significant cooling has been observed in the MSU4 record in boreal late spring and early summer.

In addition to satellite and in situ stratospheric temperature measurements, there are numerous meteorological reanalysis datasets produced by the world's meteorological services. Reanalysis products are widely used in the literature for atmospheric process studies, but developers have cautioned against their use for climate trend studies, owing to potential discontinuities in the records that can be introduced by the integration of different satellite records into the model data assimilation system (Simmons et al., 2014). The WCRP SPARC Reanalysis Intercomparison Project (S-RIP) has recently assessed the representation of long-term stratospheric temperature changes in a number of current reanalysis systems (Long et al., 2017). These reanalysis products have been compared with the NOAA STAR MSU/AMSU v3.0 and SSU v2.0 SSU1 and SSU2 records by sampling the pressure level output fields with the satellite weighting functions

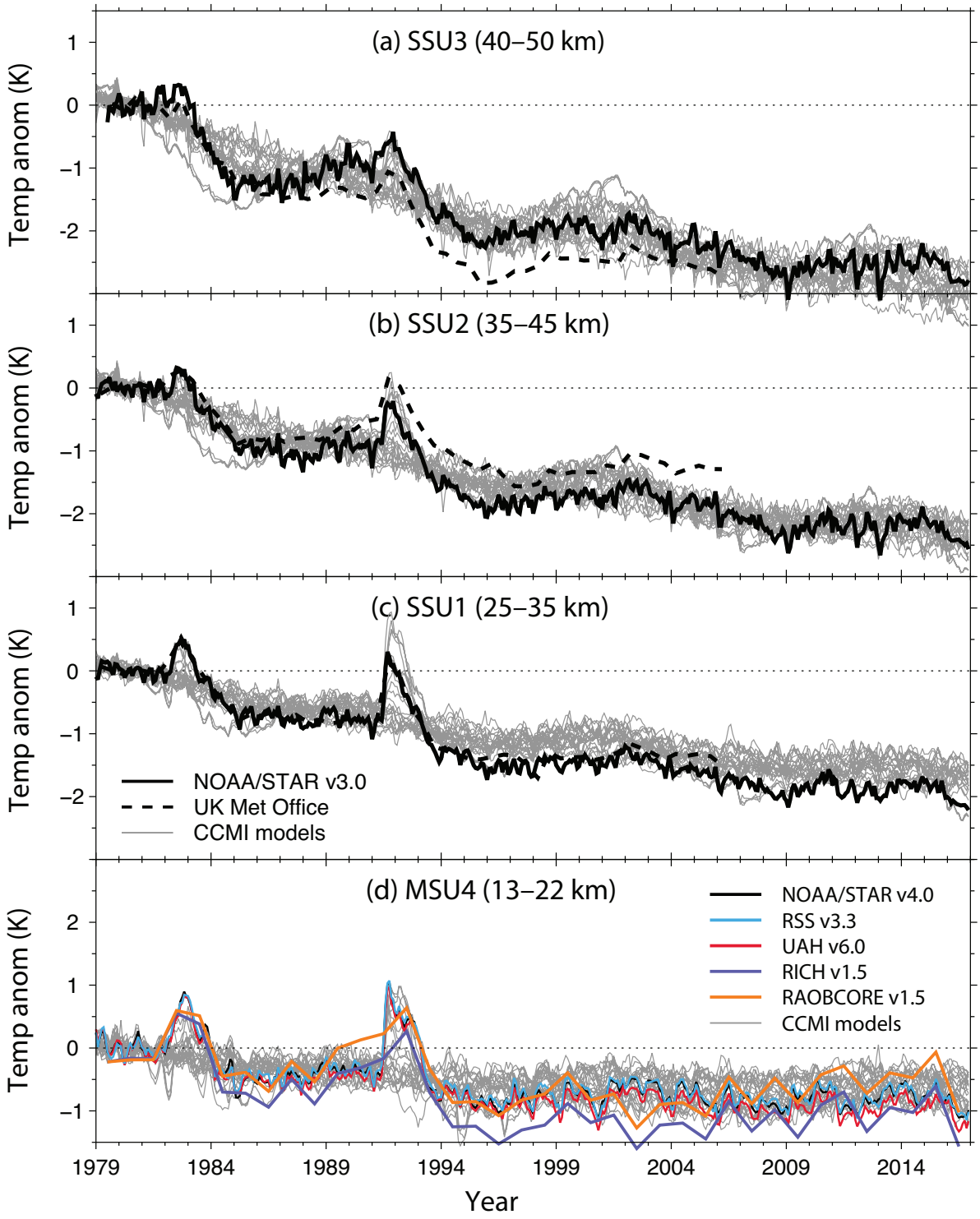

Figure 5-4. Time series of global mean stratospheric temperature anomalies from 1979 to 2016. Panels show SSU Channels 3, 2, 1 (SSU3, SSU2, SSU1; a, b, c) and MSU channel 4 (MSU4; d) for the altitude ranges, datasets, and model outputs indicated in the legends. Gray lines indicate results from a total of 23 ensemble members across 14 Chemistry-Climate Model Initiative (CCMI) models for the REF-C2 experiment, weighted by the appropriate satellite weighting function for comparison with observations. All data in panel d are shown as monthly averages except the UK Met Office dataset, which uses 6-month averages, and the two radiosonde datasets, which are annual means. The radiosonde data are as in Figure 2.8 of Blunden and Arndt (2017). Anomalies are shown relative to 1979–1981. Adapted from Maycock et al. (2018).

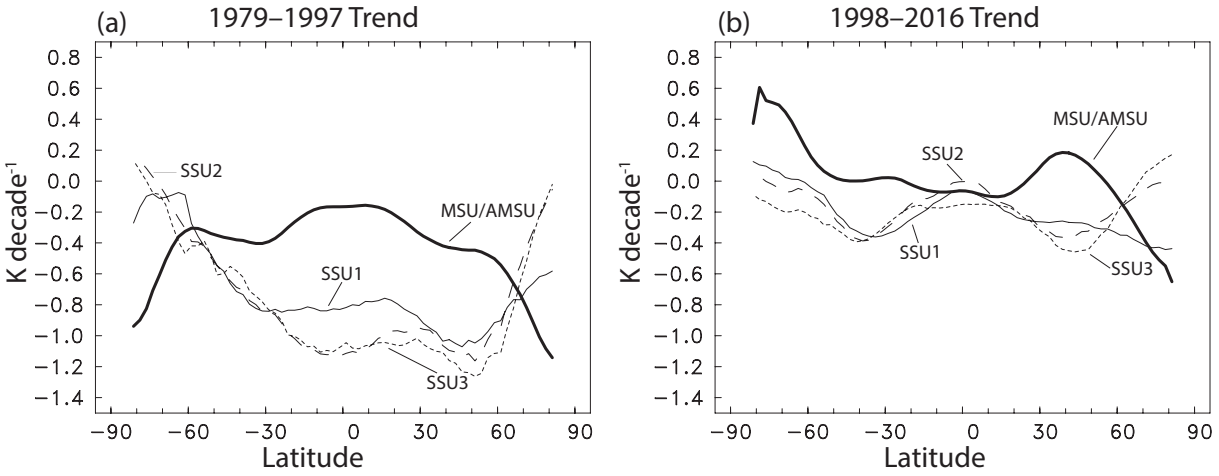

Figure 5-5. Observed annual mean stratospheric temperature trends in a merged satellite (SSU and MLS) record for the periods (a) 1979–1997 and (b) 1998–2016. Thick solid lines show MSU/AMSU, thin solid lines show SSU1, dashed lines show SSU2, and dotted lines show SSU3. Updated from Randel et al. (2016).

(Long et al., 2017). In the lower stratosphere, the reanalyses generally show weaker long-term cooling compared to MSU4, by up to ~0.5 K (~50%) over the period 1979–2015. There are larger differences in the temperature trends among the reanalyses in the middle and upper stratosphere, with the NCEP Climate Forecast System Reanalysis (CFSR) showing particularly large and unrealistic interannual and decadal variations, owing to its construction from multiple streams (Long et al., 2017). In other current reanalysis datasets, the differences in the long-term global mean temperature change in SSU1 and SSU2 compared to observations are typically <1 K over 1979–2015. In conclusion, current reanalyses show deficiencies in capturing both short- and long-term variations in stratospheric temperatures found in satellite measurements.

5.3.1.2 Simulation and Attribution of Past Global Stratospheric Temperature Changes

New studies published since the 2014 Assessment have quantified the contribution of different external factors, such as changing GHG concentrations and ozone (or ozone-depleting substance; ODS) concentrations, to observed stratospheric temperature changes over the satellite era.

According to one study, which applied a standard detection and attribution analysis to global stratospheric temperature records from the NOAA/STAR SSU v1.0 dataset, the effects of GHGs and ozone were not distinguishable separately in the middle to upper stratosphere (Mitchell, 2016), consistent with the conclusion of the 2014 Assessment. Another study, which analyzed chemistry–climate model experiments with incrementally added forcing agents and prescribed observed SSTs, found that ODSs contributed about 0.4 K (one-quarter) of the global mean cooling in SSU1 and about 0.7 K (one-third) of the cooling in SSU2 between 1979 and 1997, with virtually all cooling after 2000 being attributed to GHGs (Aquila et al., 2016) (see **Figure 5-7** for SSU2). In the upper stratosphere in SSU3, both a standard detection and attribution approach (Mitchell, 2016) and a chemistry–climate model study (Aquila et al., 2016) attribute about two-thirds of the long-term global average cooling between 1979 and 2005 to GHGs and one-third to ODSs. Chemistry–climate model experiments with incrementally added forcings further demonstrate that the relatively rapid decreases in global upper-stratospheric temperatures that occurred in the early 1980s and early 1990s were likely the result of a coincidence between a relative decrease in temperature following warming from major tropical volcanic eruptions and the declining phase of the 11-year solar cycle (Aquila et al., 2016). Stratospheric water vapor changes may have also contributed to cooling in the lower stratosphere over the last 30 years (Maycock et al., 2014); however,

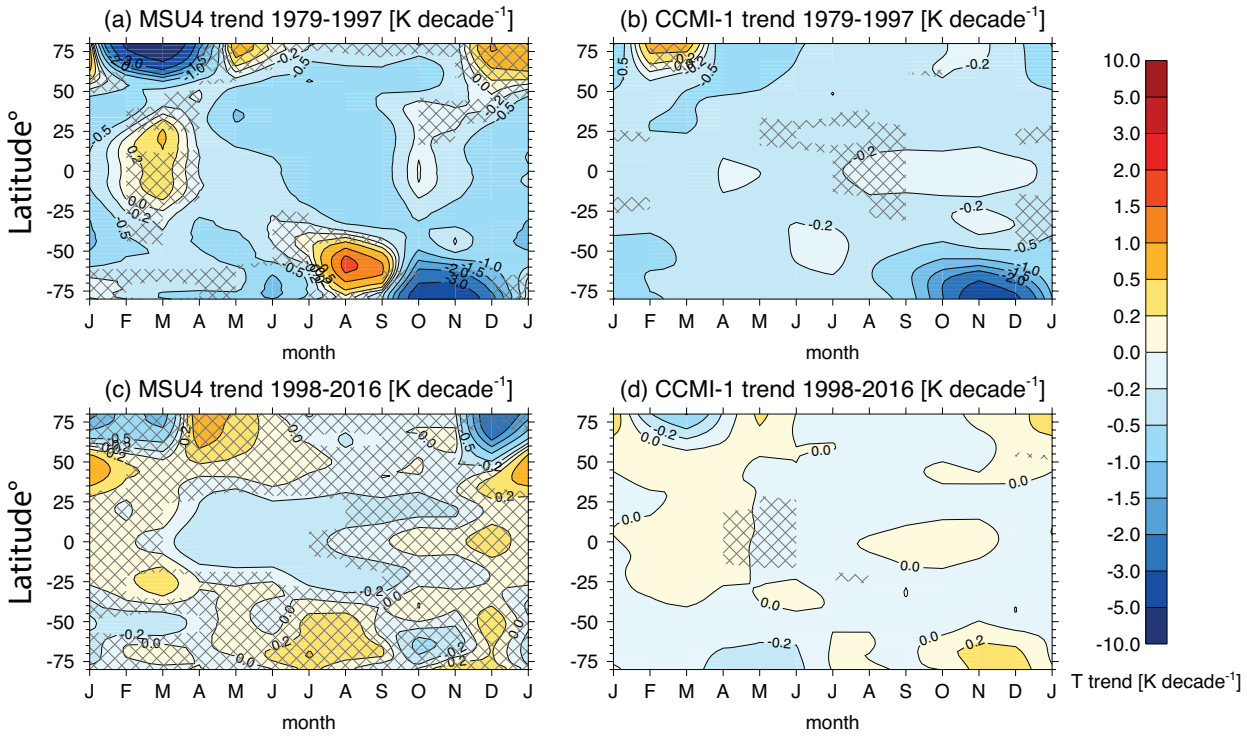

Figure 5-6. Lower-stratospheric temperature trends over the periods (a, b) 1979–1997 and (c, d) 1998–2016 in K per decade as a function of latitude and month from (a, c) satellite MSU/AMSU NOAA/STAR v4.0 (MSU4) and (b, d) multi-model mean MSU4 temperatures from 12 CCMI models for the REF-C2 simulation. The following years, which were influenced by volcanic eruptions, are treated as missing data in panels a and b: 1982, 1983, 1991, 1992, 1993. The hatching in panels a and c shows where the magnitude of the observed trend is within the 5–95% range of simulated internal variability, estimated from the spread in modeled trends, and is therefore estimated to be not statistically significant (at the 95% confidence level). Hatching in panels b and d shows where the observed MSU4 trends in panels a and c lie outside the 5–95% range of model trends, thus showing areas where the simulated and observed trends are inconsistent. Based on datasets described in Maycock et al. (2018).

the magnitude of this effect is not well constrained due to uncertainties in global long-term stratospheric water vapor trends (see **Section 5.2.2**).

In the last Assessment, simulations from climate models and chemistry–climate models were found to show weaker global average cooling than estimated from observations in the lower and upper stratosphere. In the middle stratosphere (35–45 km), the modeled trends were within the range of the observational uncertainty (Thompson et al., 2012). **Figure 5-4** shows simulated global average stratospheric temperature anomalies in the CCMI REF-C2 experiment (see **Chapter 3** and Morgenstern et al. (2017) for model details) alongside the satellite observation datasets described above (Maycock et al., 2018). The model pressure level output has been sampled according to the satellite weighting functions to facilitate the comparison with observations. The main new findings are that the model-simulated temperature changes are now in good agreement with the revised NOAA STAR SSU dataset in the upper stratosphere (40–50 km), whereas the revised UK Met Office record still shows stronger cooling than simulated in the chemistry–climate models, as was reported in the 2014 Assessment. In the lower stratosphere in the MSU4 (13–22 km) and SSU1 (25–35 km), the models show on average slightly weaker long-term cooling than observed, similar to the findings of the 2014 Assessment, though the observed trends lie within the range of individual model realizations (Maycock et al., 2018).

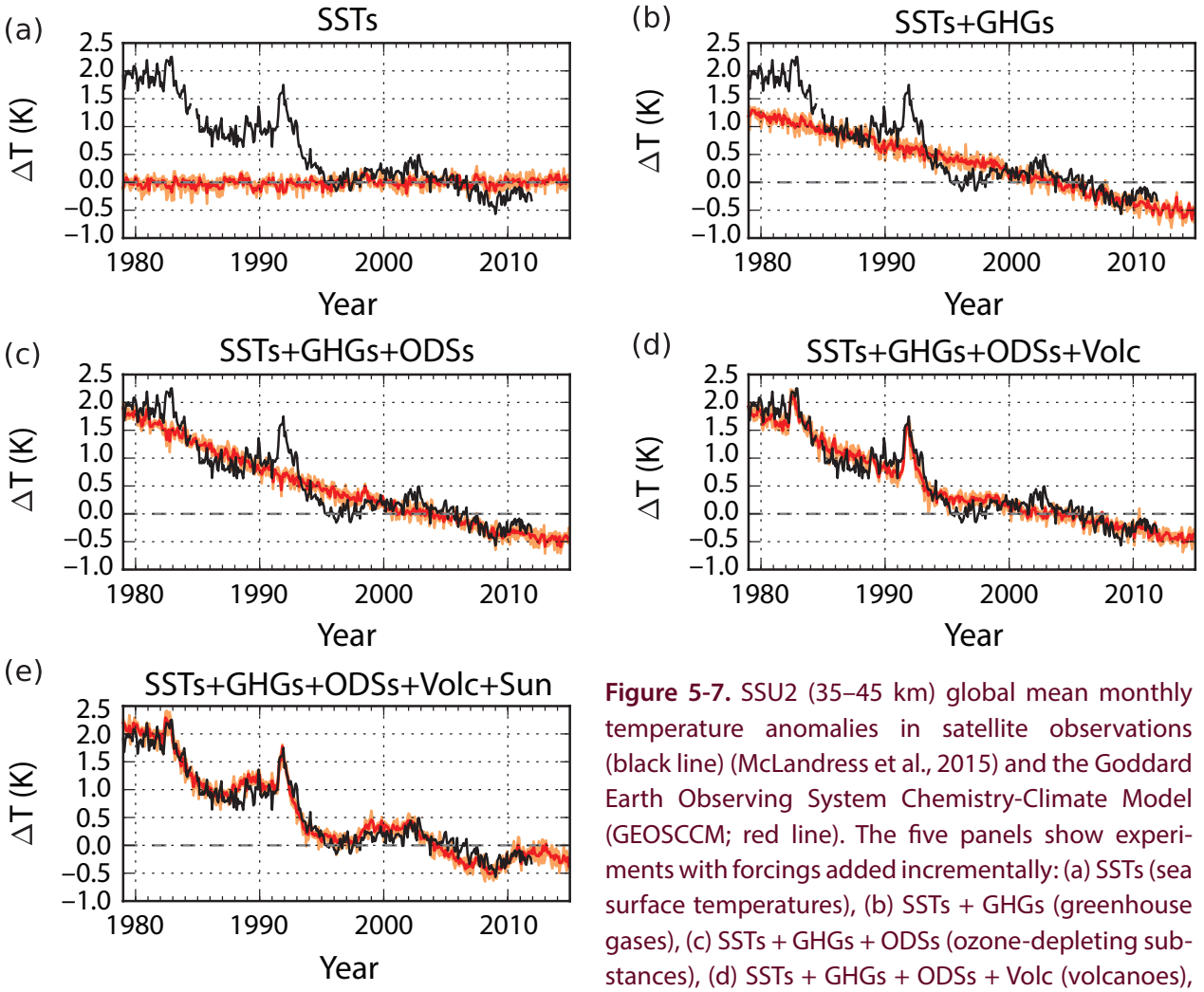

Figure 5-7. SSU2 (35–45 km) global mean monthly temperature anomalies in satellite observations (black line) (McLandress et al., 2015) and the Goddard Earth Observing System Chemistry-Climate Model (GEOSCCM; red line). The five panels show experiments with forcings added incrementally: (a) SSTs (sea surface temperatures), (b) SSTs + GHGs (greenhouse gases), (c) SSTs + GHGs + ODSs (ozone-depleting substances), (d) SSTs + GHGs + ODSs + Volc (volcanoes), (e) SSTs + GHGs + ODSs + Volc + Sun (solar). Time series are plotted as anomalies relative to the 1995–2011 average. The solid red lines show the model ensemble means, and the shaded areas show the spread across the three ensemble members. Adapted from Aquila et al. (2016).

The difference in global mean lower-stratospheric temperature trends is at least partly associated with the CCMI multi-model mean showing weaker cooling in the tropics than found in observations (**Figure 5-6b**). Note that many of the CCMI models did not include the radiative effects of volcanic aerosols in the REF-C2 experiment, following the interpretation of the experimental design by modeling groups, and hence most of the models do not capture stratospheric warming following the two major volcanic eruptions since 1979 (**Figure 5-4**). In conclusion, there is now greater consistency between observed and modeled global stratospheric temperature trends in all the SSU channels, and this is largely the result of the updates to the satellite records since the 2014 Assessment rather than any major changes in the modeled temperature trends (McLandress et al., 2015; Maycock et al., 2018).

5.3.1.3 Simulation and Attribution of Past Polar Stratospheric Temperature Trends

In addition to the attribution of global mean stratospheric temperature changes to different external factors, studies have separately analyzed the contribution of radiative and dynamical processes to seasonal polar stratospheric temperature trends. Dynamical contributions to temperature changes occur through adiabatic heating (cooling) associated with downwelling (upwelling) motion. In the Arctic, studies indicate an

important role for dynamical processes in determining the observed long-term lower-stratospheric cooling in boreal spring, though the precise magnitude of the dynamical contribution depends on the approach used to separate the radiative and dynamical contributions (Bohlinger et al., 2014; Ivy et al., 2016). In the Arctic in boreal summer, the observed stratospheric cooling at 50 hPa is smaller in magnitude and is, as expected, dominated by the radiative effects of increasing GHGs and ozone. In the Antarctic, changes in dynamics have acted to slightly enhance the radiative cooling from ozone loss in austral spring but have offset part of the radiative cooling in austral summer, resulting in weaker lower-stratospheric temperature trends than would arise from radiative effects alone (Keeley et al., 2007; Orr et al., 2013; Ivy et al., 2016). Thus, the observed long-term cooling trend in the Antarctic lower stratosphere in austral spring is slightly enhanced by the effect of dynamical feedbacks to the observed ozone trends (see **Chapter 4**). Since 2000, during the period when emergence of healing of the Antarctic ozone hole has been observed (Solomon et al., 2016), Antarctic lower-stratospheric temperature trends show a warming in austral spring, which can be partly attributed to radiative effects of ozone trends as well as to dynamical changes that may be associated with internal variability (Solomon et al., 2017).

Chemistry–climate model experiments show substantial differences in polar temperature trends, particularly in the lower stratosphere, between different ensemble members forced with identical observed SSTs, sea ice, and external forcing agents and initialized using a range of atmospheric initial conditions (Randel et al., 2017; Maycock et al., 2018) or with slight differences in the model parameterizations (Garfinkel et al., 2015a). In fact, the spread of simulated trends suggests that recent observed polar temperature trends (**Figure 5-6b**) are not inconsistent with internal variability, assuming that these models offer a realistic representation of the forced and unforced components of stratospheric temperature change. For example, although the CCMI REF-C2 multi-model mean does not capture the recent observed Arctic warming in boreal winter and cooling in boreal spring in the MSU4 (**Figure 5-6b**), the observed trends in the Arctic lie within the range of model simulations (Maycock et al., 2018). Observed SST changes have been estimated to account for about half of the recent Arctic stratospheric cooling trend in boreal spring (Garfinkel et al., 2015a), which is broadly in agreement with the estimated dynamical contribution to Arctic temperature trends discussed in **Section 5.3.1.2** (Bohlinger et al., 2014; Ivy et al., 2016). The models in **Figure 5-6b** either included a coupled ocean or used SST and sea ice boundary conditions from another model simulation, and thus the evolution of SSTs will likely differ from observations, though any forced component of SST change and its effect on polar temperature trends should be at least partly captured.

5.3.1.4 Simulated Future Stratospheric Temperature Changes

As described in the 2014 Ozone Assessment, future global stratospheric temperature trends will be determined by the relative rates of change in the major drivers of temperature in the stratosphere: CO_2, ozone, and, to a lesser extent, stratospheric water vapor. For a low GHG scenario, projected increases in ozone may result in a weak or even a small positive global temperature trend in the upper stratosphere (Maycock, 2016). For higher GHG scenarios, global cooling in the upper stratosphere due to projected CO_2 increases dominates over the warming effect from increasing ozone, and therefore temperatures are projected to decrease over the 21st century (Stolarski et al., 2010; Douglass et al., 2012; Maycock, 2016). One possible source of uncertainty in future temperature trends, particularly in the lower stratosphere, is the large spread in projected stratospheric water vapor concentrations (Smalley et al., 2017), though this effect has not yet been quantified.

The latitudinal and seasonal patterns of future temperature trends in the lower stratosphere also depend on the GHG scenario. **Figure 5-8** shows projected temperature trends at the altitude of the MSU4 channel from the CCMI REF-C2 experiment. The projected warming in the Antarctic in austral spring and summer is very prominent over the first half of this century as the ozone hole reduces in depth and extent (see **Chapter 4**). This warming is about a factor of two smaller for the medium-to-high GHG scenario (RCP-6.0; **Figure 5-8a**) than for the low GHG scenario (RCP-2.6; **Figure 5-8c**). Polar stratospheric temperature trends are also affected by changes in

the deep branch of the stratospheric overturning circulation (see **Section 4.3.4**). In the Arctic, the CCMI models simulate a mid-winter warming in the lower stratosphere over the first half of the century. Future Arctic lower-stratospheric temperature trends will be determined by a balance between changes in high-latitude wave driving and associated changes in downwelling over the pole as well as radiative effects from changes in ozone and GHGs (Oberländer et al., 2013; Rieder et al., 2014; Langematz et al., 2014; Bednarz et al., 2016). These findings are generally consistent with the 2014 Ozone Assessment. Over the second half of the 21st century, there is projected warming in the lower stratosphere across most of the tropics and subtropics in the low GHG scenario (**Figure 5-8d**), whereas the models project cooling in this region for the medium-to-high GHG scenario (**Figure 5-8b**). Thus, the sign of projected tropical lower-stratospheric temperature trends over the second half of the 21st century is dependent on the GHG scenario.

5.3.2 Brewer–Dobson Circulation

Changes in the strength of the stratospheric overturning circulation, or the Brewer–Dobson circulation (BDC), are key drivers of changes in stratospheric temperature (see **Section 5.3.1**), tracer concentrations (see **Chapter 3**, **Section 3.4.2**, and **Chapter 4**, **Section 4.3.4**), and stratosphere–troposphere exchange (**Section 5.3.3**). This section is dedicated to assessing the main advances in understanding of the BDC since the last Assessment, with special emphasis on the long-term trends.

5.3.2.1 Observations

The BDC is not directly measured and thus has to be derived indirectly from temperature observations, dynamical reanalysis fields, or tracer measurements. While a strengthening of the BDC is simulated in response to climate change, it has remained elusive in the observations. The 2014 Ozone Assessment

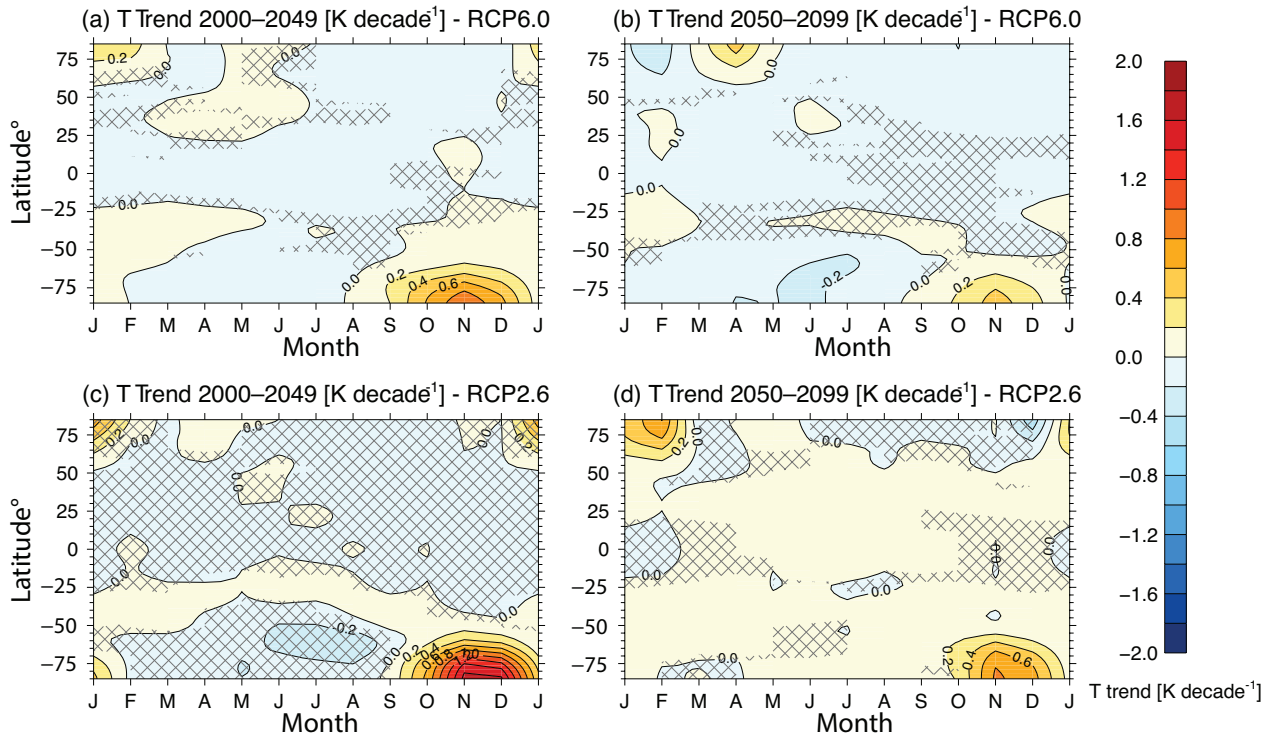

Figure 5-8. CCMI multi-model mean zonal-mean MSU4 channel (~13–22 km) temperature trends (K per decade) over the periods (a, c) 2000–2049 and (b, d) 2050–2099 under (a, b) the medium-to-high greenhouse gas (GHG) scenario (RCP-6.0; 12 models) and (c, d) the low GHG scenario (RCP-2.6; 4 models). Regions where less than two-thirds of the models agree on the sign of the trend are hatched. Based on model simulations described in Morgenstern et al. (2017) and Maycock et al. (2018).

examined a few studies that provided evidence of an acceleration in lower-stratospheric tropical upwelling in recent decades (Fu et al., 2010; Young et al., 2012), while no consistent trends in the BDC were found in the upper stratosphere. Since then, additional studies have inferred BDC trends from satellite and radiosonde temperature observations in the lower stratosphere (Ossó et al., 2015; Fu et al., 2015), obtaining an estimated acceleration of annual mean upwelling in the lower stratosphere of about 2% per decade, which is in quantitative agreement with climate model trends (e.g., Butchart, 2014). The 2014 Assessment highlighted inconclusive results on BDC trends inferred from reanalysis data; however, new studies have obtained estimates of an acceleration in lower-stratospheric tropical upwelling of 2–5% per decade in reanalyses (Fueglistaler et al., 2014; Abalos et al., 2015; Miyazaki et al., 2016), consistent with climate model trends. This advance is due to the combination of several reanalysis datasets and estimates to extract common signals among them. Nevertheless, these studies reveal a large spread in both the baseline magnitude and the long-term trends of the BDC among different reanalysis datasets and different methods for estimating the circulation. Moreover, in contrast with the broad agreement on acceleration in the lower-stratospheric BDC, the sign of the trends in the middle and upper stratosphere remains uncertain. This is because reanalyses are affected by major discontinuities above ~10 hPa, which hampers deriving trends at these levels (Simmons et al., 2014; Abalos et al., 2015). Note that in general, reanalyses are deemed to be unreliable for studying long-term stratospheric changes (see **Section 5.3.1.1**). While this undermines confidence in estimated BDC trends from reanalyses, reanalyses remain the only available observational-based source with global coverage; therefore, these estimates currently cannot be verified against independent data.

Long-lived tracer measurements in the stratosphere can be used to derive the age of air (AoA), a measure of the net tracer transport circulation strength that integrates effects of both the advection by the overturning circulation and mixing (see **Box 5-2**). Reconciling the observed and modeled AoA trends has been a major issue since an analysis of balloon measurements revealed a small aging of stratospheric air over the last decades (Engel et al., 2009), which was inconsistent with the negative AoA trends produced by climate models (Waugh, 2009). While the observed trends in AoA reported in one study (Engel et al., 2009) were not highly statistically significant, they have been recently supported with extended observations for 2015–2016 (Engel et al., 2017). In the 2014 Assessment, it was mentioned that spatiotemporal sparseness of the measurements could be a key issue for interpreting the disagreement between models and data (Garcia et al., 2011). To address this issue, long-term (>30 years) AoA trends have been obtained by combining observations with models of varying complexity (Ray et al., 2014; Hegglin et al., 2014). These combined data–model-derived AoA estimates show negative trends in the lower stratosphere and positive trends in the middle stratosphere (consistent with Engel et al., 2017). One such example is illustrated in **Figure 5-9**, which shows the AoA trends for the NH mid-latitudes as a function of altitude derived from tracer observations (Ray et al., 2014). AoA trends derived from the ERA-Interim reanalysis show a qualitatively similar structure (Diallo et al., 2012; Ploeger et al., 2015), although this result is likely to depend on the reanalysis dataset. The decrease in AoA in the NH mid-latitude lower stratosphere shown in **Figure 5-9** and in another study (Hegglin et al., 2014) is consistent with the estimated increase in the overturning circulation described above; however, as outlined in **Box 5-2**, AoA is strongly affected by mixing, and hence its local trends do not necessarily indicate changes in overturning circulation. Importantly, these new studies also demonstrate that the observed decrease in AoA in the lower stratosphere can be reconciled within uncertainties with the trends derived from chemistry–climate models, while the disagreement between observations and models remains at higher altitudes.

Global estimates of AoA from satellite tracer measurements are available only for about a decade after 2002. Over this recent period, the observations show trends of opposite sign in the two hemispheres, with AoA decreasing in the Southern Hemisphere and increasing in the Northern Hemisphere (Stiller et al., 2012; Haenel et al., 2015). This behavior is consistent with AoA trends over the same period independently derived from HCl measurements (Mahieu et al., 2014) and from the ERA-Interim reanalysis (Ploeger et al., 2015). The main difference between the decadal and the long-term trends in the reanalysis is that the

Box 5-2. What Is the Age of Stratospheric Air?

The Brewer–Dobson circulation (BDC) controls, to a large extent, the global distributions of tracers in the stratosphere, including ozone (see **Chapters 3** and **4**). Despite its relevance, there remain large uncertainties in the mean magnitude and the long-term trends of the BDC, as this planetary-scale circulation cannot be directly measured (Butchart, 2014). The mean age of stratospheric air (AoA) is an estimate of the time of residence of an air parcel in the stratosphere since it entered through the tropical tropopause (Hall and Plumb, 1994; Waugh and Hall, 2002). Mean AoA can be inferred from observations of long-lived tracers with near-linear tropospheric sources, such as SF_6 or CO_2, and thus constitutes a useful benchmark for the representation of stratospheric transport in models (Waugh and Hall, 2002). The annual mean climatology of AoA derived from the MIPAS satellite data is shown in **Box 5-2 Figure 1a**. There is broad agreement among independent observations showing ages of 4–6 years in the lower stratosphere mid-latitudes (~40–60°N, ~20–25 km) and less agreement at high and low latitudes and at higher levels (Haenel et al., 2015).

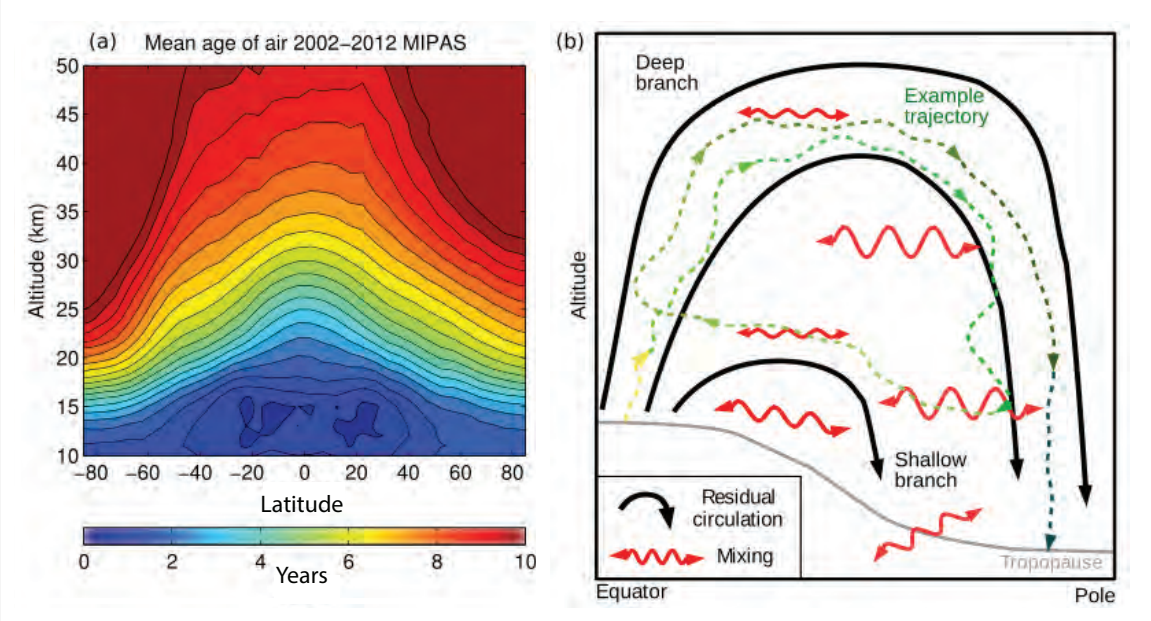

Box 5-2 Figure 1. (a) Climatology of annual mean age of air 2002–2012 from MIPAS SF_6 measurements and (b) schematic of the net stratospheric tracer transport circulation, including overturning circulation and mixing components. (a) Note that MIPAS mean age is overestimated at high latitudes due to an SF_6 mesospheric sink (Stiller et al., 2012). (a) Adapted from Haenel et al. (2015). (b) Adapted from Garny et al. (2014).

The AoA structure in **Box 5-2 Figure 1a** results from the combined effect of two components, as illustrated in **Box 5-2 Figure 1b:** slow mean advection by the overturning circulation (including shallow and deep branches; e.g., Birner and Boenisch, 2011) and rapid two-way quasi-isentropic irreversible mixing (see also Plumb, 2002; Shepherd, 2007). Accordingly, the AoA can be separated into the residual circulation transit timescale (RCTT) (Birner and Boenisch, 2011) and the time due to mixing processes (aging by mixing) (Garny et al., 2014). While the overturning circulation tends to steepen the meridional AoA gradients, mixing between the tropics and the extratropics causes recirculation of air parcels, increasing AoA throughout most of the stratosphere (see example trajectory in panel b).

Box 5-2, continued.

Furthermore, due to irreversible mixing, an air parcel traveling in the stratosphere does not maintain its identity, and the AoA at any location is fully described by a transit time distribution referred to as the age spectrum, which reflects a diversity of individual pathways followed by the elements forming the air mass (Hall and Plumb, 1994; Waugh and Hall, 2002). The mean age constitutes the first moment of the statistical distribution. Typical stratospheric age spectra feature long tails of old transit times due to aging by mixing, such that the mean age is usually longer than the modal age (peak of the age spectrum). Multiple peaks in the age spectrum reflect seasonal and interannual variability in the circulation (Ploeger and Birner, 2016). Understanding the separate contributions of the distinct transport mechanisms to the mean age and the age spectrum is key to constraining transport processes in models and their long-term trends, which are currently subject to large uncertainties.

AoA reduction in the NH lower stratosphere disappears for the most recent period. This could be related to an interruption in the acceleration of tropical upwelling in the lower stratosphere at the beginning of the 21st century (Aschmann et al., 2014), which is consistent with the observed reduced cooling of the tropical lower stratosphere over the first decade of the 21st century as compared to the previous two decades (see **Section 5.3.1.1**) (Aquila et al., 2016; Polvani et al., 2017; Randel et al., 2016; Khaykin et al., 2017). Different mechanisms have been proposed to explain the changes in tropical upwelling since around 2000, including ocean multi-decadal variability (Aschmann et al., 2014), the change in trend of atmospheric ODS concentrations since the late 1990s (see **Section 5.3.2.2**), and internal atmospheric variability (Garfinkel et al., 2017a). Moreover, the opposite sign of mean AoA trends in each hemisphere over the period 2002–2012 can be understood as a southward shift of the tropical upwelling region (Stiller et al., 2017); while the cause of this shift remains unclear, when its effects on AoA are removed, the remaining mean AoA trends are consistent with model predictions in the lower stratosphere (Stiller et al., 2017).

In addition to estimating long-term trends in the BDC, there are substantial uncertainties in estimates of the absolute strength of the overturning circulation among reanalyses (e.g., Abalos et al. (2015) estimate a 40% uncertainty). Using the meridional age gradient

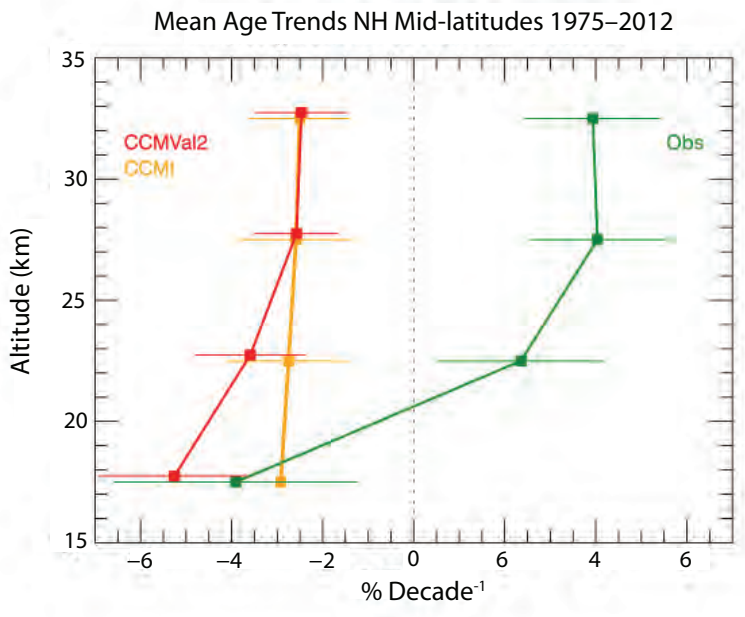

Figure 5-9. Profiles of trends in the Northern Hemisphere (NH) mid-latitude mean age of air (in percent per decade) from 1975 to 2012. Green symbols are trends derived from in situ tracer observations combined with a simple mechanistic model. Red symbols represent average trends from four ocean-coupled CCMVal2 models. Orange symbols represent average trends from nine ocean-coupled CCMI models. Error bars represent the standard deviation of the mean of all model trends at each level and, for observations, the 1σ uncertainty on the trend estimate at each level. Update to Ray et al. (2014).

as a metric of the strength of the stratospheric overturning circulation, good agreement is found between two different observational estimates at an altitude of 20 km (Neu and Plumb, 1999; Linz et al., 2016; Linz et al., 2017). The inferred value for the strength of the circulation is also shown to fall within the reanalysis uncertainty range and to agree with estimates from a climate model (Linz et al., 2017). In contrast, at higher levels, there is a 100% uncertainty in the circulation strength, with reanalyses and models showing significantly faster circulation than the observational estimate. This difference could be due to the fact that the AoA derived from SF_6 observations is overestimated, because this tracer has mesospheric sinks that lead to smaller concentrations of the tracer at high latitudes than if it were passively transported (e.g., Waugh and Hall, 2002; Haenel et al., 2015; Kovács et al., 2017). Nevertheless, the absolute strength of the overturning circulation remains highly uncertain in the middle and upper stratosphere (Linz et al., 2017).

5.3.2.2 Simulated Past and Future Changes of the BDC

The 2014 Ozone Assessment highlighted that chemistry–climate models robustly predict a long-term acceleration of the BDC in response to anthropogenic climate change (Hardiman et al., 2014; Palmeiro et al., 2014). This result stands for the new CCMI simulations (Morgenstern et al., 2018), while updated observational estimates still feature a near-zero trend or decelerating net transport circulation at mid-latitudes in the NH middle stratosphere (see **Figure 5-9**). The main recent advances in the analysis of trends in models have been through taking into account the potential contribution of large internal atmospheric variability on trends by assessing the role of the length of the period considered and through showing the importance of having several ensemble members for each simulation type. It was found that, while the BDC robustly accelerates over the last 55 years in chemistry–climate model simulations, when the period is limited to the last 25 years, some ensemble members show a slowing of tropical upwelling and an increase in NH mid-latitude mean AoA in the middle to upper stratosphere (Garfinkel et al., 2017a). It has also been found that the minimum record length needed to statistically distinguish a forced signal from the internal variability is about 30 years for a BDC trend of 2% per decade (Hardiman et al., 2017). This implies that shorter observational records do not necessarily reflect forced long-term trends. These results could potentially reconcile the modeled and observed AoA trends over shorter periods when most data have been collected, though discrepancies still remain with the longest observational records that began more than 40 years ago (**Figure 5-9**). On a wider perspective, one model study (Muthers et al., 2016) suggests that changes in mean AoA in the 20th and 21st centuries are unprecedented since the 1600s. However, this single-model result remains to be confirmed by other studies. Regarding future BDC trends, several CCMI models show the entire BDC being lifted as the tropopause rises (Oberländer-Hayn et al., 2016). Such close connection between the tropopause rise and the BDC acceleration may have implications for stratosphere–troposphere exchange (see **Section 5.3.3**).

A number of recent studies have highlighted the importance of assessing changes in isentropic eddy mixing in addition to the overturning circulation for interpreting long-term trends in the net stratospheric tracer transport and for comparing models to observations (Garny et al., 2014; Ray et al., 2014; Ploeger et al., 2015; Abalos et al., 2016; Miyazaki et al., 2016; Ray et al., 2016; Ploeger and Birner, 2016; Dietmüller et al., 2017). These studies build on a few previous studies addressing this issue (Ray et al., 2010; Li et al., 2012). They show that AoA trends derived from ERA-Interim reanalysis can be largely attributed to long-term trends in the isentropic mixing (Ploeger et al., 2015). Because isentropic mixing is a fundamental component of stratospheric tracer transport and its effect is integrated in AoA (see **Box 5-2**), it has to be adequately represented in models. Although two-way mixing and the mean overturning circulation are intrinsically coupled (both are driven by Rossby wave breaking), their combined effects on AoA, an integrated Lagrangian measure of transport, are not straightforward (Garny et al., 2014; Ploeger et al., 2015; Ploeger and Birner, 2016).

Previous model studies have examined the impact of ODS-driven ozone depletion and recovery on past and future BDC and AoA trends (e.g., Li et al., 2008; Oman et al., 2009; McLandress et al., 2010; Oberländer et al., 2013). Since the last Assessment, additional evidence from chemistry–climate model simulations has shown that Antarctic ozone depletion is the main driver of the observed BDC acceleration in the SH

summer over the past several decades (Keeble et al., 2014; Oberländer-Hayn et al., 2015; Garfinkel et al., 2017a; Polvani et al., 2018; Morgenstern et al., 2018; Li et al., 2018). **Figure 5-10a** shows the dominant role of ODSs in driving the SH polar downwelling acceleration until the year 2000. The changes in annual mean downwelling seen in **Figure 5-10a** predominantly reflect changes in austral summer (Polvani et al., 2018). Also shown in **Figure 5-10a** is a trend in polar downwelling in the 21st century of opposite sign, due to the ozone recovery (Oberländer et al., 2013; Polvani et al., 2018). The ODS influence on the BDC is not limited to the Antarctic region, and a number of recent modeling studies have quantified the global influence (Oberländer-Hayn et al., 2015; Polvani et al., 2017; Garfinkel et al., 2017a; Polvani et al., 2018). **Figure 5-10b** shows that, in a chemistry–climate model, a significant fraction (about 50%) of the past acceleration of the annual mean upwelling in the tropical lower stratosphere is attributed to ODSs. In the future, the decrease of ODSs and ozone recovery are expected to significantly reduce the GHG-driven BDC annual mean acceleration trends (**Figure 5-10b**). Finally, the ODS impact on the NH polar downwelling trends is negligible (**Figure 5-10c**). These results from a single chemistry–climate model remain to be tested in other models. Interestingly, recent modeling works have shown that the ozone hole, despite driving a strong acceleration of the downwelling over the boreal summer Antarctic lower stratosphere, leads to an increase in AoA in that region and season (Morgenstern et al., 2018; Li et al., 2018). This is attributed to the delay in the polar vortex breakup date, which implies that relatively old air remains isolated over this region. This result highlights the importance of considering changes in mixing for interpreting AoA trends.

The influence of ODS-induced ozone changes on the net overturning circulation occurs through changes in wave forcing associated with thermally driven changes in the background zonal wind. The wave forcing of the BDC cannot be viewed as predefined or fixed, as it may be affected by changes in radiation (Ming et al., 2016). Furthermore, there are important compensating processes between waves of different spatial scales, some of which cannot be directly represented in models and so are parameterized (e.g., Cohen et al., 2014; Sigmond and Shepherd, 2014).

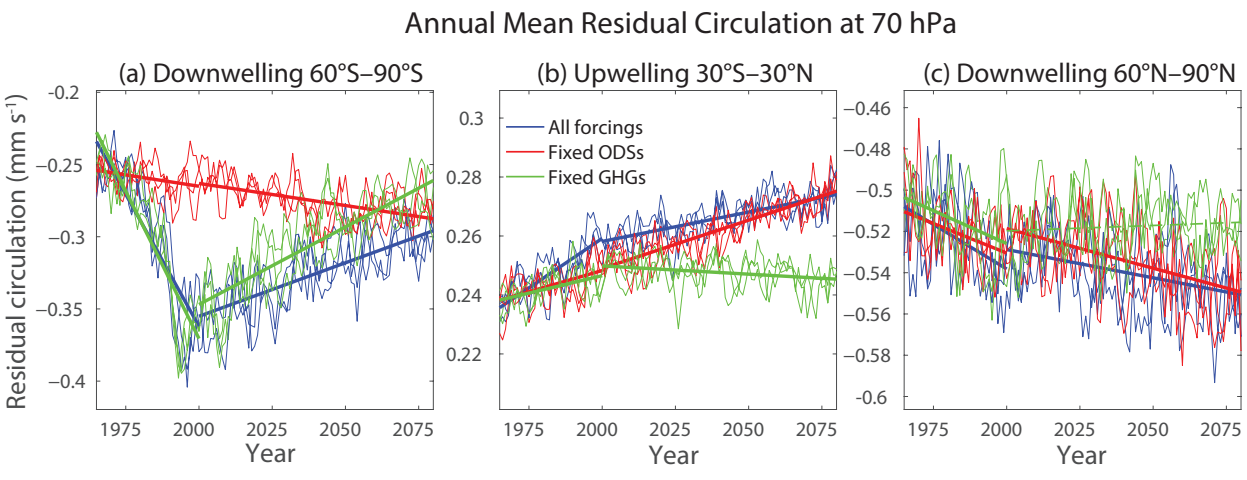

Figure 5-10. Time series of annual mean residual (overturning) circulation at 70 hPa over the (a) SH polar cap (60°S–90°S), (b) tropics (30°S–30°N), and (c) NH polar cap (60°N–90°N) for different runs from the Community Earth System Model (CESM) with Whole Atmosphere Community Climate Model (WACCM) as its atmospheric component. The thin colored lines represent all forcing runs (blue), runs with ODSs fixed to 1960 levels (red), and runs with GHGs fixed to 1960 levels (green). Three members are shown for each simulation type. Thick lines show the linear fit for each ensemble mean for the periods 1965–2000 and 2000–2080. Adapted from Polvani et al. (2018).

5.3.3 Stratosphere–Troposphere Exchange

Since ~90% of the total ozone column resides in the stratosphere, changes in stratosphere–troposphere exchange (STE) are critical to the evolution of the tropospheric ozone burden and thus air quality (e.g., Collins et al., 2003; Zeng and Pyle, 2005; Hegglin and Shepherd, 2009). Some of the factors affecting future changes in tropospheric ozone are addressed in **Section 3.4.4** of **Chapter 3** and in the recent IGAC Tropospheric Ozone Assessment Report (TOAR; see Young et al., 2018), which reports on the current understanding of tropospheric ozone in detail. Here we briefly assess the main advances since the 2014 Assessment regarding STE.

The 2014 Assessment discussed improvements to chemistry–climate models through the merging of tropospheric and stratospheric chemistry schemes, and it discussed the contribution of STE to the tropospheric ozone budget. The merged schemes resulted in improvements in modeled tropospheric ozone concentrations due to the inclusion of stratospheric ozone changes by ODSs and changes in the strength of the BDC (see **Section 5.3.2**). It was assessed that models consistently showed reduced ozone STE in the present compared to preindustrial times due to stratospheric ozone depletion, although the magnitude of the estimated change is model-dependent. On the other hand, model studies showed that concurrent ODS decreases and GHG increases in the future would lead to increased STE of ozone, with the magnitude of the change depending on the RCP scenario (see Section 4.5.3 in WMO (2014) and Section 11.3.5.1.2 in IPCC (2013)). Since the last Assessment, our qualitative understanding of the expected future changes in STE has not been modified. Stratospheric ozone influx into the troposphere is still expected to increase in the future, with the magnitude of the increase still model- and scenario-dependent, as discussed below.

STE typically occurs due to isentropic mixing, often during the formation of tropopause folds and cutoff lows associated with mid-latitude cyclonic disturbances, for example in the Atlantic and Pacific storm tracks (Stohl et al., 2003). New studies on STE have been conducted, quantifying its spatial and seasonal variability (e.g., Yang et al., 2016), investigating the mechanisms of ozone transport from the lowermost stratosphere to the surface (Škerlak et al., 2014; Lin et al., 2015; Albers et al., 2018), and giving quantitative observational constraints of the magnitude of tropospheric ozone changes due to STE (e.g., Neu et al., 2014). Stratosphere-to-troposphere ozone transport peaks in late spring and early summer in the Northern Hemisphere and shows little seasonality in the Southern Hemisphere (Yang et al., 2016). However, because it migrates seasonally in altitude following the subtropical jets, STE is strongest in winter in the Northern Hemisphere at the lower isentropes. This winter maximum is consistent with the peak of stratospheric ozone influence observed near the surface (Škerlak et al., 2014).

Nonetheless, difficulties remain in estimating the magnitude of STE. Large uncertainties have been reported in the magnitude, geographic distributions, seasonality, and long-term changes of STE, depending on the definition of the tropopause and the reanalysis dataset used (Boothe and Homeyer, 2017). In addition, it has been shown that the use of monthly mean residual circulation vertical velocities yields large errors in the estimated magnitude of ozone STE, resulting in different magnitude estimates in comparison to other methodologies (Hsu and Prather, 2014).

Ozone STE is controlled by the amount of ozone available in the lowermost stratosphere and also by the frequency and location of stratospheric intrusion events. Because these are governed by different mechanisms and their relative importance remains unclear, the variability of ozone STE, and in particular the relationship with El Niño–Southern Oscillation (ENSO), is still under discussion (Neu et al., 2014; Hess et al., 2015; Lin et al., 2015; Olsen et al., 2016; Albers et al., 2018). New research since the last Assessment provides more evidence that both the acceleration of the BDC (see **Section 5.3.2.2**) and stratospheric ozone recovery (see **Chapter 3**) will tend to increase the future global tropospheric ozone burden through enhanced STE. Two new studies find a substantial correlation between the strength of the BDC, STE, and tropospheric ozone during the observed period using satellite observations (Neu et al., 2014) and chemistry–climate model simulations constrained by observed SSTs and validated against observed ozone variability (Hess et al., 2015). The covariability between STE and tropospheric ozone from observations was used to deduce that the projected strengthening of the BDC alone (that is, without accounting for ozone recovery)

could lead to an increase in zonal mean tropospheric ozone of 2% by the end of the 21st century (Neu et al., 2014). A larger increase in mid-tropospheric ozone of 6% by 2100 due to BDC strengthening was obtained in one model study (Hess et al., 2015). The threefold difference between the two estimates highlights considerable quantitative uncertainty in the future evolution of ozone STE.

Several studies have estimated the role of STE for future tropospheric ozone using chemistry–climate model simulations that include the effects of climate change, in general agreeing that STE increases contribute importantly to future tropospheric ozone abundances. These studies examine the influence of the stratosphere on the tropospheric ozone through STE by including a stratospheric ozone tracer (no chemical ozone production in the troposphere) in the simulations (Banerjee et al., 2016; Meul et al., 2018). **Figure 5-11** shows the changes in the stratospheric ozone tracer due to climate change and ODS reduction, as a diagnostic of the impact of changes in STE on tropospheric ozone between 2000 and 2100 (Banerjee et al., 2016). A strengthened BDC under climate change following the RCP-8.5 scenario has its strongest effect on tropospheric ozone in the tropics and subtropics (**Figure 5-11a**), while stratospheric ozone recovery from declining long-lived ODSs has a larger role in the mid-latitudes and extratropics (**Figure 5-11b**). These results are consistent with recent estimates that the stratosphere-to-troposphere transport of ozone will increase more than 50% by 2100 under an RCP-8.5 scenario (Meul et al., 2018). Such increases in stratospheric ozone influx into the troposphere are consistent with those inferred in a multi-model study (Young et al., 2013) and model sensitivity studies (Kawase et al., 2011; Abalos et al., 2017). These results highlight STE as an important factor for determining future changes in tropospheric ozone, although its quantitative role remains uncertain due to the limited number of studies and the variations across current model results.

Future changes in tropospheric ozone will be determined by a complex interplay between chemical and transport processes. While all studies agree that STE changes will tend to increase future tropospheric ozone, the relative importance of STE versus tropospheric chemistry for future tropospheric ozone trends remains an open question. A strong sensitivity to GHG scenario, as reported in the last Assessment, is supported by new model results, with studies finding a net decrease in the global burden of tropospheric ozone in 2100 compared to that in 2000 in the RCP-6.0 scenario (Sekiya and Sudo, 2014; Revell et al., 2015) and an increase in the RCP8.5 scenario (Banerjee et al., 2016; Meul et al., 2018). A major source of uncertainty in projections of tropospheric ozone is the future evolution of methane concentrations, which are much larger in the RCP8.5 scenario than in the others. However, scenario dependence is not the only source of uncertainty in future tropospheric ozone. A study using new simulations from multiple chemistry–climate models finds considerable disagreement among models in tropospheric ozone even when the same scenario is considered, with much of the model spread being likely due to the uncertainty in stratospheric transport and STE trends (Morgenstern et al., 2018). A more detailed discussion of future tropospheric ozone changes is given in **Chapter 3, Section 3.4.4**.

5.3.4 Stratospheric Winds

5.3.4.1 Polar Vortices

The characteristics of stratospheric wintertime polar vortices, such as their strength and duration, have a large impact on polar stratospheric ozone variability and can also affect tropospheric climate. Observed and projected variability and long-term changes in polar vortex characteristics are discussed in **Chapter 4**. Here, we briefly review polar vortex changes with a focus on their implications for the troposphere.

Previous assessments reported an observed strengthening of the Antarctic polar vortex during austral spring and a delay in the vortex breakup date resulting from diabatic cooling associated with ozone loss. **Figure 4-3** in **Chapter 4** shows that the trend toward later breakup dates did not continue during recent years, which were instead characterized by a large variability in breakup dates ranging between mid-November and mid-December. This year-to-year variability is linked to variability in planetary wave activity, which is mostly driven by internal climate dynamics. No recent studies have analyzed projected changes in the Antarctic vortex and, in line with previous Assessments, it is expected that ozone recovery will lead to a weakening of the polar vortex

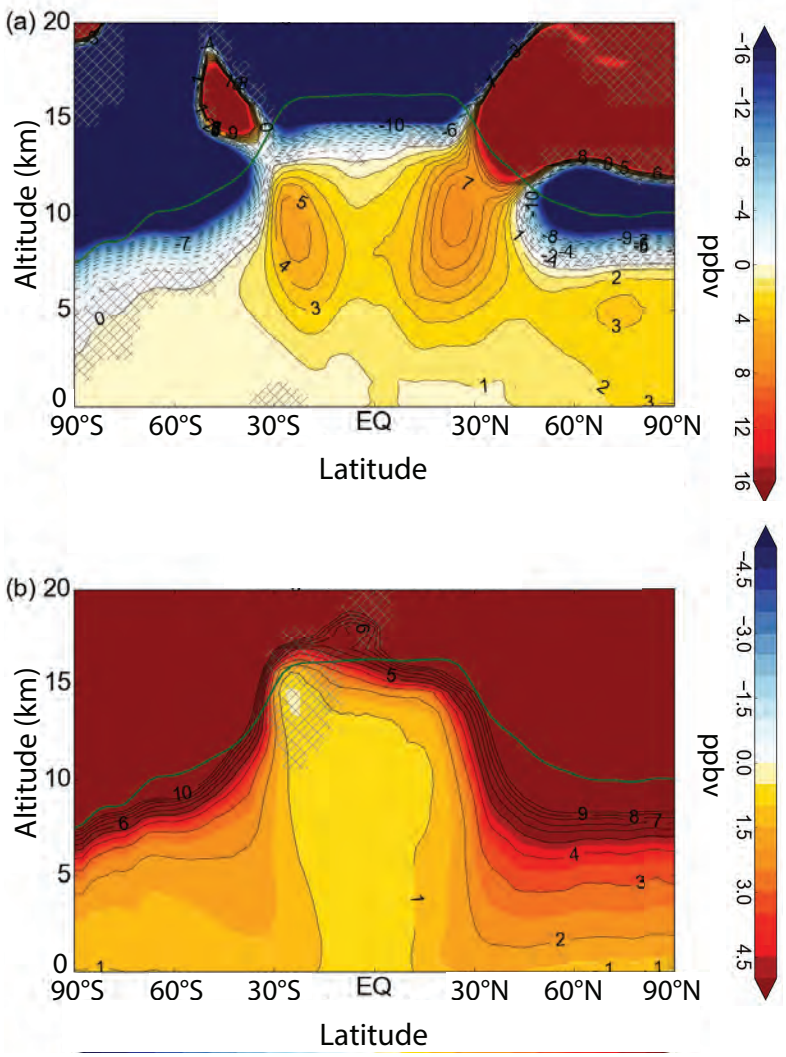

Figure 5-11. Modeled changes in ozone mixing ratio [ppbv] between 2000 and 2100 due to (a) changes in physical climate (GHGs, sea surface temperatures, and sea ice) following the RCP-8.5 scenario and (b) changes in ODS concentrations. Shown are changes for a stratospheric ozone tracer that is constrained to stratospheric values above the tropopause but that evolves freely in the troposphere and undergoes only tropospheric loss processes (i.e., there is no tropospheric ozone production). The inclusion of a separate stratospheric ozone tracer in the model simulations allows separation of the STE contribution from the changes due to tropospheric processes. Adapted from Banerjee et al. (2016).

and a return to earlier breakup dates. A trend toward later breakup dates of the Antarctic vortex may reappear in the late 21st century as a result of tropical upper-tropospheric warming driven by increased GHG concentrations and associated strengthening of the meridional temperature gradient near the tropopause (Wilcox and Charlton-Perez, 2013).

The large interannual variability in the Arctic polar vortex effectively masks any trends driven by changes in external forcings including ODSs and ozone, though there has been a shift toward weaker vortices in mid-winter since 1990 (consistent with the temperature changes discussed in **Section 5.3.1**) (Garfinkel et al., 2017b). It has been suggested in a number of studies that a loss of Arctic sea ice can lead to a weakening of the stratospheric vortex (e.g., Kim et al., 2014), and one study argued that the observed ice loss has shifted the vortex toward Eurasia (Zhang et al., 2016). However, another study demonstrated that the observed shift is also consistent with unforced decadal variability (Seviour, 2017). Two studies (Garfinkel et al., 2017b; Kretschmer et al., 2018) presented evidence that the weakening of the Arctic polar vortex since 1990 contributed to the hiatus in GHG-induced near-surface warming over Eurasia in boreal winter; however, the vortex weakening itself was not attributed to external forcing, implying that it is likely a result of internal variability.

Several new studies have analyzed future dynamical changes in the Arctic vortex and their implications

for surface climate. Coupled climate models disagree about the sign of the projected vortex changes (Simpson et al., 2018), although weakening of the polar night jet has been reported to be a preferred response across the CMIP5 multi-model ensemble (Manzini et al., 2014) and single-model large ensemble (Peings et al., 2017) by the end of the 21st century under a high GHG scenario. Nevertheless, episodes of a cold and strong polar vortex are projected to occur throughout the 21st century (Bednarz et al., 2016). While simulated future vortex changes are small in comparison to the observed large interannual variability, the intermodel spread in vortex changes is a significant component of uncertainty in future tropospheric climate change (Manzini et al., 2014; Zappa and Shepherd, 2017; Simpson et al., 2018).

The mechanisms of the projected changes in the Arctic polar vortex remain unclear. While projected Arctic amplification and sea ice loss can contribute to vortex weakening in coupled model simulations, as discussed above (Kim et al., 2014; Manzini et al., 2018), the weakening is also found in atmosphere-only model simulations omitting sea ice loss as a response to global SST warming (Karpechko and Manzini, 2017). The lack of understanding of the mechanisms, together with large intermodel spread in projections, indicates that our confidence in projected Arctic vortex changes is low.

5.3.4.2 Quasi-Biennial Oscillation Disruption and Implications

The influence of the Quasi-Biennial Oscillation (QBO) on stratospheric ozone is relatively well understood (**Chapter 3**, **Section 3.2.1.2**). However, the disruption of the QBO that took place in 2016 (see **Chapter 3** for a discussion of its effects on ozone) raised questions about how well we understand the QBO's generating mechanisms, the response of the QBO to climate change, and how the QBO will affect future ozone evolution.

During early 2016, a downward propagation of the eastward QBO phase was unexpectedly interrupted by the appearance of a westward jet at 40 hPa (Osprey et al., 2016; Newman et al., 2016). Several papers have concluded that the immediate cause of the interruption was a flux of easterly momentum associated with a pulse of planetary waves propagating from the NH extratropics (Osprey et al., 2016; Coy et al., 2017; Barton and McCormack, 2017; Watanabe et al., 2017). There is evidence that the strong 2015–2016 El Niño was implicated in forcing the wave pulse (Barton and McCormack, 2017; Hirota et al., 2018), and one study also suggests a role for the very low Arctic sea ice concentrations in that year (Hirota et al., 2018). The effect of the QBO interruption on ozone was consistent with our existing understanding of QBO–ozone linkages (see **Chapter 3, Section 3.2.1.2**). The interruption was not predicted by operational seasonal prediction models (Osprey et al., 2016), but it was reproduced retrospectively by an atmospheric model driven by observed SSTs (Watanabe et al., 2017). Although such an event is unprecedented in the more than 60 years of QBO observations (Newman et al., 2016), analogous events are found in model simulations (Osprey et al., 2016), and the effect of the anomalous wave flux on the QBO is consistent with our understanding of QBO generating mechanisms. Since the disruption in 2016, the QBO has recovered to its expected eastward phase. Analysis of simulations of future QBO, corroborated by observational evidence, suggests that QBO amplitude in the lower stratosphere will decrease (Kawatani and Hamilton, 2013; Schirber et al., 2015; Naoe et al., 2017) as a result of a projected increase in the mean tropical upwelling (see **Section 5.3.2.2**) and that the amplitude of QBO-induced ozone variability will consistently decrease in the lower stratosphere; in the upper stratosphere, it will increase due to ozone recovery (Naoe et al., 2017). However, this result is based on only a few available studies. Furthermore, our current understanding of changes in wave forcing contributing to the QBO is incomplete, which prevents firm conclusion about future QBO changes or whether QBO interruptions can occur more frequently in future climate.

5.4 EFFECTS OF CHANGES IN STRATOSPHERIC OZONE ON THE TROPOSPHERE AND SURFACE

The influence of stratospheric ozone change on SH tropospheric and surface climate has been analyzed and investigated in an increasingly mature body of research. A key result is that ozone depletion is assessed to be the dominant driver of austral summer (December–January–February; DJF) atmospheric circulation changes ranging from subpolar to tropical latitudes over the period in which stratospheric

ozone was rapidly decreasing. We focus here on what has been learned since the 2014 Ozone Assessment (Arblaster and Gillett et al., 2014). This includes improved quantification of the forced response to ozone in the context of natural internal variability and improved understanding of the role of recent changes in SSTs in driving observed SH circulation changes. We also highlight a growing body of evidence that suggests that the Southern Ocean response to ozone depletion is timescale-dependent. The effects of ozone depletion on the climate of the Southern Hemisphere, which span from the stratosphere to the oceans, are summarized in the schematic shown in **Figure 5-12**. We begin by assessing the effects of stratospheric ozone changes on the tropospheric circulation, followed by an assessment of the resultant impacts on surface climate, the ocean, and sea ice.

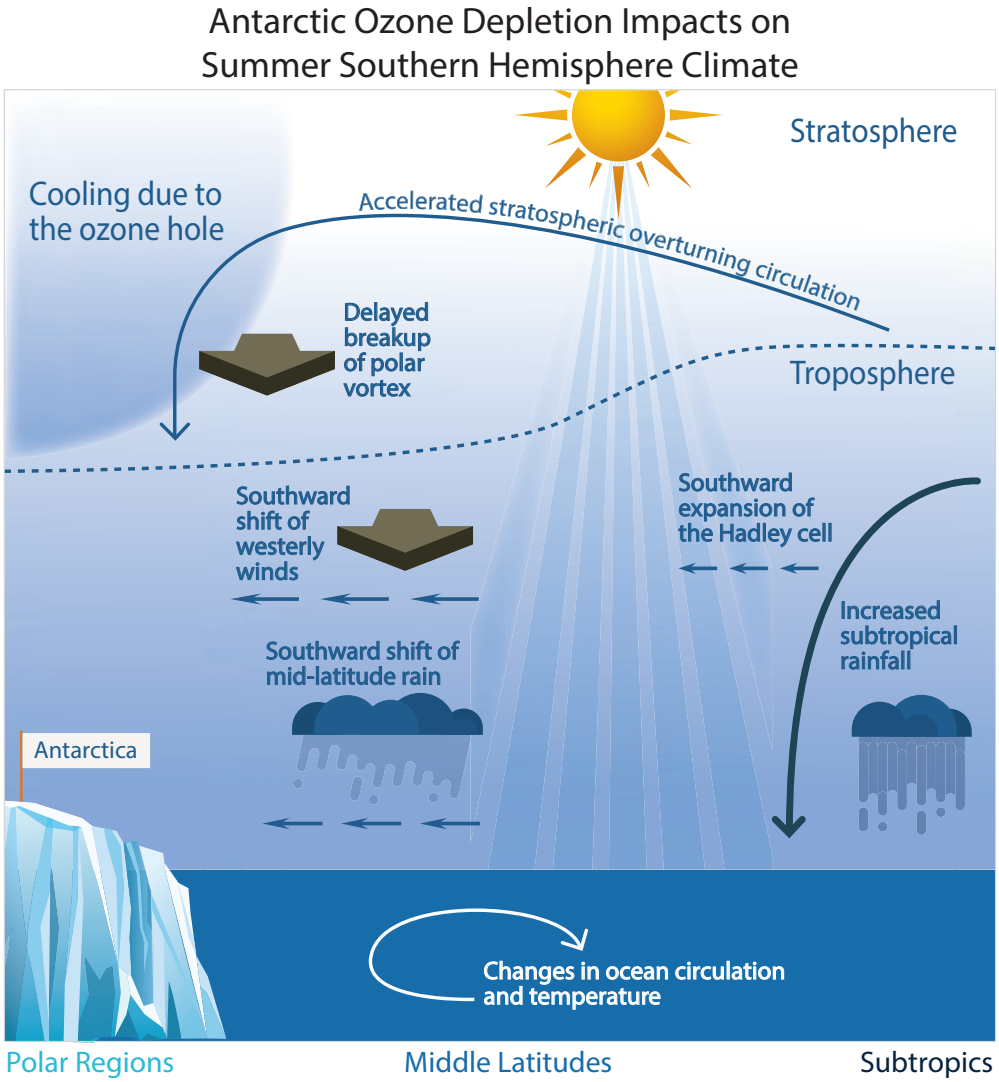

Figure 5-12. Schematic illustration of Southern Hemisphere climate impacts in austral summer associated with Antarctic ozone depletion. Ozone depletion has cooled the Antarctic stratosphere, leading to a delayed breakup of the stratospheric polar vortex and an accelerated Brewer–Dobson circulation. Impacts extended into the troposphere: A region of strong westerly winds and associated rainfall shifted southward, affecting the ocean circulation. The subtropical edge of the tropical circulation also expanded poleward, leading to reduced precipitation in mid-latitudes and enhanced precipitation in the subtropics. Update to Figure 4-22 in Arblaster and Gillett et al. (2014).

5.4.1 Tropospheric Circulation Effects

As described in **Section 5.3.1**, the primary effect of Antarctic stratospheric ozone depletion is to produce a strong cooling in the lower stratosphere over the Antarctic in austral spring. Over the period in which ozone depletion was increasing from 1960 to around 2000, large changes were observed in the SH mid-latitude and tropical circulations in austral summer: The SH tropospheric mid-latitude maximum in zonal winds (that is, the jet) shifted poleward; the Southern Annular Mode (SAM) index, which corresponds to opposite-signed changes in sea level pressure over high latitudes and mid-latitudes, shifted more into its positive phase (i.e., decreased sea level pressure over high latitudes); and the subtropical edge of the Hadley Cell shifted poleward. We first review the observational evidence for these changes and then discuss model simulations that causally link these changes to ozone depletion. An assessment of the current understanding of the mechanisms through which this shift occurs appears in **Section 5.4.2**.

5.4.1.1 The Southern Hemisphere: Observations

The SH general circulation includes a band of strong westerly winds, which are associated with the storm track (that is, synoptic-scale eddies and rainfall in the mid-latitudes). The latitude of the maximum zonal mean westerly winds in the lower troposphere is referred to as the mid-latitude near-surface jet (or for brevity, jet) and is climatologically centered around 52°S. Global monitoring of the location of the near-surface jet is available only since 1987 from the launch of the Special Sensor Microwave Imager (Goodberlet et al., 1989). Since then, a series of satellite microwave radiometers and scatterometers have continually observed near-surface wind speed. Measurements from the various satellite missions can then be combined into a gridded dataset, either with a reanalysis product or in a stand-alone product such as the Cross-Calibrated Multi-Platform (CCMP) ocean surface wind vector analyses (Atlas et al., 2011). Before 1987, winds were observed by available radiosondes and (after 1979) estimated from satellite measurements. Modern reanalysis products such as ERA-Interim and MERRA more accurately capture variability and trends in near-surface winds, wind stress, and the SAM after 1979 than earlier reanalyses (Swart et al., 2015) when compared to station data (for the SAM) and satellite data (for near-surface winds). The recent evolution of the latitude of the near-surface jet in CCMP is shown in **Figure 5-13**. Trends in the jet are strongest in DJF and are statistically significant at the 95% confidence level in that season (Swart et al., 2015), consistent with the findings of previous assessments. Since 2000, the jet in DJF has shifted equatorward, though trends are not statistically significant. Trends are weaker and not statistically significant in other seasons, with the exception of a significantly stronger jet in May (Ivy et al., 2017a).

The SAM is the leading mode of variability in the SH extratropical circulation and, as mentioned above, corresponds to opposite-signed changes in sea level pressure between subpolar latitudes and mid-latitudes. The SAM index generally tracks changes in the characteristics of the mid-latitude jet (as evidenced by the large correlation on interannual timescales in **Figure 5-13**), with the positive phase corresponding to a poleward jet shift, though the variations in the SAM can also be associated with variations in the strength of the mid-latitude jet (Monahan and Fyfe 2006; Swart et al., 2015; Solomon and Polvani, 2016).

The SAM index can be calculated from station pressure observations, which are available for a longer period than Southern Ocean surface wind observations as they do not rely on satellite retrievals. Hence the SAM has historically been used to quantify changes in the large-scale mid-latitude circulation. After 1979, there is generally good agreement between the SAM index calculated from station observations and that calculated from reanalyses, whereas prior to 1979, some reanalyses are known to have deficiencies (Marshall, 2003) and tend to simulate trends that are too strong (Swart et al., 2015).

Figure 5-13 shows the historical evolution of the SAM index from station observations of sea level pressure (based on an update of Marshall, 2003). The largest seasonal trends over the period in which ozone depletion was increasing (through 2000) are found in DJF and MAM (March–April–May), and these changes dominate the response in the annual mean. Since 2000, the SAM has stayed mostly in its positive phase (with respect to the 1971–2000 period). Evidence from paleoclimate reconstructions of the SAM index derived from networks of surface temperature proxies and from multiple studies suggests that the current

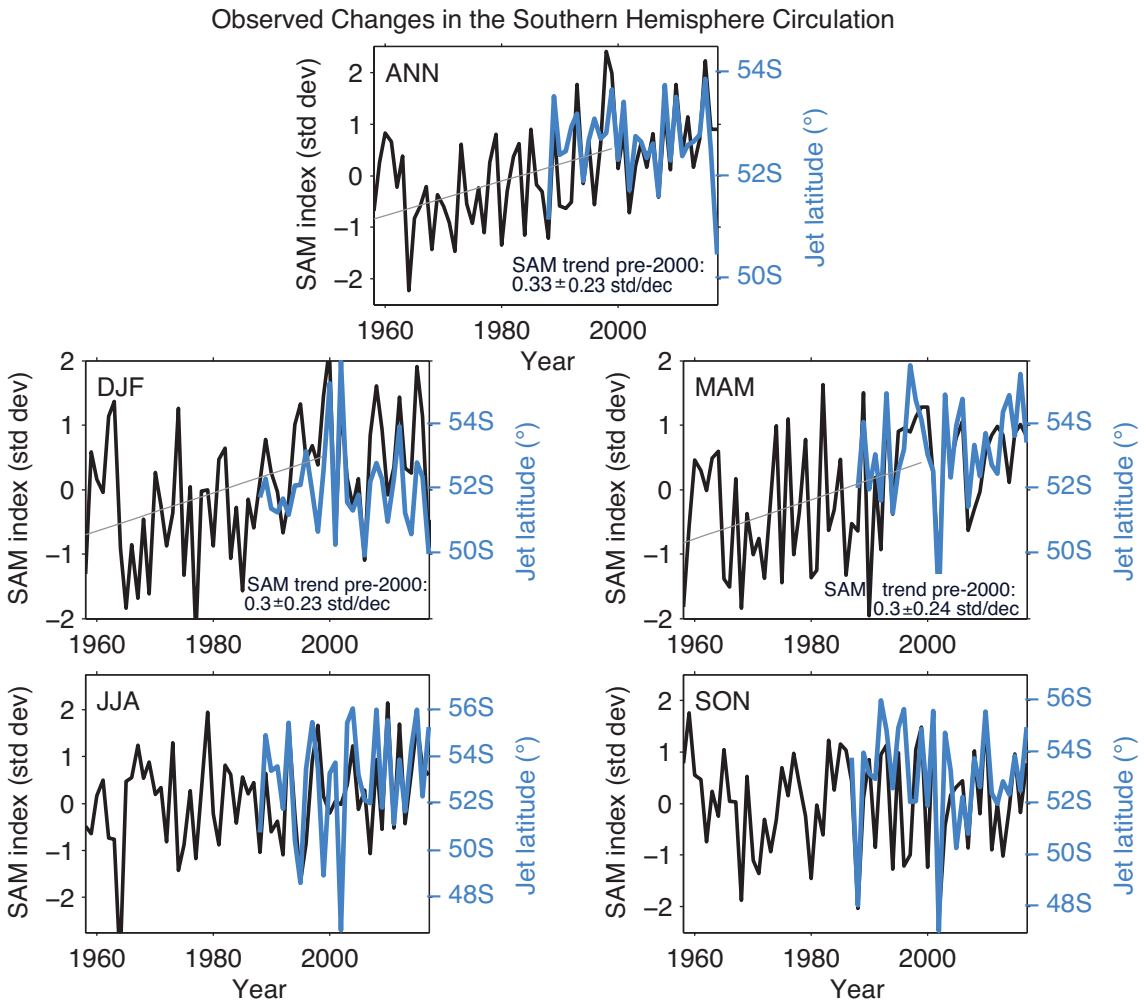

Figure 5-13. SAM index (black) and mid-latitude jet positions (blue) time series from 1958–2017 for the four seasons and annual mean. The SAM index is normalized by its standard deviation and is defined as in Marshall (2003). The jet position is based on the maximum of CCMP satellite-based surface wind speed (Atlas et al., 2011) (available for download at http://www.remss.com/measurements/ccmp), which starts in 1987. A linear trend line of the SAM changes before 2000 is shown when statistically significant, and the slope of the best fit line and its corresponding 95% uncertainty bounds are shown.

period of prolonged positive summer SAM conditions is unprecedented over at least the past 600 years (Villalba et al., 2012; Abram et al., 2014; Dätwyler et al., 2017). Reconstructions for the summer season (Dätwyler et al., 2017) are very robust across multiple methods and datasets, but some discrepancies exist in the magnitude of reconstructed low frequency SAM changes during the preindustrial period for the annually averaged SAM.

On interannual timescales, the position/strength of the mid-latitude jet and the Hadley Cell edge are correlated (Kang and Polvani, 2011; Ceppi and Hartmann, 2013; Staten and Reichler, 2014), raising the question of whether the subtropical Hadley Cell edge would also have shifted poleward. Recent studies have confirmed that the subtropical edge of the Hadley Cell has expanded poleward, confirming the results of the previous Assessment (Garfinkel et al., 2015a; Lucas and Nguyen, 2015; Davis and Birner, 2017; Solomon et al., 2017; Kim et al., 2017). This poleward shift is most pronounced in austral summer in the Atlantic and Indian Ocean sectors (Choi et al., 2014; Kim et al., 2017), the same region in which the upper-tropospheric polar

jet has shifted poleward most sharply (Manney and Hegglin, 2018). Quantifying the rate of the observed Hadley Cell expansion has been challenging, however. Different studies have used a wide variety of metrics to track Hadley Cell width, and two recent studies (Davis and Birner, 2017; Solomon et al., 2017) suggest that metrics based on upper-tropospheric quantities are only weakly correlated with metrics based on mid-tropospheric and surface processes, though another study (Mantsis et al., 2017) suggests that in CMIP5 models, a metric based on outgoing longwave radiation is well correlated with mid-tropospheric metrics. Furthermore, different reanalysis products do not agree as to the rate of expansion even when a common definition of a single metric is applied. For example, one study (Garfinkel et al., 2015a) compared five different reanalysis products (including MERRA output from two different stages in the assimilation cycle) and found that the trends in different reanalysis products (or even from two different stages in the assimilation cycle of the same reanalysis system) can be significantly different at the 90% confidence level in the Southern Hemisphere over the period 1980 to 1999, with rates of expansion ranging from 1 degree per decade to 0.3 degree per decade (**Figure 5-14**). Differences are even larger over the period from 1980 to 2009. Thus, while the Hadley Cell expansion is robust, its magnitude has large uncertainty, which is partly related to disagreement among applied metrics for the Hadley Cell edge. The development of a robust observational metric (or a set of metrics) of Hadley Cell width is still an area of active research.

5.4.1.2 The Southern Hemisphere: Model Simulations of the Past

We now assess modeling studies that have attempted to pin down the cause of the observed changes in the SH circulation, and we begin with the period in which ozone depletion was increasing, between the 1960s and 2000. The cleanest way to establish the importance of ozone for past changes in the SH circulation is to perform model simulations of the historical period both with and without ozone depletion. The 2014 Assessment described several such studies and concluded that ozone depletion is very likely the dominant driver of the changes in the SAM in summer. Since the previous Assessment, one modeling study has supported the conclusion that ozone depletion has led to a change in the summer SAM by comparing integrations with and without ozone depletion (Keeble et al., 2014). An additional study has also concluded that summertime Hadley Cell trends are strong in CMIP5 models only when ozone depletion is included (Tao et al., 2016) (**Figure 5-15**). A third study compared the summertime tropospheric response to ozone depletion from 1960 to 2000 in a suite of climate model simulations of varying configurations (for example, prescribed SSTs versus the inclusion of a coupled ocean, as well as prescribed ozone concentrations versus the inclusion of interactive chemistry) and found a consistent widening of the Hadley Cell and poleward shift of the jet in austral summer (Seviour et al., 2017a). **Figure 5-15** summarizes the trends in both the SAM and the subtropical Hadley Cell edge as simulated in the CMIP5 multi-model mean. Both the positive SAM trend and the poleward expansion of the Hadley Cell maximize in austral summer during the period from the early 1970s to around 2005, when the models are forced with all external climate drivers, including anthropogenic (ozone depletion, increasing GHG concentrations, and aerosols) and natural (solar cycle and volcanoes) factors. The separate contribution of ozone depletion and GHGs can be seen in both variables, with ozone playing a dominant role in austral summer and GHGs playing a major role during the other seasons. Overall, the majority of studies that have compared simulations forced with ozone depletion to simulations forced with no ozone depletion have concluded that ozone is the dominant forcing of changes in the SH circulation over the period in which ozone depletion was increasing.

Two studies that compared simulations with and without ozone disagreed with this consensus and concluded that ozone depletion was not the dominant cause of recent changes in the Southern Hemisphere in austral summer (Staten et al., 2012; Quan et al., 2014). However, there are methodological issues with both studies (Waugh et al., 2015): They both used prescribed ozone fields that underrepresent the magnitude of observed Antarctic ozone depletion, thus leading to a weakened response to ozone. Specifically, one of the studies (Quan et al., 2014) used ozone forcing (Lamarque et al., 2012) which underestimates observed ozone depletion by a factor of two (Figure 2f of Eyring et al., 2013). The other study (Staten et al., 2012) implicitly assumes that there was negligible ozone

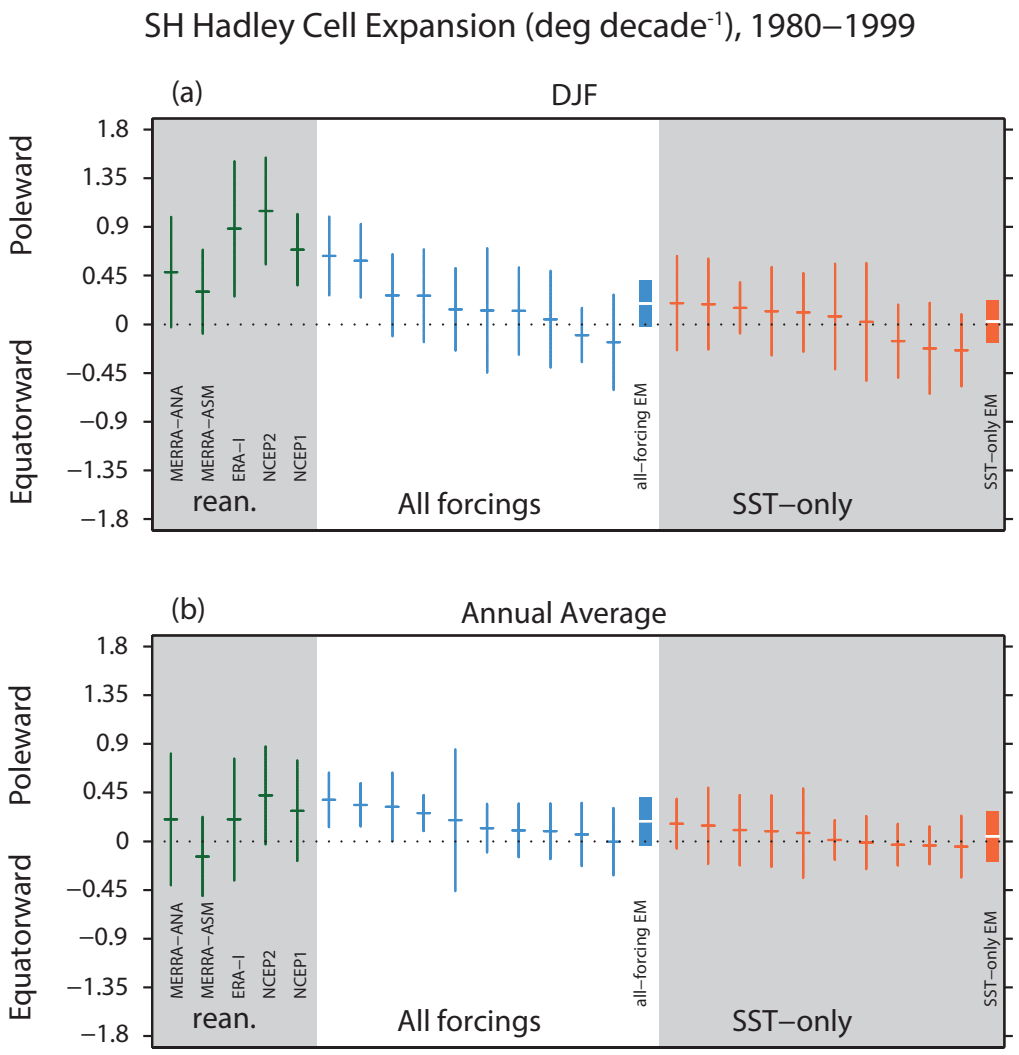

Figure 5-14. Poleward expansion of the SH Hadley Cell as determined by the zero crossing of the 500 hPa stream function in five reanalysis products and in each member of an ensemble of Goddard Earth Observing System Chemistry-Climate Model (GEOSCCM) simulations and in the ensemble mean (EM) in (a) DJF and (b) the annual average from 1980 to 1999. Integrations forced with time-varying ODS and GHG concentrations in addition to observed SSTs are in blue, while integrations with fixed ODS and GHG concentrations are in orange. Vertical lines or bars represent the 95% confidence interval on the trend as deduced by a Student's t test, and the center horizontal line indicates the trend. The uncertainty for the ensemble-mean trends are indicated by a rectangle, while that of individual ensemble members/reanalysis are indicated by a vertical line. The ensemble members for each ensemble are ordered by their expansion trend before they are plotted for clarity. Adapted from Garfinkel et al. (2015).

depletion between 1870 and 1979, as they use 1979 ozone values for their "preindustrial/1870" simulations, yet significant ozone loss occurred before this (Eyring et al., 2013) (see **Chapter 4**); hence the difference between their "preindustrial" simulation and 2000 simulation has too weak an ozone change. The net effect is that SST- and GHG-induced changes are considered over the period 1870 to 2000 as compared to ozone induced-changes from 1979 to 2000, which necessarily underestimates the relative impact of ozone on surface climate compared to other drivers.

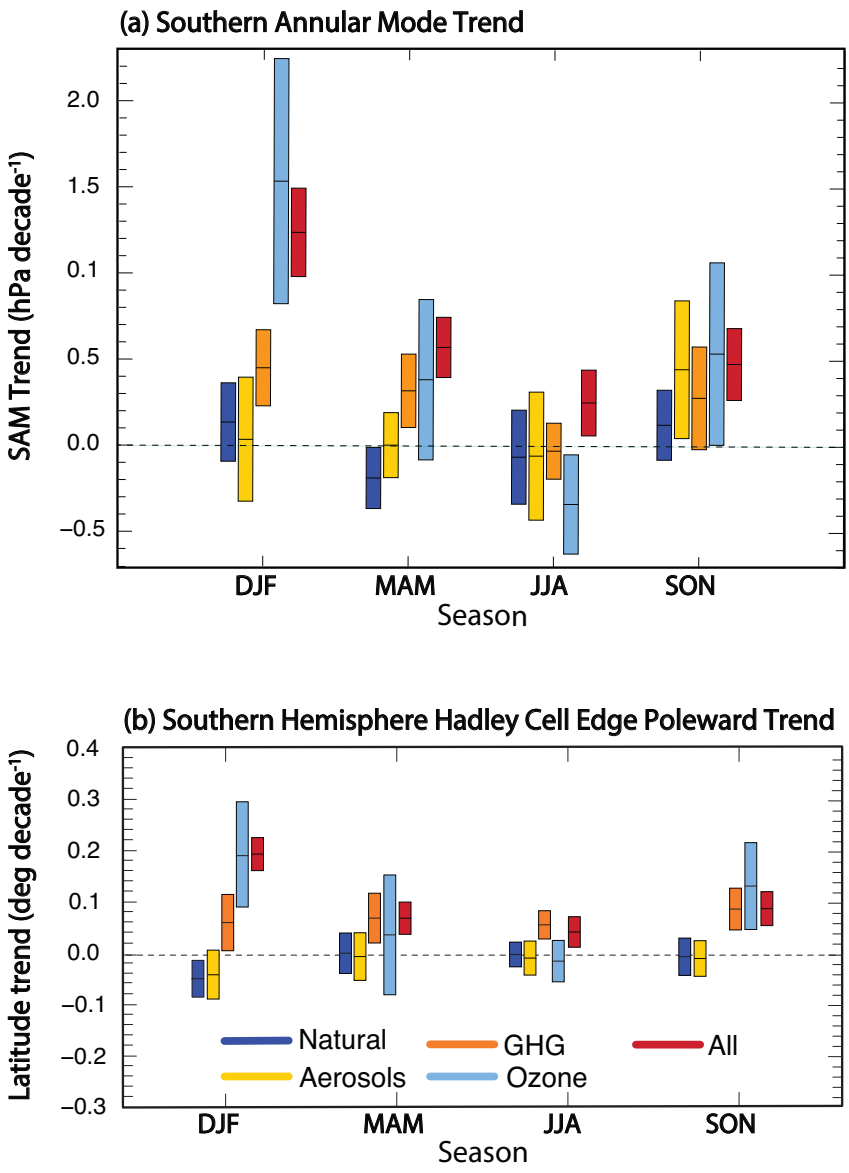

Figure 5-15. Seasonal-mean trends in the (a) SAM index for the period 1971–2006 and (b) the latitude of the poleward edge of the SH Hadley circulation at 500 hPa for the period 1970–2005 (1970–2000 for ozone only), derived from CMIP5 historical simulations. Positive trends indicate poleward expansion and negative values indicate equatorward retreat. Error bars are 90% confidence level. Units are (a) hPa per decade and (b) degree per decade. The colors denote model experiments including the following forcings: all anthropogenic and natural (red); greenhouse gases only (orange); tropospheric and stratospheric ozone only (light blue); natural (solar and volcanic) only (dark blue); and anthropogenic aerosols only (gold). Adapted from Gillett et al. (2013) and Tao et al. (2016).

The weight of the evidence from studies that have compared the impact of ozone depletion to other forcings in a methodologically appropriate manner clearly points to stratospheric ozone depletion as the dominant driver of the changes in the summer SAM over the period in which an ozone hole was formed (prior to 2000).

The trends in tropospheric zonal wind in CCMI models from 1960 to 2000, when forced with natural and anthropogenic forcings including ozone depletion, are similar to those in reanalysis data (**Figure 5-16a–c**; Son et al., 2018). Trends are somewhat weaker in CMIP5 models (**Figure 5-16d;** Rea et al., 2018); however, the weaker trends are most pronounced in those CMIP5 models that did not use interactive chemistry (**Figure 5-16f**; as noted by Eyring et al., 2013); trends in CMIP5 models that used interactive chemistry are quantitatively similar to those simulated by the CCMI models and observations (**Figure 5-16e**). While the observed zonal wind trend is generally consistent with the forced response to ozone depletion, the wind field by itself does not provide a unique fingerprint of ozone depletion due to the large internal variability in the climate system (Schneider et al., 2015).

Although there is uncertainty in the magnitude of the Hadley Cell widening (see **Section 5.4.1.3**), studies agree that the widening has continued (e.g., Mantsis et al., 2017). At the same time, the SAM has mostly

stayed in its positive phase, though the jet latitude has shifted somewhat equatorward from its 2000 position in austral summer (**Figure 5-13**). As discussed in **Chapter 4**, SH polar ozone depletion peaked around 2000 and has slowly begun its recovery, and hence ozone cannot be the sole driver of changes in the Southern Hemisphere since 2000. Rather, several studies have concluded that recent changes in tropical and subtropical SSTs (due to both internal variability and GHG-induced warming), and in particular decadal variability associated with the Pacific Decadal Oscillation (also known as the Interdecadal Pacific Oscillation), drove recent changes in SH circulation (Allen et al., 2014; Waugh et al., 2015; Garfinkel et al., 2015b; Franzke et al., 2015; Nguyen et al., 2015; Clem et al., 2016; Schneider et al., 2015; Allen and

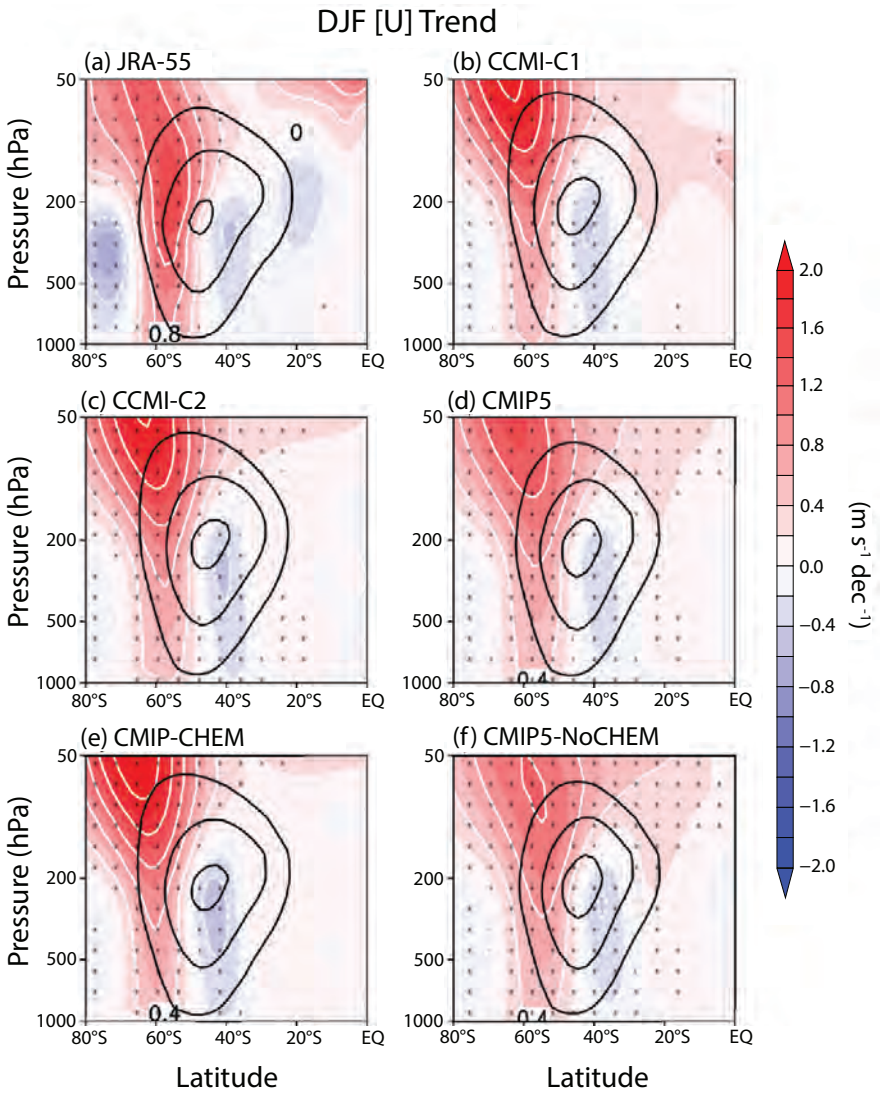

Figure 5-16. Long-term mean (thin black contour) and linear trend (color) of zonal-mean DJF zonal winds over 1960–2000 (the period of ozone loss) for (a) Japanese 55-year Reanalysis (JRA-55); (b, c) CCMI models in REF-C1 and REF-C2 simulations, respectively; and (d, e, f) CMIP5 models. The positive (negative) trends on the poleward (equatorward) flanks of the mean jet characterize a poleward shift of the jet. A comparison between CMIP5 models with and without chemistry is shown in panels e and f. The JRA-55 is the most recent reanalysis product to cover the full period of ozone loss; trends in other reanalysis products analyzed over a shorter period are quantitatively similar (e.g., Son et al., 2010). Contour interval of climatological wind is 10 m s^{-1} starting from 10 m s^{-1} at the outer-most contour. Adapted from Son et al. (2018).

Kovilakam 2017; Mantsis et al., 2017; Fogt et al., 2017; Amaya et al., 2018).

As discussed in **Section 5.4.1.1**, significant trends in the strength of the tropospheric mid-latitude jet, are also evident in May, in addition to summer; however, unlike in summer, a role of ozone depletion in the May trends is unclear. While ozone trends and stratospheric cooling have been observed in late fall, implying that they might have contributed to the tropospheric trends in May, similar stratospheric changes have also been observed earlier in fall and in summer but without concurrent significant trends in the tropospheric circulation. Furthermore, observational and modeling studies suggest a stronger role of observed changes in tropical SSTs in forcing SH tropospheric circulation changes in autumn, especially after 2000, when the ozone forcing has begun to recover (Schneider et al., 2015; Clem et al., 2016). Finally, SAM trends in autumn are not robust in modeling studies, with some studies finding positive trends (Stone et al., 2016) (see **Figure 5-15**) and others finding no trend (Swart et al., 2015; Tao et al., 2016), implying the trends may not be attributed to external forcing.

Finally, there is no consensus on the importance of changes in aerosol concentrations for changes in the SH tropospheric circulation: Some studies find that historical changes in aerosols largely canceled the effect of GHGs on the SAM in the last half of the 20th century in CMIP5 models (e.g., Fyfe et al., 2012; Gillett et al., 2013), while others find a relatively weak role for aerosols in CMIP5 models for both the SAM and the Hadley Cell changes (Steptoe et al., 2016; Tao et al., 2016). This discrepancy could be due to differences in the number of models considered by each study.

5.4.1.3 The Southern Hemisphere: Magnitude of Past Changes in Models

Modeled ensemble-mean trends in the jet position and SAM are somewhat weaker than those observed in several atmosphere–ocean and chemistry–climate model ensembles (see **Figure 5-16**) (Swart et al., 2015; Rea et al., 2018; Iglesias-Suarez et al., 2016; Purich et al., 2016a; Son et al., 2018). Climate models, on average, have been shown to underestimate trends in the *strength* of the SH mid-latitude jet (Swart and Fyfe, 2012; Swart et al., 2015; Purich et al., 2016a). These underestimations have important implications for understanding changes to SH surface wind stress and hence attribution of the trends in ocean circulation and sea ice (**Section 5.4.4**). Similarly, the ensemble, or multi-model, mean response of the Hadley Cell to historical forcings in climate models is weaker than observed, as noted in the previous Assessment (Quan et al., 2014; Garfinkel et al., 2015a). Recent research has suggested that this difference might not reflect any model biases but rather could be due to internal variability contributing to the observed trend, while averaging over an ensemble damps any such contribution from internal variability (Garfinkel et al., 2015a; Davis and Birner, 2017; Mantsis et al., 2017). Namely, the multi-model-mean trends illustrate the forced component in these circulation changes, while the reanalysis trends indicate one particular realization impacted by natural variability. For Hadley Cell expansion, individual climate simulations that include observed time-varying SSTs, ozone, and GHG concentrations can simulate trends as large as those evident in reanalysis and observational products (Garfinkel et al., 2015a; Allen and Kovilakam, 2017; Davis and Birner, 2017) (see **Figure 5-14**). According to these results, the magnitude of the forced response is comparable to the magnitude of the internal variability (**Figure 5-14**). In fact, CMIP5 models with neither time-varying GHGs nor ozone can simulate 20-year expansion trends larger than those inferred from satellite data (Mantsis et al., 2017). Similarly, individual simulations of the past climate covering the period of ozone depletion can reproduce the magnitude of the trends in the SH mid-latitude jet evident in reanalyses, implying that any discrepancy between multi-model mean and observed trends is within the uncertainty due to internal variability (Schneider et al., 2015; Swart et al., 2015; Rea et al., 2018).

There are some known model deficiencies, outlined below, that can affect the magnitude of simulated SH tropospheric circulation trends. On the one hand, in the case of models that prescribe ozone as a boundary condition rather than internally simulate it, the magnitude of simulated tropospheric circulation response to ozone depletion can be affected by unrealistic ozone forcing. For example, ozone depletion in the CMIP5 ozone forcing is weaker than observed, and it has been suggested that this may lead to an underestimation of the response in the extratropical SH circulation (**Figure 5-16d**; Young et al., 2014). In addition, a monthly-mean and zonal-mean ozone dataset misses the maximum amplitude of the ozone hole,

which may lead to an underestimated tropospheric response (Crook et al., 2008; Waugh et al., 2009; Neely et al., 2014). On the other hand, the response of the mid-latitude jet to ozone forcing does not depend on whether the atmosphere is interactively coupled with the ocean in a model or is forced with prescribed SSTs (Sigmond et al., 2010; Seviour et al., 2017a; Son et al., 2018) (see **Figure 5-16**).

Other model deficiencies that can affect simulation of tropospheric response to ozone forcing include a lack of fully resolved stratospheric dynamics (Rea et al., 2018) and an orientation of the simulated polar vortex that is too zonal (Dennison et al., 2017), both of which may lead to underestimation of the tropospheric response. By contrast, a delay in springtime breakdown of the polar vortex present in many climate models (SPARC, 2010) may lead to an overly strong response (Sheshadri and Plumb, 2016; Lin et al., 2017) (see **Section 5.4.2**).

In addition to the stratospheric biases, most current climate models exhibit an equatorward bias in the position of the SH mid-latitude jet in summer as compared to reanalysis data (Wilcox et al., 2012; Swart and Fyfe, 2012), due in part to biases in the cloud distribution (Ceppi et al., 2012), though this bias is reduced in CCMI models (Son et al., 2018). The 2014 Assessment noted that the magnitude of the simulated tropospheric response to the ozone hole may depend on the severity of this bias, with models that exhibit a more equatorward climatological jet bias also showing a larger poleward shift of the jet in response to ozone depletion (e.g., Sigmond and Fyfe, 2014). New studies, however, do not find similar relationships in the CCMI simulations (Son et al., 2018), nor in CMIP5 models when limited to the austral summer season (Simpson and Polvani, 2016), nor in ozone-only forced simulations (Seviour et al., 2017a), suggesting that the relationship between a larger climatological jet bias and a larger response to ozone depletion is not robust.

Considering the contribution of internal variability to uncertainty in simulated tropospheric circulation response to ozone depletion, new modeling studies using a large single-model ensemble (Solomon and Polvani, 2016) and long control simulations (Thomas et al., 2015) suggest that the internal variability of the SH mid-latitude jet is smaller than its forced response to combined anthropogenic forcing during the 20th century as well as its projected response during the 21st century (Solomon and Polvani, 2016), in agreement with the previous Assessment. One study reported that during the period 1980–2004, the forced component exceeds internal variability in the case of a poleward jet shift but not for the SAM trend (Thomas et al., 2015). For the SAM, a stronger forcing over a longer period is needed for a robust positive trend to emerge over internal variability (Gillett et al., 2013; see **Figure 5-15**), consistent with the previous Assessment.

Overall, we assess with high confidence that stratospheric ozone depletion is the dominant external driver of changes in the SH summer tropospheric circulation before the year 2000; however, existing model deficiencies preclude a quantitative separation of the magnitudes of the forced (mostly due to ozone) and unforced components of the observed trends.

5.4.1.4 The Southern Hemisphere: Model Simulations of the Future

The role of ozone in future changes in the SH large-scale atmospheric circulation has received comparatively little attention since the 2014 Assessment, with studies generally finding results consistent with those reported in 2014. Ozone recovery will have impacts opposite to those associated with ozone depletion (Solomon and Polvani, 2016; Dennison et al., 2016) and hence will mitigate some of the poleward shift of the jet due to projected increases in concentrations of GHGs. The degree of mitigation is dependent on the rate of increase in GHGs (Iglesias-Suarez et al., 2016; Tao et al., 2016; Rea et al., 2018). Some of the GHG-induced poleward shift will be compensated by the effect of GHGs on ozone (i.e., super-recovery; Morgenstern et al., 2014; see also **Chapter 3**). Uncertainty in the magnitude of the mitigation for a given scenario can be reduced if careful attention is paid to jet biases and to the magnitude of lower-stratospheric temperature trends over Antarctica (Wenzel et al., 2016), as well as to biases in present-day sea ice concentration for each model (Bracegirdle et al., 2018).

5.4.1.5 The Northern Hemisphere

The last Ozone Assessment found no robust linkages between stratospheric ozone depletion and tropospheric circulation in the Northern Hemisphere, though a weak positive Northern Annular Mode

trend is evident in CMIP5 models forced with ozone concentrations. While there has been little work since 2014 focusing on changes on decadal timescales, several studies have explored whether interannual variability in late spring ozone concentrations may modulate surface climate (**Section 5.4.3**).

5.4.2 Mechanisms for Stratosphere–Troposphere Dynamical Coupling

As described in **Section 5.4.1**, stratospheric ozone loss in the Southern Hemisphere has led to a poleward shift in the tropospheric mid-latitude jet. We now discuss progress toward understanding the dynamical mechanisms for this observed downward coupling. As stated in the previous Assessment, it is well established that the impact of stratospheric ozone depletion on the troposphere occurs through a cooling of the lower polar stratosphere, which is associated with anomalously strong westerly winds and a positive anomaly in stratospheric potential vorticity. It is well accepted that the balanced response in the troposphere to this positive potential vorticity anomaly is an acceleration of the zonal flow on the poleward flank of the jet (e.g., Hartley et al., 1998; Thompson et al., 2006), consistent with the sign of the observed change. However, this balanced response is too weak to explain the magnitude of the observed circulation shift.

Studies with idealized atmospheric models in particular suggest that eddy feedbacks amplify the impact of stratospheric cooling and so play a critical role in the mechanism, as discussed in the last Assessment. The relative roles of synoptic and planetary waves, with zonal wavenumbers greater than 3 and less than 3, respectively, have been the subject of two recent idealized modeling studies (Yang et al., 2015; Smith and Scott, 2016). These point to both categories of waves being important for the amplification of the tropospheric circulation response, as are substantial nonlinear eddy–eddy interactions (consistent with Orr et al., 2012). Specifically, these studies indicate that the tropospheric response cannot be due solely to the imposed radiative cooling modifying tropospheric synoptic waves alone and that planetary scale waves are crucial in the downward influence. It is very difficult to tease out the nature of these interactions, however, as it is likely impossible to clarify how the changes in waves have modified the zonal-mean flow after the zonal-mean flow has already changed (Garfinkel et al., 2013; Garfinkel and Waugh, 2014).

While the SH tropospheric response to ozone depletion in December is simulated by the climate models, it is unclear based on the current literature whether the response can be quantitatively explained by the strengthened stratospheric westerly winds and the delay in the breakdown of the stratospheric polar vortex only. Two studies (Sun et al., 2014; Byrne et al., 2017) conclude that the delay in the breakdown can account for the tropospheric impacts, but a third study (Sheshadri et al., 2014) argues that it cannot account for the full impact (though it does contribute). Finally, the onset date for the vortex breakdown is generally too late in the current climate models (e.g., Wilcox and Charlton-Perez, 2013), in part due to too-weak gravity wave drag in the polar stratosphere near 60°S (McLandress et al., 2012; Geller et al., 2013; Garcia et al., 2017; Garfinkel and Oman, 2018), and this bias impacts the magnitude and seasonality of the tropospheric response to ozone depletion (Sheshadri and Plumb, 2016; Lin et al., 2017).

5.4.3 Surface Impacts

The last Assessment noted that extratropical rainfall in the Southern Hemisphere is tied to the position of the mid-latitude jet and, for the first time, suggested that recent changes in both extratropical and subtropical austral summer rainfall may be related to ozone depletion. However, only a few studies were available, and most either did not isolate the effect of ozone depletion from other anthropogenic forcings and/or they used simplified models or experiments. Subsequent studies have sought to understand the dynamical mechanisms for the subtropical rainfall increase in summer. One study (Hendon et al., 2014), attribute it to a poleward shift of the subtropical dry zone. Understanding the extratropical rainfall response is hampered by the quality of observational products, with little in situ data and changes in satellite products leading to substantial differences across reanalysis results. Nonetheless, a weighted average across five reanalyses suggests the changes in summer from 1979 to 2010 are dynamically consistent with increases in synoptic eddy activity (Solman and Orlanski, 2016), which is primarily associated with ozone depletion. Also, one study (Bai et al., 2016), using maximum covariance analysis and principal component analysis to attribute increases in SH extratropical rainfall, found

a predominant role of ozone depletion over GHGs. However, a firm conclusion about the role of ozone depletion cannot be reached based on these statistical studies only, because statistical relationships are not typically able to determine causality.

Since the last Assessment, a small number of studies have investigated links between regional rainfall changes and ozone depletion. In particular, there has been a focus on the significant increase of austral summer rainfall in southeastern South America (SESA) over the past 50 to 100 years. This region, which includes northern Argentina, Uruguay, southern Brazil and Paraguay, has experienced one of the largest increases in rainfall worldwide (Gonzalez et al., 2014). Most studies using ensembles of climate models or single-model ensembles attribute this increase to anthropogenic forcing (Vera and Díaz, 2015; Díaz and Vera, 2017; Zhang et al., 2016; Wu and Polvani, 2017); however, they disagree on whether the increase is driven by GHG increases (Zhang et al., 2016) or by ozone depletion (Yu and Polvani, 2017). One study (Zhang et al., 2016) notes that its model may underestimate the rainfall response to ozone depletion and aerosols, which somewhat undermines its attribution of the rainfall increase to GHGs. Internal decadal variability due to changes in SSTs was also likely an important driver of the rainfall changes (Zhang et al., 2016), which could explain why the multi-model rainfall increase due to anthropogenic forcing is weaker than that observed (Vera and Díaz, 2015; Díaz and Vera, 2017). Hence, there is a wide range of conclusions for the attribution of rainfall increases in the SESA region, with a large sensitivity to the model and time period analyzed.

Other regional rainfall changes have received relatively little attention since the last Assessment. An imprint of ozone depletion has been identified in changes of the position of the South Pacific Convergence Zone (SPCZ) over the 1961–1996 period, with increases in rainfall on the northern edge and decreases to the south (Brönnimann et al., 2017). Projections by chemistry–climate models suggest that these changes will reverse as a result of ozone recovery. One study suggested the role of ozone in recent winter rainfall declines in southwestern Australia (Delworth et al., 2014), although another study argued that ozone depletion is unlikely to be an important factor in this season (Karoly, 2014). In East Africa, the SAM has been identified as the leading cause of changes in summer rainfall, surface temperature, and the diurnal temperature range, implying the role of ozone during the period of depletion (Manatsa et al., 2013, 2015, 2016). A small anthropogenic component was also found in long-term drying trends in Chile since the late 1970s, but the contribution of ozone depletion has not been isolated (Boisier et al., 2016). Given that these are single studies on each region, it is difficult to make an overall assessment of their significance.

Research since the last Assessment to tease out the impact of ozone recovery on future rainfall trends has been limited by the lack of ozone-only simulations for the 21st century under the CMIP5 framework. One study (Lim et al., 2016) discusses future rainfall changes related to the SAM, finding a robust impact of SAM changes on SH summer rainfall, with a positive SAM opposing the thermodynamically driven projected changes in the subtropics to mid-latitudes while enhancing the increases in the high latitudes. Ozone recovery would drive a more negative SAM and the reverse of these impacts on rainfall.

In terms of surface temperature changes, the previous Assessment found that the largest surface temperature response was over the high-latitude Southern Ocean (see **Section 5.4.4**) rather than Antarctica. While a contribution of ozone depletion to Antarctic surface temperature trends has been shown in a number of previous studies (e.g., McLandress et al., 2011), recent studies have emphasized an important role for natural variability in explaining some of the observed temperature changes over the Antarctic Peninsula and West Antarctica in recent decades (Jones et al., 2016; Turner et al., 2016; Smith and Polvani, 2017). One study (Smith and Polvani, 2017) analyzes the AMIP5 and CMIP5 models, as well as the observed relationship between the SAM and surface warming over Antarctica, concluding that the pattern of warming matches neither anthropogenically forced trends nor trends congruent with the SAM and that internal variability likely played a key role. Similarly, another study (Turner et al., 2016) notes both the regional and seasonal sensitivity of the temperature changes and the dominant processes involved, concluding that while ozone depletion likely contributed to warming of the eastern Antarctic Peninsula during summer, the warming across the peninsula is not inconsistent with natural variability, particularly when placed in

the context of paleoclimate records, which show previous multidecadal periods of strong warming (Jones et al., 2016). Another study (Chiodo et al., 2017) also finds a negligible radiative impact of ozone depletion on Antarctic surface temperatures, suggesting that the high albedo of the snow-covered surface simply reflects any increases in shortwave radiation. Hence, while these studies do not rule out that the ozone depletion has likely contributed to Antarctic surface temperature trends in some regions and seasons, as was previously suggested, they do show that the large natural variability of the region and the sparsity of data and large model biases in the Antarctic and Southern Ocean regions (e.g., Eyring et al., 2013; Marshall and Bracegirdle, 2014; Purich et al., 2016a; see also **Figure 5-16**) impact our confidence in attribution and projection studies there.

Several additional impacts of stratospheric ozone depletion have now been documented. For example, one study (Dennison et al., 2015), using a single chemistry–climate model, finds that ozone depletion leads to an increased frequency of extreme anomalies and increased persistence of the SAM in the stratosphere and stronger, more persistent stratosphere–troposphere coupling. Additionally, another study (Dennison et al., 2016) finds that ozone depletion leads to an increase in blocking frequency—as defined by persistent positive anomalies in 500 hPa geopotential heights—in the South Atlantic region and little change in the South Pacific in their model, consistent with ERA-Interim reanalysis trends over the satellite era. Though this indicates a potential impact of stratospheric ozone on blocking-induced heat waves and rainfall patterns, this result would need to be substantiated with additional models, particularly given well-known model biases in underestimating blocking frequency (Ummenhofer et al., 2013).

5.4.3.1 Interannual Variability

The last Assessment noted two studies (Son et al., 2013; Bandoro et al., 2014) linking interannual variability of Antarctic ozone anomalies in spring to SH summer surface temperature and rainfall changes. Recent modeling studies, using a range of approaches, have examined the possible connection between Arctic spring ozone and surface climate and have obtained mixed results. One study (Cheung et al., 2014) probed whether the extreme Arctic ozone depletion of 2011 had an effect on tropospheric climate with the UK Met Office operational weather forecasting model. It found no improvement in spring tropospheric forecast skill when forcing the model with more realistic ozone concentrations as compared to climatological ozone. Another study (Karpechko et al., 2014) found a relationship between the 2011 low-Arctic stratospheric ozone anomalies and tropospheric climate in atmospheric general circulation model simulations, but it noted that specifying the ozone anomalies in isolation of SST anomalies did not result in a significant surface impact. A third study (Smith and Polvani, 2014) found that the prescribed ozone forcing needed for a robust tropospheric response in its simulations appeared to be larger than that historically observed.

In contrast, a coupled chemistry–climate simulation study (Calvo et al., 2015) found a robust stratospheric–tropospheric response in low versus high ozone years: a positive phase of the North Atlantic Oscillation (NAO), a poleward shift of the North Atlantic tropospheric jet, and corresponding regional surface temperature anomalies. This study used an ensemble of simulations driven by historically observed ODSs, and the link between stratospheric ozone and tropospheric circulation was found only during the recent period of high ODSs, suggesting the importance of chemistry feedback on the dynamics. The fully coupled approach of this study (Calvo et al., 2015) allows consistency between the evolving ozone distributions and dynamical conditions, which may explain the differences between its conclusions and those of studies prescribing ozone concentrations. Future work is needed to evaluate whether differences in the ozone forcings, as well as other inter-model differences, among the various studies have contributed to the range of conclusions.

Two recent observational studies have also suggested that interannual variability in ozone can modify surface climate. The first study (Ivy et al., 2017b) finds that extreme Arctic stratospheric ozone anomalies in March are associated with NH tropospheric climate in spring (March–April) in specific regions of the Northern Hemisphere; the effects are generally consistent with those found in a chemistry-climate model (Calvo et al., 2015). Finally, another study (Xie et al., 2016) suggests that Arctic stratospheric ozone anomalies influence the North Pacific Oscillation (NPO)

and that an anomalous NPO modulates subtropical SSTs. This subtropical SST anomaly might then lead to improved predictability of ENSO, though future work is needed to confirm many aspects of this chain of associations (Garfinkel, 2017). However, it is well known that a delayed or advanced final warming of the Arctic stratospheric vortex can lead to surface impacts (Black and McDaniel, 2007; Ayarzagüena et al., 2009; Hardiman et al., 2011), and distinguishing the dynamical impact of the final warming from the radiative impact of the ozone anomaly that typically accompanies a final warming also requires additional work.

Thus, our assessment is that interannual variability in springtime Antarctic and Arctic ozone may be important for surface climate, but work remains to better quantify this connection.

5.4.4 Ocean and Ice Impacts

5.4.4.1 Ocean Impacts

As discussed above, observations show trends in the SAM and low-level tropospheric winds that are largest during austral summer (**Figures 5-13** and **5-15**), and these summertime trends have been mainly attributed to stratospheric ozone depletion. A positive SAM trend implies a poleward shift and/or strengthening of the surface wind stress, which plays a fundamental role in the ocean circulation. Westerly wind stress acts to drive northward transport in the underlying ocean (via Ekman transport), creating a region of divergence and upwelling on the poleward side of the surface wind maximum and a region of convergence and downwelling equatorward of the surface wind maximum (e.g., Arblaster and Gillett et al., 2014). The previous Assessment reported that observations indicate a strengthening of the horizontal and vertical circulations in the Southern Ocean, of which a substantial part was likely caused by ozone-induced westerly wind trends. These wind trends were also linked to subsurface warming below and north of the Antarctic Circumpolar Current (ACC), but the relative importance of the wind trends and other forcings (notably warming due to increased GHGs) had not been quantified.

Since the last Assessment, more evidence has appeared indicating a substantial role for ozone depletion in recent trends of the Southern Ocean circulation. For austral summer, one study (Solomon et al., 2015) showed that modeled trends in the vertical ocean circulation are mainly attributable to ozone depletion, while a different study (Wang et al., 2014) showed that ozone recovery acts to mitigate future GHG-induced changes in the horizontal ocean circulation. Observed changes in the thermal structure of the Southern Ocean (**Figure 5-17**) are dominated by a warming that maximizes along the northern flank of the ACC, around 40–50°S, with the largest warming in the upper 1,000 m (Armour et al., 2016; Schneider and Deser, 2018). Two noticeable exceptions are the regions with subsurface cooling north of 35°S (Armour et al., 2016) and widespread SST cooling that occurred since the late 1970s in the region south of 50°S (Fan et al., 2014; Jones et al., 2016; Armour et al., 2016; Schneider and Deser, 2018). The high-latitude surface cooling is intimately linked to the observed increase in Antarctic sea ice over that period (Parkinson and DiGirolamo, 2016) and will be discussed in **Section 5.4.4.2**.

Focusing first on the region between 30–60°S, a modeling study identified increasing GHGs as the main driver of the warming in this region, with ozone depletion playing a secondary role (Solomon et al., 2015). This appears consistent with a recent study (Armour et al., 2016) that suggests that the structure of upper ocean warming, with delayed warming south of the ACC and enhanced warming to the north, is fundamentally shaped by the mean (climatological) meridional circulation in the Southern Ocean. This study finds that wind-driven upwelling of water that has not been warmed by GHGs slows the warming south of the ACC, while the GHG-induced heat is taken up and transported northward and then stored just north of the ACC. This mechanism does not rely on changes in the meridional ocean circulation, possibly explaining why ozone-induced atmospheric circulation changes play a secondary role in accounting for recent Southern Ocean warming.

In conjunction with these warming trends, the Southern Ocean has also experienced freshening (i.e., a decline in salinity), with the exception of a strong salinification trend north of 45°S in the upper 500 m (**Figure 5-17**). A recent modeling study suggests that 30% of the modeled Southern Ocean freshening can be attributed to ozone depletion (Solomon et al., 2015). Sources of the freshening are believed

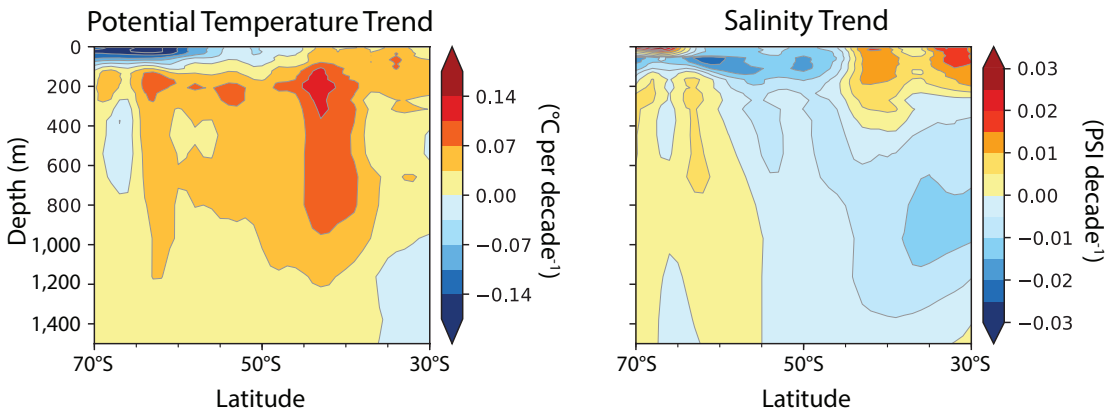

Figure 5-17. Observed 1979–2013 trend in annual-mean, zonal-mean ocean potential temperature and salinity from the Met Office Hadley Centre's EN4 dataset (Good et al., 2013).

to be located in the high latitudes and may include GHG- and ozone-induced changes in high-latitude precipitation minus evaporation (Fyfe et al., 2012), a wind-driven increase in northward freshwater transport by sea ice (Haumann et al., 2016), and basal melting of Antarctic ice shelves (Bintanja et al., 2013). Note that the melting of ice shelves was not considered by this study (Solomon et al., 2015).

Finally, we note that unforced internal variability of the Southern Ocean may have played a role in observed trends. While its magnitude is highly uncertain, some studies suggest that it is potentially large (Latif et al., 2013; Zhang et al., 2017).

5.4.4.2 Sea Ice Impacts

We now turn to the observed high-latitude (south of 50°S) surface cooling and the associated increase in Antarctic sea ice since 1979. New studies suggest that these trends reflect multi-decadal variability, with opposite trends in SSTs observed over the 1950–1978 period (Fan et al., 2014) and a recently recovered satellite-based estimate of Antarctic sea ice extent suggesting a decreasing sea ice trend from the mid-1960s to 1979 (Meier et al., 2013; Armour and Bitz, 2015; Gagné et al., 2015). The magnitude and sign of the ozone hole contribution to Southern Ocean temperature and Antarctic sea ice trends since 1979 have been topics of much discussion. In the last Assessment, it was reported that all climate model simulations that isolated the impact of stratospheric ozone depletion (including time-slice simulations in models with and without resolved ocean eddies, a fully coupled chemistry–climate model, and all six CMIP5 models with ozone-only simulations available) simulated decreased sea ice extent associated with ozone-induced changes in the Southern Ocean circulation, suggesting that ozone depletion had not contributed to the observed high-latitude ocean cooling and increase in Antarctic sea ice. The 2014 Assessment also cautioned that due to inconsistencies between the observed and modeled sea ice trends, confidence in the simulated response to the formation of the ozone hole was limited.

New modeling studies have corroborated the findings of the last Assessment that a realistic, time-evolving ozone hole leads to Antarctic sea ice decline and thus cannot explain the observed increase in sea ice since 1979 (Solomon et al., 2015) nor the regional patterns of Antarctic sea ice trends (Landrum et al., 2017). However, other recent studies have highlighted discrepancies between modeled and observed sea ice trends since 1979 (Gagné et al., 2015; Hobbs et al., 2015; Rosenblum and Eisenman, 2017), which may be related to model biases in the ocean mean state (Kostov et al., 2016, 2018; Schneider and Deser, 2018), Southern Ocean deep convection (Behrens et al., 2016), the weaker simulation of recent wind trends (Purich et al., 2016a), the underestimation of the zonal asymmetries in the atmospheric circulation (Haumann et al., 2014), the underestimation of historical surface freshening (Purich et al., 2018), and the lack of an interactive ice shelf component (Pauling et al., 2017). These studies 1) confirm that the confidence in the

simulated response to ozone depletion is still limited and 2) argue that the conclusion that the ozone hole has not contributed to recent high-latitude ocean and sea ice trends may be preliminary.

Despite these persistent model uncertainties, significant advances have been made in the understanding of processes responsible for the modeled ocean and sea ice response to ozone depletion. Idealized model simulations where the stratospheric ozone concentrations were instantaneously changed from pre-ozone hole to ozone hole conditions (Ferreira et al., 2015) demonstrated that the high-latitude ocean response entails two timescales (**Figures 5-18** and **Figure 5-19**). On the shorter timescales (months to years), the response is characterized by ocean cooling at the surface associated with increased northward Ekman transport of colder high-latitude waters. This is consistent with well-known correlations between month-to-month variations in the SAM, SST and sea ice extent. On longer timescales (years to decades), this surface cooling is then replaced by warming associated with enhanced upwelling of relatively warm waters beneath the mixed layer (see also Marshall et al., 2014). This two-timescale behavior was also seen in a different coupled climate model with significantly different characteristics of ocean convection (Seviour et al., 2016, 2017b) (**Figure 5-19c**). It should be noted that part of the initial cooling response in **Figure 5-19c** may be a reflection of the initial conditions: As a corresponding ensemble of control simulations was not available, the unforced time evolution of the SSTs was estimated indirectly. Furthermore, in spite of a relatively long cooling phase, the sea ice did not expand in those simulations. Nonetheless, based on the initial cooling of SSTs in response to instantaneous ozone forcing, some have argued that ozone

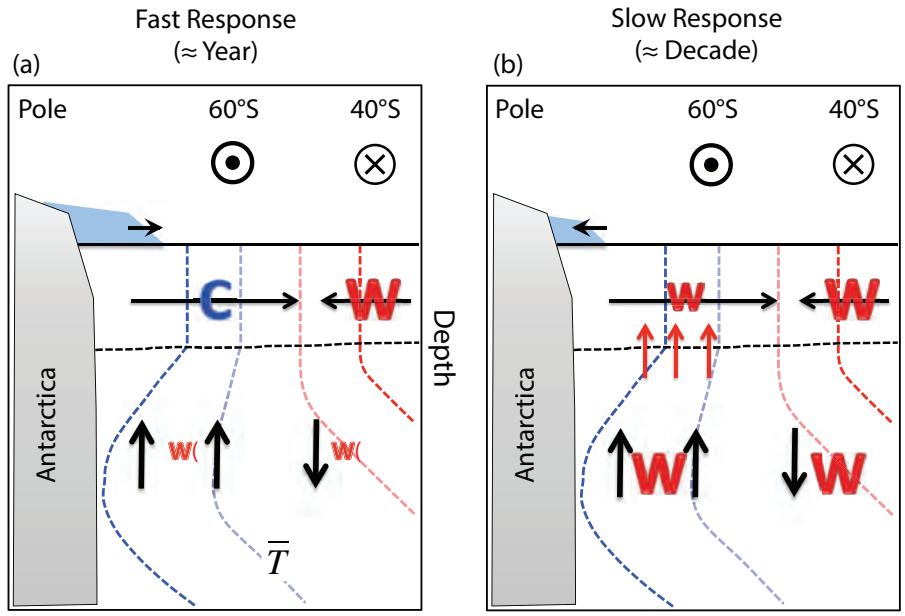

Figure 5-18. Schematic of the two-timescale response of the ocean and sea ice to a stepwise ozone hole as simulated by climate models. The dot at 60°S and × at 40°S indicate the dipole in surface wind stress associated with the strengthened SAM in response to ozone depletion. (a) The fast response is dominated by surface cooling associated with increased northward Ekman transport, whereas (b) in the slow response this cooling is replaced by warming, which is the result of enhanced upwelling of relatively warm waters from beneath the mixed layer. Blue patches represent the sea ice cover (expanding in the fast response and contracting in the slow response). Adapted from Ferreira et al. (2015).

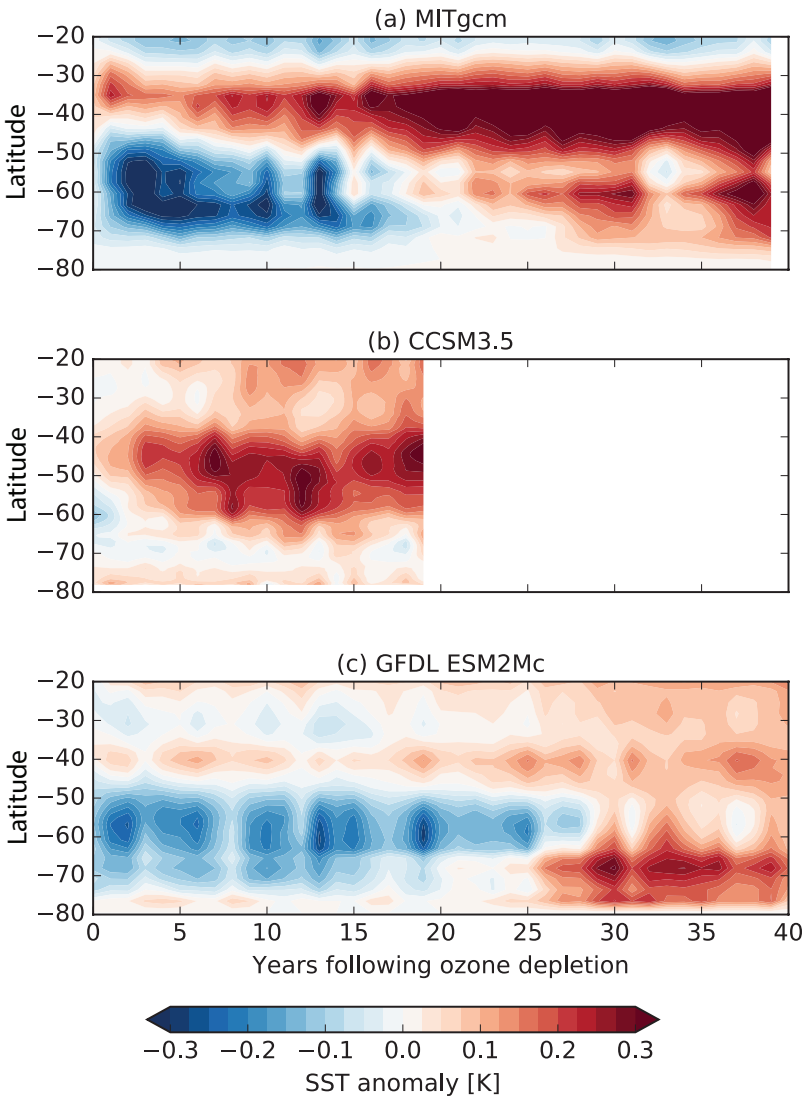

Figure 5-19. Zonal-mean and annual-mean SST response to a stepwise ozone depletion in three coupled models: (a) MITgcm, with an idealized Double-Drake configuration, and two comprehensive models, (b) CCSM3.5 and (c) GFDL ESM2Mc. All three models show a two-timescale response, consisting of a cooling followed by a warming in the Southern Ocean region (50–70°S). However, their magnitude and timescales vary greatly. The net cooling lasts approximately 20 years in the MITgcm, 3 years in CCSM3.5, and 30 years in GFDL ESM2Mc. Adapted from Ferreira et al. (2015) and Seviour et al. (2016).

depletion could drive a transient expansion of sea ice (Marshall et al., 2014; Ferreira et al., 2015). The impact of a realistically prescribed (i.e., time-varying) ozone hole on Antarctic sea ice trends critically depends on the timescale of transition from the initial cooling to subsequent warming. Unfortunately, this timescale is not well constrained, varying greatly between the three models with the prescribed stepwise ozone perturbation (**Figure 5-19**). Other attempts to quantify the impact of the ozone hole on Antarctic sea ice are more indirect and rely on statistical techniques (such as convolution theorem) to extract the SST or sea ice response to a hypothetical step increase in the SAM index. Consistent with the idealized ozone experiments, these studies find a large intermodel spread between CMIP5 models in the SST response: In response to a SAM increase, some models simulate a short transition time from initial cooling to

subsequent warming, while other models continue to cool for at least 20 years (Kostov et al., 2016, 2018). This intermodel spread has been related to biases in the models' mean ocean stratification and to dynamical processes, including oceanic (parameterized) eddy fluxes, mixed layer dynamics, and air–sea interactions (Ferreira et al., 2015; Kostov et al., 2016). This technique has also been applied to Antarctic sea ice, revealing a large range in modeled transition timescale from initial sea ice expansion to subsequent sea ice contraction in response to a step function in the SAM (Holland et al., 2016). Applying the modeled sea ice response function to SAM variability but driven by the observed SAM time series, one study (Holland et al., 2016) suggests that for the multi-model mean, the observed variations in the SAM have driven a modest sea ice decline. While these studies based on the convolution theorem are generally consistent with the idealized ozone forcing perturbations, it remains to be demonstrated that the convolution theorem can accurately predict the sea ice response to the SAM in each model.

The new studies that have quantified the response to an instantaneous ozone perturbation or SAM increase have provided important, novel insights into the physical processes involved in the sea ice response to ozone depletion. It should be emphasized, however, that these idealized experiments are tools to probe the physics of the climate system and that they were not meant to represent the real ozone hole, as its formation and the corresponding SAM increase have occurred over several decades. Nonetheless, these studies suggest that when forced with the real, time-varying ozone hole, models with a long cooling timescale would simulate increased sea ice. However, this does not seem to be consistent with the fact that all studies that have analyzed climate model experiments forced with realistic, time-varying ozone depletion consistently find decreasing sea ice.

It also needs to be emphasized that the modest increase in Antarctic sea ice extent is the result of near-canceling regional trends, with the strongest sea ice increase in the Ross Sea and strongest decrease in the Bellingshausen and Amundsen Seas (Turner et al., 2015; Hobbs et al., 2016). This pattern in the sea ice trends is qualitatively consistent with a deepening of the Amundsen Sea Low (ASL). There is some evidence that the ozone hole has contributed to these atmospheric circulation trends (England et al., 2016) in the summer months, but it has also been noted that the observed ASL trends are within the bounds of modeled internal variability (Turner et al., 2015). An increasing body of evidence suggests that the ozone hole is not the main driver of ASL trends and points to decadal variations in the tropical Pacific (Meehl et al., 2016; Purich et al., 2016b; Schneider and Deser, 2018), or possibly the Atlantic (Li et al., 2014), as the likely drivers.

We further note that during the austral spring (September, October, November; SON) of 2016, unprecedented retreat of Antarctic sea ice was observed that was 46% faster than the mean rate of loss in spring over the satellite era (Turner et al., 2017). This led to record-low sea ice extent anomalies, well exceeding 3 standard deviations of the observed 1979–2016 ice extent (Stuecker et al., 2017). This observation contrasts sharply with the long-term increasing sea ice trend discussed above. Studies have linked the unprecedented retreat to record negative values of the SAM (Turner et al., 2017; Doddridge and Marshall, 2017; Stuecker et al., 2017) and extratropical SST anomalies forced by the extreme 2015–2016 El Niño (Stuecker et al., 2017). These studies suggest that the unprecedented retreat was the result of tropically forced and internal SH atmospheric variability (and hence that it was unrelated to the slow, long-term warming simulated by the models), but more studies are needed to come to robust conclusions.

In conclusion, since the last Assessment, significant progress has been made regarding the understanding of processes involved in the response of Antarctic sea ice to ozone depletion, which is now believed to entail a fast surface cooling followed by a slow, long-term surface warming. However, the role that the ozone hole has played in observed Antarctic sea ice changes remains unclear. While the conclusion of the last Assessment that the ozone hole cannot explain recent trends in Antarctic sea ice is supported by new modeling studies, confidence in this result remains low. This is because climate models generally do not reproduce observed Antarctic sea ice trends since 1979 and because new studies have identified several systematic biases. Future progress could be made by model improvements and repetition of realistic ozone-only simulations performed with more coupled climate models.

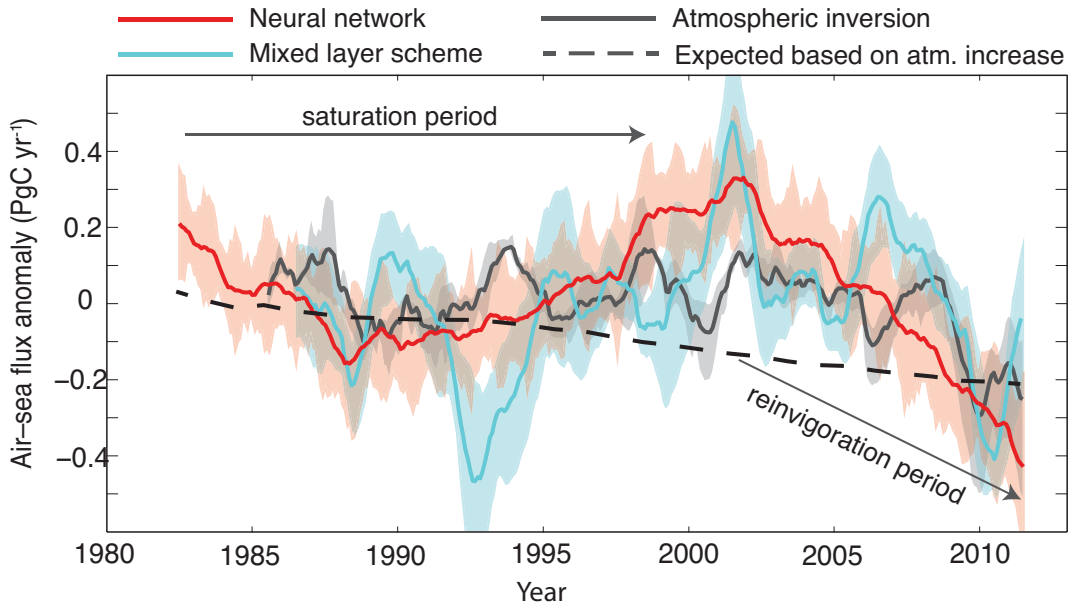

Figure 5-20. Evolution of the Southern Ocean carbon sink based on (red and blue lines and shading) two methods to interpolate surface ocean observations and (black solid line and gray shading) an atmospheric inversion method. The expected uptake based on the growth of atmospheric CO_2 alone is shown by the dashed black line. Negative values indicate anomalous uptake by the ocean. Adapted from Landschützer et al. (2015).

5.4.4.3 Ocean Carbon

The Southern Ocean plays a crucial role in the global carbon cycle, as it accounts for about 40% of the global oceanic uptake of anthropogenic CO_2 (Khatiwala et al., 2009; Frölicher et al., 2015). The strength of the carbon sink is mainly dependent on the air–sea gradients of CO_2. In the absence of other changes, the increase in anthropogenic CO_2 in the atmosphere would lead to increased air–sea gradients and hence to an increased carbon sink (dashed black line in **Figure 5-20**). It was previously suggested that the carbon sink had slowed down (Le Quéré et al., 2007) and that this slowdown was partly related to ozone-induced changes in the surface winds, which bring up carbon-rich water and hence reduce the air–sea gradient of CO_2. These results relied on atmospheric inversion methods (which estimate carbon fluxes from atmospheric CO_2 measurements) and forward ocean models. The realism of this slowdown has been debated in the literature, as inversion models have been shown to depend on data selection (Law et al., 2008) and the coarse resolution ocean models employed in most studies do not represent critical processes such as mesoscale eddies (Swart et al., 2014). Furthermore, the last Assessment reported that for the 1990–2009 period, estimates of the trends in the carbon sink depended on the analysis, with atmospheric inversions generally showing a slowdown in the uptake and ocean biogeochemical models indicating no slowdown (Lenton et al., 2013).

Since the last Assessment, further evidence has appeared suggesting that the apparent slowdown of the carbon sink is not robust (Landschützer et al., 2015, Munro et al., 2015) (**Figure 5-20**). These studies employed observations of the surface ocean CO_2 measurements and hence did not rely on imperfect ocean biogeochemical models. While they confirmed earlier studies that the carbon sink slowed down between the 1980s and early 2000s, they also found a remarkable reversal with a reinvigoration of the sink between 2002 and 2012 (**Figure 5-20**). Averaged over the Southern Ocean, these decadal variations were found to be reasonably robust to the method used to interpolate

the sparse measurements in space and time, though significant uncertainties remain on smaller spatial scales (Ritter et al., 2017). As shown in **Figure 5-20**, the strength of the carbon sink is now thought to be comparable to that expected based on atmospheric CO_2 increases alone. These results suggest that atmospheric circulation changes (whether driven by ozone or not) have not had a considerable impact on the net strength of the Southern Ocean carbon sink.

5.4.5 Changes in Radiative Forcing and Feedbacks

Since the last Assessment, there have been no major published updates to the estimated preindustrial to present-day ozone radiative forcing (RF) due to the effects of long-lived ODSs on stratospheric and tropospheric ozone abundances. However, one study (Hossaini et al., 2015) highlighted 1) that halogenated very short-lived substances (VSLSs) of both anthropogenic and natural origin tend to destroy ozone in the lower stratosphere more efficiently than long-lived ODSs and 2) that since the ozone radiative effect per molecule is stronger in the lower stratosphere than in the upper stratosphere, this may be important for the global radiative balance. This study estimated a global radiative effect from the stratospheric ozone changes in response to observed VSLSs (bromine [Br], chlorine [Cl], and iodine species) of −0.08 W m^{-2}. Although the study found no trend in the influence of VSLSs on global ozone between 1979 and 2013, the influence of brominated VSLSs on global ozone in the preindustrial (i.e., with low anthropogenic Cl) was ~30% smaller than present day owing to the coupling between Br and Cl chemical cycles. The study therefore estimated an indirect ozone RF from VSLSs of −0.014 W m^{-2}, which is about one-tenth of the study's estimated total ozone RF due to long-lived ODSs.

New studies since the last Assessment have quantified the stratospheric and tropospheric ozone RF due to the projected major drivers of atmospheric ozone concentrations over the 21st century: declining halogenated ODS concentrations, climate change due to anthropogenic forcing, changes to tropospheric ozone precursor species including methane, and changes to chemically active greenhouse gases (nitrous oxide [N_2O]). One study (Banerjee et al., 2018) used a chemistry–climate model to estimate the 21st-century ozone RF due to the projected decline in long-lived halogenated ODSs. It found a total (stratosphere and troposphere) ozone RF between 2000 and 2100 of 0.07 W m^{-2}. This is in quantitative agreement with another study (Iglesias-Suarez et al., 2018) that used a different chemistry–climate model and estimated the ozone RF due to future ODSs to be 0.129 ± 0.081 W m^{-2}. Thus, the future decline in ODSs over the 21st century will induce a small indirect positive RF from ozone. However, this positive RF is substantially smaller than the negative direct RF due to declining atmospheric ODSs as a result of the Montreal Protocol and its Amendments (see **Chapter 6**).

A number of modeling studies published since the last Assessment have examined the impact of changes in ozone in response to an abrupt increase in CO_2 on estimates of the equilibrium climate sensitivity (ECS)—the equilibrium change in global mean near-surface temperature in response to a doubling in CO_2. As discussed in **Chapters 3** and **4**, CO_2 affects stratospheric ozone abundances through effects on transport and chemistry (via changes to stratospheric temperatures). New estimates of the effect of ozone changes on ECS in different chemistry–climate models range from no change (Marsh et al., 2016) to a reduction in ECS of about 20% (Nowack et al., 2014), with some studies finding a decrease in ECS of a smaller magnitude (Dietmüller et al., 2014; Muthers et al., 2014). The differences in the relative importance of ozone changes for inferred ECS are likely to be related to the distribution and magnitude of ozone and stratospheric water vapor changes simulated in the individual models. We therefore conclude that ozone changes and their associated effect on climate feedbacks in response to increased CO_2 are more likely to reduce than to increase ECS; however, there is currently large quantitative uncertainty in the magnitude of this feedback.

5.5 CLIMATE IMPACTS OF THE MONTREAL PROTOCOL

5.5.1 World Avoided by the Montreal Protocol

World-avoided simulations evaluate the environmental and climate impacts that have been avoided as a result of the successful regulation of ODS emissions under the Montreal Protocol. This is generally done by a comparison of climate model simulations with

and without ODS emissions regulations. In the scenarios with unregulated ODSs, the ODSs are generally assumed to increase at a constant rate of 3–3.5% per year (e.g., Prather et al., 1996; Velders et al., 2007; Newman et al., 2009; Garcia et al., 2012). As reported in the 2014 Assessment, chemistry–climate models suggest that continued accumulation of ODSs in the atmosphere in the absence of the Montreal Protocol would have led to a collapse of the global ozone layer by the mid-21st century, with devastating environmental implications (Newman et al., 2009; Garcia et al., 2012). The last Assessment also reported on the additional (mostly unanticipated) benefits of ODS regulations for mitigation of global climate change. Specifically, it was reported that by later this century, unregulated ODS increases could have led to global surface temperature increases comparable to temperature increases caused by other greenhouse gases (Velders et al., 2007) and could have almost doubled changes in the hydrological cycle (precipitation minus evaporation) over the next few decades.

While new literature on this topic since the last Assessment is limited, such studies have highlighted other aspects of the climate benefits of the Montreal Protocol. One modeling study found that in the world-avoided scenario, the projected increase in the potential intensity of tropical cyclones is nearly three times larger in 2065 than in a scenario accounting for warming due to other greenhouse gases only (Polvani et al., 2016). Two other studies have attempted to quantify the implications of the avoided temperature and precipitation changes from restricting ODS emissions for global sea level rise (SLR). One study found that under an idealized scenario in which the emissions of gases regulated under the Montreal Protocol had instead been eliminated in 2050, additional thermal SLR of between 4–14 cm would be expected in the 21st century (Zickfeld et al., 2017), with the large range coming from the uncertainty in ocean heat uptake efficiencies in climate models. The other study found that by 2065, thermal SLR avoided by the Montreal Protocol is about 5 cm, but note that part of that SLR is balanced by changes in the hydrological cycle over Antarctica (Previdi and Polvani, 2017).

5.5.2 Projected Climate Impacts of the Kigali Amendment

Other new studies have simulated future climate impacts that will be avoided if nations adhere to the phasedown of hydrofluorocarbons (HFCs) under the Kigali Amendment. In the simulations without HFC regulations, a wide range of HFC scenarios is typically considered (**Chapter 2, Section 2.3.1**). As discussed in **Chapter 2**, these new studies indicate that the anticipated phasedown of HFCs is expected to avoid up to 0.4 K of global mean surface warming by 2100. The atmospheric impacts of HFC regulations have been further quantified using a 2-D (latitude–pressure) interactive chemistry, radiation, and dynamics model (Hurwitz et al., 2015, 2016). These studies found that unregulated increases in HFCs would result in a warming of the troposphere and stratosphere. In a business-as-usual HFC emissions scenario, the tropical lower stratosphere in 2050 was up to 0.41 K warmer than in a scenario with zero HFC emissions (Hurwitz et al., 2015). In that same business-as-usual scenario, the 10–16 km global mean temperature was projected to increase by 0.11–0.13 K between 2015 and 2050, while HFC mitigation scenarios similar to those proposed under the Kigali Amendment were found to avoid most of that warming (Hurwitz et al., 2016). In a business-as-usual scenario, HFCs were also found to impact the atmospheric circulation, slightly enhancing the Brewer–Dobson circulation above 18 km (resulting in a small decrease of the stratospheric mean age of air by −0.3%) and weakening the Hadley Cell circulation below 18 km (Hurwitz et al., 2015). More studies are needed to confirm this result with more comprehensive models.

REFERENCES

Abalos M., B. Legras, F. Ploeger, and W.J. Randel, Evaluating the advective Brewer-Dobson circulation in three reanalyses for the period 1979-2012, *J. Geophys. Res. Atmos., 120,* 7534–7554, doi:10.1002/2015JD023182, 2015.

Abalos M., B. Legras, and E. Shuckburgh, Interannual variability in effective diffusivity in the upper troposphere / lower stratosphere from reanalysis data, *Q. J. R. Meteorol. Soc.*, *142,* 1847–1861, doi:10.1002/qj.2779, 2016.

Abalos M., W.J. Randel, D.E. Kinnison, and R. Garcia, Using the artificial tracer e90 to examine present and future UTLS transport in WACCM, *J. Atmos. Sci.*, *74*, doi:10.1175/JAS-D-17-0135.1, 2017.

Abram, N.J., R. Mulvaney, F. Vimeux, S.J. Phipps, J. Turner, and M.H. England, Evolution of the Southern Annular Mode during the past millennium, *Nat. Clim. Change*, *4*, 564–569, doi:10.1038/nclimate2235, 2014.

Albers, J.R., J. Perlwitz, A.H. Butler, T. Birner, G.N. Kiladis, Z.D. Lawarence, G.L. Manney, A.O. Langford, and J. Dias, Mechanisms governing interannual variability of stratosphere to troposphere ozone transport, *J. Geophys. Res. Atmos.*, *123*, 234–260, doi:10.1002/2017JD026890, 2018.

Allen, R.J., and M. Kovilakam, The role of natural climate variability in recent tropical expansion, *J. Clim.*, 30, 6329–6550, doi:10.1175/JCLI-D-16-0735.1, 2017.

Allen, R.J., J.R. Norris, and M. Kovilakam, Influence of anthropogenic aerosols and the Pacific Decadal Oscillation on tropical belt width, *Nat. Geosci., 7*, 270–274, doi:10.1038/ngeo2091, 2014.

Amaya, D.J., N. Siler, S.P. Xie, and A.J. Miller, The interplay of internal and forced modes of Hadley Cell expansion: Lessons from the global warming hiatus, *Clim. Dyn.*, 51, 305–319, doi:10.1007/s00382-017-3921-5, 2018.

Anderson, J.G., D.M. Wilmouth, J.B. Smith, and D.S. Sayres, UV dosage levels in summer: Increased risk of ozone loss from convectively injected water vapor, *Science*, *337*, 835–839, doi:10.1126/science.1222978, 2012.

Anderson, J.G., D.K. Weisenstein, K.P. Bowman, C.R. Homeyer, J.B. Smith, D.M. Wilmouth, D.S. Sayres, J.E. Klobas, S.S. Leroy, J.A. Dykema, and S.C. Wofsy, Stratospheric ozone over the United States in summer linked to observations of convection and temperature via chlorine and bromine catalysis, *Proc. Natl. Acad. Sci.*, *114* (25), E4905–E4913, doi:10.1073/pnas.1619318114, 2017.

Anderson, J.G. and C.E. Clapp, Coupling free radical catalysis, climate change, and human health, *Phys. Chem. Chem. Phys., 20,* 10569–10587, doi:10.1039/C7CP08331A, 2018.

Aquila, V., W.H. Swartz, D.W. Waugh, P.R. Colarco, S. Pawson, L.M. Polvani, and R.S. Stolarski, Isolating the roles of different forcing agents in global stratospheric temperature changes using model integrations with incrementally added single forcings, *J. Geophys. Res.*, *20* (16), doi:10.1002/2015JD023841, 2016.

Arblaster, J.M., N.P Gillett (Lead Authors), N. Calvo, P.M. Forster, L.M. Polvani, S.-W. Son, D.W. Waugh, and P.J. Young, Stratospheric ozone changes and climate, Chapter 4 in *Scientific Assessment of Ozone Depletion: 2014*, Global Ozone Research and Monitoring Project–Report No. 55, World Meteorological Organization, Geneva, Switzerland, 2014.

Armour, K.C., and C.M. Bitz, Observed and projected trends in Antarctic sea ice, *U.S. Clivar Var.*, *13*, 12–19, doi:10.1175/BAMS-D-11-00244.1, 2015.

Armour, K.C., J. Marshall, J.R. Scott, A. Donohoe, and E.R. Newsom, Southern Ocean warming delayed by circumpolar upwelling and equatorward transport, *Nat. Geosci., 9*, 549–554, doi:10.1038/ngeo2731, 2016.

Aschmann, J., J.P. Burrows, C. Gebhardt, A. Rozanov, R. Hommel, M. Weber, and A.M. Thompson, On the hiatus in the acceleration of tropical upwelling since the beginning of the 21st century, *Atmos. Chem. Phys.*, *14*, 12803–12814, doi:10.5194/acp-14-12803-2014, 2014.

Atlas, R., R.N. Hoffman, J. Ardizzone, S.M. Leidner, J.C. Jusem, D.K. Smith, and D. Gombos, A cross-calibrated, multiplatform ocean surface wind velocity product for meteorological and oceanographic applications, *Bull. Am. Meteorol. Soc.*, *92* (2), 157–174, doi:10.1175/2010BAMS2949.1,2011.

Avery, M.A., S.M. Davis, K.H. Rosenlof, H. Ye, and A.E. Desser, Large anomalies in lower stratospheric water vapour and ice during the 2015–2016 El Niño, *Nat. Geosci., 10*, 405–409, doi:10.1038/ngeo2961, 2017.

Ayarzagüena, B., and E. Serrano, Monthly characterization of the tropospheric circulation over the Euro-Atlantic area in relation with the timing of stratospheric final warmings, *J. Clim., 22* (23), 6313–6324, doi:10.1175/2009JCL13565.1, 2011.

Bai, K., N.-B. Chang, and W. Gao, Quantification of relative contribution of Antarctic ozone depletion to increased austral extratropical precipitation during 1979–2013, *J. Geophys. Res.*, *121* (4), 1459–1474, doi:10.1002/2015JD024247, 2016.

Baldwin M., and M. Dameris (Lead Authors), J. Austin, S. Bekki, B. Bregman, N. Butchart, E. Cordero, N. Gillett, H.-F. Graf, C. Granier, D. Kinnison, S. Lal, T. Peter, W. Randel, J. Scinocca, D. Shindell, H. Struthers, M. Takahashi, D. Thompson, Climate-Ozone Connections, Chapter 5 in *Scientific Assessment of Ozone Depletion: 2006*, Global Ozone Research and Monitoring Project–Report No. 50, World Meteorological Organization, Geneva, Switzerland, 2007.

Bandoro, J., S. Solomon, A. Donohoe, D.W. Thompson, and B.D. Santer, Influences of the Antarctic ozone hole on Southern Hemispheric summer climate change, *J. Clim.*, *27* (16), 6245–6264, doi:10.1175/JCLI-D-13-00698.1, 2014.

Banerjee, A., A.C. Maycock, A.T. Archibald, N.L. Abraham, P. Telford, P. Braesicke, and J.A. Pyle, Drivers of changes in stratospheric and tropospheric ozone between year 2000 and 2100, *Atmos. Chem. Phys.*, *16*, 2727–2746, doi:10.5194/acp-16-2727-2016, 2016.

Banerjee, A., A.C. Maycock, and J.A. Pyle, Chemical and climatic drivers of radiative forcing due to changes in stratospheric and tropospheric ozone over the 21st century, *Atmos. Chem. Phys.*, *18*, 2899–2911, doi:10.5194/acp-2017-741, 2018.

Barton, C.A., and J.P. McCormack, Origin of the 2016 QBO disruption and its relationship to extreme El Niño events, *Geophys. Res. Lett.*, *44*, 11,150–11,157, doi:10.1002/2017GL075576, 2017.

Bednarz, E.M., A.C. Maycock, N.L. Abraham, P. Braesicke, O. Dessens, and J.A. Pyle, Future Arctic ozone recovery: The importance of chemistry and dynamics, *Atmos. Chem. Phys.*, *16*, 12159–12176, doi:10.5194/acp-16-12159-2016, 2016.

Behrens, E., G. Rickard, O. Morgenstern, T. Martin, A. Osprey, and M. Joshi, Southern Ocean deep convection in global climate models: A driver for variability of subpolar gyres and Drake Passage transport on decadal timescales, *J. Geophys. Res. Oceans*, 121, 3905–3925, doi:10.1002/2015JC011286, 2016.

Betts, R.A., C.D. Jones, J.R. Knight, R.F. Keeling, and J.J. Kennedy, El Niño and a record CO_2 rise, *Nat. Clim. Change*, *6*, 806–810, doi:10.1038/nclimate3063, 2016.

Bintanja, R., G.J. van Oldenborgh, S.S. Drijfhout, B. Wouters, and C.A. Katsman, Important role for ocean warming and increased ice-shelf melt in Antarctic sea ice expansion, *Nat. Geosci.*, *6*, 376–379, doi:10.1038/ngeo1767, 2013.

Birner, T., and H. Bönisch, Residual circulation trajectories and transit times into the extratropical lowermost stratosphere, *Atmos. Chem. Phys.*, *11*, 817–827, doi:10.5194/acp-11-817-2011, 2011.

Black, R.X., and B.A. McDaniel, The dynamics of Northern Hemisphere stratospheric finalwarming events, *J. Atmos. Sci.*, *64*, 2932-2946, doi:10.1175/JAS3981.1, 2007.

Blunden, J., and D.S. Arndt, editors, State of the Climate in 2016, *Bull. Am. Meteorol. Soc.*, *98* (8), Si–S277, doi:10.1175/2017BAMSStateoftheClimate.1, 2017.

Bohlinger, P., B.-M. Sinnhuber, R. Ruhnke, and O. Kirner, Radiative and dynamical contributions to past and future Arctic stratospheric temperature trends, *Atmos. Chem. Phys.*, *14*, 1679–1688, doi:10.5194/acp-14-1679-2014, 2014.

Boisier, J.P., R. Rondanelli, R.D. Garreaud, and F. Muñoz, Anthropogenic and natural contributions to the Southeast Pacific precipitation decline and recent megadrought in central Chile, *Geophys. Res. Lett., 43*, 413–421, doi:10.1002/2015GL067265, 2016.

Boothe, A.C., and C.R. Homeyer, Global large-scale stratosphere–troposphere exchange in modern reanalyses, *Atmos. Chem. Phys.*, *17*, 5537–5559, doi:10.5194/acp-17-5537-2017, 2017.

Bracegirdle, T.J., P. Hyder, and C.R. Holmes, CMIP5 diversity in southern westerly jet projections related to historical sea ice area: Strong link to strengthening and weak link to shift, *J. Clim.*, *31*, 195–211, doi:10.1175/JCLI-D-17-0320.1, 2018.

Brewer, A.W., Condensation Trails, *Weather*, *1*, 34–40, doi:10.1002/j.1477-8696.1946.tb00024.x, 1946.

Brinkop, S., M. Dameris, P. Jöckel, H. Garny, S. Lossow, and G. Stiller, The millennium water vapour drop in chemistry–climate model simulations, *Atmos. Chem. Phys.*, *16*, 8125–8140, doi:10.5194/

acp-16-8125-2016, 2016.

Brönnimann, S., M. Jacques-Coper, E. Rozanov, A.M. Fischer, O. Morgenstern, G. Zeng, H. Akiyoshi, and Y. Yamashita, Tropical circulation and precipitation response to ozone depletion and recovery, *Environ. Res. Lett.*, *12* (6), doi:10.1088/1748-9326/aa7416, 2017.

Butchart, N., The Brewer-Dobson circulation, *Rev. Geophys., 52*, 157–184, doi:10.1002/2013RG000448, 2014.

Byrne, N.J., T.G. Shepherd, T. Woollings, and R.A. Plumb, Nonstationarity in Southern Hemisphere Climate Variability Associated with the Seasonal Breakdown of the Stratospheric Polar Vortex. *J. Clim.,* 30, 7125–7139, doi:10.1175/JCLI-D-17-0097.1, 2017.

Calvo, N., L.M. Polvani, and S. Solomon, On the surface impact of Arctic stratospheric ozone extremes. *Environ. Res. Lett.*, *10*, 094003, doi:10.1088/1748-9326/10/9/094003, 2015.

Ceppi, P., Y.-T. Hwang, D.M.W. Frierson, and D.L. Hartmann, Southern Hemisphere jet latitude biases in CMIP5 models linked to shortwave cloud forcing, *Geophys. Res. Lett., 39*, L19708, doi:10.1029/2012GL053115, 2012.

Ceppi, P., and D.L. Hartmann, On the speed of the eddy-driven jet and the width of the Hadley cell in the Southern Hemisphere, *J. Clim.*, *26* (10), 3450–3465, doi:10.1175/JCLI-D-12-00414.1, 2013.

Cheung, J.C.H., J.D. Haigh, and D.R. Jackson, Impact of EOS MLS ozone data on medium-extended range ensemble weather forecasts, *J. Geophys. Res. Atmos.*, *119*, 9253–9266, doi:10.1002/2014JD021823, 2014.

Chiodo, G., L.M. Polvani, and M. Previdi, Large increase in incident shortwave radiation due to the ozone hole offset by high climatological albedo over Antarctica, *J. Clim.*, *30*, 4883–4890, doi:10.1175/JCLI-D-16-0842.1, 2017.

Choi, J., S.-W. Son, J. Lu, and S.-K. Min, Further observational evidence of Hadley cell widening in the Southern Hemisphere, *Geophys. Res. Lett.*, *41*, 2590–2597, doi:10.1002/2014GL059426, 2014.

Christy, J.R., R.W. Spencer, W.B. Norris, and W.D. Braswell, Error estimates of version 5.0 of MSU-AMSU bulk atmospheric temperature, *J. Atmospheric Ocean. Technol.*, *20* (5), 613–629, doi:10.1175/1520-0426, 2003.

Clem, K.R., J.A. Renwick, and J. McGregor, Relationship between eastern tropical Pacific cooling and recent trends in the Southern Hemisphere zonal-mean circulation, *Clim. Dyn.*, *49*, 113–129, doi:10.1007/s00382-016-3329-7, 2016.

Cohen, N.Y., E.P. Gerber, and O. Bühler, What Drives the Brewer–Dobson Circulation?, *J. Atmos. Sci.*, *71*, 3837–3855, doi:10.1175/JAS-D-14-0021.1, 2014.

Collins, W.J., R.G. Derwent, B. Garnier, C.E. Johnson, M.G. Sanderson, and D.S. Stevenson, Effect of stratosphere-troposphere exchange on the future tropospheric ozone trend, *J. Geophys. Res.*, *108*, 8528–8537, doi:10.1029/2002JD002617, 2003.

Coy, L., P.A. Newman, S. Pawson, and L.R. Lait, Dynamics of the disrupted 2015/16 quasi-biennial oscillation, *J. Clim.*, *30*, 5661–5674, doi:10.1175/JCLI-D-16-0663.1, 2017.

Crook, J.A., N.P. Gillett, and S.P. Keeley, Sensitivity of Southern Hemisphere climate to zonal asymmetry in ozone, *Geophys. Res. Lett.*, *35* (7), doi:10.1029/2007GL032698, 2008.

Dätwyler, C., R. Neukom, N.J. Abram, A.E. Gallant, M. Grosjean, M. Jacques-Coper, D.J. Karoly, and R. Villalba, Teleconnection stationarity, variability and trends of the Southern Annular Mode (SAM) during the last millennium, *Clim. Dyn.*, *51* (5/6), 2321–2339, doi:10.1007/s00382-017-4015-0, 2017.

Davis, N., and T. Birner, On the discrepancies in tropical belt expansion between reanalyses and climate models and among tropical belt width metrics, *J. Clim.*, *30*, 1211–1231, doi:10.1175/JCLI-D-16-0371.1, 2017.

Delworth, T.L., and F. Zeng, Regional rainfall decline in Australia attributed to anthropogenic greenhouse gases and ozone levels, *Nat. Geosci.*, *7*, 583–587, doi:10.1038/ngeo2201, 2014.

Dennison, F.W., A.J. McDonald, and O. Morgenstern, The effect of ozone depletion on the Southern Annular Mode and stratosphere-troposphere couplin, *J. Geophys. Res. Atmos.*, 120 (13), 6305–6312, doi:10.1002/2014JD023009, 2015.

Dennison, F.W., A.J. McDonald, and O. Morgenstern, The influence of ozone forcing on blocking in the Southern Hemisphere, *J. Geophys. Res. Atmos.*, *121* (24), 14,358–14,371, doi:10.1002/2016JD025033, 2016.

Dennison, F., A. McDonald, and O. Morgenstern, The evolution of zonally asymmetric austral ozone in a chemistry–climate model, *Atmos. Chem.*

Phys., *17* (22), 14075–14084, doi:10.5194/acp-17-14075-2017, 2017.

Dessler, A.E., H. Ye, T. Wang, M.R. Schoeberl, L.D. Oman, A.R. Douglass, A.H. Butler, K.H. Rosenlof, S.M Davis, and R.W. Portmann, Transport of ice into the stratosphere and the humidification of the stratosphere over the 21st century, *Geophys. Res. Lett.*, *45*, 2323–2329, doi:10.1002/2016GL06799, 2016.

Diallo, M., B. Legras, and A. Chédin, Age of stratospheric air in the ERA-Interim, *Atmos. Chem. Phys., 12*, 12133–12154, doi:10.5194/acp-12-12133-2012, 2012.

Díaz, L.B., and C.S. Vera, Austral summer precipitation interannual variability and trends over Southeastern South America in CMIP5 models, *Int. J. Climatol.*, *35* (10), 3172–3177, doi:10.1002/joc.4153, 2017.

Dietmüller, S., M. Ponater, and R. Sausen, Interactive ozone induces a negative feedback in CO_2-driven climate change simulations, *J. Geophys. Res. Atmos.*, *119*, 1796–1805, doi:10.1002/2013JD020575, 2014.

Dietmüller, S., H. Garny, F. Plöger, P. Jöckel, and D. Cai, Effects of mixing on resolved and unresolved scales on stratospheric age of air, *Atmos. Chem. Phys.*, *17*, 7703–7719, doi:10.5194/acp-17-7703-2017, 2017.

Ding, Q., and Q. Fu, A warming tropical central Pacific dries the lower stratosphere, *Clim. Dyn.*, 1–15, doi:10.1007/s00382-017-3774-y, 2017.

Dlugokencky, E.J., L.P. Steele, P.M. Lang, and K.A. Masarie, The growth rate and distribution of atmospheric methane, *J. Geophys. Res., 99*, 17,021–17,043, doi:10.1029/94JD01245, 1994.

Doddridge, E.W., & J. Marshall, Modulation of the seasonal cycle of Antarctic sea ice extent related to the Southern Annular Mode. *Geophy. Res. Lett.*, *44*, 9761–9768, doi:10.1002/2017GL074319, 2017.

Douglass, A.R., R.S. Stolarski, S.E. Strahan, and L.D. Oman, Understanding differences in upper stratospheric ozone response to changes in chlorine and temperature as computed using CCMVal-2 models, *J. Geophys. Res.*, *117*, D16306, doi:10.1029/2012JD017483, 2012.

Engel, A., T. Möbius, H. Bönisch, U. Schmidt, R. Heinz, I. Levin, E. Atlas, S. Aoki, T. Nakazawa, S. Sugawara, F. Moore, D. Hurst, J. Elkins, S. Schauffler, A. Andrews, and K. Berine, Age of stratospheric air unchanged within uncertainties over the past 30 years, *Nat. Geosci.*, *2*, 28–31, doi:10.1038/GEO388, 2009.

Engel, A., H. Bönisch, M. Ullrich, R. Sitals, O. Membrive, F. Danis, and C. Crevoisier, Mean age of stratospheric air derived from AirCore observations, *Atmos. Chem. Phys.*, *17*, 6825–6838, doi:10.5194/acp-17-6825-2017, 2017.

England, M.R., L.M. Polvani, K.L. Smith, L. Landrum, and M.M. Holland, Robust response of the Amundsen Sea Low to stratospheric ozone depletion, *Geophys. Res. Lett.*, *43*, 8207–8213, doi:10.1002/2016GL070055, 2016.

Eyring, V., J.M. Arblaster, I. Cionni, J. Sedlacek, J. Perlwitz, P.J. Young, S. Bekki, D. Bergmann, P. Cameron-Smith, W. Collins, G. Faluvegi, K.-D. Gottschaldt, L. Horowitz, D. Kinnison, J.-F. Lamarque, D.R. Marsh, D. Saint-Martin, D. Shindell, K. Sudo, S. Szopa, and S. Watanabe, Long-term changes in tropospheric and stratospheric ozone and associated climate impacts in CMIP5 simulations, *J. Geophys. Res.*, *118* , 5029–5060, doi:10.1002/jgrd.50316, 2013.

Fan, T., C. Deser, and D. Schneider, Recent sea ice trend in the context of Southern Ocean surface climate variations since 1950, *Geophys. Res. Lett., 41*, 2419–2426, doi:10.1002/2014GL059239, 2014.

Ferraro, A.J., M. Collins, and F.H. Lambert, A hiatus in the stratosphere, *Nat. Clim. Change.*, *5*, 497–498, doi:10.1038/nclimate2624, 2015.

Ferreira, D., J. Marshall, C.M. Bitz, S. Solomon, and A. Plumb, Antarctic ocean and sea ice response to ozone depletion: A two-time-scale problem, *J. Clim.*, *28*, 1206–1226, doi:10.1175/JCLI-D-14-00313.1, 2015.

Fogt, R.L., C.A. Goergens, J.M. Jones, D.P. Schneider, J.P. Nicolas, D.H. Bromwich, and H.E. Dusselier, A twentieth century perspective on summer Antarctic pressure change and variability and contributions from tropical SSTs and ozone depletion, *Geophys. Res. Lett.*, *44*, 9918–9927, doi:10.1002/2017GL075079, 2017.

Franzke, C.L.E., T.J. O'Kane, D.P. Monselesan, J.S. Risbey, and I. Horenko, Systematic attribution of observed southern hemispheric circulation trends to external forcing and internal variability, *Nonlin. Process. Geophys. 22*, 513–525, doi:10.5194/npg-22-513-2015, 2015.

Frölicher, T.L., J.L. Sarmiento, D.J. Paynter, J.P. Dunne, J.P. Krasting, and M. Winton, Dominance of the

Southern Ocean in anthropogenic carbon and heat uptake in CMIP5 models, *J. Clim.*, *28*, 862–886, doi:10.1175/JCLI-D-14-00117.1, 2015.

Fu, Q., S. Solomon, and P. Lin, On the seasonal dependence of tropical lower-stratospheric temperature trends, *Atmos. Chem. Phys.*, *10*, 2643–2653, doi:10.5194/acp-10-2643-2010, 2010.

Fu, Q., P. Lin, S. Solomon, and D.L. Hartmann, Observational evidence of strengthening of the Brewer-Dobson circulation since 1980, *J. Geophys. Res. Atmos.*, *120*, 10,214–10,228, doi:10.1002/2015JD023657, 2015.

Fueglistaler S., M. Abalos, T.J. Flannaghan, P. Lin, W.J. Randel, Variability and trends in dynamical forcing of tropical lower stratospheric temperatures, *Atmos. Chem. Phys., 14*, 13439–13453, doi:10.5194/acp-14-13439-2014, 2014.

Fyfe, J.C., N.P. Gillett, and G.J. Marshall, Human influence on extratropical Southern Hemisphere summer precipitation, *Geophys. Res. Lett.*, *39*, L23711, doi:10.1029/2012GL054199, 2012.

Gagné, M.-È., N.P. Gillett, and J.C. Fyfe, Observed and simulated changes in Antarctic sea ice extent over the past 50 years, *Geophys. Res. Lett.*, *42*, 90–95, doi:10.1002/2014GL062231, 2015.

Garcia, R.R., W.J. Randel, and D.E. Kinnison, On the determination of age of air trends from atmospheric trace species, *J. Atmos. Sci.*, 68, 139–154, doi:10.1175/2010JAS3527, 2011.

Garcia, R.R., D.E. Kinnison, and D.R. Marsh, "World avoided" simulations with the whole atmosphere community climate dodel, *J. Geophys. Res., 117*, D23303, doi:10.1029/2012JD018430, 2012.

Garcia, R.R., A.K. Smith, D.E. Kinnison, Á.D.L. Cámara, and D.J. Murphy, Modification of the gravity wave parameterization in the whole atmosphere community climate model: Motivation and results, *J. Atmos. Sci.*, *74* (1), 275–291, doi:10.1175/JAS-D-16-0104.1, 2017.

Garfinkel, C.I., D.W. Waugh, and E.P. Gerber, The effect of tropospheric jet latitude on coupling between the stratospheric polar vortex and the troposphere, *J. Clim.*, *26* (6), 2077–2095, doi:10.1175/JCLI-D-12-00301.1, 2013.

Garfinkel, C.I., and D.W. Waugh, Tropospheric Rossby wave breaking and variability of the latitude of the eddy-driven jet, *J. Clim.*, *27* (18), 7069–7085, doi:10.1175/JCLI-D-14-00081.1, 2014.

Garfinkel, C.I., M. Hurwitz, and L.D. Oman, Effect of recent sea surface temperature trends on the Arctic stratospheric vortex, *J. Geophys. Res. Atmos.*, *120*, 5404–5416, doi:10.1002/2015JD023284, 2015a.

Garfinkel, C.I., D.W. Waugh, and L.M. Polvani, Recent Hadley cell expansion: the role of internal atmospheric variability in reconciling modeled and observed trend, *Geophys. Lett., Res.*, *42,* doi:10.1002/2015GL066942, 2015b.

Garfinkel C.I., V. Aquila, D.W. Waugh, and L.D. Oman, Time-varying changes in the simulated structure of the Brewer–Dobson Circulation, *Atmos. Chem. Phys.*, *17*, 1313–1327, doi:10.5194/acp-17-1313-2017, 2017a.

Garfinkel, C.I., S.W. Son, K. Song, V. Aquila, and L.D. Oman, Stratospheric variability contributed to and sustained the recent hiatus in Eurasian winter warming, *Geophys. Res. Lett.*, *44*, doi:10.1002/2016GL072035, 2017b.

Garfinkel, C.I., Might stratospheric variability lead to improved predictability of ENSO events?, *Environ. Res. Lett.*, *12* (3), doi:10.1088/1748-9326/aa60a4, 2017.

Garfinkel, C.I., and L.D. Oman, Effect of gravity waves from small islands in the Southern Ocean on the Southern Hemisphere atmospheric circulation, *J. Geophys. Res. Atmos.*, *122*, doi:10.1002/2017JD027576, 2018.

Garfinkel, C.I., A. Gordon, L.D. Oman, F. Li, S. Davis, and S. Pawson, Nonlinear response of tropical lower stratospheric temperature and water vapor to ENSO, *Atmos. Chem. Phys.*, *18* 4597–4615, doi:10.5194/acp-2017-520, 2018.

Garny, H., T. Birner, H. Bönisch, and F. Bunzel, The effects of mixing on age of air, *J. Geophys. Res. Atmos.*, *119*, 7015–7034, doi:10.1002/2013JD021417, 2014.

Geller, M.A., M.J. Alexander, P.T. Love, J. Bacmeister, M. Ern, A. Hertzog, E. Manzini, P. Preusse, K. Sato, A.A. Scaife, and T. Zhou, A Comparison between gravity wave momentum fluxes in observations and climate models*, J. Clim.*, *26*, 6383–6405, doi:10.1175/JCLI-D-12-00545.1, 2013.

Gillett, N.P., J.C. Fyfe, and D.E. Parker, Attribution of observed sea level pressure trends to greenhouse gas, aerosol, and ozone changes, *Geophys. Res. Lett.*, *40* (10), 2302–2306, doi:10.1002/grl.50500, 2013, 2013.

Gonzalez, P., L.M. Polvani, R. Seager, and G. Correa, Stratospheric ozone depletion: A key driver

of recent precipitation trends in south eastern South America, *Clim. Dyn.*, *42* (7/8), 1775–1792, doi:10.1007/s00382-013-1777-x, 2014.

Good, S.A., M.J. Martin, and N.A. Rayner, EN4: Quality controlled ocean temperature and salinity profiles and monthly objective analyses with uncertainty estimates, *J. Geophys. Res. Ocean.*, *118*, 6704–6716, doi:10.1002/2013JC009067, 2013.

Goodberlet, M.A., C.T. Swift, and J.C. Wilkerson, Remote sensing of ocean surface winds with the Special Sensor Microwave/Imager, *J. Geophys. Res. Ocean.*, *94* (C10), 14547–14555, doi:10.1029/JC094iC10p14547, 1989.

Gray, L.J., J. Beer, M. Geller, J.D. Haigh, M. Lockwood, K. Matthes, U. Cubasch, D. Fleitmann, G. Harrison, L. Hood, J. Luterbacher, G.A. Meehl, D. Shindell, B. van Geel, and W. White, Solar influences on climate, *Rev. Geophys.*, *48* (4), doi:10.1029/2009RG000282, 2010.

Haenel, F.J., G.P. Stiller, T. Clarmann, B. Funke, E. Eckert, N. Glatthor, U. Grabowski, S. Kellmann, M. Kiefer, A. Linden, and T. Reddmann, Reassessment of MIPAS age of air trends and variability, *Atmos. Chem. Phys.*, *15*, 13161–13176, doi:10.5194/acp-15-13161-2015, 2015.

Haigh, J.D., The Sun and the Earth's climate, *Living Rev. Solar Phys.*, *4* (2), doi:10.12942/lrsp-2007-2, 2007.

Haimberger, L., C. Tavolato, and S. Sperka, Homogenization of the global radiosonde temperature dataset through combined comparison with reanalysis background series and neighboring stations, *J. Clim.*, *25*, 8108–8131, doi:10.1175/JCLI-D-11-00668.1, 2012.

Hall, T.M., and R.A. Plumb, Age as a diagnostic of stratospheric transport, *J. Geophys. Res.*, *99* (D1), 1059–1070, doi:10.1029/93JD03192, 1994.

Hardiman, S.C., N. Butchart, A.J. Charlton-Perez, T.A. Shaw, H. Akiyoshi, A. Baumgaertner, S. Bekki, P. Braesicke, M. Chipperfield, M. Dameris, R.R. Garcia, M. Michou, S. Pawson, E. Rozanov, and K. Shibata, Improved predictability of the troposphere using stratospheric final warmings, *J. Geophys. Res. Atmos.*, *116* (D18), doi:10.1029/2011JD015914, 2011.

Hardiman, S.C., N. Butchart, and N. Calvo, The morphology of the Brewer-Dobson circulation and its response to climate change in CMIP5 simulations, *Q. J. R. Meteorol. Soc.*, *140* (683), 1958–1965, doi:10.1002/qj.2258, 2014.

Hardiman, S.C., P. Lin, A.A. Scaife, N.J. Dunstone, and H.-L. Ren, The influence of dynamical variability on the observed Brewer-Dobson circulation trend, *Geophys. Res. Lett.*, *44*, 2885–2892, doi:10.1002/2017GL072706, 2017.

Hartley, D.E., J.T. Villarin, R.X. Black, and C.A. Davis, A new perspective on the dynamical link between the stratosphere and troposphere, *Nature*, *39,* 471–474, doi:10.1038/35112, 1998.

Hathaway, D.H., The Solar Cycle, *Living Rev. Solar Phys.*, *12* (4), doi:10.1007/lrsp-2015-4, 2015.

Haumann, F.A., D. Notz, and H. Schmidt, Anthropogenic influence on recent circulation-driven Antarctic sea ice changes, *Geophys. Res. Lett.*, *41*, 8429–8437, doi:10.1002/2014GL061659, 2014.

Haumann, F.A., N. Gruber, M. Münnich, I. Frenger, and S. Kern, Sea-ice transport driving Southern Ocean salinity and its recent trends, *Nature*, *537*, 89–92, doi:10.1038/nature1910, 2016.

Hegglin, M.I., and T.G. Shepherd, Large climate-induced changes in ultraviolet index and stratosphere-to-troposphere ozone flux, *Nat. Geosci.*, *2*, 687–691, doi:10.1038/ngeo604, 2009.

Hegglin, M.I., D.A. Plummer, and T.G. Shepherd, Vertical structure of stratospheric water vapour trends derived from merged satellite data, *Nat. Geosci.*, *7*, 768–776, doi:10.1038/ngeo2236, 2014.

Hendon, H.H., E.-P. Lim, and H. Nguyen, Seasonal variations of subtropical precipitation associated with the southern annular mode, *J. Clim.*, *27*, 3446–3460, doi:10.1175/JCLI-D-13-00550.1, 2014.

Hess, P., D. Kinnison, and Q. Tang, Ensemble simulations of the role of the stratosphere in the attribution of northern extratropical tropospheric ozone variability, *Atmos. Chem. Phys.*, *15*, 2341–2365, doi:10.5194/acp-15-2341-2015, 2015.

Hirota, N., H. Shiogama, H. Akiyoshi, T. Ogura, M. Takahashi, Y. Kawatani, M. Kimoto, and M. Mori, The influences of El Niño and Arctic sea-ice on the QBO disruption in February 2016, *npj Clim. and Atmos. Sci.*, *1* (10), doi:10.1038/s41612-018-0020-1, 2018.

Hobbs, W.R., N.L. Bindoff, and M.N. Raphael, New perspectives on observed and simulated Antarctic sea ice extent trends using optimal fingerprinting techniques, *J. Clim.*, *28*, 1543–1560, doi:10.1175/JCLI-D-14-00367.1, 2015.

Hobbs, W.R., R. Massom, S. Stammerjohn, P. Reid, G. Williams, and W. Meier, A review of recent changes in Southern Ocean sea ice, their drivers and forcings, *Glob. Planet. Chang.*, *143*, 228–250, doi:10.1016/j.gloplacha.2016.06.008, 2016.

Holland, M.M., L. Landrum, Y. Kostov, and J. Marshall, Sensitivity of Antarctic sea ice to the Southern Annular Mode in coupled climate models, *Clim. Dyn.*, *49* (5/6), doi:10.1007/s00382-016-3162-z., 2016.

Hossaini, R., M.P. Chipperfield, S.A. Montzka, A. Rap, S. Dhomse, and W. Feng, Efficiency of short-lived halogens at influencing climate through depletion of stratospheric ozone, *Nat. Geosci.*, *8*, 186–190, doi:10.1038/ngeo2363, 2015.

Hsu, J., and M.J. Prather, Is the residual vertical velocity a good proxy for stratosphere-troposphere exchange of ozone?, *Geophys. Res. Lett.*, *41*, 9024–9032, doi:10.1002/2014GL061994, 2014.

Hurst, D.F., S.J. Oltmans, H. Vömel, K.H. Rosenlof, S.M. Davis, E.A. Ray, E.G. Hall, and A.F. Jordan, Stratospheric water vapor trends over Boulder, Colorado: Analysis of the 30-year Boulder record, *J. Geophys. Res.*, *116*, D02306, doi:10.1029/2010JD015065, 2011.

Hurst, D.F., A. Lambert, W.G. Read, S.M. Davis, K.H. Rosenlof, E.G. Hall, A.F. Jordan, and S.J. Oltmans, Validation of Aura Microwave Limb Sounder stratospheric water vapor measurements by the NOAA frost point hygrometer, *J. Geophys. Res.*, *119*, 1612–1625, doi:10.1002/2013JD020757, 2014.

Hurst, D.F., W.G. Read, H. Vömel, H.B. Selkirk, K.H. Rosenlof, S.M. Davis, E.G. Hall, A. Jordan, S.J. Oltmans, Recent divergences in stratospheric water vapor measurements by frost point hygrometers and the Aura Microwave Limb Sounder, *Atmos. Meas. Tech.*, *9*, 447–4457, doi:10.5194/amt-2016-157, 2016.

Hurwitz, M.M., E.C. Fleming, P.A. Newman, F. Li, E. Mlawer, K. Cady-Pereira, and R. Bailey, Ozone depletion by hydrofluorocarbons, *Geophys. Res. Lett.*, *42*, 8686–8692, doi:10.1002/2015GL065856, 2015.

Hurwitz, M.M., E.L. Fleming, P.A. Newman, F. Li, and Q. Liang, Early action on HFCs,mitigates future atmospheric change, *Environ. Res. Lett.*, *11*, 114019, doi:10.1088/1748-9326/11/11/114019, 2016.

Iglesias-Suarez, F., P.J. Young, and O. Wild, Stratospheric ozone change and related climate impacts over 1850–2100 as modelled by the ACCMIP ensemble, *Atmos. Chem. Phys.*, *16* (1), 343–363, doi:10.5194/acp-16-343-2016, 2016.

Iglesias-Suarez, F., D.E. Kinnison, A. Rap, O. Wild, and P.J. Young, Key drivers of ozone change and its radiative forcing over the 21st century, *Atmos. Chem. Phys.*, *18* (9), 6121–6139, doi:10.5194/acp-2017-939, 2018.

IPCC (Intergovernmental Panel on Climate Change), *Climate Change 2013: The Physical Science Basis. Contribution of Working Group I to the Fifth Assessment Report of the Intergovernmental Panel on Climate Change*, edited by T.F. Stocker, D. Qin, G.-K. Plattner, M. Tignor, S.K. Allen, J. Boschung, A. Nauels, Y. Xia, V. Bex, and P.M. Midgley, 1535 pp., Cambridge University Press, Cambridge, United Kingdom, 2013.

Ivy, D.J., S. Solomon, and H.E. Rieder, Radiative and dynamical influences on polar stratospheric temperature trends, *J. Clim.*, doi:10.1175/JCLI-D-15-0503.1, 2016.

Ivy, D.J., C. Hilgenbrink, D. Kinnison, R.A. Plumb, A. Sheshadri, S. Solomon, and D.W.J. Thompson, Observed Changes in the southern hemispheric circulation in May, *J. Clim.*, *30* (2), 527–536, doi:10.1175/JCLI-D-16-0394.1, 2017a.

Ivy, D.J., S. Solomon, N. Calvo, and D.W.J. Thompson, Observed connections of Arctic stratospheric ozone extremes to Northern Hemisphere surface climate, *Environ. Res. Lett.*, *12* (2), 024004, doi:10.1088/1748-9326/aa57a4/, 2017b.

Jones, J.M., S.T. Gille, H. Goosse, N.J. Abram, P.O. Canziani, D.J. Charman, K.R. Clem, X. Crosta, C. de Lavergne, I. Eisenman, M.H. England, R.L. Fogt, L.M. Frankcombe, G.J. Marshall, V. Masson-Delmotte, A.K. Morrrison, A.J. Orsi, M.N. Raphael, J.A. Renwick, D.P. Schneider, G.R. Simpkins, E.R. Steig, B. Stenni, D. Swingedouw, and T.R. Vance, Assessing recent trends in high-latitude Southern Hemisphere surface climate, *Nat. Clim. Change*, *6*, 917–926, doi:10.1038/nclimate3103, 2016.

Kang, S.M., and L.M. Polvani, The interannual relationship between the latitude of the eddy-driven jet and the edge of the Hadley cell, *J. Clim.*, *24* (2), 563–568, doi:10.1175/JCLI-D-12-00414.1, 2011.

Karoly, D.J., Climate change: Human-induced rainfall changes, *Nat. Geosci.*, *7*, 551–552, doi:10.1038/ngeo2207, 2014.

Karpechko, A.Yu., J. Perlwitz, and E. Manzini. A model study of tropospheric impacts of the Arctic ozone depletion 2011, *J. Geophys. Res. Atmos.*, *119* (13),

7999–8014, doi:10.1002/2013JD021350, 2014.

Karpechko, A.Yu., and E. Manzini, Arctic stratosphere dynamical response to global warming, *J. Clim.*, *30* (17), 7071–7086, doi:10.1175/JCLI-D-16-0781.1, 2017.

Kawase, H., T. Nagashima, K. Sudo, and T. Nozawa, Future changes in tropospheric ozone under Representative Concentration Pathways (RCPs), *Geophys. Res. Lett.*, *38*, L05801, doi:10.1029/2010GL046402, 2011.

Kawatani, Y., and K. Hamilton, Weakened stratospheric quasibiennial oscillation driven by increased tropical mean upwelling, *Nature*, *497*, 478–481, doi:10.1038/nature12140, 2013.

Keeble, J., P. Braesicke, N.L. Abraham, H.K. Roscoe, and J.A. Pyle, The impact of polar stratospheric ozone loss on Southern Hemisphere stratospheric circulation and climate, *Atmos. Chem. Phys.*, *14*, 13705–13717, doi:10.5194/acp-14-13705-2014, 2014.

Keeley, S.P.E., N.P. Gillett, D.W.J. Thompson, S. Solomon, and P.M. Forster, Is Antarctic climate most sensitive to ozone depletion in the middle or lower stratosphere?, *Geophys. Res. Lett.*, *34*, L22812, doi:10.1029/2007GL031238, 2007.

Khatiwala, S., F. Primeau, and T. Hall, Reconstruction of the history of anthropogenic CO_2 concentrations in the ocean, *Nature*, *462*, 346–349, doi:10.1038/nature08526, 2009.

Khaykin, S.M., B.M. Funatsu, A. Hauchecorne, S. Godin-Beekmann, C. Claud, P. Keckhut, A. Pazmino, H. Gleisner, J.K. Nielsen, S. Syndergaard, and K.B. Lauritsen, Postmillennium changes in stratospheric temperature consistently resolved by GPS radio occultation and AMSU observations, *Geophys. Res. Lett.*, *44*, 7510–7518, doi:10.1002/2017GL074353, 2017.

Kim, B.M., S.-W. Son, S.-K. Min, J.-H. Jeong, S.-J. Kim, X. Zhang, T. Shim, and J.-H. Yoon, Weakening of the stratospheric polar vortex by Arctic sea-ice loss, *Nat. Commun., 5*, 4646, doi:10.1038/ncomms5646, 2014.

Kim, J., K.M. Grise, and S.-W. Son, Thermal characteristics of the cold-point tropopause region in CMIP5 models, *J. Geophys. Res. Atmos.*, *118*, 8827–8841, doi:10.1002/jgrd.50649, 2013.

Kim, J.-S., J.-S. Kug, J.-H. Yoon, and S.-J. Jeong, Increased atmospheric CO_2 growth rate during El Niño driven by reduced terrestrial productivity in the CMIP5 ESMs, *J. Clim.*, *29*, 8783–8805, doi:10.1175/JCLI-D-14-00672.1, 2016.

Kim, Y.-H., S.-K. Min, S.-W. Son, and J. Choi, Attribution of the local Hadley cell widening in the Southern Hemisphere, *Geophys. Res. Lett.*, *44*, 1015–1024, doi:10.1002/2016GL072353, 2017.

Klobas, J.E., D.M. Wilmouth, D.K. Weisenstein, J.G. Anderson, and R.J. Salawitch, Ozone depletion following future volcanic eruptions, *Geophys. Res. Lett.*, *44*, 7490–7499, doi: 10.1002/2017GL073972, 2017.

Konopka, P., F. Ploeger, M. Tao, and M. Riese, Zonally resolved impact of ENSO on the stratospheric circulation and water vapor entry values, *J. Geophys. Res. Atmos.*, *121* (19), 11,486–11,501, doi:10.1002/2015JD024698, 2016.

Kostov, Y., J. Marshall, U. Hausmann, K.C. Armour, D. Ferreira, and M.M. Holland, Fast and slow responses of Southern Ocean sea surface temperature to SAM in coupled climate models, *Clim. Dyn.*, 1–15, doi:10.1007/s00382-016-3162-z, 2016.

Kostov, Y., D. Ferreira, K.C. Armour, and J. Marshall, Contributions of greenhouse gas forcing and the southern annular mode to historical Southern Ocean surface temperature trends, *Geophys. Res. Lett.*, *45*, doi:10.1002/2017GL074964, 2018.

Kovács, T., W. Feng, A. Totterdill, J.M.C. Plane, S. Dhomse, J.C. Gómez-Martín, G.P. Stiller, F.J. Haenel, C. Smith, P.M. Forster, R.R. García, D.R. Marsh, and M.P. Chipperfield, Determination of the atmospheric lifetime and global warming potential of sulfur hexafluoride using a three-dimensional model, *Atmos. Chem. Phys.*, *17*, 883–898, doi:10.5194/acp-17-883-2017, 2017.

Kremser, S., L.W. Thomason, M. Hobe, M. Hermann, T. Deshler, C. Timmreck, M. Toohey, A. Stenke, J.P. Schwarz, R. Weigel, S. Fueglistaler, F.J. Prata, J.-P. Vernier, H. Schlager, J.E. Barnes, J.-C. Antuna-Marrero, D. Fairlie, M. Palm, E. Mahieu, J. Notholt, M. Rex, C. Bingen, F. Vanhellemont, A. Bourassa, J.M.C. Plane, D. Klocke, S.A. Carn, L.R. Neely, A.D. James, L. Rieger, J.C. Wilson, and B. Meland, Stratospheric aerosol - Observations, processes, and impact on climate, *Rev. Geophys.*, *54*, 278–335, doi:10.1002/2015RG000511, 2016.

Kretschmer, M., D. Coumou, L. Agel, M. Barlow, E. Tziperman, and J. Cohen, More-persistent weak stratospheric polar vortex states linked to cold extremes, *Bull. Am. Meteorol. Soc.*, *99*, 49–60, doi:10.1175/BAMS-D-16-0259.1, 2018.

Lamarque, J.F., L.K. Emmons, P.G. Hess, D.E. Kinnison, S. Tilmes, F. Vitt, and J.J. Orlando, CAM-chem: Description and evaluation of interactive atmospheric chemistry in the community Earth system model, *Geosci. Model Dev.*, *5* (2), 369–411, doi:10.5194/gmd-5-369-2012, 2012.

Landrum, L.L., M.M. Holland, M.N. Raphael, and L.M. Polvani, L., Stratospheric ozone depletion: An unlikely driver of the regional trends in Antarctic sea ice in austral fall in the late twentieth century, *Geophys. Res. Lett.*, *44*, 11,062–11,070, doi:10.1002/2017GL075618, 2017.

Landschützer, P., N. Gruber, F.A. Haumann, C. Rodenbeck, D.D. Bakker, N. Metzl, C. Sweeney, T. Takahasi, B. Tilbrook, and R. Wanninkhof, The reinvigoration of the Southern Ocean carbon sink, *Science, 349*, 1221–1224, doi:10.1126/science.aab2620, 2015.

Langematz, U., S. Meul, K. Grunow, E. Romanowsky, S. Oberländer, J. Abalichin, and A. Kubin, Future Arctic temperature and ozone: The role of stratospheric composition changes, *J. Geophys. Res. Atmos.*, *119*, 2092–2112, doi:10.1002/2013JD021100, 2014.

Lanzante, J.R., S.A. Klein, and D.J. Seidel, Temporal homogenization of monthly radiosonde temperature data, Part I: Methodology, *J. Clim.*, *16*, 224–240, doi:10.1175/1520-0442(2003)016<0224:THOMRT>2.0.CO;2, 2003.

Latif, M., T. Martin, and W. Park, Southern Ocean sector centennial climate variability and recent decadal trends, *J. Clim., 26*, 7767–7782, doi:10.1175/JCLI-D-12-00281.1, 2013.

Law, R.M., R.J. Matear, and R.J. Francey, Comment on "Saturation of the Southern Ocean CO_2 sink due to recent climate change", *Science*, *319* (5863), doi:10.1126/science.1149077, 2008.

Le Quéré, C., C. Rodenbeck, E.T. Buitenhuis, T.J. Conway, R. Langenfelds, A. Gomez, C. Labuschagne, M. Ramonet, T. Nakazawa, N. Metzl, N. Gillett, and M. Heimann, Saturation of the Southern Ocean CO_2 sink due to recent climate change, *Science*, *316*, 1735–1738, doi:10.1126/science.1136188, 2007.

Le Quéré, C., R.M. Andrew, P. Friedlingstein, S. Sitch, J. Pongratz, A.C. Manning, J.I. Korsbakken, G.P. Peters, J.G. Canadell, R.B. Jackson, T.A. Boden, P.P. Tans, O.D. Andrews, V.K. Arora, D.C.E. Bakker, L. Barbero, M. Becker, R.A. Betts, L. Bopp, F. Chevallier, L.P. Chini, P. Ciais, C.E. Cosca, J. Cross, K. Currie, T. Gasser, I. Harris, J. Hauck, V. Haverd, R.A. Houghton, C.W. Hunt, T. Ilyina, A.K. Jain, E. Kato, M. Kautz, R.F. Keeling, K. Klein Goldewijk, A. Körtzinger, P. Landschützer, N. Lefèvre, A. Lenton, S. Lienert, I. Lima, D. Lombardozzi, N. Metzl, F. Millero, P.M.S. Monteiro, D.R. Munro, J.E.M.S. Nabel, S.I. Nakaoka, Y. Nojiri, X.A. Padin, A. Peregon, B. Pfeil, D. Pierrot, B. Poulter, G. Rehder, J. Reimer, C. Rödenbeck, J. Schwinger, R. Séférian, I. Skjelvan, B.D. Stocker, H. Tian, B. Tilbrook, F.N. Tubiello, I.T. van der Laan-Luijkx, G.R. van der Werf, S. van Heuven, N. Viovy, N. Vuichard, A.P. Walker, A.J. Watson, A.J. Wiltshire, S. Zaehle, and D. Zhu, Global carbon budget 2017, *Earth Syst. Sci. Data, 10*, 405–448, doi:10.5194/essd-10-405-2018, 2018.

Lenton, A., B. Tilbrook, R.M. Law, D. Bakker, S.C. Doney, N. Gruber, M. Ishii, M. Hoppema, N.S. Lovenduski, R.J. Matear, B.I. McNeil, N. Metzl, S.E. Mikaloff Fletcher, P.M.S. Monteiro, C. Rödenbeck, C. Sweeney, and T. Takahashi, Sea-air CO_2 fluxes in the Southern Ocean for the period 1990–2009, *Biogeosci., 10*, 4037–4054, doi:10.5194/bg-10-4037-2013, 2013.

Li, F., J. Austin, and J. Wilson, The strength of the Brewer–Dobson Circulation in a changing climate: Coupled chemistry–climate model simulations, *J. Clim.*, *21*, 40–57, doi:10.1175/2007JCLI1663.1, 2008.

Li, F., D.W. Waugh, A.R. Douglass, P.A. Newman, S.E. Strahan, J. Ma, J.E. Nielsen, and Q. Liang, Long-term changes in stratospheric age spectra in the 21st century in the Goddard Earth Observing System Chemistry-Climate Model (GEOSCCM), *J. Geophys. Res.*, *117*, D20119, doi:10.1029/2012JD017905, 2012.

Li, F., P. Newman, S. Pawson, and J. Perlwitz, Effects of greenhouse gas increase and stratospheric ozone depletion on stratospheric mean age of air in 1960–2010, *J. Geophys. Res. Atmos.*, *123* (4), 2098–2110, doi:10.1002/2017JD027562, 2018.

Li, X., D.M. Holland, E.P. Gerber, and C. Yoo, Impacts of the north and tropical Atlantic Ocean on the Antarctic Peninsula and sea ice, *Nature*, *505*, 538–542, doi:10.1038/nature12945, 2014.

Lim, E.P., H.H. Hendon, J.M. Arblaster, F. Delage, H. Nguyen, S.K. Min, and M.C. Wheeler, The impact of the Southern Annular Mode on fu-

ture changes in Southern Hemisphere rainfall, *Geophys. Res. Lett.*, *43* (13), 7160–7167, doi:10.1002/2016GL069453, 2016.

Lin, M., A.M. Fiore, L.W. Horowitz, A.O. Langford, S.J. Oltmans, D. Tarasick, and H.E. Rieder, Climate variability modulates western U.S. ozone air quality in spring via deep stratospheric intrusions, *Nat. Commun.*, *6*, 7105, doi:10.1038/ncomms8105, 2015.

Lin, P., D. Paynter, L. Polvani, P. Correa, J. Gustavo, Y. Ming, and V. Ramaswamy, Dependence of model-simulated response to ozone depletion on stratospheric polar vortex climatology, *Geophys. Res. Lett.*, *17*, 14,593–14,629, doi:10.1002/2017GL073862, 2017.

Linz, M., R.A. Plumb, E.P. Gerber, and A. Sheshadri, The relationship between age of air and the diabatic circulation of the stratosphere, *J. Atmos. Sci.*, *73*, 4507–4518, doi:10.1175/JAS-D-16-0125.1, 2016.

Linz M., R.A. Plumb, E.P. Gerber, F.J. Haenel, G. Stiller, D.E. Kinnison, A. Ming, and J.L. Neu, The strength of the meridional overturning circulation of the stratosphere, *Nat. Geosci.*, *10*, 663–667, doi:10.1038/ngeo3013, 2017.

Long, C.S., M. Fujiwara, S. Davis, D.M. Mitchell, and C.J. Wright, Climatology and interannual variability of dynamic variables in multiple reanalyses evaluated by the SPARC Reanalysis Intercomparison Project (S-RIP), *Atmos. Chem. Phys.*, *17*, 14,593–14,629, doi:10.5194/acp-17-14593-2017, 2017.

Lucas, C., and H. Nguyen, Regional characteristics of tropical expansion and the role of climate variability, *J. Geophys. Res. Atmos.*, *120*, 6809–6824, doi:10.1002/2015JD023130, 2015.

Mahieu, E., M.P. Chipperfield, J. Notholt, T. Reddmann, J. Anderson, P.F. Bernath, T. Blumenstock, M.T. Coffey, S.S. Dhomse, W. Feng, B. Franco, L. Froidevaux, D.W.T. Griffith, J.W. Hannigan, F. Hase, R. Hossaini, N.B. Jones, I. Morino, I. Murata, H. Nakajima, M. Palm, C. Paton-Walsh, J.M. Russelll III, M. Schneider, C. Servais, D. Smale, and K.A. Walker, Recent Northern Hemisphere stratospheric HCl increase due to atmospheric circulation changes, *Nature*, *515*, 104–107, doi:10.1038/nature13857, 2014.

Manatsa, D., Y. Morioka, S.K. Behera, T. Yamagata, and C.H. Matarira, Link between Antarctic ozone depletion and summer warming over southern Africa, *Nat. Geosci.*, *6*, 934–939, doi:10.1038/ngeo1968, 2013.

Manatsa, D., Y. Morioka, S.K. Behera, T.D. Mushore, and R. Mugandani, Linking the southern annular mode to the diurnal temperature range shifts over southern Africa, *Int. J. Climatol.*, *35*, 4220–4236, doi:10.1002/joc.4281, 2015.

Manatsa, D., C. Mudavanhu, T.D. Mushore, and E. Mavhura, Linking major shifts in East Africa 'short rains' to the Southern Annular Mode, *Int. J. Climatol.*, *36*, 1590–1599, doi:10.1002/joc.4443, 2016.

Manney, G.L., and M.I. Hegglin, Seasonal and regional variations of long-term changes in upper-tropospheric jets from reanalyses, *J. Clim.*, *31* (1), 423–448, doi:10.1175/JCLI-D-17-0303.1, 2018.

Mantsis, D.F., S. Sherwood, R.J. Allen, and L. Shi, Natural variations of tropical width and recent trends, *Geophys. Res. Lett.*, *44*, 3825–3832, doi:10.1002/2016GL072097, 2017.

Manzini, E., A.Yu. Karpechoko, J. Anstey, M.P. Baldwin, R.X. Black, C. Cagnazzo, N. Calvo, A. Charlton-Perez, B. Christiansen, P. Davini, E. Gerber, M. Giorgetta, L. Gray, S.C. Hardiman, Y.-Y. Lee, D.R. March, B.A. McDaniel, A. Purich, A.A. Scaife, D. Shindell, S.-W. Son, S. Watanabe, and G. Zappa, Northern winter climate change: Assessment of uncertainty in CMIP5 projections related to stratosphere-troposphere coupling, *J. Geophys. Res. Atmos.*, *119*, 7979–7998, doi:10.1002/2013JD021403, 2014.

Manzini, E., A. Y., Karpechko, and L. Kornblueh, Nonlinear response of the stratosphere and the North Atlantic-European climate to global warming, *Geophys. Res. Lett.*, *45*, 4255–4263, doi:10.1029/2018GL077826, 2018.

Marsh, D.R., J.-F. Lamarque, A.J. Conley, and L.M. Polvani, Stratospheric ozone chemistry feedbacks are not critical for the determination of climate sensitivity in CESM1(WACCM), *Geophys. Res. Lett.*, *43*, 3928–3934, doi:10.1002/2016GL068344, 2016.

Marshall, G.J., Trends in the Southern Annular Mode from observations and reanalyses, *J. Clim.*, *16* (24), 4134–4143, doi: 10.1175/1520-0442(2003)016<4134:TITSAM>2.0.CO;2, 2003.

Marshall, G.J., and T. Bracegirdle, An examination of the relationship between the Southern Annular Mode and Antarctic surface air temperatures in the CMIP5 historical runs, *Clim. Dyn.*, *45* (5/6), 1513–1535, doi:10.1007/s00382-014-2406-z, 2014.

Marshall, J., K. Armour, J. Scott, Y. Kostov, U. Hausmann, D. Ferreira, T. Shepherd, T., and C. Bitz, The ocean's role in polar climate change: Asymmetric Arctic and Antarctic responses to greenhouse gas and ozone forcing, *Philos. Trans. Roy. Soc. A, 372*, doi:10.1098/rsta.2013.0040, 2014.

Masarie, K.A., and P.P. Tans, Extension and integration of atmospheric carbon dioxide data into a globally consistent measurement record, *J. Geopys. Res.*, *100*, 11,593–11,610, doi:10.1029/95JD00859, 1995.

Maycock, A.C., M.M. Joshi, K.P. Shine, S.M. Davis, and K.H. Rosenlof, The potential impact of changes in lower stratospheric water vapour on stratospheric temperatures over the past 30 years, *Q. J. R. Meteorol. Soc.*, *140*, 2176–2185, doi:10.1002/qj.2287, 2014.

Maycock, A.C., The contribution of ozone to future stratospheric temperature trends, *Geophys. Res. Lett.*, *43* (9), 4077–4658, doi:10.1002/2016GL068511, 2016.

Maycock, A.C., W.J. Randel, A.K. Steiner, A.Yu., Karpechko, J. Christy, R. Saunders, D.W.J. Thompson, C.-Z. Zou, A. Chrysanthou, N.L. Abraham, H. Akiyoshi, A.T. Archibald, N. Butchart, M. Chipperfield, M. Dameris, M. Deushi, S. Dhomse, G. Di Genova, P. Jöckel, D.E. Kinnison, O. Kirner, F. Ladstädter, M. Michou, O. Morgenstern, F. O'Connor, L. Oman, G. Pitari, D.A. Plummer, L.E. Revell, E. Rozanov, A. Stenke, D. Visioni, Y. Yamashita, and G. Zeng, Revisiting the mystery of recent stratospheric temperature trends, *Geophys. Res. Letts.*, *45*, 9919–9933, doi:10.1029/2018GL078035, 2018.

McLandress, C., A.I. Jonsson, D.A. Plummer, M.C. Reader, J.F. Scinocca, and T.G. Shepherd, Separating the dynamical effects of climate change and ozone depletion, Part I: Southern Hemisphere stratosphere, *J. Clim.*, *23*, 5002–5020, doi:10.1175/2010JCLI3586.1, 2010.

McLandress, C., T.G. Shepherd, J.F. Scinocca, D.A. Plummer, M. Sigmond, A.I. Jonsson, and M.C. Reader, Separating the dynamical effects of climate change and ozone depletion, Part II: Southern Hemisphere troposphere, J. Clim., 24, 1850–1868, doi:10.1175/2010JCLI3958.1, 2011.

McLandress, C., T.G. Shepherd, S. Polavarapu, and S.R. Beagley, Is missing orographic gravity wave drag near 60°S the cause of the stratospheric zonal wind biases in chemistry–climate models?, *J. Atmos. Sci.*, *69*, 802–818, doi:10.1175/JAS-D-11-0159.1, 2012.

McLandress, C., T.G. Shepherd, A.I. Jonsson, T. von Clarmann, and B. Funke, A method for merging nadir-sounding climate records, with an application to the global-mean stratospheric temperature data sets from SSU and AMSU, *Atmos. Chem. Phys., 15*, 9271–9284, doi:10.5194/acp-15-9271-2015, 2015.

Mears, C.A., F.J. Wentz, P. Thorne, and D. Bernie, Assessing uncertainty in estimates of atmospheric temperature changes from MSU and AMSU using a Monte-Carlo estimation technique, *J. Geophys. Res.*, *116*, D08112, doi:10.1029/2010JD014954, 2011.

Meehl, G.A., J.M. Arblaster, C.M. Bitz, C.T.Y. Chung, and H. Teng, Antarctic sea-ice expansion between 2000 and 2014 driven by tropical Pacific decadal climate variability, *Nat. Geosci., 9,* 590–595, doi:10.1038/ngeo2751, 2016.

Meier, W.N., D. Gallaher, and G.G. Campbell, New estimates of Arctic and Antarctic sea ice extent during September 1964 from recovered Nimbus I satellite imagery, *Cryosph.*, *7*, 699–705, doi:10.5194/tc-7-699-2013, 2013.

Meul, S., U. Langematz, P. Kröger, S. Oberländer-Hayn, and P. Jöckel, Future changes in the stratosphere-to-troposphere ozone mass flux and the contribution from climate change and ozone recovery, *Atmos. Chem. Phys.*, *18*, 7721–7738, doi:10.5194/acp-18-7721-2018, 2018.

Mills, M.J., A. Schmidt, R. Easter, S. Solomon, D.E. Kinnison, S.J. Ghan, R.R. Neely III, D.R. Marsh, A. Conley, C.G. Bardeen, and A. Gettelman, Global volcanic aerosol properties derived from emissions, 1990–2014, using CESM1(WACCM), *J. Geophys. Res. Atmos.*, *121*, 2332–2348, doi:10.1002/2015JD024290, 2016.

Ming, A., P. Hitchcock, and P. Haynes, The response of the lower stratosphere to zonally symmetric thermal and mechanical forcing, *J. Atmos. Sci., 73*, 1903–1922, doi:10.1175/JAS-D-15-0294.1, 2016.

Mitchell, D.M., Attributing the forced components of observed stratospheric temperature variability to external drivers, *Q. J. R. Meteorol. Soc.*, *142*, 1041–1047, doi:10.1002/qj.2707, 2016.

Miyazaki, K., T. Iwasaki, Y. Kawatani, C. Kobayashi, S. Sugawara, and M.I. Hegglin, Inter-comparison of stratospheric mean-meridional circulation and

eddy mixing among six reanalysis data sets, *Atmos. Chem. Phys.*, *16*, 6131–6152, doi:10.5194/acp-16-6131-2016, 2016.

Monahan, A.H., and J.C. Fyfe, On the nature of zonal jet EOFs, *J. Clim.*, *19*, 6409–6424, doi:10.1175/JCLI3960.1, 2006.

Morgenstern, O., G. Zeng, S.M. Dean, M. Joshi, N.L. Abraham, and A. Osprey, Direct and ozone-mediated forcing of the Southern Annular Mode by greenhouse gases, *Geophys. Res. Lett.*, *41* (24), 9050–9057, doi:10.1002/2014GL062140, 2014.

Morgenstern, O., M.I. Hegglin, E. Rozanov, F.M. O'Connor, N.L. Abraham, H. Akiyoshi, A.T. Archibald, S. Bekki, N. Butchart, M.P. Chipperfield, M. Deushi, S.S. Dhomse, R.R. Garcia, S.C. Hardiman, L.W. Horowitz, P. Jöckel, B. Josse, D. Kinnison, M. Lin, E. Mancini, M.E. Manyin, M. Marchand, V. Marécal, M. Michou, L.D. Oman, G. Pitari, D.A. Plummer, L.E. Revell, D. Saint-Martin, R. Schofield, A. Stenke, K. Stone, K. Sudo, T.Y. Tanaka, S. Tilmes, Y. Yamashita, K. Yoshida, and G. Zeng, Review of the global models used within Phase 1 of the Chemistry-Climate Model Initiative (CCMI), *Geosci. Model Dev.*, *10*, 639–671, doi:10.5194/gmd-10-639-2017, 2017.

Morgenstern, O., H. Akiyoshi, Y. Yamashita, D.E. Kinnison, R.R. Garcia, D.A. Plummer, J. Scinocca, G. Zeng, E. Rozanov, A. Stenke, L.E. Revell, G. Pitari, E. Mancini, E., G. Di Genova, S.S. Dhomse, and M.P. Chipperfield, Ozone sensitivity to varying greenhouse gases and ozone-depleting substances in CCMI-1 simulations, *Atmos. Chem. Phys.*, *18*, 1091–1114, doi:10.5194/acp-18-1091-2018, 2018.

Munro, D.R., N.S. Lovenduski, T. Takahashi, B.B. Stephens, T. Newberger, and C. Sweeney, Recent evidence for a strengthening CO_2 sink in the Southern Ocean from carbonate system measurements in the Drake Passage (2002–2015), *Geophys. Res. Lett.*, *42*, 7623–7630, doi:10.1002/2015GL065194, 2015.

Murphy, D.M., K.D. Froyd, J.P. Schwarz, and J.C. Wilson, Observations of the chemical composition of stratospheric aerosol particles, *Q. J. R. Meteorol. Soc.*, *140*, 1269–1278, doi:10.1002/qj.2213, 2014.

Muthers, S., J.G. Anet, A. Stenke, C.C. Raible, E. Rozanov, S. Brönnimann, T. Peter, F.X. Arfeuille, A.I. Shapiro, J. Beer, F. Steinhilber, Y. Brugnara, and W. Schmutz, The coupled atmosphere-chemistry-ocean model SOCOL-MPIOM, *Geosci. Model Dev.*, *7*, 2157–2179, doi:10.5194/gmd-7-2157-2014, 2014.

Muthers, S., A. Kuchar, A. Stenke, J. Schmitt, J.G. Anet, C.C. Raible, and T.F. Stocker, Stratospheric age of air variations between 1600 and 2100, *Geophys. Res. Lett.*, *43*, doi:10.1002/2016GL068734, 2016.

Myhre, G., D. Shindell, (Coordination and Lead Authors), F.-M. Bréon, W. Collins, J. Fuglestvedt, J. Huang, D. Koch, J.-F. Lamarque, D. Lee, B. Mendoza, T. Nakajima, A. Robock, G. Stephens, T. Takemura, and H. Zhang, Anthropogenic and natural radiative forcing, Chapter 8, in *Climate Change 2013: The Physical Science Basis. Contribution of Working Group I to the Fifth Assessment Report of the Intergovernmental Panel on Climate Change,* review editors D. Jacob, A.R. Ravishankara, and K. Shine, 659–740, Cambridge University Press, Cambridge, United Kingdom, doi:10.1017/ CBO9781107415324.018, 2013.

Naik, V., L.W. Horowitz, M.D. Schwarzkopf, and M. Lin, Impact of volcanic aerosols on stratospheric ozone recovery, *J. Geophys. Res. Atmos.*, *122*, 9515–9528, doi:10.1002/2016JD025808, 2017.

Naoe, H., M. Deushi, K. Yoshida, and K. Shibata, Future changes in the ozone quasi-biennial oscillation with increasing GHGs and ozone recovery in CCMI simulations, *J. Clim.*, *30*, 6977–6997, doi:10.1175/JCLI-D-16-0464.1, 2017.

Nash, J., and R. Saunders, A review of stratospheric sounding unit radiance observations for climate trends and reanalyses, *Q. J. R. Meteorol. Soc.*, *141*, 2103–2113, doi:10.1002/qj.2505, 2015.

Neely, R.R., III, O.B. Toon, S. Solomon, J.-P. Vernier, C. Alvarez, J.M. English, K.H. Rosenlof, M.J. Mills, C.G. Bardeen, J.S. Daniel, and J.P. Thayer, Recent anthropogenic increases in SO_2 from Asia have minimal impact on stratospheric aerosol, *Geophys. Res. Lett.*, *40*, doi:10.1002/grl.50263, 2013.

Neely, R.R., III, D.R. Marsh, K.L. Smith, S.M. Davis, and L.M. Polvani, Biases in Southern Hemisphere climate trends induced by coarsely specifying the temporal resolution of stratospheric ozone, *Geophys. Res. Lett.*, *41* (23), 8602–8610, doi:10.1002/2014GL061627, 2014.

Neu, J.L., and R.A. Plumb, Age of air in a leaky pipe model of stratospheric transport, *J. Geophys. Res.*, *104* (D16), 19243–19255, doi:10.1029/1999JD900251, 1999.

Neu, J.L., T. Flury, G.L. Manney, M.L. Santee, N.J. Livesey, and J. Worden, Tropospheric ozone variations governed by changes in stratospheric circulation, *Nat. Geosci.*, *7*, 340–344, doi:10.1038/ngeo2138, 2014.

Newman, P.A., L.D. Oman, A.R. Douglass, E.L. Fleming, S.M. Frith, M.M. Hurwitz, S.R. Kawa, C.H. Jackman, N.A. Krotkov, E.R. Nash, J.E. Nielsen, S. Pawson, R.S. Stolarski, and G.J.M. Velders, What would have happened to the ozone layer if chlorofluorocarbons (CFCs) had not been regulated?, *Atmos. Chem. Phys.*, *9*, 2113–2128, doi:10.5194/acp-9-2113-2009, 2009.

Newman, P.A., L. Coy, S. Pawson, and L.R. Lait, The anomalous change in the QBO in 2015–2016, *Geophys. Res. Lett.*, *43* (16), 8791–8797, doi:10.1002/2016GL070373, 2016.

Nguyen, H., C. Lucas, A. Evans, B. Timbal, and L. Hanson, Expansion of the Southern Hemisphere Hadley cell in response to greenhouse gas forcing, *J. Clim.*, *28* (20), 8067–8077, doi:10.1175/JCLI-D-15-0139.1, 2015.

Nowack, P.J., N.L. Abraham, A.C. Maycock, P. Braesicke, J.M. Gregory, M. Joshi, A. Osprey, and J.A. Pyle, A large ozone-circulation feedback and its implications for global warming assessments, *Nat. Clim. Change*, *5*, 41–45, doi:10.1038/nclimate2451, 2014.

Oberländer, S., U. Langematz, and S. Meul, Unraveling impact factors for future changes in the Brewer-Dobson circulation, *J. Geophys. Res. Atmos.*, *118*, 10,296–10,312, doi:10.1002/jgrd.50775, 2013.

Oberländer-Hayn, S., S. Meul, U. Langematz, J. Abalichin, and F. Haenel, A chemistry-climate model study of past changes in the Brewer-Dobson circulation, *J. Geophys. Res. Atmos.*, *120*, 6742–6757, doi:10.1002/2014JD022843, 2015.

Oberländer-Hayn, S., E.P. Gerber, J. Abalichin, H. Akiyoshi, A. Kerschbaumer, A. Kubin, M. Kunze, U. Langematz, S. Meul, M. Michou, O. Morgenstern, and L.D. Oman, Is the Brewer-Dobson circulation increasing or moving upward?, *Geophys. Res. Lett.*, *43*, 1772–1779, doi:10.1002/2015GL067545, 2016.

Olsen, M.A., K. Wargan, and S. Pawson, Tropospheric column ozone response to ENSO in GEOS-5 assimilation of OMI and MLS ozone data, *Atmos. Chem. Phys.*, *16*, 7091–7103, doi:10.5194/acp-16-7091-2016, 2016.

Oltmans, S.J., H. Vömel, D.J. Hofmann, K.H. Rosenlof, D. Kley, The increase in stratospheric water vapor from balloonborne, frostpoint hygrometer measurements at Washington, D.C., and Boulder, Colorado, *Geophys. Res. Lett.*, *2*, 3453–3457, doi:10.1029/2000GL012133, 2000.

Oman, L., D.W. Waugh, S. Pawson, R.S. Stolarski, and P.A. Newman, On the influence of anthropogenic forcings on changes in the stratospheric mean age, *J. Geophys. Res.*, *114*, D03105, doi:10.1029/2008JD010378, 2009.

Orr, A., T.J. Bracegirdle, J.S. Hoskings, T. Jung, J.D. Haigh, T. Phillips, and W. Feng, Possible dynamical mechanisms for Southern Hemisphere climate change due to the ozone hole, *J. Atmos. Sci.*, *69*, 2917–2932, doi:10.1175/JAS-D-11-0210.1, 2012.

Orr, A., T.J. Bracegirdle, J.S. Hoskings, W. Feng, H. Roscoe, and J.D. Haigh, Strong dynamical modulation of the cooling of the polar stratosphere associated with the Antarctic ozone hole, *J. Clim.*, *26*, 662–668, doi:10.1175/JCLI-D-12-00480.1, 2013.

Osprey, S.M., N. Butchart, J.R. Knight, A.A. Scaife, K. Hamilton, J.A. Anstey, V. Schenzinger, and C. Zhang, An unexpected disruption of the atmospheric quasi-biennial oscillation, *Science*, *353* (6306), 1424–1427, doi:10.1126/science.aah4156, 2016.

Ossó, A., Y. Sola, K.H. Rosenlof, B. Hassler, J. Bech, and J. Lorente, How robust are trends in the Brewer–Dobson circulation derived from observed stratospheric temperatures?, *J. Clim., 28*, 3024–3040, doi:10.1175/JCLI-D-14-00295.1, 2015.

Palmeiro, F.M., N. Calvo, and R.R. Garcia, Future changes in the Brewer-Dobson circulation under different greenhouse gas concentrations in WACCM4, *J. Atmos. Sci.*, *71*, 2962–2975, doi:10.1175/JAS-D-13-0289.1, 2014.

Parkinson, C.L., and N.E. DiGirolamo, New visualizations highlight new information on the contrasting Arctic and Antarctic sea-ice trends since the late 1970s, *Remote Sens. Environ.*, *183*, 198–204, doi:10.1016/j.rse.2016.05.020, 2016.

Pauling, A.G., I.J. Smith, P.J. Langhorne, and C.M. Bitz, Time-dependent freshwater input from ice shelves: Impacts on Antarctic sea ice and the Southern Ocean in an Earth system model, *Geophys. Res. Lett.*, *44*, 10,454–10,461, doi:10.1002/2017GL075017, 2017.

Peings Y., J. Cattiaux, S. Vavrus, and G. Magnusdottir, Late 21st century changes of the mid-latitude

atmospheric circulation in the CESM large ensemble, *J. Clim.*, *30*, 5943–5960, doi:10.1175/JCLI-D-16-0340.1, 2017.

Ploeger, F., M. Abalos, T. Birner, P. Konopka, B. Legras, R. Müller, and M. Riese, Quantifying the effects of mixing and residual circulation on trends of stratospheric mean age of air, *Geophys. Res. Lett.*, *42*, 2047–2054, doi:10.1002/2014GL062927, 2015.

Ploeger, F., and T. Birner, Seasonal and inter-annual variability of lower stratospheric age of air spectra, *Atmos. Chem. Phys.*, *16*, 10195–10213, doi:10.5194/acp-16-10195-2016, 2016.

Plumb, R.A., Stratospheric transport, *J. Met. Soc. Japan*, *80*, 793–809, doi:10.2151/jmsj.80.793, 2002.

Polvani, L.M., S.J. Camargo, and R.R. Garcia, The importance of the Montreal Protocol in mitigating the potential intensity of tropical cyclones, *J. Clim.*, *29*, 2275–2289, doi:10.1175/JCLI-D-15-0232.1, 2016.

Polvani, L.M., L. Wang, V. Aquila, and D.W. Waugh, The impact of ozone depleting substances on tropical upwelling, as revealed by the absence of lower stratospheric cooling since the late 1990s, *J. Clim.*, *30*, 2523–2534, doi:10.1175/JCLI-D-16-0532.1, 2017.

Polvani, L.M., M. Abalos, R. Garcia, D. Kinnison, and W.J. Randel, Significant weakening of Brewer-Dobson circulation trends over the 21st century as a consequence of the Montreal Protocol, *Geophys. Res. Lett.*, *45*, doi:10.1002/2017GL075345, 2018.

Prather, M., P. Midgley, F.S. Rowland, and R. Stolarski, The ozone layer: The road not taken, *Nature*, *381*, 551–554, doi:10.1038/381551a0, 1996.

Previdi, M., and L.M. Polvani, Impact of the Montreal Protocol on Antarctic surface mass balance and implications for global sea level rise, *J. Clim.*, *30* (18), 7247–7253, doi:10.1175/JCLI-D-17-0027.1, 2017.

Purich, A., W. Cai, M.H. England, and T. Cowan, Evidence for link between modelled trends in Antarctic sea ice and underestimated westerly wind changes, *Nat. Commun.*, *7*, (10409), doi:10.1038/ncomms10409, 2016a.

Purich, A., M.H. England, W. Cai, Y. Yoshimitsu, A. Timmermann, F.C. Fyfe, L. Frankcombe, G.A. Meehl, and J.M. Arblaster, Tropical Pacific SST drivers of recent Antarctic sea ice trends, *J. Clim.*, *29*, 8931–8948, doi:10.1175/JCLI-D-16-0440.1, 2016b.

Purich, A., M.H. England, W. Cai, A. Sullivan, and P.J. Durack, Impacts of broad-scale surface freshening of the Southern Ocean in a coupled climate model, *J. Clim.*, *31*, 2613–2632, doi:10.1175/JCLI-D-17-0092.1, 2018.

Quan, X.W., M.P. Hoerling, J. Perlwitz, H.F. Diaz, and T. Xu, How fast are the tropics expanding?, *J. Clim.*, *27* (5), 1999–2013, doi:10.1175/JCLI-D-13-00287.1, 2014.

Randel, W.J., A.K. Smith, F. Wu, C.-Z. Zou, and H. Qian, Stratospheric temperature trends over 1979–2015 derived from combined SSU, MLS and SABER satellite observations, *J. Clim.*, *29*, 4843–4859, doi:10.1175/JCLI-D-15-0629.1, 2016.

Randel, W.J., L. Polvani, F. Wu, D.E. Kinnison, C.-Z. Zou, and C. Mears, Troposphere-stratosphere temperature trends derived from satellite data compared with ensemble simulations from WACCM, *J. Geophys. Res. Atmos.*, *122*, 9651–9667, doi:10.1002/2017JD027158, 2017.

Ray, E.A., F.L. Moore, K.H. Rosenlof, S.M. Davis, H. Boenisch, O. Morgenstern, D. Smale, E. Rozanov, M. Hegglin, G. Pitari, E. Mancini, P. Braesicke, N. Butchart, S. Hardiman, F. Li, K. Shibata, and D.A. Plummer, Evidence for changes in stratospheric transport and mixing over the past three decades based on multiple data sets and tropical leaky pipe analysis, *J. Geophys. Res.*, *115*, D21304, doi:10.1029/2010JD014206, 2010.

Ray, E.A., F.L. Moore, K.H. Rosenlof, S.M. Davis, C. Sweeney, P. Tans, T. Wang, J.W. Elkins, H. Bonisch, A. Engel, S. Sugawara, T. Nakazawa, and S. Aoki, Improving stratospheric transport trend analysis based on SF_6 and CO_2 measurements, *J. Geophys. Res. Atmos.*, *119*, 14,110–14,128, doi:10.1002/2014JD021802, 2014.

Ray, E.A., F.L. Moore, K.H. Rosenlof, D.A. Plummer, F. Kolonjari, and K.A. Walker, An idealized stratospheric model useful for understanding differences between long-lived trace gas measurements and global chemistry-climate model output, *J. Geophys. Res. Atmos.*, *121*, doi:10.1002/2015JD024447, 2016.

Rea, G., A. Riccio, F. Fierli, F. Cairo, and C. Cagnazzo, Stratosphere-resolving CMIP5 models simulate different changes in the Southern Hemisphere, *Clim. Dyn.*, *50*, (5/6), 2239–2255, doi:10.1007/s00382-017-3746-2, 2018.

Revell, L.E., F. Tummon, A. Stenke, T. Sukhodolov, A. Coulon, E. Rozanov, H. Garny, V. Grewe, and T.

Peter, Drivers of the tropospheric ozone budget throughout the 21st century under the medium-high climate scenario RCP 6.0, *Atmos. Chem. Phys.*, *15*, 5887–5902, doi:10.5194/acp-15-5887-2015, 2015.

Revell, L.E., A. Stenke, E. Rozanov, W. Ball, S. Lossow, and T. Peter, The role of methane in projections of 21st century stratospheric water vapour, *Atmos. Chem. Phys.*, *16*, 13,067–13,080, doi:10.5194/acp-16-13067-2016, 2016.

Rieder, H.E., L.M. Polvani, and S. Solomon, Distinguishing the impacts of ozone-depleting substances and well-mixed greenhouse gases on Arctic stratospheric ozone and temperature trends, *Geophys. Res. Lett.*, *41* (7), 2652–2660, doi:10.1002/2014GL059367, 2014.

Ritter, R., P. Landschützer, N. Gruber, A.R. Fay, Y. Iida, S. Jones, S. Nakaoka, G.-H. Park, P. Peylin, C. Rödenbeck, K.B. Rodgers, J.D. Shutler, and J. Zeng, Observation-based trends of the Southern Ocean carbon sink, *Geophys. Res. Lett.*, *44*, 12,339–12,348, doi:10.1002/2017GL074837, 2017.

Rosenblum, E., and I. Eisenman, Sea ice trends in climate models only accurate in runs with biased global warming, *J. Clim.*, *30*, 6265–6278, doi:10.1175/JCLI-D-16-0455.1, 2017.

Rosenlof, K.H., S.J. Oltmans, D. Kley, J.M. Russell III, E.-W. Chiou, W.P. Chu, D.G. Johnson, K.K. Kelly, H.A. Michelsen, G.E. Nedoluha, E.E. Remsberg, G.C. Toon, and M.P. McCormick, Stratospheric water vapor increases over the past half century, *Geophys. Res. Lett.*, *28*,1195–1199, doi:10.1029/2000GL012502, 2001.

Rosenlof, K.H., and G.C. Reid, Trends in the temperature and water vapor content of the tropical lower stratosphere: Sea surface connection, *J. Geophys. Res.*, *113*, D06107, doi:10.1029/2007JD009109, 2008.

Saunois, M., P. Bousquet, B. Poulter, A. Peregon, P. Ciais, J.G. Canadell, E.J. Dlugokencky, G. Etiope, D. Bastviken, S. Houweling, G. Janssens-Maenhout, F.N. Tubiello, S. Castaldi, R.B. Jackson, M. Alexe, V.K. Arora, D.J. Beerling, P. Bergamaschi, D.R. Blake, G. Brailsford, V. Brovkin, L. Bruhwiler, C. Crevoisier, P. Crill, C. Curry, C. Frankenberg, N. Gedney, L. Höglund-Isaksson, M. Ishizawa, A. Ito, F. Joos, H.-S. Kim, T. Kleinen, P. Krummel J.-F. Lamarque, R. Langenfelds, R. Locatelli, T. Machida, S. Maksyutov, K.C. McDonald, J. Marshall, J.R. Melton, I. Morino, S. O'Doherty, F.-J.W. Parmentier, P.K. Patra, C. Peng, S. Peng, G.P. Peters, I. Pison, C. Prigent, R. Prinn, M. Ramonet, W.J. Riley, M. Saito, R. Schroeder, I.J. Simpson, R. Spahni, P. Steele, A. Takizawa, B.F. Thornton, H. Tian, Y. Tohjima, N. Viovy, A. Voulgarakis, M. van Weele, G. van der Werf, R. Weiss, C. Wiedinmyer, D.J. Wilton, A. Wiltshire, D. Worthy, D.B. Wunsch, X. Xu, Y. Yoshida, B. Zhang, Z. Zhang, and Q. Zhu, The global methane budget 2000–2012, *Earth Syst. Sci. Data*, *8*, 697–751, doi:10.5194/essd-8-697-2016, 2016.

Schirber, S., E. Manzini, T. Krismer, and M. Giorgetta, The quasi-biennial oscillation in a warmer climate: Sensitivity to different gravity wave parameterizations, *Clim. Dyn., 45,* 825–836, doi:10.1007/s00382-014-2314-2, 2014, 2015.

Schneider, D., C. Deser, and T. Fan, Comparing the impacts of tropical SST variability and polar tratospheric ozone loss on the Southern Ocean westerly winds, *J. Clim.*, *28*, 9350–9372, doi:10.1175/JCLI-D-15-0090.1, 2015.

Schneider, D.P., and C. Deser, Tropically driven and externally forced patterns of Antarctic sea ice change: Reconciling observed and modeled trends, *Clim. Dyn., 50*, (11/12), 4599–4618, doi:10.1007/s00382-017-3893-5, 2018.

Schwartz, M.J., W.G. Read, M.L. Santee, N.J. Livesey, L. Froidevaux, A. Lambert, and G.L. Manney, Convectively injected water vapor in the North American summer lowermost stratosphere, *Geophys. Res. Lett.*, *40*, 2316–2321, doi:10.1002/grl.50421, 2013.

Seidel, D.J., J. Li, C. Mears, I. Moradi, J. Nash, W.J. Randel, R. Saunders, D.W.J. Thompson, and C.-Z. Zou, Stratospheric temperature changes during the satellite era, *J. Geophys. Res. Atmos.*, *121*, (2), 664–681, doi:10.1002/2015JD024039, 2016.

Sekiya, T., and K. Sudo, Roles of transport and chemistry processes in global ozone change on interannual and multidecadal time scales, *J. Geophys. Res.*, *119*, 4903–4921, doi:10.1002/2013JD020838, 2014.

Seviour, W.J., A. Gnanadesikan, and D.W. Waugh, The transient response of the Southern Ocean to stratospheric ozone depletion, *J. Clim.*, *29* (20), 7383–7396, doi:10.1175/JCLI-D-16-0198.1, 2016.

Seviour, W.J.M., Weakening and shift of the Arctic stratospheric polar vortex: Internal variability or forced response?, *Geophys. Res. Lett.*, *44*, doi:10.1002/2017GL073071, 2017.

Seviour, W.J.M., D.W. Waugh, L.M. Polvani, G.J.P. Correa, and C.I. Garfinkel, Robustness of the simulated tropospheric response to ozone depletion, *J. Clim.*, *30*, 2577–2585, doi:10.1175/JCLI-D-16-0817.1, 2017a.

Seviour, W.J.M., A. Gnanadesikan, D.W. Waugh, and M.-A. Pradal, Transient response of the Southern Ocean to changing ozone: Regional responses and physical mechanisms, *J. Clim.*, *30,* 2463–2480, doi:10.1175/JCLI-D-16-0474.1, 2017b.

Shepherd, T.G., Transport in the Middle Atmosphere, *J. Meteorol. Soc. Japan, 85B*, 165–191, doi:102151/jmsj.85B.165, 2007.

Sherwood, S.C., and N. Nishant, Atmospheric changes through 2012 as shown by iteratively homogenized radiosonde temperature and wind data (IUKv2), *Environ. Res. Lett., 10* (5), doi:10.1088/1748-9326/10/5/054007, 2015.

Sheshadri, A., R.A. Plumb, and D.I.V. Domeisen, Can the delay in Antarctic polar vortex breakup explain recent trends in surface westerlies?, *J. Atmos. Sci.*, *71* (2), 566– 573, doi:10.1175/JAS-D-12-0343.1, 2014.

Sheshadri, A., and R.A. Plumb, Sensitivity of the surface responses of an idealized AGCM to the timing of imposed ozone depletion-like polar stratospheric cooling, *Geophys. Res. Lett.*, *43*, 2330–2336, doi:10.1002/2016GL067964, 2016.

Sigmond, M., J.C. Fyfe, and J.F. Scinocca, Does the ocean impact the atmospheric response to stratospheric ozone depletion?, *Geophys. Res. Lett.*, *37*, L12706, doi:10.1029/2010GL043773, 2010.

Sigmond, M., and J.C. Fyfe, The Antarctic sea ice response to the ozone hole in climate models, *J. Clim.*, *27* (3), 1336–1342, doi:10.1175/JCLI-D-13-00590.1, 2014.

Sigmond, M., and T.G. Shepherd, Compensation between resolved wave driving and parameterized orographic gravity wave driving of the Brewer–Dobson circulation and its response to climate change, *J. Clim.*, *27*, 5601–5610, doi:10.1175/JCLI-D-13-00644.1, 2014.

Simmons, A.J., P. Poli, D.P. Dee, P. Berrisford, H. Hersbach, S. Kobayashi, and C. Peubey, Estimating low-frequency variability and trends in atmospheric temperature using ERA-Interim, *Q. J. R. Meteorol. Soc.*, *140*, 329–353, doi:10.1002/qj.2317, 2014.

Simpson, I.R., and L.M. Polvani, Revisiting the relationship between jet position, forced response, and annular mode variability in the southern midlatitudes, *Geophys. Res. Lett.*, *43*, 2896–2903, doi:10.1002/2016GL067989, 2016.

Simpson, I.R., P. Hitchcock, R. Seager, Y. Wu, and P. Callaghan, The downward influence of uncertainty in the Northern Hemisphere stratospheric polar vortex response to climate change, *J. Clim.*, *31*, 6371–639, doi:10.1175/JCLI-D-18-0041.1, 2018.

Škerlak, B., M. Sprenger, and H. Wernli, A global climatology of stratosphere-troposphere exchange using the ERA-Interim data set from 1979 to 2011, *Atmos. Chem. Phys.*, *14*, 913–937, doi:10.5194/acp-14-913-2014, 2014.

Smalley, K.M., A.E. Dessler, S. Bekki, M. Deushi, M. Marchand, O. Morgenstern, D.A. Plummer, K. Shibata, Y. Yamashita, and G. Zeng, Contribution of different processes to changes in tropical lower-stratospheric water vapor in chemistry–climate models, *Atmos. Chem. Phys.*, *17*, 8031–8044, doi:10.5194/acp-17-8031-2017, 2017.

Smith, K.L., and L.M. Polvani, The surface impacts of Arctic stratospheric ozone anomalies, *Environ. Res. Lett.*, *9*, (7), doi:10.1088/1748-9326/9/7/074015, 2014.

Smith, K.L., and R.K. Scott, The role of planetary waves in the tropospheric jet response to stratospheric cooling, *Geophys. Res. Lett.*, *43*, 2904–2911, doi:10.1002/2016GL067849, 2016.

Smith, K.L., and L.M. Polvani, Spatial patterns of recent Antarctic surface temperature trends and the importance of natural variability: Lessons from multiple reconstructions and the CMIP5 models, *Clim. Dyn.*, 48 (7/8), 2653–2670, doi:10.1007/s00382-016-3230-4, 2017.

Solman, S.A., and I. Orlanski, Climate change over the extratropical Southern Hemisphere: The tale from an ensemble of reanalysis datasets, *J. Clim.*, *29*, 1673–1687, doi:10.1175/JCLI-D-15-0588.1, 2016.

Solomon, A., A.M. Polvani, K.L. Smith, and R.P. Abernathey, The impact of ozone depleting substances on the circulation, temperature, and salinity of the Southern Ocean: An attribution study with CESM1 (WACCM), *Geophys. Res. Lett.*, *42*, (13), 5547–5555, doi:10.1002/2015GL064744, 2015.

Solomon, A., L.M. Polvani, D.W. Waugh, and S.M. Davis, Contrasting upper and lower atmospheric metrics of tropical expansion in the Southern Hemisphere, *Geophys. Res. Lett., 43* (19), doi:10.1002/2016GL070917, 2016.

Solomon, A., and L.M. Polvani, Highly significant responses to anthropogenic forcings of the midlatitude jet in the Southern Hemisphere, *J. Clim.*, *29* (9), 3463–3470, doi: 0.1175/JCLI-D-16-0034.1, 2016.

Solomon, S., S. Borrmann, R.R. Garcia, R. Portmann, L. Thomason, L.R. Poole, D. Winker, and M.P. McCormick, Heterogeneous chlorine chemistry in the tropopause region, *J. Geophys. Res.*, *102*, 21,411–21,429, doi:10.1029/97JD01525, 1997.

Solomon, S., D.J. Ivy, D. Kinnison, M.J. Mills, R.R. Neely, III, and A. Schmidt, Emergence of healing in the Antarctic ozone layer, *Science, 353* (6296), 269–274, doi:10.1126/science.aae0061, 2016.

Solomon, S., D. Ivy, M. Gupta, J. Bandoro, B. Santer, Q. Fu, P. Lin, R.R. Garcia, D. Kinnison, and M. Mills, Mirrored changes in Antarctic ozone and stratospheric temperature in the late 20th versus early 21st centuries, *J. Geophys. Res. Atmos.*, *122*, 8940–8950, doi:10.1002/2017JD026719, 2017.

Son, S.-W., E.P. Gerber, J. Perlwitz, L.M. Polvani, N.P. Gillett, K.-H. Seo, V. Eyring, T.G. Shepherd, D. Waugh, H. Akiyoshi, J. Austin, A. Baumgaertner, S. Bekki, P. Braesicke, C. Brühl, N. Butchart, M.P. Chipperfield, D. Cugnet, M. Dameris, S. Dhomse, S. Frith, H. Garny, R. Garcia, S.C. Hardiman, P. Jöckel, J.F. Lamarque, E. Mancini, M. Marchand, M. Michou, T. Nakamura, O. Morgenstern, G. Pitari, D.A. Plummer, J. Pyle, E. Rozanov, J.F. Scinocca, K. Shibata, D. Smale, H. Teyssèdre, W. Tian, and Y. Yamashita, Impact of stratospheric ozone on Southern Hemisphere circulation change: A multimodel assessment, *J. Geophys. Res.*, *115*, D00M07, doi:10.1029/2010JD014271, 2010.

Son, S.-W., A. Purich, H.H. Hendon, B.-M. Kim, and L.M. Polvani, Improved seasonal forecast using ozone hole variability?, *Geophys. Res. Lett.*, *40*, 6231–6235, doi: 10.1002/2013GL057731, 2013.

Son, S.-W., B-R Han, C.I. Garfinkel, S.-Y. Kim, P. Rokjin, N.L. Abraham, H. Akiyoshi, A.T. Archibald, N. Butchart, M.P. Chipperfield, M. Dameris, M. Deushi, S.S. Dhomse, S.C. Hardiman, P. Jöckel, D. Kinnison, M. Michou, O. Morgenstern, F.M. O'Connor, L.D. Oman, D.A. Plummer, A. Pozzer, L.E. Revell, E. Rozanov, A. Stenke, K. Stone, S. Tilmes, Y. Yamashita, and G. Zeng, Tropospheric jet response to Antarctic ozone depletion: An update with Chemistry-Climate Model Initiative (CCMI) models, *Environ. Res. Lett.*, *13*, (5), doi:10.1088/1748-9326/aabf21, 2018.

SPARC CCMVal (Stratosphere-troposphere Processes And their Role in Climate) *SPARC Report on the Evaluation of Chemistry-Climate Models*, edited by V. Eyring, T.G. Shepherd, and D.W. Waugh, *SPARC Report No. 5*, WCRP-132, WMO/td-No.1526, available at: http://www.atmosp.physics.utoronto.ca/SPARC/ccmval_final/index.php, 2010.

Staten, P.W., J.J. Rutz, T. Reichler, and J. Lu, Breaking down the tropospheric circulation response by forcing, *Clim. Dyn.*, *39* (9/10), 2361–2375, doi:10.1007/s00382-011-1267-y 2012.

Staten, P.W., and T. Reichler, On the ratio between shifts in the eddy-driven jet and the Hadley-cell edge, *Clim. Dyn.*, *42* (5/6), 1229–1242, doi:10.1007/s00382-013-1905-7, 2014.

Steptoe, H., L.J. Wilcox, and E.J. Highwood, Is there a robust effect of anthropogenic aerosols on the Southern Annular Mode?, *J. Geophys. Res. Atmos.*, *121* (17), doi:10.1002/2015JD024218, 2016.

Stiller, G.P., T. von Clarmann, F. Haenel, B. Funke, N. Glatthor, U. Grabowski, S. Kellmann, M. Kiefer, A. Linden, S. Lossow, and M. López-Puertas, Observed temporal evolution of global mean age of stratospheric air for the 2002 to 2010 period, *Atmos. Chem. Phys.*, *12*, 3311–3331, doi:10.5194/acp-12-3311-2012, 2012.

Stiller, G.P., F. Fierli, F. Ploeger, C. Cagnazzo, B. Funke, F.J. Haenel, T. Reddmann, M. Riese, and T. von Clarmann, Shift of subtropical transport barriers explains observed hemispheric asymmetry of decadal trends of age of air, *Atmos. Chem. Phys.*, *17*, 11,177–11,192, doi:10.5194/acp-17-11177-2017, 2017.

Stohl, A., P. Bonasoni, P. Cristofanelli, W. Collins, J. Feichter, A. Frank, C. Forster, E. Gerasopoulos, H. Gäggeler, P. James, T. Kentarchos, H. Kromp-Kolb, B. Krüger, C. Land, J. Meloen, A. Papayannis, A. Priller, P. Seibert, M. Sprenger, G.J. Roelofs, H.E. Scheel, C. Schnabel, P. Siegmund, L. Tobler, T. Trickl, H. Wernli, V. Wirth, P. Zanis, and C. Zerefos, Stratosphere-troposphere exchange: A review, and what we have learned from STACCATO, *J. Geophys. Res.*, *108* (D12), doi:10.1029/2002JD002490, 2003.

Stolarski, R.S., A.R. Douglass, P.A. Newman, S. Pawson, and M.R. Schoeberl, Relative contribution of greenhouse gases and ozone-depleting substances to temperature trends in the stratosphere:

A chemistry-climate model study, *J. Clim.*, *23*, 28–42, doi:10.1175/2009JCLI2955.1, 2010.

Stone, K.A., O. Morgenstern, D.J. Karoly, A.R. Klekociuk, W.J. French, N.L. Abraham, and R. Schofield, Evaluation of the ACCESS-chemistry-climate model for the Southern Hemisphere, *Atmos. Chem. Phys.*, *16* (4), 2401–2415, doi:10.5194/acp-16-2401-2016, 2016.

Stuecker, M.F., C.M. Bitz, and K.C. Armour, Conditions leading to the unprecedented low Antarctic sea ice extent during the 2016 austral spring season, *Geophys. Res. Lett.*, *44*, doi:10.1002/2017GL074691, 2017.

Sun, L., G. Chen, and W.A. Robinson, The role of stratospheric polar vortex breakdown in Southern Hemisphere climate trends, *J. Atmos. Sci.*, *71* (7), 2335–2353, doi:10.1175/JAS-D-13-0290.1, 2104.

Swart, N.C., and J.C. Fyfe, Observed and simulated changes in the Southern Hemisphere surface westerly wind-stress, *Geophys. Res. Lett.*, *39*, doi:10.1029/2012GL052810, 2012.

Swart, N.C., J.C. Fyfe, O.A. Saenko, and M. Eby, Wind-driven changes in the ocean carbon sink, *Biogeosci., 11*, 6107–6117, doi:10.5194/bg-11-6107-2014, 2014.

Swart, N.C., J.C. Fyfe, N. Gillett, and G.J. Marshall, Comparing trends in the southern annular mode and surface westerly jet, *J. Clim.*, *28*, 8840–8859, doi:10.1175/JCLI-D-15-0334.1, 2015.

Tao, L., Y. Hu, and J. Liu, Anthropogenic forcing on the Hadley circulation in CMIP5 simulations, *Clim. Dyn., 46*, 3337–3350, doi:10.1007/s00382-015-2772-1, 2016.

Thomas, J.L., D.W. Waugh, and A. Gnanadesikan, Southern Hemisphere extratropical circulation: Recent trends and natural variability, *Geophys. Res. Lett., 42*, 13, 5508–5515, doi:10.1002/2015GL064521, 2015.

Thompson, D.W.J., J.C. Furtado, and T.G. Shepherd, On the tropospheric response to anomalous stratospheric wave drag and radiative heating, *J. Atmos. Sci.*, *63* (10), 2616–2629, doi:10.1175/JAS3771.1, 2006.

Thompson, D.W.J., D.J. Seidel, W.J. Randel, C.-Z. Zou, A.H. Butler, R. Lin, C. Long, C. Mears, and A. Osso, The mystery of recent stratospheric temperature trends, *Nature*, *491*, 692–697, doi:10.1038/nature11579, 2012.

Thorne, P.W., D.E. Parker, S.F.B. Tett, P.D. Jones, M. McCarthy, H. Coleman, and P. Brohan, Revisiting radiosonde upper-air temperatures from 1958 to 2002, *J. Geophys. Res.*, *110*, doi:10.1029/2004JD005753, 2005.

Turner, J., J.S. Hosking, G.J. Marshall, T. Phillips, and T.J. Bracegirdle, Antarctic sea ice increase consistent with intrinsic variability of the Amundsen Sea Low, *Clim. Dyn.*, *46*, 2391–2402, doi:10.1007/s00382-015-2708-9, 2015.

Turner, J., H. Lu, I. White, J.C. King, T. Phillips, J.S. Hosking, T.J. Bracegirdle, G.J. Marshall, R. Mulvaney, and P. Deb, Absence of 21st century warming on Antarctic Peninsula consistent with natural variability, *Nature*, *535*, 411–415, doi:10.1038/nature18645, 2016.

Turner, J., T. Phillips, G.J. Marshall, J.S. Hosking, J.O. Pope, T.J. Bracegirdle, and P. Deb, Unprecedented springtime retreat of Antarctic sea ice in 2016, *Geophys. Res. Lett.*, *44*, 6868–6875, doi:10.1002/2017GL073656, 2017.

Ueyama, R., E.J. Jensen, L. Pfister, G.S. Diskin, T.P. Bui, and J.M. Dean-Day, Dehydration in the tropical tropopause layer: A case study for model evaluation using aircraft observations, *J. Geophys. Res. Atmos.*, *119*, 5299–5316, doi:10.1002/2013JD021381, 2014.

Ummenhofer, C.C., P.C. McIntosh, M.J. Pook, J.S. Risbey, Impact of surface forcing on Southern Hemisphere atmospheric blocking in the Australia-New Zealand sector, *J. Clim.*, *26* (21), 8476–8494, doi:10.1175/JCLI-D-12-00860.1, 2013.

USGCRP, *Climate Science Special Report: Fourth National Climate Assessment, Volume I*, edited by D.J. Wuebbles, D.W. Fahey, K.A. Hibbard, D.J. Dokken, B.C. Stewart, and T.K. Maycock, U.S. Global Change Research Program, Washington, D.C., USA, 470 pp., doi:10.7930/J0J964J6, 2017.

Velders, G.J.M., S.O. Andersen, J.S. Daniel, D.W. Fahey, and M. McFarland, The Importance of the Montreal Protocol in protecting climate, *Proc. Natl. Acad. Sci.*, *104* (12), 4814–4819, doi:10.1073/pnas.0610328104, 2007.

Vera, C.S., and L. Díaz, Anthropogenic influence on summer precipitation trends over South America in CMIP5 models, *Int. J. Climatol.*, *35* (10), 3172–3177, doi:10.1002/joc.4153/full, 2015.

Vernier, J.-P., L.W. Thomason, and J. Kar, CALIPSO detection of an Asian tropo-

pause aerosol layer, *Geophys. Res. Lett.*, *38*, doi:10.1029/2010GL046614, 2011.

Vernier, J.-P., T.D. Fairlie, M. Natarajan, F.G. Wienhold, J., Bian, B.G. Martinsson, S. Crumeyrolle, L.W. Thomason, and K. M. Bedka, Increase in upper tropospheric and lower stratospheric aerosol levels and its potential connection with Asian pollution, *J. Geophys. Res. Atmos.*, *120*, 1608–1619. doi:10.1002/2014JD022372, 2015.

Villalba, R.A. Lara, M. Masiokas, R. Urrutia, E.R. Cook, D. Christie, I.A. Mundo, J. Boninsegna, P. Fenwick, R. Neukom, K. Allen, M. Morales, D.C. Araneo, G. Marshall, A. Srur, J.C. Aravena, and J. Palmer, Unusual Southern Hemisphere tree growth patterns induced by changes in the southern annular mode, *Nat. Geosci.*, *5*, 793–798, doi:10.1038/NGEO1613, 2012.

Wang, G., W. Cai, and A. Purich, Trends in Southern Hemisphere wind-driven circulation in CMIP5 models over the 21st century: Ozone recovery versus greenhouse forcing, *J. Geophys. Res. Ocean*, *119,* 2974–2984, doi:10.1002/2013JC009589, 2014.

Wang, L., C.-Z. Zou, and H. Qian, Construction of stratospheric temperature data records from Stratospheric Sounding Units, *J. Clim.*, *25*, 2931–2946, doi:10.1175/JCLI-D-11-00350.1, 2012.

Waugh, D.W., and T.M. Hall, Age of stratospheric air: Theory, observations, and models, *Rev. Geophys.*, *40* (4), doi:10.1029/2000RG000101, 2002.

Waugh D.W., Age of stratospheric air, *Nat. Geosci.*, *2*, (1), 14–16, doi:10.1038/ngeo397, 2009.

Waugh, D.W., L. Oman, P.A. Newman, R.S. Stolarski, S. Pawson, J.E. Nielsen, and J. Perlwitz, Effect of zonal asymmetries in stratospheric ozone on simulated Southern Hemisphere climate trends, *Geophys. Res. Lett.*, *36* (18), doi:10.1029/2009GL040419, 2009.

Waugh, D.W., C.I. Garfinkel, and L.M. Polvani, Drivers of the recent tropical expansion in the Southern Hemisphere: Changing SSTs or ozone depletion?, *J. Clim.*, *28*, 6581–6586, doi:10.1175/JCLI-D-15-0138.1, 2015.

Watanabe, S., K. Hamilton, S. Osprey, Y. Kawatani, and E. Nishimoto, First successful hindcasts of the 2016 Disruption of the stratospheric quasibiennial oscillation, *Geophys. Res. Lett.,44*, doi:10.1002/2017GL076406, 2017.

Wenzel, S., V. Eyring, E.P. Gerber, and A.Yu., Karpechko, Constraining future summer austral jet stream positions in the CMIP5 ensemble by process-oriented multiple diagnostic regression, *J. Clim.*, *29,* 673–687, doi:10.1175/JCLI-D-15-0412.1, 2016.

Wilcox, L.J., A.J. Charlton-Perez, and L.J. Gray, Trends in austral jet position in ensembles of high- and low-top CMIP5 models, *J. Geophys. Res.*, *117*, doi:10.1029/2012JD017597, 2012.

Wilcox, L.J., and A.J. Charlton-Perez, Final warming of the Southern Hemisphere polar vortex in high-and low-top CMIP5 models, *J. Geophys. Res. Atmos.*, *118* (6), 2535–2546, doi:10.1002/jgrd.50254, 2013.

Wu, Y., and L.M. Polvani, Recent trends in extreme precipitation and temperature over southeastern South America: The dominant role of stratospheric ozone depletion, *J. Clim.*, *30*, 6433–6441, doi:10.1175/JCLI-D-17-0124.1, 2017.

Xie, F., J. Li, W. Tian, Q. Fu, F.F. Jin, Y. Hu, J. Zhang, W. Wang, C. Sun, J. Feng, and Y. Yang, A connection from Arctic stratospheric ozone to El Niño-Southern oscillation, *Environ. Res. Lett.*, *11* (12), doi:10.1088/1748-9326/11/12/124026, 2016.

Yang, H., L. Sun, and G. Chen, Separating the mechanisms of transient responses to stratospheric ozone depletion–like cooling in an idealized atmospheric model, *J. Atmospheric Sci.*, *72* (2), 763–773, doi:10.1175/JAS-D-13-0353.1, 2015.

Yang, H., G. Chen, Q. Tang, and P. Hess, Quantifying isentropic stratosphere-troposphere exchange of ozone, *J. Geophys. Res. Atmos.*, *121*, 3372–3387, doi:10.1002/2015JD024180, 2016.

Young, P., K.H. Rosenlof, S. Solomon, S.C. Sherwood, Q. Fu, and J.-F Lamarque, Changes in stratospheric temperatures and their implications for changes in the Brewer–Dobson circulation, 1979–2005, *J. Clim.*, *25*, 1759–1772, doi:10.1175/2011JCLI4048.1, 2012.

Young, P.J., A.T. Archibald, K.W. Bowman, J.-F. Lamarque, V. Naik, D.S. Stevenson, S. Tilmes, A. Voulgarakis, O. Wild, D. Bergmann, P. Cameron-Smith, I. Cionni, W.J. Collins, S.B. Dalsøren, R.M. Doherty, V. Eyring, G. Faluvegi, L.W. Horowitz, B. Josse, Y.H. Lee, I.A. MacKenzie, T. Nagashima, D.A. Plummer, M. Righi, S.T. Rumbold, R.B. Skeie, D.T. Shindell, S.A. Strode, K. Sudo, S. Szopa, and G. Zeng, Pre-industrial to end 21st century projections of tropospheric ozone from the Atmospheric Chemistry and Climate Model Intercomparison Project (ACCMIP), *Atmos. Chem. Phys.*, *13*, 2063–2090, doi:10.5194/

acp-13-2063-2013, 2013.

Young, P.J., S.M. Davis, B. Hassler, S. Solomon, and K.H. Rosenlof, Modeling the climate impact of Southern Hemisphere ozone depletion: The importance of the ozone data set, *Geophys. Res. Lett.*, *41* (24), 9033–9039, doi:10.1002/2014GL061738, 2014.

Young, P.J., V. Naik, A.M. Fiore, A. Gaudel, J. Guo, M.Y. Lin, J.L. Neu, D.D. Parrish, H.E. Rieder, J.L. Schnell, S. Tilmes, O. Wild, L. Zhang, J. Ziemke, J. Brandt, A. Delcloo, R.M. Doherty, C. Geels, M.I. Hegglin, L. Hu, U. Im, R. Kumar, A. Luhar, L. Murray, D. Plummer, J. Rodriguez, A. Saiz-Lopez, M.G. Schultz, M.T. Woodhouse, and G. Zeng, Tropospheric Ozone Assessment Report: Assessment of global-scale model performance for global and regional ozone distributions, variability, and trends, *Elementa-Sci. Anthrop.*, *6*, (10), doi:10.1525/elementa.265, 2018.

Yu, P., D.M. Murphy, R.W. Portmann, O.B. Toon, K.D. Froyd, A.W. Rollins, R.-S. Gao, and K.H. Rosenlof, Radiative forcing from anthropogenic sulfur and organic emissions reaching the stratosphere, Geophys. *Res. Lett., 43*, 9361–9367, doi:10.1002/2016GL070153, 2016.

Yu, P., K.H. Rosenlof, S. Liu, H. Telg, T.D. Thornberry, A.W. Rollins, R.W. Portmann, Z. Bai, E.A. Ray, Y. Duan, L.L. Pan, O.B. Toon, J. Bian, and R.-S. Gao, Efficient transport of tropospheric aerosol into the stratosphere via the Asian summer monsoon anticyclone, *Proc. Natl. Acad. Sci.*, *114* (27), 6972–6977, doi:10.1073/pnas.1701170114, 2017.

Zappa, G., and T.G. Shepherd, Storylines of atmospheric circulation change for European regional climate impact assessment, *J. Clim.*, *30* (16), 6561–6577, doi:10.1175/JCLI-D-16-0807.1, 2017.

Zeng, G., and J.A. Pyle, Influence of El Ninõ Southern Oscillation on stratosphere/troposphere exchange and the global tropospheric ozone budget, *Geophys. Res. Lett.*, *32*, doi:10.1029/2004GL021353, 2005.

Zhang, H., T.L. Delworth, F. Zeng, G. Vecchi, K. Paffendorf, and L. Jia, Detection, Attribution, and Projection of Regional Rainfall Changes on (Multi-) Decadal Time Scales: A Focus on Southeastern South America, *J. Clim.*, *29* (23) 8515–8534, doi: 10.1175/JCLI-D-16-0287.1, 2016.

Zhang, J., W. Tian, M.P. Chipperfield, F. Xie, and J. Huang, Persistent shift of the Arctic polar vortex towards the Eurasian continent in recent decades, *Nat. Clim. Change*, *6*, 1094–1099, doi:10.1038/nclimate3136, 2016.

Zhang, L., T.L. Delworth, and L. Jia, Diagnosis of Decadal Predictability of Southern Ocean Sea Surface Temperature in the GFDL CM2.1 Model, *J. Clim.*, *30*, 6309–6328, doi:10.1175/JCLI-D-16-0537.1, 2017.

Zickfeld, K., S. Solomon, and D.M. Gilford, Centuries of thermal sea-level rise due to anthropogenic emissions of short-lived greenhouse gases, *Proc. Natl. Acad. Sci.*, *114* (4), 657–662, doi:10.1073/pnas.1612066114, 2017.

Zou, C.-Z., M. Goldberg, Z. Cheng, N. Grody, J. Sullivan, C. Cao, and D. Tarpley, Recalibration of microwave sounding unit for climate studies using simultaneous nadir overpasses, *J. Geophys. Res. Atmos.*, *111*, doi:10.1029/2005JD006798, 2006.

Zou, C.-Z., H. Qian, W. Wang, L. Wang, and C. Long, Recalibration and merging of SSU observations for stratospheric temperature trend studies, *J. Geophys. Res. Atmos.*, *119*, 13,180–13,205, doi:10.1002/2014JD021603, 2014.

Zou, C.-Z., and H. Qian, Stratospheric temperature climate data record from merged SSU and AMSU-A observations, *J. Atmos. Oceanic Technol.*, *33* (9), 1967–1984, doi:10.1175/JTECH-D-16-0018.1, 2016.

Chapter 6

Scenarios and Information for Policymakers

Lead Authors
L.J. Carpenter
J.S. Daniel

Coauthors
E.L. Fleming
T. Hanaoka
J. Hu
A.R. Ravishankara
M.N. Ross
S. Tilmes
T.J. Wallington
D.J. Wuebbles

Contributors
J.B. Burkholder
A. Engel
Ø. Hodnebrog
R. Hossaini
L.J.M. Kuijpers
S.A. Montzka
R.J. Salawitch
W.R. Tribett
G. Velders
H. Walter-Terrinoni

Review Editors
N.R.P Harris
M.J. Prather

Cover photo: The development of future scenarios of ODSs and HFCs are key products of the Montreal Protocol Scientific Assessment Panel. These products are developed using computer models that incorporate observed concentrations, production and consumption estimates, and the amounts of manufactured chemicals in existing equipment and application banks. These scenarios are an important part of the Executive Summary, which conveys policy relevant information to the Parties of the Montreal Protocol. Photo: Lynn Daniel and Konner Syed.

Chapter 6

Scenarios and Information for Policymakers

CONTENTS

Chapter 6

Scenarios and Information for Policymakers

SCIENTIFIC SUMMARY

In the sections below, we note the significance of various improvements in our understanding concerning actions related to the Montreal Protocol and its Amendments that could alter the recovery of the ozone layer and/or impact Earth's climate. As in previous Assessments, we use equivalent effective stratospheric chlorine (EESC) as a proxy for the amount of stratospheric ozone depletion caused by ozone-depleting substances (ODSs) that contain chlorine and/or bromine and reside in the atmosphere for more than a few months. The return of EESC to 1980 values is used as a metric to compare the effects of different future scenarios of production and emission of ozone-depleting gases on ozone layer recovery. In this chapter, we also use 2-D model simulations to estimate changes in future ozone depletion for these different scenarios. (Note that 3-D model projections of global and polar ozone and analyses of expected recovery dates are presented in Chapters 3 and 4. These calculations include changes in greenhouse gas levels and in atmospheric transport and are not expected to be equivalent to the EESC recovery dates). Our ability to predict future changes in the ozone layer is limited more by uncertainties in future levels of CO_2, CH_4, and N_2O than by uncertainties in the levels of ODSs, especially as we approach the 1980 values of EESC. Indeed, ozone levels in some regions of the atmosphere could exceed natural levels, due to climate change, with possible consequences to humans and natural ecosystems, assuming natural levels represent a harmonious balance. The influence of CO_2 occurs through its role in the climate system as a driver of change in temperature and atmospheric circulation. The influences of CH_4 and N_2O occur primarily through their roles as chemical reagents in the atmosphere. ODSs themselves are greenhouse gases, and their influence on climate and ozone layer depletion are intricately intertwined, even though we note them separately for clarity of presentation. Lastly, note that the various additional actions discussed below impact future ozone to a much smaller degree than what has already been accomplished by the Montreal Protocol.

Post-Kigali information of interest and concern

- **The Kigali Amendment to the Montreal Protocol, along with regional and national regulatory and voluntary actions taken before Kigali entered into force, is expected to substantially limit future climate forcing by HFCs.** Projections of HFC emissions that include compliance with Kigali Amendment control measures suggest that the radiative forcing (a metric for global warming) from HFCs, currently 0.025 W m^{-2} (not including HFC-23), will reach 0.13 W m^{-2} by 2050, about half as high as that projected without the Kigali Amendment and prior national and regional regulation. The estimated benefit of these actions is 2.8–4.1 Gt CO_2-eq. yr^{-1} of avoided Global Warming Potential (GWP)-weighted emissions by 2050. The projected surface temperature contribution from HFCs (excluding HFC-23) reduces from 0.3–0.5 °C to less than 0.1 °C in 2100 due to entry into force of the Kigali Amendment.

- **Options are available to further decrease the climate impact of HFCs.** Use of commercially available low-GWP alternatives in place of high-GWP HFCs in refrigeration and air-conditioning equipment, thermal insulating foam, metered-dose inhalers, fire protection, and miscellaneous HFC applications during the phasedown would further reduce climate change. Additional benefits would be gained by such actions via development of more energy-efficient equipment and thermal insulating foam that use these low-GWP replacements.

- **Sustained increases in anthropogenic chlorinated very short-lived substances (VSLSs Cl) emissions, as seen for CH_2Cl_2 in the 2000s, would decrease stratospheric ozone levels in the coming decades. However, observed growth rates of CH_2Cl_2 continue to be highly variable, and there is insufficient information to**

confidently predict future concentrations. If the growth in emission rates seen during the first decade of this century continues, CH_2Cl_2 is projected to deplete as much column ozone between 2020 and 2060 as that by the controlled ODSs emitted during that period. However, such large growth projections do not account for a more recent reduction in the CH_2Cl_2 growth rate, nor have they been shown to be consistent with expectations for global demand over the coming decades. Any control of CH_2Cl_2 production and consumption under the Montreal Protocol would be rapidly effective, since this VSLS will be cleansed out of the stratosphere within a few years.

Ozone-depleting substances (ODSs) and equivalent effective stratospheric chlorine (EESC)

Below, we discuss potential changes in the projected trajectory of ozone depletion and EESC that result from improvements in our understanding of the emissions or other characteristics of individual gases or groups of gases. We reference these potential changes to the so-called baseline scenario—which should be considered a plausible future pathway for these gases. The baseline scenario for ODSs is developed from atmospheric concentration observations, combined with estimates of the amounts of ODSs in existing equipment or other products containing ODSs, referred to as banks. The 2018 baseline scenario for HFCs takes into account global control measures introduced by the Kigali Amendment and other regional and national actions. For all baseline scenarios, we assume that the long-lived greenhouse gases N_2O, CH_4, and CO_2 follow the Representative Concentration Pathway (RCP) 6.0 scenario. Note that for some of the metrics the combined consequence of these gases is generally not simply the addition of each of the changes. It is also important to recognize that the return date of EESC to 1980 levels is quite sensitive to any change in EESC concentration because of the relatively small rate at which EESC is projected to decline in the middle of this century.

- **Global emissions of CFC-11 derived from atmospheric observations show an increase in recent years that is not consistent with our understanding of release from its banks and suggests new global production that is not reported to the United Nations Environment Programme (UN Environment). If total emissions of CFC-11 were to continue at levels experienced from 2002–2016 (67 Gg yr^{-1}), the return of mid-latitude and polar EESC to the 1980 value would be delayed by about seven years and 20 years, respectively**. Such an assumption of continuing emissions implicitly assumes that the unidentified emissions will grow to counteract the expected decline in bank emissions.

- **Emissions from current ODS banks continue to be a slightly larger future contribution than ODS production to ozone layer depletion over the next four decades, assuming maximum production levels allowed by the Montreal Protocol.** Future business-as-usual emissions from HCFCs and from banks of CFCs and banks of halons are each projected to contribute roughly comparable amounts to EESC in the next few decades.

- **Elimination of future production of methyl bromide (CH_3Br) for quarantine and pre-shipment (QPS) applications, not controlled by the Montreal Protocol, would accelerate the return of mid-latitude EESC to 1980 levels by about a year**. Production for QPS use has remained relatively stable over the last two decades and now constitutes almost 90% of the reported production of CH_3Br since emissions from other uses have declined dramatically. Non-QPS applications of CH_3Br were completely phased out in 2015, except for approved critical use exemptions, which have declined by a factor of ~30 since 2005.

- **If CCl_4 emissions continue to decline at the rate observed over the last two decades of 2.5% yr^{-1}, future concentrations will be about 14 ppt higher in 2050 than projected in the previous Assessment**. CCl_4 emissions inferred from atmospheric observations continue to be much greater than those assumed from feedstock uses as reported to UN Environment; by-product emissions from chloromethane and perchloroethylene plants and fugitive emissions from the chlor-alkali process have been quantified as significant contributors to these additional emissions. Elimination of all CCl_4 emissions in 2020 would accelerate the return of mid-latitude EESC to 1980 levels by almost three years compared to the baseline scenario

of a continued emissions decrease of 2.5% yr^{-1}. Alternatively, if future emissions do not decline but remain at the current level, the return of mid-latitude EESC to 1980 levels would be delayed almost two years.

- **The return of mid-latitude EESC to 1980 levels is estimated to be delayed by almost two years compared to the previous Assessment, due primarily to the higher projected future concentrations of CCl_4.** The mid-latitude EESC change from CCl_4 alone leads to a delay larger than two years, but future CH_3Br baseline projections are now lower than in the previous Assessment and offset some of the effect from CCl_4. The delay in polar EESC returning to 1980 levels is slightly more than two years when compared with the previous Assessment. A new EESC formalism alters the time evolution of EESC and dates when EESC returns to 1980 levels, but it has little effect on the relative impacts of the various alternative future scenarios. When compared with the previous Assessment's EESC formalism, the new EESC formalism leads to a projected EESC return to the 1980 level 11 years later at mid-latitudes and by less than two years later at polar latitudes.

- **Reducing anthropogenic emissions of N_2O from those in RCP-6.0 to the Concerted Mitigation scenario[1] would have a similar positive impact on stratospheric ozone over the next four decades as eliminating production of HCFCs from 2020. This N_2O emissions reduction would have a larger benefit to climate over 2020–2060 than the sum of all the options for controlled ODSs considered (based on GWP-weighted emissions).**

Updates on the climate impact of gases controlled by the Montreal Protocol

- **Future emissions of HFC-23, a potent greenhouse gas and a by-product of HCFC-22 production, are expected to be limited by the Kigali Amendment**, which mandates the destruction of HFC-23 to the extent practicable. Globally, HCFC-22 is currently produced in roughly equal quantities for controlled emissive uses, which are declining, and for the uncontrolled feedstock uses, which grew rapidly over the last few decades but have recently stabilized. Future emission trends will largely depend on the extent to which HFC-23 is destroyed by HCFC-22 production facilities and the amount of HCFC-22 produced.

- **Future emissions of HFCs, HCFCs, and CFCs contribute approximately 60, 9, and 3 cumulative Gt CO_2-equivalent emissions, respectively, from 2020 to 2060 in the baseline scenario.** Of the 60 Gt CO_2-eq emissions from HFCs, 53 arise from future production. For reference, cumulative CO_2 emissions from fossil fuel usage are projected over this time period to be 1,700 Gt CO_2 in the RCP-6.0 scenario and 760 Gt CO_2 in the RCP-2.6 scenario. The total radiative forcing from CFC and HCFCs and their HFC replacements is projected to continue to increase gradually for the next decade or two. After that point, the ODS and HFC restrictions of the Montreal Protocol, if adhered to, ensure a continued decline in total RF from ODSs and their replacements through the rest of the century.

- **Global warming potentials, global temperature change potentials, and ozone depletion potentials of hundreds of HCFCs are presented, most for the first time in an assessment.** This comprehensive assessment includes all the HCFCs listed under Annex C, Group I of the Montreal Protocol, many of which did not have estimated GWPs at the time of the signing of the Kigali Amendment.

Updates on impacts of climate gases and other processes on future stratospheric ozone

In this section, we summarize potentially important impacts on the future of the ozone layer that could result from anthropogenic activity not associated with ODS production or consumption and not controlled by the Montreal Protocol. As noted above, a major issue is that uncertainties in future changes in the ozone layer will be influenced more by uncertainties in CO_2, CH_4, and N_2O levels than by uncertainties in the levels of ODSs, especially as we

[1] UNEP 2013. Drawing Down N_2O to Protect Climate and the Ozone Layer. A UNEP Synthesis Report. United Nations Environment Programme (UNEP), Nairobi, Kenya.

approach the 1980 values of EESC. Increases in greenhouse gas concentrations are predicted to lead to increases in upper-stratospheric ozone at all latitudes, with a more complex pattern of ozone changes in the lower stratosphere, including a decrease in low latitudes due to changes in dynamics and transport. These processes are discussed in detail in ***Chapters 3*** *and* ***4****. Note that natural forces such as large explosive volcanic eruptions could also adversely affect ozone recovery over the next decade, while ODS levels remain high.*

- **The wide range of possible future levels of CO_2, CH_4, and N_2O represents an important limitation to making accurate projections of the ozone layer.** Global mean warming as well as stratospheric cooling will drive ozone changes through both atmospheric circulation and chemistry. Future ozone levels depend on the path of greenhouse gas and aerosol emissions as well as the sensitivity of the climate system to these emissions. Future ODS atmospheric concentrations are more certain than atmospheric concentrations of climate forcing emissions, as long as there is adherence to the Montreal Protocol. This chapter considers various climate scenarios, using the Representative Concentration Pathways (RCPs) adopted by the IPCC for its Fifth Assessment Report (AR5). The Paris Agreement, with a stated objective to limit globally averaged warming to less than 2°C, requires emissions closest to RCP-2.6, the lowest emission scenario of all the RCP scenarios.

- **Intentional long-term geoengineering applications that substantially increase stratospheric aerosols to mitigate global warming by reflecting sunlight would alter stratospheric ozone.** The estimated magnitudes and even the sign of ozone changes in some regions are uncertain because of the high sensitivity to variables such as the amount, altitude, geographic location and type of injection, and the halogen loading. An increase of stratospheric sulfate aerosol burden in amounts sufficient to substantially reduce global radiative forcing would delay the recovery of the Antarctic ozone hole. Much less is known about the effects on ozone from geoengineering solutions using non-sulfate aerosols.

- **Rocket launches presently have a small effect on total stratospheric ozone (much less than 0.1%).** Space industry developments indicate that rocket emissions may increase more significantly than reported in the previous Assessment. Their impacts will depend on rocket design (particularly the altitude of emissions), launch vehicle sizes, launch rates, spaceport locations, and fuel types. Important gaps remain in understanding rocket emissions and their combined chemical, radiative, and dynamical impacts on the global stratosphere and in projections of launch rates. These gaps limit the confidence level of predictions of present and future impacts of rocket emissions on stratospheric ozone and suggest periodic assessments are warranted. The lifetime of the most important rocket emissions is limited, and the stratospheric accumulation of rocket-emitted black carbon and alumina particles varies in correspondence with global launch rates and altitude of emissions.

Update on other environmental impacts of Montreal Protocol gases

Here, we refer to all gases controlled under the Montreal Protocol and its various Amendments, including the Kigali Amendment, as Montreal Protocol Gases.

- **There is increased confidence that trifluoroacetic acid (TFA) produced from degradation of HFCs, HCFCs, and HFOs will not harm the environment over the next few decades.** This assessment is based on the current estimates of future use of hydrocarbons, HCFCs, and HFOs. It is noteworthy that HFCs and HCFCs have atmospheric lifetimes long enough to globally distribute any TFA emissions, while HFOs have atmospheric lifetimes so short that TFA emissions are deposited near the point of emission. Periodic re-evaluation is prudent, given the uncertainties in the sources and sinks of TFA and because of its persistence in the environment.

Summary of the impacts of mitigation options and particular scenarios

Figure 6-1 (also **Figure ES-9**) shows what ozone and climate-relevant changes could be avoided if various actions were taken. These changes are shown as the differences in global total column ozone averaged over 2020–2060 and in cumulative CO_2-equivalent emissions over 2020–2060 relative to the baseline (A1) scenario (which includes the Kigali Amendment for HFCs). The options available to hasten the recovery of the ozone layer are limited, mostly because actions that could help significantly have already been taken.

- For CFCs, halons, and HCFCs, the most effective mitigation option, not considering technical feasibility, is expanded bank recapture and destruction; elimination of HCFC production starting in 2020 would be somewhat less effective.
- For CH_3Br, elimination of production for currently uncontrolled quarantine and pre-shipment (QPS) applications is shown.
- For CCl_4, the impacts of total emissions elimination starting in 2020 are shown.
- For CH_2Cl_2, an uncontrolled ozone-depleting gas whose exact sources are unknown, we show that immediate emissions elimination would have a greater positive impact on total column ozone than total emissions elimination of CCl_4.
- For N_2O, the impacts of the Concerted Mitigation average scenario from UNEP (2013) are shown, compared to the RCP-6.0 scenario. The Concerted Mitigation scenario was developed by averaging the four published mitigation scenarios (RCP-2.6, SRES B2, and scenarios 4 and 5 from Davidson, 2012) that lead to lower N_2O emissions in 2050 than were experienced in 2005.
- For HFCs, the impact of a hypothetical complete global phaseout of production (excluding HFC-23) starting in 2020 is shown. As discussed in **Chapter 2**, for this scenario the surface temperature contribution of the HFC emissions would stay below 0.02 °C for the entire 21st century and beyond.

Further detail on these options and scenarios is given in **Section 6.4** and **Table 6-5.**

All the scenarios discussed above hasten the ozone layer recovery (CFCs, halons, HCFCs, CH_3Br, CCl_4, CH_2Cl_2 and N_2O) and reduce warming (HFCs, CFCs, halons, HCFCs, CCl_4, and N_2O). An additional scenario for emissions that may result from a violation of the Montreal Protocol is shown, namely continuing unexplained emissions of CFC-11 at 67 Gg yr^{-1}, which is the average calculated annual emission from atmospheric concentration observations over 2002–2016. This scenario leads to more ozone depletion and climate warming. Avoiding this scenario would have a larger positive impact on future ozone than any of the other mitigation options considered here.

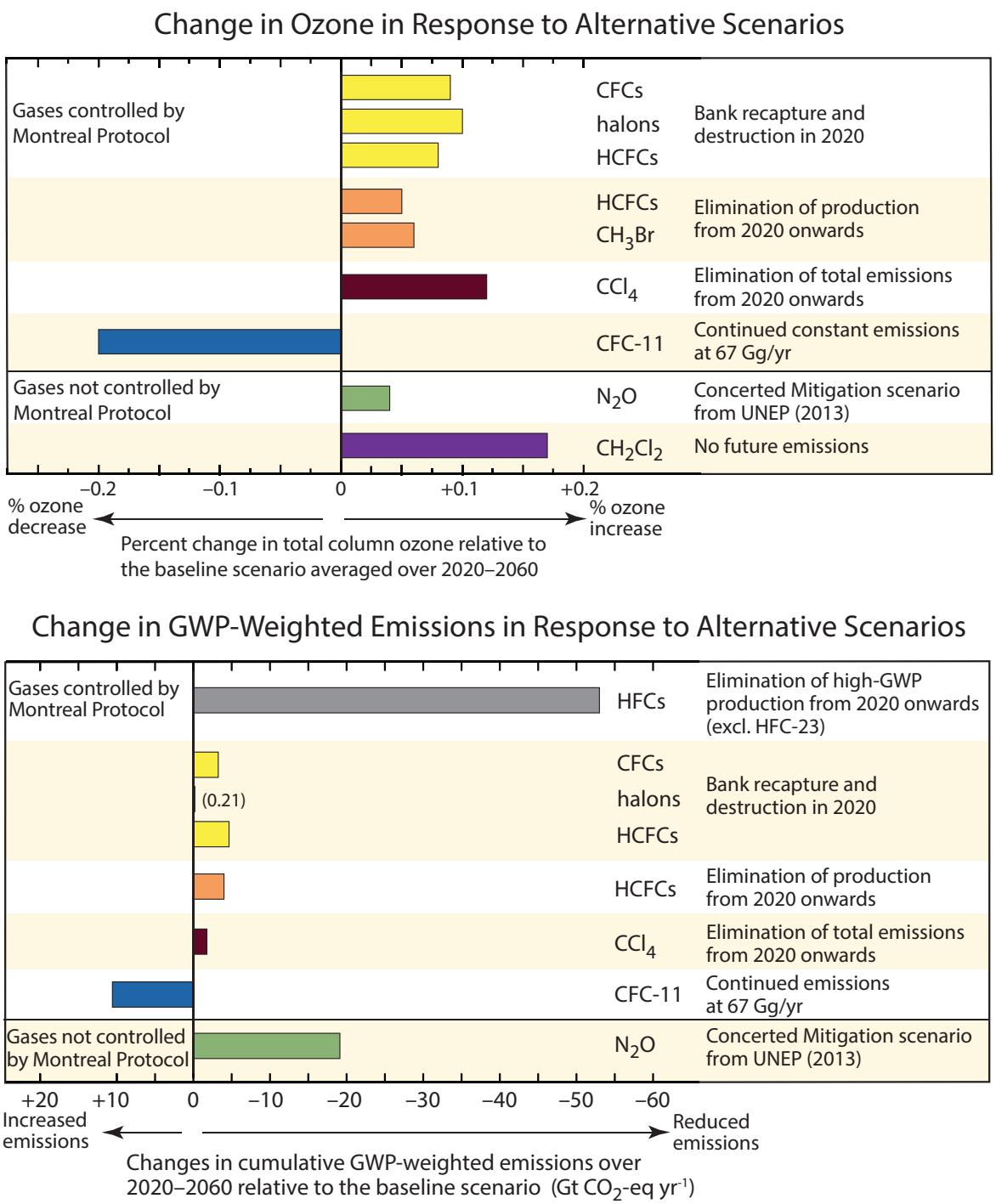

Figure 6-1. Ozone and climate-relevant impacts of alternative future scenarios compared with the baseline scenario. The climate-relevant metric is chosen to be the integrated GWP-weighted emission from 2020 to 2060, and the ozone-relevant metric is the percentage change in total column ozone averaged over 2020 to 2060. A decrease in total ozone and an increase in GWP-weighted emissions occur when future emissions are higher than in the baseline scenario for the compounds considered. Numerical values of these changes are shown in **Table 6-5**.

Chapter 6

Scenarios and Information for Policymakers

6.1 INTRODUCTION

The World Meteorological Organization (WMO) Ozone Assessments have reported on the ozone layer and related processes since the 1980s. Since 1989, the Assessments have focused on reviewing progress of the control measures introduced under the 1987 Montreal Protocol and its subsequent Amendments and adjustments. The Protocol is widely acknowledged to have been highly successful, resulting in striking reductions in the total amount of ODSs in the atmosphere (see **Chapter 1**) and more recently in an upturn in upper-stratospheric ozone levels (**Chapter 3**), giving confidence in the projections that ozone will recover sometime around mid-century at mid-latitudes and the Arctic, and somewhat later for the Antarctic. In addition, it was shown around a decade ago that the Montreal Protocol and its Amendments and adjustments had contributed more to climate change mitigation than any other existing international agreement at that time (Velders et al., 2007).

In this chapter, we focus on possible options and scenarios to aid policymakers in decisions related to protecting stratospheric ozone and minimizing effects on climate from ODS halocarbons and their replacements. As production and consumption of controlled ODSs have continued to decline, options for reducing their future emissions have become somewhat more limited but still exist and with significant potential for ozone and climate protection. One potentially important new result is a slower decline in CFC-11 atmospheric concentrations than projected in the last Assessment; the implications of this result are discussed in **Section 6.4**. Also, growth in very short-lived substances, such as CH_2Cl_2, and other compounds not covered by the Protocol (e.g., N_2O) could have important effects on the future evolution of stratospheric ozone.

A major new development relating to policy is the Kigali Amendment to the Montreal Protocol, which introduces controls on HFCs. HFCs are replacement compounds that have only small effects on ozone depletion. However, many of these compounds in current commercial use are strong greenhouse gases and therefore affect climate. The Kigali Amendment comes into force on January 1, 2019, as it has now been ratified by the threshold 20 parties to the Montreal Protocol. This chapter summarizes the projected impacts of the Kigali Amendment on climate (which are discussed in detail in **Chapter 2**) and also examines some other processes and policies unrelated to Montreal Protocol gases, including impacts of proposed stratospheric aerosol geoengineering interventions that might alter stratospheric ozone.

6.1.1 Summary of Findings from the Previous Ozone Assessment

Chapter 5 of the previous Assessment evaluated the impacts of various hypothetical policy options for reducing future emissions of ODSs, including elimination of production and bank recapture and destruction (Harris and Wuebbles et al., 2014). Updates to Ozone Depletion Potentials (ODPs), Global Warming Potentials (GWPs) and, for the first time in an Ozone Assessment, Global Temperature change Potentials (GTPs), were also presented. The main findings were

- Emissions from the 2015 ODS banks through to 2050 were projected to lead to greater future ozone depletion and climate forcing than those caused by future ODS production. Halon banks were projected to contribute most to ozone depletion, while CFC and HCFC banks were expected to contribute most in terms of GWP-weighted emissions.

- The impact on the recovery of stratospheric ozone of further policy actions on ODSs that had already been controlled was becoming smaller, but if all ODS emissions ceased (including from banks), then the return to 1980 mid-latitude equivalent effective stratospheric chlorine (EESC) values would be brought forward by about 11 years from the baseline scenario of 2047.

- Global ozone was expected to increase to above pre-1980 levels due to future projected increases

in carbon dioxide (CO_2) and methane (CH_4), which act to increase globally averaged ozone.

- Future CCl_4 emissions remained more uncertain than for other ODSs due to incomplete understanding of the current budget—with likely missing source(s)—but were expected to remain an important factor in the evolution of EESC.
- There was still insufficient research available to confidently compare the options of mitigating emissions of anthropogenic very short-lived substances (VSLSs) with those of the longer-lived ODSs, but VSLSs were expected to play a relatively larger role in future ozone depletion if long-lived controlled halocarbons followed their projected decline.
- Quarantine and pre-shipment (QPS) uses of CH_3Br—which are exempted uses not controlled by the Montreal Protocol—constituted an annual consumption that was larger than that from uses controlled by the Protocol. The elimination of future emissions from QPS uses would have brought forward the date of EESC return to 1980 levels by 1.1 years relative to the baseline scenario.
- The direct radiative forcing (RF) from ODS halocarbons (CFCs, halons, and HCFCs) in 2014 was about 0.33 W m^{-2} and near its expected peak. The RF was projected to decrease to about 0.20 W m^{-2} by 2050 and to near 0.10 W m^{-2} by 2100, assuming continued compliance with the Montreal Protocol.
- While HFCs constituted less than 1% of the RF on climate (0.02 W m^{-2}), if the mix of HFCs remained unchanged, increasing demand would have implied a radiative forcing for HFCs as high as 0.4 W m^{-2} by 2050. Replacement of the current mix of high-GWP HFCs with low-GWP compounds was projected to have the potential to lead to a decrease in the projected RF possibly by as much as 0.07 W m^{-2} by 2030 relative to the baseline scenario. HFC banks were also stated to be an important consideration when estimating the impact of HFC mitigation on future climate change.
- If (hypothetical) geoengineering of the climate system via anthropogenic increases of stratospheric sulfate aerosols were to occur within the next few decades, it could deplete stratospheric ozone, with the largest effects in the polar regions, although quantitative studies were limited.

Since the last Assessment, in addition to peer-reviewed publications, several reports have addressed topics of direct interest for this chapter:

- The SPARC report, Solving the Mystery of Carbon Tetrachloride (SPARC, 2016). This report identifies four specific emission pathways for CCl_4, which have not been well quantified by previous Ozone Assessments, and shows that these pathways, combined with revised lifetime estimates for CCl_4, result in a reduced discrepancy between known atmospheric sources and sinks. These pathways are (1) fugitive emissions from incineration, feedstock usage, and process agents; (2) unreported non-feedstock emissions during production of chlorinated methanes and perchloroethylene; (3) unreported inadvertent emissions during the production and use of chlorine gas; and (4) legacy emissions from contaminated land areas.
- Reports produced by the UNEP Technology and Economic Assessment Panel (TEAP). These reports continue to assess the technological and economic possibilities for phasing in commercially available replacements for ODSs (e.g., UNEP, 2016). This provides key information on the technical feasibility of scenarios considered in this chapter that assume reductions in future production or the capture and destruction of banks.

6.1.2 Key Issues to Be Addressed in This Assessment

The majority of this chapter is dedicated to assessing the potential future impacts of a number of ozone-relevant processes and activities on ozone depletion and climate forcing, in order to aid policy decisions regarding stratospheric ozone protection and related climate issues. Simple, well-established metrics are used to provide information about the effect of emissions from human activity on stratospheric ozone and climate. Ozone metrics include Ozone Depletion Potentials (ODPs) and equivalent effective stratospheric chlorine (EESC). Climate metrics used are Global Warming Potentials (GWPs), Global Temperature change Potentials (GTPs), and radiative

forcing (RF). GWPs and GTPs are presented for an extensive set of less common HCFCs for the first time and are updated for other HCFCs and HFCs in Group I of Annexes A, C, and F of the Kigali Amendment. New ozone and climate metrics for short-lived haloolefins, which are characterized by very small ODPs, GWPs, and GTPs, are also reported.

New scenarios that incorporate previously reported bottom-up bank estimates, the latest ODS mixing ratio observations, and reported production are generated in this chapter, and the potential impacts on future ozone depletion and climate forcing are calculated. These scenarios investigate effects of hypothetical changes in emissions and are illustrative of potential mitigation actions. For the first time, projections of an anthropogenic VSLS (CH_2Cl_2) are incorporated into these scenarios. The impact of future HFC abundances on climate forcing, with regard to the Kigali Amendment (**Section 6.2.1.2**), is also assessed, using the scenarios presented in **Chapter 2**.

Consistent with **Chapters 3** and **4** in this Assessment in their analyses of future projections of ozone, we use the Representative Concentration Pathway (RCP) 6.0 scenario (IPCC, 2013) as the baseline emission scenario for CO_2, CH_4, and N_2O. The sensitivity of the projected impacts of these greenhouse gases on stratospheric ozone is investigated by additionally using the RCP2.6, RCP4.5, and RCP8.5 scenarios. Our primary reason for using a variety of future greenhouse gas (GHG) scenarios is to assess the range of ozone impacts of the compounds relative to those controlled under the Montreal Protocol. The RCP2.6 scenario is the one that most closely complies with the stated goal of the Paris Agreement to hold "the increase in the global average temperature to well below 2°C above pre-industrial levels and pursuing efforts to limit the temperature increase to 1.5°C above preindustrial levels" (IPCC, 2013a). It should be noted that a new group of scenarios (Shared Socioeconomic Pathways, or SSPs) has recently been developed. The SSPs are based on alternative socioeconomic projections that could arise from plausible major global developments (O'Neill et al., 2017; Riahi et al., 2017). This new scenario framework, established by the climate change research community, will be used for the new generation of earth system models as part of the Coupled Model Intercomparison Project Phase 6 (CMIP6). Here, in common with the rest of this Assessment, we use the RCP scenarios that were adopted by the IPCC for its Fifth Assessment Report (IPCC, 2013b).

In common with previous Assessments, this chapter also assesses some other potential influences on stratospheric ozone that do not involve the emission of chlorine- and bromine-containing source gases, including deliberate climate intervention and rockets. Here, and elsewhere in the chapter, key gaps in our understanding that prevent a firm assessment of future ozone levels are identified.

6.2 ISSUES OF POTENTIAL IMPORTANCE TO STRATOSPHERIC OZONE AND CLIMATE

6.2.1 Halocarbons Controlled Under the Montreal Protocol

Implementation of the Montreal Protocol controls has resulted in significantly lower EESC than would otherwise have occurred (WMO, 2014, and preceding reports) as well as significant reductions in radiative forcing of climate change. The majority of ODSs that were originally controlled under the Montreal Protocol are now declining in the atmosphere. The atmospheric abundance of CFCs has declined substantially (**Chapter 1**) mainly due to their substitution by HCFCs, HFCs, and not-in-kind (NIK) solutions including non-fluorinated compounds; although some CFCs, notably CFC-11, have not dropped as quickly as expected over the last few years, and the reasons for this are not well understood. The observed rate of decline of atmospheric CCl_4 also remains slower than predicted, and there is new understanding of potential additional sources that include by-product emissions from chloromethane and perchloroethylene plants, although a discrepancy between sources and sinks still exists. **Section 6.4** discusses the implications of these uncertainties on future EESC.

Atmospheric CH_3Br results from both natural and anthropogenic emissions, the latter mainly from its use as a fumigant. The atmospheric abundance of CH_3Br has continued to decline, most likely due to the phase-out (completed in 2015) of controlled industrial production and consumption (**Chapter 1**). Critical use exemptions (CUEs) for the controlled uses, applied for by developed countries since 2005 and by developing countries since 2015, have declined dramatically from

their peak in 2005 of 21.8 Gg yr^{-1} and now represent only a small fraction (<10% or 0.7 Gg) of annual use of CH_3Br. Quarantine and pre-shipment (QPS) uses of CH_3Br, which are not controlled by the Montreal Protocol, have remained relatively stable over the last decade and in 2016 constituted an annual consumption of 8.4 Gg.

HCFCs, which are transitional replacement compounds, are still increasing in the atmosphere, although growth rates have slowed in response to their phaseout schedules, which were established first in 1992 with an accelerated phaseout established in 2007 (Harris and Wuebbles et al., 2014). In non–Article 5 countries, HCFC production started decreasing around 2000, well before the phaseout schedule started in 2004, whereas the production of HCFCs in Article 5 parties continued to rise until 2012 and started decreasing just when the phaseout schedule went into effect in 2013 (UNEP, 2017). The consumption of HCFCs in Asia in Article 5 parties in 2015 accounts for the majority of global consumption at around 70%. Thus, for achieving further global HCFC emissions reductions, complying with or even accelerating the earlier phaseout schedule (by promoting the replacement of HCFCs by low-GWP fluorinated compounds or non-fluorinated compounds and other NIK solutions) in Asia plays an important role in reducing future HCFC emissions. An important source of emissions not controlled by the Montreal Protocol is emissions from banked ODSs, mainly from uses such as refrigerants and foams. If no further policy actions for banked ODSs are considered in Article 5 parties, especially in Asia, emissions from banked HCFCs will become larger than those of banked CFCs (Daniel et al., 2011). Thus, banked HCFCs will be a major source of both ODSs and climate emissions in the coming decades. Effective measures for reducing emissions from banked HCFCs are recovery and destruction from banked ODSs when equipment that uses refrigerants and foams is disposed, together with appropriate management for reducing leakage during the operation of such equipment (Box 5-1 of Harris and Wuebbles et al., 2014). In **Section 6.4** we discuss the effect on future EESC and ozone of policy options that include reducing HCFC leakage by bank recapture and destruction and eliminating production of HCFCs.

Halons are particularly important to ozone depletion because they contain bromine, which is roughly 60 times more effective at depleting ozone than chlorine. However, because of their smaller atmospheric concentrations, halons influence climate to a much smaller degree than other ODSs such as CFCs, HCFCs, and CCl_4. In Harris and Wuebbles et al. (2014), future leakage of halons from their banks was found to be the largest contributor to ozone depletion through to 2050. While, for the Assessments, we assume that bank capture is 100% effective, in reality the accessibility and profitability of the various banks are important factors in destroying emissions; for example, halon bank capture from fire-fighting equipment for use in new aircraft where alternatives are not available is generally much more cost effective than CFC and HCFC bank capture from foams used in home insulation where alternatives are widely available.

6.2.1.1 Replacement Compounds

The reduction in ODS emissions has occurred as a result of NIK technology; containment, recovery, and recycling actions; and replacement by compounds that do not have significant ODPs. Examples of NIK technology include mechanical pumps or hydrocarbons to replace ODS propellants in consumer and commercial applications, CO_2 or hydrocarbons to replace ODSs in foam-blowing applications, and ammonia in industrial refrigeration. Ammonia and the hydrocarbons used (ethane, propane, and butane) do not have any significant impact on stratospheric ozone or radiative forcing of climate change. Of the in-kind replacement compounds, HFCs are by far the most important (for climate; they are non-ozone depleting), with HFC-134a accounting for the majority of HFC production, emissions, atmospheric concentration, and radiative forcing (see **Chapter 2**). Oxygenated compounds (e.g., hydrofluoroethers) have found use in niche applications. The decreased use of CFCs, and now HCFCs, has resulted in increased HFC use, particularly in the refrigeration and air conditioning sectors and, to a lesser degree, in the foam and fire protection sectors. Annual global production of CFCs peaked in the late 1980s (UNEP, 2017), HCFC production peaked in the late 2000s (UNEP, 2017), and HFC production and emissions continue to increase (McCulloch and Midgley, 2001; Velders et al., 2015a) (see also **Chapters 1** and **2**). As

will be discussed in **Section 6.2.6**, the atmospheric degradation of HFCs neither contributes significantly to tropospheric ozone formation nor yields products that pose a significant known risk to human or ecosystem health.

HFCs typically have lower GWPs than the CFCs and HCFCs they have replaced. Yet, some HFCs such as HFC-23 (GWP =12,400), HFC-143a (GWP = 3,170), and HFC-125 (GWP = 4,800), and to a lesser extent HFC-134a (GWP = 1,300), have high GWPs. While the current contribution of HFCs to radiative forcing of climate is small at approximately 0.02 W m^{-2} (see **Chapter 2**), the potential future growth in the emissions of high-GWP HFCs has given rise to concerns about their possible future climate impact (UNEP, 2011; Velders et al., 2009; Velders et al., 2015b; Velders et al., 2012; WMO, 2011; 2014; Wuebbles et al., 2013) and to the Kigali Amendment of the Montreal Protocol discussed in the next section.

To minimize ozone layer depletion and have minimal impact on climate, ODS replacements need to have low ODPs and low GWPs. Meeting such conditions requires replacement compounds to not contain chlorine or bromine, have short lifetimes, and/or have weak infrared (IR) absorption cross-sections.

Halogenated alkenes (halogenated olefins, HFOs) such as HFO-1234yf, HFO-1234ze(*E*), HCFO-1233zd(*Z*), and HCFO-1233zd(*E*) are commercially important short-lived replacement compounds (Brown, 2009; Burkholder et al., 2015; Wallington et al., 2010; 2017). Members of this class of compounds have low ODPs and GWPs (**Appendix A**) and have been developed for use as refrigerants, aerosol propellants, degreasing agents, and foam-blowing agents (Burkholder et al., 2015; Wallington et al., 2017). HFOs can be used on their own or as blends with HFCs. A number of other short-lived compounds have also been proposed as replacements for long-lived ODSs and HFCs (see **Chapter 1**).

The energy efficiency of the equipment used can also be very important to the indirect impact of replacement compounds on climate forcing. In fact, for some applications, the indirect impact on climate through energy efficiency can be far more important than the direct impact through emissions of the gas itself, as discussed below and in **Chapter 2**.

6.2.1.2 Kigali Amendment

The Kigali Amendment comes into force on January 1, 2019, as it has now been ratified by the threshold 20 parties to the Montreal Protocol. Under Annex F, it includes 18 controlled HFC substances and forms a framework of regulations in 4 country groupings; the main non–Article 5 (non-A5) parties, other non-A5 parties, Group I A5 parties, and Group II A5 parties. It subsumes all current policies for HFCs. Unlike the current restriction of ODSs listed in the Montreal Protocol, rather than aim for a complete phaseout, the amendment aims to achieve 80–85% phaseout of production and consumption of HFCs compared to baseline levels. The amendment aims to implement the phasedown of HFC production and consumption starting in 2019 for most developed countries, in 2024 for most developing countries, and in 2028 for some developing countries. The Amendment also mandates that HFC-23 emissions should be destroyed to the extent practicable by all countries.

The Kigali Amendment will significantly limit the future production and consumption of HFCs. Under the current control measures, emissions of HFCs are projected to peak around 2035, about a decade after the peak in global production and consumption, due to gradual emissions from refrigeration and air-conditioning equipment (so-called banks). The HFC bank, therefore, represents a substantial source of emissions and radiative forcing after production is phased down (Velders et al., 2014). Emissions of HFC-23 (formed as a by-product of HCFC-22 manufacture, see **Section 6.2.1.3**) should also be significantly limited. The contribution of HFCs (excluding HFC-23) to the global average surface temperature change is projected to reach a maximum—assuming compliance with the Kigali Amendment—of around 0.07°C by 2060, after which it decreases slowly to about 0.06°C by 2100 (**Chapter 2**). Without Kigali, surface temperature warming from HFCs might have been as high as 0.3°–0.5°C by 2100 (**Chapter 2**). Of course, adjustments to the HFC control schedules analogous to historical adjustments to the ODS control schedules could substantially reduce the climate impact.

The Kigali Amendment regulations mandate not only different phasedown schedules of production and consumption (for the different country groupings) but also different settings of base year and baseline

expressed in CO_2 equivalents. The baselines in non-A5 parties are set based on historical data of HFCs (2011–2013) plus 15% of the baseline consumption of HCFCs, whereas the baselines in A5 parties are set at the average amounts of HFCs from 2020 to 2022 in Group I countries, and the average amounts of HFCs from 2024 to 2026 in Group II countries, plus 15% of the baseline consumption of HCFCs for both groups (**Chapter 2**, **Table 2-3**). Thus, the effects of emissions reductions due to the Kigali Amendment will depend on the levels of baseline consumption in A5 parties even before the phasedown schedule starts, which in turn depends on incentives to reduce the consumption of HFCs and promote the replacement to non-fluorinated compounds.

Options are available to accelerate the phasedown schedule and provide additional avoided GWP-weighted emissions of HFCs, including use of technologically feasible low-GWP alternatives in place of high-GWP HFCs in refrigeration and air-conditioning equipment during the phasedown (Xu et al., 2013). Additional benefits of the Kigali Amendment could be gained via the development of more energy-efficient equipment that uses these low-GWP replacements, since the CO_2 emissions resulting from the energy used by the equipment are important contributors to the total climate impact related to refrigerant use (e.g., Shah et al., 2015).

6.2.1.3 HFC-23

HFC-23 is formed as a by-product at the reactor stage of the manufacture of HCFC-22. Atmospheric emissions can be avoided if HCFC-22 production is managed for better containment and if the HFC-23 is incinerated. Incineration projects in developing countries have been supported through the Clean Development Mechanism (CDM) of the Kyoto Protocol (http://cdm.unfccc.int), allowing a significant fraction of the HFC-23 produced in HCFC-22 facilities to be incinerated during the period 2006–2013. Despite these mitigation efforts, there has been a resurgence in emissions since 2009 (Rigby et al., 2014), with emissions in 2013–2015 similar to or slightly higher than in 2006, when CDM-facilitated destruction had yet to be fully implemented (Simmonds et al., 2018). This increase in emissions is attributed mainly to the fact that no new CDM projects were awarded after 2009, while HCFC-22 production for feedstock use in non–Annex 1 countries (mainly China) was increasing, including from plants that did not have abatement technology (Fang et al., 2014; Simmonds et al., 2018). The Montreal Protocol regulates for dispersive uses of HCFC-22 (such as refrigerants and foams), which are being reduced. However, around half of the current production of HCFC-22 is for feedstock uses (Miller et al., 2010; WMO, 2014) (such as fluorine-contained resin and components of sophisticated technologies), which are uncontrolled. Total HCFC-22 production increased rapidly in the past few decades but has recently stabilized (Miller et al., 2010), showing that expansion of feedstock use has not matched the decrease in emissive uses and indeed also appears to have stabilized over the last few years.

The Kigali Amendment mandates all HCFC-22 producing facilities to collect and destroy the emitted HFC-23 by-product "to the extent practicable," although reduction schedules and frameworks are still under discussion. The emission reductions can be gained for most developing countries because many companies set up destruction facilities under the CDM. However, although the incremental cost of HFC-23 destruction is far less than the price paid by the CDM, the cost for renewal of the destruction facilities and operating the incineration may be an issue for some developing countries. In summary, emissions of HFC-23 are expected to be reduced under the full implementation of the Kigali Amendment, assuming declines mandated by the Protocol outpace any increases in HCFC-22 production. However, the future trajectory of HFC-23 emissions is uncertain and depends on the amount of HCFC-22 produced, the efficiency of avoiding unwanted HFC-23 by-products, and whether the amount of HFC-23 incinerated increases or decreases.

6.2.2 Breakdown Products

The atmospheric degradation of HCFCs, HFCs, and HFOs is initiated by reaction with OH radicals leading to the formation of halogenated carbonyl compounds, which undergo further oxidation to yield HF, HCl, CO_2, and, in some cases, trifluoroacetic acid (TFA) (Burkholder et al., 2015; Calvert et al., 2008; IPCC/TEAP, 2005; Wallington et al., 1994; WMO, 2011, 2014). The photochemical ozone creation potentials of HCFCs, HFCs, and HFOs are very small, and tropospheric ozone formation resulting from their

degradation is of negligible importance (Hayman and Derwent, 1997; Luecken et al., 2010; Wallington et al., 2015; WMO, 2011, 2014). The additional burden of HF, HCl, and CO_2 at the concentrations expected from atmospheric degradation of HCFCs, HFCs, and HFOs is of no consequence.

TFA is a product of the atmospheric degradation of HCFC-123 and several commercially important ODS replacement compounds such as HFC-134a, HFO-1234yf, and HFC-227ea. HFO-1234yf has five times the TFA breakdown products than the HFC-134a it replaces in mobile air conditioners. TFA is a ubiquitous natural component of the hydrosphere, with many sources beyond the halocarbons controlled under the Montreal Protocol (e.g., Scheurer et al., 2017). It is present in ocean water, even at great depths and in remote locations, at a concentration of approximately 200 ng /l (Solomon et al., 2016). In surface freshwater, TFA levels are typically 10–300 ng l^{-1}. TFA is stable in the environment and accumulates in terminal water bodies such as salt lakes. TFA levels in the Dead Sea have been reported to be 6,400 ng l^{-1} (Boutonnet et al., 1999). Currently, the oxidation of HFC-134a makes the largest contribution from ODS replacements to TFA formation. The global background atmospheric concentration of HFC-134a is approximately 100 ppt. Assuming a 7–20% molar yield of TFA (Wallington et al., 1996), rainout as the sole atmospheric fate of TFA, and annual global precipitation of 5 x 10^{17} liters Warneck and Williams (2012) give an estimate of 20–50 ng l^{-1} for the current average TFA concentration in global precipitation resulting from HFC-134a degradation. Local concentrations will be higher or lower than the global average depending on local precipitation volumes and photochemical activity. The concentrations of TFA observed in rainwater typically substantially exceed those that can be accounted for by HFC-134a degradation, indicating the presence of significant sources other than HFC degradation (Frank et al., 1996; McCulloch and Lindley, 2003; Wu et al., 2014a, b). HFC-134a is currently being replaced by HFO-1234yf in applications such as mobile air conditioners. HFO-1234yf has a higher, 100%, molar TFA yield and degrades more rapidly and closer to its emission sources than HFC-134a with 20% molar TFA yield. Luecken et al. (2010), Russell et al. (2012), Henne et al. (2012), Kazil et al. (2014), and Wang et al. (2018) have estimated TFA concentrations in rainwater resulting from future use of HFO-1234yf and report similar findings. Average concentrations in rainwater are projected to be of the order of 1,000 ng l^{-1}. Regions with lower rainfall have higher concentrations but lower total deposition. Increases in TFA levels in terminal water bodies in North America of 1,000–15,000 ng l^{-1} with a maximum of 200,000 ng l^{-1} in the Sonoran Desert were projected in a modeling study of 50 years of future HFO-1234yf use (Russell et al., 2012).

It has been shown recently that the reaction of Criegee intermediates with TFA in the gas phase is extremely rapid (Chhantyal-Pun et al., 2017). Criegee intermediates are present in the atmosphere as a result of the reaction of ozone with alkenes and play an important role in atmospheric chemistry over landmasses with vegetation, where biogenic emissions of alkenes (e.g., isoprene and terpenes) are significant and ozone is available. Reactive loss of TFA via reaction with Criegee intermediates could be an important loss mechanism for TFA, and it has not been accounted for in atmospheric models of TFA deposition. Inclusion of this new gas-phase chemistry in atmospheric models could decrease the projected deposition of TFA over landmasses (by as much as a factor of two) (Chhantyal-Pun et al., 2017).

The effects of TFA on human and ecosystem health resulting from the use of compounds regulated under the Montreal Protocol have been assessed by Solomon et al. (2016). Mammals are insensitive to TFA (Boutonnet et al., 1999), and plants and other animals have a high tolerance to TFA. Solomon et al. (2016) tested a worst-case scenario with upper-limit TFA levels estimated for the future use of HFC-134a, HFO-1234yf, HFC-143a, and HFC-227ea through the year 2050 and selecting the most sensitive biological endpoints for different species. The no-observed-effect-concentrations for aquatic organisms considered by Solomon et al. (2016) were in the range 3 x 10^{7}–2.4 x 10^{9} ng l^{-1}, with an outlier at 1.2 x 10^{5} ng l^{-1}. Risks for humans, terrestrial vertebrates, plants exposed via soil, and aquatic plants and animals were assessed to be de minimis (Solomon et al., 2016). Risks for organisms in salt lakes and playas were not assessed because there are no data on the toxicity of TFA for such organisms. It was noted that future increases in TFA levels resulting from ODS replacement degradation in salt lakes will be small compared to the

existing burden of other natural salts in such locations (Solomon et al., 2016). The large body of published field measurements, toxicological studies, modeling studies, and environmental assessments point to a clear conclusion: The current and estimated future concentrations of TFA and its salts resulting from degradation of HCFCs, HFCs, and HFOs do not pose any known significant risk to human or ecosystem health (Solomon et al., 2016).

6.2.3 Very Short-Lived Substances (VSLSs; Biogenic and Anthropogenic)

VSLSs have not been controlled by the Montreal Protocol since it has been mistakenly assumed they have a negligible impact on stratospheric ozone due to their short atmospheric lifetimes and/or because they are dominated by biogenic sources. Previous Assessments had considered n-propyl bromide as an ODS with a latitude-dependent ODP. Since the last Assessment, a number of new studies predict a significant impact of VSLSs on ozone as discussed below.

Chlorinated VSLSs are predominantly anthropogenic in origin (**Chapter 1**). They currently contribute only a small fraction (<10%) to total stratospheric chlorine but are becoming more relevant for stratospheric ozone due to increased emissions of CH_2Cl_2, which is used as an industrial solvent, as a blowing agent in the production of foam plastics, and as a feedstock or by-product in the production of other chemicals (Campbell and Shende, 2005; Simmonds et al., 2006). Surface concentrations have increased by around 8% (2.85 ppt) per year between 2004 and 2014 (Hossaini et al., 2017). Assuming this mean growth rate continues linearly, Hossaini et al. (2017) predict that CH_2Cl_2 could delay the return of total lower stratospheric Cl_y to pre-1980 levels by 15–17 years, and by 2050, reduce annual mean ozone concentrations in the lower stratosphere by 6%—effects that are much larger than the influence of potentially eliminating future small levels of production or emission of CFCs and HCFCs. In **Section 6.4** we examine the effects of eliminating emissions of CH_2Cl_2 on future ozone and the influence of different RCPs and varying OH levels on projections of the impact of CH_2Cl_2 on future ozone.

Biogenic VSLSs—mainly $CHBr_3$ and CH_2Br_2—account for an appreciable fraction (~30%) of total stratospheric bromine. The majority of $CHBr_3$ and CH_2Br_2 emissions come from oceanic marine algae, mainly seaweeds (Carpenter and Liss, 2000). While most models currently assume fixed emissions or atmospheric mixing ratios of VSLS Br (Hossaini et al., 2016), oceanic emissions may undergo future climate-induced or other anthropogenically induced changes. Changes in surface winds and sea surface temperature and removal of sea ice would likely increase the oceanic sea–air fluxes of VSLS Br (Tegtmeier et al., 2015; Falk et al., 2017); however, possible changes in biological oceanic production are not sufficiently well understood. While currently believed to be small (Leedham et al., 2013), future anthropogenic emissions of VSLS Br in the form of seaweed aquaculture have also been projected to substantially increase over the next years, particularly from Southeast Asia (Radulovich et al., 2015; WMO, 2014). The ODPs of VSLSs are highly sensitive to growing emissions in this region (e.g., Tegtmeier et al., 2015).

The effectiveness of both brominated and chlorinated VSLSs as ODSs depends not only on their emissions but also on chemical processing and the strength and location of convective transport (**Chapter 1**). In addition, the phaseout of the long-lived chlorinated source gases under the Montreal Protocol and the resulting decline in stratospheric chlorine mean that bromine-mediated O_3 destruction via the BrO + ClO catalytic cycle will decrease over the 21st century. However, there is not currently a consensus on whether the combination of these factors causes a delay in the return of Antarctic ozone to pre-1980 levels due to bromine VSLS. Falk et al. (2017) find that changes in atmospheric chemistry and transport and a decrease of anthropogenic chlorine may result in a decrease in the total amount of stratospheric Br_y VSLS and its impact on ozone during the 21st century, despite increasing VSLS Br emissions. In contrast, Tegtmeier et al. (2015) project a 31% increase of the ODP-weighted emissions of $CHBr_3$ by 2100, compared to present values under the RCP8.5 scenario, due to a larger convective updraft mass flux in the upper troposphere and increasing emissions, offset by less effective catalytic ozone destruction. Fernandez et al. (2017) find that VSLS Br chemistry affects the depth and duration of the Antarctic ozone hole and will dominate Antarctic ozone seasonality by 2100, but that its inclusion in a global model does not result in a significant delay to the modelled ozone return date to 1980 levels.

Conversely, Yang et al. (2014) and Oman et al. (2016) derived an increase of between 7 and 10 years in the return date when VSLS Br are included.

In summary, emissions of VSLS Br from seaweed farming and from physical sea–air exchange may increase in the future, but overall changes in VSLS Br emissions from these combined effects, along with potential climate-induced changes in natural oceanic production, are not known to any degree of certainty. Whether increased future VSLS Br emissions would actually lead to a delay in O_3 recovery is also highly uncertain, with contrasting results due to structural differences between models and internal model variability.

Previous Assessments have concluded that iodine chemistry likely has a negligible role in determining levels of stratospheric ozone, based on available remote-sensing measurements of iodine in the lowermost stratosphere. Saiz-Lopez et al. (2015) however calculate that significant levels of total reactive iodine, between two and five times larger than the currently assumed upper limits, can be injected into the stratosphere and exert an ODP similar to, or even larger than, that of VSLS Br. There are currently no projections of how iodinated VSLSs might affect the future evolution of the stratospheric ozone layer, although oceanic iodine emissions are predicted to have increased over the 20th century due to increases in surface ozone concentrations (Sherwen et al., 2017).

6.2.4 The Key Climate Gases: Carbon Dioxide, Methane, and Nitrous Oxide

The most important drivers of climate change over the last century are the well-mixed greenhouse gases (GHGs) carbon dioxide (CO_2), methane (CH_4), and nitrous oxide (N_2O), with HFCs as a growing new threat to climate as a consequence of its widespread use as a transitional substitute for ODSs. With atmospheric lifetimes of a decade or more, these gases are circulated and mixed around the globe to yield small inter-hemispheric gradients. The atmospheric abundances and associated radiative forcings on climate from these gases have increased substantially in the industrial era (see **Chapters 1**, **3**, and **5**). Future changes in halogen concentrations will take place against the backdrop of the changes occurring in the climate and in the chemical and radiative effects of these GHGs. The Paris Agreement within the United Nations Framework Convention on Climate Change (UNFCCC) enhances previous UNFCCC targets for reducing overall climate forcing, starting in the year 2020, and aims to limit the global average temperature increase this century to well below 2°C above preindustrial levels and to pursue efforts to limit the temperature increase to 1.5°C. Within the Agreement, each country determines its own contribution towards the global goals, called Nationally Determined Contributions (NDCs). One key aspect for the Montreal Protocol is that the Paris Agreement does not give stringent guidance on the levels of the most important climate gases for stratospheric ozone, namely CH_4 and N_2O. Changing concentrations of CH_4 and N_2O can significantly affect the amounts of hydrogen oxides (HO_x) and nitrogen oxides (NO_x) concentrations in the stratosphere, which also affect the concentration and distribution of ozone. The NO_x produced from dissociation of N_2O decreases stratospheric ozone, while CH_4 can lead to regions of net ozone production, particularly in the troposphere, and to regions of depletion, but in the global average leads to additional ozone. The continuing increase in the global CO_2 concentration and, to a lesser degree, the increase in global CH_4 concentration also have important effects on stratospheric ozone through cooling of the stratosphere, which slows the ozone chemical loss rates. The resulting climate change from increasing GHGs also strengthens the stratospheric Brewer–Dobson circulation (BDC), which will redistribute ozone (see **Chapter 5**).

Future ozone levels will be strongly dependent on the actual future emissions and concentrations of these climate gases. Once the NDCs of the major countries are available beyond the current estimates of 2030, going out to mid-century or beyond, it will be possible to better estimate the impact of the Paris Agreement on the future state of the ozone layer and also better determine the dates for the return of the ozone layer to its 1980 values. As shown in Rogelj et al. (2016), the initial NDCs do not hold globally averaged temperature increases below 2°C, and so further reductions in projected GHG emissions, with associated different impacts on stratospheric ozone, are expected if climate actions are taken to meet the Paris Agreement. **Section 6.4** examines how the changing concentrations of these gases according to selected RCPs

adopted by the IPCC for its Fifth Assessment Report (IPCC, 2013b) could affect future changes in ozone relative to the changing emissions and concentrations of halogens. Of the RCPs, the RCP2.6 scenario is the closest one holding global temperature increase below 2°C (IPCC, 2013a).

6.2.5 Deliberate Climate Intervention

6.2.5.1 Geoengineering via Stratospheric Sulfate Aerosol Modifications

Increasing the burden of stratospheric aerosols, also called stratospheric aerosol geoengineering, has been proposed as a method to increase the reflectivity of Earth's atmosphere in order to counteract some effects of climate change. The most discussed application is using the continuous injection of SO_2 (or H_2SO_4) into the tropical stratosphere. Despite similarities to short-term impacts of volcanic eruptions, the impact of geoengineering strategies on the climate system would be different, since they would have to be applied over an extended period of time to continuously cool Earth's surface. The increase in stratospheric aerosol surface area density (SAD) as a result of increasing sulfur injections over a continuous time period would increase surface cooling, but it would also cause an increase in heterogeneous ozone loss cycles involving reactive chlorine (ClO_x), bromine (BrO_x), and hydrogen (HO_x) (see **Appendix 6A**). On the other hand, the reduction of nitrogen oxides through increasing heterogeneous reactions (mostly important in the tropical mid-stratosphere) could actually increase ozone and counteract a potential decrease in tropical column ozone as the result of projected increasing GHGs. These chemical effects of geoengineering on ozone would be reduced by the end of the 21st century because of the projected future decrease in ODSs and consequent halogen activation through heterogeneous reactions.

In addition to chemical changes, an increased stratospheric aerosol burden could also cause larger dynamical changes, including heating of the lower tropical stratosphere and a speedup of the BDC, including changes in tracer transport towards high latitudes, which in part would counteract the change in ozone due to chemistry (**Appendix 6A**). For large injection amounts, this may even cause an increase in column ozone in the Northern Hemisphere (NH) winter mid-latitudes compared to a non-geoengineering scenario (Tilmes et al., 2018). Changes in tracer transport and UV as a result of changes in column ozone and aerosol scatter may also increase tropospheric methane lifetime (Visioni et al., 2017b), may alter stratosphere-to-troposphere exchange of ozone and other tracers (Xia et al., 2017), and would weaken the tropospheric jet streams (Richter et al., 2018). The potential heating of the tropopause may further cause a significant increase in stratospheric water vapor, impacting radiation and chemistry.

Column ozone changes as the result of stratospheric aerosol geoengineering therefore depends on the injection amount, timing (ODS loading), and injection strategy (influencing aerosol size and location; **Appendix 6A**). Relatively small and constant injections of 2.5–4 Tg S yr^{-1} between 2020 and 2070, which would result in 0.5°C of surface cooling, are calculated to lead to an approximately 4% reduction in the global stratospheric column ozone for 2020 and only 1% reduction by 2070 (Pitatry et al., 2014; Xia et al., 2017). Much larger injection amounts that would lead to a surface temperature cooling of around 2°C in 2040–2050, based on a single model study, would result in reductions in column ozone of 28–40% in October over Southern Hemisphere (SH) high latitudes and 8–18% for NH high latitudes in March, with varying values depending on the injection altitude (Tilmes et al., 2018). Injections closer to the tropopause cause a stronger dynamical response and could result in up to an 8% increase in column ozone in NH winter mid- and high latitudes. A single modeling transient simulation based on RCP8.5 greenhouse gas forcings with continuously increasing SO_2 injections between 2020 and 2099 and decreasing ODSs would result in approximately constant change in column ozone in high polar latitudes (20–23% in October over the SH and 10–12% in March over the NH polar latitudes) and slightly larger (3–5%) column ozone values compared to non-geoengineering conditions for tropics and winter northern mid-latitudes by the end of the 21st century (Richter et al., 2018).

Use of Other Aerosols

The use of high refractive index solid particles such as Al_2O_3, TiO_2, and $CaCO_3$ have been suggested as stratospheric aerosol geoengineering options with lower stratospheric heating and lower surface areas

for heterogeneous reactions than sulfate aerosols (Dykema et al., 2014; Keith et al., 2016). Limited heating in the stratosphere and reduced reactivity of the particles may change the dynamical response compared to sulfate aerosols. Based on simple 2-D model simulations, Keith et al. (2016) estimate that a radiative forcing of –1 W m^{-2} achieved using stratospheric injection of $CaCO_3$ particles could result in a 3.8% increase in global column ozone. Estimated aerosol properties and uptake rates still need to be confirmed by lab studies. Impacts on chemistry and dynamics in comprehensive earth system models have not been investigated.

6.2.5.2 Geoengineering via Solar Irradiance Reduction

Other geoengineering activities proposed to help counteract climate change via solar radiation management involve modifying Earth's energy balance by

Box 6-1. Stratospheric Aerosol Geoengineering

Climate geoengineering via reduction of incoming solar radiation is a strategy to deliberately mitigate some of the effects of anthropogenic global warming (Crutzen, 2006). Since it does not address the cause of climate change (the increase in greenhouse gases) it could be only a temporary solution to help reduce the worst impacts, including heat waves, floods, sea level rise, etc., until decarbonization has effectively stabilized the climate (Tilmes et al., 2016; Wigley, 2006). Stratospheric aerosol geoengineering is a proposed method to reflect incoming shortwave solar radiation to cool Earth's surface, also called solar radiation management. The idea of this approach is to inject aerosols or gases that form aerosols (most studies have performed calculations for sulfur dioxide [SO_2]) into the tropical stratosphere. These are distributed around the globe within approximately 1–2 months, similar to what has been observed after large volcanic eruptions. The continuous injection of SO_2 or aerosols is assumed to form a persistent aerosol layer that achieves a certain amount of global cooling, with a cooling efficiency reaching up to 1°C per 10 $TgSO_2$ yr^{-1} injections (Pierce et al., 2011; Kravitz et al., 2018), although with potentially reduced efficiency with increasing injection amounts (Niemeier and Schmidt, 2017). Earth system models have a range of approximately a factor of three in the forcing efficiency per injection amount, which depends on the aerosol microphysical descriptions and radiation scheme, as well as feedbacks including changes in ice clouds and assumptions regarding levels of other greenhouse gases (Visioni et al., 2017). There is large uncertainty in the regional impacts of stratospheric aerosol geoengineering. The following is a brief overview of currently known potential benefits, side effects, and risks (Robock, 2016).

Benefits: Earth system models have shown that globally averaged temperatures can be balanced (Kravitz et al., 2013), extreme temperatures and large precipitation events can be reduced (Curry et al., 2014), aridity can be reduced (Tilmes et al., 2016), and the melting of the Arctic sea ice can be significantly slowed or even reversed (Kravitz et al., 2017). The cooling of Earth's surface via stratospheric aerosol geoengineering has potential positive impacts on air quality (Xia et al., 2017) and agriculture and crop yields (Pongratz et al., 2012). Limited investigation also suggests surface ozone levels could decline (Eastham et al., 2018; Xia et al., 2017), which would lead to health benefits. A potential decrease in column ozone may be beneficial if it counteracts the increasing column ozone above preindustrial levels from a projected super recovery. Strategically placed injections may reverse the shortening of the Quasi-Biennial Oscillation (QBO) period from increasing greenhouse gases in the future (Richter et al., 2018). Changes in direct to diffuse radiation ratio have been shown to be beneficial for plant growth and may have other benefits for the biosphere (Xia et al., 2016). The strong cooling potential of stratospheric aerosols would allow for a quick response to sudden climate changes, and the relatively short lifetime of stratospheric sulfate aerosols of about 2 years would allow for a phaseout of geoengineering in a short time if required. The approach would not largely change ocean acidification but may reduce the bleaching of coral reefs (Zhang et al., 2017).

Box 6-1, continued.

Side Effects: Models show that past or present-day climate conditions cannot be perfectly restored with geo-engineering and that, depending on how it is implemented, it may lead to unintended side effects. Models agree that cooling Earth's surface via shortwave radiation (as opposed to mitigating the heating caused by increased trapping of longwave radiation) slows the hydrological cycle, which leads to reductions in global precipitation (Tilmes et al., 2013). While the largest reductions occur over the oceans, this method may lead to a disruption of the monsoonal precipitation. Other side effects include significant heating in the tropical stratosphere, a substantial increase in stratospheric water vapor, a strengthening of the polar night jets, and a weakening of subtropical jets and tropospheric storm tracks (Tilmes et al., 2018; Richter et al., 2018). Changes in stratosphere–troposphere exchange may impact tropospheric ozone and methane lifetimes (Visioni et al., 2017b). Enhanced sulfur deposition resulting from injections was shown to be unimportant (Kravitz et al., 2009). Changes in stratospheric ozone, including the delay of the recovery of ozone at high altitudes and the potential increase of ozone for some regions and seasons, and changes in aerosols impact surface ultraviolet (UV) radiation. Substantial changes in UV, either increased or decreased from pre-ozone hole values, may be harmful for life on Earth. Further, potential side effects include changes in ocean currents, carbon budget, effects on land and ocean biosphere, energy production for solar generators, and visible astronomy. New strategies are being currently developed that aim to reduce some of these side effects (Kravitz et al., 2017).

Risks: Attempting to offset elevated global temperatures requires consistent injections until greenhouse gases are sufficiently reduced. Depending on the pathway, this approach may require hundreds of years of application (Tilmes et al., 2016). A sudden termination of such an application would lead to significant climate change within 10 years after the termination (Jones et al., 2013). Uncertainties regarding future climate change mean that the injection amounts may be higher than anticipated. There are other possible risks that are not included in the models, for example, impacts on the biosphere and continued sea level rise. Additionally, feedback processes might be larger than model predictions, and the current model parameterizations might not be correct in a "geo-engineered" world. Technical injection strategies have not been developed to date, and the required costs would depend on many factors (McClellan et al., 2012).

reflecting sunlight before it enters Earth's atmosphere (e.g., Early, 1989; Seifritz, 1989; Angel, 2006). Recent model studies investigating the stratospheric response in the Geoengineering Model Intercomparison Project (GeoMIP) G1 experiment computed a global ozone increase of 2–8% throughout most of the stratosphere due to a 4% reduction in the total solar irradiance (TSI), with a global total column ozone increase of 1.6% (Jackman and Fleming, 2014; Nowack et al., 2016). This resulted in up to a 20% reduction in local UV radiation, with potential adverse effects on life on Earth, including vitamin-D deficiency and an increase in tropospheric ozone. The main drivers of the ozone increase were reductions in atomic oxygen and temperature caused by the 4% TSI decrease, which subsequently slowed the ozone photochemical loss rates. Reductions in stratospheric water vapor and atomic oxygen excited state, $O(^1D)$, also contributed to the ozone enhancement by decreasing odd hydrogen concentrations and therefore the HO_x-ozone loss rates.

6.2.6 Other Potential Influences on Stratospheric Ozone

Emissions from Rockets

Since WMO (2014), the orbital launch rate has increased by about a factor of two (Doncaster et al., 2016; FAA, 2016). Recent developments suggest that rocket launches and emissions will continue to increase and possibly accelerate. New space systems, such as reusable and heavy-lift launch vehicles and communication satellite constellations using thousands of satellites in low earth orbit, have emerged (Klinkrad, 2017; Pelton and Jacque, 2016). Maturation of these

systems ensures that launch emissions will increase in coming years. Detailed scenarios of future launch emissions based on known, likely, or speculative future space transportation requirements have not been developed.

Studies of the atmospheric impacts of rockets have primarily focused on stratospheric chemical perturbations associated with the various components of rocket engine emissions. In particular, ozone loss caused by solid rocket motors (ammonium perchlorate oxidizer) occupies the greatest portion of the literature, as summarized in Harris and Wuebbles et al. (2014). Existing model predictions are necessarily incomplete, however, because they do not account for the several types of fuels used by the space industry or the rapid evolution in the global space launch industry and because of the sparsity of new research using modern models that couple atmospheric radiation and chemistry.

For several decades (1981–2011), the Space Shuttle was the largest single rocket emission source, and research focused on its solid rocket motor emissions. After the Space Shuttle ended service in 2011, solid rocket motor emissions from other launch vehicles (Ariane V, Vega, and others) have increased such that solid rocket motor emissions into the stratosphere (~4 Gg yr^{-1}) have remained nearly constant over the past decade. Global models (Voigt et al., 2013), using prescribed HCl and alumina aerosol emissions, generally agree that as recently as a few years ago, solid rocket motor emissions produce a global total column ozone loss of about 0.03%, approximately equally partitioned between HCl gas-phase reactions and alumina surface heterogeneous chlorine activation reactions. The alumina surface heterogeneous contribution is not well understood, however. Two microphysical parameters, acknowledged as poorly understood in Daniel et al. (2011), determine the magnitude of the alumina impact. These are (1) the size distribution of emitted alumina (specifically, the submicron mode mass fraction, which determines steady-state stratospheric alumina surface area density) and (2) the chlorine activation rate constant. Models have tended to adopt values representative of lower bounds for these parameters. Extrapolations of model results to parameter upper bounds suggest that alumina-related global ozone loss could be a factor of 10 larger than the widely assumed value of 0.03% (Voigt et al., 2013). No research has been done since WMO (2014) to conclusively eliminate the possibility of upper-bound submicron mass fraction or chlorine activation rate.

Ross and Sheaffer (2014) considered the radiative effects of the black carbon (BC; i.e., "soot") and alumina aerosol components of rocket emissions and noted that coupling between radiative and chemical impacts presents a potentially important path for ozone loss from rocket emissions. BC emissions from kerosene-fueled rockets have a relatively long stratospheric lifetime (~3 years) and accumulate in the upper stratosphere (Ross et al., 2010). This BC scatters and absorbs incoming solar radiation, possibly increasing stratospheric temperatures and thereby accelerating the rate of ozone-destroying chemical reactions. Models of BC-based geoengineering (Kravitz et al., 2012) and limited nuclear exchanges (Mills et al., 2014) can be viewed as analogues to rocket BC emissions, though scaled up by orders of magnitude. Downward extrapolations using these models suggest that stratospheric heating in the present-day rocket BC accumulation (Ross et al., 2010) could produce global ozone loss comparable to that purely from chemical loss from solid rocket motors. The fraction of global launches using propellants that have a relatively large BC emission index (mainly kerosene) has trended upward in recent years, increasing the steady-state BC accumulation. Indirect ozone loss caused by stratospheric heating associated with rocket BC emissions has yet to be studied using the required coupled chemistry and climate models.

Larson et al. (2017) modeled the impact of hydrogen-fueled rockets emitting only water vapor (typically, propellants emit ~400 g [H_2O] per kg of fuel). They found global ozone loss from rocket H_2O emissions to be three orders of magnitude less than from an equivalent emission from solid rocket motors. The present water vapor component of rocket emissions produces ozone loss less than 0.0001%. Even under the most expansive plausible launch growth scenario, ozone loss from hydrogen-fueled rockets does not become significant.

Larson et al. (2017) also examined ozone loss caused by spacecraft descent from orbit. Intense atmospheric heating in the mesospheric portion of the reentry corridor produces NO_x, which while not directly emitted is a source arising from rocket activity. Larsen et al.

Table 6-1. Atmospheric lifetimes, fractional halogen release factors, and Ozone Depletion Potentials (ODPs) for long-lived halocarbons. In this Assessment, lifetimes are based on SPARC (2013) and SPARC (2016). Fractional release factors (mid-latitude conditions) used in this Assessment are from Newman et al. (2007), with ODPs calculated using the fractional release values from Laube et al. (2013), shown in parentheses. Lifetime uncertainties are based on SPARC (2013) lifetimes as evaluated by Velders and Daniel (2014); the uncertainty associated with the CCl_4 lifetime has not been updated for the revised lifetime and so is left blank. See **Chapter 1** for further discussion on atmospheric lifetimes.

Halocarbon	Atmospheric Lifetime (years)			Fractional Release Factors	ODPs	
	WMO (2014)	This Assessment	Lifetime Uncertainty (1σ)	WMO (2014) and this Assessment	This Assessment Recommendation	In Montreal Protocol
Annex A-I						
CFC-11	52	52	±22%	0.47	1.0	1.0
CFC-12	102	102	±15%	0.23	0.73 (0.81)	1.0
CFC-113	93	93	±17%	0.29	0.81 (0.82)	0.8
CFC-114	189	189	±12%	0.12	0.50	1.0
CFC-115	540	540	±17%	0.04	0.26	0.6
Annex A-II						
halon-1301	72	72	±13%	0.28	15.2 (19.0)	10.0
halon-1211	16	16	±29%	0.62	6.9 (7.7)	3.0
halon-2402	28	28	±19%	0.65	15.7	6.0
Annex B-II						
CCl_4	26[a]	32		0.56	0.87 (0.87)	1.1
Annex B-III						
CH_3CCl_3	5.0[b]	5.0[b]	±3%	0.67	0.14 (0.17)	0.1
Annex C-I						
HCFC-22	12	12	±16%	0.13	0.034 (0.024)	0.055
HCFC-123	1.3	1.3			0.02[c]	0.02
HCFC-124	5.9	5.9			0.022[c]	0.022
HCFC-141b	9.4	9.4	±15%	0.34	0.102 (0.069)	0.11
HCFC-142b	18	18	±14%	0.17	0.057 (0.023)	0.065
HCFC-225ca	1.9	1.9			0.025[c]	0.025
HCFC-225cb	5.9	5.9			0.033[c]	0.033
Annex E						
CH_3Br	0.8[d]	0.8[d]	±17%	0.60	0.57	0.6
Others						
halon-1202	2.5	2.5	±33%	0.62	1.7	
CH_3Cl	0.9[e]	0.9[e]	±18%	0.44	0.015	

Notes:

[a] The partial lifetime for CCl_4 is 44 years for atmospheric loss (from SPARC, 2013) and is assumed to be 183 years for oceanic loss (Butler et al., 2016) and 375 years for soil loss for a total lifetime of 32 years (see **Chapter 1**).

[b] The partial lifetime for CH_3CCl_3 is 5 years for atmospheric loss (from SPARC, 2013).

[c] ODPs taken from Papanastasiou et al. (2018).

[d] The total lifetime for CH_3Br is 1.5 years for atmospheric loss (from SPARC, 2013), 3.1 years for oceanic loss, and 3.3–3.4 years for soil loss.

[e] The partial lifetime for CH_3Cl is 1.3 years for atmospheric loss (from SPARC, 2013) and 3 years for oceanic and soil losses.

(2017) modeled the NO_x emission for spacecraft returning from orbit, finding ozone column loss would not exceed 0.1% at a rate of 10^5 reentries per year. For comparison, the present reentry rate (including large space debris) is less than 10^2 per year so that current ozone loss from reentry NO_x emissions is inferred to be less than 0.0001%.

6.3 METRICS FOR CHANGES IN OZONE AND CLIMATE

6.3.1 Metrics for Changes in Ozone

The two primary metrics for studies of stratospheric ozone are equivalent effective stratospheric chlorine (EESC) and Ozone Depletion Potentials (ODPs). An updated analysis of ODPs was given in the last Assessment (see Section 5.3 and especially Box 5-2 in Harris and Wuebbles et al. (2014) for the basic description of the EESC and ODP concepts; see also Tables 5-2 and 5-3 in that Assessment for the derived values of ODPs). Uncertainty estimates of the ODPs were also included in Table 5-2, and to our knowledge, have not been updated. A discussion of the uncertainties associated with ODPs and EESC from a variety of sources can be found in Velders and Daniel (2014). Semi-empirical ODPs (see Box 5-2 in Harris and Wuebbles et al., 2014) and EESC take advantage of observations to determine fractional release factors (FRFs), which quantifies how much of a trace gas is broken down by the time it reaches a particular region of the stratosphere. **Section 6.4** and **Chapter 1** describe a recent update to the FRF formalism for chlorine- and bromine-containing compounds. This leads to relatively minor changes in FRFs, and thus to semi-empirical ODPs, and to more significant changes in calculated EESC. This update does not, however, affect model-calculated ODPs. Relative to the last Assessment, the only lifetime change for the most important long-lived halocarbons is for CCl_4. As discussed in **Chapter 1**, the CCl_4 lifetime has been updated from 26 to 32 years, leading to a 23% increase in its ODP (**Table 6-1** and **Appendix A**). It is also important to recognize that ODPs can depend on the background atmosphere. Revell et al. (2015) have confirmed that this is especially the case for nitrous oxide (N_2O), where ODP values are likely to be larger (by as much as a factor of two depending on levels of chlorine and methane in the stratosphere) for 2100 than in the present day.

In addition to the updates above, there are only a few new studies of ODPs since WMO (2014), primarily for compounds considered to play a relatively minor role in ozone depletion. The discussion of these follows below in two parts, for long-lived gases (atmospheric lifetimes greater than 1 year) and for short-lived gases. Overall, the findings for ODPs are similar to prior Assessments, but this Assessment includes ODP estimates for a few additional compounds.

Long-Lived Gases

Davis et al. (2016), using the NASA Goddard two-dimensional chemistry-climate model, evaluated the atmospheric lifetimes, ODPs, and GWPs for several CFCs not previously examined, namely CFC-112, CFC-112a, CFC-113a, and CFC-114a. The first observations of the small atmospheric concentrations of CFC-112, CFC-112a, and CFC-113a were reported by Laube et al. (2014), along with budget analyses with emission sources dating back to the 1960s (see **Chapter 1**). The first long-term measurements of CFC-114 and CFC-114a, separately (Laube et al.,

2016), have also been reported since WMO (2014). As expected, the ODPs for these CFCs are quite large: 0.98, 0.86, 0.73, and 0.72 for CFC-112, CFC-112a, CFC-113a, and CFC-114a, respectively.

Short-Lived Gases

Wallington et al. (2015) analyzed the atmospheric chemistry for a number of different short chain haloolefins; however, only HCFO-1233zd(*E*) (26-day lifetime using a simple scaling relative to global-averaged OH (hydroxyl) concentrations) and HCFO-1233zd(*Z*) (12-day lifetime) had non-zero ODPs, and these were already included in Harris and Wuebbles et al. (2014) based on the earlier study by Patten and Wuebbles (2010). Patten and Wuebbles (2010), using a three-dimensional atmospheric chemistry-climate model, found an atmospheric lifetime of 40 days (for emissions assumed to be on all landmasses from 30°N to 60°N) and an ODP of 0.00034 for HCFO-1233zd(*E*) and an atmospheric lifetime of 13 days and an ODP of <0.00034 for HCFO-1233zd(*Z*). In a new study updating the reaction rates, Sulbaek Andersen et al. (2017) found a slightly smaller lifetime for HCFO-1233zd(*E*) of 36 days and reduced the ODP to 0.00030 for the same emissions assumptions as made in Patten and Wuebbles (2010). As emphasized in prior assessments, ODPs for very short-lived substances (VSLSs) that contain bromine or chlorine are strongly dependent on the geographic location and season of emission. Therefore, it is important to provide the emissions assumptions when reporting VSLS ODP derivations. Although ODP-weighted emissions have been used for some time in analyses of long-lived gases, Tegtmeier et al. (2015) extend this approach to short-lived compounds through analyses of $CHBr_3$ emissions from the ocean by accounting for the area-based variations in ODPs and emissions. They found that ODP-weighted emissions of $CHBr_3$ were about 9% of the total ODP-weighted emissions by the long-lived halogenated ODPs and that they are expected to grow over the rest of the century due to climate change.

Indirect ODPs

As strong radiative forcers, HFCs increase tropospheric and lower-stratospheric temperatures, thereby enhancing ozone-destroying catalytic cycles and modifying the atmospheric circulation. These changes lead to a weak indirect depletion of stratospheric ozone. Incorporating the interactions between chemistry, radiation, and dynamics, model-calculated ODPs for HFC-32, HFC-134a, HFC-125, HFC-143a, and HFC-23 range from 0.39×10^{-3} to 30.0×10^{-3} (Hurwitz et al., 2015). These values are approximately 100 times larger than previous ODP estimates, which were based solely on the direct chemical potential to deplete ozone via catalytic loss cycles that involve fluorine (Ravishankara et al., 1994). Nevertheless, their total projected impact on globally averaged total ozone from HFCs remains less than 0.1 DU (Dobson unit) by 2050 (Hurwitz et al., 2016), even for the high-growth HFC scenario from Velders et al. (2015).

6.3.2 Metrics for Changes in Climate

Radiative forcing (RF), Global Warming Potentials (GWPs), and Global Temperature change Potentials (GTPs) are the primary metrics used to consider the climate effects of halocarbons and other gases. An updated analysis of GWPs and GTPs was given in the last Assessment (see section 5.3 and especially Box 5-3 in Harris and Wuebbles et al. (2014) for the basic description of the GWP and GTP concepts; Table 5A-1 in that Assessment gives the derived values of GWPs and GTPs from IPCC, 2013b). Table 5-5 in Harris and Wuebbles et al. (2014) provides an update for a number of halocarbons based on the updated SPARC (2013) lifetimes, while Section 5.3.2 (and Tables 5-6 and 5-7) discuss uncertainties in the GWP and GTP derivations. Shortcomings of using RF, GWPs, and GTPs as proxies for climate response have been studied extensively and are summarized in Chapter 8 of IPCC (2013b). More recent work has examined how the GWP concept can be appropriately used to compare different climate-forcing agents (Allen et al., 2016).

In this Assessment, updates for many GWPs and GTPs are provided. **Table 6-2** presents values for selected long-lived ODSs and HFCs, following the approach used in IPCC AR5 (2013b) that is currently being used by policymakers. This Assessment also includes GWPs and GTPs for the 274 HCFCs in Annex C of the Montreal Protocol (**Appendix A**). These values are potentially useful as the Parties continue the process of phasing out HCFC production and consumption; many of them are provided for the first time in

an assessment. The new values are based on estimates of lifetimes and calculations of infrared absorption characteristics (Papanastasiou et al., 2018). Because these quantities are not experimentally measured, the metrics calculated from this information typically have larger uncertainties associated with them than those based on laboratory measurements.

As in the last Assessment, these metrics were calculated based on the evaluation and assessment of IPCC (Myhre et al., 2013), with updates based on Etminan et al. (2016). The new analyses by Etminan et al. (2016) include shortwave effects not adequately considered previously; these affect the radiative forcing efficiency and GWP for CH_4 but have no significant effects on the GWPs for other compounds. Also shown are the atmospheric lifetimes and radiative efficiencies used in these analyses. As in WMO (2014) and IPCC (2013b), the CO_2 radiative efficiencies (and hence the GWPs and GTPs) of non-CO_2 greenhouse gases presented in **Table 6-2** and **Appendix A** are calculated with a CO_2 level corresponding to 391 ppm.

The following discusses the few new studies of GWPs and GTPs (based on updates to atmospheric lifetimes or new radiative efficiencies for the compounds in question) that have been published since WMO (2014) in two parts: long-lived gases (atmospheric lifetimes greater than 1 year) and short-lived gases. Overall, with the exception of the values for CH_4, there have been minor changes in the derived GWPs and GTPs for the compounds evaluated.

Long-Lived Gases

As mentioned above (**Section 6.3.1**), Davis et al. (2016) have provided 100-year GWP values for CFCs that have not previously received much attention: CFC-112, CFC-112a, CFC-113a, and CFC-114a. Lu et al. (2017) updated analyses of the radiative forcing for NF_3 and derived GWPs and GTPs for 20- and 100-year integrations. Their GWP and GTP values are smaller than those derived previously by IPCC (2013b), primarily due to their derivation of a smaller radiative efficiency. In contrast, a study by Totterdill et al. (2016) found a 25% larger radiative efficiency for NF_3 than IPCC (2013b) and therefore larger GWP and GTP values.

Short-Lived Gases

Most of the new analyses since WMO (2014) of short-lived halocarbons have been associated with short-lived haloolefins, which generally have extremely small GWP values. A short description is provided of some of the key studies. Wallington et al. (2015), along with their analyses of ODPs, provide estimated GWPs for a number of HCFOs, all having 100-year GWPs of 1 or less. Sulbaek Andersen et al. (2017) derive GWP values for HCFO-1233zd(*E*) of 19, 5, and 1 for 20-, 100- and 500-year time horizons, respectively, using the radiative forcing three-dimensional modeling studies from Wuebbles et al. (2013) for emissions assumed to be distributed across all landmasses from 30°N to 60°N; these GWPs are larger than prior values but reasonable for the assumed landmass emissions. Orkin et al. (2014) examined the photochemical properties of HCFO-1233zd(*Z*) and estimated an atmospheric lifetime of 46 days assuming a well-mixed distribution (which would be very unlikely for such a short-lived gas) and a relatively small 100-year GWP of 14 (but this again reflects an even distribution of the concentration of the gas).

Climate Carbon-Cycle Feedbacks

New studies of the Climate–Carbon cycle Feedbacks (CCFs) on GWPs and GTPs show the potential importance of accounting for these feedbacks with an explicit CCF model rather than with a linear feedback approach, especially for long-time horizons (Sterner and Johansson, 2017). While values of GWPs and GTPs change less than 10% for all well-mixed greenhouse gases when the time horizon is limited to 100 years or less, the values for long time horizons, such as 500 years, can be substantially lower (by up to 30% for the GWP and up to 90% for the GTP) with the explicit CCF model than with the linear feedback approach. This Assessment does not account for the CCF effects in the values of GWPs and GTPs presented here.

Indirect GWPs

There are multiple types of indirect (100-yr) GWPs that have been discussed in the literature. Usually, these relate to the chemical impact a source gas has on other gases and their subsequent climate forcing. One indirect effect that has been shown to be important

Table 6-2. Lifetimes, radiative efficiencies, direct global warming potentials (GWPs), and Global Temperature change Potentials (GTPs) for selected gases (based on a radiative efficiency for CO_2 based on [CO_2] = 391 ppm). The CO_2 AGWPs[a] for the 20- and 100-yr time horizons are 2.495×10^{-14} and 9.171×10^{-14} W yr $(m^2\ kg)^{-1}$; the CO_2 AGTPs[a] for the 20-, 50-, and 100-yr time horizons are 6.841×10^{-16}, 6.167×10^{-16}, and 5.469×10^{-16} K kg^{-1}. GTPs for the 50-yr time horizon are not included in this table but may be found in Appendix A.

Industrial Designation or Common Name	Lifetime (years)	GWP 20-yr	GWP 100-yr	GTP 20-yr	GTP 100-yr
Annex A-I					
CFC-11	52	7,090	5,160	7,160	2,920
CFC-12	102	10,800	10,300	11,300	8,590
CFC-113	93	6,560	6,080	6,830	4,860
CFC-114	189	7,710	8,580	8,180	8,530
CFC-115	540	5,780	7,310	6,210	8,290
Annex A-II					
halon-1301	72	7,930	6,670	8,160	4,700
halon-1211	16	4,590	1,750	3,950	300
halon-2402	28	3,920	2,030	3,730	615
Annex B-II					
CCl_4	32	3,790	2,110	3,670	750
Annex B-III					
CH_3CCl_3	5	555	153	300	21
Annex C-I					
HCFC-22	12	5,310	1,780	4,230	265
HCFC-141b	9.4	2,590	800	1,900	114
HCFC-142b	18	5,140	2,070	4,530	390
Annex E					
CH_3Br	0.8	7.6	2	2.4	<1
Others					
halon-1202	2.5	720	196	285	27
CH_3Cl	0.9	16	4.3	5.1	<1
HFC-23	228	11,085	12,690	11,825	13,150
HFC-32	5.4	2,530	705	1,440	90
HFC-125	30	6,280	3,450	6,040	1,180
HFC-134a	14	3,810	1,360	3,170	215
HFC-143a	51	7,050	5,080	7,110	2,830
HFC-152a	1.6	545	148	190	21
HFC-227ea	36	5,250	3,140	5,140	1,260
HFC-245fa	7.9	2,980	880	2,040	124

Notes:

[a] From the mass of the atmosphere (5.135×10^{18} kg; Trenberth and Smith, 2005), average molecular mass of dry air (28.964 g mol^{-1}; Warneck and Williams, 2012), and molecular mass of CO_2 (44.01 g mol^{-1}) the conversion factor 1 ppm $CO_2 = 7.803 \times 10^{12}$ kg is derived. This conversion factor can be used to convert the CO_2 AGWPs and AGTPs given above to units of per ppm rather than per kg.

results from the destruction of stratospheric ozone by the ODSs. Because ozone is a greenhouse gas itself, destruction of ozone will lead to a cooling influence on climate. For gases like the halons, this indirect effect is actually larger than, and opposite in sign to, the direct forcing caused by the presence of the halons themselves. There have been no new studies updating this indirect effect for the ODSs, so we update them here (**Table 6-3**) only for the revised CO_2 AGWP (absolute GWP, which is the radiative forcing integrated over a given time horizon, resulting from a pulse emission of the gas) and the updated lifetime of CCl_4.

As interest in shorter-lived compounds replacing longer-lived greenhouse gases has grown, the importance of identifying the degradation products of these compounds and understanding the physical properties of the products has been pointed out. This is another situation in which the indirect GWP can actually be larger than the direct GWP of an emitted compound (Bravo et al., 2011; Jubb et al., 2015).

6.4 SCENARIOS AND SENSITIVITY ANALYSES

6.4.1 Tools Used in Analyses of Ozone and Climate Effects

In this chapter, as in the past two Ozone Assessments (WMO, 2011, 2014), we use two primary tools to compare the climate and ozone impacts of various future scenarios. The first is a simple box model (Harris and Wuebbles et al., 2014), which allows for the calculation of the ozone metrics EESC and ODP-weighted emissions and of the climate metrics RF (radiative forcing) and GWP-weighted emissions (100-yr time horizon). EESC has been shown to be a reasonable proxy for the amount of stratospheric ozone depletion caused by a given abundance of a long-lived ODS (Daniel et al., 2010), and RF is a quantity that describes the energy imbalance often due to the presence of some compound in the atmosphere, and is roughly proportional to the global average surface temperature change it will produce (Myhre et al., 2013). The second evaluation tool used in this chapter is the NASA/Goddard Space Flight Center (GSFC) 2-D coupled chemistry–radiation–dynamics model (Fleming et al., 2011) driven with mixing ratio boundary conditions calculated from the box model. Earlier versions of this model were also used in Daniel and Velders, et al. (2011) and Harris and Wuebbles et al. (2014). The inclusion of the 2-D model allows us to compare impacts of the long-lived ODSs that are controlled by the Montreal Protocol with the impacts of CO_2, CH_4, and N_2O as well as with very short-lived (VSLS) compounds like CH_2Cl_2. The GSFC 2-D model compares well with observations and with the 3-D Goddard Earth Observing System Chemistry Climate Model (GEOSCCM) in simulating temperature and various transport-sensitive features in the meridional plane, such as the horizontal and vertical gradients of long-lived stratospheric tracers and age of air (Fleming et al., 2011; SPARC, 2013). Projections of future ozone using this 2-D model are also in very good agreement with those of more complex 3-D models used in **Chapters 3**, **4**, and **5** of this Assessment to examine the impacts of various processes and emissions on ozone and climate (see **Appendix 6A**). 3-D models provide our best understanding of chemical, dynamical, and radiative processes and how they interact to explain the past and future state of the atmosphere. However, these models take large amounts of computer time, which makes evaluation of many dozens of alternative scenarios impractical. Thus, in this chapter, we do not use any 3-D model calculations.

RF is calculated throughout this chapter as it was in Harris and Wuebbles et al. (2014), using the radiative efficiencies found in the **Appendix Table A-1**. EESC is also calculated as in WMO (2014) and is used as the basis for comparison of different scenarios (**Section 6.4.3.1**). However, we also discuss calculations of EESC using the updated approach of Ostermoller et al. (2017) and Engel et al. (2017). The fundamental advance in these papers is the recognition that the difference between the average age of ODSs that have dissociated and the average age of inert tracers can be important to the estimated amount of Cl_y and Br_y in the stratosphere and thus for EESC. They demonstrate that the use of mean age of air in the calculation of both fractional release and in EESC (Newman et al., 2007) leads to a bias in those quantities. The impact of the updated theoretical approach on calculated fractional release factors (FRFs) is not large overall, but it does alter the FRF of a few compounds (Engel et al., 2017). The effect on the change to polar EESC is also not particularly large since the average age of the dissociated ODSs

Table 6-3. Indirect GWPs from ozone depletion (direct forcing from ODSs, themselves, is not included). Approach is taken from Daniel et al. (1995), assuming a radiative forcing due to ozone depletion in 2011 of –0.15 W m^{-2} (IPCC, 2013b). Uncertainty in this radiative forcing leads to an uncertainty in these GWPs of ±100%. Direct GWPs are shown for comparison.

GAS	Indirect GWP 100-yr	Direct GWP 100-yr
CFC-11	–2,860	5,160
CFC-12	2,050–2,050	10,300
CFC-113	–2,180	6,080
CFC-114	–880	8,580
CFC-115	–210	7,310
HCFC-22	–98	1,780
HCFC-123	–35	80
HCFC-124	–45	530
HCFC-141b	–250	800
HCFC-142b	–160	2,070
CH_3CCl_3	–310	153
CCl_4	–2,610	2,110
CH_3Br	–1,210	2
halon-1211	–18,500	1,750
halon-1301	–46,100	6,670
halon-2402	–44,800	2,030
HCFC-225ca	–39	127
HCFC-225cb	–58	525

are generally not too different from the mean age of an inert tracer. At mid-latitudes, on the other hand, the new approach leads to significantly older effective ages for dissociated ODSs than for an inert tracer in many cases, assumed to be three years here and in previous Assessments (WMO, 2007, 2011, 2014).

The return of EESC to 1980 levels continues to be a useful metric to compare future scenarios. It is important to recognize, however, that relatively small changes in stratospheric chlorine and bromine loading (i.e., EESC) can lead to large changes in this return time because of how gradually EESC is declining in the baseline scenario. It is also important to recognize that while numerous sources of uncertainty, particularly in atmospheric lifetimes, limit our ability to pinpoint the return of EESC to 1980 levels to within 25–40 years (95% confidence interval) (Velders and Daniel, 2014), this metric can be used meaningfully to compare differences in return dates of various scenarios, assuming that the relative atmospheric lifetimes, production, and bank estimates of different substances or groups of substances are well defined.

6.4.2 Baseline Scenario for Ozone and Climate

Future atmospheric concentrations of ODSs depend on the amount emitted to the atmosphere and the rate at which destruction occurs. The destruction rate can change over time due to changes in atmospheric circulation, changes in solar irradiances at the relevant wavelengths, or changes in reactive chemicals like OH, O(1D), and atomic chlorine. Release to the atmosphere depends on multiple factors, which can include the amount released during and after production, whether production is ultimately for use as a feedstock or for dispersive uses, and on the rate at which the ODS is released from existing applications, also called banks.

Because of inherent uncertainties in these sources and sinks, it is not possible to perfectly predict future ODS concentrations. Therefore, the baseline (A1) scenario should be considered a plausible future pathway, and not the most likely future pathway in some statistical sense. In fact, here and in Chapter 1 we show the extent to which historical observations have differed from the baseline scenario projections of past Assessments. It is also important to keep in mind that the purpose of the projections in this chapter is not for them to serve as predictions, but instead to be used to evaluate the impact of potential policy options regarding the future production and consumption of various ODSs as well as emissions from banks.

The baseline scenario in this Assessment has been developed using the same methodology as has been used in the past several Assessments (WMO, 2007, 2011, 2014). Observations from **Chapter 1** are used to constrain the mixing ratios over the time period when they are available, which is generally from around 1980 through 2016. Before this time period, mixing ratios are taken from the previous Assessment (Harris and Wuebbles et al., 2014), except for CFC-114 (see discussion below). The recent mixing ratios are used in conjunction with the bottom-up bank estimates for 2008 (UNEP, 2009) and the annual production reported to the Ozone Secretariat to estimate bank values through the beginning of 2016 using the relationship

$$B_{i+1} = B_i + P_i - E_i$$

where B_i is the bank at the beginning of year i, and P_i and E_i are the production and emission, respectively, throughout year i. Knowing the annual emissions and bank values allow for a calculation of the bank fraction that is annually released over the past several years. The annual release fractions, averaged over the last 7 years, are then assumed to remain constant in the future; by assuming that future production is equal to what is permitted by the fully adjusted and amended Montreal Protocol and that this is added to the banks, these release fractions can be used to estimate future annual emissions.

Table 6-4 contains the long-lived ODS mixing ratios for the baseline scenario, and Figure 6-2 includes a comparison of the current baseline scenario with the baseline scenario from WMO (2014). Many of the current projections remain very similar to the previous ones (e.g., CFC-12, CFC-113, and CFC-114 and halons 1211 and 1301). Such agreement is to be expected since our understanding of global lifetimes for most of the compounds has not changed, there has been no reported production to UNEP for CFCs and halons, and we continue to assume the same 2008 bank levels as in Harris and Wuebbles et al. (2014). There has been a slight downward revision in the CFC-114 mixing ratios from 1979 through the mid-1980s because of recent additions of firn data to the historical record (**Chapter 1**) (Laube et al., 2014). Thus, CFC-114 mixing ratios preceding the atmospheric measurement record have been scaled by a constant factor (0.92) to avoid a discontinuity in 1979. **Figure 6-2** also shows how the individual mixing ratios change in the different alternative scenarios. For the scenarios shown, the HCFCs show much more dependence on future emissions than do the CFCs in relation to their current atmospheric concentrations, but CFC emissions, in particular those from the CFC-11 banks, remain significant.

The CCl_4 projection in the current Assessment is higher than in Harris and Wuebbles et al. (2014) because emissions are assumed to decline at a rate of 2.5% yr^{-1} rather than the 6% yr^{-1} assumed in Harris and Wuebbles et al. (2014). There is substantial interannual variability in the emission trend, but the updated rate is more consistent with the long-term trend over the last two decades.

HCFC projections are similar to those of the previous Assessment (Harris and Wuebbles et al., 2014), although the three major HCFCs shown in **Figure 6-2**

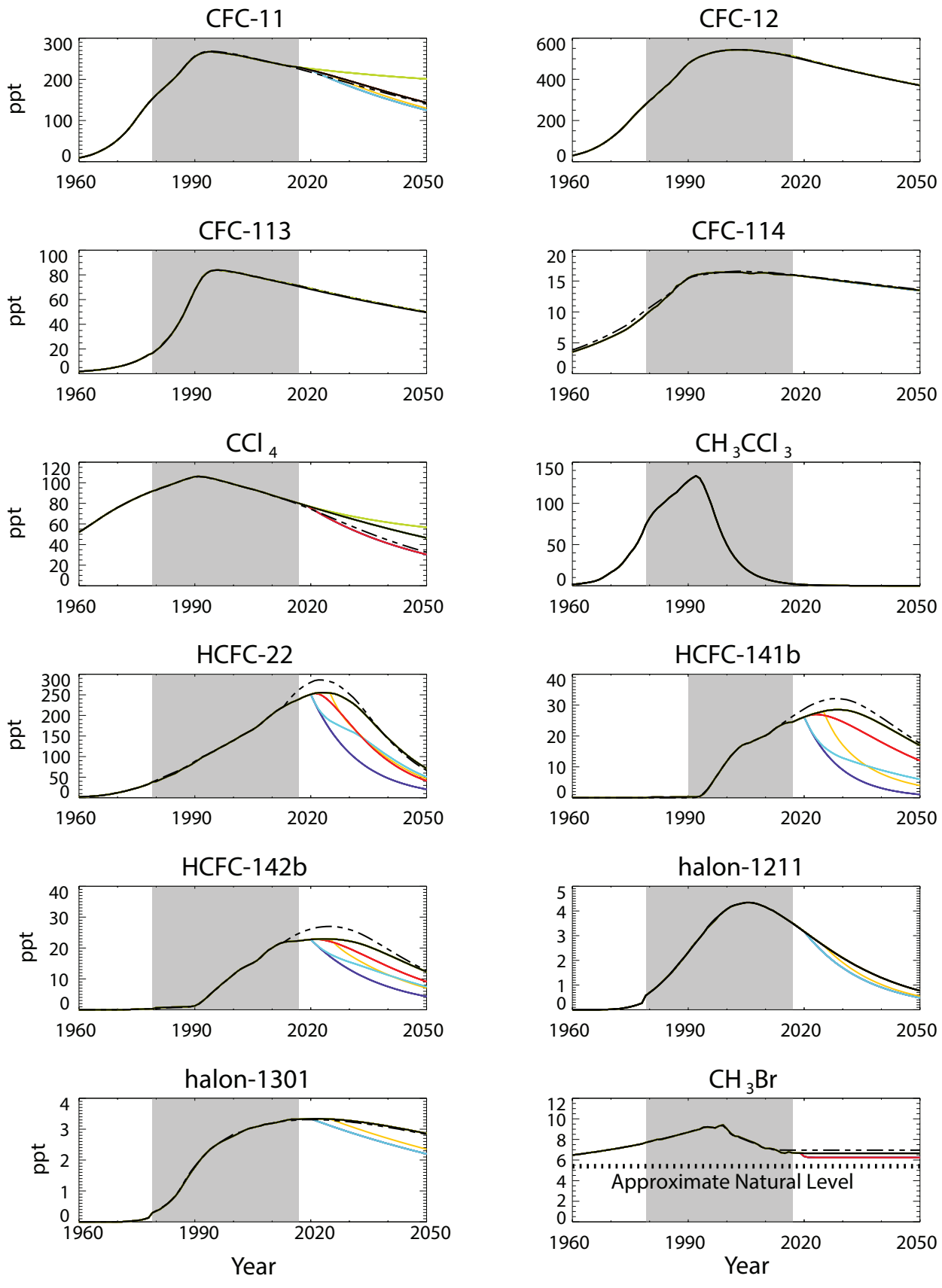
CFC-11
CFC-12
CFC-113
CFC-114
CCl 4
CH 3CCl 3
HCFC-22
HCFC-141b
HCFC-142b
halon-1211
halon-1301
CH 3Br
ppt
Approximate Natural Level
1960
1990
2020
2050
Year

all have concentrations somewhat lower for the next few years, owing to recent growth in concentrations that was less than projected previously and to the fact that reported production over the past few years has been less than was assumed in Harris and Wuebbles et al. (2014) .

CH_3Br projections are developed by calculating the total atmospheric loss of CH_3Br (using the approach used in Table 1-4 of Carpenter and Reimann et al., 2014) with a global atmospheric lifetime of 0.8 years, and assuming equivalent total atmospheric emissions. (Note that the baseline scenario of the previous Assessment assumed a global atmospheric CH_3Br lifetime of 0.75 years as in WMO, 2011). All emissions, including QPS and CUE emissions, are assumed to continue at the 2016 level indefinitely into the future. This is a minor difference from the baseline scenario of the last Assessment, where CUE emissions were assumed to be zero after 2012. This change makes little difference to the calculations since production under CUE has continued to decline and was less than a tenth of production for QPS in 2016.

A lower assumed total atmospheric emission is the primary reason for a slight lowering of future CH_3Br atmospheric concentrations in the baseline scenario when compared with the previous Assessment (6.7 ppt currently relative to the previous 7.0 ppt). Note that the CH_3Br budget continues to have a significant imbalance between sources and sinks, and there is a large uncertainty in both terms (WMO, 2014). The key issue, however, is the level of anthropogenic production and consumption that could be controlled, if desired, which is well defined. We also note that (continued) reduction in the global atmospheric mole fraction of CH_3Br leads to an increase in the net sea–air flux of CH_3Br, which can somewhat dampen policy actions taken to reduce anthropogenic emissions. While the ocean response to recent and predicted future changes in atmospheric CH_3Br is now very small (resulting in a calculated increase in net ocean emissions according to the budget terms of Carpenter and Reimann et al. (2014) of ~0.4 Gg yr^{-1} from 2012 to 2016), we note that since the mid-1990s, the net ocean source has likely increased by ~10 Gg yr^{-1} (Hu et al., 2012; WMO, 2014).

The baseline scenario for HFCs is taken directly from **Chapter 2** and includes global control measures introduced by the Kigali Amendment and other regional and national actions. In order to estimate the impact of the Kigali actions, we use the reference scenarios for HFCs developed in Velders et al. (2015a), which are projections without consideration of specific global control measures. These HFC scenarios are discussed in detail in **Chapter 2**, **Section 2.5.1**.

Potentially, one of the more important differences from projections of previous Assessments is that CFC-11 has declined more slowly than projected for a number of years, and the discrepancy has increased since 2012. While this is not apparent from **Figure 6-2** due to the large scale on the y-axis, it has the potential to be important and will be discussed later in **Section 6.4.3**. We continue to treat CFC-11 emission in the baseline scenario as has been done in previous Assessments, i.e., as arising solely from its banks. This does lead to a higher implied annual bank release fraction, since the ratio of emissions to bank size has gone up substantially since 2013.

In addition to evaluating the impact of future ODS emissions and concentrations, we use the 2-D model to examine the impact of future concentrations of N_2O, CH_4, and CO_2, as well as of short-lived halocarbon (i.e., CH_2Cl_2) emissions, on stratospheric ozone.

Figure 6-2. Comparison of long-lived halocarbon mixing ratios in the current baseline scenario (shown as solid black curve) with those from the baseline scenario of WMO (2014) (dot-dashed black line); future mixing ratio projections for the "no emission from 2020 onward" (dark blue), "bank capture and destruction in 2020" (cyan), "bank capture and destruction in 2025" (yellow), and "no production from 2020 onward" (red) scenarios. Shaded regions represent the time periods when mixing ratios are constrained to observational estimates (see **Chapter 1**). The approximate natural concentration of CH_3Br is noted by the dotted blue line in the lower right-hand panel (see **Chapter 1**). The green curves for CFC-11 and CCl_4, respectively, show concentrations for scenarios in which annual emissions remain at 67 Gg yr^{-1} of CFC-11 and 33 Gg yr^{-1} of CCl_4.

Table 6-4. Mixing ratios (ppt) of the ODSs considered in the baseline scenario. Values are for the beginning of the corresponding year. Shaded areas indicate when the mixing ratio values are forced to equal global average estimates inferred from observations (see **Chapter 1**).

Year	CFC-11	CFC-12	CFC-113	CFC-114	CFC-115	CCl_4	CH_3CCl_3
1955	3.3	14.3	1.3	2.4	0.0	42.3	0.1
1960	9.5	29.5	1.9	3.5	0.0	52.1	1.5
1965	23.5	58.8	3.1	4.6	0.0	64.4	4.7
1970	52.8	114.3	5.5	5.9	0.2	75.9	16.3
1975	106.1	203.1	10.4	7.6	0.6	85.5	40.0
1980	162.4	296.6	19.0	10.1	1.6	93.0	82.3
1981	170.7	311.3	21.5	10.6	1.9	94.6	89.0
1982	179.4	329.6	25.3	11.0	2.2	96.0	93.9
1983	187.6	345.4	28.5	11.6	2.4	97.2	97.8
1984	196.4	362.8	32.0	12.2	2.8	98.5	102.1
1985	205.6	378.1	36.8	12.7	3.1	99.8	106.6
1986	215.4	397.2	41.9	13.3	3.5	101.1	110.2
1987	226.5	415.9	47.4	14.2	3.9	102.7	113.3
1988	237.6	437.9	54.2	14.5	4.3	103.7	118.3
1989	247.5	458.8	61.1	15.0	4.8	104.9	122.9
1990	255.2	476.2	67.7	15.5	5.2	106.0	127.2
1991	260.6	489.6	73.3	15.8	5.7	106.2	130.7
1992	264.0	500.6	78.4	16.0	6.1	105.8	133.3
1993	266.3	510.1	81.3	16.1	6.5	105.3	130.4
1994	266.9	516.3	83.1	16.2	6.9	104.4	122.1
1995	266.3	522.4	83.7	16.3	7.2	103.8	110.6
1996	265.2	528.5	83.8	16.3	7.5	102.8	98.2
1997	264.2	533.0	83.6	16.4	7.7	101.8	84.1
1998	262.8	536.3	83.2	16.4	7.9	100.8	71.1
1999	261.5	539.1	82.7	16.4	8.0	99.8	59.5
2000	259.9	541.2	82.1	16.4	8.1	98.6	49.7
2001	258.4	542.9	81.8	16.4	8.2	97.6	41.5
2002	256.7	543.6	81.2	16.4	8.3	96.6	34.5
2003	254.5	543.6	80.4	16.4	8.3	95.6	28.8
2004	252.5	543.5	79.6	16.4	8.3	94.6	24.0
2005	250.5	542.7	78.9	16.3	8.3	93.7	20.0
2006	248.4	541.8	78.4	16.2	8.4	92.6	16.7

HCFC-22	HCFC-141b	HCFC-142b	halon-1211	halon-1202	halon-1301	halon-2402	CH_3Br	CH_3Cl
1.0	0.0	0.0	0.00	0.00	0.00	0.00	6.3	491.3
2.1	0.0	0.0	0.00	0.00	0.00	0.00	6.5	510.3
4.9	0.0	0.0	0.00	0.00	0.00	0.00	6.7	528.1
12.1	0.0	0.0	0.02	0.00	0.00	0.02	7.0	539.9
23.8	0.0	0.2	0.12	0.01	0.04	0.06	7.4	545.8
39.6	0.2	0.7	0.70	0.01	0.35	0.15	7.8	548.4
43.8	0.2	0.7	0.82	0.01	0.41	0.17	7.9	548.6
48.0	0.2	0.8	0.94	0.01	0.50	0.19	8.0	548.9
52.0	0.2	0.8	1.09	0.01	0.59	0.21	8.0	549.1
55.6	0.2	0.8	1.25	0.01	0.71	0.23	8.1	549.3
59.7	0.2	0.9	1.40	0.01	0.84	0.25	8.2	549.4
65.6	0.2	0.9	1.56	0.02	1.01	0.27	8.3	549.5
71.1	0.2	1.0	1.75	0.02	1.21	0.30	8.4	549.6
75.1	0.2	1.0	1.94	0.02	1.41	0.32	8.5	549.7
80.2	0.2	1.1	2.13	0.02	1.60	0.35	8.6	549.8
86.3	0.3	1.3	2.33	0.02	1.77	0.38	8.7	549.8
92.5	0.3	1.9	2.55	0.02	1.94	0.40	8.8	549.9
98.8	0.3	2.8	2.74	0.03	2.10	0.42	8.9	549.9
103.3	0.5	3.9	2.92	0.03	2.23	0.44	9.0	549.9
108.4	1.3	5.0	3.11	0.03	2.35	0.46	9.2	550.0
113.2	2.6	6.2	3.32	0.04	2.44	0.47	9.2	560.9
119.0	4.5	7.2	3.48	0.04	2.53	0.48	9.2	544.9
123.7	6.4	8.4	3.63	0.04	2.60	0.48	9.1	535.0
128.4	8.2	9.3	3.81	0.04	2.66	0.49	9.3	555.4
134.3	10.1	10.4	3.95	0.05	2.72	0.49	9.4	563.3
139.1	11.8	11.4	4.07	0.05	2.78	0.49	9.0	552.6
144.7	13.5	12.4	4.17	0.04	2.84	0.49	8.6	540.2
150.5	14.8	13.3	4.23	0.04	2.91	0.49	8.3	536.3
155.4	16.1	13.9	4.27	0.04	2.97	0.49	8.3	541.5
160.5	17.0	14.6	4.31	0.04	3.02	0.48	8.1	536.4
165.7	17.5	15.2	4.34	0.03	3.05	0.48	8.0	538.7
171.9	17.9	15.9	4.34	0.03	3.08	0.48	7.8	537.1

Year	CFC-11	CFC-12	CFC-113	CFC-114	CFC-115	CCl_4	CH_3CCl_3
2007	246.2	539.8	77.7	16.3	8.4	91.5	14.0
2008	244.1	537.6	76.9	16.3	8.4	90.3	11.7
2009	242.2	535.5	76.1	16.4	8.4	89.1	9.9
2010	240.4	532.8	75.7	16.3	8.4	87.9	8.3
2011	238.4	530.2	75.0	16.3	8.4	86.7	6.9
2012	236.4	527.7	74.4	16.1	8.4	85.5	5.8
2013	234.4	524.8	73.7	16.1	8.4	84.5	4.8
2014	232.9	521.9	73.0	16.1	8.4	83.3	4.0
2015	231.7	519.1	72.4	16.0	8.5	82.3	3.4
2016	230.3	515.9	71.7	16.0	8.5	81.1	2.7
2017	229.2	512.6	71.2	16.0	8.5	79.9	2.3
2018	227.0	507.6	70.4	15.9	8.5	78.8	1.8
2019	224.8	502.6	69.7	15.8	8.5	77.8	1.5
2020	222.5	497.7	68.9	15.8	8.5	76.7	1.2
2021	220.1	492.9	68.2	15.7	8.5	75.6	1.0
2022	217.6	488.1	67.4	15.6	8.5	74.5	0.8
2023	215.1	483.3	66.7	15.5	8.5	73.4	0.7
2024	212.5	478.6	66.0	15.5	8.5	72.3	0.6
2025	209.9	473.9	65.3	15.4	8.5	71.2	0.5
2030	196.4	451.2	61.9	15.0	8.5	65.9	0.2
2035	182.6	429.7	58.6	14.6	8.5	60.7	0.1
2040	168.9	409.1	55.6	14.2	8.4	55.8	0.0
2045	155.7	389.5	52.7	13.9	8.4	51.1	0.0
2050	143.1	370.9	49.9	13.5	8.3	46.7	0.0
2055	131.2	353.2	47.3	13.2	8.2	42.6	0.0
2060	120.0	336.3	44.8	12.8	8.2	38.8	0.0
2065	109.7	320.2	42.5	12.5	8.1	35.2	0.0
2070	100.1	304.9	40.3	12.2	8.0	31.9	0.0
2075	91.3	290.3	38.1	11.8	8.0	28.9	0.0
2080	83.2	276.4	36.1	11.5	7.9	26.1	0.0
2085	75.7	263.2	34.3	11.2	7.8	23.6	0.0
2090	68.9	250.6	32.5	10.9	7.7	21.3	0.0
2095	62.7	238.6	30.8	10.6	7.7	19.2	0.0
2100	57.0	227.2	29.2	10.4	7.6	17.2	0.0

	HCFC-22	HCFC-141b	HCFC-142b	halon-1211	halon-1202	halon-1301	halon-2402	CH_3Br	CH_3Cl
	179.1	18.5	16.9	4.32	0.03	3.11	0.47	7.7	542.0
	187.3	19.1	18.1	4.28	0.03	3.15	0.47	7.5	544.7
	195.2	19.6	19.3	4.22	0.02	3.17	0.46	7.3	543.0
	202.5	20.1	20.0	4.16	0.02	3.19	0.46	7.1	539.1
	210.0	20.9	20.8	4.08	0.02	3.21	0.45	7.1	534.7
	216.0	21.9	21.5	4.01	0.02	3.24	0.44	7.1	535.8
	221.4	22.8	21.8	3.91	0.02	3.27	0.44	6.9	542.3
	226.5	23.5	22.1	3.81	0.02	3.30	0.43	6.7	538.7
	231.5	24.1	22.2	3.71	0.01	3.32	0.42	6.7	546.0
	235.3	24.4	22.2	3.61	0.01	3.32	0.42	6.8	555.3
	239.3	24.5	22.3	3.51	0.01	3.32	0.41	6.8	550.6
	244.0	25.1	22.5	3.40	0.01	3.33	0.40	6.7	539.5
	247.9	25.6	22.7	3.29	0.01	3.33	0.39	6.7	539.5
	251.1	26.1	22.8	3.17	0.00	3.34	0.39	6.7	539.5
	253.7	26.6	22.9	3.06	0.00	3.34	0.38	6.7	539.5
	255.0	27.0	22.9	2.94	0.00	3.34	0.37	6.7	539.5
	255.5	27.4	22.9	2.83	0.00	3.34	0.37	6.7	539.5
	255.2	27.7	22.9	2.72	0.00	3.33	0.36	6.7	539.5
	254.3	28.0	22.9	2.61	0.00	3.33	0.35	6.7	539.5
	235.0	28.5	22.2	2.10	0.00	3.28	0.31	6.7	539.5
	193.4	26.9	20.5	1.66	0.00	3.20	0.28	6.7	539.5
	144.6	23.9	17.8	1.30	0.00	3.10	0.25	6.7	539.5
	103.1	20.4	15.0	1.01	0.00	2.98	0.22	6.7	539.5
	71.1	16.9	12.3	0.77	0.00	2.86	0.19	6.7	539.5
	48.1	13.8	9.9	0.59	0.00	2.73	0.17	6.7	539.5
	32.2	11.2	7.9	0.44	0.00	2.60	0.15	6.7	539.5
	21.5	8.9	6.2	0.34	0.00	2.46	0.13	6.7	539.5
	14.2	7.1	4.9	0.25	0.00	2.33	0.11	6.7	539.5
	9.4	5.6	3.8	0.19	0.00	2.20	0.10	6.7	539.5
	6.2	4.5	2.9	0.14	0.00	2.08	0.08	6.7	539.5
	4.1	3.5	2.2	0.10	0.00	1.96	0.07	6.7	539.5
	2.7	2.8	1.7	0.08	0.00	1.84	0.06	6.7	539.5
	1.8	2.2	1.3	0.06	0.00	1.73	0.05	6.7	539.5
	1.2	1.7	1.0	0.04	0.00	1.62	0.05	6.7	539.5

RCP6.0 is used in the baseline scenario, with sensitivity calculations performed using RCP2.6, RCP4.5, and RCP8.5 scenarios. While the specific RCP does not affect conclusions regarding the importance of the various ODS emission sources to future ozone depletion, the wide range of concentrations of N_2O, CH_4, and CO_2 across the RCPs can lead to a rather large difference in the date when global column ozone returns to 1980 levels.

Given the multiple sources of CH_2Cl_2 (Leedham Elvidge et al., 2015) and continued variability in growth rates, we assume that it is reasonable to project constant emissions forward; thus, the baseline for CH_2Cl_2 maintains current atmospheric mixing ratios into the future. We note, however, that there are major uncertainties in future emissions of CH_2Cl_2 due to a lack of bottom-up information on its industrial sources. A constant stratospheric VSLS Br of 5 ppt is used in all the 2-D model runs.

6.4.3 Alternative Future Scenarios

As in past Assessments, we consider multiple alternative future sensitivity cases to assess which emission sources are responsible for the projected concentrations of the various ODSs and of EESC. This information can inform policy discussions by quantifying the effects of various potential policy controls.

Zero-emission scenarios are run for all ODSs, both individually and collectively, and assume no future anthropogenic emission into the atmosphere from any source; thus, the future concentrations are governed exclusively by the current concentrations and the global lifetimes. These scenarios represent minimum concentrations that can be achieved through direct controls, assuming the lifetimes used in the model are accurate and unchanging. There are also scenarios in which there is continued production into the future as allowed by the Montreal Protocol but current banks are eliminated, and other scenarios in which current banks continue to emit into the future but future production is eliminated. None of these alternative scenarios is presented as a likely, or even necessarily a possible, future path. Instead, they are meant as sensitivity studies, which can aid in determining the impact of some lesser reduction. For example, if 10% of the CFC bank were captured and destroyed in 2020, the magnitude of the impact is expected to be about 10% of the effect of the case considered here, in which the entire CFC bank in 2020 was captured and destroyed. There is a slight nonlinearity introduced tied to the return of EESC to 1980 levels, because a larger mitigation will cause EESC to cross below the 1980 threshold sooner, thus changing the ending time of the integration. The time when emissions occur can also lead to a response that does not scale linearly. Thus, for example, some metrics for the combined impact of a zero-production scenario with a zero-bank scenario are not expected to be exactly the same as the metrics for a zero-emission scenario.

Designing the alternative scenarios for most ODSs is relatively straightforward since they are entirely, or almost entirely, emitted from human activity. CH_3Br is an exception. As discussed previously, the key aspect to evaluating the controllable contribution of CH_3Br to stratospheric bromine and ozone depletion is the amount that is emitted from human activity in comparison to natural emissions. As in previous Assessments, we consider emissions from QPS (7.3 Gg yr^{-1} in 2016) and CUE (0.7 Gg yr^{-1} in 2016) to be the controllable emissions. We do not consider emissions from indoor or outdoor biomass burning as being controllable, nor do we consider any potential emissions reduction from leaded gasoline, due to its small estimated contribution to total emissions.

As stated above, the concentration of CFC-11 has not dropped as quickly as expected over the last few years or as quickly as it had been dropping over the preceding ten years. This observation is particularly unexpected because reported global production of the CFCs, in total, has been below zero (i.e., more destruction than production) since 2010 (UNEP, 2017). This discrepancy could be attributed to several potential causes: (1) a circulation change that resulted in lower natural loss rates; (2) increased emission from existing equipment; or (3) emissions from production that have not been reported to the Ozone Secretariat for allowed uses as feedstock or process agents or from illegal uses for new equipment or to service existing equipment. Identifying the underlying cause(s) is key to quantifying the potential implication for ozone depletion. If, for example, a temporary circulation change is entirely responsible for the slower decline, there is little long-term impact. While atmospheric circulation changes have likely played a role, 3-D models cannot explain the observed atmospheric concentrations without

emission increases after 2012 (Montzka et al., 2018). An abrupt and substantial increase in emissions from existing banks, required to solely explain the observations, is considered highly unlikely: While building demolition may lead to increasing CFC-11 emissions as the insulating foams in the buildings are destroyed, such emissions are expected to ramp up slowly and to primarily occur in developed countries, which is not shown by the observations (Montzka et al., 2018). These lines of evidence suggest the possibility that the emissions could be related to unreported production (Montzka et al., 2018). Thus, we have included an additional sensitivity case in which we assume the future emissions of CFC-11 do not decline but remain at 67 Gg yr^{-1}, the average calculated top-down emissions over 2002–2016.

As discussed previously and in **Chapter 1**, new potential sources of CCl_4 emissions have been identified from industry and from legacy uses that are currently not captured in reporting to UNEP. There are also likely additional missing source(s). Given that future CCl_4 emissions remain uncertain, we have included an additional alternative scenario for CCl_4 in which current estimated top-down emissions (33 Gg yr^{-1}) remain constant indefinitely.

Projecting future CH_2Cl_2 emissions is one of the more uncertain aspects of the scenarios considered here. As discussed in **Chapter 1**, tropospheric mixing ratios of CH_2Cl_2 demonstrated strong growth from the early 2000s to around 2014. Growth has slowed since then, although growth rates continue to be highly variable. A potentially large source of CH_2Cl_2 is as a co-product of $CHCl_3$ manufacture, which is used almost entirely for HCFC-22 production (Oram et al., 2017). Oram et al. (2017) calculate that around 715 kt of CH_2Cl_2 (in 2015) could be produced in association with HCFC-22 production in China, of which ~455 Gg (nearly half of estimated global CH_2Cl_2 annual emissions) could be used for emissive applications. If indeed CH_2Cl_2 production is closely linked to the demand for HCFC-22, then its emissions could decline in the future, as long as noncontrolled feedstock production of HCFC-22 does not outweigh declines in controlled HCFC-22 emissions mandated by the Montreal Protocol. However, the variable growth rates of CH_2Cl_2 and the lack of a definitive understanding of its global budget mean that reliable projections are currently not possible. Thus, we develop two alternative scenarios for CH_2Cl_2, intended as sensitivity studies to examine the potential influence on stratospheric O_3: (1) continued strong growth in emissions, assuming that surface mole fractions grow consistently at 2.85 ppt per year (the mean rate observed during 2004–2014 as in scenario 1 from Hossaini et al., 2017), and (2) immediate cessation of emissions.

It is important to recognize that N_2O remains the most significant ODP-weighted emission among all the ODSs. Thus, even though N_2O is not controlled under the Montreal Protocol, we run two mitigation scenarios to compare with the ODS emission cases. These alternative scenarios will also have climate implications because N_2O is a long-lived greenhouse gas. The two scenarios are unchanged from Harris and Wuebbles et al. (2014). In one, all future anthropogenic emissions are eliminated, and in the other, the average of the "concerted mitigation" scenarios from UNEP (2013) is assumed. These scenarios are RCP2.6, SRES B2, and scenarios 4 and 5 from Davidson (2012). Future assumptions in these scenarios vary, but as an example, scenario 4 in Davidson (2012) considered improved agricultural efficiency and emissions reductions of 50% in the transportation/industrial sectors and from biomass burning relative to a baseline scenario in 2050. Scenario 5 incorporates scenario 4 assumptions, as well as a reduction in meat consumption.

Policy options can be directly compared with the baseline scenario of this Chapter (**Table 6-5**) using: (1) the return of EESC to 1980 levels, (2) integrated EESC above 1980 levels, (3) integrated ODP- and (4) GWP-weighted ODS emissions from 2020 through 2060, and (5) integrated ozone depletion. As in past Assessments, 1980 is the reference year—identified as a time when the return of EESC or global column ozone to levels experienced then signifies an important milestone in moving towards recovery. It is important to recognize, however, that even when EESC or global column ozone returns to 1980 levels, there will almost certainly be differences in the ozone spatial distribution both for the total column as well as in the vertical profile. These differences are unavoidable as long as greenhouse gases like CO_2, CH_4, and N_2O remain perturbed from their 1980 levels. The actual year of return to 1980 global column ozone also will depend on natural variations (e.g., in meteorology and atmospheric circulation) that can affect ozone,

Table 6-5. Comparison of scenarios and cases[a]: the year when EESC[b] drops below the 1980 value for both mid-latitude and Antarctic vortex, and integrated EESC differences (mid-latitude case) relative to the baseline (A1) scenario[c]. Also shown are changes in integrated ODP- and GWP-weighted emissions and, for selected cases, integrated global ozone depletion for 2020–2060. Future changes in CH_4 and CO_2 may also significantly alter ozone levels, potentially by amounts larger than any of the cases considered in this table.

Scenario and Cases	Percent Difference in Integrated EESC Relative to Baseline Scenario for the Mid-latitude Case		Year When EESC is Expected to Drop Below 1980 Value		Change in Cumulative ODP-Weighted[e] Emission: 2020–2060	Change in Cumulative GWP-Weighted[f] Emission: 2020–2060	Percent Difference in Integrated O_3 Depletion[g]: 2020–2060
	Mid-latitude[c,d]			Antarctic Vortex[d]			
	$\int_{1980}^{\chi} EESC\,dt$	$\int_{2020}^{\chi} EESC\,dt$			(Million tons CFC-11-eq)	(Billion tons CO_2-eq)	
Scenarios							
A1: Baseline scenario	0.0	0.0	2049.4	2075.7	0.00	0.0	0.00
Cases[a] of zero production from 2020 onward of:							
P0: All ODS	–4.2	–19.1	2044.6	2070.3	–0.88	–5.8	–0.21
CFCs	–0.0	–0.0	2049.4	2075.7	–0.00	–0.0	–0.00
Halons	–0.0	–0.0	2049.4	2075.7	–0.00	–0.0	–0.00
HCFCs	–0.8	–3.9	2048.6	2075.3	–0.12	–4.0	–0.05
CH_3Br for QPS and CUE[h]	–1.5	–6.8	2048.2	2074.2	–0.18	–0.0	–0.06
CCl_4	–2.2	–9.9	2046.6	2072.3	–0.59	–1.8	–0.17
Cases[a] of zero emissions from 2020 onward of:							
E0: All ODS (does not include N_2O)	–8.0	–36.8	2039.6	2064.2	–2.30	–13.9	–0.48
CFCs	–1.7	–7.9	2047.3	2073.2	–0.62	–3.3	–0.09
Halons	–2.2	–9.9	2047.1	2073.0	–0.61	–0.2	–0.10
HCFCs	–2.4	–11.0	2047.5	2074.7	–0.30	–8.7	–0.12
CCl_4[i]	–2.2	–9.9	2046.6	2072.4	–0.59	–1.8	–0.12
CH_3CCl_3	–0.0	–0.0	2049.4	2075.7	–0.00	–0.0	–0.00
CH_3Br for QPS and CUE[h]	–1.5	–6.8	2048.2	2074.2	–0.18	–0.0	–0.06
Total anthropogenic N_2O[j]	-	-	-	-	–5.25	–81.8	–0.45
N_2O mitigation	-	-	-	-	–1.23	–19.1	–0.04

Cases[a] of full recovery of the 2020 banks of:							
B0: All ODS	–5.1	–23.2	2043.9	2069.7	–1.42	–8.1	–0.27
CFCs	–1.7	–7.9	2047.3	2073.2	–0.62	–3.3	–0.09
Halons	–2.2	–9.9	2047.1	2073.0	–0.61	–0.2	–0.10
HCFCs	–1.6	–7.4	2048.3	2075.1	–0.19	–4.7	–0.08
Cases[a] of full recovery of the 2025 banks of:							
B1: All ODS	–3.1	–14.1	2045.0	2070.6	–1.09	–6.9	–0.18
CFCs	–0.9	–4.3	2047.9	2073.8	–0.46	–2.4	–0.06
Halons	–1.2	–5.5	2047.7	2073.5	–0.46	–0.2	–0.06
HCFCs	–1.2	–5.7	2048.1	2074.9	–0.18	–4.3	–0.07
Continued emission of CFC-11:							
Constant at 67 Gg yr^{-1}	+4.0	+18.3	2056.7	2096.0	+2.06	+10.6	+0.20
Continued emission of CCl_4:							
	+0.9	+4.0	2051.2	2080.6	+0.42	1.3	+0.05
Cases relating to the VSLS CH_2Cl_2:							
No future anthropogenic emission	-	-	-	-	-	-	-0.17
Increasing emission	-	-	-	-	-		+0.17

Notes:

[a] Significance of ozone-depleting substances for future EESC were calculated in the hypothetical "cases" by setting production or emission to zero in 2020 and subsequent years or the bank of the ODS to zero in the year 2020 or 2025.

[b] EESC is calculated as in WMO (2014).

[c] EESC is integrated above the 1980 level and until it returns to this level, denoted as year "x"

[d] For mid-latitude conditions, an average age of air of 3 years, corresponding fractional release values, and a bromine efficiency factor (alpha) of 60 are assumed. For Antarctic vortex conditions, an average age of air of 5.5 years, corresponding fractional release values, and an alpha value of 65 are assumed. In all cases, age spectra are applied as in Newman et al. (2007).

[e] Semi-empirical ODPs from **Table 6-1**.

[f] GWPs with 100-year time horizon (**Table 6-2**).

[g] Integrated globally averaged total column ozone changes are taken from 2-D model runs described in this chapter.

[h] It is assumed that 84% of production for QPS use is emitted to the atmosphere and that 65% of production under CUE is emitted (Harris and Wuebbles et al., 2014). The alternative scenario evaluated here includes elimination of emissions from both QPS use and under CUE. Note that emissions under CUE are 15 times smaller than emissions from QPS use in future years of the baseline scenario.

[i] Banks are assumed to be zero. Emissions include uncertain sources such as possible fugitive emissions and unintended other emissions.

[j] The integrated ODP- and GWP-weighted emissions correspond to the reduction of anthropogenic N_2O emissions from RCP6.0 to two mitigation cases (see text). The weaker "N_2O mitigation" scenario is only projected through 2050, so ODP- and GWP-weighted emissions are calculated for 2020–2050.

regardless of EESC levels and the amount of anthropogenic climate change.

6.4.3.1 Stratospheric Ozone Implications

We project that mid-latitude EESC will return to 1980 levels around 2049 and polar EESC will return around 2076 for the baseline scenario. This is almost 2 years later for mid-latitude EESC and slightly more than 2 years later for polar EESC when compared with the baseline scenario of WMO (2014). Both of these differences are primarily a result of higher concentrations of CCl_4, which are caused primarily by slower projected decreases in future emissions. The difference in total EESC between the WMO (2014) baseline scenario and the current one is shown in **Figure 6-3**. The differences appear very small at the scale shown all the way to 2100.

The "No Future Emissions" scenario represents the fastest that EESC could recover, assuming no changes in lifetimes or fractional release values in the future. The close alignment of the "Zero 2020 Bank," "Zero 2025 Bank," and "No Future Production" cases demonstrates the comparable importance of current banks and future production when ODSs are examined together. If emissions were completely stopped in 2020, it could result in an earlier return of mid-latitude and polar EESC to 1980 levels by about a decade. However, for perspective, it is important to recognize the relatively small impacts that additional controls could have on ODSs when compared with what the Montreal Protocol has already accomplished (e.g., Figures 5-6 and 5-8 of Harris and Wuebbles et al., 2014).

As previously discussed, a new approach to calculate EESC (Engel et al., 2017) has been proposed, which

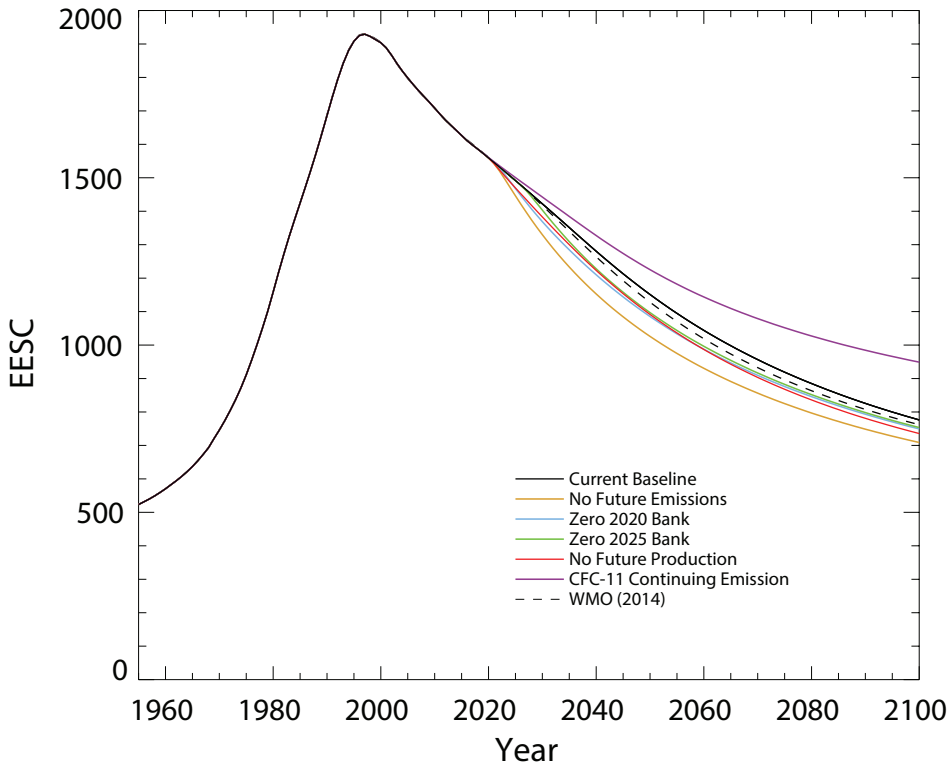

Figure 6-3. EESC for the current baseline scenario (mid-latitude conditions) compared with EESC from the WMO (2014) baseline scenario; also shown are the four major alternative scenarios that represent current mitigation examples considered in this Assessment, and a scenario that assumes a continuation of CFC-11 emissions through the end of the century at the level estimated over 2002–2016 (67 Gg yr^{-1}) (Montzka et al., 2018). All of the EESC curves are calculated using the approach from Newman (2007). The difference between the current baseline curve and the WMO (2014) curve is indistinguishable until after 2020.

differs from the methodology used in this chapter and in previous Assessments in that it attempts to account for the fact that the average age of air for source gases that have been dissociated in the stratosphere is longer than the average age of inert tracers in the same stratospheric location. For the scenarios considered in this chapter, the use of the new EESC approach leads to a delay in mid-latitude return to 1980 levels of about another decade, with a much smaller effect for polar EESC. Despite these quite large changes in the return dates for mid-latitude EESC, the relative importance of the various ODS emission sources to ozone depletion metrics changes little between the two approaches (cf. **Tables 6-5** and **6C-1**). For the rest of this chapter we will use the older EESC approach.

The importance of future emissions from CFCs, halons, HCFCs, CCl_4, and CH_3Br (mainly from QPS) are all comparable, even more so than in the previous Assessment. As in WMO (2014), future emissions from CFCs and halons in the baseline scenario continue to arise entirely from the existing banks, while banks of CCl_4 and CH_3Br are assumed to be negligibly small, so future emissions for them arise exclusively from future production. Future HCFC emissions arise from both current banks as well as future projected production, with current banks contributing more than future production.

If the emissions indicated from the recent slowdown in the decline of CFC-11 concentrations continue into the future, the recovery of EESC and ozone will be delayed. As stated above, we have included a scenario in which CFC-11 emissions continue at 67 Gg yr^{-1} indefinitely. This is the level implied by atmospheric concentration trends over 2002–2016 if it is assumed that atmospheric dynamics played no role in the changing trends (Montzka et al., 2018) (**Chapter 1**). In this alternative scenario, the mid-latitude EESC return to 1980 levels is delayed by about 7 years, and polar EESC return is delayed by about 20 years. For context, the ODP-weighted CFC-11 emissions in this scenario exceed those of the baseline scenario by 2.1 million ODP-weighted tons over 2020–2060, thus almost doubling ODP-weighted emissions from the long-lived halocarbon ODSs over that period compared with the baseline scenario. Continuing emission of CCl_4 at 33 Gg yr^{-1} also has implications for ozone recovery: It delays the return of EESC to 1980 levels at mid-latitudes and in the Antarctic vortex by ~2 years and ~5 years, respectively, relative to the baseline scenario.

Figure 6-4a compares the impact of selected scenarios on the globally averaged total column ozone as calculated with the 2-D model. As expected, the ozone response exhibits a roughly inverse relationship with the EESC curves shown in **Figure 6-3**. Continued CFC-11 emissions at 67 Gg yr^{-1} causes a change in ozone that grows over time and eventually leads to more ozone depletion than is caused by all future halocarbon ODS emissions in the baseline scenario. Shown in **Figure 6-4b** are the responses for the N_2O mitigation scenarios. N_2O exerts a similar ozone response to that shown in Harris and Wuebbles et al. (2014). After about 30 years, the impact of future anthropogenic N_2O emissions on ozone is larger than the combined impact of all future long-lived halogenated ODS emissions, and the N_2O influence continues to grow. The significance of N_2O is also apparent from its cumulative ODP- and GWP-weighted emissions shown in **Table 6-5**; the total N_2O anthropogenic emissions over 2020–2060 are more than two times that of the ODSs for ODP-weighted emissions, and six times for GWP-weighted emissions.

Figure 6-4c shows the impacts on ozone of the range of RCP scenarios (RCP2.6, 4.5, 6.0, and 8.5). The influences of CO_2, CH_4, and N_2O are shown, individually, by varying each one alone while holding the other two gases at 2015 levels. The baseline ODS scenario is used in all runs. The processes responsible for the ozone impacts of these greenhouse gases (GHGs) are discussed in **Chapter 3**. When compared with **Figure 6-4a**, it is apparent that the variations of each of these three gases across the RCP scenarios lead to a substantially wider range of possible future ozone levels than from the ODS scenarios alone. For example, the difference in global ozone in 2100 between the baseline ODS scenario and a scenario with no ODS emissions from 2020 is less than 1 DU (**Figure 6-4a**). This contrasts with differences of 11, 16, and 6 DU, due to differences in CO_2, CH_4, and N_2O, respectively, between the RCP2.6 and RCP8.5 scenarios. Thus, policies that affect the future evolution of these three GHGs in particular will be important for predicting how ozone will change. Furthermore, the potential increase of global ozone above preindustrial levels means that in the future, policy decisions that lead to less climate forcing and less ozone depletion may no

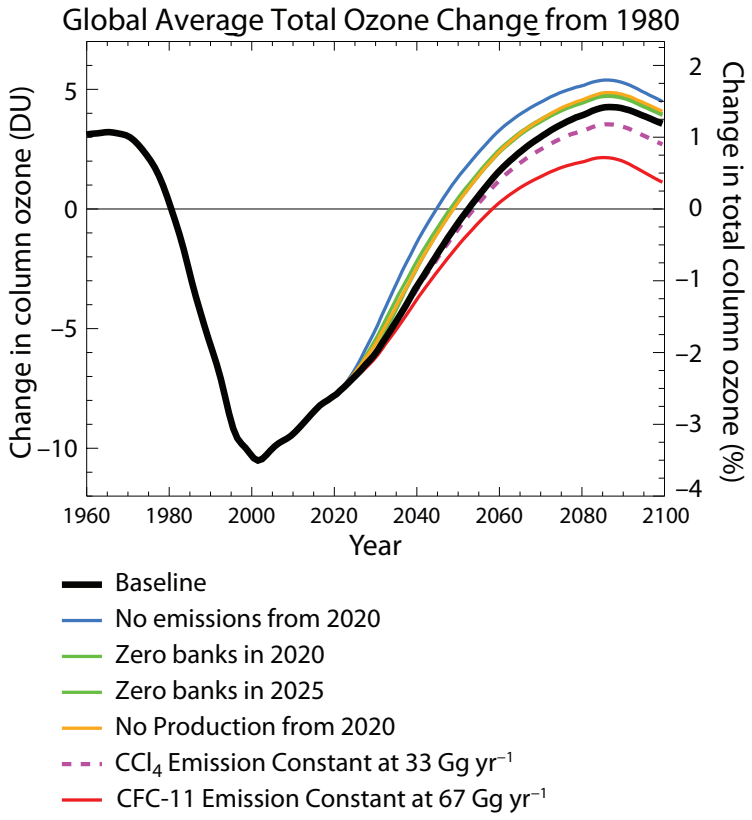

Figure 6-4a. Influence of selected scenarios on globally averaged total ozone. The scenarios include the baseline scenario; no long-lived ODS emissions from 2020; full capture and destruction of the bank in 2020, but allowing continued production; full capture and destruction of the bank in 2025, but allowing continued production; no production of long-lived ODSs from 2020, but allowing banks to continue to emit; continued annual emission of CFC-11 at 67 Gg yr^{-1}; and continued annual emission of CCl_4 at 33 Gg yr^{-1}, with all other assumptions following the baseline scenario. Calculations are from the GSFC 2-D model. In all scenarios shown, the decline just before 2100 is caused by a decrease in tropospheric column ozone and is not due to additional stratospheric ozone depletion. The zero line represents 1980 levels.

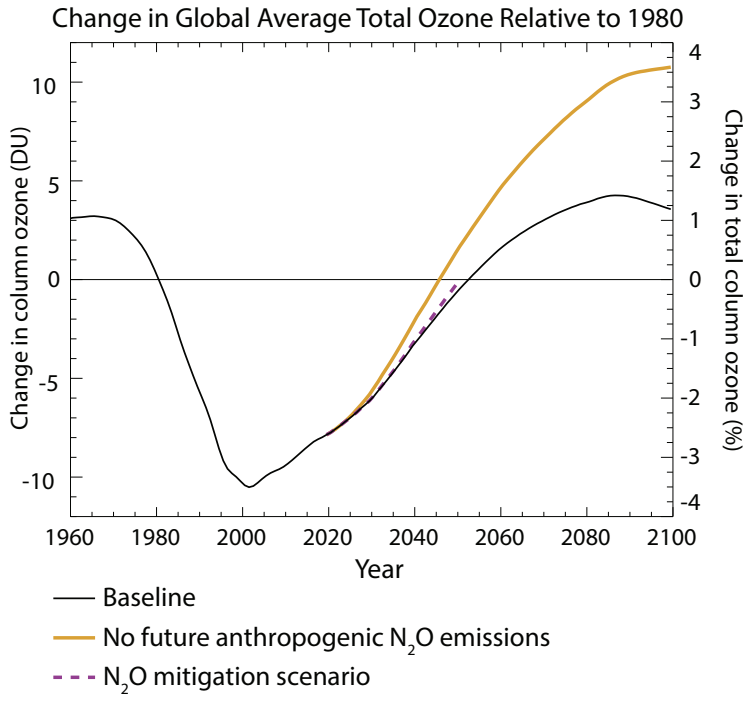

Figure 6-4b. Influence of N_2O mitigation on future ozone. Globally averaged total column ozone for the baseline scenario (black) is compared with the scenarios in which no future anthropogenic N_2O emissions occur and for a weaker N_2O mitigation scenario (see text). Calculations are from the GSFC 2-D model.

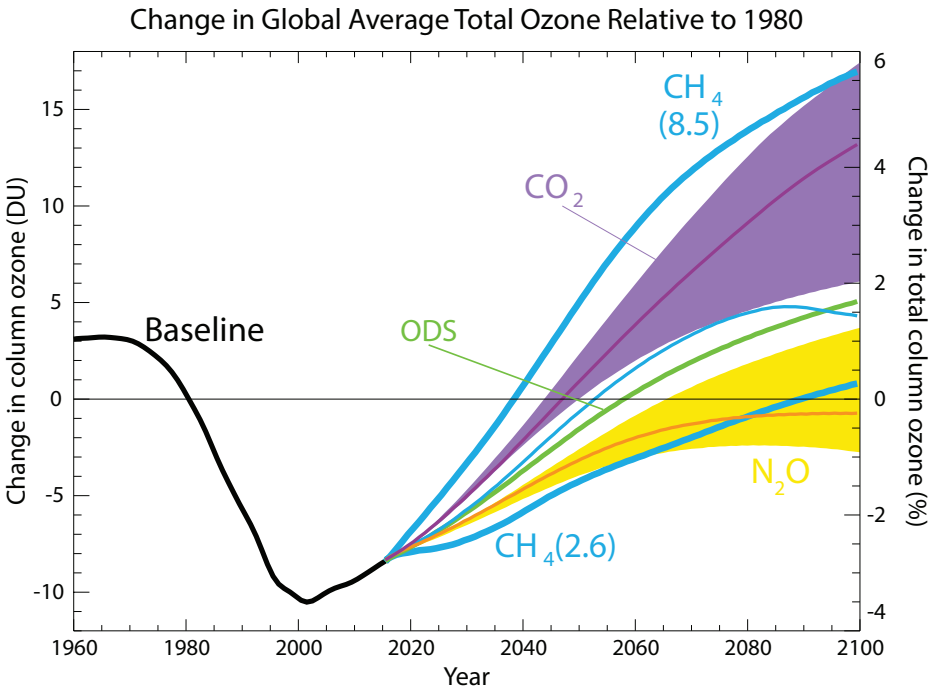

Figure 6-4c. Separate influence of N_2O, CH_4, and CO_2 on future global ozone in the presence of decreasing ODSs. The baseline ODS scenario is used in all runs. The shading depicts the range of impacts, among RCP2.6, 4.5, 6.0, and 8.5, due to future increasing CO_2 (purple) and N_2O (yellow). The CH_4 impacts for RCP2.6 and 8.5 are depicted by the thick blue lines. The thinner colored lines show the separate impacts of N_2O (yellow), CH_4 (blue), and CO_2 (purple) under the RCP6.0 scenario. The thick green line shows the response to only decreasing ODSs. For CO_2, RCP8.5 gives the largest ozone response and RCP2.6, the smallest. For N_2O, RCP8.5 gives the most negative ozone response relative to ODS only, and RCP2.6 gives the least negative ozone response. For all simulations, the gases (of N_2O, CH_4, and CO_2) that are not being varied are fixed at 2015 levels. Calculations are from the GSFC 2-D model, which compares well with 3-D models, including for CH_4 perturbations (see **Appendix 6B**).

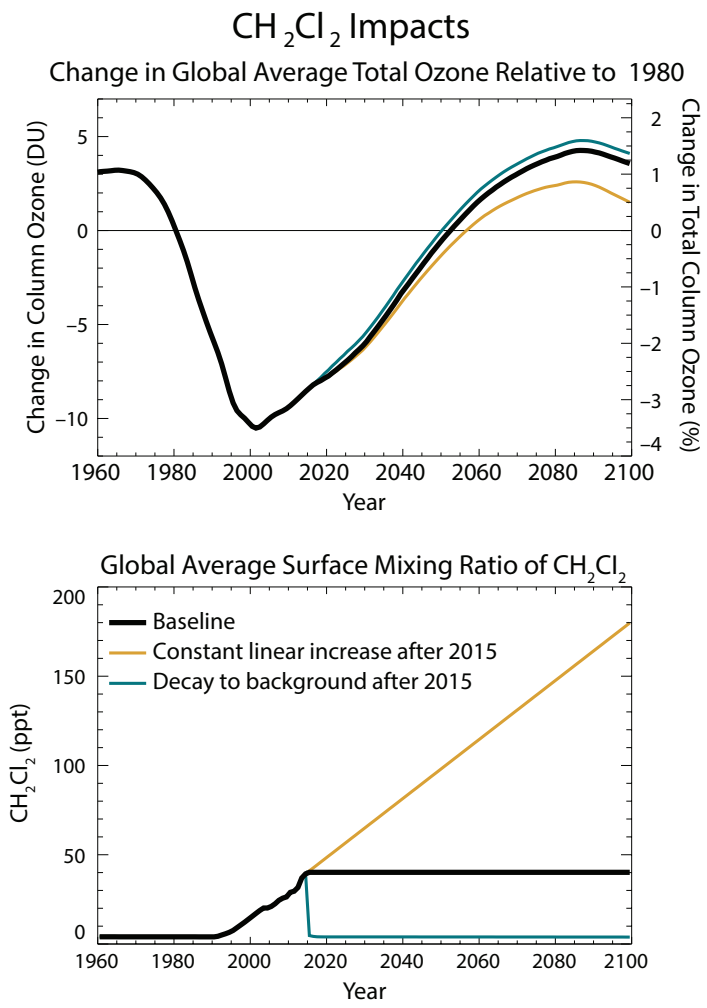

Figure 6-5. Influence of CH_2Cl_2 on globally averaged total ozone. The change in total ozone from 1960 through 2100 is shown for the three CH_2Cl_2 scenarios considered (*upper panel*); assumed constant emissions (our baseline scenario), linearly increasing emissions (adapted from Hossaini et al., 2017), and an elimination of anthropogenic emissions beginning in 2015. Surface concentrations of CH_2Cl_2 for the three scenarios are also shown (*lower panel*). Calculations are from the GSFC 2-D model.

longer be considered a win-win proposition (Butler et al., 2016).

The two alternative scenarios for CH_2Cl_2, namely (1) continued strong growth in emissions and (2) immediate cessation of emissions, are shown in **Figure 6-5** along with its mixing ratios in the baseline scenario. Unlike the CFCs, CH_2Cl_2 has a short lifetime and thus responds rapidly to changes in emissions. If emissions quickly decrease in the future, the contribution of CH_2Cl_2 to stratospheric chlorine will also fall rapidly. Under scenario (1), the 2-D model predicts that integrated ozone depletion over 2020–2060 (shown in the final column of **Table 6-5)** would increase by even more than it would decrease if all future controlled ODS production were eliminated beginning in 2020. However, the continuing large variability in its surface abundances causes us to be unable to confidently predict future concentrations or to evaluate the plausibility of this scenario. If, on the other hand, all anthropogenic emissions of CH_2Cl_2 had ceased in 2015, the effect on integrated ozone depletion from 2020–2060 would be about two-thirds of the effect of eliminating production of all controlled ODSs beginning in 2020.

6.4.3.2 Climate Implications

From the projections for 2020 through 2060, HCFC emissions contribute about two-thirds to the total GWP-weighted emissions for all ODSs (not including N_2O), with both future production and current banks playing comparable roles. Projected CFC banks in 2020 represent the next most important class of GWP-weighted emissions, contributing just over 20% of the total in the baseline scenario. If, however, unreported CFC-11 production is and continues to be an important factor, the GWP-weighted emissions of all the controlled ODSs from 2020 to 2060 would almost double compared with the baseline

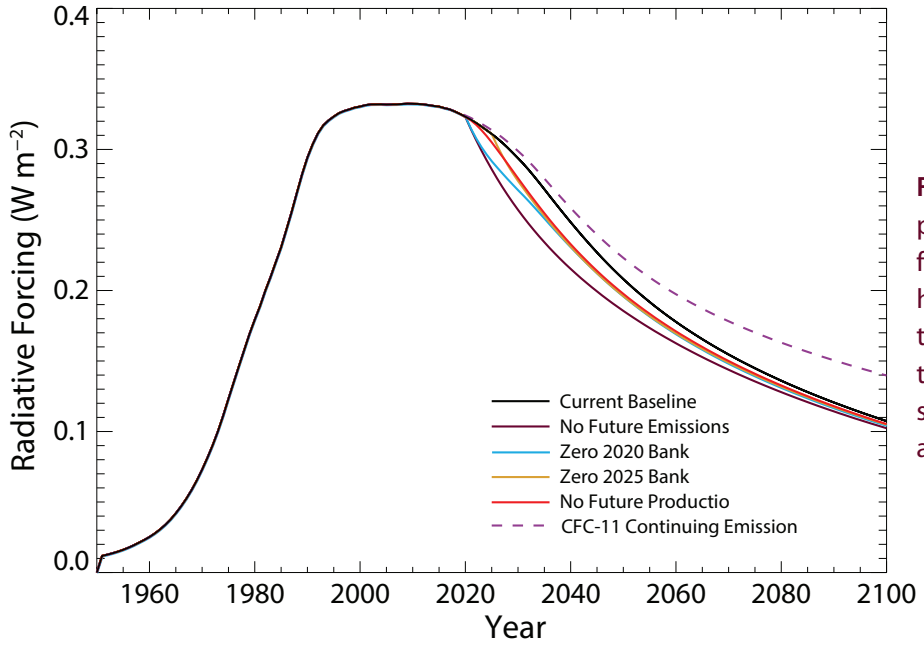

Figure 6-6. Historical and projected future radiative forcing from long-lived ODS halocarbons. The forcing for the mitigation scenarios and the constant CFC-11 emission scenario shown in Figure 6.2 and 6.3 are also shown.

scenario (assuming CFC-11 emissions continue at 67 Gg yr^{-1}), and CFCs would be the ODS group whose future emissions contribute most to climate change. Continuing CCl_4 emissions at 2016 levels lead to a much smaller additional climate impact. As a point of comparison, the amount of CO_2 emitted in 2015 from fuel combustion was 32 Gt CO_2, and the sum from 2020 to 2060 in the RCP6.0 scenario is 1,700 Gt CO_2 (IEA, 2017), while the total CO_2-equivalent emissions in the baseline scenario from ODSs controlled by the Montreal Protocol over 2020–2060 is projected to be 13.8 Gt CO_2-eq yr^{-1}.

As seen in **Figure 6-6**, the maximum difference in radiative forcing between the baseline scenario and the zero-emission scenario is less than 0.05 W m^{-2}, and by 2100, no ODS policy action could reduce ODS radiative forcing by as much as 0.01 W m^{-2} when compared with the baseline scenario, which assumes compliance with the Montreal Protocol. If there is not complete adherence to the Protocol, the RF would be expected to rise above the current baseline curve, with the actual RF path depending on the extent of the Montreal Protocol violation. If, for example, CFC-11 emissions were to continue at 67 Gg yr^{-1} indefinitely, RF would be 0.03 W m^{-2} higher in 2100 than in the baseline scenario (**Figure 6-6**).

Figure 6-7 shows the contribution of the various ODSs and their replacements, specifically HFCs, to future RF. The RF from CFCs has been declining since the latter half of the 20th century. The subsequent increase in the HCFC replacement compounds is projected to offset this decline through to about 2020. Once the transition to HFCs advances, the projected HFC concentration increases more than offset the decline in ODS RF for at least a decade. After that point, the HFC restrictions of the Kigali Amendment, if adhered to, ensure a continued decline in total RF from ODSs and their replacements through the rest of the century. This is one of the primary expected successes of the Kigali Amendment; in the absence of Kigali, there would have been a possibility that uncontrolled growth of HFCs could have led to increasing total RF through the end of the century. Our current projections suggest that the total RF from ODSs and their replacements will be below 0.2 W m^{-2} by the end of the century if there is global adherence to the Kigali Amendment, meaning the RF from all Montreal Protocol gases (ODSs and HFCs) would be only slightly higher than the RF of CFC-12, by itself, in the early 2000s, when it was at its peak concentration. Cumulative GWP-weighted HFC emissions under the Kigali Amendment (excluding HFC-23) are calculated to be 62–63 Gt CO_2-eq yr^{-1} from 2020 to 2060 compared with potential emissions in the absence of

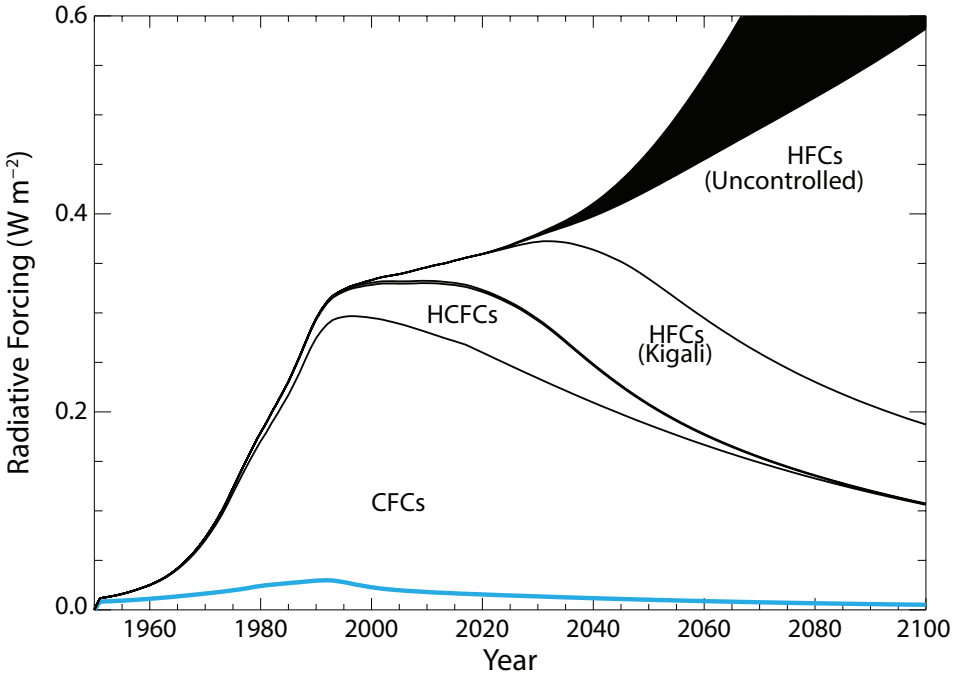

Figure 6-7. Contribution to historical and projected future radiative forcing from long-lived ODS halocarbons and HFCs (not including HFC-23). The lowest black line represents the forcing from CH_3Cl and the cyan line represents the additional contribution from CH_3CCl_3 and CCl_4. The shaded range for uncontrolled HFCs represents that range between the "low" and "high" projections in Velders et al. (2015b). HFC-23 is not included in the RF contributions from HFCs since it is generally not used as a replacement compound in applications that traditionally used ODSs, and it is also in a separate group in the Kigali Amendment (see **Chapter 3, Section 2.5.1.5**).

Kigali (baseline scenario of Velders et al., 2015b) over the same time period of 125–155 Gt CO_2-eq yr^{-1}. A hypothetical immediate global phaseout of HFC production in 2020 could reduce these cumulative emissions to 9.5–9.6 Gt CO_2-eq yr^{-1}, which represent continuing emissions from the banks. See **Chapter 2** for further discussion.

The climatic influence of the ODSs and their replacements are shown in comparison with the three dominant GHGs, CO_2, CH_4, and N_2O, in **Figure 6-8**. The figure demonstrates the large range in CO_2-equivalent emissions and radiative forcing for these three climatically important gases (using the RCP2.6 projection as the minimum and the RCP8.5 projection as the maximum emissions scenario). The substantial benefit of the Kigali Amendment is apparent from the figure, in comparing the HFC curves without the Kigali Amendment (red dashed) with the Kigali curves (red solid). The sizable reduction in the climate impact of ODSs, in response to actions taken as a consequence of the Montreal Protocol, is also evident. In contrast, the relative reductions that can be made in future ODS and HFC emissions lead to a substantially smaller climate influence, assuming compliance with the Protocol.

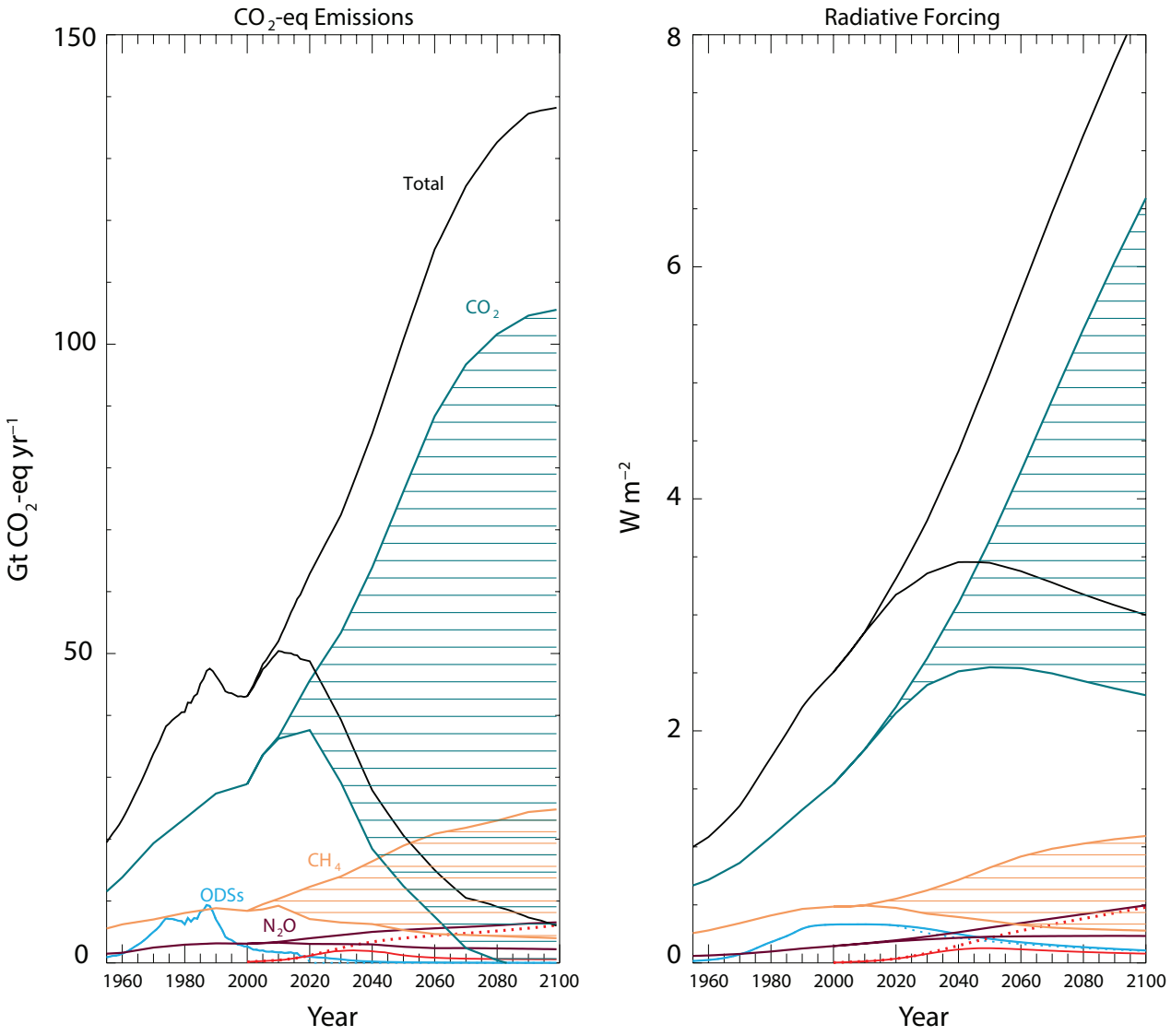

Figure 6.8. Emissions and radiative forcing of ODSs and HFCs compared to these quantities for the three long-lived greenhouse gases: CO_2, CH_4, and N_2O. Maximum (minimum) values for CO_2, CH_4, and N_2O represent the RCP8.5 (RCP2.6) future projections. The total represents the sum of all curves, with the maximum total including the baseline curves for ODSs and HFCs, and the RCP8.5 scenario for the other three greenhouse gases. The minimum total is the baseline ODS and HFC scenario and the RCP2.6 scenario for CO_2, CH_4, and N_2O. The HFC curves (red) are not labeled due to the lack of available space. The solid red curves are the baseline HFC scenario consistent with the Kigali Amendment and the dashed HFC curves represent the "low growth" future HFC scenario described in **Chapter 2** and is from Velders et al. (2015a). The dashed ODS curves represent the "no future ODS emission" scenario described in the text.

REFERENCES

Allen, M.R., J.S. Fuglestvedt, K.P. Shine, A. Reisinger, R.T. Pierrehumbert, and P.M. Forster, New use of global warming potentials to compare cumulative and short-lived climate pollutants, *Nat. Clim. Change*, *6* (8), 773–776, doi:10.1038/nclimate2998, 2016.

Anderson, J.G., D.K. Weisenstein, K.P. Bowman, C.R. Homeyer, J.B. Smith, D.M. Wilmouth, D.S. Sayres, J.E. Klobas, S.S. Leroy, J.A. Dykema, and S.C. Wofsy, Stratospheric ozone over the United States in summer linked to observations of convection and temperature via chlorine and bromine catalysis, *Proc. Natl. Acad. Sci.*, *114* (25), E4905–E4913, doi:10.1073/pnas.1619318114, 2017.

Angel, R., Feasibility of cooling the Earth with a cloud of small spacecraft near the inner Lagrange point (L1), *Proc. Natl. Acad. Sci.*, *103* (46), 17,184–17,189, doi:10.1073/pnas.0608163103, 2006.

Aquila, V., C.I. Garfinkel, P.A. Newman, L.D. Oman, and D.W. Waugh, Modifications of the quasi-biennial oscillation by a geoengineering perturbation of the stratospheric aerosol layer, *Geophys. Res. Lett.*, *41* (5), 1738–1744, doi:10.1002/2013gl058818, 2014.

Benduhn, F., J. Schallock, and M.G. Lawrence, Early growth dynamical implications for the steerability of stratospheric solar radiation management via sulfur aerosol particles, *Geophys. Res. Lett.*, *43* (18), 9956–9963, doi:10.1002/2016GL070701, 2016.

Berthet, G., F. Jegou, V. Catoire, G. Krysztofiak, J.B. Renard, A.E. Bourassa, D.A. Degenstein, C. Brogniez, M. Dorf, S. Kreycy, K. Pfeilsticker, B. Werner, F. Lefevre, T.J. Roberts, T. Lurton, D. Vignelles, N. Begue, Q. Bourgeois, D. Daugeron, M. Chartier, C. Robert, B. Gaubicher, and C. Guimbaud, Impact of a moderate volcanic eruption on chemistry in the lower stratosphere: balloon-borne observations and model calculations, *Atmos. Chem. Phys.*, *17* (3), 2229–2253, doi:10.5194/acp-17-2229-2017, 2017.

Boutonnet, J.C., P. Bingham, D. Calamari, C. de Rooij, J. Franklin, T. Kawano, J.M. Libre, A. McCulloch, G. Malinverno, J.M. Odom, G.M. Rusch, K. Smythe, I. Sobolev, R. Thompson, and J.M. Tiedje, Environmental risk assessment of trifluoroacetic acid, *Hum. Ecol. Risk. Assess.*, *5* (1), 59–124, doi:10.1080/10807039991289644, 1999.

Bravo, I., Y. Diaz-de-Mera, A. Aranda, E. Moreno, D.R. Nutt, and G. Marston, Radiative efficiencies for fluorinated esters: indirect global warming potentials of hydrofluoroethers, *Phys. Chem. Chem. Phys.*, *13* (38), 17185–17193, doi:10.1039/c1cp21874c, 2011.

Brown, J., HFOs New, Low Global Warming Potential Refrigerants, *ASHRAE J.*, *51* (8), 22–29, 2009.

Burkholder, J.B., R.A. Cox, and A.R. Ravishankara, Atmospheric degradation of ozone depleting substances, their substitutes, and related species, *Chem. Rev.*, *115* (10), 3704–3759, doi:10.1021/cr5006759, 2015.

Butler, A.H., J.S. Daniel, R.W. Portmann, A.R. Ravishankara, P.J. Young, D.W. Fahey, and K.H. Rosenlof, Diverse policy implications for future ozone and surface UV in a changing climate, *Environ. Res. Lett.*, *11* (6), doi:10.1088/1748-9326/11/6/064017, 2016.

Calvert, J.G., R.G. Derwent, J.J. Orlando, G.S. Tyndall, and T.J. Wallington, Mechanisms of atmospheric oxidation of the alkanes, 992 pp., Oxford University Press, New York, New York, 2008.

Campbell, N., and R. Shende, HFCs and PFCs: Current and Future Supply, Demand and Emissions, plus Emissions of CFCs, HCFCs and Halons, in *Safeguarding the Ozone Layer and the Global Climate System: Issues Related to Hydrofluorocarbons and Perfluorocarbons*, edited by B. Metz, L. Kuijpers, S. Solomon, S.O. Andersen, O. Davidson, J. Pons, D. de Jager, T. Kestin, M. Manning, and L.A. Meyer, 403–436, Cambridge University Press, Cambridge, United Kingdom, 2005.

Carpenter, L.J., and P.S. Liss, On temperate sources of bromoform and other reactive organic bromine gases, *J. Geophys. Res. Atmos.*, *105* (D16), 20539–20547, doi:10.1029/2000JD900242, 2000.

Carpenter, L.J., and S. Reimann (Lead Authors), J.B. Burkholder, C. Clerbaux, B.D. Hall, R. Hossaini, J.C. Laube, and S.A. Yvon-Lewis, Update on Ozone-Depleting Substances (ODSs) and Othe Gases of Interest to the Montreal Protocol, Chapter 1 in *Scientific Assessment of Ozone Depletion: 2014*, Global Ozone research and Monitoring Project–Report No. 55, World Meteorological Organization, Geneva, Switzerland, 2014.

Chhantyal-Pun, R., M.R. McGillen, J.M. Beames,

M.A.H. Khan, C.J. Percival, D.E. Shallcross, and A.J. Orr-Ewing, Temperature-dependence of the rates of reaction of trifluoroacetic acid with Criegee intermediates, *Angew. Chem. Int. Ed.*, *56*, 9044-9047, doi:10.1002/anie/201703700, 2017.

Crutzen, P.J., Albedo enhancement by stratospheric sulfur injections: A contribution to resolve a policy dilemma?, *Climate Change*, *77*, 211–220, doi:10.1007/s10584- 006-9101-y, 2006.

Dai, Z., D.K. Weisenstein, and D.W. Keith, Tailoring meridional and seasonal radiative forcing by sulfate aerosol solar geoengineering, *Geophys. Res. Lett.*, *45*, 1030–1039, doi:10.1002/2017GL076472, 2018.

Daniel, J.S., S. Solomon, and D.L. Albritton, On the evaluation of halocarbon radiative forcing and global warming potentials, *J. Geophys. Res. Atmos.*, *100* (D1), 1271–1285, doi:10.1029/94JD02516, 1995.

Daniel, J.S., E.L. Fleming, R.W. Portmann, G.J.M. Velders, C.H. Jackman, and A.R. Ravishankara, Options to accelerate ozone recovery: ozone and climate benefits, *Atmos. Chem. Phys.*, *10*, 7697–7707, doi:10.5194/acp-7697-2010, 2010.

Davidson, E.A., Representative concentration pathways and mitigation scenarios for nitrous oxide, *Environ. Res. Lett.*, *7*, doi:10.1088/1748-9326/7/2/024005, 2012.

Davis, M.E., F. Bernard, M.R. McGillen, E.L. Fleming, and J.R. Burkholder, UV and infrared absorption spectra, atmospheric lifetimes, and ozone depletion and global warming potentials for CCl_2FCCl_2F (CFC-112), CCl_3CClF_2 (CFC-112a), CCl_3CF_3 (CFC-113a), and CCl_2FCF_3 (CFC-114a), *Atmos. Chem. Phys.*, *16* (12), 8043–8052, doi:10.5194/acp-16-8043-2016, 2016.

Dhomse, S.S., D. Kinnison, M.P. Chipperfield, R.J. Salawitch, I. Cionni, M.I. Hegglin, N.L. Abraham, H. Akiyoshi, A.T. Archibald, E.M. Bednarz, S. Bekki, P. Braesicke, N. Butchart, M. Dameris, M. Deushi, S. Frith, S.C. Hardiman, B. Hassler, L.W. Horowitz, R.-M. Hu, P. Jöckel, B. Josse, O. Kirner, S. Kremser, U. Langematz, J. Lewis, M. Marchand, M.Y. Lin, E. Mancini, V. Marécal, M. Michou, O. Morgenstern, F.M. O'Connor, L. Oman, G. Pitari, D.A. Plummer, J.A. Pyle, L.E. Revell, E. Rozanov, R. Schofield, A. Stenke, K. Stone, K. Sudo, S. Tilmes, D. Visioni, Y. Yamashita, and G. Zeng, Estimates of ozone return dates from Chemistry-Climate Model Initiative simulations, *Atmos. Chem. Phys.*, *18* (11), 8409–8438, doi:10.5194/acp-18-8409-2018, 2018.

Doncaster, B., J. Shulman, J. Bradford, and J. Olds, *SpaceWorks 2016 Nano/Microsatellite Market Forecast Report*, 20 pp., SpaceWorks Enterprises, Inc., Atlanta, Georgia, 2016.

Douglass, A.R., R.S. Stolarski, S.E. Strahan, and L.D. Oman, Understanding differences in upper stratospheric ozone response to changes in chlorine and temperature as computed using CCM-Val-2 models, *J. Geophys. Res., 117* (D15), D16306, doi:10.1029/2012JD017483, 2012.

Dykema, J.A., D.W. Keith, J.G. Anderson, and D. Weisenstein, Stratospheric controlled perturbation experiment: a small-scale experiment to improve understanding of the risks of solar geoengineering, *Phil. Trans. R. Soc. A 372* (2031), doi:10.1098/rsta.2014.0059, 2014.

Early, J.T., Space-based solar shield to offset greenhouse effect, *J. Br. Interplanet. Soc.*, *42* (12), 567–569, 1989.

Eastham, S.D., D.W. Keith, and S.R.H. Barrett, Mortality tradeoff between air quality and skin cancer from changes in stratospheric ozone, *Environ. Res. Lett.*, *13*, doi:10.1088/1748-9326/aaad2e, 2018.

Engel, A., H. Bonisch, J. Ostermoller, M.P. Chipperfield, S. Dhomse, and P. Jockel, A refined method for calculating equivalent effective stratospheric chlorine *Atmos. Chem. Phys.*, *18*, 601–619, doi:10.5194/acp-18-601-2018, 2018.

English, J.M., O.B. Toon, and M.J. Mills, Microphysical simulations of sulfur burdens from stratospheric sulfur geoengineering, *Atmos. Chem. Phys.*, *12* (10), 4775–4793, doi:10.5194/acp-12-4775-2012, 2012.

Etminan, M., G. Myhre, E.J. Highwood, and K.P. Shine, Radiative forcing of carbon dioxide, methane, and nitrous oxide: A significant revision of the methane radiative forcing, *Geophys. Res. Lett.*, *43*, 12614–12623, doi:10.1002/2016GL071930, 2016.

FAA (Federal Aviation Administration), *Commercial Space Transportation Forecast, Executive Summary Report*, 177 pp., FAA Office of Commercial Space Transportation, Washington, D.C., 2016.

Fahey, D.W., S.R. Kawa, E.L. Woodbridge, P. Tin, J.C. Wilson, H.H. Jonsson, J.E. Dye, D. Baumgardner, S. Borrmann, D.W. Toohey, L.M. Avallone,

M.H. Proffitt, J. Margitan, M. Loewenstein, J.R. Podolske, R.J. Salawitch, S.C. Wofsy, M.K.W. Ko, D.E. Anderson, M.R. Schoeberl, and K.R. Chan, In situ measurements constraining the role of sulphate aerosols in mid-latitude ozone depletion, *Nature*, *363*, 509–514, doi:10.1038/363509a0, 1993.

Falk, S., B.M. Sinnhuber, G. Krysztofiak, P. Jokel, P. Graf, and S.T. Lennartz, Brominated VSLS and their influence on ozone under a changing climate, *Atmos. Chem. Phys.*, *17* (18), 11,313–11,329, doi:10.5194/acp-17-11313-2017, 2017.

Fang, X.K., B.R. Miller, S.S. Su, J. Wu, J.B. Zhang, and J.X. Hu, Historical Emissions of HFC-23 (CHF_3) in China and Projections upon Policy Options by 2050, *Environ. Sci. Technol.*, *48* (7), 4056–4062, doi:10.1021/es404995f, 2014.

Fernandez, R.P., D.E. Kinnison, J.-F. Lamarque, S. Tilmes, and A. Saiz-Lopez, Impact of biogenic very short-lived bromine on the Antarctic ozone hole during the 21st century, *Atmos. Chem. Phys.*, *17* (3), 1673–1688, doi:10.5194/acp-17-1673-2017, 2017.

Fioletov, V.E., G.E. Bodeker, A.J. Miller, R.D. McPeters, and R. Stolarski, Global ozone and zonal total ozone variations estimated from ground-based and satellite measurements: 1964–2000, *J. Geophys. Res., 107* (D22), ACH21-1–ACH21-14, doi:10.1029/2001JD001350, 2002.

Fiore, A.M., J.J. West, L.W. Horowitz, V. Naik, and M.D. Schwarzkopf, Characterizing the tropospheric ozone response to methane emission controls and the benefits to climate and air quality, *J. Geophys. Res.*, *113*, D08307, doi:10.1029/2007JD009162, 2008.

Fleming, E.L., C.H. Jackman, R.S. Stolarski, and A.R. Douglass, A model study of the impact of source gas changes on the stratosphere for 1850-2100, *Atmos. Chem. Phys.*, *11* (16), 8515–8541, doi:10.5194/acp-11-8515-2011, 2011.

Froidevaux, L., J. Anderson, H.-J. Wang, R.A. Fuller, M.J. Schwartz, M.L. Santee, N.J. Livesey, H.C. Pumphrey, P.F. Bernath, J.M. Russell III, and M.P. McCormick, Global OZone Chemistry And Related trace gas Data records for the Stratosphere (GOZCARDS): Methodology and sample results with a focus on HCl, H_2O, and O_3, *Atmos. Chem. Phys.*, *15* (18), 10,471–10,507, doi:10.5194/acp-15-10471-2015, 2015.

Frank, H., A. Klein, and D. Renschen, Environmental trifluoroacetate, *Nature*, *382* (34), doi:10.1038/382034a0, 1996.

Harris, N.R.P., and D.J. Wuebbles (Lead Authors), J.S. Daniel, J. Hu, L.J.M. Kuijpers, K.S. Law, M.J. Prather, and R. Schofield, Scenarios and Information for Policymakers, Chapter 5 in *Scientific Assessment of Ozone Depletion: 2014*, Global Ozone research and Monitoring Project–Report No. 55, World Meteorological Organization, Geneva, Switzerland, 2014.

Hayman, G.D., and R.G. Derwent, Atmospheric chemical reactivity and ozone-forming potentials of potential CFC replacements, *Environ. Sci. Technol.*, *31* (2), 327–336, doi:DOI 10.1021/es950775l, 1997.

Heckendorn, P., D. Weisenstein, S. Fueglistaler, B.P. Luo, E. Rozanov, M. Schraner, L.W. Thomason, and T. Peter, The impact of geoengineering aerosols on stratospheric temperature and ozone, *Environ. Res. Lett.*, *4* (4), 108, doi:10.1008/1748-9326/4/4/045108, 2009.

Henne, S., D.E. Shallcross, S. Reimann, P. Xiao, D. Brunner, S. O'Doherty, and B. Buchmann, Future Emissions and Atmospheric Fate of HFC-1234yf from Mobile Air Conditioners in Europe, *Environ. Sci. Technol.*, *46* (3), 1650–1658, doi:10.1021/es2034608, 2012.

Hossaini, R., P.K. Patra, A.A. Leeson, G. Krysztofiak, N.L. Abraham, S.J. Andrews, A.T. Archibald, J. Aschmann, E.L. Atlas, D.A. Belikov, H. Bonisch, L.J. Carpenter, S. Dhomse, M. Dorf, A. Engel, W. Feng, S. Fuhlbrugge, P.T. Griffiths, N.R.P. Harris, R. Hommel, T. Keber, K. Kruger, S.T. Lennartz, S. Maksyutov, H. Mantle, G.P. Mills, B.R. Miller, S.A. Montzka, F. Moore, M.A. Navarro, D.E. Oram, K. Pfeilsticker, J.A. Pyle, B. Quack, A.D. Robinson, E. Saikawa, A. Saiz-Lopez, S. Sala, B.M. Sinnhuber, S. Taguchi, S. Tegtmeier, R.T. Lidster, C. Wilson, and F. Ziska, A multi-model intercomparison of halogenated very short-lived substances (TransCom-VSLS): linking oceanic emissions and tropospheric transport for a reconciled estimate of the stratopsheric source gas injection of bromine, *Atmos. Chem. Phys.*, *16* (14), 9163–9187, doi:10.5194/acp-16-9163-2016, 2016.

Hossaini, R., M.P. Chipperfield, S.A. Montzka, A.A. Leeson, S.S. Dhomse, and J.A. Pyle, The increasing threat to stratospheric ozone from dichloro-

methane, *Nature*, doi:10.1038/ncomms15962, 2017.

Hu, L., S. Yvon-Lewis, Y.N. Liu, and T.S. Bianchi, The ocean in near equilibrium with atmospheric methyl bromide, *Global Biogeochem. Cycles*, *26*, doi:10.1029/2011GB004272, 2012.

Hurwitz, M.M., E.L. Fleming, P.A. Newman, F. Li, E. Mlawer, K. Cady-Pereira, and R. Bailey, Ozone depletion by hydrofluorocarbons, *Geophys. Res. Lett.*, *42*, doi:10.1002/2015GL065856, 2015.

Hurwitz, M.M., E.L. Fleming, P.A. Newman, F. Li, and Q. Liang, Early action on HFCs mitigates future atmospheric change, *Environ. Res. Lett.*, *11*, doi:10.1008/1748-9326/11/11/114019, 2016.

IEA (International Energy Agency), *Key World Energy Statistics 2017*, Paris, France, 2017.

IPCC (Intergovernmental Panel on Climate Change), *Climate Change 2013: The Physical Science Basis: Contribution of Working Group I to the Fifth Assessment Report of the Intergovernmental Panel on Climate Change*, edited by T.F. Stocker, D. Qin, G.-K. Plattner, M. Tignor, S.K.Allen, J. Boschung, A. Nauels, Y. Xia, V. Bex, and P.M. Midgley, 1535 pp., Cambridge University Press, Cambridge, United Kingdom, 2013.

IPCC/TEAP (Intergovernmental Panel on Climate Change, Technology and Economic Assessment Panel), *Special Report on Safeguarding the Ozone Layer and the Global Climate System: Issues Related to Hydrofluorocarbons and Perfluorocarbons*, 478 pp., Cambridge University Press, Cambridge, United Kingdom, doi:10.13140/2.1.4337.2161, 2005.

Jackman, C.H., and E.L. Fleming, Stratospheric ozone response to a solar irradiance reduction in a quadrupled CO_2 environment, *Earth's Future*, *2*, 331–340, doi:10.1002/2014EF000244, 2014.

Jacob, D.J., *Introduction to Atmospheric Chemistry*, 266 pp., Princeton University Press, Princeton, New Jersey, 1999.

Jones, A., J.M. Haywood, K. Alterskjaer, O. Boucher, J.N.S. Cole, C.L. Curry, P.J. Irvine, D.Y. Ji, B. Kravitz, J.E. Kristjansson, J.C. Moore, U. Niemeier, A. Robock, H. Schmidt, B. Singh, S. Tilmes, S. Watanabe, and J.H. Yoon, The impact of abrupt suspension of solar radiation management (termination effect) in experiment G2 of the Geoengineering Model Intercomparison Project (GeoMIP), *J. Geophys. Res. Atmos.*, *118* (17), 9743–9752, doi:10.1002/jgrd.50762, 2013.

Jubb, A.M., M.R. McGillen, R.W. Portmann, J.S. Daniel, and J.B. Burkholder, An atmospheric photochemical source of the persistent greenhouse gas CF_4, *Geophys. Res. Lett.*, *42* (21), 9505–9511, doi:10.1002/2015GL066193, 2015.

Kawase, H., T. Nagashima, K. Sudo, and T. Nozawa, Future changes in tropospheric ozone under Representative Concentration Pathways (RCPs), *Geophys. Res. Lett.*, *38*, L05801, doi:10.1029/2010GL046402, 2011.

Kazil, J., S. McKeen, S.W. Kim, R. Ahmadov, G.A. Grell, R.K. Talukdar, and A.R. Ravishankara, Deposition and rainwater concentrations of trifluoroacetic acid in the United States from the use of HFO-1234yf, *J. Geophys. Res. Atmos.*, *119* (24), 14059–14079, doi:10.1002/2014JD022058, 2014.

Keith, D.W., D.K. Weisenstein, J.A. Dykema, and F.N. Keutsch, Stratospheric solar geoengineering without ozone loss?, *Proc. Nat. Acad. Sci.*, *113* (52), 14,910–14,914, doi:10.1073/pnas.161557211, 2016.

Klinkrad, Large satellite constellations and related challenges for space debris mitigation, *J. Space Safety Eng.*, *4* (2), 59–60, doi:10.1016/j.jsse.2017.06.002, 2017.

Kravitz, B., A. Robock, L. Oman, G. Stenchikov, and A.B. Marquardt, Sulfuric acid deposition from stratospheric geoengineering with sulfate aerosols, *J. Geophy. Res.*, *115* (D16), doi:10.1029/2009JD011918, 2009.

Kravitz, B., A. Robock, D.T. Shindell, and M.A. Miller, Sensitivity of stratospheric geoengineering with black carbon to aerosol size and altitude of injection, *J. Geophys. Res. Atmos.*, *117*, doi:10.1029/2011JD017341, 2012.

Kravitz, B., K. Caldeira, O. Boucher, A. Robock, P.J. Rasch, K. Alterskjaer, D.B. Karam, J.N.S. Cole, C.L. Curry, J.M. Haywood, P.J. Irvine, D. Ji, A. Jones, J.E. Kristjánsson, D.J. Lunt, J.C. Moore, U. Niemeier, H. Schmidt, M. Schulz, B. Singh, S. Tilmes, S. Watanabe, S. Yang, and J.-H. Yoon, Climate model response from the Geoengineering Model Intercomparison Project (GeoMIP), *J. Geophy. Res.*, *118* (15), 8320, doi:10.1002/jgrd.50646, 2013.

Kravitz, B., D.G. MacMartin, M.J. Mills, J.H. Richter, S. Tilmes, J.-F. Lamarque, J.J. Tribbia, and F. Vitt, First simulations of designing stratospheric sulfate

aerosol geoengineering to meet multiple simultaneous climate objectives, *J. Geophys. Res. Atmos.*, *122*, 12,616–12,634, doi:10.1002/2017JD026874, 2017.

Laakso, A., H. Korhonen, S. Romakkaniemi, and H. Kokkola, Radiative and climate effects of stratospheric sulfur geoengineering using seasonally varying injection areas, *Atmos. Chem. Phys.*, *17*, 6957-6974, doi:10.5194/acp-17-6957-2017, 2017.

Larson, E.J.L., R.W. Portmann, K.H. Rosenlof, D.W. Fahey, J.S. Daniel, and M.N. Ross, Global atmospheric response to emissions from a proposed reusable space launch system *Earth's Future*, *5* (1), 37–48, doi:10.1002/2016EF000399 2017.

Laube, J.C., A. Keil, H. Bonisch, A. Engel, T. Rockmann, C.M. Volk, and W.T. Sturges, Observation-based assessment of stratospheric fractional release, lifetimes, and ozone depletion potentials of ten important source gases, *Atmos. Chem. Phys.*, *13* (5), 2779–2791, doi:10.5194/acp-13-2779-2013, 2013.

Laube, J.C., M.J. Newland, C. Hogan, C.A.M. Brenninkmeijer, P.J. Fraser, P. Martinerie, D.E. Oram, C.E. Reeves, T. Röckmann, J. Schwander, E. Witrant, and W.T. Sturges, Newly detected ozone-depleting substances in the atmosphere, *Nat. Geosci.*, *7*, 266–269, doi:10.1038/ngeo2109, 2014.

Laube, J.C., N.M. Hanif, P. Martinerie, E. Gallacher, P.J. Fraser, R. Langenfelds, C.A.M. Brenninkmeijer, J. Schwander, E. Witrant, J.L. Wang, C.F. Ou-Yang, L.J. Gooch, C.E. Reeves, W.T. Sturges, and D.E. Oram, Tropospheric observations of CFC-114 and CFC-114a with a focus on long-term trends and emissions, *Atmos. Chem. Phys.*, *16* (23), 15347–15358, doi:10.5194/acp-16-15347-2016, 2016.

Leedham, E.C., C. Hughes, F.S.L. Keng, S.M. Phang, G. Malin, and W.T. Sturges, Emission of atmospherically significant halocarbons by naturally occurring and farmed tropical macroalgae, *Biogeosciences*, *10* (6), 3615–3633, doi:10.5194/bg-10-3615-2013, 2013.

Leedham Elvidge, E.C., D.E. Oram, J.C. Laube, A.K. Baker, S.A. Montzka, S. Humphrey, D.A. O'Sullivan, and C.A.M. Brenninkmeijer, Increasing concentrations of dichloromethane, CH_2Cl_2, inferred from CARIBIC air samples collected 1998–2012, *Atmos. Chem. Phys.*, *15* (4), 1939–1958, doi:10.5194/acp-15-1939-2015, 2015.

Lu, P., H. Zhang, and J. Wu, Inhomgeneous radiative forcing of NF3, *Atmosphere*, *8* (1), doi:10.3390/atmos8010017, 2017.

Luecken, D.L., R.L. Waterland, S. Papasavva, K. Taddonio, W.T. Hutzell, J.P. Rugh, and S.O. Andersen, Ozone and TFA impacts in North America from degradation of 2,3,3,3-tetrafluoropropene (HFO-1234yf), a potential greenhouse gas replacement, *Environ. Sci. Technol.*, *44* (1), 343–348, doi:10.1021/es902481f, 2010.

McCulloch, A., and P.M. Midgley, The history of methyl chloroform emissions: 1951–2000, *Atmos. Environ.*, *35* (31), 5311–5319, doi:10.1016/S1352-2310(01)00306-5, 2001.

McCulloch, A., and A. Lindley, From mine to refrigeration: a life cycle inventory analysis of the production of HFC-134a, *International Journal of Refrigeration-Reveu Internationale du Froid*, *26* (8), 865–872, doi:10.1016/S0140-7007(03)00095-1 2003.

Miller, B.R., M. Rigby, L.J.M. Kuijpers, P.B. Krummel, L.P. Steele, M. Leist, P.J. Fraser, A. McCulloch, C. Harth, P. Salameh, J. Muhle, R.F. Weiss, R.G. Prinn, R.H.J. Wang, S. O'Doherty, B.R. Greally, and P.G. Simmonds, HFC-23 (CHF_3) emission trend response to HCFC-22 ($CHClF_2$) production and recent HFC-23 emission abatement measures, *Atmos. Chem. Phys.*, *10* (16), 7875–7890, doi:10.5194/acp-10-7875-2010, 2010.

Mills, M.J., O.B. Toon, J. Lee-Taylor, and A. Robock, Multidecadal global cooling and unprecedented ozone loss following a regional nuclear conflict *Earth's Future*, *2* (4), 161–176, doi:10.1002/2013EF000205 2014.

Mills, M.J., J. Richter, S. Tilmes, B. Kravitz, D.G. MacMartin, S.A. Glanville, J.J. Tribbia, J.F. Lamarque, F. Vitt, A. Schmidt, A. Gettelman, R.B. Neale, C. Hannay, J. Bacmeister, and D.E. Kinnison, Radiative and chemical response to interactive stratospheric aerosols in fully coupled CESM1(WACCM), *J. Geophys. Res. Atmos.*, *122*, 13,061–13,078, doi:10.1002/2017JD027006, 2017.

Montzka, S.A., G.S. Dutton, P. Yu, E. Ray, R.W. Portmann, J.S. Daniel, L. Kuijpers, B.D. Hall, D. Mondeel, C. Siso, J.D. Nance, M. Rigby, A.J. Manning, L. Hu, F. Moore, B.R. Miller, and J.W. Elkins, An unexpected and persistent increase in global emissions of ozone-depleting CFC-11, *Nature*, *557* (7705), 413–417, doi:10.1038/s41586-018-

0106-2, 2018.

Myhre, G., and D. Shindell (Coordinating Lead Authors), F.-M. Breon, W. Collins, J.S. Fuglestvedt, J. Huang, D. Koch, J.-F. Lamarque, D. Lee, B. Mendoza, T. Nakajima, A. Robock, G. Stephens, T. Takemura, and H. Zhang, Anthropogenic and natural radiative forcing. In: *Climate Change 2013: The physical science basis, contribution of working group I to the fifth assessment report of the intergovernmental panel on climate change*, 659–740 pp., Cambridge, United Kingdom and New York, New York, USA, 2013.

Nevison, C. V.K. Gupta, and L. Klinger, Self-sustained temperature oscillations on Daisyworld, *Tellus B*, *51* (4), 806–814, doi:10.1034/j.1600-0889.1999.t01-3-00005.x, 1999.

Newman, P.A., J.S. Daniel, D.W. Waugh, and E.R. Nash, A new formulation of equivalent effective stratospheric chlorine (EESC), *Atmos. Chem. Phys.*, *7* (17), 4537–4552, doi:10.5194/acp-7-4537-2007, 2007.

Niemeier, U., and C. Timmreck, What is the limit of climate engineering by stratospheric injection of SO_2, *Atmos. Chem. Phys.*, *15* (16), 9128–9141, doi:10.5194/acp-15-9129-2015, 2015.

Niemeier, U., and H. Schmidt, Changing transport processes in the stratosphere by radiative heating of sulfate aerosols, *Atmos. Chem. Phys.*, *17*, 14,871–14,886, doi:10.5194/acp-2017-470, 2017.

Nowack, P.J., N.L. Abraham, P. Braesicke, and J.A. Pyle, Stratospheric ozone changes under solar geoengineering: implications for UV exposure and air quality, *Atmos. Chem. Phys.*, *16*, 4191–4203, doi:10.5194/acp-16-4191-2016, 2016.

O'Neill, B.C., E. Kriegler, K.L. Ebi, E. Kemp-Benedict, K. Riahi, D.S. Rothman, B.J. van Ruijven, D.P. van Vuuren, J. Birkmann, K. Kok, M. Levy, and W. Solecki, The roads ahead: Narratives for shared socieconomic pathways describing world futures in the 21st century, *Global Environ. Change*, *42*, 169–180, doi:10.1016/j.gloenvcha.2015.01.004, 2017.

Oman, L.D., A.R. Douglass, R.J. Salawitch, T.P. Canty, J.R. Ziemke, and M. Manyin, The effect of representing bromine from VSLS on the simulation and evolution of Antarctic ozone, *Geophys. Res. Lett.*, *43*, 9869–9876, doi:10.1002/2016GL070471, 2016.

Oram, D.E., M.J. Ashfold, J.C. Laube, L.J. Gooch, S. Humphrey, W.T. Sturges, E. Leedham-Elvidge, G.L. Forster, N.R.P. Harris, M.I. Mead, A. Abu Samah, S.M. Phang, C.F. Ou-Yang, N.H. Lin, J.L. Wang, A.K. Baker, C.A.M. Brenninkmeijer, and D. Sherry, A growing threat to the ozone layer from short-lived anthropogenic chlorocarbons, *Atmos. Chem. Phys.*, *17* (19), 11,929–11,941, doi:10.5194/acp-17-11929-2017, 2017.

Orkin, V.L., L.E. Martynova, and M.J. Kurylo, Photochemical properties of trans-1-chloro-3,3,3-trifluoropropene (trans-CHCl=CHCF$_3$): OH reaction rate constant, UV and IR absorption spectra, global warming potential, and ozone depletion potential, *J. Phys. Chem. A*, *118* (28), 5263–5271, doi:10.1021/jp5018949, 2014.

Ostermoller, J., H. Bonisch, P. Jockel, and A. Engel, A new time-independent formulation of fractional release, *Atmos. Chem. Phys.*, *17*, 3785–3797, doi:10.5194/acp-17-3785-2017, 2017.

Papanastasiou, D.K., A. Beltrone, P. Marshall, and J.B. Burkholder, Global warming potentials for the C_1-C_3 hydrochlorofluorocarbons (HCFCs) included in the Kigali Amendment to the Montreal Protocol, *Atmos. Chem. Phys.*, doi:10.5194/acp-2018-27, 2018.

Patten, K.O., and D.J. Wuebbles, Atmospheric lifetimes and Ozone Depletion Potentials of trans-1-chloro-3,3,3- trifluoropropylene and trans-1,2-dichloroethylene in a three-dimensional model, *Atmos. Chem. Phys.*, *10* (22), 10867–10874, doi:10.5194/acp-10-10867-2010, 2010.

Pelton, J., and B. Jacque, Distrtibuted internet-optimized services via satellite constellations, in *Handbook of Satellite Applications*, Springer, New York, New York, doi:10.1007/978-1-614-6423-5_96-1, 2016.

Pitari, G., V. Aquila, B. Kravitz, A. Robock, S. Watanabe, N.D. Luca, G.D. Genova, E. Mancini, S. Tilmes, and I. Cionni, Stratospheric ozone response to sulfate geoengineering: Results from the Geoengineering Model Intercomparison Project (GeoMIP), *J. Geophy. Res.*, *119* (5), 2629–2653, doi:10.1002/2013JD020566, 2014.

Pongratz, J., D.B. Lobell, L. Cao, and K. Caldeira, Crop yields in a geoengineered climate, *Nat. Clim. Change*, *2*, 101–105, doi:10.1038/nclimate1373, 2012. Haigh, J.D., and J.A. Pyle, Ozone perturbation experiments in a two-dimensional

circulation model, *Q. J. Roy. Meteorol. Soc., 108,* 551–574, doi:10.1002/qj.49710845705, 1982.

Jackman, C.H., D.R. Marsh, D.E. Kinnison, C.J. Mertens, and E.L. Fleming, Atmospheric changes caused by galactic cosmic rays over the period 1960-2010, *Atmos. Chem. Phys.*, *16*, 5853–5866, doi:10.5194/acp-16-5853-2016, 2016.

Portmann, R.W., and S. Solomon, Indirect radiative forcing of the ozone layer during the 21st century, *Geophys. Res. Lett.*, *34*, L02813, doi:10.1029/2006GL028252, 2007.

Radulovich, R., A. Neori, D. Valderrama, C.R.K. Reddy, H. Cronin, and J. Forster, Farming of seaweeds, Chapter 3 in *Seaweed Sustainability: Food and Non-Food Applications*, edited by B.K. Tiwari and D.J. Troy, pp. 27–59, Elsevier, Amsterdam, 2015.

Randeniya, L., P.F. Vohrolik, and I.C. Plumb, Stratospheric ozone depletion at northern mid latitudes in the 21st century: The importance of futue concentrations of greenhouse gases nitrous oxide and methane, *Geophys. Res. Lett.*, *29* (4), doi:10.1029/2001GL014295, 2002.

Ravishankara, A.R., A.A. Turnipseed, N.R. Jensen, S. Barone, M. Mills, C.J. Howard, and S. Solomon, Do hydrofluorocarbons destroy stratospheric ozone, *Science*, *263* (5143), 71–75, doi:10.1126/science.263.5143.71, 1994.

Revell, L.E., G.E. Bodeker, P.E. Huck, B.E. Williamson, and E. Rozanov, The sensitivity of stratospheric ozone changes through the 21st century to N_2O and CH_4, *Atmos. Chem. Phys.*, *12*, 11,309–11,317, doi:10.5194/acp-12-11309-2012, 2007.

Revell, L.E., F. Tummon, R.J. Salawitch, A. Stenke, and T. Peter, The changing ozone depletion potential of N_2O in a future climate, *Geophys. Res. Lett.*, *42* (22), 10,047–10,055, doi:10.1002/2015GL065702, 2015.

Riahi, K., D.P. van Vuuren, E. Kriegler, J. Edmonds, B.C. O'Neill, S. Fugimori, N. Bauer, K. Calvin, R. Delink, O. Fricko, W. Lutz, A. Popp, J.C. Cuaresma, S. KC, Leimbach, M., L. Jiang, T. Kram, S. Rao, J. Emmerling, K. Ebi, T. Hasegawa, P. Havlik, F. Humpenoder, L.A. Da Silva, S. Smith, E. Stehfest, V. Bosetti, J. Eom, D. Gernaat, T. Masui, J. Rogelj, J. Strefler, L. Drouet, V. Krey, G. Luderer, M. Harmsen, K. Takahashi, L. Baumstark, J.C. Doelman, M. Kainuma, Z. Klimont, G. Marangoni, H. Lotze-Campen, M. Obersteiner, A. Tabeau, and M. Tavoni, The shared socieconomic pathways and their energy, land use, and greenhouse gas emissions implications: An overview, *Global Environ. Change*, *42*, 153–168, doi:10.1016/j.gloenvcha.2016.05.009, 2017.

Richter, J.H., S. Tilmes, M.J. Mills, J.J. Tribbia, B. Kravitz, D.G. MacMartin, F. Vitt, and J.F. Lamarque, Stratospheric Dynamical Response and Ozone Feedbacks in the Presence of SO_2 Injections, *J. Geophys. Res. Atmos.*, *122* (23), 12,557–12,573, doi:10.1002/2017jd026912, 2017.

Richter, J.H., S. Tilmes, A.S. Glanville, M.J. Mills, J.J. Tribbia, B. Kravitz, F. Vitt, and J.-F. Lamarque, Stratospheric response in geoengineering simulation meeting multiple surface climate objectives, *J. Geophys. Res. Atmos.*, *123*, 5762–5782, doi:10.1029/2018JD028285, 2018.

Rigby, M., R.G. Prinn, S. O'Doherty, B.R. Miller, D. Ivy, J. Muhle, C.M. Harth, P.K. Salameh, T. Arnold, R.F. Weiss, P.B. Krummel, L.P. Steele, P.J. Fraser, D. Young, and P.G. Simmonds, Recent and future trends in synthetic greenhouse gas radiative forcing, *Geophys. Res. Lett.*, *41* (7), 2623–2630, doi:10.1002/2013gl059099, 2014.

Robock, A., Albedo enhancement by stratospheric sulfur injections: More research needed, *Earths Future*, *4* (12), 644–648, doi:10.1002/2016ef000407, 2016.

Rogelj, J., M. den Elzen, N. Hohne, T. Fransen, H. Fekete, H. Winkler, R. Schaeffer, F. Sha, K. Riahi, and M. Meinshausen, Paris Agreement climate proposals need a boost to keep warming well below 2 degrees C, *Nature*, *534* (7609), 631–639, doi:10.1038/nature18307, 2016.

Ross, M.N., and P.M. Sheaffer, Radiative forcing caused by rocket engine emissions, *Earth's Future*, *2* (4), 177–196, doi:10.1002/2013EF000160 2014.

Ross, M., M.J. Mills, and D. Toohey, Potential climate impact of black carbon emitted by rockets, *Geophys. Res. Lett.*, *37*, doi:10.1029/2010GL044548 2010.

Russell, M.H., G. Hoogeweg, E.M. Webster, D.A. Ellis, R.L. Waterland, and R.A. Hoke, TFA from HFO-1234yf: Accumulation and aquatic risk in terminal water bodies, *Environ. Toxicol. Chem.*, *31* (9), 1957–1965, doi:10.1002/etc.1925, 2012.

Saiz-Lopez, A., S. Baidar, C.A. Cuevas, T.K. Koenig, R.P. Fernandez, B. Dix, D.E. Kinnison, J.-F. Lamarque, X. Rodriguez-Lloveras, T.L. Campos,

and R. Volkamer, Injection of iodine to the stratosphere, *Geophys. Res. Lett.*, *42* (16), 6852–6859, doi:10.1002/ 2015GL064796, 2015.

Scheurer, M., K. Nödler, F. Freeling, J. Janda, O. Happel, M. Riegel, U. Müller, F.R. Storck, M. Fleig, F.T. Lange, A. Brunsch, and H.-J. Brauch, Small, mobile, persistent: Trifluoroacetate in the water cycle - overlooked sources, pathways, and consequences for drinking water supply, *Water Res.*, *126*, 460–471, doi:10.1016/j.watres.2017.09.045, 2017.

Seifritz, W., Mirrors to halt global warming?, *Nature*, *340*, 603, doi:10.1038/340603a0, 1989.

Shah, N., M. Wei, V.E. Letschert, and A.A. Phadke, Benefits of leapfrogging to superefficiency and low global warming potential refrigerants in room air conditioning, *Report LBNL-1003671*, Lawrence Berkeley National Laboratory, Berkeley, California, 2015.

Sherwen, T., M.J. Evans, L.J. Carpenter, J.A. Schmidt, and L. Mickley, Halogen chemistry reduces tropospheric O3 radiative forcing, *Atmos. Chem. Phys.*, *17* (2), 1557–1569, doi:10.5194/acp-17-1557-2017, 2017.

Simmonds, P.G., A.J. Manning, D.M. Cunnold, A. McCulloch, S. O'Doherty, R.G. Derwent, P.B. Krummel, P.J. Fraser, B. Dunse, L.W. Porter, R.H.J. Wang, B.R. Greally, B.R. Miller, P. Salameh, R.F. Weiss, and R.G. Prinn, Global trends, seasonal cycles, and European emissions of dichloromethane, trichloroethene, and tetrachloroethene from the AGAGE observations at Mace Head, Ireland, and Cape Grim, Tasmania, *J. Geophy. Res.*, *111*, doi:10.1029/2006JD007082, 2006.

Smalley, K.M., A.E. Dessler, S. Bekki, M. Deushi, M. Marchand, O. Morgenstern, D.A. Plummer, K. Shibata, Y. Yamashita, and G. Zeng, Contribution of different processes to changes in tropical lower-stratospheric water vapor in chemistry-climate models, *Atmos. Chem. Phys.*, *17* (13), 8031–8044, doi:10.5194/acp-17-8031-2017, 2017.

Solomon, K.R., G.J.M. Velders, S.R. Wilson, S. Madronich, J. Longstreth, P.J. Aucamp, and J.F. Bornman, Sources, fates, toxicity, and risks of trifluoroacetic acid and its salts: Relevance to substances regulated under the Montreal and Kyoto Protocols, *J. Toxicol. Environ. Health Part B*, *19* (7), 289–304, doi:1080/10937404.2016.1175981, 2016.

SPARC CCMVal (Stratospheric Processes and their Role in Climate), *SPARC CCMVal Report on the Evaluation of Chemistry-Climate Models*, edited by V. Eyring, T.G. Shepherd, D.W. Waugh, *SPARC Report No. 5*, WCRP-132, WMO/TD-No. 1526, 2010.

SPARC, (Stratosphere-troposphere Processes And their Role in Climate), *SPARC Report on Lifetimes of stratospheric ozone-depleting substances, their replacements, and related species*, edited by M.K.W. Ko, P.A. Newman, S. Reimann, and S.E. Strahan, *SPARC Report No. 6*, WCRP-15/2013, https://www.sparc-climate.org/publications/sparc-reports/, 2013.

SPARC, (Stratosphere-troposphere Processes And their Role in Climate), *SPARC Report on the Mystery of Carbon Tetrachloride*, edited by Q. Liang, P.A. Newman, and S. Reimann, *SPARC Report No. 7*, WCRP-13/2016, https://www.sparc-climate.org/publications/sparc-reports/, 2016.

Sterner, E.O., and D.J.A. Johansson, The effect of climate–carbon cycle feedbacks on emission metrics, *Environ. Res. Lett.*, *12* (3), doi:10.1088/1748-9326/aa61dc, 2017.

Strahan, S.E., A.R. Douglass, R.S. Stolarski, H. Akiyoshi, S. Bekki, P. Braesicke, N. Butchart, M.P. Chipperfield, D. Cugnet, S. Dhomse, S.M. Frith, A. Gettelman, S.C. Hardiman, D.E. Kinnison, J.-F. Lamarque, E. Mancini, M. Marchand, M. Michou, O. Morgenstern, T. Nakamura, D. Olivié, S. Pawson, G. Pitari, D.A. Plummer, J.A. Pyle, J.F. Scinocca, T.G. Shepherd, K. Shibata, D. Smale, H. Teyssèdre, W. Tian, and Y. Yamashita, Using transport diagnostics to understand chemistry climate model ozone simulations, *J. Geophy. Res.*, *116* (D17), doi:10.1029/2010jd015360, 2011.

Sulback Andersen, M.P., J.A. Schmidt, A. Volkova, and D.J. Wuebbles, A three-dimensional model of the atmospheric chemistry of *E* and *Z*-CF_3CH=CHCl (HCFO-1233(zd) (E/Z)), *Atmos. Environ.*, *179*, 250–259, doi:10.1016/j.atmosenv.2018.02.018, 2018.

Tegtmeier, S., F. Ziska, I. Pisso, B. Quack, and G.J.M. Velders, Oceanic bromoform emissions weighted by their ozone depletion potential, Atmos. Chem. Phys., 15, 13,647–13,663, doi:10.5194/acp-15-13647-2015, 2015.

Tilmes, S., R.R. Garcia, D.E. Kinnison, A. Gettelman, and P.J. Rasch, Impact of geoengineered aerosols on the troposphere and stratosphere, *J. Geophy.*

Res., *114* (D12), doi:10.1029/2008JD011420, 2009.

Tilmes, S., D.E. Kinnison, R.R. Garcia, R. Salawitch, T. Canty, J. Lee-Taylor, S. Madronich, and K. Chance, Impact of very short-lived halogens on stratospheric ozone abundance and UV radiation in a geo-engineered atmosphere, *Atmos. Chem. Phys.*, *12* (22), 10,945–10, 955, doi:10.5194/acp-12-10945-2012, 2012.

Tilmes, S., J. Fasullo, J.-F. Lamarque, D.R. Marsh, M. Mills, K. Alterskjær, H. Muri, J.E. Kristjánsson, O. Boucher, M. Schulz, J.N.S. Cole, C.L. Curry, A. Jones, J. Haywood, P.J. Irvine, D. Ji, J.C. Moore, D.B. Karam, B. Kravitz, P.J. Rasch, B. Singh, J.-H. Yoon, U. Niemeier, H. Schmidt, A. Robock, S. Yang, and S. Watanabe, The hydrological impact of geoengineering in the Geoengineering Model Intercomparison Project (GeoMIP), *J. Geophy. Res.*, *118* (19), 11,036–011,058, doi:10.1002/jgrd.50868, 2013.

Tilmes, S., B.M. Sanderson, and B.C. O'Neill, Climate impacts of geoengineering in a delayed mitigation scenario, *Geophys. Res. Lett.*, *43*, 8222–8229, doi:10.1002/2016GL070122, 2016.

Tilmes, S., J.H. Richter, M.J. Mills, B. Kravitz, D.G. MacMartin, F. Vitt, J.J. Tribbia, and J.F. Lamarque, Sensitivity of aerosol distribution and climate response to stratospheric SO_2 injection locations, *J. Geophy. Res.*, *122*, 12,591–12,615, doi:10.1002/2017JD026888, 2017.

Tilmes, S., J.H. Richter, M.J. Mills, B. Kravitz, D.G. MacMartin, R.R. Garcia, D.E. Kinnison, J.F. Lamarque, J. Tribbia, and F. Vitt, Effects of Different Stratospheric SO_2 Injection Altitudes on Stratospheric Chemistry and Dynamics, *J. Geophys. Res. Atmos.*, *123* (9), 4654–4673, doi:10.1002/2017jd028146, 2018.

Totterdill, A., T. Kovacs, W. Feng, S. Dhomse, C.J. Smith, J.C. Gomez-Martin, M.P. Chipperfield, P.M. Forster, and J.M.C. Plane, Atmospheric lifetimes, infrared absorption spectra radiative forcings and global warming potentials of NF_3 and CF_3CF_2Cl (CFC-115), *Atmos. Chem. Phys.*, *16*, 11,451–1,1463, doi:10.5194/acp-16-11451-2016, 2016.

Trenberth, K.E., and L. Smith, The mass of the atmosphere: A constraint on global analyses, *J. Climate*, doi:10.1175/JCLI-3299.1, 2005.

UNEP (United Nations Environment Programme), *Assessment of Alternatives to HCFCs and HFCs and Update of the TEAP 2005 Supplement Report Data*, Report of the UNEP Technology and Economic Assessment Panel, Task Force Decision XX/8 Report, 129 pp, Nairobi, Kenya, https://unep.ch/ozone/Assessment_Panels/TEAP/Reports/TEAP_Reports/teap-may-2009-decisionXX-8-task-force-report.pdf, 2009.

UNEP (United Nations Environment Programme), *HFCs: A Critical Link in Protecting Climate and the Ozone Layer*, 40 pp., Nairobi, Kenya, 2011.

UNEP (United Nations Environment Programme), *Drawing down N_2O to protect climate and the ozone layer*, A UNEP Synthesis Report, Nairobi, Kenya, 2013.

UNEP (United Nations Environment Programme), Data Access Centre, Ozone Secretariat, Nairobi, Kenya, 2017.

UNEP/TEAP (United Nations Environment Programme, Technology and Economic Assessment Panel) *September Decision XXVII/4 Task Force Update Report Further information on Alternatives to Ozone-Depleting Substances*, *Volume 1*, 179 pp., Nairobi, Kenya, 2016.

Velders, G.J.M., and J.S. Daniel, Uncertainty analysis of projections of ozone-depleting substances: Mixing ratios, EESC, ODPs, and GWPs, *Atmos. Chem. Phys.*, *14* (6), 2757–2776, doi:10.5194/acp-14-2757-2014, 2014.

Velders, G.J.M., S.O. Andersen, J.S. Daniel, D.W. Fahey, and M. McFarland, The importance of the Montreal Protocol in protecting climate, *Proc. Natl. Acad. Sci.*, *104* (12), 4814–4819, doi:10.1073/pnas.0610328104, 2007.

Velders, G.J.M., D.W. Fahey, J.S. Daniel, M. McFarland, and S.O. Andersen, The large contribution of projected HFC emissions to future climate forcing, *Proc. Natl. Acad. Sci.*, *106* (27), 10,949–10,954, doi:10.1073/pnas.0902817106, 2009.

Velders, G.J.M., A.R. Ravishankara, M.K. Miller, M.J. Molina, J. Alcamo, J.S. Daniel, D.W. Fahey, S.A. Montzka, and S. Reimann, Preserving Montreal Protocol climate benefits by limiting HFCs, *Science*, *335* (6071), 922–923, doi:10.1126/science.1216414, 2012.

Velders, G.J.M., S. Solomon, and J.S. Daniel, Growth of climate change commitments from HFC banks and emissions, *Atmos. Chem. Phys.*, *14* (9), 4563–4572, doi:10.5194/acp-14-4563-2014, 2014.

Velders, G.J.M., D.W. Fahey, J.S. Daniel, S.O. Anderson, and M. McFarland, Future atmospheric abundances and climate forcings from scenarios of global and regional hydrofluorocarbon (HFC) emissions, *Atmos. Environ.*, *123* (A), 200–209, doi:10.1016/j.atmosenv.2015.10.071, 2015.

Visioni, D., G. Pitari, and V. Aquila, Sulfate geoengineering: a review of the factors controlling the needed injection of sulfur dioxide, *Atmos. Chem. Phys.*, *17* (6), 3878–3889, doi:10.5194/acp-17-3879-2017, 2017.

Visioni, D., G. Pitari, V. Aquila, S. Tilmes, I. Cionni, G. Di Genova, and E. Mancini, Sulfate geoengineering impact on methane transport and lifetime: Results from the Geoengineering Model Intercomparison Project (GeoMIP), *Atmos. Chem. Phys.*, *17*, 11,209–11,226, doi:10.5194/acp-17-11209-2017, 2017.

Voigt, C., U. Schumann, K. Graf, and K.-D. Gottschaldt, Impact of rocket exhaust plumes on atmospheric composition and climate, *Prog. Propulsion Phys.*, *4*, 657–670, doi:10.1051/eucass/201304657, 2013.

Wallington, T.J., W.F. Schneider, D.R. Worsnop, O.J. Nielsen, J. Sehested, W. DeBruyn, and J.A. Shorter, Atmospheric chemistry and environmental impact of CFC replacements: HFCs and HCFCs, *Environ. Sci. Technol.*, *28* (7), 320A–326A, doi:10.1021/es00056a002, 1994.

Wallington, T.J., M.D. Hurley, J.M. Fracheboud, J.J. Orlando, G.S. Tyndall, J. Sehested, T.E. Møgelberg, and O.J. Nielsen, Role of excited CF_3CFHO radicals in the atmospheric chemistry of HFC-134a, *J. Phys. Chem.*, *100* (46), 8116–1812, doi:10.1021/jp9624764, 1996.

Wallington, T.J., M.P. Sulbaek Andersen, and O.J. Nielsen, Estimated Photochemical Ozone Creation Potentials (POCPs) of $CF_3CF{=}CH_2$ (HFO-1234yf) and Related Hydrofluoroolefins (HFOs), *Atmos. Environ.*, *44* (11), 1478, doi:10.1016/j.atmosenv.2010.01.040, 2010.

Wallington, T.J., M.P. Sulbaek Andersen, and O.J. Nielsen, Atmospheric chemistry of short-chain haloolefins: Photochemical ozone creation potentials (POCPs), global warming potentials (GWPs), and ozone depletion potentials (ODPs), *Chemosphere*, *129*, 135–141, doi:10.1016/j.chemosphere.2014.06.092, 2015.

Wallington, T.J., M.P. Sulbaek Andersen, and O.J. Nielsen, Advances in Atmospheric Chemistry, World Scientific Publishing Company, 2017.

Wang, Z.Y., Y.H. Wang, J.F. Li, S. Henne, B.Y. Zhang, J.X. Hu, and J.B. Zhang, Impacts of the Degradation of 2,3,3,3-Tetrafluoropropene into Trifluoroacetic Acid from Its Application in Automobile Air Conditioners in China, the United States, and Europe, *Environ. Sci. Technol.*, *52* (5), 2819–2826, doi:10.1021/acs.est.7b05960, 2018.

Warneck, P., and J. Williams, The atmospheric chemist's companion: Numerical data for use in the atmospheric sciences, Springer, New York, NY, 2012.

Wigley, T.M.L., A combined mitigation/geoengineering approach to climate stabilization, *Science*, *314* (5798), 452–454, doi:10.1126/science.1131728, 2006.

WMO (World Meteorological Organization), *Scientific Assessment of Ozone Depletion: 2006*, Global Ozone Research and Monitoring Project–Report No. 50, 572 pp, Geneva, Switzerland, 2007.

WMO (World Meteorological Organization), *Scientific Assessment of Ozone Depletion: 2010*, Global Ozone Research and Monitoring Project–Report No. 52, 516 pp., Geneva, Switzerland, 2011.

WMO (World Meteorological Organization), *Scientific Assessment of Ozone Depletion: 2014*, Global Ozone Research and Monitoring Project–Report No. *55*, 416 pp., Geneva, Switzerland, 2014.

Wu, J., J.W. Martin, Z. Zhai, K. Lu, X. Fang, and H. Jin, Airborne trifluoroacetic acid and its fraction from the degradation of HFC-134a in Beijing, China, *Environ. Sci. Technol.*, *48* (7), 3675–3681, doi:10.1021/es4050264, 2014a.

Wu, J., J.W. Martin, Z. Zhai, K. Lu, X. Fang, and H. Jin, Response to comment on "Airborne trifluoroacetic acid and its fraction from the degradation of HFC-134a in Beijing, China," *Environ. Sci. Technol.*, *48* (7), 9949, doi:10.1021/es5032568, 2014b.

Wuebbles, D.J., D. Wang, K.O. Patten, and S.C. Olsen, Analyses of short-lived replacements for HFCs with large GWPs, *Geophys. Res. Lett.*, *40* (17), 4767–4771, doi:10.1002/grl.50908, 2013.

Xia, L., A. Robock, S. Tilmes, and R.R. Neely III, Stratospheric sulfate geoengineering could enhance the terrestrial photosynthesis rate, *Atmos. Chem. Phys.*, *16*, 1479–1489, doi:10.5194/acp-16-1479-2016, 2016.

Xia, L., P.J. Nowack, S. Tilmes, and A. Robock, Impacts of stratospheric sulfate geoengineering

on tropospheric ozone, *Atmos. Chem. Phys.*, *17*, 11,913-11,928, doi:10.5194/acp-17-11913-2017, 2017.

Xu, Y., D. Zaelke, G.J.M. Velders, and V. Ramanathan, The role of HFCs in mitigating 21st century climate change, *Atmos. Chem. Phys.*, *13*, 6083–6089, doi:10.5194/acp-13-6083-2013, 2013.

Yang, X., N.L. Abraham, A.T. Archibald, P. Braesicke, J. Keeble, P.J. Telford, N.J. Warwick, and J.A. Pyle, How sensitive is the recovery of stratospheric ozone to changes in concentrations of very short-lived bromocarbons?, *Atmos. Chem. Phys.*, *14* (19), 10,431–10,438, doi:10.5194/acp-14-10431-2014, 2014.

Ziemke, JR., and O.R. Cooper, Tropospheric ozone, in State of the Climate in 2016, *Bull. Am. Meteorol. Soc., 98*, S52–S54, doi:10.1175/2017BAMS-StateofClimate.1, 2017.

Ziemke, J.R., and O.R. Cooper, Tropospheric ozone, in State of the Climate in 2017, *Bull. Am. Meteorol. Soc., 99* (8), doi:10.1175/2018BAMSStateof-Climate.1, 2018.

Appendix 6A
Current State of Knowledge on Stratospheric Sulfate Geoengineering

Since geoengineering may be considered in the future, chemical and dynamical changes and their impacts on future column ozone have to be understood. Models incorporate stratospheric chemistry and dynamics with varying degrees of sophistication, and very few single-model studies have investigated changes in ozone due to geoengineering with consideration of interactions between dynamics, chemistry, aerosols, and climate. In this appendix, the current state of knowledge on stratospheric sulfate geoengineering is summarized in more detail than covered in the main chapter.

6A.1 Impact of Stratospheric Sulfate Geoengineering on Net Chemical Ozone Production

An increasing sulfate aerosol burden from possible continuous injection of SO_2 into the tropical stratosphere would result in an enhanced aerosol surface area density in the mid- and lower stratosphere (i.e., up to about 10 hPa in the tropics). This would increase the surface area available for heterogeneous reactions, similar to that observed after large volcanic eruptions (Heckendorn et al., 2009; Pitari et al., 2014; Tilmes et al., 2009; Tilmes et al., 2012; Visioni et al., 2017a). The magnitude and spatial pattern of the increased aerosol surface area density and the associated mass and size distributions, which are strongly model dependent, vary with the amount and location of injections (e.g., Dai et al., 2018; English et al., 2012; Laakso et al., 2017; Niemeier and Timmreck, 2015; Pitari et al., 2014; Tilmes et al., 2017) and on the injection substance. The impact of increased aerosol surface area is particularly significant for three heterogeneous reactions:

$$N_2O_5 + H_2O \rightarrow 2HNO_3 \quad (1)$$

$$ClONO_2 + H_2O \rightarrow HOCl + HNO_3 \quad \text{for } T < 200 \quad (2)$$

$$ClONO_2 + HCl \rightarrow Cl_2 + HNO_3 \quad \text{for } T < 200K \quad (3)$$

Reaction (1), the reduction of nitrogen oxides (NO_y) via hydrolysis of N_2O_5 (e.g., Fahey et al., 1993) would increase ozone abundance, which is in part counteracted by the increase in ozone loss cycles involving reactive chlorine (ClOx), bromine (BrO_x), and hydrogen (HOx) families. This reaction is dominant in the tropical mid-stratosphere (**Figure 6A-1**, top left).

Increasing/decreasing the surface area density and NO_y would result in an increase/decrease of the importance of reaction (1), although this effect would saturate at very high aerosol loadings (e.g., Berthet et al., 2017). Reaction (2), the hydrolysis of $ClONO_2$, results in production of HOCl, increased HOx and ClO concentrations, and increased ozone loss via the catalytic ClOx and HOx cycles. Heterogeneous reactions of $ClONO_2$ with hydrogen chloride HCl result in additional reactive chlorine. Reactions (2) and (3) are most important in cold regions, especially in the lower stratosphere in polar regions in winter and spring (**Figure 6A-1**, top left). Additional reactions, including the hydrolysis of $BrONO_2$, play an important role for warmer conditions (Tilmes et al., 2012), as recent observations after small volcanic eruptions have demonstrated (Berthet et al., 2017). The importance of these reactions will decline with the projected decreasing stratospheric halogen burden. A potential increase in the cold point temperature, as the result of aerosol geoengineering and a resulting increase in stratospheric water vapor content (see **Section 6.2.5**), leads to an additional increase in the HO_x ozone loss cycle throughout the stratosphere. Resulting changes in net chemical ozone production are most important in the lower and upper tropical stratosphere, especially in the summer Northern Hemisphere (Tilmes et al., 2018). An increase in the odd oxygen cycle involving reactive oxygen (O_x), resulting from a temperature increase in

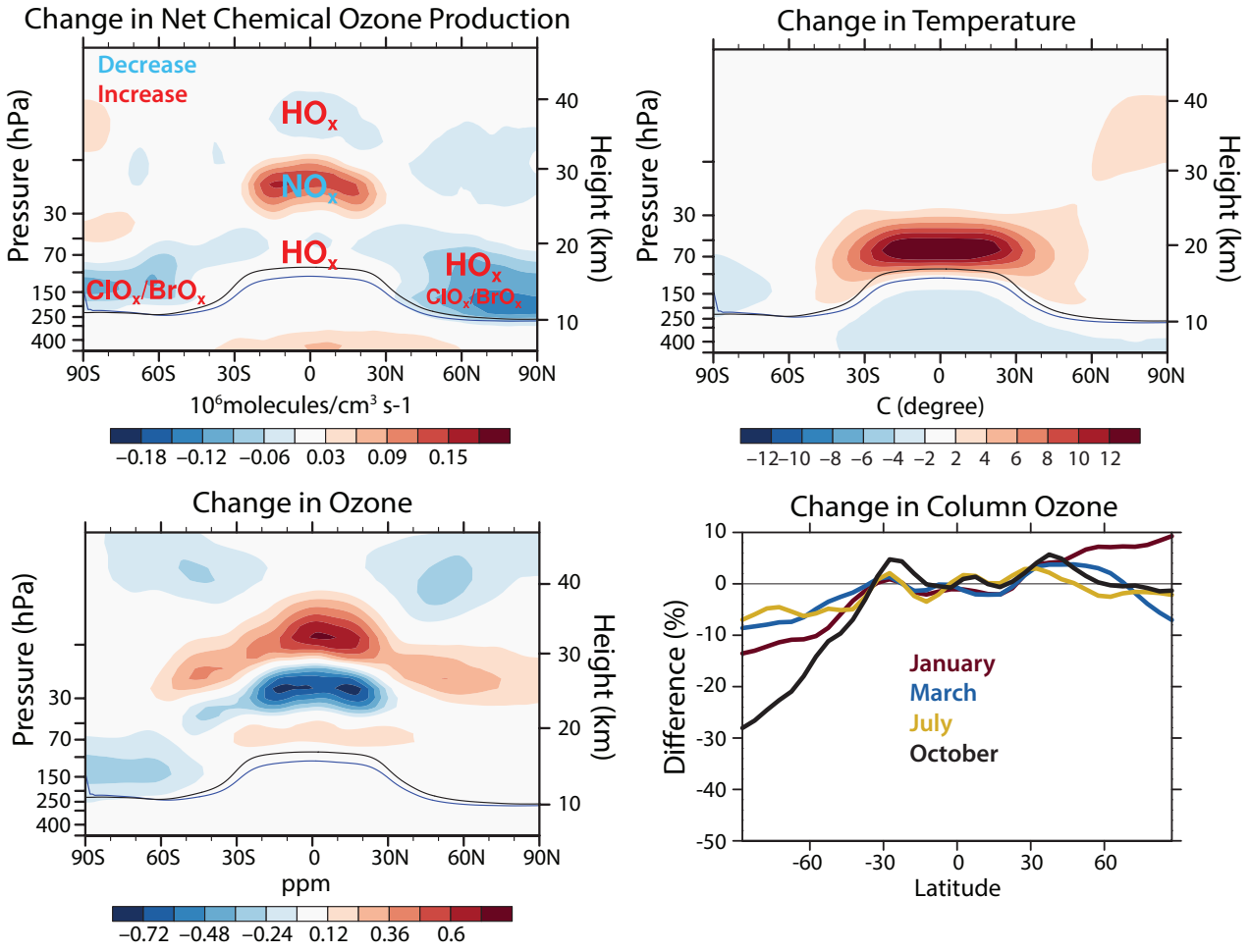

Figure 6A-1. Processes impacting stratospheric ozone in 2042–2049 following RCP8.5 for 16 Tg S yr^{-1} injections at 15°N/15°S. Impact of enhanced sulfate aerosols on zonal and annual averaged net rate of chemical production of ozone (*top left*), temperature (*top right*), and ozone concentration (*bottom left*). Changes in the dominant ozone loss cycles are shown in blue if decreasing (net chemical production is increasing) and in red if increasing (net chemical production decreasing) (*top left*). The example is based on a RCP8.5 control simulation between 2042 and 2049 and a geoengineering simulation with injection of 16 Tg S yr^{-1} evenly distributed between two single injection locations at 15°N and 15°S latitude, 180° longitude, and at 70 hPa (about 19 km) to counteract surface warming of about 2°C, using a fully interactive model, CESM1 (WACCM) (Richter et al., 2018; Tilmes et al., 2018). The tropopauses in the control and geoengineering simulations are shown by the black and blue lines, respectively. Changes in ozone concentration with geoengineering are driven mainly by dynamical changes, especially in the tropics and the Northern Hemisphere; changes in ozone concentration in polar regions mainly reflect enhanced chemical loss. Differences in column ozone (%) between the geoengineering and the control simulation in 2042–2049 are illustrated for different months (*bottom right*).

the tropical stratosphere, would also contribute to the change in net chemical ozone. Finally, the decrease in photolysis rates due to scatter by aerosols has been estimated to decrease ozone in the tropical lower stratosphere (Pitari et al., 2014).

6A.2 Impact of Stratospheric Sulfate Geoengineering on Dynamics

According to modeling studies, geoengineering via stratospheric aerosol injection would affect dynamics through two main processes: (1) cooling of the troposphere as the result of reduced incoming shortwave radiation and (2) substantial warming of the tropical stratosphere as the result of diabatic heating caused by the increased sulfate aerosol layer (**Figure 6A-1**, top right) (e.g., Pitari et al., 2014; Tilmes et al., 2018; Richter et al., 2018). These processes result in a drop in tropopause altitude, a weakening of the subtropical jets, and an increase in the tropical cold point temperature, which may increase stratospheric water vapor by up to 90% for very large injections of 40 Tg SO_2 yr^{-1} (Richter et al., 2018; Tilmes et al., 2018). The vertical component of the residual circulation in the tropics is reduced below the injection location as the result of a decrease in the temperature gradient between the tropics and mid-latitudes above the subtropical jets. On the other hand, the increased tropical upwelling above the injection locations and increased downwelling in high latitudes is consistent with a strengthening of the gravity wave drag and Eliassen–Palm flux (EPF) divergence in mid- and high latitudes and is aligned with a strengthening of the polar night jet (Tilmes et al., 2018; Richter et al., 2018). The strengthening of the polar night jet in high latitudes results in additional ozone depletion (Tilmes et al., 2009), while increases in horizontal advection, especially in winter mid-latitudes in the Northern Hemisphere stratosphere, can result in an increase of ozone above values of non-geoengineered conditions, for example, as shown for large injections of 16 Tg S yr^{-1} at about 1 km above the tropical tropopause (**Figure A6-1**, bottom left). Changes in advection of ozone, other gases, and sulfate aerosols interact with chemical changes as well as stratosphere-to-troposphere exchange. Resulting changes in tropospheric chemistry, temperature, and UV are estimated to increase methane lifetime by 16% for continuous 4 Tg S yr^{-1} injections (Visioni et al., 2017b).

Simulations with injections of sulfur at the equator identified a significant prolonging of the westerly phase of the Quasi-Biennial Oscillation (QBO) with increasing injection amounts (Aquila et al., 2014). This would lead to a stronger confinement of particles in the tropics (Niemeier and Schmidt, 2017). However, Richter et al. (2017) have shown that geoengineering in a model with interactive stratospheric chemistry and coupled ocean has a reduced impact on the QBO due to reductions in heating as the result of reductions in ozone around 30 hPa. Furthermore, different injection scenarios at 15°N and 15°S or in addition at 30°N and 30°S with injections up to 25 Tg S yr^{-1} by the end of the 21st century (Richter et al., 2018) would instead lead to a QBO that is closer to present-day conditions. Large differences and shortcomings in the representation of the QBO in different models exist, and differences in the response to geoengineering have to be investigated in more detail.

6A.3 Impact of Sulfate Aerosol Geoengineering on Column Ozone

In addition to potential changes in column ozone as the result of increasing greenhouse gases (GHGs) (Butler et al., 2016), chemical and dynamical changes due to geoengineering, as discussed above, would affect future column ozone and in part counteract the projected increase of column ozone ("super-recovery") over most latitudes (**Chapter 3**). In one modeling study, a fixed injection of 4 Tg S yr^{-1} between 2020 and 2070, which results in 0.5°C of surface cooling, leads to approximately a 4% reduction in the global stratospheric column ozone for 2020 and only a 1% reduction by 2070 (Xia et al., 2017). These results are similar to calculations based on four models using fixed injections of 2.5 Tg S yr^{-1}, which show an average decrease in global column ozone of 2.8% over the same period (Visioni et al., 2017a). The impact of aerosols geoengineering on ozone is therefore small if applied later in the century, when global column ozone absent geoengineering is projected to increase by about ~4% (from 2020 to 2070) due to changes in ODS and GHG concentrations (Cionni et al., 2017).

Simulations using a fully interactive earth system model that includes an interactive aerosol microphysical

scheme coupled to interactive chemistry and radiation, and with an internally generated QBO (Mills et al., 2017), point to the importance of chemistry and dynamical changes on column ozone. Very large injections of 16 Tg S yr^{-1}, to cool the surface by about 2°C in 2042–2049, reduce column ozone values towards present-day conditions in winter and spring high altitudes for both hemispheres (**Figure 6A-1**, bottom right). Maximum reductions of 8% in March over the Arctic, and 28% in October over Antarctica are reached in comparison to the RCP8.5 control simulation (**Figure 6A-1**, bottom right). On the other hand, an increase of column ozone above non-geoengineered levels up to 8% is simulated for the Northern Hemisphere mid-latitudes in winter. A different experiment that reached the same surface cooling but applied injections at higher altitudes (~5 km about the tropopause) indicated that advection is less important and resulted in a larger decrease in column ozone at high latitudes, with up to 18% loss over the Arctic and up to 40% over Antarctica in spring. The impact on column ozone is therefore dependent on the injection strategy (Richter et al., 2018; Tilmes et al., 2018).

A transient simulation based on RCP8.5 GHG forcings with continuously increasing SO_2 injections at 15°N, 15°S, 30°N, and 30°S at ~5 km about the tropopause required injections up to 25 Tg S yr^{-1} by the end of the century to maintain temperatures at 2020 levels (Kravitz et al., 2017). In this simulation, ozone recovery in the Southern Hemisphere polar vortex was delayed until the end of the 21st century. Besides, column ozone reached values close to pre-ozone hole conditions for the Southern Hemisphere and tropics and well above pre-ozone hole conditions for northern mid-latitudes in winter and spring (Richter et al., 2018). By the end of the 21st century, geoengineering resulted in higher column ozone values compared to non-geoengineering conditions for tropics and winter northern mid-latitudes.

Appendix 6B

Comparison of Past and Future Ozone Projections of the GSFC 2-D Model with GEOSCCM 3-D Simulations

In this appendix, predictions of past and future ozone with the GSFC 2-D model (GSFC 2D), used in this chapter, are shown to be in very good agreement with the GEOSCCM 3-D simulations used in **Chapters 3**, **4**, and **5**. The GEOSCCM has a comprehensive tropospheric and stratospheric chemical mechanism (e.g., Oman et al., 2016) and performed well in both chemical- and transport-related process evaluations (SPARC CCMVal, 2010; Strahan et al., 2011; Douglass et al., 2012). The GSFC 2-D model has complete stratospheric chemistry but contains a limited subset of tropospheric species (Fleming et al., 2011; Jackman et al., 2016). The GSFC 2-D model compares well with observations and the GEOSCCM in simulating various transport-sensitive features in the meridional plane (e.g., long-lived tracers), as well as long-term changes in temperature and age of air over the 1950–2100 period (Fleming et al., 2011; SPARC, 2013). In this appendix, we also show comparisons of the baseline simulation with the CCMI multi-model mean (MMM, ±1σ) for the total and stratospheric column, and with selected observations where available.

Figure 6B-1 shows comparisons of the GSFC 2-D model and GEOSCCM global/annually averaged ozone from the CCMI baseline REF-C2 simulations for 1960–2100. These simulations include past stratospheric aerosol variations and solar ultraviolet flux variability associated with the 11-year solar cycle, with a repeating 11-year cycle projected out to 2100. The 2-D model stratospheric column ozone agrees quite well with the GEOSCCM, both in absolute amount and the pre-2000 decline and future ozone recovery out to 2100 (**Figure 6B-1b**). While tropospheric column ozone is similar in the two models during the 1960s, GSFC 2-D underestimates the time-dependent increases in tropospheric ozone in the GEOSCCM from ~1970 through the mid-21st century (**Figure 6B-1c**). This is likely due to the limited tropospheric chemical scheme used in the 2-D model, as mentioned above. This results in a low bias in tropospheric ozone throughout the 21st century, which is as large as 15% (5 DU) in 2050–2060. This low bias is also reflected in the future total column ozone comparison through the 21st century (**Figure 6B-1a**). For the total and stratospheric column, GSFC 2D and GEOSCCM show overall agreement with the observations but show a stronger decline and stronger recovery compared with the CCMI MMM (gray shading indicates ±1σ). For the tropospheric column, the limited available data fall between the two models (see the figure caption for details of the observations and MMM).

Figure 6B-2 shows stratospheric column ozone from the REF-C2 simulations at selected latitude zones. The GSFC 2D low bias in tropospheric ozone, and therefore in the total column, is similar to that of the global average (**Figure 6B-1**); therefore, the focus here is on stratospheric ozone. The 2-D model captures well the decline and recovery of stratospheric ozone simulated by the GEOSCCM and CCMI MMM during the Antarctic spring and the tropical and Northern mid-latitude annual average. The models show general agreement with the observations, which have significant year-to-year variability, although the CCMI MMM shows a somewhat weaker ozone decline during the Antarctic spring. The models also show the GHG-induced "super-recovery" at Northern Hemisphere mid-latitudes, where stratospheric ozone is 15–20 DU higher in 2100 than in 1960 (the CCMI MMM shows a somewhat smaller increase). The GEOSCCM, GSFC 2D, and CCMI MMM all show a similar decrease in tropical stratospheric ozone during the late 21st century, again driven primarily by GHG changes as discussed in **Chapter 3** (see **Sections 3.4.2** and **3.4.3.1** and **Figures 3-26**, **3-29**, and **3-30**).

GSFC 2D also compares well with the GEOSCCM in simulating the ozone response to the CH_4 perturbations discussed in **Chapters 3** and **4**. **Figure 6B-3** shows the profile ozone mixing ratio difference (ppm) between the RCP8.5 (high) CH_4 simulation and REF-C2 (RCP6.0 CH_4), averaged over 2070–2100. In the stratosphere, increased CH_4 loading leads to increased ozone due to the conversion of active chlorine to reservoir chlorine via the reaction $CH_4 + Cl \rightarrow HCl + CH_3$, which reduces the chlorine-catalyzed ozone loss, although this process will

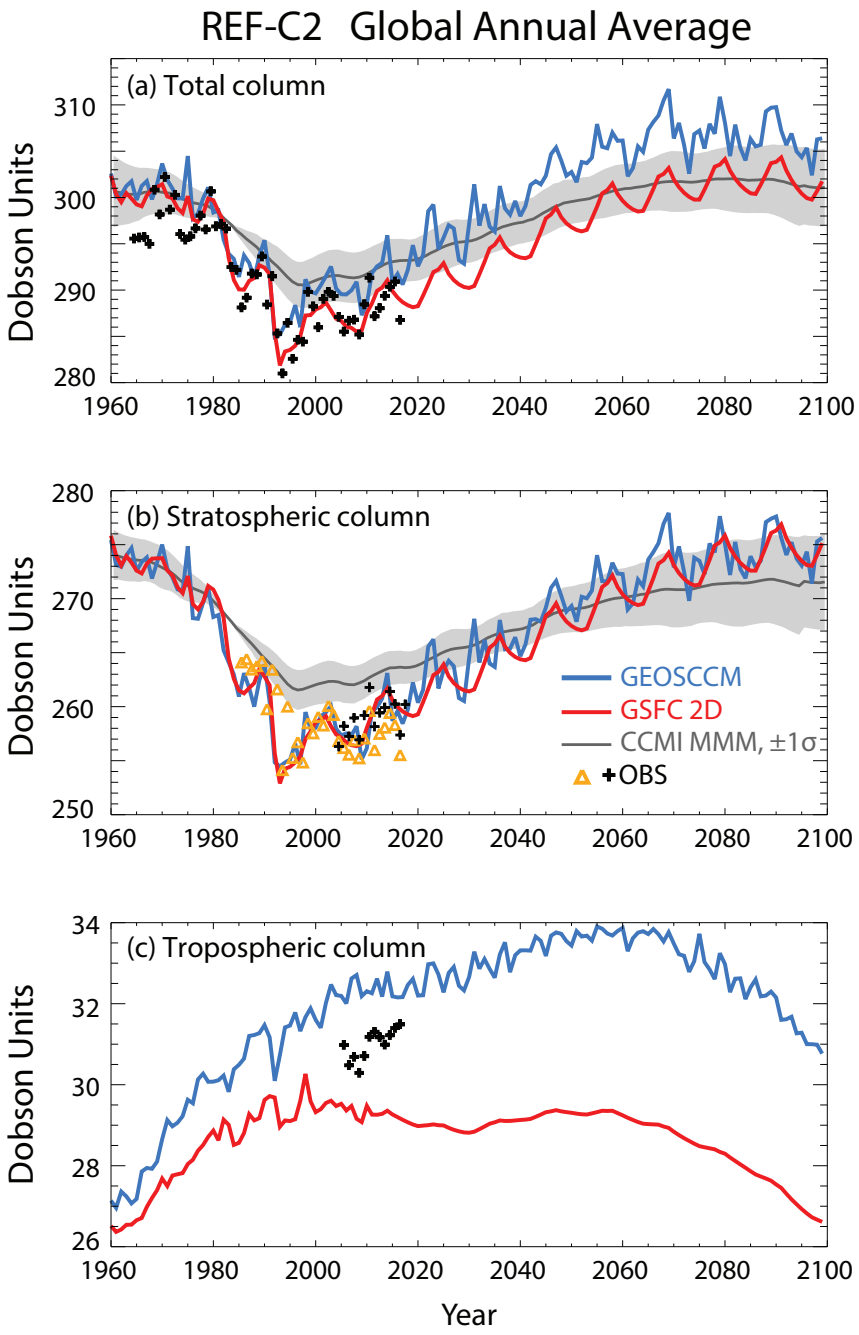

Figure 6B-1. Comparison of past and future globally averaged ozone from the REF-C2 simulations and observations. This shows the ozone columns below (c) and above (b) the latitude- and seasonally-dependent tropopause, and the total column (a), from the GSFC 2-D model (red line) and GEOSCCM 3-D model (blue line) for 1960–2100. Also shown are the CCMI multi-model mean (MMM, dark gray line) with ±1σ (gray shading) (see **Sections 3.4** and **4.5** of this Assessment, and Dhomse et al., 2018 for details). The observations are (a) ground-based total ozone for 1964–2016 updated from Fioletov et al. (2002); (b) stratospheric column ozone from: Aura/MLS version 4.2 for 2005–2017 (black +), and Global OZone Chemistry And Related trace gas Data records for the Stratosphere (GOZCARDS) version 2.20 for 1985–2016, updated from Froidevaux et al. (2015) and time-interpolated to fill in missing data (orange Δ); and (c) tropospheric column ozone derived from OMI/MLS averaged over 60°S to 60°N for 2005–2016 (Ziemke and Cooper, 2017; 2018). To facilitate visual comparison and minimize the model biases in the 1960s, the following offsets were applied: (a) MMM: +6.5 DU; (b) MMM: –3 DU, GOZCARDS: +3 DU.

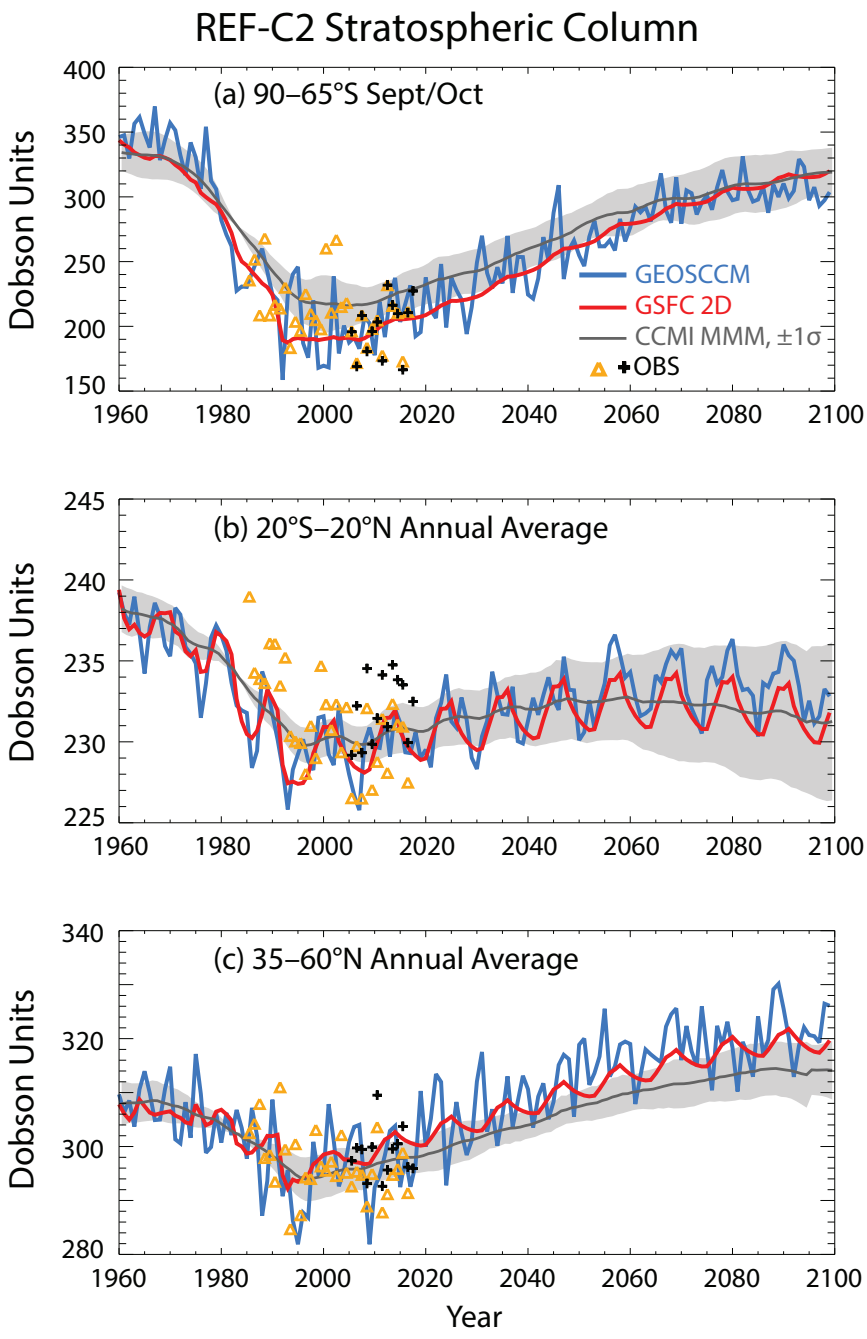

Figure 6B-2. Comparison of past and future stratospheric column ozone in select latitude bands from the baseline REF-C2 simulations and observations. This shows the ozone column above the tropopause (seasonally- and latitude-dependent) from the GSFC 2-D model (red line) and GEOSCCM 3-D model (blue line) for 1960–2100. Also shown are the CCMI multi-model mean (MMM, dark gray line) with ±1σ (gray shading) (see **Sections 3.4** and **4.5** of this Assessment, and Dhomse et al., 2018 for details). The observations are stratospheric column ozone from: Aura/MLS version 4.2 for 2005–2017 (black +), and Global OZone Chemistry And Related trace gas Data records for the Stratosphere (GOZCARDS) version 2.20 for 1985–2016, updated from Froidevaux et al., 2015 and time-interpolated to fill in missing data (orange Δ). To facilitate visual comparison and minimize the model biases in the 1960s, the following offsets were applied: (a) MMM: +15 DU; (b) MMM: –16 DU, GOZCARDS: +2 DU; (c) GEOSCCM: –5 DU, GOZCARDS: +2 DU.

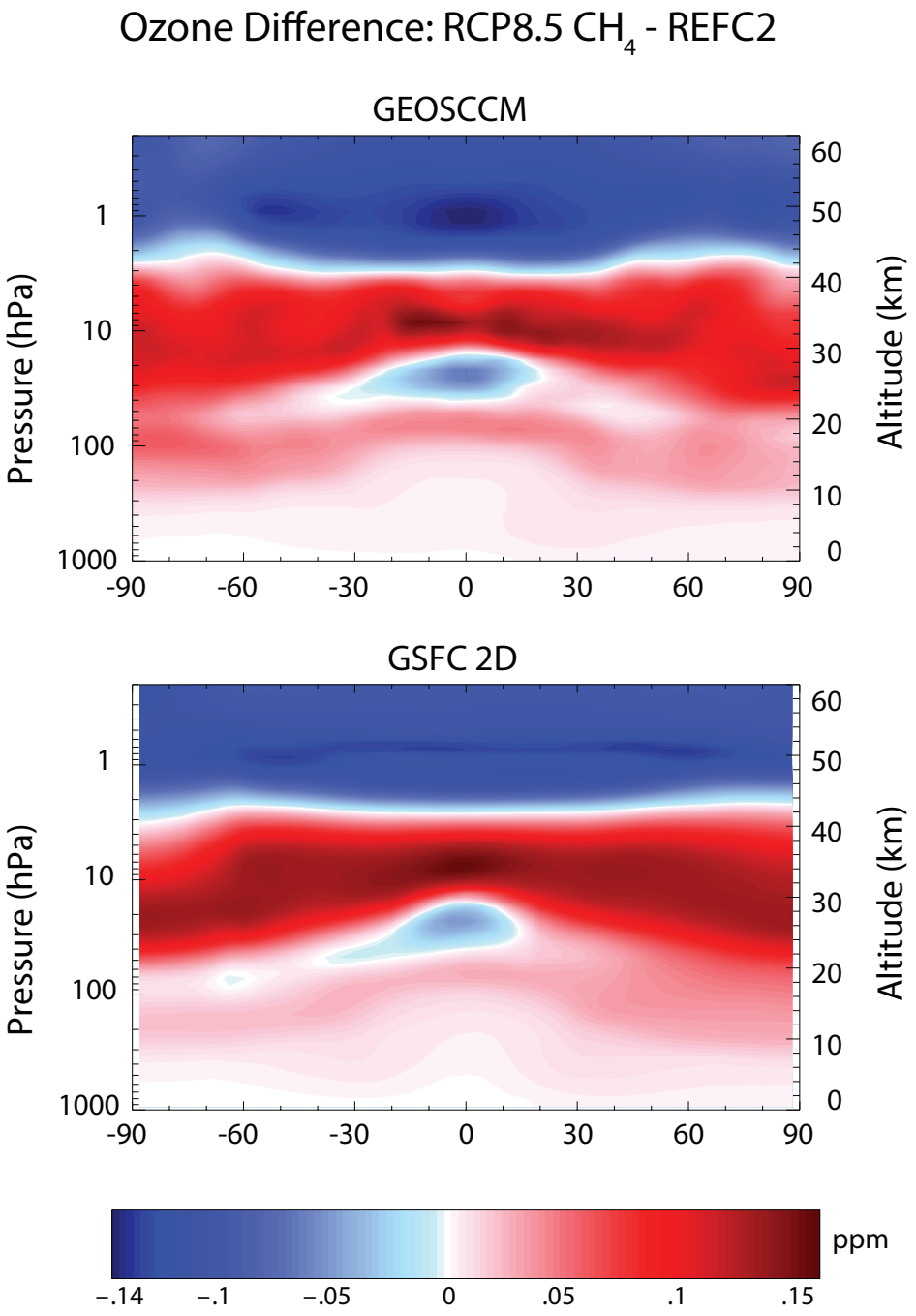

Figure 6B-3. Profile ozone sensitivity to CH_4. This shows the ozone mixing ratio difference (ppm) between simulations using the RCP8.5 CH_4 (high) scenario and the baseline REF-C2 (RCP6.0 CH_4) from the GEOSCCM and GSFC 2-D model, averaged over the period 2070–2099 to minimize interannual variability in the GEOSCCM. Negative differences are indicated by the blue colors, positive differences by the red colors.

become less important as chlorine diminishes through the late 21st century. Methane oxidation also increases stratospheric HO_x, which (1) increases the HO_x-ozone loss and (2) sequesters NO_x in the reservoir HNO_3 via the reaction OH + NO_2, thereby reducing ozone loss in the mid-stratosphere (Nevison et al., 1999; Randeniya et al., 2002). There is also a contribution due to the increased water vapor from methane oxidation, which enhances stratospheric cooling and reduces the ozone chemical loss rates (e.g., WMO, 2014). In the troposphere and lowermost stratosphere, CH_4 oxidation leads to enhanced NO_x-induced ozone production, which is strongly dependent on the amount of ambient NO_x (e.g., see Jacob, 1999; Portmann and Solomon, 2007; Fiore et al., 2008; Kawase et al., 2011; WMO, 2014). The net impact of these processes yields ozone increases throughout most of the stratosphere below ~42 km and ozone decreases above ~42 km. The small area of negative ozone change in the tropical mid-stratosphere is likely due to "reverse self-healing," in which increased ozone concentrations at higher altitudes allow less UV radiation to penetrate to lower altitudes, thereby reducing ozone production (e.g., Haigh and Pyle, 1982; Portmann and Solomon, 2007).

Figure 6B-4 shows time series of the global ozone difference from the REF-C2 simulation using (1) fixed (low) 1960 CH_4 throughout 1960–2100 and (2) RCP8.5 (high) CH_4 for 2000–2100. Globally, tropospheric and stratospheric column ozone both increase with larger methane concentrations and decrease with smaller methane concentrations. GEOSCCM and GSFC 2D give very similar global tropospheric and stratospheric ozone responses to both low and high methane concentrations throughout 1960–2100 (**Figure 6B-4b** and **c**). Although GSFC 2D has limited tropospheric chemistry and underestimates the GEOSCCM baseline tropospheric ozone, the large-scale NO_x distribution is similar to the GEOSCCM. As a result, GSFC 2D simulates quite well the methane-induced global tropospheric ozone perturbations (difference from REF-C2) simulated by GEOSCCM (**Figure 6B-4c**). The total column ozone responses are therefore also quite similar between the two models (**Figure 6B-4a**), which gives confidence in the fidelity of the 2-D model total ozone responses to the CH_4 sensitivity simulations discussed in **Section 6.4.3.1** (**Figure 6-4c**). **Figure 6B-4** also indicates that changes in stratospheric and tropospheric ozone each account for roughly 50% of the total ozone response to the CH_4 sensitivity simulations shown in **Figure 6-4c**.

Figure 6B-5 shows the model ozone mixing ratio sensitivity to N_2O as discussed in **Chapters 3** and **4**. The difference between simulations using fixed (low) 1960 N_2O versus the baseline REF-C2 (RCP6.0 N_2O) results in positive ozone changes in the mid-upper stratosphere, owing to the reduced NO_x-ozone loss. Negative ozone changes occur in the lower stratosphere and upper troposphere as the reduced NO_x decreases the NO_x-induced ozone production cycle. Some of the negative changes are also likely caused by "reverse self-healing" as discussed above. The zero ozone difference line occurs at ~28 km in the tropics and descends with latitude to ~18 km at the poles (see also Revell et al., 2012; Figure 2-25 of Parwon, Steinbrecht, et al., 2014; and **Chapter 3** of this Assessment). To emphasize these positive and negative ozone differences, time series of the global column ozone below and above this zero difference line are shown in **Figure 6B-6c** and **d**. GSFC 2D is similar to the GEOSCCM in simulating the positive ozone changes above the zero difference line through the 21st century (**Figure 6B-6c**). However, GSFC 2D underestimates the negative ozone differences below the zero difference line at Northern Hemisphere mid-high latitudes at 10–18 km (**Figure 6B-5**) and in the global average (**Figure 6B-6d**). As a result, the 2-D model has larger positive changes in the global total column in the later part of the 21st century (**Figure 6B-6a**). However, GSFC 2D is very similar to the GEOSCCM in simulating the positive column ozone differences above 28 km, the primary region of stratospheric NO_x-ozone loss (**Figure 6B-6b**).

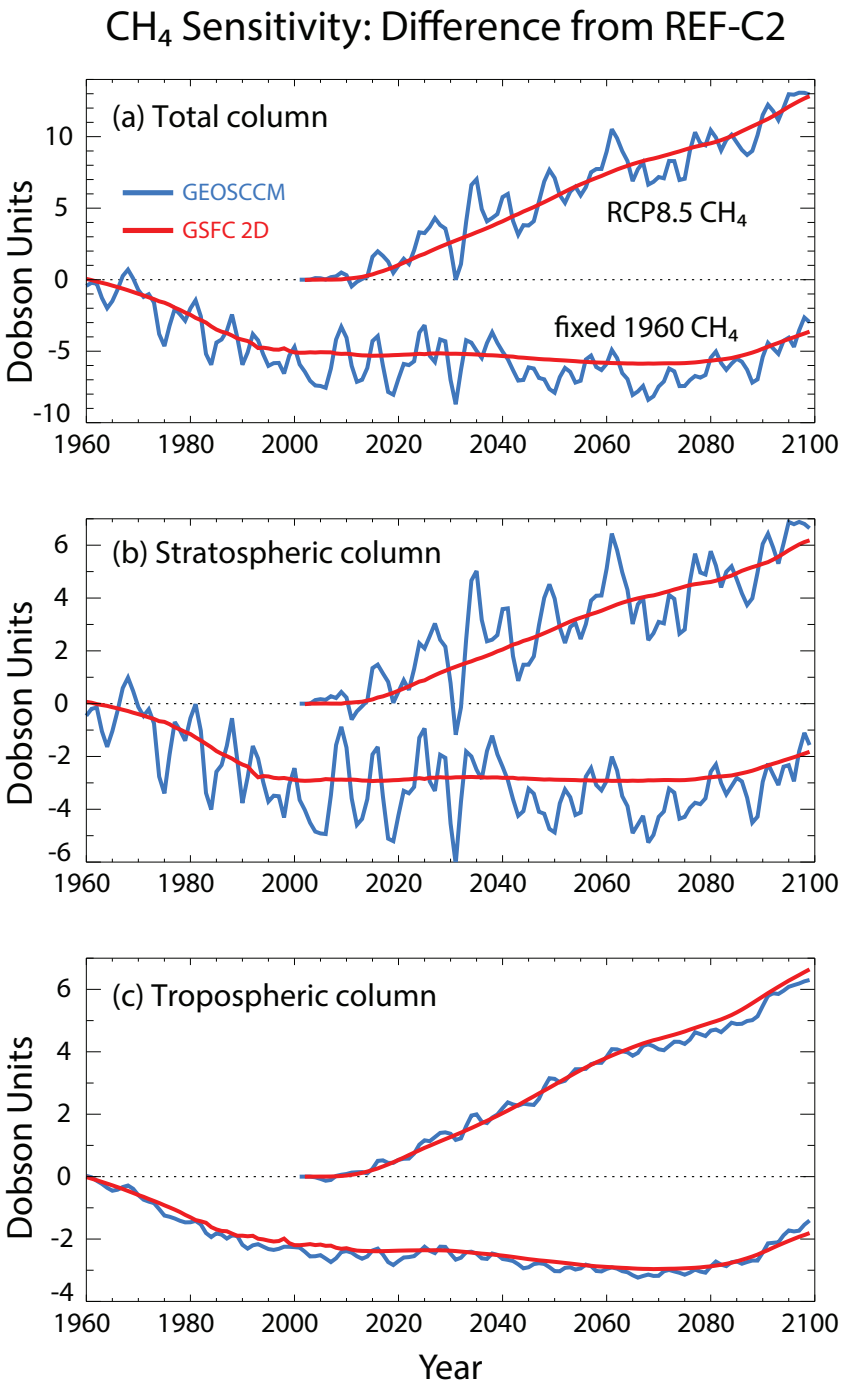

Figure 6B-4. Comparison of the past and future global ozone sensitivity to CH_4 variations. This shows the 1960–2100 global ozone difference from the baseline REF-C2 (RCP6.0 CH_4) of simulations using fixed (low) 1960 CH_4 (negative ozone anomalies) and the RCP8.5 CH_4 (high) scenario (positive ozone anomalies). Shown are the global tropospheric (c) and stratospheric (b) columns (separated by the latitude- and seasonally-dependent tropopause), and the total column (a) from the GSFC 2-D model (red line) and GEOSCCM 3-D model (blue line). Note that interannual variability in the 2-D model, due to tropospheric NO_x and CO emissions and the 11-year solar cycle, is the same for all simulations, so that the 2-D model difference curves (red) show minimal variability.

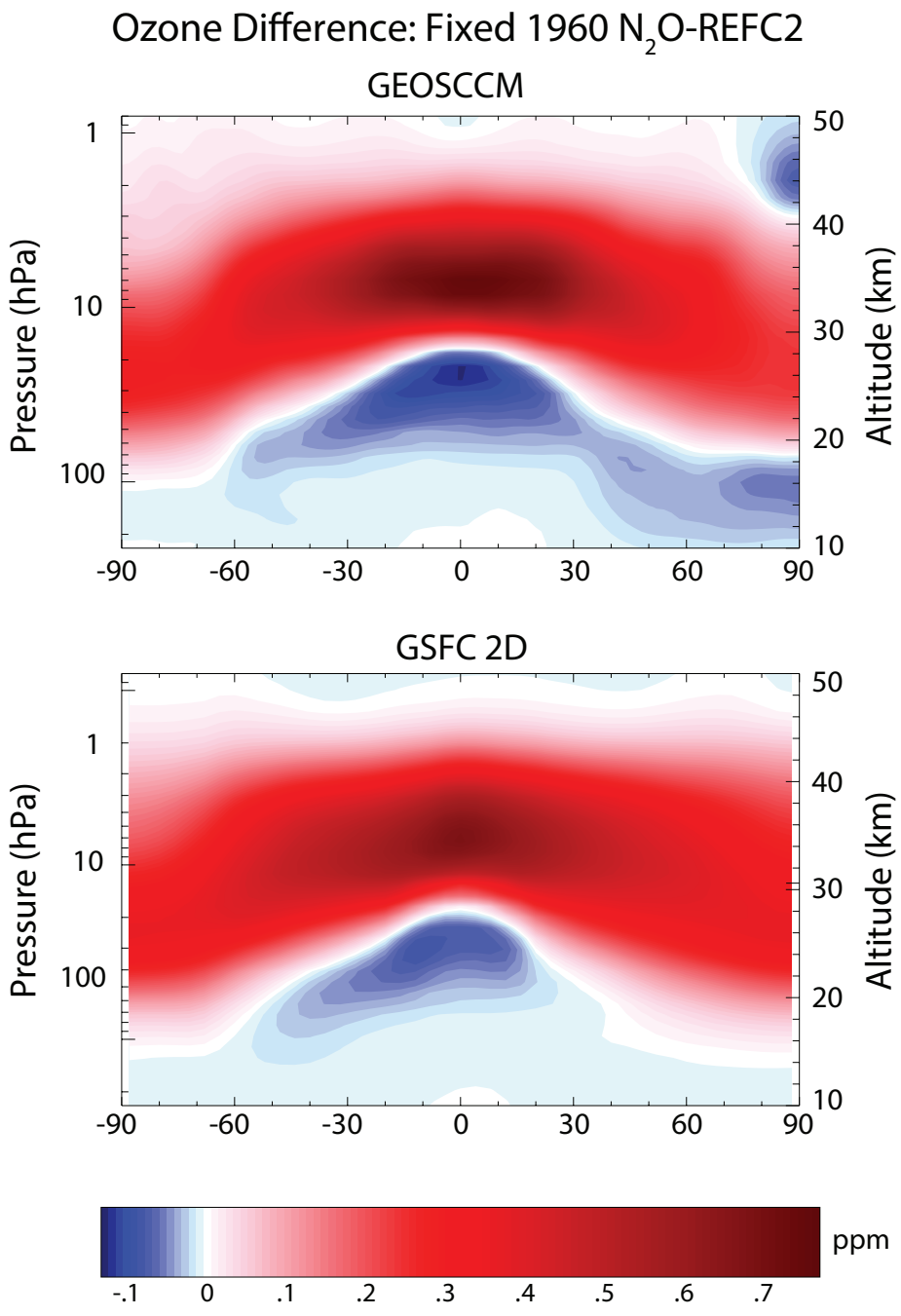

Figure 6B-5. Profile ozone sensitivity to N_2O. This shows the ozone mixing ratio difference (ppm) between simulations using fixed (low) 1960 N_2O and the baseline REF-C2 (RCP6.0 N_2O) from the GEOSCCM and GSFC 2-D model, both averaged over the period 2070–2099 to minimize interannual variability in the GEOSCCM. Negative differences are indicated by the blue colors, positive differences by the red colors.

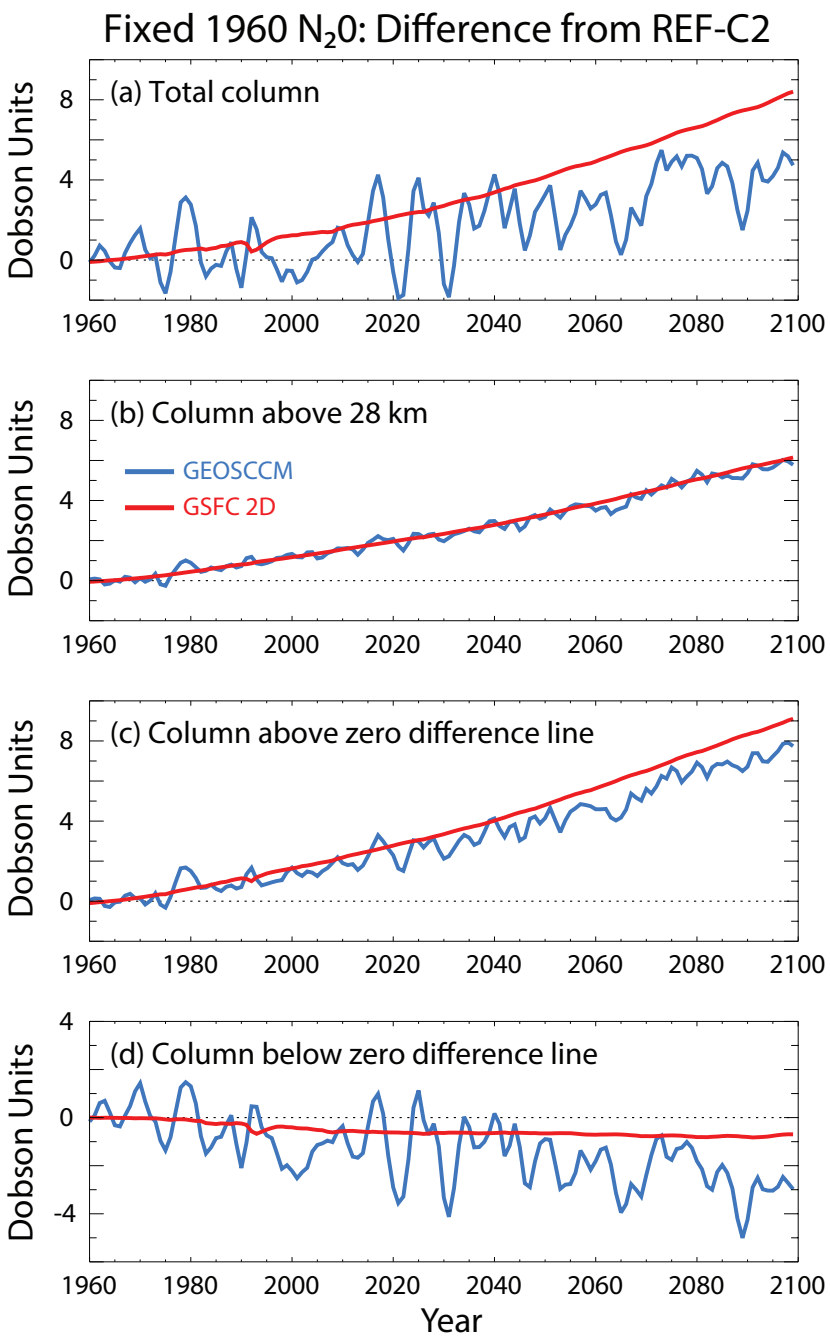

Figure 6B-6. Comparison of the past and future global ozone sensitivity to N_2O. This shows the 1960–2100 global ozone difference between simulations using fixed (low) 1960 N_2O and the baseline REF-C2 (RCP6.0 N_2O). As seen in **Figure 6A-5**, positive ozone differences occur in the mid-upper stratosphere, and negative differences in the lower stratosphere: the zero difference line occurs at ~28 km in the tropics and descends with latitude to ~18 km at the poles (see also Figure 2-25 of Pawson, Steinbrecht, et al., 2014, and **Chapter 3** of this Assessment). To emphasize these positive and negative differences, the column ozone below (d) and above (c) the zero difference line is shown in the bottom two panels. Also shown is column ozone above 28 km (b), the primary region of NO_x ozone loss, and the total column (a), from the GSFC 2-D model (red line) and GEOSCCM 3-D model (blue line). Note that interannual variability in the 2-D model, due to tropospheric NO_x and CO emissions and the 11-year solar cycle, is the same for all simulations, so that the 2-D model difference curves (red) show minimal variability.

Appendix 6C

Evaluation of Alternative Scenarios Using New EESC Formalism

Table 6C-1. Same as **Table 6-5**, for the part shown, but using the approach to calculating EESC and the fractional release values from Engel et al. (2017). **Table 6-5** and its footnotes provide additional information about the scenarios and the calculations used to populate the table.

Scenario and Cases	Percent Difference in Integrated EESC Relative to Baseline Scenario for the Mid-latitude Case		Year When EESC is Expected to Drop Below 1980 Value	
	Mid-latitude			Antarctic Vortex
	$\int_{1980}^{\chi} EESC\,dt$	$\int_{2020}^{\chi} EESC\,dt$		
Scenarios				
A1: Baseline scenario	0.0	0.0	2060.4	2077.3
P0: All ODS	–5.0	–16.4	2054.7	2071.9
CFCs	0.0	0.0	2060.4	2077.3
Halons	0.0	0.0	2060.4	2077.3
HCFCs	–0.9	–3.0	2059.8	2076.9
CH_3Br for QPS and CUE	–1.6	–5.4	2058.9	2075.8
CCl_4	–2.7	–8.9	2056.9	2073.9
E0: All ODS (does not include N_2O)	–9.9	–32.3	2048.9	2065.6
CFCs	–2.1	–6.7	2058.0	2074.9
Halons	–2.6	–8.6	2057.8	2074.6
HCFCs	–2.5	–8.3	2058.8	2076.2
CCl_4	–2.7	–8.9	2056.9	2073.9
CH_3CCl_3	0.0	0.0	2060.4	2077.3
CH_3Br for QPS and CUE	–1.6	–5.4	2058.9	2075.8
B0: All ODS	–6.0	–19.5	2054.4	2071.3
CFCs	–2.1	–6.7	2058.0	2074.9
Halons	–2.6	–8.6	2057.8	2074.6
HCFCs	–1.6	–5.3	2059.5	2076.7
B1: All	–4.0	–13.1	2055.4	2072.4
CFCs	–1.3	–4.1	2058.6	2075.4
Halons	–1.6	–5.3	2058.4	2075.1
HCFCs	–1.4	–4.5	2059.3	2076.5
Continued emission of CFC-11:				
Constant at 67 Gg yr^{-1}	+6.0	+19.7	2072.7	2098.4
Continued emission of CCl_4 at current levels:				
	+1.5	+4.9	2063.7	2080.8

Appendix A

Summary of Abundances, Lifetimes, Ozone Depletion Potentials (ODPs), Radiative Efficiencies (REs), Global Warming Potentials (GWPs), and Global Temperature change Potentials (GTPs)

Lead Author
J.B. Burkholder

Contributors
Ø. Hodnebrog
V.L. Orkin

Cover photo: Experimental apparatus used in fundamental kinetic and photochemical laboratory studies. Laboratory measurements provide key input to the derivation of the parameters reported in this appendix. Photo: W. von Dauster, NOAA.

Appendix A

Summary of Abundances, Lifetimes, Ozone Depletion Potentials (ODPs), Radiative Efficiencies (REs), Global Warming Potentials (GWPs), and Global Temperature change Potentials (GTPs)

CONTENTS

This page was intentionally left blank.

Appendix A

Introduction

Table A-1 in this appendix contains a compilation of atmospheric abundance, lifetime, ozone depletion potential (ODP), and radiative metrics for ozone depleting substances (ODSs), replacement compounds, and related species covered under the umbrella of the present ozone assessment. The table builds upon the metrics reported in various previous assessments from the Intergovernmental Panel on Climate Change (IPCC, 2013) and the World Meteorological Organization and United Nations – Environment (WMO, 2014).

The abundances and metrics reported in Table A-1 were evaluated based on the best available data and analysis methods as described in the table heading footnotes. Table entries have associated abundance, lifetime, ODP, and radiative metric footnotes that provide the literature source, parameters, or method used to derive the reported metric. Long- and short-lived (lifetimes <~0.5 years) source compounds are included in the table. Metrics given for short-lived species are dependent on the time and location of their emission because they do not become atmospherically well-mixed and, hence, the abundances and metrics reported are not valid for all emission scenarios.

In the absence of experimental kinetic or photochemical data for some molecules, the OH radical reactivity and UV photolysis rates were estimated using structure activity relationships (SARs), trends in reactivity and photolysis for a class of compounds, or comparison with similar molecules where experimental data are available. In the absence of experimental infrared absorption spectra, radiative efficiencies were calculated, in some cases, based on theoretically calculated spectra (e.g. for many of the hydrochlorofluorocarbons (HCFCs) included in the table).

The ODPs and global warming potentials (GWPs) given in the table may differ, in some cases, from the official metrics for controlled substances reported in the Montreal Protocol Handbook (Handbook, 2018) due to consideration of recent experimental data, methods of analysis, and/or assessment recommendations (Ammann et al., 2017; Burkholder et al., 2015; IPCC, 2013; Ko et al., 2013; WMO, 2014).

Appendix A

Summary of Abundances, Lifetimes, Ozone Depletion Potentials (ODPs), Radiative Efficiencies (REs), Global Warming Potentials (GWPs), and Global Temperature change Potentials (GTPs)

Table A-1. Atmospheric abundances, lifetimes, ozone depletion potential (ODPs), radiative efficiencies (REs), Global Warming Potentials (GWPs) for 20 and 100-year time horizons, and Global Temperature change Potentials (GTPs) for 20, 50, and 100-year time horizons. Atmospheric abundances are taken from the present Assessment as noted in the footnotes. Global, annually averaged, atmospheric lifetimes (total, arising from tropospheric OH reaction, and arising from stratospheric loss) were derived using the methods and kinetic and photochemical data described in the footnotes. The ODPs reported here are semi-empirical values or from atmospheric model calculations as cited in the compounds footnote. The radiative metrics reported here are based on a CO_2 abundance of 391 ppm (the CO_2

Industrial Designation or Chemical Name	Chemical Formula	Atmospheric Abundance (2016) [a]	WMO (2014) Total Lifetime (years) [b]	Total Lifetime (years) [c]	Tropospheric (OH Reactive loss) Lifetime (years) [d]	
Carbon dioxide	CO_2	402.9 ppm			–	
Methane	CH_4	1842 ppb	12.4	12.4	10.4	
Fossil methane #	CH_4		12.4	12.4	10.4	
Nitrous oxide	N_2O	329 ppb	121	123	–	
Hydrocarbons						
Propene	CH_2=$CHCH_3$	–	0.35 days (0.27–0.50 days)	0.4 days (0.27–0.50 days)	0.4 days (0.27–0.50 days)	
Isobutene	$(CH_3)_2C$=CH_2	–	0.20 days (0.15–0.29 days)	0.2 days (0.15–0.29 days)	0.2 days (0.15–0.29 days)	
Propane, R-290	$CH_3CH_2CH_3$	–	12.5 days (9.9–27 days)	15 days (9.9–27 days)	15 days (9.9–27 days)	
Isobutane, R-600a	$(CH_3)_2CHCH_3$	–	6.0 days (5.2–10.7 days)	7 days (5.2–10.7 days)	7 days (5.2–10.7 days)	
n-pentane	$CH_3CH_2CH_2CH_2CH_3$	–	3.4 days (2.7–6.5 days)	3 days (2.7–6.5 days)	3 days (2.7–6.5 days)	
Cyclopentane	c-$CH_2CH_2CH_2CH_2CH_2$	–	2.7 days (2.2–5.3 days)	3 days (2.2–5.3 days)	3 days (2.2–5.3 days)	
Isopentane	$(CH_3)_2CHCH_2CH_3$	–	3.4 days (2.9–6.0 days)	4 days (2.9–6.0 days)	4 days (2.9–6.0 days)	
Oxygenated Hydrocarbons						
Methyl formate	CH_3OCHO	–	66 days (60–143 days)	87 days (60–143 days)	87 days (60–143 days)	
Isopropanol	$(CH_3)_2CHOH$	–	2.0 days (1.5–2.9 days)	2 days (1.5–2.9 days)	2 days (1.5–2.9 days)	
Methylal	$CH_3OCH_2OCH_3$	–	2.2 days (1.5–2.8 days)	2 days (1.5–2.8 days)	2 days (1.5–2.8 days)	
Chlorofluorocarbons						
CFC-11	CCl_3F	230.2 ppt	52	52	–	
CFC-12	CCl_2F_2	515.9 ppt	102	102	–	
CFC-13	$CClF_3$	3.0 ppt	640	640	–	
CFC-112	CCl_2FCCl_2F	0.4 ppt	59	63.6	–	

absolute GWPs for the 20- and 100-yr time horizons are 2.495×10^{-14} and 9.171×10^{-14} W yr/(m^2 kg); the CO_2 absolute GTPs for the 20-, 50-, and 100-yr time horizons are 6.841×10^{-16}, 6.167×10^{-16}, and 5.469×10^{-16} K/kg, see Chapter 6) and are consistent with the values reported in IPCC (2013) and the last ozone assessment (WMO, 2014). Radiative efficiencies were calculated using the methods given in Hodnebrog et al. (2013) with lifetime and stratospheric temperature change adjustments applied. Climate-carbon feedbacks are included for CO_2 (see IPCC (2013) for further details). The derivation of GTP assumes a climate sensitivity of 1.06 K (W m^{-2})$^{-1}$, equivalent to a 3.9 K equilibrium temperature increase in response to a doubling of CO_2, toward the higher end of the uncertainty in climate sensitivity. For further details on the specific values used see Supplementary Material Section S8.12 and references therein in IPCC (2013).

		Stratospheric Lifetime (years) [e]	ODP [f]	Radiative Efficiency (W m^{-2} ppb^{-1}) [g]	GWP 20-yr [h]	GWP 100-yr	GTP 20-yr [i]	GTP 50-yr	GTP 100-yr	Footnotes A: Abundance L: Lifetime		O: ODP R: RE, GWP, & GTP	
			0	1.375e-5	1	1	1	1	1	A1	L1		R1
			0	3.63e-4	84	28	67	14	4	A2	L1		R1
			0	3.63e-4	85	30	68	15	6	A2	L1		R1
		123	–	3.00e-3	264	265	277	282	234	A3	L:2,3	O1	R1
		–	0	1.5e-4	<<1	<<1	<<1	<<1	<<1			O2	R2
		–	0	6.8e-5	<<1	<<1	<<1	<<1	<<1			O2	R2
		–	0	3.6e-4	<1	<1	<1	<1	<1			O2	R2
		–	0	2.5e-4	<<1	<<1	<<1	<<1	<<1		L4	O2	R2
		–	0	1.7e-4	<<1	<<1	<<1	<<1	<<1		L4	O2	R2
		–	0	1.3e-4	<<1	<<1	<<1	<<1	<<1		L4	O2	R2
		–	0	2.4e-4	<<1	<<1	<<1	<<1	<<1		L4	O2	R2
		–	0	0.045	40	11	12	1.8	1.5		L5	O2	R2
		–	0	1.4e-3	<<1	<<1	<<1	<<1	<<1			O2	R2
		–	0	4.0e-3	<<1	<<1	<<1	<<1	<<1		L6	O2	R2
		55	1.0	0.26	7,090	5,160	7,160	5,480	2,920	A4	L:2,3		R3
		103	0.73–0.81	0.32	10,800	10,300	11,300	11,000	8,590	A4	L:2,3	O:3,4	R3
		–	1.0	0.25	10,900	13,900	11,700	14,200	15,900	A4	L7	O5	R3
		65.4	0.98	0.29	5,500	4,370	5,631	4,715	2,875	A4	L:2,8	O6	R4

Industrial Designation or Chemical Name	Chemical Formula	Atmospheric Abundance (2016) [a]	WMO (2014) Total Lifetime (years) [b]	Total Lifetime (years) [c]	Tropospheric (OH Reactive loss) Lifetime (years) [d]	
CFC-112a	$CClF_2CCl_3$	0.07 ppt	51	52	–	
CFC-113	CCl_2FCClF_2	71.7 ppt	93	93	–	
CFC-113a	CCl_3CF_3	0.66 ppt	59	55	–	
CFC-114	$CClF_2CClF_2$	15 ppt	189	189	–	
CFC-114a	CCl_2FCF_3	1 ppt	~100	105	–	
CFC-115	$CClF_2CF_3$	8.5 ppt	540	540	–	
CFC-216ba	$CClF_2CClFCF_3$	38 ppq	–	135	–	
CFC-216ca	$CClF_2CF_2CClF_2$	20 ppq	–	~135	–	
(E)-R316c (*(E)*-1,2-dichlorohexafluoro-cyclobutane)	*(E)*-1,2-c-$C_4F_6Cl_2$		75	75	–	
(Z)-R316c (*(Z)*-1,2-dichlorohexafluoro-cyclobutane)	*(Z)*-1,2-c-$C_4F_6Cl_2$		114	114	–	
Hydrochlorofluorocarbons						
HCFC-21	$CHFCl_2$		1.7	1.7	1.8	
HCFC-22	CHF_2Cl	235.3 ppt	11.9	11.9	13.0	
HCFC-31	CH_2FCl	0.080 ppt	1.2	1.2	1.3	
HCFC-121	$CHCl_2CCl_2F$		–	1.11	1.17	
HCFC-121a	$CHClFCCl_3$		–	2.67	2.96	
HCFC-122	$CHCl_2CClF_2$		–	0.9	0.96	
HCFC-122a	$CHClFCCl_2F$		–	3.1	3.4	
HCFC-122b	CHF_2CCl_3		–	9.31	12.6	
HCFC-123	$CHCl_2CF_3$		1.3	1.3	1.38	
HCFC-123a	$CHClFCClF_2$		4.0	4.0	4.3	
HCFC-123b	CHF_2CCl_2F		~6	11.8	15.1	
HCFC-124	$CHClFCF_3$	1.1 ppt	5.9	5.9	6.3	
HCFC-124a	CHF_2CClF_2		~9.2	17	19	
HCFC-131	$CHCl_2CHClF$		–	0.76	0.752	
HCFC-131a	CH_2ClCCl_2F		–	2.57	2.8	
HCFC-131b	CH_2FCCl_3		–	2.33	2.55	
HCFC-132	$CHClFCHClF$		–	1.73	1.81	
HCFC-132a	$CHCl_2CHF_2$		–	1.12	1.18	
HCFC-132b	$CH_2ClCClF_2$		–	3.5	3.7	
HCFC-132c	CH_2FCCl_2F		4.3	4.1	4.5	
HCFC-133	$CHClFCHF_2$		–	3.1	3.21	
HCFC-133a	CH_2ClCF_3	0.38 ppt	4.0	4.6	4.7	
HCFC-133b	CH_2FCClF_2		–	7.2	7.71	
HCFC-141	$CH_2ClCHClF$		–	1.14	1.19	
HCFC-141a	CH_2FCHCl_2		–	0.50	0.49	

		Stratospheric Lifetime (years) [e]	ODP [f]	Radiative Efficiency ($W\ m^{-2}\ ppb^{-1}$) [g]	GWP 20-yr [h]	GWP 100-yr	GTP 20-yr [i]	GTP 50-yr	GTP 100-yr	Footnotes A: Abundance L: Lifetime		O: ODP R: RE, GWP, & GTP	
		53.8	0.86	0.26	4,770	3,455	4,823	3,690	1,970	A4	L:2,8	O6	R4
		94.5	0.81–0.82	0.30	6,560	6,080	6,830	6,510	4,860	A4	L:2,3	O:3,4	R3
		57.5	0.73	0.25	5,040	3,750	5,114	4,020	2,230	A4	L:2,8	O6	R4
		191	0.50	0.31	7,710	8,580	8,180	9,010	8,530	A4	L:2,3	O:3,4	R3
		106.7	0.72	0.29	6,960	6,670	7,287	7,175	5,650	A4	L:2,8	O6	R4
		664	0.26	0.20	5,780	7,310	6,210	7,500	8,290	A4	L:3,9	O:3,4	R3
		135	0.35							A4	L10	O7	
		~135	~0.35							A4	L10	O7	
		76	0.46	0.28	4,750	4,050	4,909	4,375	2,935		L11	O8	R5
		115	0.54	0.31	5,500	5,400	5,773	5,800	4,715		L11	O8	R5
		~35	0.036	0.15	545	150	190	26	20	A5	L:12,13	O9	R3
		161	0.024–0.034	0.21	5,310	1,780	4,230	845	265	A5	L:3,12,13	O3	R3
		~35	0.019	0.0587	230	65	77	11	9	A5	L1	O9	R6
		20	0.030	0.183	245	65	80	11	9	A5	L14	O10	R7
		27.3	0.066	0.180	580	160	235	29	22	A5	L14	O10	R7
		21	0.022	0.17	220	60	70	10	8	A5	L14	O9	R3
		34	0.067	0.21	865	235	375	44	33	A5	L14	O9	R3
		35.5	0.170	0.213	2,330	715	1,705	255	102	A5	L14	O10	R7
		31	0.01	0.15	290	80	98	14	11	A5		O11	R3
		65	0.039	0.23	1,350	370	660	72	51	A5		O9	R3
		54	0.124	0.24	3,400	1,130	2,700	530	168	A5	L14	O10	R7
		98	0.022	0.20	1,870	530	1,120	121	74	A5		O5	R3
		161	0.026	0.241	4,675	1,825	4,085	1,260	330	A5	L14	O10	R7
		20	0.019	0.101	115	30	36	5	4	A5	L14	O10	R7
		31	0.056	0.169	645	175	260	32	24	A5	L14	O10	R7
		26	0.054	0.132	460	125	175	22	17	A5	L14	O10	R7
		39	0.025	0.152	440	120	155	21	17	A5	L14	O10	R7
		24	0.020	0.131	245	65	81	12	9	A5	L14	O10	R7
		67	0.038	0.202	1,175	320	540	61	45	A5	L14	O10	R6
		41	0.062	0.17	1,155	315	570	62	44	A5		O9	R3
		68	0.017	0.173	1,010	275	435	51	38	A5	L14	O10	R7
		103	0.019	0.15	1,295	355	680	72	50	A5	L15	O9	R8
		110	0.024	0.206	2,645	765	1,740	205	108	A5	L14	O10	R7
		30	0.022	0.0772	170	45	56	8	6	A5	L14	O10	R7
		20	0.011	0.0594	55	15	17	3	2	A5	L14	O10	R7

Industrial Designation or Chemical Name	Chemical Formula	Atmospheric Abundance (2016) [a]	WMO (2014) Total Lifetime (years) [b]	Total Lifetime (years) [c]	Tropospheric (OH Reactive loss) Lifetime (years) [d]	
HCFC-141b	CH_3CCl_2F	24.4 ppt	9.4	9.4	10.7	
HCFC-142	CH_2ClCHF_2		–	2.6	2.73	
HCFC-142a	$CH_2FCHClF$		–	1.58	1.64	
HCFC-142b	CH_3CClF_2	22.2 ppt	18	18	19.3	
HCFC-151	CH_2ClCH_2F		–	0.49	0.487	
HCFC-151a	CH_3CHClF		–	1.16	1.2	
HCFC-221aa	$CHCl_2CCl_2CCl_2F$		–	0.93	0.98	
HCFC-221ab	$CHClFCCl_2CCl_3$		–	2.67	2.96	
HCFC-221ba	$CHCl_2CClFCCl_3$		–	1.11	1.17	
HCFC-221da	$CCl_3CHClCCl_2F$		–	3.29	3.71	
HCFC-221ea	$CCl_3CHFCCl_3$		–	3.52	3.99	
HCFC-222aa	$CHCl_2CCl_2CClF_2$		–	1.11	1.17	
HCFC-222ab	$CHClFCCl_2CCl_2F$		–	2.67	2.96	
HCFC-222ac	$CHF_2CCl_2CCl_3$		–	9.29	12.6	
HCFC-222ba	$CHCl_2CClFCCl_2F$		–	1.11	1.17	
HCFC-222bb	$CHClFCClFCCl_3$		–	3.15	3.54	
HCFC-222ca	$CHCl_2CF_2CCl_3$		–	1.38	1.47	
HCFC-222da	$CCl_2FCHClCCl_2F$		–	4.48	5.23	
HCFC-222db	$CCl_3CHClCClF_2$		–	4.62	5.42	
HCFC-222ea	$CCl_3CHFCCl_2F$		–	4.68	5.49	
HCFC-223aa	$CHCl_2CCl_2CF_3$		–	1.11	1.17	
HCFC-223ab	$CHClFCCl_2CClF_2$		–	3.18	3.54	
HCFC-223ac	$CHF_2CCl_2CCl_2F$		–	9.29	12.6	
HCFC-223ba	$CHCl_2CClFCClF_2$		–	1.39	1.47	
HCFC-223bb	$CHClFCClFCCl_2F$		–	3.18	3.54	
HCFC-223bc	$CHF_2CClFCCl_3$		–	10.6	15.1	
HCFC-223ca	$CHCl_2CF_2CCl_2F$		–	1.38	1.47	
HCFC-223cb	$CHClFCF_2CCl_3$		–	3.88	4.45	
HCFC-223da	$CCl_2FCHClCClF_2$		–	6.48	7.86	
HCFC-223db	$CCl_3CHClCF_3$		–	6.47	8.02	
HCFC-223ea	$CCl_2FCHFCCl_2F$		–	6.28	7.74	
HCFC-223eb	$CCl_3CHFCClF_2$		–	6.46	8.02	
HCFC-224aa	$CHClFCCl_2CF_3$		–	3.15	3.54	
HCFC-224ab	$CHF_2CCl_2CClF_2$		–	11.3	15.1	
HCFC-224ba	$CHCl_2CClFCF_3$		–	1.39	1.47	
HCFC-224bb	$CHClFCClFCClF_2$		–	4.1	4.45	

	Stratospheric Lifetime (years) [e]	ODP [f]	Radiative Efficiency ($W\ m^{-2}\ ppb^{-1}$) [g]	GWP 20-yr [h]	GWP 100-yr	GTP 20-yr [i]	GTP 50-yr	GTP 100-yr	Footnotes A: Abundance L: Lifetime		O: ODP R: RE, GWP, & GTP	
	72.3	0.069–0.102	0.16	2,590	800	1,900	285	114	A5	L:3,13	O4	R3
	60	0.019	0.110	645	175	260	32	24	A5	L14	O10	R7
	42	0.015	0.113	400	110	140	19	15	A5	L14	O10	R7
	212	0.023-0.057	0.19	5,140	2,070	4,530	1,490	390	A5	L:3,13	O4	R3
	20	0.008	0.0306	40	10	12	2	2	A5	L14	O10	R7
	33	0.015	0.0629	200	55	66	9	7	A5	L14	O10	R7
	20	0.027	0.183	140	38	46	7	5		L14	O10	R7
	27	0.069	0.181	405	110	165	20	15		L14	O10	R7
	20	0.032	0.174	160	44	53	8	6		L14	O10	R7
	29	0.083	0.243	670	180	300	34	25		L14	O10	R7
	30	0.088	0.219	640	175	295	33	24		L14	O10	R7
	20	0.028	0.224	220	60	73	10	8		L14	O10	R7
	27	0.061	0.234	560	150	225	28	21		L14	O10	R7
	35	0.191	0.221	1,620	500	1,185	175	71		L14	O10	R7
	20	0.028	0.210	210	56	68	10	8		L14	O10	R7
	29	0.071	0.199	560	150	245	28	21		L14	O10	R7
	22	0.034	0.205	250	68	86	12	10		L14	O10	R7
	31	0.097	0.283	1,120	305	580	62	43		L14	O10	R7
	31	0.100	0.265	1,080	295	570	61	41		L14	O10	R7
	31	0.101	0.245	1,010	280	535	57	39		L14	O10	R7
	20	0.024	0.195	205	56	68	10	8		L14	O10	R7
	31	0.059	0.282	855	230	375	43	32		L14	O10	R7
	35	0.164	0.289	2,265	695	1,660	245	99		L14	O10	R7
	23	0.029	0.258	340	92	116	16	13		L14	O10	R7
	31	0.059	0.235	710	195	310	36	27		L14	O10	R7
	36	0.185	0.249	2,140	680	1,640	282	99		L14	O10	R7
	22	0.029	0.234	310	83	105	15	12		L14	O10	R7
	30	0.073	0.238	875	240	420	46	33		L14	O10	R7
	37	0.111	0.313	1,850	525	1,155	129	74		L14	O10	R7
	33	0.117	0.229	1,350	385	845	94	54		L14	O10	R7
	33	0.114	0.282	1,620	460	1000	110	64		L14	O10	R7
	33	0.117	0.262	1,540	440	965	108	62		L14	O10	R7
	29	0.049	0.247	800	215	345	40	30		L14	O10	R7
	45	0.141	0.306	2,945	960	2,305	430	142		L14	O10	R7
	24	0.023	0.215	310	83	105	14	12		L14	O10	R7
	51	0.047	0.283	1,180	320	585	64	45		L14	O10	R7

Industrial Designation or Chemical Name	Chemical Formula	Atmospheric Abundance (2016) [a]	WMO (2014) Total Lifetime (years) [b]	Total Lifetime (years) [c]	Tropospheric (OH Reactive loss) Lifetime (years) [d]	
HCFC-224bc	$CHF_2CClFCCl_2F$		–	11.3	15.1	
HCFC-224ca	$CHCl_2CF_2CClF_2$		–	1.79	1.92	
HCFC-224cb	$CHClFCF_2CCl_2F$		–	1.57	1.64	
HCFC-224cc	$CHF_2CF_2CCl_3$		–	12.5	19	
HCFC-224da	$CClF_2CHClCClF_2$		–	10.4	12.3	
HCFC-224db	$CCl_2FCHClCF_3$		–	9.39	12	
HCFC-224ea	$CCl_2FCHFCClF_2$		–	9.16	11.6	
HCFC-224eb	CCl_3CHFCF_3		–	8.88	11.9	
HCFC-225aa	$CHF_2CCl_2CF_3$		–	11.8	15.1	
HCFC-225ba	$CHClFCClFCF_3$		–	4.2	4.45	
HCFC-225bb	$CHF_2CClFCClF_2$		–	15.9	19	
HCFC-225ca	$CHCl_2CF_2CF_3$		0.02 ppt	1.9	2.0	
HCFC-225cb	$CHClFCF_2CClF_2$		0.04 ppt	5.9	6.3	
HCFC-225cc	$CHF_2CF_2CCl_2F$		–	14.1	19	
HCFC-225da	$CClF_2CHClCF_3$		–	16.3	19.5	
HCFC-225ea	$CClF_2CHFCClF_2$		–	15.3	18.1	
HCFC-225eb	$CCl_2FCHFCF_3$		–	13.4	17.7	
HCFC-226ba	$CHF_2CClFCF_3$		–	17	19	
HCFC-226ca	$CHClFCF_2CF_3$		–	5.47	5.8	
HCFC-226cb	$CHF_2CF_2CClF_2$		–	21.6	24.7	
HCFC-226da	$CF_3CHClCF_3$		–	27.7	32.6	
HCFC-226ea	$CClF_2CHFCF_3$		–	24.9	28.8	
HCFC-231aa	$CHCl_2CCl_2CHClF$		–	0.799	0.839	
HCFC-231ab	$CH_2ClCCl_2CCl_2F$		–	1.61	1.73	
HCFC-231ac	$CH_2FCCl_2CCl_3$		–	2.33	2.55	
HCFC-231ba	$CHCl_2CClFCHCl_2$		–	0.56	0.586	
HCFC-231bb	$CH_2ClCClFCCl_3$		–	2.54	2.8	
HCFC-231da	$CHCl_2CHClCCl_2F$		–	0.54	0.557	
HCFC-231db	$CHClFCHClCCl_3$		–	1.34	1.43	
HCFC-231ea	$CHCl_2CHFCCl_3$		–	0.76	0.799	
HCFC-231fa	$CCl_2FCH_2CCl_3$		–	6.26	7.71	
HCFC-232aa	$CHClFCCl_2CHClF$		–	1.65	1.77	
HCFC-232ab	$CHCl_2CCl_2CHF_2$		–	1.01	1.07	
HCFC-232ac	$CH_2ClCCl_2CClF_2$		–	2.56	2.8	
HCFC-232ad	$CH_2FCCl_2CCl_2F$		–	2.33	2.55	
HCFC-232ba	$CHCl_2CClFCHClF$		–	0.99	1.04	

	Stratospheric Lifetime (years) [e]	ODP [f]	Radiative Efficiency ($W\ m^{-2}\ ppb^{-1}$) [g]	GWP 20-yr [h]	GWP 100-yr	GTP 20-yr [i]	GTP 50-yr	GTP 100-yr	Footnotes A: Abundance L: Lifetime		O: ODP R: RE, GWP, & GTP	
	45	0.141	0.308	2,965	970	2,320	430	142		L14	O10	R7
	28	0.028	0.262	480	130	173	23	18		L14	O10	R7
	35	0.022	0.248	400	108	139	19	15		L14	O10	R7
	37	0.174	0.314	3,215	1,090	2,600	550	165		L14	O10	R7
	67	0.096	0.349	3,180	1,010	2,425	410	146		L14	O10	R7
	43	0.119	0.285	2,420	745	1,780	265	107		L14	O10	R7
	43	0.117	0.312	2,600	795	1,895	275	114		L14	O10	R7
	35	0.126	0.235	1,915	580	1,380	195	83		L14	O10	R7
	54	0.094	0.264	2,820	935	2,240	440	139		L14	O10	R7
	74	0.025	0.254	1,175	320	590	65	45		L14	O10	R7
	100	0.069	0.319	4,030	1,520	3,470	985	260		L14	O10	R7
	44	0.025	0.220	470	127	170	22	18	A5	L3	O5	R3
	101	0.033	0.290	1,860	525	1,110	120	73	A5	L3	O5	R3
	55	0.110	0.344	4,080	1,455	3,410	835	230		L14	O10	R7
	100	0.071	0.302	3,860	1,475	3,340	980	255		L14	O10	R7
	99	0.068	0.340	4,210	1,560	3,590	975	260		L14	O10	R7
	55	0.105	0.287	3,310	1,155	2,725	630	180		L14	O10	R7
	161	0.019	0.267	3,790	1,480	3,310	1,020	265		L14	O10	R7
	98	0.013	0.261	1,680	465	965	105	66		L14	O10	R7
	174	0.022	0.341	5,370	2,385	4,915	1,970	540		L14	O10	R7
	185	0.025	0.251	4,315	2,210	4,105	2,075	665		L14	O10	R7
	180	0.023	0.307	5,095	2,455	4,775	2,195	650		L14	O10	R7
	20	0.022	0.128	98	27	31	5	4		L14	O10	R7
	23	0.042	0.180	280	75	98	13	10		L14	O10	R7
	26	0.058	0.156	350	94	135	17	13		L14	O10	R7
	20	0.015	0.114	62	17	19	3	2		L14	O10	R7
	27	0.063	0.163	400	108	159	20	15		L14	O10	R7
	20	0.015	0.136	70	19	22	3	3		L14	O10	R7
	21	0.036	0.144	185	50	63	9	7		L14	O10	R7
	20	0.021	0.131	96	26	30	4	4		L14	O10	R7
	33	0.143	0.213	1,230	350	755	83	49		L14	O10	R7
	245	0.036	0.177	300	82	106	14	11		L14	O10	R7
	20	0.024	0.143	150	41	49	7	6		L14	O10	R7
	29	0.053	0.222	590	160	235	29	22		L14	O10	R7
	26	0.050	0.213	515	140	198	25	19		L14	O10	R7
	20	0.023	0.162	165	45	54	8	6		L14	O10	R7

Industrial Designation or Chemical Name	Chemical Formula	Atmospheric Abundance (2016) [a]	WMO (2014) Total Lifetime (years) [b]	Total Lifetime (years) [c]	Tropospheric (OH Reactive loss) Lifetime (years) [d]	
HCFC-232bb	$CH_2ClCClFCCl_2F$		–	2.56	2.8	
HCFC-232bc	$CH_2FCClFCCl_3$		–	3.64	4.14	
HCFC-232ca	$CHCl_2CF_2CHCl_2$		–	0.70	0.737	
HCFC-232cb	$CH_2ClCF_2CCl_3$		–	4.47	5.21	
HCFC-232da	$CHCl_2CHClCClF_2$		–	0.82	0.859	
HCFC-232db	$CHClFCHClCCl_2F$		–	1.51	1.61	
HCFC-232dc	$CHF_2CHClCCl_3$		–	2.83	3.15	
HCFC-232ea	$CHCl_2CHFCCl_2F$		–	0.83	0.872	
HCFC-232eb	$CHClFCHFCCl_3$		–	2.04	2.22	
HCFC-232fa	$CCl_2FCH_2CCl_2F$		–	9.23	12.5	
HCFC-232fb	$CCl_3CH_2CClF_2$		–	10.2	14.4	
HCFC-233aa	$CHClFCCl_2CHF_2$		–	2.63	2.87	
HCFC-233ab	$CH_2ClCCl_2CF_3$		–	2.57	2.8	
HCFC-233ac	$CH_2FCCl_2CClF_2$		–	3.71	4.14	
HCFC-233ba	CHClFCClFCHClF		–	2.1	2.23	
HCFC-233bb	$CHCl_2CClFCHF_2$		–	1.27	1.34	
HCFC-233bc	$CH_2ClCClFCClF_2$		–	4.75	5.21	
HCFC-233bd	$CH_2FCClFCCl_2F$		–	3.71	4.14	
HCFC-233ca	$CHCl_2CF_2CHClF$		–	1.27	1.34	
HCFC-233cb	$CH_2ClCF_2CCl_2F$		–	4.57	5.21	
HCFC-233cc	$CH_2FCF_2CCl_3$		–	6.26	7.71	
HCFC-233da	$CHCl_2CHClCF_3$		–	0.896	0.939	
HCFC-233db	$CHClFCHClCClF_2$		–	2.37	2.52	
HCFC-233dc	$CHF_2CHClCCl_2F$		–	3.55	3.96	
HCFC-233ea	$CHCl_2CHFCClF_2$		–	0.982	1.03	
HCFC-233eb	$CHClFCHFCCl_2F$		–	2.32	2.51	
HCFC-233ec	$CHF_2CHFCCl_3$		–	4.13	4.77	
HCFC-233fa	$CCl_2FCH_2CClF_2$		–	15.4	23.3	
HCFC-233fb	$CCl_3CH_2CF_3$		–	16.4	29.3	
HCFC-234aa	$CHF_2CCl_2CHF_2$		–	6.51	7.54	
HCFC-234ab	$CH_2FCCl_2CF_3$		–	3.76	4.14	
HCFC-234ba	$CHClFCClFCHF_2$		–	3.39	3.61	
HCFC-234bb	$CH_2ClCClFCF_3$		–	4.84	5.21	
HCFC-234bc	$CH_2FCClFCClF_2$		–	7.01	7.71	
HCFC-234ca	$CHClFCF_2CHClF$		–	2.74	2.9	
HCFC-234cb	$CHCl_2CF_2CHF_2$		–	1.65	1.74	

	Stratospheric Lifetime (years) [e]	ODP [f]	Radiative Efficiency ($W\ m^{-2}\ ppb^{-1}$) [g]	GWP 20-yr [h]	GWP 100-yr	GTP 20-yr [i]	GTP 50-yr	GTP 100-yr	Footnotes A: Abundance L: Lifetime		O: ODP R: RE, GWP, & GTP	
	29	0.053	0.222	590	160	235	29	22		L14	O10	R7
	30	0.075	0.205	770	210	360	40	29		L14	O10	R7
	20	0.017	0.130	95	26	30	4	4		L14	O10	R7
	31	0.090	0.208	950	260	490	53	37		L14	O10	R7
	20	0.019	0.178	151	41	48	7	6		L14	O10	R7
	24	0.033	0.200	310	84	108	15	12		L14	O10	R7
	28	0.060	0.184	540	145	225	27	20		L14	O10	R7
	20	0.019	0.165	142	38	45	7	5		L14	O10	R7
	25	0.045	0.183	390	104	143	19	15		L14	O10	R7
	35	0.176	0.267	2,255	690	1,645	242	99		L14	O10	R7
	36	0.194	0.249	2,255	710	1,710	280	103		L14	O10	R7
	32	0.043	0.185	545	145	220	27	20		L14	O10	R7
	31	0.042	0.194	560	150	225	27	21		L14	O10	R7
	35	0.057	0.250	1,030	280	490	54	39		L14	O10	R7
	38	0.031	0.202	475	128	178	23	18		L14	O10	R7
	23	0.023	0.171	245	66	81	11	9		L14	O10	R7
	53	0.057	0.261	1,365	375	730	78	53		L14	O10	R7
	35	0.057	0.257	1,060	290	500	56	40		L14	O10	R7
	23	0.023	0.174	245	67	83	12	9		L14	O10	R7
	37	0.069	0.250	1,260	345	660	71	49		L14	O10	R7
	33	0.100	0.246	1,650	465	1,020	112	66		L14	O10	R7
	20	0.017	0.142	142	38	46	7	5		L14	O10	R7
	40	0.034	0.238	630	170	245	31	24		L14	O10	R7
	35	0.055	0.245	970	265	445	50	37		L14	O10	R7
	20	0.019	0.183	200	54	65	9	8		L14	O10	R7
	30	0.038	0.221	575	155	220	28	22		L14	O10	R7
	31	0.068	0.236	1,080	295	540	58	41		L14	O10	R7
	46	0.207	0.321	4,020	1,495	3,435	940	250		L14	O10	R7
	37	0.247	0.204	2,635	1,010	2,285	675	175		L14	O10	R7
	47	0.062	0.198	1,500	425	940	105	60		L14	O10	R7
	41	0.039	0.215	980	265	465	51	37		L14	O10	R7
	57	0.028	0.215	885	240	400	45	34		L14	O10	R7
	67	0.035	0.218	1,265	350	680	73	49		L14	O10	R7
	77	0.045	0.279	2,245	645	1,455	170	91		L14	O10	R7
	51	0.025	0.205	685	185	280	34	26		L14	O10	R7
	29	0.020	0.199	400	110	141	19	15		L14	O10	R7

Industrial Designation or Chemical Name	Chemical Formula	Atmospheric Abundance (2016) [a]	WMO (2014) Total Lifetime (years) [b]	Total Lifetime (years) [c]	Tropospheric (OH Reactive loss) Lifetime (years) [d]	
HCFC-234cc	$CH_2ClCF_2CClF_2$		–	9.46	10.6	
HCFC-234cd	$CH_2FCF_2CCl_2F$		–	6.64	7.71	
HCFC-234da	$CHClFCHClCF_3$		–	2.67	2.82	
HCFC-234db	$CHF_2CHClCClF_2$		–	5.69	6.18	
HCFC-234ea	$CHCl_2CHFCF_3$		–	1.06	1.11	
HCFC-234eb	$CHClFCHFCClF_2$		–	2.88	3.04	
HCFC-234ec	$CHF_2CHFCCl_2F$		–	5.32	6.04	
HCFC-234fa	$CClF_2CH_2CClF_2$		–	31	43.4	
HCFC-234fb	$CCl_2FCH_2CF_3$		~45	45	98	
HCFC-235ba	$CHF_2CClFCHF_2$		–	8.8	9.5	
HCFC-235bb	$CH_2FCClFCF_3$		–	7.21	7.71	
HCFC-235ca	$CH_2ClCF_2CF_3$		–	9.82	10.6	
HCFC-235cb	$CHClFCF_2CHF_2$		–	4.45	4.7	
HCFC-235cc	$CH_2FCF_2CClF_2$		–	14.2	15.7	
HCFC-235da	$CHF_2CHClCF_3$		–	7.55	8.09	
HCFC-235ea	$CHClFCHFCF_3$		–	7.36	7.88	
HCFC-235eb	$CHF_2CHFCClF_2$		–	3.18	3.33	
HCFC-235fa	$CClF_2CH_2CF_3$		–	61.7	88.6	
HCFC-241aa	CH_2ClCCl_2CHClF		–	1.43	1.52	
HCFC-241ab	$CH_2FCCl_2CHCl_2$		–	0.77	0.803	
HCFC-241ac	$CH_3CCl_2CCl_2F$		–	5.18	6.18	
HCFC-241ba	$CH_2ClCClFCHCl_2$		–	0.79	0.826	
HCFC-241bb	$CH_3CClFCCl_3$		–	7.76	10	
HCFC-241da	$CHCl_2CHClCHClF$		–	0.56	0.581	
HCFC-241db	$CH_2ClCHClCCl_2F$		–	0.53	0.549	
HCFC-241dc	$CH_2FCHClCCl_3$		–	0.75	0.786	
HCFC-241ea	$CHCl_2CHFCHCl_2$		–	0.42	0.429	
HCFC-241eb	$CH_2ClCHFCCl_3$		–	1.05	1.11	
HCFC-241fa	$CHCl_2CH_2CCl_2F$		–	0.53	0.555	
HCFC-241fb	$CHClFCH_2CCl_3$		–	1.48	1.59	
HCFC-242aa	$CHF_2CCl_2CH_2Cl$		–	2.13	2.29	
HCFC-242ab	CH_2FCCl_2CHClF		–	1.78	1.91	
HCFC-242ac	$CH_3CCl_2CClF_2$		–	8.09	10	
HCFC-242ba	$CHClFCClFCH_2Cl$		–	1.99	2.11	
HCFC-242bb	$CHCl_2CClFCH_2F$		–	1.03	1.09	
HCFC-242bc	$CH_3CClFCCl_2F$		–	8.09	10	

	Stratospheric Lifetime (years) [e]	ODP [f]	Radiative Efficiency ($W\ m^{-2}\ ppb^{-1}$) [g]	GWP 20-yr [h]	GWP 100-yr	GTP 20-yr [i]	GTP 50-yr	GTP 100-yr	Footnotes A: Abundance L: Lifetime		O: ODP R: RE, GWP, & GTP	
	85	0.054	0.267	2,705	835	1,990	300	120		L14	O10	R7
	48	0.063	0.281	2,160	615	1,370	155	87		L14	O10	R7
	50	0.024	0.203	660	180	268	33	25		L14	O10	R7
	72	0.039	0.271	1,820	510	1,070	115	71		L14	O10	R7
	23	0.014	0.158	205	55	67	10	8		L14	O10	R7
	52	0.026	0.241	845	230	355	42	32		L14	O10	R7
	45	0.052	0.276	1,745	485	990	105	68		L14	O10	R7
	108	0.132	0.347	6,225	3,405	6,005	3,330	1,170		L14	O10	R7
	58	0.40	0.264	5,190	3,490	5,190	3,685	1,760			O9	R7
	121	0.018	0.225	2,375	715	1,700	238	102		L14	O10	R7
	110	0.017	0.237	2,140	620	1,410	167	87		L14	O10	R7
	126	0.018	0.215	2,455	765	1,830	288	110		L14	O10	R7
	85	0.014	0.234	1,375	375	710	76	53		L14	O10	R7
	146	0.021	0.282	4,040	1,450	3,385	840	230		L14	O10	R7
	112	0.017	0.227	2,130	620	1,430	175	88		L14	O10	R7
	111	0.017	0.227	2,085	605	1,385	165	86		L14	O10	R7
	69	0.012	0.274	1,160	315	510	59	44		L14	O10	R7
	204	0.051	0.297	6,780	5,320	6,930	5,730	3,430		L14	O10	R7
	24	0.035	0.116	187	51	64	9	7		L14	O10	R7
	20	0.020	0.0937	81	22	25	4	3		L14	O10	R7
	32	0.112	0.191	1,090	300	610	65	42		L14	O10	R7
	20	0.020	0.121	108	29	34	5	4		L14	O10	R7
	34	0.163	0.191	1,545	450	1,050	131	64		L14	O10	R7
	20	0.014	0.100	63	17	19	3	2		L14	O10	R7
	20	0.014	0.119	71	19	22	3	3		L14	O10	R7
	20	0.019	0.115	97	26	31	5	4		L14	O10	R7
	20	0.011	0.081	38	10	12	2	1		L14	O10	R7
	20	0.027	0.125	147	40	48	7	6		L14	O10	R7
	20	0.014	0.117	70	19	22	3	3		L14	O10	R7
	22	0.037	0.152	255	69	87	12	10		L14	O10	R7
	29	0.039	0.131	340	93	129	17	13		L14	O10	R7
	27	0.034	0.132	290	78	103	14	11		L14	O10	R7
	42	0.125	0.227	2,065	610	1,430	185	87		L14	O10	R7
	37	0.033	0.151	370	100	135	18	14		L14	O10	R7
	21	0.021	0.133	168	46	55	8	6		L14	O10	R7
	42	0.125	0.244	2,220	655	1,535	199	93		L14	O10	R7

Industrial Designation or Chemical Name	Chemical Formula	Atmospheric Abundance (2016) [a]	WMO (2014) Total Lifetime (years) [b]	Total Lifetime (years) [c]	Tropospheric (OH Reactive loss) Lifetime (years) [d]	
HCFC-242ca	$CHCl_2CF_2CH_2Cl$		–	1.09	1.15	
HCFC-242cb	$CH_3CF_2CCl_3$		–	12.3	18.7	
HCFC-242da	$CHClFCHClCHClF$		–	1.32	1.38	
HCFC-242db	$CHCl_2CHClCHF_2$		–	0.73	0.761	
HCFC-242dc	$CH_2ClCHClCClF_2$		–	1.2	1.25	
HCFC-242dd	$CH_2FCHClCCl_2F$		–	0.83	0.871	
HCFC-242ea	$CHCl_2CHFCHClF$		–	0.72	0.756	
HCFC-242eb	$CH_2ClCHFCCl_2F$		–	1.24	1.31	
HCFC-242ec	$CH_2FCHFCCl_3$		–	1.7	1.84	
HCFC-242fa	$CHCl_2CH_2CClF_2$		–	0.74	0.768	
HCFC-242fb	$CHClFCH_2CCl_2F$		–	1.61	1.71	
HCFC-242fc	$CHF_2CH_2CCl_3$		–	4.14	4.78	
HCFC-243aa	$CHF_2CCl_2CH_2F$		–	2.99	3.25	
HCFC-243ab	$CH_3CCl_2CF_3$		–	8.33	10	
HCFC-243ba	$CHF_2CClFCH_2Cl$		–	3.63	3.88	
HCFC-243bb	$CHFClCClFCH_2F$		–	2.67	2.82	
HCFC-243bc	$CH_3CClFCF_2Cl$		–	15.6	18.7	
HCFC-243ca	CH_2ClCF_2CHClF		–	2.89	3.14	
HCFC-243cb	$CHCl_2CF_2CH_2F$		–	1.46	1.54	
HCFC-243cc	$CH_3CF_2CFCl_2$		19.5	18	27.1	
HCFC-243da	$CHF_2CHClCHFCl$		–	1.97	2.07	
HCFC-243db	$CH_2ClCHClCF_3$		–	1.44	1.51	
HCFC-243dc	$CH_2FCHClCF_2Cl$		–	2.03	2.13	
HCFC-243ea	$CHFClCHFCHFCl$		–	1.57	1.64	
HCFC-243eb	$CHCl_2CHFCHF_2$		–	0.90	0.938	
HCFC-243ec	$CH_2ClCHFCF_2Cl$		–	1.7	1.78	
HCFC-243ed	$CH_2FCHFCFCl_2$		–	2.03	2.17	
HCFC-243fa	$CHCl_2CH_2CF_3$		–	0.78	0.813	
HCFC-243fb	$CHFClCH_2CF_2Cl$		–	2.24	2.36	
HCFC-243fc	$CHF_2CH_2CFCl_2$		–	5.07	5.73	
HCFC-244ba	$CH_2FCClFCHF_2$		–	5.17	5.49	
HCFC-244bb	$CH_3CClFCF_3$		–	16.6	18.7	
HCFC-244ca	$CH_2ClCF_2CHF_2$		–	6.39	6.82	
HCFC-244cb	CH_2FCF_2CHFCl		–	4.02	4.24	
HCFC-244cc	$CH_3CF_2CF_2Cl$		–	31.2	38.1	
HCFC-244da	$CHF_2CHClCHF_2$		–	3.88	4.09	

	Stratospheric Lifetime (years) [e]	ODP [f]	Radiative Efficiency ($W\ m^{-2}\ ppb^{-1}$) [g]	GWP 20-yr [h]	GWP 100-yr	GTP 20-yr [i]	GTP 50-yr	GTP 100-yr	Footnotes			
									A: Abundance L: Lifetime		O: ODP R: RE, GWP, & GTP	
	22	0.022	0.144	193	52	63	9	7		L14	O10	R7
	36	0.206	0.251	3,045	1,025	2,450	510	154		L14	O10	R7
	29	0.024	0.147	238	64	80	11	9		L14	O10	R7
	20	0.015	0.119	106	29	33	5	4		L14	O10	R7
	28	0.023	0.170	250	68	83	12	9		L14	O10	R7
	20	0.017	0.159	162	44	52	8	6		L14	O10	R7
	20	0.015	0.119	106	29	33	5	4		L14	O10	R7
	23	0.025	0.167	255	69	85	12	10		L14	O10	R7
	24	0.034	0.174	365	98	129	17	14		L14	O10	R7
	20	0.015	0.153	138	37	43	6	5		L14	O10	R7
	26	0.031	0.203	400	109	140	19	15		L14	O10	R7
	31	0.075	0.198	1000	270	500	54	38		L14	O10	R7
	37	0.036	0.154	620	168	265	31	23		L14	O10	R7
	49	0.085	0.205	2,095	625	1,465	195	89		L14	O10	R7
	58	0.033	0.146	710	195	330	37	27		L14	O10	R7
	50	0.027	0.161	580	157	235	29	22		L14	O10	R7
	94	0.088	0.264	4,010	1,500	3,440	955	252		L14	O10	R7
	37	0.035	0.182	710	192	295	35	27		L14	O10	R7
	27	0.020	0.147	290	78	99	14	11		L14	O10	R7
	54	0.19	0.315	5,130	2,060	4,540	1,495	390			O9	R6
	42	0.022	0.162	430	116	158	21	16		L14	O10	R7
	34	0.018	0.138	270	73	92	13	10		L14	O10	R7
	43	0.023	0.203	555	150	206	27	21		L14	O10	R7
	36	0.019	0.172	365	99	127	17	14		L14	O10	R7
	21	0.014	0.141	170	46	55	8	6		L14	O10	R7
	38	0.020	0.182	420	113	148	20	16		L14	O10	R7
	32	0.026	0.215	590	159	218	28	22		L14	O10	R7
	20	0.012	0.120	125	34	40	6	5		L14	O10	R7
	45	0.024	0.231	700	189	265	34	26		L14	O10	R7
	44.0	0.056	0.263	1,765	490	975	104	68		L14	O10	R7
	90	0.017	0.173	1,310	360	730	78	51		L14	O10	R7
	148	0.027	0.238	4,140	1,600	3,600	1,080	280		L14	O10	R7
	101	0.018	0.173	1,580	450	985	109	63		L14	O10	R7
	79	0.015	0.178	1,065	290	520	57	41		L14	O10	R7
	173	0.039	0.277	6,120	3,360	5,905	3,290	1,160		L14	O10	R7
	77	0.015	0.182	1,050	285	505	56	40		L14	O10	R7

Industrial Designation or Chemical Name	Chemical Formula	Atmospheric Abundance (2016) [a]	WMO (2014) Total Lifetime (years) [b]	Total Lifetime (years) [c]	Tropospheric (OH Reactive loss) Lifetime (years) [d]	
HCFC-244db	$CH_2FCHClCF_3$		–	2.44	2.54	
HCFC-244ea	$CHF_2CHFCHFCl$		–	2.39	2.5	
HCFC-244eb	$CH_2ClCHFCF_3$		–	2.04	2.12	
HCFC-244ec	$CH_2FCHFCF_2Cl$		–	2.88	3.01	
HCFC-244fa	$CHFClCH_2CF_3$		–	2.37	2.48	
HCFC-244fb	$CHF_2CH_2CF_2Cl$		–	7.76	8.35	
HCFC-251aa	$CH_2FCCl_2CH_2Cl$		–	1.26	1.34	
HCFC-251ab	CH_3CCl_2CHFCl		–	1.73	1.85	
HCFC-251ba	$CH_2ClCClFCH_2Cl$		–	1.34	1.4	
HCFC-251bb	$CH_3CClFCHCl_2$		–	1.02	1.07	
HCFC-251da	$CH_2ClCHClCHFCl$		–	0.69	0.719	
HCFC-251db	$CH_2FCHClCHCl_2$		–	0.40	0.416	
HCFC-251dc	$CH_3CHClCFCl_2$		–	0.52	0.535	
HCFC-251ea	$CH_2ClCHFCHCl_2$		–	0.47	0.489	
HCFC-251eb	$CH_3CHFCCl_3$		–	0.68	0.709	
HCFC-251fa	$CHClFCH_2CCl_2H$		–	0.33	0.339	
HCFC-251fb	$CH_2ClCH_2CCl_2F$		–	0.45	0.467	
HCFC-251fc	$CH_2FCH_2CCl_3$		–	0.65	0.676	
HCFC-252aa	$CH_2FCCl_2CH_2F$		–	1.94	2.07	
HCFC-252ab	$CH_3CCl_2CHF_2$		–	4.41	4.93	
HCFC-252ba	$CH_2ClCClFCH_2F$		–	2.19	2.31	
HCFC-252bb	$CH_3CClFCHClF$		–	2.87	3.04	
HCFC-252ca	$CH_2ClCF_2CH_2Cl$		–	2.47	2.61	
HCFC-252cb	$CH_3CF_2CHCl_2$		–	1.19	1.25	
HCFC-252da	$CH_2ClCHClCHF_2$		–	1.0	1.04	
HCFC-252db	$CH_2FCHClCHClF$		–	1.15	1.2	
HCFC-252dc	$CH_3CHClCClF_2$		–	0.77	0.799	
HCFC-252ea	$CH_2ClCHFCHClF$		–	1.02	1.06	
HCFC-252eb	$CH_2FCHFCHCl_2$		–	0.65	0.67	
HCFC-252ec	$CH_3CHFCCl_2F$		–	0.84	0.882	
HCFC-252fa	$CHClFCH_2CHClF$		–	1.15	1.19	
HCFC-252fb	$CHCl_2CH_2CHF_2$		–	0.66	0.684	
HCFC-252fc	$CH_2ClCH_2CClF_2$		–	0.94	0.972	
HCFC-252fd	$CH_2FCH_2CCl_2F$		–	0.70	0.732	
HCFC-253ba	$CH_2FCClFCH_2F$		–	3.66	3.86	
HCFC-253bb	$CH_3CClFCHF_2$		–	7.85	8.46	

	Stratospheric Lifetime (years) [e]	ODP [f]	Radiative Efficiency ($W\ m^{-2}\ ppb^{-1}$) [g]	GWP 20-yr [h]	GWP 100-yr	GTP 20-yr [i]	GTP 50-yr	GTP 100-yr	Footnotes			
									A: Abundance L: Lifetime		O: ODP R: RE, GWP, & GTP	
	57	0.012	0.164	600	162	235	29	23		L14	O10	R7
	57	0.012	0.191	685	185	267	33	26		L14	O10	R7
	51	0.011	0.151	460	125	170	22	17		L14	O10	R7
	64	0.013	0.226	975	265	410	49	37		L14	O10	R7
	56	0.012	0.185	655	178	255	32	25		L14	O10	R7
	111	0.020	0.285	3,060	900	2,080	260	127		L14	O10	R7
	23	0.028	0.0752	129	35	43	6	5		L14	O10	R7
	27	0.037	0.110	260	70	93	12	10		L14	O10	R7
	29	0.027	0.0951	173	47	59	8	7		L14	O10	R7
	21	0.023	0.109	151	41	49	7	6		L14	O10	R7
	20	0.016	0.0821	77	21	24	4	3		L14	O10	R7
	20	0.009	0.0631	35	9	11	2	1		L14	O10	R7
	20	0.012	0.122	85	23	26	4	3		L14	O10	R7
	20	0.011	0.0776	50	14	15	2	2		L14	O10	R7
	20	0.016	0.134	124	34	39	6	5		L14	O10	R7
	20	0.008	0.0739	33	9	10	2	1		L14	O10	R7
	20	0.011	0.107	66	18	20	3	2		L14	O10	R7
	20	0.015	0.103	91	25	28	4	3		L14	O10	R7
	31	0.029	0.105	310	83	113	15	12		L14	O10	R7
	42	0.056	0.153	1,010	275	520	56	39		L14	O10	R7
	44	0.027	0.0992	330	89	125	16	12		L14	O10	R7
	51	0.032	0.147	640	173	265	32	24		L14	O10	R7
	47	0.029	0.126	470	127	186	23	18		L14	O10	R7
	24	0.019	0.146	265	71	87	12	10		L14	O10	R7
	27	0.016	0.0897	135	37	44	6	5		L14	O10	R7
	29	0.017	0.101	176	48	58	8	7		L14	O10	R7
	22	0.013	0.149	174	47	55	8	7		L14	O10	R7
	27	0.016	0.112	173	47	57	8	7		L14	O10	R7
	20	0.011	0.0922	90	24	28	4	3		L14	O10	R7
	20	0.015	0.175	223	60	71	10	8		L14	O10	R7
	29	0.017	0.143	250	67	82	12	9		L14	O10	R7
	20	0.011	0.114	113	31	35	5	4		L14	O10	R7
	25	0.015	0.153	217	59	70	10	8		L14	O10	R7
	20	0.012	0.155	164	45	52	8	6		L14	O10	R7
	73	0.017	0.131	810	221	380	42	31		L14	O10	R7
	108	0.024	0.184	2,260	665	1,545	195	94		L14	O10	R7

Industrial Designation or Chemical Name	Chemical Formula	Atmospheric Abundance (2016) [a]	WMO (2014) Total Lifetime (years) [b]	Total Lifetime (years) [c]	Tropospheric (OH Reactive loss) Lifetime (years) [d]	
HCFC-253ca	$CH_2ClCF_2CH_2F$		–	4.23	4.47	
HCFC-253cb	CH_3CF_2CHClF		–	3.48	3.66	
HCFC-253da	$CH_2FCHClCHF_2$		–	1.67	1.74	
HCFC-253db	$CH_3CHClCF_3$		–	1.02	1.06	
HCFC-253ea	$CH_2ClCHFCHF_2$		–	1.44	1.5	
HCFC-253eb	$CH_2FCHFCHClF$		–	1.5	1.56	
HCFC-253ec	$CH_3CHFCClF_2$		–	1.13	1.17	
HCFC-253fa	$CHClFCH_2CHF_2$		–	1.83	1.9	
HCFC-253fb	$CH_2ClCH_2CF_3$		–	1.05	1.09	
HCFC-253fc	$CH_2FCH_2CClF_2$		–	1.48	1.54	
HCFC-261aa	$CH_3CCl_2CH_2F$		–	1.06	1.11	
HCFC-261ba	$CH_3CClFCH_2Cl$		–	2.19	2.31	
HCFC-261da	$CH_2ClCHClCH_2F$		–	0.45	0.462	
HCFC-261db	$CH_3CHClCHClF$		–	0.47	0.478	
HCFC-261ea	$CH_2ClCHFCH_2Cl$		–	0.54	0.554	
HCFC-261eb	$CH_3CHFCHCl_2$		–	0.31	0.315	
HCFC-261fa	CH_2ClCH_2CHClF		–	0.57	0.591	
HCFC-261fb	$CH_2FCH_2CHCl_2$		–	0.33	0.339	
HCFC-261fc	$CH_3CH_2CCl_2F$		–	0.61	0.638	
HCFC-262ba	$CH_3CClFCH_2F$		–	3.4	3.59	
HCFC-262ca	$CH_3CF_2CH_2Cl$		–	3.2	3.33	
HCFC-262da	$CH_2FCHClCH_2F$		–	0.92	0.956	
HCFC-262db	$CH_3CHClCHF_2$		–	0.64	0.662	
HCFC-262ea	$CH_2FCHFCH_2Cl$		–	0.83	0.856	
HCFC-262eb	$CH_3CHFCHFCl$		–	0.66	0.685	
HCFC-262fa	$CH_2ClCH_2CHF_2$		–	0.80	0.828	
HCFC-262fb	CH_2FCH_2CHFCl		–	0.87	0.902	
HCFC-262fc	$CH_3CH_2CF_2Cl$		–	1.2	1.24	
HCFC-271ba	$CH_3CClFCH_3$		–	5.0	5.37	
HCFC-271da	$CH_3CHClCH_2F$		–	0.27	0.278	
HCFC-271ea	CH_3CHFCH_2Cl		–	0.30	0.302	
HCFC-271fa	$CH_2ClCH_2CH_2F$		–	0.34	0.345	
HCFC-271fb	CH_3CH_2CHClF		–	0.49	0.506	
Hydrofluorocarbons						
HFC-23	CHF_3	28.9 ppt	228	228	243	
HFC-32	CH_2F_2	10 ppt	5.4	5.4	5.5	

	Stratospheric Lifetime (years) [e]	ODP [f]	Radiative Efficiency ($W\ m^{-2}\ ppb^{-1}$) [g]	GWP 20-yr [h]	GWP 100-yr	GTP 20-yr [i]	GTP 50-yr	GTP 100-yr	Footnotes A: Abundance L: Lifetime		O: ODP R: RE, GWP, & GTP	
	79	0.018	0.135	960	265	485	52	37		L14	O10	R7
	71	0.017	0.183	1,080	295	490	56	41		L14	O10	R7
	44	0.012	0.118	335	91	118	16	13		L14	O10	R7
	30	0.009	0.120	208	56	68	10	8		L14	O10	R7
	39	0.011	0.113	275	75	95	13	10		L14	O10	R7
	40	0.011	0.125	320	86	110	15	12		L14	O10	R7
	33	0.009	0.183	350	95	116	16	13		L14	O10	R7
	46	0.012	0.175	545	147	196	26	20		L14	O10	R7
	31	0.009	0.121	215	58	70	10	8		L14	O10	R7
	40	0.011	0.194	490	132	168	23	18		L14	O10	R7
	23	0.020	0.0727	132	36	43	6	5		L14	O10	R7
	44	0.031	0.0827	310	84	118	15	12		L14	O10	R7
	20	0.009	0.0338	26	7	8	1	1		L14	O10	R7
	20	0.009	0.0625	50	14	15	2	2		L14	O10	R7
	20	0.010	0.0493	45	12	14	2	2		L14	O10	R7
	20	0.006	0.0618	33	9	10	2	1		L14	O10	R7
	20	0.011	0.0746	73	20	23	3	3		L14	O10	R7
	20	0.006	0.0557	32	9	10	1	1		L14	O10	R7
	20	0.012	0.137	145	39	45	7	5		L14	O10	R7
	69	0.020	0.125	835	227	380	43	32		L14	O10	R7
	66	0.019	0.117	730	197	320	37	27		L14	O10	R7
	28	0.009	0.0587	107	29	34	5	4		L14	O10	R7
	21	0.007	0.0813	103	28	32	5	4		L14	O10	R7
	25	0.009	0.0657	107	29	34	5	4		L14	O10	R7
	21	0.007	0.0982	128	35	40	6	5		L14	O10	R7
	25	0.008	0.0858	135	37	43	6	5		L14	O10	R7
	26	0.009	0.0991	170	46	54	8	6		L14	O10	R7
	34	0.011	0.168	395	107	131	18	15		L14	O10	R7
	83	0.028	0.106	1,225	340	675	72	47		L14	O10	R7
	20	0.004	0.0261	17	5	5	1	1		L14	O10	R7
	20	0.004	0.0330	23	6	7	1	1		L14	O10	R7
	20	0.004	0.0284	22	6	7	1	1		L14	O10	R7
	20	0.007	0.0652	75	20	23	3	3		L14	O10	R7
	4420	0	0.18	11,085	12,690	11,825	13,340	13,150	A6	L3		R3
	124	0	0.11	2,530	705	1,440	154	98	A6	L3		R3

Industrial Designation or Chemical Name	Chemical Formula	Atmospheric Abundance (2016) [a]	WMO (2014) Total Lifetime (years) [b]	Total Lifetime (years) [c]	Tropospheric (OH Reactive loss) Lifetime (years) [d]	
HFC-41	CH_3F		2.8	2.8	2.9	
HFC-125	CHF_2CF_3	20.4 ppt	31	30	32	
HFC-134	CHF_2CHF_2		9.7	10	10.5	
HFC-134a	CH_2FCF_3	90 ppt	14	14	14.1	
HFC-143	CH_2FCHF_2		3.5	3.6	3.70	
HFC-143a	CH_3CF_3	19.1 ppt	51	51	57	
HFC-152	CH_2FCH_2F		146 days (114-335 days)	172 days (114-335 days)	172 days (114-335 days)	
HFC-152a	CH_3CHF_2	6.7 ppt	1.6	1.6	1.55	
HFC-161	CH_3CH_2F		66 days (51–154 days)	80 days (51–154 days)	80 days (51–154 days)	
HFC-227ca	$CF_3CF_2CHF_2$		28.2	30	32	
HFC-227ea	CF_3CHFCF_3	1.2 ppt	36	36	37.5	
HFC-236cb	$CH_2FCF_2CF_3$		~13	13.4	14	
HFC-236ea	CHF_2CHFCF_3		11.0	11.4	11.9	
HFC-236fa	$CF_3CH_2CF_3$	0.15 ppt	222	213	253	
HFC-245ca	$CH_2FCF_2CHF_2$		6.5	6.6	6.9	
HFC-245cb	$CF_3CF_2CH_3$		47.1	39.9	43	
HFC-245ea	$CHF_2CHFCHF_2$		3.2	3.2	3.3	
HFC-245eb	$CH_2FCHFCF_3$		3.2	3.2	3.3	
HFC-245fa	$CHF_2CH_2CF_3$	2.4 ppt	7.9	7.9	8.2	
HFC-263fb	$CH_3CH_2CF_3$		1.1	1.1	1.16	
HFC-272ca	$CH_3CF_2CH_3$		2.6	9	9.7	
HFC-281ea	CH_3CHFCH_3		23 days (19–46 days)	27 days (19–46 days)	27 days (19–46 days)	
HFC-329p	$CHF_2CF_2CF_2CF_3$		~30	32	34	
HFC-338pcc	$CHF_2CF_2CF_2CHF_2$		12.9	13.5	14.0	
HFC-356mcf	$CH_2FCH_2CF_2CF_3$		1.2	1.2	1.26	
HFC-356mff	$CF_3CH_2CH_2CF_3$		8.3	8.5	8.9	
HFC-365mfc	$CH_3CF_2CH_2CF_3$	0.94 ppt	8.7	8.9	9.3	
HFC-43-10mee	$CF_3CHFCHFCF_2CF_3$	0.27 ppt	16.1	17.0	17.9	
HFC-458mfcf	$CF_3CH_2CF_2CH_2CF_3$		22.9	23.8	25.5	
HFC-55-10mcff	$CF_3CF_2CH_2CH_2CF_2CF_3$		7.5	7.7	8.0	
HFC-52-13p	$CHF_2CF_2CF_2CF_2CF_2CF_3$		32.7	35.2	37.0	
HFC-72-17p	$CHF_2CF_2CF_2CF_2CF_2CF_2$-$CF_2CF_3$		–	23.8	24.9	
Unsaturated Hydrofluorocarbons						
HFO-1123	$CHF=CF_2$		–	1.4 days	1.4 days	

		Stratospheric Lifetime (years) [e]	ODP [f]	Radiative Efficiency ($W\ m^{-2}\ ppb^{-1}$) [g]	GWP 20-yr [h]	GWP 100-yr	GTP 20-yr [i]	GTP 50-yr	GTP 100-yr	Footnotes A: Abundance L: Lifetime		O: ODP R: RE, GWP, & GTP	
		65	0	0.02	430	116	177	21	16		L:12,13		R3
		595	0	0.23	6,280	3,450	6,040	3,350	1180	A6	L:3,13		R3
		240	0	0.19	3,625	1,135	2,725	440	164				R3
		267	0	0.16	3,810	1,360	3,170	770	215	A6	L:3,13		R3
		100	0	0.13	1,250	340	580	64	48				R3
		612	0	0.16	7,050	5,080	7,110	5,390	2,830	A6	L3		R3
		–	0	0.04	64	17	20	3.0	2.4				R3
		39	0	0.10	545	148	190	26	21	A6	L:3,13		R3
		–	0	0.02	20	6	6	<1	<1				R3
		640	0	0.27	5,260	2,865	5,070	2,795	975		L16		R3
		673	0	0.26	5,250	3,140	5,140	3,180	1,260	A6	L:3,17		R3
		305	0	0.23	3,540	1,235	2,915	670	192				R3
		270	0	0.30	4,190	1,370	3,290	620	202				R3
		1350	0	0.24	6,785	7,680	7,230	8,090	7,870				R3
		165	0	0.24	2,530	720	1,600	180	102				R3
		550	0	0.24	6,340	4,000	6,280	4,150	1,800				R3
		95	0	0.16	860	233	375	44	32				R3
		90	0	0.20	1,070	290	460	54	40				R3
		149	0	0.24	2,980	880	2,040	260	124	A6	L3		R3
		40	0	0.10	250	68	83	12	9.5				R3
		185	0	0.07	1,580	480	1,140	163	69		L18		R3
		–	0	–	–	–	–	–	–	A6			R9
		675	0	0.31	4,720	2,630	4,565	2,595	935		L19		R3
		360	0	–	–	–	–	–	–				R9
		40	0	–	–	–	–	–	–				R9
		190	0	–	–	–	–	–	–				R9
		190	0	0.22	2,660	810	1,915	271	115	A6			R3
		365	0	0.359	3,770	1,470	3,295	1,015	265	A6			R10
		375	0	–	–	–	–	–	–				R9
		175	0	–	–	–	–	–	–				R9
		710	0	–	–	–	–	–	–		L20		R9
		525	0	–	–	–	–	–	–		L21		R9
		–	0	0.0019	<1	<<1	<<1	<<1	<<1		L22		R11

Industrial Designation or Chemical Name	Chemical Formula	Atmospheric Abundance (2016) [a]	WMO (2014) Total Lifetime (years) [b]	Total Lifetime (years) [c]	Tropospheric (OH Reactive loss) Lifetime (years) [d]	
HFO-1132a	$CH_2=CF_2$		4.0 days (3–5.7 days)	4.6 days (3–5.7 days)	4.6 days (3–5.7 days)	
HFO-1141	$CH_2=CHF$		2.1 days (1.4–3.1 days)	2.5 days (1.4–3.1 days)	2.5 days (1.4–3.1 days)	
HFO-1234ye*(E)*	*(E)*-$CHF=CFCHF_2$		<5 days	<5 days	<5 days	
HFO-1234ye*(Z)*	*(Z)*-$CHF=CFCHF_2$		<5 days	<5 days	<5 days	
HFO-1225ye*(E)*	*(E)*-$CF_3CF=CHF$		4.9 days (3.7–6.9 days)	5.7 days (3.7–6.9 days)	5.7 days (3.7–6.9 days)	
HFO-1225ye*(Z)*	*(Z)*-$CF_3CF=CHF$		8.5 days (6.2–12 days)	10 days (6.2–12 days)	10 days (6.2–12 days)	
2,3,3,4,4-pentafluorocyclobut-1-ene	c-$CH=CFCF_2CF_2$-		–	270 days	270 days	
HFO-1234ze*(E)*	*(E)*-$CF_3CH=CHF$		16.4 days (12.8–24 days)	19 days (12.8–24 days)	19 days (12.8–24 days)	
HFO-1234ze*(Z)*	*(Z)*-$CF_3CH=CHF$		10.0 days	10.0 days	10.0 days	
3,3,4,4-tetrafluorocyclobut-1-ene	c-$CH=CHCF_2CF_2$-		–	84 days	84 days	
HFO-1234yf	$CF_3CF=CH_2$		10.5 days (8.4–16 days)	12 days (8.4–16 days)	12 days (8.4–16 days)	
HFO-1261zf	$CH_2FCH=CH_2$		0.7 days (0.5–1.0 days)	0.8 days (0.5–1.0 days)	0.8 days (0.5–1.0 days)	
HFO-1234yc	$CF_2=CFCH_2F$		~2 days	~2 days	~2 days	
HFO-1225zc	$CF_2=CHCF_3$		~2 days	~2 days	~2 days	
HFO-1234zc	$CF_2=CHCHF_2$		<5 days	<5 days	<5 days	
HFO-1336mzz*(E)*	*(E)*-$CF_3CH=CHCF_3$		– (~16–30 days)	122 days	122 days	
HFO-1336mzz*(Z)*	*(Z)*-$CF_3CH=CHCF_3$		22 days (16.3–32 days)	27 days (16.3–32 days)	27 days (16.3–32 days)	
HFO-1243zf	$CF_3CH=CH_2$		7.0 days (5.5–11 days)	9 days (5.5–11 days)	9 days (5.5–11 days)	
HFO-1345zf	$C_2F_5CH=CH_2$		7.6 days (5.8–11.4 days)	9 days (5.8–11.4 days)	9 days (5.8–11.4 days)	
HFO-1438mzz*(E)*	*(E)*-$CF_3CH=CHCF_2CF_3$		– (16–30 days)	122 days	122 days	
HFO-1447zf	$CH_2=CHCF_2CF_2CF_3$		– (6–10 days)	9 days (6–10 days)	9 days (6–10 days)	
3,3,4,4,5,5,6,6,6-Nonafluorohex-1-ene	$C_4F_9CH=CH_2$		7.6 days	9 days	9 days	
3,3,4,4,5,5,6,6,7,7,8,8,8-Tridecafluorooct-1-ene HFO-174-13fz	$C_6F_{13}CH=CH_2$		7.6 days	9 days	9 days	
3,3,4,4,5,5,6,6,7,7,8,8,9,9,10,10,10-Heptadecafluorodec-1-ene HFO-194-17fz	$C_8F_{17}CH=CH_2$		7.6 days	9 days	9 days	
HFO-1438ezy*(E)*	*(E)*-$(CF_3)_2CFCH=CHF$		–	43 days	43 days	
Chlorocarbons and Hydrochlorocarbons						
Methyl chloroform	CH_3CCl_3	2.6 ppt	5.0	5.0	6.1	
Carbon tetrachloride	CCl_4	80.5 ppt	26.0	32	–	
Methyl chloride	CH_3Cl	555 ppt	0.9	0.9	1.57	

	Stratospheric Lifetime (years) [e]	ODP [f]	Radiative Efficiency ($W\ m^{-2}\ ppb^{-1}$) [g]	GWP 20-yr [h]	GWP 100-yr	GTP 20-yr [i]	GTP 50-yr	GTP 100-yr	Footnotes A: Abundance L: Lifetime		O: ODP R: RE, GWP, & GTP	
	–	0	0.004	<1	<1	<1	<1	<1				R3
	–	0	0.002	<1	<1	<1	<1	<1				R3
	–	0	–	–	–	–	–	–		L23		R9
	–	0	–	–	–	–	–	–		L23		R9
	–	0	0.01	<1	<1	<1	<1	<1				R3
	–	0	0.02	<1	<1	<1	<1	<1				R3
	–	0	0.20	236	64	74	11	8.8		L24		R12
	–	0	0.04	4	<1	<1	<1	<1				R3
	–	0	0.02	1	<1	<1	<1	<1		L21		R3
	–	0	0.10	40.6	11	12	1.8	1.5		L24		R12
	–	0	0.02	1	<1	<1	<1	<1	A7			R3
	–	0	–	–	–	–	–	–				R9
	–	0	–	–	–	–	–	–		L23		R9
	–	0	–	–	–	–	–	–		L23		R9
	–	0	–	–	–	–	–	–		L23		R9
	–	0	0.13	60	16	18	2.7	2.2		L25		R13
	–	0	0.07	6	2	2	<1	<1				R3
	–	0	0.01	<1	<1	<1	<1	<1				R3
	–	0	0.01	<1	<1	<1	<1	<1				R3
	–	0	–	–	–	–	–	–		L26		R9
	–	0	–	–	–	–	–	–				R9
	–	0	0.03	<1	<1	<1	<1	<1		L27		R3
	–	0	0.03	<1	<1	<1	<1	<1		L27		R3
	–	0	0.03	<1	<1	<1	<1	<1		L27		R3
	–	0	0.34	42	11	12	1.9	1.6		L28		R14
	38	0.14–0.17	0.07	555	153	300	32	21	A8	L:3,13	O3	R3
	44	0.89	0.174	3,790	2,110	3,670	2,080	750	A8	L:13,29	O3	R15
	30.4	0.015	0.004	16	4.3	5.1	<1	<1	A8	L:3,13,30	O3	R15

Industrial Designation or Chemical Name	Chemical Formula	Atmospheric Abundance (2016) [a]	WMO (2014) Total Lifetime (years) [b]	Total Lifetime (years) [c]	Tropospheric (OH Reactive loss) Lifetime (years) [d]	
Methylene chloride	CH_2Cl_2	34 ppt	144 days (95–1070 days)	180 days (95–1070 days)	180 days (95–1070 days)	
Chloroform	$CHCl_3$	8.9 ppt	149 days (97–1145 days)	183 days (97–1145 days)	183 days (97–1145 days)	
1,2-Dichloroethane	CH_2ClCH_2Cl	12.8 ppt (10.4–18.3)	65.0 days (41–555 days)	82 days (41–555 days)	82 days (41–555 days)	
Chloroethane	CH_3CH_2Cl		39 days (26–280 days)	48 days (26–280 days)	48 days (26–280 days)	
1-Chloropropane	$CH_3CH_2CH_2Cl$		14 days (10–80 days)	16 days (10–80 days)	16 days (10–80 days)	
2-Chloropropane	$CH_3CHClCH_3$		18 days (13–95 days)	22 days (13–95 days)	22 days (13–95 days)	
Unsaturated Hydrochlorocarbons and Chlorocarbon						
Chloroethene (vinyl chloride)	CH_2=CHCl		1.5 days (0.9–2.2 days)	1.7 days (0.9–2.2 days)	1.7 days (0.9–2.2 days)	
1,2-dichloroethene	CH_2=CCl_2		0.9 days (0.5–1.3 days)	1 days (0.5–1.3 days)	1 days (0.5–1.3 days)	
(E)-1,2-dichloroethene	*(E)*-CClH=CClH		– (3.2–6.7 days)	5.5 days (3.2–6.7 days)	5.5 days (3.2–6.7 days)	
(Z)-1,2-dichloroethene	*(Z)*-CClH=CClH		– (3.2–6.7 days)	5.2 days (3.2–6.7 days)	5.2 days (3.2–6.7 days)	
Trichloroethene	CHCl=CCl_2	0.3 ppt	4.9 days (3.3–7.1 days)	5.6 days (3.3–7.1 days)	5.6 days (3.3–7.1 days)	
Perchloroethene	CCl_2=CCl_2	1.5 ppt	90 days (66–245 days)	110 days (66–245 days)	110 days (66–245 days)	
Unsaturated Chlorofluorocarbons and Hydrochlorofluorocarbons						
CFO-1113 Chlorotrifluoroethene	CF_2=CFCl		1.4 days (0.8–2.1 days)	1.5 days (0.8–2.1 days)	1.5 days (0.8–2.1 days)	
HCFO-1233zd*(E)*	*(E)*-CF_3CH=CHCl		26 days (21–39 days)	42.5 days (34–64 days)	42.5 days (34–64 days)	
HCFO-1233zd*(Z)*	*(Z)*-CF_3CH=CHCl		– ~(20–40) days	13 days	13 days	
HCFO-1233xf (2-chloro-3,3,3-fluoro-1-propene)	CF_3CCl=CH_2		– ~(20–40) days	42.5 days (34–64 days)	42.5 days (34–64 days)	
CFO-1215yc (3-chloro-1,1,2,3,3-fluoro-1-propene)	CF_2=$CFCF_2Cl$		~5 days ~(3–7 days)	~5 days ~(3–7 days)	~5 days ~(3–7 days)	
CFO-1316yff (4,4-dichloro-1,1,2,3,3,4-fluoro-1-butene)	CF_2=$CFCF_2CFCl_2$		~5 days ~(3–7 days)	~5 days ~(3–7 days)	~5 days ~(3–7 days)	
Bromocarbons, Hydrobromocarbons and Halons						
Methyl bromide	CH_3Br	6.8 ppt	0.8	0.8	1.8	
Methylene bromide	CH_2Br_2	0.9 ppt (0.6–1.7)	123 days (80–890 days)	150 days (80–890 days)	150 days (80–890 days)	
Bromoform	$CHBr_3$	1.2 ppt (0.4–4.0)	24 days (15–88 days)	16 days (8–23 days)	57 days (15–88 days)	
Halon-1201	$CHBrF_2$		5.2	4.9	5.7	
Halon-1202	CBr_2F_2	0.01 ppt	2.9	2.5	–	
Halon-1211	$CBrClF_2$	3.6 ppt	16.0	16	–	
Halon-1301	$CBrF_3$	3.3 ppt	65.0	72	–	

	Stratospheric Lifetime (years) [e]	ODP [f]	Radiative Efficiency ($W\ m^{-2}\ ppb^{-1}$) [g]	GWP 20-yr [h]	GWP 100-yr	GTP 20-yr [i]	GTP 50-yr	GTP 100-yr	Footnotes A: Abundance L: Lifetime		O: ODP R: RE, GWP, & GTP	
	–	–	0.028	37	10	11	1.7	1.4	A8			R15
	–	–	0.07	66	18	20	3.0	2.2	A8			R15
	–	–	0.01	5.1	1.4	1.5	<1	<1	A8			R3
	–	–	0.004	1.8	<1	<1	<1	<1				R2
	–	–	–	–	–	–	–	–				R9
	–	–	0.005	0.9	<1	<1	<1	<1				R2
	–	–	8.8e-4	<1	<<1	<<1	<<1	<<1				R2
	–	–	1.17e-3	<<1	<<1	<<1	<<1	<<1				R2
	–	<0.0003	–	–	–	–	–	–			O12	R9
	–	<0.0003	2.95e-4	<<1	<<1	<<1	<<1	<<1			O12	R2
	–	<0.004	5.74e-3	<1	<1	<1	<<1	<<1	A9		O12	R2
	–	–	0.053	21.7	5.9	6.5	1.0	0.8	A9			R2
	–	–	–	–	–	–	–	–				R9
	–	<0.0004	0.067	13.5	3.7	4.0	0.6	0.5			O12	R16
	–	<0.0004	0.025	1.5	0.4	0.45	0.07	0.06			O12	R16
	–	–	–	–	–	–	–	–		L31		R9
	–	–	–	–	–	–	–	–		L32		R9
	–	–	–	–	–	–	–	–		L32		R9
	26.3	0.57	0.004	7.6	2	2.4	<1	<1	A9	L:3,13	O3	R3
	–	3–4	0.01	5.3	1.4	1.6	<1	<1	A9	L2	O12	R3
	–	1–5	0.003	<1	<1	<1	<<1	<<1	A9	L2	O12	R9
	35		0.15	1,240	340	675	72	48		L33		R3
	36	1.7	0.27	720	196	285	35	27	A9	L:2,3	O3	R3
	41	6.9–7.7	0.29	4,590	1,750	3,950	1,130	300	A9	L:2,3	O3	R3
	73.5	15.2–19.0	0.30	7,930	6,670	8,160	7,160	4,700	A9	L:2,3	O3	R3

Industrial Designation or Chemical Name	Chemical Formula	Atmospheric Abundance (2016) [a]	WMO (2014) Total Lifetime (years) [b]	Total Lifetime (years) [c]	Tropospheric (OH Reactive loss) Lifetime (years) [d]	
Bromochloromethane	CH_2BrCl	0.10 ppt (0.07–0.12)	137 days (89–1050 days)	165 days (89–1050 days)	165 days (89–1050 days)	
Bromodichloromethane	$CHBrCl_2$	0.3 ppt (0.1–0.9)	78 days (38–250 days)	66 days (38–250 days)	95 days (56–460 days)	
Dibromochloromethane	$CHBr_2Cl$	0.3 ppt (0.1–0.8)	59 days (28–225 days)	59 days (28–225 days)	71 days (45–325 days)	
bromoethane	CH_3CH_2Br		41 days (28–260 days)	50 days (30–260 days)	50 days (30–260 days)	
1,2-dibromoethane	CH_2BrCH_2Br		70 days (44–590 days)	89 days (44–590 days)	89 days (44–590 days)	
n-bromopropane	$CH_3CH_2CH_2Br$		12.8 days (9–65 days)	15 days (9–65 days)	15 days (9–65 days)	
Iso-bromopropane	$CH_3CHBrCH_3$		16.7 days (12–88 days)	20 days (12–88 days)	20 days (12–88 days)	
Halon-2301	CH_2BrCF_3		3.4	3.2	3.2	
Halon-2311 / Halothane	$CHBrClCF_3$	0.010 ppt	1.0	1.0	1.1	
Halon-2401	$CHFBrCF_3$		2.9	2.9	3.1	
Halon-2402 isomer	CF_3CFBr_2		–	2.5	–	
Halon-2402	$CBrF_2CBrF_2$	0.42 ppt	20.0	28	–	
Unsaturated Bromofluorocarbons						
Bromothrifluoroethene	$CFBr=CF_2$		1.4 days (0.9–2.0 days)	1.6 days (0.9–2.0 days)	1.6 days (0.9–2.0 days)	
1-Bromo-2,2-fluoroethene	$CHBr=CF_2$		2.3 days (1.5–3.4 days)	2.7 days (1.5–3.4 days)	2.7 days (1.5–3.4 days)	
2-Bromo-3,3,3-fluoro-1-propene	$CH_2=CBrCF_3$		2.7 days (1.8–3.9 days)	3.2 days (1.8–3.9 days)	3.2 days (1.8–3.9 days)	
2-bromo-3,3,4,4,4-fluoro-1-butene	$CH_2=CBrCF_2CF_3$		3.1 days (2.0–4.6 days)	3.7 days (2.0–4.6 days)	3.7 days (2.0–4.6 days)	
4-bromo-3,3,4,4-fluoro-1-butene	$CH_2=CHCF_2CF_2Br$		6.5 days (4.7–9.5 days)	7.5 days (4.7–9.5 days)	7.5 days (4.7–9.5 days)	
Unsaturated Bromochlorofluorocarbons						
4-bromo-3-chloro-3,4,4-trifluoro-1-butene	$CH_2=CHCClFCBrF_2$		–	4.5 days	4.5 days	
Fully Fluorinated Species						
Nitrogen trifluoride	NF_3	1.5 ppt	500.0	569	–	
Perfluorotriethylamine	$N(C_2F_5)_3$		–	>1000	–	
Perfluorotripropylamine	$N(C_3F_7)_3$		–	>1000	–	
Perfluorotributylamine	$N(C_4F_9)_3$		–	>1000	–	
Perfluorotripentylamine	$N(C_5F_{11})_3$		–	>1000	–	
Sulphur hexafluoride	SF_6	8.9 ppt	3,200.0	3,200	–	
(Trifluoromethyl)sulfur pentafluoride	SF_5CF_3	0.153 ppt	800.0	650–950	–	
PFC-14 (Perfluoromethane)	CF_4	82.7 ppt	50,000.0	50,000	–	
PFC-116 (Perfluoroethane)	C_2F_6	4.6 ppt	10,000.0	10,000	–	

	Stratospheric Lifetime (years) [e]	ODP [f]	Radiative Efficiency ($W\ m^{-2}\ ppb^{-1}$) [g]	GWP 20-yr [h]	GWP 100-yr	GTP 20-yr [i]	GTP 50-yr	GTP 100-yr	Footnotes A: Abundance L: Lifetime		O: ODP R: RE, GWP, & GTP	
	–	–	0.022	17	4.7	5.2	0.8	0.6	A9			R2
	–	–	–	–	–	–	–	–	A9	L2		R9
	–	–	–	–	–	–	–	–	A9	L2		R9
	–	<0.46	0.0060	1.7	0.5	0.5	<1	<1			O12	R2
	–	–	0.012	3.7	1.0	1.1	0.17	0.14				R2
	–	<0.17	0.002	0.2	<1	<1	<<1	<<1			O12	R2
	–	–	0.004	0.4	0.1	0.1	<1	<1				R2
	–	–	0.14	620	167	270	31	23				R3
	20	~1.6	0.13	151	41	49	7	6	A9		O13	R3
	45	–	0.19	675	184	285	34	25		L33		R3
	–	–	–	–	–	–	–	–		L34		R9
	41	15.7	0.31	3,920	2,030	3,730	1,900	615	A9	L:3,13	O3	R3
	–	–	–	–	–	–	–	–			O14	R9
	–	–	–	–	–	–	–	–			O14	R9
	–	<0.05	–	–	–	–	–	–			O12	R9
	–	–	–	–	–	–	–	–			O14	R9
	–	–	–	–	–	–	–	–			O14	R9
	–	–	0.0135	<1	<1	<1	<<1	<<1		L35	O14	R17
	740	0	0.20	12,460	15,750	13,420	16,250	18,035	A10	L:3,36		R3
	–	0	0.68	8,150	10,610	8,800	10,880	12,500		L37		R18
	–	0	0.82	7,055	9,180	7,620	9,410	10,815		L37		R18
	–	0	0.97	6,470	8,420	6,980	8,630	9,910	A10	L37		R18
	–	0	1.07	5,780	7,520	6,240	7,710	8,860		L37		R18
	–	0	0.57	17,500	23,500	18,900	23,800	28,200	A10	L7		R3
	–	0	0.59	13,500	17,400	14,500	17,800	20,200	A10	L38		R3
	–	0	0.09	4,880	6,630	5,270	6,690	8,040	A10	L7		R3
	–	0	0.25	8,210	11,100	8,880	11,200	13,500	A10	L7		R3

Industrial Designation or Chemical Name	Chemical Formula	Atmospheric Abundance (2016) [a]	WMO (2014) Total Lifetime (years) [b]	Total Lifetime (years) [c]	Tropospheric (OH Reactive loss) Lifetime (years) [d]	
PFC-c216 (Perfluorocyclopropane)	c-C_3F_6		3,000.0	3,000	–	
PFC-218 (Perfluoropropane)	C_3F_8	0.63 ppt	2,600.0	2,600	–	
PFC-c316 (Perfluorocyclobutene)	c-C_4F_6		–	1.2	1.2	
PFC-c318 (Perfluorocyclobutane)	c-C_4F_8	1.44 ppt	3,200.0	3,200	–	
PFC-31-10 (Perfluorobutane)	n-C_4F_{10}		2,600.0	2,600	–	
PFC-c418 (Perfluorocyclopentene)	c-C_5F_8		31.0 days	1.1	1.1	
PFC-41-12 (Perfluoropentane)	n-C_5F_{12}	0.148 ppt	4,100.0	4,100	–	
PFC-51-14 (Perfluorohexane)	n-C_6F_{14}		3,100.0	3,100	–	
PFC-61-16 (Perfluoroheptane)	n-C_7F_{16}		3,000.0	3,000	–	
PFC-71-18 (Perfluorooctane)	n-C_8F_{18}		3,000.0	3,000	–	
PFC-91-18 (isomer mixture)	$C_{10}F_{18}$		2,000.0	2,000	–	
PFC-c91-18*(Z)* (Perfluorodecalin*(Z)*)	*(Z)*-$C_{10}F_{18}$		2,000.0	2,000	–	
PFC-c91-18*(E)* (Perfluorodecalin*(E)*)	*(E)*-$C_{10}F_{18}$		2,000.0	2,000	–	
PFC-1114	$CF_2=CF_2$		1.1 days (0.7–1.6 days)	1.2 days (0.7–1.6 days)	1.2 days (0.7–1.6 days)	
PFC-1216	$CF_3CF=CF_2$		4.9 days (3.3–7.1 days)	5.5 days (3.3–7.1 days)	5.5 days (3.3–7.1 days)	
Perfluorobuta-1,3-diene	$CF_2=CFCF=CF_2$		1.1 days	1.1 days	1.1 days	
Perfluorobut-1-ene	$CF_3CF_2CF=CF_2$		6.0 days	6 days	6 days	
Perfluorobut-2-ene (71% *(E)* and 29% *(Z)* isomer blend)	$CF_3CF=CFCF_3$		31.0 days	31 days	31 days	
(E)-Perfluoro-2-butene	*(E)*-$CF_3CF=CFCF_3$		–	22 days	22 days	
(Z)-Perfluoro-2-butene	*(Z)*-$CF_3CF=CFCF_3$		–	35 days	35 days	
Perfluoro(2-methyl-2-pentene)	$(CF_3)_2C=CFCF_2CF_3$		–	192 days	192 days	
Halogenated Ethers						
HFE-125	CHF_2OCF_3		119.0	135	147	
HFE-134 (HG-00)	CHF_2OCHF_2		25.4	26.9	28.4	
HFE-143a	CH_3OCF_3		4.8	4.9	5.05	
HFE-152a	CH_3OCHF_2		–	1.8	1.85	
HFE-227ea	$CF_3CHFOCF_3$		46.7	54.8	58	
HCFE-235ca2 (enflurane)	CHF_2OCF_2CHFCl		4.3	4.42	4.62	
HCFE-235da2 (isoflurane)	$CHF_2OCHClCF_3$	0.11 ppt	3.5	3.5	3.7	
HFE-236ca	$CHF_2OCF_2CHF_2$		20.8	22.0	23.1	
HFE-236ea2 (desflurane)	$CHF_2OCHFCF_3$	3.2 ppt	10.8	14.1	14.8	
HFE-236fa	$CF_3CH_2OCF_3$		~7.5	~7.5	~8	
HFE-245cb2	$CF_3CF_2OCH_3$		5.0	5.0	5.24	
HFE-245fa1	$CHF_2CH_2OCF_3$		6.6	~6.7	~7	

		Stratospheric Lifetime (years) [e]	ODP [f]	Radiative Efficiency ($W\ m^{-2}\ ppb^{-1}$) [g]	GWP 20-yr [h]	GWP 100-yr	GTP 20-yr [i]	GTP 50-yr	GTP 100-yr	Footnotes A: Abundance L: Lifetime		O: ODP R: RE, GWP, & GTP	
		–	0	0.23	6,850	9,200	7,400	9,310	11,000	A10	L39		R19
		–	0	0.28	6,640	8,900	7,180	9,010	10,700	A10	L39		R3
		–	0	0.25	425	115	141	20	16		L24		R12
		–	0	0.32	7,110	9,540	7,680	9,660	11,500	A10	L7		R3
		–	0	0.36	6,870	9,200	7,420	9,320	11,000	A10	L39		R3
		–	0	0.28	322	87	106	15	12		L40		R20
		–	0	0.41	6,350	8,550	6,860	8,650	10,300	A10	L7		R3
		–	0	0.44	5,890	7,910	6,370	8,010	9,490	A10	L7		R3
		–	0	0.50	5,830	7,820	6,290	7,920	9,380	A10	L39		R3
		–	0	0.55	5,680	7,620	6,130	7,710	9,140	A10	L39		R3
		–	0	0.55	5,390	7,190	5,820	7,290	8,570		L39		R3
		–	0	0.56	5,430	7,240	5,860	7,340	8,630		L39		R3
		–	0	0.48	4,720	6,290	5,090	6,380	7,500		L39		R3
		–	0	0.002	<1	<1	<1	<1	<1				R3
		–	0	0.01	<1	<1	<1	<1	<1				R3
		–	0	0.003	<1	<1	<1	<1	<1				R3
		–	0	0.02	<1	<1	<1	<1	<1		L41		R3
		–	0	0.07	6	2	2	<1	<1				R3
		–	0	0.068	5	1.3	1.4	<1	<1				R3
		–	0	–	–	–	–	–	–				R9
		–	0	–	–	–	–	–	–				R9
		1665	0	0.41	12,615	12,980	13,315	13,860	11,960				R3
		500	0	0.44	11,840	5,965	11,215	5,530	1,735				R3
		130	0	0.18	1,950	540	1,060	113	75				R3
		56	0	–	–	–	–	–	–				R9
		968	0	0.44	8,920	6,630	9,060	7,110	3,930				R3
		100	0.04	0.41	2,190	600	1,125	121	84			O13	R3
		86	0.03	0.42	1,800	490	820	93	68	A11		O13	R3
		436	0	0.56	9,855	4,420	9,050	3,700	1,020				R19
		316	0	0.45	6,440	2,300	5,385	1,320	365	A11		O13	R3
		196	0	0.36	3,350	980	2,240	273	138		L42		R3
		134	0	0.33	2,360	655	1,280	136	91				R3
		168	0	0.31	2,960	845	1,880	214	119		L43		R3

Industrial Designation or Chemical Name	Chemical Formula	Atmospheric Abundance (2016) [a]	WMO (2014) Total Lifetime (years) [b]	Total Lifetime (years) [c]	Tropospheric (OH Reactive loss) Lifetime (years) [d]	
HFE-245fa2	$CHF_2OCH_2CF_3$		5.5	5.5	5.8	
HFE-254cb1	$CH_3OCF_2CHF_2$		2.5	2.5	2.62	
HFE-254eb2	$CH_3OCHFCF_3$		88 days (69–200 days)	110 days (69–200 days)	110 days (69–200 days)	
HFE-263fb2	$CF_3CH_2OCH_3$		23 days (19–47 days)	28 days (19–47 days)	28 days (19–47 days)	
HFE-263m1	$CF_3OCH_2CH_3$		0.4	~145 days	~145 days	
HFE-329mcc2	$CHF_2CF_2OCF_2CF_3$		~25	~25	~25	
HFE-338mmz1	$(CF_3)_2CHOCHF_2$		21.2	22.3	23.5	
HFE-338mcf2	$CF_3CH_2OCF_2CF_3$		~7.5	~7.5	~8	
HFE-347mmz1 (Sevoflurane)	$(CF_3)_2CHOCH_2F$	0.16 ppt	~2	1.9	1.96	
HFE-347mcc3 (HFE-7000)	$CH_3OCF_2CF_2CF_3$		5.0	5.1	5.3	
HFE-347mcf2	$CHF_2CH_2OCF_2CF_3$		~6.6	~6.7	~7	
HFE-347pcf2	$CHF_2CF_2OCH_2CF_3$		5.9	6.1	6.3	
HFE-347mmy1	$(CF_3)_2CFOCH_3$		3.7	3.7	3.8	
HFE-347mcf	$CHF_2OCH_2CF_2CF_3$		5.6	5.8	6.0	
HFE-356mec3	$CH_3OCF_2CHFCF_3$		~3	2.5	2.62	
HFE-356mff2	$CF_3CH_2OCH_2CF_3$		105 days (79–270 days)	128 days (79–270 days)	128 days (79–270 days)	
HFE-356pcf2	$CHF_2CH_2OCF_2CHF_2$		~6	~6	~6	
HFE-356pcf3	$CHF_2OCH_2CF_2CHF_2$		3.5	3.5	3.7	
HFE-356pcc3	$CH_3OCF_2CF_2CHF_2$		~3	2.5	2.62	
HFE-356mmz1	$(CF_3)_2CHOCH_3$		61 days (49–128 days)	65 days (49–128 days)	65 days (49–128 days)	
HFE-365mcf3	$CF_3CF_2CH_2OCH_3$		19.3 days (17–42 days)	25 days (17–42 days)	25 days (17–42 days)	
HFE-365mcf2	$CF_3CF_2OCH_2CH_3$		0.6	219 days	219 days	
HFE-374pc2	$CHF_2CF_2OCH_2CH_3$		64 days (49–128 days)	76 days (49–128 days)	76 days (49–128 days)	
HFE-43-10pccc124 (H-Galden 1040x, HG-11)	$CHF_2OCF_2OC_2F_4OCHF_2$		13.5	14.1	14.7	
HFE-449s1 (HFE-7100)	$C_4F_9OCH_3$		4.7	4.8	5.0	
n-HFE-7100	*n*-$C_4F_9OCH_3$		4.7	4.8	5.0	
i-HFE-7100	*i*-$C_4F_9OCH_3$		4.7	4.8	5.0	
HFE-54-11mecf	$CF_3CHFCF_2OCH_2CF_2CF_3$		8.8	9.1	9.5	
HFE-569sf2 (HFE-7200, isomer mix)	$C_4F_9OC_2H_5$		~0.8	0.8	0.8	
n-HFE-7200	*n*-$C_4F_9OC_2H_5$		0.8	0.8	0.8	
i-HFE-7200	*i*-$C_4F_9OC_2H_5$		0.8	0.63	0.65	
HFE-236ca12 (HG-10)	$CHF_2OCF_2OCHF_2$		25.0	26.5	28.0	
HFE-338pcc13 (HG-01)	$CHF_2OCF_2CF_2OCHF_2$		12.9	13.4	14.0	

	Stratospheric Lifetime (years) [e]	ODP [f]	Radiative Efficiency ($W\ m^{-2}\ ppb^{-1}$) [g]	GWP 20-yr [h]	GWP 100-yr	GTP 20-yr [i]	GTP 50-yr	GTP 100-yr	Footnotes A: Abundance L: Lifetime		O: ODP R: RE, GWP, & GTP	
	145	0	0.36	2,910	810	1,670	179	114				R3
	74	0	0.26	1,110	300	440	54	42				R3
	–	0	–	–	–	–	–	–				R9
	–	0	0.04	6	1.6	1.8	<1	<1		L44		R3
	–	0	0.13	102	28	31	4.7	3.8		L45		R3
	580	0	0.53	6,960	3,360	6,520	3,010	895		L46		R3
	440	0	0.44	6,000	2,715	5,525	2,290	635				R3
	196	0	0.44	3,180	930	2,120	259	131		L47		R3
	46	0	0.32	685	185	250	33	26	A11		O13	R3
	135	0	0.35	1,970	545	1,090	116	76				R3
	168	0	0.42	3,010	860	1,910	215	121				R3
	155	0	0.48	3,170	890	1,930	211	126				R3
	104	0	0.32	1,330	365	625	69	51				R3
	150	0	–	–	–	–	–	–				R9
	74	0	0.30	930	250	370	46	35		L48		R3
	–	0	0.17	74	20	22	3.4	2.8				R3
	145	0	0.37	2,650	745	1,595	174	105		L49		R3
	97	0	0.38	1,640	445	750	84	62				R3
	74	0	0.32	990	270	390	48	37		L48		R3
	–	0	0.15	33	8.9	9.8	1.5	1.2		L35		R3
	–	0	0.05	4.7	1.3	1.4	<1	<1		L50		R3
	–	0	0.26	215	58	66	10	8		L51		R19
	–	0	0.30	97	26	29	4.4	3.6				R3
	315	0	1.02	8,180	2,920	6,835	1,680	464				R3
	128	0	0.36	1,530	420	825	88	59				R3
	128	0	0.42	1,790	490	960	102	69				R3
	128	0	0.35	1,490	410	800	85	57				R3
	212	0	–	–	–	–	–	–		L52		R9
	27	0	0.30	210	57	66	10	8		L53		R3
	27	0	0.35	235	65	75	11	9		L53		R19
	22	0	0.24	129	35	40	5.9	4.8		L53		R3
	500	0	0.65	11,165	5,575	10,550	5,140	1,591		L54		R3
	304	0	0.86	8,595	3,000	7,085	1,630	466				R3

Industrial Designation or Chemical Name	Chemical Formula	Atmospheric Abundance (2016) [a]	WMO (2014) Total Lifetime (years) [b]	Total Lifetime (years) [c]	Tropospheric (OH Reactive loss) Lifetime (years) [d]	
HG-02 (1,1′-Oxybis[2-(difluoromethoxy)-1,1,2,2-tetrafluoroethane)	$HF_2C(OCF_2CF_2)_2OCF_2H$		26	26.9	28.4	
HG-03 (1,1,3,3,4,4,6,6,7,7,9,9,10,10,12,12-Hexadecafluoro-2,5,8,11-tetraoxadodecane)	$HF_2C(OCF_2CF_2)_3OCF_2H$		26	26.9	28.4	
HG-04(1,1,3,3,4,4,6,6,7,7,9,9,10,10,12,12,13,13,15,15-Eicosafluoro-2,5,8,11,14-pentaoxapentadecane)	$HCF_2O(CF_2CF_2O)_4CF_2H$		26	26.9	28.4	
HG-20	$HF_2C(OCF_2)_2OCF_2H$		25.0	26.5	28.0	
HG-21	$HF_2COCF_2CF_2OCF_2OCF_2O-CF_2H$		13.5	13.4	14.0	
HG-30	$HF_2C(OCF_2)_3OCF_2H$		25.0	26.5	28.0	
1-Ethoxy-1,1,2,2,3,3,3-heptafluoropropane	$CF_3CF_2CF_2OCH_2CH_3$		0.8	0.75	0.77	
Fluoroxene	$CF_3CH_2OCH=CH_2$		3.6 days	3.6 days	3.6 days	
1,1,2,2-Tetrafluoro-1-(fluoromethoxy) ethane	$CH_2FOCF_2CF_2H$		6.2	6.2	6.5	
2-Ethoxy-3,3,4,4,5-pentafluorotetrahydro-2,5-bis[1,2,2,2-tetrafluoro-1-(trifluoromethyl)ethyl]-furan	$C_{12}H_5F_{19}O_2$		1.0	0.81	0.83	
Fluoro(methoxy)methane	CH_3OCH_2F		73.0 days	73 days	73 days	
Difluoro(methoxy)methane	CH_3OCHF_2		1.1	1.1	1.1	
Fluoro(fluoromethoxy)methane	CH_2FOCH_2F		0.9	0.9	0.9	
Difluoro(fluoromethoxy)methane	CH_2FOCHF_2		3.3	3.2	3.3	
Trifluoro(fluoromethoxy)methane	CH_2FOCF_3		4.4	4.2	4.4	
HG′-01	$CH_3OCF_2CF_2OCH_3$		2.0	1.7	1.74	
HG′-02	$CH_3O(CF_2CF_2O)_2CH_3$		2.0	1.7	1.74	
HG′-03	$CH_3O(CF_2CF_2O)_3CH_3$		2.0	1.7	1.74	
HFE-329me3	$CF_3CFHCF_2OCF_3$		40.0	33.6	35.3	
2-Chloro-1,1,2-trifluoro-1-methoxyethane	CH_3OCF_2CHFCl		1.4	1.43	1.49	
PFPMIE (perfluoropolymethylisopropyl ether)	$CF_3OCF(CF_3)CF_2OCF_2OCF_3$		800.0	800	–	
HFE-216	$CF_3OCF=CF_2$		8.4 days	1.6 days	1.6 days	
Fluoroesters						
Trifluoromethyl formate	$HC(O)OCF_3$		<3.5	<3.5	3.7	
Perfluoroethyl formate	$HC(O)OCF_2CF_3$		<3.5	<3.6	3.7	
Perfluoropropyl formate	$HC(O)OCF_2CF_2CF_3$		<2.6	<2.6	2.7	
Perfluorobutyl formate	$HC(O)OCF_2CF_2CF_2CF_3$		3.0	<2.6	2.7	
2,2,2-Trifluoroethyl formate	$HC(O)OCH_2CF_3$		0.4	200 days	204 days	
3,3,3-Trifluoropropyl formate	$HC(O)OCH_2CH_2CF_3$		0.3	99 days	110 days	
1,2,2,2-Tetrafluoroethyl formate	$HC(O)OCHFCF_3$		3.2	3.1	3.2	

	Stratospheric Lifetime (years) [e]	ODP [f]	Radiative Efficiency ($W\ m^{-2}\ ppb^{-1}$) [g]	GWP 20-yr [h]	GWP 100-yr	GTP 20-yr [i]	GTP 50-yr	GTP 100-yr	Footnotes A: Abundance L: Lifetime O: ODP R: RE, GWP, & GTP			
	500	0	1.15	10,435	5,260	9,885	4,875	1,527		L54		R3
	500	0	1.43	9,745	4,910	9,230	4,550	1,426		L54		R3
	500	0	1.46	7,970	4,015	7,545	3,720	1,166		L54		R3
	500	0	0.92	11,630	5,810	10,995	5,350	1,658		L55		R19
	304	0	1.71	10,925	3,815	9,005	2,070	592		L56		R19
	500	0	1.65	16,500	8,240	15,600	7,595	2,352		L55		R19
	25	0	0.28	221	60	70	10	8.3		L51		R19
	–	0	0.01	<1	<1	<1	<1	<1		L51		R19
	153	0	0.34	3,040	855	1,860	205	121		L51		R19
	28	0	0.49	165	45	52	7.6	6.2		L57		R3
	–	0	0.07	46	13	14	2	2		L58		R19
	35	0	0.17	515	139	168	24	19		L59		R19
	30	0	0.19	470	127	150	22	18		L59		R19
	92	0	0.30	2,155	585	950	109	82		L59		R19
	120	0	0.33	2,620	715	1,315	142	100		L59		R19
	51	0	0.29	685	185	245	33	26		L60		R19
	51	0	0.56	770	210	275	37	29		L60		R3
	51	0	0.76	740	200	260	35	28		L60		R3
	680	0	0.48	6,900	3,955	6,715	3,955	1,485		L61		R3
	42	0	0.21	455	123	156	22	17		L62		R3
	–	0	0.65	7,500	9,710	8,070	9,910	11,300		L63		R3
	–	0	0.02	<1	<1	<1	<1	<1		L64		R3
	110	0	0.31	2,150	590	985	111	82		L65		R19
	110	0	0.44	2,130	580	970	110	81		L66		R19
	83	0	0.50	1,380	375	555	68	52		L66		R19
	83	0	0.56	1,240	335	500	61	47		L66		R19
	20	0	0.16	155	42	48	7	6		L67		R19
	20	0	0.13	56	15	17	2.5	2.1		L68		R19
	98	0	0.35	1,670	455	720	84	63		L69		R19

Industrial Designation or Chemical Name	Chemical Formula	Atmospheric Abundance (2016) [a]	WMO (2014) Total Lifetime (years) [b]	Total Lifetime (years) [c]	Tropospheric (OH Reactive loss) Lifetime (years) [d]	
1,1,1,3,3,3-Hexafluoropropan-2-yl formate	$HC(O)OCH(CF_3)_2$		3.2	3.1	3.2	
Perfluorobutyl acetate	$CH_3C(O)OCF_2CF_2CF_2CF_3$		21.9 days	22 days	22 days	
Perfluoropropyl acetate	$CH_3C(O)OCF_2CF_2CF_3$		21.9 days	22 days	22 days	
Perfluoroethyl acetate	$CH_3C(O)OCF_2CF_3$		21.9 days	22 days	22 days	
Trifluoromethyl acetate	$CH_3C(O)OCF_3$		21.9 days	22 days	22 days	
Methyl carbonofluoridate	$FCOOCH_3$		1.8	1.8	1.8	
1,1-Difluoroethyl carbonofluoridate	$FC(O)OCF_2CH_3$		0.3	110 days	110 days	
1,1-Difluoroethyl 2,2,2-trifluoroacetate	$CF_3C(O)OCF_2CH_3$		0.3	110 days	110 days	
Ethyl 2,2,2-trifluoroacetate	$CF_3C(O)OCH_2CH_3$		21.9 days	22 days	22 days	
2,2,2-Trifluoroethyl 2,2,2-trifluoroacetate	$CF_3C(O)OCH_2CF_3$		54.8 days	180 days	180 days	
Methyl 2,2,2-trifluoroacetate	$CF_3C(O)OCH_3$		0.6	1.0	1.0	
Methyl 2,2-difluoroacetate	$HCF_2C(O)OCH_3$		40.1 days	124 days	124 days	
Difluoromethyl 2,2,2-trifluoroacetate	$CF_3C(O)OCHF_2$		0.3	110 days	110 days	
1,1,2-Trifluoro-2-(trifluoromethoxy)-ethane	$CHF_2CHFOCF_3$		9.8	9.0	9.3	
1-Ethoxy-1,1,2,3,3,3-hexafluoropropane	$CF_3CHFCF_2OCH_2CH_3$		0.4	147 days	150 days	
1,1,1,2,2,3,3-Heptafluoro-3-(1,2,2,2-tetrafluoroethoxy)-propane	$CF_3CF_2CF_2OCHFCF_3$		67.0	59.4	62	
1,1,2,2-Tetrafluoro-3-methoxypropane	$CHF_2CF_2CH_2OCH_3$		14.2 days	26 days	26 days	
3,3,3-Trifluoro-propanal	CF_3CH_2CHO		2 days	5 days	5 days	
Halogenated Alcohols						
3,3,3-Trifluoropropan-1-ol	$CF_3CH_2CH_2OH$		12 days	15 days	15 days	
2,2,3,3,3-Pentafluoropropan-1-ol	$CF_3CF_2CH_2OH$		0.3	172 days	172 days	
4,4,4-Trifluorobutan-1-ol	$CF_3(CH_2)_2CH_2OH$		4 days	5.4 days	5.4 days	
2,2,3,3,4,4,5,5-Octafluorocyclopentanol	$-(CF_2)_4CH(OH)-$		0.3	110 days	110 days	
1,1,1,3,3,3-Hexafluoropropan-2-ol	$(CF_3)_2CHOH$		1.9	1.9	1.95	
3,3,4,4,5,5,6,6,7,7,7-Undecafluoroheptan-1-ol	$CF_3(CF_2)_4CH_2CH_2OH$		20 days	17 days	17 days	
3,3,4,4,5,5,6,6,7,7,8,8,9,9,9-Pentadecafluorononan-1-ol	$CF_3(CF_2)_6CH_2CH_2OH$		20 days	17 days	17 days	
3,3,4,4,5,5,6,6,7,7,8,8,9,9,10,10,11,11,11-Nonadecafluoroundeca-1-o1	$CF_3(CF_2)_8CH_2CH_2OH$		20 days	17 days	17 days	
2,2,3,3,4,4,4-Heptafluorobutan-1-ol	$CF_3CF_2CF_2CH_2OH$		0.6	0.55	0.55	
2,2,3,3-Tetrafluoro-1-propanol	$CHF_2CF_2CH_2OH$		91.2 days	93 days	93 days	
2,2,3,4,4,4-Hexafluoro-1-butanol	$CF_3CHFCF_2CH_2OH$		112 days (85–280 days)	134 days (85–280 days)	134 days (85–280 days)	
2-Fluoroethanol	CH_2FCH_2OH		20.4 days	16 days	16 days	
2,2-Difluoroethanol	CHF_2CH_2OH		40 days	61 days	61 days	
2,2,2-Trifluoroethanol	CF_3CH_2OH		0.3	167 days	167 days	

		Stratospheric Lifetime (years) [e]	ODP [f]	Radiative Efficiency ($W\ m^{-2}\ ppb^{-1}$) [g]	GWP 20-yr [h]	GWP 100-yr	GTP 20-yr [i]	GTP 50-yr	GTP 100-yr	Footnotes			
										A: Abundance L: Lifetime		O: ODP R: RE, GWP, & GTP	
		96	0	0.33	1,175	320	510	59	44		L68		R19
		–	0	0.12	6	2	2	<1	<1		L70		R19
		–	0	0.11	6	2	2	<1	<1		L71		R19
		–	0	0.10	8	2	2	<1	<1		L71		R19
		–	0	0.07	8	2	2	<1	<1		L71		R19
		58	0	0.07	350	95	126	17	13		L69		R19
		–	0	0.17	90	24	27	4.1	3.4		L72		R19
		–	0	0.27	103	28	31	4.7	3.9		L68		R19
		–	0	0.05	5	1	1	<1	<1		L73		R19
		–	0	0.15	85	23	26	3.9	3.2		L73		R19
		34	0	0.18	315	86	103	15	12		L73		R19
		–	0	0.05	35	9	10	1.6	1.3		L73		R19
		–	0	0.24	99	27	30	5	4		L68		R19
		250	0	0.35	3,765	1,145	2,720	390	164		L74		R3
		20	0	0.19	88	24	27	4	3		L74		R3
		1400	0	0.58	7,750	5,980	7,910	6,435	3,755		L74		R3
		–	0	0.03	3	0.9	1	<1	<1		L75		R3
		–	0	0.004	<1	<1	<1	<1	<1		L76		R3
		–	0	0.02	1.6	<1	<1	<1	<1		L77		R3
		–	0	0.14	99	27	30	4.6	3.7				R3
		–	0	0.01	<1	<1	<1	<1	<1				R3
		–	0	0.16	47	13	14	2	2		L78		R3
		62	0	0.26	670	182	245	32	25				R3
		–	0	0.06	2	<1	<1	<1	<1		L79		R3
		–	0	0.07	1.8	<1	<1	<1	<1		L79		R3
		–	0	0.05	<1	<1	<1	<1	<1		L79		R3
		–	0	0.20	124	34	38	5.7	4.6		L80		R3
		–	0	0.11	48	13	14	2	1.8		L81		R3
		–	0	0.19	86	23	26	4.0	3.2				R3
		–	0	0.02	3	0.8	0.9	<1	<1				R3
		–	0	0.04	18	5	5	0.8	0.7				R3
		–	0	0.10	103	28	31	4.7	3.8				R3

Industrial Designation or Chemical Name	Chemical Formula	Atmospheric Abundance (2016) [a]	WMO (2014) Total Lifetime (years) [b]	Total Lifetime (years) [c]	Tropospheric (OH Reactive loss) Lifetime (years) [d]	
2,2-3,3,4,4,5,5,5-fluoro-1-pentanol	$CF_3CF_2CF_2CF_2CH_2OH$		142 days (111–330 days)	172 days (111–330 days)	172 days (111–330 days)	
Halogenated Ketones						
NOVEC-1230, FK-5-1-12 Perfluoro(2-methyl-3-pentanone)	$CF_3CF_2C(O)CF(CF_3)_2$		7.0 days (7–14 days)	7 days (7–14 days)	–	
NOVEC-774 Tetradecafluoro-2,4-dimethylpentan-3-one	$(CF_3)_2CFC(O)CF(CF_3)_2$		–	–	–	
Perfluoro(2-methyl-3-hexanone)	$CF_3CF_2CF_2C(O)CF(CF_3)_2$		–	–	–	
Iodocarbons						
Methyl iodide	CH_3I	0.8 ppt (0.3–2.1)	7 days (3.5–9.6 days)	<14 days (3.5–14 days)	197 days	
Trifluoroiodomethane	CF_3I		4 days (0.7–4 days)	<5 days (0.7–5 days)	3.0	
Bromoiodomethane	CH_2BrI		–	≤60 mins	145 days	
Chloroiodomethane	CH_2ClI		–	<100 mins	145 days	
Diiodomethane	CH_2I_2		–	≤5 mins	4 days	
Iodoethane	CH_3CH_2I		4 days (2.4–13.9 days)	<4 days (2.4–13.9 days)	52 days (13–94 days)	
n-iodopropane	$CH_3CH_2CH_2I$		–	<2 days	15 days	
i-iodopropane	CH_3CHICH_3		–	<1 day	13 days	
1-iodo-heptafluoropropane	$CF_3CF_2CF_2I$		<2 days	<2 days	3.0	
Special Compounds						
Carbonyl fluoride	COF_2		– (5–10 days)	7 days (5–10 days)	–	
Phosphorus tribromide	PBr_3		– (<0.01 days)	– (<0.01 days)	–	
Ammonia	NH_3	–	– (Few days)	– (Few days)	110 days	
Carbonyl Sulfide	COS	505 ppt	–	2	–	
Sulfuryl fluoride	SO_2F_2	2.3 ppt	36.0	36.0	>300	

		Stratospheric Lifetime (years) [e]	ODP [f]	Radiative Efficiency ($W\ m^{-2}\ ppb^{-1}$) [g]	GWP 20-yr [h]	GWP 100-yr	GTP 20-yr [i]	GTP 50-yr	GTP 100-yr	Footnotes A: Abundance L: Lifetime		O: ODP R: RE, GWP, & GTP	
		–	0	–	–	–	–	–	–				R9
		–	0	0.03	<1	<1	<1	<1	<1		L82		R3
		–	0	–	–	–	–	–	–		L83		R21
		–	0	–	–	–	–	–	–		L83		R21
		–	<0.42	6.0e-4	<<1	<<1	<<1	<<1	<<1	A12	L:20,84, 85,86	O12	R2
		–	<0.09	–	–	–	–	–	–	A12	L:84, 85,86	O12	R22
		–	–	–	–	–	–	–	–	A12	L:84, 87,88	O15	R22
		–	<0.07	–	–	–	–	–	–	A12	L:84, 87,88	O12	R22
		–	–	–	<<1	<<1	<<1	<<1	<<1	A12	L:84, 87,89	O15	R2
		–	–	–	–	–	–	–	–		L:84,86, 87,90	O15	R22
		–	–	–	–	–	–	–	–		L:84, 87,90	O15	R22
		–	–	–	<<1	<<1	<<1	<<1	<<1		L:84,87, 90	O15	R2
		–	<0.04	–	–	–	–	–	–		L:84,91	O16	R23
		0	–	8.0e-3	<1	<1	<1	<1	<1		L92		R2
		–	–	–	–	–	–	–	–		L92	O14	R9
		0	–	1.4e-3	<1	<1	<1	<1	<1		L82		R2
		0	–	5.7e-3	43	12	16	2.0	1.6	A10	L93		R2
		630	0	0.20	6,840	4,090	6,690	4,140	1,650	A10	L:13,94		R3

Table Heading Footnotes

a The data given in the abundance column are only intended to provide a "snapshot" of the compound's atmospheric abundance. The chapter and table(s) cited in the compound's footnote provides the analysis details, previously reported abundances and trends, and references. This summary does not represent a comprehensive survey of the abundance of all molecules included in the table. Compounds included in this table fall into several different abundance classifications: (1) compounds with known sources and global observations for which values are reported in the table, (2) compounds with known sources, but with only local or regional observations for which some values are reported in the table (note that the abundances for very short-lived substances (VSLSs) may represent local observations that can vary with location, altitude, and season), (3) compounds with natural and/or man-made sources that are not addressed in the report chapters, and (4) compounds with no presently known sources or observations.

b Total lifetime reported in WMO (2014).

c Total lifetime (τ_{Total}) is defined as the combination of the total atmospheric lifetime (τ^{Atm}_{Total}), which includes tropospheric loss (OH reaction and UV photolysis) and stratospheric loss (reactions with OH and O(^{1}D) and UV photolysis), with the lifetimes due to ocean and soil uptake. Except where noted in the footnotes, tropospheric loss due to Cl atom reaction is not included. Mesospheric loss processes are negligible except for very long-lived compounds as noted in the footnotes.

$$\frac{1}{\tau^{Atm}_{Total}} = \frac{1}{\tau_{Trop}} + \frac{1}{\tau_{Strat}} + \frac{1}{\tau_{Meso}}$$

$$\frac{1}{\tau_{Trop}} = \frac{1}{\tau^{Trop}_{OH}} + \frac{1}{\tau^{Trop}_{h\nu}}$$

$$\frac{1}{\tau_{Strat}} = \frac{1}{\tau^{Strat}_{OH}} + \frac{1}{\tau^{Strat}_{O(^1D)}} + \frac{1}{\tau^{Strat}_{h\nu}}$$

$$\frac{1}{\tau_{Total}} = \frac{1}{\tau^{Atm}_{Total}} + \frac{1}{\tau_{Ocean}} + \frac{1}{\tau_{Soil}}$$

d The tropospheric partial lifetime due reaction with the OH radical was calculated relative to the lifetime for CH_3CCl_3 (6.1 years) using a temperature of 272 K. OH reaction rate coefficients are taken from Burkholder et al. (2015) unless stated otherwise in the footnote. Lifetimes for very short-lived substances (VSLSs) are reported, although their local lifetimes will depend on the time and location of their emission. A representative range of VSLS local lifetimes taken from WMO (2014) Chapter 1 (Tables 1-5, 1-11) are given in parenthesis where available. The tropospheric OH partial lifetime for CH_3CCl_3 (6.1 years) was calculated from an overall lifetime of 5.0 years derived from the AGAGE and NOAA networks using a stratospheric partial lifetime of 38 years and an ocean partial lifetime of 94 years (Prinn et al., 2005).

e The stratospheric partial lifetime was estimated based on atmospheric model calculations, where available, and empirical relationships for the OH, O(^{1}D), and photolysis partial lifetimes. Stratospheric lifetimes are not reported for very short-lived substances (VSLSs). The minimum stratospheric partial lifetime was taken to be 20 years.

* Stratospheric OH reactive loss partial lifetimes were estimated based on the empirical correlation derived using 2-D model results reported in Ko et al. (2013): $\log_{10}(\tau^{Strat}_{OH}) = 1.528 + 0.901 \times \log_{10}(\tau^{Trop}_{OH})$.
* The O(^{1}D) lifetime was based on measured or estimated reaction rate coefficients ($k_{reactive}$, cm^3 molecule^{-1} s^{-1}) and estimated using the empirical lifetime relationship; $\tau(years) = 3.7 \times 10^{-8}/k_{reactive}$. Where experimental data were not available, the O(^{1}D) reactivity was estimated using the activity relationship for H atom and Cl atom abstraction given in Baasandorj et al. (2013).
* Stratospheric photolysis partial lifetimes were taken from model calculations or based on the empirical estimates given in Orkin et al. (2013) or for the HCFCs from Papanastasiou et al. (2018).

f Atmospheric model calculated and semi-empirical values as cited in the footnotes.

g Radiative efficiency (RE) values were calculated using the empirical approach given in Hodgenbrog et al. (2013). The values reported in this table are lifetime adjusted using the exponential expression reported in Hodgenbrog et al., (2013) for compounds primarily removed by UV photolysis in the stratosphere and the S shaped curve for compounds primarily removed by reaction with the OH radical. The values also include a +10% stratospheric temperature change adjustment.

h Global warming potentials (GWPs) are calculated relative to CO_2.

i Global temperature change potentials (GTPs) calculated relative to CO_2 using the parameterization given in Supplementary Material Section S8.12 and references therein in IPCC (2013).

Abundance Footnotes

A1. See Chapter 6.
A2. See Chapter 1, Section 1.5.2 and Table 1-8.
A3. See Chapter 1, Section 1.5.1 and Table 1-8.
A4. See Chapter 1, Section 1.2.1 and Table 1-1.
A5. See Chapter 1, Section 1.2.5 and Table 1-1.
A6. See Chapter 2, Section 2.3 and Table 2-3.
A7. See Chapter 2, Section 2.3.5.
A8. See Chapter 1, Section 1.2 and Tables 1-1, 1-2, 1-3 and 1-4.
A9. See Chapter 1, Section 1.2 and 1.3 and Tables 1-1 and 1-4.
A10. See Chapter 1, Section 1.5 and Table 1-8.
A11. See Chapter 1, Section 1.5.
A12. See Chapter 1, Section 1.3 and Table 1-4.

Lifetime Footnotes

L1. Total lifetime reported in WMO (2014).
L2. Tropospheric photolysis partial lifetimes

Molecule	Formula	Lifetime (years)	Reference
Nitrous oxide	N_2O	14,600	SPARC Lifetime Report (Ko et al., 2013) *
Carbon tetrachloride	CCl_4	1,230	SPARC Lifetime Report (Ko et al., 2013) *
CFC-11	CCl_3F	1,770	SPARC Lifetime Report (Ko et al., 2013) *
CFC-12	CCl_2F_2	12,500	SPARC Lifetime Report (Ko et al., 2013) *
CFC-112	CCl_2FCCl_2F	2,280	Davis et al. (2016)
CFC-112a	CCl_3CClF_2	1,190	Davis et al. (2016)
CFC-113	CCl_2FCClF_2	8,120	SPARC Lifetime Report (Ko et al., 2013) *
CFC-113a	CCl_3CF_3	1,480	Davis et al. (2016)
CFC-114	$CClF_2CClF_2$	19,600	SPARC Lifetime Report (Ko et al., 2013) *
CFC-114a	CCl_2FCF_3	8,300	Davis et al. (2016)
(E)-R316c	*(E)*-1,2-c-$C_4F_6Cl_2$	3,600	Papadimitriou et al. (2013b)
(Z)-R316c	(*Z*)-1,2-c-$C_4F_6Cl_2$	10,570	Papadimitriou et al. (2013b)
Bromodichloromethane	$CHBrCl_2$	222 days	WMO (2014) Table 1-5
Dibromochloromethane	$CHBr_2Cl$	160 days	WMO (2014) Table 1-5
Methylene bromide	CH_2Br_2	13.7	WMO (2014) Table 1-5
Bromoform	$CHBr_3$	~23 days	Papanastasiou et al. (2014)
Halon-1202	CBr_2F_2	2.74	Papanastasiou et al. (2013)
Halon-1211	$CBrClF_2$	27.2	Papanastasiou et al. (2013)
Halon-1301	$CBrF_3$	4,050	SPARC Lifetime Report (Ko et al., 2013) **
Halon-2402	$CBrF_2CBrF_2$	85.5	Papanastasiou et al. (2013)

* Model mean given in SPARC Table 5.6 scaled to recommended total lifetime.

** Model mean given in SPARC Table 5.6 scaled to $CBrF_3$ UV cross section reported by Bernard et al. (2015).

L3. Atmospheric lifetimes recommended in the SPARC Lifetime report (Ko et al., 2013). Note, in some cases there are slight differences between the combination of the partial lifetimes and the recommended total atmospheric lifetime, which was derived from multi-model results and field observations.

L4. OH rate coefficient taken from Atkinson (2003).

L5. OH rate coefficient taken from Le Calve et al. (1997).

L6. Room temperature OH rate coefficient taken from Wallington et al. (1997) and *E*/R assumed to be 1000 K.

L7. Total lifetime is the best estimate taken from Ravishankara et al. (1993) that includes mesospheric loss due to Lyman-α (121.567 nm) photolysis. Electron reactive loss was included for SF_6.

L8. Stratospheric partial lifetime was taken from the 2-D model calculations in Davis et al. (2016). These values are in agreement with the values reported in Laube et al. (2014) [59 (43–95) years for CFC-112, 51 (32–113) years for CFC-112a, and 59 (31–305) years for CFC-113a (scaled to a CFC-11 lifetime of 52 years)], but of higher precision.

L9. The total lifetime includes mesospheric loss due to Lyman-α (121.567 nm) photolysis.

L10. Lifetime taken from Kloss et al. (2014).

L11. Stratospheric partial lifetime taken from 2-D model calculations in Papadimitriou et al. (2013b).

L12. *k*(OH) in the NASA/JPL (Burkholder et al., 2015) data evaluation was updated since the previous assessment resulting in a slight change in the OH tropospheric loss partial lifetime from that given in WMO (2014).

L13. Ocean and soil loss partial lifetimes

Molecule	Formula	Soil Lifetime (years)	Reference	Ocean Lifetime (years)	Reference
Methyl chloride	CH_3Cl	4.2	Hu et al. (2012)	12	Hu et al. (2013)
Methyl bromide	CH_3Br	3.35	Montzka and Reimann et al. (WMO, 2014)	3.1	Hu et al. (2012)
Carbon tetrachloride	CCl_4	375 (288–536)*	Rhew and Happell (2016), SPARC (2016)	183 (147–241)*	Butler et al. (2016)
HCFC-21	$CHCl_2F$	–		673	Yvon-Lewis and Butler (2002)
HCFC-22	$CHClF_2$	–		1,174	Yvon-Lewis and Butler (2002)
HCFC-124	$CHClF\text{-}CF_3$	–		1,855	Yvon-Lewis and Butler (2002)
HCFC-141b	$CH_3C\text{-}Cl_2F$	–		9,190	Yvon-Lewis and Butler (2002)
HCFC-142b	$CH_3C\text{-}ClF_2$	–		122,200	Yvon-Lewis and Butler (2002)
HFC-41	CH_3F	–		1,340	Yvon-Lewis and Butler (2002)
HFC-125	CHF_2CF_3	–		10,650	Yvon-Lewis and Butler (2002)
HFC-134a	CH_2FCF_3	–		5,909	Yvon-Lewis and Butler (2002)
HFC-152a	CH_3CHF_2	–		1,958	Yvon-Lewis and Butler (2002)
Methyl chloroform	CH_3CCl_3	–		94	Yvon-Lewis and Butler (2002)
Sulfuryl fluoride	SO_2F_2	–		40	Mühle et al. (2009)

* Possible range of lifetime given in parenthesis.

L14. Lifetimes taken from Papanastasiou et al. (2018) where *k*(OH) was calculated using the structure activity relationship (SAR) of DeMore (1996) and stratospheric lifetime estimated as described in footnote e.

L15. 2-D model calculated stratospheric lifetime reported in McGillen et al. (2015).

L16. OH reactivity assumed the same as CHF_2CF_3 (HFC-125).

L17. Stratospheric partial lifetime calculated using 2-D model with OH and $O(^1D)$ rate coefficients recommended in SPARC lifetime report, Chapter 3 (Ko et al., 2013).

L18. OH reactivity calculated using the structure activity relationships of DeMore (1996) with an assumed *E*/R of 1700 K.
L19. OH reactivity calculated using the room temperature rate coefficient reported by Young et al. (2009a) with an assumed *E*/R of 1700 K.
L20. OH reactivity taken from IUPAC evaluation (Ammann et al., 2017).
L21. OH reactivity taken from Chen et al. (2011).
L22. The OH rate coefficient data were taken from Baasandorj and Burkholder (2016).
L23. No experimental data available for the OH reaction and the lifetimes were estimated based on reactivity trends of fluorinated ethenes and propenes.
L24. The OH rate coefficient was taken from Jia et al. (2013).
L25. The OH rate coefficient data were taken from Baasandorj et al. (2018).
L26. Assumed to be the same as HFO-1336mzz*(E)*.
L27. OH reactivity was calculated using the room temperature rate coefficient reported by Sulbaek Andersen et al. (2005) with the *E*/R obtained for the OH + CH_2=$CHCF_3$ reaction, -170 K.
L28. OH reactivity was calculated using the rate coefficient data from Papadimitriou and Burkholder (2016).
L29. Lifetimes recommended in the SPARC CCl_4 report (2016).
L30. Lifetime due to reaction with Cl-atom of 259 years taken from the SPARC lifetime report, Chapter 5 model-mean (Ko et al., 2013).
L31. Local lifetime estimated as similar to that of *(E)*-CF_3CH=$CHCl$.
L32. Local lifetime estimated as similar to that of CF_3CF=CF_2.
L33. Stratospheric photolysis lifetime was estimated using the empirical relationship given in Orkin et al. (2013).
L34. Lifetime estimated to be similar to that of CBr_2F_2.
L35. OH rate coefficient taken from Orkin et al. (2017).
L36. Tropospheric (84,150 years) and mesospheric (2,531 years) lifetimes taken from 2-D model calculations in Papadimitriou et al. (2013a).
L37. Estimated total lifetime lower-limit.
L38. Total lifetime range taken from Takahashi et al. (2002) including mesospheric loss due to Lyman-α (121.567 nm) photolysis, dissociative electron attachment, and solar proton event loss processes.
L39. Total lifetime estimate based on the increase in Lyman-α (121.567 nm) absorption cross section (increased photolysis rate) with increasing number of –CF_2- groups in the perfluorocarbon.
L40. OH rate coefficient taken from Zhang et al. (2017).
L41. Room temperature OH rate coefficient taken from Young et al. (2009b) with the *E*/R assumed to be the same as for the OH + CF_3CF=CF_2 reaction, -415 K.
L42. Tropospheric OH partial lifetime estimated from that for $CF_3CH_2OCF_2CHF_2$ by adjusting for the reactivity contribution of –CF_2CHF_2 determined from the reactivity of $CF_3CF_2OCF_2CHF_2$.
L43. Tropospheric OH partial lifetime estimated from those for CF_3OCH_3 and $CHF_2CH_2CF_3$.
L44. Room temperature OH rate coefficient taken from Oyaro et al. (2005) with an assumed *E*/R of 500 K.
L45. Estimated OH reactivity.
L46. Tropospheric OH partial lifetime estimated to be greater than that of $CHF_2CF_2OCHF_2$ and less than that of $CHF_2CF_2CF_2CF_3$.
L47. Tropospheric OH partial lifetime estimated to be the same as for $CF_3OCH_2CF_3$.
L48. Tropospheric OH partial lifetime estimated to be the same as for $CH_3OCF_2CHF_2$.
L49. Tropospheric OH partial lifetime estimated from the sum of the OH partial lifetimes of $CF_3CF_2OCF_2CHF_2$ and $CF_3CF_2OCH_2CHF_2$.
L50. Room temperature OH rate coefficient taken from Oyaro et al. (2004) with an assumed *E*/R of 500 K.
L51. Tropospheric OH partial lifetime estimated in Bravo et al. (2011b).
L52. Tropospheric OH partial lifetime calculated using the OH rate coefficient from Chen et al. (2005).
L53. Tropospheric OH partial lifetime calculated using the room temperature OH rate coefficient from Christensen et al. (1998) with an assumed *E*/R of 1000 K.
L54. OH reactivity assumed to be similar to that of HCF_2OCF_2H.
L55. OH reactivity assumed to be similar to HG-10.
L56. OH reactivity assumed to be similar to HG-01.
L57. Tropospheric OH partial lifetime calculated using the room temperature OH rate coefficient from Javadi et al. (2007) with an assumed *E*/R of 1000 K.

L58. Tropospheric OH partial lifetime calculated using the structure activity relationship estimated OH rate coefficient in Urata et al. (2003).
L59. OH rate coefficient calculated theoretically in Blowers et al. (2008).
L60. Tropospheric OH partial lifetime calculated using the room temperature OH rate coefficient from Sulbaek Andersen et al. (2004) with an assumed *E*/R of 1000 K.
L61. Tropospheric OH partial lifetime calculated using the room temperature OH rate coefficient from Wallington et al. (2004) with an assumed *E*/R of 1000 K.
L62. Tropospheric OH partial lifetime calculated using the OH rate coefficient from Tokuhashi et al. (1999).
L63. Lifetime estimated in Young et al. (2006).
L64. Tropospheric OH partial lifetime calculated using the room temperature OH rate coefficient from Mashino et al. (2000) with an assumed *E*/R of -400 K.
L65. Tropospheric OH partial lifetime calculated using the OH rate coefficient from Chen et al. (2004a).
L66. Tropospheric OH partial lifetime calculated using the OH rate coefficient from Chen et al. (2004b). There is no experimental data available for perfluorobutyl formate and it is assumed to be similar to perfluoroporopyl formate.
L67. Tropospheric OH partial lifetime calculated using the room temperature OH rate coefficient from Oyaro et al. (2004) with an assumed *E*/R of 500 K.
L68. Lifetime estimated in Bravo et al. (2011a).
L69. Tropospheric OH partial lifetime calculated using the OH rate coefficient from Chen et al. (2006).
L70. Tropospheric OH partial lifetime estimated in Christensen et al. (1998) based on comparison with Cl atom reactivity.
L71. OH reactivity assumed to be the same as for perfluorobutyl acetate.
L72. OH reactivity assumed to be the same as for $CF_3C(O)OCH_2CH_3$.
L73. Tropospheric OH partial lifetime calculated using the room temperature OH rate coefficient from Blanco and Teruel (2007) with an assumed *E*/R of 1000 K.
L74. Tropospheric OH partial lifetime calculated using the room temperature OH rate coefficient from Oyaro et al. (2005) with an assumed *E*/R of 1500 K.
L75. Tropospheric OH partial lifetime calculated using the room temperature OH rate coefficient from Oyaro et al. (2004) with an assumed *E*/R of 1000 K.
L76. Tropospheric OH partial lifetime calculated using the OH rate coefficient from Antiñolo et al. (2010).
L77. OH rate coefficient taken from Antiñolo et al. (2011).
L78. OH reactivity estimated by comparison with other fluoroalcohols.
L79. OH reactivity calculated using the room temperature rate coefficient reported by Ellis et al. (2003) with an assumed *E*/R of 1000 K.
L80. OH rate coefficient taken from Bravo et al. (2010).
L81. OH rate coefficient taken from Antiñolo et al. (2012).
L82. Tropospheric photolysis is the dominant loss process for perfluoroketones (Jackson et al., 2011; Taniguchi et al., 2003).
L83. OH reactivity assumed to be similar to that of NOVEC-1230.
L84. Lifetime primarily determined by UV photolysis with a decreasing local lifetime with increasing altitude.
L85. Lifetime estimates taken from the 3-D model simulations of Youn et al. (2010).
L86. Lifetime range is representative of the variation in local photolysis partial lifetime with time and location of emission.
L87. Photolysis lifetimes taken from Mössinger et al. (1998) for CH_2BrI and Roehl et al. (1997) for CH_2ClI, CH_3CH_2I, $CH_3CH_2CH_2I$, CH_3CHICH_3.
L88. OH reactivity assumed to be similar to that of CH_2Br_2.
L89. OH reactivity taken from Zhang et al. (2011).
L90. OH reactivity taken from Zhang et al. (2012)
L91. Photolysis and OH reactivity assumed the same as for CF_3I.
L92. Heterogeneous processing is the predominate removal process.
L93. Lifetime reported in Brühl et al. (2012).
L94. Lifetimes taken from Papadimitrou et al. (2008) and Mühle et al. (2009).

ODP Footnotes

O1. See Chapter 1, Section 1.5.1.

O2. Negligible and assigned a value of zero.
O3. ODP taken from WMO (2014) Table 5.2.
O4. A greater ODP value was reported from the 2-D model calculations in Davis et al. (2016): 0.95 (CFC-113), 0.78 (CFC-114), 0.44 (CFC-115), 1.01 (CFC-12), and 1.06 (CCl_4).
O5. Taken from Montreal Protocol.
O6. ODP taken from the 2-D model calculations in Davis et al. (2016). The semi-empirical ODP reported in Laube et al. (2014) is consistent with the latter Davis et al. (2016) value, but has a larger uncertainty range.
O7. ODP taken from Kloss et al. (2014).
O8. ODP taken from the 2-D model calculations in Papadimitriou et al. (2013b).
O9. Semi-empirical ODP calculated using empirical relationship of the fractional release factor with stratospheric lifetime given in Papanastasiou et al. (2018).
O10. Taken from Papanastasiou et al. (2018).
O11. ODP taken from WMO (2011).
O12. Upper-limit of ODPs of short-lived substances reported in the studies of Brioude et al. (2010) (C_2H_5Br, CH_2CBrCF_3, n-C_3H_7Br, C_2HCl_3, CCl_3CHO, CH_3I, CF_3I, C_3F_7I, CH_2ClI, $CHBr_3$), Wuebbles and co-workers (Patten et al., 2011; Patten and Wuebbles, 2010; Wuebbles et al., 2011; Wuebbles et al., 2009; Youn et al., 2010) (C_3H_7Br, C_2HCl_3, C_2Cl_4, HFO-1233zd, *(E)*-CHCl=CHCl, CF_3I, and CH_3I), and Tegtmeier et al. (2012) (CH_2Br_2, $CHBr_3$). The derived ODPs in these studies were shown to be strongly dependent on the region and season of the substance emission with the greatest values obtained for emissions in the Indian subcontinent.
O13. Taken from Langbein et al. (1999).
O14. Value not available.
O15. Assumed to be <0.02 for surface emission.
O16. Assumed to be the same as for CF_3I.

RE, GWP, and GTP Footnotes

R1. Radiative metrics taken from IPCC (2013).
R2. RE calculated using the room temperature infrared absorption spectrum reported in the Pacific Northwest National Laboratory (PNNL) database, https://secure2.pnl.gov/nsd/nsd.nsf (Sharpe et al., 2004).
R3. RE taken from recommendation given in Hodnebrog et al. (2013), which was based on a combination of literature review of experimental data and re-analysis.
R4. Radiative metrics calculated using the infrared absorption spectrum reported in Davis et al. (2016) and the lifetime reported here.
R5. Radiative metrics calculated using the infrared absorption spectrum reported in Papadimitriou et al. (2013b) and the lifetime reported here.
R6. Radiative metrics calculated using the theoretically calculated infrared absorption spectrum in Papanastasiou et al. (2018) and lifetimes given here.
R7. Radiative metrics calculated using the theoretically calculated infrared absorption spectrum and lifetimes reported in Papanastasiou et al. (2018).
R8. Radiative metrics calculated using the infrared spectrum and lifetimes reported in McGillen et al. (2015).
R9. Radiative efficiency not available.
R10. Radiative metrics calculated using the RE reported in Le Bris et al. (2018) and the lifetime reported here.
R11. Radiative metrics calculated using the infrared spectrum in Baasandorj and Burkholder (2016).
R12. Radiative metrics calculated using the RE reported in Jai et al. (2013) with lifetime and stratospheric temperature corrections applied here using the lifetimes reported here.
R13. Radiative metrics calculated using the infrared spectrum in Baasandorj et al. (2018).
R14. Radiative metrics calculated using the infrared spectrum in Papadimitriou and Burkholder (2016).
R15. Radiative metrics calculated using the infrared spectrum in Wallington et al. (2016).
R16. Radiative metrics calculated using the infrared spectrum in Gierczak et al. (2014).
R17. Radiative metrics calculated using the infrared spectrum in Orkin et al. (2017).
R18. Infrared absorption spectrum taken from Bernard et al. (2018).
R19. RE taken from recommendation given in Hodnebrog et al. (2013), which was based on theoretically calculated infrared absorption spectra and analysis.

R20. Radiative metrics calculated using the RE reported in Zhang et al. (2017) and the lifetime reported here.
R21. Assumed to be similar to NOVEC-1230.
R22. Assumed negligible.
R23. Assumed to be similar to that of CF_3I.

REFERENCES

Ammann, M., R.A. Cox, J.N. Crowley, H. Herrmann, M.E. Jenkin, V.F. McNeil, A. Mellouki, M.J. Rossi, J. Troe, and T.J. Wallington, IUPAC Task Group on Atmospheric Chemical Kinetic Data Evaluation, 2017.

Antiñolo, M., E. Jiménez, A. Notario, E. Martínez, and J. Albaladejo, Tropospheric photooxidation of CF_3CH_2CHO and $CF_3(CH_2)_2CHO$ initiated by Cl atoms and OH radicals, *Atmos. Chem. Phys.*, *10*, 1911–1922, doi:10.5194/acp-10-1911-2010, 2010.

Antiñolo, M., E. Jiménez, and J. Albaladejo, Temperature effects on the removal of potential HFC replacements, $CF_3CH_2CH_2OH$ and $CF_3(CH_2)_2CH_2OH$, initiated by OH radicals, *Environ. Sci. Technol.*, *45*, 4323–4330, doi:10.1021/es103931s, 2011.

Antiñolo, M., S. González, B. Ballesteros, J. Albaladejo, and E. Jiménez, Laboratory studies of $CHF_2CF_2CH_2OH$ and $CF_3CF_2CH_2OH$: UV and IR absorption cross sections and OH rate coefficients between 263 and 358 K, *J. Phys. Chem. A*, *116*, 6041–6050, doi:10.1021/jp2111622, 2012.

Atkinson, R., Kinetics of the gas-phase reactions of OH radicals with alkanes and cycloalkanes, *Atmos. Chem. Phys.*, *3*, 2233–2307, doi:10.5194/acp-3-2233-2003, 2003.

Baasandorj, M., and J.B. Burkholder, Rate coefficient for the gas-phase OH + $CHF{=}CF_2$ reaction between 212 and 375 K, *Int. J. Chem. Kinet.*, *48*, 714–723, doi:10.1002/kin.21027, 2016.

Baasandorj, M., E.L. Fleming, C.H. Jackman, and J.B. Burkholder, $O(^1D)$ kinetic study of key ozone depleting substances and greenhouse gases, *J. Phys. Chem. A*, *117*, 2434–2445, doi:10.1021/j312781c, 2013.

Baasandorj, M., P. Marshall, A.R. Ravishankara, and J.B. Burkholder, Rate coefficient measurements and theoretical analysis of the OH + (*E*)-$CF_3CH{=}CHCF_3$ reaction, *J. Phys. Chem. A*, *122*, doi:10.1021/acs.jpca.8b02771, 2018.

Bernard, F., M.R. McGillen, E.L. Fleming, C.H. Jackman, and J.B. Burkholder, $CBrF_3$ (Halon-1301): UV absorption spectrum between 210 and 320 K, atmospheric lifetime, and ozone depletion potential, *J. Photochem. Photobio.*, *306*, 13–20, doi:10.1016/j.jphotochem.2015.03.012, 2015.

Bernard, F., D.K. Papanastasiou, V.C. Papadimitriou, and J.B. Burkholder, Infrared absorption spectra of $N(C_xF_{2x+1})_3$, × = 2-5 perfluoroamines, *J. Quant. Spectrosc. Rad. Trans.*, *211*, 166–171, doi:10.1016/j.jqsrt.2018.02.039, 2018.

Blanco, M.B., and M.A. Teruel, Atmospheric degradation of fluoroesters (FESs): Gas-phase reactivity study towards OH radicals at 298 K, *Atmos. Environ.*, *41*, 7330–7338, doi:10.1016/j.atmosenv.2007.05.013, 2007.

Blowers, P., K.F. Tetrault, and Y. Trujilo-Morehead, Global warming potential predictions for hydrofluoroethers with two carbon atoms, *Theor. Chem. Acc.*, *119*, 369–381, doi:10.1007/s00214-007-0394-3, 2008.

Bravo, I., Y. Díaz-de-Mera, A. Aranda, K. Smith, K.P. Shine, and G. Marston, Atmospheric chemistry of $C_4F_9OC_2H_5$ (HFE-7200), $C_4F_9OCH_3$ (HFE-7100), $C_3F_7OCH_3$ (HFE-7000) and $C_3F_7H_2OH$: Temperature dependence of the kinetics of their reactions with OH radicals, atmospheric lifetimes and global warming potentials, *Phys. Chem. Chem. Phys.*, *12*, 5115–5125, doi:10.1039/b923092k, 2010.

Bravo, I., Y. Diaz-de-Mera, A. Aranda, E. Moreno, D.R. Nutt, and G. Marston, Radiative efficiencies for fluorinated esters: indirect global warming potentials of hydrofluoroethers, *Phys. Chem. Chem. Phys.*, *13*, 17185–17193, doi:10.1039/c1cp21874c, 2011a.

Bravo, I., G. Marston, D.R. Nutt, and K.P. Shine, Radiative efficiencies and global warming potentials using theoretically determined absorption cross-sections for several hydrofluoroethers (HFEs) and hydrofluoropolyethers (HFPEs), *J. Quant. Spectrosc. Rad. Trans.*, *112*, 1967–1977, doi:10.1016/j.jqsrt.2011.05.001, 2011b.

Brioude, J., R.W. Portmann, J.S. Daniel, O.R. Cooper, G.J. Frost, K.H. Rosenlof, C. Granier, A.R. Ravishankara, S.A. Montzka, and A. Stohl, Variations in ozone depletion potentials of very short-lived substances with season and emission region, *Geophys. Res. Lett.*, *37*, L19804, doi:10.1029/2010GL044856, 2010.

Brühl, C., J. Lelieveld, P.J. Crutzen, and H. Tost, The role of carbonyl suphide as a source of stratospheric sulphate aerosol and its impact on climate, *Atmos. Chem. Phys.*, *12*, 1239–1253, doi:10.5194/acp-12-1239-2012, 2012.

Burkholder, J.B., S.P. Sander, J. Abbatt, J.R. Barker, R.E. Huie, C.E. Kolb, M.J. Kurylo, V.L. Orkin, D.M. Wilmouth, and P.H. Wine, *Chemical Kinetics and Photochemical Data for Use in Atmospheric Studies, Evaluation No. 18*, JPL Publication 15-10, Jet Propulsion Laboratory, Pasadena, California, http://jpldataeval.jpl.nasa.gov., 2015.

Butler, J.H., S.A. Yvon-Lewis, J.M. Lobert, D.B. King, S.A. Montzka, J.L. Bullister, V. Koropalov, J. Elkins, B.D. Hall, L. Hu, and Y. Liu, A comprehensive estimate for loss of atmospheric carbon tetrachloride (CCl_4) to the ocean, *Atmos. Chem. Phys.*, *16*, 10899–10910, doi:10.5194/acp-16-10899-2016, 2016.

Chen, L., S. Kutsuna, K. Tokuhashi, and A. Sekiya, Kinetics of the gas-phase reaction of $CF_3OC(O)H$ with OH radicals at 242–328 K, *Int. J. Chem. Kinet.*, *36*, 337–344, doi:10.1002/kin.20004, 2004a.

Chen, L., S. Kutsuna, K. Tokuhashi, and A. Sekiya, Kinetics study of the gas-phase reactions of $C_2F_5OC(O)H$ and *n*-$C_3F_7OC(O)H$ with OH radicals at 253–328 K, *Chem. Phys. Lett.*, *400*, 563–568, doi:10.1016/j.cplett.2004.11.019, 2004b.

Chen, L., S. Kutsuna, K. Tokuhashi, and A. Sekiya, Kinetics study of the gas-phase reactions of $CHF_2CF_2OCHF_2$ and $CF_3CHFCF_2OCH_2CF_2CF_3$ with OH radicals at 253–328 K, *Chem. Phys. Lett.*, *403*, 180–184, doi:10.1016/j.cplett.2005.01.002, 2005.

Chen, L., S. Kutsuna, K. Tokuhashi, and A. Sekiya, Kinetics and mechanisms of $CF_3CHFOCH_3$, $CF_3CHFOC(O)H$, and $FC(O)OCH_3$ reactions with OH radicals, *J. Phys. Chem. A*, *110*, 12845–12851, doi:10.1021/jp064917h, 2006.

Chen, L., T. Uchimaru, S. Kutsuna, K. Tokuhashi, A. Sekiya, and H. Okamoto, Kinetics and mechanism of gas-phase reaction of $CF_3CF_2CF_2CF_2CF_2CF_2CF_2H$ with OH radicals in an environmental reaction chamber at 253–328 K, *Chem. Phys. Lett.*, *501*, 263–266, doi:10.1016/j.cplett.2010.12.009, 2011.

Christensen, L.K., J. Sehested, O.J. Nielsen, M. Bilde, T.J. Wallington, A. Guschin, L.T. Molina, and M.J. Molina, Atmospheric chemistry of HFE-7200 ($C_4F_9OC_2H_5$): Reaction with OH radicals and fate of $C_4F_9OCH_2CH_2O(\bullet)$ and $C_4F_9OCHO(\bullet)CH_3$ radicals, *J. Phys. Chem. A*, *102*, 4839–4845, doi:10.1021/jp981128u, 1998.

Davis, M.E., F. Bernard, M.R. McGillen, E.L. Fleming, and J.B. Burkholder, UV and infrared absorption spectra, atmospheric lifetimes, and ozone depletion and global warming potentials for CCl_2FCCl_2F (CFC-112), CCl_3CClF_2 (CFC-112a), CCl_3CF_3 (CFC-113a), and CCl_2FCF_3 (CFC-114a), *Atmos. Chem. Phys.*, *16*, 8043–8052, doi:10.5194/acp-16-8043-2016, 2016.

DeMore, W.B., Experimental and estimated rate constants for the reactions of hydroxyl radicals with several halocarbons, *J. Phys. Chem.*, *100*, 5813–5820, doi:10.1021/jp953216%2B, 1996.

Ellis, D.A., J.W. Martin, S.A. Mabury, M.D. Hurley, M.P. Sulbaek Andersen, and T.J. Wallington, Atmospheric lifetime of fluorotelomer alcohols, *Environ. Sci. Technol.*, *37*, 3816–3820, doi:10.1021/es034136j, 2003.

Gieczak, T., M. Baasandorj, and J.B. Burkholder, OH + (*E*)- and (*Z*)-1-chloro-3,3,3-trifluoropropene-1 ($CF_3CH=CHCl$) reaction rate coefficients: Stereoisomer-dependent reactivity, *J. Phys. Chem. A*, *118*, 11,015–11,s025, doi:10.1021/jp509127h, 2014.

Handbook for the Montreal Protocol on Substances that Deplete the Ozone Layer, Twelfth Edition, Ozone Secretariat, Secretariat of the Vienna Convention for the Protection of the Ozone Layer and of the Montreal Protocol on Substances the Deplete the Ozone Layer, United Nations Environment Programme, Nairobi, Kenya, 2018. http://ozone.unep.org/sites/default/files/MP_handbook-english-2018.pdf

Hodnebrog, Ø., M. Etminan, J.S. Fuglestvedt, G. Marston, G. Myhre, C.J. Nielsen, K.P. Shine, and T.J. Wallington, Global warming potentials and radiative efficiencies of halocarbons and related compounds: A comprehensive review,

Rev. Geophys., *51*, 300–378, doi:10.1002/rog.20013, 2013.

Hu, L., S.A. Yvon-Lewis, Y. Liu, and T.S. Bianchi, The ocean in near equilibrium with atmospheric methyl bromide, *Global Biogeochem. Cycles*, *26*, GB3016, doi:10.1029/2011GB004272, 2012.

Hu, L., S.A. Yvon-Lewis, J.H. Butler, J.M. Lobert, and D.B. King, An improved oceanic budget for methyl chloride, *J. Geophys. Res.*, *118*, 715–725, doi:10.1029/2012JC008196, 2013.

IPCC, *Climate Change 2013: The Physical Science Basis. Contribution of Working Group 1 to the Fifth Assessment Report of the Intergovernmental Panel on Climate Change*, edited by T.F. Stocker, D. Qin, G.-K. Plattner, M. Tignor, S.K. Allen, J. Boschung, A. Nauels, Y. Xia, V. Bex, and P.M. Midgley, 1535 pp., Cambridge University Press, Cambridge, United Kingdom, 2013.

Jackson, D.A., C.J. Young, M.D. Hurley, T.J. Wallington, and S.A. Mabury, Atmospheric degradation of perfluoro-2-methyl-3-pentanone: Photolysis, hydrolysis and hydration, *Environ. Sci. Technol.*, *45*, 8030–8036, doi:10.1021/es104362g, 2011.

Javadi, M.S., O.J. Nielsen, T.J. Wallington, M.D. Hurley, and J.G. Owens, Atmospheric chemistry of 2-ethoxy-3,3,4,4,5-pentafluorotetrahydro-2,5-bis[1,2,2,2-tetrafluoro-1-(trifluoromethyl)ethyl]-furan: Kinetics, mechanisms, and products of Cl atom and OH radical initiated oxidation, *Environ. Sci. Technol.*, *41*, 7389–7395, doi:10.1021/es071175c, 2007.

Jia, X., L. Chen, J. Mizukado, S. Kutsuna, and K. Tokuhashi, Rate constants for the gas-phase reactions of cyclo-CX=CXCF_2CF_2- (X = H, F) with OH radicals at a temperature range of 253–328 K, *Chem. Phys. Lett.*, *572*, 21–25, doi:10.1016/j.cplett.2013.04.020, 2013.

Kloss, C., M.J. Newland, D.E. Oram, P.J. Fraser, C.A.M. Brenninkmeijer, T. Röckmann, and J.C. Laube, Atmospheric abundances, trends and emissions of CFC-216ba, CFC-216ca and HCFC-225ca, *Atmos.*, *5*, 420–434, doi:10.3390/atmos5020420, 2014.

Ko, M.K.W., P.A. Newman, S. Reimann, S.E. Strahan, R.A. Plumb, R.S. Stolarski, J.B. Burkholder, W. Mellouki, A. Engel, E.L. Atlas, M. Chipperfield, and Q. Liang, Lifetimes of stratospheric ozone-depleting substances, their replacements, and related species, *SPARC Report No. 6*, WCRP-15/2013, 2013.

Langbein, T., H. Sonntag, D. Trapp, A. Hoffmann, W. Malms, E.-P. Röth, V. Mörs, and R. Zellner, Volatile anaesthetics and the atmosphere: Atmospheric lifetimes and atmospheric effects of halothane, enflurane, isoflurane, desflurane and sevoflurane, *Br. J. Anaesth.*, *82*, 66–73, doi:10.1093/bja/82.1.66, 1999.

Laube, J.C., M.J. Newland, C. Hogan, C.A.M. Brenninkmeijer, P.J. Fraser, P. Martinerie, D.E. Oram, C.E. Reeves, T. Röckmann, J. Schwander, E. Witrant, and W.T. Sturges, Newly detected ozone-depleting substances in the atmosphere, *Nat. Geosci.*, *7*, 266–269, doi:10.1038/ngeo2109, 2014.

Le Bris, K., J. DeZeeuw, P.J. Godin, and K. Strong, Infrared absorption cross-sections, radiative efficiency and global warming potential of HFC-43-10mee, *J. Mol. Spectrosc.*, *348*, 64–67, doi:10.1016/j.jms.2017.06.004, 2018.

Le Calve, S., G. Le Bras, and A. Mellouki, Temperature dependence for the rate coefficients of the reactions of the OH radical with a series of formates, *J. Phys. Chem. A*, *101*, 5489–5493, doi:.1021/jp970554x, 1997.

Mashino, M., Y. Ninomiya, M. Kawasaki, T.J. Wallington, and M.D. Hurley, Atmospheric chemistry of $CF_3CF{=}CF_2$: Kinetics and mechanism of its reactions with OH radicals, Cl atoms, and ozone, *J. Phys. Chem. A*, *104*, 7255–7260, doi:10.1021/jp000498r, 2000.

McGillen, M.R., F. Bernard, E.L. Fleming, and J.B. Burkholder, HCFC-133a (CF_3CH_2Cl): OH rate coefficient, UV and infrared absorption spectra, and atmospheric implications, *Geophys. Res. Lett.*, *42*, 6098–6105, doi:10.1002/2015GL064939, 2015.

Mössinger, J.C., D.E. Shallcross, and R.A. Cox, UV-VIS absorption cross-sections and atmospheric lifetimes of CH_2Br_2, CH_2I_2 and CH_2BrI, *J. Chem. Soc. Faraday Trans.*, *94*, 1391–1396, doi:10.1039/A709160E, 1998.

Mühle, J., J. Huang, R.F. Weiss, R.G. Prinn, B.R. Miller, P.K. Salameh, C.M. Harth, P.J. Fraser, L.W. Porter, B.R. Greally, S.

O'Doherty, and P.G. Simonds, Sulfuryl fluoride in the global atmosphere, *J. Geophys. Res.*, *114*, D05306, doi:10.1029/2008JD011162, 2009.

Orkin, V.L., V.G. Khamaganov, E.E. Kasimovskaya, and A.G. Guschin, Photochemical properties of some Cl containing halogenated alkanes, *J. Phys. Chem. A*, *117*, 5483–5490, doi:10.1021/jp400408y, 2013.

Orkin, V.L., L.E. Martynova, and M.J. Kurylo, Photochemical properties of CH_2=CH-CFCl-CF_2Br (4-bromo-3-chloro-3,4,4-trifluoro-1-butene) and CH_3-O-CH(CF_3)$_2$ (Methyl Hexafluoroisopropyl Ether): OH reaction rate constants and UV and IR absorption spectra, *J. Phys. Chem. A*, *121* (30) , 5675–5680, doi:10.1021/acs.jpca.7b04256, 2017.

Oyaro, N., S.R. Sellevåg, and C.J. Nielsen, Study of the OH and Cl-initiated oxidation, IR absorption cross-section, radiative forcing, and global warming potential of four C_4-hydrofluoroethers, *Environ. Sci. Technol.*, *38*, 5567–5576, doi:10.1021/es0497330, 2004.

Oyaro, N., S.R. Sellevåg, and C.J. Nielsen, Atmospheric chemistry of hydrofluoroethers: Reaction of a series of hydrofluoroethers with OH radicals and Cl atoms, atmospheric lifetimes, and global warming potentials, *J. Phys. Chem. A*, *109*, 337–346, doi:10.1021/jp047860c, 2005.

Papadimitriou, V.C., and J.B. Burkholder, OH radical reaction rate coefficients, infrared spectrum, and global warming potential of (CF_3)$_2$CFCH=CHF (HFO-1438ezy(*E*)), *J. Phys. Chem. A*, *120*, 6618–6628, doi:10.1021/acs.jpca.6b06096, 2016.

Papadimitriou, V.C., R.W. Portmann, D.W. Fahey, J. Mühle, R.F. Weiss, and J.B. Burkholder, Experimental and theoretical study of the atmospheric chemistry and global warming potential of SO_2F_2, *J. Phys. Chem. A*, *112*, 12657–12666, doi/abs/10.1021/jp806368u, 2008.

Papadimitriou, V.C., M.R. McGillen, E.L. Fleming, C.H. Jackman, and J.B. Burkholder, NF_3: UV absorption spectrum temperature dependence and the atmospheric and climate forcing implications, *Geophys. Res. Lett.*, *40*, 1–6, doi:10.1002/grl.50120, 2013a.

Papadimitriou, V.C., M.R. McGillen, S.C. Smith, A.M. Jubb, R.W. Portmann, B.D. Hall, E.L. Fleming, C.H. Jackman, and J.B. Burkholder, 1,2-Dichlorohexafluoro-cyclobutane (1,2-c-$C_4F_6Cl_2$, R-316c) a potent ozone depleting substance and greenhouse gas: Atmospheric loss processes, lifetimes, and ozone depletion and global warming potentials for the (*E*) and (*Z*) stereoisomers, *J. Phys. Chem. A*, *117*, 11,049–11,065, doi:10.1021/jp407823k, 2013b.

Papanastasiou, D.K., N. Rontu Carlon, J.A. Neuman, E.L. Fleming, C.H. Jackman, and J.B. Burkholder, Revised UV absorption spectra, ozone depletion potentials, and global warming potentials for the ozone-depleting substances CF_2Br_2, CF_2ClBr, and CF_2BrCF_2Br, *Geophys. Res. Lett.*, *40*, doi:10.1002/GRL.50121, 2013.

Papanastasiou, D.K., S.A. McKeen, and J.B. Burkholder, The very short-lived ozone depleting substance $CHBr_3$ (bromoform): Revised UV absorption spectrum, atmospheric lifetime and ozone depletion potential, *Atmos. Chem. Phys.*, *14*, 3017–3025, doi: 10.5194/acpd-13-32963-2013, 2014.

Papanastasiou, D.K., A. Beltrone, P. Marshall, and J.B. Burkholder, Global warming potential estimates for C_1-C_3 hydrochlorofluorocarbons (HCFCs) included in the Kigali amendment to the Montreal Protocol, *Atmos. Chem. Phys.*, *18*, 6317–6330, doi:10.5194/acp-18-6317-2018, 2018.

Patten, K.O., and D.J. Wuebbles, Atmospheric lifetimes and Ozone Depletion Potentials of trans-1-chloro-3,3,3-trifluoropropylene and trans-1,2-dichloroethylene in a three-dimensional model, *Atmos. Chem. Phys.*, *10*, 10867–10874, doi:10.5194/acp-10-10867-2010, 2010.

Patten, K.O., V.G. Khamaganov, V.L. Orkin, S.L. Baughcum, and D.J. Wuebbles, OH reaction rate constant, IR absorption spectrum, ozone depletion potentials and global warming potentials of 2-bromo-3,3,3-trifluoropropene, *J. Geophys. Res.*, *116*, D24307, doi:10.1029/2011JD016518, 2011.

Prinn, R.G., J. Huang, R.F. Weiss, D.M. Cunnold, P.J. Fraser, P.G. Simmonds, A. McCulloch, C. Harth, S. Reimann, P. Salameh, S. O'Doherty, R.H.J. Wang, L.W. Porter, B.R. Miller, and P.B. Krummel, Evidence for variability of atmospheric hydroxyl radicals over the past quarter century, *Geophys. Res. Lett.*, *32*, L07809, doi:10.1029/2004GL022228, 2005.

Ravishankara, A.R., S. Solomon, A.A. Turnipseed, and R.F. Warren, Atmospheric lifetimes of long-lived halogenated species, *Science*, *259*, 194–199, doi:10.1126/science.259.5092.194, 1993.

Rhew, R.C., and J.D. Happell, The atmospheric partial lifetime of carbon tetrachloride with respect to the global soil sink, *Geophys. Res. Lett.*, *43*, 2889–2895, doi:10.1002/2016GL067839, 2016.

Roehl, C.M., J.B. Burkholder, G.K. Moortgat, A.R. Ravishankara, and P.J. Crutzen, Temperature dependence of UV absorption cross sections and atmospheric implications of several alkyl iodides, *J. Geophys. Res.*, *102*, 12,819–12,829, doi:10.1029/97JD00530, 1997.

Sharpe, S.W., T.J. Johnson, R.L. Sams, P.M. Chu, G.C. Rhoderick, and P.A. Johnson, Gas-phase databases for quantitative infrared spectroscopy, *Appl. Spectrosc.*, *58*, 1452–1461, doi:10.1366/0003702042641281, 2004.

SPARC, *Report on the Mystery of Carbon tetrachloride*, edited by Q. Liang, P.A. Newman, and S. Reimann, *SPARC Report No. 7*, WCRP-13/2016, 2016.

Sulbaek Andersen, M.P., M.D. Hurley, T.J. Wallington, F. Blandini, N.R. Jensen, V. Librando, J. Hjorth, G. Marchionni, M. Avataneo, M. Visca, F.M. Nicolaisen, and O.J. Nielsen, Atmospheric chemistry of $CH_3O(CF_2CF_2O)_nCH_3$ (n=1-3): Kinetics and mechanism of oxidation initiated by Cl atoms and OH radicals, IR spectra, and global warming potentials, *J. Phys. Chem. A*, *108*, 1964–1972, doi:10.1021/jp036615a, 2004.

Sulbaek Andersen, M.P., O.J. Nielsen, A. Toft, T. Nakayama, Y. Matsumi, R.L. Waterland, R.C. Buck, M.D. Hurley, and T.J. Wallington, Atmospheric chemistry of $C_xF_{2x+1}CH=CH_2$ (x=1, 2, 4, 6, and 8): Kinetics of gas-phase reactions with Cl atoms, OH radicals, and O_3, *J. Photochem. Photobio.*, *176*, 124–128, doi:10.1016/j.jphotochem.2005.06.015, 2005.

Takahashi, K., T. Nakayama, Y. Matsumi, S. Solomon, T. Gejo, E. Shigemasa, and T.J. Wallington, Atmospheric lifetime of SF_5CF_3, *Geophys. Res. Lett.*, *29*, doi:10.1029/2002GL015356, 2002.

Taniguchi, N., T.J. Wallington, M.D. Hurley, A.G. Guschin, L.T. Molina, and M.J. Molina, Atmospheric chemistry of $C_2F_5C(O)CF(CF_3)_2$: Photolysis and reaction with Cl atoms, OH radicals, and ozone, *J. Phys. Chem. A*, *107*, 2674–2679, doi:10.1021/jp0220332, 2003.

Tegtmeier, S., K. Krüger, B. Quack, E.L. Atlas, I. Pisso, A. Stohl, and X. Yang, Emission and transport of bromocarbons: From the West Pacific ocean into the stratosphere, *Atmos. Chem. Phys.*, *12*, 10,633–10,648, doi:10.5194/acp-12-10633-2012, 2012.

Tokuhashi, K., A. Takahashi, M. Kaise, and S. Kondo, Rate constants for the reactions of OH radials with CH_3OCF_2CHFCl, CHF_2OCF_2CHFCl, $CHF_2OCHClCF_3$, and $CH_3CH_2OCF_2CHF_2$, *J. Geophys. Res.*, *104*, 18,681–18,688, doi:10.1029/1999JD900278, 1999.

UNEP (United Nations Environment Programme), Handbook for the Montreal Protocol on Substances that Deplete the Ozone Layer, Ozone Secretariat, Vienna Convention for the Protection of the Ozone Layer and the Montreal Protocol on Substances that Deplete the Ozone Layer, 895 pp., Nairobi, Kenya, 2018.

Urata, S., A. Takada, T. Uchimaru, and A.K. Chandra, Rate constants estimation for the reaction of hydrofluorocarbons and hydrofluoroethers with OH radicals, *Chem. Phys. Lett.*, *368*, 215–223, 2003.

Wallington, T.J., M.D. Hurley, J.C. Ball, A.M. Straccia, J. Platz, L.K. Christensen, J. Sehested, and O.J. Nielsen, Atmospheric chemistry of dimethoxymethane ($CH_3OCH_2OCH_3$): Kinetics and mechanism of its reaction with OH radicals and fate of the alkoxy radicals $CH_3OCHO(\bullet)OCH_3$ and $CH_3OCH_2OCH_2O(\bullet)$, *J. Phys. Chem. A*, *101*, 5302–5308, doi:10.1021/jp9631184, 1997.

Wallington, T.J., M.D. Hurley, O.J. Nielsen, and M.P. Sulbaek Andersen, Atmospheric chemistry of $CF_3CFHCF_2OCF_3$ and $CF_3CFHCF_2OCF_2H$: Reaction with Cl atoms and OH radicals, degradation mechanism, and global warming potentials, *J. Phys. Chem. A*, *108*, 11,333–11,338, doi:10.1021/jp046454q, 2004.

Wallington, T.J., B.P. Pivesso, A.M. Lira, J.E. Anderson, C.J. Nielsen, N.H. Andersen, and Ø. Hodnebrog, CH_3Cl, CH_2Cl_2, $CHCl_3$, and CCl_4: Infrared spectra, radiative efficiencies, and global warming potentials, *J. Quant. Spectrosc. Rad. Trans.*, *174*, 56–64, doi:10.1016/j.jqsrt.2016.01.029, 2016.

WMO (World Meteorological Organization), *Scientific Assessment of Ozone Depletion: 2014*, Global Ozone Research and Monitoring Project–Report No. 55, World Meteorological Organization, Geneva, Switzerland, 2014.

Wuebbles, D.J., D. Youn, K. Patten, D. Wang, and M. Martinez-Aviles., Metrics for ozone and climate: Threedimensional modeling studies of ozone depletion potentials and indirect global warming potentials, in Twenty Years of Ozone Decline, in *Proceedings of the Symposium for the 20th Anniversary of the Montreal Protocol*; edited by C. Zerefos, G. Contopoulos, and G. Skalkeas, 297–326, Springer, Netherlands, 2009.

Wuebbles, D.J., K.O. Patten, D. Wang, D. Youn, M. Martínez-Avilés, and J.S. Francisco, Three-dimensional model evaluation of the ozone depletion potentials for n-propyl bromide, trichloroethylene and perchloroethylene, *Atmos. Chem. Phys.*, *11*, 2371–2380, doi:10.5194/acp-11-2371-2011, 2011.

Youn, D., K.O. Patten, D.J. Wuebbles, H. Lee, and C.-W. So, Potential impact of iodinated replacement compounds CF_3I and CH_3I on atmospheric ozone: A three-dimensional modeling study, *Atmos. Chem. Phys.*, *10*, 10,129–10,144, doi:10.5194/acp-10-10129-2010, 2010.

Young, C.J., M.D. Hurley, T.J. Wallington, and S.A. Mabury, Atmospheric lifetime and global warming potential of a perfluoropolyether, *Environ. Sci. Technol.*, *40*, 2242–2246, doi:10.1021/es052077z, 2006.

Young, C.J., M.D. Hurley, T.J. Wallington, and S.A. Mabury, Atmospheric chemistry of CF_3CF_2H and $CF_3CF_2CF_2CF_2H$: Kinetics and products of gas-phase reactions with Cl atoms and OH radicals, infrared spectra, and formation of perfluorocarboxylic acids, *Chem. Phys. Lett.*, *473*, 251–256, doi:10.1016/j.cplett.2009.04.001, 2009a.

Young, C.J., M.D. Hurley, T.J. Wallington, and S.A. Mabury, Atmospheric chemistry of perfluorobutenes ($CF_3CF=CFCF_3$ and $CF_3CF_2CF=CF_2$): Kinetics and mechanisms of reactions with OH radicals and chlorine atoms, IR spectra, global warming potentials, and oxidation to perfluorocarboxylic acids, *Atmos. Environ.*, *43*, 3717–3724, doi:10.1016/j.atmosenv.2009.04.025, 2009b.

Yvon-Lewis, S.A., and J.H. Butler, Effect of oceanic uptake on atmospheric lifetimes of selected trace gases, *J. Geophys. Res.*, *107* (D20), doi:10.1029/2001JD001267, 2002.

Zhang, N., T. Uchimaru, Q. Guo, F. Qing, L. Chen, and J. Mizukado, Atmospheric chemistry of perfluorocyclopentene (cyc-$CF_2CF_2CF_2CF=CF$-): Kinetics, products and mechanism of gas-phase reactions with OH radicals, and atmospheric implications, *Atmos. Environ.*, *160*, 46–54, doi:10.1016/j.atmosenv.2017.04.012, 2017.

Zhang, S., R. Strekowski, L. Bosland, A. Monod, and C. Zetzsch, Kinetic study of the reaction of OH with CH_2I_2, *Phys. Chem. Chem. Phys.*, *13*, 11,671–11,677, doi:10.1039/c1cp20885c, 2011.

Zhang, S., R. Strekowski, A. Monod, L. Bosland, and C. Zetzsch, Temperature-dependent kinetics study of the reactions of OH with C_2H_5I, *n*-C_3H_7I, and iso-C_3H_7I, *J. Phys. Chem. A*, *116*, 9497–9506, doi:10.1021/jp300575f, 2012.

Appendix B

Chemical Formulae and Nomenclature

Reactive Halogen-Containing Species

Cl	atomic chlorine	Br	atomic bromine
Cl_y	total inorganic chlorine	Br_y	total inorganic bromine
Cl_2	molecular chlorine	Br_2	molecular bromine
ClO	chlorine monoxide	BrO	bromine monoxide
ClO_x	(ClO + 2 ClOOCl)	Br_2O	dibromine monoxide
Cl_2O_2, ClOOCl	dichlorine peroxide (ClO dimer)	BrO_x	(Br, BrO, $BrONO_2$, HOBr, ...)
$ClONO_2$, $ClNO_3$	chlorine nitrate	$BrONO_2$, $BrNO_3$	bromine nitrate
HCl	hydrogen chloride (hydrochloric acid)	HBr	hydrogen bromide
HOCl	hypochlorous acid	HOBr	hypobromous acid

F	atomic fluorine	I	atomic iodine
F_2	molecular fluorine	I_2	molecular iodine
F_y	total inorganic fluorine	I_y	total inorganic iodine
HF	hydrogen fluoride (hydrofluoric acid)	IO	iodine monoxide
FO_x	F + FO	IO_x	iodine radicals

Other Reactive Species

O	atomic oxygen	H	atomic hydrogen
$O(^3P)$	atomic oxygen (ground state)	H_2	molecular hydrogen
$O(^1D)$	atomic oxygen (first excited state)	OH	hydroxyl radical
O_2	molecular oxygen	HO_2	hydroperoxyl radical
O_3	ozone	H_2O	water
O_x	odd oxygen (O, $O(^1D)$, O_3)	HO_x	odd hydrogen (H, OH, HO_2, H_2O_2)

N	atomic nitrogen	HNO_2, HONO	nitrous acid
N_2	molecular nitrogen	HOONO	pernitrous acid
N_2O	nitrous oxide	HNO_3	nitric acid
NO	nitric oxide	HNO_4, $HOONO_2$	peroxynitric acid
NO_2	nitrogen dioxide	NH_3	ammonia
NO_3	nitrogen trioxide, nitrate radical	NH_4NO_3	ammonium nitrate
N_2O_5	dinitrogen pentoxide	NO_x	nitrogen oxides ($NO + NO_2$)

Other Reactive Species (continued)

$HNO_3 \bullet 3H_2O$	nitric acid trihydrate condensate (NAT)	NO_y	total reactive nitrogen (NO, NO_2, NO_3, N_2O_5, $ClONO_2$, HNO_4, HNO_3)
S	atomic sulfur		
SO_2	sulfur dioxide	H_2S	hydrogen sulfide
H_2SO_4	sulfuric acid	CS_2	carbon disulfide
CH_3SCH_3	dimethyl sulfide (DMS)	COS, OCS	carbonyl sulfide
C	carbon atom		
CO	carbon monoxide	CO_2	carbon dioxide
CH_3	methyl radical	CH_3CH_3	ethane
CH_4	methane	$CH_3CH_2CH_3$	propane
CH_3OH	methyl alcohol, methanol	$CH_3CH_2CH_2CH_3$	butane
$CF_3C(O)OH$, CF_3CO_2H	trifluoroacetic acid (TFA)	CH_2O	formaldehyde
$CaCO_3$	calcite, calcium carbonate		
TiO_2	titanium dioxide		
Al_2O_3	aluminum oxide		

Note: Table A-1 in Appendix A provides an extensive listing of chemical names and formulas, including many ozone depleting substances, their replacements, and other substances of interest to the Montreal Protocol.

Appendix C

2018 Ozone Assessment Acronym Dictionary

A1	baseline (or most likely) halocarbon scenario of the Ozone Assessment
A1-2006	baseline (or most likely) halocarbon scenario of the 2006 Ozone Assessment
A1-2010	baseline (or most likely) halocarbon scenario of the 2010 Ozone Assessment
A1B	scenario of the IPCC Special Report on Emissions Scenarios (SRES)
A5	Article 5 countries of the Montreal Protocol
AGAGE	Advanced Global Atmospheric Gases Experiment
AAO	Antarctic oscillation
AC	air conditioning
ACC	Antarctic Circumpolar Current
ACCMIP	Atmospheric Chemistry and Climate Model Intercomparison Project
ACE-FTS	Fourier Transform Spectrometer instrument on the Atmospheric Chemistry Experiment satellite
AGAGE	Advanced Global Atmospheric Gases Experiment (atmospheric monitoring surface sites)
AGWP	absolute GWP, which is the radiative forcing integrated over a given time horizon, resulting from a pulse emission of the gas
AMIP	Atmospheric Model Intercomparison Project
AMSU	Advanced Microwave Sounding Unit (satellite-based instrument)
AO	Arctic oscillation
AoA	age of stratospheric air
AR5	IPCC Fifth Assessment Report
ASL	Amundsen Sea Low
ATAL	Asian Tropopause Aerosol Layer
ATLAS	a Lagrangian chemistry and transport model (CTM)
ATT	Cross-Calibrated Multi-Platform products
CCMVal	Chemistry-Climate Model Validation Activity (e.g. CCMVal-2 = Phase 2 of CCMVal)
CDM	Clean Development Mechanism of the Kyoto Protocol
CFCs	chlorofluorocarbons
CFSR	Climate Forecast System Reanalysis
CGAA	Cape Grim Air Archive (atmospheric monitoring surface sites)
CIMS	Chemical Ionization Mass Spectrometer instrument
CLAES	Cryogenic Limb Array Etalon Spectrometry (satellite-based instrument)
CLaMS	Chemical Lagrangian Model of the Stratosphere
CMEs	coronal mass ejections
CMIP	Climate Model Intercomparison Project (e.g. CMIP5 = Phase 5 of CMIP)
CONTRAST	Convective Transport of Active Species in the Tropics (aircraft-based field campaign)
CPT	cold point tropopause
CR-AVE	Costa Rica Aura Validation Experiment (aircraft-based field campaign)
CSIRO	Commonwealth Scientific and Industrial Research Organisation
CTM	chemistry transport model
CUE	Critical use exemption

DJF	December-January-February
DOAS	Differential Optical Absorption Spectroscopy instrument
DU	Dobson Units
ECMWF	European Centre for Medium-Range Weather Forecasts (forecast model)
ECS	equilibrium climate sensitivity
EDGAR	Emissions Database for Global Atmospheric Research
EESC	Equivalent Effective Stratospheric Chlorine
EHF	eddy heat flux
ENSO	El Niño–Southern Oscillation
ENVISAT	Environmental Satellite
EOFs	empirical orthogonal functions
EPA	Environmental Protection Agency
EPP	energetic particle precipitation
ERA	ECMWF Re-Analysis (a global atmospheric reanalysis data product)
EAR-40	ECMWF 40-year Re-Analysis
ERA-Interim	ECMWF Interim Re-Analysis
FPH	frost point hygrometer
FRF	fractional release factor
FTIR	Fourier transform infrared
GAW	Global Atmosphere Watch programme of WMO
GC-ECD	gas chromatography-electron capture detection instrument
GC-MS	gas chromatography-mass spectrometry instrument
GCM	general circulation model
GDP	gross domestic product
GeoMIP	Geoengineering Model Intercomparison Project
GEOSCCM	Goddard Earth Observing System Chemistry Climate Model
GHG	greenhouse gas
GOME	Global Ozone Monitoring Experiment spectrometer (satellite-based instrument)
GOMOS	Global Ozone Monitoring by Occultation of Stars (satellite-based instrument)
GOZCARDS	Global OZone Chemistry And Related trace gas Data records for the Stratosphere
GPS	global positioning system
GSG	GOME-SCIAMACHY-GOME-2 merged dataset
$GtCO_2$-eq	gigatonnes of carbon dioxide equivalent
GTO	the GOME-type Total Ozone column ozone product
GTP	global temperature potential
GWP	global warming potential
HALOE	HALogen Occultation Experiment (satellite-based instrument)
HF	hydrogen fluoride
HCFC	hydrochlorofluorocarbon
HCFO	hydrochlorofluoroolefin
HFC	hydrofluorocarbon
HFE	halogenated ether
HFO	hydrofluoroolefin
HIAPER	High-performance Instrumented Airborne Platform for Environmental Research
HIPPO	HIAPER Pole-to-Pole Observations (aircraft-based field campaign)

HTOC	Halon Technical Options Committee
IASI	Infrared Atmospheric Sounding Interferometer (satellite-based instrument)
IGAC	International Global Atmospheric Chemistry project
IHD	interhemispheric difference
ILT	independent linear trend
IPCC	Intergovernmental Panel on Climate Change
JJA	June-July-August
LCCP	Life Cycle Climate Performance
LIMS	Limb Infrared Monitor of the Stratosphere (satellite-based instrument)
LOTUS	Long-term Ozone Trends and Uncertainties in the Stratosphere (a SPARC activity)
LS	lower stratosphere
LZRH	level of zero radiative heating
MAC	mobile air conditioning
MAGICC6	Model for the Assessment of Greenhouse Gas Induced Climate Change
MAM	March-April-May
MBL	marine boundary layer
MERRA	Modern Era Retrospective-analysis for Research and Applications (e.g. MERRA-2 = version 2 of MERRA)
MIPAS	Michelson Interferometer for Passive Atmospheric Sounding
MIPAS-B	balloon-based Michelson Interferometer for Passive Atmospheric Sounding
MLF	Montreal Protocol's Multilateral Fund
MLR	multiple linear regression
MLS	Microwave Limb Sounder (satellite-based instrument)
MMM	multi-model mean
MOD	merged ozone dataset
MSU	Microwave Sounding Unit (satellite-based instrument)
MZM	monthly zonal mean
NAM	Northern Annular Mode
NAO	North Atlantic oscillation
NASA	National Aeronautics and Space Administration (United States)
NAT	nitric acid trihydrate
NCEP	National Centers for Environmental Prediction (NOAA; United States)
NCEP/CFSR	NCEP Climate Forecast System Reanalysis (data product)
NDACC	Network for the Detection of Atmospheric Composition Change
NDCs	Nationally Determined Contributions within the Paris Agreement within the UNFCCC
NH	Northern Hemisphere
NIES	National Institute for Environmental Studies (Japan)
NIK	not-in-kind
NOAA	National Oceanic and Atmospheric Administration (United States)
NRLSSI	Naval Research Laboratory Spectral Solar Irradiance model
OCS	carbonyl sulfide (also COS)
ODP	ozone depletion potential
ODS	ozone-depleting substance
OMD	ozone hole mass deficit

OMI	Ozone Monitoring Instrument (satellite-based instrument)
OMPS	Ozone Mapping Profiler Suite (satellite-based instrument)
OPCs	optical particle counters
OSIRIS	Optical Spectrograph and InfraRed Imaging System (satellite-based instrument)
PCE	perchloroethylene, also known as tetrachloroethylene
PCO	partial column ozone
PFC	perfluorocarbon
PG	product gas
PGI	product gas injection
Pre-AVE	Pre- Aura Validation Experiment (field campaign)
PSC	polar stratospheric cloud
PWLT	piecewise linear trend
PWT	piecewise trend
QBO	Quasi-Biennial Oscillation
QPS	quarantine and pre-shipment
RCP	Representative Concentration Pathway (used by IPCC)
RF	radiative forcing
S-RIP	WCRP SPARC Reanalysis Intercomparison Project
SABER	Sounding of the Atmosphere using Broadband Emission Radiometry (satellite-based instrument)
SAGE	Stratospheric Aerosol and Gas Experiment (satellite-based instrument)
SAM	southern annular mode
SAP	UNEP Scientific Assessment Panel to the Parties of the Montreal Protocol
SATIRE-S	Spectral and Total Irradiance Reconstruction—Satellite era model
SBUV / SBUV MOD / SBUV COH	Solar Backscatter Ultraviolet (satellite-based instrument) / Merged Ozone Data (MOD) product / SBUV Cohesive dataset
SCIAMACHY	SCanning Imaging Absorption spectroMeter for Atmospheric CHartographY (satellite-based instrument)
SCISAT	SCIence SATellite
SG	source gas
SGI	source gas injection
SH	Southern Hemisphere
SHADOZ	Southern Hemisphere Additional Ozonesondes
SHIVA	Stratospheric ozone Halogen Impacts in a Varying Atmosphere (field experiment)
SLIMCAT	Single-Layer Isentropic Model of Chemistry and Transport
SLR	sea level rise
SNAP	Significant New Alternatives Policy
SON	September-October-November
SOR	solar ozone response
SORCE	Solar Radiation and Climate Experiment
SPARC	Stratospheric Processes And their Role in Climate (project of WCRP)
SPEs	solar proton events
SRES	Special Report on Emissions Scenarios (used by IPCC)
SSI	solar spectral irradiance
SSP	Shared Socioeconomic Pathway

SST	sea surface temperature
SSU	Stratospheric Sounding Unit (satellite-based instrument)
SSW	sudden stratospheric warming
STAR	The NOAA Center for Satellite Applications and Research
STE	stratosphere-troposphere exchange
STT	stratosphere-to-troposphere transport
Suomi NPP	Suomi National Polar-orbiting Partnership weather satellite
SWOOSH	Stratospheric Water and OzOne Satellite Homogenized (merged data record)
SWV	stratospheric water vapor
SZA	solar zenith angle
TC4	Tropical Composition, Cloud and Climate Coupling (aircraft-based field experiment)
TCE	trichloroethene, trichloroethylene
TCO	total column ozone
TEAP	UNEP Technology and Economic Assessment Panel to the Parties of the Montreal Protocol
TELIS	TEtrahertz and submillimeter LImb Sounder (satellite-based instrument)
TES	Tropospheric Emission Spectrometer
TFA	trifluoroacetic acid
TOAR	Tropospheric Ozone Assessment Report
TOMCAT	Toulouse Off-line Model of Chemistry and Transport
TOMS	Total Ozone Mapping Spectrometer (satellite-based instrument)
TP	tropopause pressure
TransCom-VSLS	A multi-model intercomparison of halogenated very short-lived substances
TSI	total solar irradiance
TTL	tropical tropopause layer
UARS	Upper Atmosphere Research Satellite
UCI	University of California Irvine
UEA	University of East Anglia
UNEP	United Nations Environment Programme
UNFCCC	United Nations Framework Convention on Climate Change
US	upper stratosphere
UT	upper troposphere
UTLS	upper troposphere/lower stratosphere
UV	ultraviolet
VEI	Volcanic Explosivity Index
VSL SG	Very Short-Lived Source Gas
VSLS	very short-lived substance
WACCM	Whole Atmosphere Community Climate Model
WCRP	World Climate Research Programme
WMO	World Meteorological Organization
WOUDC	World Ozone and Ultraviolet Radiation Data Centre of WMO/GAW

Appendix D

List of Authors, Contributors, and Reviewers

Assessment Co-chairs

David W. Fahey	NOAA Earth System Research Laboratory, Chemical Sciences Division	USA
Paul A. Newman	NASA Goddard Space Flight Center	USA
John A. Pyle	University of Cambridge and the National Centre for Atmospheric Science	UK
Bonfils Safari	University of Rwanda, College of Science and Technology, Kigali	Rwanda

Assessment Scientific Steering Committee

David W. Fahey	NOAA Earth System Research Laboratory, Chemical Sciences Division	USA
Paul A. Newman	NASA Goddard Space Flight Center	USA
John A. Pyle	University of Cambridge and the National Centre for Atmospheric Science	UK
Bonfils Safari	University of Rwanda, College of Science and Technology, Kigali	Rwanda
Martyn P. Chipperfield	University of Leeds	UK
David J. Karoly	Climate Science Centre, Commonwealth Scientific and Industrial Research Organisation (CSIRO), Aspendale, Victoria	Australia
Doug Kinnison	National Center for Atmospheric Research (NCAR)	USA
Malcolm K. Ko	NASA Langley Research Center	USA
Michelle Santee	NASA Jet Propulsion Laboratory (JPL)	USA

Assessment Coordinator

Sarah J. Doherty	University of Colorado, Cooperative Institute for Research in Environmental Sciences at NOAA Earth System Research Laboratory, Chemical Sciences Division	USA

Coordinating Lead Authors

Chapter 1: Update on Ozone-Depleting Substances (ODSs) and Other Gases of Interest to the Montreal Protocol

Andreas Engel	Goethe Universität, Frankfurt	Germany
Matthew Rigby	University of Bristol, School of Chemistry	UK

Chapter 2: Hydrofluorocarbons (HFCs)

Stephen A. Montzka	NOAA Earth System Research Laboratory, Global Monitoring Division	USA
Guus J.M. Velders	Dutch National Institute for Public Health and Environment (RIVM), Bilthoven & Utrecht University	The Netherlands

Chapter 3: Update on Global Ozone: Past, Present, and Future

Peter Braesicke	Institute of Meteorology and Climate Research (IMK) Atmospheric Trace Gases and Remote Sensing (ASF) Karlsruher Institut für Technologie (KIT)	Germany
Jessica Neu	NASA Jet Propulsion Laboratory (JPL)	USA

Chapter 4: Polar Stratospheric Ozone: Past, Present, and Future

Ulrike Langematz	Freie Universität Berlin, Berlin	Germany
Matthew B. Tully	Bureau of Meteorology, Melbourne	Australia

Chapter 5: Stratospheric Ozone Changes and Climate

Alexey Yu. Karpechko	Finnish Meteorological Institute, Helsinki	Finland
Amanda C. Maycock	University of Leeds	UK

Chapter 6: Scenarios and Information for Policymakers

Lucy J. Carpenter	University of York	UK
John S. Daniel	NOAA Earth System Research Laboratory, Chemical Sciences Division	USA

Scientific Assessment of Ozone Depletion: 2018: Appendix A Table

James B. Burkholder	NOAA Earth System Research Laboratory, Chemical Sciences Division	USA

20 Questions and Answers About the Ozone Layer

Sarah J. Doherty	University of Colorado, Cooperative Institute for Research in Environmental Sciences at NOAA Earth System Research Laboratory, Chemical Sciences Division	USA
David W. Fahey	NOAA Earth System Research Laboratory, Chemical Sciences Division	USA
Michaela I. Hegglin	University of Reading	UK
Ross J. Salawitch	Department of Atmospheric and Oceanic Science & Department of Chemistry and Biochemistry, Earth System Science Interdisciplinary Center, University of Maryland, College Park	USA

Co-Authors

Chapter 1: Update on Ozone-Depleting Substances (ODSs) and Other Gases of Interest to the Montreal Protocol

James B. Burkholder	NOAA Earth System Research Laboratory, Chemical Sciences Division	USA
Rafael P. Fernandez	Consejo Nacional de Investigaciones Cientificas y Técnicas (CONICET)	Argentina
Lucien Froidevaux	NASA Jet Propulsion Laboratory (JPL), California Institute of Technology	USA
Bradeley D. Hall	NOAA Earth System Research Laboratory, Global Monitoring Division	USA
Ryan Hossaini	Lancaster Environment Centre, Lancaster University	UK
Takuya Saito	National Institute for Environmental Studies (NIES) Center for Environmental Measurement and Analysis	Japan
Martin K. Vollmer	Swiss Federal Laboratories for Materials Science and Technology (EMPA)	Switzerland
Bo Yao	China Meteorological Administration (CMA) Meteorological Observation Centre (MOC)	China

Chapter 2: Hydrofluorocarbons (HFCs)

Paul B. Krummel	Climate Science Centre, Commonwealth Scientific and Industrial Research Organisation (CSIRO) Oceans and Atmosphere	Australia
Jens Mühle	Scripps Institution of Oceanography, University of California, San Diego	USA
Vladimir Orkin	National Institute of Standards and Technology (NIST)	USA
Sunyoung Park	Department of Oceanography, School of Earth System Sciences Kyungpook National University	South Korea
Nihar Shah	Lawrence Berkeley National Laboratory	USA
Helen Walter-Terrinoni	Technology and Econominc Assessment Panel (TEAP) of the Montreal Protocol The Chemours Company	USA

Chapter 3: Update on Global Ozone: Past, Present, and Future

Vitali Fioletov	Environment and Climate Change Canada (ECCC)	Canada
Sophie Godin-Beekmann	Laboratoire Atmosphères, Milieux, Observations Spatiales (LATMOS), Centre National de la Recherche Scientifique (CNRS), Sorbonne University	France
Daan Hubert	Royal Belgian Institute for Space Aeronomy (BIRA-IASB)	Belgium
Irina Petropavlovskikh	University of Colorado, Cooperative Institute for Research in Environmental Sciences at NOAA Earth System Research Laboratory, Global Monitoring Division	USA
Masato Shiotani	Research Institute for Sustainable Humanosphere, Kyoto University	Japan
Björn-Martin Sinnhuber	Institute of Meteorology and Climate Research (IMK) Atmospheric Trace Gases and Remote Sensing (ASF) Karlsruher Institut für Technologie (KIT)	Germany

Chapter 4: Polar Stratospheric Ozone: Past, Present, and Future

Natalia Calvo	Universidad Complutense de Madrid	Spain
Martin Dameris	Deutsches Zentrum für Luft- und Raumfahrt (DLR) Institut für Physik der Atmosphäre	Germany
A. T. J. de Laat	Royal Netherlands Meteorological Institute	The Netherlands
Andrew Klekociuk	Australian Antarctic Division	Australia
Rolf Müller	Forschungszentrum Jülich GmbH	Germany
Paul Young	Lancaster University	UK

Chapter 5: Stratospheric Ozone Changes and Climate

Marta Abalos	Universidad Complutense de Madrid	Spain
Hideharu Akiyoshi	National Institute for Environmental Studies (NIES)	Japan
Julie Arblaster	Monash University	Australia
Chaim Garfinkel	The Hebrew University of Jerusalem	Israel
Karen H. Rosenlof	NOAA Earth System Research Laboratory, Chemical Sciences Division	USA
Michael Sigmond	Environment and Climate Change Canada (ECCC)	Canada

Chapter 6: Scenarios and Information for Policymakers

Eric L. Fleming	Science Systems and Applications, Inc. & NASA Goddard Space Flight Center	USA
Tatsuya Hanaoka	National Institute for Environmental Studies	Japan
Jianxin Hu	Peking University	China
A.R. Ravishankara	Colorado State University, Fort Collins, Colorado	USA
Martin N. Ross	The Aerospace Corporation	USA
Simone Tilmes	National Center for Atmospheric Research (NCAR)	USA
Timothy J. Wallington	Ford Motor Company	USA

Donald J. Wuebbles	University of Illinois	USA

Contributing Authors

Chapter 1: Update on Ozone-Depleting Substances (ODSs) and Other Gases of Interest to the Montreal Protocol

Elliot L. Atlas	University of Miami, Rosenstiel School of Marine and Atmospheric Science, Department of Atmospheric Sciences	USA
Peter F. Bernath	Old Dominion University, Department of Chemistry and Biochemistry & University of Waterloo, Department of Chemistry	USA/Canada
Donald R. Blake	University of California, Irvine, Department of Chemistry	USA
Geoff Dutton	NOAA Earth System Research Laboratory, Global Monitoring Division	USA
Paul B. Krummel	Climate Science Centre, Commonwealth Scientific and Industrial Research Organisation (CSIRO) Oceans and Atmosphere	Australia
Johannes C. Laube	University of East Anglia, School of Environmental Sciences	UK
Emmanuel Mahieu	University of Liège, Institute of Astrophysics and Geophysics	Belgium
Stephen A. Montzka	NOAA Earth System Research Laboratory, Global Monitoring Division	USA
Jens Mühle	Scripps Institution of Oceanography, University of California, San Diego	USA
Gerald Nedoluha	Naval Research Laboratory	USA
Simon O'Doherty	University of Bristol, School of Chemistry	UK
David E. Oram	University of East Anglia, School of Environmental Sciences and National Centre for Atmospheric Sciences	UK
Klaus Pfeilsticker	University of Heidelberg, Institut für Umweltphysik	Germany
Ronald G. Prinn	Massachusetts Institute of Technology (MIT), Center for Global Change Science	USA
Birgit Quack	GEOMAR Helmholtz Centre for Ocean Research Kiel	Germany
Isobel J. Simpson	University of California, Irvine, Department Of Chemistry	USA
Ray F. Weiss	Scripps Institution of Oceanography, University of California, San Diego	USA

Chapter 2: Hydrofluorocarbons (HFCs)

Peter F. Bernath	Old Dominion University, Department of Chemistry and Biochemistry & University of Waterloo, Department of Chemistry	USA/Canada
Chris Boone	Department of Chemistry, University of Waterloo	Canada
Lei Hu	University of Colorado, Cooperative Institute for Research in Environmental Sciences at NOAA Earth System Research Laboratory, Global Monitoring Division	USA
Michael J. Kurylo	Universities Space Research Association Goddard Earth Sciences, Technology, and Research (USRA/GESTAR)	USA
Emma Leedham Elvidge	Center for Ocean and Atmospheric Sciences School of Environmental Sciences, University East Anglia	UK
Michela Maione	Univerità di Urbino and National Research Council	Italy
Benjamin R. Miller	University of Colorado, Cooperative Institute for Research in Environmental Sciences at NOAA Earth System Research Laboratory, Global Monitoring Division	USA
Simon O'Doherty	University of Bristol, School of Chemistry	UK
Matthew Rigby	University of Bristol, School of Chemistry	UK
Isobel J. Simpson	University of California, Irvine, Department of Chemistry	USA
Martin K. Vollmer	Swiss Federal Laboratories for Materials Science and Technology (EMPA)	Switzerland
Ray F. Weiss	Scripps Institution of Oceanography, University of California, San Diego	USA

Chapter 3: Update on Global Ozone: Past, Present, and Future

William Ball	Institute for Atmospheric and Climate Science, ETH Zürich & Physikalisch-Meteorologisches Observatorium Davos World Radiation Center	Switzerland
Kai-Lan Chang	NOAA Earth System Research Laboratory, Global Monitoring Division	USA
Robert Damadeo	NASA Langley Research Center	USA
Sandip Dhomse	School of Earth and Environment, University of Leeds	UK
Stacey M. Frith	Science Systems and Applications, Inc. & NASA Goddard Space Flight Center	USA
Audrey Gaudel	University of Colorado, Cooperative Institute for Research in Environmental Sciences at NOAA Earth System Research Laboratory, Chemical Sciences Division	USA
Birgit Hassler	Institut für Physik der Atmosphäre (IPA) Deutsches Zentrum für Luft- und Raumfahrt (DLR)	Germany
Stefanie Kremser	Bodeker Scientific	New Zealand
Stergios Misios	Atmospheric Physics Clarendon Laboratory, University of Oxford	UK
Olaf Morgenstern	National Institute of Water and Atmospheric Research Ltd (NIWA)	New Zealand
Ross J. Salawitch	Department of Atmospheric and Oceanic Science & Department of Chemistry and Biochemistry, Earth System Science Interdisciplinary Center, University of Maryland, College Park	USA
Viktoria F. Sofieva	Finnish Meteorological Institute, Helsinki	Finland
Kleareti Tourpali	Laboratory of Atmospheric Physics, Aristotle University of Thessaloniki	Greece
Olga Tweedy	Johns Hopkins University, Department of Earth and Planetary Sciences	USA
Daniel Zawada	University of Saskatchewan, Department of Physics and Engineering Physics	Canada

Chapter 4: Polar Stratospheric Ozone: Past, Present, and Future

Simon Alexander	Australian Antarctic Division	Australia
Sandip Dhomse	University of Leeds	UK
Bernd Funke	Instituto de Astrofísica de Andalucía, CSIC	Spain
Peter von der Gathen	Alfred Wegener Institute, Helmholtz Centre for Polar and Marine Research	Germany
Jens-Uwe Grooß	Forschungszentrum Jülich GmbH	Germany
Stefanie Kremser	Bodeker Scientific	New Zealand
Gloria L. Manney	NorthWest Research Associates & New Mexico Institute of Mining and Technology	USA
Sergej Molleker	Max-Planck-Institut for Chemistry	Germany
Eric Nash	Science Systems and Applications, Inc.	USA
Michael C. Pitts	NASA Langley Research Center	USA
Alfonso Saiz-López	Institute of Physical Chemistry Rocasolano	Spain
Franziska Schmidt	Freie Universität Berlin, Institut für Meteorologie	Germany
Miriam Sinnhuber	Karlsruher Institut für Technologie (KIT)	Germany
Reinhold Spang	Forschungszentrum Jülich GmbH	Germany
Ines Tritscher	Forschungszentrum Jülich GmbH	Germany
Mark Weber	Institute of Environmental Physics, Universität Bremen	Germany

Chapter 5: Stratospheric Ozone Changes and Climate

Valentina Aquila	American University, Washington, DC	USA
Antara Banerjee	Columbia University	USA
Andreas Chrysanthou	University of Leeds	UK
David Ferreira	University of Reading	UK

Hella Garny	Deutsches Zentrum für Luft- und Raumfahrt (DLR)	Germany
Nathan P. Gillett	Canadian Centre for Climate Modelling and Analysis and Environment and Climate Change Canada (ECCC)	Canada
Peter Landschützer	Max-Planck-Institut für Meteorologie	Germany
Eun-Pa Lim	Bureau of Meteorology	Australia
Michael J. Mills	Atmospheric Chemistry Observations & Modeling (ACOM) National Center for Atmospheric Research (NCAR)	USA
William J. Randel	Atmospheric Chemistry Observations & Modeling (ACOM) National Center for Atmospheric Research (NCAR)	USA
Eric Ray	University of Colorado, Cooperative Institute for Research in Environmental Sciences at NOAA Earth System Research Laboratory, Chemical Sciences Division	USA
William Seviour	Johns Hopkins University	USA
Seok-Woo Son	Seoul National University	South Korea
Neil Swart	Environment and Climate Change Canada (ECCC)	Canada

Chapter 6: Scenarios and Information for Policymakers

James B. Burkholder	NOAA Earth System Research Laboratory, Chemical Sciences Division	USA
Andreas Engel	Goethe Universität, Frankfurt	Germany
Øivind Hodnebrog	Center for International Climate Research (CICERO)	Norway
Ryan Hossaini	Lancaster Environment Centre, Lancaster University	UK
Lambert J.M. Kuijpers	Eindhoven University of Technology, A/genT Consultancy	The Netherlands
Stephen A. Montzka	NOAA Earth System Research Laboratory, Global Monitoring Division	USA
Ross J. Salawitch	Department of Atmospheric and Oceanic Science & Department of Chemistry and Biochemistry, Earth System Science Interdisciplinary Center, University of Maryland, College Park	USA
Walter Tribett	University of Maryland, College Park	USA
Guus J.M. Velders	Dutch National Institute for Public Health and Environment (RIVM), Bilthoven & Utrecht University	The Netherlands
Helen Walter-Terrinoni	Technology and Econominc Assessment Panel (TEAP) of the Montreal Protocol The Chemours Company	USA

Scientific Assessment of Ozone Depletion: 2018: Appendix Tables

Øivind Hodnebrog	Center for International Climate Research (CICERO)	Norway
Vladimir L. Orkin	National Institute of Standards and Technology	USA

Review Editors

Chapter 1: Update on Ozone-Depleting Substances (ODSs) and Other Gases of Interest to the Montreal Protocol

Qing Liang	NASA Goddard Space Flight Center	USA
Stefan Reimann	Swiss Federal Laboratories for Materials Science and Technology (EMPA)	Switzerland

Chapter 2: Hydrofluorocarbons (HFCs)

Lambert J.M. Kuijpers	Eindhoven University of Technology, A/genT Consultancy	The Netherlands
Bill Sturges	School of Environmental Sciences, University of East Anglia	UK

Chapter 3: Update on Global Ozone: Past, Present, and Future

Wolfgang Steinbrecht	Meteorological Observatory Hohenpeissenberg Deutscher Wetterdienst (DWD)	Germany
Mark Weber	Institute of Environmental Physics, Universität Bremen	Germany

Chapter 4: Polar Stratospheric Ozone: Past, Present, and Future

William J. Randel	Atmospheric Chemistry Observations & Modeling (ACOM) National Center for Atmospheric Research (NCAR)	USA
Susan Solomon	Massachusetts Institute of Technology (MIT)	USA

Chapter 5: Stratospheric Ozone Changes and Climate

Chiara Cagnazzo	Italian National Research Council, Rome	Italy
Lorenzo Polvani	Columbia University, New York	USA

Chapter 6: Scenarios and Information for Policymakers

Neil Harris	Cranfield University	UK
Michael Prather	University of California, Irvine	USA

Reviewers

Georgios Amanatidis	European Parliament	Belgium
Mads P. Sulbæk Andersen	California State University, Northridge & University of Copenhagen	USA/Denmark
Valentina Aquila	American University, Washington, D.C.	USA
Tim Arnold	National Physical Laboratory & University of Edinburgh	UK
Matthew Ashfold	University of Nottingham Malaysia Campus	Malaysia
Pieter Aucamp	Environmental Effects Assessment Panel (EEAP) / Ptersa Environmental Consultants	South Africa
Alkiviadis F. Bais	Aristotle University of Thessaloniki, Laboratory of Atmospheric Physics	Greece
William Ball	Institute for Atmospheric and Climate Science, ETH Zürich & Physikalisch-Meteorologisches Observatorium Davos World Radiation Centre	Switzerland
Slimane Bekki	Centre National de la Recherche Scientifique (CNRS)	France
Germar Bernhard	Biospherical Instruments, Inc.	USA
P.K. Bhartia	NASA Goddard Space Flight Center	USA
Nicola Blake	University of California, Irvine, Department of Chemistry	USA
Greg Bodeker	Bodeker Scientific	New Zealand
Adam Bourassa	University of Saskatchewan	Canada
John Burrows	University of Bremen	Germany
Amy Butler	University of Colorado, Cooperative Institute for Research in Environmental Sciences at NOAA Earth System Research Laboratory, Chemical Sciences Division	USA
Pablo Canziani	Consejo Nacional de Investigaciones Cientificas y Técnicas (CONICET) Universidad Tecnológica Nacional, Buenos Aires (UTN.BA)	Argentina
Andrew Charlton-Perez	University of Reading	UK
Cathy Clerbaux	Centre National de la Recherche Scientifique (CNRS) & Université Pierre et Marie Curie	France
Melanie Coldewey-Egbers	Deutsches Zentrum für Luft- und Raumfahrt (DLR)	Germany
Robert Damadeo	NASA Langley Research Center	USA

Sean Davis	University of Colorado, Cooperative Institute for Research in Environmental Sciences at NOAA Earth System Research Laboratory, Chemical Sciences Division	USA
Mohamdou Diallo	Institute for Energy and Climate Research Stratosphere (IEK-7) & Forschungszentrum Jülich GmbH	Germany
Anne Douglass	NASA Goddard Space Flight Center	USA
Richard Eckman	NASA Headquarters	USA
Paul Fraser	Climate Science Centre, Commonwealth Scientific and Industrial Research Organization (CSIRO)	Australia
Lucien Froidevaux	NASA Jet Propulsion Laboratory (JPL), California Institute of Technology	USA
Jan Fuglestvedt	Center for International Climate Research (CICERO)	Norway
Ann M. Gabriel	Department of the Environment and Energy	Australia
Hella Garny	Deutsches Zentrum für Luft- und Raumfahrt (DLR)	Germany
Jimmy Gasore	University of Rwanda, College of Science and Technology Department of Physics, Kigali	Rwanda
Edwin P. Gerber	Courant Institute of Mathematical Sciences, New York University	USA
Andrew Gettleman	National Center for Atmospheric Research (NCAR)	USA
Nathan P. Gillett	Canadian Centre for Climate Modelling and Analysis and Environment and Climate Change Canada (ECCC)	Canada
William Goetzler	Navigant Consulting, Inc.	USA
Jens-Uwe Grooß	Forschungszentrum Jülich GmbH	Germany
Joanna Haigh	Imperial College London	UK
Alain Hauchecorne	Laboratoire Atmosphères, Milieux, Observations Spatiales (LATMOS), Centre National de la Recherche Scientifique (CNRS)/IPSL Université de Versailles Staint Quentin-en-Yvelines (UVSQ), UPMC	France
Peter Hitchcock	Laboratoire de Meteorologie Dynamique (LMD) Ecole polytechnique, Palaiseau	France
Lei Hu	University of Colorado, Cooperative Institute for Research in Environmental Sciences at NOAA Earth System Research Laboratory, Global Monitoring Division	USA
Nathalie Huret	LPC2E Centre National de la Recherche Scientifique (CNRS)	France
Imre M. Jánosi	ELTE Eötvös Loránd University, Budapest	Hungary
Julie Jones	Department of Geography, University of Sheffield	UK
Yasuko Kasai	National Institute of Information and Communications (NICT), Tokyo	Japan
Jooil Kim	Scripps Institution of Oceanography, University of California, San Diego	USA
Jeff Knight	Met Office Hadley Center	UK
Michael J. Kurylo	Universities Space Research Association Goddard Earth Sciences, Technology, and Research) (USRA/GESTAR)	USA
Susan Gabriela Lakkis	Pontificia Universidad Católica Argentina, Facultad de Ingeniería y Ciencias Agrarias (UCA); Universidad Tecnológica Nacional Unidad de Investigación y Desarrollo de las Ingenierías Facultad Regional Buenos Aires (UTN.BA)	Argentina
Johannes C. Laube	University of East Anglia, School of Environmental Sciences	UK
Kathy Law	Laboratoire Atmosphères, Milieux, Observations Spatiales (LATMOS), Centre National de la Recherche Scientifique (CNRS)/IPSL Université de Versailles Staint Quentin-en-Yvelines (UVSQ), UPMC	France
Sunday Leonard	STAP-GEF, UN Environment	Kenya
Pu Lin	Program in Atmospheric and Oceanic Sciences, Princeton University & NOAA Geophysical Fluid Dynamics Laboratory	USA
Jintai Lin	Peking University	China

Nathaniel Livesey	NASA Jet Propulsion Laboratory (JPL), California Institute of Technology	USA
Sasha Madronich	National Center for Atmospheric Research (NCAR)	USA
Michela Maione	Univerità di Urbino and National Research Council	Italy
Martin R. Manning	Victoria University of Wellington	New Zealand
Katja Matthes	GEOMAR Helmholtz Centre for Ocean Research Kiel & Christian-Albrechts-Universität zu Kiel	Germany
Archie McCulloch	Atmospheric Chemistry Research Group, University of Bristol	UK
Richard L. McKenzie	National Institute of Water and Atmospheric Research Ltd (NIWA Lauder)	New Zealand
Johan Mellqvist	Chalmers University of Technology	Sweden
Pauline M. Midgley	Independent Consultant	Germany
Olaf Morgenstern	National Institute of Water and Atmospheric Research Ltd (NIWA)	New Zealand
Vaishali Naik	NOAA Geophysical Fluid Dynamics Laboratory	USA
Hiroaki Naoe	Meteorological Research Institute	Japan
Simon O'Doherty	University of Bristol, School of Chemistry	UK
Luke Oman	NASA Goddard Space Flight Center	USA
David E. Oram	University of East Anglia, School of Environmental Sciences and National Centre for Atmospheric Sciences	UK
Andrew Orr	British Antarctic Survey (BAS)	UK
Prabir Patra	JAMSTEC (Japan Agency for Marine-Earth Science & Technology)	Japan
Andrea Pazmiño	Laboratoire Atmosphères, Milieux, Observations Spatiales (LATMOS), Centre National de la Recherche Scientifique (CNRS) Université de Versailles Staint Quentin-en-Yvelines (UVSQ)	France
Judith Perlwitz	University of Colorado, Cooperative Institute for Research in Environmental Sciences at NOAA Earth System Research Laboratory, Physical Sciences Division	USA
Thomas Peter	ETH Zürich	Switzerland
Damaris Kirsch Pinheiro	UFSM - Federal University of Santa Maria	Brazil
Giovanni Pitari	Università dell'Aquila - Department of Physical and Chemical Sciences	Italy
Michael C. Pitts	NASA Langley Research Center	USA
Marta Pizano	Consultant	Colombia
Felix Ploeger	Institute of Energy and Climate Research (IEK-7) Forschungszentrum Jülich GmbH	Germany
David Plummer	Environment and Climate Change Canada (ECCC)	Canada
Jean-Pierre Pommereau	Laboratoire Atmosphères, Milieux, Observations Spatiales (LATMOS), Centre national de la recherche scientifique (CNRS) Université de Saint Quentin (UVSQ)	France
Robert W. Portmann	University of Colorado, Cooperative Institute for Research in Environmental Sciences at NOAA Earth System Research Laboratory, Chemical Sciences Division	USA
V. Ramaswamy	NOAA Geophysical Fluid Dynamics Laboratory	USA
Marilyn Raphael	University of California, Los Angeles	USA
Piera Raspollini	Istituto di Fisica Applicata "Nello Carrara" Consiglio Nazionale delle Ricerche (IFAC-CNR)	Italy
Claire Reeves	University of East Anglia	UK
Andy Reisinger	New Zealand Agricultural Greenhouse Gas Research Centre	New Zealand
James Renwick	Victoria University of Wellington	New Zealand
Rob Rhew	University of California, Berkeley	USA
Harald Rieder	University of Graz, Wegener Center for Climate and Global Change	Austria
Martin Riese	Forschungszentrum Jülich GmbH	Germany

Alan Robock	Rutgers University	USA
Karen H. Rosenlof	NOAA Earth System Research Laboratory, Chemical Sciences Division	USA
Alfonso Saiz-López	Institute of Physical Chemistry Rocasolano	Spain
Ross J. Salawitch	Department of Atmospheric and Oceanic Science & Department of Chemistry and Biochemistry, Earth System Science Interdisciplinary Center, University of Maryland, College Park	USA
Kaoru Sato	Department of Earth and Planetary Science, University of Tokyo	Japan
Adam Scaife	Met Office Hadley Center (MOHC)	UK
Sue Schauffler	National Center for Atmospheric Research (NCAR)	USA
Robyn Schofield	University of Melbourne	Australia
Jonathan Shanklin	British Antarctic Survey (BAS)	UK
Rajendra Shende	Technology, Education, Research and Rehabilitation for the Environment (TERRE) Policy Centre	India
Keith Shine	Department of Meteorology, University of Reading	UK
Rajiv Singh	Honeywell International	USA
Miriam Sinnhuber	Karlsruher Institut für Technologie (KIT)	Germany
Karen Smith	University of Toronto Scarborough	Canada
Keith Solomon	UN Environment, Ozone Secretariat & Center for Toxicology, University of Guelph	Kenya/Canada
Gabi Stiller	Karlsruher Institut für Technologie (KIT) Institute of Meteorology and Climate Research (IMK)	Germany
Susan Strahan	NASA Goddard Space Flight Center	USA
Tove Svendby	Norwegian Institute for Air Research (NILU)	Norway
David Tarasick	Environment and Climate Change Canada (ECCC)	Canada
Larry W. Thomason	NASA Langley Research Center	USA
Roland van der A	Royal Netherlands Meteorological Institute (RNMI)	The Netherlands
Carolina Vera	Universidad Tecnológica Nacional, Buenos Aires (UTN.BA) Centro de Investigaciones del Mar y de la Atmoósfera (CIMA) Consejo Nacional de Investigaciones Cientificas y Técnicas (CONICET)	Argentina
Jean-Paul Vernier	NASA Langley Research Center	USA
Thomas von Clarmann	Karlsruher Institut für Technologie (KIT) Institute of Meteorology and Climate Research (IMK)	Germany
Christian von Savigny	University of Greifswald	Germany
Krzysztof Wargan	Science Systems and Applications (SSAI) & Global Modeling and Assimilation Office NASA Goddard Space Flight Center	USA
Ray F. Weiss	Scripps Institution of Oceanography, Univesity of California, San Diego	USA
David Wilmouth	Harvard University	USA
Stephen Wilson	Centre for Atmospheric Chemistry, University of Wollongong	Australia
Caradee Wright	South African Medical Research Council and University of Pretoria	South Africa
Yangyang Xu	Texas A&M University	USA
Shigeo Yoden	Kyoto University	Japan
Yoko Yokouchi	National Institute for Environmental Studies (visiting scientist)	Japan
Adrián Yuchechen	Universidad Tecnológica Nacional, Buenos Aires (UTN.BA) Consejo Nacional de Investigaciones Científicas y Técnicas (CONICET) Unidad de Investigación y Desarrollo de las Ingenierías (UIDI)	Argentina
Durwood Zaelke	Institute for Governance and Sustainable Development (IGSD)	USA

Sponsoring Organizations and Liaisons

Tina Birmpili	UN Environment, Ozone Secretariat	Kenya
Geir Braathen	World Meteorological Organization (WMO)	Switzerland
Vincent-Henri Peuch	European Commission, Liaison European Centre for Medium-Range Weather Forecasts (ECMWF)	UK
Jack Kaye	NASA Headquarters	USA
David W. Fahey	NOAA Earth System Research Laboratory, Chemical Sciences Division	USA
David Dokken	United States Global Change Research Program (USGCRP)	USA

Organizational Liaisons

Pieter Aucamp	Environmental Effects Assessment Panel (EEAP) of the Montreal Protocol & Ptersa Environmental Consultants	South Africa
Marco Gonzáles	Senior member Technology and Economic Assessment Panel (TEAP) of the Montreal Protocol & Former Executive Secretary, Ozone Secretariat	Costa Rica
Lambert J.M. Kuijpers	Eindhoven Univeisty of Technology, A/genT Consultancy	The Netherlands
Bella Maranion	Co-Chair of the Technology and Economic Assessment Panel (TEAP) of the Montreal Protocol & U.S. Environmental Protection Agency (EPA)	USA
Helen Walter-Terrinoni	Technology and Econominc Assessment Panel (TEAP) of the Montreal Protocol The Chemours Company	USA
Sophia Mylona	UN Environment, Ozone Secretariat	Kenya

Final Author Team Meeting

16-20 July 2018

Les Diablerets, Switzerland by Jean-Pierre Pommereau - June 2010

Steve Andersen	Institute for Governance & Sustainable Development (IGSD)	USA
Pieter Aucamp	Environmental Effects Assessment Panel (EEAP) & Ptersa Environmental Consultants	South Africa
Tina Birmpili	UN Environment, Ozone Secretariat	Kenya
Geir Braathen	World Meteorological Organization (WMO)	Switzerland

Peter Braesicke	Institute of Meteorology and Climate Research (IMK) Atmospheric Trace Gases and Remote Sensing (ASF) Karlsruher Institut für Technologie (KIT)	Germany
Chiara Cagnazzo	Italian National Research Council , Rome	Italy
Lucy J. Carpenter	University of York	UK
Martyn P. Chipperfield	University of Leeds	UK
Debra Dailey-Fisher	NOAA Earth System Research Laboratory, Chemical Sciences Division	USA
Martin Dameris	Deutsches Zentrum für Luft- und Raumfahrt (DLR) Institut für Physik der Atmosphäre	Germany
John S. Daniel	NOAA Earth System Research Laboratory, Chemical Sciences Division	USA
Sarah J. Doherty	University of Colorado, Cooperative Institute for Research in Environmental Sciences at NOAA Earth System Research Laboratory, Chemical Sciences Division	USA
Andreas Engel	Goethe Universität, Frankfurt	Germany
David W. Fahey	NOAA Earth System Research Laboratory, Chemical Sciences Division	USA
Paul Fraser	Climate Science Centre, Commonwealth Scientific and Industrial Research Organization (CSIRO)	Australia
Sophie Godin-Beekmann	Laboratoire Atmosphères, Milieux, Observations Spatiales (LATMOS), Centre National de la Recherche Scientifique (CNRS), Sorbonne University	France
Marco Gonzáles	Senior member Technology and Economic Assessment Panel (TEAP) Former Executive Secretary, Ozone Secretariat	Costa Rica
Neil Harris	Cranfield University	UK
Michaela I. Hegglin	University of Reading	UK
Jianxin Hu	Peking University	China
Kenneth W. Jucks	NASA Headquarters	USA
Elizabeth M. Juvera	Bay Area Environmental Research Institute (BAERI) & NASA Earth Science Project Office	USA
David J. Karoly	Climate Science Centre, Commonwealth Scientific and Industrial Research Organisation (CSIRO), Aspendale, Victoria	Australia
Alexey Yu. Karpechko	Finnish Meteorological Institute, Helsinki	Finland
Doug Kinnison	National Center for Atmospheric Research (NCAR)	USA
Ronda Knott	Science and Technology Corporation NOAA Earth System Research Laboratory, Chemical Sciences Division	USA
Malcolm J. Ko	NASA Langley Research Center	USA
Lambert J.M. Kuijpers	Eindhoven University of Technology, A/genT Consultancy	The Netherlands
Michael J. Kurylo	Universities Space Research Association Goddard Earth Sciences, Technology, and Research USRA/GESTAR)	USA
Ulrike Langematz	Freie Universität Berlin, Berlin	Germany
Qing Liang	NASA Goddard Space Flight Center	USA
Bella Maranion	Technology and Economic Assessment Panel (TEAP) & U.S. Environmental Protection Agency	USA
Amanda C. Maycock	University of Leeds	UK
Pauline Midgley	Independent Consultant	Germany
Suzette Milano-Schoser	Science and Technology Corporation NOAA Earth System Research Laboratory, Chemical Sciences Division	USA
Stephen A. Montzka	NOAA Earth System Research Laboratory, Global Monitoring Division	USA
Olaf Morgenstern	National Institute of Water and Atmospheric Research Ltd (NIWA)	New Zealand
Rolf Müller	Forschungszentrum Jülich GmbH	Germany

Sophia Mylona	UN Environment, Ozone Secretariat	Kenya
Jessica Neu	NASA Jet Propulsion Laboratory (JPL)	USA
Paul A. Newman	NASA Goddard Space Flight Center	USA
Tyeisha B. Philson	Science Systems and Applications, Inc. & NASA Earth System Project Office	USA
David Plummer	Environment and Climate Change Canada (ECCC)	Canada
Lorenzo Polvani	Columbia University, New York	USA
Michael Prather	University of California, Irvine	USA
John A. Pyle	University of Cambridge and the National Centre for Atmospheric Science	UK
A.R. Ravishankara	Colorado State University, Fort Collins, Colorado	USA
Claire Reeves	University of East Anglia	UK
Stefan Reimann	Swiss Federal Laboratories for Materials Science and Technology (EMPA)	Switzerland
Ann M. Reiser	NOAA Earth System Research Laboratory, Office of the Executive Director	USA
Matthew Rigby	University of Bristol, School of Chemistry	UK
Karen H. Rosenlof	NOAA Earth System Research Laboratory, Chemical Sciences Division	USA
Bonfils Safari	University of Rwanda, College of Science and Technology, Kigali	Rwanda
Ross J. Salawitch	Department of Atmospheric and Oceanic Science & Department of Chemistry and Biochemistry, Earth System Science Interdisciplinary Center, University of Maryland, College Park	USA
Michelle Santee	NASA Jet Propulsion Laboratory (JPL)	USA
Rajendra Shende	Technology, Education, Research and Rehabilitation for the Environment (TERRE) Policy Centre	India
Michael Sigmond	Environment and Climate Change Canada (ECCC)	Canada
Susan Solomon	Massachusetts Institute of Technology (MIT)	USA
Wolfgang Steinbrecht	Meteorological Observatory Hohenpeissenberg Deutscher Wetterdienst (DWD)	Germany
Bill Sturges	School of Environmental Sciences, University of East Anglia	UK
Simone Tilmes	National Center for Atmospheric Research (NCAR)	USA
Matthew B. Tully	Bureau of Meteorology, Melbourne	Australia
Guus J.M. Velders	Dutch National Institute for Public Health and Environment (RIVM), Bilthoven & Utrecht University	The Netherlands
Timothy J. Wallington	Ford Motor Company	USA
Helen Walter-Terrinoni	Technology and Econominc Assessment Panel (TEAP) of the Montreal Protocol The Chemours Company	USA
Mark Weber	Institute of Environmental Physics, Universität Bremen	Germany
Ray F. Weiss	Scripps Institution of Oceanography, University of California, San Diego	USA
Donald J. Wuebbles	University of Illinois	USA

Graphic Design and Layout

Debra Dailey-Fisher	NOAA Earth System Research Laboratory, Chemical Sciences Division	USA
Nada Derek	Climate Science Centre, Commonwealth Scientific and Industrial Research Organisation (CSIRO) Oceans and Atmosphere	Australia
F. Dennis Dickerson	Respond Grafiks	USA
Netta Kasher	The Hebrew University of Jerusalem	Israel
Sydnee Masias	Science and Technology Corporation NOAA Office of the Chief Administrative Officer	USA
Ann M. Reiser	NOAA Earth System Research Laboratory, Office of the Executive Director	USA

Albert Romero	NOAA Office of the Chief Administrative Officer	USA

Editorial Team

Sarah J. Doherty	University of Colorado, Cooperative Institute for Research in Environmental Sciences at NOAA Earth System Research Laboratory, Chemical Sciences Division	USA
Tiffany Means	North Carolina State University and NOAA Cooperative Institute for Climate and Satellites -NC, National Centers for Environmental Information (NCEI)	USA
Brooke C. Stewart	North Carolina State University and NOAA Cooperative Institute for Climate and Satellites -NC, National Centers for Environmental Information (NCEI)	USA
Andrea McCarrick	North Carolina State University and NOAA Cooperative Institute for Climate and Satellites -NC, National Centers for Environmental Information (NCEI)	USA
Debra Dailey-Fisher	NOAA Earth System Research Laboratory, Chemical Sciences Division	USA
Ann M. Reiser	NOAA Earth System Research Laboratory, Office of the Executive Director	USA

Administrative Support

Debra Dailey-Fisher	NOAA Earth System Research Laboratory, Chemical Sciences Division	USA
Elizabeth M. Juvera	Bay Area Environmental Research Institute (BAERI) & NASA Earth Science Project Office (ESPO)	USA
Ronda Knott	Science and Technology Corporation NOAA Earth System Research Laboratory, Chemical Sciences Division	USA
Suzette Milano-Schoser	Science and Technology Corporation NOAA Earth System Research Laboratory, Chemical Sciences Division	USA
Tyeisha B. Philson	Science Systems and Applications, Inc. (SSAI) & NASA Earth System Project Office (ESPO)	USA
Ann M. Reiser	NOAA Earth System Research Laboratory, Office of the Executive Director	USA
Kathy A. Thompson	Science Systems and Applications, Inc.	USA

Computing, Technical, and Network Support

Catherine Burgdorf Rasco	University of Colorado, Cooperative Institute for Research in Environmental Sciences at NOAA Earth System Research Laboratory, Chemical Sciences Division	USA
Jenny Fox	NOAA Earth System Research Laboratory, Chemical Sciences Division	USA
Mike Mascola	Cherokee Services Group NOAA Earth System Research Laboratory, Office of the Executive Director	USA
Douglas Ohlhorst	NOAA Earth System Research Laboratory, Chemical Sciences Division	USA
Richard Tisinai	University of Colorado, Cooperative Institute for Research in Environmental Sciences at NOAA Earth System Research Laboratory, Chemical Sciences Division	USA

Reference Research and Editing

Debra Dailey-Fisher	NOAA Earth System Research Laboratory, Chemical Sciences Division	USA
Jenn Kinkade	University of Colorado, Cooperative Institute for Research in Environmental Sciences at NOAA Earth System Research Laboratory, Chemical Sciences Division	USA
Ann M. Szczurek Davis	University of Colorado, Cooperative Institute for Research in Environmental Sciences at NOAA Earth System Research Laboratory, Chemical Sciences Division	USA
Sydnee Masias	Science and Technology Corporation NOAA Office of the Chief Administrative Officer	USA
Suzette Milano-Schoser	Science and Technology Corporation NOAA Earth System Research Laboratory, Chemical Sciences Division	USA
Ann M. Reiser	NOAA Earth System Research Laboratory, Office of the Executive Director	USA

World Meteorological Organization
Global Ozone Research and Monitoring Project—Report No. 58

Scientific Assessment of Ozone Depletion: 2018